

University of Nebraska - Lincoln

DigitalCommons@University of Nebraska - Lincoln

Civil Engineering Theses, Dissertations, and
Student Research

Civil Engineering

Summer 6-2016

Development of a Transition Between an Energy-Absorbing Concrete Barrier and a Rigid Concrete Buttress

Tyler Schmidt

University of Nebraska-Lincoln, t.schmidt@huskers.unl.edu

Follow this and additional works at: <http://digitalcommons.unl.edu/civilengdiss>



Part of the [Structural Engineering Commons](#)

Schmidt, Tyler, "Development of a Transition Between an Energy-Absorbing Concrete Barrier and a Rigid Concrete Buttress" (2016).
Civil Engineering Theses, Dissertations, and Student Research. 97.
<http://digitalcommons.unl.edu/civilengdiss/97>

This Article is brought to you for free and open access by the Civil Engineering at DigitalCommons@University of Nebraska - Lincoln. It has been accepted for inclusion in Civil Engineering Theses, Dissertations, and Student Research by an authorized administrator of DigitalCommons@University of Nebraska - Lincoln.

DEVELOPMENT OF A TRANSITION BETWEEN AN ENERGY-ABSORBING
CONCRETE BARRIER AND A RIGID CONCRETE BUTTRESS

by

Tyler L. Schmidt

A THESIS

Presented to the Faculty of
The Graduate College at the University of Nebraska
In Partial Fulfillment of Requirements
For the Degree of Master of Science

Major: Civil Engineering

Under the Supervision of Professor Ronald K. Faller

Lincoln, Nebraska

June, 2016

DEVELOPMENT OF A TRANSITION BETWEEN AN ENERGY-ABSORBING
CONCRETE BARRIER AND A RIGID CONCRETE BUTTRESS

Tyler L. Schmidt, M.S.

University of Nebraska, 2016

Advisor: Ronald K. Faller

From 2010 to 2015, MwRSF researchers developed the RESTORE barrier, which is a restorable MASH TL-4 median barrier with a steel and concrete rail supported by elastomer posts and steel skids. The research effort reported herein describes the initial development of a transition from the RESTORE barrier to a rigid TL-4 concrete buttress.

The previously-developed RESTORE barrier LS-DYNA model was validated against three full-scale vehicle crash tests. Several design concepts were generated through a series of brainstorming efforts. The primary transition concept consisted of a pin and loop connection between the RESTORE barrier and rigid concrete buttress, which was designed and evaluated with LS-DYNA computer simulation. Vehicle and system behavior were investigated using MASH test designation nos. 4-20, 4-21, and 4-22. Six horizontal gusset plates and drop-down pin allowed for limited deflection and rotation at the transition joint, but provided shear continuity between the two systems. A rounded-edge cover plate mitigated vehicle snag on the transition joint hardware. Eleven impact points were evaluated with each vehicle model to determine critical impact points for use in a future full-scale crash testing program. All occupant risk measures and vehicle stability were within MASH limits. Further design modifications are recommended to limit stresses in the transition joint hardware and to reduce excessive

occupant compartment deformation that occurred when the small car impacted the concrete buttress end.

ACKNOWLEDGEMENTS

I would like to thank all of the people who contributed in some way to the work described herein. First and foremost, I would like to thank Dr. Ronald Faller who spent long hours working with me, giving me advice, and helping me finish writing this document. Thank you for continuing to challenge me, teach me how to think more critically, and demanding further detail on everything so a reader could fully understand. The whole thesis process provided me a great tool for me to become a successful structural engineer.

I would also like to thank the members of my graduate committee, Dr. Jennifer Schmidt and Dr. John Reid. I have learned a great deal about engineering and research from each of you and it was a pleasure to have you on my committee. I would like to specifically like to thank Dr. Jennifer Schmidt for taking time out of her day to answer my smallest questions and help me succeed in graduate school and with my thesis.

I would like to thank the entire staff of the Midwest Roadside Safety Facility for providing a positive work environment and great learning opportunity. It has been a pleasure working with all of you over the last four years.

Lastly, and most importantly, I want to thank my family and friends. My parents, Michael and Brenda always supported me and gave me encouragement through all of my years of schooling. My siblings, Greg and Danielle always made me aim higher through all of their endeavors and helped me to succeed just like them. Lastly, to my friends who showed me that it is nice to have some fun and not work all of the time. Thank you to all who helped me through school and my thesis process.

TABLE OF CONTENTS

ACKNOWLEDGEMENTS	iv
TABLE OF CONTENTS	v
LIST OF FIGURES	x
LIST OF TABLES	xxiii
1 INTRODUCTION	1
1.1 Background and Problem Statement.....	1
1.2 Objective.....	8
1.3 Scope.....	9
2 LITERATURE REVIEW	10
2.1 Introduction.....	10
2.2 Transition Design Considerations.....	10
2.3 Common Connections Between Concrete Barriers	12
2.3.1 Portable Concrete Barriers.....	12
2.3.2 PCB Termination and Anchorage Methods.....	14
2.3.3 MASH TL-3 Median Barrier Gate.....	17
2.4 Lateral Stiffness Transitions	20
2.4.1 Guardrail to Portable Concrete Barriers	20
2.4.2 SAFER Barrier Between Portable Concrete Barrier and Rigid Buttress	23
2.4.3 Portable Concrete Barriers to Permanent Concrete Roadside Barriers.....	29
2.5 Transitions Between Different Barrier Heights and Widths.....	31
2.5.1 Single-Slope Approach Guardrail Height Transition	31
2.5.2 PCBs to Permanent Concrete Median Barriers for Median Applications	34
2.5.3 PCBs to Permanent Concrete Median Barriers for Roadside Applications	35
2.5.4 Steel Bridge Railing and Transition on a Longitudinal Glue- Laminated Timber Deck	36
2.5.5 TL-4 Bridge Railing and Transition on a Transverse Glue- Laminated Timber Deck	37
2.5.6 Horizontal Flare Rates for Concrete Barriers	38
2.6 MASH TL-4 Barrier Loading.....	40
2.6.1 Introduction.....	40
2.6.2 AASHTO Design Impact Loads	40
2.6.3 MASH TL-4 Barrier Force Investigation Based on Previous Test Data	41
2.6.4 Precast Concrete Bridge Rail Study.....	42
2.6.5 TTI Mechanically Stabilized Earth Wall	44
2.6.6 TTI Tall MSE Wall.....	46

2.6.7 TTI Simulation on TL-4 Impact Loads.....	49
2.6.8 MwRSF RESTORE Barrier.....	51
2.6.9 AASHTO Update to MASH Design Loads.....	52
2.7 MASH TL-4 Barrier Heights.....	52
2.7.1 Minimum MASH TL-4 Rail Height Using Simulation.....	53
2.7.2 Minimum MASH TL-4 Rail Height Using Crash Testing.....	54
2.8 Concrete Barrier Design Methodologies.....	55
2.8.1 Yield-Line Theory.....	55
2.8.2 Torsional Resistance Footer Design.....	56
3 RESTORE BARRIER OVERVIEW.....	58
3.1 Introduction.....	58
3.2 Coupon Material Testing and Simulation.....	58
3.3 Individual Component Testing.....	62
3.3.1 Introduction.....	62
3.3.2 16-in. (406-mm) Tall Elastomer Shear Fenders.....	63
3.3.3 11 ⁵ / ₈ -in. (295-mm) Tall Elastomer Shear Fenders.....	65
3.4 Component Testing Simulation.....	67
3.5 Sub-System Testing.....	67
3.6 Interior System Moment Connection.....	69
3.7 LS-DYNA Simulations of Final Barrier Concept.....	71
3.7.1 RESTORE Barrier Model.....	71
3.7.2 TL-4 MASH Longitudinal Barrier Impact Requirements and Evaluation Criteria.....	75
3.7.3 Simulation Results.....	75
3.8 Final Design of RESTORE Barrier Before Crash Testing.....	77
3.9 Full-Scale Crash Tests and Results.....	78
3.9.1 Background.....	78
3.9.2 Test No. SFH-1 – MASH Test Designation No. 4-11.....	79
3.9.3 Test No. SFH-2 – MASH Test Designation No. 4-10.....	80
3.9.4 Test No. SFH-3 – MASH Test Designation No. 4-12.....	81
3.9.5 Full-Scale Crash Test Recommendations.....	84
4 SIMULATION AND FULL-SCALE TEST COMPARISON – 1100C.....	85
4.1 Purpose.....	85
4.2 Overall Model Comparisons.....	85
4.3 Vehicle Stability.....	93
4.4 Occupant Risk Analysis.....	96
4.5 Deflection and Snag.....	97
4.6 Impact Force Investigation.....	98
4.7 Discussion.....	101
5 SIMULATION AND FULL-SCALE TEST COMPARISON – 2270P.....	103
5.1 Overall Model Comparisons.....	103
5.2 Vehicle Stability.....	110
5.3 Occupant Risk Analysis.....	113
5.4 Deflection and Snag.....	114

5.5 Impact Force Investigation	114
5.6 Discussion	116
6 SIMULATION AND FULL-SCALE TEST COMPARISON – 10000S	119
6.1 Overall Model Comparisons	119
6.2 Vehicle Stability.....	128
6.3 Occupant Risk Analysis.....	131
6.4 Deflection and Snag.....	131
6.5 Impact Force Investigation	132
6.6 Discussion.....	135
7 DESIGN CONSIDERATIONS	138
7.1 Introduction.....	138
7.2 Design Impact Forces	139
7.3 Degrees of Freedom and Tolerances.....	140
7.4 Rigid Concrete Buttress Geometry	144
7.5 Lateral Stiffening in Transition Region	145
7.6 Highway Geometry.....	145
7.6.1 Superelevation.....	145
7.6.2 Horizontal Curves	146
7.6.3 Vertical Curves	148
7.6.4 Conclusions.....	151
7.7 Modifications to RESTORE Barrier.....	152
8 BRAINSTORMING, CONCEPT DEVELOPMENT, AND DESIGN	153
8.1 Introduction.....	153
8.2 Drop-Down RESTORE Barrier and Bollard Concept.....	154
8.3 Pin and Loop Concept.....	158
8.3.1 Distribution of Lateral Load on Pin and Gussets.....	158
8.3.2 Distribution of Longitudinal Barrier Load on Vertical Pin and Gusset Plates	166
8.3.3 Combined Loading on Pin and Gusset Plates	168
8.3.4 Pin Selection	169
8.3.4.1 Shear Design	169
8.3.4.2 Bending Design.....	170
8.3.5 Gusset Plate Design	171
8.3.6 Back Plate and Connection Bolt Design.....	177
8.3.7 Weld Design.....	184
8.3.8 Top Steel Tube Moment Connection.....	188
8.3.9 Concrete Steel Reinforcement and Anchorage	194
8.3.10 Steel Anchor Hardware and Chemical Adhesive Systems for Concrete Sections.....	195
8.4 Moment Connection.....	196
9 INITIAL MODELING OF PINNED CONNECTION.....	197
9.1 Background	197
9.2 Scope.....	197

9.3 RESTORE Barrier Model Modifications.....	197
9.4 1100C Vehicle Simulations	201
9.4.1 Dodge Neon	201
9.4.2 Toyota Yaris Simulation.....	204
9.5 2270P Chevrolet Silverado Simulations	208
9.6 Conclusions.....	211
10 PREFERRED DESIGN MODEL CONFIGURATION	213
10.1 Introduction.....	213
10.2 LS-DYNA Model for RESTORE Barrier Transition	213
10.3 Initial Simulation	216
10.3.1 Initial Cover Plate – 1100C Yaris.....	218
10.3.2 Initial Cover Plate – 2270P Silverado.....	223
10.3.3 Recommendations and Changes	227
10.4 Cover Plate Design	227
10.4.1 Design Calculations	227
10.4.2 Straight Cover Plate Model.....	231
10.4.3 Straight Cover Plate Simulations.....	232
10.4.4 Rounded Cover Plate Model.....	235
10.5 Epoxy Anchorage Modeling	238
11 CIP DETERMINATION – MODELING TEST DESIGNATION NO. 4-20	240
11.1 Purpose.....	240
11.2 CIP Location Simulation Results.....	244
11.2.1 Yaris Vehicle Model	244
11.2.2 Neon Vehicle Model	258
11.3 Upstream Location Simulation Results	271
11.3.1 Yaris Vehicle Model	271
11.3.2 Neon Vehicle Model	285
11.4 Reverse-Direction Impact Location Simulation Results.....	299
11.4.1 Yaris Vehicle Model	300
11.4.2 Neon Vehicle Model	310
11.5 1100C Simulation Summary.....	320
12 CIP DETERMINATION – MODELING TEST DESIGNATION NO. 4-21	326
12.1 Purpose.....	326
12.2 CIP Location Simulation Results.....	327
12.3 Upstream Location Simulation Results	342
12.4 Reverse-Direction Impact Location Simulation Results.....	356
12.5 2270P Simulation Summary	365
13 CIP DETERMINATION – MODELING TEST DESIGNATION NO. 4-22	370
13.1 Purpose.....	370
13.2 CIP Location Simulation Results.....	371
13.3 Upstream Location Simulation Results	388
13.4 Reverse-Direction Impact Location Simulation Results.....	403
13.5 10000S Simulation Summary	413

14 SUMMARY, CONCLUSIONS, AND RECOMMENDATIONS	419
14.1 Summary and Conclusions	419
14.2 Recommendations.....	434
15 REFERENCES	439
16 APPENDICES	448
Appendix A. MASH TL-4 Safety Criteria.....	449
Appendix B. RESTORE Barrier Drawing Set	452
Appendix C. Accelerometer and Rate Transducer Data Plots, 1100C Interior Simulation.....	477
Appendix D. Accelerometer and Rate Transducer Data Plots, 2270P Interior Simulation	484
Appendix E. Accelerometer and Rate Transducer Data Plots, 10000S Interior Simulation	492
Appendix F. Design Concepts.....	499
Appendix G. RISA Indeterminate Beam Analysis.....	523
Appendix H. Concrete Buttress – Preliminary Design Only – Internal Reinforcement and Footer.....	527
Appendix I. RESTORE Barrier Transition with No Cover Plate	539
Appendix J. RESTORE Barrier Transition with Straight Cover Plate Drawing Modifications	571
Appendix K. RESTORE Barrier Transition with Rounded Cover Plate Drawing Set	583
Appendix L. Comparison Bar Graphs for 1100C Vehicles	617
Appendix M. Comparison Bar Graphs for 2270P Vehicle	622
Appendix N. Comparison Bar Graphs for 10000S Vehicle.....	627

LIST OF FIGURES

Figure 1. Double-Sided Concrete Barrier in Narrow Median [1].....	2
Figure 2. Front-Face Geometries for Safety-Shape Concrete Median Barriers [3-8].....	2
Figure 3. Front-Face Geometries for Single-Slope and Vertical-Face Concrete Median Barriers [9-14]	4
Figure 4. Redirective Force Comparison [7-8].....	4
Figure 5. Overview of RESTORE Barrier.....	6
Figure 6. Cross Section of RESTORE Barrier.....	7
Figure 7. Critical Pocketing Angle [25-26]	11
Figure 8. General PCB Connectors [28-29].....	13
Figure 9. Loading Conditions at PCB Joints [28].....	14
Figure 10. Portable Concrete Barrier (PCB) Anchorage and Termination [31-32].....	16
Figure 11. Original Emergency Opening System [33]	18
Figure 12. Modified Emergency Opening System [33].....	19
Figure 13. Final Design of the Emergency Opening System [34-35].....	20
Figure 14. NDOR PCB to Guardrail Stiffness Transition, Test Nos. MGSPCB-1 through MGSPCB-3 [38].....	22
Figure 15. Portable Concrete Barrier Design for Iowa Speedway [39-40].....	26
Figure 18. Free-Standing PCB to Rigid Concrete Barrier Transition Schematic [41- 42]	30
Figure 19. Free-Standing PCB to Rigid Concrete Barrier Transition, Test No. FTB- 2 [41-42].....	31
Figure 20. Two Height Transitions for Single-Slope Concrete Median Barrier [43- 44]	33
Figure 21. Free-Standing PCB to Rigid Barrier Height Transition for Median Applications on Asphalt [45].....	35
Figure 22. Free-Standing PCB to Rigid Barrier Height Transition for Roadside Applications on Concrete [46].....	36
Figure 23. TBC-8000 Bridge Rail Transition [47-49].....	37
Figure 24. TL-4 Transition on Transverse Glue-Laminated Timber Deck [51-52]	38
Figure 25. Horizontal Flare Rate of 6H:1V Barrier Toe [53-54].....	39
Figure 26. Modified Horizontal Flare Rate with Chamfer [53-54]	40
Figure 27. Comparison of Lateral Impact Loads – Simulation and TTI Test No. 476460-1b	48
Figure 28. SUT Impact Forces on MSE Wall from Simulation [66].....	50
Figure 29. Lateral Impact Forces rom Simulation Contact with 50-msec Average [22-23].....	51
Figure 30. SUT Lateral Barrier Forces, Rigid Single-Slope Concrete Barrier vs. Original RESTORE Barrier Simulation [16-17].....	52
Figure 31. 10000S SUT Vehicle Impacting 34½-in. (816-mm) Tall, Rigid Vertical Barrier [22-23]	54
Figure 33. Summary of Material Tests at 100 Percent Strain.....	61
Figure 34. Simulation of Shear Fender Tensile Test – Stress vs. Strain.....	62
Figure 35. Maritime International, Inc. HSF-14 Marine Shear Fender [16-18]	64

Figure 36. Energy vs. Deflection Comparison Plot, Test Nos. HSF14-1 and HSF14-2 [16-18].....	65
Figure 37. Bogie Test Setup for Beam and Shear Fenders, Test No. SFHT-1 [18]	68
Figure 38. Simulated Dynamic Barrier Deflections with Varied Concrete Beam Splices – 2270P MASH TL-3 Condition [19]	71
Figure 39. RESTORE Barrier – Simulation Part Numbers: (a) Isometric View; and (b) Top View at Concrete Beam Splice [19]	72
Figure 40. RESTORE Barrier Damage, Test No. SFH-1 [20-21]	80
Figure 41. RESTORE Barrier Damage, Test No. SFH-2 [20-21]	82
Figure 42. RESTORE Barrier Damage, Test No. SFH-3 [20-21]	83
Figure 43. RESTORE Barrier Damage, After ACJ Removal, Test No. SFH-3 [20-21]	83
Figure 44. Vehicle Comparison, Pre- and Post-Test.....	86
Figure 45. 1100C Simulation vs. Test No. SFH-2 Sequential Photographs, Downstream View	90
Figure 46. 1100C Simulation vs. Test No. SFH-2 Sequential Photographs, Overhead View	91
Figure 47. Lateral and Longitudinal Change in Velocity Comparison, 1100C	92
Figure 48. Interior Impact Roll Angle Comparison, 1100C	95
Figure 49. Interior Impact Pitch Angle Comparison, 1100C.....	95
Figure 50. Interior Impact Yaw Angle Comparison, 1100C	96
Figure 51. Lateral Force Comparison, 1100C Dodge Neon	100
Figure 52. Lateral Force Comparison, 1100C Toyota Yaris	100
Figure 53. Vehicle Comparison, Pre- and Post-Test, 2270P	103
Figure 54. 2270P Simulation vs. Test No. SFH-1 Sequential Photographs, Downstream View	106
Figure 55. 2270P Simulation vs. Test No. SFH-1 Sequential Photographs, Overhead View	107
Figure 56. 2270P Lateral and Longitudinal Change in Velocity Comparison	109
Figure 57. Interior Impact Roll Angle Comparison, 2270P.....	111
Figure 58. Interior Impact Pitch Angle Comparison, 2270P	112
Figure 59. Interior Impact Yaw Angle Comparison, 2270P	112
Figure 60. Lateral Force Comparison, 2270P	116
Figure 61. Vehicle Comparison, Pre- and Post-Test, 10000S	120
Figure 62. 10000S Simulation vs. Test No. SFH-3 Sequential Photographs, Downstream View	122
Figure 63. 10000S Simulation vs. Test No. SFH-3 Sequential Photographs, Overhead View	123
Figure 64. 10000S Lateral and Longitudinal Change in Velocity Comparison	125
Figure 65. Comparison Between Simulation and Full-Scale Vehicle Box Attachment Damage.....	127
Figure 66. Interior Impact Roll Angle Comparison, 10000S.....	129
Figure 67. Interior Impact Pitch Angle Comparison, 10000S	130
Figure 68. Interior Impact Yaw Angle Comparison, 10000S.....	130
Figure 69. Lateral Impact Force Comparison, 10000S.....	134
Figure 70. Barrier Coordinate System	139

Figure 71. Proposed Buttress Geometry at New Transition Joint Location	144
Figure 72. Typical Parabolic Vertical Curve	149
Figure 73. Bollard Cantilevered Moment Arm.....	155
Figure 74. Lateral Design Load and Location, Isometric View	159
Figure 75. Initial Schematic Pin and Gusset Concept (See Appendix F).....	160
Figure 76. Pin and Support Approximation for Analysis and Design with Dimensions (Horizontal View).....	160
Figure 77. Approximated Design Load Scenarios: (a) Case 1 and (b) Case 2	161
Figure 78. Reactions Due to Applied Moment	162
Figure 79. Combined Loading, Eccentricity and Point Load, Case 1.....	163
Figure 80. Shear and Moment Diagrams, Case 1	164
Figure 81. Combined Loading, Eccentricity and Point Load, Case 2.....	165
Figure 82. Shear and Moment Diagrams, Case 2	165
Figure 83. Estimated Longitudinal Loading Scenario	166
Figure 84. Longitudinal Loading Free-Body Diagram	167
Figure 85. Shear Diagram, Longitudinal Loading	168
Figure 86. Types of Failure for Steel [86]	173
Figure 87. Types of Block Shear Failure of Steel [86].....	175
Figure 88. Description of Block Shear Areas of Gusset Plates	176
Figure 89. Back Plate and Connection Bolt Design Loads and Orientation.....	178
Figure 90. 3D Analysis of Back Plate and Connections, Y-Z Plane	178
Figure 91. 3D Analysis of Back Plate and Connections, X-Y Plane.....	179
Figure 92. 3D Analysis of Back Plate and Connections, Rotated X-Y Plane	180
Figure 93. 3D Analysis of Back Plate and Connections, Z-y' Plane.....	181
Figure 94. 3D Analysis of Back Plate and Connections, x'-Z Plane.....	181
Figure 95. Back Plate Dimensions and Block Shear Lines	184
Figure 96. Tension, Bending, and Shear Stresses within Fillet Welds.....	185
Figure 97. Loading and Dimension of Gusset Plate Fillet Welds.....	185
Figure 98. Upper Splice Tube Bolt Spacing Requirements.....	192
Figure 99. Top Tube and Inner Splice Tube with Bolt Configurations, Option 1	192
Figure 100. Inner Splice Tube Connection, Option 2.....	193
Figure 101. RESTORE Barrier Pin-and-Loop Simulation Part Numbers	198
Figure 102. Initial Simulations with the Pin-and-Loop Concept.....	200
Figure 103. Lateral Loop Contact Forces – 5 ft Upstream from Pin – 1100C Neon.....	203
Figure 104. Lateral Loop Contact Forces – 20 ft Upstream from Pin – 1100C Neon.....	203
Figure 105. Lateral Loop Contact Forces – 40 ft Upstream from Pin – 1100C Neon.....	204
Figure 106. Lateral Loop Contact Forces – 5 ft Upstream from Pin – 1100C Yaris.....	206
Figure 107. Lateral Loop Contact Forces – 20 ft Upstream from Pin – 1100C Yaris.....	207
Figure 108. Lateral Loop Contact Forces – 40 ft Upstream from Pin – 1100C Yaris.....	207
Figure 109. Lateral Loop Contact Forces – 5 ft Upstream from Pin – 2270P.....	210
Figure 110. Lateral Loop Contact Forces – 20 ft Upstream from Pin – 2270P.....	210
Figure 111. Lateral Loop Contact Forces – 40 ft Upstream from Pin – 2270P.....	211
Figure 112. Simulation Part Numbers – No Cover Plate.....	214
Figure 113. Initial Concept for Lateral Vehicle Snag Prevention	217
Figure 114. Initial Cover Plate Concept	218
Figure 115. Roll Angle Comparison, With and Without Cover Plate, 1100C Yaris.....	219

Figure 116. Pitch Angle Comparison, With and Without Cover Plate, 1100C Yaris.....	220
Figure 117. Yaw Angle Comparison, With and Without Cover Plate, 1100C Yaris	220
Figure 118. 1100C Yaris Simulation, Cover Plate Comparison, Sequential Photographs.....	221
Figure 119. Lateral Change in Velocity Comparison, With and Without Cover Plate Trials, 1100C Yaris	222
Figure 120. Longitudinal Change in Velocity Comparison, With and Without Cover Plate Trials, 1100C Yaris	223
Figure 121. Roll Angle Comparison, With and Without Cover Plate, 2270P	224
Figure 122. Pitch Angle Comparison, With and Without Cover Plate, 2270P	224
Figure 123. Yaw Angle Comparison, With and Without Cover Plate, 2270P	225
Figure 124. Lateral Change in Velocity Comparison, With and Without Cover Plate Trials, 2270P	226
Figure 125. Longitudinal Change in Velocity Comparison, With and Without Cover Plate Trials, 2270P	226
Figure 126. Cover Plate Gusset Locations.....	228
Figure 127. β Coefficient for Stress on Flat Plate.....	229
Figure 128. Simulation Part Numbers – Straight Cover Plate	232
Figure 129. Compressed and Extended Joint Views, Straight Cover Plate	233
Figure 130. 1100C Yaris Model Snag on Upstream End of Straight Cover Plate.....	234
Figure 131. 2270P Silverado Model Snag on Upstream End of Straight Cover Plate ...	235
Figure 132. Simulation Part Numbers – Rounded Cover Plate	237
Figure 133. Before and After Photographs of Simulated Epoxy Anchors in Buttress ...	239
Figure 134. Von Mises Stresses, Before and After Simulated Epoxy Anchors, 100 msec	239
Figure 135. RESTORE Barrier Transition Impact Locations for Simulations	241
Figure 136. Compressed and Extended Joint Views	241
Figure 137. Von Mises and Tresca Failure Surfaces [89]	243
Figure 138. RESTORE Barrier Transition, 1100C Yaris Simulation Comparison, CIP Locations, Downstream View	246
Figure 139. RESTORE Barrier Transition, 1100C Yaris Simulation Comparison, CIP Locations, Downstream View	247
Figure 140. RESTORE Barrier Transition, 1100C Yaris Simulation Comparison, CIP Locations, Overhead View	248
Figure 141. RESTORE Barrier Transition, 1100C Yaris Simulation Comparison, CIP Locations, Overhead View	249
Figure 142. Lateral Change in Velocity, CIP Locations, 1100C Toyota Yaris	251
Figure 143. Longitudinal Change in Velocity, CIP Locations, 1100C Toyota Yaris.....	252
Figure 144. Lateral Force Comparison, CIP Locations, 1100C Toyota Yaris	253
Figure 145. Roll Angle Comparison, CIP Locations, 1100C Toyota Yaris	254
Figure 146. Pitch Angle Comparison, CIP Locations, 1100C Toyota Yaris	255
Figure 147. Yaw Angle Comparison, CIP Locations, 1100C Toyota Yaris.....	255
Figure 148. Von Mises Stress and Plastic Strain Comparison on Horizontal Gussets, Trial No. 44 at 40 msec, 1100C Yaris	257
Figure 149. Von Mises Stress on Cover Plate Gussets (GPa), Trial No. 70 at 40 msec, 1100C Yaris	258

Figure 150. RESTORE Barrier Transition, 1100C Neon Simulation Comparison, CIP Locations, Downstream View	260
Figure 151. RESTORE Barrier Transition, 1100C Neon Simulation Comparison, CIP Locations, Downstream View	261
Figure 152. RESTORE Barrier Transition, 1100C Neon Simulation Comparison, CIP Locations, Overhead View	262
Figure 153. RESTORE Barrier Transition, 1100C Neon Simulation Comparison, CIP Locations, Overhead View	263
Figure 154. Lateral Change in Velocity, CIP Locations, 1100C Dodge Neon.....	265
Figure 155. Longitudinal Change in Velocity, CIP Locations, 1100C Dodge Neon	265
Figure 156. Lateral Force Comparison, CIP Locations, 1100C Dodge Neon	266
Figure 157. Roll Angle Comparison, CIP Locations, 1100C Dodge Neon.....	267
Figure 158. Pitch Angle Comparison, CIP Locations, 1100C Dodge Neon.....	268
Figure 159. Yaw Angle Comparison, CIP Locations, 1100C Dodge Neon	268
Figure 160. Bolt Von Mises Stresses and Deformation (GPa), Trial No. 33 at 40 msec, 1100C Neon	270
Figure 161. RESTORE Barrier Transition, 1100C Yaris Simulation Comparison, Upstream Impact Locations, Downstream View	274
Figure 162. RESTORE Barrier Transition, 1100C Yaris Simulation Comparison, Upstream Impact Locations, Downstream View	275
Figure 163. RESTORE Barrier Transition, 1100C Yaris Simulation Comparison, Upstream Impact Locations, Overhead View	276
Figure 164. RESTORE Barrier Transition, 1100C Yaris Simulation Comparison, Upstream Impact Locations, Overhead View	277
Figure 165. Lateral Change in Velocity, Upstream Impact Locations, 1100C Toyota Yaris.....	279
Figure 166. Longitudinal Change in Velocity, Upstream Impact Locations, 1100C Toyota Yaris.....	280
Figure 167. Lateral Force Comparison, Upstream Impact Locations, 1100C Toyota Yaris.....	281
Figure 168. Vehicle Roll Comparison, Upstream Impact Locations, 1100C Toyota Yaris.....	282
Figure 169. Vehicle Pitch Comparison, Upstream Impact Locations, 1100C Toyota Yaris.....	283
Figure 170. Vehicle Yaw Comparison, Upstream Impact Locations, 1100C Toyota Yaris.....	283
Figure 171. RESTORE Barrier Transition, 1100C Neon Simulation Comparison, Upstream Impact Locations, Downstream View	288
Figure 172. RESTORE Barrier Transition, 1100C Neon Simulation Comparison, Upstream Impact Locations, Downstream View	289
Figure 173. RESTORE Barrier Transition, 1100C Neon Simulation Comparison, Upstream Impact Locations, Overhead View	290
Figure 174. RESTORE Barrier Transition, 1100C Neon Simulation Comparison, Upstream Impact Locations, Overhead View	291
Figure 175. Rubber-on-Rubber Contact Issue	292

Figure 176. Lateral Change in Velocity, Upstream Impact Locations, 1100C Dodge Neon.....	294
Figure 177. Longitudinal Change in Velocity, Upstream Impact Locations, 1100C Dodge Neon	294
Figure 178. Lateral Force Comparison, Upstream Impact Locations, 1100C Dodge Neon.....	295
Figure 179. Vehicle Roll Comparison, Upstream Impact Locations, 1100C Dodge Neon.....	296
Figure 180. Vehicle Pitch Comparison, Upstream Impact Locations, 1100C Dodge Neon.....	297
Figure 181. Vehicle Yaw Comparison, Upstream Impact Locations, 1100C Dodge Neon.....	298
Figure 182. RESTORE Barrier Transition, 1100C Yaris Simulation Comparison, Reverse-Direction Locations, Downstream View	302
Figure 183. RESTORE Barrier Transition, 1100C Yaris Simulation Comparison, Reverse-Direction Locations, Overhead View	303
Figure 184. Lateral Change in Velocity, Reverse-Direction Locations, 1100C Toyota Yaris.....	305
Figure 185. Longitudinal Change in Velocity, Reverse-Direction Locations, 1100C Toyota Yaris.....	305
Figure 186. Lateral Force Comparison, Reverse-Direction Locations, 1100C Toyota Yaris.....	307
Figure 187. Longitudinal Force Comparison, Reverse-Direction Locations, 1100C Toyota Yaris.....	307
Figure 188. Roll Angle Comparison, Reverse-Direction Locations, 1100C Toyota Yaris.....	308
Figure 189. Pitch Angle Comparison, Reverse-Direction Locations, 1100C Toyota Yaris.....	309
Figure 190. Yaw Angle Comparison, Reverse-Direction Locations, 1100C Toyota Yaris.....	310
Figure 191. RESTORE Barrier Transition, 1100C Neon Simulation Comparison, Reverse-Direction Locations, Downstream View	312
Figure 192. RESTORE Barrier Transition, 1100C Neon Simulation Comparison, Reverse-Direction Locations, Overhead View	313
Figure 193. Occupant Compartment Deformations, Slope-Break Point, 1100C Neon ...	314
Figure 194. Lateral Change in Velocity, Reverse-Direction Locations, 1100C Dodge Neon	315
Figure 195. Longitudinal Change in Velocity, Reverse-Direction Locations, 1100C Dodge Neon	316
Figure 196. Lateral Force Comparison, Reverse-Direction Locations, 1100C Dodge Neon.....	317
Figure 197. Longitudinal Force Comparison, Reverse-Direction Locations, 1100C Dodge Neon	317
Figure 198. Roll Angle Comparison, Reverse-Direction Locations, 1100C Dodge Neon.....	318

Figure 199. Pitch Angle Comparison, Reverse-Direction Locations, 1100C Dodge Neon.....	319
Figure 200. Yaw Angle Comparison, Reverse-Direction Locations, 1100C Dodge Neon.....	320
Figure 201. RESTORE Barrier Transition, 2270P Silverado Simulation Comparison, CIP Locations, Downstream View.....	330
Figure 202. RESTORE Barrier Transition, 2270P Silverado Simulation Comparison, CIP Locations, Downstream View.....	331
Figure 203. RESTORE Barrier Transition, 2270P Silverado Simulation Comparison, CIP Locations, Overhead View.....	332
Figure 204. RESTORE Barrier Transition, 2270P Silverado Simulation Comparison, CIP Locations, Overhead View.....	333
Figure 205. Lateral Change in Velocity, CIP Locations, 2270P Chevrolet Silverado	335
Figure 206. Longitudinal Change in Velocity, CIP Locations, 2270P Chevrolet Silverado	336
Figure 207. Lateral Force Comparison, CIP Locations, 2270P Chevrolet Silverado.....	337
Figure 208. Roll Angle Comparison, CIP Locations, 2270P Chevrolet Silverado	338
Figure 209. Pitch Angle Comparison, CIP Locations, 2270P Chevrolet Silverado	339
Figure 210. Yaw Angle Comparison, CIP Locations, 2270P Chevrolet Silverado	339
Figure 211. RESTORE Barrier Transition, 2270P Silverado Simulation Comparison, Upstream Impact Locations, Downstream View	344
Figure 212. RESTORE Barrier Transition, 2270P Silverado Simulation Comparison, Upstream Impact Locations, Downstream View	345
Figure 213. RESTORE Barrier Transition, 2270P Silverado Simulation Comparison, Upstream Impact Locations, Overhead View	346
Figure 214. RESTORE Barrier Transition, 2270P Silverado Comparison, Upstream Impact Locations, Overhead View	347
Figure 215. Lateral Change in Velocity, Upstream Impact Locations, 2270P Silverado	349
Figure 216. Longitudinal Change in Velocity, Upstream Impact Locations, 2270P Silverado	350
Figure 217. Lateral Force Comparison, Upstream Impact Locations, 2270P Silverado	351
Figure 218. Vehicle Roll Comparison, Upstream Impact Locations, 2270P Silverado	352
Figure 219. Vehicle Pitch Comparison, Upstream Impact Locations, 2270P Silverado	353
Figure 220. Vehicle Yaw Comparison, Upstream Impact Locations, 2270P Silverado	354
Figure 221. RESTORE Barrier Transition, 2270P Silverado Simulation Comparison, Reverse-Direction Locations, Downstream View.....	358
Figure 222. RESTORE Barrier Transition, 2270P Silverado Simulation Comparison, Reverse-Direction Locations, Overhead View.....	359
Figure 223. Lateral Change in Velocity, Reverse-Direction Locations, 2270P Silverado	361

Figure 224. Longitudinal Change in Velocity, Reverse-Direction Locations, 2270P Silverado	361
Figure 225. Lateral Force Comparison, Reverse-Direction Locations, 2270P Silverado	362
Figure 226. Longitudinal Force Comparison, Reverse-Direction Locations, 2270P Silverado	363
Figure 227. Roll Angle Comparison, Reverse-Direction Locations, 2270P Silverado ...	364
Figure 228. Pitch Angle Comparison, Reverse-Direction Locations, 2270P Silverado	364
Figure 229. Yaw Angle Comparison, Reverse-Direction Locations, 2270P Silverado...	365
Figure 230. RESTORE Barrier Transition, 10000S F800 Simulation Comparison, CIP Locations, Downstream View	374
Figure 231. RESTORE Barrier Transition, 10000S F800 Simulation Comparison, CIP Locations, Downstream View	375
Figure 232. RESTORE Barrier Transition, 10000S F800 Simulation Comparison, CIP Locations, Overhead View	376
Figure 233. RESTORE Barrier Transition, 10000S F800 Simulation Comparison, CIP Locations, Overhead View	377
Figure 234. Lateral Change in Velocity, CIP Locations, 10000S F800 Simulation.....	379
Figure 235. Longitudinal Change in Velocity, CIP Locations, 10000S F800 Simulation	379
Figure 236. Lateral Force Comparison, CIP Locations, 10000S F800 Simulation	380
Figure 237. Roll Angle Comparison, CIP Locations, 10000S F800 Simulation	381
Figure 238. Pitch Angle Comparison, CIP Locations, 10000S F800 Simulation.....	382
Figure 239. Yaw Angle Comparison, CIP Locations, 10000S F800 Simulation	382
Figure 240. Von Mises Stress (GPa) of Cover Plate Bolts, Trial No. 36 at 100 msec, 10000S F800 Model.....	385
Figure 241. Cover Plate Bolt Von Mises Stress Anomalies (GPa), Trial 32	386
Figure 242. Von Mises Stress and Plastic Strain Comparison on Horizontal Gussets, Trial No. 32 at 240 msec, 10000S F800 Model	387
Figure 243. Von Mises Stress and Plastic Strain Comparison on Cover Plate, Trial No. 36 at 100 msec, 10000S F800 Model.....	388
Figure 244. RESTORE Barrier Transition, 10000S F800 Simulation Comparison, Upstream Impact Locations, Downstream View	391
Figure 245. RESTORE Barrier Transition, 10000S F800 Simulation Comparison, Upstream Impact Locations, Downstream View	392
Figure 246. RESTORE Barrier Transition, 10000S F800 Simulation Comparison, Upstream Impact Locations, Overhead View	393
Figure 247. RESTORE Barrier Transition, 10000S F800 Simulation Comparison, Upstream Impact Locations, Overhead View	394
Figure 248. Lateral Change in Velocity, Upstream Impact Locations, 10000S F800 Simulation	396
Figure 249. Longitudinal Change in Velocity, Upstream Impact Locations, 10000S F800 Simulation.....	397
Figure 250. Lateral Force Comparison, Upstream Impact Locations, 10000S F800 Simulation	398

Figure 251. Vehicle Roll Comparison, Upstream Impact Locations, 10000S F800 Simulation	399
Figure 252. Vehicle Pitch Comparison, Upstream Impact Locations, 10000S F800 Simulation	400
Figure 253. Vehicle Yaw Comparison, Upstream Impact Locations, 10000S F800 Simulation	401
Figure 254. RESTORE Barrier Transition, 10000S F800 Simulation Comparison, Reverse-Direction Locations, Downstream View	405
Figure 255. RESTORE Barrier Transition, 10000S F800 Simulation Comparison, Reverse-Direction Locations, Overhead View	406
Figure 256. Lateral Change in Velocity, Reverse-Direction Locations, 10000S F800 Model	408
Figure 257. Longitudinal Change in Velocity, Reverse-Direction Locations, 10000S F800 Model	408
Figure 258. Lateral Force Comparison, Reverse-Direction Locations, 10000S F800 Model	410
Figure 259. Longitudinal Force Comparison, Reverse-Direction Locations, 10000S F800 Model	410
Figure 260. Roll Angle Comparison, Reverse-Direction Locations, 10000S F800 Model	411
Figure 261. Pitch Angle Comparison, Reverse-Direction Locations, 10000S F800 Model	412
Figure 262. Yaw Angle Comparison, Reverse-Direction Locations, 10000S F800 Model	412
Figure B-1. System Layout, RESTORE Barrier [20]	453
Figure B-2. Barrier Assembly, RESTORE Barrier [20]	454
Figure B-3. Post and Tubing Details, RESTORE Barrier [20]	455
Figure B-4. Splice Details, RESTORE Barrier [20]	456
Figure B-5. Splice Details, RESTORE Barrier [20]	457
Figure B-6. Splice 5-6 Instrumentation Details, RESTORE Barrier [20]	458
Figure B-7. Concrete Beam Geometry, RESTORE Barrier [20]	459
Figure B-8. Concrete Beam Details, RESTORE Barrier [20]	460
Figure B-9. Concrete Beam and Rebar Assembly, RESTORE Barrier [20]	461
Figure B-10. Concrete Beam, Rebar Assembly Details, RESTORE Barrier [20]	462
Figure B-11. Concrete Beam, Rebar Assembly Details, RESTORE Barrier [20]	463
Figure B-12. Concrete Beam, Rebar Assembly Details, RESTORE Barrier [20]	464
Figure B-13. Bill of Bars, RESTORE Barrier [20]	465
Figure B-14. Skid Details, RESTORE Barrier [20]	466
Figure B-15. Skid Assembly Details, RESTORE Barrier [20]	467
Figure B-16. Skid Component Details, RESTORE Barrier [20]	468
Figure B-17. Skid Top Plate Detail, RESTORE Barrier [20]	469
Figure B-18. Upper Tube Assembly, RESTORE Barrier [20]	470
Figure B-19. Steel End Tubing Assembly, RESTORE Barrier [20]	471
Figure B-20. Steel Tubing Components, RESTORE Barrier [20]	472
Figure B-21. Angle Joint Details, RESTORE Barrier [20]	473
Figure B-22. Rubber Post Details, RESTORE Barrier [20]	474

Figure B-23. Fastener Details, RESTORE Barrier [20]	475
Figure B-24. Bill of Materials, RESTORE Barrier [20].....	476
Figure C-1. 10-ms Average Longitudinal Deceleration Comparison, 1100C Vehicles.....	478
Figure C-2. Longitudinal Occupant Impact Velocity Comparison, 1100C Vehicles	479
Figure C-3. Longitudinal Occupant Displacement Comparison, 1100C Vehicles	480
Figure C-4. 10-ms Average Lateral Deceleration Comparison, 1100C Vehicles.....	481
Figure C-5. Lateral Occupant Impact Velocity Comparison, 1100C Vehicles	482
Figure C-6. Lateral Occupant Displacement Comparison, 1100C Vehicles	483
Figure D-1. 10-ms Average Longitudinal Deceleration Comparison, 2270P Vehicles.....	485
Figure D-2. 10-ms Average Longitudinal Deceleration Comparison, 2270P Vehicles.....	486
Figure D-3. Longitudinal Occupant Impact Velocity Comparison, 2270P Vehicles	487
Figure D-4. Longitudinal Occupant Displacement Comparison, 2270P Vehicles	488
Figure D-5. 10-ms Average Lateral Deceleration Comparison, 2270P Vehicles.....	489
Figure D-6. Lateral Occupant Impact Velocity Comparison, 2270P Vehicles.....	490
Figure D-7. Lateral Occupant Displacement Comparison, 2270P Vehicles	491
Figure E-1. 10-ms Average Longitudinal Deceleration Comparison, 10000S Vehicles.....	493
Figure E-2. Longitudinal Occupant Impact Velocity Comparison, 10000S Vehicles.....	494
Figure E-3. Longitudinal Occupant Displacement Comparison, 10000S Vehicles.....	495
Figure E-4. 10-ms Average Lateral Deceleration Comparison, 10000S Vehicles	496
Figure E-5. Lateral Occupant Impact Velocity Comparison, 10000S Vehicles.....	497
Figure E-6. Lateral Occupant Displacement Comparison, 10000S Vehicles.....	498
Figure F-1. RESTORE Barrier Transition Brainstorming Designs – Phase 1	500
Figure F-2. RESTORE Barrier Transition Brainstorming Designs – Phase 1	501
Figure F-3. RESTORE Barrier Transition Brainstorming Designs – Phase 1	502
Figure F-4. RESTORE Barrier Transition Brainstorming Designs – Phase 1	503
Figure F-5. RESTORE Barrier Transition Brainstorming Designs – Phase 1	504
Figure F-6. RESTORE Barrier Transition Brainstorming Designs – Phase 1	505
Figure F-7. RESTORE Barrier Transition Brainstorming Designs – Phase 2.....	506
Figure F-8. RESTORE Barrier Transition Brainstorming Designs – Phase 2.....	507
Figure F-9. RESTORE Barrier Transition Brainstorming Designs – Phase 2.....	508
Figure F-10. RESTORE Barrier Transition Brainstorming Designs – Phase 2.....	509
Figure F-11. RESTORE Barrier Transition Brainstorming Designs – Phase 2.....	510
Figure F-12. RESTORE Barrier Transition Brainstorming Designs – Phase 2.....	511
Figure F-13. RESTORE Barrier Transition Brainstorming Designs – Phase 2.....	512
Figure F-14. RESTORE Barrier Transition Brainstorming Designs – Phase 2.....	513
Figure F-15. RESTORE Barrier Transition Brainstorming Designs – Phase 2.....	514
Figure F-16. RESTORE Barrier Transition Brainstorming Designs – Phase 2.....	515
Figure F-17. RESTORE Barrier Transition Brainstorming Designs – Phase 3.....	516
Figure F-18. RESTORE Barrier Transition Brainstorming Designs – Phase 3.....	517
Figure F-19. RESTORE Barrier Transition Brainstorming Designs – Phase 3.....	518
Figure F-20. RESTORE Barrier Transition Brainstorming Designs – Phase 3.....	519
Figure F-21. RESTORE Barrier Transition Brainstorming Designs – Phase 3.....	520

Figure F-22. RESTORE Barrier Transition Brainstorming Designs – Phase 3.....	521
Figure F-23. Block Shear Calculations and Surfaces of Horizontal Gusset Plates	522
Figure G-1. Case 1 RISA Analysis	524
Figure G-2. Case 2 RISA Analysis	525
Figure G-3. Longitudinal Loading RISA Analysis.....	526
Figure H-2. Profile Barrier Segments for Simplification of Reinforcement Design	527
Figure H-3. RESTORE Barrier Transition Buttress Internal Reinforcement Calculations.....	530
Figure H-4. RESTORE Barrier Transition Buttress Internal Reinforcement Calculations.....	531
Figure H-5. RESTORE Barrier Transition Buttress Internal Reinforcement Calculations.....	532
Figure H-6. Torsional Footer Design Spreadsheet, RESTORE Barrier Transition Buttress	534
Figure H-7. Buttress and Foundation Assembly.....	535
Figure H-8. Buttress Rebar Layout.....	536
Figure H-9. Buttress Rebar Detail	537
Figure H-10. Foundation Rebar Layout.....	538
Figure I-1. System Layout, No Cover Plate, RESTORE Barrier Transition	540
Figure I-2. System Layout, No Cover Plate, RESTORE Barrier Transition	541
Figure I-3. Barrier Adjustment Details, No Cover Plate, RESTORE Barrier Transition	542
Figure I-4. Barrier Assembly, No Cover Plate, RESTORE Barrier Transition	543
Figure I-5. Post and Tubing Details, No Cover Plate, RESTORE Barrier Transition.....	544
Figure I-6. Splice Details, No Cover Plate, RESTORE Barrier Transition.....	545
Figure I-7. Concrete Rail Geometry, No Cover Plate, RESTORE Barrier Transition	546
Figure I-8. Concrete Rail Details, No Cover Plate, RESTORE Barrier Transition.....	547
Figure I-9. Concrete Rail and Rebar Assembly, No Cover Plate, RESTORE Barrier Transition	548
Figure I-10. Concrete Rail Rebar Assembly Details, No Cover Plate, RESTORE Barrier Transition.....	549
Figure I-11. Concrete Rail Rebar Assembly Details, No Cover Plate, RESTORE Barrier Transition.....	550
Figure I-12. Concrete Rail Rebar Assembly Details, No Cover Plate, RESTORE Barrier Transition.....	551
Figure I-13. Bill of Bars, No Cover Plate, RESTORE Barrier Transition.....	552
Figure I-14. Skid Details, No Cover Plate, RESTORE Barrier Transition.....	553
Figure I-15. Skid Assembly Details, No Cover Plate, RESTORE Barrier Transition.....	554
Figure I-16. Skid Component Details, No Cover Plate, RESTORE Barrier Transition	555
Figure I-17. Skid Top Plate Detail, No Cover Plate, RESTORE Barrier Transition.....	556
Figure I-18. Steel Rail Assembly, No Cover Plate, RESTORE Barrier Transition.....	557
Figure I-19. Steel Rail Components, No Cover Plate, RESTORE Barrier Transition	558
Figure I-20. Steel Rail Splice Components, No Cover Plate, RESTORE Barrier Transition	559
Figure I-21. Angle Joint Details, No Cover Plate, RESTORE Barrier Transition	560

Figure I-22. Rubber Post Details, No Cover Plate, RESTORE Barrier Transition	561
Figure I-23. Buttress Assembly, No Cover Plate, RESTORE Barrier Transition	562
Figure I-24. Buttress Connection Details, No Cover Plate, RESTORE Barrier Transition	563
Figure I-25. Buttress Details, No Cover Plate, RESTORE Barrier Transition.....	564
Figure I-26. Buttress Steel Rail Tube, No Cover Plate, RESTORE Barrier Transition	565
Figure I-27. Buttress Connection Components, No Cover Plate, RESTORE Barrier Transition	566
Figure I-28. Fastener Details, No Cover Plate, RESTORE Barrier Transition	567
Figure I-29. Fastener Details, No Cover Plate, RESTORE Barrier Transition	568
Figure I-30. Bill of Materials, No Cover Plate, RESTORE Barrier Transition.....	569
Figure I-31. Bill of Materials, No Cover Plate, RESTORE Barrier Transition.....	570
Figure J-1. Buttress Assembly, Straight Cover Plate, RESTORE Barrier Transition	572
Figure J-2. Buttress Connection Details, Straight Cover Plate, RESTORE Barrier Transition	573
Figure J-3. Buttress Details, Straight Cover Plate, RESTORE Barrier Transition.....	574
Figure J-4. Buttress Steel Rail Tube, Straight Cover Plate, RESTORE Barrier Transition	575
Figure J-5. Buttress Connection Components, Straight Cover Plate, RESTORE Barrier Transition.....	576
Figure J-6. Buttress Connection Details, Straight Cover Plate, RESTORE Barrier Transition	577
Figure J-7. Buttress Connection Cover Plate, Straight Cover Plate, RESTORE Barrier Transition.....	578
Figure J-8. Fastener Details, Straight Cover Plate, RESTORE Barrier Transition	579
Figure J-9. Fastener Details, Straight Cover Plate, RESTORE Barrier Transition	580
Figure J-10. Bill of Materials, Straight Cover Plate, RESTORE Barrier Transition.....	581
Figure J-11. Bill of Materials, Straight Cover Plate, RESTORE Barrier Transition.....	582
Figure K-1. System Layout, RESTORE Barrier Transition	584
Figure K-2. System Layout, RESTORE Barrier Transition	585
Figure K-3. Barrier Adjustment Details, RESTORE Barrier Transition	586
Figure K-4. Barrier Assembly, RESTORE Barrier Transition	587
Figure K-5. Post and Tubing Details, RESTORE Barrier Transition.....	588
Figure K-6. Splice Details, RESTORE Barrier Transition.....	589
Figure K-7. Concrete Rail Geometry, RESTORE Barrier Transition	590
Figure K-8. Concrete Rail Details, RESTORE Barrier Transition.....	591
Figure K-9. Concrete Rail and Rebar Assembly, RESTORE Barrier Transition.....	592
Figure K-10. Concrete Rail Rebar Assembly Details, RESTORE Barrier Transition	593
Figure K-11. Concrete Rail Rebar Assembly Details, RESTORE Barrier Transition	594
Figure K-12. Concrete Rail Rebar Assembly Details, RESTORE Barrier Transition	595
Figure K-13. Bill of Bars, RESTORE Barrier Transition.....	596
Figure K-14. Skid Details, RESTORE Barrier Transition.....	597
Figure K-15. Skid Assembly Details, RESTORE Barrier Transition.....	598
Figure K-16. Skid Component Details, RESTORE Barrier Transition	599
Figure K-17. Skid Top Plate Detail, RESTORE Barrier Transition.....	600

Figure K-18. Steel Rail Assembly, RESTORE Barrier Transition.....	601
Figure K-19. Steel Rail Components, RESTORE Barrier Transition	602
Figure K-20. Steel Rail Splice Components, RESTORE Barrier Transition	603
Figure K-21. Angle Joint Details, RESTORE Barrier Transition	604
Figure K-22. Rubber Post Details, RESTORE Barrier Transition	605
Figure K-23. Buttress Assembly, RESTORE Barrier Transition	606
Figure K-24. Buttress Connection Details, RESTORE Barrier Transition	607
Figure K-25. Buttress Details, RESTORE Barrier Transition	608
Figure K-26. Buttress Steel Rail Tube, RESTORE Barrier Transition	609
Figure K-27. Buttress Connection Components, RESTORE Barrier Transition.....	610
Figure K-28. Buttress Connection Details, RESTORE Barrier Transition	611
Figure K-29. Buttress Connection Cover Plate, RESTORE Barrier Transition	612
Figure K-30. Fastener Details, RESTORE Barrier Transition	613
Figure K-31. Fastener Details, RESTORE Barrier Transition	614
Figure K-32. Bill of Materials, RESTORE Barrier Transition.....	615
Figure K-33. Bill of Materials, RESTORE Barrier Transition.....	616
Figure L-1. Lateral and Longitudinal ORA Comparison, 1100C Simulations.....	618
Figure L-2. Lateral and Longitudinal OIV Comparison, 1100C Simulations	619
Figure L-3. Maximum Deflection and Lateral Force Comparisons, 1100C Simulations	620
Figure L-4. Maximum Roll, Pitch, and Yaw Angle Comparisons, 1100C Simulations	621
Figure M-1. Lateral and Longitudinal ORA Comparison, 2270P Simulations	623
Figure M-2. Lateral and Longitudinal OIV Comparison, 2270P Simulations	624
Figure M-3. Maximum Deflection and Lateral Force Comparisons, 2270P Simulations	625
Figure M-4. Maximum Roll, Pitch, and Yaw Angle Comparisons, 2270P Simulations	626
Figure N-1. Maximum Deflection and Lateral Force Comparisons, 10000S Simulations	628
Figure N-2. Maximum Roll, Pitch, and Yaw Angle Comparisons, 10000S Simulations	629

LIST OF TABLES

Table 1. PCB Connection Strengths [30].....	14
Table 2. Estimated Peak Lateral Impact Force - MASH TL-4 Impact Conditions [57-58].....	42
Table 3. Estimated MASH TL-4 Peak Lateral Impact Forces – LS-DYNA Simulations [58].....	44
Table 4. Lateral Design Force Calculation Studies [63-64]	46
Table 5. Shear Fender Dynamic Testing Results [16-18].....	64
Table 6. Dynamic Testing Results – All Component Tests [19].....	66
Table 7. Dynamic Testing Results – All Component Tests, Continued [19]	67
Table 8. Elastomer Shear Fender Deflection and Energy Absorption, Test No. SFHT-1	69
Table 9. RESTORE Barrier Model Parts, Elements, and Materials [19]	73
Table 10. Comparison Between Test No. SFH-2 and 1100C Simulations.....	89
Table 11. Summary of OIV and ORA, 1100C Vehicles.....	97
Table 12. Dynamic Deflection, Working Width, and Post Snag, 1100C Vehicles	98
Table 13. 1100C Lateral Force Comparison.....	101
Table 14. Comparison Between Test No. SFH-1 and 2270P Simulation.....	105
Table 15. Summary of OIV and ORA, 2270P Vehicles	113
Table 16. Dynamic Deflection, Working Width, and Post Snag, 2270P Vehicles.....	114
Table 17. 2270P Lateral Impact Force Comparison	116
Table 18. Comparison of Results Between Test No. SFH-3 and 10000S Simulation.....	121
Table 19. Summary of OIV and ORA, 10000S Vehicles	131
Table 20. Dynamic Deflection, Working Width, and Post Snag, 10000S Vehicles.....	132
Table 21. 10000S Lateral Impact Force Comparison	135
Table 22. Barrier and Tube Rotations and Translations for Interior SUT Impact Event	142
Table 23. Minimum Section Modulus and Diameter for Vertical Bollard in Drop- Down Buttress Concept	156
Table 24. Determination of Pin Diameter to Resist Shear.....	170
Table 25. Summary of 3D Back Plate and Connection Bolt Analysis	182
Table 26. Gusset Plate Weld Design Summary	188
Table 27. Summary of Splice Tube Section Moduli and Thickness Calculations.....	190
Table 28. RESTORE Barrier Pin-and-Loop Model Parts, Elements, and Materials.....	199
Table 29. Simulation Results for 1100C Vehicle, Dodge Neon, at Varying Impact Locations.....	202
Table 30. Simulation Results for 1100C Vehicle, Toyota Yaris, Varying Impact Locations.....	205
Table 31. Simulation Results for 2270P Vehicle, Chevrolet Silverado, Varying Impact Locations.....	208
Table 32. Barrier Model Parts, Elements, and Materials – No Cover Plate	215
Table 33. Barrier Model Parts, Elements, and Materials – Straight Cover Plate	232
Table 34. Barrier Model Parts, Elements, and Materials – Rounded Cover Plate.....	237
Table 35. Comparison Matrix of CIP Locations, 1100C Toyota Yaris	245

Table 36. RESTORE Barrier Component Stress Comparison, 1100C Toyota Yaris, CIP Locations.....	257
Table 37. Comparison Matrix of CIP Locations, 1100C Dodge Neon.....	259
Table 38. RESTORE Barrier Component Stress Comparison, 1100C Dodge Neon, CIP Locations.....	269
Table 39. Comparison Matrix of Upstream Impact Locations, 1100C Toyota Yaris.....	273
Table 40. RESTORE Barrier Component Stress Comparison, 1100C Toyota Yaris, Upstream Locations	284
Table 41. Comparison Matrix of Upstream Impact Locations, 1100C Dodge Neon	287
Table 42. RESTORE Barrier Component Stress Comparison, 1100C Dodge Neon, Upstream Locations	299
Table 43. Comparison Matrix of Reverse-Direction Locations, 1100C Toyota Yaris	301
Table 44. Comparison Matrix of Reverse-Direction Locations, 1100C Dodge Neon.....	311
Table 45. Comparison Matrix of CIP Locations, 2270P Silverado	329
Table 46. RESTORE Barrier Component Stress Comparison, 2270P Silverado, CIP Locations.....	341
Table 47. Comparison Matrix of Upstream Impact Locations, 2270P Chevrolet Silverado	343
Table 48. RESTORE Barrier Component Stress Comparison, 2270P Silverado, Upstream Locations	356
Table 49. Comparison Matrix of Reverse-Direction Locations, 2270P Silverado	357
Table 50. Comparison Matrix of CIP Locations, 10000S F800 Simulation.....	373
Table 51. RESTORE Barrier Component Stress Comparison, 10000S F800 Simulation, CIP Locations	383
Table 52. Comparison Matrix of Upstream Impact Locations, 10000S F800 Simulation	390
Table 53. RESTORE Barrier Component Stress Comparison, 10000S F800 Simulation, Upstream Locations.....	402
Table 54. Comparison Matrix of Reverse-Direction Locations, 10000S F800 Model....	404
Table 55. MASH TL-4 Crash Test Conditions [15]	449
Table 56. MASH Evaluation Criteria for Longitudinal Barriers [15]	451

1 INTRODUCTION

1.1 Background and Problem Statement

Each year throughout the transportation industry, numerous fatalities and serious injuries occur during run-off-road, motor-vehicle crashes along U.S. highways and roadways. A common practice to reduce the number of serious injuries and fatalities has been to remove nearby fixed object hazards (e.g., trees) or shield hazards (e.g., steep slopes) with crashworthy barriers located near the roadway edge.

Further, errant vehicles can also enter into medians between divided highways, which pose undue risks to occupants entering into opposing traffic lanes and potentially striking oncoming traffic. For very wide medians, barriers may not necessarily be used to prevent cross-median crashes. However, cable median barrier systems have often been utilized to eliminate cross-median crashes in these wide medians. For narrow medians, which are often associated with urban/suburban freeways and interstate highways, rigid concrete barriers have been successfully utilized to separate traffic and prevent crashes into oncoming traffic, as depicted in Figure 1 [1].

These rigid concrete barriers have evolved over time and have varied in shape, height, and strength. Early safety-shape concrete barriers, such as the General Motors (GM) shape concrete barrier [2], were developed with the intent to minimize vehicle damage during shallow-angle impact events but still redirect errant vehicles during larger-angle encroachments. As depicted in Figure 2, the GM shape used multiple slopes, which allowed the vehicle's tires to climb up the lower slope at low impact angles without damaging the sheet metal of the vehicle. The upper slope allowed for the barrier to redirect errant vehicles at larger impact angles. However, the GM shape was shown to

cause vehicle rollover and was never implemented on the roadway. Therefore, the New Jersey safety shape [3-4] and F-shape [5] concrete barriers were developed and utilized the same concept of multiple slopes on a given barrier face. The newer barriers were very similar to the GM shape with the main difference pertaining to the location of the slope break point between the two sloped faces, as shown in Figure 2.



Figure 1. Double-Sided Concrete Barrier in Narrow Median [1]

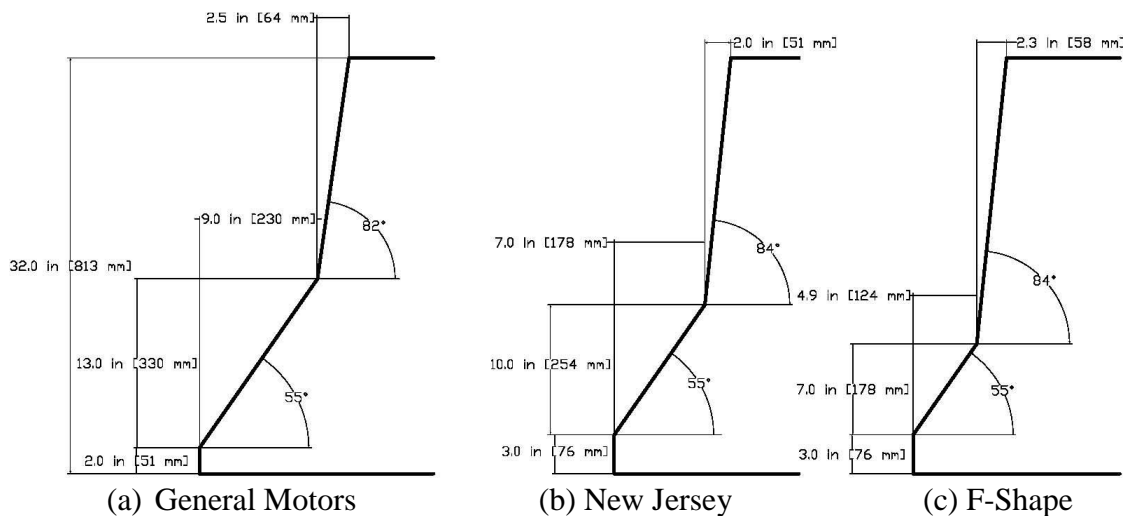


Figure 2. Front-Face Geometries for Safety-Shape Concrete Median Barriers [3-8]

For years, the design of the dual-slope barriers were believed to help mitigate the vehicle's impact energy during rigid barrier crashes as a result of tire climbing up the lower face [7-8]. Thus, these barriers were historically referred to as safety-shape barriers. The New Jersey- and F-shape barriers were successful in containing and redirecting errant vehicles as well as eliminating cross-median crashes on urban/suburban freeways and interstate highways. However, vehicle climb was shown to cause increased roll angles, and even rollover, in small cars as well as higher center-of-mass passenger vehicles, which increases the risks of severe injuries [7-11]. As such, other concrete barrier shapes were then developed.

Subsequently, a concrete barrier with a constant slope (i.e., single slope) was developed to limit tire climb on the barrier face [12-13]. Many different slopes were considered, but a slope of approximately 10 degrees away from vertical was the most successful selection, as shown in Figure 3. Similarly, a vertical-face concrete barrier (i.e., slope equal to 0 degrees relative to vertical) was considered where the potential for vehicle climb on the barrier face would be further minimized. The single-slope and vertical-face concrete barriers helped to increase vehicle stability, although vehicle damage and lateral impact forces were increased due to limiting the vehicular movements throughout impact event [9-11].

In a MwRSF safety study, Albuquerque used a small car with an impact height of 9 in. (229 mm) to compare a vertical barrier to a safety shape barrier [7-8]. Albuquerque noted that the redirective lateral forces were higher with a vertical barrier than a safety shape barrier due to the orientation of the front slope, as shown in Figure 4. Using Newton's Second Law of Motion, Albuquerque also stated that higher lateral forces also

resulted in higher lateral accelerations during impacts with vertical-face concrete barriers as compared to safety-shape barriers. Thus, there existed a need to develop a vertical-face concrete median barrier that imparts reduced lateral accelerations to passenger vehicles as compared to rigid barriers but would not increase vehicle climb and rollover tendencies.

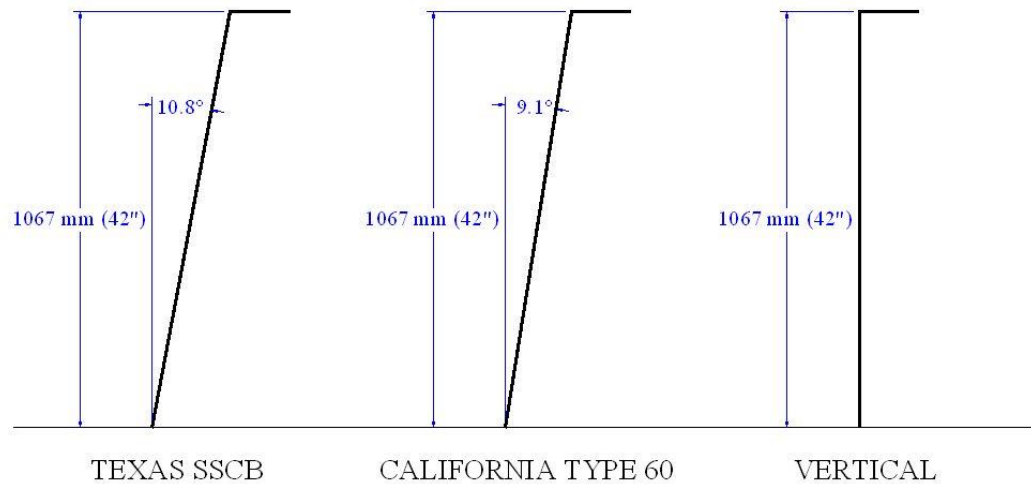


Figure 3. Front-Face Geometries for Single-Slope and Vertical-Face Concrete Median Barriers [9-14]

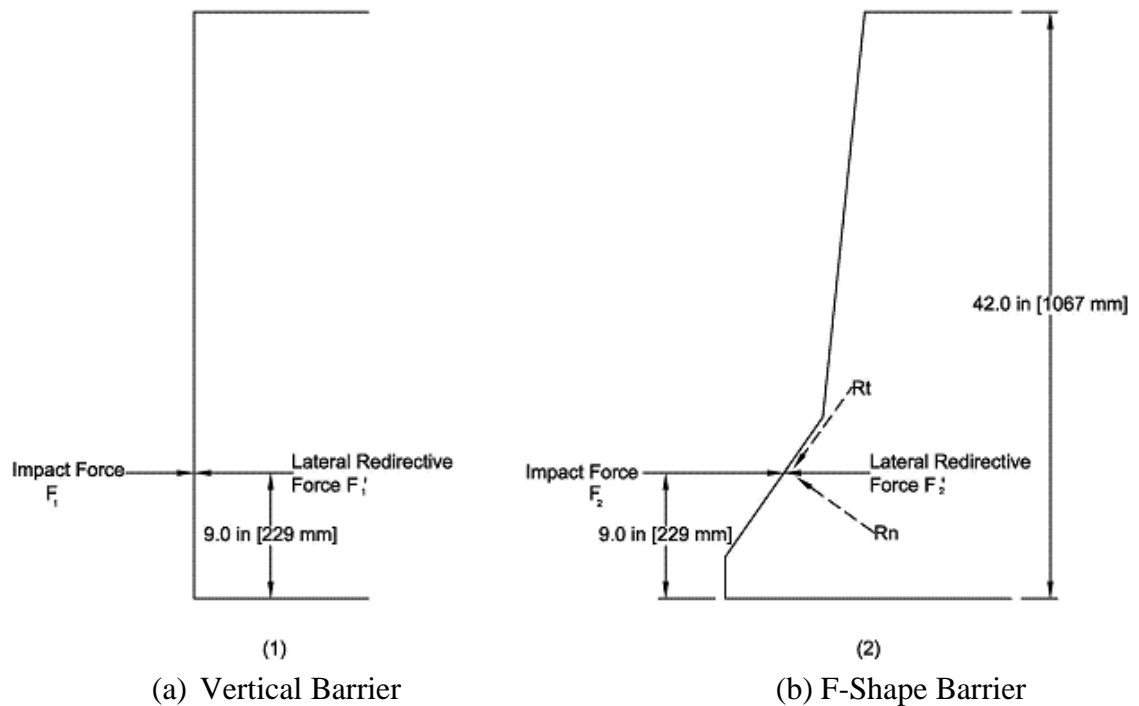


Figure 4. Redirective Force Comparison [7-8]

In 2010, MwRSF researchers initiated a study to develop a next-generation, energy-absorbing barrier system. Several design criteria were identified for the barrier system. First, the barrier was to satisfy the American Association of State Highway and Transportation Officials (AASHTO's) Manual Assessing Safety Hardware (MASH) Test Level 4 (TL-4) crash testing criteria [15]. A 30 percent decrease in the lateral accelerations on passenger vehicles was desired for impacts with the new barrier as compared to impacts with rigid barriers. Furthermore, the barrier width should be less than or equal to 36 in. (914 mm) to accommodate current urban median footprint widths. The front-face geometry should reduce concerns for vehicle climb and instability during impact events. Next, fabrication and installation costs should eventually be competitive with current concrete barriers but no more than 2 times the costs of existing rigid concrete median barrier and foundation systems. Maintenance costs for the new barrier system should be virtually zero under normal impact conditions. Lastly, the system should be restorable and reusable, with no structural damage occurring during passenger vehicle impacts. However, minimal barrier damage was permissible during single-unit truck impact events.

Although numerous concepts were generated, Schmidt, et al. [16-21] created a new barrier concept, designated the RESTORE barrier, that reduced lateral accelerations in impact events up to 47 percent for pickup trucks and as much as 21 percent for small cars as compared to impacts with rigid barriers, as shown in Figure 5. Other occupant risk measures were reduced even further. The RESTORE barrier was comprised of concrete barrier segments placed on top of elastomer shear fenders spaced at 60 in. (1,524 mm) and steel skids spaced at 120 in. (3,048 mm). The concrete barrier segments were

connected with a moment connection, designated as the Adjustable Continuity Joint (ACJ), to provide continuity between adjacent barrier segments. The concrete barrier segments that were positioned on top of the shear fenders and skids had a top mounting height of approximately 30¹/₈ in. (765 mm).

Based on previous crash testing, the lowest mounting height for a concrete barrier to successfully contain and redirect the 10000S vehicle was 36 in. (914 mm) [22-23]. Therefore, a steel tube assembly was considered to increase the top mounting height of the barrier system to approximately 38⁵/₈ in. (981 mm), as shown in Figure 6.



Figure 5. Overview of RESTORE Barrier

Three full-scale crash tests were previously performed on the RESTORE Barrier according to the TL-4 impact safety standards found in MASH [16-21]. During the full-scale crash testing program, the RESTORE barrier experienced up to 11.2 in. (284 mm)

and 7.3 in. (185 mm) of dynamic deflection and up to 33.5 in. (851 mm) and 29.6 in. (752 mm) of working width with the 2270P and 1100C passenger vehicles, respectively.

Further, during the impact event with the 10000S vehicle, the barrier experienced a maximum dynamic deflection of 13.9 in. (353 mm) and 15.1 in. (384 mm) at the top of the concrete barrier and the top of the steel tube, respectively. The working width was found to be 60.2 in. (1,529 mm). In addition, the new barrier system successfully met the TL-4 safety criteria, safely contained and redirected the vehicles, and performed as intended with minor design modifications to be considered in the future.

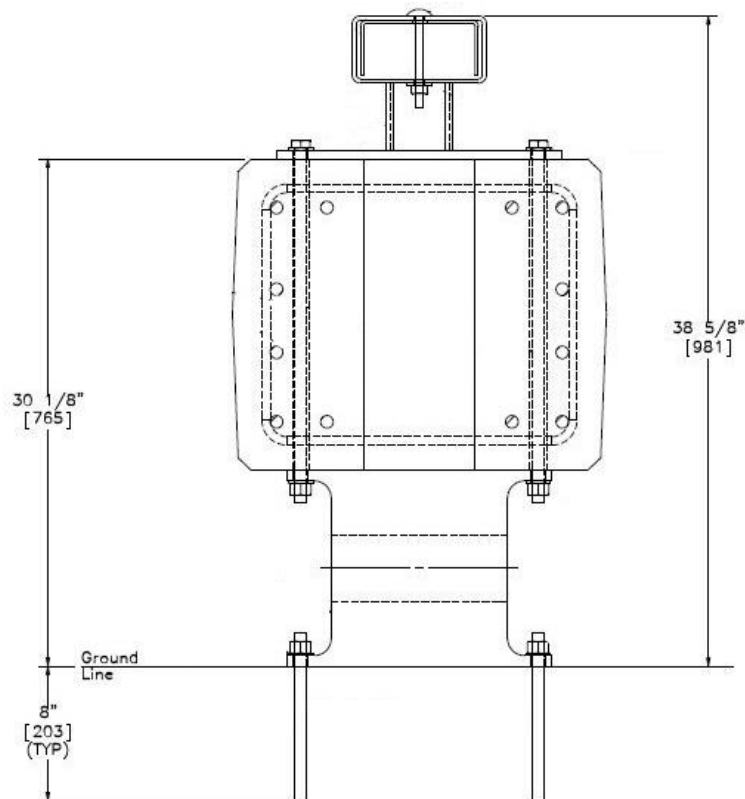


Figure 6. Cross Section of RESTORE Barrier

In order for any new longitudinal barrier to be accepted for use on the roadway, it also has to have a crashworthy termination. Two common methods for terminating longitudinal barriers are to: (1) use a crashworthy crash cushion or guardrail end terminal

on the ends or (2) use a crashworthy transition from the RESTORE barrier to a rigid concrete barrier or buttress, which in turn would be shielded with crashworthy crash cushion or transitioned to a concrete buttress. The RESTORE barrier was designed to allow for lateral deflection but limited rotation about the vertical and longitudinal axes. In the absence of an integrated crashworthy end treatment, a stiffness transition may be needed to gradually adapt the RESTORE Barrier to a rigid concrete buttress, which provides sufficient continuity across this region. Therefore, it is necessary to develop a rigid buttress that will satisfy the MASH TL-4 impact safety standards as well as allow the RESTORE barrier to be adapted to other rigid barrier shapes.

1.2 Objective

Several research objectives were considered for this study. The primary objective included the development of a stiffness transition between the RESTORE barrier and a rigid concrete buttress. The transition was designed to meet the Test Level 4 (TL-4) impact safety standards found in MASH [15]. LS-DYNA computer simulation [24] was used to investigate vehicle behavior and design impact forces at both interior and transition regions, evaluate the safety performance and structural adequacy of the prototype concepts for the stiffness transition system, as well as identify a final design deemed ready for full-scale crash testing with 1100C, 2270P, and 10000S vehicles. The transition system was configured to fit within the same footprint as the RESTORE barrier, utilize as much standard hazard as possible, and withstand impact events on either side and from any direction. The final concept would mitigate concerns for vehicle pocketing, vehicle snag, as well as vehicle instabilities. The transition system also

accommodated height differences and connection gaps between the RESTORE barrier and the rigid concrete buttress end.

1.3 Scope

The research objectives were completed through several tasks. First, literature was reviewed including connections between barriers, stiffening techniques, and previous simulation and full-scale testing of various transition systems. Several design concepts for the stiffness transition between the RESTORE barrier and the rigid concrete buttress were brainstormed, designed, and evaluated. A computer simulation effort was undertaken to investigate vehicle behavior and impact forces, as well as to analyze, refine, and evaluate several concepts under MASH TL-4 impact scenarios using LS-DYNA, a 3-D nonlinear finite element code [24]. Finally, a preferred concept was selected, and recommendations for full-scale crash testing were provided.

2 LITERATURE REVIEW

2.1 Introduction

A literature search was conducted in order to review and gain knowledge of (1) transition design considerations, (2) common connections between concrete barriers, (3) lateral stiffness transitions, (4) transitions between different barrier heights and widths, (5) MASH TL-4 barrier loading, (6) MASH TL-4 barrier heights, and (7) concrete barrier design methodologies. A summary of all barrier transitions is not included herein. The compiled results aided in the formulation of design concepts for the transition between the RESTORE barrier and a rigid concrete buttress.

2.2 Transition Design Considerations

When two connected barriers have varying strengths, stiffnesses, and/or geometries, a barrier transition is required to smoothly and effectively provide continuity between the two different containment systems. Transitions contain and redirect errant vehicles, limit barrier deflection, and mitigate concerns for vehicle pocketing and snagging. Vehicle pocketing can occur when the lateral barrier deflection of an upstream region of a guardrail system is much greater than that in the adjacent downstream region, thus creating a sharp bend or high slope in the guardrail system as the impacting vehicle approaches the stiffer region. Excessive pocketing may lead to vehicle snagging on system components as well as excessive vehicle deceleration and occupant compartment deformation. A critical pocketing angle has previously been used to estimate when pocketing may become a critical concern. The pocketing angle has been defined as the angle between the guardrail region in advance of the impacting vehicle and the downstream section of the rail, as shown in Figure 7. For angles smaller than the critical

pocketing angle, the vehicle would be expected to be safely redirected. For angles larger than the critical angle, the vehicle may encounter undesirable behavior and not pass the safety criteria provided in the *Manual for Assessing Safety Hardware* (MASH) [15].

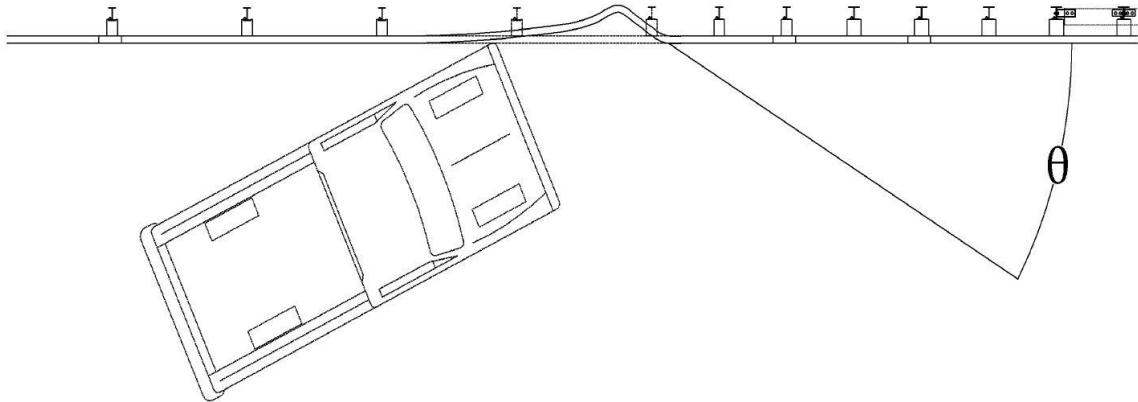


Figure 7. Critical Pocketing Angle [25-26]

In 2010, researchers at Midwest Roadside Safety Facility (MwRSF) reviewed many guardrail transition tests [26] that were performed with either the National Cooperative Highway Research Program (NCHRP) Report No. 350 [27] or MASH impact safety testing standards [15]. With the NCHRP Report No. 350 standards, the critical pocketing angle was believed to be approximately 23 degrees for steel guardrail [25]. NCHRP Report No. 350 [27] utilized testing with a 4,409-lb (2,000-kg) pickup truck, designated 2000P, while the updated standards in MASH [15] included a 5,000-lb (2,268-kg) pickup truck, designated 2270P. Previously, researchers had noted that the 2270P pickup truck, as found in MASH, was believed to be more stable than the 2000P vehicle found in NCHRP Report No. 350. Taking into account the increased vehicle stability, MwRSF researchers believed that the critical pocketing angle for a 2270P vehicle impacting a steel corrugated beam guardrail system was higher than 23 degrees,

maybe closer to 30 degrees [26]. Without an effective stiffness transition design, a serious potential existed for vehicle pocketing into the barrier, wheel snag, snag with other vehicle components on elements in the stiffer barrier, as well as vehicle instability.

2.3 Common Connections Between Concrete Barriers

Due to the vast selection of barriers with each having different functions, properties, and degrees of freedom, many connections were created and successfully implemented. These connections have been used for attaching both similar and different barrier segments. For this review, only a limited number of connections that provided information pertaining to permanent and portable concrete barriers are listed herein.

2.3.1 Portable Concrete Barriers

In 1987, Graham-Migletz Enterprises, Inc. conducted an extensive literature search to identify and evaluate available connections between adjacent portable concrete barriers (PCBs) [28]. In 1985, the Federal Highway Administration (FHWA) also conducted a literature search to determine the most common type of PCB connectors that were used throughout the States [29]. The results from the survey by FHWA, as depicted in Figure 8, revealed several common types of connectors for PCBs, such as: pin and loop; pin and wire rope; tongue and groove; plate insert; or dowel rods.

Several important factors were considered for each type of connection, such as gap width between barriers, cross-sectional area of connection components, thickness or diameter of connector piece, number of pieces used in connection, and fabrication materials. Further, the four loading conditions that were analyzed for each connection were: (1) ultimate tensile strength in the longitudinal direction (F); (2) ultimate moment (M); (3) ultimate shear strength in the lateral direction (V); and (4) ultimate torsion (T),

as shown in Figure 9 [28]. Various barriers were analyzed by the Texas Transportation Institute (TTI), and the strengths of each connection were determined, as shown in Table 1 [30].

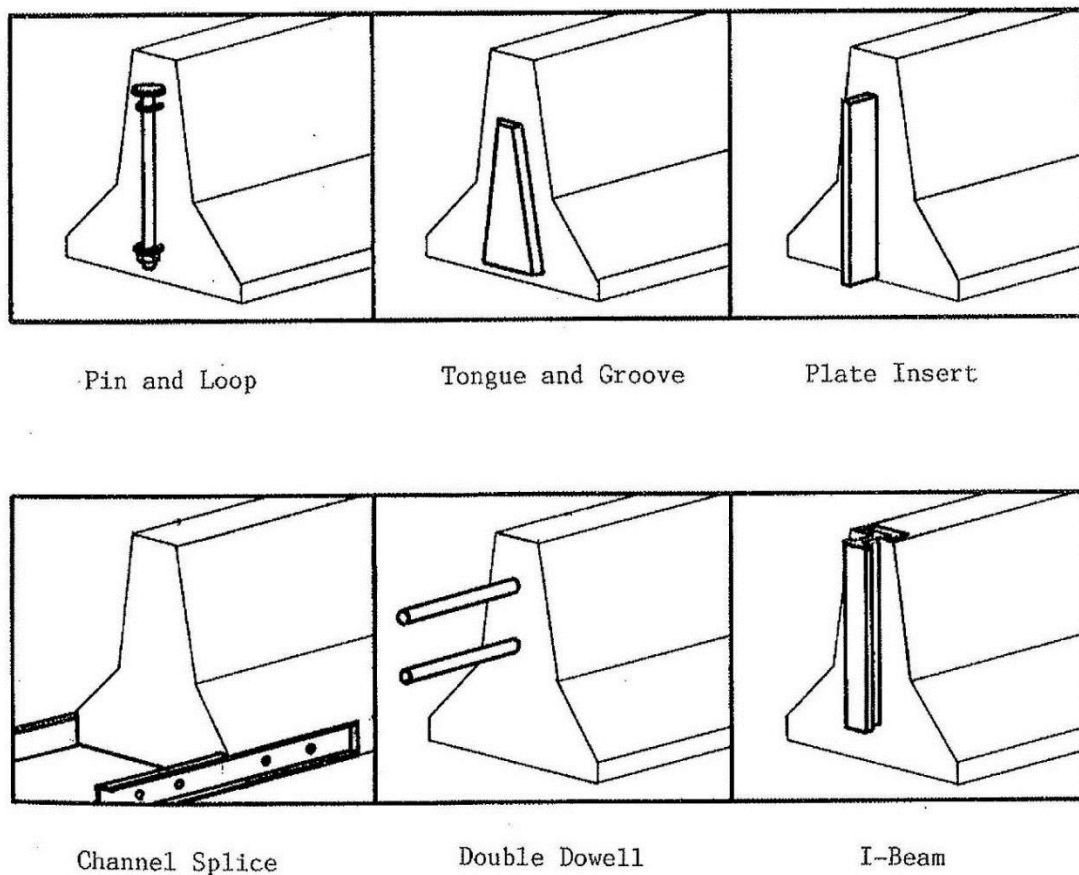


Figure 8. General PCB Connectors [28-29]

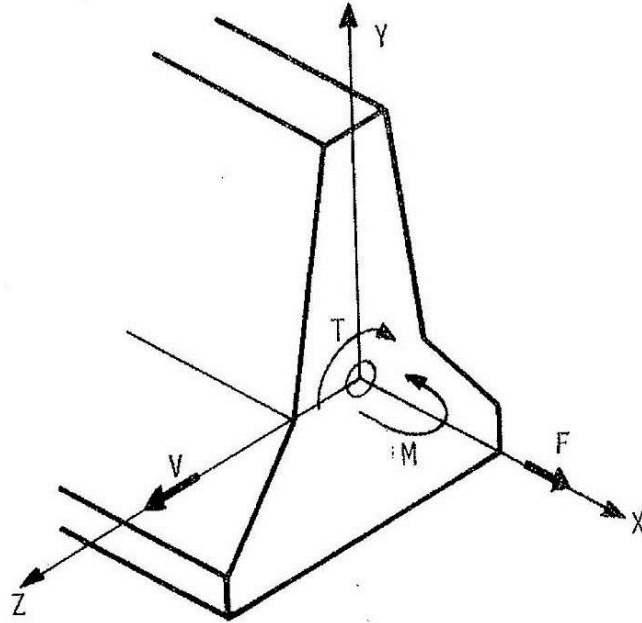


Figure 9. Loading Conditions at PCB Joints [28]

Table 1. PCB Connection Strengths [30]

Connection Type	Tensile Capacity kip (kN)	Shear Capacity kip (kN)	Moment Capacity k-ft (kJ)	Torsion Capacity k-ft (kJ)
I-Lock	92 (409)	208 (925)	61 (83)	87 (118)
Pin and Rebar (CA)	85 (378)	85 (378)	57 (77)	60 (81)
Pin and Wire Rope	61 (271)	61 (271)	41 (56)	41 (56)
Pin and Rebar (GA)	46 (205)	46 (205)	31 (42)	31 (42)
Dowel	0 (0)	60 (267)	0 (0)	37 (50)
Tongue and Groove (OR)	0 (0)	27 (120)	0 (0)	9 (12)
Tongue and Groove (VA)	0 (0)	32 (142)	0 (0)	7 (9)

2.3.2 PCB Termination and Anchorage Methods

In 2009, researchers at MwRSF investigated the termination and end anchorage requirements for PCB systems [31-32]. The impact behavior of a free standing PCB system with anchored ends, when struck near the upstream end of the system, had never been previously investigated. Following a review of previous crashworthy PCB systems,

computer simulation was used to analyze, design, and modify the anchorage system before conducting full-scale vehicle crash testing on the proposed system.

LS-DYNA computer simulations were conducted to determine impact loads for use in the analysis and design of the anchorage system. From the simulation effort, MwRSF researchers decided that the termination and anchorage system should withstand an 80-kip (356-kN) load over approximately 10 in. (254 mm) of deflection for the TL-3 impact event. A driven, steel anchor post system was subjected to full-scale crash testing. The end barrier was anchored by two cable assemblies that connected the end connector pin to two driven steel anchor posts. The pin sleeve was a 1½-in. (38-mm) diameter schedule 40 pipe, and the inserted pin was a 1¼-in. (32-mm) diameter grade 60 steel pin. The anchor posts were installed in soil with an embedment depth of 8 ft (2.4 m). One post was located along the longitudinal axis of the system, 45¾ in. (1,153 mm) upstream from the first barrier. The second post was located 29¾ in. (746 mm) upstream from the first barrier and offset 11½ in. (292 mm) laterally away from the connection pin towards the roadway, as shown in Figure 10.



Figure 10. Portable Concrete Barrier (PCB) Anchorage and Termination [31-32]

The MASH test designation no. 3-11 full-scale crash test was performed on a system consisting of twelve 12-ft 6-in. (3,810-mm) long, F-shape PCB segments that utilized the end anchorage system noted above, for a total system length of 156 ft – 6 in. (47.7 m). The PCB system utilized a pin and loop barrier-to-barrier connection. During test no. TPCB-1, a 4,991-lb (2,264-kg) pickup truck impacted the system 9 ft – $\frac{5}{8}$ in. (2,759 mm) downstream from the upstream end of barrier no. 1 at a speed of 62.9 mph (101.2 km/h) and at an angle of 25.5 degrees. The maximum dynamic anchor deflections were 5.3 in. (135 mm) for the offset anchorage and 6.2 in. (157 mm) for the in-line anchorage, measured from string potentiometers mounted on the anchors. The PCB end anchorage system contained and redirected the vehicle with a maximum lateral permanent set barrier deflection of 66½ in. (1,689 mm). The system was determined to be successful according to the TL-3 safety criteria found in MASH.

2.3.3 MASH TL-3 Median Barrier Gate

In 2010, researchers at the Texas A&M Transportation Institute (TTI) crash tested the Texas Department of Transportation's (TxDOT's) Emergency Opening System (EOS) according to MASH TL-3 conditions [33-35]. The original EOS was fabricated with two 8-in. x 8-in. x $\frac{3}{8}$ -in. (203-mm x 302-mm x 10-mm) A500 Grade B steel tubes offset vertically 3 in. (76 mm) away from one another and separated by a C3x6 steel channel, as shown in Figure 11. The length of the gate was 30 ft (9.1 m), extending between two rigid concrete buttresses. The gate was connected to the end brackets using a $3\frac{1}{4}$ -in. (83-mm) diameter x 26-in. (660 mm) long A572 Grade 42 steel pin located on both ends of the gate. The top mounting height of the barrier was $30\frac{1}{4}$ in. (768 mm), and the concrete buttresses were 32 in. (813 mm) tall and had a 6-in. (152-mm) radius curb under the end brackets. Three tests were conducted to evaluate the performance of the EOS.

During the MASH test designation no. 3-11 crash test, the pickup truck was contained and redirected. After the test, the concrete buttress had experienced extensive spalling, exposing the reinforcing bars. The maximum occupant compartment deformation was 8.3 in. (211 mm), which was located near the left-side floor pan. Thus, the system was redesigned to prevent buttress damage. The test was unsuccessful due to occupant compartment deformation limits being violated.



Figure 11. Original Emergency Opening System [33]

The concrete was recast with a straight taper instead of the rounded curb protruding from the end of the concrete buttress. The taper extended 8 in. (203 mm) away from the end of the buttress and narrowed from 12 in. (152 mm) to 3¼ in. (63 mm). A second test was performed according to MASH test designation no. 3-10. Multiple limits from MASH were violated due to vehicle snag on the end of the concrete buttress and the steel gussets between the two steel tubes. The steel gussets extended outward 1 in. (25 mm) on either direction of the steel tube with a 2H:1V coped corner. The maximum occupant compartment deformation was 10.8 in. (274 mm) in the right-front firewall area, which exceeded the limit provided in MASH. Additionally, the longitudinal impact velocity did not satisfy the recommendations found in MASH. Therefore, test designation no. 3-10 did not pass the MASH impact safety requirements.

Several modifications were made to the end of the median barrier gate to help mitigate the vehicle snagging observed in the previous test, as shown in Figure 12. The welded tubing that connected the EOS with the buttress was tapered outward 2 in. (51

mm) on each side of the gate to give a total width of 12 in. (305 mm) and then tapered inward to 8 in. (203 mm) over a distance of 23 in. (584 mm) to match the overall width of the steel beams. The pin connecting the gate to the end bracket retained its diameter of 3¼ in. (83 mm). Other details of the EOS, including the concrete buttress details, remained the same as used in the previous tests.



Figure 12. Modified Emergency Opening System [33]

Another MASH test designation no. 3-10 crash test was conducted on the modified EOS. However, the test was again unsuccessful due to excessive occupant compartment deformation limits. Vehicle snag occurred between the two longitudinal gussets, against the back plate. The 1100C vehicle occupant compartment experienced interior deformations equal to 12.0 in. (305 mm) in the right-front firewall area, which violated the limits provided in MASH.

Additional design and finite element analysis was utilized to mitigate snag potential and optimize the gate [34-35]. From the simulation results, two 29-ft (8.8-m)

long, 12-in. x 12-in. x ¼-in. (305-mm x 605-mm x 6-mm) A500 Grade B steel tubes stacked vertically on top of one another and bolted together effectively contained and redirected the passenger vehicles. The height of the gate was modified to 35 in. (889 mm). The tubes were connected to end brackets located at each exposed end of the concrete median barrier with a 2¼-in. (57-mm) diameter by 32-in. (813-mm) long A36 steel pin. Each pin was inserted from the top and through both tubes and then inserted into the concrete under the bolted tubes. The final EOS is shown in Figure 13.

Three full-scale crash tests were conducted on the developed EOS using test designation nos. 3-11, 3-20, and 3-21. All three crash tests met the required evaluation criteria provided in MASH.



Figure 13. Final Design of the Emergency Opening System [34-35]

2.4 Lateral Stiffness Transitions

2.4.1 Guardrail to Portable Concrete Barriers

In 2014, MwRSF sought to develop a stiffness transition between portable concrete barriers (PCB) and a W-beam guardrail for the Nebraska Department of Roads

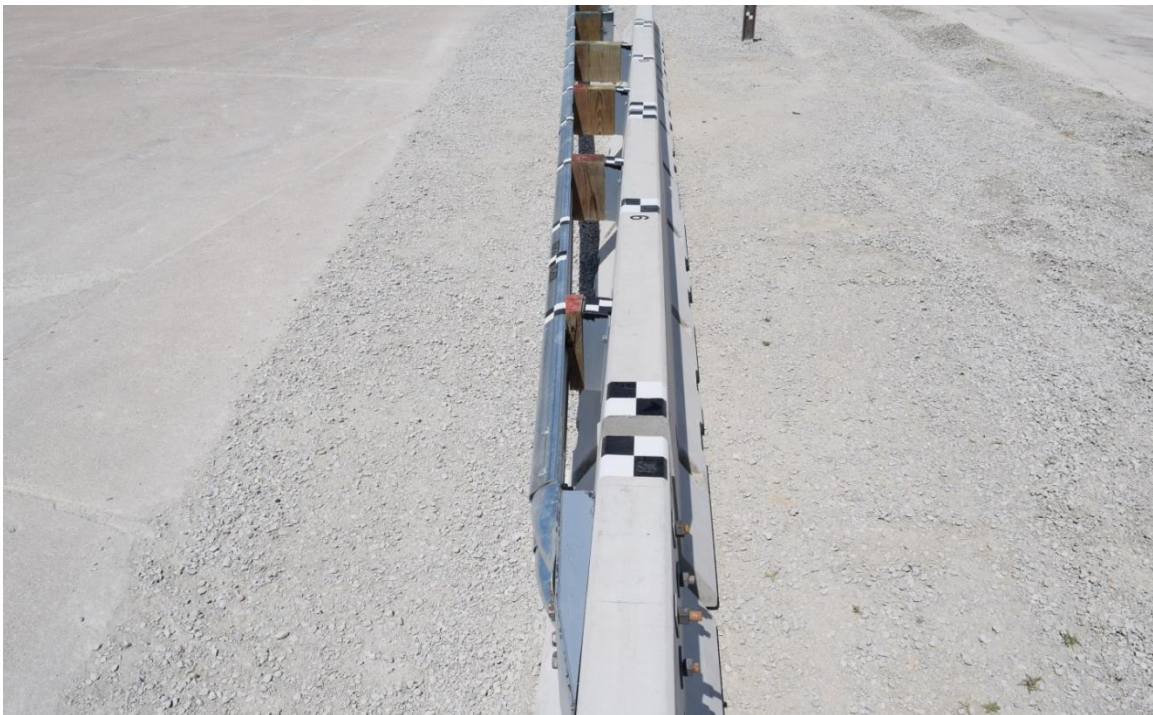
(NDOR) in order to improve safety within a construction or work zone [36-38]. Within a construction zone adjacent to existing W-beam guardrail systems, a portion of the W-beam guardrail is often removed during bridge rehabilitation activities. Thus, a PCB system is often used to shield the work-zone area when installed at a 15H:1V flare rate. For this research and development effort, it was preferred that the PCBs not be anchored nor pinned to the roadway surface.

LS-DYNA simulations were run to better understand the inherent risks associated with barriers not containing a proper transition from guardrail to PCBs. The evaluation criteria included vehicle behavior, occupant risk, and rail pocketing. In order to be considered successful, the vehicle should not penetrate, underride, or override the barrier and should satisfy the occupant risk values deemed safe according to MASH. The maximum pocking angle was chosen to be 23 degrees, as determined as a lower bound from the previous research. Two different semi-rigid guardrail systems were investigated for the barrier system leading into the transition region: the modified G4(1S) guardrail system and the Midwest Guardrail System (MGS). Numerous transition concepts were configured for connection to both flared and parallel PCBs, when attached to both W-beam guardrail systems. Some of the stiffening techniques that were explored utilized three beams, blockout additions, cantilever beams extending behind the guardrail systems, and guardrail nesting.

Through LS-DYNA simulation, multiple design configurations were impacted and evaluated according to the criteria listed previously. The modified G4(1S) system was selected to be modeled first, although it had some limitations. The MGS was modeled second. Through the stiffening technique of guardrail nesting, a design

configuration that met all of the evaluation criteria was chosen, as shown in Figure 14. As such, a compliant crash testing program was initiated.

Test designation nos. 3-20, 3-21, and a reverse direction test no. 3-21, were performed on the selected configuration. All of the TL-3 tests passed the MASH safety criteria, and the transition was deemed acceptable for use along highways and roadways [38].



(a)



(b)

Figure 14. NDOR PCB to Guardrail Stiffness Transition, Test Nos. MGSPCB-1 through MGSPCB-3 [38]

2.4.2 SAFER Barrier Between Portable Concrete Barrier and Rigid Buttress

Racetracks commonly use PCBs to shield openings or protect portions of the infield. Some of these installations are located in areas where current safety guidance would recommend treatment with the Steel And Foam Energy-Reduction (SAFER) barrier. Therefore, a shielding method was developed to effectively cover the opening for racing events while still being removable at other times [39-40].

Various simulations were conducted to determine the most effective PCB configuration, transition layout, and necessary anchorage hardware. A previously-developed PCB for the Iowa Speedway was selected for initial consideration due to several advantages over other PCB systems. The Iowa Speedway PCB featured a robust connection and a significant quantity of reinforcing steel to increase barrier capacity, as shown in Figure 15. The PCB also used a relatively-short, 8-ft (2.4-m) segment length, which allowed it to be easily placed around curves.

An opening size of approximately 114 ft – 5⁷/₈ in. (34.9 m) was chosen for simulation, design, and testing, so that an even number of 8-ft (2.4-m) long segments could be used. The opening size was believed to be large enough to reflect the upper end of the opening size on most race track walls.

Alternatively, a secondary series of simulations was performed to investigate the effects of placing the SAFER barrier in front of free-standing PCBs, which were transitioned to the ends of rigid concrete buttresses. The main concerns for impacts near the rigid barrier ends were pocketing within the SAFER barrier, excessive loading to connections within the barrier system, and concerns for kinking the steel SAFER barrier panels as the PCB deflected in advance of the rigid wall, thus potentially resulting in

vehicle pocketing or snag. Due to overall system deflections being higher than desired and a risk for pocketing in the SAFER barrier, a second row of PCB segments were placed behind the original row of PCB segments. Both the original and second rows were anchored to the rigid barrier ends.

The PCB segments were 8 ft (2.4 m) long by 18 in. (457 mm) wide x 36 in. (914 mm) tall with a vertical front face and a sloped back face. The reinforced concrete barrier segments were connected with rebar loops and a 1¼-in. (32-mm) diameter, A36 steel pin passing through the loops. The end anchorage for the original row consisted for a ¾-in. (19-mm) thick, “L” shaped A572 Grade 50 steel plate anchored to the end of the rigid barrier and attached with an oversized 1½-in. (38-mm) diameter, A36 steel pin through the loops of the end PCB and the pin plates. It was believed that the “L” shaped steel anchor plate could be adjusted up to ¾ in. (19 mm) by the addition of spacers under the plates to address small variations and construction tolerances. The second row PCB segments were attached with a cable anchor assembly. An oversized 1½-in. (38-mm) diameter, A36 steel pin was placed through the loops of the end PCB segment. The cables were ¾-in. (19 mm) diameter 6x19 IWRC IPS wire rope with a thimble assembly on one end and Grade 5 threaded stud on the other end. Pipe sleeve spacers were utilized to keep the cable assemblies attached at a consistent height to the end pin of the PCB segment. Photographs of the system are shown in Figures 16 and 17.

The test set-up was configured for a 135 mph (60.4 m/s) impact of a NASCAR stock car vehicle at an angle of 25 degrees with the SAFER attached to PCB barrier. The impact point was 12 ft (3.7 m) upstream from the end of the rigid, concrete buttress. After the test, the maximum dynamic deflection of the original row of the PCB segments was

determined to be 15.0 in. (381 mm) at the top of the first row of barriers. The maximum dynamic deflection of the second row of PCB segments was determined to be 24.7 in. (627 mm) at the top of the second row of barriers. The maximum permanent set of the first row of PCB segments was determined to be 11.5 in. (292 mm), and the second row was determined to be 21.0 in. (533 mm).



Figure 15. Portable Concrete Barrier Design for Iowa Speedway [39-40]

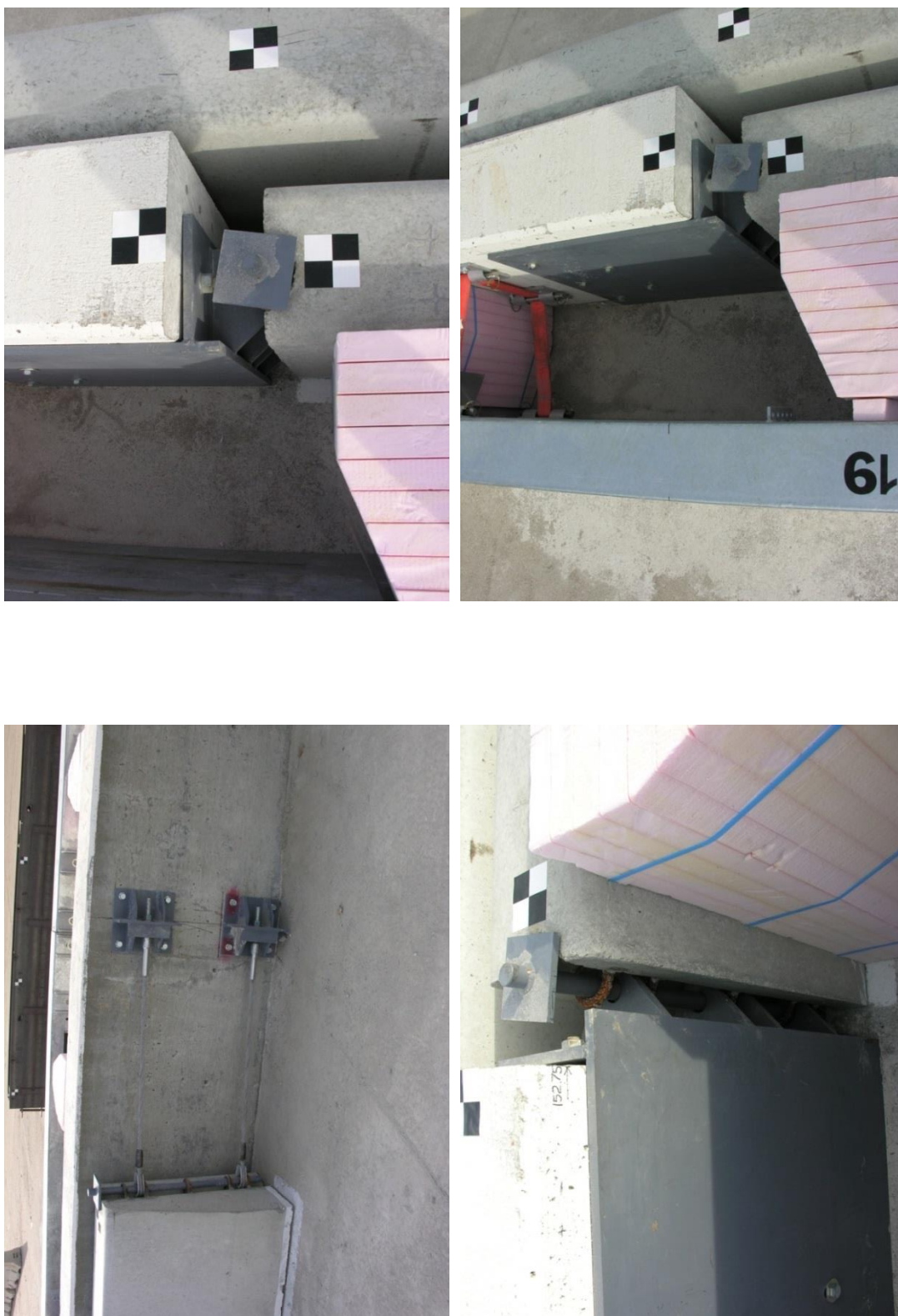


Figure 16. Pre-Test Photographs of SAFER on PCB Installed Across Opening, Test No. SPCB-1 [39-40]



Figure 17. Pre-Test Photographs of SAFER on PCB Installed Across Opening, Test No. SPCB-1 [39-40]

To accommodate differences between the available gap between the rigid barriers and the overall barrier length, some alternatives were presented. The end anchor plates for the first row of PCB segments were designed to allow for $\frac{3}{4}$ in. (19 mm) of shimming underneath the end plates to adjust the fit of the segments. The concrete buttress ends could be cut and recast to fit an even number of PCB segments, which may be necessary to provide sufficient structural capacity for the end sections. Lastly, a special, shortened PCB segment could be cast in a shorter length for the last barrier in the first row in order to provide an improved fit.

2.4.3 Portable Concrete Barriers to Permanent Concrete Roadside Barriers

In 2007, MwRSF aimed to develop a tie-down system for PCBs and then utilize that tie-down system within an approach transition from free-standing barriers to a rigid concrete barrier [41-42]. This research effort was evaluated according to the TL-3 safety performance criteria set forth in the NCHRP Report No. 350 [27].

The first phase of the project included full-scale crash testing to determine the characteristics of an asphalt pinned tie-down PCB system. Test no. FTB-1 utilized barriers with a pin and loop type connection comprised of two sets of three rebar loops on each barrier interconnection. The vertical connection pin consisted of a $1\frac{1}{4}$ -in. (32-mm) diameter by 28-in. (711 mm) long, A36 steel bar. The system with three $1\frac{1}{2}$ -in. (38-mm) diameter by 36-in. (914-mm) long, A36 steel pins with 3 in. x 3 in. x $\frac{1}{2}$ in. (76 mm x 76 mm x 13 mm) steel caps was crash tested and found acceptable according to NCHRP Report No. 350 criteria for test designation no. 3-11. It was recommended that the steel caps be strengthened to account for the fracture of some welds.

The second phase included the development and full-scale testing of a transition from a free-standing PCB to rigid concrete barrier. The considered transition utilized a number of asphalt tie-down pins within the transition section to stiffen the PCB as it approached the stiffer barrier. For test no. FTB-2, the only system change was an increased number of barriers to account for the free-standing section, the transition section, and the rigid barrier end. The rigid barrier end was simulated by bolting down the final five F-shape barriers with epoxied anchors. The transition utilized a varied spacing of the pins to create a transition in stiffness over a series of four barrier segments. The tie-down pins were modified slightly prior to the transition test to prevent the disengagement of the top caps observed in test no. FTB-1. This modification strengthened the connection of the cap to the pin but did not change the embedment depth. In addition, a nested 12-gauge (2.7 mm) thrie beam was bolted across both sides of the barrier at the joint between the pinned barriers and the rigid barrier system in order to reduce the potential for vehicle snag at the joint. The free-standing to rigid concrete barrier transition schematic is shown in Figure 18, and the as-tested system is shown in Figure 19.

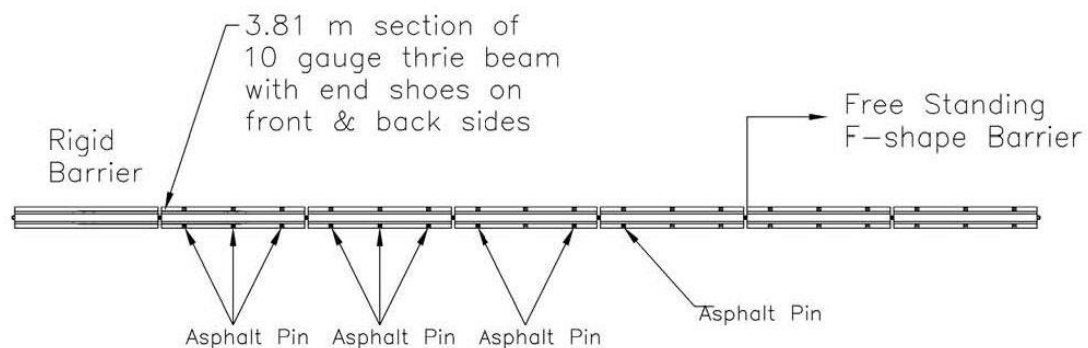


Figure 18. Free-Standing PCB to Rigid Concrete Barrier Transition Schematic [41-42]

The system was impacted near the middle of the first transition barrier, just upstream from the first asphalt pin, traveling downstream towards the rigid barrier. The maximum permanent set and dynamic barrier deflections were measured to be $5\frac{1}{4}$ in. and $18\frac{3}{8}$ in. (133 mm and 467 mm), respectively. It should be noted that the degree of vehicle roll and pitch observed in this test were a cause for concern, but the test was still successful. Researchers believed that barriers with a vertical front face would demonstrate better vehicle stability when impacted.



Figure 19. Free-Standing PCB to Rigid Concrete Barrier Transition, Test No. FTB-2 [41-42]

2.5 Transitions Between Different Barrier Heights and Widths

2.5.1 Single-Slope Approach Guardrail Height Transition

In 1995, MwRSF conducted two crash tests on a transition between a single-slope concrete median barrier and a semi-rigid guardrail system. The original upstream top slope of the concrete median barrier was 2H:1V. However, the impacting pickup truck experienced excessive contact between the vehicle's right-front hood and quarter panel and the top end of the buttress, which contributed to the an unsuccessful crash test due to

vehicle snag. As a result, a modified barrier design was configured to include an 8H:1V top slope for the end of the concrete median barrier to reduce vehicle contact. The modified transition system was retested and shown to effectively mitigate vehicle snag on the concrete barrier positioned above the three beam approach guardrail with different heights [43-44], as shown in Figure 20.



2H:1V Slope



8H:1V Slope

Figure 20. Two Height Transitions for Single-Slope Concrete Median Barrier [43-44]

2.5.2 PCBs to Permanent Concrete Median Barriers for Median Applications

In 2010, MwRSF aimed to identify locations where temporary concrete barriers were currently being transitioned to other barriers, determine if those barrier transitions were crashworthy, identify locations where transitions were still needed, and rank the most important need. From a survey sent to the Midwest States Pooled Fund members, a transition from a PCB to a permanent concrete barrier was deemed to be the most important. Later, a second survey determined that an end-to-end transition would be most beneficial [45].

Multiple permanent concrete barrier systems were compared to a 32-in. (813-mm) tall F-shape PCB. From the comparison, it was determined that the 42-in. (1,067-mm) tall California (CA) single-slope concrete median barrier provided the most critical scenario for the approach transition. This finding was due to the major differences in geometry, which would likely cause an increased potential for vehicle snag. Further, a 10-in. (254-mm) height difference existed between the CA single-slope concrete median barrier and typical 32-in. (813-mm) tall PCBs. Therefore, a height transition segment was needed to mitigate vehicle snag on the taller barrier end. Since the height would be transitioned with a steel cap instead of the sloped concrete barrier, previously configured with a 8H:1V slope [43-44], a more aggressive slope of 5H:1V was explored, as shown in Figure 21. The test installation consisted of a rigid buttress, four transition PCBs, eight free-standing PCBs, and a steel transition cap. The stiffness transition system utilized varied spacing of the asphalt pin tie-down components as well as a nested 12-gauge (2.7 mm) thrie beam bolted across the joint between the pinned barrier and the rigid buttress.

The transition system was successfully crash tested through the use of two crash tests at different impact points according to test designation no. 3-21 in MASH.



Figure 21. Free-Standing PCB to Rigid Barrier Height Transition for Median Applications on Asphalt [45]

2.5.3 PCBs to Permanent Concrete Median Barriers for Roadside Applications

In 2012, researchers at TTI developed a transition between portable safety shape barriers and permanent concrete barriers [46], similar to the study conducted by MwRSF. Unlike the MwRSF median transition for asphalt pavement, the TTI transition was intended for roadside applications and use on concrete pavement. The final design incorporated a transition between a 32-in. (813-mm) tall, F-shape PCB and a 42-in. (1,067-mm) tall, rigid single-slope concrete barrier and an 11-degree slope on a steel transition cap, as shown in Figure 22. Due to the height difference between the barriers, a transition cap was used with approximately a 5H:1V slope. The barriers were connected

with a pin-and-loop connection, and the portable barriers had 2 pins anchoring the barrier on the traffic side only. The impact side of the barrier had a thrie beam, while the non-impact side of the barrier used a ¼-in. (6-mm) thick, steel plate and a wood spacer. The transition section was successfully crash tested according to test designation 3-21 in MASH.



Figure 22. Free-Standing PCB to Rigid Barrier Height Transition for Roadside Applications on Concrete [46]

2.5.4 Steel Bridge Railing and Transition on a Longitudinal Glue-Laminated Timber Deck

In 1992, researchers at MwRSF developed and tested a thrie beam and channel bridge railing system, designated TBC-8000, for use on a longitudinal timber bridge deck [47-49]. The bridge railing consisted of a thrie beam rail, an upper C8x11.5 (C200x17) channel rail, and W6x15 (W152x22.3) steel posts and spacer blocks. An approach guardrail transition was configured on the upstream end of the bridge rail. The steel

channel rail was transitioned both vertically and laterally when exiting off of the bridge. The TBC-8000 transitioned vertically with approximately a 10H:1V slope and then transitioned laterally with approximately 10H:1V slope, as shown in Figure 23. The bridge rail passed the performance level 2 (PL-2) safety performance criteria set forth by the American Association of State Highway and Transportation Officials' *Guide Specifications for Bridge Railings (1989)* [50]. However, a transition test was not conducted, but the upper channel was tapered to prevent snag and was configured to be similar to previously crash-tested systems.



Figure 23. TBC-8000 Bridge Rail Transition [47-49]

2.5.5 TL-4 Bridge Railing and Transition on a Transverse Glue-Laminated Timber Deck

In 1995, researchers at MwRSF developed and tested a TL-4 bridge railing and transition system for a transverse glue-laminated timber deck [51-52]. The bridge rail and approach guardrail transition system was tested according to the NCHRP Report No. 350 TL-4 safety criteria. The design of the transition, followed a similar design to what had been configured previously for TBC-8000, which was used on longitudinal timber deck

panels [47]. Instead of an upper C-section for the top rail element, a HSS tubular section was used and attached to the top of the steel spacer blocks. Further, the top rail was sloped differently, using a more aggressive slope. The vertical slope was approximately 5H:1V with a lateral transition of 4H:1V, as shown in Figure 24 [51-52]. The bridge rail and transition systems contained and redirected the 4,409-lb (2,000-kg) pickup truck and the 17,637-lb (8,000-kg) single-unit truck. The bridge rail and transition systems were deemed successful according to the NCHRP Report No. 350 TL-4 safety criteria.



Figure 24. TL-4 Transition on Transverse Glue-Laminated Timber Deck [51-52]

2.5.6 Horizontal Flare Rates for Concrete Barriers

In 1998, a research study was conducted by MwRSF to develop and test three beam transitions to rigid concrete safety shape barriers [53-54]. The approach guardrail transition was evaluated according to the NCHRP Report No. 350 safety criteria. Since

curbs are often used to provide hydraulic drainage near the ends of a bridge (i.e., the transition region), a 4-in. (102-mm) tall triangular-shape concrete curb was constructed below the thrie-beam, as shown in Figure 25. The horizontal flare rate for the lower toe of the concrete barrier was approximately 6H:1V. After the first full-scale crash test, it was determined that barrier deflections were excessive, resulting in vehicle rollover. Therefore, various stiffening techniques were explored in the approach guardrail transition. A deeper post embedment was utilized in the modified design as well as a 1-in. (25-mm) chamfer was added to the upstream impact-side corner of the barrier end. With the system modifications, the approach guardrail transition was successfully crash tested with the 6H:1V horizontal slope, as shown in Figure 26. Therefore, a 6H:1V horizontal slope of the barrier toe was deemed acceptable for tapering the lower region of a concrete barrier end.



Figure 25. Horizontal Flare Rate of 6H:1V Barrier Toe [53-54]

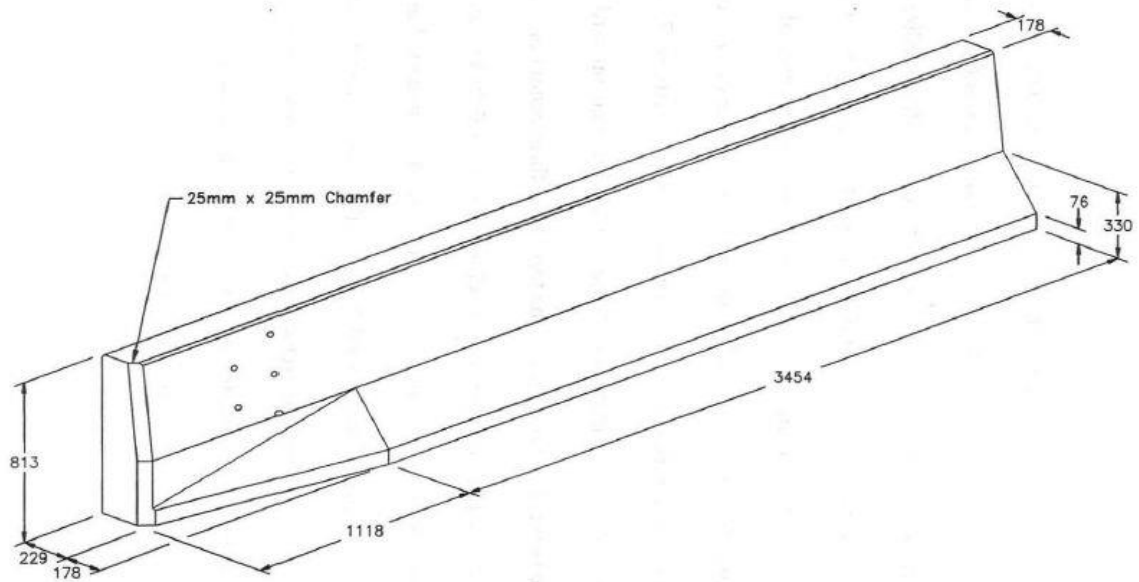


Figure 26. Modified Horizontal Flare Rate with Chamfer [53-54]

2.6 MASH TL-4 Barrier Loading

2.6.1 Introduction

The transition between the RESTORE barrier and rigid concrete barriers was expected to meet the MASH TL-4 impact safety standards. To complete this effort, it was deemed important to further investigate TL-4 barrier loading. Many research groups have investigated the magnitude of impact loads pertaining to the TL-4 impact safety standards. Over the years, researchers have occasionally identified different loads based on design values, physical test results, and simulation results. Therefore, researchers have used slightly different TL-4 design impact loads for configuring barrier systems.

2.6.2 AASHTO Design Impact Loads

The 1989 AASHTO *Guide Specifications for Bridge Railings* [55] specifies a lateral design load of 80 kips (356 kN) for configuring PL-2 barriers using a load application height ranging between 17 in. (432 mm) and “H” minus 7 in. (178 mm),

where “H” equals the overall system height. Over the years, crash testing guidelines have changed along with codes for designing bridge railings. For example, the AASHTO *LRFD Bridge Design Specifications* [56] now specifies a lateral design load of 54.0 kips (240 kN) for configuring TL-4 barriers using a load application height of 32 in. (813 mm).

2.6.3 MASH TL-4 Barrier Force Investigation Based on Previous Test Data

In 2007, Eller and Reid conducted a research study to investigate techniques for approximating lateral and longitudinal barrier forces from existing crash data [57]. First, sensors located near the center of gravity in full-scale tests were used to provide accelerations along the X, Y, and Z axes. Second, overhead film data was analyzed and used to determine the instantaneous vehicle yaw angle relative to the rail. As part of this method, several assumptions were made. The assumptions were: (1) the barrier is rigid and non-deforming; (2) the test vehicle is rigid with uniform accelerations; and (3) the vehicle motion is confined to the X-Y plane. After accelerations were converted to forces, the lateral and longitudinal barrier forces were acquired using Equations 1 and 2 along with the vehicle yaw data.

$$F_n = F_x \sin(\theta) + F_y \cos(\theta) \quad (1)$$

$$F_t = F_x \cos(\theta) - F_y \sin(\theta) \quad (2)$$

Where: F_n = Lateral barrier force
 F_t = Longitudinal barrier force
 F_x = Force along the x-axis
 F_y = Force along the y-axis
 θ = Instantaneous angle between vehicle and original barrier face

From scaling of previous crash test results, the NCHRP Report No. 350 TL-4 peak lateral loads, as reported by Eller and Reid [57], were multiplied by the ratio of the

MASH target impact severity (154.4 k-ft (209 kJ)) divided by the actual impact severity obtained from the NCHRP Report No. 350 crash tests to estimate MASH TL-4 lateral barrier forces. From the calculation, the peak lateral loads were approximated to range between 88 and 95 kips (391 and 4,253 kN), as shown in Table 2.

Table 2. Estimated Peak Lateral Impact Force - MASH TL-4 Impact Conditions [57-58]

Test No.	Ref No.	Weight	Impact Speed	Impact Angle (deg)	Actual Impact Severity	NCHRP 350 TL-4 Peak Lateral Impact Force	MASH TL-4 Predicted Peak Lateral Impact Force
		lbs (kg)	mph (km/h)		k-ft (kJ)	kips (kN)	kips (kN)
CYRO-1	[59-60]	17,840 (8,092)	51.2 (82.4)	17.7	145 (196)	87.2 (388)	93.3 (415)
ZOI-1	[61]	17,605 (7,985)	50.4 (81.1)	15.64	108 (146)	66.8 (297)	88.7 (395)
ZOI-3	[61]	17,637 (8,000)	50.2 (80.8)	16.32	117 (159)	66.9 (298)	94.5 (421)

2.6.4 Precast Concrete Bridge Rail Study

In 2012, MwRSF researchers developed a MASH TL-4 precast concrete bridge rail for use on cast-in-place and precast concrete bridge deck systems [58]. Unfortunately, only a small number of full-scale crash tests with SUT vehicles had been conducted on barriers under the MASH impact safety standards. Three different methods were explored to determine design impact loads: (1) numerical approximations; (2) scaling of results from previous crash tests; and (3) computer simulations.

Using a numerical approximation outlined in NCHRP Report No. 86 [62], the equations to calculate vehicle impact loads are shown below:

$$G_{LAT} = \frac{(V_I * \sin\theta)^2}{2g[AL * \sin\theta - b(1 - \cos\theta) + D]} \quad (3)$$

$$F_{LAT-AVE} = G_{LAT} * Wt \quad (4)$$

Where: V_1 = Initial impact speed
 θ = Initial impact angle
 AL = Distance from the front of the vehicle to the center of gravity
 $2B$ = Width of the vehicle
 D = Barrier lateral deflection
 g = Gravitational constant
 Wt = Vehicle weight

Using TL-4 impact conditions, AL and B distances of 16.4 and 3.5 ft (5.0 and 1.1 m), respectfully, and the assumption of a rigid barrier, the average lateral impact force was determined to be 37.5 kips (167 kN). Assuming a dynamic impact factor of 2, the peak lateral impact force was determined to be 75 kips (334 kN), based on the equations above.

The second method of scaling results from previous crash tests was shown by Eller and Reid, as described in Chapter 2.6.3. The final method, LS-DYNA computer simulation, was also used to approximate the MASH TL-4 peak lateral loads for two different barrier heights. The first barrier configuration was 34½ in. (876 mm) tall, and the other barrier configuration was 36½ in. (927 mm) tall. Two simulations were run for each barrier height – one with suspension failure and one without suspension failure. From the analysis, the peak lateral impact force was found to range from 75 to 98 kips (334 to 436 kN), as shown in Table 3. Therefore, MwRSF researchers conservatively selected a design lateral impact force of 100 kips (445 kN) for use in the development of a new, aesthetic TL-4 precast concrete bridge rail.

Table 3. Estimated MASH TL-4 Peak Lateral Impact Forces – LS-DYNA Simulations [58]

Case No.	Barrier Height in. (mm)	Simulation Conditions	Peak Lateral Impact Load	
			(kips)	(kN)
A	36½ (927)	Suspension attached	81	360
B	36½ (927)	Front suspension deleted at 100 ms	98	436
C	34½ (876)	Suspension attached	75	334
D	34½ (876)	Front suspension deleted at 100 ms	86	383

2.6.5 TTI Mechanically Stabilized Earth Wall

In 2009, TTI developed procedures for designing roadside barrier systems placed on mechanically stabilized earth (MSE) retaining walls as part of NCHRP project nos. 22-20 and 22-20(2) [63-64]. Several tasks were performed, including a literature review, engineering analyses, computer simulations of TL-3 through TL-5 impacts, full-scale crash testing, and guideline development.

The barrier design loads, first published by the Bureau of Public Roads (BPR), now the Federal Highway Administration (FHWA) were reviewed. In 1962, the BPR proposed that bridge railings and buttresses should be designed for a transverse load of 30 kips (133 kN) using plastic design procedures [65]. In 1965, the railing specifications changed such that bridge railings and buttresses should be designed for a transverse load of 10 kips (45 kN), divided among the various rail members using an elastic analysis. Even with the change, Bligh, et al. noted that the 10-kip (45-kN) load with the rail resistance defined by an elastic analysis was roughly equivalent to the 30-kip (133-kN) load defined by a plastic analysis. When NCHRP Report No. 350 was published in 1993, the bridge design specifications were modified to phase out a design load of 10 kips (45 kN) and move toward using a design load of 54 kips (240 kN) for configuring traffic

barriers to meet the TL-4 criteria. Bligh, et al. noted that a larger force was based on dynamic impact testing results obtained with an instrumented rigid wall. Therefore, the 54-kip (240-kN) load was used with an ultimate strength analysis.

To further determine a more accurate MASH TL-4 design impact load, multiple processes were explored including: (1) a combination of a mass-spring model and a mathematical model described in NCHRP Report No. 86 (Equation 5) [62]; (2) Newton's second law of motion (Equation 6); (3) NCHRP Report No. 86 equations to compute lateral accelerations and average lateral impact force (Equations 3-4), however, including a dynamic increase factor of $\pi/2$; and (4) LS-DYNA computer simulation.

$$F_2 = F_1 \left(\frac{V_2}{V_1} \right)^2 \left(\frac{\sin\theta_2}{\sin\theta_1} \right) \left(\frac{A_1 L_1}{A_2 L_2} \right) \sqrt{\frac{K_2}{K_1}} \sqrt{\frac{W_2}{W_1}} \quad (5)$$

Where: F_1 = Dynamic impact force of vehicle 1, kips (kN)
 F_2 = Dynamic impact force of vehicle 2, kips (kN)
 V_1 = Impact velocity of vehicle 1, ft/sec (m/s)
 V_2 = Impact velocity of vehicle 2, ft/sec (m/s)
 θ_1 = Impact angle of vehicle 1, degrees
 θ_2 = Impact angle of vehicle 2, degrees
 $A_1 L_1$ = Distance from the front of vehicle 1 to the center of mass, ft (m)
 $A_2 L_2$ = Distance from the front of vehicle 2 to the center of mass, ft (m)
 K_1 = Stiffness of vehicle 1
 K_2 = Stiffness of vehicle 2
 W_1 = Mass of vehicle 1, lb (kg)
 W_2 = Mass of vehicle 2, lb (kg)

$$F_{lat} = m a_{lat} \quad (6)$$

Where: F_{lat} = Lateral impact force
 m = Mass of vehicle, lb (kg)
 a_{lat} = Maximum lateral acceleration, g's

LS-DYNA computer simulation was used to investigate the MASH TL-4 peak lateral forces for vehicle impacts into a rigid vertical concrete wall. Various wall heights,

ranging between 36 in. (914 mm) and an infinitely tall wall, were explored in the simulation study. The peak load was determined using the command *CONTACT_FORCE_TRANSDUCER_PENALTY [24] along with a 50-msec moving average. From all of the methods noted above, including the design guide, the peak lateral loads ranged from 54 kips (240 kN) and 99 kips (440 kN), as shown in Table 4.

Table 4. Lateral Design Force Calculation Studies [63-64]

Method No.	Equation No.	Model/Method	Peak Load kip (kN)
1	5	Mass-Spring Model with NCHRP Report No. 86	80.3 (357)
2	6	Equation of Motion	99.0 (440)
3	3-4	Lat. Accel. to get Lat. Impact Force with DMF	78.5 (349)
4	NA	36 in. (914 mm) Tall Wall Simulation	67.2 (299)
4	NA	39 in. (991 mm) Tall Wall Simulation	72.3 (322)
4	NA	42 in. (1,067 mm) Tall Wall Simulation	79.1 (352)
4	NA	Tall Wall Simulation	93.3 (415)
NA	NA	AASHTO Bridge Recommendation	54.0 (240)

2.6.6 TTI Tall MSE Wall

In 2011, TTI researchers analyzed MSE wall panels as well as investigated crash wall configurations to determine whether a secondary barrier is needed to protect a MSE wall from vehicular impacts [66-67]. Before the MSE wall was crash-tested, the SUT simulation model needed to be modified to meet the MASH test vehicle specifications. The model previously met the NCHRP Report No. 350 requirements, but the mass of the SUT need to be increased, the impact speed needed to be increased, and the ballast height needed to be changed. Therefore, a validation of the SUT simulation model was performed with test no. 476460-1b on a rigid NJ shape concrete barrier [67-68].

Two different methods were used to calculate the impact forces from the simulation results. The first method used the contact forces, between the vehicle and the

barrier as determined by *CONTACT_FORCE_TRANSDUCER_PENALTY [24], both with and without a 50-msec moving average. The second method used the local lateral and longitudinal accelerations from the accelerometer placed at the c.g. of the vehicle coupled with the local yaw angles. The acceleration data was filtered using a SAE 60 Hz filter and a 50-msec moving average. Similarly using data from test no. 476460-1b, the lateral impact forces were calculated by using the lateral and longitudinal accelerations coupled with the yaw angles along with a 50-msec moving average. The comparison between these two methods and test no. 476460-1b are shown in Figure 27. The peak force imparted to the barrier during test no. 476460-1b was 83.9 kips (373 kN). The simulated peak forces imparted to the using accelerations coupled with the yaw data and contact forces were 90.1 kips (401 kN) and 60.8 kips (271 kN), respectively.

After validation, three models were run to determine the forces imparted to the MSE wall. The first model represented an impact with a typical section of a MSE wall. The other two models used the same MSE wall, but an additional wall was placed adjacent to the MSE. However, there were two different methods to represent the interaction between the MSE wall and the additional wall. The first method used contacts to essentially glue the MSE wall to an additional wall, and the second used simulated embedded anchors between the MSE wall and additional wall. The impact forces were determined from the contact forces between the vehicle and the impacted wall and were filtered with a SAE 60 Hz filter.

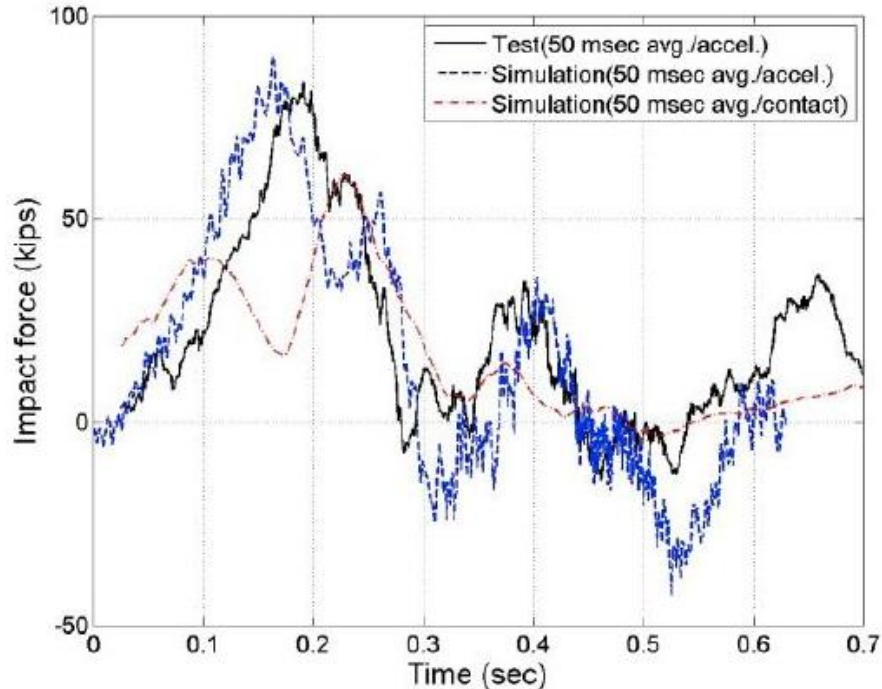


Figure 27. Comparison of Lateral Impact Loads – Simulation and TTI Test No. 476460-1b

There were three distinct peak forces shown in the first case where the SUT impacted the MSE wall directly. The peak forces were 73.3 kips (326 kN) when the left-front bumper contacted the wall, 131.1 kips (584 kN) when the left-front of the box contacted the wall, and 134.2 kips (597 kN) when the left-rear contacted the wall, as shown in Figure 28a.

There were three distinct peak forces shown in the second case where the SUT impacted the crash wall placed next to the MSE wall and used contacts defined in LS-DYNA. The peak forces were 94.8 kips (422 kN) when the left-front bumper contacted the wall, 129.2 kips (575 kN) when the left-front of the box contacted the wall, and 331.9 kips (1,476 kN) when the left-rear contacted the wall, as shown in Figure 28b.

There were three distinct peak forces shown in the third case where the SUT impacted the crash wall placed next to the MSE wall and used embedded anchors to

support the wall. The peak forces were 100.9 kips (449 kN) when the left-front bumper contacted the wall, 130.3 kips (580 kN) when the left-front of the box contacted the wall, and 362.2 kips (1,611 kN) when the left-rear contacted the wall, as shown in Figure 28c.

2.6.7 TTI Simulation on TL-4 Impact Loads

In 2011, TTI researchers investigated single-unit truck impacts into rigid concrete barriers under MASH TL-4 impact conditions with LS-DYNA [22-23]. Multiple rail heights were explored to determine the lowest height that would safely contain and redirect the updated MASH SUT vehicle. Rail heights of 42, 39, 38, 37 and 36 in. (1,067, 991, 965, 940, and 914 mm) were simulated, and vehicle stability and impact forces were accessed using the simulations. The lateral impact forces were obtained by summing the lateral contact forces applied to the barrier by the SUT and then taking a 50-msec moving average of the data. The peak forces for the 36-, 39- and 42-in. (914-, 991-, and 1,067-mm) tall barriers were approximately 67, 73, and 81 kips (298, 325, and 360 kN), respectively, as shown in Figure 29. From the study, the peak impact force increased as the height of the barrier increased. Thus, researchers conservatively selected a lateral design load of 80 kips (356 kN).

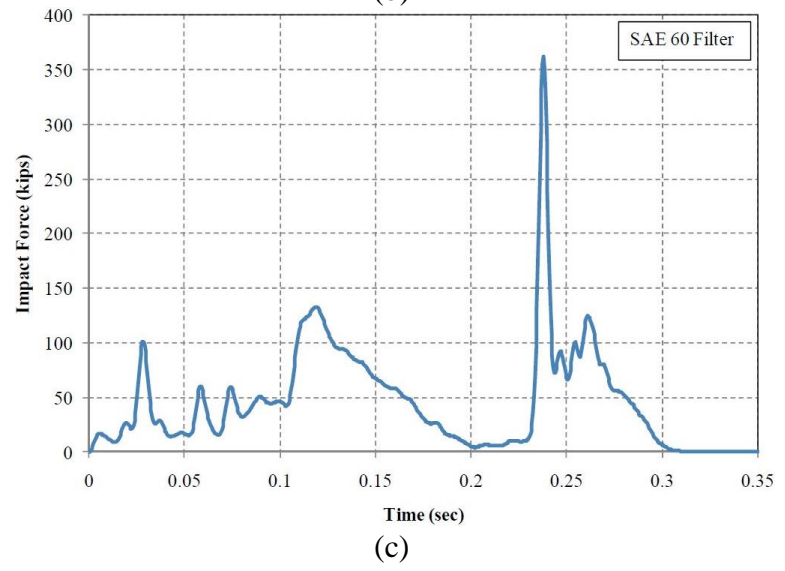
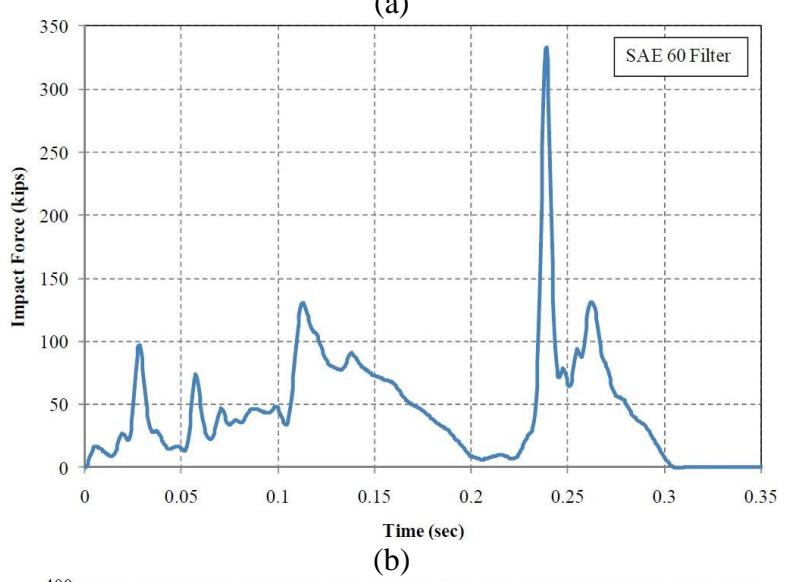
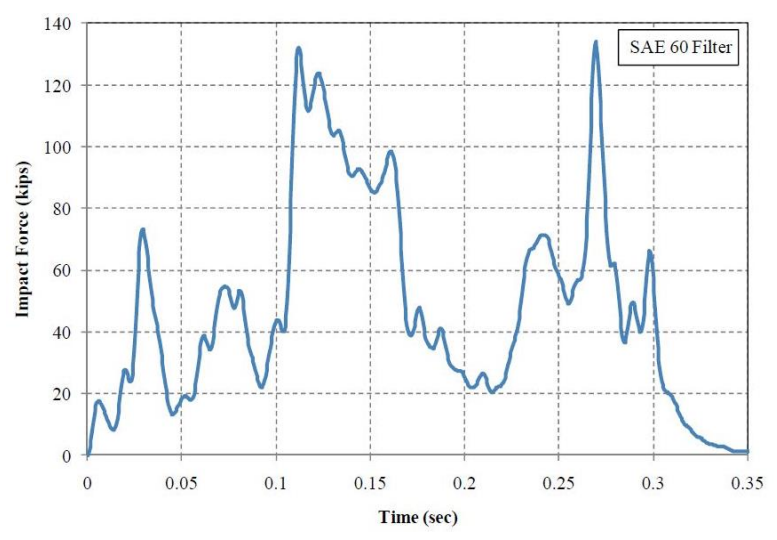


Figure 28. SUT Impact Forces on MSE Wall from Simulation [66]

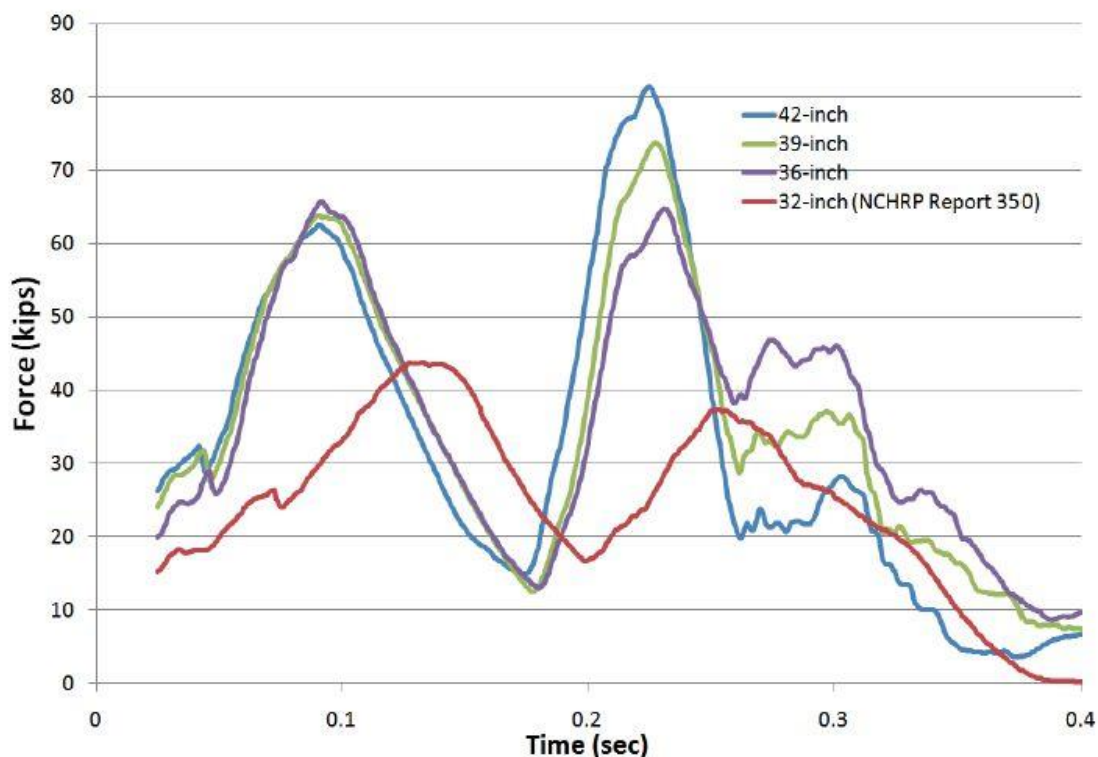


Figure 29. Lateral Impact Forces rom Simulation Contact with 50-msec Average [22-23]

2.6.8 MwRSF RESTORE Barrier

Numerical approximations, scaling of NCHRP Report No. 350 crash test results, and computer simulations were used to estimate an appropriate design impact load for a MASH TL-4 concrete barrier, as described in Chapter 2.6.4. Similarly, TTI researchers recommended that a lateral design load of 80 kips (356 kN) be used to design TL-4 bridge rails, as described in Chapter 2.6.7. Thus, an original lateral design load of 80 to 100 kips (356 to 445 kN) was used for initially configuring the barrier using an assumption that any dynamic barrier deflection would reduce peak lateral loading. Simulation between an initial barrier design with elastomer shear fenders was compared to a baseline simulation of a rigid, single-slope concrete barrier, as shown in Figure 30. Since the simulation showed lower forces than what was expected for the targeted barrier

concept, a reduced impact load of 75 kips (334 kN) was used for configuring the RESTORE barrier under SUT impacts [16-17].

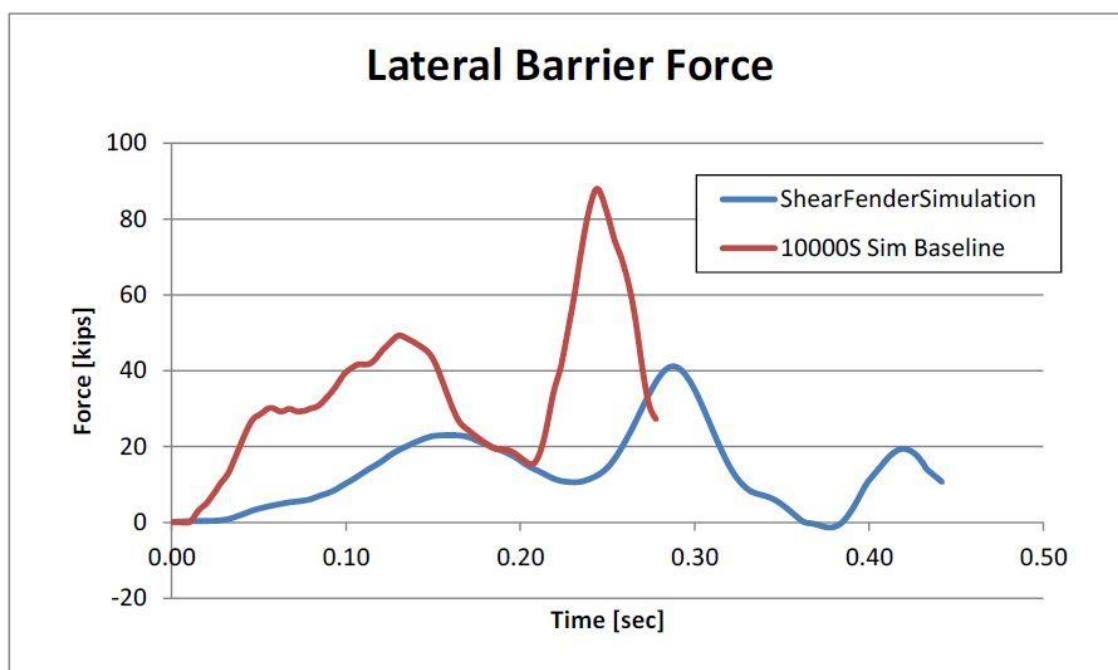


Figure 30. SUT Lateral Barrier Forces, Rigid Single-Slope Concrete Barrier vs. Original RESTORE Barrier Simulation [16-17]

2.6.9 AASHTO Update to MASH Design Loads

On August 17, 2015, AASHTO presented a webinar update on a AASHTO/FHWA joint implementation plan regarding the MASH safety performance criteria [69]. Potential changes to bridge railing design guidelines were also discussed, including acceptable design loads and load application heights necessary to meet MASH TL-4 impact safety standards. Based on LS-DYNA simulations, TTI researchers suggested that a lateral design load of a 67.2 kips (299 kN) be used for a 36-in. (914-mm) tall, TL-4 barrier.

2.7 MASH TL-4 Barrier Heights

Concrete barrier heights have typically ranged from 32 to 42 in. (813 to 1,067 mm) for TL-4 and TL-5 systems, respectively. These heights have also been adequate for

passenger vehicles due to the center of gravity of those vehicles being below 30 in. (762 mm). However, taller vehicles, such as single-unit trucks, have a much higher center of gravity and increased risk of override for shorter barriers. Multiple barriers were successfully tested according to TL-4 of NCHRP Report No. 350. Due to the increased vehicle weight and impact speed for the SUT according to the standards in MASH, further research was needed to investigate minimum barrier heights under MASH TL-4 impact conditions.

2.7.1 Minimum MASH TL-4 Rail Height Using Simulation

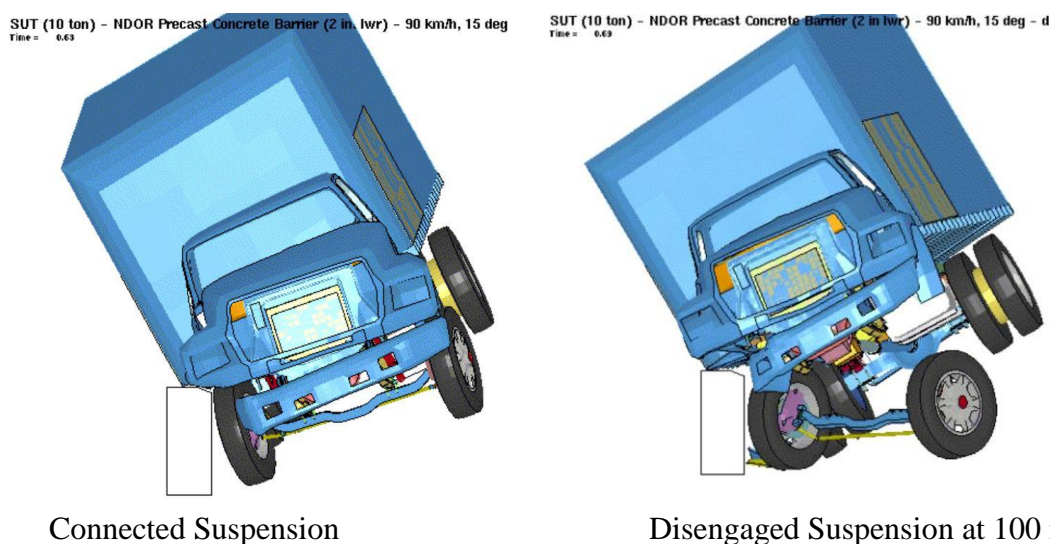
In 2006, MwRSF designed a new precast, aesthetic, concrete bridge rail that would meet the MASH TL-4 impact conditions [58]. For the design process, it was necessary to determine a barrier height that would successfully meet the updated guidelines listed in MASH. The single-unit truck found in NCHRP Report 350 weighed 17,637 lb (8,000 kg) and used a target speed of 50 mph (80 km/h). However, the single-unit truck found in MASH weighed 22,046 lb (10,000 kg) and used a target speed of 56 mph (90 km/h). These changes resulted in a 56 percent increase in impact severity and an increased risk for override on a 32-in. (813-mm) tall rigid barrier. Therefore, a simulation effort was utilized to determine the barrier height necessary to prevent barrier override.

The barrier geometry was modeled so that the vertical height could be easily changed between trials. If the initial simulation provided satisfactory results, then a second simulation was conducted at the same barrier height in which the suspension was disconnected from the front axle during impact. That type of damage was commonly observed in previous TL-4 full-scale crash tests, which could cause vehicle instabilities. From the simulation effort, a rigid, vertical barrier with a 34½ in. (876 mm) height was

deemed adequate for redirecting a single-unit truck and preventing barrier override, even with the disconnected suspension, as shown in Figure 31.

2.7.2 Minimum MASH TL-4 Rail Height Using Crash Testing

In 2011, TTI researchers conducted a research study to investigate the minimum rail height to safely withstand a TL-4 SUT impact condition according to the new MASH testing criteria [22-23]. Multiple models were run using LS-DYNA with barrier heights ranging from 36 in. (914 mm) to 42 in. (1,067 mm). The vehicle stability was reviewed with each barrier height, and a 36-in. (914-mm) tall barrier height was determined to be the shortest barrier to successfully contain and redirect the vehicle while satisfying the MASH criteria. Note that barrier heights lower than 36 in. (914 mm) were not simulated. Therefore, a 36-in. (914-mm) tall barrier was constructed and subjected to full-scale crash testing. Researchers conducted a yield-line analysis on the Texas single-slope concrete barrier under the TL-4 impact conditions. The barrier was deemed capable of withstanding a lateral load of 80 kips (356 kN). Following the full-scale crash test, the barrier was found acceptable according to the MASH TL-4 testing criteria.



Connected Suspension
Disengaged Suspension at 100 ms
Figure 31. 10000S SUT Vehicle Impacting 34½-in. (816-mm) Tall, Rigid Vertical Barrier [22-23]

2.8 Concrete Barrier Design Methodologies

2.8.1 Yield-Line Theory

In 1978, Hirsch developed a procedure, based on yield-line theory described in advanced reinforced concrete textbooks to determine the ultimate redirective capacity of a concrete buttress [70]. The yield-line theory calculated the ultimate redirective capacity of a barrier by treating it like a flat slab and using the conservation of energy principle with an assumed failure shape. The external work, or energy applied to the barrier system, is equivalent to the impact load multiplied by a displacement. The internal energy absorbed is calculated as the sum of the bending moments multiplied by the displacement angle along each edge of the predicted failure shape, also called yield lines [56,70]. From previous research and observation, the predicted yield lines are generally a saw tooth shape, as shown in Figure 32. The redirective capacity of different barriers were found by calculating the critical length of the failure shape and then the redirective capacity of the barrier as a function of the individual bending moments combined with the critical length, as shown in Equations 7 and 8 for internal regions.

$$L_c = \frac{L_t}{2} + \sqrt{\left(\frac{L_t}{2}\right)^2 + \frac{8H(M_b + M_w H)}{M_c}} \quad (7)$$

$$R_w = \frac{8M_b}{L_c - \frac{L_t}{2}} + \frac{8M_w H}{L_c - \frac{L_t}{2}} + \frac{M_c L_c^2}{H \left(L_c - \frac{L_t}{2}\right)} \quad (8)$$

Where: L_c = Critical wall length over which the yield line mechanism occurs

L_t = Longitudinal length of distribution of impact force (ft)

M_c = Ultimate flexural resistance of wall about horizontal axis (kip-ft/ft)

M_b = Ultimate moment capacity of beam at top of wall (kip-ft)

M_w = Ultimate flexural resistance of wall about vertical axis (kip-ft/ft)

H = Height of wall (ft)

R_w = Nominal railing redirective capacity to transverse loads

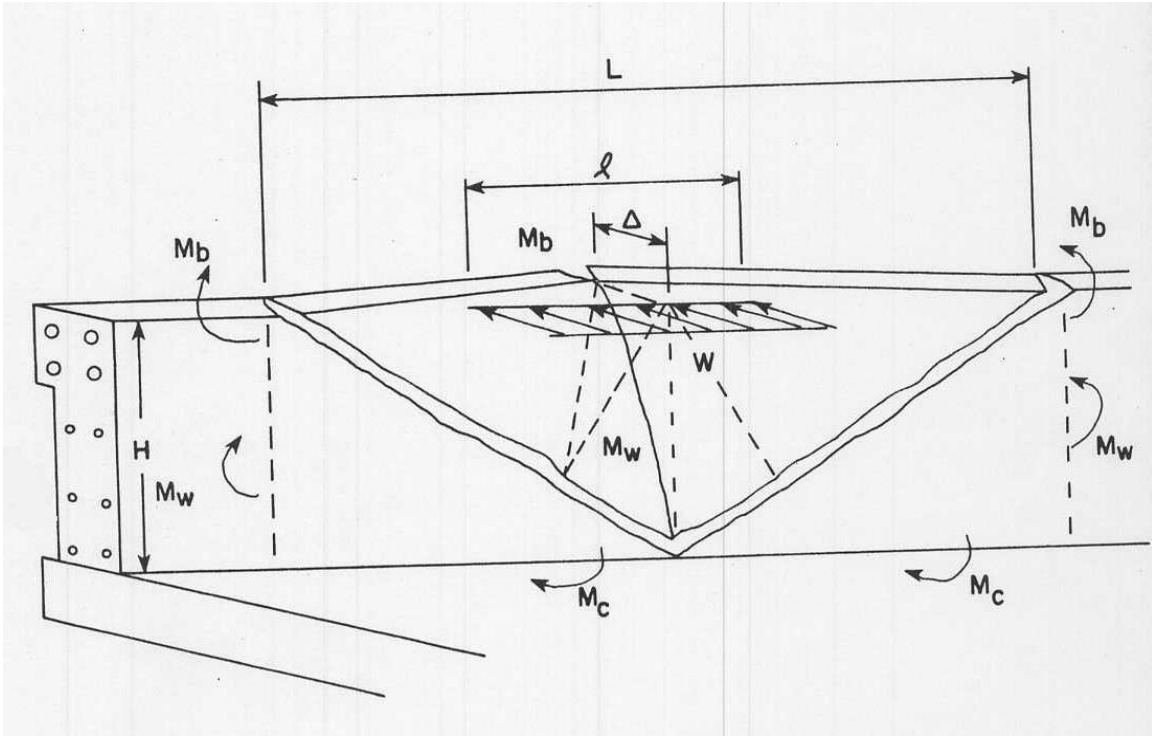


Figure 32. Yield-Line Failure Shape with Bending Moments [9-11,56,70]

The redirective capacity of a barrier can also be calculated at end sections using a similar process to that noted above but with modified equations [56,70]. The only difference is that the saw tooth shape is cut in half to resemble a single fracture line. The modified equations are then used to find the critical length and the ultimate strength, as shown in Equations 9 and 10.

$$L_c = \frac{L_t}{2} + \sqrt{\left(\frac{L_t}{2}\right)^2 + H \frac{(M_b + M_w H)}{M_c}} \quad (9)$$

$$R_w = \frac{M_b}{L_c - \frac{L_t}{2}} + \frac{M_w H}{L_c - \frac{L_t}{2}} + \frac{M_c L_c^2}{H \left(L_c - \frac{L_t}{2}\right)} \quad (10)$$

2.8.2 Torsional Resistance Footer Design

During an impact, the barrier will transfer load into the footing by both lateral shear and moment about the longitudinal axis. By extending stirrups from the barrier into

the footing, the shear is transferred from the barrier to the footing, and finally to the soil around the barrier. Thus, lateral shear is not a major design concern for the footing. The moment about the longitudinal axis, or the barrier overturning resistance, becomes torsion when transferred to the footing. This torsion was the critical design load for the footing.

Therefore, the design of a footer utilized a modified process to ensure that sufficient torsional resistance was provided to match the overturning moment of the end section [9-11,71]. Other design loads, including the moment capacity of the beam or the flexural resistance about the vertical axis, did not need to be applied. Therefore, the cantilever moment per unit length of the barrier, M_c , was multiplied by the critical length, L , to obtain the torsion load on the footer. The torsion load was then divided by a strength reduction factor of $\phi=0.75$ to obtain the design load for the footer. The torsion strength of the concrete would be subtracted out and the steel reinforcement would be designed to carry the remainder of the load by following the standards listed in the American Concrete Institute (ACI) manual [72].

3 RESTORE BARRIER OVERVIEW

3.1 Introduction

Previous research was conducted by Schmidt, et al. to design and evaluate various reusable energy-absorbing components for use in a restorable barrier system [16-21]. An intensive search identified several different energy-absorbing materials and components. Elastomer was selected as the preferred material for the energy-absorbing components. Biaxial extension, planar tension, and simple tension were conducted on ethylene propylene diene monomer (EPDM) and AASHTO D2000 elastomer coupons to determine the force vs. deflection, engineering stress vs. strain, and bulk and shear moduli. The material properties obtained from the physical testing were implemented into elastomer material models for simulation of the tests in order to select the most accurate material model. Selected energy-absorber components were physically tested, and the results were compared to LS-DYNA simulations. Additionally, prototype barrier designs were evaluated, and the preferred concept was successfully evaluated according to MASH TL-4 safety performance criteria.

3.2 Coupon Material Testing and Simulation

Initial simple tensile testing provided the necessary material properties for the EPDM elastomer. In order to simulate the EPDM, a material model needed to be selected. There are several elastomer material formulation models in LS-DYNA [24]. However, Schmidt et al. selected the following to be evaluated with the EPDM elastomer:

MAT_BLATZ-KO_RUBBER (MAT_007)
MAT_MOONEY-RIVLIN_RUBBER (MAT_027)
MAT_FRAZER_NASH_RUBBER_MODEL (MAT_031)
MAT_HYPERELASTIC_RUBBER (MAT_077_H)

MAT_OGDEN_RUBBER (MAT_077_O)
MAT_CELLULAR_RUBBER (MAT_087)
MAT_ARRUDA_BOYCE_RUBBER (MAT_127)
MAT_SIMPLIFIED_RUBBER/FOAM (MAT_181)
MAT_SIMPLIFIED_RUBBER_WITH_DAMAGE (MAT_183)

Solid elements were preferred over shell elements to model the complicated geometries of the energy absorbers. However, there were hourglassing and inconsistencies with the constant-stress solid elements that were used during initial simulations with the EPDM elastomer. Hexahedral elements were considered, but they could also deform with hourglassing. Therefore, one-point, nodal-pressure, tetrahedron elements were recommended for use; because, they deformed well, couldn't hourglass, and the forces accurately represented the tension tests.

Using the one-point, nodal-pressure, tetrahedron elements and 80 durometer EPDM elastomer, most of the material model simulations followed the tensile forces and were only slightly higher than the actual tensile tests. However, the Simplified Rubber/Foam material model was the most accurate at modeling the elastomers in tension through the evaluation process.

Three loading cases – biaxial extension, planar tension, and simple tension – were conducted using D2000 elastomer coupons. Each loading case was tested at various strains between 25 and 150 percent. The stress vs. strain for the three different types of loading at 100 percent strain are shown in Figure 33. The shear modulus was calculated to be 88 psi (0.616 MPa).

Since the A2000 elastomer was the selected material for the shear fenders, a simulation effort was performed to determine the most accurate material model. The models were formulated with one-point, nodal-pressure, tetrahedron elements. Multiple

material formulations were evaluated through LS-DYNA simulation. The first selected material model was the Blatz-Ko material model. It was used due to it being the most basic rubber model in LS-DYNA. The only material properties that are input into the model are shear modulus and mass density, where the model assumes the Poisson's ratio of 0.463. The Ogden model was considered, because it allowed for multiple inputs to be included. Therefore, three types of experimental test data could be input into the model including: uniaxial tensile data; biaxial data; and pure shear data. With the inputted test data, the model would perform a curve fitting with the Poisson's ratio set to 0.495. The shear and compression models were not important when modeling the tension tests. However, they were important to consider for energy-absorber simulations. Lastly, the Simplified Rubber/Foam material model was selected, because it performed the best during previous simulations with the EPDM rubber. Similar to the Ogden, tensile test data could be input into the material model. However, this material formulation does not use a strain-energy density function to curve fit the data as used by the Ogden model.

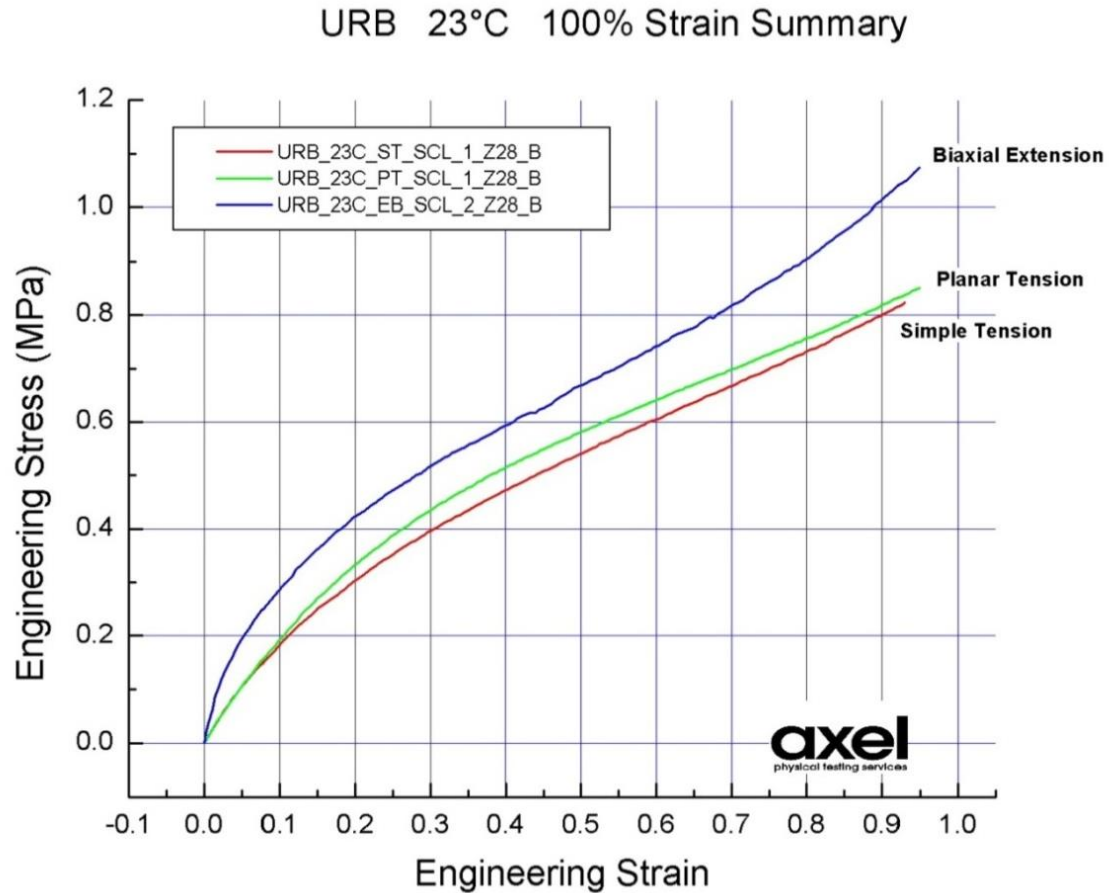


Figure 33. Summary of Material Tests at 100 Percent Strain

The stress vs. strain for each of the material models was compared to the tension test, as shown in Figure 34. The Ogden material model with tension test data input and the Simplified Rubber/Foam material model compared very well to the test data. However, the Simplified Rubber/Foam model was selected to be the most promising and would be further investigated with other load scenarios through component test simulations.

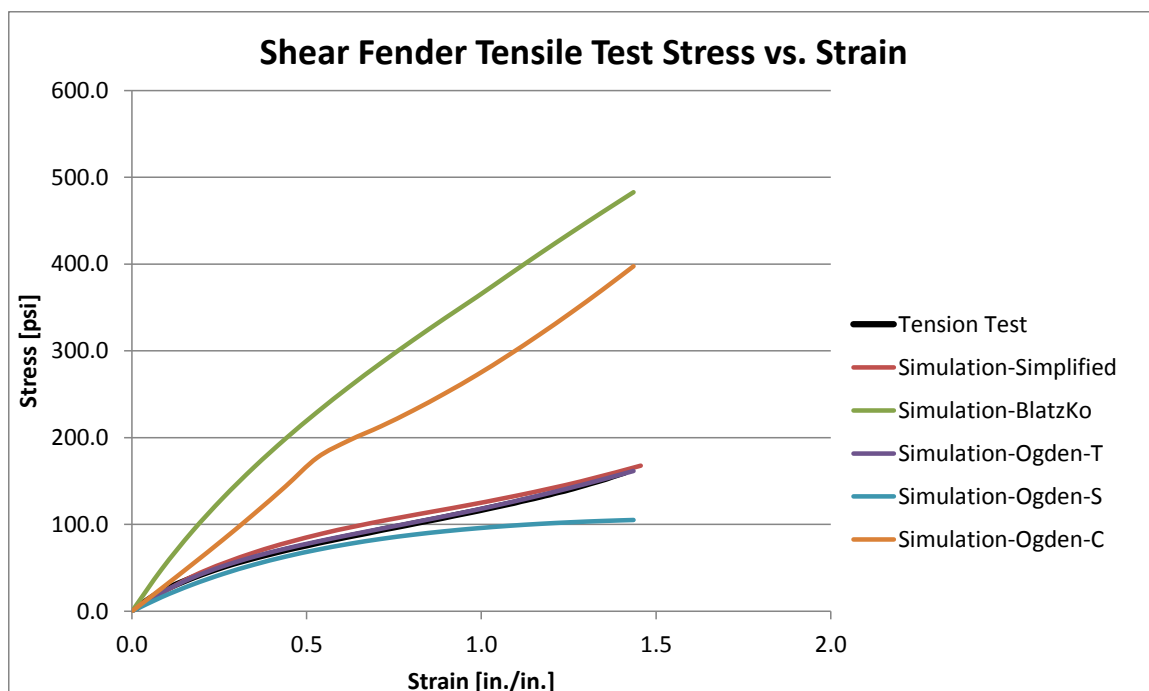


Figure 34. Simulation of Shear Fender Tensile Test – Stress vs. Strain

3.3 Individual Component Testing

3.3.1 Introduction

Dynamic component tests were conducted to verify energy absorber simulations and to evaluate energy dissipation. Approximately 52.8 to 211.2 k-in. (6.0 to 23.9 kJ) of kinetic energy per energy absorber was estimated by Schmidt, et al. [16-17] to be necessary to achieve the desired acceleration reductions.

LS-DYNA simulation was used to assist in the selection of the shapes that would be further explored with physical testing. Multiple shapes were considered including cone, cylinder, and shear fender. The cone-shaped energy absorber was simulated. However, a physical component test was required to validate component behavior, and there existed limited availability of pre-made conical fender sizes. Therefore, conical fenders were not further investigated.

Twelve EPDM elastomer cylinders with thicknesses of either 1 or 2 in. (25 or 51 mm) and durometer of either 60 or 80 were component tested. All of the EPDM cylinders absorbed less energy than what was desired. The 2-in. (51-mm) thick cylinders were not loaded to their maximum deflection, so they were expected to absorb significantly more energy if impacted with a larger load. However, they did not satisfy the original design goal to create a new barrier system, and not retrofit an existing barrier. Therefore, they were not selected for further evaluation.

3.3.2 16-in. (406-mm) Tall Elastomer Shear Fenders

Elastomer shear fenders were investigated for use in the barrier. Five component tests were conducted 16-in. high x 14-in. wide x 22-in. long (406-mm x 356-mm x 559-mm) shear fenders, as shown in Figure 35. The elastomer was 50- to 55-durometer AASHTO D2000. The shear fenders were loaded along the lateral and longitudinal axes.

Three of the five tests showed that the shear fenders absorbed energies within the desired range, as shown in Table 5. The laterally-impacted shear fender deflected almost 1 in. (25 mm) farther than the longitudinally-impacted shear fender, but it did not absorb additional energy, as shown in Table 5 and Figure 36. Therefore, the shear fenders were recommended for further evaluation along the longitudinal axis.



Figure 35. Maritime International, Inc. HSF-14 Marine Shear Fender [16-18]

Table 5. Shear Fender Dynamic Testing Results [16-18]

Test No.	Bogie Weight		Impact Direction	Surface Temp		Impact Velocity		Max. Deflection		Peak Force		Total Energy	
	lb	(kg)		^o F	(^o C)	mph	(km/h)	in.	(mm)	kip	(kN)	k-in.	(kJ)
HSF14-1	1818	(825)	Lateral	84	(52)	4.9	(8)	6.2	(157)	12.1	(54)	17.8	(2.0)
HSF14-2	1818	(825)	Longitudinal	73	(41)	5.0	(8)	5.3	(135)	13.0	(58)	18.2	(2.1)
HSF14-3	1818	(825)	Longitudinal	66	(34)	9.1	(15)	10.5	(267)	26.5	(118)	60.5	(6.8)
HSF14-4	1818	(825)	Longitudinal	75	(43)	14.3	(23)	37.3	(947)	42.9	(191)	149.7	(16.9)
HSF14-5	4946	(2243)	Longitudinal	138	(106)	11.9	(19)	28.5	(724)	41.2	(183)	268.4	(30.3)

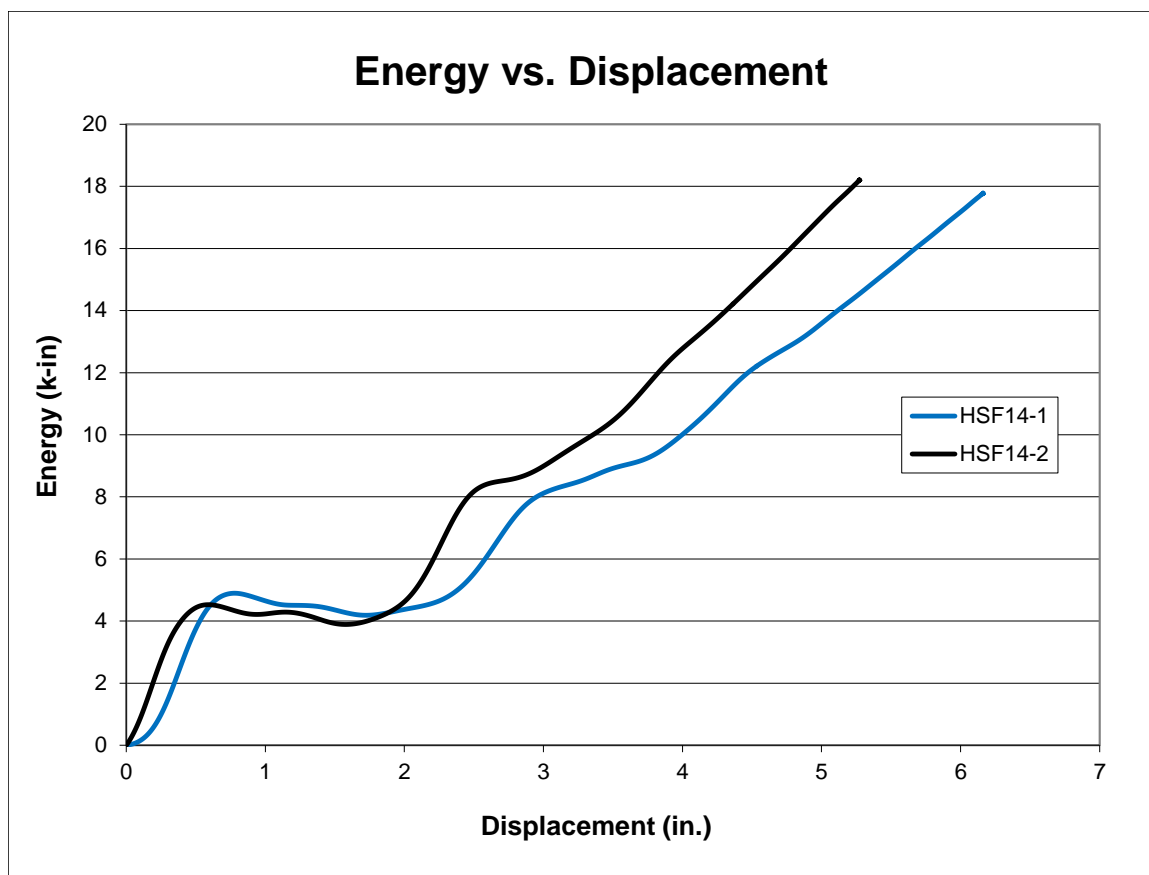


Figure 36. Energy vs. Deflection Comparison Plot, Test Nos. HSF14-1 and HSF14-2 [16-18]

3.3.3 11 $\frac{5}{8}$ -in. (295-mm) Tall Elastomer Shear Fenders

During the study, a smaller shear fender was selected to lower the bottom height of the concrete rail when placed on top of the elastomer posts to mitigate post snag. As such, dynamic component testing was used to evaluate the new shear fenders. A total of nine dynamic bogie tests were conducted on a shear fender with dimensions of 11 $\frac{5}{8}$ in. tall x 10 in. wide x 15 $\frac{3}{4}$ in. long (295 mm x 254 mm x 400 mm) with a 4-in. (102-mm) diameter hole lengthwise through the shear fender. All of the tests were conducted with the post loaded longitudinally, which is parallel to the length of the hole. Seven of the bogie tests were without a steel pipe positioned through the longitudinal hole, and test

nos. SF10P-1 and SF10P-2 were with a 3½-in. (89-mm) diameter pipe placed through the longitudinal hole.

The results from the bogie testing program are summarized in Tables 6 and 7. The energy that was absorbed by the 16-in. (406-mm) tall shear fenders varied from 1.5 to 1.9 times greater than the 11½ (295-mm) tall posts at 4, 6, 8 and 10 in. (102, 152, 203, and 254 mm) of deflection. Since the energy absorbed by the smaller post was almost half as much as the larger post, the post spacing was chosen to be 5 ft (1.5 m) so that the system with the smaller posts would absorb approximately the same energy as the system with the larger posts at 10 ft (3.0 m) spacing.

Table 6. Dynamic Testing Results – All Component Tests [19]

Test No.	Bogie Weight lb (kg)	Impact Velocity mph (km/h)	Max. Deflection in. (mm)	Peak Force kips (kN)
SF10-1	1,854 (841)	6.3 (10.1)	8.4 (213)	17.1 (76.1)
SF10-2	1,854 (841)	8.0 (12.9)	11.7 (297)	18.4 (81.8)
SFD-1	1,886 (855)	11.1 (17.8)	17.8 (452)	24.8 (110.3)
SFD-2	1,886 (855)	8.2 (13.2)	11.8 (300)	25.2 (112.1)
SFD-3	1,886 (855)	8.6 (13.9)	13.5 (343)	19.3 (85.9)
SFD-4	1,886 (855)	8.4 (13.5)	13.5 (343)*	15.4 (68.5)
SFD-5	1,886 (855)	8.6 (13.9)	14.2 (361)	19.2 (85.4)
SF10P-1	1,886 (855)	6.6 (10.6)	9.9 (251)	13.8 (61.4)
SF10P-2	1,886 (855)	9.5 (15.3)	14.6 (371)	21.2 (94.3)

*taken from film analysis

Table 7. Dynamic Testing Results – All Component Tests, Continued [19]

Test No.	Energy at Deflection k-in. (kJ)				Total Energy k-in. (kJ)
	4 in. (102 mm)	6 in. (152 mm)	8 in. (203 mm)	10 in. (254 mm)	
SF10-1	11.0 (1.2)	18.2 (2.1)	27.4 (3.1)	NA	29.4 (3.3)
SF10-2	11.9 (1.3)	17.4 (2.0)	26.2 (3.0)	36.9 (4.2)	47.4 (5.4)
SFD-1	13.0 (1.5)	23.1 (2.6)	27.7 (3.1)	37.6 (4.2)	93.0 (10.5)
SFD-2	17.9 (2.0)	22.8 (2.6)	31.6 (3.6)	41.1 (4.6)	51.0 (5.8)
SFD-3	12.6 (1.4)	19.5 (2.2)	27.2 (3.1)	36.1 (4.1)	56.1 (6.3)
SFD-4	9.1 (1.0)	15.7 (1.8)	23.2 (2.6)	30.8 (3.5)	52.9 (6.0)
SFD-5	10.2 (1.2)	17.0 (1.9)	23.9 (2.7)	32.3 (3.6)	56.3 (6.4)
SF10P-1	9.4 (1.1)	15.4 (1.7)	23.4 (2.6)	NA	32.5 (3.7)
SF10P-2	12.4 (1.4)	20.8 (2.4)	28.5 (3.2)	38.5 (4.3)	68.2 (7.7)

3.4 Component Testing Simulation

Simulations of test no. HSF14-4 were used to select a LS-DYNA elastomer material model. An existing bogie model was modified to be similar to the bogie vehicle used in test no. HSF14-4. The elastomer was meshed with one-point, nodal-pressure, tetrahedron solid elements. Two different elastomer material models were considered: the Simplified Rubber/Foam from performing the best previously and Blatz-Ko from being the most basic material model in LS-DYNA. The two parameters that were adjusted in the models were the material model properties and the friction between the impact head and the steel impact structure attached to the shear fender. Both of the material models showed similar results. Since tensile test data was obtained, the Simplified Rubber/Foam model was selected as the best fit and was used within future models.

3.5 Sub-System Testing

A small-scale system was tested involving four shear fenders, acting as posts with a timber beam placed on top as the rail [18]. The system was impacted between the

middle two posts. The shear fenders used in this test were 10 in. wide x $11\frac{5}{8}$ in. tall x $15\frac{3}{4}$ in. long (254 mm x 295 mm x 400 mm). The shear fenders were spaced at 8 ft (2.4 m), as shown in Figure 37.

The 4,871-lb (2,209-kg) bogie impacted the small-scale system at 15.2 mph (24.5 km/h). The maximum deflection was found to be 35 in. (889 mm), which was right before the timber beam fractured. As the system was impacted, each of the four elastomer posts rotated, deflected, and absorbed energy differently during the impact event, as shown in Table 8. The bogie's kinetic energy was absorbed by the system primarily through the deflection of the elastomer shear fenders bending and the fracture of the timber beam.



Figure 37. Bogie Test Setup for Beam and Shear Fenders, Test No. SFHT-1 [18]

Table 8. Elastomer Shear Fender Deflection and Energy Absorption, Test No. SFHT-1

Shear Fender No.	Deflection in. (mm)	Energy Absorption k-in. (kJ)
1	13.5 (343)	45 (5.1)
2	21.8 (554)	115 (13.0)
3	23 (584)	115 (13.0)
4	16.3 (414)	70 (7.9)

The energy absorbed by the shear fenders alone was estimated to be 345 k-in. (39 kJ) in the test, which was 76 percent of the total energy absorbed by the barrier. It was believed to be a reasonable estimate of the energy-absorbing capacity of the shear fenders and a preliminary evaluation of the beam and post concept. However, an optimized rail and splice was desired to better distribute the impact load to multiple shear fenders, so that the barrier could reduce lateral accelerations up to 30 percent as compared to impacts with a rigid barrier.

3.6 Interior System Moment Connection

Several rounds of static load testing with a concrete beam on top of elastomer shear fenders found the optimal weight for a 20-ft (6.1-m) long rail segment to be approximately 320 lb/ft (467 kg/m), excluding bolts, nuts and washers, with 1 1/8-in. (295-mm) tall posts spaced at 5 ft (1.5 m) center to center. A hybrid steel and precast concrete rail was optimized to meet the height and provide a structural capacity of 2,250 kip-in. (225 kN). Moment and shear continuity was desired between adjacent precast concrete barriers to distribute the impact force across multiple shear fenders. Therefore, the concrete rail splice was designed to meet several criteria: (1) provide continuity to the concrete rail; (2) provide a structural capacity greater than that provided by the rail; (3) accommodate construction tolerances (4) provide a smooth front and back face for aesthetics and to reduce snag potential; and (5) not interfere with concrete rail

reinforcement. The preferred rail splice would be robust, reduce relative rotation angles at beam ends, and provide the lowest dynamic barrier deflection.

Several splices were considered, including: splice plates on the top and bottom faces; splice tubes at the center of the top and bottom faces; a cross-bolted connection (X-connection) through the front and back faces, which was originally developed at the Texas A&M Transportation Institute (TTI) as a connection between temporary concrete barriers [73]; and a wedge-shaped connection through the front and back faces, denoted as the Adjustable Continuity Joint (ACJ).

Each of the concepts was simulated using LS-DYNA, and the X-connection and the ACJ provided the lowest dynamic deflections, as shown in Figure 38. However, the cross-bolted connection required 1¾-in. (44-mm) diameter bolts to provide adequate strength and larger bolt holes and cavities in the concrete to accommodate construction tolerances. These aspects hindered the placement of internal steel reinforcement and created voids on the front and back rail faces. The ACJ also had open hardware on the front and back faces of the rail. However, a cover plate could be designed to cover the exposed hardware. The ACJ was selected for use in the barrier system, which was designed to have a nominal ½-in. (13-mm) gap and +/- ¼ in. (6 mm) of construction tolerances between adjacent barriers. The ACJ was designed with two 6-in. x 6-in. x ½-in. (152-mm x 152-mm x 13-mm) steel angles attached vertically to the front and back faces of the concrete beams with a total of eight 1-in. (25-mm) diameter bolts at each joint.

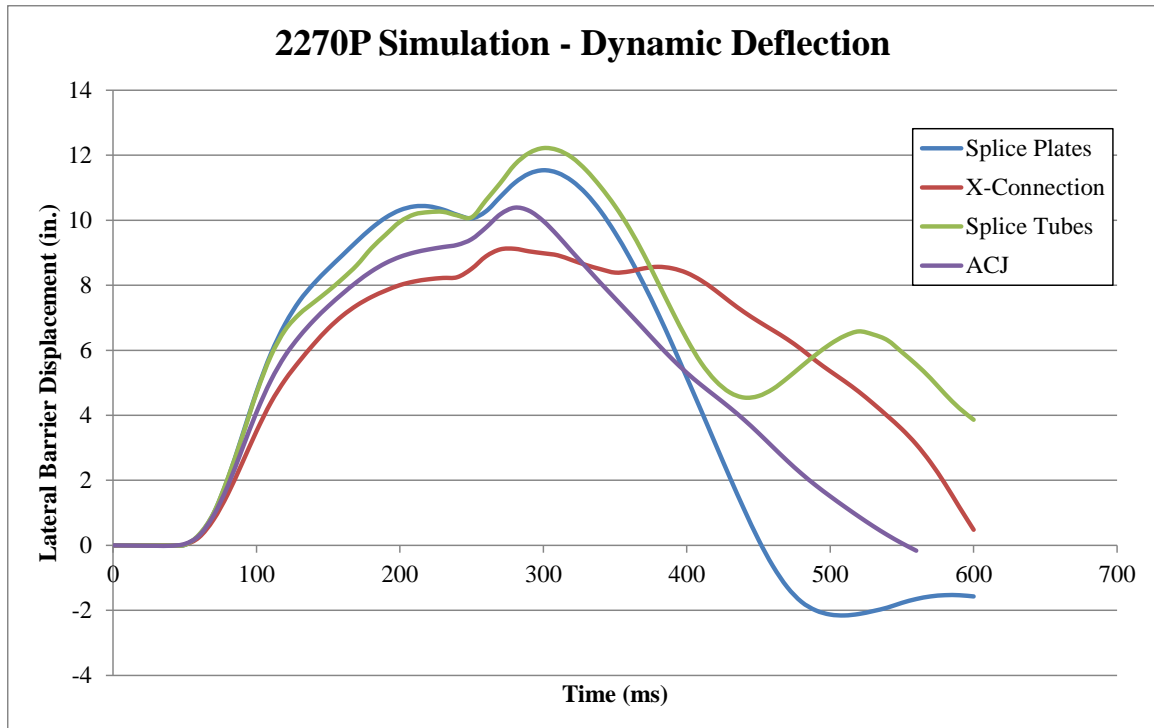


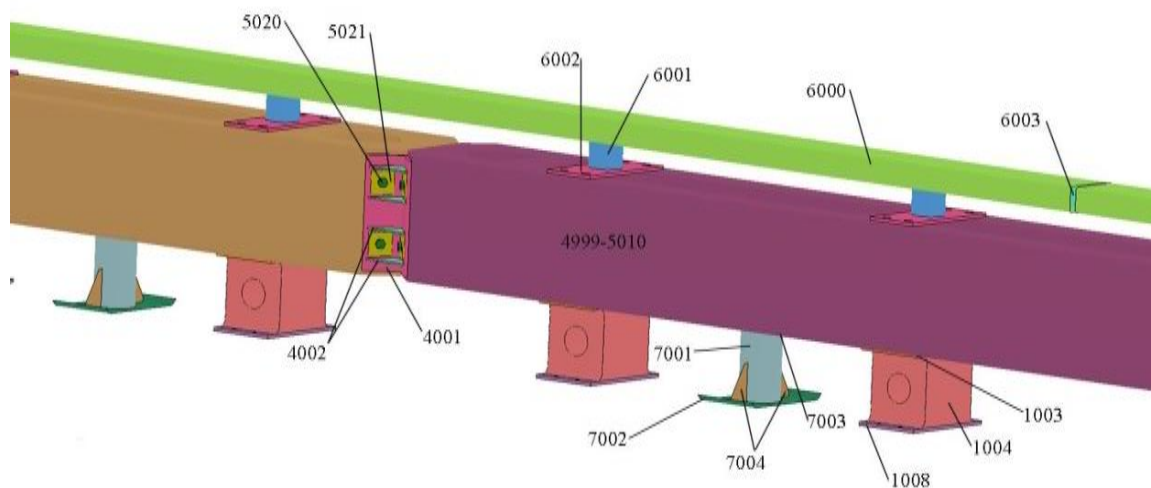
Figure 38. Simulated Dynamic Barrier Deflections with Varied Concrete Beam Splices – 2270P MASH TL-3 Condition [19]

3.7 LS-DYNA Simulations of Final Barrier Concept

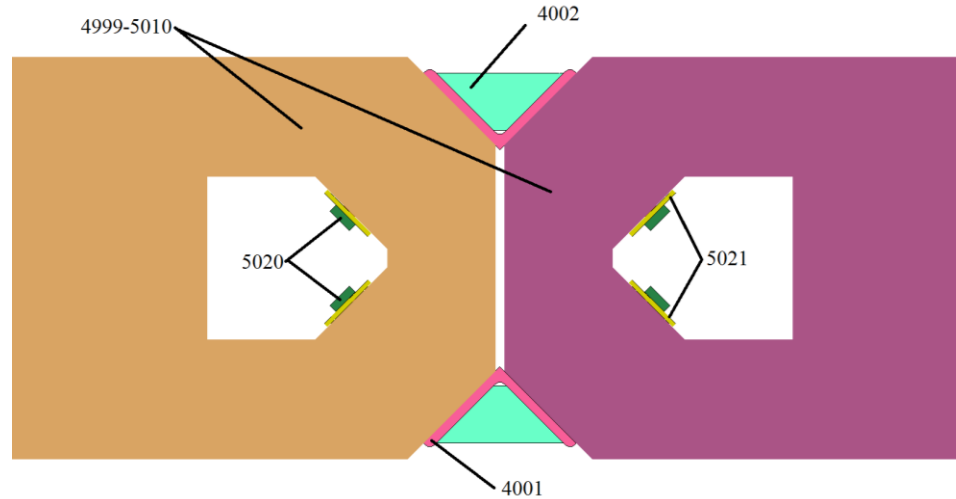
3.7.1 RESTORE Barrier Model

LS-DYNA simulation was performed to evaluate the safety performance and dynamic behavior of the prototype barrier system (i.e., RESTORE), which included precast concrete beams, an upper tubular steel beam and post system, the ACJ, elastomer shear fender posts, steel skids (or ski support posts), and various connection hardware. The general barrier configuration was depicted in Figures 5 and 6. The overall simulation model is shown in Figure 39.

The RESTORE barrier model, originally configured by Schmidt, et al. [19], was 240 ft (73 m) long. The primary barrier model parts are shown in Figure 39, and the associated parts, element types, and material models are shown in Table 9.



(a) Isometric View



(b) Top View at Concrete Beam Splice

Figure 39. RESTORE Barrier – Simulation Part Numbers: (a) Isometric View; and (b) Top View at Concrete Beam Splice [19]

Table 9. RESTORE Barrier Model Parts, Elements, and Materials [19]

Part Description	Simulation Part No.	Element Type	Material
Post - Top Steel	1003	Type 1 Solid	*MAT_PIECEWISE_LINEAR_PLASTICITY
Post - Elastomer	1004	Type 13 Solid	*MAT_SIMPLIFIED_RUBBER/FOAM
Post - Bottom Steel	1008	Type 1 Solid	*MAT_RIGID
ACJ Angle	4001	Type 2 Solid	*MAT_PIECEWISE_LINEAR_PLASTICITY
ACJ Gussets	4002	Type 2 Solid	*MAT_PIECEWISE_LINEAR_PLASTICITY
Concrete Beam	4999-5010	Type 2 Shell	*MAT_RIGID
Splice Bolt Heads/Nuts	5020	Type 2 Solid	*MAT_PIECEWISE_LINEAR_PLASTICITY
Splice Bolt Washers	5021	Type 2 Solid	*MAT_PIECEWISE_LINEAR_PLASTICITY
Splice Bolt Shafts	5022	Type 2 Solid	*MAT_PIECEWISE_LINEAR_PLASTICITY
Top Tubes	6000	Type 2 Shell	*MAT_PIECEWISE_LINEAR_PLASTICITY
Tube Posts	6001	Type 2 Shell	*MAT_PIECEWISE_LINEAR_PLASTICITY
Post Base Plates	6002	Type 1 Solid	*MAT_PIECEWISE_LINEAR_PLASTICITY
Tube Splices	6003	Type 2 Shell	*MAT_PIECEWISE_LINEAR_PLASTICITY
Skid Cylinder	7001	Type 2 Shell	*MAT_PIECEWISE_LINEAR_PLASTICITY
Skid Baseplate	7002	Type 2 Shell	*MAT_PIECEWISE_LINEAR_PLASTICITY
Skid Top Plate	7003	Type 2 Shell	*MAT_PIECEWISE_LINEAR_PLASTICITY
Skid Gussets	7004	Type 2 Shell	*MAT_PIECEWISE_LINEAR_PLASTICITY

The elastomer shear fenders were modeled with the material formulation *MAT_SIMPLIFIED_RUBBER/FOAM using the type 13 solid elements, as previously developed by Schmidt, et al. [16-17]. The concrete beams were modeled with type 2 rigid-shell elements that were free to move in all translational and rotational directions; since, significant damage to the concrete beams was not anticipated. Each concrete beam was assigned a separate part number from 4999 to 5010 and used *MAT_RIGID, and the translational mass, center of gravity location, and inertia properties were assigned for each beam as calculated in a 3D-CAD model.

The ACJ angle, ACJ gussets, splice bolt heads/nuts, splice bolt washers, and splice bolt shafts (part nos. 4001, 4002, 5020, 5021, and 5022) used type 2 fully-integrated, selectively-reduced, solid-element formulations to control the hourglass

energy along with *MAT_PIECEWISE_LINEAR_PLASTICITY. The post base plates (part no. 6002) had hourglass control type 3 to control the hourglass energy along with type 1 solid elements and *MAT_PIECEWISE_LINEAR_PLASTICITY.

The top and bottom of the elastomer posts (part nos. 1003 and 1008) used type 1 solid elements along with *MAT_PIECEWISE_LINEAR_PLASTICITY. The top tubes, tube posts, tube splices, skid cylinders, skid baseplate, skid top plate and skid gussets (part nos. 6000, 6001, 6003, 7001, 7002, 7003, and 7004) used type 2 shell elements along with *MAT_PIECEWISE_LINEAR_PLASTICITY.

For Schmidt's modeling effort, several parts were connected with merged nodes and are noted as follows:

- 1) top and bottom steel in the elastomer posts (part nos. 1003 and 1008) and the elastomer in the post (part no. 1004) to make the post a continuous part;
- 2) splice bolt heads/nuts (part no. 5020) and the splice bolt shaft (part no. 5022) to make continuous bolts;
- 3) ACJ angle (part no. 4001) and the ACJ gussets (part no. 4002), which is similar to welded parts with no failure;
- 4) tube posts (part no. 6001), post base plates, and top tubes (part nos. 6002 and 6000), which is similar to welded parts with no failure; and
- 5) skid parts (part nos. 7001, 7002, 7003, 7004).

Tied contacts were used between the concrete beams (part nos. 4999-5010) and the top steel in the elastomer posts (part no. 1003) as well as the post base plates (part no. 6002) to simulate the through-bolts. The bottom steel in the posts (part no. 1008) was constrained from all motion to simulate anchorage via threaded rods epoxied into concrete. The skid top plate was tied to the bottom of each beam rather than modeling the cylinder extending into the holes in the concrete beam.

The static and dynamic coefficients of friction defined in the contacts between the vehicles' bodies/tires and the barrier were as follows:

- 1) 0.1 for the 1100C Neon body and 0.3 for its tires;
- 2) 0.1 for the 2270P Silverado body and 0.1 for its tires;
- 3) 0.1 for the 10000S Ford Single-Unit Truck body and 0.1 for its tires; and
- 4) 0.3 for the bottom of the skids and the ground.

The static and dynamic coefficients of friction defined as surface-to-surface contacts between the ACJ, washers, and bolt heads were 0.3.

3.7.2 TL-4 MASH Longitudinal Barrier Impact Requirements and Evaluation Criteria

Three full-scale vehicle crash tests are recommended for evaluating longitudinal barriers according to the MASH TL-4 safety performance criteria [15]. According to TL-4 of MASH, longitudinal barrier systems must be subjected to three full-scale vehicle crash tests. Further detail can be found in Appendix A. The three full-scale crash tests are as follows:

1. Test Designation No. 4-10 consists of a 2,425-lb (1,100-kg) passenger car impacting the system at a nominal speed and angle of 62 mph (100 km/h) and 25 degrees, respectively.
2. Test Designation No. 4-11 consists of a 5,000-lb (2,268-kg) pickup truck impacting the system at a nominal speed and angle of 62 mph (100 km/h) and 25 degrees, respectively.
3. Test Designation No. 4-12 consists of a 22,046-lb (10,000-kg) single-unit truck impacting the system at a nominal speed and angle of 56 mph (90 km/h) and 15 degrees, respectively.

3.7.3 Simulation Results

In lieu of full-scale crash testing, the MASH required impacts were initially simulated using LS-DYNA. The vehicle models used during Schmidt's final LS-DYNA

simulation effort consisted of the 1100C Dodge Neon model developed by the National Crash Analysis Center (NCAC) [74] and modified by MwRSF, the 2270P Chevrolet Silverado model developed by NCAC [75-76] and modified by MwRSF, and the 10000S single-unit truck model originally developed by NCAC and calibrated by TTI against available full-scale crash test data [68].

Two different systems were evaluated, one with metal skids underneath the barrier, and one without metal skids. The addition of the metal skids was to evaluate barrier performance and deflection to determine the most successful barrier before full-scale crash testing.

The 1100C Neon and 2270P Silverado models impacted the RESTORE barrier at a speed of 62 mph (27.8 m/s) and an angle of 25 degrees. The maximum lateral dynamic deflection found in the 1100C simulation was 7.4 in. (189 mm) without skids and 6.6 in. (168 mm) with skids, respectively. Similarly, the maximum lateral dynamic deflection found in the 2270P simulation was 9.9 in. (251 mm) without skids and 8.2 in. (203 mm) with skids, respectively. Both vehicles were successfully contained and redirected, and the vehicle's roll and pitch values were acceptable according to MASH safety performance criteria. The 10000S single-unit truck model impacted the RESTORE barrier at a speed of 56 mph (25 m/s) and an angle of 15 degrees approximately 78 in. (1,981 mm) upstream from the splice between concrete beam nos. 5 and 6. The lateral dynamic deflection found in simulation was 13.5 in. (342 mm) without skids and was not determined during the impact with skids as the tire and post (rubber to rubber) contact created model instability. However, during the impact with skids, the vehicle appeared to be captured by the barrier. As the single-unit truck was being redirected away from the

system, the system started to restore to its original position but then deflected farther when the back of the cargo box contacted the rail during the simulation without skids. The cargo box floor support I-beams snagged on the steel rail base plates, which accentuated pitch and roll motions late in the impact event. Since there were many parts of the model that had yet to be validated, it was difficult to make predictive conclusions as to the performance of the 10000S vehicle and barrier.

The final simulations were used to investigate barrier performance as well as the benefits of incorporating support skids during impact events. The skids limited the roll motion of the barrier as compared to the barrier without the skids and did not negatively affect the barrier performance for any of the simulations. Therefore, the skids were recommended for use in the final design.

3.8 Final Design of RESTORE Barrier Before Crash Testing

The system consisted of twelve 19-ft 11½-in. (6.1-m) long x 18½-in. (470-mm) tall x 21½-in. (546-mm) wide concrete beams. The concrete beams were chamfered to have a maximum width of 22¼ in. (565 mm) at the center and had 4½ in. (114 mm) coped ends to allow for the ACJ to be inserted. Complete design details for the barrier system are shown in Appendix B. The concrete beam was designed with a light-weight concrete mix with a minimum 28-day compressive strength of 5,000 psi (34 MPa) and a density of 110 pcf (1,762 kg/m³). The concrete beams were placed on top of the 11⁵/₈ in. (295 mm) tall shear fenders spaced at 5 ft (1.5 m). The nominal height of the top of the concrete rail was 30¹/₈ in. (765 mm). To accommodate the TL-4 height requirement, a steel tube assembly was installed on top of the concrete beams to reach a nominal height of 38⁵/₈ in. (981 mm). The steel tube assembly was constructed with an 8-in. x 4-in. x ¼-

in. (203-mm x 102-mm x 6-mm) steel HSS section. The metal skids below the concrete for stability were spaced every 120 in. (3.0 m) on-center. They were made out of a 6 ½ in. (165-mm) outer diameter pipe that was ⅜-in. (10-mm) thick and was welded to a metal ski with flared ends. A metal plate was welded at a height of 11 in. (279 mm) for the concrete segment to rest on. A ½-in. (13-mm) thick elastomer pad was inserted between the metal plate and the concrete to allow for construction variances.

3.9 Full-Scale Crash Tests and Results

3.9.1 Background

According to TL-4 of MASH, longitudinal barrier systems must be subjected to three full-scale vehicle crash tests, as described in Section 3.7.2. Therefore, three full-scale vehicle crash tests were performed to evaluate the RESTORE barrier according to the MASH TL-4 safety performance criteria [15].

After each test, all TL-4 MASH safety criteria were evaluated, including occupant risk values and occupant compartment deformations. The lateral, or perpendicular, impact force was also estimated [20-21] and compared to test results obtained with similar vehicles impacting rigid barriers. As part of the investigation, the barrier forces were determined from the longitudinal and lateral vehicle accelerations, as measured at the vehicle's c.g., and were processed using a filtered 50-msec moving average. The filtered 50-msec moving average vehicle accelerations were then combined with the uncoupled yaw angle versus time data in order to estimate the vehicular loading applied to the barrier system.

3.9.2 Test No. SFH-1 – MASH Test Designation No. 4-11

For the first full-scale test, a 2270P pickup truck impacted the barrier system at a speed of 63.4 mph (102.1 km/h) and an angle of 24.8 degrees [20-21]. Impact occurred $41\frac{3}{16}$ in. (1,046 mm) upstream from the joint between barrier nos. 5 and 6 and was successfully captured and redirected. The vehicle impacted the first two posts downstream from the impact point along the front face and part of the upstream face. The permanent set of the barrier was estimated to be $\frac{7}{8}$ in. (22 mm). The maximum lateral dynamic deflection for the top of the concrete beam was 11.2 in. (284 mm) at the upstream end of barrier no. 6, as determined from high-speed digital video analysis.

Barrier damage was minimal and consisted of contact marks, concrete spalling, gouges, and hairline concrete cracks, as shown in Figure 40. The barrier damage did not affect the system's structural capacity. Vehicle damage was moderate and was mainly concentrated on the left-front corner and left side of the vehicle, where the impact occurred. All of the occupant risk values were within the suggested limits provided in MASH. Therefore, test no. SFH-1 was determined to be acceptable according to the MASH safety performance criterion for test designation no. 4-11. The maximum lateral load imparted to the barrier was estimated to range between 58 and 62 kips (258 and 276 kN), as determined from the accelerometer and yaw data.



Figure 40. RESTORE Barrier Damage, Test No. SFH-1 [20-21]

3.9.3 Test No. SFH-2 – MASH Test Designation No. 4-10

For the second full-scale test, an 1100C small car impacted the barrier system at a speed of 64.3 mph (103.5 km/h) and an angle of 24.8 degrees [20-21]. The impact occurred $8\frac{5}{16}$ in. (211 mm) upstream from the joint between barrier nos. 7 and 8 and was successfully captured and redirected. The vehicle impacted the first two posts downstream of the impact point causing a cut on both posts due to the vehicle's rim. The permanent set of the barrier was approximately $1\frac{3}{4}$ in. (44 mm), which was measured at the joint between barrier nos. 7 and 8. The maximum lateral dynamic barrier deflection for the top of the concrete beam, including barrier rotation backward, was 7.1 in. (180 mm) at the upstream end of barrier no. 8, as determined from high-speed digital video analysis.

Barrier damage was minimal and consisted of gouging and contact marks on the front face of the concrete segments as well as cuts in the elastomer posts, as shown in Figure 41. The barrier damage did not affect the system's structural capacity, if re-impacted. Vehicle damage was moderate and was mainly concentrated on the left-front corner and left side of the vehicle, where the impact occurred. All of the occupant risk

values were within the suggested limits provided in MASH. Therefore, test no. SFH-2 was determined to be acceptable according to the MASH safety performance criterion for test designation no. 4-10. The maximum lateral load imparted to the barrier was estimated to range between 46 and 48 kips (206 and 215 kN), as determined from the accelerometer and yaw data.

3.9.4 Test No. SFH-3 – MASH Test Designation No. 4-12

For the final full-scale test, a 10000S single-unit truck impacted the barrier system at a speed of 56.5 mph (90.9 km/h) and an angle of 14.9 degrees [20-21]. Impact occurred 55¾ in. (1,416 mm) upstream from the joint between barrier nos. 5 and 6 and was successfully captured and redirected. The permanent set of the barrier was approximately 1½ in. (38 mm). The maximum lateral dynamic barrier deflection for the top upstream end of concrete barrier no. 6 and the top of the upper tube assembly at the same location, including barrier rotation backward, were 13.9 in. (353 mm) and 15.1 in. (384 mm), respectively.



Concrete Damage



Elastomer Post Damage

Figure 41. RESTORE Barrier Damage, Test No. SFH-2 [20-21]

Barrier damage was minimal and consisted of contact marks and gouging on the front face of the concrete beams, cracking and spalling at the joint connections, contact marks along the top of the concrete beams and along the upper tube assembly, and contact with the elastomer posts, as shown in Figure 42. Concrete spalling occurred behind multiple ACJ connections, after removal, as shown in Figure 43. The barrier

damage likely did not affect the system's structural capacity. Vehicle damage was moderate and was mainly concentrated on the left-front corner and the frame under the cargo box, where the impact occurred. All of the occupant risk values were within the suggested limits provided in MASH. Therefore, test no. SFH-3 was determined to be acceptable according to the MASH safety performance criterion for test designation no. 4-12. The maximum lateral load imparted to the barrier was estimated to range between 95 and 105 kips (422 and 467 kN), as determined from the accelerometer and yaw data.



Figure 42. RESTORE Barrier Damage, Test No. SFH-3 [20-21]



Figure 43. RESTORE Barrier Damage, After ACJ Removal, Test No. SFH-3 [20-21]

3.9.5 Full-Scale Crash Test Recommendations

During the full-scale crash testing, several barrier elements were damaged. During the passenger vehicle testing, the damage found was believed to not negatively affect the structural performance of the barrier. However, the cuts in the posts may not have allowed the barrier to fully restore in test no. SFH-2, and modifications to protect the elastomer posts were to be considered in the future. Damage found during all the full-scale tests included spalling of the concrete, which was not a concern for structural performance, but modifications were to be considered to reduce concrete spalling and cracking in the future.

4 SIMULATION AND FULL-SCALE TEST COMPARISON – 1100C

4.1 Purpose

Previous finite element analysis simulations investigated the performance of the RESTORE barrier system before full-scale crash testing was completed [19], and the simulations were not validated against the full-scale crash tests [20-21]. Therefore, a comparison study was needed in order to determine how accurate the previous simulations were in predicting the vehicle and barrier behavior including (1) vehicle stability, (2) occupant risk, (3) dynamic deflection, (4) snag, and (5) the lateral impact force. After comparison, a transition design could then be evaluated using the validated barrier model. Note that the Roadside Safety Verification and Validation Program (RSVVP) [79] was not used as it was outside the scope of this study. The purpose of these next chapters was to evaluate the similarities between the full-scale crash test and simulation to aid in the design and evaluation of the transition region. The transition will then be subjected to full-scale testing to determine if it satisfies the safety performance criteria presented in MASH.

4.2 Overall Model Comparisons

Two different small car vehicle models, the Dodge Neon and the Toyota Yaris [74, 80], impacted the barrier model from the initial simulations and were compared to test no. SFH-2. The test and simulation vehicles had different dimensions and mass. The Toyota Yaris model had a mass of 2,775 lb (1,259 kg) and the Dodge Neon model had a mass of 2,591 lb (1,175 kg). The vehicle used in the full-scale crash test, test no. SFH-2, was a Kia Rio that had a test inertial mass of 2,406 lb (1,091 kg). A visual comparison of the bumper heights and hood lengths is shown in Figure 44. Note that the Yaris model

mass included an additional 351 lb (159 kg) for two simulated occupants. The Neon model included an additional mass of 170 lb (75 kg) for one simulated occupant on the driver side. Test no. SFH-2 utilized a 166-lb (75-kg) test dummy on the front, impact-side seat for a total vehicle mass of 2,572 lb (1,167 kg).

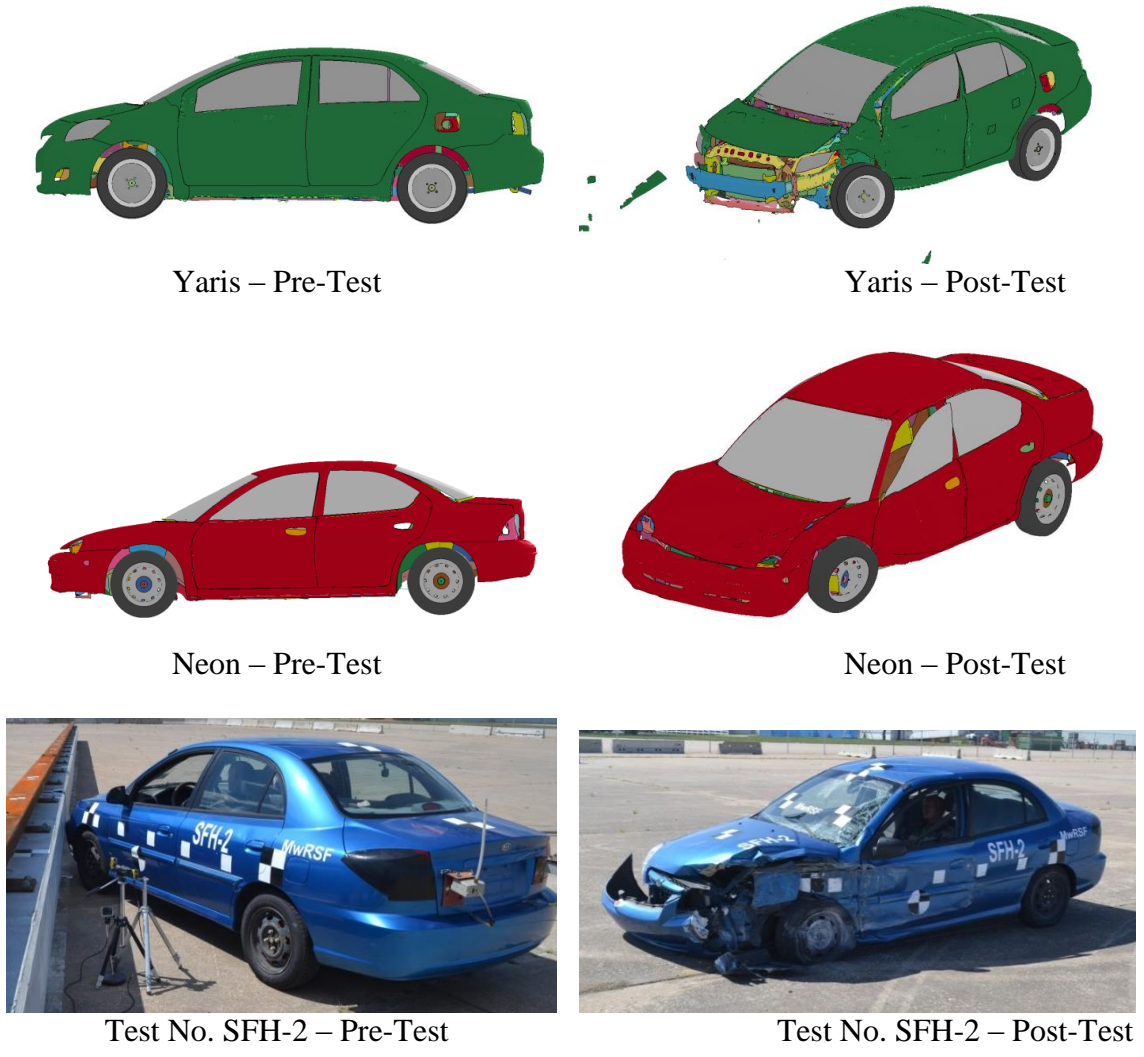


Figure 44. Vehicle Comparison, Pre- and Post-Test

The simulated vehicle impact velocity was modified to 64.3 mph (103.5 km/h) to correlate with test no. SFH-2. The impact angle during test no. SFH-2 was 24.8 degrees, while the impact angle used in the simulations was 25 degrees. Each of the vehicles were

targeted to impact 3 ft – 7 in. (1.1 m) upstream from the upstream face of the first post downstream from the joint between adjacent barriers. In the simulation, the Neon impacted the barrier 41¾ in. (1,060 mm) upstream from the first post, and the Yaris impacted the barrier 43¾ in. (1,111 mm) upstream from the first post. The vehicle in test no. SFH-2 impacted the barrier 37⁵/₁₆ in. (948 mm) upstream from the first post. The static and dynamic coefficients of friction between the Yaris and Neon vehicle model body/tires and the barrier was 0.1. Comparisons between the two simulations and the full-scale crash test results are shown in Table 10. Test sequential photographs are shown in Figures 45 and 46.

The overall length of contact was subjective. The Yaris vehicle model lost contact with the barrier 180 msec after impact, and the lateral and longitudinal velocities changed minimally, as shown in Figure 47. The Yaris recontacted the system at 260 msec, just before it was parallel to the system. Due to the loss in contact, the Yaris model became parallel with the barrier 44 msec later than what was seen in test no. SFH-2 and had a parallel velocity 6.0 percent lower than what was determined in test no. SFH-2. Additionally, the loss of contact with the barrier may have been contributed to the Yaris model exiting the system 60 msec later than in test no. SFH-2 even through the exit angle was within 0.9 degrees of test no. SFH-2. The overall length of contact, including the length where contact was lost, was 15 ft 11 in. (4.9 m) for the Yaris model.

The Neon model stayed in contact with the system for the duration of the impact event for a total length of contact of 16 ft – 7 in. (5.1 m). The Neon became parallel to the barrier 11 msec sooner than observed in test no. SFH-2, and it had a parallel velocity within 2 percent of test no. SFH-2. However, the exit angle that was calculated for the

Neon model was 3.4 degrees lower than observed in test no. SFH-2. The Neon and Yaris model exit velocities were 1.5 percent lower and 10.4 percent lower than test no. SFH-2, respectively.

Table 10. Comparison Between Test No. SFH-2 and 1100C Simulations

Comparison of Results		MASH Test Designation No. 4-10 RESTORE Barrier		
Test		SFH-2	Yaris Sim.	Neon Sim.
Reference Number		[20-21]	NA	NA
Vehicle	Designation	1100C	1100C	1100C
	Test Inertial, lb (kg)	2,406 (1,091)	2,775 (1,259)	2,591 (1,175)
Impact Conditions	Velocity, mph (km/h)	64.3 (103.5)	64.3 (103.5)	64.3 (103.5)
	Angle, deg.	24.8	25	25
Impact Severity, kip-ft (kJ)		58.3 (79.1)	68.5 (92.9)	64.0 (86.8)
Parallel Conditions	Velocity, mph (km/h)	41.7 (67.1)	39.2 (63.0)	42.4 (68.2)
	Time, ms	228	272	217
Exit Conditions	Velocity, mph (km/h)	41.4 (66.6)	37.1 (59.6)	40.8 (65.7)
	Angle, deg.	4.4	3.5	1.0
	Time, ms	336	396	291
Length of Contact		12 ft – 7 in. (3.8 m)	15 ft – 11 in. (4.9 m)	16 ft – 7 in. (5.1 m)
ORA, g's	Longitudinal	-5.06	-10.14	-6.36
	Lateral	8.19	9.82	9.11
OIV, ft/s (m/s)	Longitudinal	-26.51 (-8.08)	-28.46 (-8.67)	-28.34 (-8.64)
	Lateral	25.59 (7.80)	24.08 (7.34)	27.78 (8.47)
Test Article Deflections, in. (mm)	Dynamic of Concrete	7.1 (180)	7.5 (191)	7.7 (196)
	Dynamic of Steel Rail	7.3 (185)	7.4 (188)	7.6 (193)
	Working Width	29.6 (752)	30.0 (762)	30.2 (767)
Vehicle Stability, deg.	Max Roll	-4.4	5.6	4.7
	Max Pitch	-4.6	-20.9	-2.6
	Max Yaw	30.6	28.5	26.0
Impact Point in relation to upstream face of first elastomer post downstream of impact in. (mm)		37 ⁵ / ₁₆ (948)	43 ³ / ₄ (1,111)	41 ³ / ₄ (1,060)
No. of posts hit by leading tire (wheel snag)		2	2	0
Max. Lateral Impact Force, kips (kN) ¹		48.4 (215)	46.0 (205)	42.7 (190)

¹ Calculated using CFC60 50-msec moving average lateral and longitudinal accelerations coupled with Euler yaw angle.

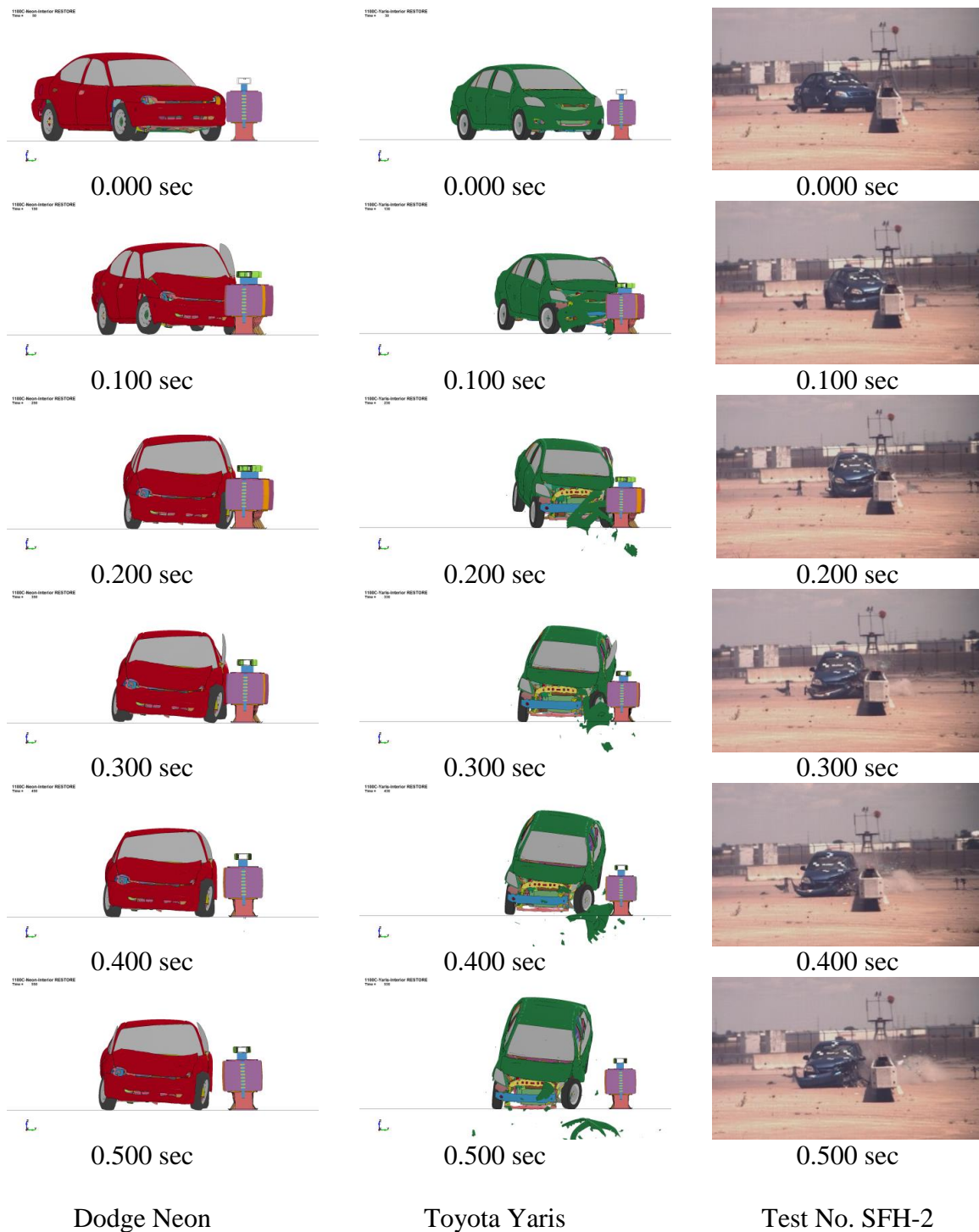


Figure 45. 1100C Simulation vs. Test No. SFH-2 Sequential Photographs, Downstream View

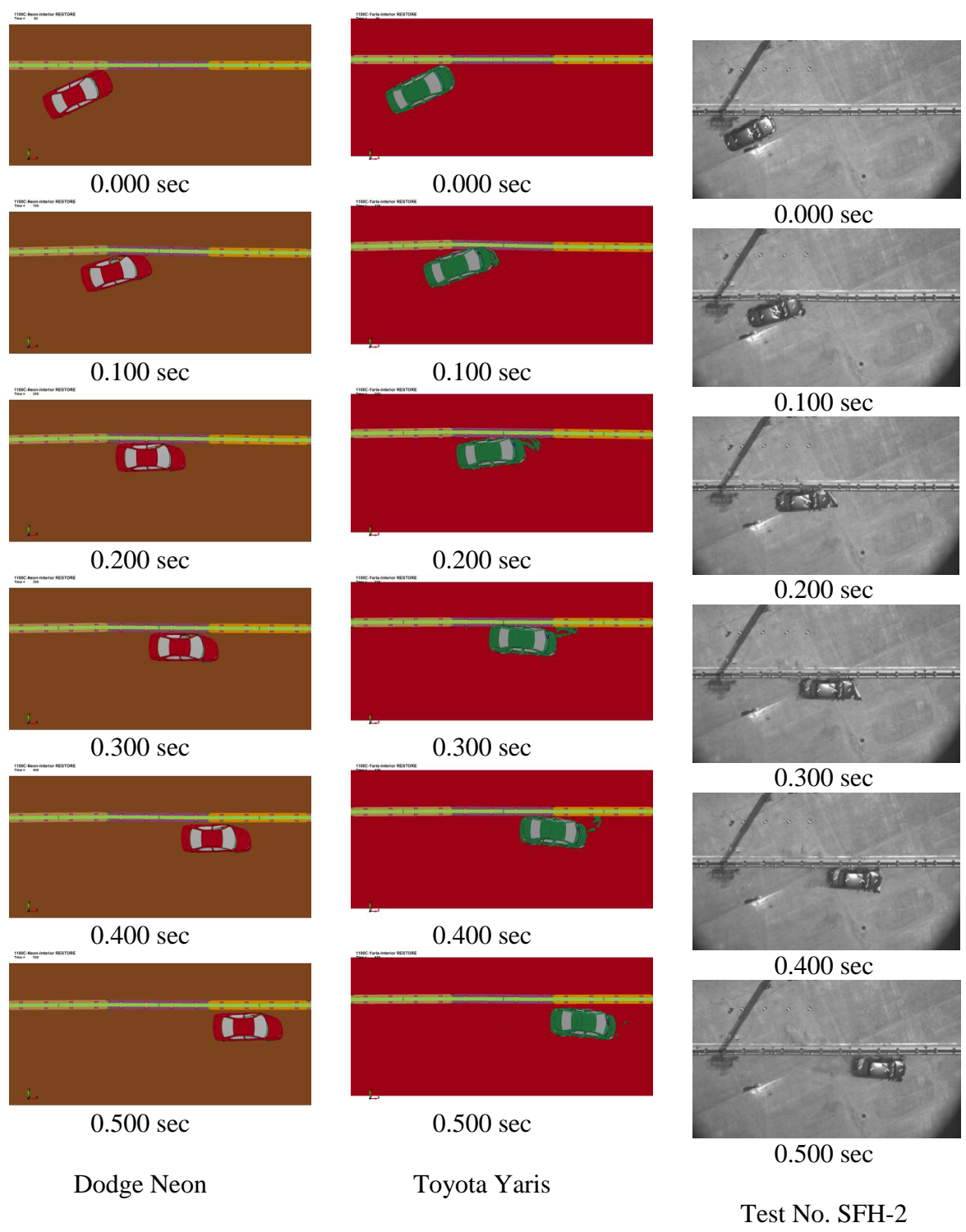


Figure 46. 1100C Simulation vs. Test No. SFH-2 Sequential Photographs, Overhead View

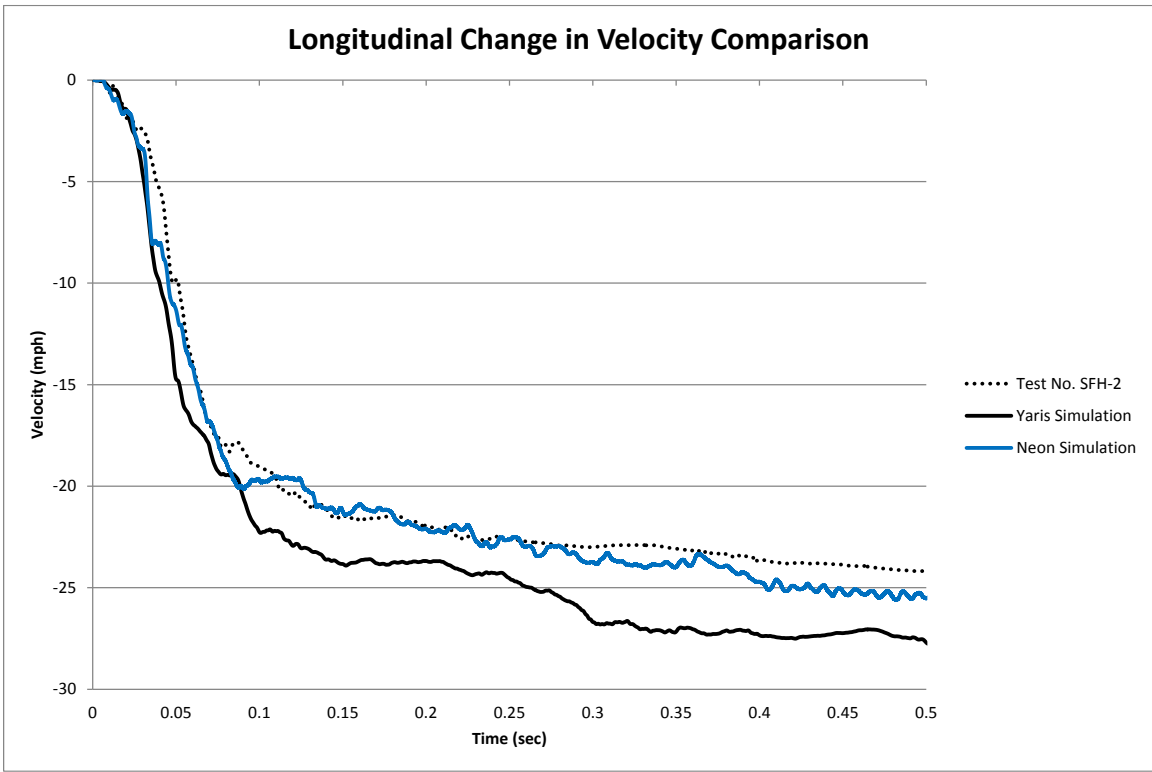
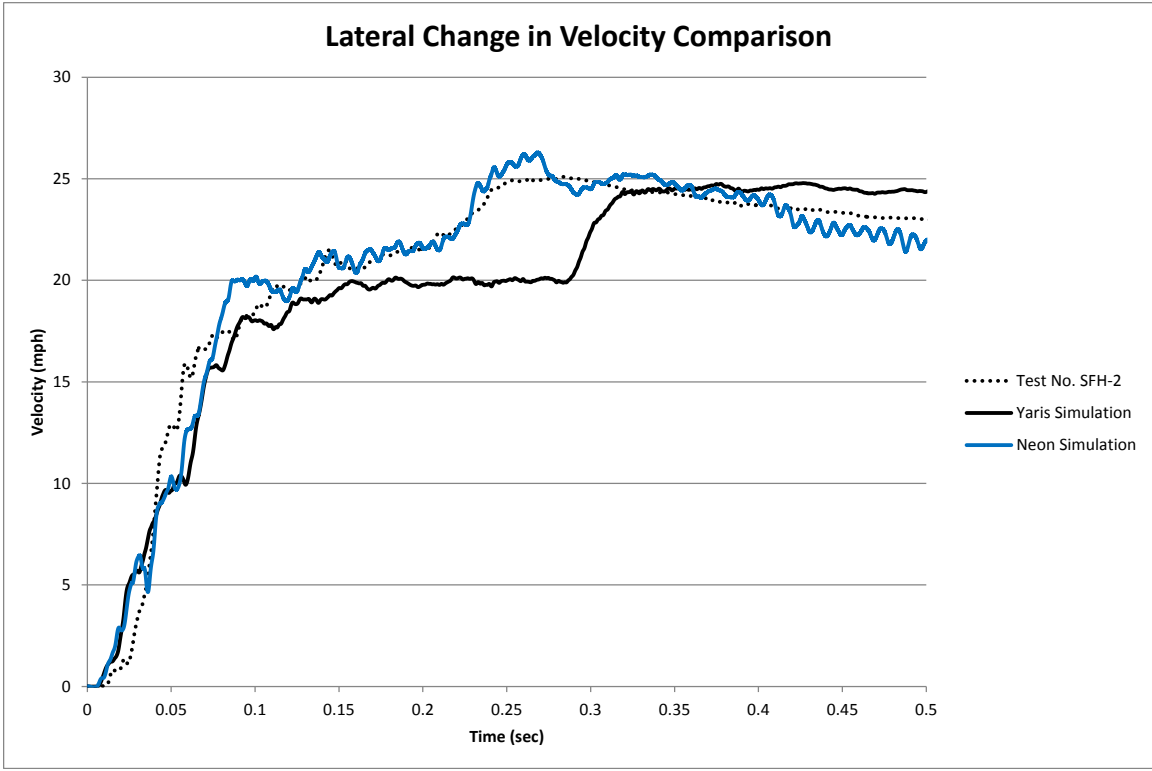


Figure 47. Lateral and Longitudinal Change in Velocity Comparison, 1100C

No permanent system damage occurred in the LS-DYNA simulations; since, the concrete was modeled with a rigid material definition and could not fracture, and failure could not occur in the elastomer posts. However, during the Yaris simulation, the left-front tire contacted the upstream corner of the RESTORE barrier and eroded the bottom corner of the ACJ 45 msec after impact, which may have increased the vehicle instability. The Yaris contacted two posts, similar to test no. SFH-2, but the simulation showed no visual evidence that the rim would cut the post if failure were to be modeled. The Neon did not contact any of the posts.

The Yaris's front plastic bumper cover fractured and disengaged, which was not found during the full-scale crash test. The top of the left-front door on the Yaris bent outward 5.7 in. (145 mm). The Neon vehicle damage more closely resembled the vehicle damage found in the full-scale crash test. The left-front corners of both vehicle models were crushed inward, as shown previously in Figure 44. Detailed comparisons of vehicle stability, occupant risk, dynamic deflection, snag, and lateral impact force are discussed in the following sections.

4.3 Vehicle Stability

Simulation data was processed similarly to the full-scale crash test data. The raw local angular rates were extracted and converted into Euler angles based on the MASH vehicle orientation. Both the simulation and full-scale crash test angular rate data were processed in the order of yaw, pitch, then roll with a pitch singularity of 90 degrees.

Some noise occurred in the simulation roll angles, as shown in Figure 48. The Yaris and the Neon both started to roll in the opposite direction as the full-scale crash test and had large roll angles over the first 50 msec. The extracted roll angle of the Neon

changed approximately 8 degrees from 30 to 40 msec after impact. The simulation did not visually exhibit that behavior, as shown previously in Figure 48. The Yaris did not appear to roll from 5.6 degrees to -3 degrees over the course of the impact. However, it was difficult to determine which direction the vehicles rolled visually; since, all of the roll angles were small. The maximum calculated roll angles were -4.4, 5.6, and 4.7 degrees for test no. SFH-2 vehicle, the Yaris model, and the Neon model, respectively.

The maximum pitch angle for the Neon was 43.5 percent less than observed in test no. SFH-2, as shown in Figure 49. However, the pitch angles for both the Neon simulation and crash test were below 5 degrees. Due to the left-front tire of the Yaris impacting the lower corner of a concrete beam, some snagging occurred, which resulted in a pitch angle 78.0 percent greater than observed in test no. SFH-2. Note that the Yaris pitch angles were still increasing at the end of the simulation. The maximum pitch angles were -4.6, -20.9, and -2.6 degrees for test no. SFH-2 vehicle, the Yaris model, and the Neon model, respectively.

The yaw angles for both of the vehicle models were similar to full-scale crash test, as shown in Figure 50. However, the Toyota Yaris had a delayed yaw after impact due to the plastic bumper cover fracture before the structural components of the frame impacted the barrier and caused the progression of the yaw. The Yaris yaw angle was 6.7 percent less than observed in test no. SFH-2. However, the Dodge Neon started to yaw at the appropriate time and followed a similar trend to test no. SFH-2 but had a 15.0 percent lower peak angle. The maximum yaw angles were 30.6, 28.5, and 26.0 degrees for test no. SFH-2 vehicle, the Yaris model, and the Neon model, respectively.

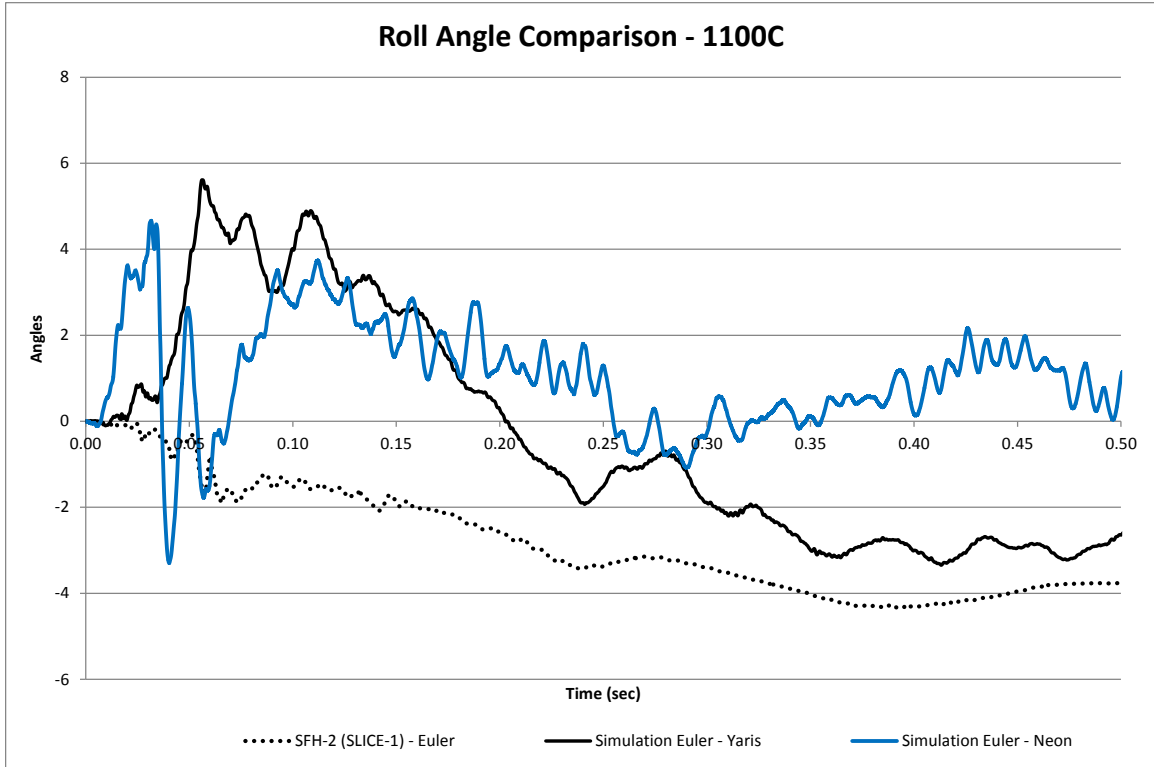


Figure 48. Interior Impact Roll Angle Comparison, 1100C

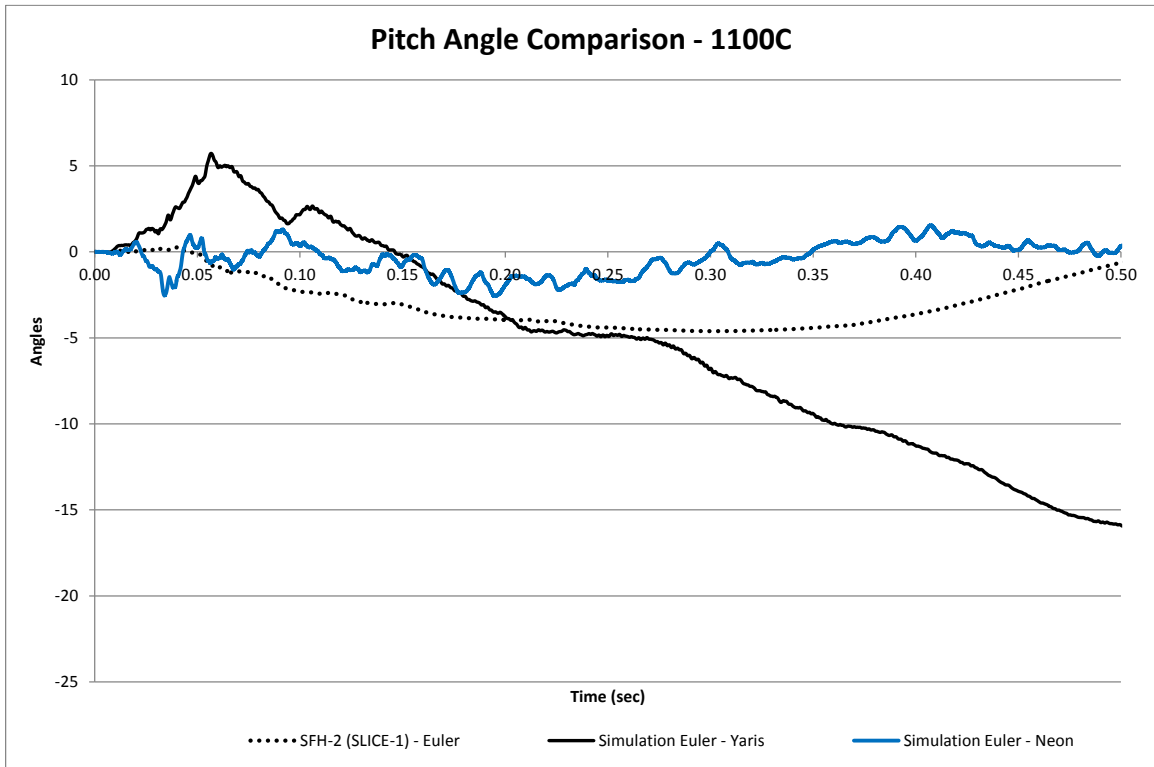


Figure 49. Interior Impact Pitch Angle Comparison, 1100C

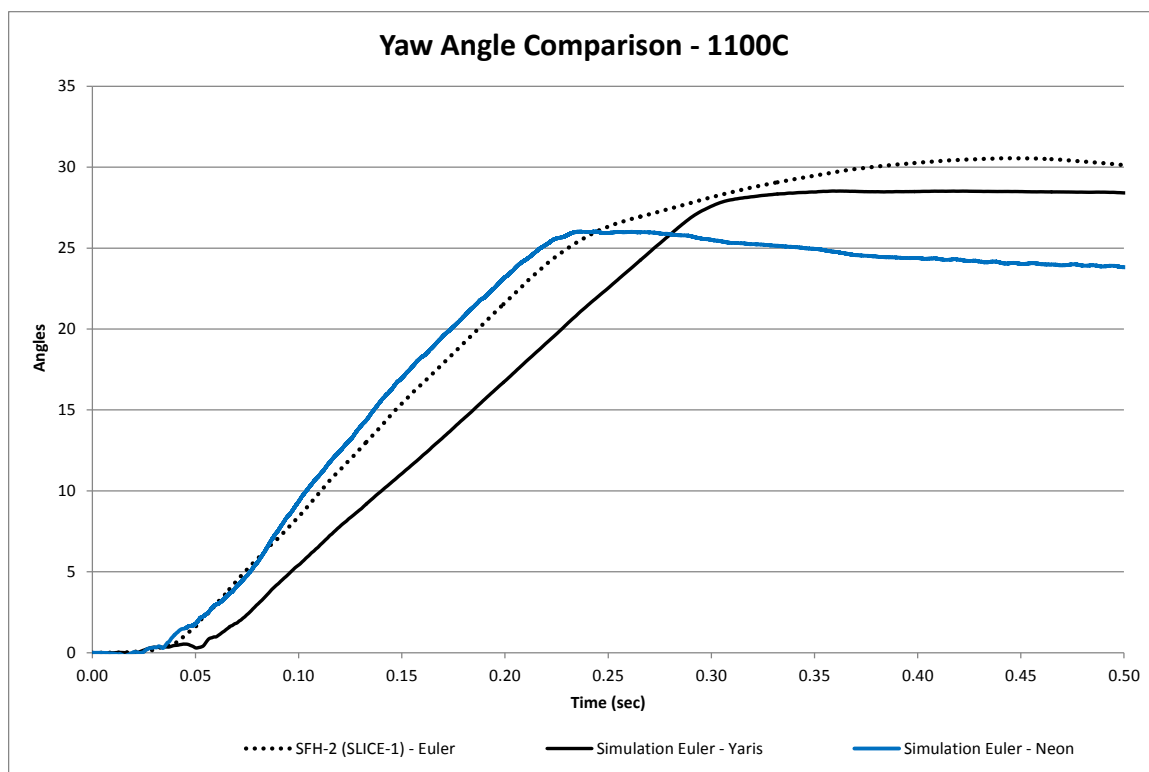


Figure 50. Interior Impact Yaw Angle Comparison, 1100C

4.4 Occupant Risk Analysis

The calculated occupant impact velocities (OIVs) and maximum 0.010-sec occupant ridedown accelerations (ORAs) in both the longitudinal and lateral directions were extracted from the accelerometer on each of the vehicle models and processed the same as used for the full-scale crash test accelerations, as shown in Table 11. The longitudinal OIV for the Yaris and the Neon models were 3.4 and 6.9 percent greater than observed in test no. SFH-2, while the lateral OIV for the Yaris and Neon models were 5.9 percent less than and 8.6 percent greater than observed in test no. SFH-2, respectively. However, the longitudinal ORA for the Yaris model was 50.1 percent greater than the longitudinal ORA found in test no. SFH-2. The large ORA occurred shortly after the calculated t^* value and may be due to the Yaris model losing contact with the barrier

during the impact event. The transducer data plots can be found in Appendix C. For the 1100C models, the Neon model provided more accurate occupant risk values due to the loss of contact between the barrier and the Yaris model.

Table 11. Summary of OIV and ORA, 1100C Vehicles

Evaluation Criteria		Transducer		
		SFH-2 SLICE-1	Dodge Neon Simulation	Toyota Yaris Simulation
OIV ft/s (m/s)	Longitudinal	-26.51 (-8.08)	-28.34 (-8.64)	-28.46 (-8.67)
	Lateral	25.59 (7.80)	27.78 (8.47)	24.08 (7.34)
ORA g's	Longitudinal	-5.06	-6.36	-10.14
	Lateral	8.19	9.11	9.82

4.5 Deflection and Snag

The dynamic deflection of the concrete beams and working widths were recorded using video analysis for test no. SFH-2, and were determined to be 7.1 in. (180 mm) and 29.6 in. (752 mm), respectively. Similarly, the maximum dynamic deflection of the concrete beams in the simulations was determined to be 7.5 in. (191 mm) with the Toyota Yaris and 7.7 in. (196 mm) with the Dodge Neon. The working widths were calculated to be 30.0 and 30.2 in. (762 and 767 mm) for the Toyota Yaris and Dodge Neon, as shown in Table 12, respectively.

During the test no. SFH-2, the left-front tire of the Kia Rio sedan contacted the first two posts downstream from impact. The tire contact on the upstream face of the first post was approximately 3½ in. (89 mm) with a cut along the impact face. On the second post, the tire contact on the upstream face was approximately 5¼ in. (133 mm) with a cut along the impact face. In the simulation with the Toyota Yaris model, approximately 1.3

in. (33 mm) of contact occurred on the upstream face of the first post downstream of the joint, and 2.1 in. (53 mm) of contact occurred on the upstream face of the second post.

The Dodge Neon model tire did not contact any posts. For the 1100C models, the Yaris model provided the closest representation of the post snag and dynamic deflection.

Table 12. Dynamic Deflection, Working Width, and Post Snag, 1100C Vehicles

Vehicle Type	Dynamic Concrete Deflection in. (mm)	Dynamic Steel Deflection in. (mm)	Working Width in. (mm)	Amount of Snag Post 1 in. (mm)	Amount of Snag Post 2 in. (mm)
Kia Rio (SFH-2)	7.1 (180)	7.3 (185)	29.6 (752)	3.5 (89)	5.25 (133)
Toyota Yaris	7.5 (191)	7.4 (188)	30.0 (762)	1.3 (33)	2.1 (53)
Dodge Neon	7.7 (196)	7.6 (193)	30.2 (767)	0 (0)	0 (0)

4.6 Impact Force Investigation

Methods for determining the lateral barrier force for the 1100C vehicle were investigated. Previous studies have explored the different methods for determining barrier forces but have not compared the results from full-scale tests and simulations. Four different methods were investigated through simulation for estimating lateral barrier forces. The baseline method to determine the lateral barrier forces during the full-scale crash test used local lateral and longitudinal accelerations coupled with the Euler yaw angle multiplied by vehicle mass. The different methods to calculate barrier force from the simulation results were: (1) local lateral and longitudinal accelerations coupled with the calculated Euler yaw angle multiplied by vehicle mass; (2) global lateral accelerations multiplied by the vehicle mass; (3) contact forces between the vehicle and the barrier components with a CFC 60 filter; and (4) contact forces between the vehicle and the

barrier components with a CFC 60 filter and a 50-msec moving average. The accelerations were obtained using the command

*ELEMENT_SEATBELT_ACCELEROMETER and outputted with

*DATABASE_HISTORY_NODE. Contact forces were obtained using the command

*CONTACT_FORCE_TRANSDUCER and included the exterior shell of the vehicles and all of the barrier parts.

The filtered contact force with the Yaris and Neon resulted in peak lateral impact forces approximately 41 and 29 percent greater than what was experienced during test no. SFH-2, as shown in Figures 51 and 52. However, after applying a 50-msec moving average, the peak force with the Yaris and Neon was 6.1 and 16.3 percent less than what was experienced during test no. SFH-2. The global acceleration multiplied by the vehicle mass as well as the local accelerations coupled with yaw multiplied by vehicle mass gave similar force trends. The global acceleration multiplied by vehicle mass resulted in peak forces within 4 percent for the Yaris model and 13 percent with the Neon model. The local accelerations coupled with yaw multiplied by vehicle mass resulted in peak forces within 5 percent for the Yaris model and 13 percent with the Neon model, as shown in Table 13. The Toyota Yaris model mass was approximately 13 percent greater in mass than the Kia Rio used in the full-scale crash test and the Dodge Neon was approximately 7 percent greater in mass; which may have contributed to differences in barrier forces. Tail slap for the Yaris model occurred approximately 100 ms later than the crash test due to the vehicle not remaining in contact with the barrier for the entirety of the impact event. For the 1100C models, the global acceleration multiplied by the mass provided the closest peak lateral impact force.

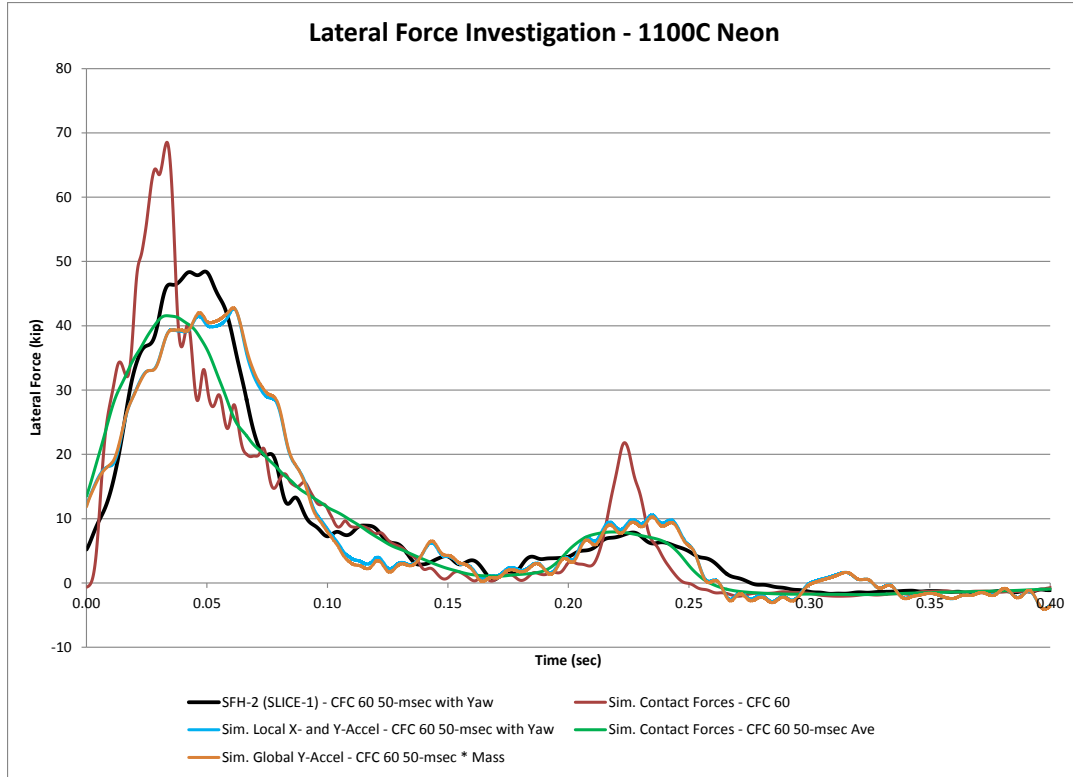


Figure 51. Lateral Force Comparison, 1100C Dodge Neon

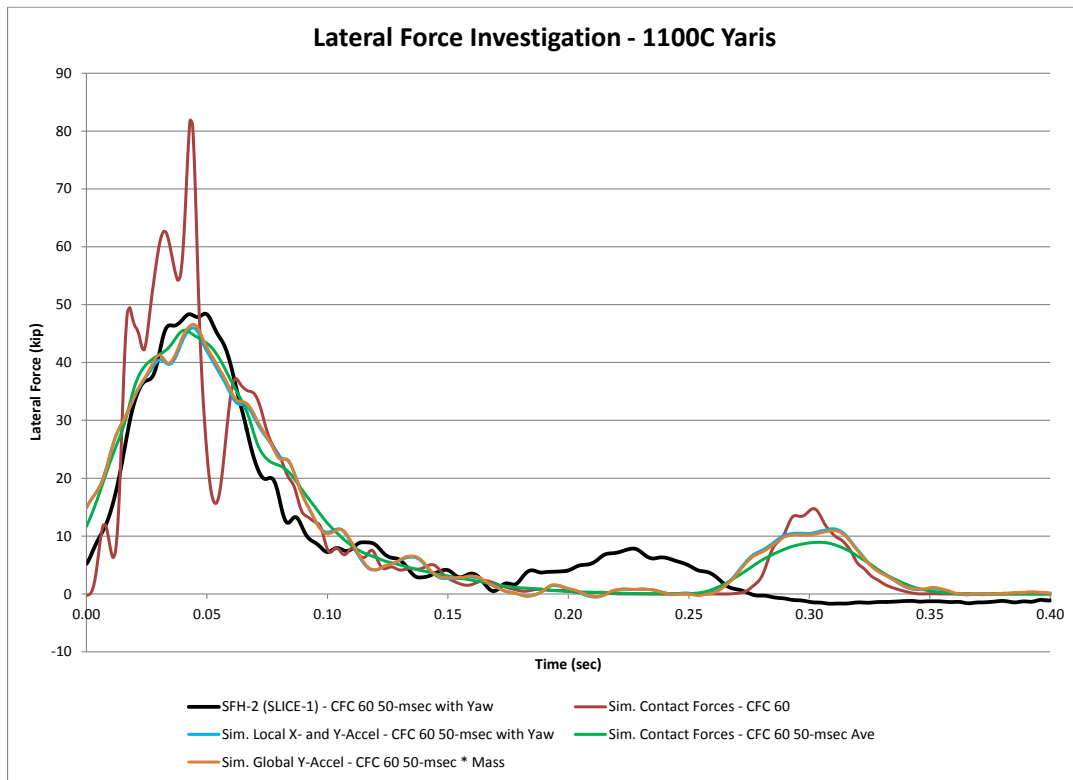


Figure 52. Lateral Force Comparison, 1100C Toyota Yaris

Table 13. 1100C Lateral Force Comparison

Method	Max. Force kip (kN)	% Difference from Baseline SLICE 1
Full-Scale Local X- and Y- Accelerations with Yaw *Mass	48.4 (215)	Baseline
NEON Simulation		
Sim. Local X- and Y- Accelerations with Yaw *Mass	42.7 (190)	-13.3%
Sim. Global Y-Acceleration * Mass	42.8 (190)	-13.1%
Sim. Contact Forces CFC60	68.5 (305)	29.3%
Sim. Contact Forces CFC60 50-ms Average	41.6 (185)	-16.3%
YARIS Simulation		
Sim. Local X- and Y- Accelerations with Yaw *Mass	46.0 (205)	-5.2%
Sim. Global Y-Acceleration * Mass	46.6 (207)	-3.9%
Sim. Contact Forces CFC60	81.8 (364)	40.8%
Sim. Contact Forces CFC60 50-ms Average	45.6 (203)	-6.1%

4.7 Discussion

During the original simulations run by Schmidt, et al., the Dodge Neon was used to simulate the 1100C impact. However, the Toyota Yaris model was also available, and it was necessary to select the vehicle model that best represented the full-scale crash test. Multiple factors were considered in the selection and comparison of the vehicles including: vehicle stability; occupant risk; dynamic deflection; vehicle snag; working width; and lateral impact forces. For the transition design, the amount of snag that will occur under and at the joint was important for the small car simulations.

The Dodge Neon vehicle roll, pitch, and yaw angles were most similar to test no. SFH-2. However, the tires did not contact the posts, which occurred in the full-scale crash test. The Toyota Yaris showed 78.0 percent more pitch than what was expected, but the left-front tire of the Yaris model impacted the same two posts that were impacted in the full-scale crash test.

Both of the vehicle models had similar occupant risk values as the full-scale crash test. However, the Yaris model showed had a maximum longitudinal ORA value double than what was calculated in the full scale crash test. The large ORA value in the Yaris simulation occurred shortly after t^* and may have been contributed to the Yaris losing contact with the system during the impact event. When trying to obtain the lateral barrier forces from the model, the Yaris model with the global lateral acceleration multiplied by vehicle mass was most similar to the lateral barrier force calculated in the full-scale crash test. Therefore, neither vehicle model was accurate for all comparison parameters, and both vehicles will be used to evaluate the transition region. The Dodge Neon was most accurate for ORA, OIV, and vehicle stability, while the Toyota Yaris was most accurate for snag, deflection, and lateral impact force.

5 SIMULATION AND FULL-SCALE TEST COMPARISON – 2270P

5.1 Overall Model Comparisons

The Chevrolet Silverado vehicle model [75-76] impacted the barrier model from the initial simulations and was compared to test no. SFH-1. The test and simulation vehicles had different dimensions and masses. The Chevrolet Silverado model had a mass of 5,008 lb (2,272 kg). The vehicle used in the full-scale crash test, test no. SFH-1, was a Dodge Ram 1500 that had a test inertial mass of 5,021 lb (2,277 kg). A 165-lb (75-kg) test dummy was seated in the front, impact-side seat in the full-scale crash test, so the total vehicle mass was 5,186 lb (2,352 kg). Note that the Silverado model mass did not include additional mass for simulated occupants. A visual comparison of the vehicles is shown in Figure 53.

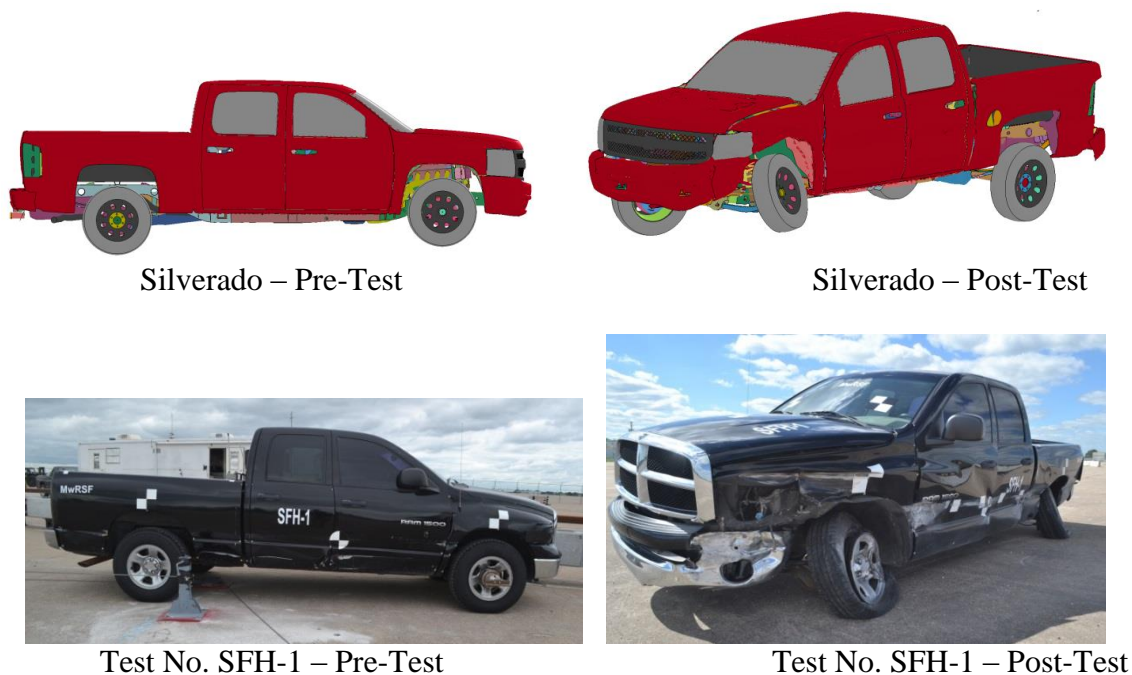


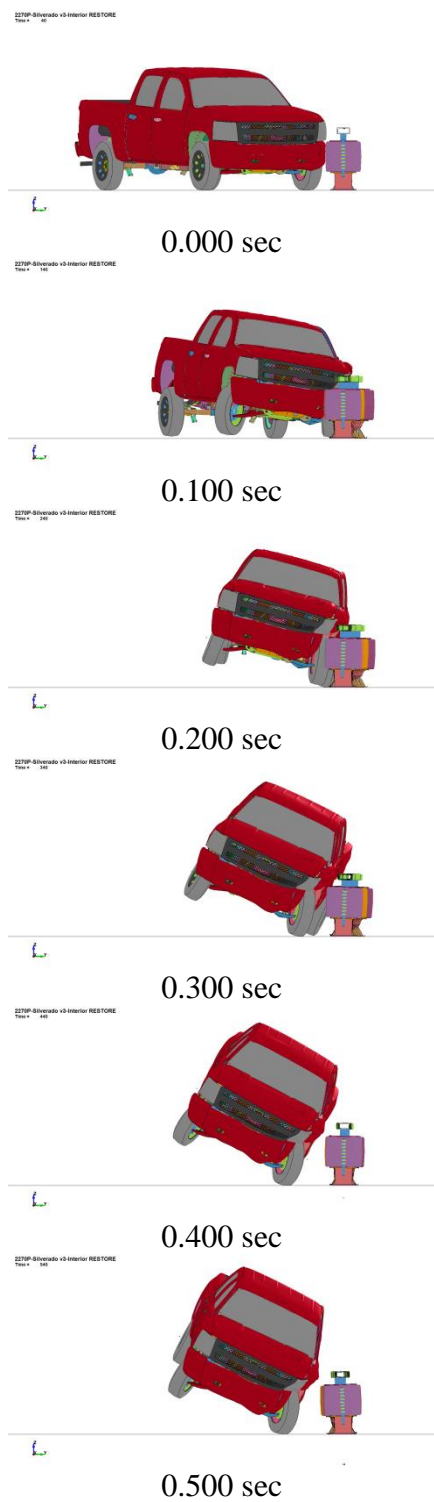
Figure 53. Vehicle Comparison, Pre- and Post-Test, 2270P

The Silverado impact velocity was modified to 63.4 mph (102.1 km/h) to correlate with test no. SFH-1. The impact angle during test no. SFH-1 was 24.8 degrees, while the impact angle used in the simulation was 25 degrees. The vehicles were targeted to impact 4 ft – 3 in. (1.3 m) upstream from the ACJ between two adjacent barriers. In the simulation, the Silverado impacted the barrier 4 ft – 5 in. (1.3 m) upstream from the ACJ. The vehicle in test no. SFH-1 impacted the barrier 4 ft – 8 in. (1.4 m) upstream from the ACJ. The static and dynamic coefficients of friction between the Silverado vehicle model body/tires and the barrier was 0.1. Comparisons between the simulation and the full-scale crash test results are shown in Table 14. Test sequential photographs are shown in Figures 54 and 55.

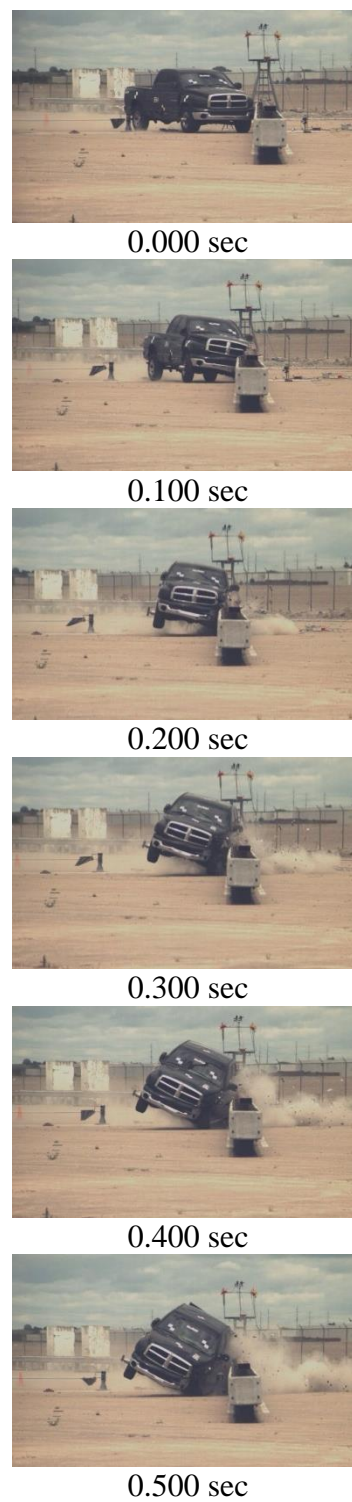
Table 14. Comparison Between Test No. SFH-1 and 2270P Simulation

Comparison of Results		MASH Test Designation No. 4-11 RESTORE Barrier	
Test		SFH-1	Silverado Sim.
Reference Number		[20-21]	NA
Vehicle	Designation	2270P	2270P
	Test Inertial Weight, lb (kg)	5,021 (2,277)	5,008 (2,272)
Impact Conditions	Velocity, mph (km/h)	63.4 (102.1)	63.4 (102.1)
	Angle, deg.	24.8	25
Impact Severity, kip-ft (kJ)		118.6 (160.8)	120.3 (163.1)
Parallel Conditions	Velocity, mph (km/h)	48.6 (78.2)	51.8 (83.4)
	Time, ms	193	200
Exit Conditions	Velocity, mph (km/h)	43.5 (69.9)	51.3 (82.5)
	Angle, deg.	10.6	4.2
	Time, ms	540	310
Length of Contact		15 ft – ¼ in. (4.6 m)	10 ft – 10 in. (3.3 m)
ORA, g's	Longitudinal	-4.81	11.15
	Lateral	8.40	12.51
OIV, ft/s (m/s)	Longitudinal	-17.62 (-5.37)	-15.75 (-4.80)
	Lateral	21.29 (6.49)	19.46 (5.93)
Test Article Deflections, in. (mm)	Dynamic of Concrete	11.2 (284)	9.9 (251)
	Dynamic of Steel Rail	10.9 (277)	10.1 (257)
	Working Width	33.5 (851)	32.2 (818)
Vehicle Stability, deg.	Max Roll	-27.3	-29.8
	Max Pitch	-8.0	-9.7
	Max Yaw	36.4	29.5
Impact Point in relation to center of ACJ between two adjacent barriers in. (mm)		56½ (1,435)	53 (1,346)
No. of posts hit by leading tire (wheel snag)		2	1
Max. Lateral Impact Force, kips (kN) ¹		58.6 (261)	60.3 (268)

¹ Calculated using CFC60 50-msec moving average lateral and longitudinal accelerations coupled with Euler yaw angle.

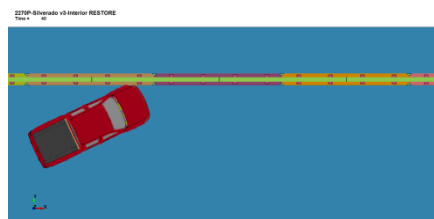


Chevy Silverado



Test No. SFH-1

Figure 54. 2270P Simulation vs. Test No. SFH-1 Sequential Photographs, Downstream View



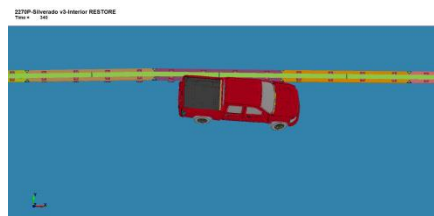
0.000 sec



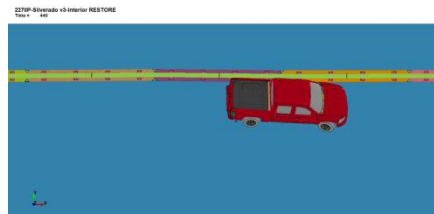
0.100 sec



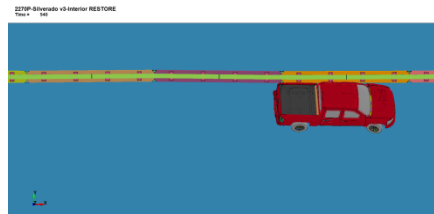
0.200 sec



0.300 sec



0.400 sec



0.500 sec

Chevy Silverado



0.000 sec



0.100 sec



0.200 sec



0.300 sec



0.400 sec



0.500 sec

Test No. SFH-1

Figure 55. 2270P Simulation vs. Test No. SFH-1 Sequential Photographs, Overhead View

The lateral change in velocity of the Silverado model matched test no. SFH-1 very well, as shown in Figure 56. The longitudinal change in velocity started to deviate from test no. SFH-1 around 100 msec. The difference in longitudinal velocities could be accounted to the Silverado model not having the full vehicle length in contact with the system like the full-scale crash vehicle did. The longitudinal change in velocity of the Silverado model plateaued around 200 to 250 msec due to the vehicle starting to yaw away from the barrier, with only the rear region remaining in contact. The Silverado model stayed in contact with the system for the duration of the impact event for a total length of contact of 10 ft – 10 in. (3.3 m), which was 4 ft – 3 in. (1.3 m) shorter than observed in test no. SFH-1. The Silverado model became parallel to the barrier 7 msec later than observed in test no. SFH-1, and had a parallel velocity 6 percent greater than observed in test no. SFH-1. However, the exit angle calculated for the Silverado model was 6.4 degrees lower than observed in test no. SFH-1. The Silverado model exit velocity was 15.2 percent higher than observed in test no. SFH-1, respectively.

No permanent system damage occurred in the LS-DYNA simulations; since, the concrete was modeled with a rigid material definition and could not fracture, and failure could not occur in the elastomer posts. The Silverado model left-front wheel contacted the second post downstream of impact, similar to test no. SFH-1. However, the Silverado model left-front wheel did not contact the first post downstream of impact, as seen in test no. SFH-1.

The Silverado vehicle model damage closely resembled the vehicle damage found in the full-scale crash test. The left-front corner of the vehicle model was crushed inward, as shown previously in Figure 53. Detailed comparisons of vehicle stability, occupant

risk, dynamic deflection, snag, and lateral impact force are discussed in the following sections.

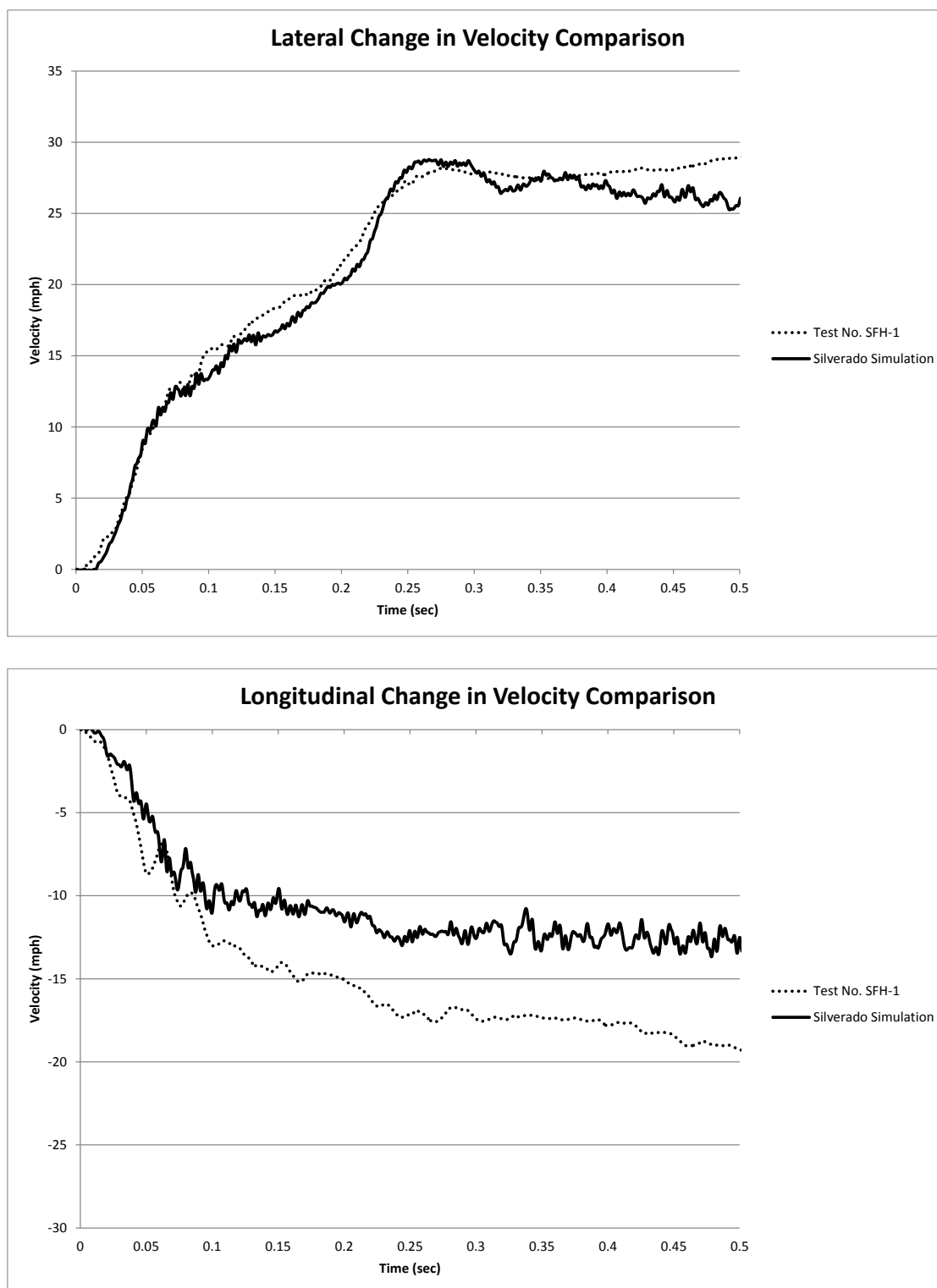


Figure 56. 2270P Lateral and Longitudinal Change in Velocity Comparison

5.2 Vehicle Stability

Simulation data was processed similarly to the full-scale crash test data. The raw local angular rates were extracted and converted into Euler angles based on the MASH vehicle orientation. Both the simulation and full-scale crash test angular rate data were processed in the order of yaw, pitch, then roll with a pitch singularity of 90 degrees.

The Silverado model did not show a positive roll angle directly after impact which was observed in test no. SFH-1, as shown in Figure 57. However, there was a similar trend in the change in the roll angle where there was an approximate 5 degree difference through 400 msec. Between 400 and 500 msec, the Silverado model started to match the full-scale crash test roll angles. The maximum calculated roll angles were -27.3 and -29.8 degrees for test no. SFH-1 and the Silverado model, respectively.

Some noise occurred in the simulation pitch angles, as shown in Figure 58. The simulation did not visually exhibit the -4 degree spike after 50 msec, but it did exhibit similar pitch angles as the full-scale test through the remainder of the simulation. The maximum pitch angle for the Silverado model was within 2 degrees of test no. SFH-2. However, the Silverado model continued to pitch at the end of the simulation, but the pitch did not exceed the limits listed in MASH. The maximum pitch angles were -8.0 and -9.7 degrees for test no. SFH-1 and the Silverado model, respectively.

The yaw angles for the Silverado model were similar to test no. SFH-1 through 200 msec, as shown in Figure 59. At 200 msec, the Silverado model became parallel to the system and started to yaw away from the barrier. The Silverado model visually started to yaw back toward the barrier at 300 msec, as shown previously in Figure 54. As a result, the Silverado model had a peak yaw angle 23.4 percent lower than the peak yaw

angle observed in test no. SFH-1. The maximum yaw angles were 36.4 and 29.5 degrees for test no. SFH-1 and the Silverado model, respectively.

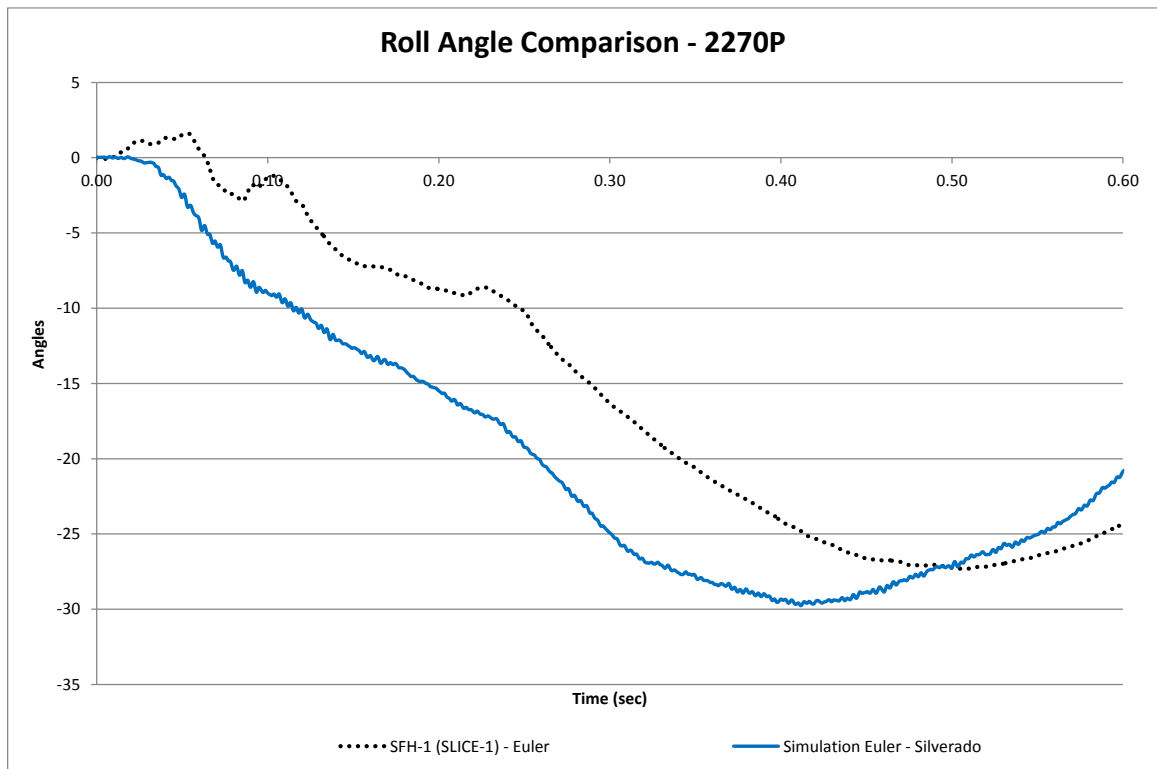


Figure 57. Interior Impact Roll Angle Comparison, 2270P

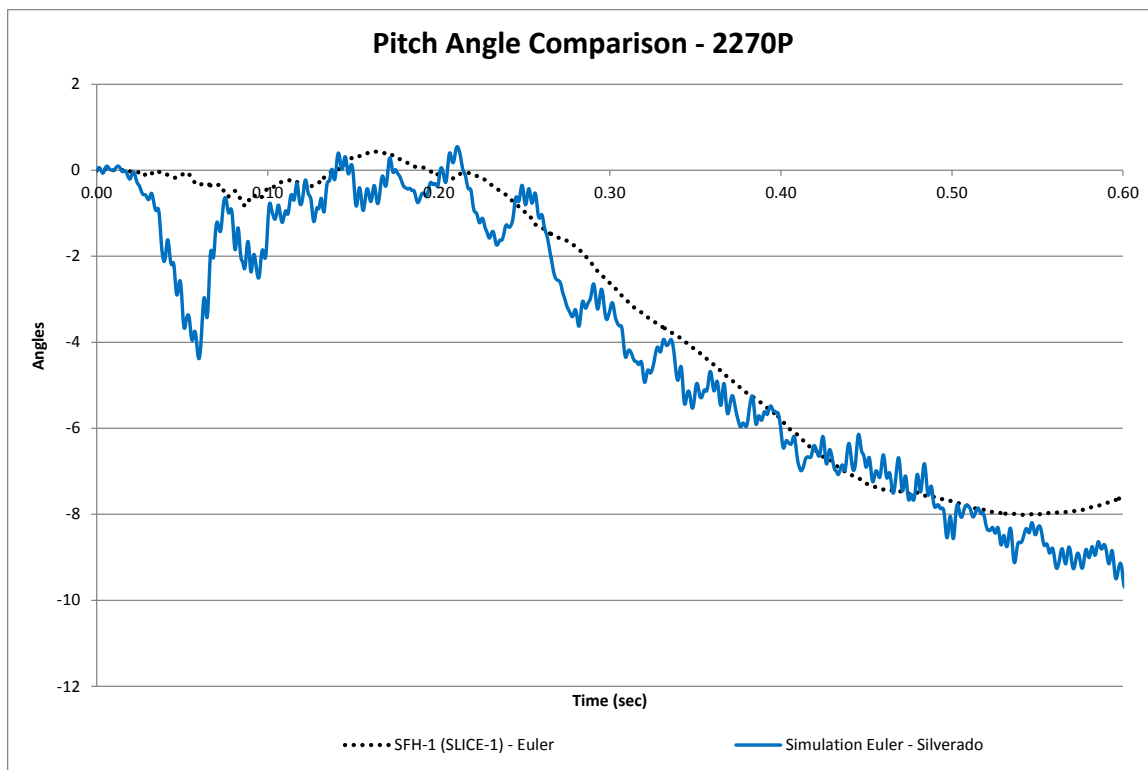


Figure 58. Interior Impact Pitch Angle Comparison, 2270P

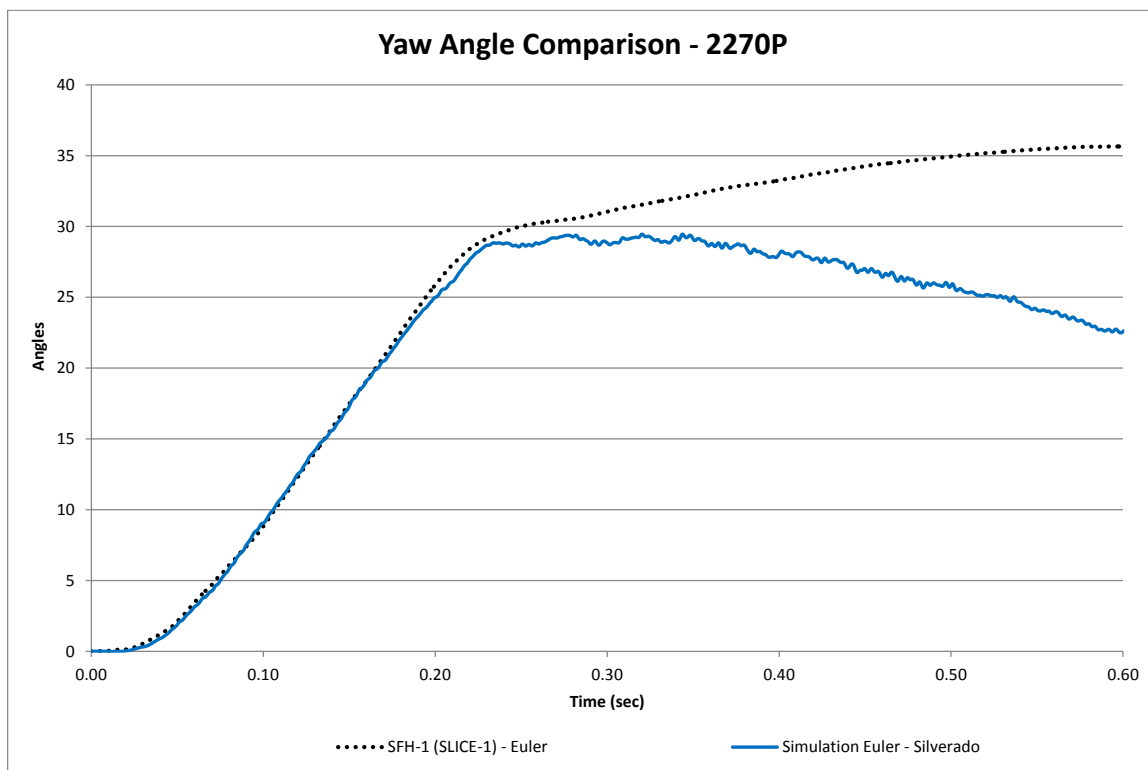


Figure 59. Interior Impact Yaw Angle Comparison, 2270P

5.3 Occupant Risk Analysis

The calculated occupant impact velocities (OIVs) and maximum 0.010-sec occupant ridedown accelerations (ORAs) in both the longitudinal and lateral directions were extracted from the accelerometer on each the vehicle model and processed the same as used for the full-scale crash test accelerations, as shown in Table 15. The longitudinal and lateral ORA for the Silverado model were 143 and 33 percent greater than observed in test no. SFH-1, respectively. The longitudinal accelerations were still very noisy after the CFC 180 filter and 10 msec moving average. Further, the longitudinal ORA occurred after the vehicle had already exited the system and most likely occurred due to the left-front tire re-impacting the ground. The differences in ORA showed that the accelerations after the vehicle exited the system cannot be accurately determined from simulation with the Silverado model. However, the longitudinal and lateral OIV more closely matched the results observed in the full-scale crash test. The lateral OIV was 9.4 percent lower than observed in test no. SFH-1, and the longitudinal OIV was 10.6 percent greater than observed in test no. SFH-1. The transducer data plots can be found in Appendix D.

Table 15. Summary of OIV and ORA, 2270P Vehicles

Evaluation Criteria		Transducer	
		SFH-1 SLICE-1	Silverado Simulation
OIV ft/s (m/s)	Longitudinal	-17.62 (-5.37)	-15.75 (-4.80)
	Lateral	21.29 (6.49)	19.46 (5.93)
ORA g's	Longitudinal	-4.81	11.15
	Lateral	8.40	12.51

5.4 Deflection and Snag

The dynamic deflection of the concrete beams and working width were determined to be 11.2 in. (284 mm) and 33.5 in. (851 mm), respectively from video analysis for test no. SFH-1. Similarly, the maximum dynamic deflection of the concrete beams in the simulation was determined to be 9.9 in. (251 mm) with the Chevrolet Silverado model. The working width of the simulation was calculated to be 32.2 in. (818 mm), as shown in Table 16.

During test no. SFH-1, the left-front tire of the Dodge Ram 1500 contacted the first two posts downstream from impact. The tire contact on the upstream face of the first post was approximately 6 in. (152 mm) laterally. On the second post, the tire contact on the upstream face was approximately 4¾ in. (121 mm) laterally. In the simulation with the Silverado model, the left-front tire did not contact the first post downstream from impact, but approximately 0.75 in. (19 mm) of contact occurred on the upstream face of the second post downstream from impact.

Table 16. Dynamic Deflection, Working Width, and Post Snag, 2270P Vehicles

Vehicle Type	Dynamic Concrete Deflection in. (mm)	Dynamic Steel Deflection in. (mm)	Working Width in. (mm)	Amount of Snag Post 1 in. (mm)	Amount of Snag Post 2 in. (mm)
Dodge Ram 1500 (SFH-1)	11.2 (284)	10.9 (277)	33.5 (851)	6.0 (152)	4.75 (121)
Silverado Model	9.9 (251)	10.1 (257)	32.2 (818)	0 (0)	0.75 (19)

5.5 Impact Force Investigation

The same methods for determining lateral barrier force that were explored with the small car impacts were investigated with the pickup truck impacts. The baseline

method to determine the lateral barrier forces during the full-scale crash test used local lateral and longitudinal accelerations coupled with the Euler yaw angle multiplied by vehicle mass. The different methods to calculate barrier force from the simulation results were: (1) local lateral and longitudinal accelerations coupled with the calculated Euler yaw angle multiplied by vehicle mass; (2) global lateral accelerations multiplied by the vehicle mass; (3) contact forces between the vehicle and the barrier components with a CFC 60 filter; and (4) contact forces between the vehicle and the barrier components with a CFC 60 filter and a 50-msec moving average. The accelerations were obtained using the command *ELEMENT_SEATBELT_ACCELEROMETER and outputted with *DATABASE_HISTORY_NODE. Contact forces were obtained using the command *CONTACT_FORCE_TRANSDUCER and included the exterior shell of the vehicle and all of the barrier parts.

The filtered contact force with the Silverado model resulted in peak lateral impact forces approximately 40 percent greater than what was experienced during test no. SFH-1, as shown in Figure 60. However, after applying a 50-msec moving average, the peak force was 10.6 percent less than what was experienced during test no. SFH-1. The global acceleration multiplied by the vehicle mass as well as the local accelerations coupled with yaw multiplied by vehicle mass gave similar force trends. The global acceleration multiplied by vehicle mass resulted in a peak force within 4 percent. The local accelerations coupled with yaw multiplied by vehicle mass resulted in a peak force within 3 percent, as shown in Table 17. Higher forces occurred around tail slap in the Silverado simulation due to the rear tires and axle being stronger than observed for the full-scale crash test vehicle.

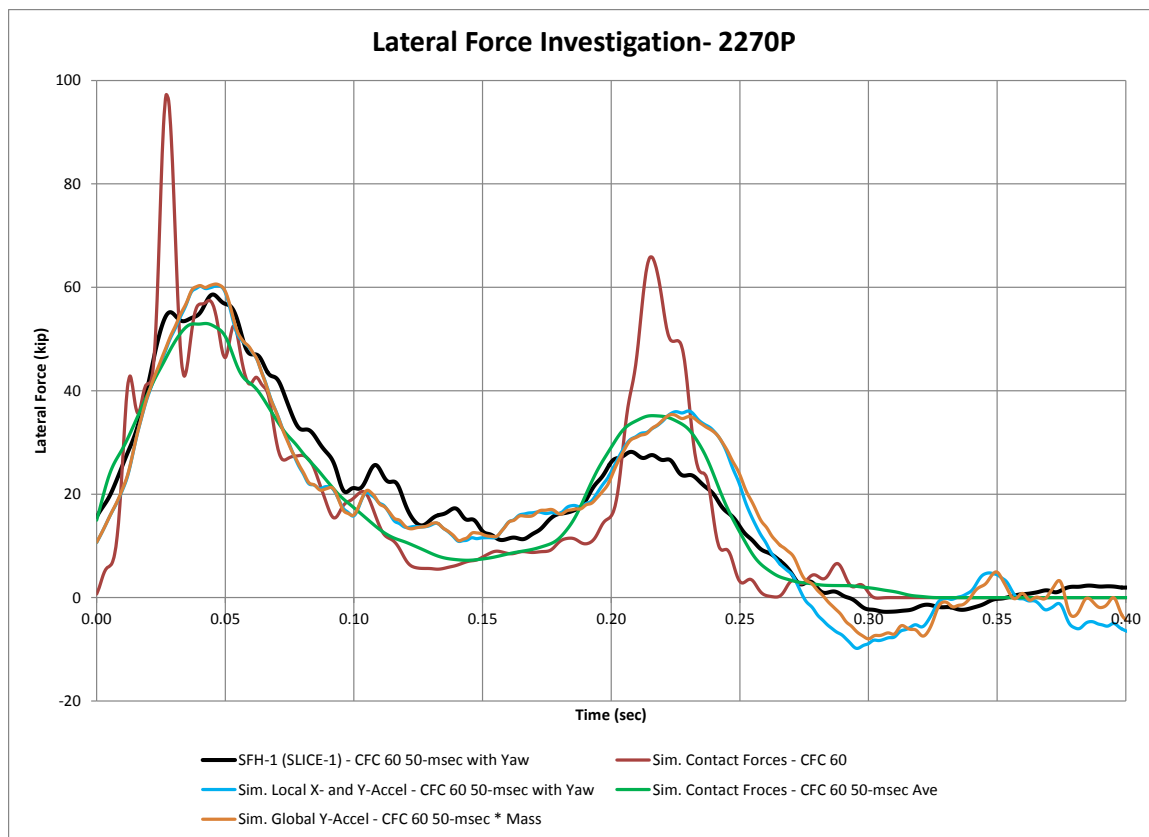


Figure 60. Lateral Force Comparison, 2270P

Table 17. 2270P Lateral Impact Force Comparison

Method	Max. Force kip (kN)	% Difference from Baseline SLICE 1
Full-Scale Local X- and Y- Accelerations with Yaw *Mass	58.6 (261)	Baseline
SILVERADO Simulation		
Sim. Local X- and Y- Accelerations with Yaw *Mass	60.3 (268)	2.8%
Sim. Global Y-Acceleration * Mass	60.6 (270)	3.3%
Sim. Contact Forces CFC60	97.2 (432)	39.7%
Sim. Contact Forces CFC60 50-ms Average	53.0 (236)	-10.6%

5.6 Discussion

During the original simulations run by Schmidt, et al., the Chevrolet Silverado model was used to simulate the 2270P impact event. However, the full-scale crash test

results had never been validated and compared to the simulation. Therefore, a simulation effort to validate the system was needed.

The Silverado model showed similar vehicle behaviors to those observed in test no. SFH-1. The Silverado vehicle model mass was within 4 percent of the full-scale test vehicle mass. The length of contact was accurately shown through simulation with the parallel times being 7 msec apart. However, the exit angle for the Silverado model was approximately 68 percent lower than observed in the full-scale crash test. Similarly, the Silverado model started to yaw back towards the barrier after exiting the system. The roll and pitch angles compared well with the full-scale crash test.

The occupant risk values showed varying results. The OIV values between the Silverado simulation and test no. SFH-1 were within 13 percent for the longitudinal direction and 10 percent for the lateral direction, respectively. However, the ORA values did not compare well with the full-scale crash test. The lateral ORA was 33 percent larger than test no. SFH-1, which was caused by the tail slap of the Silverado model against the barrier. The rear tires and axle in the model were believed to be stronger than the full-scale crash test vehicle tires, so the lateral ORA was not accurate. Similarly, the longitudinal ORA value was over 100 percent different due to the left-front tire re-impacting the ground after impact. The ORA values in simulation with the Silverado model were not representative of the full-scale crash test after the vehicle exited the system.

Lastly, different methods were used to determine the forces imparted on the barrier. Using filtered contact forces provided lateral impact forces within 40 percent of what was found in test no. SFH-1. The other three methods for determining the lateral

impact forces gave a closer approximation to the full-scale crash test. The global y-acceleration multiplied by the Silverado vehicle model mass was selected for use since it was within 1 percent of the local accelerations coupled with yaw, but took less time to calculate. This method resulted in a peak lateral force approximately 3 percent greater than observed in test no. SFH-1, and the lateral force trends followed the full-scale crash test through the duration of the impact event.

6 SIMULATION AND FULL-SCALE TEST COMPARISON – 10000S

6.1 Overall Model Comparisons

The Ford F800 vehicle model [68] impacted the barrier model in the initial simulation effort for comparison to physical results obtained in test no. SFH-3. The test and simulation vehicles had different dimensions and mass distributions. The main differences were the location and amount of ballast. Further, the connection of the box to the frame in the F800 simulation model did not include any shear plates, and the simulation used ½-in. (13-mm) diameter U-bolts opposed to the ⅝-in. (16-mm) diameter U-bolts used in test no. SFH-3. The U-bolts in the F800 vehicle model were connected to the frame with simulated washers and plates. The suspension of the F800 vehicle model did not have failure enabled, not allowing the tires to disengage. A visual comparison of the vehicles is shown in Figure 61. The F800 model had a tire diameter of 37 in. (940 mm), while the full-scale vehicle had a tire diameter of 39½ in. (1,003 mm). The top of the bumper in the F800 was 32 in. (813 mm) above the ground, while the full-scale vehicle top bumper height was 29⅞ in. (759 mm) above the ground. The Ford F800 simulation model had a mass of 22,142 lb (10,043 kg). The actual test vehicle used in test no. SFH-3, utilized a Ford F800 with a test inertial mass of 21,746 lb (9,864 kg). Test no. SFH-3 utilized a 166-lb (75-kg) test dummy on the front, impact-side seat for a total vehicle mass of 21,912 lb (9,939 kg). The simulated F800 vehicle did not include additional mass for simulated occupants.

The F800 vehicle model impacted the barrier at a velocity of 56.5 mph (90.9 km/h) to correlate with test no. SFH-3. The impact angle during test no. SFH-3 was 14.9 degrees, while the impact angle used in the simulation was 15 degrees. The vehicles were

targeted to impact 4 ft – 11 in. (1.5 m) upstream from the ACJ between barrier nos. 5 and 6. In the simulation, the F800 impacted the barrier 4 ft – 7 in. (1.4 m) upstream from the ACJ. The vehicle in test no. SFH-3 impacted the barrier 5 ft – 1 in. (1.5 m) upstream from the ACJ. The static and dynamic coefficients of friction between the F800 vehicle model body/tires and the barrier was 0.1. Comparisons between the simulation and full-scale crash test results are shown in Table 18. Test sequential photographs are shown in Figures 62 and 63. Note that the extraction time for the accelerometer in the F800 model was determined based on the initial contact time, whereas the extraction time determined from test no. SFH-3 was based on the accelerations from the transducers placed in the box at the vehicle c.g.

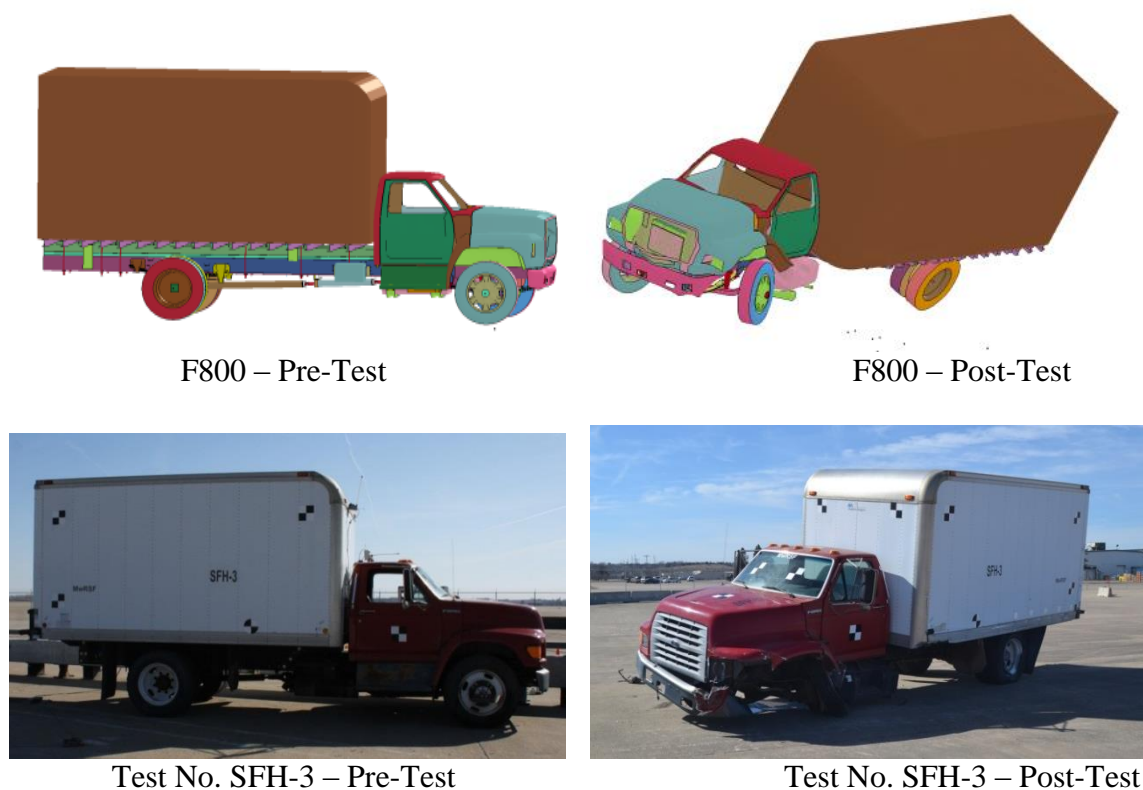
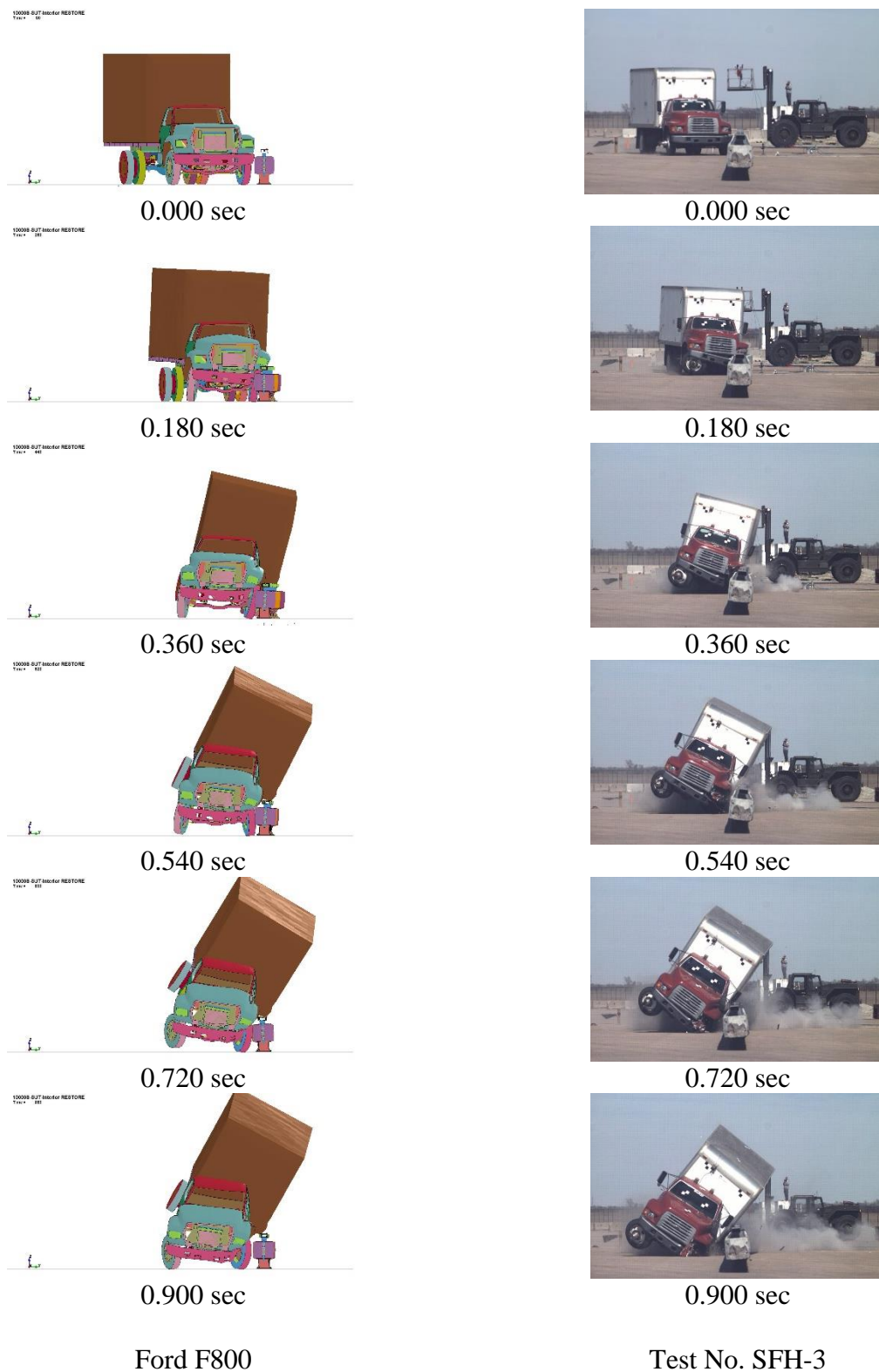


Figure 61. Vehicle Comparison, Pre- and Post-Test, 10000S

Table 18. Comparison of Results Between Test No. SFH-3 and 10000S Simulation

Item Description		MASH Test Designation No. 4-12 RESTORE Barrier	
Test		SFH-3	F800 Simulation
Reference Number		[20-21]	NA
Vehicle	Designation	10000S	10000S
	Test Inertial, lb (kg)	21,746 (9,864)	22,142 (10,043)
Impact Conditions	Velocity, mph (km/h)	56.5 (90.9)	56.5 (90.9)
	Angle, deg.	14.9	15.0
Impact Severity, kip-ft (kJ)		154.4 (209.3)	158.5 (214.9)
Parallel Conditions	Velocity, mph (km/h)	47.9 (77.0)	48.5 (78.0)
	Time, ms	326	380
Exit Conditions	Velocity, mph (km/h)	38.7 (62.3)	44.5 (71.7)
	Angle, deg.	9.0	3.4
	Time, ms	1,320	830
Length of Contact		59 ft – 3 in. (18.1 m)	51 ft – 8 in. (15.7 m)
ORA, g's	Longitudinal	-6.70	-6.62
	Lateral	7.82	9.58
OIV, ft/s (m/s)	Longitudinal	-8.30 (-2.53)	-6.89 (-2.10)
	Lateral	13.25 (4.04)	9.15 (2.79)
Test Article Deflections, in. (mm)	Dynamic of Concrete	13.9 (353)	12.4 (315)
	Dynamic of Steel Rail	15.1 (384)	12.5 (318)
	Working Width	60.2 (1,529)	68.0 (1,727)
Vehicle Stability, deg.	Max. Roll	-33.8	-32.1
	Max. Pitch	-10.7	-13.3
	Max. Yaw	25.7	19.1
Impact Point in relation to center of ACJ between barrier nos. 5 and 6 in. (mm)		4 ft – 7 in. (1.4 m)	5 ft – 1 in. (1.5 m)
No. of posts hit by leading tire (wheel snag)		1	0
Max. Lateral Impact Force, kips (kN) ¹		105.0 (467)	81.4 (362)

¹ Calculated using CFC60 50-msec moving average lateral and longitudinal accelerations coupled with Euler yaw angle.



Ford F800

Test No. SFH-3

Figure 62. 10000S Simulation vs. Test No. SFH-3 Sequential Photographs, Downstream View

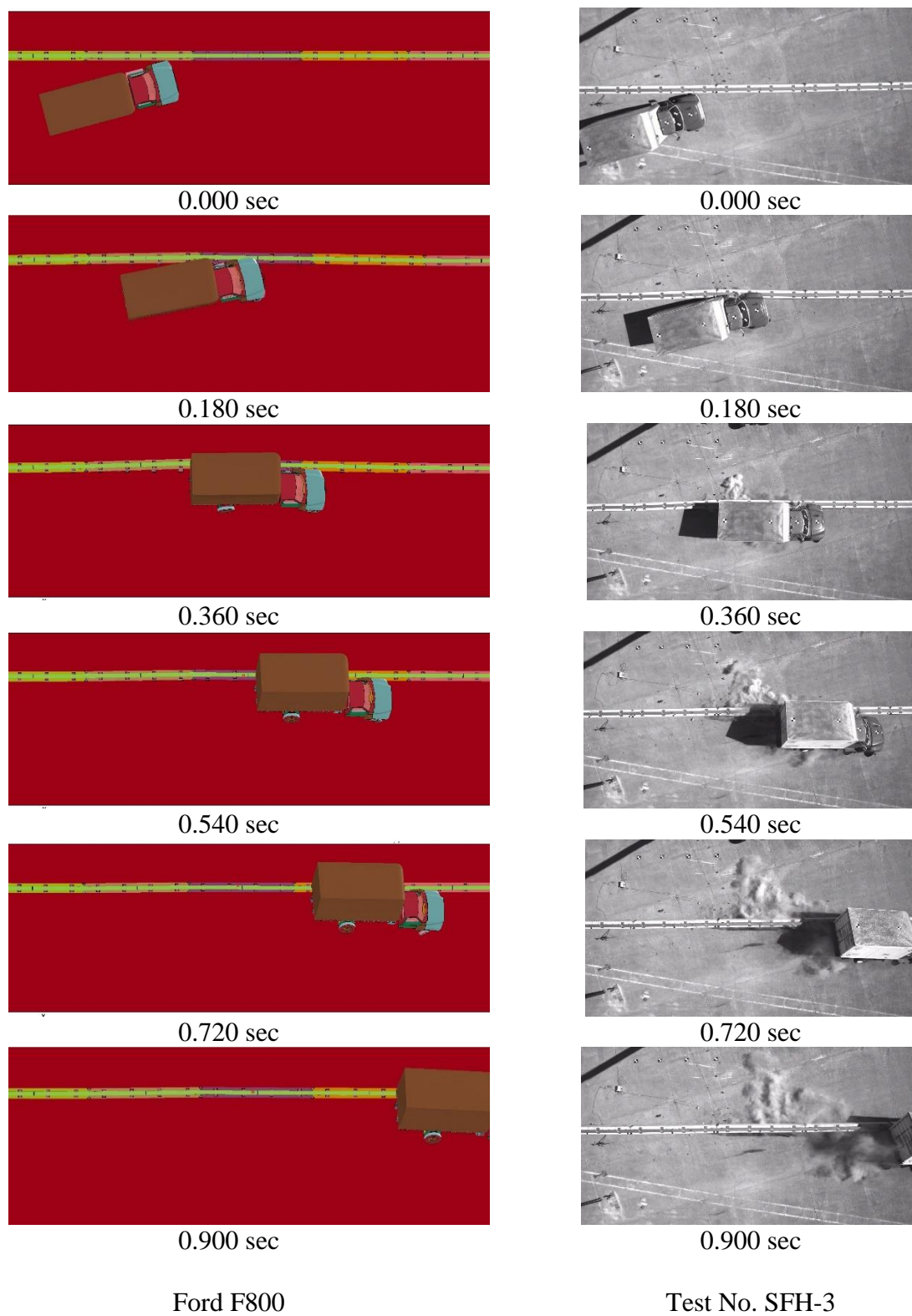


Figure 63. 10000S Simulation vs. Test No. SFH-3 Sequential Photographs, Overhead View

The lateral change in velocity for the F800 simulated vehicle model followed the same curve as observed for test no. SFH-3 through approximately 150 msec, as shown in Figure 64. Between 200 and 400 msec, the lateral change in velocity was greater than test no. SFH-3. After 400 msec, the F800 model was not laterally impacting the RESTORE barrier as severe, and was mainly traveling longitudinally, whereby the lateral change in velocity slightly decreased. The full-scale test vehicle lateral velocity decreased through the whole impact event. The longitudinal change in velocity of the F800 model more closely matched the results from test no. SFH-3 through 900 msec, as shown in Figure 64.

The barrier had accentuated dynamic deflection and working width due to the impact with the cargo box and excessive barrier rotations. The F800 model became parallel to the barrier at 380 msec, which was 54 msec later than observed in test no. SFH-3, and it had a parallel velocity 11.6 percent greater than observed in test no. SFH-3. The exit angle in the full-scale test was 62 percent greater than the angle observed through simulation.

No permanent system damage occurred in the LS-DYNA simulations; since, the concrete was modeled with a rigid material definition and could not fracture, and failure could not occur in the elastomer posts. The F800 left-front wheel did not contact any of the posts located downstream from impact, unlike observed in test no. SFH-3. The first post downstream of impact had a cut on the front face due to contact between the left-front tire lug nuts with the vehicle from test no. SFH-3.

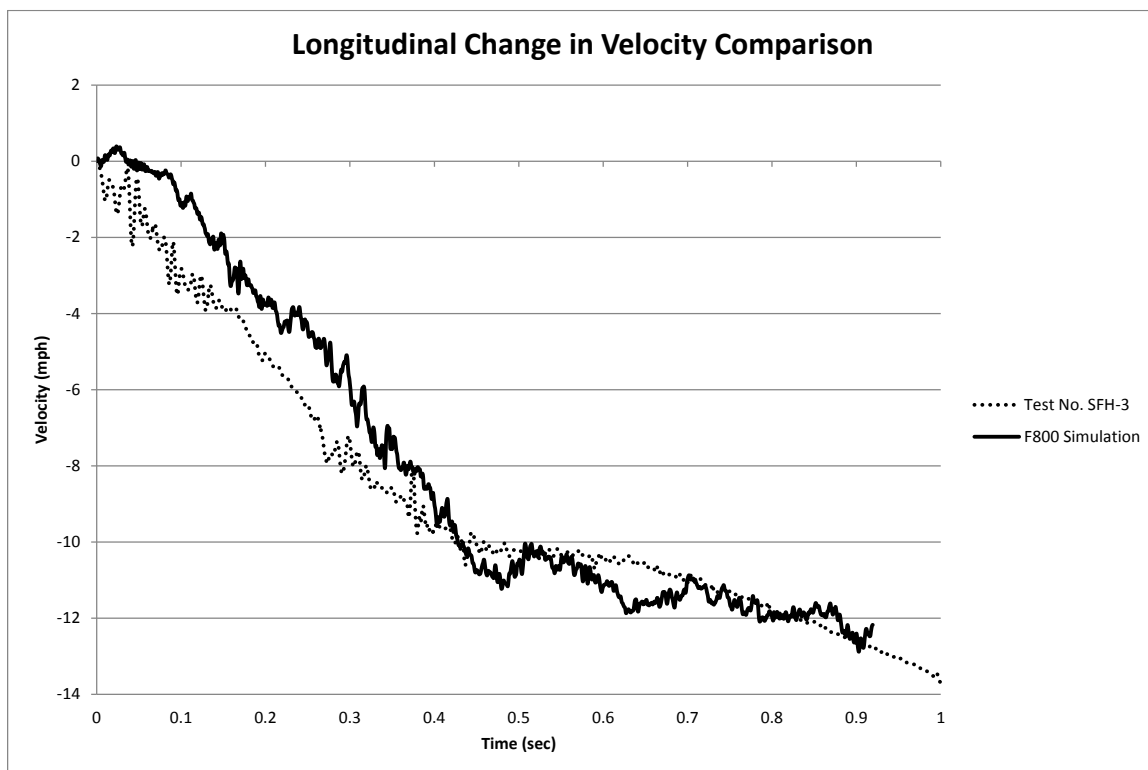
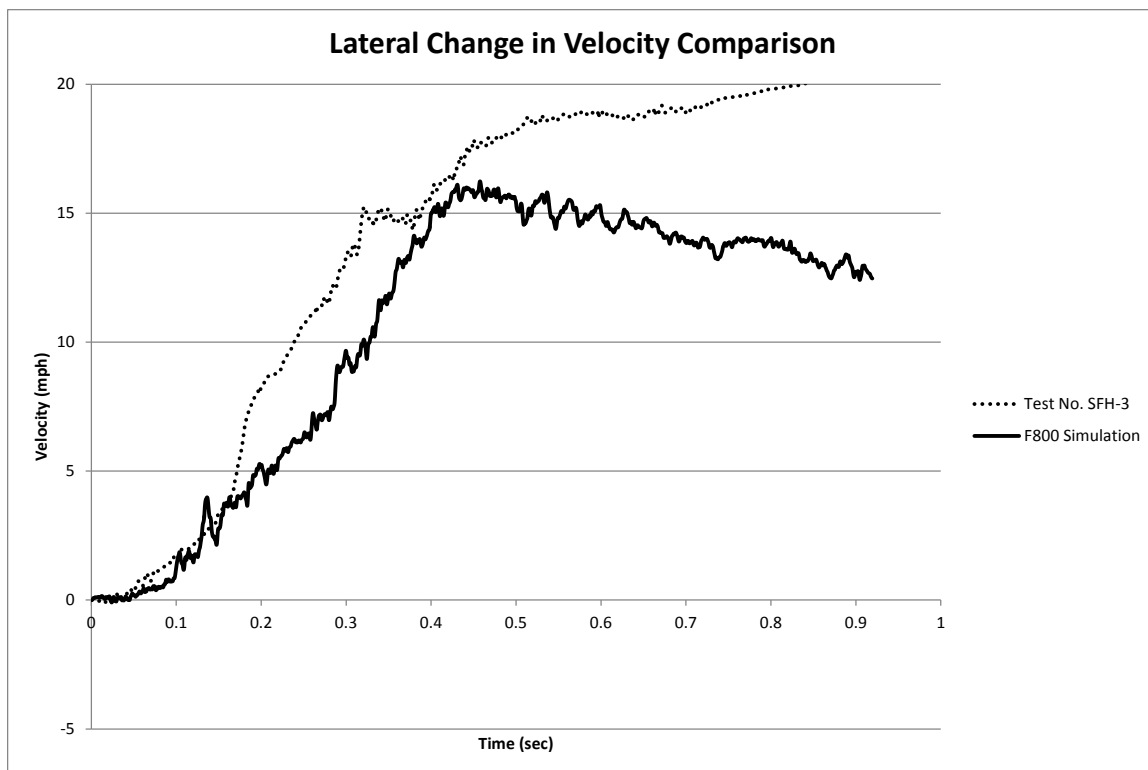
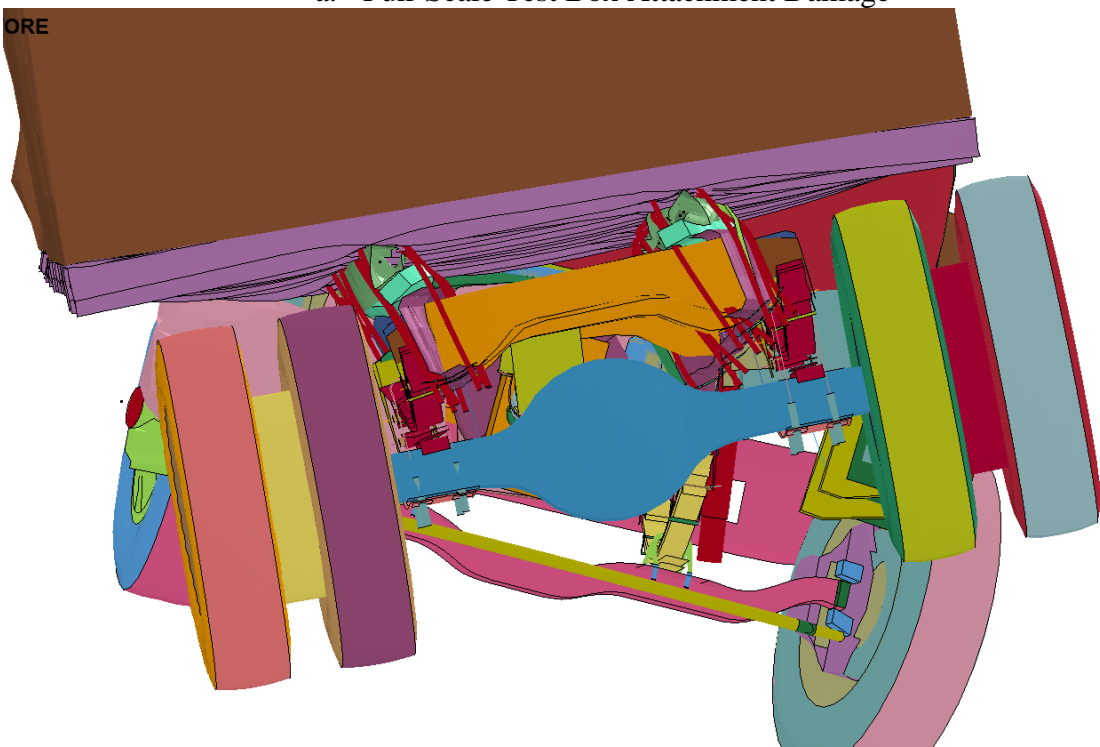


Figure 64. 1000S Lateral and Longitudinal Change in Velocity Comparison

The simulated vehicle damage for the F800 model through 900 msec varied compared to the damage found in the full-scale vehicle crash test. The left-front corner of the vehicle model was crushed inward and upward more in the F800 vehicle model, as compared to test no. SFH-3, as shown previously in Figure 61. The suspension in the F800 vehicle model was not enabled, thus not allowing the left-front tire to partially disengage as observed for the actual vehicle in the full-scale crash test. Further, the box frame in the F800 vehicle model deformed more than observed for the full-scale test vehicle. Whereas the U-bolts in the F800 model deformed more than observed in the full-scale crash test, as shown in Figure 65. Detailed comparisons of vehicle stability, occupant risk, dynamic deflection, snag, and lateral impact force are discussed in the following sections.



a. Full-Scale Test Box Attachment Damage



b. Simulation Box Attachment Damage

Figure 65. Comparison Between Simulation and Full-Scale Vehicle Box Attachment Damage

6.2 Vehicle Stability

Simulation data was processed similarly to that used for the full-scale crash test data. The raw local angular rates at the F800 model c.g. were extracted and converted into Euler angles based on the MASH vehicle orientation. Both the simulation and full-scale crash test angular rate data from the accelerometer placed at the c.g. of the vehicles in the box were processed in the order of yaw, pitch, then roll with a pitch singularity of 90 degrees.

The F800 model showed similar roll angles through the impact, as shown in Figure 66. The maximum roll angle through 900 msec for the F800 model was 5 percent more than the roll angle observed at 900 msec in test no. SFH-3. However, the maximum roll angles were approximately 30 msec apart. The maximum calculated roll angles through 685 msec were -32.1 and -33.8 degrees for test no. SFH-3 and the F800 model, respectively.

The F800 model showed pitch angles in the opposite direction directly after impact through approximately 300 msec, as shown in Figure 67. The F800 model pitched positively through 100 msec and proceeded to pitch negatively afterward. Test no. SFH-3 showed that the vehicle pitched negatively through 250 msec. After which, the vehicle in test no. SFH-3 pitched positively for approximately 50 msec and then proceeded to pitch negatively for the remainder of the impact event. The maximum pitch values were -10.7 and -13.3 degrees for test no. SFH-3 and the F800 model, respectively.

The yaw angles for the F800 model were similar to test no. SFH-3 through 200 msec, as shown in Figure 68. At 200 msec, the F800 model started to yaw more gradually than observed in test no. SFH-3. As a result, the maximum yaw angle of the F800 model

was 35 percent lower than observed in test no. SFH-3. The maximum yaw angles were 25.7 and 19.1 degrees for test no. SFH-3 and the F800 model, respectively.

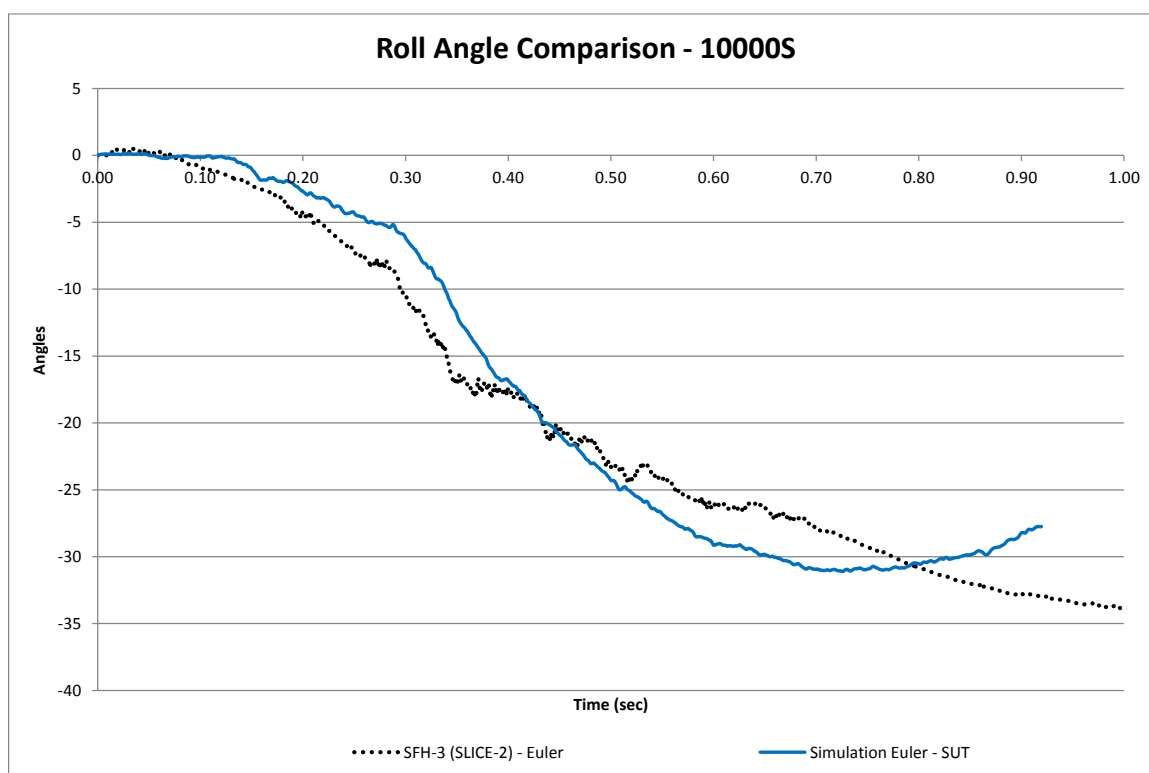


Figure 66. Interior Impact Roll Angle Comparison, 10000S

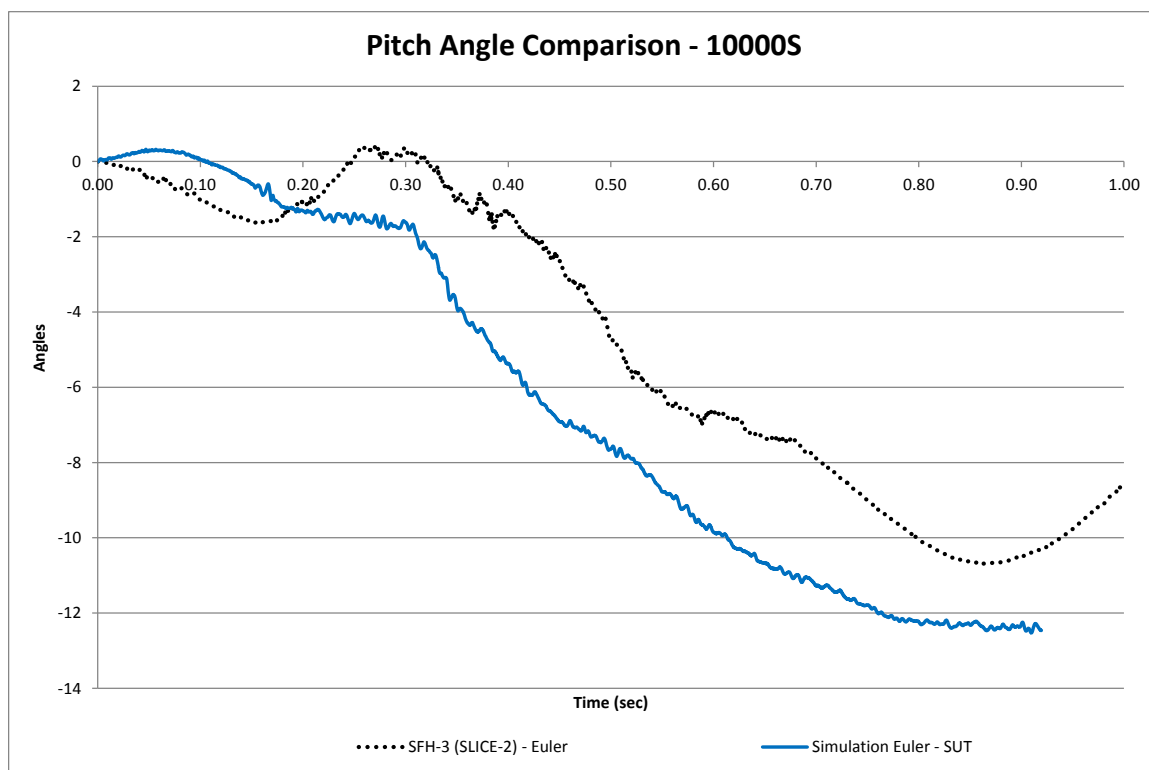


Figure 67. Interior Impact Pitch Angle Comparison, 10000S

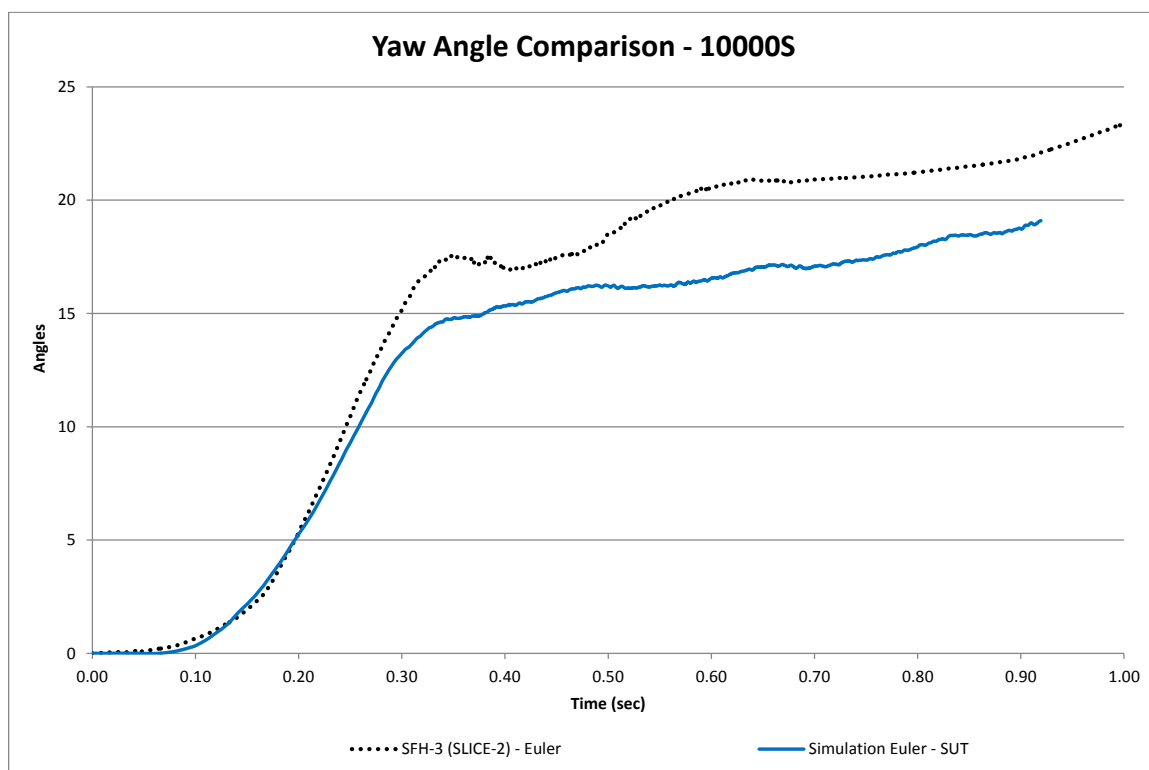


Figure 68. Interior Impact Yaw Angle Comparison, 10000S

6.3 Occupant Risk Analysis

Occupant risk values are not a required evaluation criteria for test designation no. 4-12. However, the calculated occupant impact velocities (OIVs) and maximum 0.010-sec occupant ridedown accelerations (ORAs) in both the longitudinal and lateral directions were extracted from the accelerometer located at the c.g. under the cargo box in the vehicle model and processed the same as used for the full-scale crash test accelerations, as compared in Table 19. The longitudinal and lateral ORA for the F800 model were 1 percent less and 23 percent greater than observed in test no. SFH-3, respectively. The accelerations may be different due to variations in the box attachment between the F800 vehicle model and the full-scale vehicle, as described earlier. The longitudinal and lateral OIV for the F800 vehicle model were 17 and 31 percent less than observed in test no. SFH-3. The transducer comparison data plots can be found in Appendix E.

Table 19. Summary of OIV and ORA, 10000S Vehicles

Evaluation Criteria		Transducer	
		SFH-3 SLICE-2	F800 Simulation
OIV ft/s (m/s)	Longitudinal	-8.30 (-2.53)	-6.89 (-2.10)
	Lateral	13.25 (4.04)	9.15 (2.79)
ORA g's	Longitudinal	-6.7	-6.62
	Lateral	7.82	9.58

6.4 Deflection and Snag

The maximum dynamic deflection of the concrete beam and steel tube as well as working width for test no. SFH-3 were 13.9 in. (353 mm), 15.1 in. (384 mm), and 60.2 in.

(1,529 mm), respectively. Similarly, the maximum dynamic deflection of the concrete beam and steel tube in the simulation were determined to be 12.4 in. (315 mm) and 12.5 in. (318 mm) with the Ford F800 model. The simulated working width was determined to be 68.0 in. (1,727 mm), as shown in Table 20, respectively.

During test no. SFH-3, the left-front tire of the vehicle contacted the first post downstream from impact. The lug nut from the tire caused a tear in the impact face of the elastomer post. In the simulation with the F800 model, the left-front tire did not contact any of the posts.

Table 20. Dynamic Deflection, Working Width, and Post Snag, 10000S Vehicles

Vehicle Type	Dynamic Concrete Deflection in. (mm)	Dynamic Steel Deflection in. (mm)	Working Width in. (mm)
Ford F800 (SFH-3)	13.9 (353)	15.1 (384)	60.2 (1,529)
F800 Model	12.4 (315)	12.5 (318)	68.0 (1,727)

6.5 Impact Force Investigation

The same methods for determining lateral barrier force that were explored with the small car and pickup truck impacts were investigated with the single-unit truck impacts. The baseline method to determine the lateral barrier forces during the full-scale crash test used local lateral and longitudinal accelerations coupled with the Euler yaw angle multiplied by vehicle mass. The different methods to calculate barrier force from the simulation results were: (1) local lateral and longitudinal accelerations coupled with the calculated Euler yaw angle multiplied by vehicle mass; (2) global lateral accelerations multiplied by the vehicle mass; (3) contact forces between the vehicle and the barrier

components with a CFC 60 filter; and (4) contact forces between the vehicle and the barrier components with a CFC 60 filter and a 50-msec moving average. The accelerations were obtained using the command

*ELEMENT_SEATBELT_ACCELEROMETER and outputted with

*DATABASE_HISTORY_NODE. The accelerometer was placed at the c.g. of the F800 vehicle model under the cargo box. Contact forces were obtained using the command *CONTACT_FORCE_TRANSDUCER and included the exterior shell of the vehicles and all of the barrier parts.

The peak forces between the full-scale crash test and the simulation occurred at different times. The peak observed in test no. SFH-3 occurred during the initial impact, while the peak observed in the simulations with the F800 vehicle model occurred during the tail slap. The differences may be due to the suspension failure not being enabled or the box attachment in the simulation.

The filtered contact force with the F800 model resulted in peak lateral impact forces approximately 65 percent greater than what was experienced during test no. SFH-3, as shown in Figure 69. After applying a 50-msec moving average, the peak force was reduced to 43 percent less than what was experienced during test no. SFH-3. The global acceleration multiplied by the vehicle mass compared well to the local accelerations coupled with yaw multiplied by vehicle mass. They were consistent through approximately 250 msec, where they started to diverge slightly. The global acceleration multiplied by vehicle mass resulted in a peak force approximately 30 percent less than observed in test no. SFH-3. The local accelerations coupled with yaw multiplied by vehicle mass resulted in a peak force 23 percent less than observed in test no. SFH-3, as

shown in Table 21. However, the tail slap in test no. SFH-3 was calculated to be approximately 75.1 kips (334 kN) at approximately 300 msec, respectively. The global Y-acceleration multiplied by the vehicle mass resulted in a tail slap force approximately 2 percent smaller than observed in the full-scale crash test at approximately 340 msec. Similarly, the local accelerations coupled with yaw and multiplied by mass resulted in a tail slap force approximately 8 percent larger than observed in test no. SFH-3. Both of the simulated lateral tail slap forces were approximately 50 msec later than observed during the full-scale crash test.

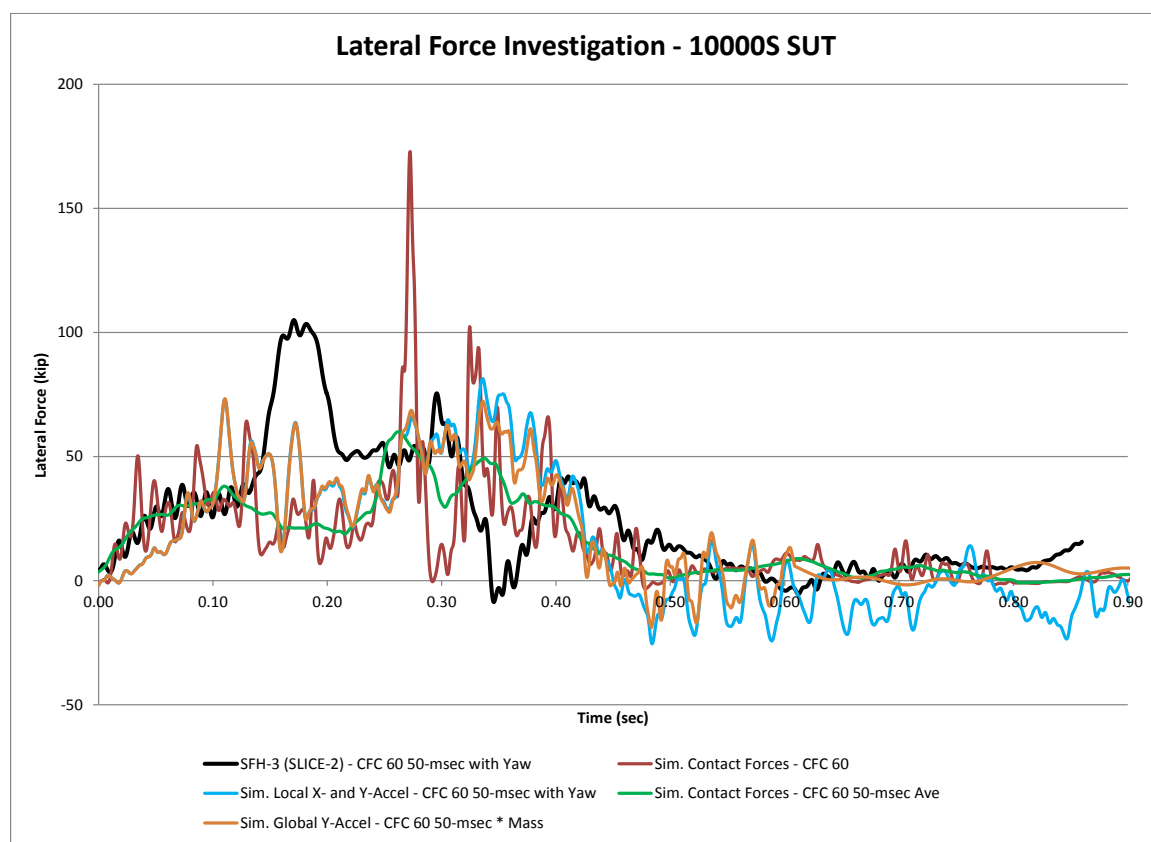


Figure 69. Lateral Impact Force Comparison, 10000S

Table 21. 10000S Lateral Impact Force Comparison

Method	Max. Force kip (kN)	% Difference from Baseline SLICE 1
Full-Scale Local X- and Y- Accelerations with Yaw *Mass	105.0 (467)	Baseline
SUT Simulation		
Sim. Local X- and Y- Accelerations with Yaw *Mass	81.4 (362)	-22.5%
Sim. Global Y-Acceleration * Mass	73.3 (326)	-30.2%
Sim. Contact Forces CFC60	172.8 (769)	64.6%
Sim. Contact Forces CFC60 50-ms Average	60.0 (267)	-42.9%

6.6 Discussion

During the original simulations run by Schmidt, et al., the Ford F800 model was used to simulate the 10000S impact event. However, the full-scale crash test results had never been validated and compared to the simulation. Therefore, a validation effort was needed to validate the barrier system.

The F800 model showed some similar vehicle behaviors to those observed in test no. SFH-3. The F800 vehicle model showed dynamic deflections of the concrete rail within 10 percent of those observed in test no. SFH-3 and a working width within 14 percent. The simulation showed similar trends in roll and yaw. However, the F800 model did not yaw as much as observed in test no. SFH-3. The pitch angles between the F800 vehicle model and the full-scale crash test vehicle did not follow the same trend. However pitch was minimal and the magnitudes varied by 3 to 4 degrees.

Occupant risk values were not a required evaluation criteria for test designation no. 4-12. However, they were used for comparison purposes. The longitudinal and lateral ORA values for the F800 model were 1 percent less and 23 percent greater than observed in test no. SFH-3. The larger lateral ORA in the simulation may be due to variations in the box attachment between the F800 vehicle model and the full-scale test vehicle. The

longitudinal and lateral OIV values were 17 and 31 percent less than observed in test no. SFH-3.

Lastly, different methods were used to determine the forces imparted on the barrier. None of the methods were similar to the full-scale crash test as all of the methods used under predicted the peak force observed during the initial impact. However, the methods were considered when determining the tail slap of the single-unit truck impact. The use of filtered contact forces provided lateral impact forces within 65 percent of what was observed in test no. SFH-3. The other three methods provided a closer approximation to the results observed in the full-scale crash test. The global Y-acceleration multiplied by vehicle mass and the local x- and y-accelerations coupled with yaw and multiplied by vehicle mass followed a similar trend, but the peak lateral forces were 8 percent different. The local x- and y-accelerations coupled with yaw and multiplied by the vehicle mass was the closest representation to the peak force observed in test no. SFH-3. However, the global Y-acceleration multiplied by the vehicle mass was within 2 percent of the tail slap force observed in test no. SFH-3. Therefore, the global Y-acceleration multiplied by the vehicle mass is suggested for use in estimating lateral impact force for the single-unit truck crash events.

The SUT vehicle model was good at predicting the maximum tail slap force, however the tail slap peak force occurred later than observed in test no. SFH-3. The dynamic deflection of the RESTORE barrier model closely resembled the dynamic barrier deflections found in test no. SFH-3. The roll angles before 700 msec and the the pitch angles were also close representations to the full-scale crash test. However, the

F800 model box attachment was not a good representation to the full-scale crash test vehicle.

7 DESIGN CONSIDERATIONS

7.1 Introduction

The RESTORE barrier system was initially targeted for urban roadside/median applications. The barrier met the TL-4 safety performance requirements set forth in MASH [15]. Therefore, the transition section must also meet MASH TL-4 safety performance criteria. Since the RESTORE barrier can be used as a median barrier, the transition must also be designed for reverse-direction impacts. Further, the transition between the RESTORE barrier and a rigid concrete buttress should accommodate differences in design impact forces, degrees of freedom, tolerances, geometry (height, width, and shape), stiffness, and roadway geometry, and successfully contain and redirect an errant vehicle.

During testing, the RESTORE barrier deflected in the Y-direction and rotated about the X- and Z-axes within interior regions. The rigid concrete buttress will be constrained in all directions. As a vehicle travels toward the stiffer barrier, vehicle pocketing and snag can occur, similar to approach guardrail transitions, as explained in Section 2.2. If excessive vehicle pocketing and snag are prevalent, excessive decelerations and/or occupant compartment deformations may occur. When a vehicle travels toward the stiffer barrier, a gradual change in barrier deflection is required before reaching the rigid concrete buttress. When configuring the transition section, connections between the RESTORE barrier and the rigid buttress as well as connections between adjacent interior components were considered.

For the RESTORE barrier, a coordinate system was used to describe the forces, moments, rotations, and displacements, as shown in Figure 70. The lateral direction is the Y-axis, the longitudinal direction is the X-axis and the vertical direction is the Z-axis.



Figure 70. Barrier Coordinate System

7.2 Design Impact Forces

The RESTORE barrier was originally designed to withstand a 75-kip (333-kN) point load during an interior impact event [16-17]. Based on the results obtained from test no. SFH-3, the maximum lateral load imparted on the barrier was estimated to range between 94.9 and 105.0 kips (422 and 467 kN), as determined from the SLICE-1 and SLICE-2 accelerometer and rate transducer data, as previously described in Section 3.9.4. However, different studies and references have provided varying design lateral impact forces for TL-4 crash events according to the MASH safety performance criteria, as outlined in Section 2.6. Based on previous research as well as the estimated loading observed in a full-scale crash test with the interior region of the RESTORE barrier, a lateral design load of 100 kips (445 kN) was chosen for use in the transition region. As

such, it may be necessary to examine and redesign the steel reinforcement near the concrete segment ends to account for the increased lateral, longitudinal, torsional, and bending loads imparted to the stiffened RESTORE barrier within transition regions.

Following an analysis of data from test no. SFH-3, a coefficient of friction of 0.45 was estimated by dividing the calculated maximum tangential barrier force of 47.4 kips (211 kN) by the calculated perpendicular barrier force of 105.0 (467 kN). The product of a 100-kip (445-kN) design load and a coefficient of friction of 0.45 provided an initial longitudinal design force of 45 kips (200 kN) within the transition region.

7.3 Degrees of Freedom and Tolerances

The RESTORE barrier allows translation in the X- and Y-directions and limited compression and tension in the Z-direction due to the addition of the metal skids in previous work. The RESTORE barrier can also rotate about the X-, Y-, and Z-axes. The joints at the ends of the concrete segments are configured with the ACJ hardware, which largely provides shear and moment transfer. Due to the need to accommodate some construction tolerance, limited joint rotations relative to one another were observed in the full-scale crash testing program and are described below.

The rigid concrete buttress cannot translate in the X-, Y- and Z-directions, and cannot rotate about the X-, Y-, and Z-axes. Thus, some degrees of freedom of the joint within the transition region may need to allow translation and/or rotation in order for the RESTORE barrier to connect to a rigid concrete buttress. For example, the joint may likely be configured to prevent translation in the Y-direction but allow limited translation in the X- and Z- directions. The joint may also be configured to prevent rotation about the X-direction but allow partial or full rotation about the Y- and Z-axes, respectively.

Results from the interior testing program may provide additional insights into the selection of fixed, free, or partially-free degrees of freedom for rotations and translations as well as construction tolerances. Dynamic barrier deflections during test no. SFH-3 were measured using an overhead view through video analysis on targets located on the upstream and downstream ends. Note that targets were placed on the top of the concrete beam segments and the top of the steel tube assembly. The vertical difference between the concrete and steel tube targets was 8½ in. (216 mm) in the non-impacted position. The maximum difference in lateral deflection between the concrete and upper tube targets was calculated to be 2.3 in. (58 mm). From geometry, a maximum rotation angle of 15.7 degrees was calculated about the longitudinal X-axis during an interior impact scenario, as shown in Table 22. If excessive rotation is found, there is a higher risk of vehicle snag on the elastomer posts or metal skids with the wheel or fender, which could lead to excessive instabilities. Therefore, the new joint at the transition region should limit barrier rotations about the X-axis. To accommodate minimal rotation about the X-axis, the last barrier segment(s) should withstand torsional loading near the ends of the installation, and the need for additional metal skids and elastomer posts should be evaluated.

During test no. SFH-3, 13.9 in. (353 mm) and 15.1 in. (283 mm) of dynamic deflection occurred in the concrete barrier and upper steel tube assembly located at the upstream end of barrier no. 6, respectively. Multiple barrier segments translated backward during the impact event. The longitudinal difference (X-axis) between the upstream and downstream concrete barrier targets was approximately 19 ft – 3 in. (5.9 m). Similarly, the top steel tube had four targets placed on each segment, where the steel

tube posts were located. The longitudinal difference between each target was approximately 5 ft (1.5 m). At the time of maximum deflection, displacement measurements were recorded for the concrete barrier segments near the impact location. Due to multiple barriers deflecting during impact, the maximum rotation angle of a single barrier with respect to the global Z-axis was calculated. The maximum global rotation of a single concrete beam was calculated to be 1.6 degrees about the Z-axis. Further, the maximum global rotation of the top steel tube was calculated to be 1.9 degrees. Thus, a maximum relative angle between the RESTORE barrier segment ends could be determined, as shown in Table 22.

Table 22. Barrier and Tube Rotations and Translations for Interior SUT Impact Event

Target Location	Deflections from Test No. SFH-3 in. (mm)		Max. Rotation about Z-axis (degrees)			Lateral Displacement Difference Between Concrete and Tube Targets in. (mm)	Max. Rotation about X-axis (degrees)
	Concrete Beam	Upper Tube	Across Concrete Segment	Across Steel Tube Segment	Max. Relative Angle Between Barriers		
Upstream Barrier No. 5	7.0 (178)	7.7 (196)	1.6	1.9		0.7 (18)	4.7
Downstream Barrier No. 5	13.6 (345)	13.8 (351)			0.4	0.2 (5)	1.3
Upstream Barrier No. 6	13.9 (353)	15.1 (384)	1.2	1.6	0.3	1.2 (30)	8.1
Downstream Barrier No. 6	8.9 (226)	10.0 (254)				1.1 (28)	7.4
Upstream Barrier No. 7	8.2 (208)	9.5 (241)	1.2	1.3		1.3 (33)	8.8
Downstream Barrier No. 7	3.2 (81)	5.5 (140)				2.3 (58)	15.7

Note: Barriers in table were the only barriers in view during overhead video analysis

In the transition region, the last 20 ft (6.1 m) concrete barrier segment could be assumed to rotate from a zero displacement position to a deflection of approximately 13.9 in. (353 mm), as observed in test no. SFH-3. The maximum estimated rotation over

the 20 ft (6.1 m) long barrier segment would be approximately 3.3 degrees, if hinged at the far end. For the transition configuration, the joint should accommodate a rotation angle of +/- 4 degrees about the vertical Z-axis, if the concrete sections remain the same length.

Real-world installations may be several miles long. As such, a construction tolerance of +/- ¼ in. (6 mm) was provided for the ACJ to allow sufficient clearance to connect both ends of the concrete segments. The new joint within the transition region will be designed to accommodate +/- 1½ in. (38 mm) of axial translation in the X-direction for construction tolerance.

Barrier stiffening may be needed to limit lateral deflection (Y-direction) before the system terminates in order to reduce the potential for vehicle snag on the rigid concrete buttress end. Further, the RESTORE barrier utilized metal skids to reduce rotations about the X- and Y-axes during interior impact events. Thus, the metal skids should be retained through the transition region to limit rotations about the X- and Y-axes.

After the metal skids were implemented into the RESTORE barrier, as noted in Chapter 3.7, the vertical deflection in the Z-direction was virtually zero at the interior locations. Thus, the joint between the RESTORE barrier and the rigid concrete buttress should be designed to limit the vertical displacements. The limited displacements will assist in reducing concerns for excessively loading the transition hardware in the vertical direction.

7.4 Rigid Concrete Buttress Geometry

Multiple concrete barrier configurations are used in roadside and median applications. Thus, a universal rigid concrete buttress was desired to more easily transition from the RESTORE barrier to all common barrier shapes. The common barrier shapes used in roadside and median applications are safety-shaped barriers (i.e., F-shape or New Jersey shape), single-slope barriers, or vertical barriers, as described in Chapter 1. Therefore, a standard buttress end was desired to largely mirror the RESTORE barrier on the other side of the transition joint, except that the lower region consisted of a narrow concrete wall, as shown in Figure 71. This geometry was chosen to mitigate concerns for wheel snag on the end of the lower buttress.

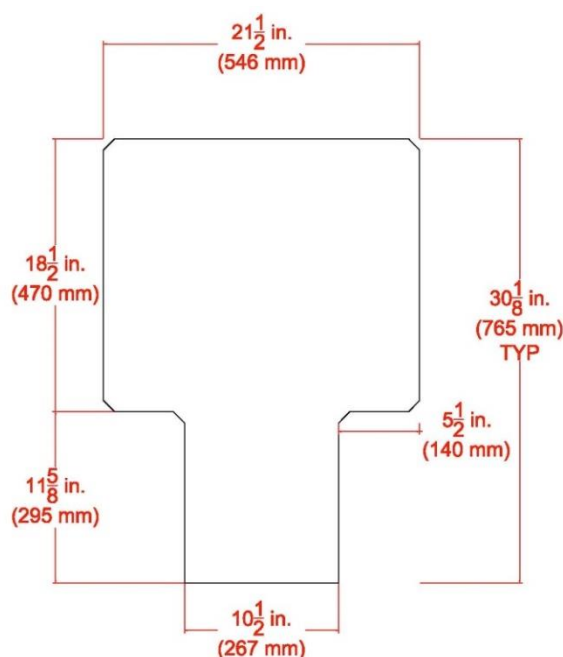


Figure 71. Proposed Buttress Geometry at New Transition Joint Location

The rigid concrete buttress was expected to be approximately 10 ft (3.0 m) long to allow for a gentle height, width, and shape transition to other common barrier shapes.

Based on prior research noted in Section 2.5, a horizontal flare rate of 6:1, a vertical

concrete flare rate of 8H:1V, and a vertical steel flare rate of 5H:1V have been effectively used. Note that the horizontal flare rate was only successfully crash tested on a concrete toe, and no research has been conducted on a full barrier height horizontal flare rate. A reinforced concrete foundation should be provided under the buttress to adequately anchor it and prevent translations and rotations. Further, a foundation is also required under the RESTORE barrier to adequately anchor the elastomer posts, which use threaded rods that are epoxied into a concrete foundation, and support the steel skids.

7.5 Lateral Stiffening in Transition Region

Many steel approach guardrail transitions to rigid concrete buttresses incorporate the use of larger, stronger, and longer posts, as well as reduced post spacing, to gradually reduce lateral barrier deflections. When transitioning the RESTORE barrier to a rigid concrete buttress, it may be necessary to change the number and/or size of elastomer posts as well as the steel skids. Therefore, a simulation study, combined with analytical calculations, will be conducted to evaluate if the current configuration is adequate and determine if any changes to posts or metal skids are needed.

7.6 Highway Geometry

7.6.1 Superelevation

During the initial barrier testing, a total of ten static tests were conducted on the elastomer posts [19]. During static testing, the fenders were loaded in compression at different superelevations to determine the optimal rail weight and post spacing at various temperatures. The preliminary design concept had 14-in. (356-mm) wide elastomer posts able to support a uniform dead load of 460 lb/ft (685 kg/m). Through static testing, several of the component tests showed that this static load would have been too great for

the system to remain stable. Based on the performance of the system through static testing, the targeted rail weight was approximately 320 lb/ft (476 kg/m) or less when the 10-in. (254-mm) wide elastomer posts were spaced at 5 ft (1.5 m) centers [19]. For the RESTORE barrier, an 8 percent maximum superelevation was considered practical for use on a high-speed urban roadway. However, a 14 percent grade was used in the static testing program. The 10-in. (254-mm) wide elastomer posts were used for the evaluation with 5-ft (1.5-m) post spacing. The system was stable through at least a 218-lb/ft (325-kg/m) uniform load. However, it was anticipated that there would not be a problem using an 8 percent horizontal grade and including steel supports with a 320-lb/ft (476-kg/m) uniform load. The 8 percent superelevation was not explicitly evaluated but would be further explored after the barrier design was finalized.

7.6.2 Horizontal Curves

Previous research was not documented to determine the minimum horizontal curve accommodated by the RESTORE barrier. Therefore, a study was considered to determine if the RESTORE barrier could accommodate large horizontal curves.

The AASHTO Green Book, *A Policy on Geometric Design of Highways and Streets*, refers to the minimum horizontal radius being determined from the maximum rate of superelevation, the maximum side friction factor, and the given design speed [81]. The U.S. customary calculation for the minimum horizontal radius is shown in Equation 11. With the determined superelevation, as noted previously as 8 percent, a design speed of 62 mph (100 km/h), and the side friction of value interpolated from Table 3-7 in the AASHTO Green Book [81] as 0.12, a minimum horizontal radius was calculated to be 1,281 ft (390.4 m). To be conservative, the minimum horizontal curve for a highway

where the RESTORE barrier will be used was determined to be approximately 1,300 ft (396.2 m).

$$R_{\min} = \frac{V^2}{15(0.01e_{\max} + f_{\max})} \quad (11)$$

Where: R_{\min} = Minimum horizontal radius, ft (m)

V = Design speed, mph (km/h)

e_{\max} = Maximum superelevation, percent

f_{\max} = Maximum side friction factor

The concrete barrier segment length was 20 ft (6.1 m) and the maximum tolerance that the ACJ was allowed to tolerate was +/- ¼ in. (6 mm), as stated previously. Thus, the joint could be positioned that one side has a ¼ in. gap and the other side has a ¾ in. (19 mm) gap. The distance between the largest and smallest gap widths between the two ACJs was 12½ in. (318 mm), as shown in the drawing set in Appendix B. From geometry, the maximum angle that the joint could accommodate would be approximately 2.3 degrees about the Z-axis.

Highway geometry is typically measured in 100 ft (30.5 m) increments. The degree of curvature for a 100 ft (30.5 m) centerline is given in Equation 12. With the determined minimum radius of 1,300 ft (396.2 m), the degree of curvature for the horizontal curve was 4.4 degrees over a 100 ft (30.5 m) distance. Over a 100 ft (30.5 m) distance, five RESTORE barrier segments will be used, with a total of 5 joints in consideration. Thus, each joint would have to accommodate approximately 0.9 degrees of rotation about the Z-axis. Since the joint can accommodate 2.3 degrees about the Z-axis, the ACJ hardware satisfies the minimum horizontal curvature requirements.

$$D = \frac{36,000}{2\pi R} = \frac{5,729.6}{R} \quad (12)$$

Where: D = Degree of curvature per 100 ft (30.5 m) of centerline, degrees

R = Radius of curve, ft (m)

7.6.3 Vertical Curves

Similarly, previous research was not documented to determine the maximum vertical curve that could be accommodated by the RESTORE barrier. However, it was designed for with both the ACJ and the elastomer pads utilized with the steel support skids. Therefore, a study was considered to determine if the RESTORE barrier could accommodate typical vertical curves. The determination of the vertical curves followed a design process derived by Bateman, et al. [82-83].

Vertical curves along roadways are designed to be parabolic in shape. For a parabolic curve, the rate of change of the slope (the slope gradient) is constant. The general equation for a parabola is shown in Equation 13. The Green Book refers to the tangent slopes of the roadway as grades, which are expressed as a percent [81]. A vertical curve with horizontal length, L , and tangent grades, G_1 and G_2 , at its ends, as shown in Figure 72, will have a value, K , associated with it such that $K = L/A$, where A is the algebraic difference between the two tangent grades.

$$y = ax^2 + bx + c \quad (13)$$

Where: y = vertical coordinate of the roadway
 x = horizontal coordinate of the roadway
 a , b , and c are coefficients

The first derivative of the quadratic equation provides the general form of the equation for the slope gradient, as shown in Equation 14.

$$\frac{dy}{dx} = 2ax + b \quad (14)$$

If the origin is placed at the beginning of the vertical curve, as shown in Figure 72, where the tangent grade is G_1 (a percent), the slope gradient at $x = 0$ is given by Equation 15.

$$\left(\frac{dy}{dx}\right)_{x=0} = b = \frac{G_1}{100} \quad (15)$$

Where: G_1 = tangent grade (as a percent) at the beginning of the vertical curve (i.e., $x = 0$)

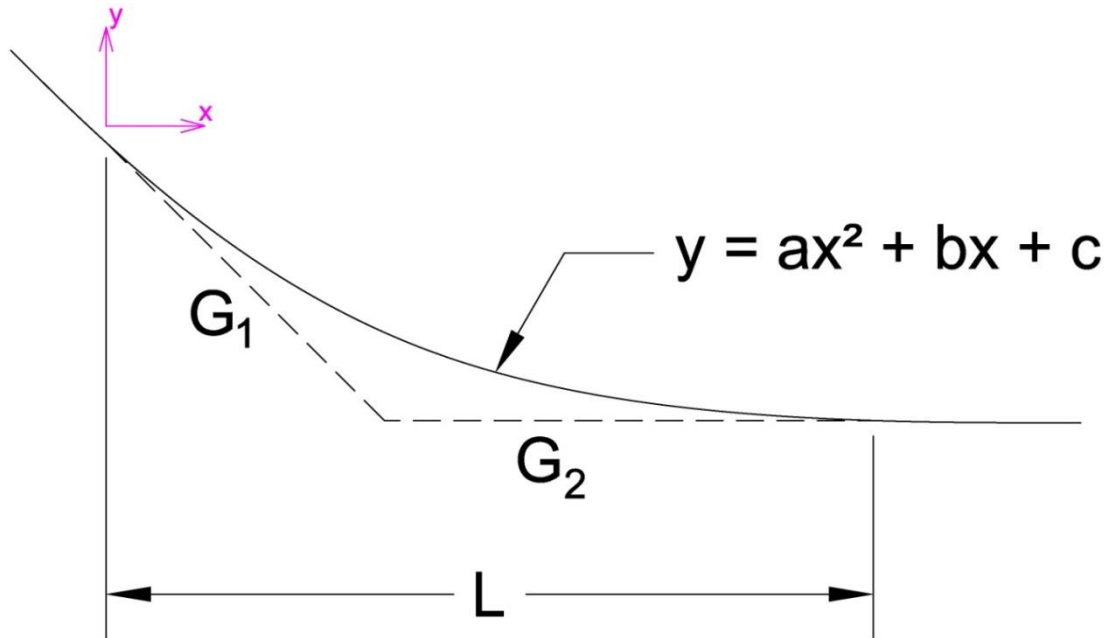


Figure 72. Typical Parabolic Vertical Curve

At $x = L$, the end of the curve, the tangent grade is G_2 (a percent), as shown in Equation 16.

$$\left(\frac{dy}{dx}\right)_{x=L} = 2aL + b = 2aL + \frac{G_1}{100} = \frac{G_2}{100} \quad (16)$$

Where: L = horizontal length of curve

G_2 = tangent grade (as a percent) at the end of the vertical curve (i.e., $x = L$)

Solving for “a” in Equation 16 gives Equation 17.

$$a = \frac{G_2 - G_1}{200L} = \frac{A}{200L} = \frac{1}{200\left(\frac{L}{A}\right)} \quad (17)$$

Where: A = algebraic difference between the two tangent grades

Recall that $K = L/A$. Therefore, the coefficient, a , can be expressed in terms of K , as shown in Equation 18.

$$a = \frac{1}{200K} \quad (18)$$

The Green Book specifies minimum K -values for different types of curves, sag and crest, and for different highway design speeds [81]. A sag curve is designed as the driver is traveling downward, and a crest curve is designed as the driver is traveling upward. The guidance for curvature design accounts for both stopping and passing sight distances for vehicles. More information on highway design geometry is found in the AASHTO Green Book [81].

The K -value based on stopping sight distance for a sag vertical curve on a highway with a design speed of 62 mph (100 km/h) is 144 ft (43.9 m), as determined from interpolation from Table 3-36 in the AASHTO Green Book [81]. As stated previously, the minimum horizontal length of the curve determined was 1,300 ft (396.2 m). From a combination of Equations 17 and 18 and the simplification of making G_2 zero, assuming the exit elevation is horizontal, it was determined that the sag vertical curve was 9.0 percent. Similarly, the Green Book states the K -value for a crest vertical curve on a highway with a design speed of 62 mph (100 km/h) is 168 ft (51.2 m) determined from interpolation from Table 3-34 in the AASHTO Green Book [81]. Similarly by substituting the new K -value into Equations 17 and 18, the crest vertical curve was 7.7 percent. Since the sag vertical curve had a greater grade and would then govern the slope of the curve, a 9.0 percent vertical curve was to be accommodated in the design of the RESTORE barrier.

Similar to the horizontal curve, the ACJ was taken into consideration for the maximum amount of rotation. If the joint would be positioned that the top side had a $\frac{1}{4}$ in. gap and the bottom side had a $\frac{3}{4}$ in. (19 mm) gap, and the distance between the top and bottom was 17 in. (432 mm), as shown in the drawing set in Appendix B, the maximum angle that the joint could accommodate would be approximately 1.7 degrees about the Y-axis. Further, the steel support skids utilized a $\frac{1}{2}$ in. (13 mm) thick elastomer pad which would be compressed for differences in vertical curvature.

Highway geometry is typically measured in 100 ft (30.5 m) increments. The percent grade for the vertical curve considered is 9 percent, which would mean a 5 degree curvature over 100 ft (30.5 m). Similar to before, five RESTORE barrier segments would be installed over 100 ft (30.5 m) with five ACJs in consideration. Thus, each joint would have to accommodate approximately 1.0 degrees of rotation about the Y-axis. Since the joint can accommodate 1.7 degrees about the Y-axis, the ACJ hardware satisfies the minimum vertical curvature requirements.

7.6.4 Conclusions

Previous guidance was reviewed to determine the maximum superelevation that would be used on a roadway where the RESTORE barrier may be located. However, the horizontal and vertical curves had not been documented. Therefore, calculations determined that the RESTORE barrier should be able to be installed on a roadway with a minimum horizontal radius of 1,300 ft (396.2 m) and a vertical curve of 9.0 percent. The horizontal degree of curvature for one ACJ needed to be at least 0.9 degrees about the Z-axis. The ACJ hardware could accommodate 2.3 degrees. The vertical degree of curvature for one ACJ needed to be 1.0 degrees about the Y-axis. The ACJ hardware

could accommodate 1.7 degrees. Thus, evaluation proved that the ACJ could accommodate the minimum required curvatures if the hardware and concrete barrier segments remained the same.

Through the determination of the design limits for the RESTORE barrier, the transition region was required to satisfy the same superelevation, vertical and horizontal curvature. The joint between the RESTORE barrier and the rigid buttress needs to accommodate an 8 percent superelevation, 1,300 ft (396.2 m) horizontal radius, and a 9.0 percent vertical curve.

7.7 Modifications to RESTORE Barrier

The upper tube rail was spliced at the midspan regions of the concrete segments for test nos. SFH-1 through SFH-3. However, construction feedback noted that a steel splice relocation near or at the ACJ locations would greatly increase ease of construction. Therefore, any modified rail splice configuration at the ACJ locations should provide equal or greater bending capacity, and possibly equivalent axial capacity, to that provided by a solid tube between rigid posts if retesting is not desired. The current rail section utilizes a 8-in. x 4-in. x 1/4-in. (203-mm x 102-mm x 6-mm) HSS steel tube, with a yield strength of 46 ksi (317 GPa), which provided an elastic bending capacity of 612 k-in. (69.1 kJ) without considering reduction factors. Therefore, a modified connection should provide an elastic bending capacity equal to or greater than 612 k-in. (69.1 kJ).

8 BRAINSTORMING, CONCEPT DEVELOPMENT, AND DESIGN

8.1 Introduction

Initial design considerations were brainstormed for the connection between the RESTORE barrier and a rigid concrete buttress. Ideally, the initial designs aimed to mitigate snag, reduce risk for rollover, provide structural continuity, and follow the design criteria given in Chapter 7. Three phases of brainstorming were performed to generate transition prototypes, each phase involving increased detail, as shown in Appendix F. Eleven concepts were developed in Phase 1, which were placed within three general categories during Phases 2 and 3, which included: (1) drop-down RESTORE barrier and bollard or under shoe; (2) pin and loop or female-female connections; and (3) adjustable-length, end fittings. The adjustable-length end fittings would transition the RESTORE barrier to a vertical concrete barrier with a pre-fabricated mold and the length of the pre-fabricated mold could vary in length. Since one of the original design goals was to maintain 20-ft (6.1-m) long concrete barrier sections, if possible, the adjustable-length end fittings group was not pursued at this time. Through further brainstorming, a moment connection was recommended to be explored for use in the transition system, similar to that provided at the interior barrier connection locations. However, this connection type was not explored herein and would need to be investigated in a future effort. Further, a simulation study was completed during the design process to determine if the pin and loop concept had merit and to determine the force distribution imparted to the end loops. That investigation is reported in Chapter 9.

8.2 Drop-Down RESTORE Barrier and Bollard Concept

Three concepts were developed to utilize the vertical holes and openings in the RESTORE barrier to connect to a bollard including: extending a shoe or a toe under the RESTORE barrier, placing a bollard through the pentagon hole in the RESTORE barrier, or creating an end attachment to allow a bollard to terminate the system.

The concepts required a vertical bollard to extend upward from the ground approximately 30 in. (762 mm) and connect extend through the pentagon hole in the RESTORE barrier or connect to the RESTORE barrier end. For this concept, a vertical bollard would need to fit within the vertical pentagon hole in order to not change the barrier geometry. The pentagon hole measured approximately 6½ in. x 7½ in. (165 mm x 191 mm). When configuring the transition joint concept, a dynamic lateral design load of 100 kips (445 kN), using a load factor of 1.0, was applied at the top of the concrete rail, which was 30⅛ in. (765 mm) above the groundline, as shown in Figure 73. A vertical bollard would be connected to the ground with a welded base plate using epoxy anchors or embedded into a reinforced concrete foundation. Thus, it was assumed to behave as a cantilever beam, which would need to withstand a maximum moment of 3,012.5 k-in. (340.4 kN-m). With this large design moment, it would be challenging to configure a useable and realistic epoxy anchorage system. Thus, a vertical bollard would likely need to be embedded into a rigid concrete foundation.

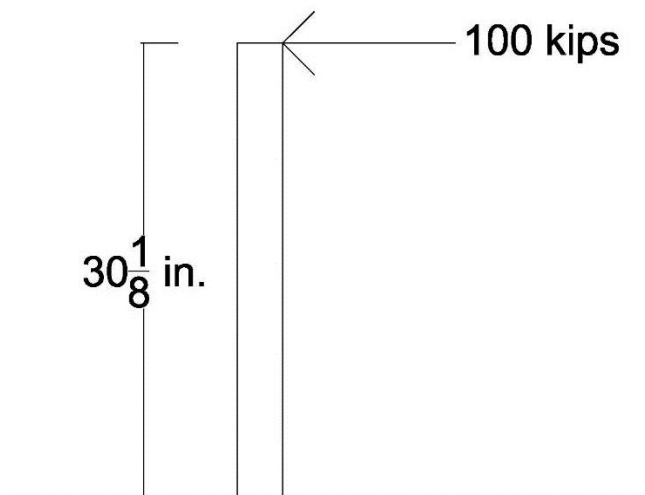


Figure 73. Bollard Cantilevered Moment Arm

To estimate the vertical bollard sizes, a basic elastic bending analysis was considered. Using the yield strengths for known circular sections, the section modulus was calculated for each material type, as summarized in Table 23. The basic equation that was used for the analysis is shown in Equation 19. For an ASTM A53 Grade B steel round bar, the required section modulus was found to be 86 in.^3 ($1,409 \text{ cm}^3$). Using this section modulus in combination with Equation 20, the minimum diameter for a solid circular bollard was approximately $9\frac{1}{2} \text{ in.}$ (241 mm). However, this bollard size would be too large to fit within the pentagon opening in the RESTORE barrier. For ASTM A500 Grade B HSS material, the required section modulus was 72 in.^3 ($1,180 \text{ cm}^3$) for a round, hollow tube. Using this section modulus, the smallest diameter pipe within the 14th Edition AISC Steel Construction Manual [85] was 14 in. (356 mm), which was provided by a HSS14x0.625 section. As such, ASTM A500 Grade B round HSS will not work in this application, as a 14-in. (356-mm) diameter pipe section will not fit within the vertical pentagon opening.

Table 23. Minimum Section Modulus and Diameter for Vertical Bollard in Drop-Down Buttress Concept

Description	Steel Specification	Yield Strength, ksi (GPa)	Required Section Modulus in. ³ (cm ³)	Minimum Required Diameter for Solid Round Bar, in. (mm)	Minimum Available Size for Hollow Circular Section to Meet Requirements, in. (mm)
Round Solid Bar	ASTM A53 Grade B	35 (241)	86 (1,409)	9½ (241)	NA
Round HSS	ASTM A500 Grade B	42 (290)	72 (1,180)	NA	HSS 14x0.625
Heavy Weight Drill Core Pipe	AISI 1340-modified	65 (448)	46.3 (759)	NA	6⅝ (168) O.D. x 5 (127) I.D. ¹
High Strength Drill Core Pipe	Grade VM-165	140 (965)	21.5 (352)	NA	6⅝ (168) O.D. x 5.97 (152) I.D. ¹

¹ The section listed is the maximum size that is available; however, it does not meet the required section modulus.

$$\sigma_y = \frac{Mc}{I} = \frac{M}{S} = \frac{PL}{S} = \frac{100 k (30.125 in.)}{S} \quad (19)$$

$$S_{solid} = \frac{\pi d_2^3}{32} \quad (20)$$

$$S_{hollow} = \frac{\pi(d_2^4 - d_1^4)}{32d_2} \quad (21)$$

Where: σ_y = Yield stress of material, ksi (MPa)

M = Moment applied, k-in. (kN-m)

P = Applied load, kip (kN)

L = Distance between applied load and axis of revolution, in. (mm)

c = Perpendicular distance to neutral axis, in. (mm)

I = Second moment of area about neutral axis, in.⁴ (mm⁴)

S = Section modulus, in.³ (cm³)

S_{solid} = Section modulus of a solid circular cross section, in.³ (cm³)

S_{hollow} = Section modulus of a hollowed circular cross section, in.³ (cm³)

d₁ = Inner diameter of section, in. (mm)

d₂ = Outer diameter of section, in. (mm)

Drill core pipe is generally available with increased section moduli and yield strengths as compared to ASTM A53 or ASTM A500 HSS. For a heavy-weight, drill core

pipe with a yield strength of 65 ksi (448 MPa), the required section modulus was 46.3 in.³ (759 cm³). The largest-available drill core pipe with a 65 ksi (448 MPa) yield strength capable of fitting within the vertical opening has a 6⁵/₈ in. (168 mm) outer diameter and a thickness and section modulus of 1³/₁₆ in. (21 mm) and 19.3 in.³ (316 cm³), respectively. For a high-strength, drill core pipe with a yield strength of 130 ksi (896 MPa), the required section modulus was found to be 21.5 in.³ (352 cm³). Again, the largest-available drill core pipe with a 130 ksi (896 MPa) yield strength capable of fitting within the vertical opening has a 6⁵/₈ in. (168 mm) outer diameter and a thickness and section modulus of 0.33 in. (8 mm) and 9.8 in.³ (161 cm³), respectively. For both drill core pipe examples with different material strengths, neither option provided sufficient resistance to bending.

As noted above, all bollard sections were too large to fit within the vertical pentagon opening in the RESTORE barrier without modifying the barrier geometry. A shoe or toe would be created under the RESTORE barrier as an extruded portion of the rigid concrete buttress that would allow a bollard to be embedded within it. Utilizing a shoe or toe under the RESTORE barrier would allow for the vertical bollard to have a smaller applied moment due to the shortened cantilever length, as shown in Figures F-1, F-12, and F-20. This concept would likely require the concrete buttress to be constructed after the RESTORE barrier was installed. Further, the shoe/toe would add complexity and allow for only minimal construction tolerances, which may not satisfy the design goals of providing a longitudinal tolerance of +/- 1½ in. (38 mm). Thus, the bollard section would need to be placed outside of the RESTORE barrier. An external bollard would require additional protection in order to mitigate potential vehicle snag on the lower exposed end

section due to its large diameter required to resist the lateral design load. With the needs for a large section and additional snag mitigation, the drop-down RESTORE barrier and bollard concept was not pursued at this time.

8.3 Pin and Loop Concept

Initial design concepts incorporated a pin and loop concept similar to that used for PCB connections, often configured with three loops on each barrier end, making it a female-to-female connection. At the transition joint, each barrier end would utilize a similar steel bracket. The hardware on each side of the pin could be interchangeable where the gusset plates on the RESTORE barrier side could be used on the buttress side, and vice versa, as shown in Figures F-17, F-21, and F-22. The pin and loop concept with three loops (i.e. horizontal gusset plates with holes) was initially preferred to reduce the number of different parts, use practical hardware, and improve constructability. Further, it was preferred that the RESTORE barrier segments do not change geometry. Thus, the sloped ends would be utilized when attaching the connection hardware at the joint. Rebar loops would be difficult to externally anchor to the barrier ends at the transition joint without requiring special barrier segments to be fabricated. Therefore, horizontal gusset plates with holes, as shown in Figure F-22, were chosen for use in connecting the RESTORE barrier to a rigid buttress via a pin and loop connection concept.

8.3.1 Distribution of Lateral Load on Pin and Gussets

A 100-kip (445-kN) lateral design load was used to size the connection hardware, which consisted of a point load applied to the top downstream end of the RESTORE barrier, as shown in Figure 74. An initial design schematic is provided in Figure 75, and a beam (representing the pin) approximation with gusset plates (i.e. supports) is shown in

Figure 76. The lateral design load would be transferred from the top of the RESTORE barrier to the RESTORE gusset plate system. The load would then be transferred to the buttress gusset plate system through shear in the vertical drop-down pin. The RESTORE gusset and buttress gusset configurations were represented by two different shapes to distinguish between the different horizontal gussets acting on the drop-down pin. The circles represented the RESTORE gussets, the triangles represented the buttress gussets, and the gusset locations resulted in a reaction on the pin. The dimensions between gussets are shown in Figure 76, where the left-side represents the top of the pin. Each gusset reaction imparts a lateral force on the pin at the center of each gusset.

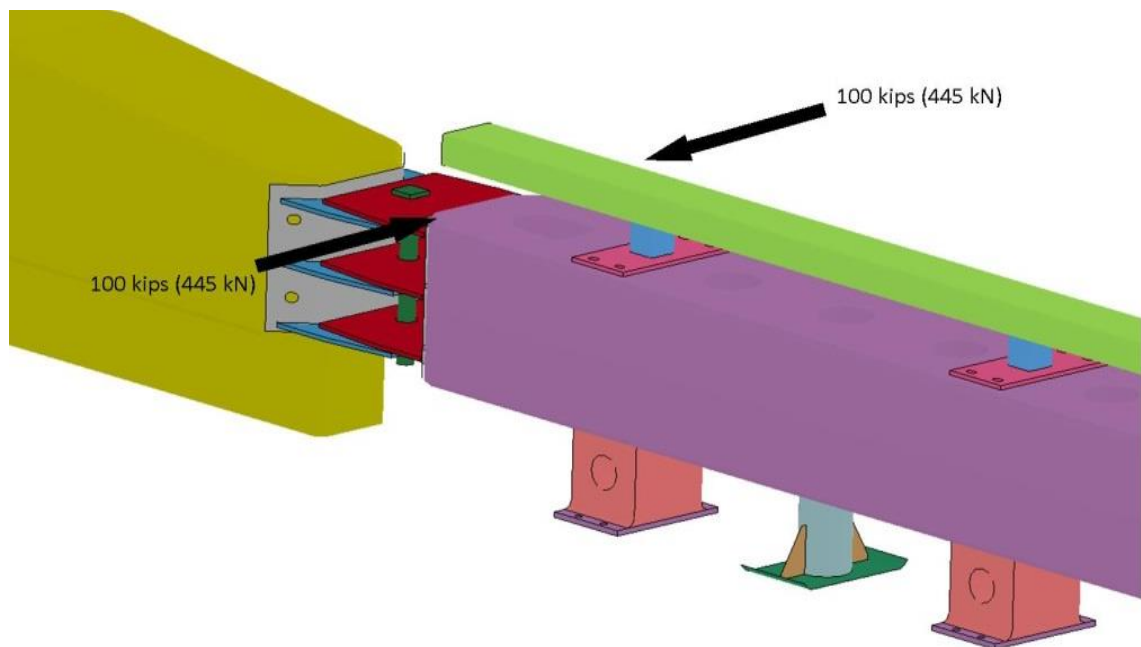


Figure 74. Lateral Design Load and Location, Isometric View

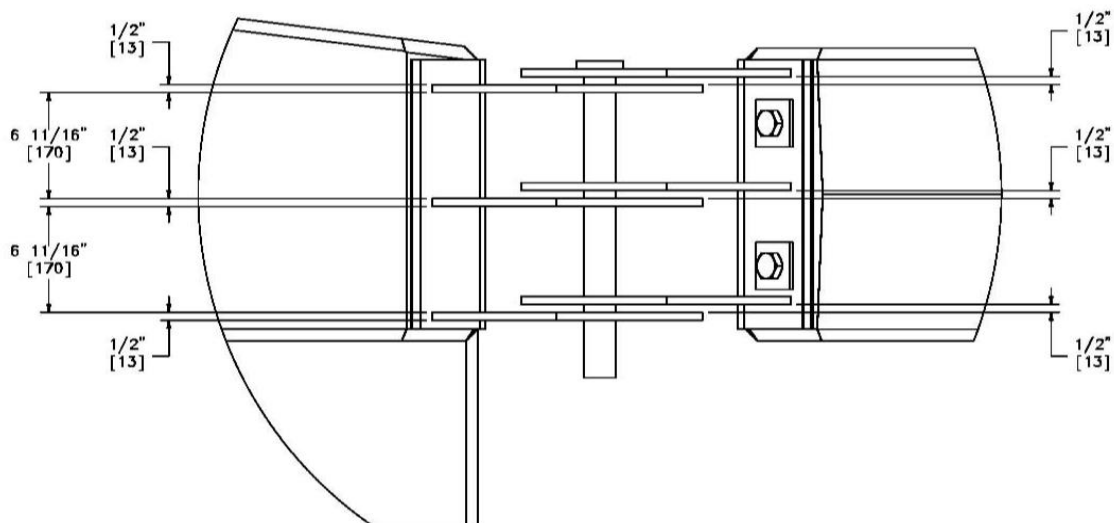


Figure 75. Initial Schematic Pin and Gusset Concept (See Appendix F)

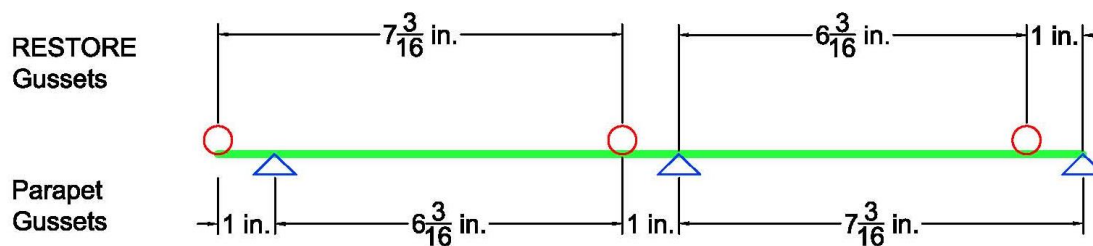
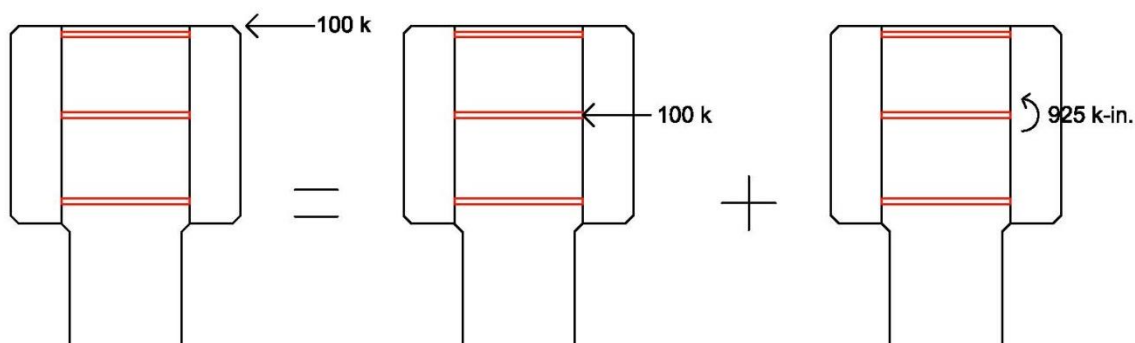


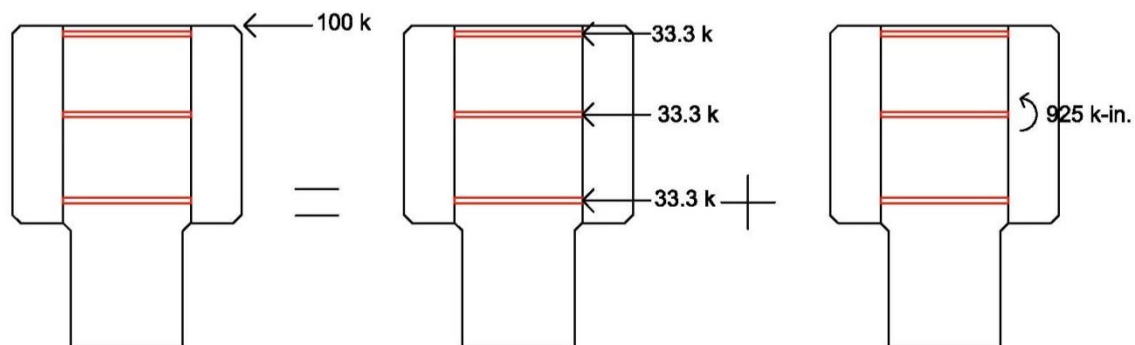
Figure 76. Pin and Support Approximation for Analysis and Design with Dimensions (Horizontal View)

The 100-kip (445-kN) lateral design load was transferred to the RESTORE gussets using two different approximations. The first approximation, denoted as Case 1 shown in Figure 77a, translated the 100-kip (445-kN) point load to the center of the buttress or RESTORE barrier gusset plate assembly and applied an eccentric moment about the center of the RESTORE barrier segment. The moment was determined by multiplying the design load by one-half the RESTORE concrete beam height, or $9\frac{1}{4}$ in. (235 mm). The second approximation, denoted as Case 2 shown in Figure 77b, distributed the 100-kip (445-kN) load evenly between the three RESTORE barrier gusset

plates, and an eccentric moment was applied about the center of the RESTORE barrier segment. Note that the same eccentric moment was used for both cases.



(a) Case 1



(b) Case 2

Figure 77. Approximated Design Load Scenarios: (a) Case 1 and (b) Case 2

Since the same eccentric moment was produced for Cases 1 and 2, an analysis was performed to determine the reactions that the moment would produce on the top and bottom gusset plates (R1 and R3). The analysis assumed that the moment was applied about the middle gusset, therefore only rotating the pin and not producing a reaction at R2. Thus, the top and bottom gusset plates had equal and opposite reactions of 64.4 kips (287 kN), respectively. The free-body, shear, and moment diagrams are shown in Figure 78. The reactions on the top and bottom gusset plates will be combined with the

respective placement of the 100-kip (445-kN) load for Cases 1 or 2, as described in Figure 77.

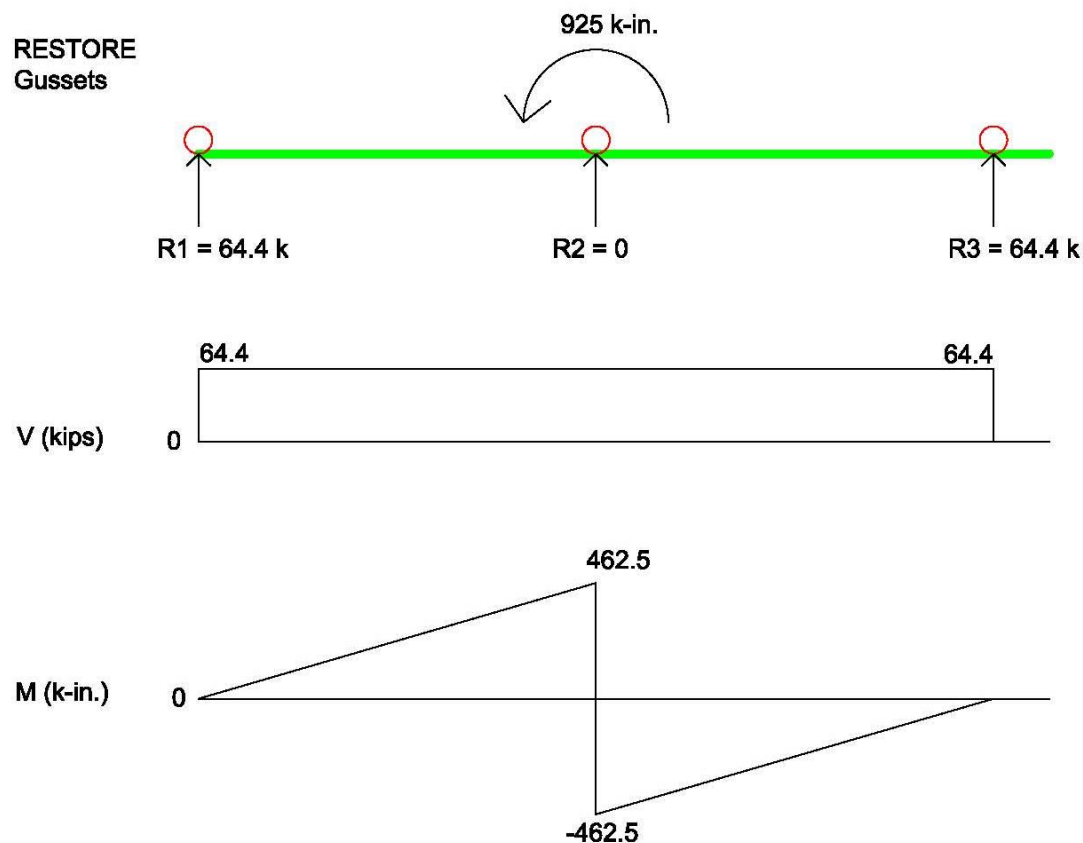


Figure 78. Reactions Due to Applied Moment

Since the free-body diagram for both Case 1 and Case 2 resulted in an indeterminate analysis, a computer program named Rapid Interactive Structural Analysis (RISA) [84] was used to assist in determining the member forces and reactions on the buttress gusset plates. The results from RISA can be found in Appendix G.

The reactions determined from the eccentric moment were combined with the loading scenario for Case 1 to get the resultant forces on the pin and loop system, as shown in Figure 79. From the RISA analysis of Case 1, the reactions (R1, R2, and R3)

were calculated to be 86.1, 70.5 and -56.6 kips (383, 314, and -252 kN), respectively. The free-body, shear and moment diagrams for Case 1 are shown in Figure 80.

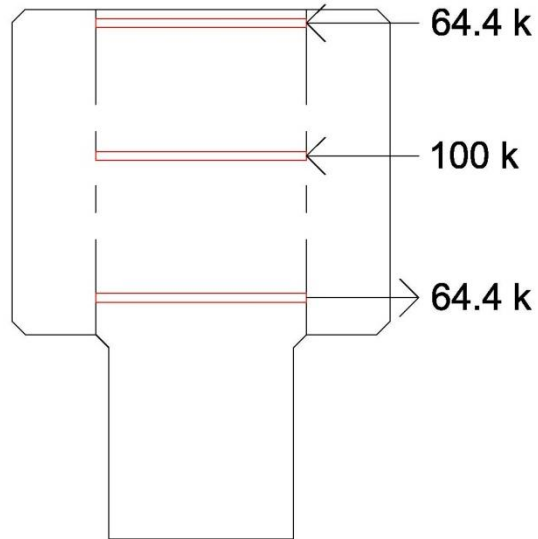


Figure 79. Combined Loading, Eccentricity and Point Load, Case 1

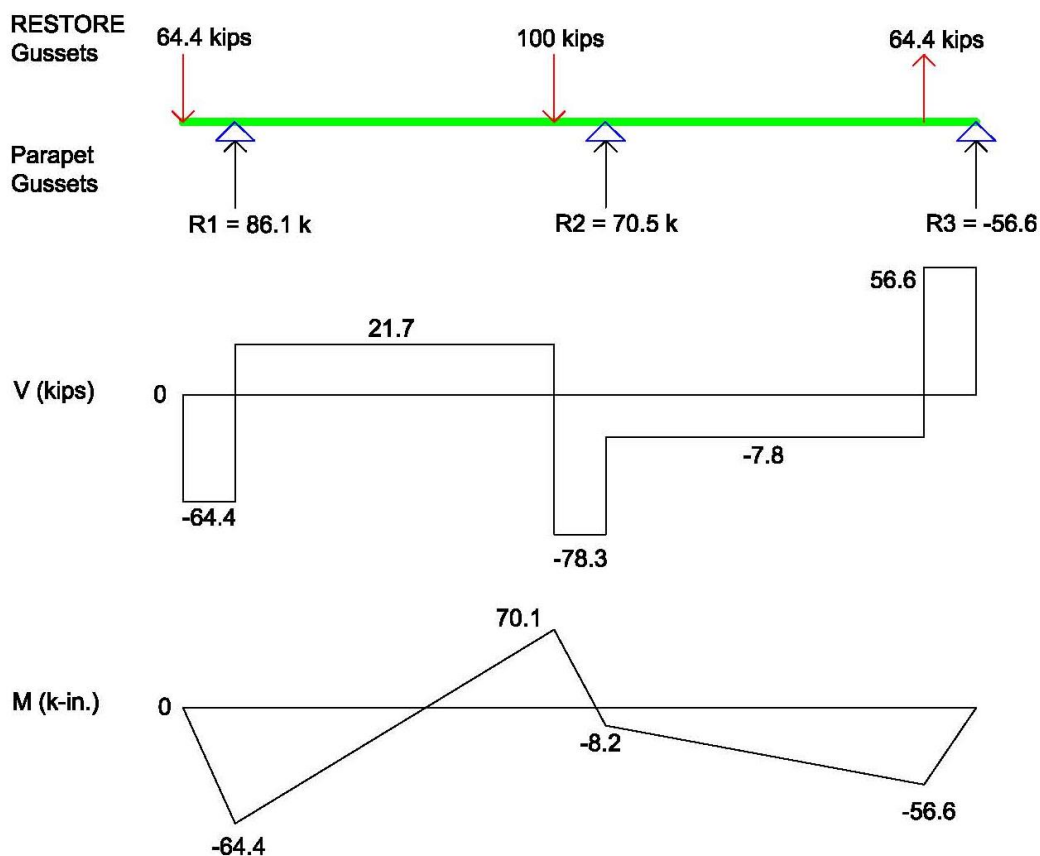


Figure 80. Shear and Moment Diagrams, Case 1

Similarly, the reactions determined from the eccentric moment and the loading scenario for Case 2 were combined, as shown in Figure 81. From the RISA analysis of Case 2, the reactions (R1, R2, and R3) were calculated to be 118.5, 5.6, and -24.1 kips (527, 25, and -107 kN), respectively. The free-body, shear and moment diagrams for Case 2 are shown in Figure 82.

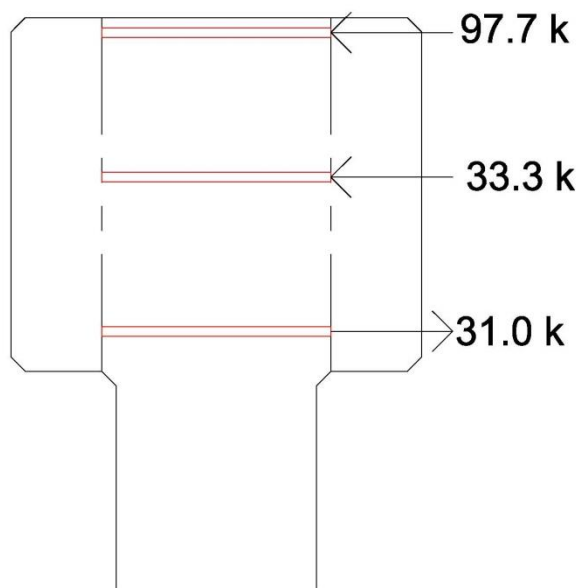


Figure 81. Combined Loading, Eccentricity and Point Load, Case 2

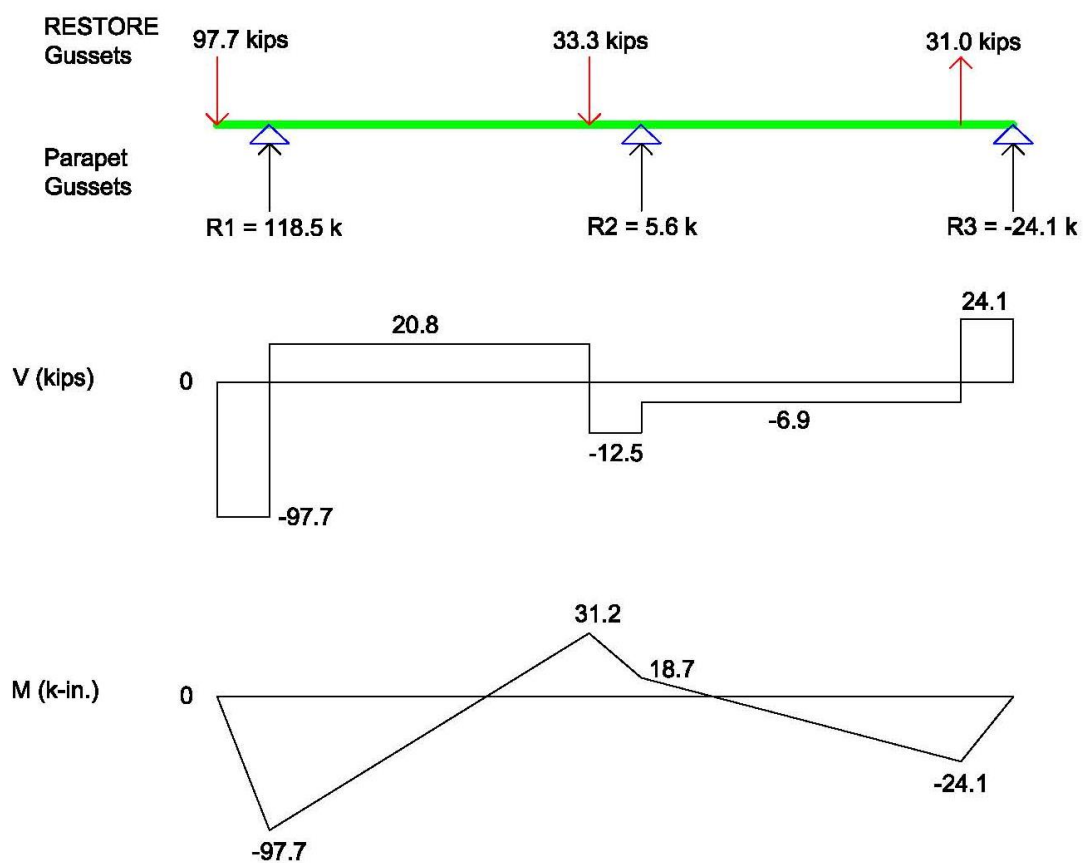


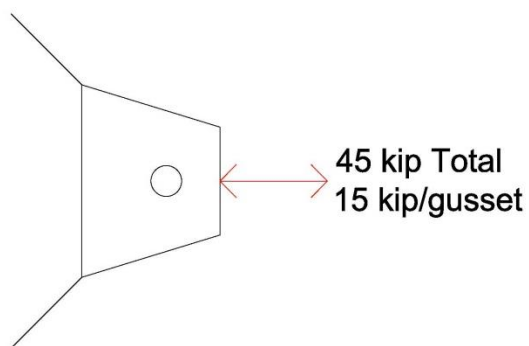
Figure 82. Shear and Moment Diagrams, Case 2

8.3.2 Distribution of Longitudinal Barrier Load on Vertical Pin and Gusset Plates

The longitudinal barrier load from an impacting vehicle was unknown. An approximation for this load was to utilize the lateral impact load multiplied by the coefficient of friction. Based on full-scale crash testing results from test no. SFH-3, the coefficient of friction was calculated to be approximately 0.45 for the RESTORE barrier during the SUT impact event. Using the determined coefficient of friction and the lateral design load of 100 kips (445 kN), a longitudinal design force of 45 kips (200 kN) was determined, as noted in Section 7.2 using Equation 22. The longitudinal force could apply either a compression or tension load on the joint, depending from which direction in a median configuration it is impacted. Since the metal skids under the concrete rail allow for vertical support, the longitudinal force was assumed to be distributed evenly across the three gusset plates, as shown in Figures 83 and 84.

$$F_{long} = F_{lat} * \mu \quad (22)$$

Where: F_{long} = Longitudinal force
 F_{lat} = Lateral force
 μ = Coefficient of friction



PLAN VIEW

Figure 83. Estimated Longitudinal Loading Scenario

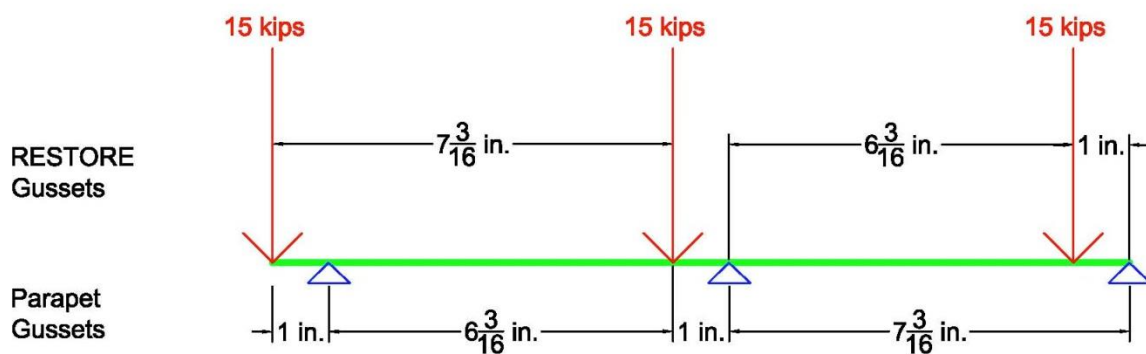


Figure 84. Longitudinal Loading Free-Body Diagram

Similar to the lateral load, RISA analysis was used to determine the reactions of each of the supports, or buttress gusset plates. From the RISA analysis, the reactions (R1, R2, and R3) were calculated to be 18.3, 14.6, and 12.1 kips (81, 65, and 54 kN), respectively. The free-body, shear and moment diagrams for the longitudinal loading case are shown in Figure 85. The 15-kip (67-kN) loads could be applied in the opposite direction, which would result in the reaction and the shear and moment diagrams in the opposite direction.

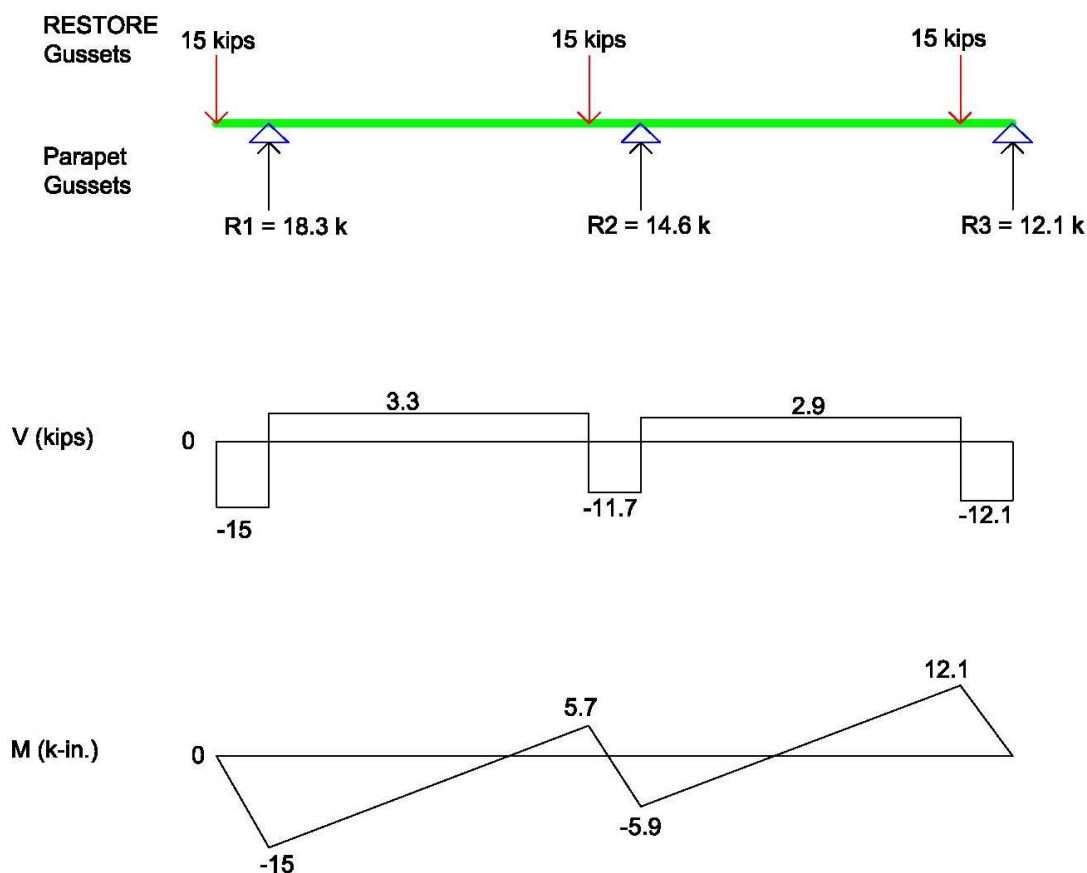


Figure 85. Shear Diagram, Longitudinal Loading

8.3.3 Combined Loading on Pin and Gusset Plates

Through previous testing, virtually no vertical deflection occurred after the implementation of the metal skids. Thus, the vertical force applied to the joint would be virtually zero. Therefore, the combined loading only considered the lateral and longitudinal loads. Based on the results obtained for the lateral and longitudinal loading configurations, the maximum shear force would be the maximum of the sum of the squares of the lateral and longitudinal shear forces along the pin. The maximum shear force occurred between the top RESTORE and top buttress gusset plates and was calculated to be 98.8 kips (439 kN) using Equation 23.

$$V_{\max} = \sqrt{V_{\max,\text{lateral}}^2 + V_{\max,\text{longitudinal}}^2} \quad (23)$$

Where: $V_{\max,\text{lateral}}$ = Maximum lateral shear force, kips (kN)
 $V_{\max,\text{longitudinal}}$ = Maximum longitudinal shear force, kips (kN)
 V_{\max} = Maximum resultant shear force, kips (kN)

8.3.4 Pin Selection

8.3.4.1 Shear Design

As noted earlier, the pin would transfer the load from the RESTORE gussets to the buttress gussets through shear. Therefore, the pin diameter was determined based on the equations for shear noted in Equation J-4 from the AISC Steel Construction Manual [85]. Two equations were used in the determination of the pin size, as shown in Equations 24 and 25. According to the AISC Steel Construction Manual, the equation that produces the lowest available shear strength (ϕR_n) in the pin would control the design. Thus, the equations were used to determine the pin diameter. The resultant shear force applied to the pin was $\phi R_n = 98.8$ kip (439 kN), which was used in Equations 24 and 25 to select a minimum diameter. Note that the gross area and net area subjected to shear were assumed to be equal.

$$\phi R_n = \phi 0.6 F_y A_{gv} \quad (\text{J4-3}) \quad \phi = 1.0 \quad (24)$$

$$\phi R_n = \phi 0.6 F_u A_{nv} \quad (\text{J4-4}) \quad \phi = 0.75 \quad (25)$$

Where: F_y = Minimum yield stress (ksi)
 F_u = Tensile stress (ksi)
 A_{gv} = Gross area subject to shear (in.²)
 A_{nv} = Net area subject to shear (in.²)
 ϕ = Resistance factor

For A36 and A529 steel materials, the pin diameters from these equations are shown in Table 24. Using ASTM A36 steel material, the pin diameter would be 2½ in. (64 mm). Using ASTM A529 steel material, the pin diameter would be 2¹/₁₆ in. (52 mm).

An ASTM A529 steel pin with 50 ksi (335 GPa) material was selected due to a smaller required diameter, thus requiring a smaller hole within the gusset plate. The selected pin size was approximately $2\frac{1}{16}$ in. (52 mm) using the A529 steel.

Table 24. Determination of Pin Diameter to Resist Shear

Pin Material	Yield Strength, F_y ksi (MPa)	Tensile Strength, F_u ksi (MPa)	Eqtn. No.	Required Pin Diameter in. (mm)	Required Pin Area in. ² (cm ²)	Selected Pin Diameter in. (mm)	Selected Pin Area in. ² (cm ²)	Min. Hole Size in Gusset Plate in. (mm)
A36	36 (248)	58 (400)	24	2.41 (61)	4.6 (30)	$2\frac{1}{2}$ (64)	4.9 (32)	3 (76)
			25	2.20 (56)	3.8 (25)	$2\frac{1}{4}$ (57)	4.0 (26)	$2\frac{3}{4}$ (70)
A529	50 (345)	70 (483)	24	2.05 (52)	3.3 (21)	$2\frac{1}{16}$ (52)	3.3 (21)	$2\frac{1}{2}$ (64)
			25	2.00 (51)	3.1 (20)	2 (51)	3.1 (20)	$2\frac{1}{2}$ (64)

8.3.4.2 Bending Design

As noted earlier, the pin was assumed to transfer the load from the RESTORE gussets to the buttress gussets through shear. However, a vertical gap of 1 in. (25 mm) from center to center existed between adjacent gusset plates. Further, a maximum span between farther gussets was $6\frac{3}{16}$ in. (157 mm). Thus, a bending analysis was also conducted to determine if the section would yield under bending. The basic elastic bending equation is shown in Equations 26 and 27. The maximum bending moment of 97.7 kip-in. (132 kN-m) would be imparted to the pin, as determined previously with Case 2. The required pin diameter based on a simple elastic analysis using A529 steel material was found to be 2.71 in. (69 mm), respectively.

$$M_{Applied} = S\sigma_y \quad (26)$$

$$S = \frac{\pi d^3}{32} \quad (27)$$

Where: $M_{Applied}$ = Moment about the axis of bending, k-in. (kN-m)
 S = Elastic section modulus, in.³ (mm³)

σ_y = Yield strength of material, ksi (MPa)
 d = Pin diameter, in. (mm)

Next, a basic plastic bending analysis was performed using Equations 28 and 29.

For this basic plastic analysis, the required pin diameter for A529 steel material was found to be 2.27 in. (58 mm), respectively.

$$M_{applied} = Z\sigma_y \quad (28)$$

$$Z = \frac{d^3}{6} \quad (29)$$

Where: Z = Plastic section modulus, in.³ (mm³)

Thus, the pin diameters required to resist bending were estimated to approximately range between 2¼ and 2¾ in. (57 and 70 mm), which were larger than those required to resist the shear loading. Thus, an aggressive approach was utilized to initially begin the design with the 2-in. (51-mm) pin diameter that would be evaluated through computer simulation and stress analysis. If the stress analysis showed concerns with excessive pin deformations and stresses, then larger pin diameters would need to be investigated.

8.3.5 Gusset Plate Design

The gusset plates were designed to withstand the maximum shear forces calculated from Cases 1 and 2, as shown previously in Sections 8.3.1 and 8.3.2. To determine the minimum thickness of each gusset plate, a combined force of 98.8 kips (439 kN) was used in the bearing strength equations from the AISC Steel Manual Equations J3-6a and J3-6c [85], as shown in Equations 30 and 31. Equation 30 was used for the RESTORE barrier gussets because they were designed to incorporate a standard hold for the vertical pin. Equation 31 was used for the buttress gussets because they were designed to incorporate a long slot to accommodate for construction tolerances. The first

part of the equation represents tear out of the steel, as shown in Figure 86b, and the second part of the equation represents ovalization of the holes, as shown in Figure 86d. Other types of failures exist, as shown in Figure 86, but they were not considered in the initial sizing design. The clear distance from the center of the hole to the edge of the gusset plate was initially estimated as being greater than or equal to $2d$, as determined by solving for the clear distance in either Equation 30 or 31. With a 2-in. (51-mm) diameter pin, the clear distance would need to be greater than 4 in. (102 mm). Two different material strengths were considered during the design of the gusset, ASTM A36 and ASTM A572 steel. The ultimate stresses for A36 and A572 steel are 58 and 65 ksi (400 and 448 GPa), respectively.

$$\phi R_n = \phi 1.2 l_c t F_u \leq \phi 2.4 d t F_u \quad (\text{J3-6a}) \quad \phi = 0.75 \quad (30)$$

$$\phi R_n = \phi 1.0 l_c t F_u \leq \phi 2.0 d t F_u \quad (\text{J3-6c}) \quad \phi = 0.75 \quad (31)$$

Where: R_n = Nominal bearing strength of the material, kips (kN)

ϕR_n = Available bearing strength at pin holes, kips (kN)

l_c = clear distance between center of hole and material edge in direction of force, in. (mm)

t = thickness of connected material, in. (mm)

d = nominal bolt diameter, in. (mm)

F_u = Specified minimum tensile strength of connected material, ksi (MPa)

ϕ = Resistance factor

Based on the bearing strength calculation, the minimum thickness for the gusset plates was calculated to be approximately 0.47 and 0.42 in. (12 and 11 mm) with a normal size hole or 0.57 and 0.51 in. (14 and 13 mm) with a long slot, for A36 and A572 steel, respectively. Thus, an initial plate thickness of $\frac{1}{2}$ in. (13 mm) was selected to be evaluated through the block shear analysis.

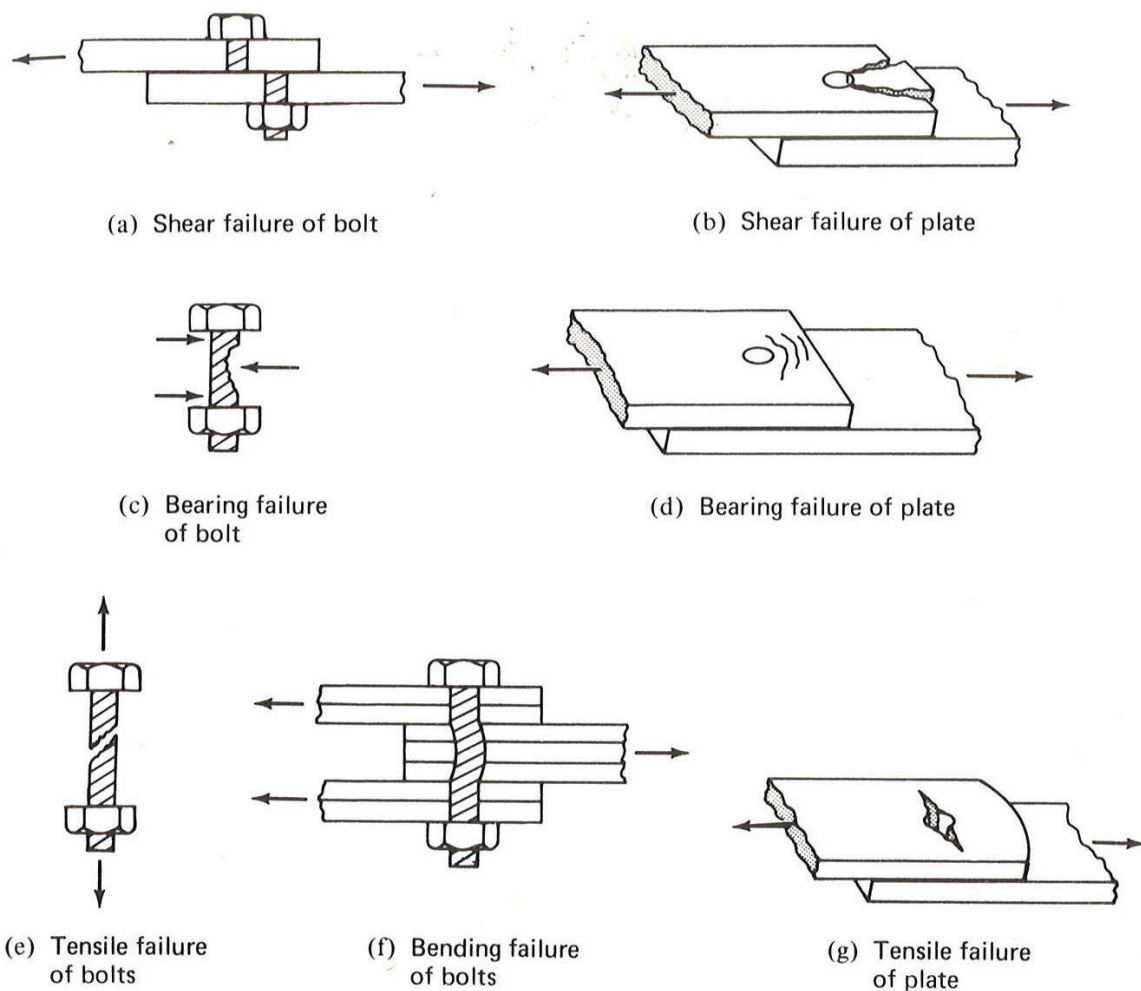


Figure 86. Types of Failure for Steel [86]

Block shear is generally referred to as a tearing limit state where a portion of the connecting material is torn in order for the connection bolt to be released, as shown in Figure 87. Since block shear failure often governs during plate design, further analysis was performed to determine the appropriate plate distances on each side of the pin hole as well as confirm if the chosen plate thickness was adequate. The lateral design load used within the block shear equations was the maximum shear force determined from Case 2, which was 97.7 kips (435 kN). Similarly, the longitudinal design load used within the block shear equations was the maximum shear force determined from the longitudinal

loading, which was 15.0 kips (67 kN). Thus, the lateral and longitudinal distances between the pin hole and the edges of the plate were designed to withstand a $R_n=97.7$ kip (435 kN) lateral load and a $R_n=15.0$ kip (67 kN) longitudinal load, as determined from the vertical drop pin analysis in Sections 8.3.1 and 8.3.2. The block shear equations were taken from Chapter 16, Equation J4-5, in the AISC Steel Manual [85] and are shown in Equation 32. The left side of the equation represents a rupture condition, while the right side of the equation represents a yield condition. A visual representation of the shear and tension areas are depicted in Figure 87 for the standard hole. The slotted hole used the same clear distance between the edge of the hold and the edge of the plate. The equations for block shear are given below, and the failure surfaces were simplified to a rectangle for calculations, instead of the targeted trapezoidal shape, as shown in Figure 88. The areas noted in Figure 88 were the lengths shown, multiplied by the thickness of the plate. The simplification of the shapes to rectangles, instead of trapezoids, allows for a conservative design due to additional material in the lateral direction, which has higher applied forces. Note that uniform tension stress was assumed during the analysis.

$$R_n = 0.6F_u A_{nv} + U_{bs}F_u A_{nt} \leq 0.6F_y A_{gv} + U_{bs}F_u A_{nt} \quad (J4-5) \quad \phi = 0.75 \quad (32)$$

Where: R_n = Nominal strength of plate, kips (kN)

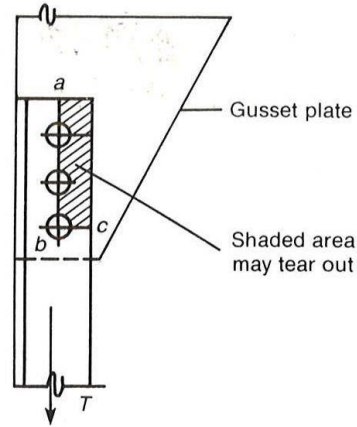
ϕR_n = Available strength of plate, kips (kN)

A_{nv} = Net area subject to shear, in.²

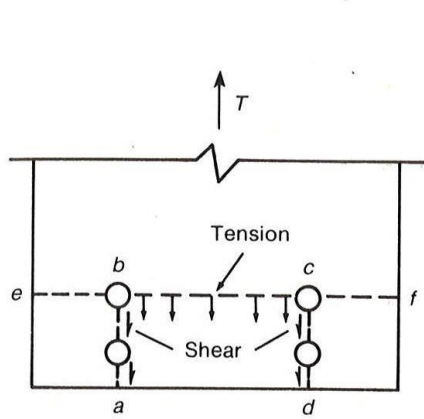
A_{nt} = Net area subject to tension, in.²

A_{gv} = Gross area subject to shear, in.²

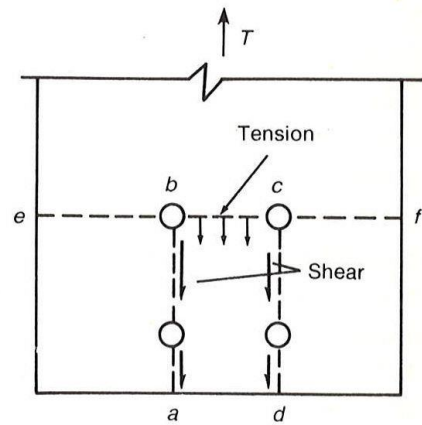
U_{bs} = Tension stress coefficient (1.0 when tension stress is uniform, 0.5 when tension stress is nonuniform)



(a) Failure by tearing out



(b) Large tension, small shear



(c) Large shear, small tension

Figure 87. Types of Block Shear Failure of Steel [86]

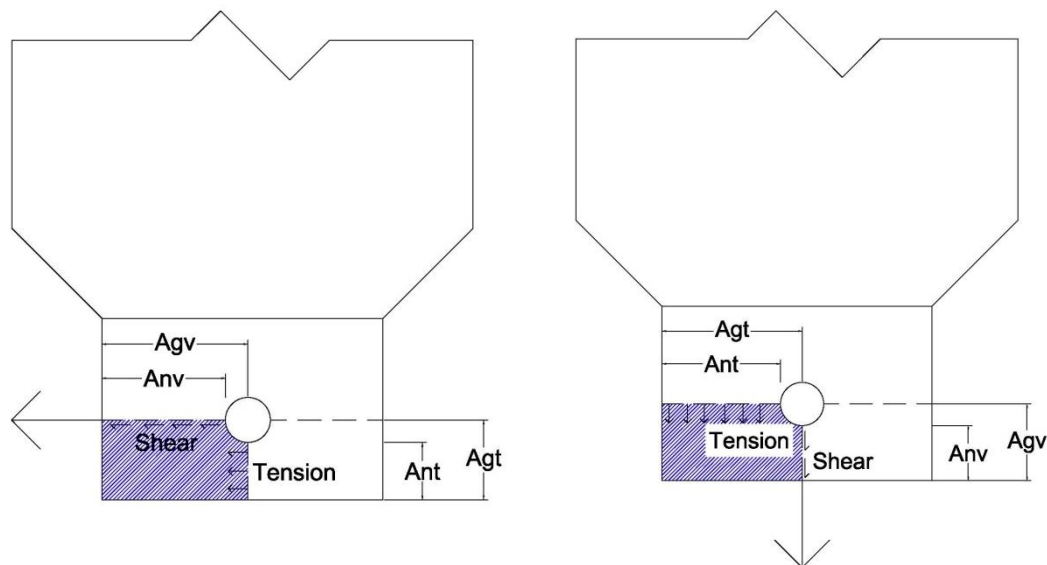


Figure 88. Description of Block Shear Areas of Gusset Plates

The pin size, as previously determined, was 2 in. (51 mm). To provide adequate constructability, the hole was oversized to allow for the pin to be easily dropped down. Thus, the hole size was chosen to be 2½ in. (64 mm) diameter. Both A36 and A572 steel materials were considered for the gusset plates. The results from the block shear calculations, as shown in Figure F-23, determined that the gusset plates fabricated with A36 steel needed to be 10½ in. (267 mm) wide laterally. Similarly, the A572 steel gusset plates needed to be 8 in. (203 mm) wide laterally. Due to the narrower width and desire to use consistent steel grades (i.e., strengths) throughout the configuration, the A572 steel 50 ksi (344 GPa) steel material option was selected in the transition design.

Note that further evaluation will be performed with computer simulation to determine if a cover plate can prevent vehicle snag between the horizontal gusset plates or on the upstream concrete buttress end.

8.3.6 Back Plate and Connection Bolt Design

For the design of the back plate, which provides the connection between the gussets and the RESTORE barrier or buttress, a 3D force distribution was used. Similar to the design of the pin and the gusset plates, a design load of 100 kip (445 kN) was applied to the top of the concrete on the RESTORE barrier side, as shown in Figure 89. From the load, an eccentric moment of 925 k-in (105 kN-m) was created when the load was translated to the center of the RESTORE barrier. With respect to the Y-Z plane, the 100-kip (445-kN) lateral load was evenly distributed to the four connecting bolts. Similarly, the moment was distributed evenly to each of the bolts in terms of a shear force perpendicular to a radius drawn from a center rotation point, as shown in Figure 90. Based on the loads applied, resultant forces imparted to bolts 1 through 4, were 42.0, 42.0, 8.0, and 8.0 kips (187, 187, 36, and 36 kN) in the Y-direction and 17.0, -17.0, 17.0, and -17.0 kips (76, -76, 76, and -76 kN) in the Z-direction, respectively. Similarly, the bolt forces were considered in the X-Y plane, as shown in Figure 91. The 45 kip (200 kN) load applied at the center was evenly distributed between the four bolts. The forces for bolts 1 through 4 were all -11.3 kips (50 kN) in the X-direction. The Y-direction forces remained the same from what was calculated in the Y-Z plane.

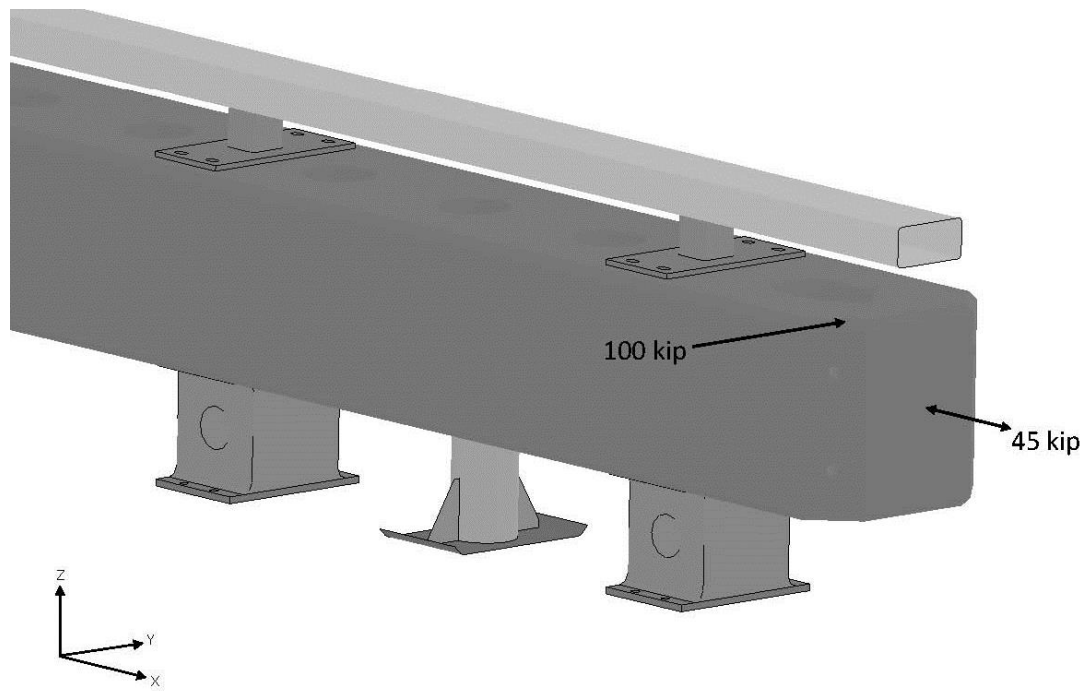


Figure 89. Back Plate and Connection Bolt Design Loads and Orientation

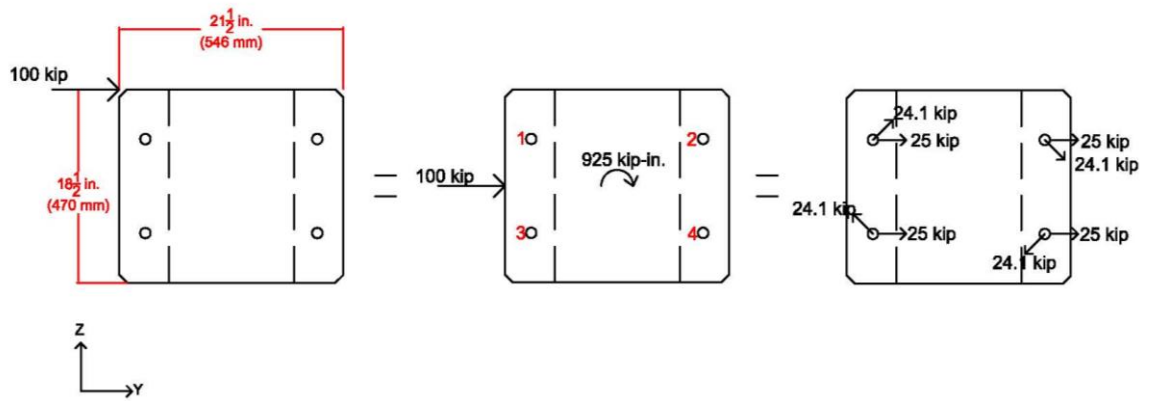


Figure 90. 3D Analysis of Back Plate and Connections, Y-Z Plane

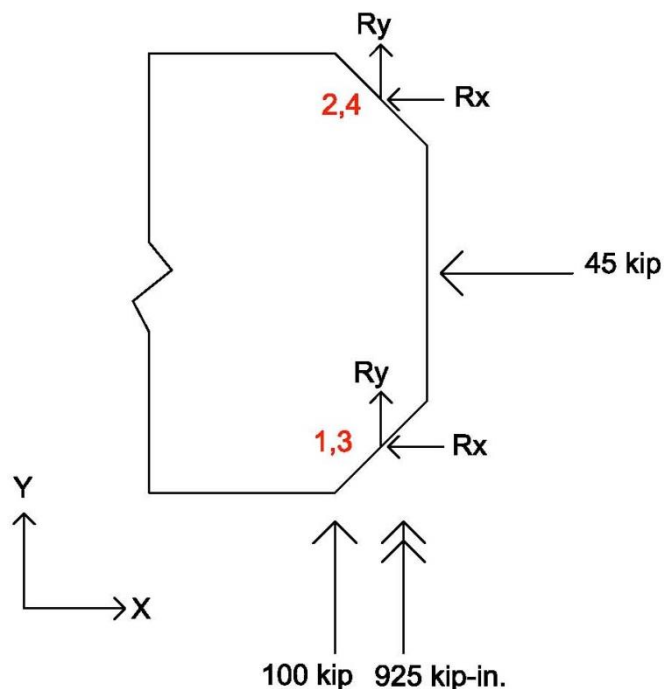


Figure 91. 3D Analysis of Back Plate and Connections, X-Y Plane

Based on the resultant loading in the X-Y plane, a rotated $x'-y'$ plane was used to determine the maximum tensile load and the maximum shear load with respect to that plane, as shown in Figure 92. The maximum tensile forces were calculated to be -37.7, 21.8, -13.6, and 2.3 kips (-168, 97, -60, and 10 kN) for bolts 1 through 4, respectively. The shear forces in the bolts with respect to the $x'-y'$ plane were found to be -21.8, -37.7, 2.3, and -13.6 kips (-97, -168, 10, and -60 kN) for bolts 1 through 4, respectively. However, the shear also had a vertical component, so a resultant maximum shear was calculated based on the rotated axes forces and the vertical axis forces, as shown in Figures 93 and 94. The maximum combined shear for bolts 1 through 4 were 27.7, 41.4, 17.2, and 21.8 kips (123, 184, 77, and 97 kN), respectively. Therefore, the maximum shear load of 41.4 kips (184 kN) was utilized in the design of the bolts and the back plate. Since the 45-kip (200-kN) longitudinal load could be applied in the positive or negative

direction, the process was repeated utilizing a positive 45-kip (200-kN) longitudinal load. The maximum combined shear on any one bolt was still 41.4 kips (184 kN). A summary of the resultant forces in the X, Y, and Z directions, as well as the tensile and shear in the x' , and y' directions is shown in Table 25.

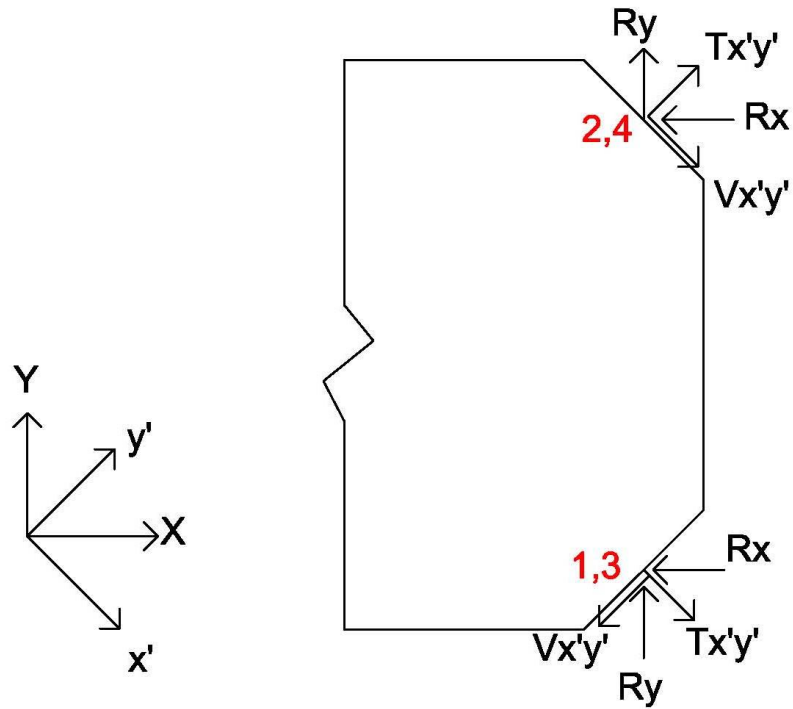


Figure 92. 3D Analysis of Back Plate and Connections, Rotated X-Y Plane

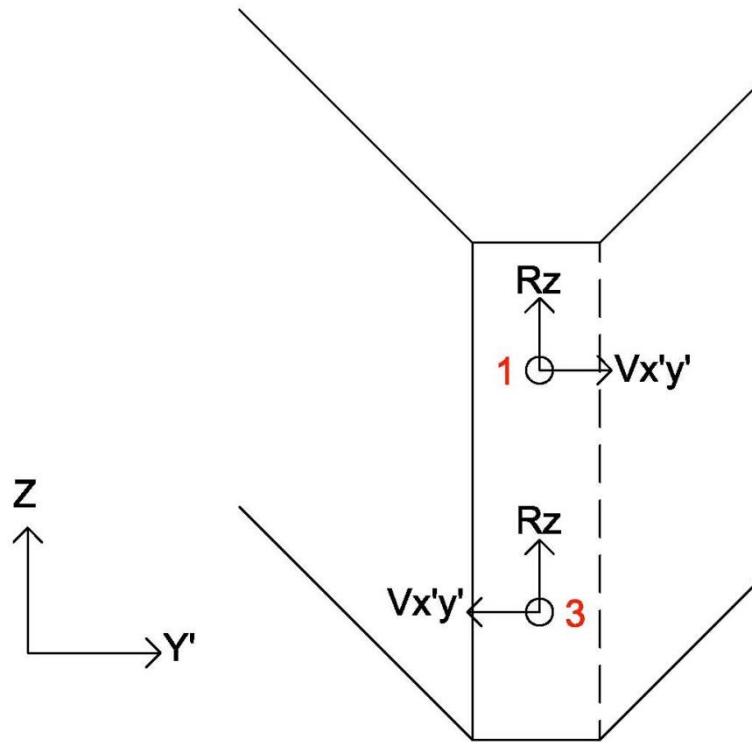


Figure 93. 3D Analysis of Back Plate and Connections, Z - y' Plane

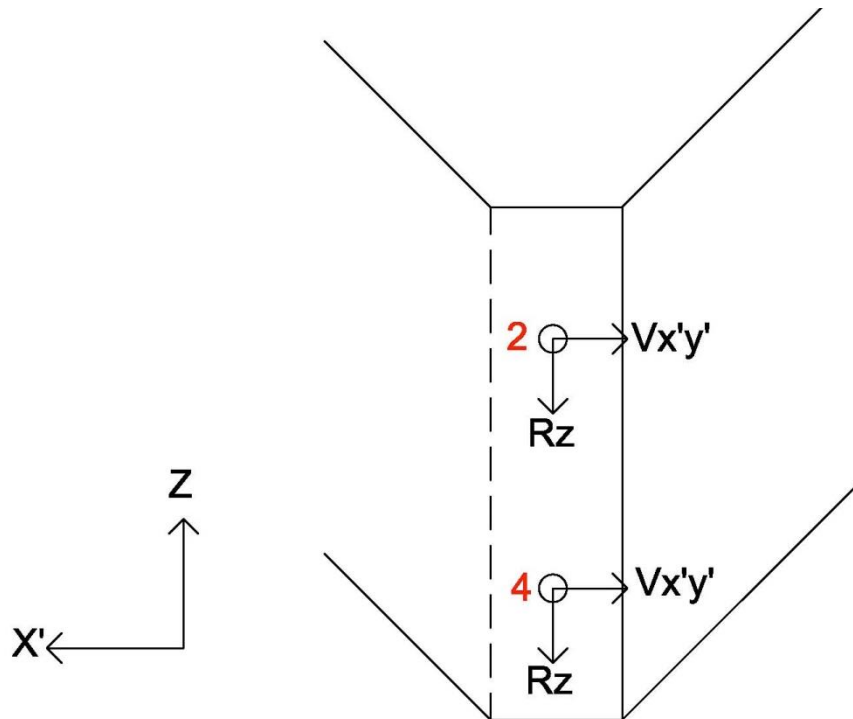


Figure 94. 3D Analysis of Back Plate and Connections, x' - Z Plane

Table 25. Summary of 3D Back Plate and Connection Bolt Analysis

Force Descriptions	Bolt Numbers (-45 kip Longitudinal Force)			
	1	2	3	4
X resultant (Rx) kip (kN)	-11.3 (50)	-11.3 (50)	-11.3 (50)	-11.3 (50)
Y resultant (Ry) kip (kN)	42.0 (187)	42.0 (187)	8.0 (36)	8.0 (36)
Z resultant (Rz) kip (kN)	17.0 (76)	-17.0 (-76)	17.0 (76)	-17.0 (-76)
$T_{x'y'}$ kip (kN)	-37.7 (-168)	21.8 (97)	-13.6 (-60)	2.3 (10)
$V_{x'y'}$ kip (kN)	-21.8 (-97)	-37.7 (-168)	2.3 (10)	-13.6 (-60)
ABS (Resultant V) kip (kN)	27.7 (123)	41.4 (184)	17.2 (77)	21.8 (97)
ABS (Resultant T) kip (kN)	37.7 (168)	21.8 (97)	13.6 (60)	2.3 (10)

Force Descriptions	Bolt Numbers (+45 kip Longitudinal Force)			
	1	2	3	4
X resultant (Rx) kip (kN)	11.3 (50)	11.3 (50)	11.3 (50)	11.3 (50)
Y resultant (Ry) kip (kN)	42.0 (187)	42.0 (187)	8.0 (36)	8.0 (36)
Z resultant (Rz) kip (kN)	17.0 (76)	-17.0 (-76)	17.0 (76)	-17.0 (-76)
$T_{x'y'}$ kip (kN)	-21.8 (-97)	37.7 (168)	2.3 (10)	13.6 (60)
$V_{x'y'}$ kip (kN)	-37.7 (-168)	-21.8 (-97)	-13.6 (-60)	2.3 (10)
ABS (Resultant V) kip (kN)	41.4 (184)	27.7 (123)	21.8 (97)	17.2 (77)
ABS (Resultant T) kip (kN)	21.8 (97)	37.7 (168)	2.3 (10)	13.6 (60)

A 27.7 kip (123 kN) resultant shear and a 37.7 kip (168 kN) tension force were used in the calculation of the back plate thickness and bolt diameter. The back plate and bolts were desired to be used within the same chamfered corners and bolts as the ACJ. Therefore, the bolt size was determined using Equation C-J3-6a in the AISC manual [85], shown in Equation 33. The values for the factored nominal tensile and shear stresses can

be found in Table J3.2 of the AISC manual. Solving the equation for the diameter that would satisfy the required shear and tensile stresses, a minimum diameter of 1¼ in. (32 mm) was needed. Using the other specified approach of Equation J3-2 in the AISC manual [85], as shown in Equations 34 and 35, a similar diameter of 1¼ in. (32 mm) was determined. However, a more aggressive diameter of 1 in. (25 mm) would be evaluated through simulation to maintain the same connection hardware throughout the system.

$$\left(\frac{f_t}{\phi F_{nt}}\right) + \left(\frac{f_v}{\phi F_{nv}}\right) = 1.3 \quad (\text{J3-6a}) \quad \phi = 0.75 \quad (33)$$

$$\phi R_n = \phi F'_{nt} A_b \quad (\text{J3-2}) \quad \phi = 0.75 \quad (34)$$

$$F'_{nt} = 1.3F_{nt} - \frac{F_{nt}}{\phi F_{nv}} f_v \leq F_{nt} \quad (\text{J3-3a}) \quad \phi = 0.75 \quad (35)$$

Where: F_{nt} = Nominal tensile stress, ksi (MPa)

f_t = Required tensile stress, ksi (MPa)

f_v = Required shear stress, ksi (MPa)

F_{nv} = Nominal shear stress, ksi (MPa)

Φ = Resistance factor

R_n = Nominal strength of bolt, kips (kN)

ϕR_n = Available strength of bolt, kips (kN)

A_b = Area of bolt, in.² (mm²)

F'_{nt} = Nominal tensile stress modified to include effects of shear stress, ksi (MPa)

A similar design process to that shown in Section 8.3.5 and Equation 32 was used to calculate block shear capacity of the back plate. In this case, the dimensions that were considered were in the x'-Z or Z-y' planes, as shown in Figure 95. The forces that were used in the design process were the maximum resultant shear of 37.7 kips (168 kN) and the maximum resultant z-direction force of 17.0 kips (76 kN). ASTM A572 steel was used throughout the block shear calculations. From the block shear analysis, a plate thickness of 3/8 in. (10 mm) was required to withstand the loading. However, a back plate thickness of 1/2 in. (13 mm) and ASTM A572 steel was selected in order to be

conservative and maintain similar material grade and thickness throughout the transition hardware. The plate thickness was checked with Equation 30 and provided satisfactory structural resistance to prevent tear out and ovalization.

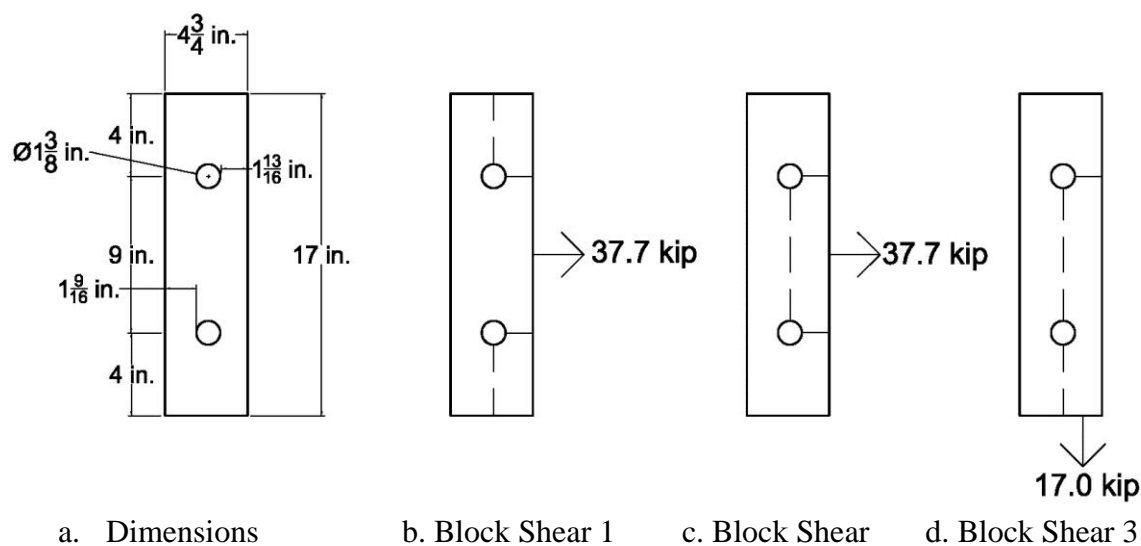


Figure 95. Back Plate Dimensions and Block Shear Lines

8.3.7 Weld Design

The minimum size of a fillet weld for a $\frac{1}{2}$ -in. (13-mm) thick steel material is $\frac{3}{16}$ in. (5 mm), as determined from Table J2.4 in the AISC Steel Manual, Chapter 16 [85]. The maximum allowable weld size for a $\frac{1}{2}$ -in. (13-mm) thick plate is $\frac{7}{16}$ in. (11 mm), as determined by Section J2.J2b in the AISC Steel Manual, Chapter 16 [85]. The weld analysis considered each gusset to be a cantilevered plate where the stress in the welds were calculated in terms of tension, bending, and shear, as shown in Figure 96. For this analysis, assumed dimensions were made for the gusset plate configuration. The gusset plate was assumed to be rectangular with a $12\frac{1}{2}$ in. (318 mm) weld length (l), an $8\frac{3}{4}$ in. (222 mm) moment arm between the applied load and the vertical back plate (c), and the plate thickness was $\frac{1}{2}$ in. (13 mm), as determined from previous analysis, as shown in

Figure 97. The moment about the weld was 854.9 k-in. (96.6 kN-m) from the 97.7 kip (435 kN) load being translated 8¾ in. (222 mm) to the weld.

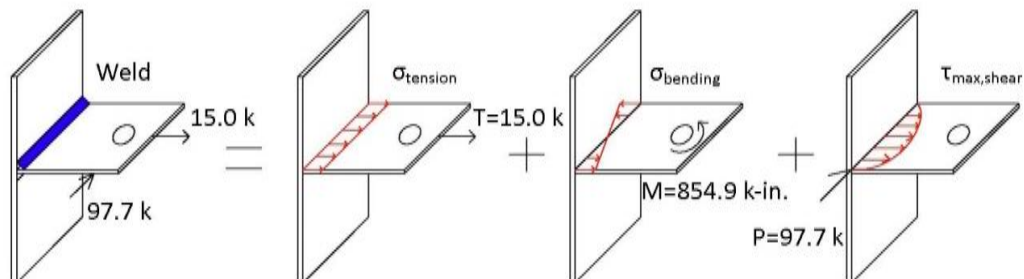


Figure 96. Tension, Bending, and Shear Stresses within Fillet Welds

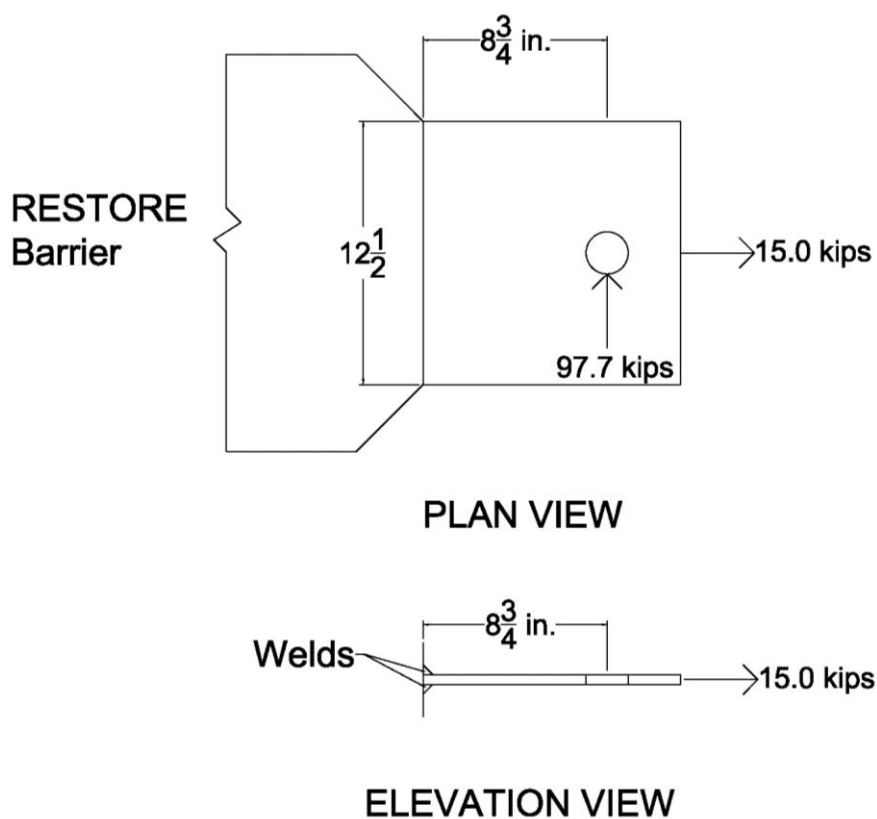


Figure 97. Loading and Dimension of Gusset Plate Fillet Welds

For the analysis, the moment of inertia of the fillet weld group was calculated, as shown in Equation 36. Then, the bending stress was determined using the moment

produced by the 97.7-kip (435-kN) lateral load determined from Section 8.3.1, as shown in Equation 37. The area of the fillet welds was calculated by multiplying the effective throat thickness by the weld length. From the calculation of the area, the tension stress could be found using the 15.0-kip (67-kN) longitudinal load determined from Section 8.3.2, as shown in Equation 38. If the ratio of thickness to width of a plate was less than or equal to $\frac{1}{4}$, then plate could be considered as a narrow rectangular beam and the maximum shear stress, τ_{shear} , would be located at the center of the width, and calculated using Equation 39 [87]. The ratio of thickness to width of the gusset plate was 0.04. The maximum lateral load of $P=97.7$ kips (435 kN) was used to calculate the maximum shear stress. The maximum shear stresses in the weld were determined by combining tension, bending and shear stresses. At the ends of the weld, the combination of the tension and bending stresses produced a maximum normal or principal stress without shear stress, as shown in Equation 41. Further, by using the tension and shear stresses in Equation 42, the maximum principal stress could be determined at the center of the gusset plate and weld. Note that the shear stresses are zero at the ends of the weld, and the bending stress is zero at the center of the weld.

Three weld sizes were examined: $\frac{5}{16}$, $\frac{3}{8}$, and $\frac{7}{16}$ in. (8, 10, and 11 mm). A weld filler material had a strength of 70 ksi (483 MPa). All of the welds would fail in bending with the 50 ksi (345 MPa) material based on the maximum concentrated stress calculations, as shown in Table 26. However, a $\frac{7}{16}$ in. (11 mm) fillet weld provided a maximum stress of 55 ksi (379 MPa), which was within 10 percent of the 50 ksi (345 MPa) material grade. The initial weld calculations were approximate based on assumed plate widths. It was known that gusset plate widths would likely be increased, thus

allowing for longer welds and a reduction in the maximum stress in the welds. Thus, a $7/16$ in. (11 mm) fillet weld was selected and recommended to be further evaluated.

$$I = 2 * \frac{bh^3}{12} = \frac{t_e h^3}{12} \quad (36)$$

$$\sigma_{bending} = \frac{Mc}{I} \quad (37)$$

$$\sigma_{tension} = \frac{P}{A} = \frac{P}{2(t_e l)} \quad (38)$$

$$\tau_{shear,center} = \frac{PQ}{It} = \frac{3}{2} * \frac{P}{A} = \frac{3}{2} * \frac{P}{2 * t_e l} \quad (39)$$

$$\tau_{shear,end} = 0 \quad (40)$$

$$\sigma_{max,end} = \sigma_{bending} + \sigma_{tension} \quad (41)$$

$$\sigma_{max,center} = \frac{\sigma_x + \sigma_y}{2} \pm \sqrt{\left(\frac{\sigma_x - \sigma_y}{2}\right)^2 + \tau_{xy}^2} = \frac{\sigma_x}{2} \pm \sqrt{\frac{\sigma_x^2}{4} + \tau_{shear,center}^2} \quad (42)$$

Where: I = Moment of inertia of fillet weld, in.⁴ (mm⁴)

t_e = Effective throat thickness, 0.707*t, in. (mm)

t = Weld size, in. (mm)

l = Weld length, in. (mm)

M = Moment about bending arm, kip-in. (kN-m)

c = Perpendicular distance to the neutral axis, in. (mm)

P = Load applied, kips (kN)

$\sigma_{bending}$ = Elastic bending stress, ksi (MPa)

$\sigma_{tension}$ = Tension stress, ksi (MPa)

τ_{shear} = Shear stress, ksi (MPa)

$\sigma_{max,end}$ = Maximum principal stress on end of plate, ksi (MPa)

$\sigma_{max,center}$ = Maximum principal stress at center of plate, ksi (MPa)

Table 26. Gusset Plate Weld Design Summary

		Weld Sizes		
t, in. (mm)		$\frac{5}{16}$ (8)	$\frac{3}{8}$ (10)	$\frac{7}{16}$ (11)
I, in. ⁴ (mm ⁴)		71.9 (2.99E7)	86.3 (3.59E7)	100.7 (4.19E7)
A, in. ² (mm ²)		5.5 (3,564)	6.6 (4,276)	7.7 (4,989)
σ_{bending} , ksi (MPa)		74.3 (512)	61.9 (427)	53.1 (366)
σ_{tension} , ksi (MPa)		2.7 (19)	2.3 (16)	1.9 (13)
τ_{shear} , ksi (MPa)		26.5 (183)	22.1 (152)	19.0 (131)
σ_{max} , ksi (MPa)	End	77.0 (531)	64.2 (442)	55.0 (379)
	Center	29.3 (202)	24.4 (168)	20.0 (138)

8.3.8 Top Steel Tube Moment Connection

For the termination of the top steel tube railing, a connection was designed between the last RESTORE barrier and the concrete buttress (i.e., the region above the gusset plate assemblies). Thus, a moment connection was selected for use to limit tube rail rotation about the vertical axis. However, a rail splice was necessary to accommodate construction tolerances. The rail splice configuration with moment and shear continuity was designed to provide equal or greater strength than the tube rail itself.

The current upper steel tube was fabricated using a ASTM A500 Grade B 46 ksi (317 MPa) material configured with a 8-in. x 4-in. x $\frac{1}{4}$ -in. (203-mm x 102-mm x 6-mm) HSS section, which has an elastic and a plastic section modulus of 10.6 in.³ (174 cm³) and 13.3 in.³ (218 cm³) about the x-x, or strong axis of bending, respectively. The yielding and plastic moment capacities of the section were calculated to be 488 k-in. (55 kN-m) and 612 k-in. (69 kN-m), respectively.

Using ASTM A36 and A572 material steel in Equations 43 or 44, the elastic section modulus of the inner section had to be equal to, or greater than, 13.6 in.³ (223 cm³) for 36 ksi (248 MPa) steel and 9.8 in.³ (161 cm³) for 50 ksi (345 MPa) steel.

Further, the plastic section modulus of the inner section had to be equal to, or greater than, 17.0 in.³ (279 cm³) for 36 ksi (248 MPa) steel and 12.3 in.³ (201 cm³) for 50 ksi (345 MPa) steel.

To allow for minimal clearance between the inner splice tube and outer tube sections, the inner splice tube was desired to be 7¼ in. x 3¼ in. (184 mm x 83 mm), which would provide an ⅛-in. (3-mm) clear gap on each side between the inner and outer sections. HSS sections were desired but none provided the desired external dimensions. Therefore, a tube section with the desired external dimension would be fabricated from welded plates. The thickness of the inner splice tube was found using Equations 45 and 46 along with the moduli noted above. The tube thickness results are shown in Table 27. The required section would utilize a thickness of 5/16 and 7/16 in. (8 and 11 mm) with 50 and 36 ksi (345 and 248 MPa) steel, respectively, when considering full cross-sectional yield. However, if no yielding were allowed, a tube thickness of ½ and ¾ in. (13 and 19 mm) would be required with A572 and A36 material steel, respectively. In summary, the thinnest inner tube splice would result using ASTM A572 steel material, which was 5/16 and ½ in. (8 and 13 mm) thick based on no yielding and reaching full-cross sectional yield, respectively. Using an aggressive design approach, the inner splice tube section was configured with welded 5/16-in. (8-mm) thick plates with widths of 6⅝ in. (168 mm) and 2⅝ in. (67 mm) to maintain the outer dimensions determined previously. The weld would use a maximum leg size of ¼ in. (6 mm) in order to round the corners and create an artificial HSS section.

$$M_p = F_y Z \quad (43)$$

$$M_y = F_y S \quad (44)$$

$$Z = \frac{bh^2}{4} - (b - 2t) \left(\frac{h}{2} - t \right)^2 \quad (45)$$

$$S = \frac{bh^2}{6} - \frac{b(h - 2t)^3}{6h} \quad (46)$$

Where: M_p = Plastic moment capacity, k-in. (kN-m)
 M_y = Yielding moment capacity, k-in. (kN-m)
 F_y = Yield strength of material, ksi (MPa)
 Z = Plastic section modulus, in.³ (cm³)
 S = Elastic section modulus, in.³ (cm³)
 b = Outer length of shorter side of section, in. (mm)
 h = Outer length of longer side of section, in. (mm)
 t = Thickness of inner splice tube section, in. (mm)

Table 27. Summary of Splice Tube Section Moduli and Thickness Calculations

Required Values	Steel Material Grade, ksi (MPa)	
	36 (248)	50 (345)
Elastic Section Modulus (S), in. ³ (cm ³) ¹	13.6 (223)	9.8 (161)
Plastic Section Modulus (Z), in. ³ (cm ³) ¹	17.0 (279)	12.3 (201)
Minimum thickness to meet S, in. (mm) ¹	$\frac{3}{4}$ (19)	$\frac{1}{2}$ (13)
Minimum thickness to meet Z, in. (mm) ¹	$\frac{7}{16}$ (11)	$\frac{5}{16}$ (8)

¹ Does not consider a reduction for potential bolt holes.

To maintain the same moment capacity as the outer tube, two connection methods were evaluated to connect the inner splice tube and outer tube. The first connection method was a series of bolts to develop the moment connection's capacity. The second connection method was a sufficiently long inner splice tube that would develop the moment capacity through lateral bearing on the inside of the outer tube rail.

Due to the tube splice being implemented above the pin and gusset configuration and the need for construction tolerances, small rotation angle of 1 degree was assumed to be across the tube splice. In the full-scale crash test no. SFH-3, permanent bending occurred in the top tube. Thus, slight movement within the joint would allow the section to rotate slightly before loading occurred.

For the first method, to determine the necessary spacing of the bolts, the bolt holes were oversized by $\frac{1}{8}$ in. (3 mm), and the 1 degree rotation was assumed. From geometry, the center to center bolt spacing distance was calculated to be 7.16 in. (182 mm), as shown in Figure 98. By incorporating two bolts per side with a total of four bolts in the connection, each bolt would have to withstand approximately 43 kips (191 kN) in shear with one shear plane between the top of the tubes and one shear plane between the bottoms of the tube, as shown in Figure 99a, and, the required bolt diameter was $1\frac{1}{4}$ in. (32 mm). However, due to the bearing capacity of the sections using Equation 30 and the width of the plate being $6\frac{5}{8}$ in. (168 mm), the required tube thickness would have to be increased to $\frac{7}{16}$ in. (11 mm) in order to resist tear out of the bolt hole. Thus, four bolts per side were considered, with a total of eight bolts in the connection to obtain four shear planes, as shown in Figure 99b. For this configuration with bolts spaced at least 7.16 in. (182 mm) apart, each bolt would have to withstand approximately 22 kips (98 kN), in shear. The required bolt diameter was calculated to be $\frac{7}{8}$ in. (22 mm) and the $\frac{5}{16}$ in. (8 mm) thicknesses of the tube materials was satisfactory to resist the loads through bearing capacities. The overall length of the tube splice with four bolts would need to be approximately $22\frac{1}{8}$ in. (562 mm) long.

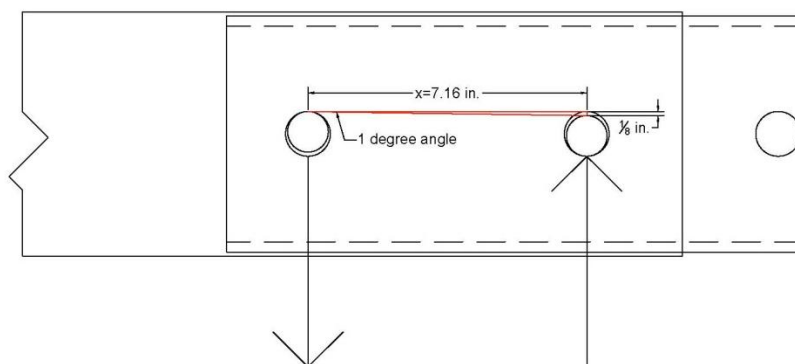


Figure 98. Upper Splice Tube Bolt Spacing Requirements

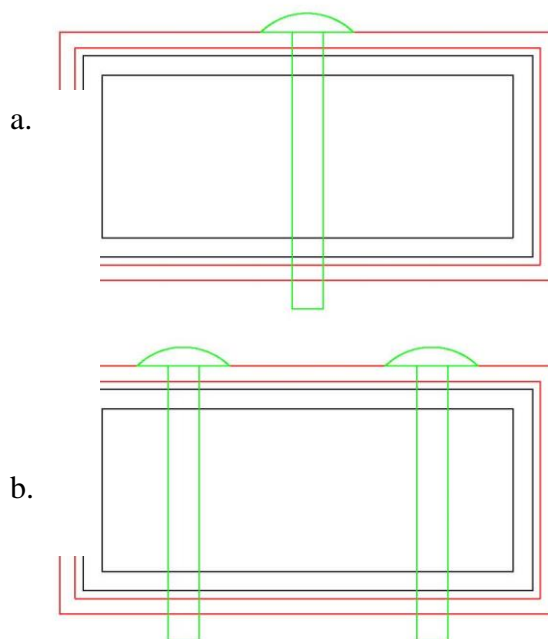


Figure 99. Top Tube and Inner Splice Tube with Bolt Configurations, Option 1

For the second method, the minimum length of the inner splice tube section was based on it developing the moment capacity as the outer tube rail section through bearing on the inside of the outer walls. Incorporating the same design rotation of 1 degree, the required inner splice tube length was $14\frac{1}{4}$ in. (362 mm) into each end of the outer tube.

Considering a nominal gap of $\frac{1}{2}$ in. (13 mm), the required total length of the inner splice tube was 29 in. (737 mm), as shown in Figure 100. One bolt on each side of the splice, would secure the inner splice tube during an impact event; since, there would be limited longitudinal loading imparted on the top tube rail. The bolt holes on each side would be oversized by $\frac{1}{4}$ in. (6 mm) to allow for bearing to occur on the outer tube before the bolt holes. The first method required a total of eight $\frac{7}{8}$ in. (22 mm) diameter bolts and a tube splice thickness of $\frac{5}{16}$ in. (8 mm) to maintain the same capacity as the RESTORE barrier top tube. The second design required a 29 in. (737 mm) long splice tube and two $\frac{1}{2}$ in. (13 mm) diameter connection bolts and was selected for further evaluation through simulation due to fewer required bolts.

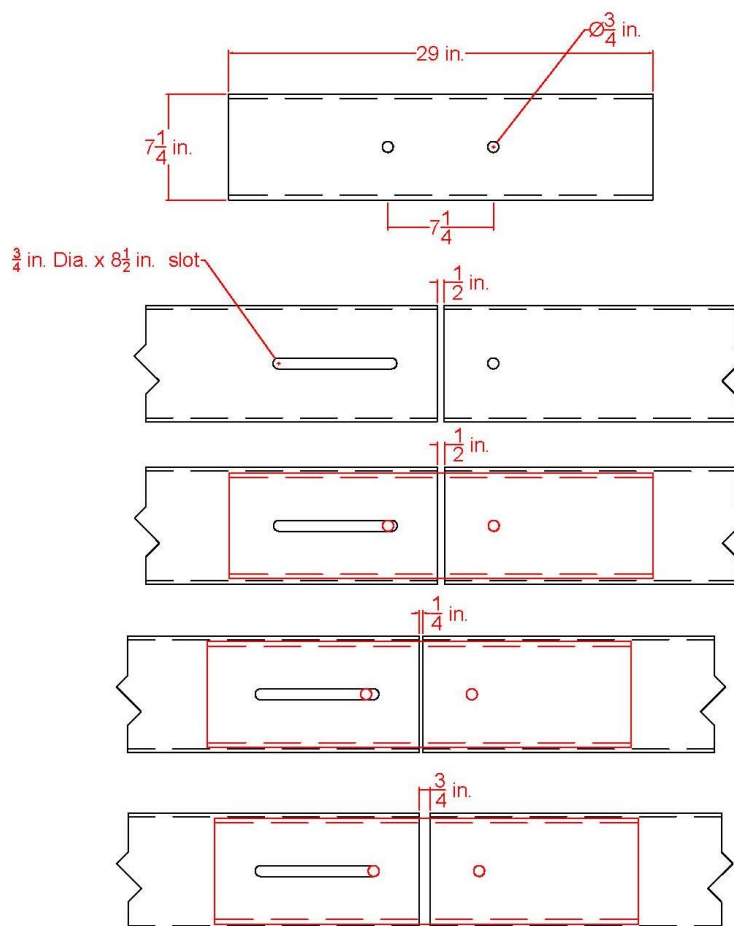


Figure 100. Inner Splice Tube Connection, Option 2

8.3.9 Concrete Steel Reinforcement and Anchorage

The concrete buttress was designed to transition from a 30-in. (762-mm) tall modified “T” shape, which resembled the RESTORE barrier, to a vertical 36-in. (914-mm) tall median barrier. A preliminary design was created for internal reinforcement within the buttress. The preliminary design utilized the yield line theory [70], as described in Chapter 2. The concrete had a compressive strength of 5,000 psi (34.5 MPa). A clear cover of 1½ in. (38 MM) was used with a total of twelve no. 7 longitudinal bars throughout buttress with eight of the longitudinal bars within the concrete beam and the other four were within the bottom post. Seventeen vertical stirrups were spaced throughout the 10-ft (3.0-m) long buttress at various spacing between 4 and 12 in. (102 and 305 mm). The calculations and design for the preliminary buttress reinforcement are provided in Appendix H. Further analysis needs to be completed to determine if the internal reinforcement is adequate to withstand a TL-4 design impact load.

Further, an initial reinforced concrete foundation was determined using a modified torsional capacity procedure, per Rosenbaugh, et al. [9-11]. The footer was designed with a concrete compressive strength of 5,000 psi (34.5 MPa). The footer was determined to be 45 in. wide by 30 in. deep (1,143 mm by 762 mm). The reinforcement consisted of no. 4 stirrups every 12 in. (305 mm) and four no. 6 longitudinal bars evenly spaced. The overturning capacity was calculated through the buttress design, and the buttress reinforcement and the foundation design are dependent on one another. The calculations and design for the preliminary buttress reinforcement are provided in Appendix H. Further, no foundation system has been designed for the RESTORE barrier. However, the foundation design for the concrete buttress would provide sufficient

structural capacity for use with the RESTORE barrier system. Further design and analysis of a RESTORE barrier foundation system is warranted to provide a more economical solution.

8.3.10 Steel Anchor Hardware and Chemical Adhesive Systems for Concrete Sections

An initial epoxy anchorage sizing was completed for the elastomer post anchorage prior to the bogie testing done in the initial energy-absorber selection phases. Through bogie testing, four $\frac{3}{4}$ -in. (19-mm) diameter by 15 in. (381 mm) long threaded steel rods were epoxied 12 in. (305 mm) into the concrete foundation in order to support the 16-in. (406-mm) tall elastomer posts [18]. However, the 12-in. (305-mm) embedment depth did not show any signs of anchor, concrete, or epoxy failure during the testing with the 16-in. (406-mm) tall elastomer posts. Thus, a decreased embedment depth of 8 in. (203 mm) was bogie tested and evaluated with the $1\frac{5}{8}$ -in. (295-mm) tall elastomer posts [19]. Four $\frac{3}{4}$ -in. (19-mm) diameter steel rods at each post were embedded in a concrete tarmac 8 in. (203 mm) which provided sufficient strength to anchor the elastomer posts during the full-scale crash testing program [20-21]. The epoxy had a minimum bond strength of 1,300 psi (9.0 MPa). However, further analysis, testing, and evaluation must be completed with the design of a concrete foundation system.

The back plate was configured with a $\frac{1}{2}$ -in. (13-mm) thick plate that would utilize the chamfered corners, similar to the RESTORE barrier so that the same hardware could be utilized throughout the system. From prior analysis and design effort, $1\frac{1}{4}$ -in. (32-mm) diameter bolts were needed to resist impact loading. A more aggressive design approach was considered where a 1-in. (25-mm) diameter bolt was used to be consistent with interior ACJ bolts. This smaller bolt diameter would be investigated through simulation

on the RESTORE barrier side. However, the back plate will be connected to the buttress using epoxy anchors, and will need to be further evaluated as they were not calculated and included in the simulation effort.

Design calculations were not completed to determine the anchorage design for the top steel tube termination to the concrete buttress. However, the top tube termination would likely be connected to a welded base plate, similar to the top tube connection in the interior section, and would be anchored into the top of the concrete buttress using epoxied threaded rods. However, calculations were never completed on the epoxy anchorage system to terminate the top tube and welded base plate. Thus, further design and evaluation must be completed prior to full-scale crash testing the transition system.

8.4 Moment Connection

Through the design process, further brainstorming led to a transition joint concept utilizing a moment connection to the buttress end, which would need to withstand a TL-4 impact event with all three vehicle types. The moment connection may consider utilizing hardware similar to the ACJ but would need to be strengthened to accommodate the constrained conditions. Thus, future design efforts may consider a moment if an alternate transition section is desired.

9 INITIAL MODELING OF PINNED CONNECTION

9.1 Background

The original LS-DYNA model of the RESTORE barrier, as created by Schmidt, et al. [19], was modified to incorporate a pinned end for use in determining if the pin-and-loop concept had merit. The initial development of the pinned end connection as well as some of the model components are outlined herein. This simulation effort and the design of the gusset concept, which resembled the pin-and-loop configuration, were completed simultaneously.

9.2 Scope

During the initial simulation efforts by Schmidt, et al., the RESTORE barrier did not include any end constraints, which allowed for increased barrier deflections and rotations as well as the propensity for vehicle instability to be magnified [19]. Therefore, the force distribution within the pin and loop end connection and vehicle stability when impacted near a constrained pinned end was unknown. Therefore, simulations with impact locations ranging between 5 and 40 ft (0.3 and 12.2 m) upstream from the downstream pinned end of the RESTORE barrier were modeled to determine the maximum lateral force distributions on the loops, the maximum vehicle underride, vehicle stability problems, and determine the number of required posts and skids.

9.3 RESTORE Barrier Model Modifications

For the purpose of this simulation effort, slight modifications were made to the original model. The model incorporated eight loops to simulate rebar on both the upstream and downstream ends of the barrier, which were utilized to compare barrier performance for both constrained and unconstrained ends. Since the distribution of forces

on the pin and loops was being investigated and one design concept had three gussets, the number of loops on the downstream end of the barrier was reduced to three, as shown in Figure 101. The pin was modeled with *MAT_RIGID using type 2 solid elements. The pin was constrained in all directions to simulate a connection to a rigid concrete buttress. The rebar loops were configured with a material having a yield strength of 60 ksi (413 MPa), which were modeled with *MAT_PIECEWISE_LINEAR_PLASTICITY using type 2 solid elements, as shown in Figure 101 and Table 28. Note that steel gusset plates were concurrently being designed to replace the rebar loops. Each of the loops were modeled with two different parts using merged nodes to connect them in order to obtain contact forces on either the impact or non-impact side.

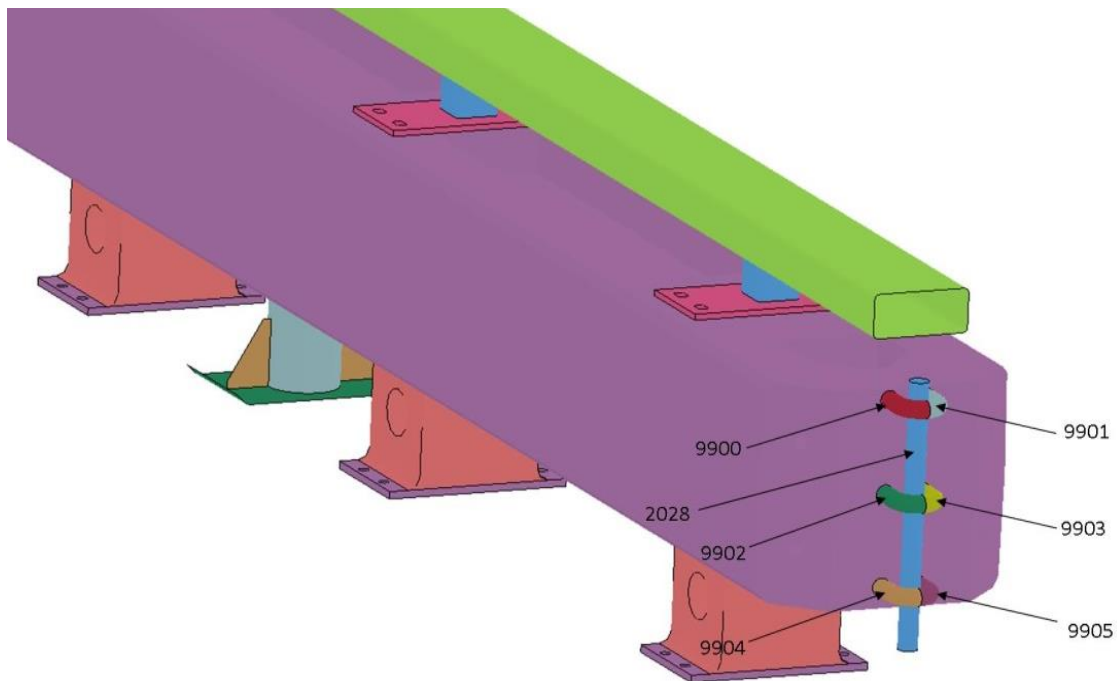


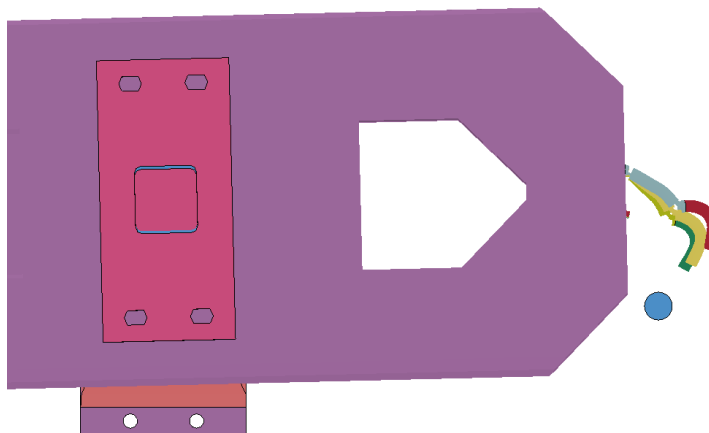
Figure 101. RESTORE Barrier Pin-and-Loop Simulation Part Numbers

Table 28. RESTORE Barrier Pin-and-Loop Model Parts, Elements, and Materials

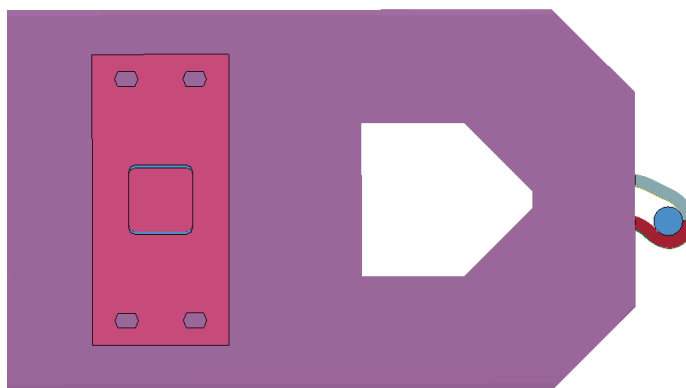
Part Description	Simulation Part No.	Element Type	Material
Pin	2028	Type 2 Solid	*MAT_RIGID
Impact Side Top Loop	9900	Type 2 Solid	*MAT_PIECEWISE_LINEAR_PLASTICITY
Non-Impact Side Top Loop	9901	Type 2 Solid	*MAT_PIECEWISE_LINEAR_PLASTICITY
Impact Side Middle Loop	9902	Type 2 Solid	*MAT_PIECEWISE_LINEAR_PLASTICITY
Non-Impact Side Middle Loop	9903	Type 2 Solid	*MAT_PIECEWISE_LINEAR_PLASTICITY
Impact Side Bottom Loop	9904	Type 2 Solid	*MAT_PIECEWISE_LINEAR_PLASTICITY
Non-Impact Side Bottom Loop	9905	Type 2 Solid	*MAT_PIECEWISE_LINEAR_PLASTICITY

The loops are generally embedded into the concrete barrier. However, the concrete RESTORE barrier segments were modeled with a rigid material definition and further efforts to remodel the end barrier segments were not desired. Therefore, the simulated loops were connected to the RESTORE barrier segments using *CONSTRAINED_EXTRA_NODES, which constrains the nodes at the end of the loops as part of the rigid barrier segment. The 60 ksi (413 MPa) steel loops were originally modeled to fail when the effective plastic strain reached a limit value of 0.29, which caused the loops to fail, as shown in Figure 102a. Shortly after failure, the simulation stopped running. To determine if the loops experienced large forces, the material failure option was removed. However, with failure removed, the loops deformed more than what was desired, as shown in Figure 102b. The pin-and-loop connection was desired to not allow barrier translation and loop deformations. Thus, the cross-section of the loops were changed in order to get the desired behavior for the joint and determine if the pin-and-loop concept had merit.

The diameter of the loops was increased from $\frac{3}{4}$ in. (19 mm) to $1\frac{1}{4}$ in. (32 mm) to prevent excessive deformation and fracture when the effective plastic strain reached a limit of 0.29. With an increased loop diameter at the downstream end, the loops did not fracture and large deformations did not occur.



a. Failure Defined



b. Failure Removed

Figure 102. Initial Simulations with the Pin-and-Loop Concept

The transition system was impacted at 5, 20, and 40 ft (1.5, 6.1 and 12.2 m) upstream from the downstream pinned end of the system to evaluate the barrier deflections while traveling toward a stiffer end, vehicle stability, maximum lateral impact

force, and force distribution into the loops. Impacts with the 1100C and 2270P vehicle models were evaluated with the pin-and-loop concept.

9.4 1100C Vehicle Simulations

Two 2,425-lb (1,100-kg) small car vehicle models impacted the barrier system: a Dodge Neon and Toyota Yaris. As mentioned in Chapter 4, the Dodge Neon model was most accurate for representing the ORA, OIV and vehicle stability. The Toyota Yaris was most accurate for representing the vehicle snag, barrier deflections, and lateral impact force. However, all parameters were compared for both vehicles.

9.4.1 Dodge Neon

The Dodge Neon model impacted the barrier at 62.1 mph (100 km/h) and an angle of 25 degrees for each impact upstream from the pin-and-loop connection. The Neon model had a mass of 2,591 lb (1,175 kg). The impact locations and corresponding results are shown in Table 29. The maximum lateral impact force increased as the impact location was closer to the fixed pin. The impact 5 ft (1.5 m) upstream from the pin showed approximately a 10 percent higher force than the impacts farther upstream. The 20 and 40 ft (6.1 and 12.2 m) impact location forces were within 3 percent of each other.

Similarly, the simulated dynamic deflection increased as the impact event occurred farther upstream from the pinned connection. The vehicle roll, pitch, and yaw behavior for each of the impact points was not a cause for concern and were all determined to be minimal. The unfiltered contact forces, as determined from *CONTACT_FORCE_TRANSducer between the impact and non-impact sides of each downstream loop and the pin, are shown in Figures 103 through 105 for impacts located 5, 20, and 40 ft (1.5, 6.1, and 12.2 m) upstream from the pin, respectively. The

barrier did not rotate about the X-axis in the impact 5 ft (1.5 m) upstream from the pin, and only the front of the loops were loaded laterally. The maximum lateral load during the initial impact for each loop varied from 17, 31, and 54 kips (76, 138, and 240 kN) for the impact side on the top, middle and bottom loops, respectively. For the impact 20 ft (6.1 m) upstream from the pin, the barrier rotated along the X-axis, which loaded the top impact side 40 percent more than the bottom non-impact side. Similarly for the impact 40 ft (12.2 m) upstream from the pin, the top impact side of the loops experienced a force 13 percent greater than the bottom non-impact side. Post snag was not observed for any of the impact locations with the Neon model.

Table 29. Simulation Results for 1100C Vehicle, Dodge Neon, at Varying Impact Locations

Simulation Parameter		Results at Impact Location Upstream from Pin and Loop Connection		
		5 ft (1.5 m)	20 ft (6.1 m)	40 ft (12.2 m)
ORA, g's	Longitudinal	-5.58	-4.88	-10.88
	Lateral	11.51	7.15	11.42
OIV, ft/s (m/s)	Longitudinal	-24.70 (-7.53)	-24.15 (-7.36)	-24.90 (-7.59)
	Lateral	30.48 (9.29)	28.41 (8.66)	27.30 (8.32)
Test Article Deflections, in. (mm)	Dynamic of Concrete Rail	0.7 (18)	6.8 (173)	6.4 (163)
	Dynamic of Steel Rail	0.6 (15)	7.0 (178)	6.5 (165)
	Location of Maximum Deflection Upstream From Pin	20 ft (6.1 m)	20 ft (6.1 m)	40 ft (12.2 m)
	Working Width	23 (584)	29.1 (739)	28.7 (729)
Parallel Time, msec		199	198	209
Vehicle Stability	Max. Roll, deg.	6.9	4.9	4.9
	Max. Pitch, deg.	3.3	-2.5	-2.7
	Max. Yaw, deg.	33.6	29.0	26.9
Posts hit by leading tire (wheel snag)		0	0	0
Max. Lateral Impact Force, kips (kN) ¹		49.3 (219)	43.9 (195)	45.2 (201)

¹Calculated using CFC60 50-msec moving average of global Y-acceleration multiplied by mass.

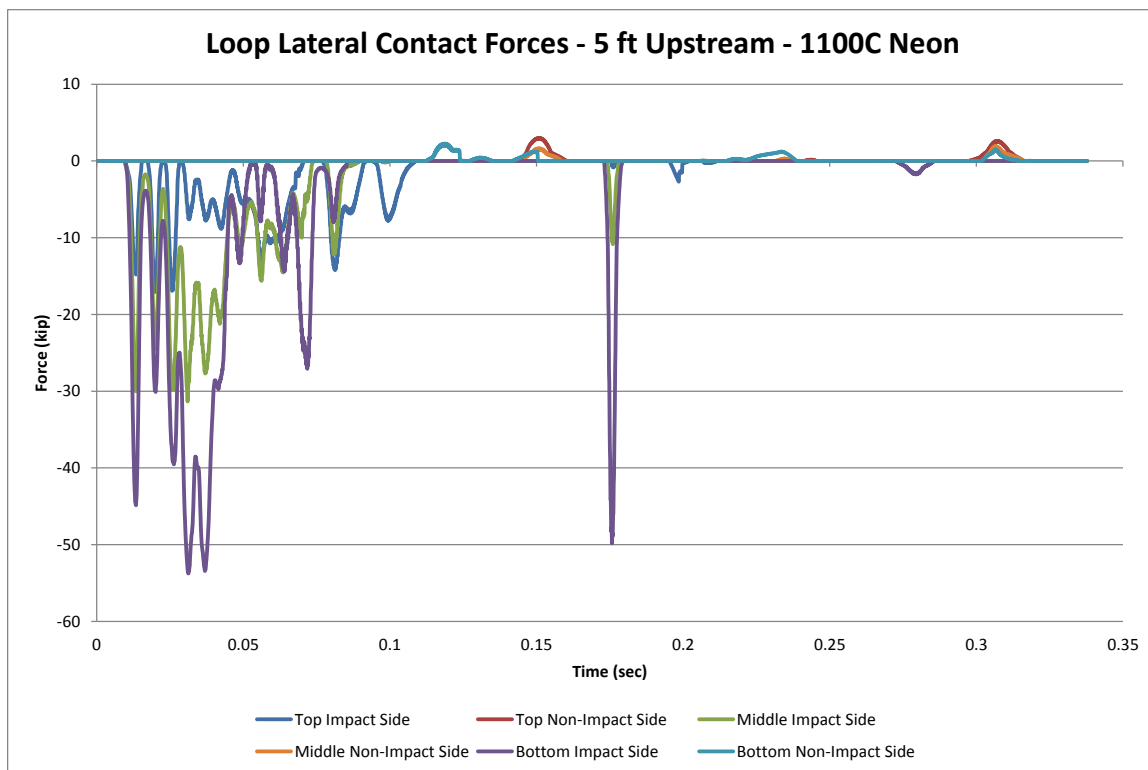


Figure 103. Lateral Loop Contact Forces – 5 ft Upstream from Pin – 1100C Neon

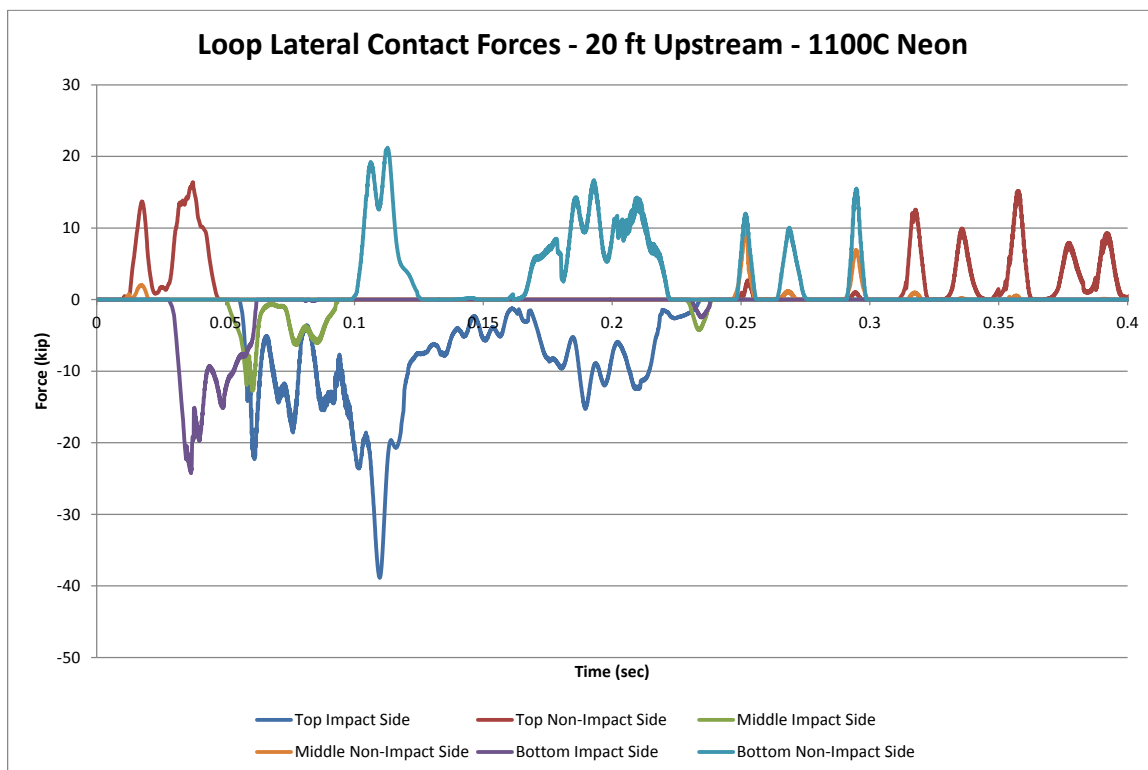


Figure 104. Lateral Loop Contact Forces – 20 ft Upstream from Pin – 1100C Neon

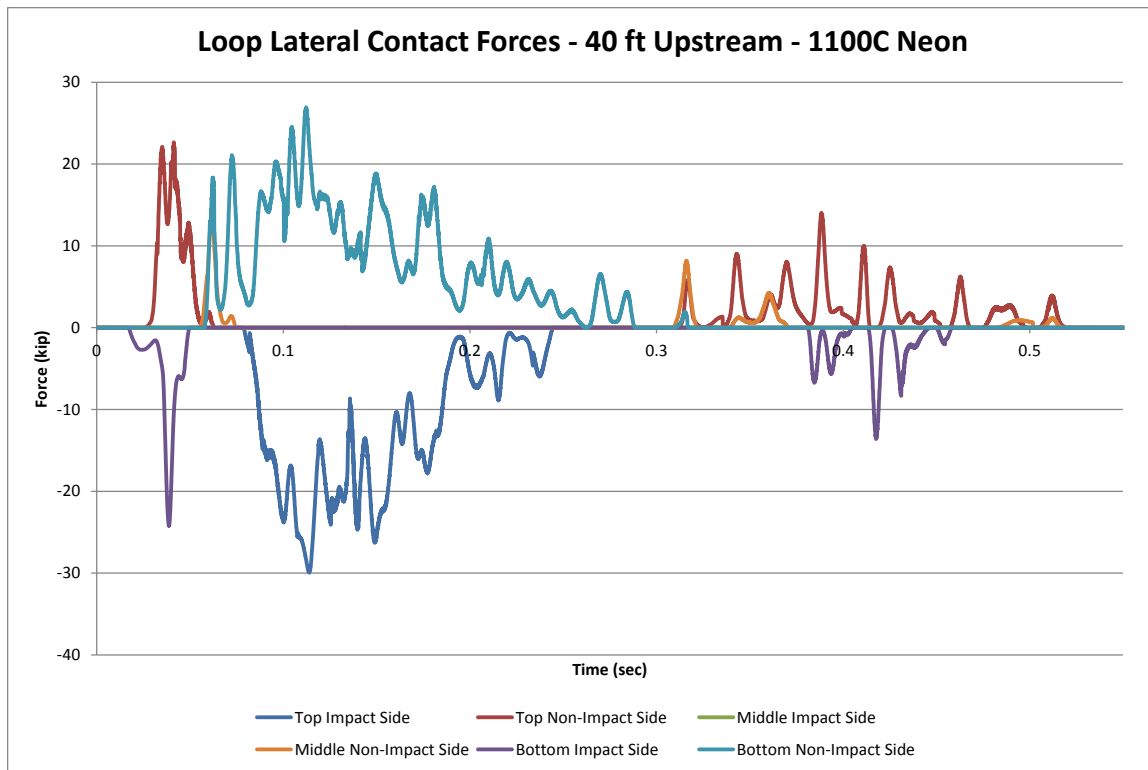


Figure 105. Lateral Loop Contact Forces – 40 ft Upstream from Pin – 1100C Neon

9.4.2 Toyota Yaris Simulation

The Toyota Yaris model impacted the barrier at 62.1 mph (100 km/h) and an angle of 25 degrees for each impact upstream from the pin-and-loop connection. The Yaris model had a mass of 2,775 lb (1,259 kg). The impact locations and corresponding results are shown in Table 30. The maximum lateral impact force increased as the impact location was closer to the fixed pin. The impact 5 ft (1.5 m) upstream from the pin showed approximately a 10 percent higher lateral force than the impacts farther upstream. The 20 and 40 ft (6.1 and 12.2 m) impact location lateral forces were calculated to be approximately within 100 lb (445 N).

Table 30. Simulation Results for 1100C Vehicle, Toyota Yaris, Varying Impact Locations

Simulation Parameter		Results at Impact Location Upstream from Pin and Loop Connection		
		5 ft (1.5 m)	20 ft (6.1 m)	40 ft (12.2 m)
ORA, g's	Longitudinal	-6.71	-5.61	-4.48
	Lateral	3.65	6.13	9.61
OIV, ft/s (m/s)	Longitudinal	-28.08 (-8.56)	-28.77 (-8.77)	-28.22 (-8.60)
	Lateral	27.85 (8.49)	23.13 (7.05)	23.56 (7.18)
Test Article Deflections, in. (mm)	Dynamic of Concrete Rail	1.0 (25)	7.5 (191)	7.1 (180)
	Dynamic of Steel Rail	0.9 (23)	7.7 (196)	7.2 (183)
	Location of Maximum Deflection Upstream from Pin	20 ft (6.1 m)	20 ft (6.1 m)	40 ft (12.2 m)
	Working Width	23.3 (592)	29.8 (757)	29.4 (747)
Parallel Time, msec		205	299	269
Vehicle Stability	Max. Roll, deg.	9.1	13.8	13.1
	Max. Pitch, deg.	-7.9	-11.1	-13.9
	Max. Yaw, deg.	48.4	34.9	28.2
Posts hit by leading tire (wheel snag)		0	1	2
Max. Lateral Impact Force, kips (kN) ¹		55.6 (247)	49.8 (222)	49.9 (222)

¹Calculated using CFC60 50-msec moving average of global Y-acceleration multiplied by mass

Similarly, the simulated dynamic deflection increased as the impact event occurred farther upstream from the pinned connection. The vehicle roll, pitch, and yaw behavior for each of the impact locations was not a cause for concern and were all deemed to be minimal. Unfiltered contact forces, as determined from *CONTACT_FORCE_TRANSDUCER between the impact and non-impact sides of each downstream loop and the pin, are shown in Figures 106 through 108 for impacts located 5, 20, and 40 ft (1.5, 6.1, and 12.2 m) upstream from the pin, respectively. The barrier did not rotate about the X-axis in the impact 5 ft (1.5 m) upstream from the pin, and only the front of the loops were loaded laterally. The maximum lateral load during the initial impact for each loop varied from 12, 24, and 36 kips (53, 107 and 160 kN) for

the impact side on the top, middle and bottom loops, respectively. For the impact 20 ft (6.1 m) upstream from the pin, the barrier rotated about the X-axis, which loaded the top impact side 39 percent more than the bottom non-impact side. However for the impact 40 ft (12.2 m) upstream from the pin, the top impact side of the loops experienced a force 15 percent less than the bottom non-impact side. Further, wheel snag occurred on one post during the impact 20 ft (6.1 m) upstream from the pin, and wheel snag was seen on 2 posts during the impact 40 ft (12.2 m) upstream from the pin.

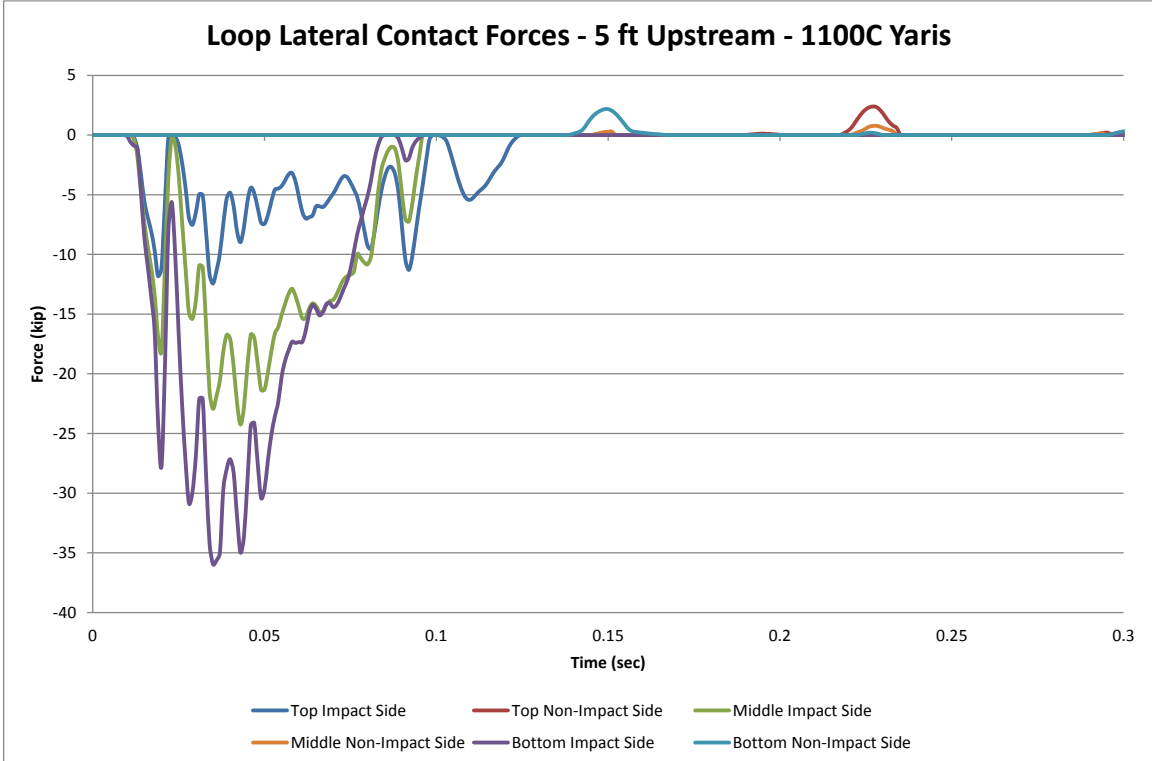


Figure 106. Lateral Loop Contact Forces – 5 ft Upstream from Pin – 1100C Yaris

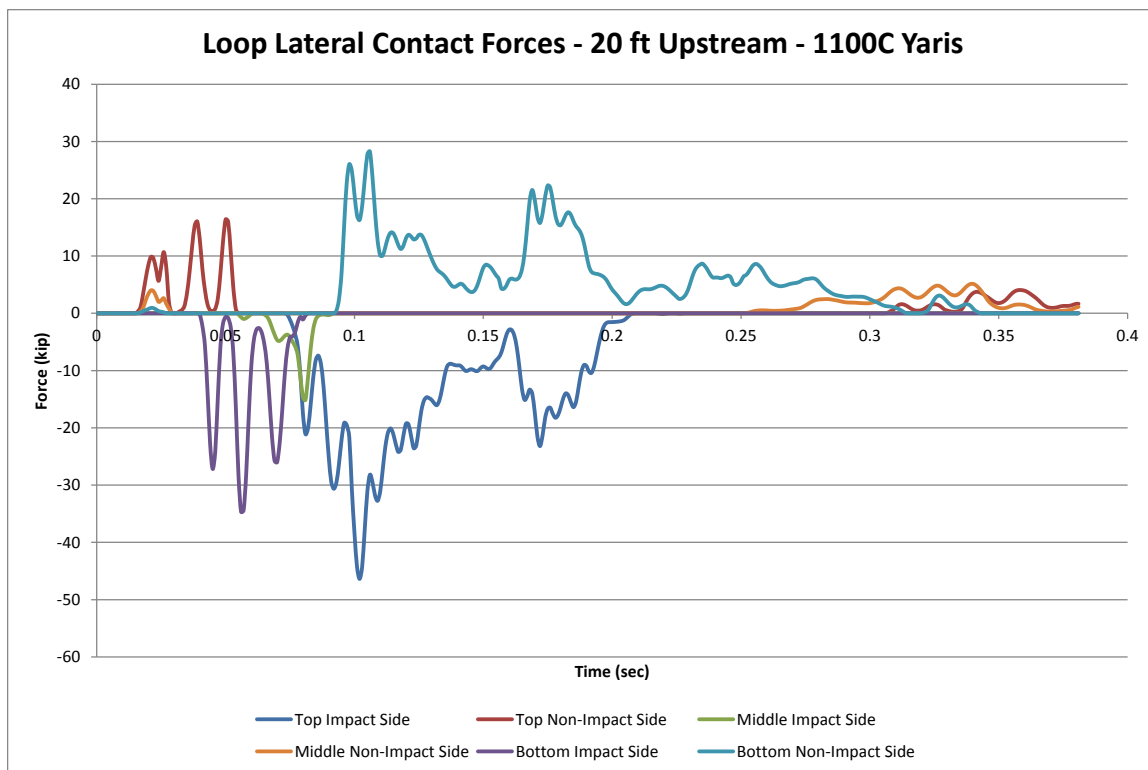


Figure 107. Lateral Loop Contact Forces – 20 ft Upstream from Pin – 1100C Yaris

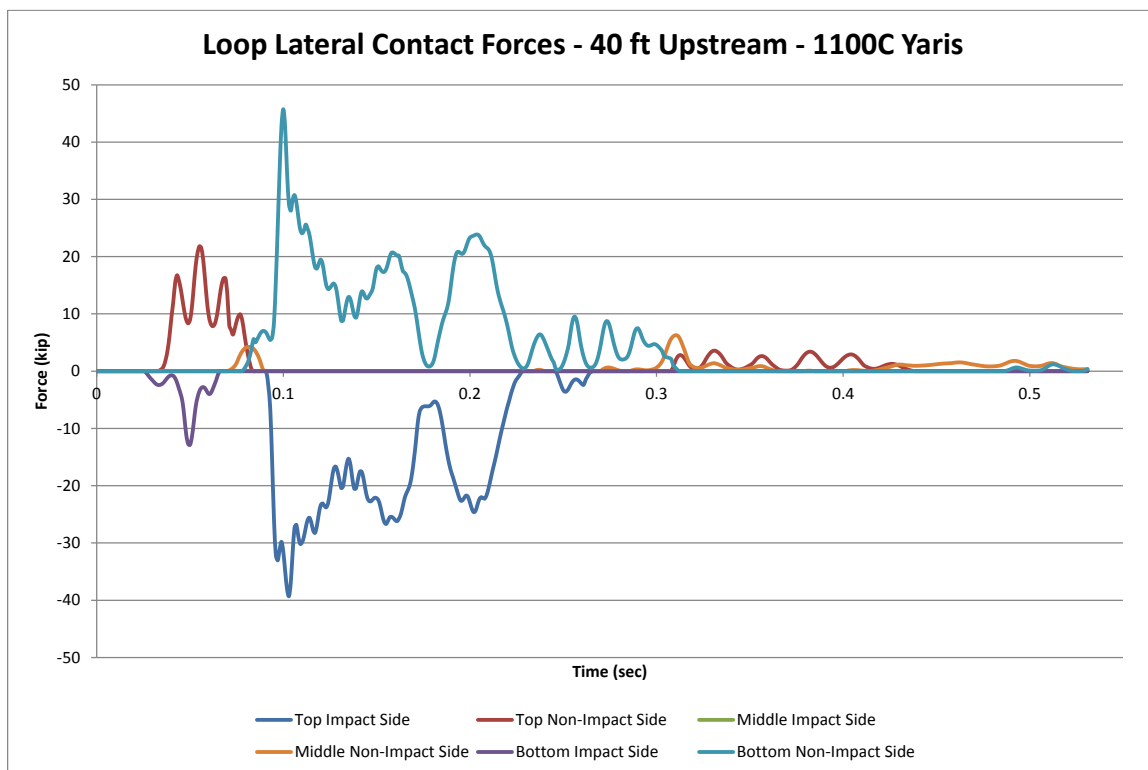


Figure 108. Lateral Loop Contact Forces – 40 ft Upstream from Pin – 1100C Yaris

9.5 2270P Chevrolet Silverado Simulations

The Chevrolet Silverado model impacted the barrier at 62.1 mph (100 km/h) and an angle of 25 degrees for each impact location upstream from the pin-and-loop connection. The Silverado model had a mass of 5,008 lb (2,272 kg). The impact locations and corresponding results are shown in Table 31. The maximum lateral impact force increased as the impact location was closer to the fixed pin connection. The impact 5 ft (1.5 m) upstream from the pin showed approximately a 16 percent higher lateral force than the impacts farther upstream. The lateral forces for the 20 and 40 ft (6.1 and 12.2 m) impact locations were within 1 percent.

Table 31. Simulation Results for 2270P Vehicle, Chevrolet Silverado, Varying Impact Locations

Simulation Parameter		Results at Impact Location Upstream from Pin and Loop Connection		
		5 ft (1.5 m)	20 ft (6.1 m)	40 ft (12.2 m)
ORA, g's	Longitudinal	-13.21	13.13	-13.58
	Lateral	15.79	14.37	17.22
OIV, ft/s (m/s)	Longitudinal	-16.86 (-5.14)	-16.21 (-4.94)	-16.27 (-4.96)
	Lateral	22.67 (6.91)	20.87 (6.36)	6.18 (20.28)
Test Article Deflections, in. (mm)	Dynamic of Concrete Rail	1.0 (25)	7.5 (191)	7.9 (201)
	Dynamic of Steel Rail	1.0 (25)	7.6 (193)	7.9 (201)
	Location of Maximum Deflection Upstream from Pin	20 ft (6.1 m)	20 ft (6.1 m)	40 ft (12.2 m)
	Working Width	23.3 (592)	29.9 (759)	30.2 (767)
Parallel Time, msec		197	186	195
Vehicle Stability	Max. Roll, deg.	-20.4	-29.1	-27.1
	Max. Pitch, deg.	-14.3	-7.2	-9.2
	Max. Yaw, deg.	27.3	31.0	28.6
Posts hit by leading tire (wheel snag)		0	0	0
Max. Lateral Impact Force, kips (kN) ¹		78.1 (347)	67.5 (300)	68.1 (303)

¹Calculated using CFC60 50-msec moving average of global Y-acceleration multiplied by mass

Similarly, the simulated dynamic deflection increased as the impact event occurred farther upstream from the pin. The vehicle roll, pitch, and yaw behavior for each of the impact locations was not a cause for concern and were all deemed to be minimal. Unfiltered contact forces, as determined from *CONTACT_FORCE_TRANSDUCER between the impact and non-impact sides of each downstream loop and the pin, are shown in Figures 109 through 111 for impacts located 5, 20, and 40 ft (1.5, 6.1, and 12.2 m) upstream from the pin, respectively. The barrier did not rotate about the X-axis in the impact 5 ft (1.5 m) upstream from the pin, and only the front of the loops were loaded laterally. The maximum lateral load during the first impact for each loop were within 20 percent. The secondary impact occurred when the rear of the vehicle impacted the barrier. However, the contact forces during tail slap for the 2270P vehicle may be greater than what would be observed during full-scale crash testing due to the rear axle and wheels being stronger than the full-scale crash test vehicle. As the impact occurred farther upstream, rotation in the barrier was present where the top impact and bottom non-impact sides of the loops were loaded. The top impact side loops experienced 22 and 26 percent higher loads than the bottom non-impact side during the impacts at 20 and 40 ft (6.1 and 12.2 m) upstream from the pin, respectively.

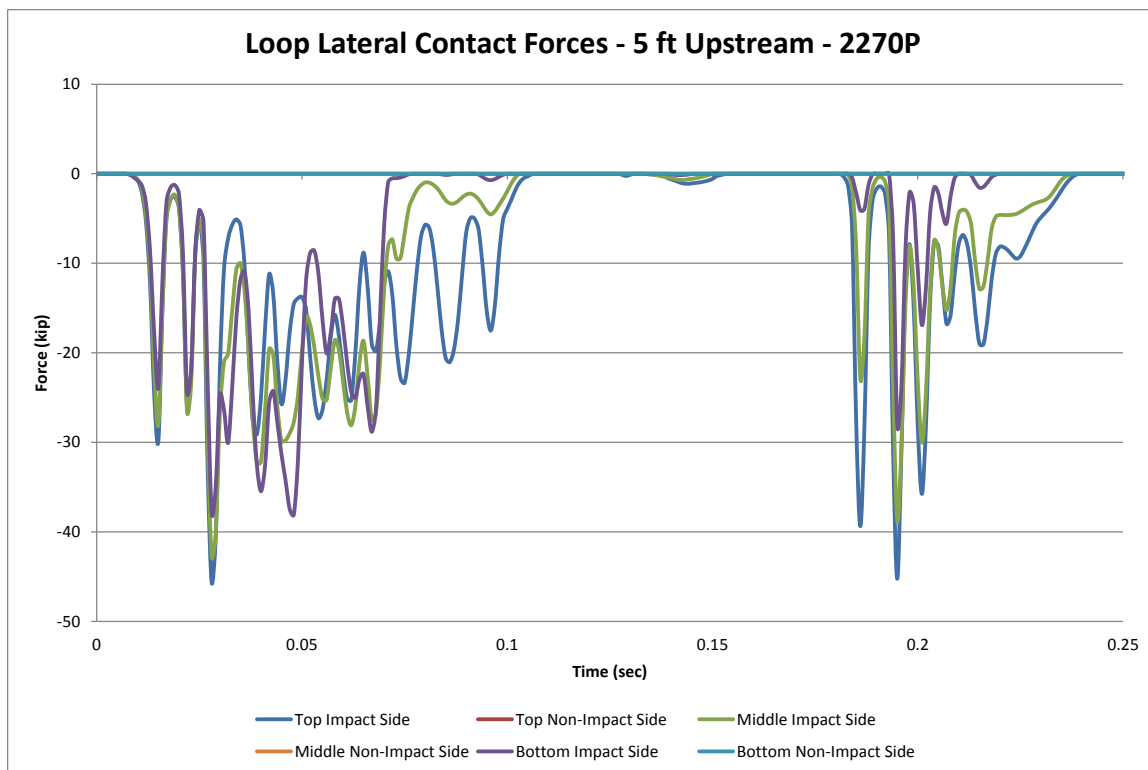


Figure 109. Lateral Loop Contact Forces – 5 ft Upstream from Pin – 2270P

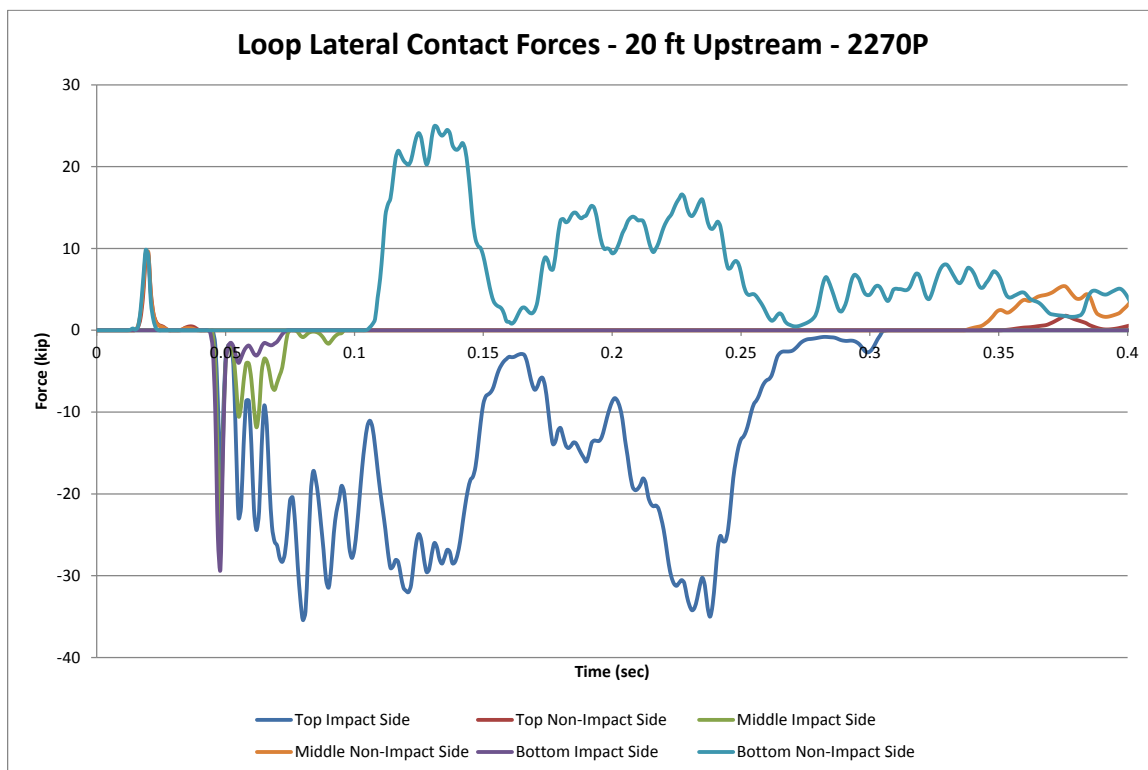


Figure 110. Lateral Loop Contact Forces – 20 ft Upstream from Pin – 2270P

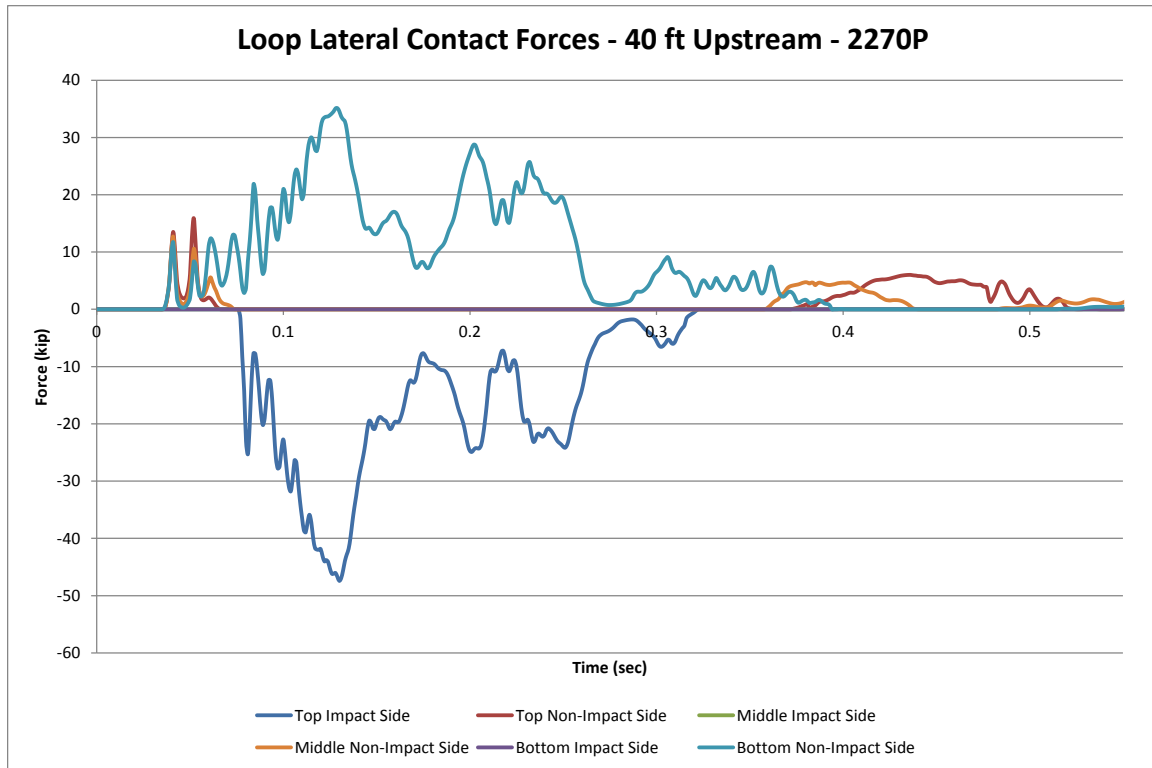


Figure 111. Lateral Loop Contact Forces – 40 ft Upstream from Pin – 2270P

9.6 Conclusions

Computer simulation was used to evaluate whether the pin-and-loop concept had merit. The simulation study utilized the loops that were already incorporated in the model but were modified to represent the scenario that was being designed. Multiple results were tabulated and evaluated, including the force distribution across the loops at various impact locations, concerns for post snag, vehicle underride, and vehicle stability.

The simulation study used both Dodge Neon and Toyota Yaris small car models as well as the Chevrolet Silverado pickup truck model. During the simulations with each of the vehicle models, the maximum lateral force imparted on the barrier increased and the deflections decreased as the impact location moved closer to the downstream pinned-end connection. Wheel snag occurred on posts that were downstream from impact during

the Yaris simulations at 20 and 40 ft (6.1 and 12.2 m) upstream from the pin. The simulated wheel snag was similar to that observed during the interior region impact event, and should be further evaluated using more impact locations. The determination of the addition of more posts and shear fenders should also be further evaluated through computer simulation. Due to the small vehicle roll, pitch, and yaw angles, deflections not cause a concern for vehicle instability, and similar vehicle snag on the post as observed at the interior location, the pin-and-loop concept shows potential merit for use in a transition and is recommended for further evaluation through LS-DYNA simulations.

The simulations did not load the non-impact side of the loops at all when the impact location was 5 ft (1.5 m) upstream from the pin. The forces exerted on the impact side of the loops were nearly even between each loop during the simulation with the pickup truck model. However, the force distribution on the impact side of the loops showed higher forces on the bottom loop, as compared to the top loop. Thus, it is believed that the SUT model would exhibit a similar trend with the top loop experiencing a greater load than the bottom loop due to the higher bumper height. This loading scenario resembles the force approximation where the 100 kip (445 kN) lateral point load was distributed across the gusset plates evenly with the eccentric moment. Further, that force approximation produced the larger peak shear value and was used throughout the pin and gusset plate assembly calculations.

10 PREFERRED DESIGN MODEL CONFIGURATION

10.1 Introduction

Based on the results found in Chapter 9, the pin-and-gusset concept showed promise and potential for use in transitioning the RESTORE barrier to a rigid concrete buttress. However, further simulation efforts had to be completed to evaluate the design from Section 8.3. The computer-aided drawing set for the transition region without a cover plate can be found in Appendix G.

10.2 LS-DYNA Model for RESTORE Barrier Transition

The transition barrier model was 211 ft – 4½ in. +/- 1½ in. (64.4 m +/- 38 mm) long. Ten RESTORE barrier segments were inter-connected, while the upstream end had no constraints and the downstream end was connected to a rigid buttress with a vertical drop pin and gusset plate assembly. The RESTORE barrier transition was evaluated at various impact points with various vehicle models, including: 1100C Neon and Yaris passenger cars, a 2270P Silverado pickup truck, and a 10000S single-unit truck.

The RESTORE barrier model parts were previously shown in Section 3.7.1 and remained the same throughout the simulations. The transition model parts are shown in Figure 112, and the parts, element types, and material models are shown in Table 32. The corresponding part reference numbers from the drawing set in Appendix I are also shown in Table 32. Reference numbers b1-b4 and d6-d7 (bolted connections), c1-c5 (rebar), and d9 (epoxy) were not modeled as discrete parts.

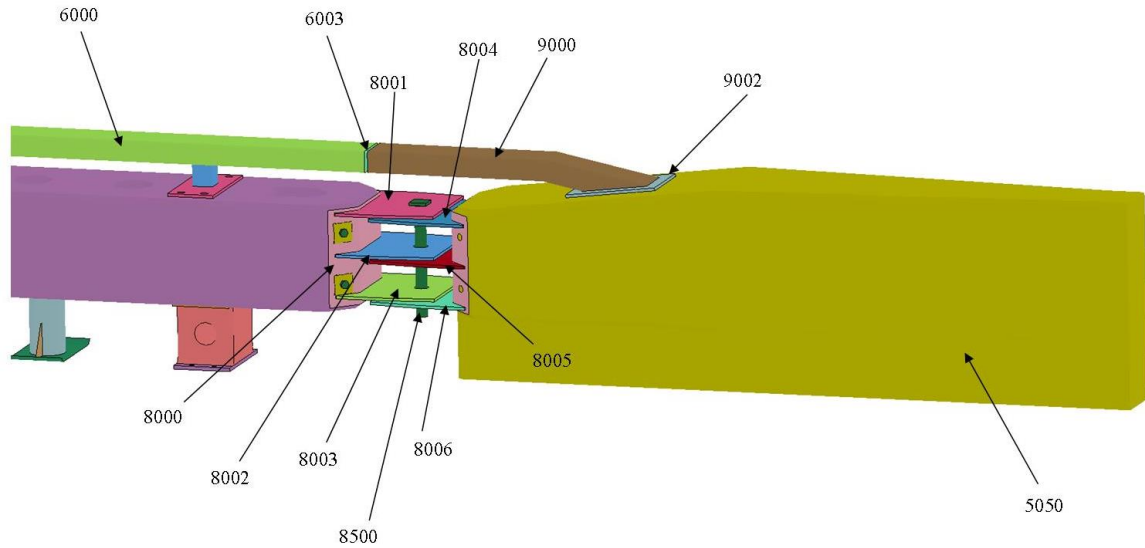


Figure 112. Simulation Part Numbers – No Cover Plate

The RESTORE and buttress gusset plates, and pin (part nos. 8001 through 8006 and 8500) used fully-integrated, selectively-reduced solid element formulations. Previous simulations conducted by Schmidt, et al. modeled the ACJ with solid elements in order to provide a consistent surface when prestressing the splice bolts. However, the back plate was modeled with a Belytschko-Tsay element formulation (Type 2 shell elements) to reduce the number of elements within the transition region. The buttress was designed to restrict motion, so it was modeled as a rigid part with a Belytschko-Tsay element formulation (Type 2 shell elements). The top tube termination used the same material properties as the internal RESTORE barrier top tube with a Belytschko-Tsay element formulation (Type 2 shell elements). The tube base plate used a constant stress solid element (Type 1 solid elements). The back plate, gusset plates, pin, tube, tube splice, and tube base plate (part nos. 8000-8006, 8500, 9000, 9002, 6000 and 6003) were simulated using an actual yield strength of 62 ksi (427 MPa). None of the material models incorporated failure.

Table 32. Barrier Model Parts, Elements, and Materials – No Cover Plate

Part Description	Drawing Reference No.	Simulation Part No.	Element Type	Element Thickness, in. (mm)	Material
Back Plate	a6	8000	Type 2 Shell	$\frac{1}{2}$ (13)	*MAT_PIECEWISE_LINEAR_PLASTICITY
Top RESTORE Gusset	a7	8001	Type 2 Solid	NA	*MAT_PIECEWISE_LINEAR_PLASTICITY
Middle RESTORE	a7	8002	Type 2 Solid	NA	*MAT_PIECEWISE_LINEAR_PLASTICITY
Bottom RESTORE	a7	8003	Type 2 Solid	NA	*MAT_PIECEWISE_LINEAR_PLASTICITY
Top Buttress Gusset	a8	8004	Type 2 Solid	NA	*MAT_PIECEWISE_LINEAR_PLASTICITY
Middle Buttress Gusset	a8	8005	Type 2 Solid	NA	*MAT_PIECEWISE_LINEAR_PLASTICITY
Bottom Buttress Gusset	a8	8006	Type 2 Solid	NA	*MAT_PIECEWISE_LINEAR_PLASTICITY
Pin	b11	8500	Type 2 Solid	NA	*MAT_PIECEWISE_LINEAR_PLASTICITY
Buttress	a5	5050	Type 2 Shell	$\frac{1}{16}$ (2)	*MAT_RIGID
Top Tube Termination	d5	9000	Type 2 Shell	$\frac{1}{4}$ (6)	*MAT_PIECEWISE_LINEAR_PLASTICITY
Tube Base Plate	d4	9002	Type 1 Solid	NA	*MAT_PIECEWISE_LINEAR_PLASTICITY
Tube Splice ¹	d11 and d12	6003	Type 2 Shell	$\frac{1}{4}$ (6)	*MAT_PIECEWISE_LINEAR_PLASTICITY
Top Tube	d3	6000	Type 2 Shell	$\frac{1}{4}$ (6)	*MAT_PIECEWISE_LINEAR_PLASTICITY

¹ Noted part was simulated with a smaller thickness than designed. Use thickness defined in drawing set for any future work.

The gusset nodes were merged to the back plate. Similarly, the top nodes for the tube termination hardware were merged to the tube base plate. The merged nodes simulated a weld between the respective parts.

Tied contacts were used between the tube base plate and the rigid concrete buttress (part nos. 5050 and 9002) to simulate the epoxy anchorage. A

*CONTACT_TIED_NODES_TO_SURFACE was originally used to attach the entire back plate to the buttress. However, this option did not allow the back plate to deform.

Thus, the nodes around the bolt holes in the back plate were constrained to the buttress

using *CONSTRAINED_EXTRA_NODES. This option allowed more realistic deformation in the back plate.

The top tube splice locations were moved from the midspan on the concrete barrier to the ends of the concrete barriers, above the ACJ. This splice movement caused a need for a new part, as shown in Appendix G. The top tube connection was not simulated with bolts, as it required more difficult meshing of parts when the bolts in the top tube were designed to solely hold the tube splices in place and not to withstand any of the loading. Thus, the tube splices (part no. 6003) were connected to the top tube and sloped tube (part nos. 6000 and 9000) with four *CONSTRAINED_SPOTWELD connections on each side of the tube splice. Four spotwelds were implemented to simulate an area where a bolt would be connected. Inputs for the shear and normal force at failure were defined as 1.0 (4.4 kN) and 1.7 kips (7.6 kN), which is one fourth of the shear and tensile failure forces for ½-in. (13-mm) diameter, A307 Grade A bolts. The purpose of the constraints was to hold the tube splices in the correct location during the impact event.

10.3 Initial Simulation

Simulations using LS-DYNA were used to determine if excessive vehicle snag occurred at the transition joint. Two concepts were considered for preventing lateral vehicle pocketing. The first was to extend the gusset plates so that they were nearly flush with the front faces of the RESTORE barrier and buttress, as shown in Figure 113. However, this concept would have higher risk for vehicle components to penetrate between the gusset plate and snag on the buttress end. The second concept was to incorporate a cover plate that would reduce concerns for vehicle snag but require

additional hardware. The nominal vertical gap between the gusset plates was $5^{11}/16$ in. (144 mm).

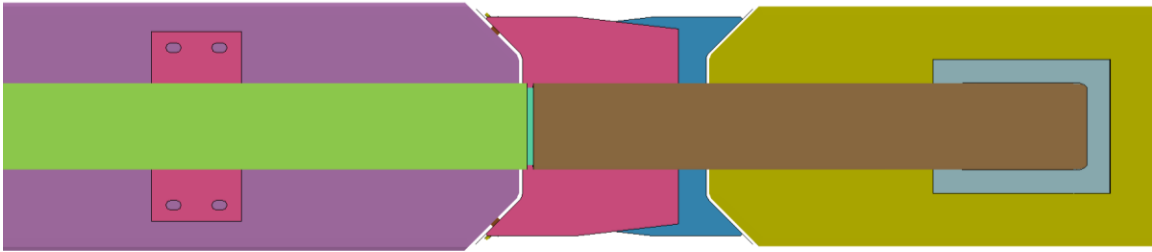


Figure 113. Initial Concept for Lateral Vehicle Snag Prevention

The Yaris and the Silverado model impacts were evaluated to determine if there would be any vehicle snag within the transition region. During the simulation with the Yaris model, the left fender penetrated between the vertical gusset plates, and the left-front tire underrode the transition hardware. The left-front tire had approximately $1\frac{3}{4}$ in. (44 mm) of lateral snag on the lower buttress wall. The snag on the lower buttress caused the Yaris model to never become parallel to the system. The simulated vehicle exited the system with a negative yaw angle, thus, causing the vehicle to become perpendicular to the barrier with large roll angles. The vehicle snag on the buttress face also caused the Yaris model to have a change in pitch of approximately 8 degrees over 15 msec. The simulation with the Silverado model had issues with negative volumes within the engine compartment due to the left-front fender penetrating between the vertical gusset plates, thus causing vehicle snag on the upstream concrete buttress face. Therefore, a cover plate was implemented in the model in order to resolve the vehicular snag issues.

The cover plate was modeled using $1/16$ -in. (2-mm) thick shell elements with a rigid material formulation. The shell cover plate was then attached to the longitudinal

sides of the gusset plates using merged nodes, as shown in Figure 114. When modeling the cover plate in this manner, a rigid connection was created between the RESTORE barrier and the rigid concrete buttress. However, this configuration and approach would provide insight into the potential benefits for using a cover plate to reduce vehicle snag at this location.

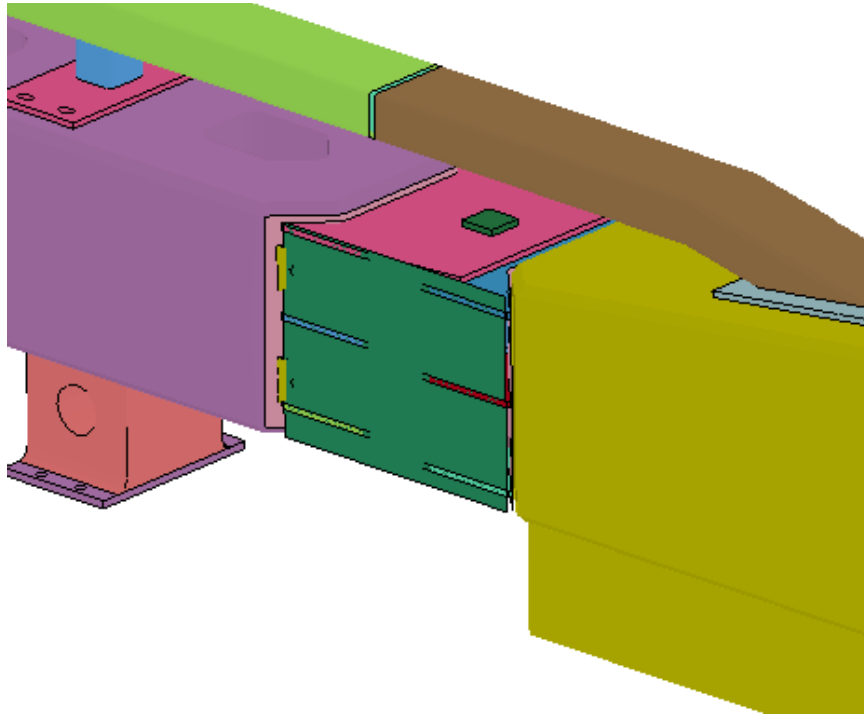


Figure 114. Initial Cover Plate Concept

10.3.1 Initial Cover Plate – 1100C Yaris

The left fender and left-front tire of the Yaris model snagged on the rigid concrete buttress during the impact without the cover plate. The snag caused the Yaris model to exhibit a maximum roll angle of 33.7 degrees between 50 and 100 msec after impact, as shown in Figure 115. After the addition of the cover plate, the roll angle decreased by 279 percent at approximately 90 msec. Further, vehicle snag was shown through the comparison of vehicle pitch angles, as shown in Figure 116. Without a cover plate and

where the left-front tire had contacted the upstream face of the buttress, the maximum pitch angles exceeded 10 degrees. With the cover plate included, the pitch angles remained below 5 degrees, as shown in Figure 117. Lastly, the Yaris model had yaw angles in the opposite direction during the impact without the cover plate, which did not allow the Yaris model to become parallel to the system. The Yaris model with the cover plate continued to yaw in the same direction, becoming parallel after exiting the system. The Yaris model exited the system at approximately 150 msec and continued to gradually yaw. This vehicle behavior can also be seen in the sequential photographs provided in Figure 118.

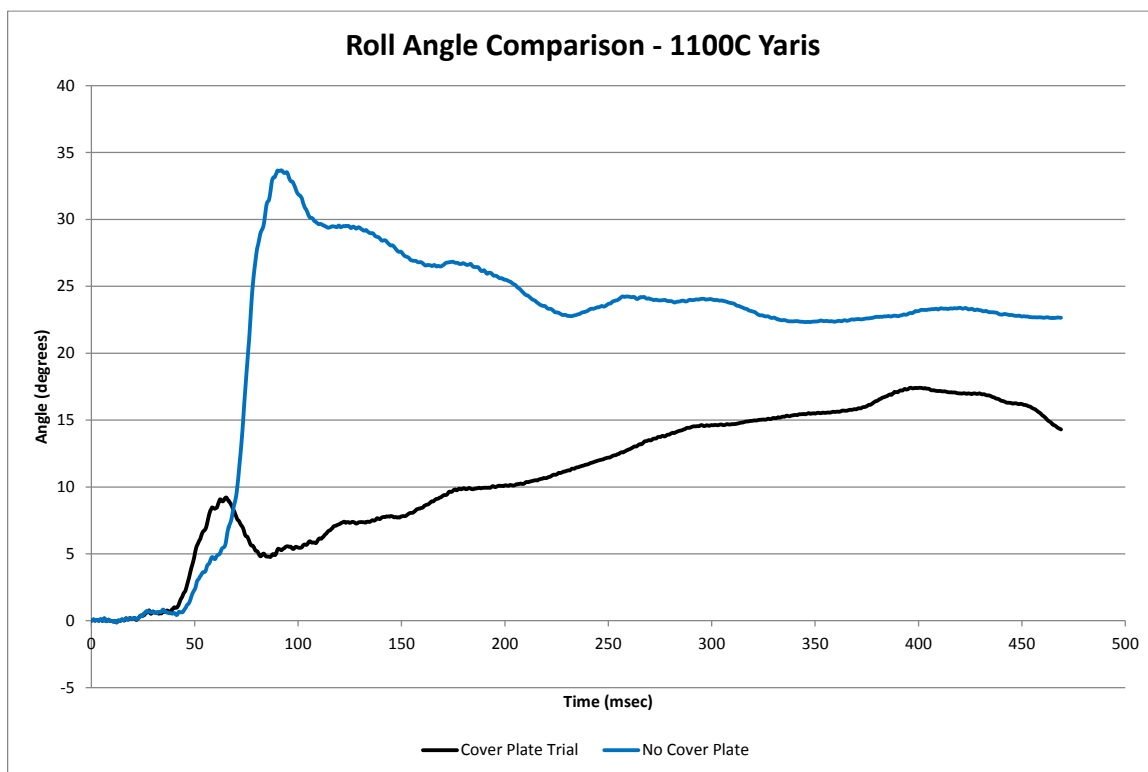


Figure 115. Roll Angle Comparison, With and Without Cover Plate, 1100C Yaris

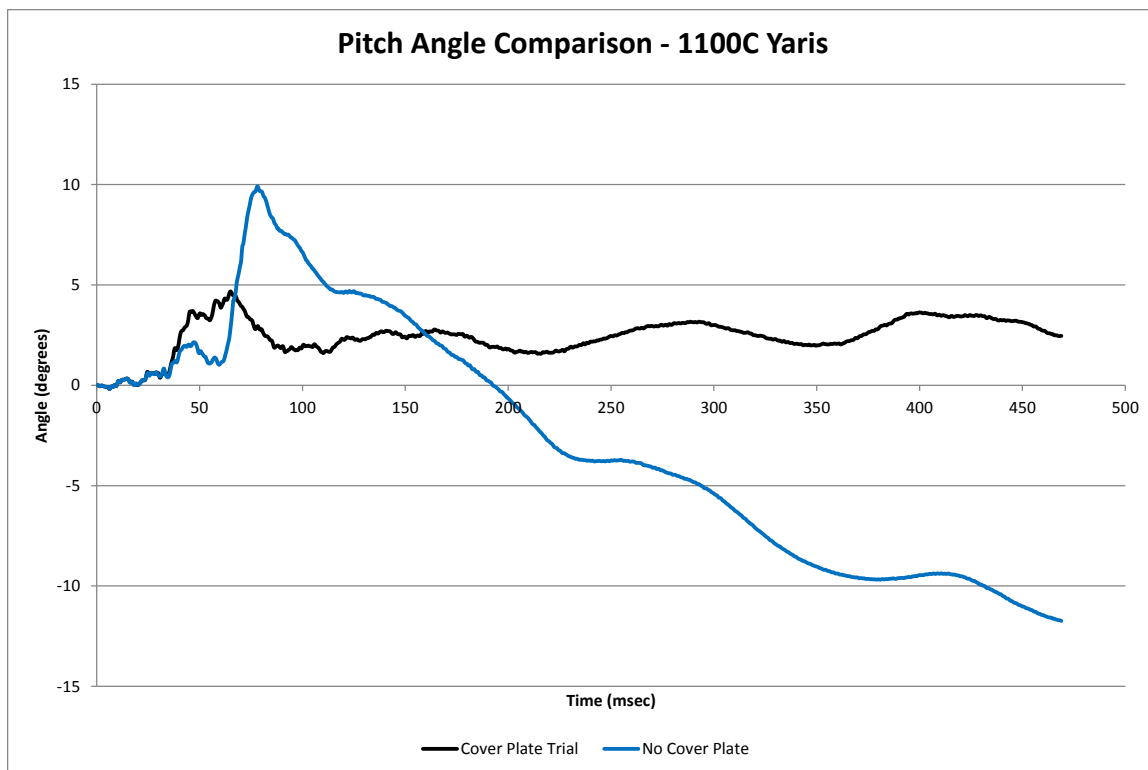


Figure 116. Pitch Angle Comparison, With and Without Cover Plate, 1100C Yaris

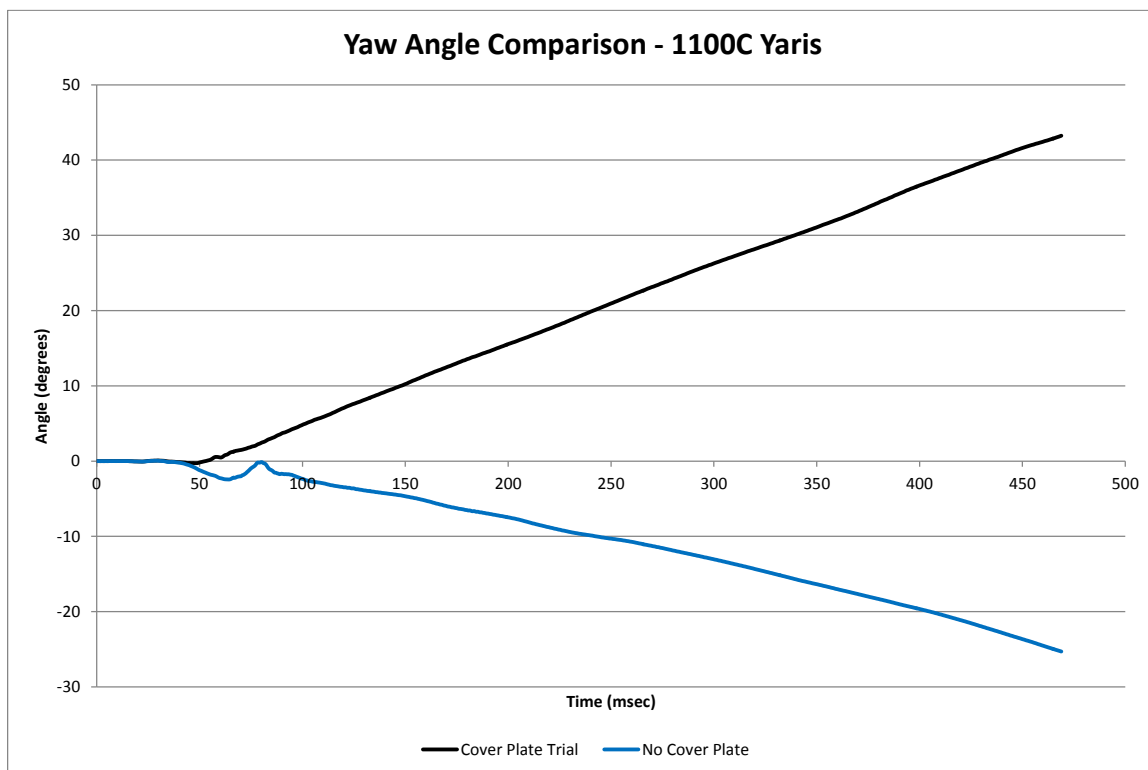


Figure 117. Yaw Angle Comparison, With and Without Cover Plate, 1100C Yaris

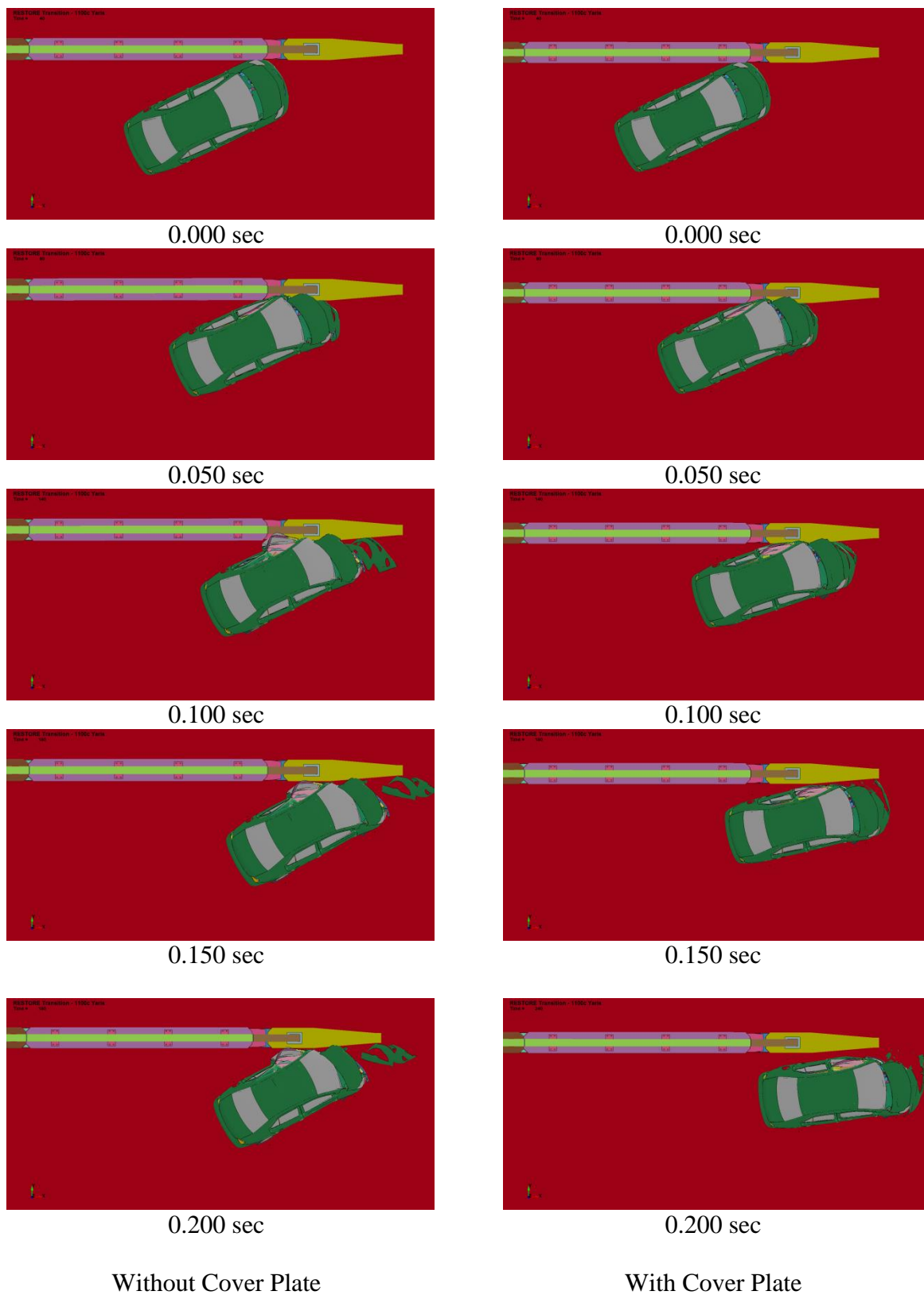


Figure 118. 1100C Yaris Simulation, Cover Plate Comparison, Sequential Photographs

The lateral change in velocity for the impacts with the Yaris vehicle model with and without a cover plate matched through approximately 400 msec after impact, as shown in Figure 119. However, the longitudinal change in velocity for the simulation without the cover plate was approximately 40 percent greater than observed during the simulation with the cover plate, as shown in Figure 120. Therefore, the cover plate was beneficial as it reduced vehicle snag in the transition region.

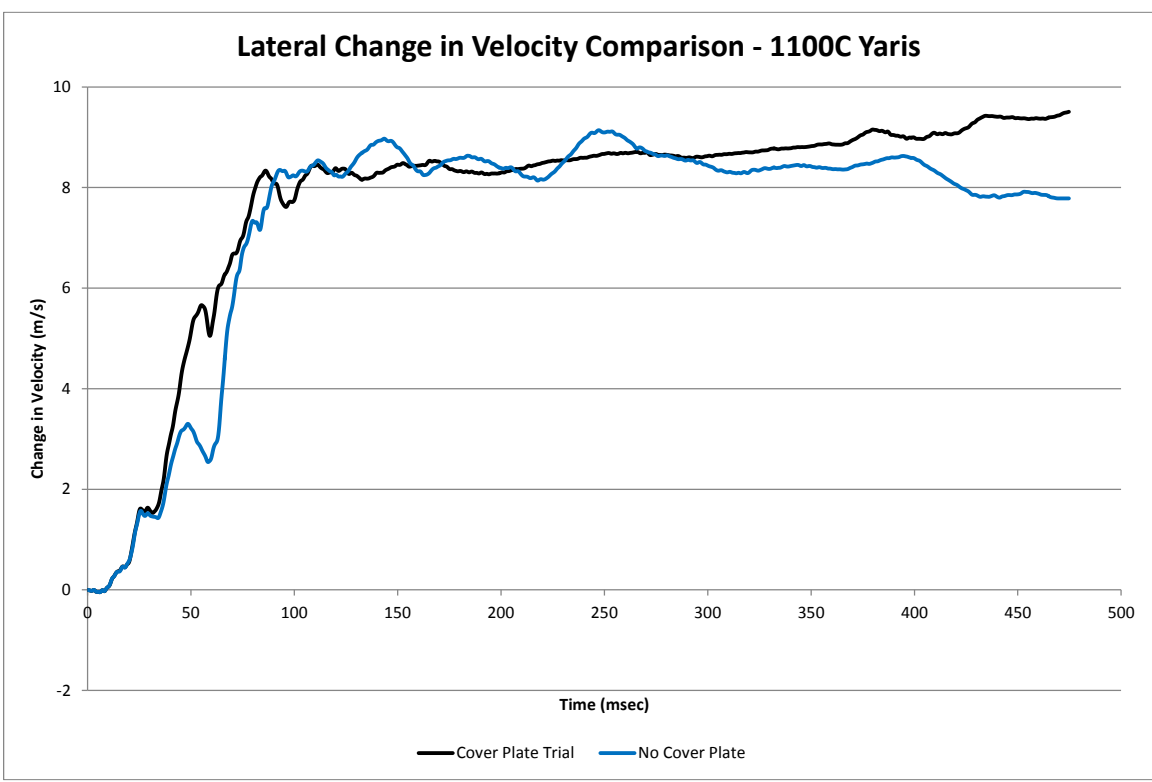


Figure 119. Lateral Change in Velocity Comparison, With and Without Cover Plate Trials, 1100C Yaris

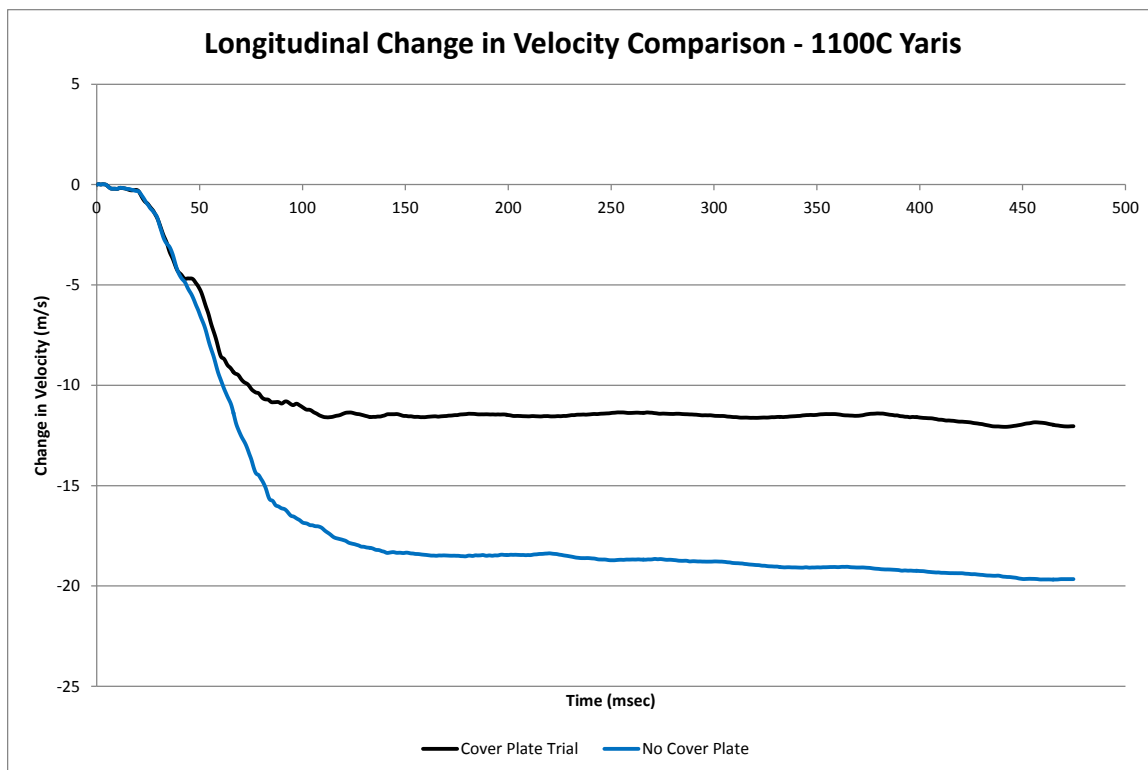


Figure 120. Longitudinal Change in Velocity Comparison, With and Without Cover Plate Trials, 1100C Yaris

10.3.2 Initial Cover Plate – 2270P Silverado

The Silverado vehicle model's left-front fender snagged on the rigid concrete buttress during the impact event without the cover plate. The vehicle snag through simulation caused negative volumes within the engine compartment, thus causing the simulation to stop running after approximately 100 msec. However, when the cover plate was implemented, the roll, pitch, and yaw behavior with and without a cover plate were similar through 100 msec, as shown in Figures 121 through 123.

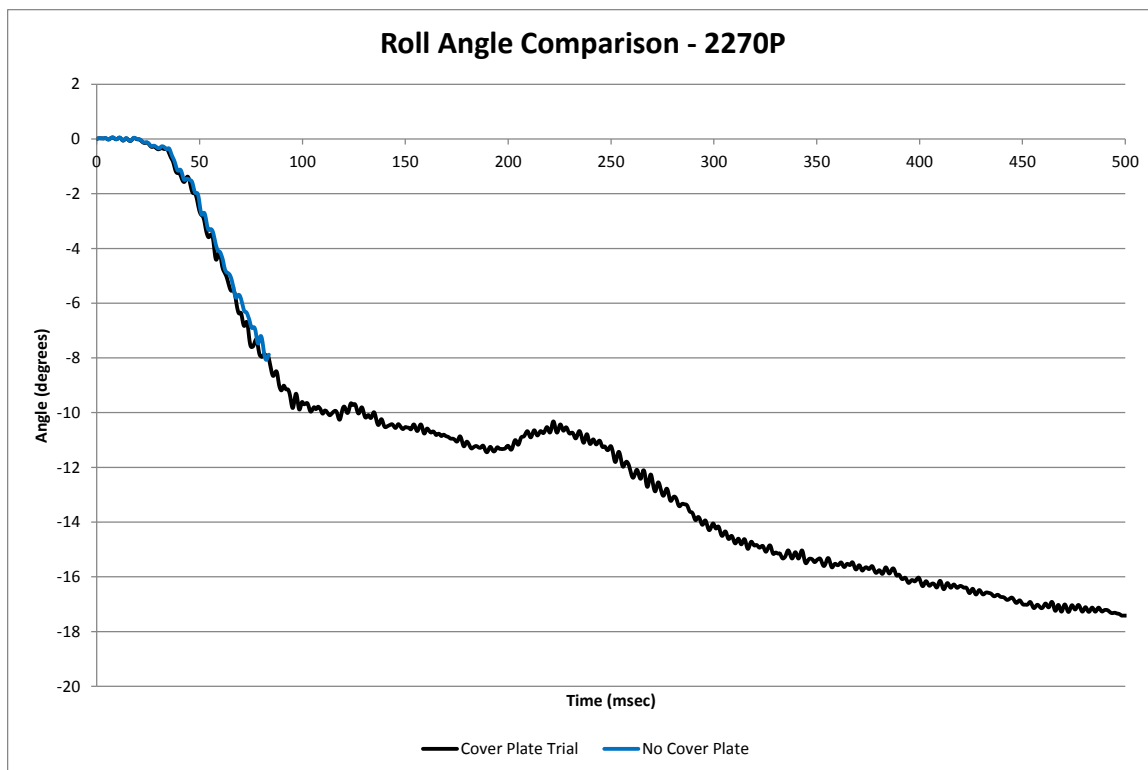


Figure 121. Roll Angle Comparison, With and Without Cover Plate, 2270P

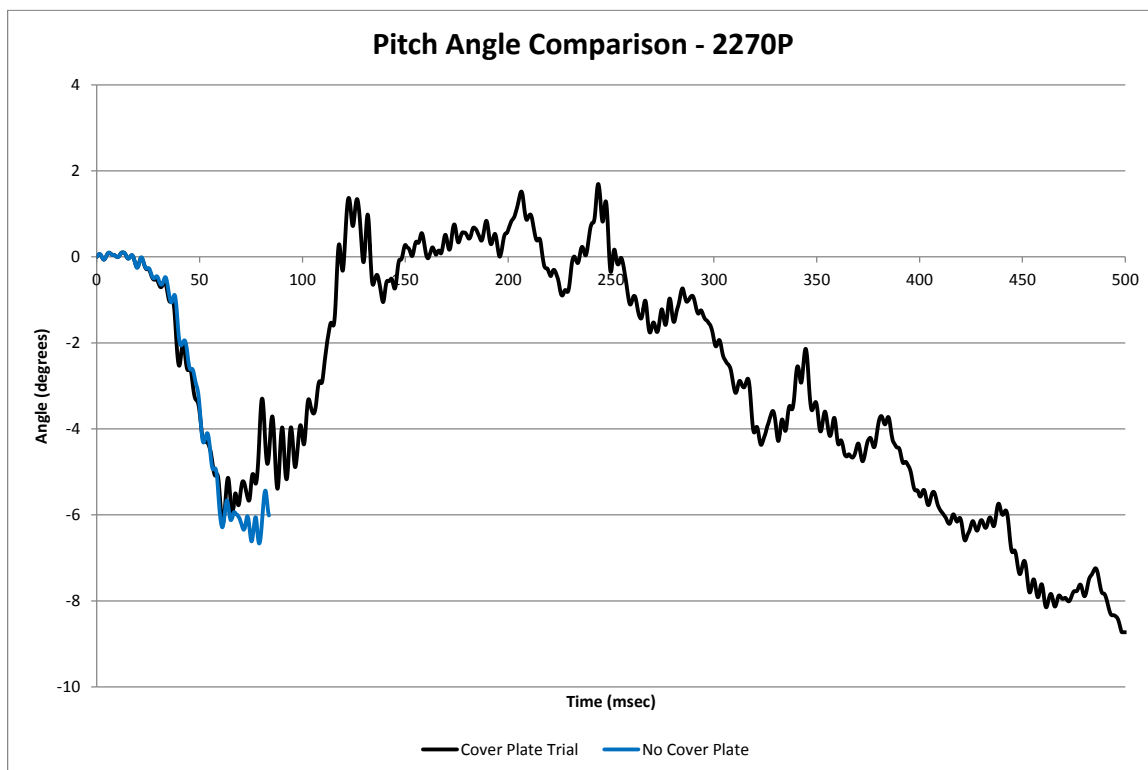


Figure 122. Pitch Angle Comparison, With and Without Cover Plate, 2270P

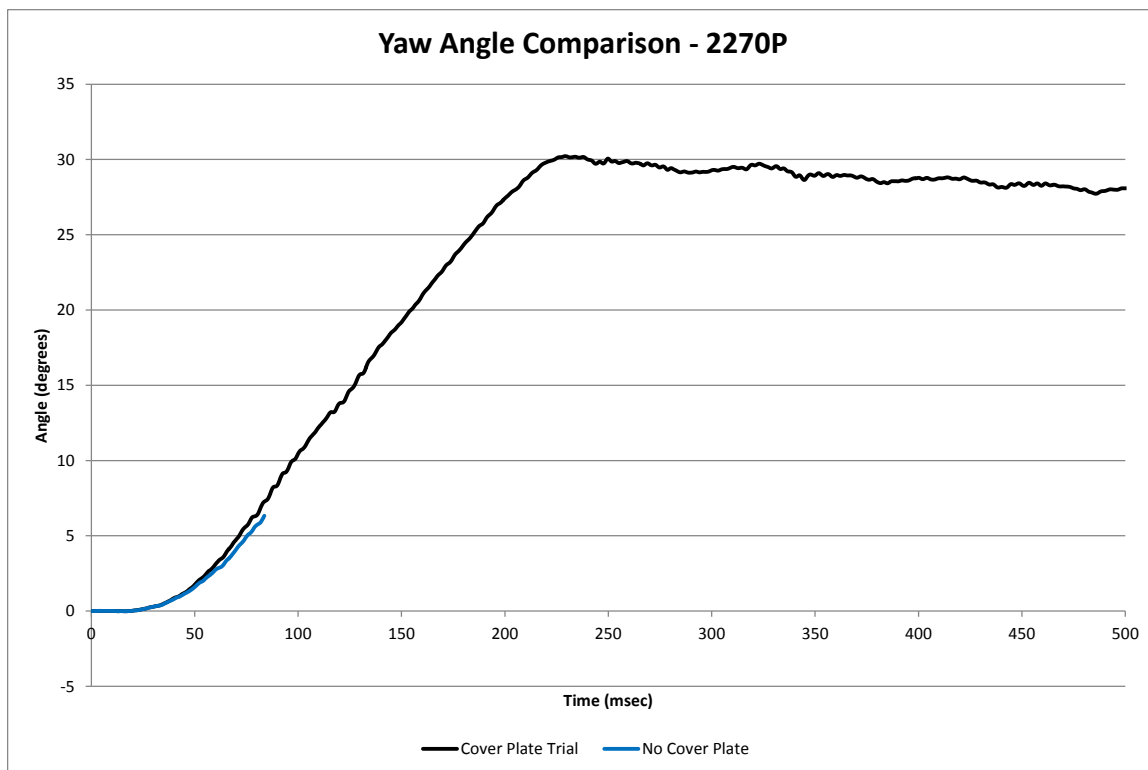


Figure 123. Yaw Angle Comparison, With and Without Cover Plate, 2270P

The lateral change in velocity for the Silverado impact event with and without a cover plate matched through 100 msec, as shown in Figure 124. However, the longitudinal change in velocity for the simulation without the cover plate increased significantly more than observed with the simulation pertaining to the cover plate option, actually around 60 msec, as shown in Figure 125. Therefore, the cover plate was deemed to be beneficial as it reduced vehicle snag within the transition region.

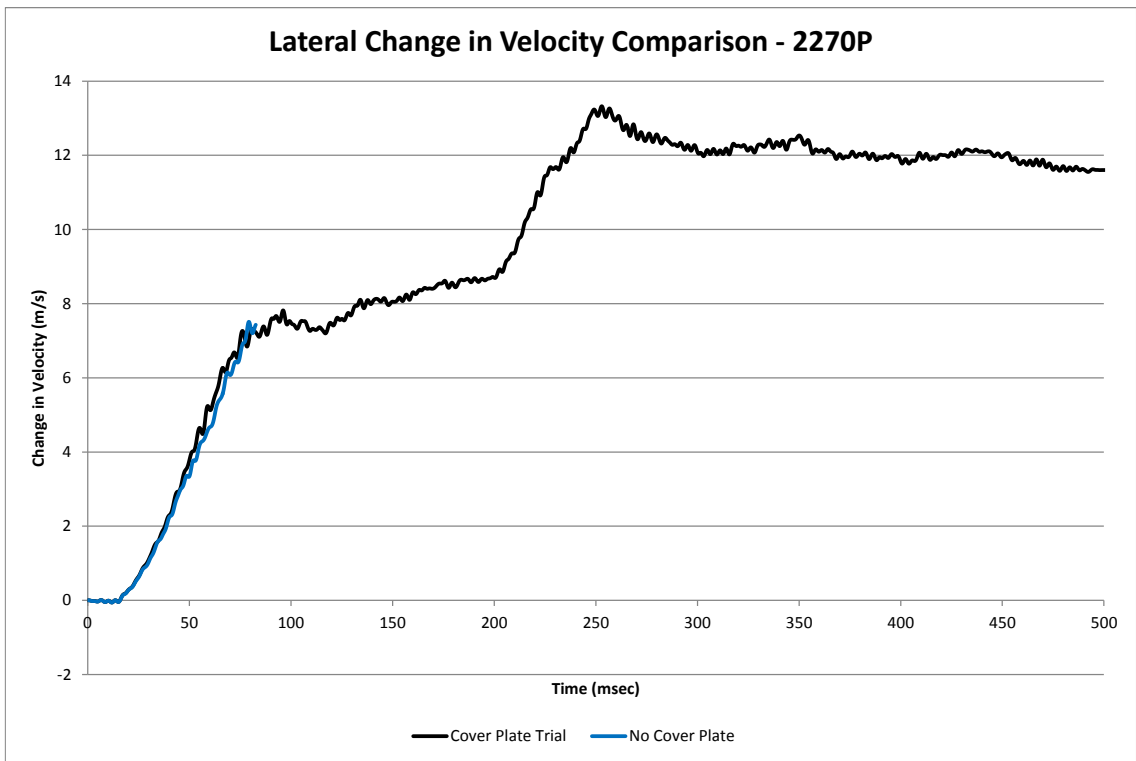


Figure 124. Lateral Change in Velocity Comparison, With and Without Cover Plate Trials, 2270P

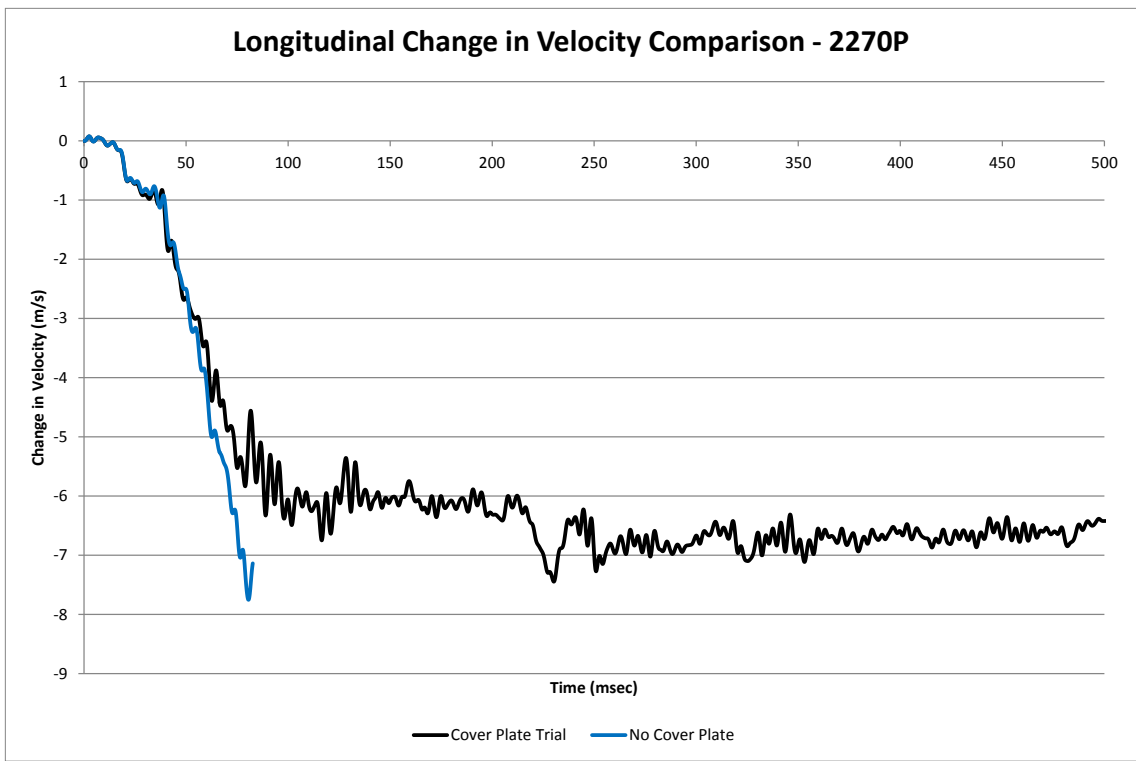


Figure 125. Longitudinal Change in Velocity Comparison, With and Without Cover Plate Trials, 2270P

10.3.3 Recommendations and Changes

The gusset plate configuration without a cover plate exhibited passenger vehicle snag on the rigid concrete buttress in the simulations. The longitudinal velocity decreased 40 percent quicker without a cover plate with the Yaris model, which indicated that significant vehicle snag had occurred. The Silverado vehicle model's longitudinal velocity also decreased quicker without a cover plate, and the vehicle model became unstable. However, the negative volumes were resolved when a cover plate shielded the vertical opening between the gusset plates. Therefore, the cover plate concept greatly improved vehicle behavior during impacts near the transition region. Thus, the cover plate and gusset plate assembly is recommended for further evaluation.

10.4 Cover Plate Design

10.4.1 Design Calculations

The cover plate was desired to be a simple piece that could be used on either side of the transition joint, thus not requiring different pieces for each side. The cover plate should extend to the height of the back plate and minimize the gap between the edge of the cover plate and the RESTORE barrier or buttress when the joint is fully compressed. The cover plate hardware incorporated three horizontal gusset plates. The top gusset plate prevented the cover plate from translating upward, while the bottom two gusset plates prevented downward translation, as shown in Figure 126.

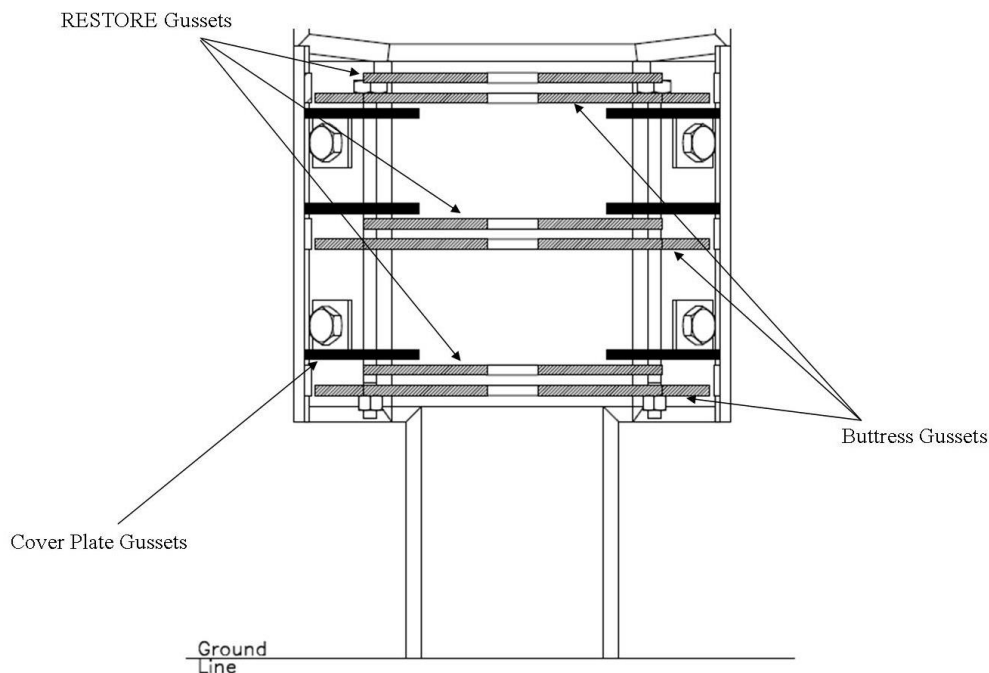


Figure 126. Cover Plate Gusset Locations

The cover plate needed to prevent vehicle snag on the upstream buttress face and accommodate the desired $\pm 1\frac{1}{2}$ in. (38 mm) construction tolerances. Therefore, the outer overall dimensions of the cover plate were 20 in. x $18\frac{1}{2}$ in. (508 mm x 470 mm). In order to determine the thickness of the cover plate, an approximate analysis was completed using a concept published by Roark and Young [87] to calculate the bending stress of a flat plate with straight boundaries and constant thickness, as shown in Equation 47 and Figure 127.

$$\sigma = \frac{\beta W}{t^2} \quad (47)$$

Where: σ = Maximum stress of plate, ksi (GPa)

β = Coefficient determined from Figure 127

t = Thickness of plate, in. (mm)

a_1 = Longer width of rectangular load applied, in. (mm)

b_1 = Shorter width of rectangular load applied, in. (mm)

$W = qa_1b_1 = 50 \text{ kip (222 kN)}$

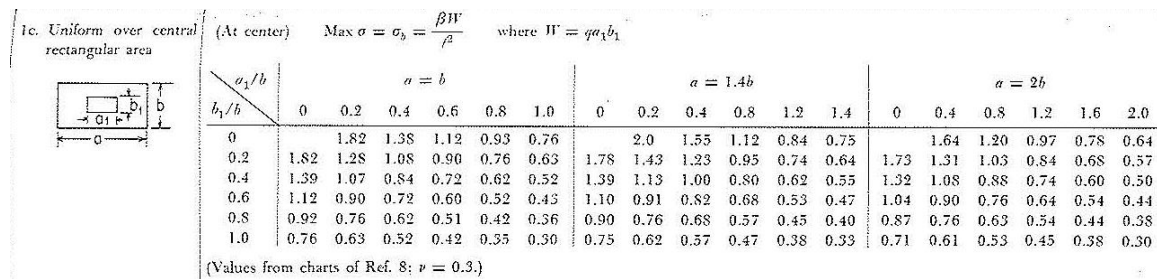


Figure 127. β Coefficient for Stress on Flat Plate

The governing dimensions of the unsupported area to determine the coefficient β were 20 in. (508 mm) long (a) and $6^{11}/16$ in. (170 mm) tall (b). The size of a single-unit truck bumper is approximately 12 in. (305 mm) tall. Therefore the rectangular area where the load was applied to the cover plate was assumed to be 12 in. x 6 in. (305 mm x 152 mm). Note that load application area may vary. The design load through the analysis process was a 100-kip (445-kN) lateral load applied at the top of the RESTORE barrier. However, the governing unsupported area was located at the bottom half of the RESTORE barrier, so a design load of 50 kips (222) was selected for use. The cover plate was designed with a steel material yield strength of 50 ksi (344 GPa). Poisson's ratio was considered to be 0.3. Therefore, using Equation 47 with a determined β coefficient of 0.44 shown in Figure 127, the approximate thickness of the plate was determined to be $5/8$ in. (16 mm). Due to the assumptions made, a more aggressive thickness of $1/2$ in. (13 mm) was considered for evaluation through simulation.

To determine the thickness of the cover plate gussets, welds, and bolt sizes, similar processes as described in Sections 0, 8.3.5, and 8.3.7 were used. Two bolts were desired to hold each cover plate, with one bolt extending through the RESTORE gussets and one bolt extending through the buttress gussets. The bolt size that would hold the cover plate and cover plate gussets in place was determined from using a 100-kip (445-

kN) design load and Equations 24 and 25. The total area needed to withstand a 100-kip (445-kN) shear load was 1.52 in.^2 (981 mm^2). The bolts should experience minimal tensile load, so it was not considered in the determination of the bolt diameter. Due to each side having three gussets, the total area could be divided across the six shear planes for a diameter of $\frac{5}{8} \text{ in.}$ (16 mm) using A325 hex bolts with a yield stress of 92 ksi (634 GPa). Therefore, a bolt diameter of $\frac{5}{8} \text{ in.}$ (16 mm) was used to restrain the cover plates. A hole diameter of $\frac{3}{4} \text{ in.}$ (19 mm) was selected for the cover plate bolts.

The cover plate was assumed to act as a rigid plate, which would distribute the 100-kip (445-kN) design load evenly over the three cover plate gussets, resulting in a design load of 33.3 kips (148 kN). The required gusset thickness using the bearing strength equation, as shown previously in Equation 30, was $\frac{1}{2} \text{ in.}$ (13 mm) using ASTM A572 steel plate. Thus, the block shear was evaluated using Equation 32. Based on the loading scenario, the most likely block shear occurrence would be in the longitudinal direction. With $\frac{1}{2}$ -in. (13-mm) thick steel plate, the required lateral distance between the hole and the edge of the plate was $1\frac{3}{4} \text{ in.}$ (44 mm), and the required longitudinal distance between the hole and the edge of the plate was $2\frac{1}{4} \text{ in.}$ (57 mm). The width of the gusset plate was chosen to be $18\frac{3}{4} \text{ in.}$ (476 mm) to allow for clear space on each side between the edge of the gusset and the edge of the cover plate.

The range of leg lengths that were considered in the determination of the weld sizes was between $\frac{3}{16}$ and $\frac{5}{16} \text{ in.}$ (5 and 8 mm) based on the thickness of the material. From calculations using Equations 36 through 42 and considering the bending stress equal to zero due to the design of the cover plate bearing on the barrier gussets before

bending could occur in the cover plate gussets, the required weld size was $3/16$ in. (5 mm). The modifications to the drawing set can be found in Appendix J.

10.4.2 Straight Cover Plate Model

The straight cover plate that was added to the transition model incorporated coped corners to mitigate vehicle snag. The cover plate parts are shown in Figure 128, and the parts, element types, and material models are shown in Table 33.

The cover plate gussets and the cover plate bolts (part nos. 9501 and 9502) used fully-integrated, type 2 solid element formulations. The bolts were simplified to have a cylindrical tube represent the bolts with a solid cylindrical head on the top and the bottom, simulating the bolt head and washer. The head and washer were not modeled discretely; since, the purpose of the bolts was only to hold the cover plate in place. Two bolts (part no. 9502) held the cover plates and cover plate gussets in place, and were extended vertically through either the RESTORE gussets or the buttress gussets. The cover plate (part no. 9500) used $1/2$ -in. (13-mm) thick, type 2 shell elements. The gussets nodes were merged with the cover plate to simulate a welded connection. The cover plate and cover plate gussets (part nos. 9500 and 9501) were simulated using a yield strength of 62 ksi (427 MPa). The cover plate bolts (part no. 9502) were simulated with a yield strength of 105 ksi (724 MPa) which was scaled up from Grade B bolt properties.

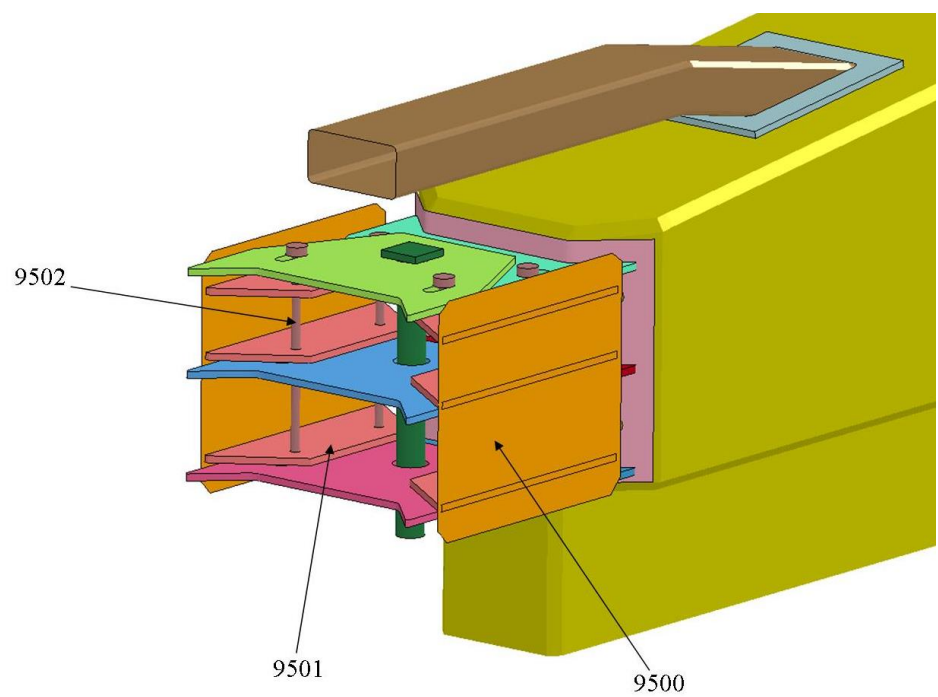


Figure 128. Simulation Part Numbers – Straight Cover Plate

Table 33. Barrier Model Parts, Elements, and Materials – Straight Cover Plate

Part Description	Drawing Reference No.	Simulation Part No.	Element Type	Element Thickness, in. (mm)	Material
Cover Plate	a9	9500	Type 2 Shell	1/2 (13)	*MAT_PIECEWISE_LINEAR_PLASTICITY
Cover Plate Gusset	a11	9501	Type 2 Solid	NA	*MAT_PIECEWISE_LINEAR_PLASTICITY
Cover Plate Bolts	b12	9502	Type 2 Solid	NA	*MAT_PIECEWISE_LINEAR_PLASTICITY

10.4.3 Straight Cover Plate Simulations

Further simulations were run with the straight cover plate added to the joint when both extended and compressed in order to evaluate the extents of the construction tolerances, as shown in Figure 129. During the initial simulations, the Yaris vehicle model impacted the system 3 ft – 7 in. (1.1 m) upstream from the upstream buttress face with the extended joint. This position was denoted as the critical impact point for rigid buttresses in MASH based on the concern for snag with small cars. The simulation results

with the Yaris model successfully contained and redirected the vehicle during the impact event with the straight cover plate. However, during the impact with the extended joint, the left-front fender of the Yaris model had approximately 2 in. (51 mm) of snag on the upstream edge of the cover plate, as shown in Figure 130. Note that the RESTORE barrier, buttress, and back plate were removed in order to clearly see the snag on the upstream side. The fender snag in the model indicated that it may occur in full-scale crash testing on the upstream side and either allow occupant compartment intrusions or vehicle instability.

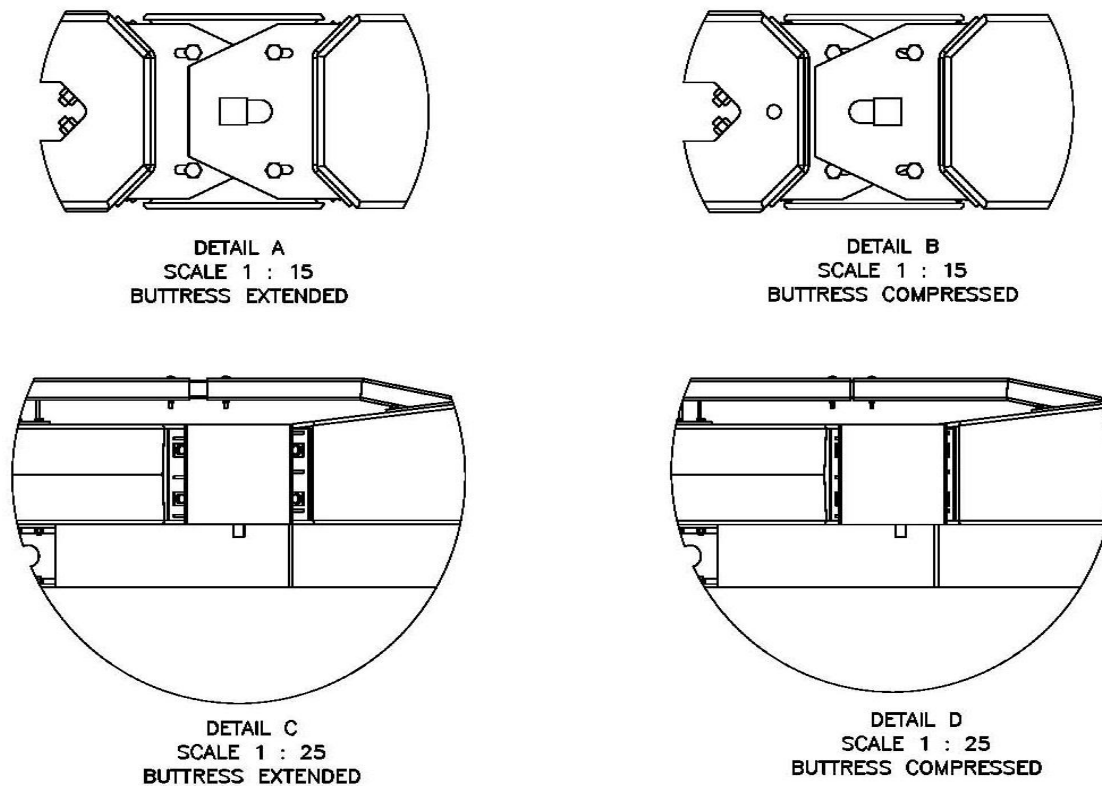


Figure 129. Compressed and Extended Joint Views, Straight Cover Plate

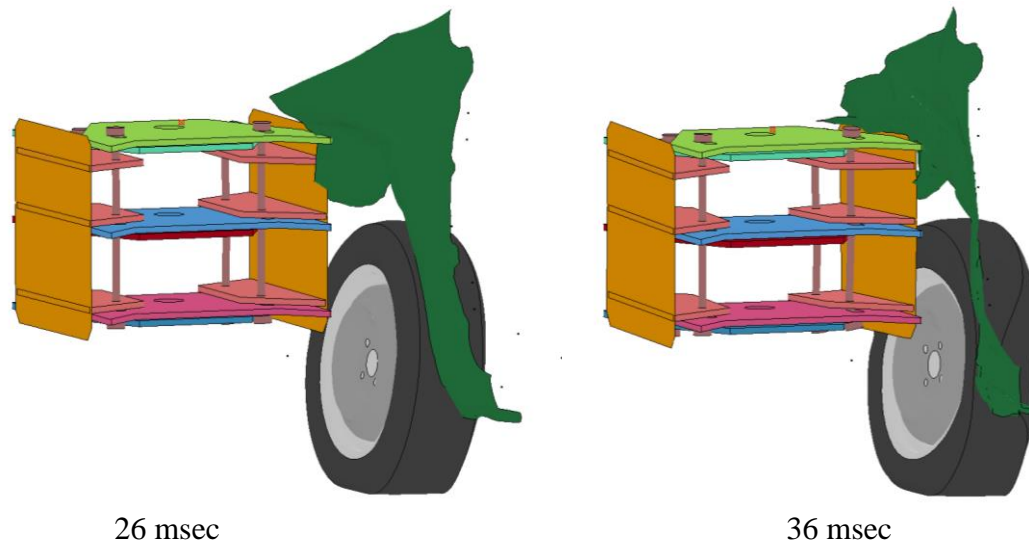


Figure 130. 1100C Yaris Model Snag on Upstream End of Straight Cover Plate

Similarly, the Silverado vehicle model impacted the system 4 ft – 3 in. (1.3 m) upstream from the pin with the extended joint, as denoted as the critical impact point in MASH for rigid buttress impacts with other passenger vehicles. The left-front door of the Silverado model snagged approximately ½ in. (13 mm) on the upstream top corner of the cover plate, as shown in Figure 131. The sheet metal on the Silverado model did not have failure enabled. However, the snag started to excessively deform the cover plate at 76 msec, causing the cover plate bolts to produce negative volumes. The snag on the upstream side of the cover plate excessively deformed the plate and the bolts restraining the cover plate, which was not desired. Therefore, further evaluation was warranted to prevent snag with passenger vehicles.

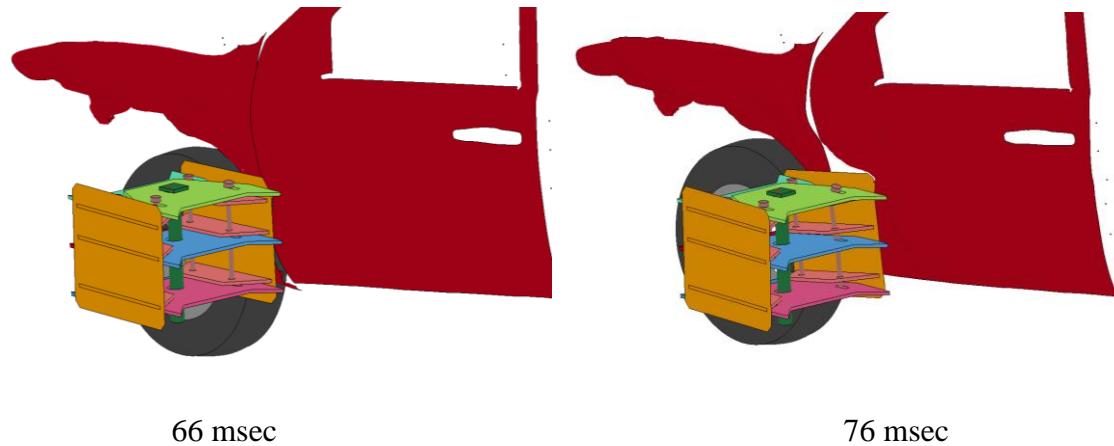


Figure 131. 2270P Silverado Model Snag on Upstream End of Straight Cover Plate

10.4.4 Rounded Cover Plate Model

Multiple options were considered to reduce the amount of snag on the cover plate. The options included translating the cover plates farther back from the RESTORE barrier and buttress faces, thus minimizing the gap between the RESTORE barrier and buttress and the cover plate, and rounding/tapering the edges of the cover plate. Setting the cover plate farther back was not recommended as it could provide additional vehicle snag on the rigid concrete buttress. The gap between the barriers and the cover plate was already minimized while still allowing for the construction tolerances. Therefore, the rounded edges on the cover plate were recommended for further evaluation. The rounded cover plate simulation results are presented in the subsequent chapters. The drawing set for the rounded cover plate is shown in Appendix K.

Due to rounding the corners of the cover plate, the lateral width of the RESTORE gussets and buttress gussets had to be minimized to allow for the face of the cover plate to not exceed the faces of the RESTORE barrier and buttress. Thus, a larger gap between the cover plate and the gussets led to the cover plate bolts to withstand some of the lateral

impact force during an impact event. Therefore, longitudinal metal strips were welded on the backside of the cover plate at the locations of the RESTORE barrier and buttress gussets to allow bearing between the cover plate and the gussets during impacts and to prevent the vertical bolts from being loaded.

The rounded cover plate parts are shown in Figure 132, and the parts, element types, and material models are shown in Table 34. The cover plate, cover plate gussets, and cover plate bolts (part nos. 9500 through 9502) remained the same from the straight cover plate model. Similarly, the cover plate gusset nodes were merged with the cover plate. The cover plate strips were added to ensure that the plate would bear on the transition gussets and not excessively load the cover plate bolts; since, the bolts were designed to restrain the cover plate and not take much of the impact load. The cover plate strips (part no. 9503) used fully-integrated type 2 solid elements. The cover plate strip nodes were merged with the cover plate to simulate a welded connection. The cover plate strips (part no. 9503) were simulated using actual yield strength of 62 ksi (427 MPa). Failure was not enabled for any of the parts within the pin and gusset configuration due to not being able to accurately depict when failure may occur based on the different loading conditions and stress states present during a full-scale impact simulation.

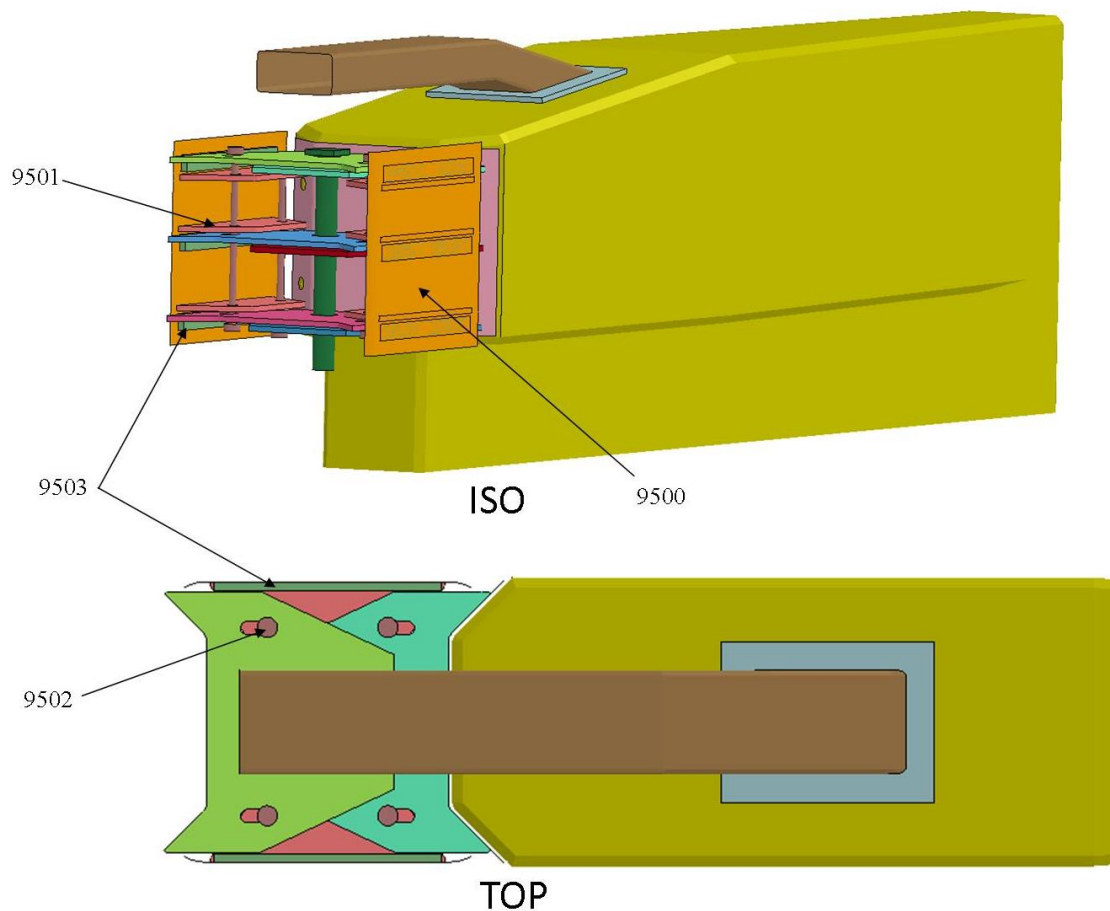


Figure 132. Simulation Part Numbers – Rounded Cover Plate

Table 34. Barrier Model Parts, Elements, and Materials – Rounded Cover Plate

Part Description	Drawing Reference No.	Simulation Part No.	Element Type	Element Thickness, in. (mm)	Material
Cover Plate	a9	9500	Type 2 Shell	1/2 (13)	*MAT_PIECEWISE_LINEAR_PLASTICITY
Cover Plate Gusset	a11	9501	Type 2 Solid	NA	*MAT_PIECEWISE_LINEAR_PLASTICITY
Cover Plate Bolts	b12	9502	Type 2 Solid	NA	*MAT_PIECEWISE_LINEAR_PLASTICITY
Cover Plate Strips	a10	9503	Type 2 Solid	NA	*MAT_PIECEWISE_LINEAR_PLASTICITY

10.5 Epoxy Anchorage Modeling

During the initial simulations with the various cover plate concepts, the back plate on the buttress side did not exhibit the anticipated stresses. The *CONSTRAINED_EXTRA_NODES connection between the back plate bolt hole nodes and buttress restrained the back plate from deformation. Thus, a bolted connection similar to the actual design was incorporated into the model. The buttress was modified to have bolt holes extend from the face into the rigid concrete barrier, as shown in Figure 133. This modification was possible due to the buttress being modeled with rigid shell elements, thus the interior was hollow. The same through bolts from the RESTORE barrier ACJ connection were placed through the bolt holes in the buttress. The washer located on the inside of the hollowed buttress had a rigid material definition and was constrained in all directions within the *MAT_RIGID card to simulate the anchorage. The same bolt prestressing that was used throughout the RESTORE barrier was utilized with the anchorage bolts as well. The stresses in the back plate before and after implementing the simulated anchor bolts are shown in Figure 134.



a. Before Simulated Anchors



b. After Simulated Anchors

Figure 133. Before and After Photographs of Simulated Epoxy Anchors in Buttress

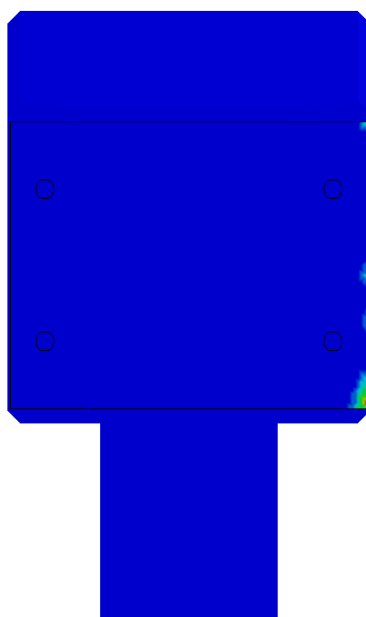
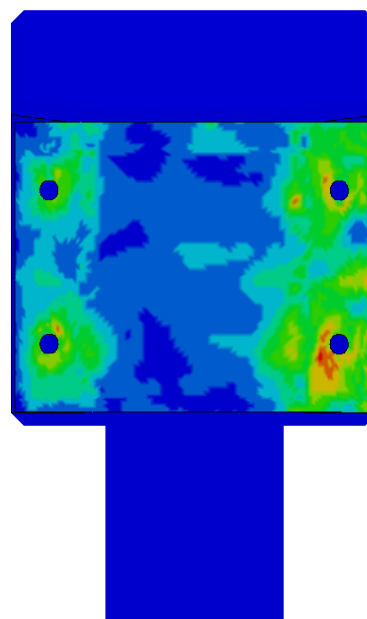
100 msec
Before Simulated Anchors100 msec
After Simulated Anchors

Figure 134. Von Mises Stresses, Before and After Simulated Epoxy Anchors, 100 msec

11 CIP DETERMINATION – MODELING TEST DESIGNATION NO. 4-20

11.1 Purpose

In lieu of full-scale crash testing, further computer simulation was utilized to evaluate the transition design according to the MASH safety performance criteria for test designation no. 4-20. The vehicle models impacted at a speed of 62.1 mph (100 km/h) and an angle of 25 degrees, as recommended by MASH. Several impact points were evaluated to determine vehicle and barrier performance. Therefore, the proposed transition incorporating the curved cover plate, as determined from the research explained in Chapter 10 and shown in Appendix K, was evaluated with LS-DYNA.

Multiple impact points were considered upstream from the buttress end and in the reverse direction, as shown in Figure 135. Two barrier configurations were considered due to the +/- 1½ in. (38 mm) construction tolerance: the joint fully extended and the joint fully compressed. MASH states that computer simulation with LS-DYNA should be performed to evaluate the CIPs when practical and accessible. However, if computer simulation is unavailable, the CIP for a stiffness transition should be either 3 ft – 7 in. (1.1 m) upstream from the location with the greatest potential for wheel snag (i.e., upstream end of buttress) or 3 ft – 7 in. (1.1 m) upstream from the location with the potential for the largest load (i.e., drop-down pin) or deflection (i.e., upstream locations) for test designation no. 4-20. The largest load is expected to occur at an impact point near the pin and gusset plate assemblies due to the constraint in the lateral y-direction. However, impact locations farther upstream would need to be evaluated to determine the location of the maximum barrier deflection and/or flare rate. To accommodate all of the CIP possibilities, computer simulation was used to consider the suggested CIP locations

in MASH as well as upstream impact locations to determine the worse-case vehicle and/or barrier performance. Each suggested CIP impact location in MASH was simulated with the Dodge Neon and Toyota Yaris vehicle models when the joint was fully extended and when the joint was fully compressed, as shown in Figure 136.

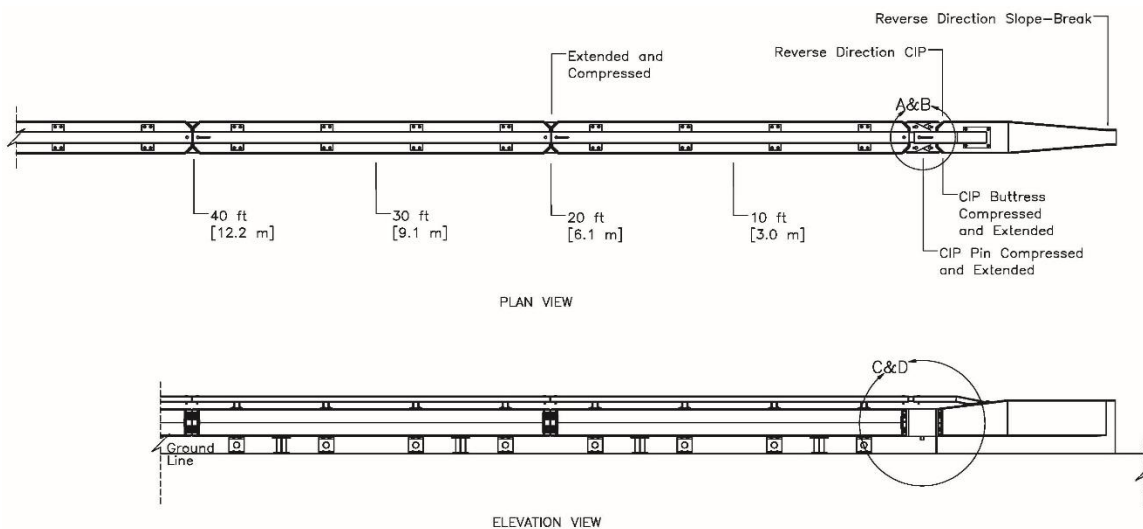


Figure 135. RESTORE Barrier Transition Impact Locations for Simulations

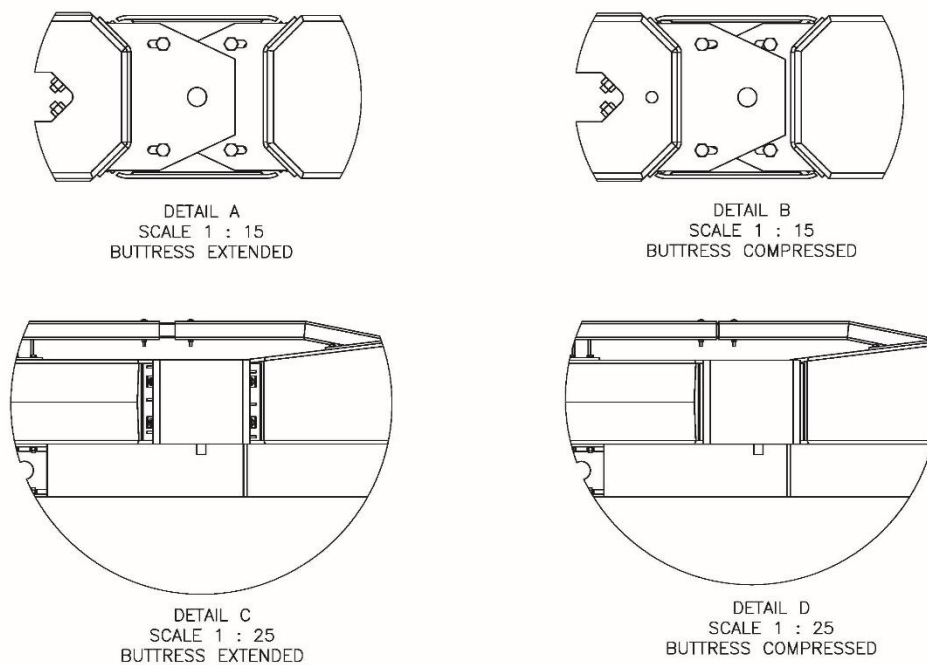


Figure 136. Compressed and Extended Joint Views

Impact locations farther upstream from the pin were simulated at intervals of 10 ft (3.0 m) and up to 40 ft (12.2 m) away from the pin. Each impact location was simulated 3 ft – 7 in. (1.1 m) upstream from the four locations positioned at 10 ft (3.0 m) intervals, as shown in Figure 135 and with the joint fully extended. However, at the location 20 ft (6.1 m) upstream from the pin, the compressed joint was also investigated to determine if restricted joint movement affected the results.

Lastly, the reverse-direction simulations evaluated performance at impact locations directly at the slope-break point of the buttress on the downstream end with a horizontal flare rate of 6:1. A horizontal flare rate of 6:1 over the full barrier height has not been previously crash tested under the MASH safety performance criteria. The impact location 3 ft – 7 in. (1.1 m) upstream from the upstream corner of the cover plate was evaluated in the reverse direction with the joint fully extended to evaluate the potential for snag behind the cover plate.

The most commonly-used yield criterion is the von Mises yield criterion. The von Mises criterion utilized a formulation in which the yield strength is the same in both tension and compression. The Tresca criterion, or maximum shear-stress criterion, states that yielding begins when the maximum shear stress at a point equals the maximum shear stress at yield in uniaxial tension or compression. It should be noted that the shear stress associated with the von Mises criterion is less conservative than the similar maximum shear stress criterion, noted as the Tresca yield criterion. The Tresca yield criterion is represented by the dashed line forming a hexagon and the von Mises criterion is represented by the solid oval line under a plane stress condition, as shown in Figure 137. The von Mises and Tresca conditions under three-dimensional loading are given by

Equations 48 and 49. Note that the material is believed to be yielded when the von Mises condition exceeds the yield stress of the material, or when the Tresca condition exceeds one-half of the yield stress of the material. The yield strength for the ACJ bolts and cover plate bolts was 105.0 ksi (724 MPa) which was scaled up from Grade B bolt properties, and the yield strength for the top tube, gusset plates, and drop-down pin was 62.4 ksi (430 MPa). The ultimate strength for the ACJ bolts and cover plate bolts was 137.5 ksi (948 MPa) and the ultimate stress for the top tube, gusset plates, and drop-down pin was 101.2 ksi (698 MPa).

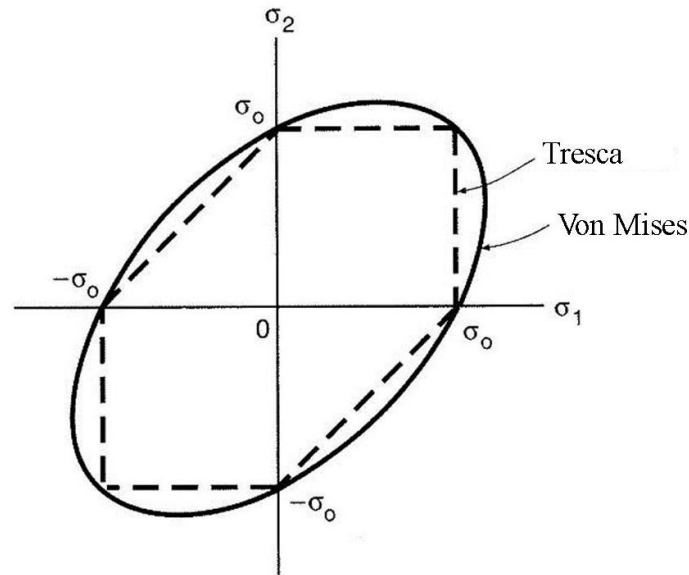


Figure 137. Von Mises and Tresca Failure Surfaces [89]

$$\sigma_{VM} = \frac{1}{\sqrt{2}} \sqrt{(\sigma_1 - \sigma_2)^2 + (\sigma_2 - \sigma_3)^2 + (\sigma_3 - \sigma_1)^2} \geq \sigma_y \quad (48)$$

$$\tau_o = \text{MAX} \left(\frac{|\sigma_1 - \sigma_2|}{2}, \frac{|\sigma_2 - \sigma_3|}{2}, \frac{|\sigma_3 - \sigma_1|}{2} \right) \geq \frac{\sigma_y}{2} \quad (49)$$

Where: σ_{vm} = Von Mises or effective stress yield condition, ksi (MPa)

$\sigma_1, \sigma_2, \sigma_3$ = Principal stresses, ksi (MPa)

τ_o = Tresca shear stress yield condition, ksi (MPa)

σ_v = Yield strength of material, ksi (MPa)

As described in Chapter 4, the Dodge Neon model provided the most reliable results for ORA, OIV, and vehicle stability. The Toyota Yaris provided the most reliable results for vehicle snag, barrier deflections, and lateral impact force. However, all simulation results will be compared for both vehicle models.

11.2 CIP Location Simulation Results

Two reference locations were considered during the simulations of the suggested MASH CIP locations. The first suggested CIP location was 3 ft – 7 in. (1.1 m) upstream from the location with the greatest potential for wheel snag (i.e., upstream end of buttress), while the second CIP location was 3 ft – 7 in. (1.1 m) upstream from the location with the potential for largest load (i.e., pin). During the rounded cover plate implementation, the initial design had interference between the cover plate and the washers on the bolts when fully-compressed. Therefore, the joint was ½ in. (13 mm) extended from the fully compressed configuration during the CIP simulations. However, the details are correct in the drawing set in Appendix K.

11.2.1 Yaris Vehicle Model

The comparison of results for the Yaris vehicle model between the simulations at the suggested MASH CIP locations is shown in Table 35. The simulations at each impact point successfully contained and redirected the Yaris model, as shown in Figures 138 through 141. The simulation end times were different for the simulations. However, the vehicles had redirected by the end of the simulations.

During the simulations at each of the impact locations, the Yaris model became parallel to the barrier after the model had already exited the system. Similar behavior was

observed with the Yaris model in the interior impact location, as described in Chapter 4. Thus, the parallel velocity was less than the exit velocity for the Yaris model at each of the impact locations.

The Yaris model experienced more vehicle damage in the simulations at the suggested MASH CIP locations as compared to the interior region simulations. The left-front corner of the Yaris model in the CIP location simulations had more lateral crush, causing the left-front headlight compartment to intrude farther into the engine compartment. Further, the top front of the left-front door in the simulations at the CIP location showed more lateral outward extensions than the interior location.

Table 35. Comparison Matrix of CIP Locations, 1100C Toyota Yaris

Simulation Parameters		Impact Location and Trial No.			
		30	34	44	70
		CIP Buttress Extended ²	CIP Buttress Compressed ²	CIP Pin Extended ²	CIP Pin Compressed ²
End Time, ms		206	206	266	266
Parallel Conditions	Time, ms	192	189	224	187
	Velocity, mph (km/h)	39.0 (62.7)	39.0 (62.8)	39.1 (62.9)	39.9 (64.3)
Exit Conditions	Velocity, mph (km/h)	39.3 (63.2)	39.3 (63.2)	39.3 (63.2)	40.2 (64.7)
	Angle, deg.	-9.9	-9.4	-9.1	-9.4
	Time, ms	136	136	136	136
Length of Contact		8 ft - 10 in. (2.7 m)	9 ft - 2 in. (2.8 m)	9 ft - 1 in. (2.8 m)	9 ft - 1 in. (2.8 m)
t*, ms		81.0	80.2	80.6	80.0
ORA, g's	Longitudinal	-8.83	-8.26	-8.99	-4.67
	Lateral	8.68	9.09	9.48	7.61
OIV, ft/s (m/s)	Longitudinal	-31.07 (-9.47)	-30.05 (-9.16)	-29.13 (-8.88)	-28.84 (-8.79)
	Lateral	22.97 (7.00)	28.71 (8.75)	28.77 (8.77)	29.63 (9.03)
Test Article Deflections, in. (mm)	Dynamic of Concrete	0.6 (15)	0.8 (20)	0.8 (20)	0.9 (23)
	Dynamic of Steel Rail	0.7 (18)	0.9 (23)	0.8 (20)	0.9 (23)
	Working Width	22.9 (582)	23.1 (587)	23.1 (587)	23.2 (589)
Location of Max. Deflection Upstream from Pin		20 ft (6.1 m)	20 ft (6.1 m)	20 ft (6.1 m)	20 ft (6.1 m)
Vehicle Stability	Max. Roll, deg.	8.1	9.6	9.5	9.8
	Max. Pitch, deg.	-4.1	-4.6	-4.9	-5.2
	Max. Yaw, deg.	29.2	29.8	36.9	36.8
Posts Hit by Leading Tire (wheel snag)		0	0	0	0
Max. Lateral Impact Force, kips (kN) ¹		58.2 (258.9)	58.7 (261.1)	57.1 (254.0)	57.8 (257)

¹ Calculated using global Y-acceleration multiplied by mass.

² Impacted 3 ft – 7 in. (1.1 m) upstream from noted location.



Figure 138. RESTORE Barrier Transition, 1100C Yaris Simulation Comparison, CIP Locations, Downstream View

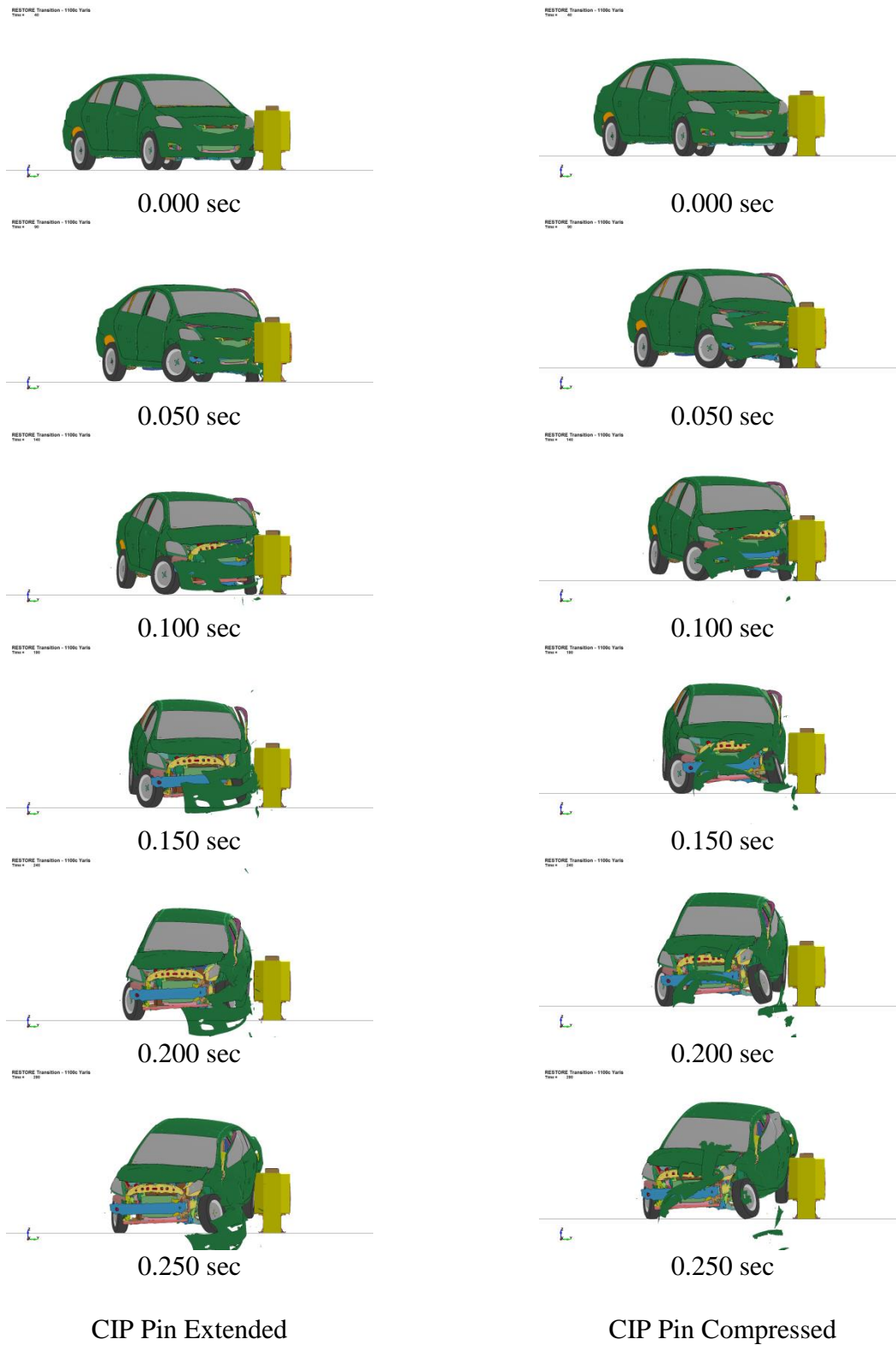


Figure 139. RESTORE Barrier Transition, 1100C Yaris Simulation Comparison, CIP Locations, Downstream View

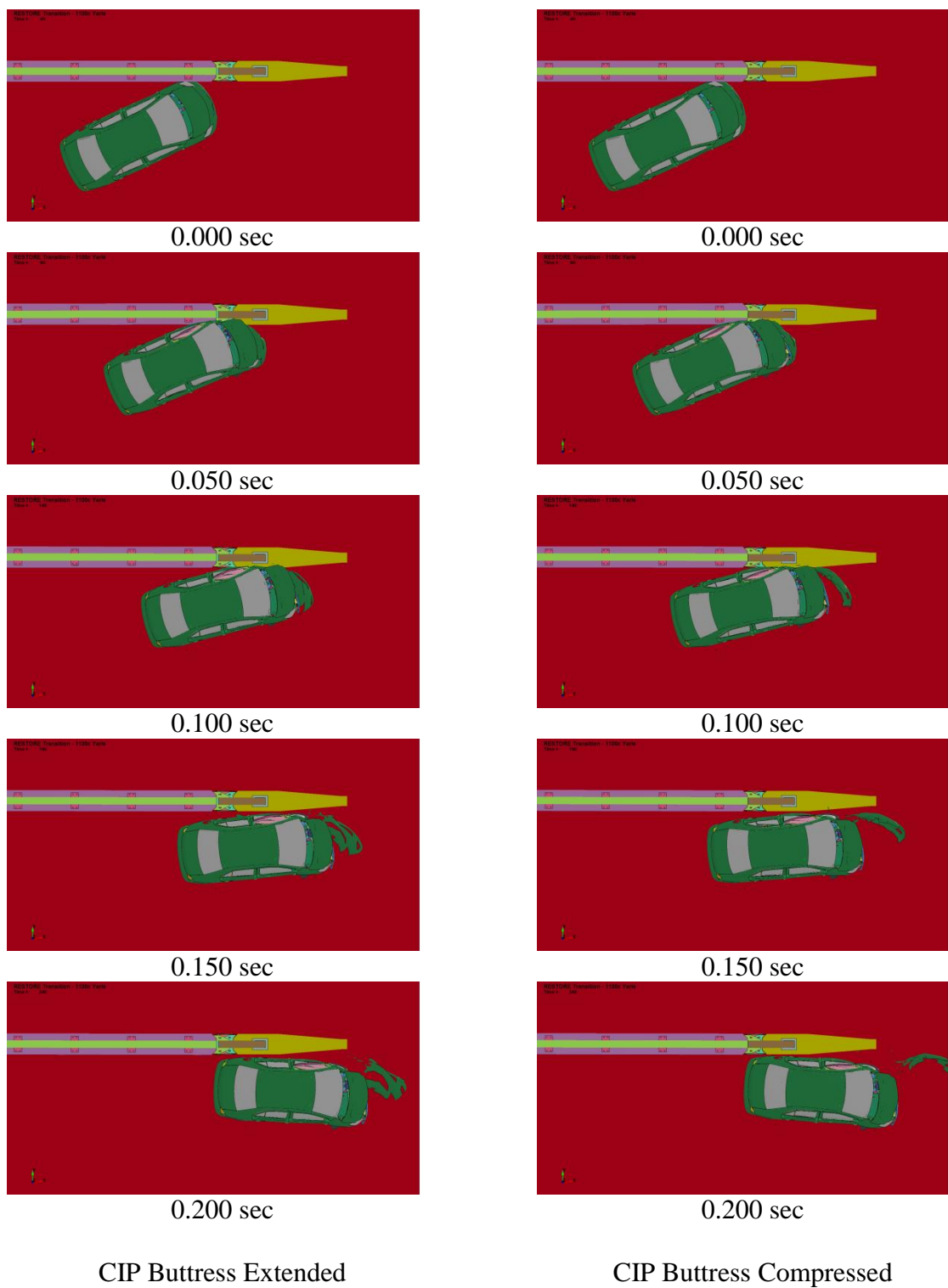


Figure 140. RESTORE Barrier Transition, 1100C Yaris Simulation Comparison, CIP Locations, Overhead View

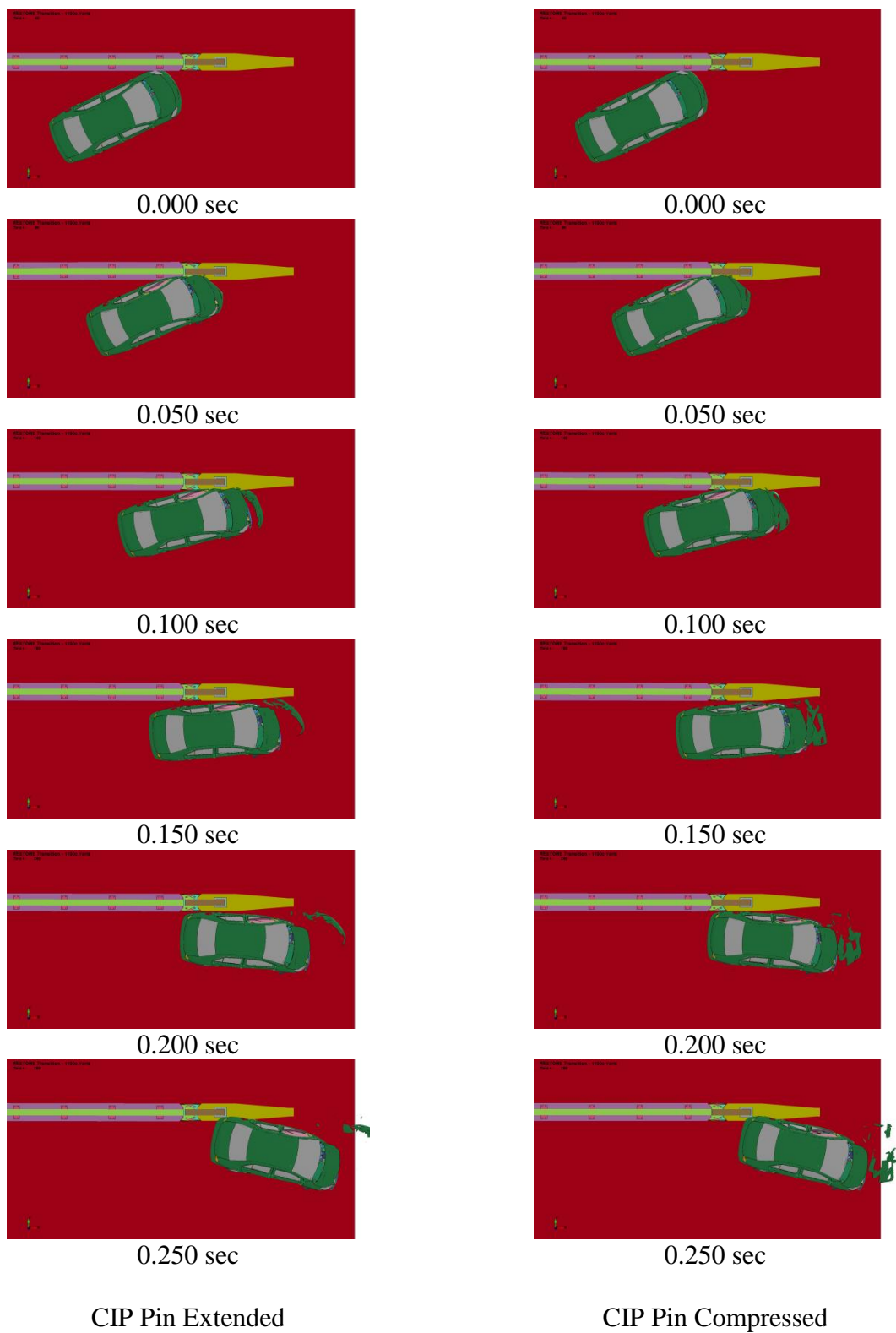


Figure 141. RESTORE Barrier Transition, 1100C Yaris Simulation Comparison, CIP Locations, Overhead View

Since all degrees of freedom in the rigid concrete buttress were constrained, the buttress did not have any damage nor deflections. The simulations with the extended and the compressed joints showed similar dynamic deflections, with the maximum deflection located at the upstream end of the last RESTORE barrier segment (i.e., 20 ft (6.1 m) upstream from the pin). The RESTORE barrier segments did rotate about the longitudinal x-axis, with the exception of the compressed joint with an impact location relative to the buttress face, in which the last RESTORE barrier segment rotated less than 1 degree due to the lateral tolerances in the vertical pin holes.

The lateral and longitudinal changes in velocity for each of the impact locations were similar, as shown in Figures 142 and 143. The main difference in the lateral change in velocity was that the CIP locations relative to the pin had an extended run-time. The longitudinal change in velocity was nearly identical through approximately 75 msec. The longitudinal change in velocity varied between the simulations between 75 msec and 100 msec by a maximum of 8 percent. The impact location relative to the buttress when the joint was fully extended resulted in the highest change in longitudinal velocity. The lateral and longitudinal OIV for each simulation were similar, as shown in Table 35.

The lateral and longitudinal ORAs for each simulation are shown in Table 35. The lateral ORA for the impact location relative to the buttress with the joint hardware fully extended provided a negative value as compared to the positive values observed at the other impact locations. The lateral ORA values were expected to be positive based on the orientation of the vehicle and observed lateral change in velocity. The longitudinal ORA for the impact location relative to the pin when the joint was fully compressed was approximately 50 percent less than the longitudinal ORAs for the other impact locations.

The lower longitudinal ORA indicates that when the cover plate is fully compressed, vehicle snagging is reduced.

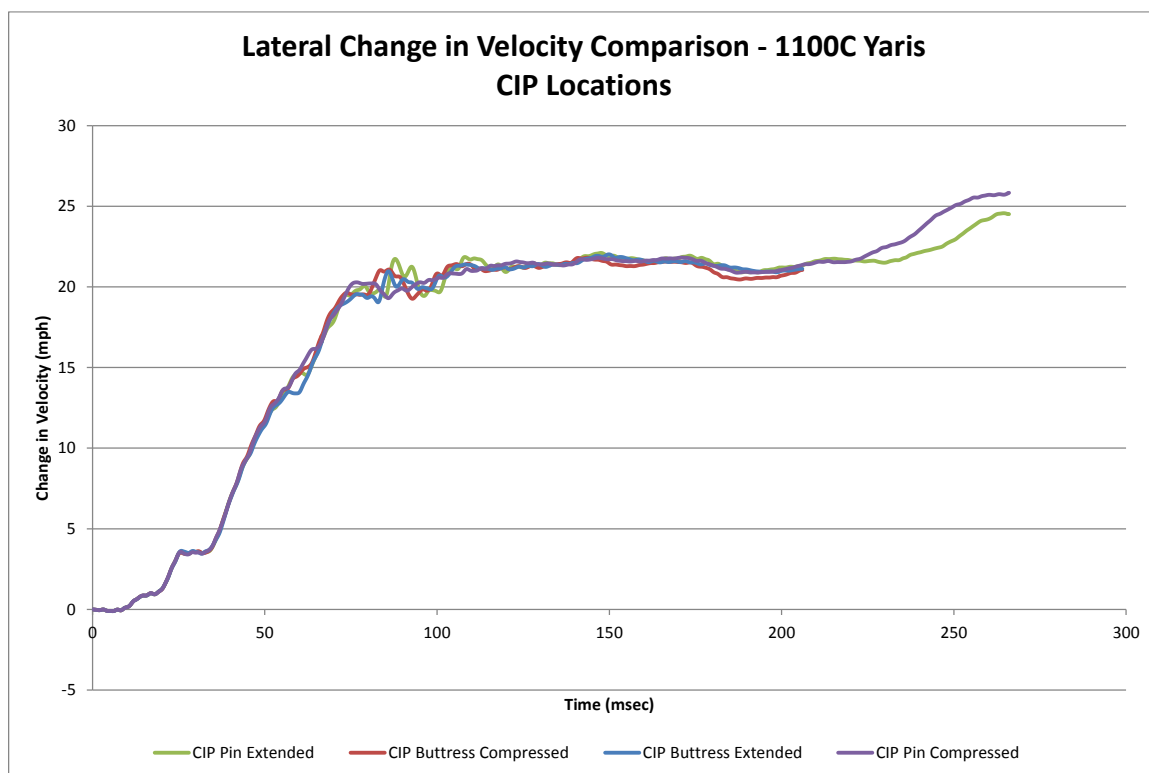


Figure 142. Lateral Change in Velocity, CIP Locations, 1100C Toyota Yaris

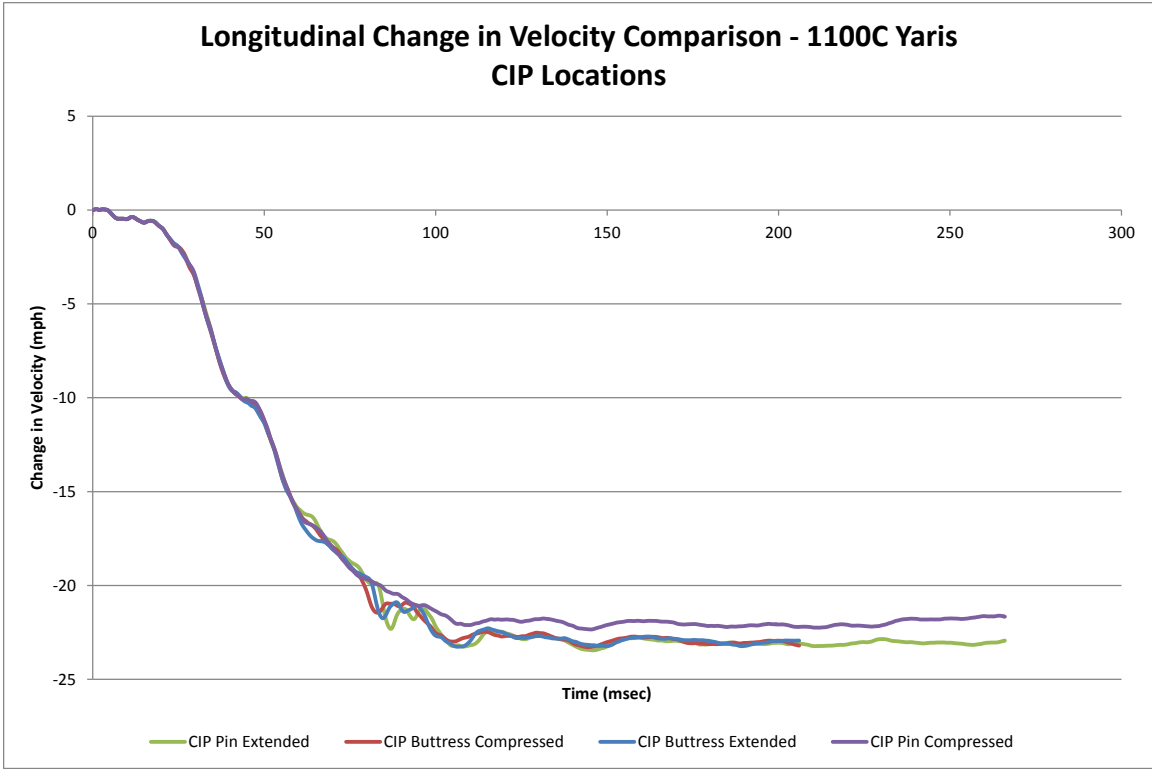


Figure 143. Longitudinal Change in Velocity, CIP Locations, 1100C Toyota Yaris

The lateral barrier impact forces were calculated using the CFC60 filtered 50-msec global Y-accelerations multiplied by the mass. Each of the impact location simulations exhibited a similar force trend through 100 msec, as shown in Figure 144. After 100 msec, the simulations relative to the pin with the compressed and extended joint and the simulation relative to the buttress with the compressed joint showed some slight vehicle snagging, with force fluctuations of approximately 6 kips (26.7 kN) at 125 msec. Note that the Yaris model did not become parallel to the barrier until after it had already exited the system. Thus, tail slap was not observed.

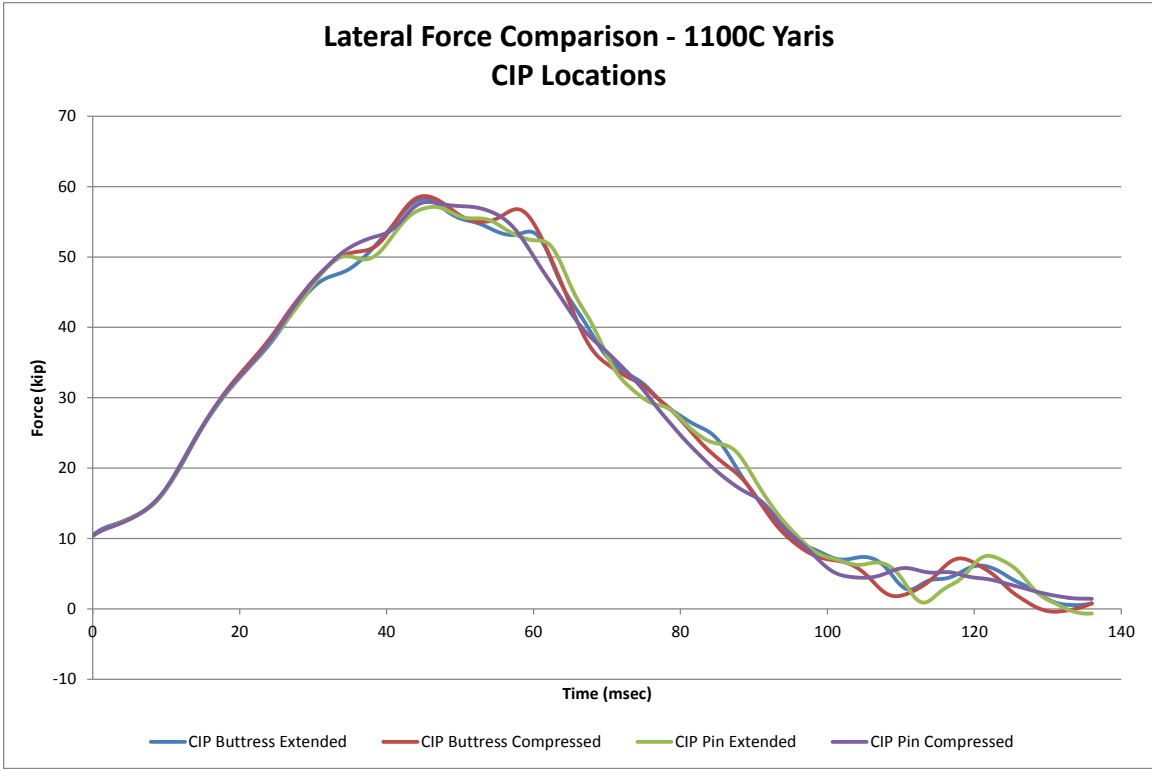


Figure 144. Lateral Force Comparison, CIP Locations, 1100C Toyota Yaris

The vehicles in each simulation rolled approximately 9 degrees from 45 to 55 msec after impact, as shown in Figure 145. After 50 msec, each of the roll angles started to roll towards zero again. The maximum roll angles for each of the impact location simulations were within 9 percent of each other.

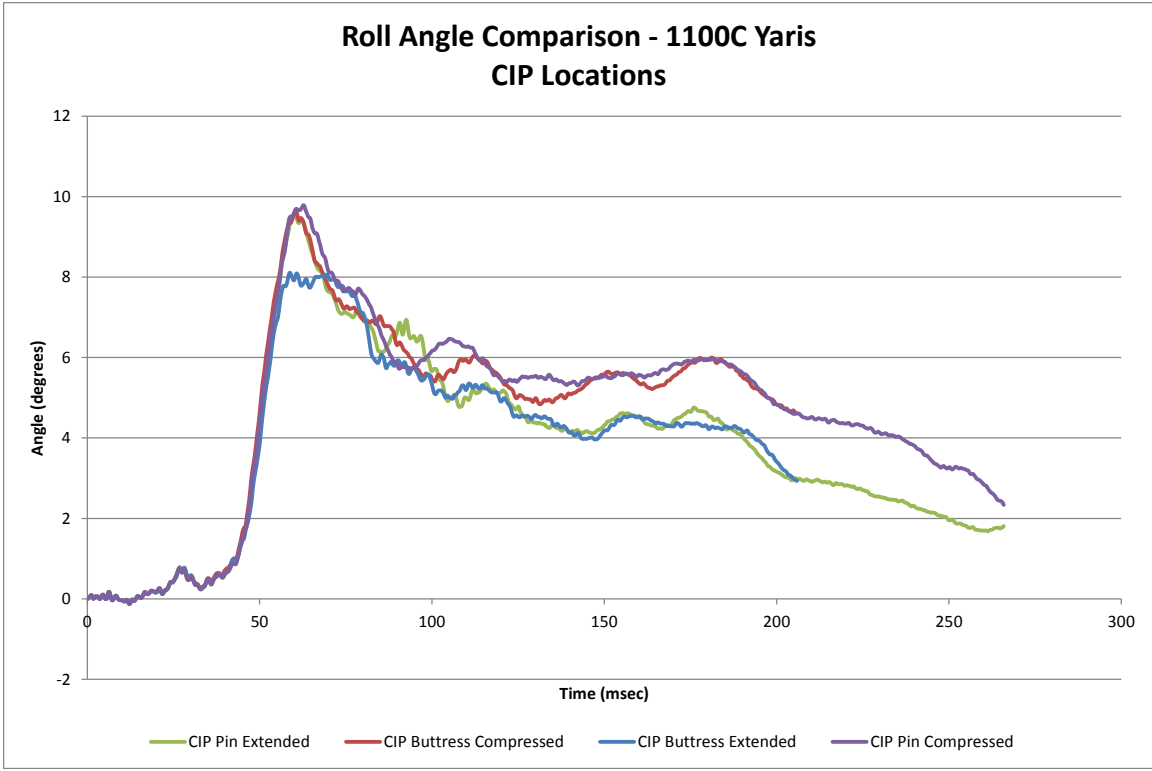


Figure 145. Roll Angle Comparison, CIP Locations, 1100C Toyota Yaris

The pitch angles for each of the impact location simulations were similar, as shown in Figure 146. The pitch angles had a spike of approximately 4.0 degrees before reaching the maximum pitch values of approximately -5.0 degrees. Similarly, the yaw angles were almost identical in the simulations with four different impact locations, as shown in Figure 147. However, for each of the impact locations, the parallel time for the Yaris model occurred after the vehicle had exited the system.

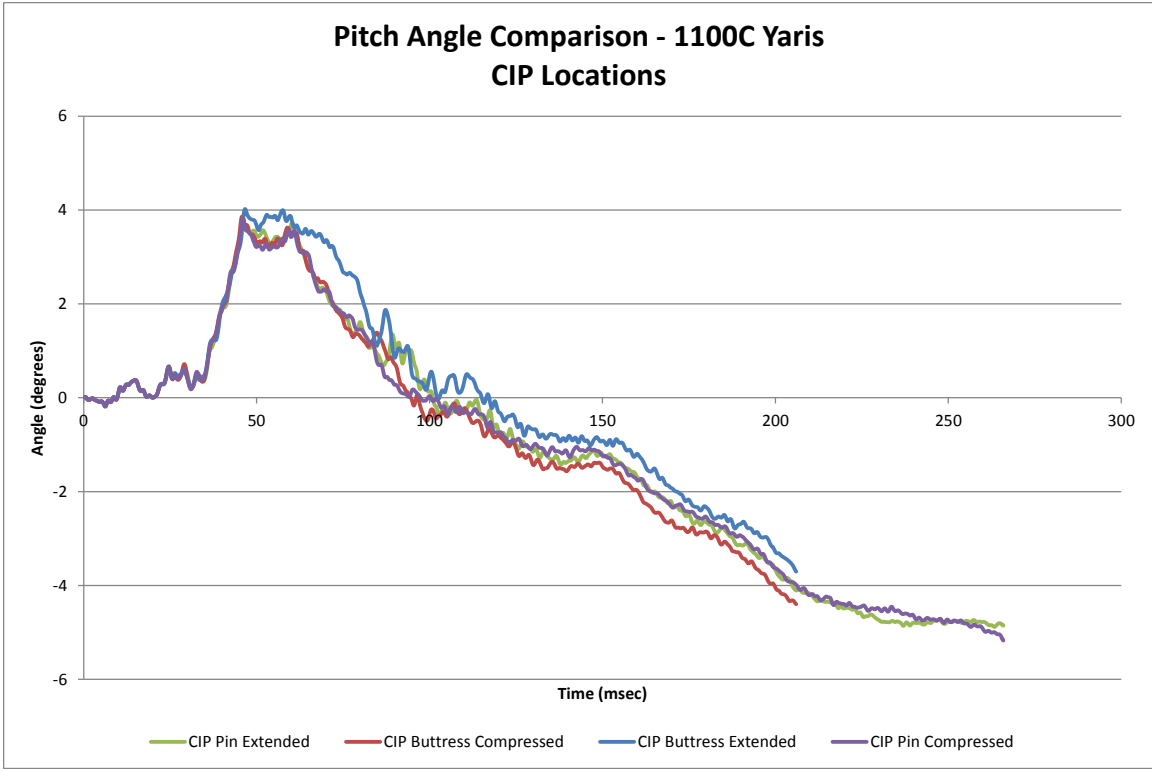


Figure 146. Pitch Angle Comparison, CIP Locations, 1100C Toyota Yaris

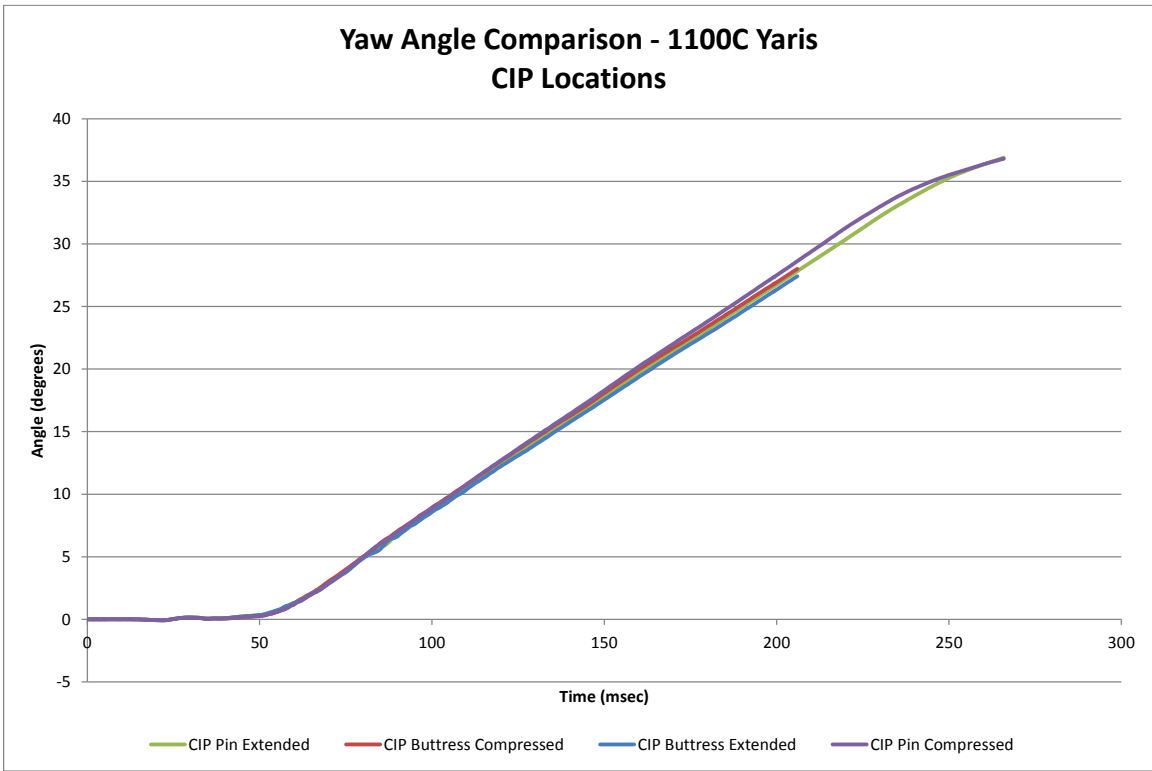


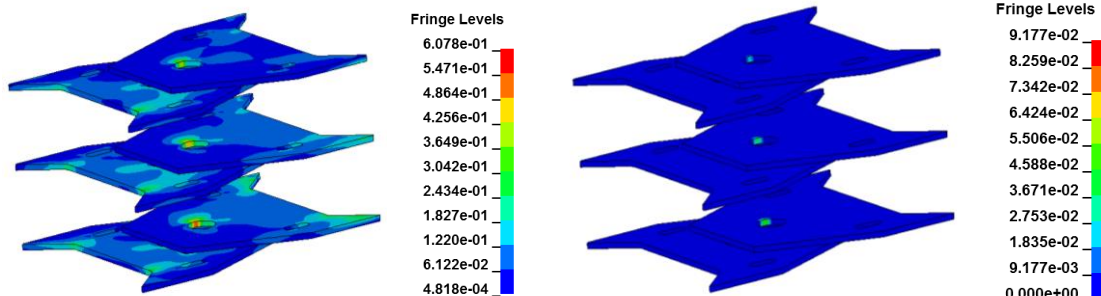
Figure 147. Yaw Angle Comparison, CIP Locations, 1100C Toyota Yaris

The von Mises and Tresca yield conditions were considered to evaluate the stresses within the parts of the pin-and-gusset configuration. A description of each part in relation to each yield condition, and the results can be found in Table 36. For some of the parts, the two yield conditions did not agree as to whether the material yielded or not. The vertical pin yielded during the simulation with the compressed hardware relative to the buttress using the von Mises yield condition, while the pin did not reach yield in the other impact location simulations. However, the Tresca condition showed that the pin yielded at all of the impact location simulations. Similarly, differences between the two yield conditions were found when evaluating the cover plate bolts. In most simulations, the cover plate bolts did not yield, and permanent deformation of the bolts was not observed through the simulations.

The horizontal gusset plates exceeded the Tresca and von Mises yield conditions. However, the peak stresses in the gusset plates occurred at the edges of the pin hole where the pin was bearing on the gusset plates, as shown in Figure 148. Due to the localization of the stresses, the gusset holes may have ovalized due to high bearing stresses, but they would not likely have ruptured and could be reloaded during subsequent impact events.

Table 36. RESTORE Barrier Component Stress Comparison, 1100C Toyota Yaris, CIP Locations

Simulation Parameters			Impact Location and Trial No.			
			30	34	44	70
Vertical Pin	Max.Tresca Stress	Stress, ksi (MPa)	33.4 (231)	35.5 (245)	33.9 (234)	35.0 (241)
		$\tau \geq 0.5\sigma_y ?$	Yes	Yes	Yes	Yes
Horizontal Gusset Plates	Max.von Mises Stress	Stress, ksi (MPa)	60.8 (419)	62.5 (431)	61.1 (421)	61.3 (422)
		$\sigma_{vm} \geq \sigma_y ?$	No	Yes	No	No
Cover Plate Bolts	Max.Tresca Stress	Stress, ksi (MPa)	50.4 (348)	49.1 (338)	50.6 (349)	48.6 (335)
		$\tau \geq 0.5\sigma_y ?$	Yes	Yes	Yes	Yes
Cover Plate Gussets	Max.von Mises Stress	Stress, ksi (MPa)	87.6 (604)	85.4 (589)	88.2 (608)	84.4 (582)
		$\sigma_{vm} \geq \sigma_y ?$	Yes	Yes	Yes	Yes
Cover Plate Bolts	Max.von Mises Stress	Stress, ksi (MPa)	45.1 (311)	55.4 (382)	53.5 (369)	51.4 (354)
		$\tau \geq 0.5\sigma_y ?$	No	Yes	Yes	No
Cover Plate Gussets	Max.Tresca Stress	Stress, ksi (MPa)	90.1 (621)	103.9 (716)	105.8 (730)	89.0 (614)
		$\sigma_{vm} \geq \sigma_y ?$	No	No	Yes	No
Cover Plate Gussets	Max.von Mises Stress	Stress, ksi (MPa)	31.6 (218)	34.5 (238)	32.2 (222)	38.6 (266)
		$\tau \geq 0.5\sigma_y ?$	Yes	Yes	Yes	Yes
Cover Plate Gussets	Max.von Mises Stress	Stress, ksi (MPa)	59.5 (410)	69.2 (477)	55.9 (385)	67.5 (466)
		$\sigma_{vm} \geq \sigma_y ?$	No	Yes	No	Yes



a. Von Mises Stress (GPa)

b. Plastic Strain

Figure 148. Von Mises Stress and Plastic Strain Comparison on Horizontal Gussets, Trial No. 44 at 40 msec, 1100C Yaris

The cover plate gussets were also believed to have yielded based on the yield conditions. The location of the peak stress on the corners of the cover plate gussets due to contact with the horizontal gusset plates are shown in Figure 149. The area of stresses that exceeded their yield conditions were relatively small and were believed to not have affected the structural capacity of the part.

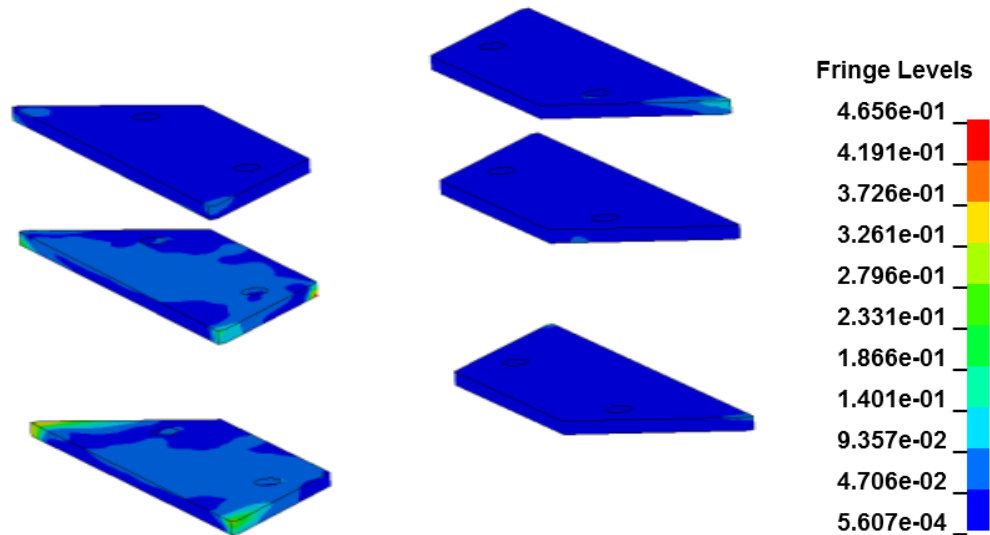


Figure 149. Von Mises Stress on Cover Plate Gussets (GPa), Trial No. 70 at 40 msec, 1100C Yaris

11.2.2 Neon Vehicle Model

The comparison of results for the Neon model between the simulations at the suggested MASH CIP locations is shown in Table 37. The simulations at each impact point successfully contained and redirected the Neon model, as shown in Figures 150 through 153. Each simulation had a different run time based on the computational speed of the computer. However, the desired data for each simulation was obtained.

The damage to the Neon vehicle model was similar between the suggested MASH CIP locations and the interior impact location. Although additional crushing may have occurred on the left-front corner of the vehicle due to impacting a stiffer system, the damage was not visually distinguishable.

Table 37. Comparison Matrix of CIP Locations, 1100C Dodge Neon

Simulation Parameters		Impact Location and Trial No.			
		29	33	43	69
		CIP Buttress Extended ²	CIP Buttress Compressed ²	CIP Pin Extended ²	CIP Pin Compressed ²
End Time, msec		350	350	280	343
Parallel Conditions	Time, ms	168	169	221	174
	Velocity, mph (km/h)	42.4 (68.3)	42.4 (68.2)	41.2 (66.3)	41.8 (67.2)
Exit Conditions	Velocity, mph (km/h)	41.5 (66.8)	38.4 (61.9)	40.7 (65.5)	40.0 (64.5)
	Angle, deg.	6.3	5.4	1.4	4.8
	Time, ms	241	241	232	251
Length of Contact		7 ft - 10 in. (2.4 m)	7 ft - 10 in. (2.4 m)	6 ft - 11 in. (2.1 m)	8 ft - 5 in. (2.6 m)
t*, ms		74.3	73.6	74.4	75.7
ORA, g's	Longitudinal	-5.31	-5.32	-6.71	-6.67
	Lateral	13.83	11.63	10.38	10.67
OIV, ft/s (m/s)	Longitudinal	-27.69 (-8.44)	-27.59 (-8.41)	-27.78 (-8.47)	-28.28 (-8.62)
	Lateral	33.00 (10.06)	32.35 (-.86)	33.62 (10.25)	32.51 (9.91)
Test Article Deflections, in. (mm)	Dynamic of Concrete	0.5 (13)	0.8 (20)	0.6 (15)	0.8 (20)
	Dynamic of Steel Rail	0.6 (15)	0.8 (20)	0.7 (18)	0.9 (23)
	Working Width	22.8 (579)	23.2 (589)	23.0 (584)	23.2 (589)
Location of Max. Deflection Upstream from Pin		20 ft (6.1 m)	20 ft (6.1 m)	20 ft (6.1 m)	20 ft (6.1 m)
Vehicle Stability	Max. Roll, deg.	-4.7	-4.7	-5.2	5.5
	Max. Pitch, deg.	-2.7	-2.9	-2.9	-2.4
	Max. Yaw, deg.	33.6	30.8	28.9	30.7
Posts Hit by Leading Tire (wheel snag)		0	0	0	0
Max. Lateral Impact Force, kips (kN) ¹		55.6 (247.3)	54.6 (242.9)	54.5 (242.4)	53.5 (238.0)

¹ Calculated using global Y-acceleration multiplied by mass.

² Impacted 3 ft – 7 in. (1.1 m) upstream from noted location.



Figure 150. RESTORE Barrier Transition, 1100C Neon Simulation Comparison, CIP Locations, Downstream View

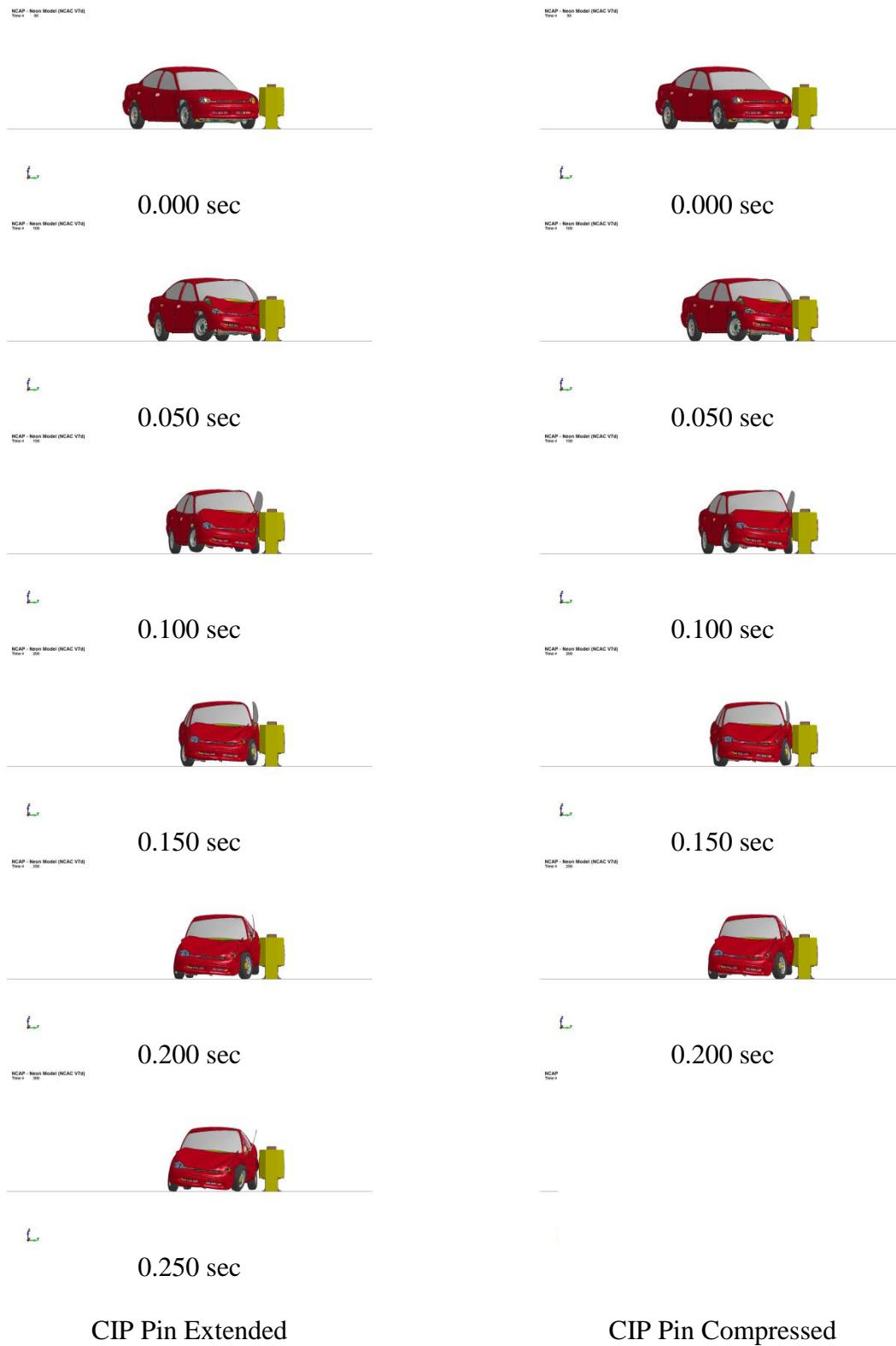
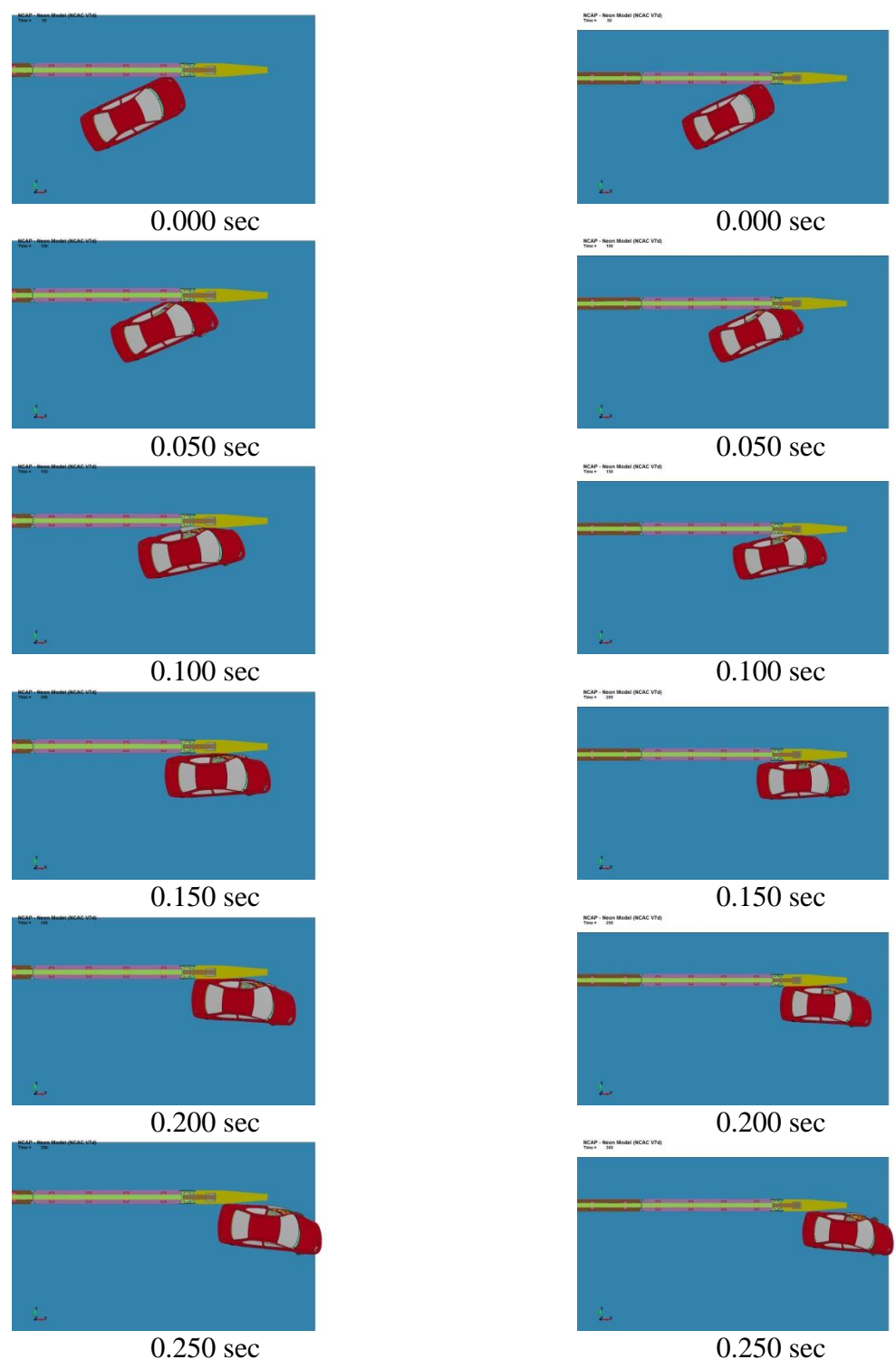


Figure 151. RESTORE Barrier Transition, 1100C Neon Simulation Comparison, CIP Locations, Downstream View



CIP Buttress Extended

CIP Buttress Compressed

Figure 152. RESTORE Barrier Transition, 1100C Neon Simulation Comparison, CIP Locations, Overhead View

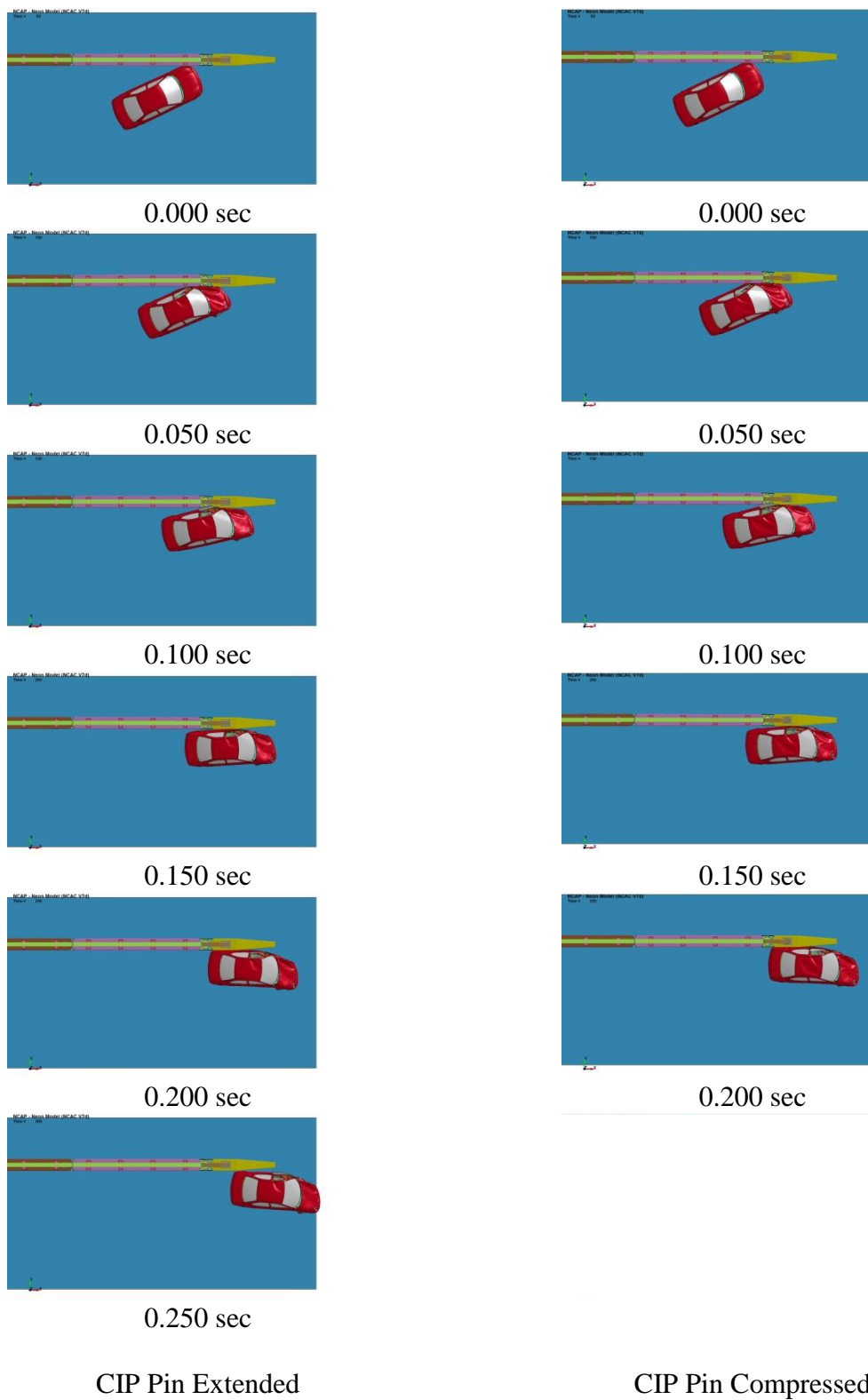


Figure 153. RESTORE Barrier Transition, 1100C Neon Simulation Comparison, CIP Locations, Overhead View

Since all degrees of freedom in the rigid concrete buttress were constrained, the buttress did not have any damage nor deflections. The simulations with the extended and the compressed joints showed similar dynamic deflections, with the maximum deflection located at the upstream end of the last RESTORE barrier segment (i.e., 20 ft (6.1 m) upstream from the pin). The last RESTORE barrier segment experienced up to 1 degrees of rotation about the longitudinal x-axis during the simulations when the Neon model impacted the system with the extended and compressed joint at the locations relative to the pin and the compressed joint relative to the buttress end. Rotation was experienced and allowed based on the tolerances provided within the vertical pin holes and slots.

The lateral and longitudinal changes in velocity of each simulation for each impact location correlated well, as shown in Figures 154 and 155. The main difference in the lateral change in velocity was that the CIP location simulations relative to the pin had an extended run-time. The longitudinal change in velocity was nearly identical through approximately 75 msec. After 75 msec, the longitudinal change in velocity varied in each impact location simulation, but they were all within 3 mph (4.8 km/h). The lateral and longitudinal ORA and OIV values were similar throughout each impact location simulation with the Neon model.

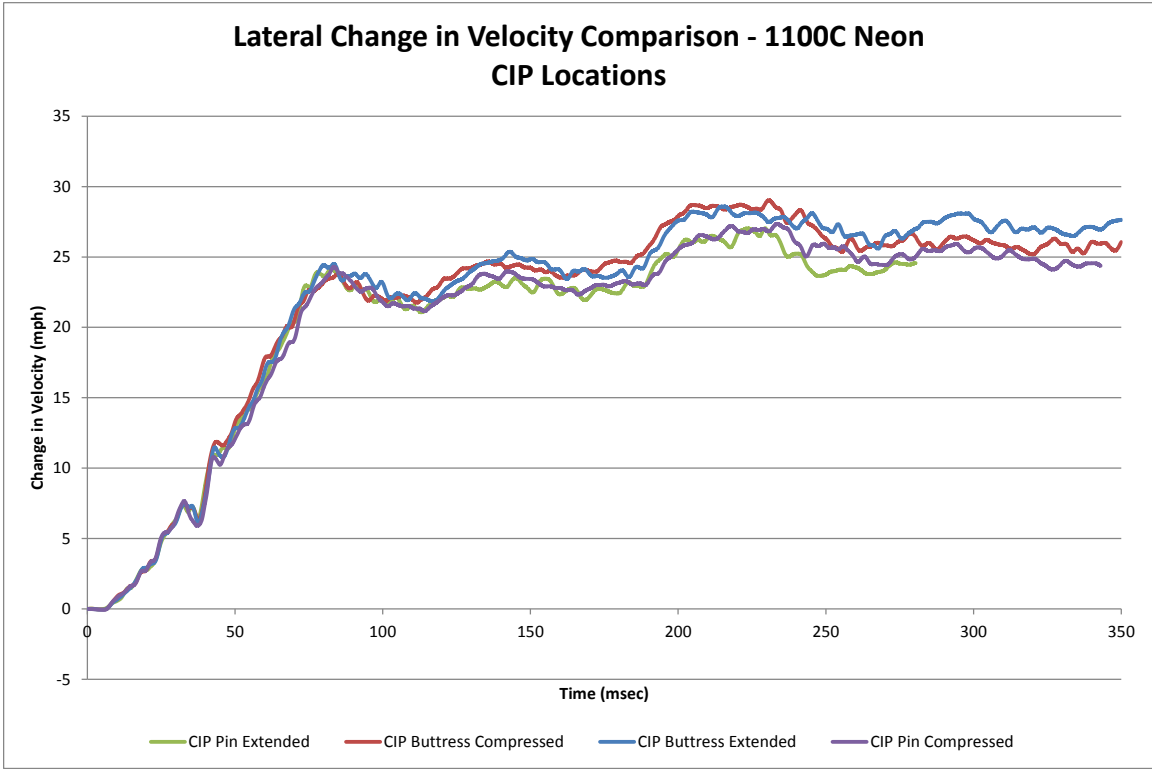


Figure 154. Lateral Change in Velocity, CIP Locations, 1100C Dodge Neon

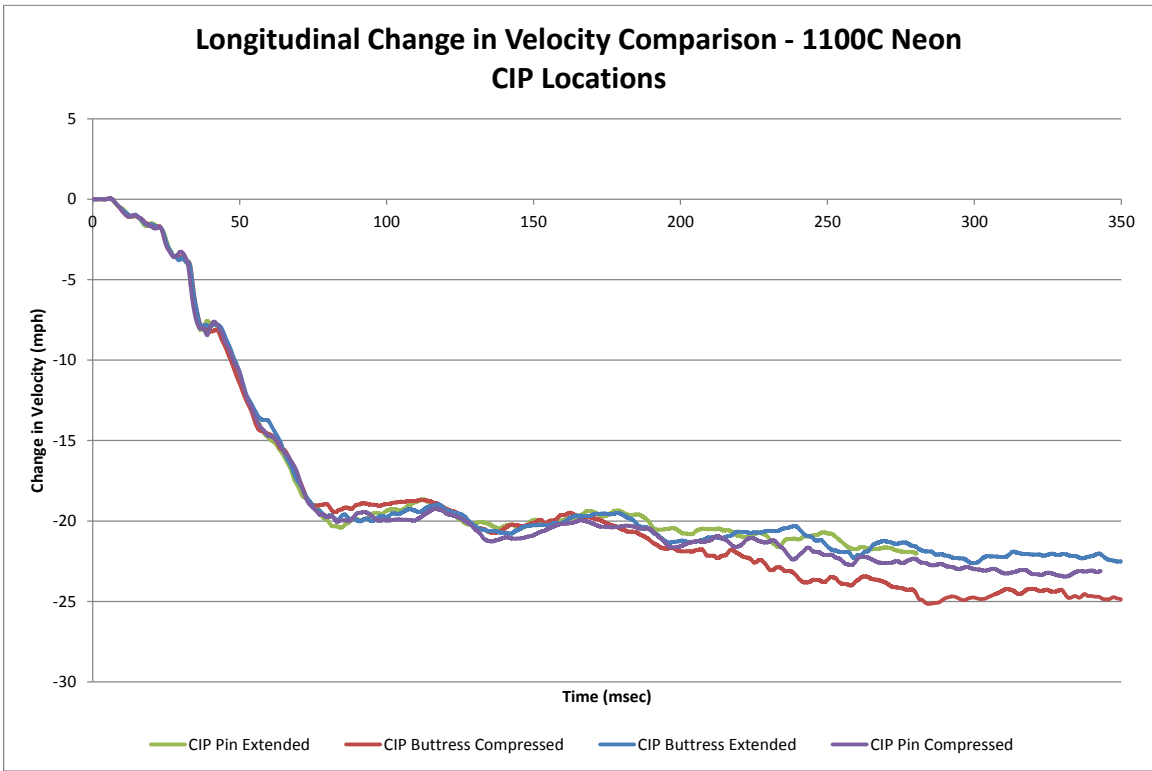


Figure 155. Longitudinal Change in Velocity, CIP Locations, 1100C Dodge Neon

The lateral barrier impact forces were calculated using the CFC60 filtered 50-msec global Y-accelerations multiplied by the vehicle mass. Each of the location simulations exhibited a similar force trend through approximately 150 msec, as shown in Figure 156. After 150 msec, the tail slap of the Neon model deviated with the extended joint simulation relative to the pin, as compared to the other three location simulations.

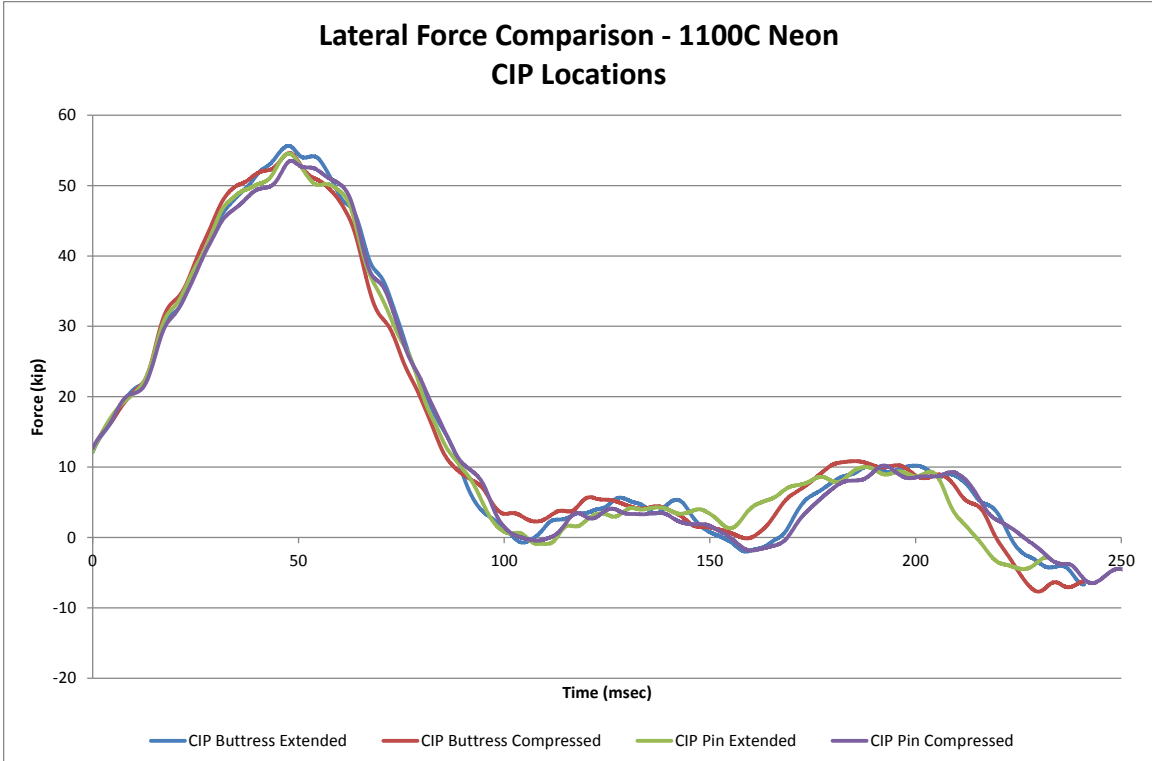


Figure 156. Lateral Force Comparison, CIP Locations, 1100C Dodge Neon

The roll angles for each impact location simulation correlated with each other over the first 40 msec, and all had a positive change in roll angle of approximately 5.5 degrees, as shown in Figure 157. By 50 msec, each of the roll angles were approximately -4.0 degrees. The roll angles fluctuated with limited roll angles for the remainder of the simulation.

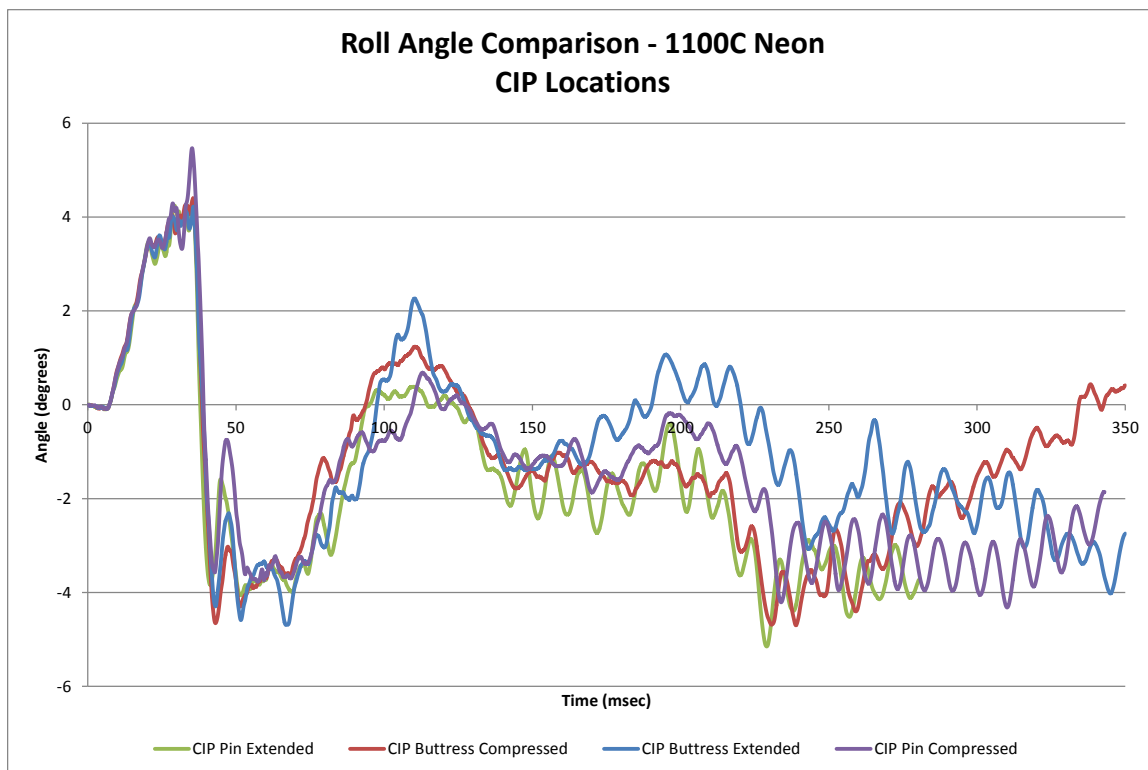


Figure 157. Roll Angle Comparison, CIP Locations, 1100C Dodge Neon

The pitch angles for each of the impact location simulations were similar through approximately 50 msec, as shown in Figure 158. The pitch angles for each impact location simulations were small, with a variance within 5 degrees, fluctuating around no pitch and making the angle curves look noisy. The yaw angles were also similar to each other in each simulation, as shown in Figure 159. The peak yaw angles were within 3.0 percent of one another.

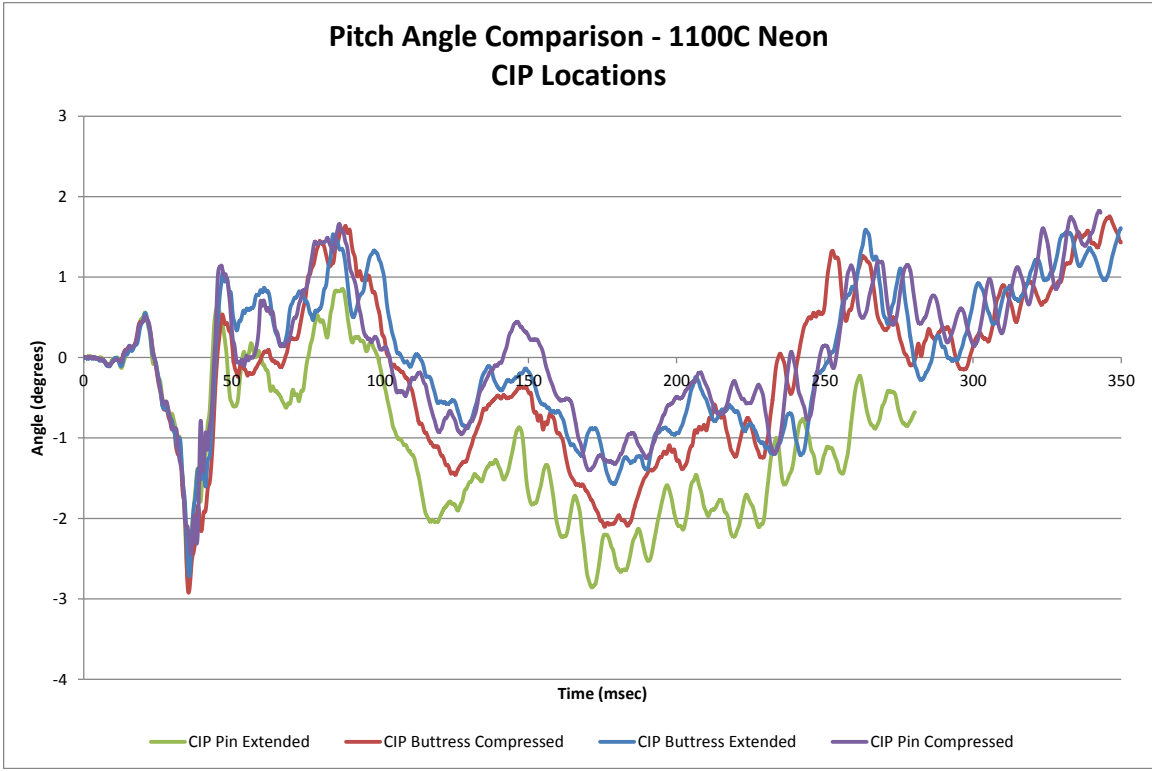


Figure 158. Pitch Angle Comparison, CIP Locations, 1100C Dodge Neon

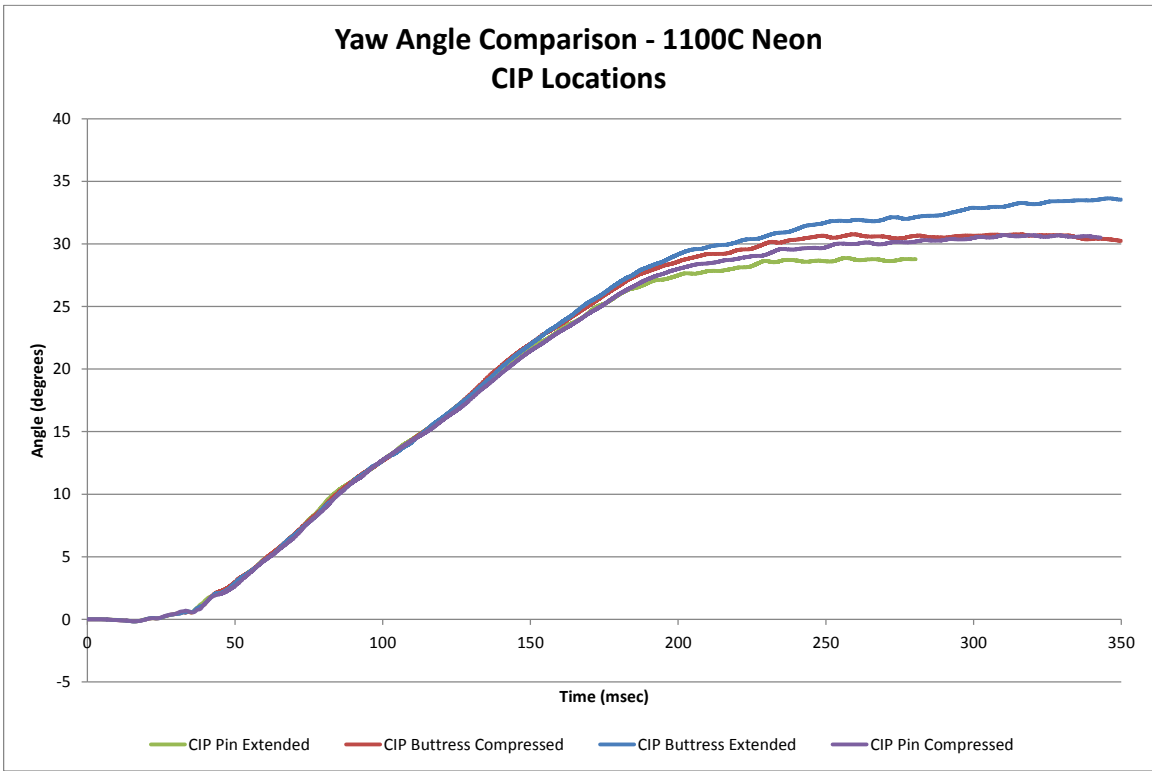


Figure 159. Yaw Angle Comparison, CIP Locations, 1100C Dodge Neon

The von Mises and Tresca yield conditions were considered to evaluate the stresses within the parts of the pin and gusset configuration. A description of each part with relation to each yield condition, and the results are shown in Table 38. For some of the parts, the von Mises and Tresca yield conditions did not correspond to each other. During the simulation impact events relative to the buttress end, the maximum stress of the vertical pin did not exceed the von Mises condition whereas the maximum stress exceeded the Tresca condition. During the simulations with the Neon model, the cover plate bolts experienced stresses that exceeded yield conditions, causing permanent deformations, as shown in Figure 160.

Table 38. RESTORE Barrier Component Stress Comparison, 1100C Dodge Neon, CIP Locations

Simulation Parameters			Impact Location and Trial No.			
			29	33	43	69
			CIP Buttress Extended	CIP Buttress Compressed	CIP Pin Extended	CIP Pin Compressed
Vertical Pin	Max. Tresca Stress	Stress, ksi (MPa)	33.5 (231)	36.0 (248)	32.9 (227)	38.0 (262)
		$\tau \geq 0.5\sigma_y$?	Yes	Yes	Yes	Yes
	Max. von Mises Stress	Stress, ksi (MPa)	58.5 (403)	63.3 (437)	63.1 (435)	66.1 (456)
		$\sigma_{vm} \geq \sigma_y$?	No	Yes	Yes	Yes
Horizontal Gusset Plates	Max. Tresca Stress	Stress, ksi (MPa)	51.9 (358)	51.2 (353)	52.1 (360)	47.7 (329)
		$\tau \geq 0.5\sigma_y$?	Yes	Yes	Yes	Yes
	Max. von Mises Stress	Stress, ksi (MPa)	90.5 (624)	90.6 (625)	90.8 (626)	79.2 (546)
		$\sigma_{vm} \geq \sigma_y$?	Yes	Yes	Yes	Yes
Cover Plate Bolts	Max. Tresca Stress	Stress, ksi (MPa)	57.6 (397)	60.5 (417)	55.5 (383)	61.6 (425)
		$\tau \geq 0.5\sigma_y$?	Yes	Yes	Yes	Yes
	Max. von Mises Stress	Stress, ksi (MPa)	105.1 (724)	107.2 (739)	106.1 (732)	107.1 (739)
		$\sigma_{vm} \geq \sigma_y$?	Yes	Yes	Yes	Yes
Cover Plate Gussets	Max. Tresca Stress	Stress, ksi (MPa)	24.2 (167)	31.5 (217)	33.2 (229)	30.2 (208)
		$\tau \geq 0.5\sigma_y$?	No	Yes	Yes	No
	Max. von Mises Stress	Stress, ksi (MPa)	45.6 (314)	61.4 (423)	57.8 (399)	56.0 (386)
		$\sigma_{vm} \geq \sigma_y$?	No	No	No	No
Top Tube, Splice, and Termination	Max. Tresca Stress	Stress, ksi (MPa)	35.5 (245)	34.9 (241)	36.0 (148)	36.0 (248)
		$\tau \geq 0.5\sigma_y$?	Yes	Yes	Yes	Yes
	Max. von Mises Stress	Stress, ksi (MPa)	61.6 (425)	61.0 (420)	62.4 (430)	62.4 (430)
		$\sigma_{vm} \geq \sigma_y$?	No	No	Yes	Yes
Cover Plate	Max. Tresca Stress	Stress, ksi (MPa)	33.1 (228)	33.4 (230)	35.3 (244)	34.7 (239)
		$\tau \geq 0.5\sigma_y$?	Yes	Yes	Yes	Yes
	Max. von Mises Stress	Stress, ksi (MPa)	57.4 (396)	58.3 (402)	61.9 (427)	62.4 (430)
		$\sigma_{vm} \geq \sigma_y$?	No	No	No	Yes

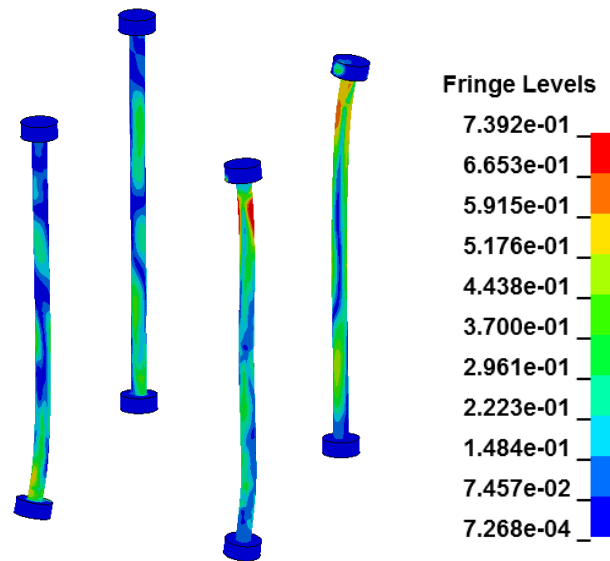


Figure 160. Bolt Von Mises Stresses and Deformation (GPa), Trial No. 33 at 40 msec, 1100C Neon

The horizontal gusset plates and cover plate gussets were believed to have yielded based on the von Mises and Tresca yield conditions for all of the simulations with the Neon model, except the simulation relative to the buttress with the extended joint. However, similar to the Yaris simulations, as explained in Section 11.2.1, the horizontal gusset plates in each of the simulations had localized stresses and strains, causing ovalization in the gusset, but rupture would not likely be experienced. Similarly, the cover plate gussets had some slight deformations at the corner due to the peak stresses exceeding the yield conditions but were not believed to have affected the structural capacity of the part. The simulation relative to the buttress with the extended joint had maximum stresses in the cover plate gussets well below the other simulations where the stresses did not exceed the yield conditions.

The top tube, tube splices, and tube termination had peak stresses that exceeded the yield conditions in the simulations at each impact location based on the Tresca yield conditions. However, the impact location simulation relative to the buttress end with the

compressed joint did not show that the tube parts would yield based on the von Mises yield condition. The other three impact location simulations had maximum stresses of 62.4 ksi (430 MPa), which was the yield stress, thus making the condition true.

Lastly, the cover plate stresses during all of the impacts at the MASH suggested CIP locations exceeded the Tresca yield conditions. The stresses within the cover plate were not greater than the von Mises condition in the simulation relative to the buttress with the compressed joint, and the simulation relative to the pin with the extended joint. The von Mises stresses in the other two simulations were 62.4 ksi (430 MPa), which was the yield stress of the material. The majority of the stresses on the cover plate were concentrated on the curved sides due to contact between the cover plate and the horizontal gusset plates.

11.3 Upstream Location Simulation Results

Impact points upstream from the pin and gusset plate assemblies were simulated at intervals of 10 ft (3.0 m). The impact point occurred 3 ft – 7 in. (1.1 m) upstream from locations of 10, 20, 30, and 40 ft (3.0, 6.1, 9.1, 12.2 m) away from the downstream end of the last concrete RESTORE barrier in order to determine the maximum load imparted to the ACJ hardware and investigate the potential for vehicle snag on posts when traveling toward a stiffened barrier.

11.3.1 Yaris Vehicle Model

The comparison of results for the Yaris vehicle model between the simulations at the upstream impact locations is shown in Table 39. The simulations at each impact point successfully contained and redirected the Yaris model, as shown in Figures 161 through

164. The simulation end times were different for each of the simulations. However, the desired data was obtained for each of the impact locations.

The left-front tire of the Yaris model penetrated under the RESTORE barrier and contacted posts at the 20 ft (6.1 m) impact location when the joint was both extended and compressed. For both simulations at the 20-ft (6.1-m) impact locations, the left-front tire contacted the upstream face approximately across 2 in. (51 mm) on the first post downstream from impact and approximately across 1 in. (25 mm) on the second post downstream from impact.

In the simulations with the Yaris model impacting upstream from the pin, the left-front corner of the vehicle model had similar crush as the simulation at the interior location. However, as the impact location moved closer to the rigid concrete buttress end, the deformations at the top of the left-front door extended farther outward laterally than the door extensions found during the interior location simulation.

Table 39. Comparison Matrix of Upstream Impact Locations, 1100C Toyota Yaris

Simulation Parameters		Impact Location and Trial No.				
		53	54	66	55	56
		10 ft Upstream Extended ²	20 ft Upstream Extended ²	20 ft Upstream Compressed ²	30 ft Upstream Extended ²	40 ft Upstream Extended ²
End Time, ms		316	416	416	516	566
Parallel Conditions	Time, ms	229	286	246	243	288
	Velocity, mph (km/h)	40.5 (65.2)	38.1 (61.2)	39.5 (63.5)	41.9 (67.3)	38.6 (62.2)
Exit Conditions	Velocity, mph (km/h)	38.1 (61.3)	37.6 (60.4)	36.8 (59.2)	39.2 (63.0)	37.3 (60.1)
	Angle, deg.	6.7	2.6	3.6	3.0	4.6
	Time, ms	300	310	346	310	340
Length of Contact t*, ms		13 ft - 2 in. (4.0 m) 81.7	14 ft - 5 in. (4.4 m) 88.3	14 ft - 9 in. (4.5 m) 87.9	12 ft - 4 in. (3.7 m) 82.7	13 ft - 4in. (4.0 m) 87.6
ORA, g's	Longitudinal	-5.96	-4.81	-5.24	-4.04	-5.63
	Lateral	11.68	9.41	8.37	14.33	9.65
OIV, ft/s (m/s)	Longitudinal	-27.20 (-8.29)	-27.62 (-8.42)	-26.74 (-8.15)	-25.61 (-7.81)	-27.80 (-8.47)
	Lateral	25.95 (7.91)	22.08 (6.73)	21.81 (6.65)	23.48 (7.16)	22.70 (6.92)
Test Article Deflections, in. (mm)	Dynamic of Concrete	5.8 (147)	9.1 (231)	9.0 (229)	6.3 (160)	8.8 (224)
	Dynamic of Steel Rail	6 (152)	9.3 (236)	9.3 (236)	6.8 (173)	9.2 (234)
	Working Width	28.1 (714)	31.4 (798)	31.3 (795)	28.6 (726)	31.1 (790)
Location of Max. Deflection Upstream from Pin		20 ft (6.1 m)	20 ft (6.1 m)	20 ft (6.1 m)	20 ft (6.1 m)	40 ft (12.2 m)
Vehicle Stability	Max. Roll, deg.	8.3	6.3	6.3	7.9	6.0
	Max. Pitch, deg.	-7.8	-11.2	-11.0	-11.3	-17.6
	Max. Yaw, deg.	32.6	28.5	29.1	28.0	29.6
Posts Hit by Leading Tire (wheel snag)		0	2	2	0	2
Max. Lateral Impact Force, kips (kN) ¹		51.8 (230.4)	47.6 (211.7)	44.9 (199.7)	49.8 (221.5)	47.7 (212.0)

¹ Calculated using global Y-acceleration multiplied by mass.

² Impacted 3 ft – 7 in. (1.1 m) upstream from noted location.

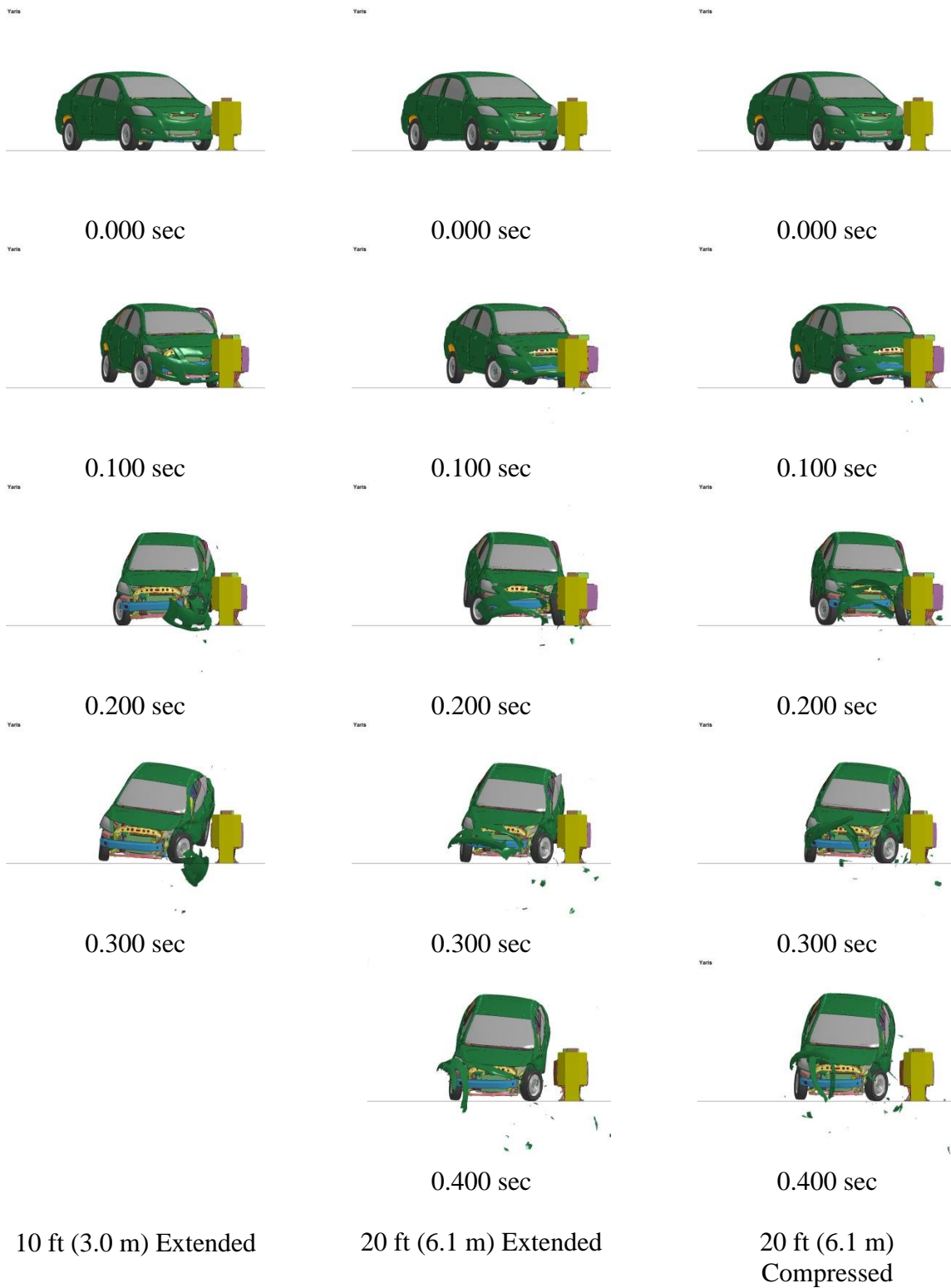


Figure 161. RESTORE Barrier Transition, 1100C Yaris Simulation Comparison, Upstream Impact Locations, Downstream View



Figure 162. RESTORE Barrier Transition, 1100C Yaris Simulation Comparison, Upstream Impact Locations, Downstream View

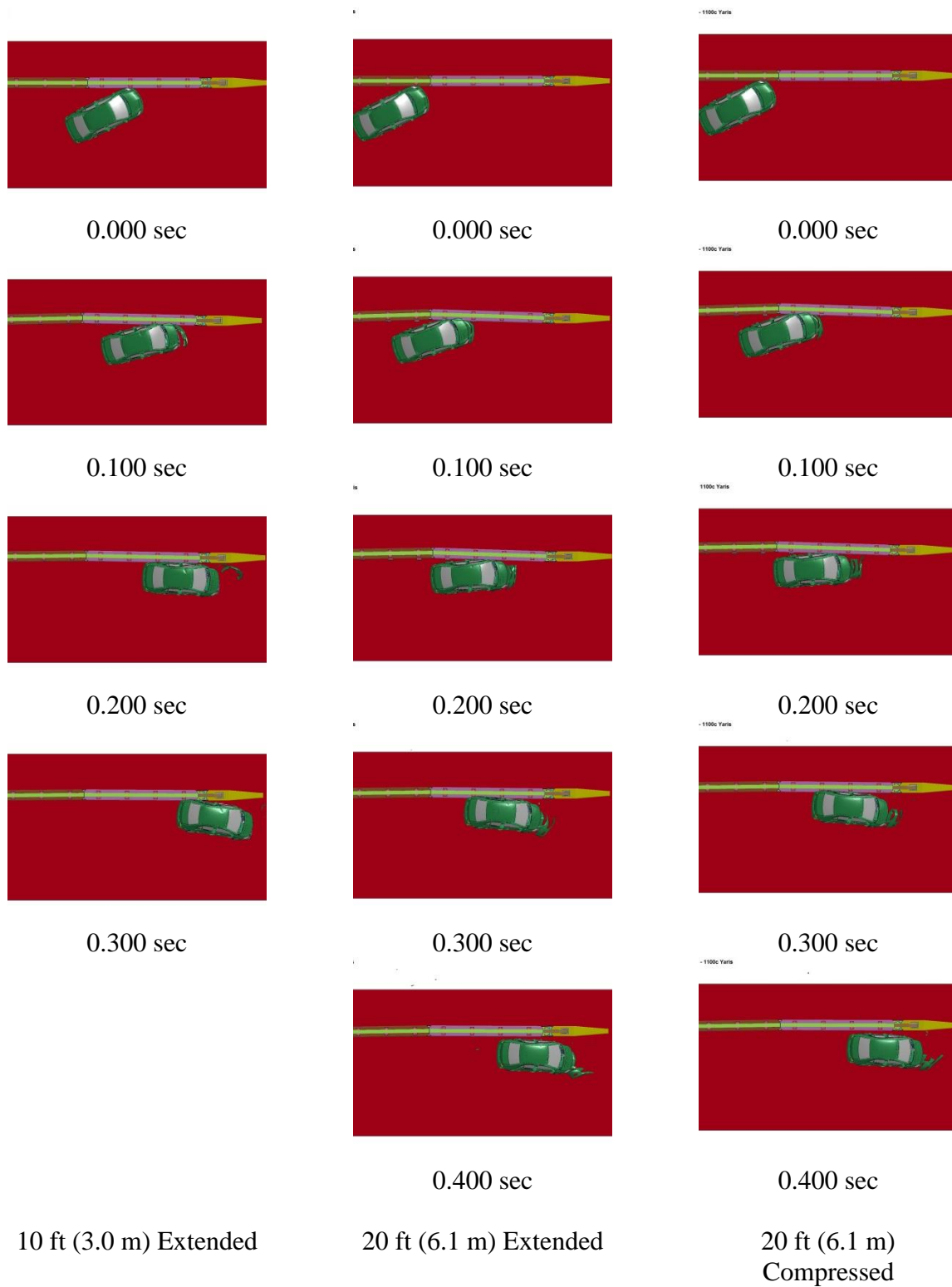


Figure 163. RESTORE Barrier Transition, 1100C Yaris Simulation Comparison, Upstream Impact Locations, Overhead View

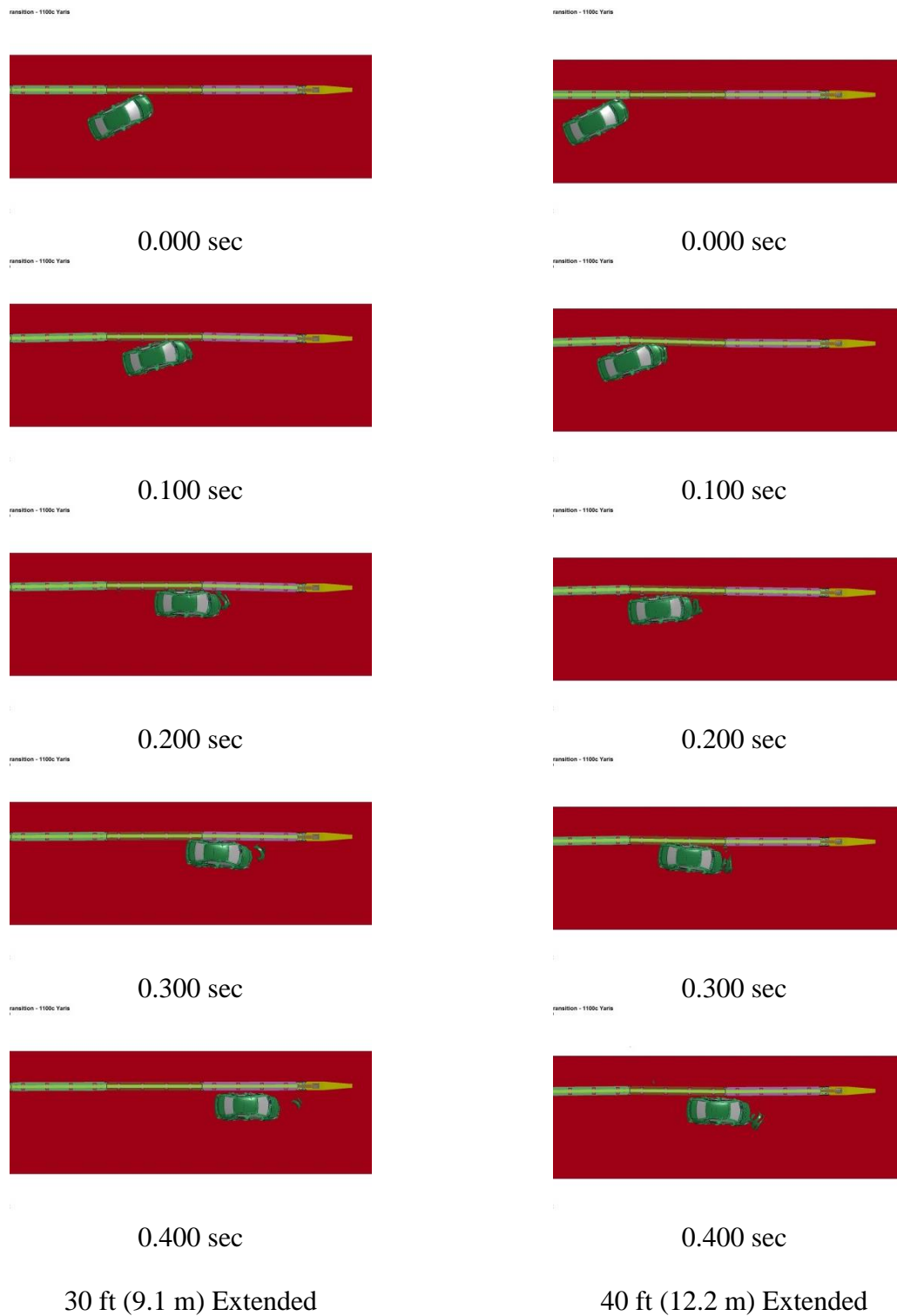


Figure 164. RESTORE Barrier Transition, 1100C Yaris Simulation Comparison, Upstream Impact Locations, Overhead View

The simulated dynamic barrier deflection of the RESTORE barrier at each impact location showed a trend where the deflections increased as the impact occurred farther upstream from the pin. However, the maximum dynamic deflection was found to occur in the 20-ft (6.1-m) impact location simulation when considering impact locations of 10, 20, 30 and 40 ft (3.0, 6.1, 9.1, and 12.2 m). The simulation at the 20-ft (6.1-m) impact location with extended joint showed an 18 percent larger dynamic deflection than observed in the simulation at the interior location. The larger deflections were likely caused by the presence of a nearby hinge or pin, ACJ widening at 20 ft (6.1 m), and preventing the distribution of load across multiple barrier segments, thus, changing the constraints of the system limited the transfer of impact force, causing an increase at the 20-ft (6.1-m) impact location simulation.

The lateral change in velocity between each impact location simulation upstream from the pin followed a similar trend through approximately 50 msec, as shown in Figure 165. However, the lateral change in velocity in the simulations for 10 and 30 ft (3.0 and 9.1 m) upstream from the pin were greater than the simulations for 20 and 40 ft (6.1 and 12.2 m) upstream from the pin between 200 and 300 msec. The difference in the lateral velocity could possibly be contributed to the smaller observed dynamic deflections. The simulations at the 20- and 40-ft (6.1- and 12.2-m) impact locations deflected laterally approximately 30 percent more than the simulations at the 10- and 30-ft (3.0- and 9.1-m) impact locations. The longitudinal change in velocity was similar through each impact location simulation, as shown in Figure 166. However, the longitudinal change in velocity for the Yaris model at the 30-ft (9.1-m) impact location did not decrease as much as observed for the other impact location simulations. The longitudinal ORA and OIV

values were similar throughout each upstream impact location simulation with the Yaris model. However, the lateral ORA and OIV values were larger during the simulations for 10 and 30 ft (3.0 and 9.1 m) upstream from the joint, which may have been due to the impact at the midspan of the barrier segments, where less deflection and post energy absorption occurred.

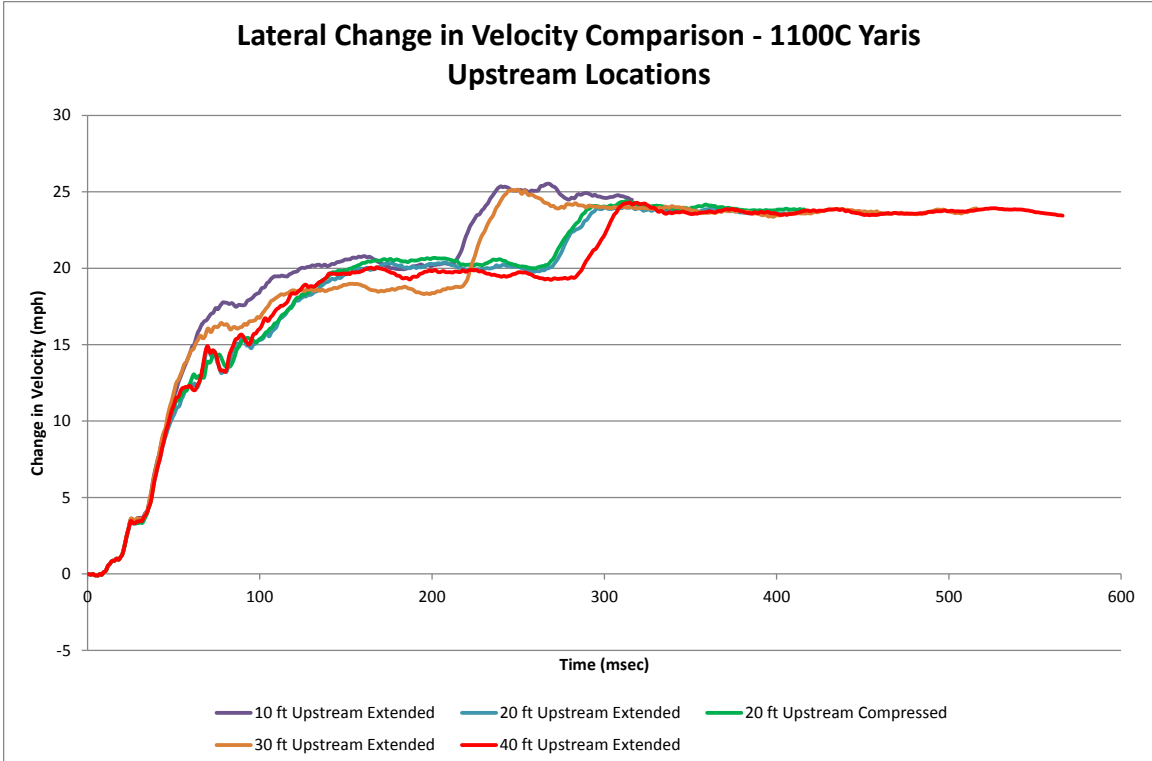


Figure 165. Lateral Change in Velocity, Upstream Impact Locations, 1100C Toyota Yaris

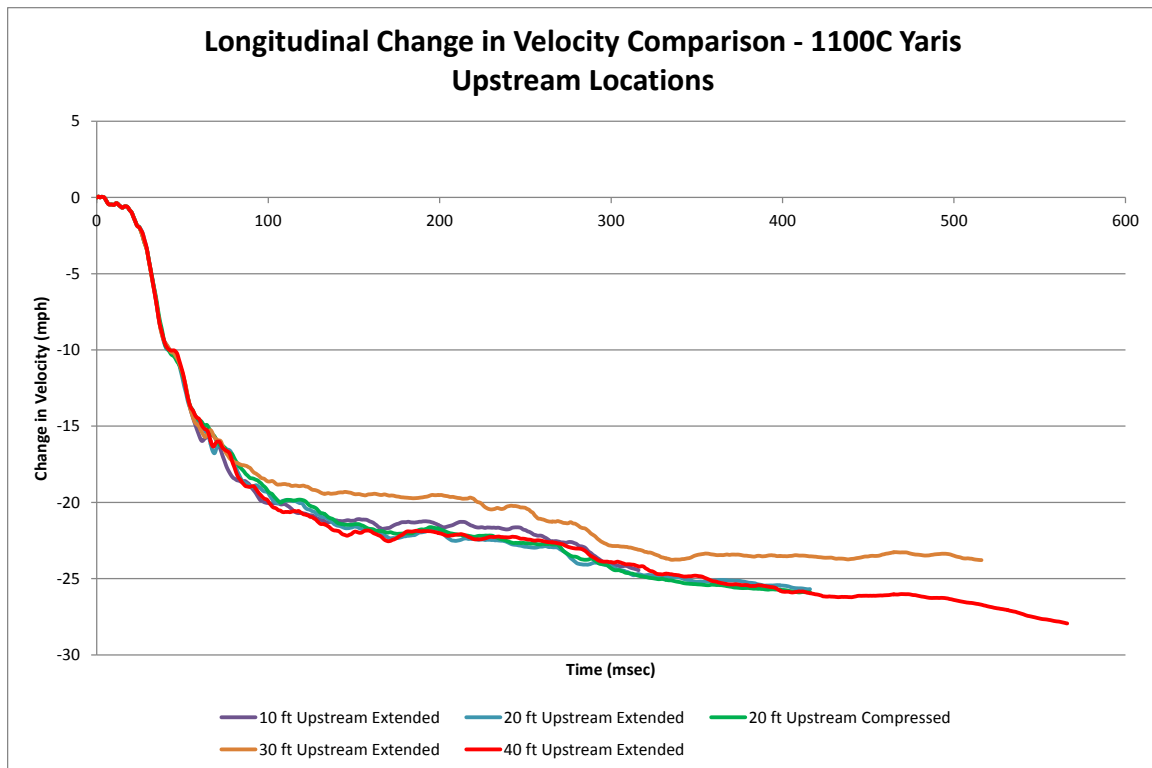


Figure 166. Longitudinal Change in Velocity, Upstream Impact Locations, 1100C Toyota Yaris

The lateral barrier impact forces were calculated using the CFC60 filtered 50-msec global Y-accelerations multiplied by the mass. The 10- and 30-ft (3.0- and 9.1-m) impact location simulations had a higher peak lateral forces of 51.8 and 49.8 kips (230 and 222 kN), respectively, as compared to the extended and compressed 20-ft (6.1-m) and extended 40-ft (12.2 m) impact location simulations of 47.6, 44.9 and 47.7 kips (212, 200, and 212 kN), respectively, as shown in Figure 167. It was expected that the lateral barrier force would increase closer to the pin due to the constraint in the lateral y-direction, which limited dynamic barrier deflection. The 10-ft (3.0-m) impact location simulation had approximately a 4 percent larger force than observed for the 30-ft (9.1-m) impact location simulation and approximately a 10 percent greater impact force than

observed for the 20- and 40-ft (6.1- and 12.2-m) impact location simulations. The tail slap for the 10- and 30-ft (3.0- and 9.1-m) impact location simulations occurred 50 msec prior to the 20- and 40-ft (6.1- and 12.2-m) location simulations.

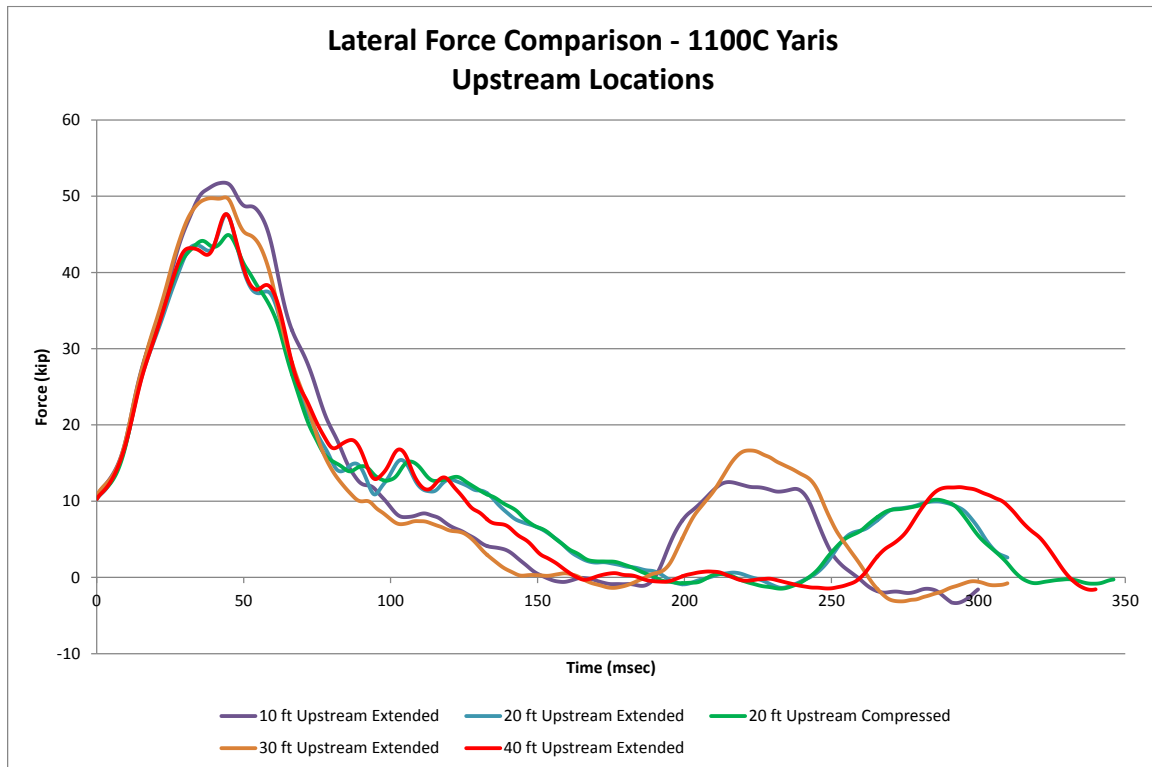


Figure 167. Lateral Force Comparison, Upstream Impact Locations, 1100C Toyota Yaris

The roll angles of the Yaris simulations at the upstream impact locations showed similar trends through approximately 50 msec. Next, the simulations at 10 and 30 ft (3.0 and 9.1 m) upstream from the pin resulted in higher peak roll angles of 8.3 and 7.9 degrees, as shown in Figure 168, respectively. The peak roll angles for the 10- and 30-ft (3.0- and 9.1-m) impact location simulations were approximately 28 percent larger than observed for the 20- and 40-ft (6.1- and 12.2-m) impact location simulations.

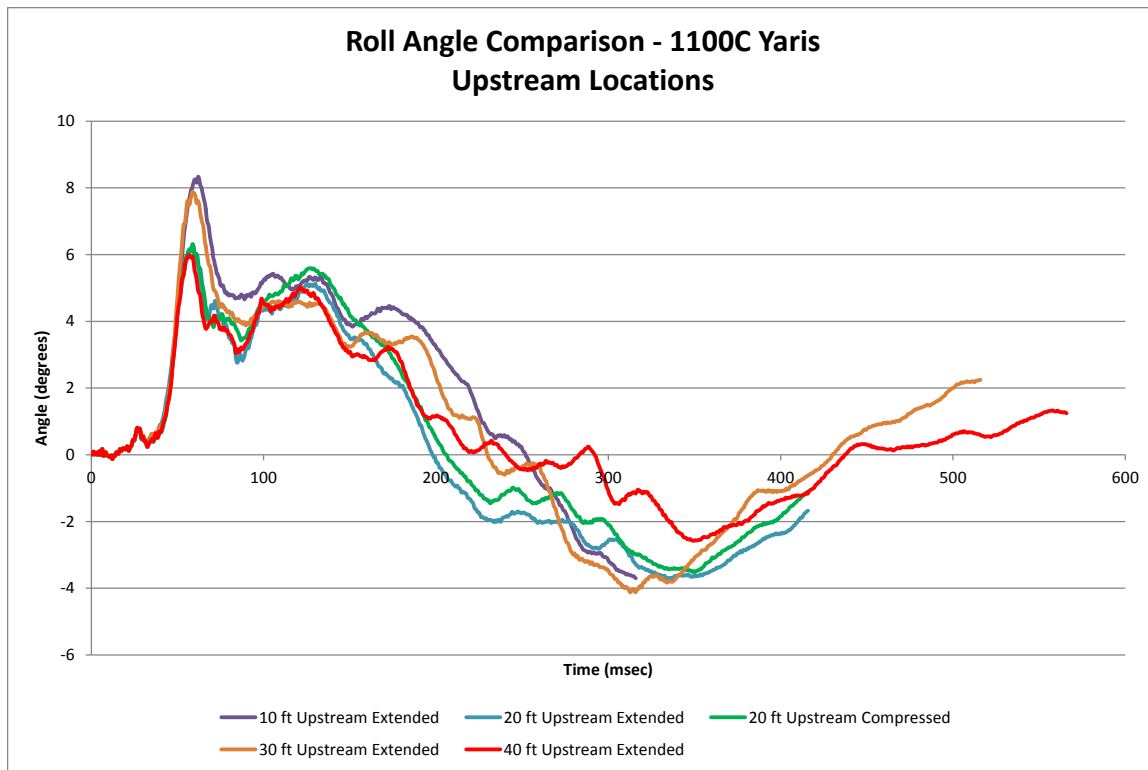


Figure 168. Vehicle Roll Comparison, Upstream Impact Locations, 1100C Toyota Yaris

The pitch angles of the Yaris simulations at each impact location were similar, as shown in Figure 169. The impact location simulations at 10 and 30 ft (3.0 and 9.1 m) upstream from the pin increased more with time, as compared to the impact location simulations at 20 and 40 ft (6.1 and 12.2 m), as shown in Figure 170. The 10-ft (3.0-m) impact location simulation yaw angle was approximately 35 percent higher than observed for the 20- and 40-ft (6.1- and 12.2-m) impact location simulations at 200 msec. The 30-ft (9.1-m) impact location simulation had a yaw angle approximately 20 percent higher than observed for the 20- and 40-ft (6.1- and 12.2-m) impact location simulations at 200 msec. However, the maximum yaw angles for all of the simulations were within 5 degrees, and they were still increasing when the simulations ended.

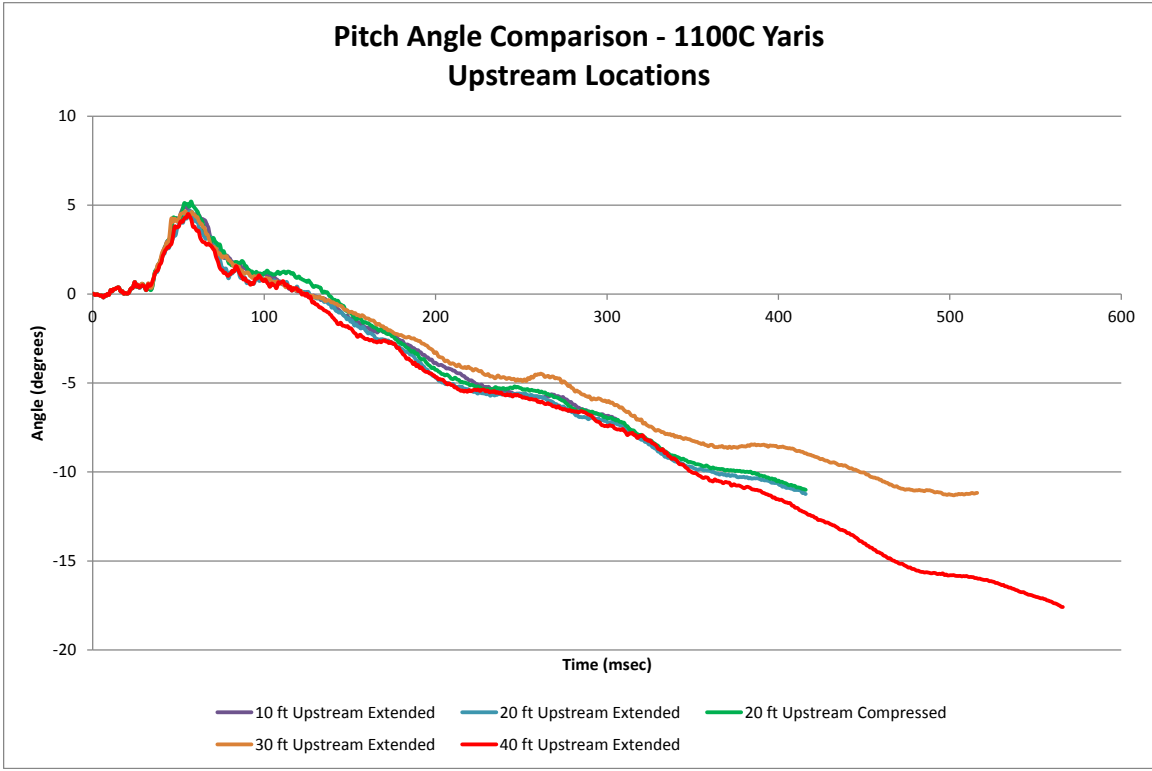


Figure 169. Vehicle Pitch Comparison, Upstream Impact Locations, 1100C Toyota Yaris

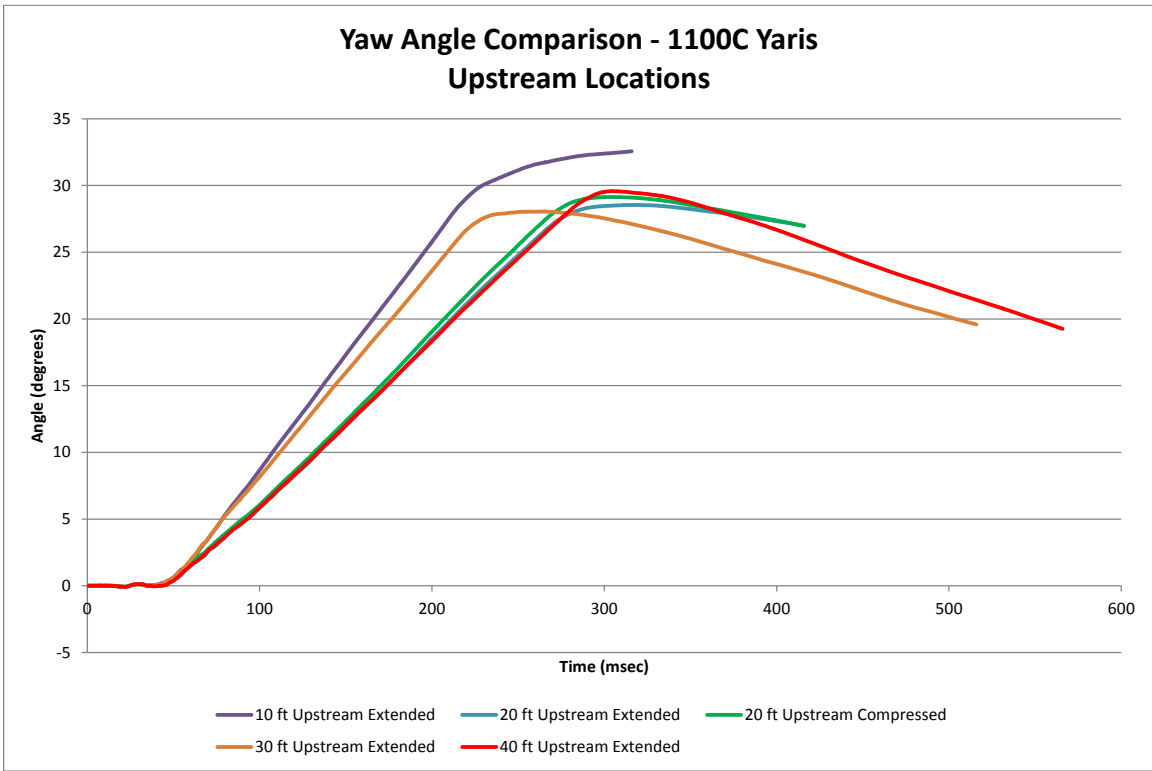


Figure 170. Vehicle Yaw Comparison, Upstream Impact Locations, 1100C Toyota Yaris

The von Mises and Tresca yield conditions were considered to evaluate the stresses within the different parts as the Yaris model impacted the system upstream from the pin and gusset plate assemblies. Each of the impact location simulations upstream from the transition hardware were compared to the interior Yaris model simulation, as noted in Chapter 4 and shown in Table 40. The interior region simulation was considered the baseline for the comparison, as the steel component did not have noticeable permanent deformation. The Yaris simulation at the interior location showed that the ACJ bolts had stresses that exceeded the Tresca yield condition, but they did not exceed the von Mises yield condition. The impact location simulations upstream from the transition hardware showed that the Tresca stresses were up to 22.3 percent greater than observed for the interior location simulation. Similarly, the von Mises stresses for the upstream impact location simulations were up to 20.7 percent greater than the interior simulation. The simulated ACJ bolts had the largest stress increases at the 20- and 40-ft (6.1- and 12.2-m) impact locations based on both the Tresca and von Mises yield conditions. However, the ACJ bolts connected two adjacent rigid barriers, not allowing the concrete to fracture which may have increased the stresses within the bolts.

Table 40. RESTORE Barrier Component Stress Comparison, 1100C Toyota Yaris, Upstream Locations

Simulation Parameters			Impact Location and Trial No.					
			NA	53	54	66	55	56
ACJ Bolts	Max. Tresca Stress	Stress, ksi (MPa)	Interior Model	10 ft Upstream Extended	20 ft Upstream Extended	20 ft Upstream Compressed	30 ft Upstream Extended	40 ft Upstream Extended
		57.0 (393)	57.1 (394)	68.3 (471)	69.7 (480)	55.1 (380)	62.5 (431)	
		$\tau \geq 0.5\sigma_y$?	Yes	Yes	Yes	Yes	Yes	Yes
	% Different Than Interior	NA	0.3	19.9	22.3	-3.2	9.8	
	Max. von Mises Stress	Stress, ksi (MPa)	103.9 (0.737)	117.6 (0.811)	129.1 (0.890)	120.7 (0.832)	108.8 (0.750)	126.8 (0.874)
		$\sigma_{vm} \geq \sigma_y$?	No	Yes	Yes	Yes	Yes	Yes
% Different Than Interior		NA	10	20.7	12.9	1.8	18.6	

11.3.2 Neon Vehicle Model

The comparison of results for the Neon vehicle model between the simulations at upstream impact locations is shown in Table 41. The simulations at each impact point successfully contained and redirected the Neon model, as shown in Figures 171 through 174. The simulation end times were different, but all of the desired information was obtained through each simulation. However, the Dodge Neon model showed post-tire interaction in the simulation with the impact location 20 ft (6.1 m) upstream from the pin and gusset plate configuration when the joint was extended, which caused the simulation to become unstable. Due to the model instability, the vehicle did not reach parallel, and several results in Table 41 could not be obtained. The post and tire contact problem that occurred is shown in Figure 175.

Another simulation in which the Neon vehicle model impacted 20 ft (6.1 m) upstream from the pin was simulated with the fully compressed joint, instead of the extended joint. During the impact with the compressed joint, the Neon model did not contact any posts, and the simulation successfully ran. Similarly, the other impact location simulations upstream from the pin did not show any post-tire interaction.

The simulation at 20 ft (6.1 m) upstream from the pin with the compressed joint caused the vehicle to snag on the upstream face of the RESTORE barrier, just downstream from impact. The slight vehicle snag on the joint caused the vehicle to exit the system before becoming parallel to the system. Thus, the exit velocity for that impact location simulation was slightly larger than the parallel velocity.

The Neon vehicle model did not have many significant differences in damage between the upstream impact location simulations and the interior impact location

simulation. The main difference between the vehicle model damage was concentrated on the left-front corner of the vehicle, where the upstream impact location simulations experienced slightly more crush and the wheel assembly appeared experience further detachment from the vehicle body. However, the wheel suspension failure was not enabled, so wheel damage may not be predictive of actual damage.

Table 41. Comparison Matrix of Upstream Impact Locations, 1100C Dodge Neon

Simulation Parameters		Impact Location and Trial No.				
		49	50	65	51	52
		10 ft Upstream Extended ²	20 ft Upstream Extended ²	20 ft Upstream Compressed ²	30 ft Upstream Extended ²	40 ft Upstream Extended ²
End Time, msec		301	185	401	460	551
Parallel Conditions	Time, ms	220	NA	344	254	338
	Velocity, mph (km/h)	41.0 (66.0)	NA	35.3 (56.8)	40.1 (64.5)	36.7 (59.0)
Exit Conditions	Velocity, mph (km/h)	39.7 (63.9)	NA	35.6 (57.2)	38.9 (62.6)	35.9 (57.7)
	Angle, deg.	3.6	NA	-2.2	0.6	1.2
	Time, ms	252	NA	302	312	372
Length of Contact		8 ft - 10 in. (2.7 m)	NA	16 ft - 9 in. (5.1 m)	18 ft - 8 in. (5.7 m)	16 ft - 8 in. (4.9 m)
t*, ms		75.7	81.0	82.1	76.7	82.3
ORA, g's	Longitudinal	-4.28	NA	-10.49	-7.71	-9.29
	Lateral	8.30	NA	10.11	8.99	8.44
OIV, ft/s (m/s)	Longitudinal	-25.20 (-7.69)	-26.84 (-8.18)	-26.87 (-8.19)	-24.74 (-7.54)	-27.58 (-8.41)
	Lateral	29.63 (9.03)	25.61 (7.80)	25.02 (7.62)	27.38 (8.35)	26.21 (7.99)
Test Article Deflections, in. (mm)	Dynamic of Concrete	5.6 (142)	10.0 (254)	10.2 (259)	6.8 (173)	9.2 (234)
	Dynamic of Steel Rail	5.8 (147)	10.3 (262)	10.5 (267)	7.2 (183)	9.6 (244)
	Working Width	27.9 (709)	32.3 (820)	32.5 (826)	29.1 (739)	31.5 (800)
Location of Max. Deflection Upstream from Pin		20 ft (6.1 m)	20 ft (6.1 m)	20 ft (6.1 m)	20 ft (6.1 m)	40 ft (12.1 m)
Vehicle Stability	Max. Roll, deg.	4.8	5.5*	4.9	-4.9	-4.9
	Max. Pitch, deg.	-2.8	-3.6*	-4.4	-5.4	-5.4
	Max. Yaw, deg.	29.4	17.3*	29.7	26.6	26.6
Posts Hit by Leading Tire (wheel snag)		0	2	0	0	0
Max. Lateral Impact Force, kips (kN) ¹		49.4 (219.6)	41.4 (184.2)	40.0 (177.7)	46.4 (206.4)	39.2 (174.4)

*These values are only accurate through 184.8 msec

¹ Calculated using global Y-acceleration multiplied by mass.

² Impacted 3 ft – 7 in. (1.1 m) upstream from noted location.

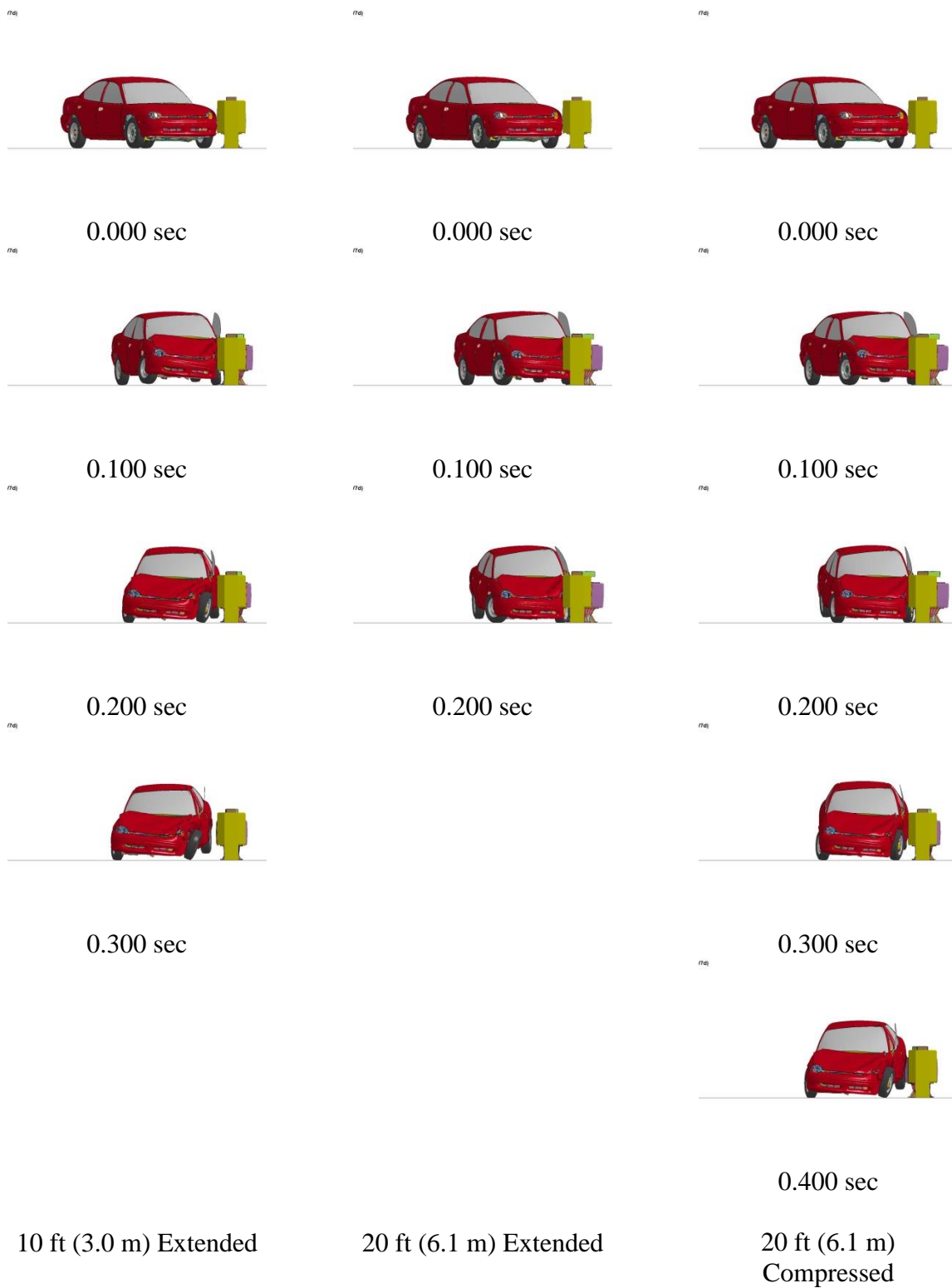


Figure 171. RESTORE Barrier Transition, 1100C Neon Simulation Comparison, Upstream Impact Locations, Downstream View

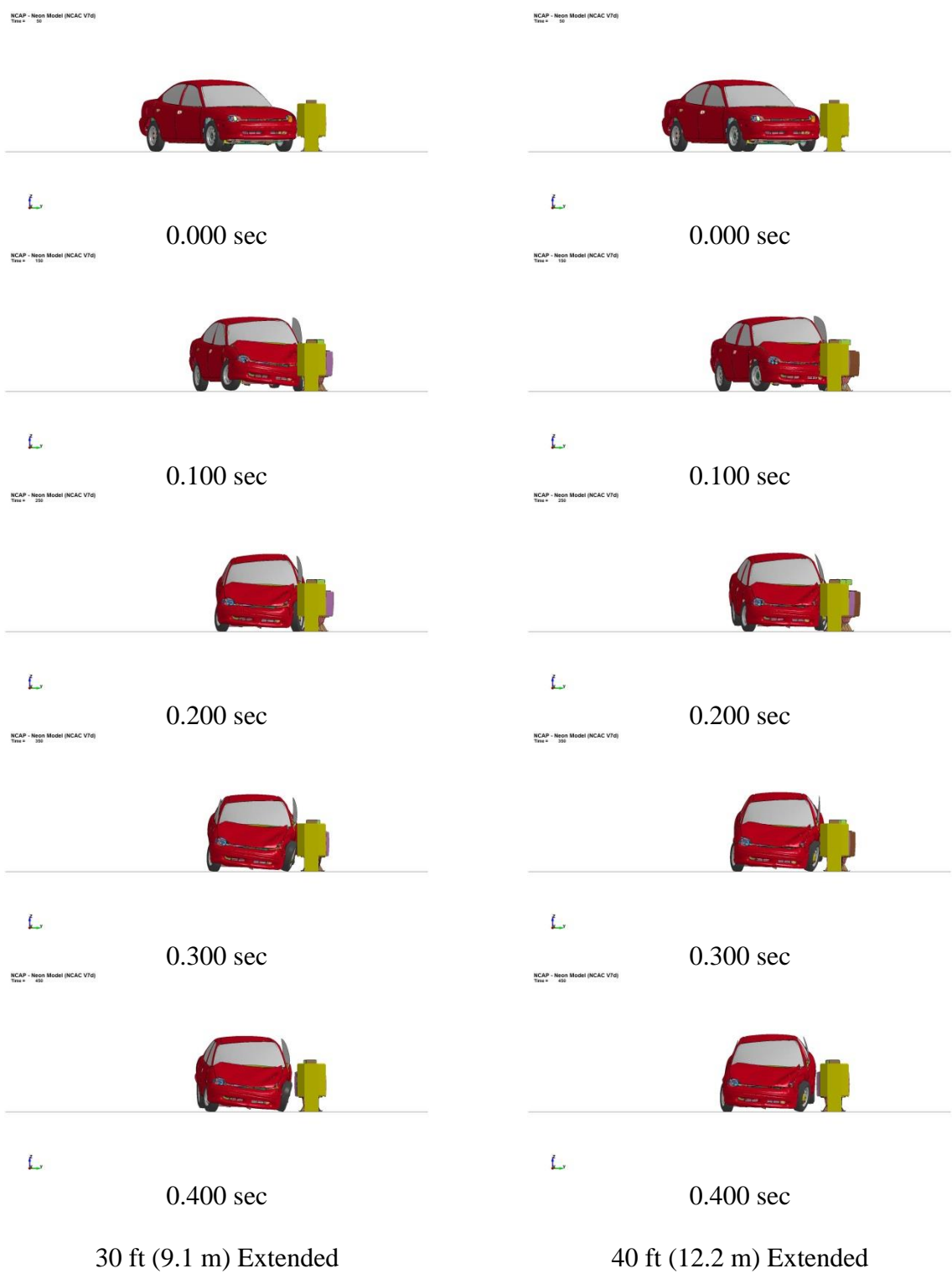


Figure 172. RESTORE Barrier Transition, 1100C Neon Simulation Comparison, Upstream Impact Locations, Downstream View

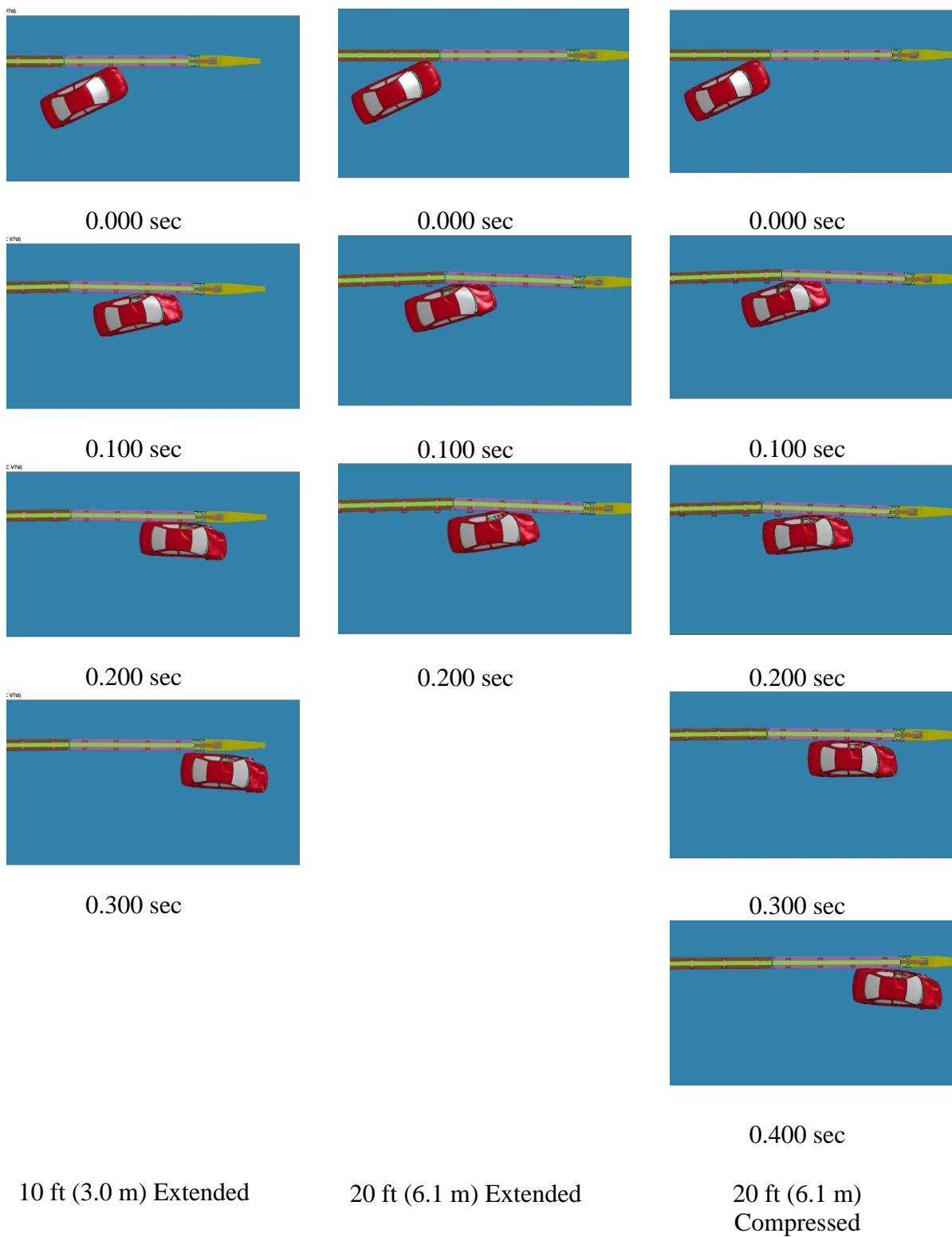


Figure 173. RESTORE Barrier Transition, 1100C Neon Simulation Comparison, Upstream Impact Locations, Overhead View

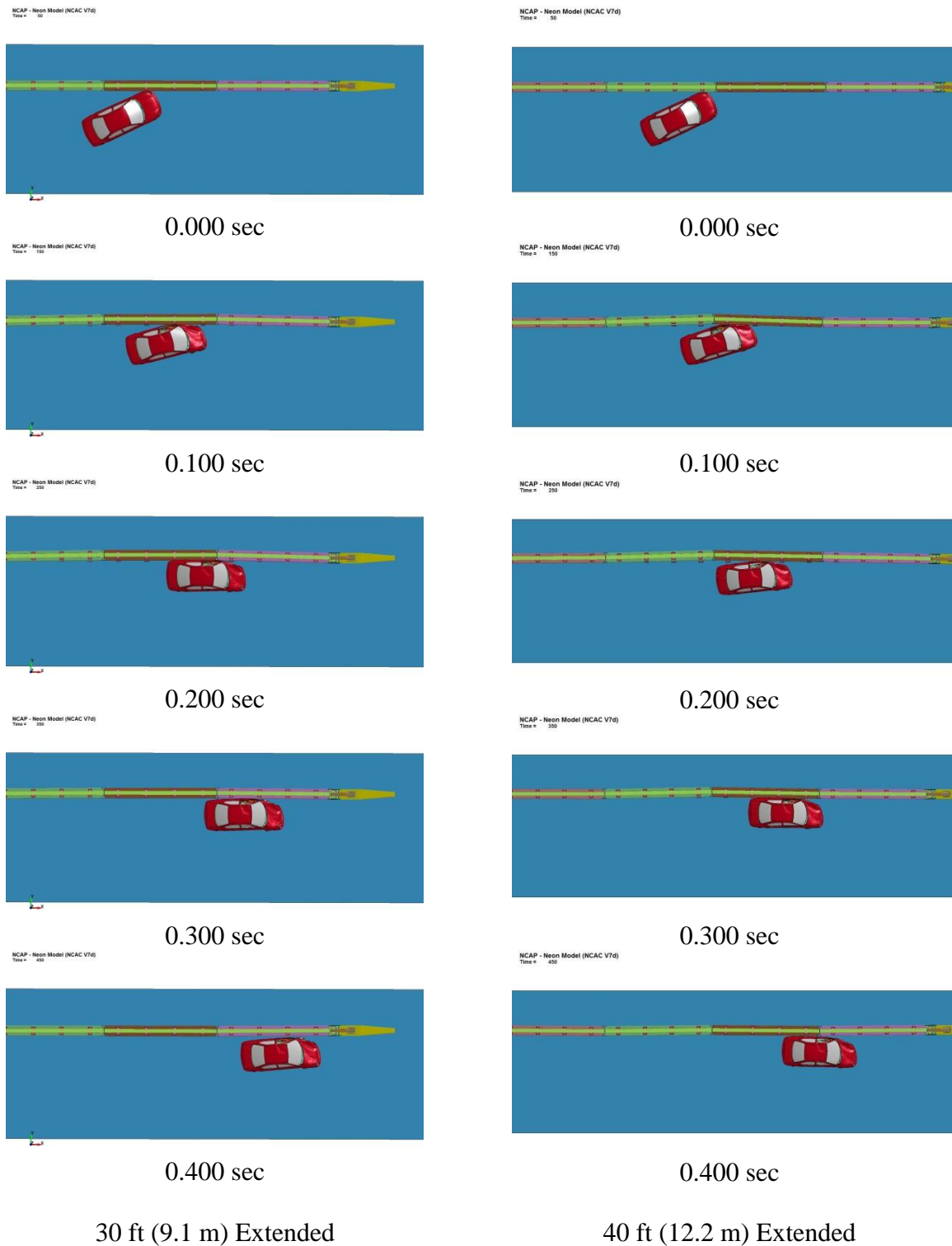


Figure 174. RESTORE Barrier Transition, 1100C Neon Simulation Comparison, Upstream Impact Locations, Overhead View

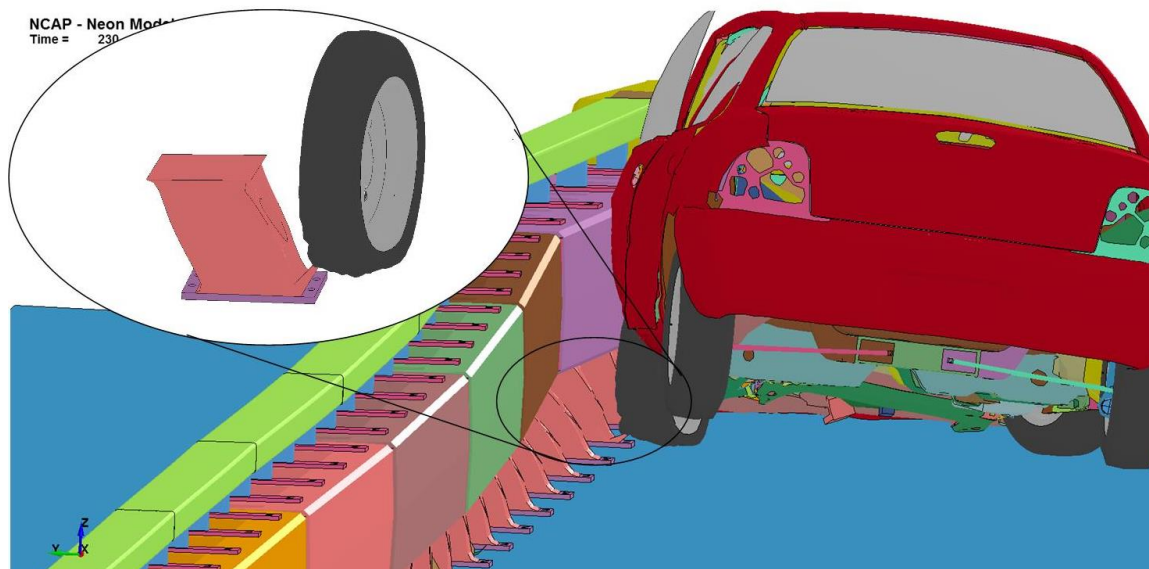


Figure 175. Rubber-on-Rubber Contact Issue

The simulation barrier deflections at each impact location showed a trend where the deflections increased as the impact occurred farther upstream from the pin. However, the maximum dynamic deflection was greatest in the 20-ft (6.1-m) impact location simulation. The simulation at the 20-ft (6.1-m) impact location showed a 25 percent larger deflection than observed in the simulation at the interior location. The larger deflections were likely caused by the presence of a nearby hinge or pin, ACJ widening at 20 ft (6.1 m), and preventing the distribution of load across multiple barrier segments, thus, changing the constraints of the system limited the transfer of the impact force, causing an increase at the 20 ft (6.1 m) impact location simulation.

The lateral change in velocity between of the impact location simulations followed a similar trend. However, the lateral change in velocity for the simulations for 10 and 30 ft (3.0 and 9.1 m) upstream from the pin were greater through 100 msec than the simulations for 20 and 40 ft (6.1 and 12.2 m) upstream from the pin, as shown in Figure 176. The longitudinal velocity for the simulations for 10 and 30 ft (3.0 and 9.1 m)

upstream from the pin did not decrease as rapidly as observed for the 20- and 40-ft (6.1- and 12.2-m) simulation locations, as shown in Figure 177. The greater longitudinal change in velocity for the 20- and 40-ft (6.1- and 12.2-m) impact location simulations could be contributed to the larger dynamic deflections experienced at those locations. Note the simulation for 20 ft (6.1 m) upstream from the pin with the extended joint had a large change in the longitudinal velocity starting at approximately 175 msec and, then the simulation became unstable and terminated. The change in longitudinal velocity was contributed to the rubber-on-rubber contact noted earlier. The lateral and longitudinal OIV values were similar between the different impact location simulations. The longitudinal ORA values were smaller during the simulations 10 and 30 ft (3.0 and 9.1 m) upstream from the pin, which may have been due to the impact at the midspan of the barrier segments where there was no joint for which the vehicle could snag. The lateral ORA values were similar, with the exception of the simulation 20 ft (6.1 m) upstream of the pin with compressed joint. The lateral ORA value was approximately 12 percent greater than observed for the other impact location simulations.

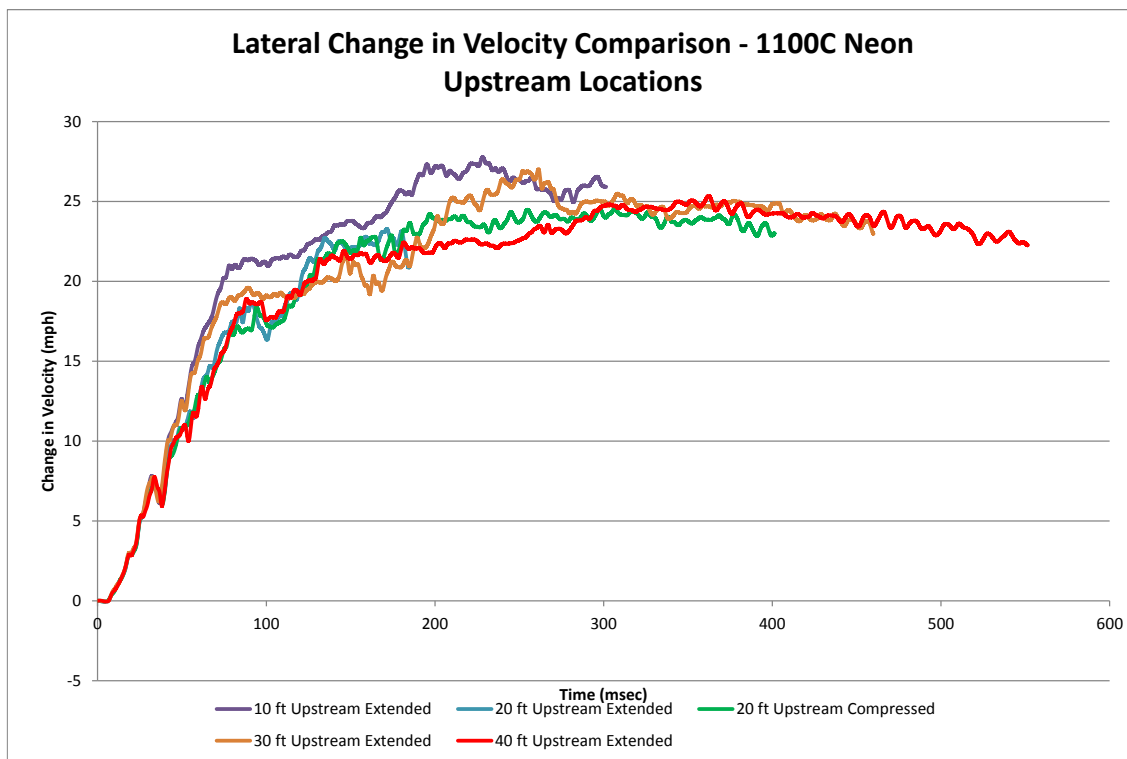


Figure 176. Lateral Change in Velocity, Upstream Impact Locations, 1100C Dodge Neon

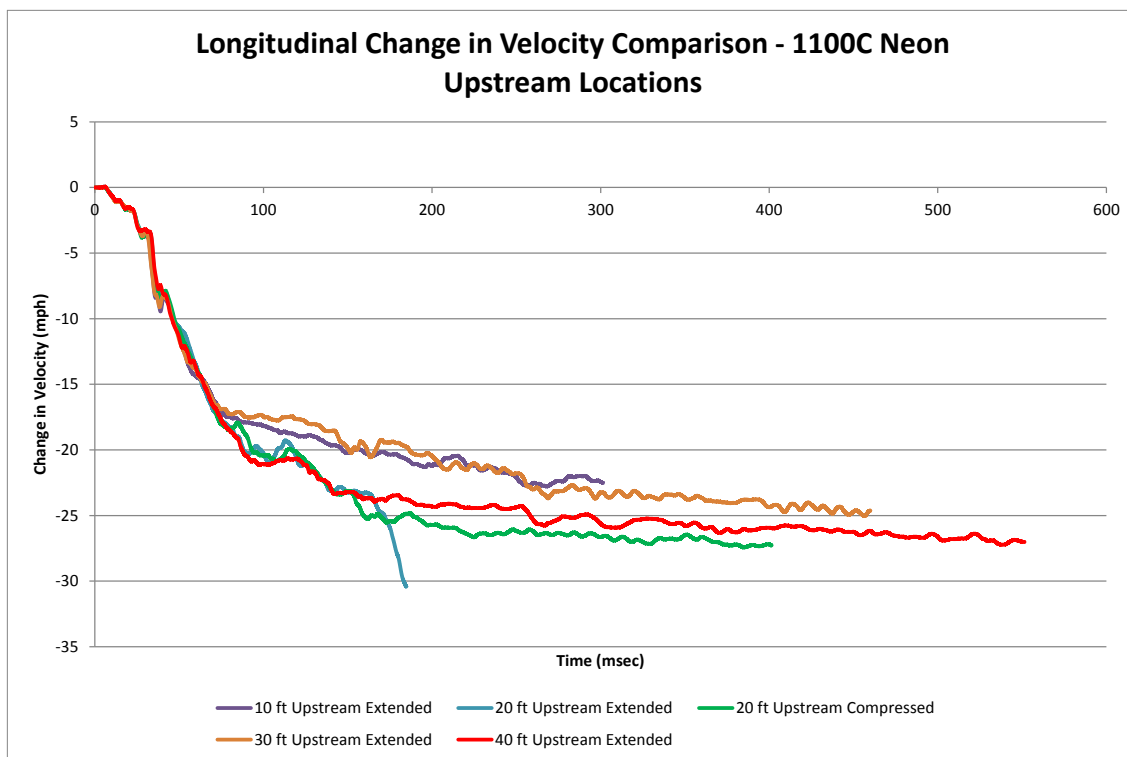


Figure 177. Longitudinal Change in Velocity, Upstream Impact Locations, 1100C Dodge Neon

The lateral barrier impact forces were calculated using the CFC60 filtered 50-msec global Y-accelerations multiplied by the mass. The simulations at 10 and 30 ft (3.0 and 9.1 m) upstream from the pin showed a higher peak lateral force as compared to the simulations for 20 and 40 ft (6.1 and 12.2 m) upstream from the pin, as shown in Figure 178. It was expected that there would be an increase in the lateral barrier force closer to the pin due to the constraints in the lateral y-direction decreasing the dynamic barrier deflections. The 10-ft (3.0-m) impact location simulation had approximately a 10 percent larger force than observed for the 30-ft (9.1-m) impact location simulation and approximately a 20 percent greater impact force than observed for the 20- and 40-ft (6.1- and 12.2-m) impact location simulations.

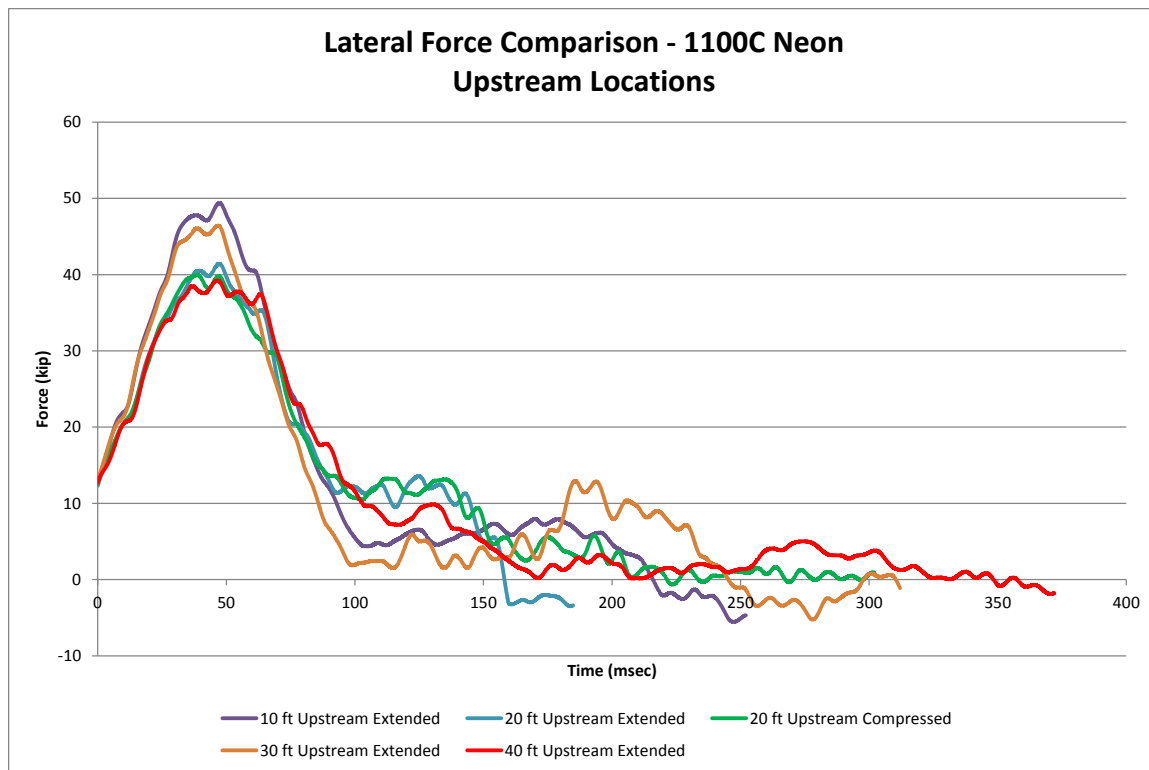


Figure 178. Lateral Force Comparison, Upstream Impact Locations, 1100C Dodge Neon

The roll and pitch of the Neon model at each impact location showed similar angles through approximately 50 msec, as shown in Figures 179 and 180, respectively. The roll angles during the simulations at each impact location experienced up to a 9.0 degree change in roll between 40 and 50 msec. At 120 msec, the roll angles for the simulations at 10 and 30 ft (3.0 and 9.1 m) upstream from the pin were approximately 50 percent less than the roll angles observed for the simulations for 20 and 40 ft (6.1 and 12.2 m) upstream from the pin. The trend was opposite for the pitch angles where the angles for the simulations 20 and 40 ft (6.1 and 12.2 m) upstream from the pin were approximately 50 percent less than the simulations for 10 and 30 ft (3.0 and 9.1 m) upstream from the pin at approximately 100 msec.

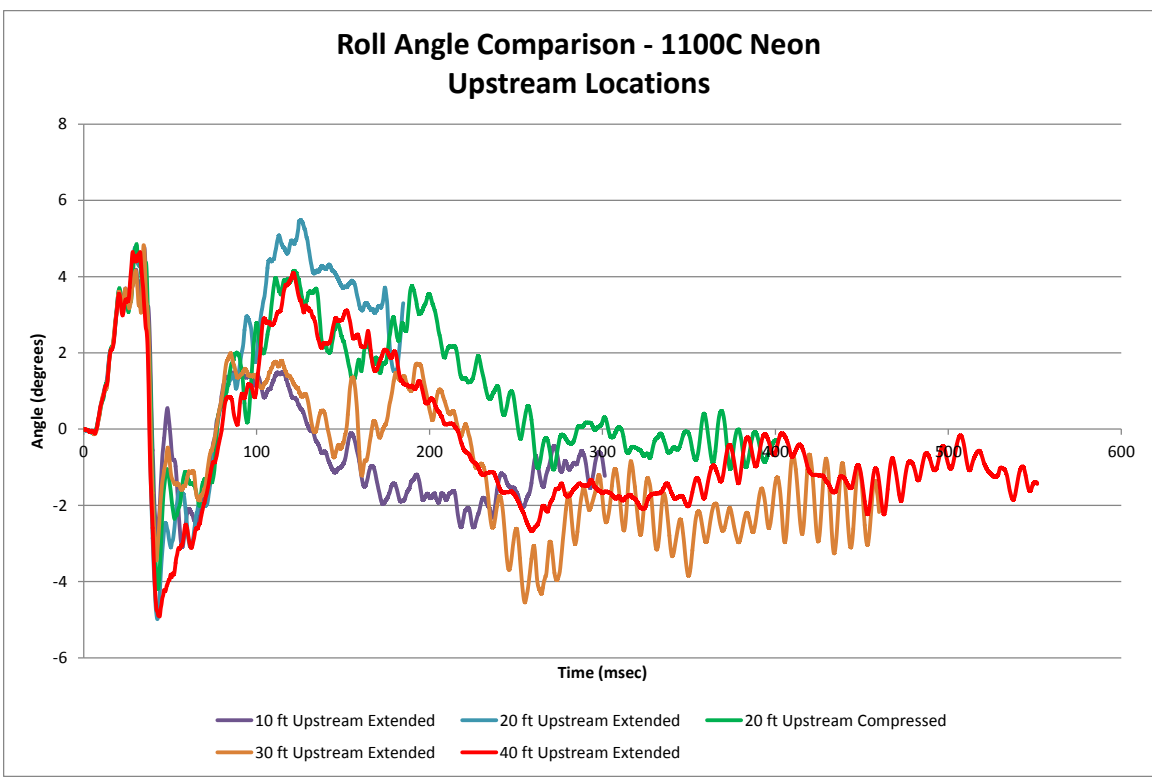


Figure 179. Vehicle Roll Comparison, Upstream Impact Locations, 1100C Dodge Neon

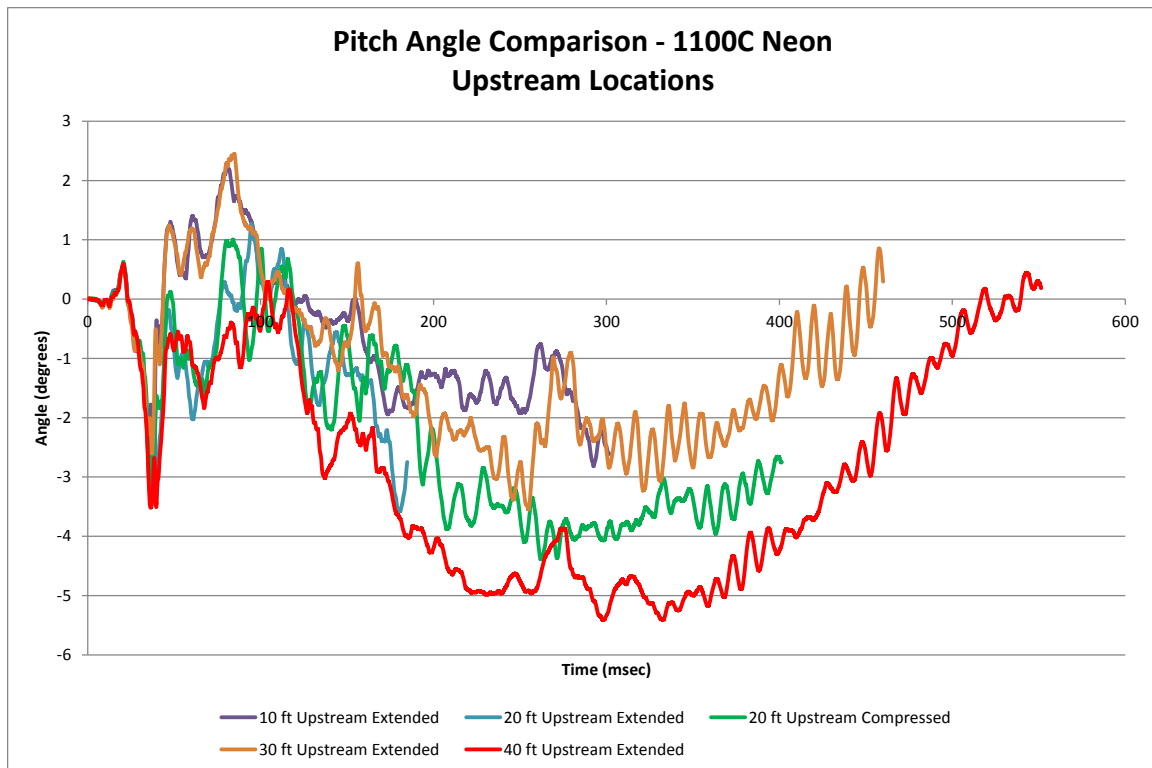


Figure 180. Vehicle Pitch Comparison, Upstream Impact Locations, 1100C Dodge Neon

The simulations for 10 and 30 ft (3.0 and 9.1 m) upstream from the pin showed a faster change in yaw angle as compared to the simulations at 20 and 40 ft (6.1 and 12.2 m), as shown in Figure 181. The yaw angle for the simulation at 10 ft (3.0 m) upstream from the pin was approximately 40 percent higher than observed in the simulation at 20 and 40 ft (6.1 and 12.2 m) upstream from the pin at 200 msec. The 30-ft (9.1-m) impact location simulation had a yaw angle approximately 32 percent higher than observed for the 20- and 40-ft (6.1- and 12.2-m) impact location simulations at 200 msec. However, the maximum yaw angles for all of the impact location simulations were within 5 degrees.

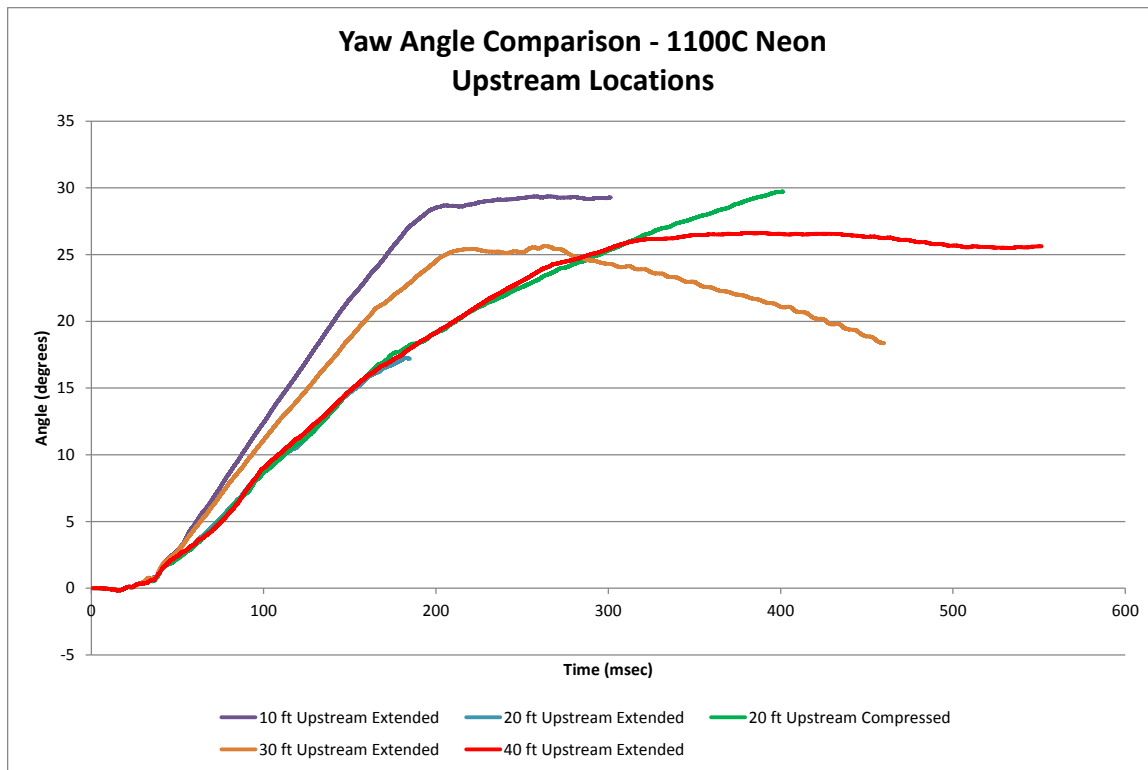


Figure 181. Vehicle Yaw Comparison, Upstream Impact Locations, 1100C Dodge Neon

The von Mises and Tresca yield conditions were considered to evaluate the stresses within the parts of the pin and gusset plate assemblies. Each simulation with impact locations upstream from the transition hardware were compared to the interior Neon simulation, as noted in Chapter 4 and shown in Table 42. The interior simulation was considered the baseline, as the barrier components did not have noticeable permanent deformations. The Neon simulation at the interior location showed that the ACJ bolts had peak stresses that exceeded the Tresca yield condition, but they did not exceed the von Mises yield condition. The impact location simulations upstream from the transition hardware showed Tresca stresses that were up to 26.1 percent greater than the interior location simulation. Similarly, the von Mises stresses for the upstream impact location simulations were up to 19.7 percent greater than the interior simulation. However, the

ACJ bolts connected two adjacent rigid barriers, not allowing the concrete to fracture which may have increased the stresses within the bolts.

The top tube and tube connections had stresses exceeding both the Tresca and von Mises yield conditions during the interior simulation impact event. Note the stresses presented were the maximum stresses for the top tube and tube splice connection. The maximum von Mises stress was 62.4 ksi (430 MPa) during the interior simulation, which was the yield stress of the tube material. Most of the upstream impact location simulations did not negatively affect the stresses in the top tube. The simulations at the 20-ft (6.1-m) impact location upstream from the pin with the compressed joint had the largest maximum stress difference of 7.6 percent. The other impact location simulations had lower maximum stresses within the top tube at the upstream locations.

Table 42. RESTORE Barrier Component Stress Comparison, 1100C Dodge Neon, Upstream Locations

Simulation Parameters			Impact Location and Trial No.					
			NA	49	50	65	51	52
			Interior Model	10 ft Upstream Extended	20 ft Upstream Extended	20 ft Upstream Compressed	30 ft Upstream Extended	40 ft Upstream Extended
ACJ Bolts	Max. Tresca Stress	Stress, ksi (MPa)	56.1 (387)	56.4 (389)	69.3 (478)	70.7 (488)	58.5 (403)	60.7 (418)
		$\tau \geq 0.5\sigma_y$?	Yes	Yes	Yes	Yes	Yes	Yes
		% Different Than Interior	NA	0.6	23.6	26.1	4.3	8.2
	Max. von Mises Stress	Stress, ksi (MPa)	104.8 (723)	116.6 (804)	125.8 (867)	123.9 (855)	112.4 (775)	128.0 (883)
		$\sigma_{vm} \geq \sigma_y$?	No	Yes	Yes	Yes	Yes	Yes
		% Different Than Interior	NA	9.0	17.6	15.9	5.1	19.7
Top Tube and Tube Splice	Max. Tresca Stress	Stress, ksi (MPa)	36.0 (248)	33.5 (231)	36.7 (253)	37.1 (256)	35.3 (243)	35.8 (247)
		$\tau \geq 0.5\sigma_y$?	Yes	Yes	Yes	Yes	Yes	Yes
		% Different Than Interior	NA	-6.9	2.1	3.3	-1.9	-0.6
	Max. von Mises Stress	Stress, ksi (MPa)	62.4 (430)	58.0 (400)	65.0 (0.449)	67.2 (463)	62.4 (430)	62.0 (427)
		$\sigma_{vm} \geq \sigma_y$?	Yes	No	Yes	Yes	Yes	No
		% Different Than Interior	NA	-7.1	4.2	7.6	0.0	-0.7

11.4 Reverse-Direction Impact Location Simulation Results

Simulations of impact points in the reverse direction were performed at the slope-break point of the rigid concrete buttress while traveling toward the RESTORE barrier as well as 3 ft – 7 in. (1.1 m) upstream from the upstream corner of the cover plate. These locations were evaluated with the joint extended to investigate vehicle snag and excessive

OIVs and ORAs. Prior MASH testing on a concrete barrier with a horizontal flare rate of 6:1 over the full height has never been conducted. Therefore, a simulation effort was conducted to evaluate an impact at the horizontal slope-break point.

11.4.1 Yaris Vehicle Model

The comparison of results for the Yaris model in simulations under reverse-direction locations is shown in Table 43. The simulations at each impact point successfully contained and redirected the Yaris model, as shown in Figures 182 and 183. The simulations had varying end times. However, all of the desired information was obtained. The stresses within the transition hardware were acceptable and are not reported herein.

The left-front of the Yaris model had significantly more inward crush during the reverse-direction simulations at the slope-break point and CIP location as compared to the simulations at interior and upstream locations. The top of the left-front door separated farther away from the vehicle during impacts in the reverse direction. The increase in damage of the Yaris model was expected as the buttress was stiffer than the RESTORE barrier and transition region.

Table 43. Comparison Matrix of Reverse-Direction Locations, 1100C Toyota Yaris

Simulation Parameters		Impact Location and Trial No.	
		38	62
		Reverse-Direction Slope-Break Point	Reverse-Direction CIP ³
End Time, ms		453	366
Parallel Conditions	Time, ms	230	225
	Velocity, mph (km/h)	35.8 (57.6)	40.4 (65.0)
Exit Conditions	Velocity, mph (km/h)	36.9 (59.4)	39.1 (62.9)
	Angle, deg.	-7.3	5.9
	Time, ms	140	270
Length of Contact		8 ft - 0 in. (2.4 m)	9 ft - 0 in. (2.7 m)
t*, ms		72.4	78.3
ORA, g's	Longitudinal	-6.13	-5.38
	Lateral	3.98	11.68
OIV, ft/s (m/s)	Longitudinal	-31.82 (-9.70)	-27.28 (-8.32)
	Lateral	31.86 (9.71)	28.19 (8.59)
Test Article Deflections, in. (mm)	Dynamic of Concrete	0.5 (13)	0.6 (15)
	Dynamic of Steel Rail	0.4 (10)	0.4 (10)
	Working Width	22.8 (579)	22.9 (582)
Location of Max. Deflection Upstream from Pin		0 ft (0 m)	0 ft (0 m)
Vehicle Stability	Max. Roll, deg.	9.1	8.1
	Max. Pitch, deg.	6.9	-8.7
	Max. Yaw, deg.	50.1	31.9
Posts Hit by Leading Tire (wheel snag)		0	0
Max. Lateral Impact Force, kips (kN) ¹		68.4 (304.3)	56.6 (251.6)
Max. Longitudinal Impact Force, kips (kN) ²		26.6 (118.3)	20.6 (91.6)

¹ Calculated using global Y-acceleration multiplied by mass.

² Calculated using local X- and Y- accelerations coupled with yaw, multiplied by mass.

³ Impacted 3 ft – 7 in. (1.1 m) upstream from cover plate edge.



Figure 182. RESTORE Barrier Transition, 1100C Yaris Simulation Comparison, Reverse-Direction Locations, Downstream View

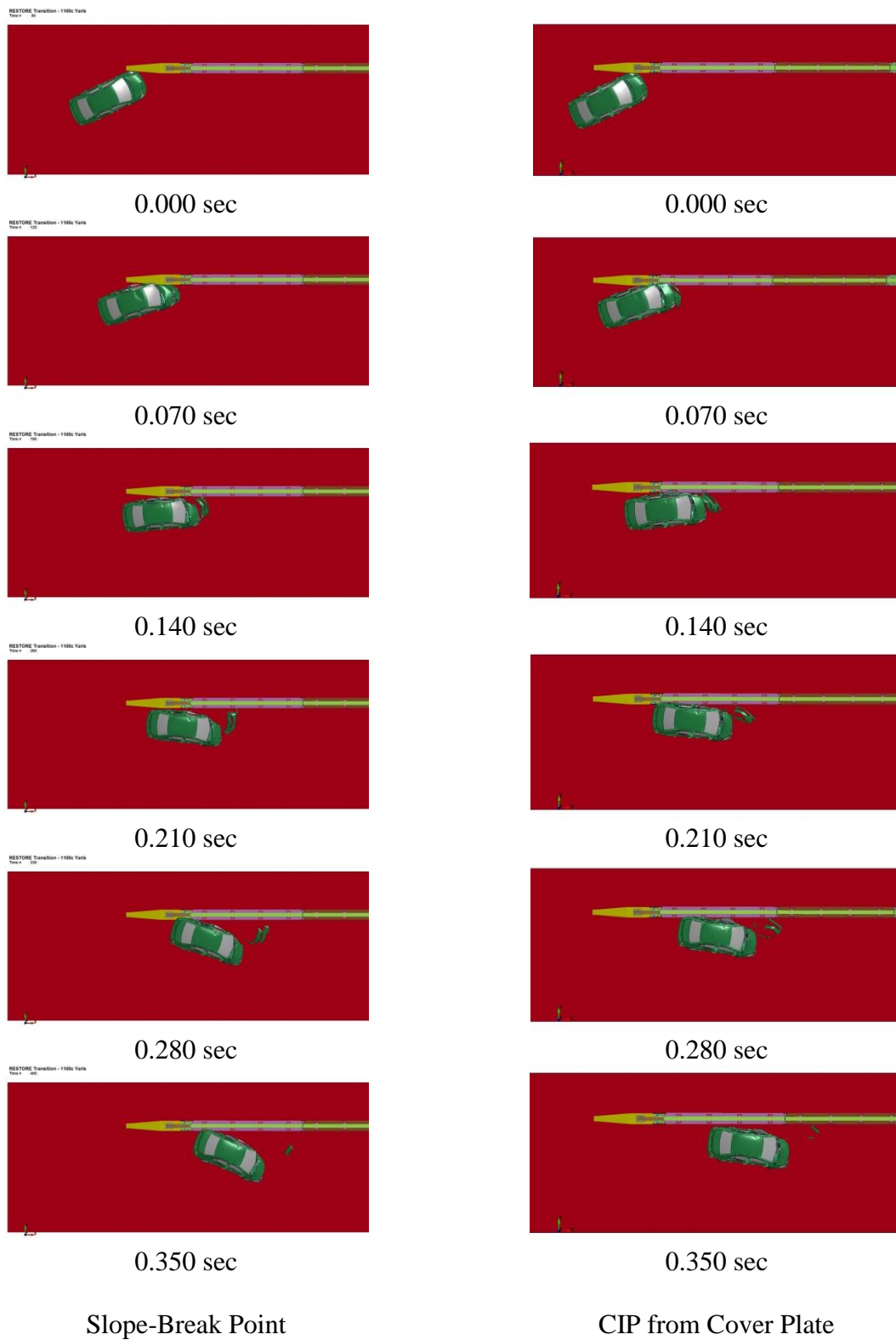


Figure 183. RESTORE Barrier Transition, 1100C Yaris Simulation Comparison, Reverse-Direction Locations, Overhead View

Since all degrees of freedom in the rigid concrete buttress were constrained, the buttress did not have any damage nor deflections. However, the upstream end of the RESTORE barrier dynamically deflected 0.6 in. (15 mm) during the simulation at the CIP location upstream from the cover plate corner. Similarly, the upstream end of the RESTORE barrier dynamically deflected 0.5 in. (13 mm) during the impact located at the slope-break point.

The lateral change in velocity in simulations into the two reverse-direction impact locations were similar over the first 50 msec, as shown in Figure 184. The plateau that was observed with the slope-break impact location simulation was due to the vehicle model losing contact with the system. The change in lateral velocity at approximately 200 msec for the Yaris model that impacted the CIP location was due to the vehicle re-contacting the system. Similarly, the longitudinal change in velocity was greater for the simulation at the slope-break impact location as compared to the CIP location, as shown in Figure 185. The longitudinal velocity was similar for both impact location simulations through 50 msec. However, the longitudinal change in velocity was 20 percent greater than observed for the impact at the CIP location at 100 msec for the Yaris model at the slope-break point.

The simulated lateral and longitudinal OIVs were 14.3 and 11.5 percent greater for the slope-break point location as compared to the CIP location. However, the lateral ORA value for the CIP location simulation was 65.9 percent larger than observed for the slope-break point location. The occupant risk values were expected to increase as a rigid barrier was impacted. Each of the values were within the MASH limits.

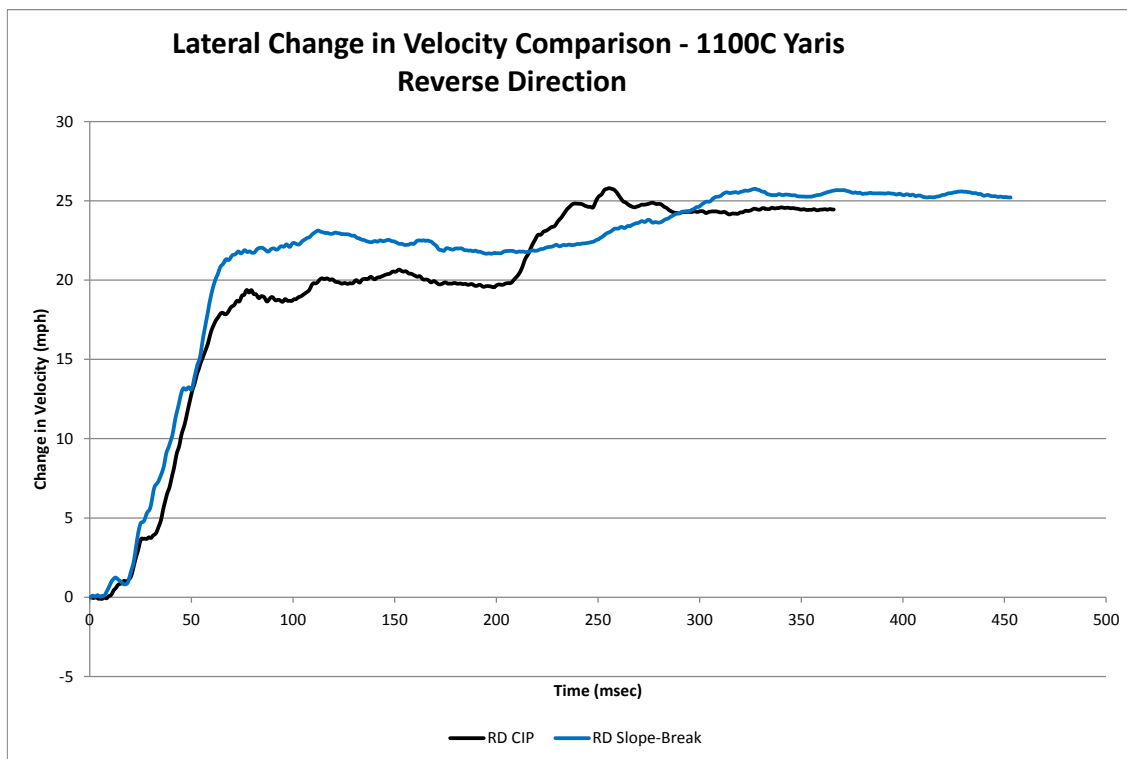


Figure 184. Lateral Change in Velocity, Reverse-Direction Locations, 1100C Toyota Yaris

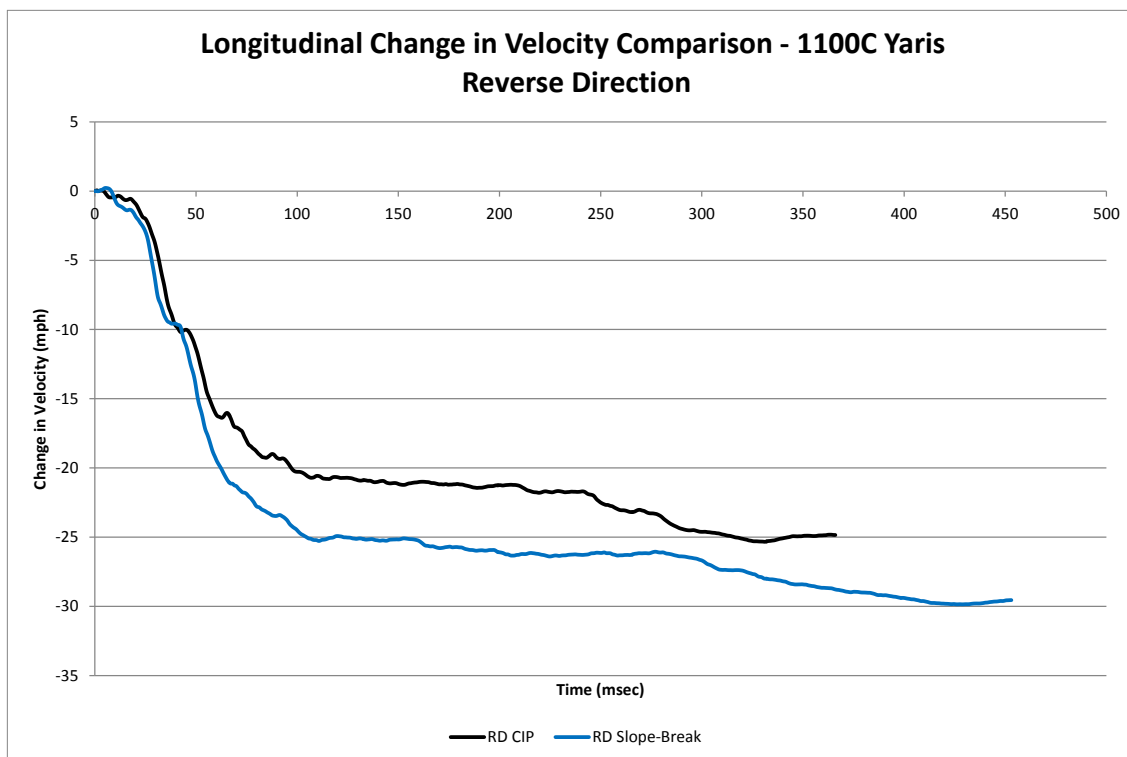


Figure 185. Longitudinal Change in Velocity, Reverse-Direction Locations, 1100C Toyota Yaris

The lateral impact forces were calculated using the CFC60 filtered 50-msec global Y-accelerations multiplied by the mass. Each of the simulations impacted the rigid concrete buttress. The slope-break point simulation experienced a 17 percent higher maximum lateral impact force, as shown in Figure 186. After the peak force was reached, the two impact location simulations exhibited similar forces through 150 msec. During the simulation at the CIP location, a 10-kip (445-kN) higher load occurred during the tail slap as compared to the slope-break simulation. The longitudinal impact force was calculated using the local X- and Y-accelerations coupled with the yaw angle and multiplied by the mass of the vehicle model. The simulation that impacted the slope-break point experienced a 23 percent higher maximum longitudinal impact force than observed for the CIP location simulation, as shown in Figure 187. The simulation at the slope-break point exited the system at approximately 140 msec and recontacted the buttress around 200 msec.

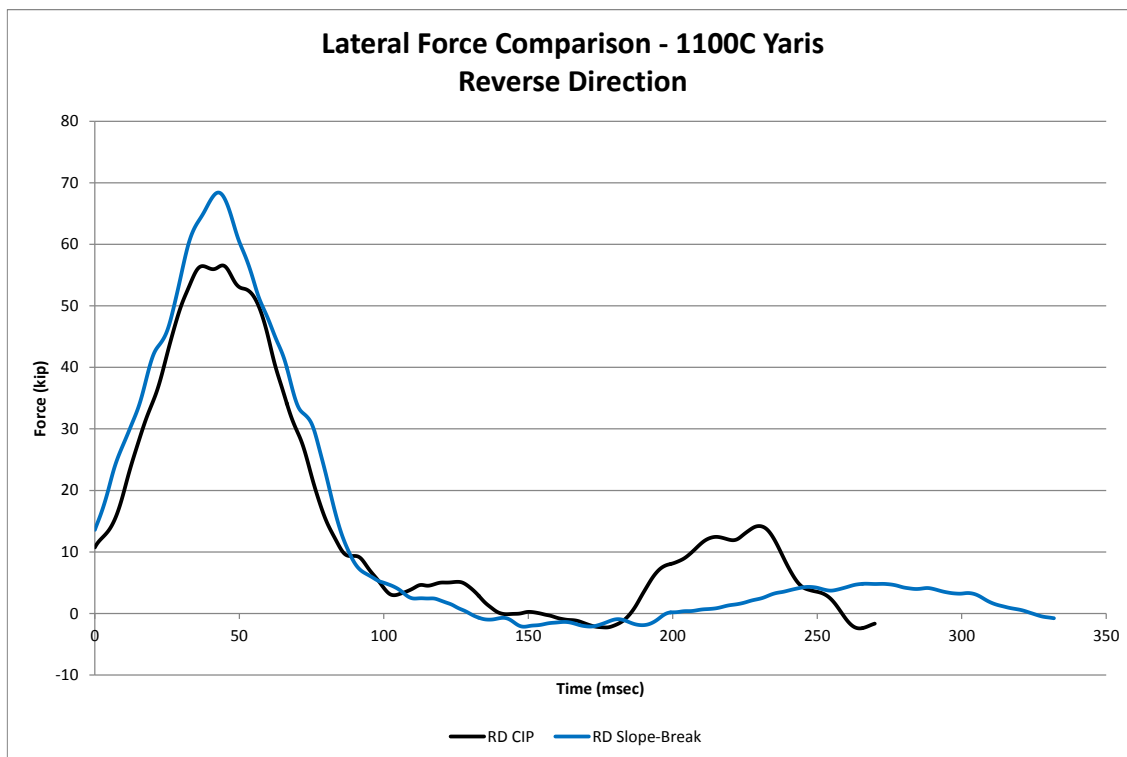


Figure 186. Lateral Force Comparison, Reverse-Direction Locations, 1100C Toyota Yaris

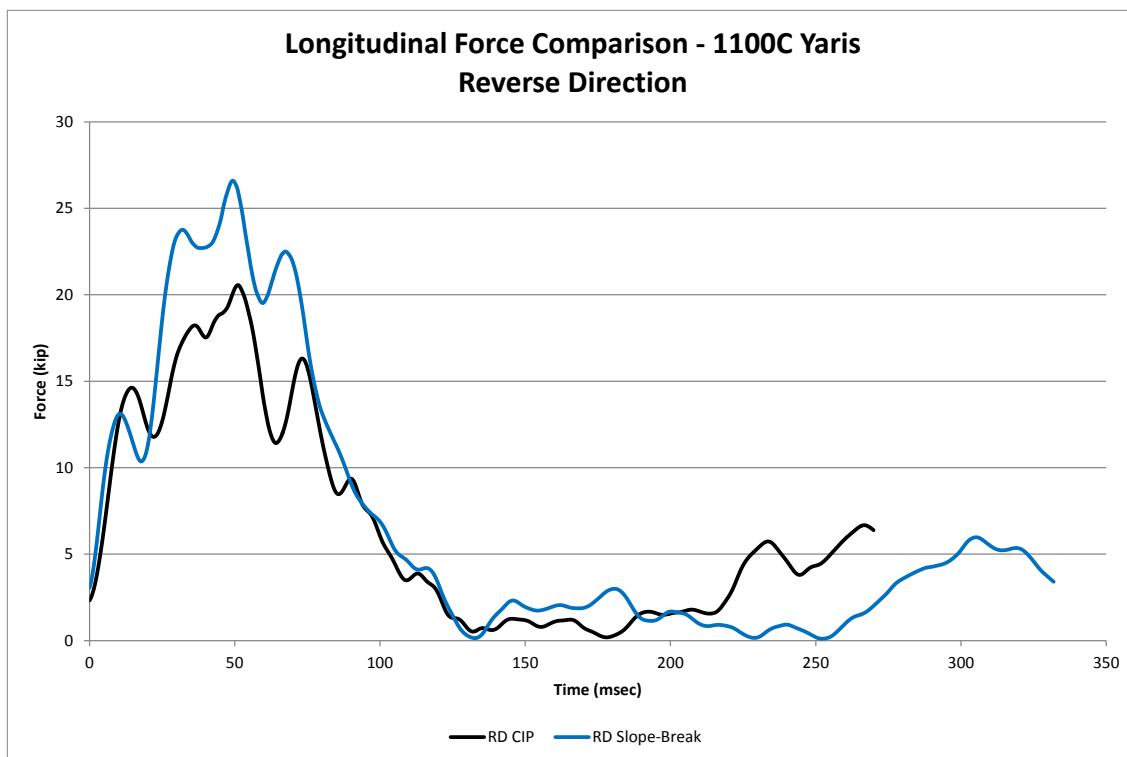


Figure 187. Longitudinal Force Comparison, Reverse-Direction Locations, 1100C Toyota Yaris

The vehicles in each simulation had similar roll angle trends. However, a peak roll angle of 9.1 degrees occurred at 50 msec in the slope-break point impact location simulation, and a peak roll angle of 8.1 degrees occurred at 55 msec in the CIP impact location simulation, as shown in Figure 188. Further, the simulation at the slope break point experienced an 11 percent higher roll angle as compared to the CIP impact location.

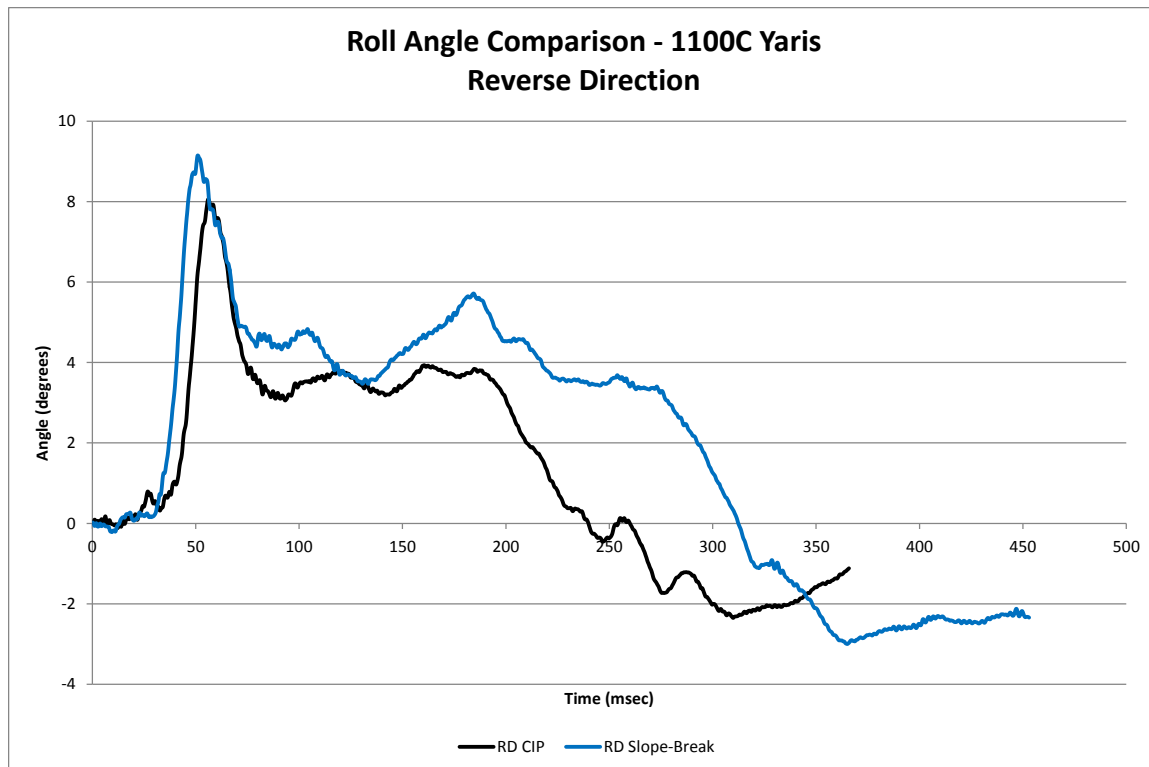


Figure 188. Roll Angle Comparison, Reverse-Direction Locations, 1100C Toyota Yaris

The pitch angles for the slope-break point impact location simulation resulted in an approximately 25 percent higher initial peak than observed for the CIP location simulation, as shown in Figure 189. The larger initial peak corresponded to a greater change in longitudinal velocity with the slope-break point as compared to the CIP impact location simulation. After the initial peak, the simulation with respect to the CIP impact

location experienced approximately a 24 percent larger maximum pitch angle at 350 msec. The Yaris model pitch angles were still increasing at the end of the simulations.

The yaw angles for each simulation were approximately zero through 50 msec, which was the time that the plastic outer bumper was being impacted. At 50 msec, the structural bumper was impacted and each vehicle model started to yaw, as shown in Figure 190. The Yaris model at the slope-break point exited the system before becoming parallel to the system. However, a 36 percent higher peak yaw angle was experienced as compared to the simulation location at the CIP location.

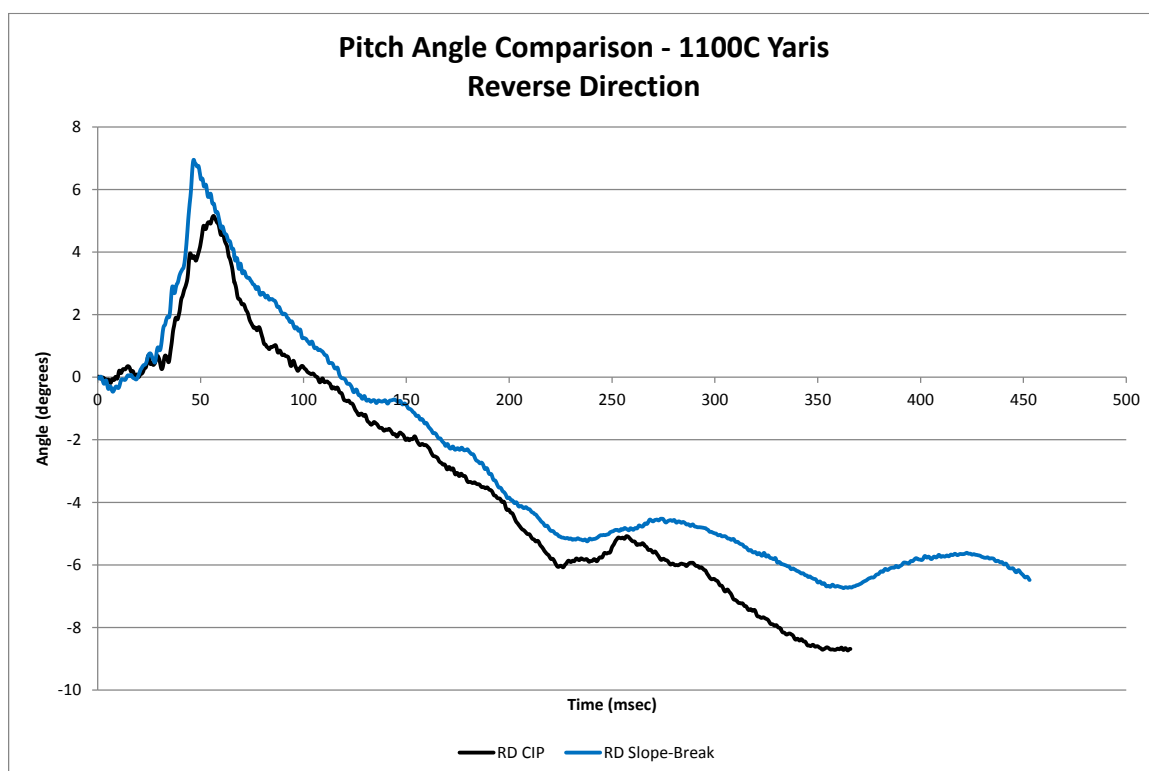


Figure 189. Pitch Angle Comparison, Reverse-Direction Locations, 1100C Toyota Yaris

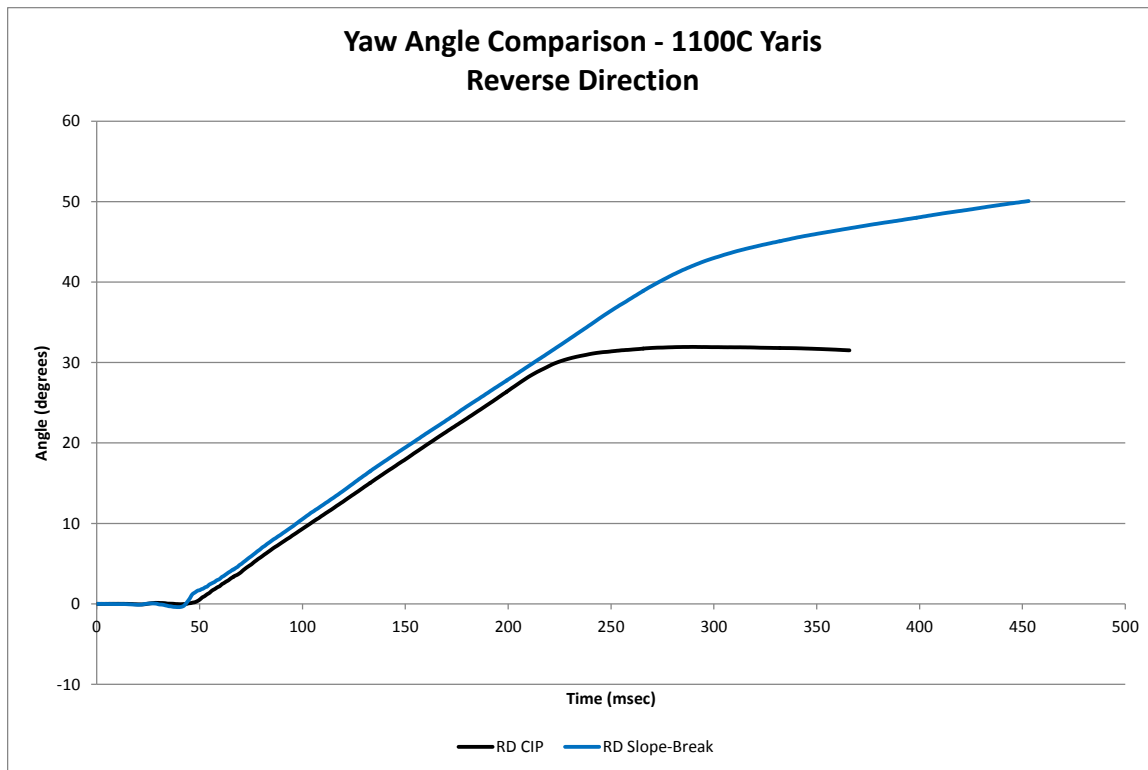


Figure 190. Yaw Angle Comparison, Reverse-Direction Locations, 1100C Toyota Yaris

11.4.2 Neon Vehicle Model

The comparison of results for the Neon model in the simulations under reverse-direction locations is shown in Table 44. The simulations at each impact point successfully contained and redirected the Neon model, as shown in Figures 191 and 192. The simulation end times varied, but the desired information was obtained through each impact event. The stresses within the transition hardware were acceptable, and they were not reported herein.

The left front of the Neon model had significantly more inward crush during the reverse-direction simulations at the slope-break point and CIP location as compared to the simulations at interior and upstream locations. The Neon vehicle model also experienced crush at the bottom front of the left-front door, causing approximately 11 in.

(279 mm) of occupant compartment deformations in the toe pan during the simulation with the slope-break point, as shown in Figure 193. Further, the roof was dented near the top of the left-front door. The increase in damage of the Neon model was expected as the buttress was stiffer than the RESTORE barrier and transition.

Table 44. Comparison Matrix of Reverse-Direction Locations, 1100C Dodge Neon

Simulation Parameters		Impact Location and Trial No.	
		37	61
		Reverse-Direction Slope-Break Point	Reverse-Direction CIP ³
End Time, ms		384	351
Parallel Conditions	Time, ms	202	216
	Velocity, mph (km/h)	38.4 (61.8)	41.2 (66.3)
Exit Conditions	Velocity, mph (km/h)	37.9 (60.9)	41.3 (66.5)
	Angle, deg.	5.8	1.0
	Time, ms	232	223
Length of Contact		6 ft - 3 in. (1.9 m)	6 ft - 11 in. (2.1 m)
t*, ms		69.9	75.1
ORA, g's	Longitudinal	-5.66	-6.10
	Lateral	12.80	9.51
OIV, ft/s (m/s)	Longitudinal	-29.68 (-9.05)	-27.60 (-8.40)
	Lateral	34.74 (10.59)	32.38 (9.87)
Test Article Deflections, in. (mm)	Dynamic of Concrete	0	0.6 (15)
	Dynamic of Steel Rail	0	0.4 (10)
	Working Width	22.3 (566)	22.9 (582)
Location of Max. Deflection Upstream from Pin		0 ft (0 m)	0 ft (0 m)
Vehicle Stability	Max. Roll, deg.	4.4	5.6
	Max. Pitch, deg.	-1.9	-2.4
	Max. Yaw, deg.	39.5	29.7
Posts Hit by Leading Tire (wheel snag)		0	0
Max. Lateral Impact Force, kips (kN) ¹		63.2 (281.0)	54.9 (244.4)
Max. Longitudinal Impact Force, kips (kN) ²		23.8 (105.9)	20.1 (89.4)

¹ Calculated using global Y-acceleration multiplied by mass.

² Calculated using local X- and Y- accelerations coupled with yaw, multiplied by mass.

³ Impacted 3 ft – 7 in. (1.1 m) upstream from cover plate edge.



Figure 191. RESTORE Barrier Transition, 1100C Neon Simulation Comparison, Reverse-Direction Locations, Downstream View

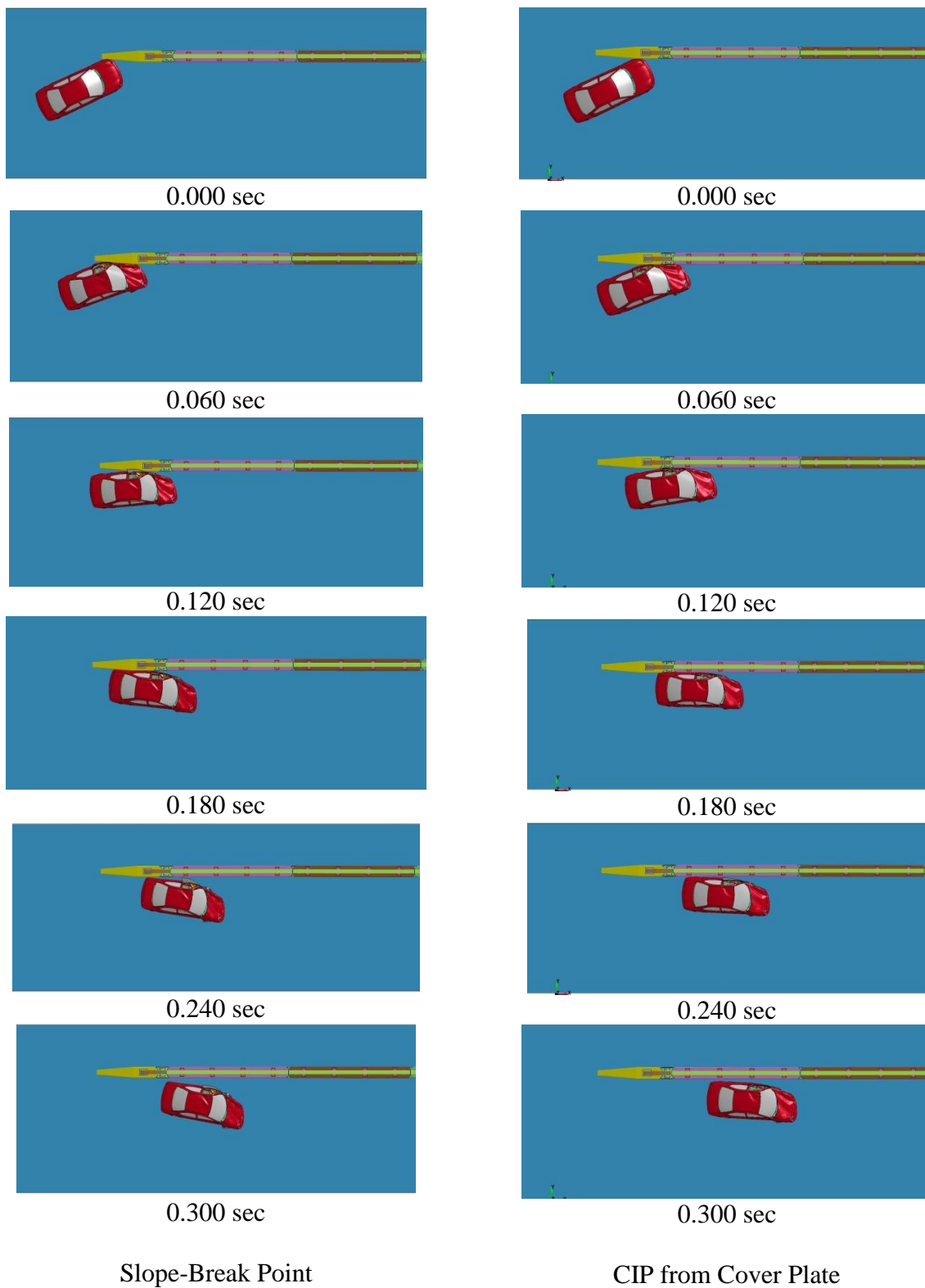


Figure 192. RESTORE Barrier Transition, 1100C Neon Simulation Comparison, Reverse-Direction Locations, Overhead View

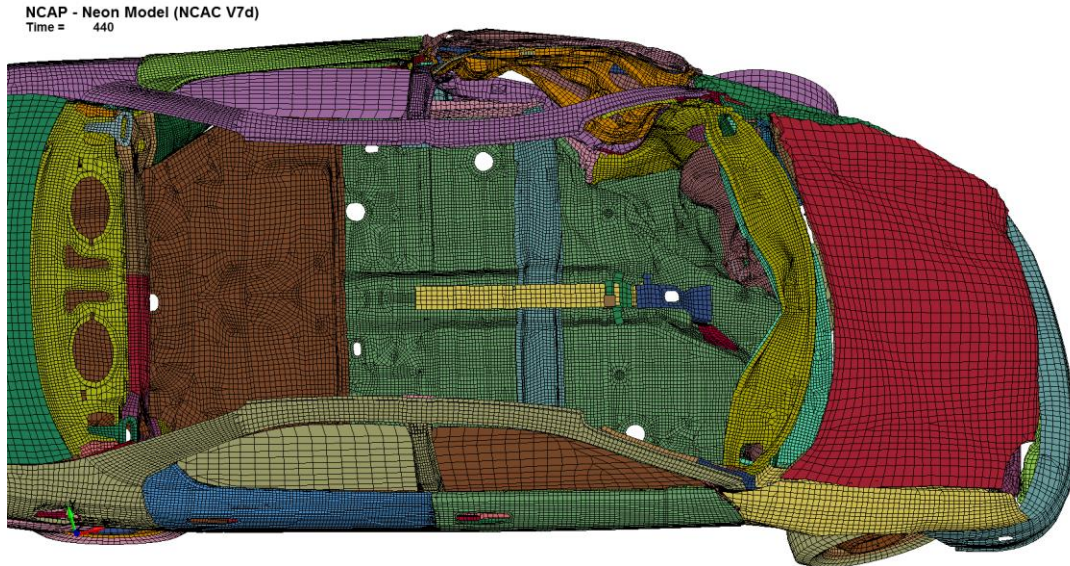


Figure 193. Occupant Compartment Deformations, Slope-Break Point, 1100C Neon

Since all degrees of freedom in the rigid concrete buttress were constrained, the buttress did not have any damage nor deflections. However, the upstream end of the RESTORE barrier dynamically deflected 0.6 in. (15 mm) during the simulation at the CIP location relative to the cover plate. The Neon model did not impact the RESTORE barrier in the simulation at the slope-break point, thus not causing any dynamic deflections.

The lateral change in velocity in simulations into the two reverse-direction impact locations exhibited similar trends but had different magnitudes, as shown in Figure 194. In general, the slope-break point simulation had a magnitude approximately 20 percent larger than observed for the CIP impact location simulation from 75 msec through the end of the simulation. The lateral change in velocity difference can be contributed to the horizontal flare rate of 6:1 over its full height that was impacted. Similarly, the longitudinal change in velocity was greater for the slope-break impact location simulation as compared to the CIP location, as shown in Figure 195. The longitudinal velocity was

similar for both impact location simulations through 50 msec. Next, the Neon model impact at the slope-break point had a greater change in longitudinal velocity due to the larger horizontal flare rate. By the end of the simulation, the slope-break point simulation had a 20 percent higher change in the longitudinal velocity at 350 msec.

The lateral and longitudinal OIV and ORA values were similar between the two simulations. Higher OIV and ORA values were expected due to impacting a rigid barrier. However, they were well within the limits presented in MASH.

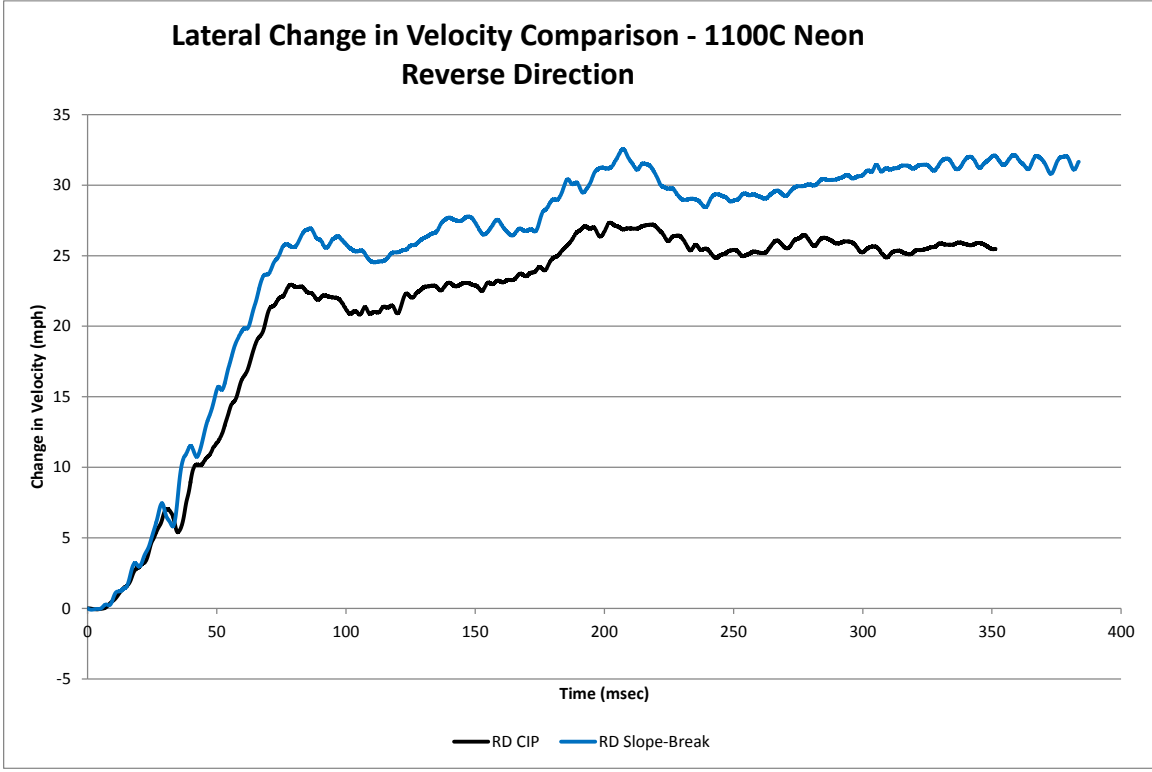


Figure 194. Lateral Change in Velocity, Reverse-Direction Locations, 1100C Dodge Neon

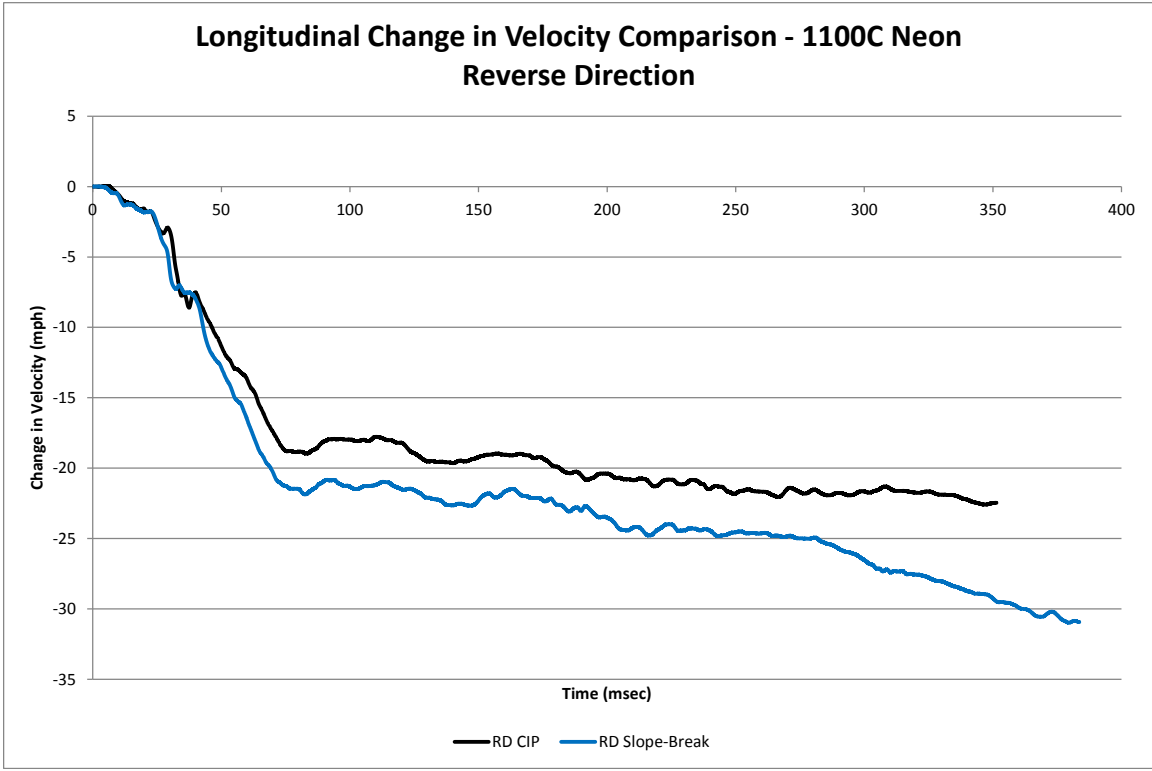


Figure 195. Longitudinal Change in Velocity, Reverse-Direction Locations, 1100C Dodge Neon

The lateral impact forces were calculated using the CFC60 filtered 50-msec global Y-accelerations multiplied by the mass. Each of the locations impacted the rigid concrete buttress. The slope-break point location simulation experienced a 13 percent higher maximum lateral impact force, as shown in Figure 196. After the peak force, the two impact location simulations exhibited similar forces through the remainder of the impact event. Similarly, the longitudinal barrier impact force was calculated, and the slope-break point simulation location experienced a 16 percent higher maximum longitudinal impact force, as shown in Figure 197. Note that the longitudinal barrier force was calculated using the local X- and Y- accelerations coupled with the yaw angle and multiplied by the mass of the vehicle model.

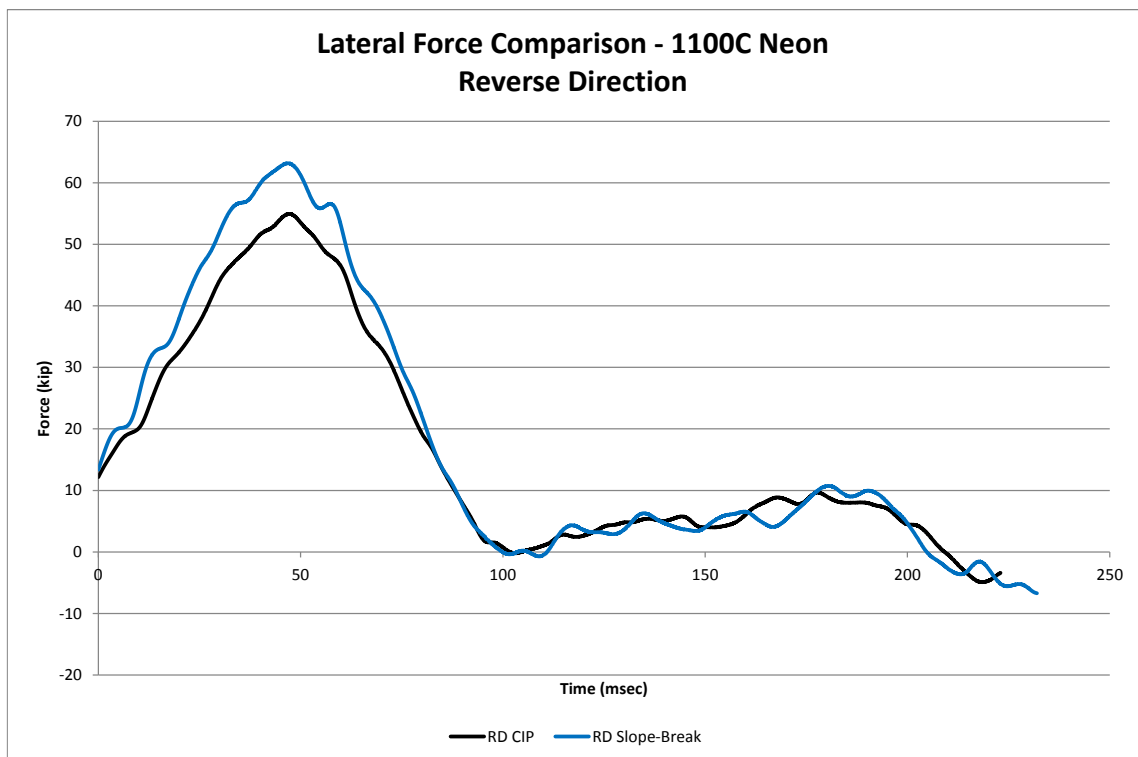


Figure 196. Lateral Force Comparison, Reverse-Direction Locations, 1100C Dodge Neon

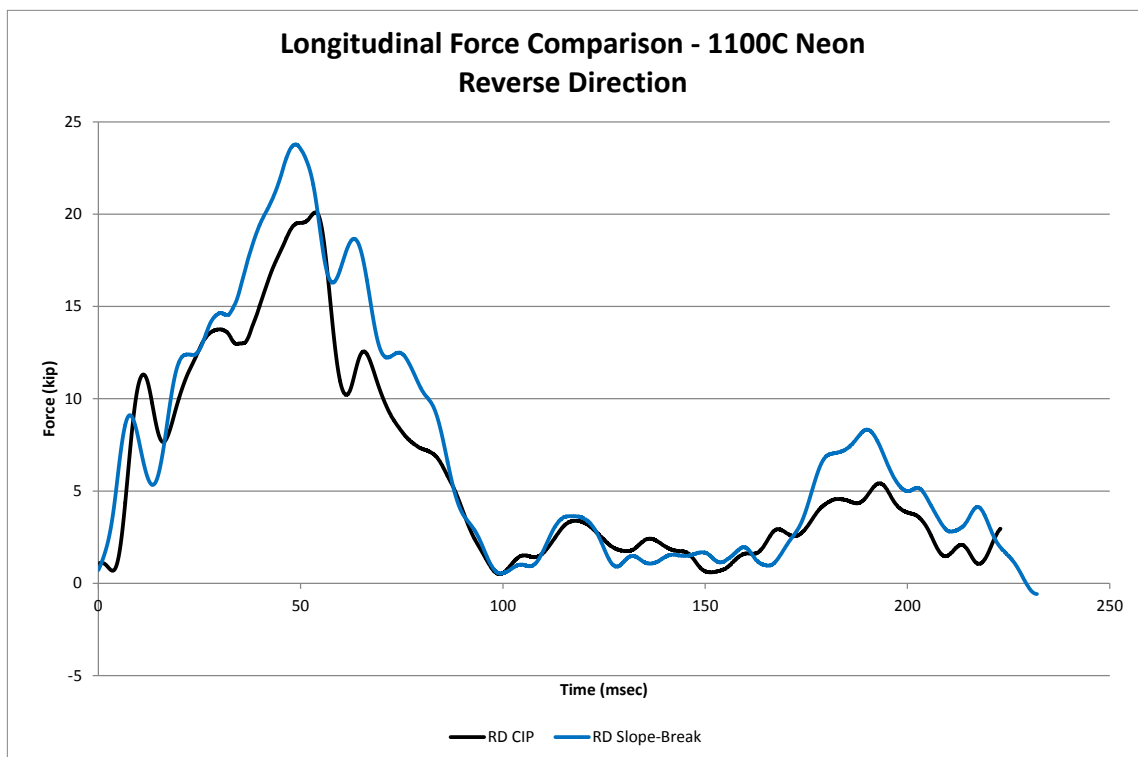


Figure 197. Longitudinal Force Comparison, Reverse-Direction Locations, 1100C Dodge Neon

The roll angles for the Neon model were nearly identical through approximately 25 msec, as shown in Figure 198. However, the roll angle during the simulation at the CIP location decreased approximately 10 degrees, while the slope-break point simulation had a reduction of approximately 4 degrees at 40 msec. Next, the roll angles varied 5 degrees at 110 msec. Through the duration of the simulation events for both impact locations, the roll angles were acceptable and low.

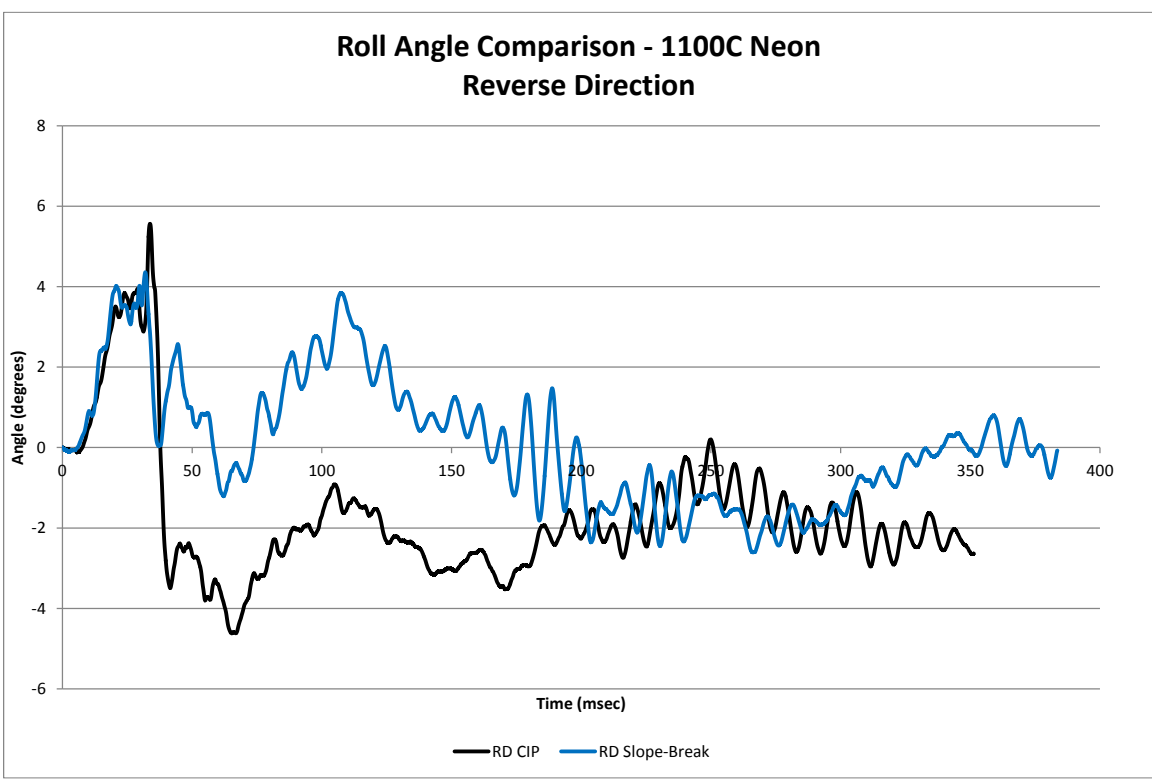


Figure 198. Roll Angle Comparison, Reverse-Direction Locations, 1100C Dodge Neon

The pitch angles for the simulations at the slope-break point and the CIP location were similar through approximately 100 msec, as shown in Figure 199. The two simulated pitch angles varied by less than 1.0 percent throughout the impact event. The maximum pitch angles were -1.9 and -2.4 for the simulations at the slope-break point and the CIP location, respectively.

The yaw angle for the simulation at the slope-break point location increased more quickly than observed for the CIP location, as shown in Figure 200. The slope-break point simulation location had a maximum yaw angle 25 percent larger than observed for the CIP location. The yaw angle for the simulation at the slope-break point was approximately 20 percent larger at 175 msec and 25 percent larger at 350 msec than observed for the CIP location simulation.

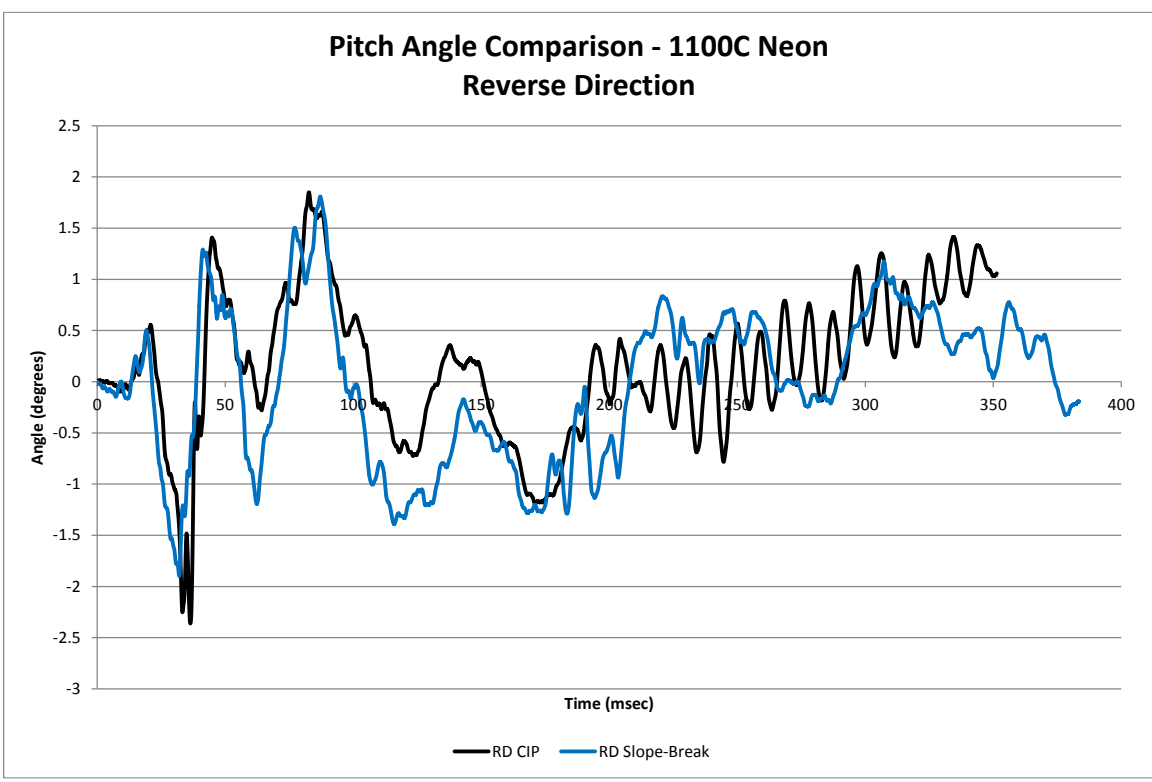


Figure 199. Pitch Angle Comparison, Reverse-Direction Locations, 1100C Dodge Neon

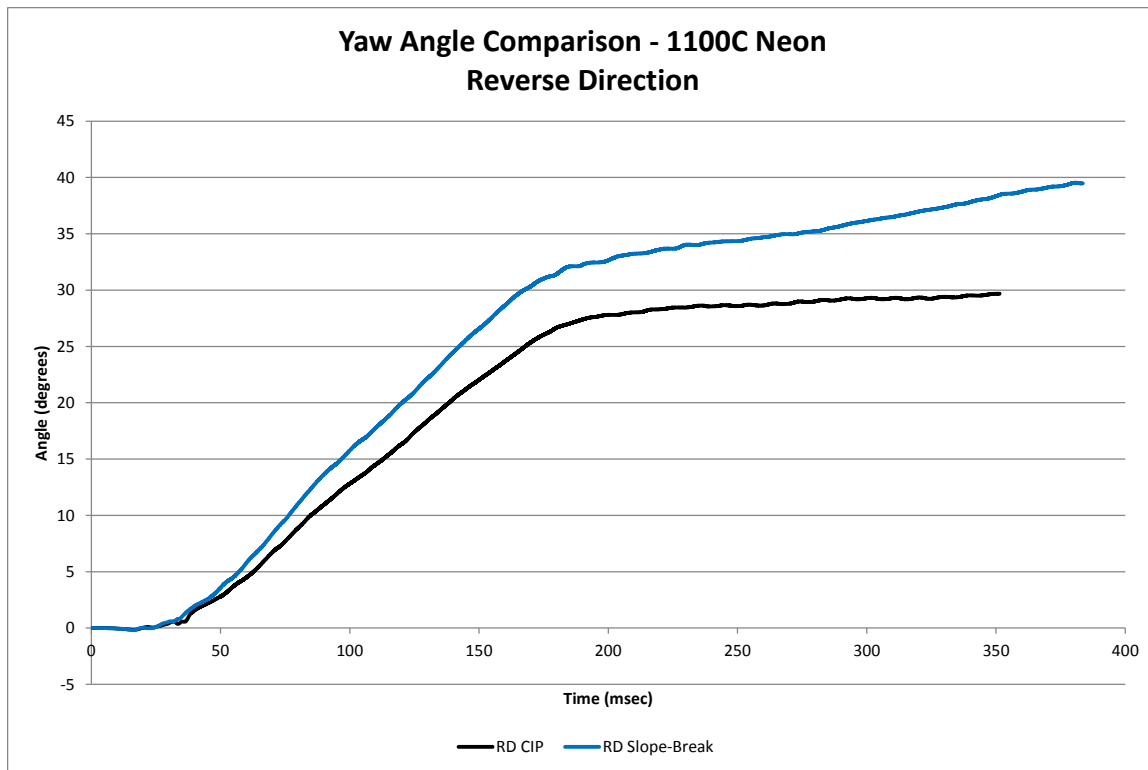


Figure 200. Yaw Angle Comparison, Reverse-Direction Locations, 1100C Dodge Neon

11.5 1100C Simulation Summary

Various impact locations were simulated to evaluate the RESTORE barrier transition to a rigid concrete buttress according to MASH test designation no. 4-20 impact conditions. Impact locations at the suggested CIP location of 3 ft – 7 in. (1.1 m) in MASH were simulated with respect to the upstream buttress end and the drop-down pin locations. Impact locations were also simulated in 10 ft (3.0 m) increments upstream from the pin-and-gusset plate assemblies to find the worst-case critical impact points, as recommended in MASH. Further, two simulations in the reverse direction were used to determine if the transition can be used in median applications with vehicles traveling in both directions. The 1100C vehicle models, the Dodge Neon and Toyota Yaris, indicated that the pin-and-gusset plate assemblies with the rounded cover plates have the potential

for being successfully used in a MASH TL-4 barrier transition that accommodates the degrees of freedom of the RESTORE barrier. Comparison plots between all of the impact locations with both small car vehicle models are shown in Appendix L.

The simulations at the suggested CIP locations in MASH around the transition hardware did not cause major concerns for occupant safety. However, many of the stresses within the parts located in the pin and gusset plate assemblies exceeded the Tresca and von Mises yield conditions. In order for the transition to be maintenance free, the vertical drop-down cover plate bolts were recommended to be re-designed so that they do not exhibit permanent deformation, which occurred in simulations at the suggest CIP locations in MASH during the Neon and Yaris model impacts. The original design intended for the vertical bolts to secure the cover plates and not experience much loading. The horizontal gusset plates exceeded the yield conditions. However, the maximum stresses were localized at the edges of the pin holes, which may have caused the holes to ovalize but not for the plates to have ruptured. The cover plate gussets did not exceed any of the von Mises yield conditions during the simulations with the Neon model. The cover plate gussets exceeded the von Mises yield conditions during the Yaris model simulations with respect to the pin and the buttress with the compressed joint. The location of the stresses on the cover plate gussets were at the inner corners due to contact with the horizontal gusset plates. The cover plate gussets may experience some permanent deformation, but they would have likely been able to be impacted again. The top tube, tube connection, and termination exceeded the yield condition in all simulations, except for one simulation at a suggested CIP location noted in MASH. Lastly, the cover plate exceeded the yield conditions with the maximum stress located on the rounded edges of

the cover plate. Deformations on the cover plate occurred from the plate contacting the horizontal gusset plates. The cover plate would still have structural capacity and could be impacted again if the permanent deformations did not cause the rounded edges to extend past the RESTORE or buttress face. If the cover plate edges extend past the RESTORE or buttress face, the cover plates would need to be replaced due to an increased potential for snag behind the cover plate.

Through the simulations upstream from the transition hardware, the 20-ft (6.1-m) impact location upstream from the pin-and-gusset plate assemblies was observed to provide the worst-case impact location. At the 20-ft (6.1-m) impact location with the joint extended and compressed, the system experienced dynamic deflections and ACJ bolt stresses greater than observed at the other simulated impact locations. The RESTORE barrier was designed to distribute the impact force across multiple barrier segments. With the downstream end of the barrier segment pinned, the system did not distribute the impact force to as many RESTORE barrier segments, which led to increased barrier deflections. The stresses in the ACJ bolts were up to 26 percent higher than observed in the interior simulation. However, the stresses in the ACJ bolts were likely as the concrete RESTORE barrier segments were modeled with a rigid-element formulation that was unable to fracture and spall, as was observed in the concrete beams in test no. SFH-2. Thus, the concrete segments in the model did not have any stress, and the bolts were loaded more.

Lastly, the reverse-direction simulations found that the barrier successfully contained and redirected the small car models. The ORA and OIV values were higher than observed for the impacts upstream from the drop-down pin due to primary contact

with a rigid barrier. The impacts at the slope-break point resulted in up to 23 percent higher lateral and longitudinal impact forces imparted to the barrier as compared to the impacts at the CIP location with respect to the cover plate. The increased impact forces and ORA and OIV values were believed to be acceptable as they did not negatively affect the vehicle behavior and were below the MASH limits. However, it may be advisable to consider flatter horizontal flare rates over the full barrier height in order to largely eliminate concerns for increased forces, ORAs and OIVs.

In the simulations near the transition hardware, the vehicle model damage increased as compared to the interior simulation. The greatest vehicle damage occurred during the slope-break impact location simulation with the Neon model. The left-front corner of the vehicle model crushed inward, which included the bottom of the left-front door, causing approximately 11 in. (279 mm) of deformation to the toe pan. The Yaris model did not exhibit as severe of crush on the left-front corner of the vehicle at the same impact location.

Note that the Dodge Neon model provided the most accurate ORA, OIV, and vehicle stability results in the simulation at the interior location. The Toyota Yaris provided the most accurate vehicle snag, barrier deflections, and lateral impact force results, in the simulation at the interior location. Thus, some results may not be predictive of full-scale crash test results within the transition region. It is recommended that the RESTORE barrier transition be full-scale crash tested at multiple impact points. MASH suggests that rigid transitions should be evaluated at the location 3 ft – 7 in. (1.1 m) upstream of the buttress face with the small car vehicle. Through the simulation analysis, it was determined the extended and compressed joint at each suggested CIP location in

MASH showed similar results, when compared to each other. However, the suggest CIP location in MASH upstream of the buttress with extended joint has a higher potential for vehicle snag on the upstream edge of the cover plate and wheel snag on the upstream buttress face.

The second impact location is 3 ft – 7 in. (1.1 m) upstream from the 20-ft (6.1-m) location with the extended joint. The extended joint simulations with the Neon and Yaris vehicle models had higher lateral barrier forces and slightly greater deflections than the compressed joint. This impact location provided the greatest barrier deflections, which may lead to a greater potential for vehicle snag on posts and vehicle instability. The Neon and Yaris models impacted the first post downstream of impact during the simulation. Note, the Neon model did not impact any posts during the simulation at the interior region, and the post contact led to model instabilities, which may be an indication that vehicle snag on posts is a greater concern. Thus, the location 20 ft (6.1 m) upstream from the pin with the extended joint would most likely provide the worst-case snag potential for the small car vehicle.

The third impact location may be the slope-break point of the horizontal flare rate of 6:1 on a concrete buttress. This slope-break point has never been full-scale crash tested according to MASH on full barrier heights and may need to be evaluated before considered for use on the roadway. The slope-break impact location experienced higher occupant risk values for the Neon and Yaris vehicle models as well as higher lateral and longitudinal barrier forces. Further, the Neon model had occupant compartment deformations that exceeded the limits in MASH, which could cause concern during a full-

scale crash test. Other flatter horizontal flare rates, 10:1 or flatter, should be considered and evaluated to minimize occupant risk values and occupant compartment deformations.

12 CIP DETERMINATION – MODELING TEST DESIGNATION NO. 4-21

12.1 Purpose

In lieu of full-scale crash testing, further computer simulation was utilized to evaluate the transition design according to the MASH safety performance criteria for test designation no. 4-21. The Silverado model impacted at a speed of 62.1 mph (100 km/h) and an angle of 25 degrees, as recommended by MASH. Several impact points were evaluated to determine vehicle and barrier performance. Multiple impact points were considered upstream from the buttress and in the reverse direction, as shown in previously in Figure 135. Two barrier configurations were considered due to the +/- 1½ in. (38 mm) construction tolerance: the joint fully extended and the joint fully compressed.

MASH states that computer simulation with LS-DYNA should be performed to evaluate CIPs when practical and accessible. However, if computer simulation is unavailable, the CIP for a stiffness transition should be either 4 ft – 3 in. (1.3 m) upstream from the location with the greatest potential for wheel snag (i.e., upstream end of buttress) or 4 ft – 3 in. (1.3 m) upstream from the location with the potential for the largest load (i.e., drop-down pin) or deflection (i.e., upstream locations) for test designation no. 4-21. The largest load is expected to occur at an impact point near the pin and gusset plate assemblies due to the constraint in the lateral y-direction. However, impact locations farther upstream would need to be evaluated to determine the location of the maximum barrier deflection and/or flare rate. To accommodate all of the CIP possibilities, computer simulation was used to consider the suggested CIP locations in MASH as well as upstream impact locations to determine the worse-case vehicle and/or

barrier performance. Each suggested CIP impact location in MASH was simulated with the Chevrolet Silverado vehicle model when the joint was fully extended and when the joint was fully compressed, as shown previously in Figure 136.

Impact locations farther upstream from the pin were simulated at intervals of 10 ft (3.0 m) and up to 40 ft (12.2 m) away from the pin. Each impact location was simulated 4 ft – 3 in. (1.3 m) upstream from the four locations positioned at 10 ft (3.0 m) intervals, as shown previously in Figure 135 and with the joint fully extended. However, at the location 20 ft (6.1 m) upstream from the pin, the compressed joint was also investigated to determine if restricted joint movement affected the results.

Lastly, the reverse-direction simulations evaluated performance at impact locations directly at the slope-break point of the buttress on the downstream end with a horizontal flare rate of 6:1. A horizontal flare rate of 6:1 over the full barrier height has not been previously crash tested under the MASH safety performance criteria. Also, an impact location 4 ft – 3 in. (1.3 m) upstream from the upstream corner of the cover plate was evaluated in the reverse direction with the joint fully extended to evaluate the potential for snag behind the cover plate.

12.2 CIP Location Simulation Results

Two reference locations were considered during the simulations of the suggested MASH CIP locations. The first suggested CIP location was 4 ft – 3 in. (1.3 m) upstream from the location with the greatest potential for wheel snag (i.e., upstream end of buttress), while the second CIP location was 4 ft – 3 in. (1.3 m) upstream from the location with the potential for largest load (i.e., drop-down pin). During the rounded cover plate implementation, the initial design had interference between the cover plate

and the washers on the bolts when fully-compressed. Therefore, the joint was ½ in. (13 mm) extended from the fully-compressed configuration during the CIP simulations.

However, the details are correct in the drawing set in Appendix K.

The comparison of results for the Silverado model between the simulations at the suggested MASH CIP locations is shown in Table 45. The simulations at each impact point successfully contained and redirected the Silverado model, as shown in Figures 201 through 204. All of the simulations took additional computational time, and the vehicles did not fully redirect by the end of the simulation. Thus, the results will be updated as they become available.

More damage on the Silverado model was found during the impacts at the suggested MASH CIP locations. The left-front hood and the left-front fender had more separation during the suggested MASH CIP simulations than observed for the simulation at the interior location. Further, the top of the left-front door was separated from the vehicle during the simulations at the suggested MASH CIP locations. The door separation did not occur during the impacts at the interior location simulation. Overall, the simulated impacts at the suggested MASH CIP locations showed more vehicle model damage as compared to the interior impact simulation. The increased damage to the Silverado model was expected as the buttress was stiffer than the RESTORE barrier and approach transition.

Table 45. Comparison Matrix of CIP Locations, 2270P Silverado

Simulation Parameters		Impact Location and Trial No.			
		31	35	41	71
		CIP Buttress Extended	CIP Buttress Compressed	CIP Pin Extended	CIP Pin Compressed
End Time, ms		266	366	266	366
Parallel Conditions	Time, ms	125	124	209	177
	Velocity, mph (km/h)	49.3 (79.3)	49.7 (79.9)	47.1 (75.8)	49.9 (80.3)
Exit Conditions	Velocity, mph (km/h)	NA	48.8 (78.5)	NA	48.5 (78.1)
	Angle, deg.	NA	4.3	NA	4.9
	Time, ms	NA	256	NA	266
Length of Contact		NA	6 ft - 4 in. (1.9 m)	NA	6 ft - 7 in. (2.0 m)
t*, ms		90.0	89.6	94.6	88.9
ORA, g's	Longitudinal	-10.96	-10.31	11.56	10.58
	Lateral	15.61	15.12	17.28	16.65
OIV, ft/s (m/s)	Longitudinal	-20.10 (-6.13)	-17.42 (-5.31)	-21.29 (-6.49)	-17.78 (-5.42)
	Lateral	24.81 (7.56)	25.23 (7.69)	28.31 (8.63)	25.13 (7.66)
Test Article Deflections, in. (mm)	Dynamic of Concrete	0.8 (20)	0.8 (20)	0.9 (23)	0.9 (23)
	Dynamic of Steel Rail	0.5 (13)	0.5 (13)	0.5 (13)	0.6 (15)
	Working Width	23.1 (587)	23.1 (587)	23.2 (589)	23.2 (589)
Location of Max. Deflection	Upstream from Pin	0 ft (0 m)	0 ft (0 m)	0 ft (0 m)	0 ft (0 m)
Vehicle Stability	Max. Roll, deg.	-11.4	-16.4	-19.8	-18.1
	Max. Pitch, deg.	-6.5	-4.9	-6.2	-6.1
	Max. Yaw, deg.	30.4	29.9	34.2	30.5
Posts Hit by Leading Tire (wheel snag)		0	0	0	0
Max. Lateral Impact Force, kips (kN)		83.6 (371.9)	79.9 (355.4)	80.8 (359.4)	84.3 (375.0)

¹ Calculated using global Y-acceleration multiplied by mass.

² Impacted 4 ft – 3 in. (1.3 m) upstream from noted location.



Figure 201. RESTORE Barrier Transition, 2270P Silverado Simulation Comparison, CIP Locations, Downstream View

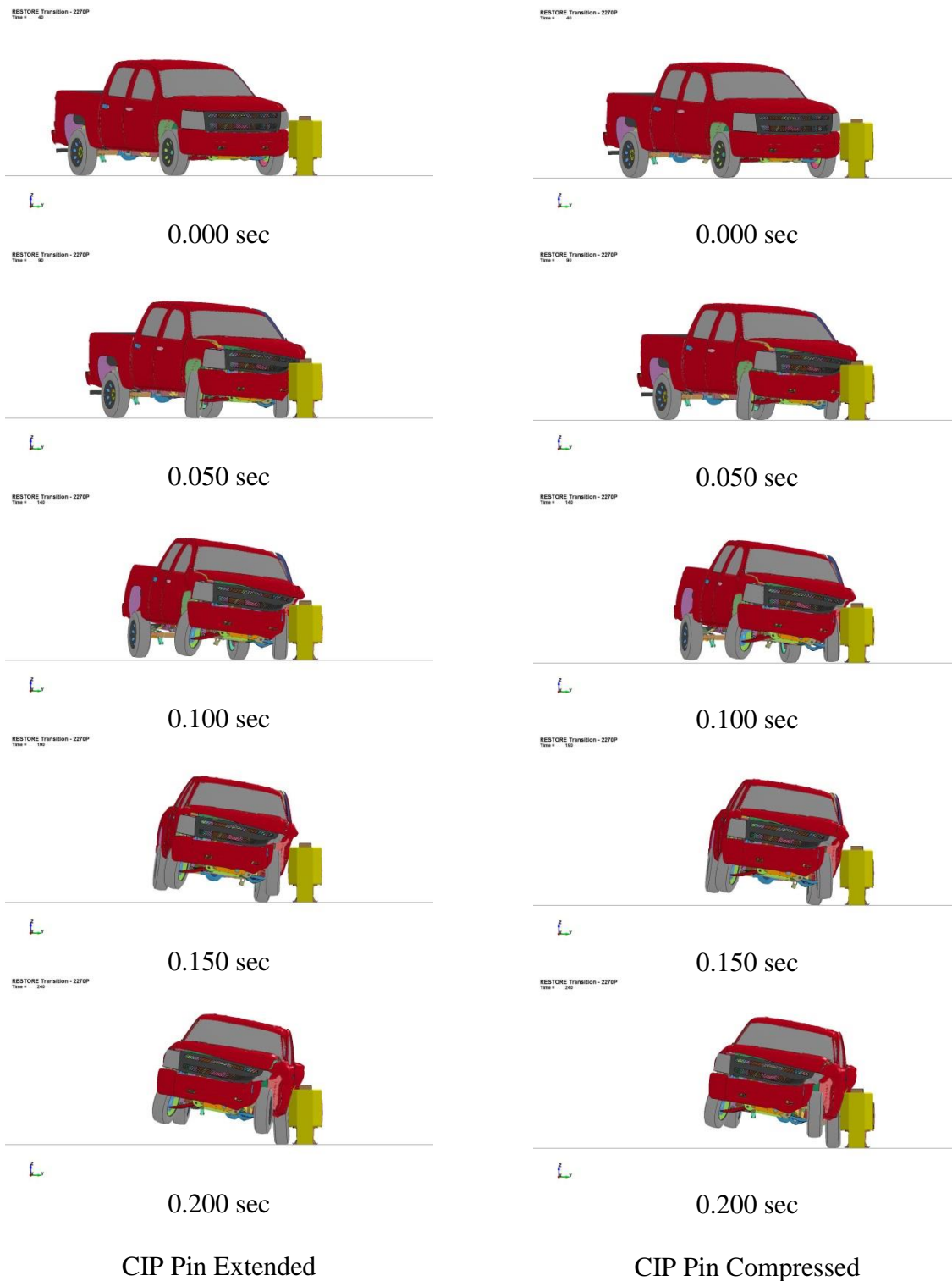


Figure 202. RESTORE Barrier Transition, 2270P Silverado Simulation Comparison, CIP Locations, Downstream View

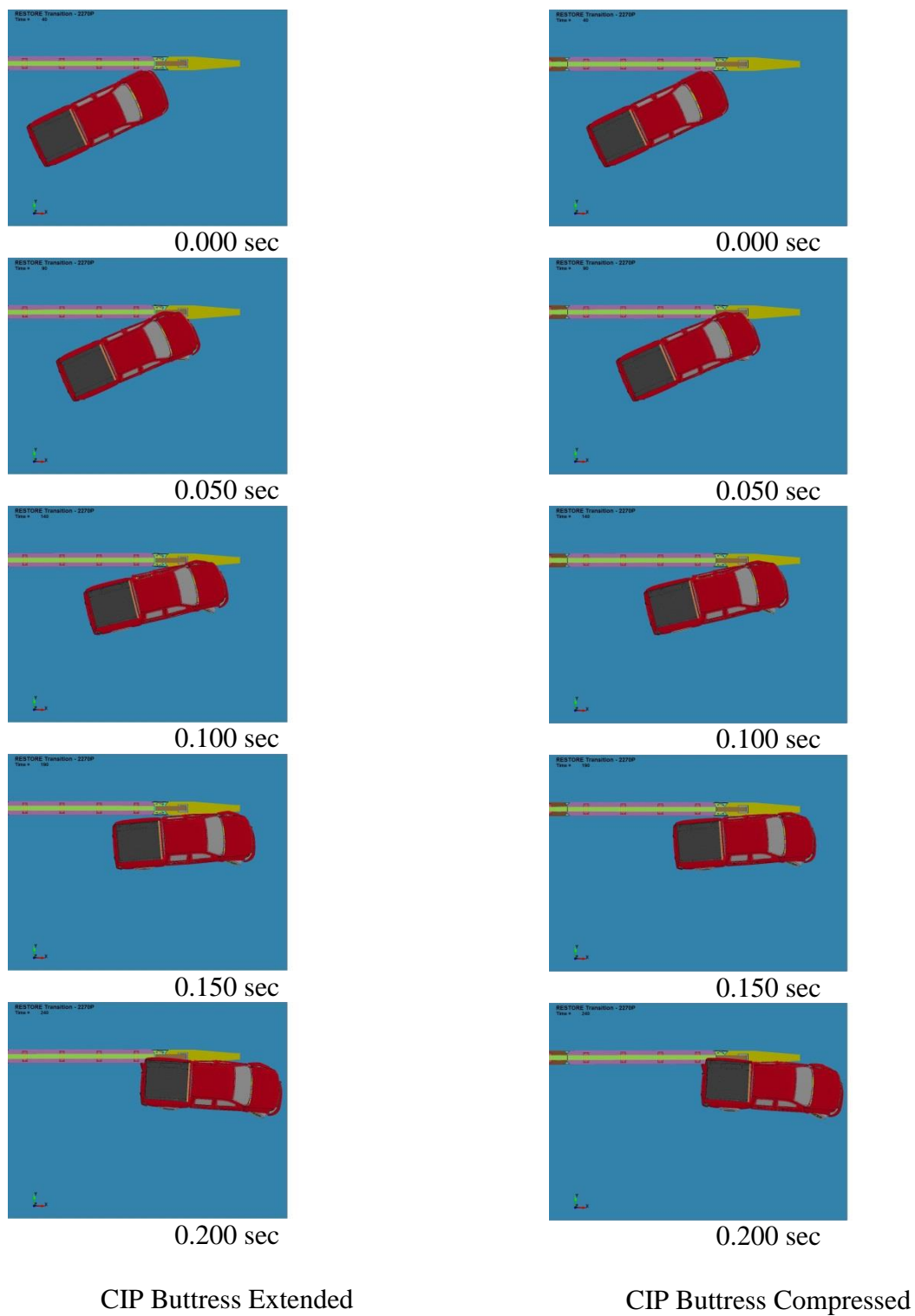


Figure 203. RESTORE Barrier Transition, 2270P Silverado Simulation Comparison, CIP Locations, Overhead View

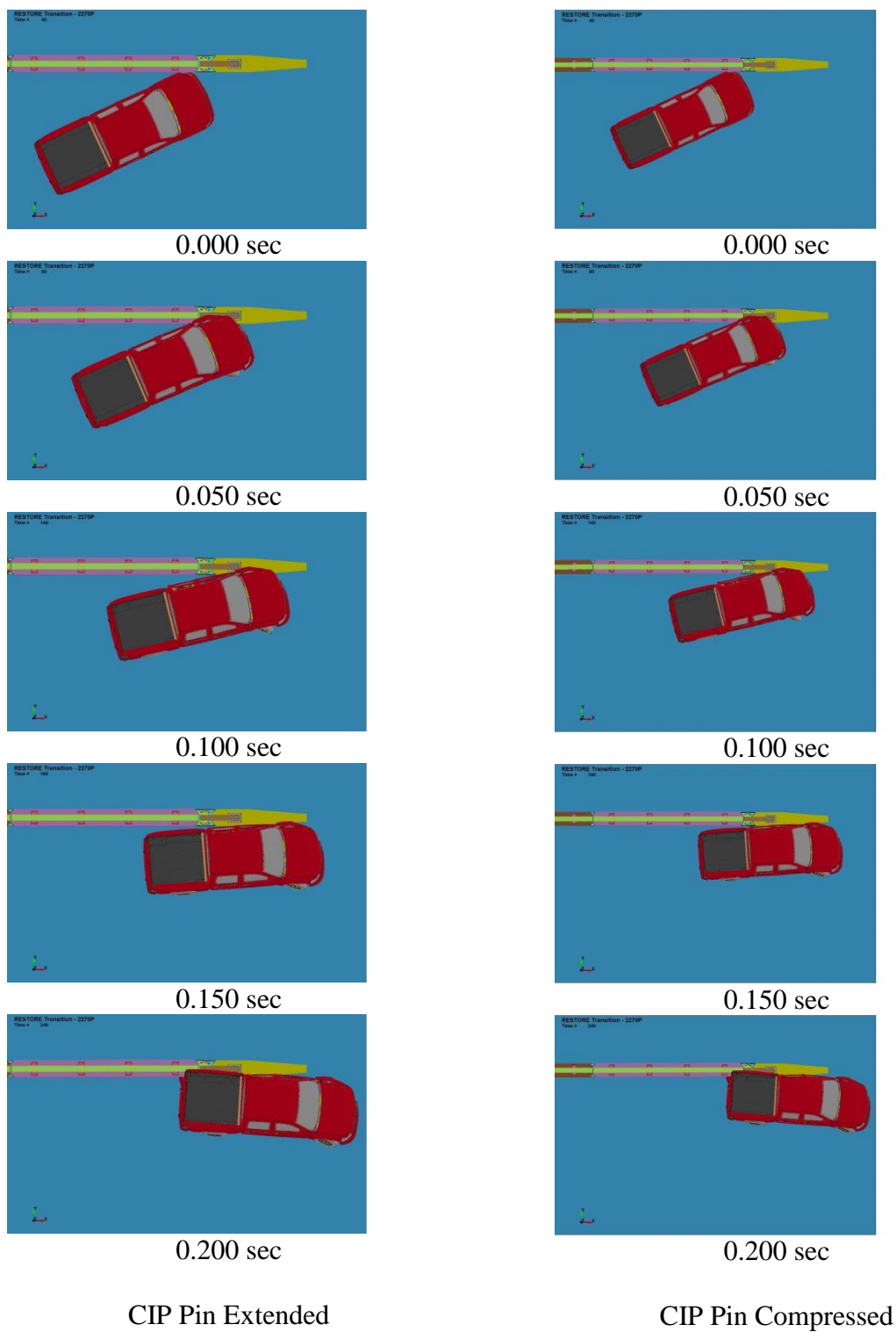


Figure 204. RESTORE Barrier Transition, 2270P Silverado Simulation Comparison, CIP Locations, Overhead View

Since all degrees of freedom in the rigid concrete buttress were constrained, the buttress did not have any damage nor deflections. The simulations with the extended and the compressed joints showed similar dynamic deflections, with the maximum deflection located at the downstream end of the last RESTORE barrier segment (i.e., RESTORE barrier end at the pin). The last RESTORE barrier segment experienced up to 3 degrees of simulated rotation about the longitudinal x-axis under impacts with the Silverado model with the extended and compressed joint at the locations relative to the pin and the compressed joint relative to the buttress. The vertical drop-down pin also rotated back slightly about the longitudinal x-axis to the extent allowed by the slot and hole tolerances within the gusset plates.

The lateral and longitudinal changes in velocity of each simulation at each impact location were similar, as shown in Figures 205 and 206, respectively. The simulation with an impact location 4 ft – 3 in. (1.3 m) upstream from the pin and fully extended joint experienced a delayed change in both lateral and longitudinal velocity due to the joint able to compress while the RESTORE barrier rotated about the pin. That impact location had a 7 percent greater change in lateral velocity at 100 msec and again at 250 msec. The longitudinal change in velocity was similar for all impact location simulations through approximately 100 msec. The simulation with an impact location 4 ft – 3 in. (1.3 m) upstream from the pin and fully extended joint experienced a greater change in longitudinal velocity between 100 msec through the end of the impact event. The longitudinal OIVs for the compressed joint simulations were approximately 20 percent less than observed for the extended joint simulations. The lateral OIVs were all within 13 percent of each other. The longitudinal ORAs for the simulations that impacted the

barrier relative to the pin were both positive, where the expected sign was negative based on the vehicle orientation.

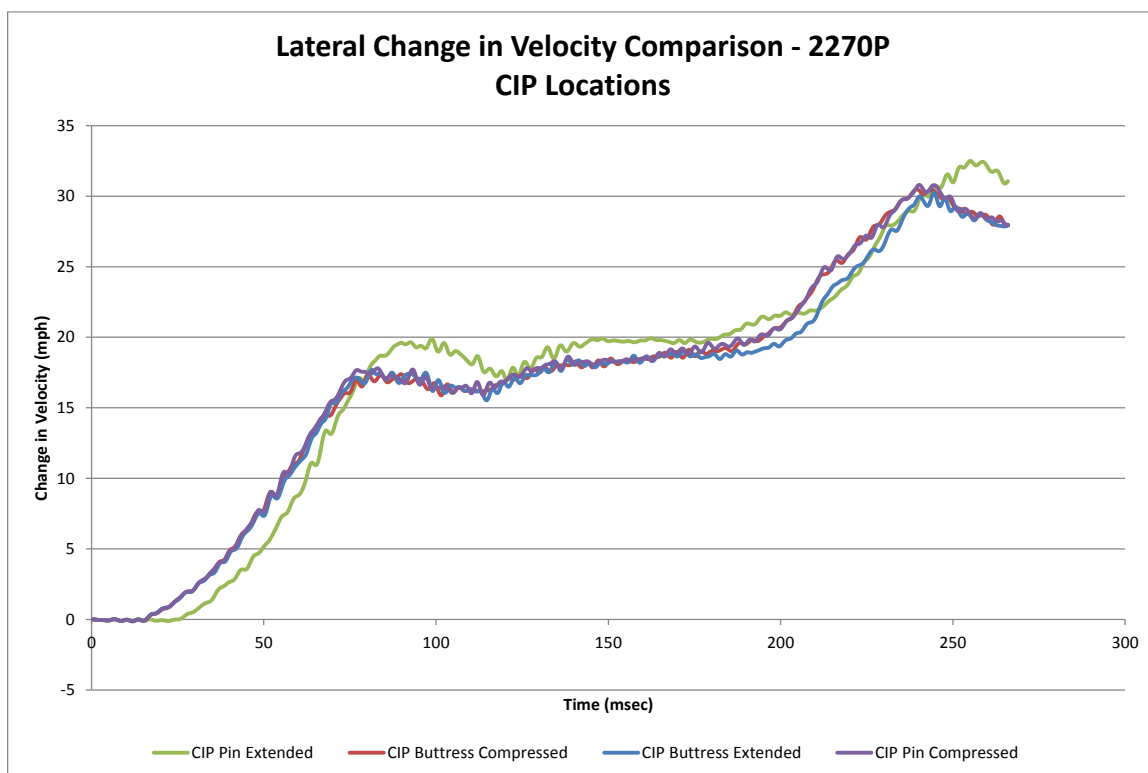


Figure 205. Lateral Change in Velocity, CIP Locations, 2270P Chevrolet Silverado

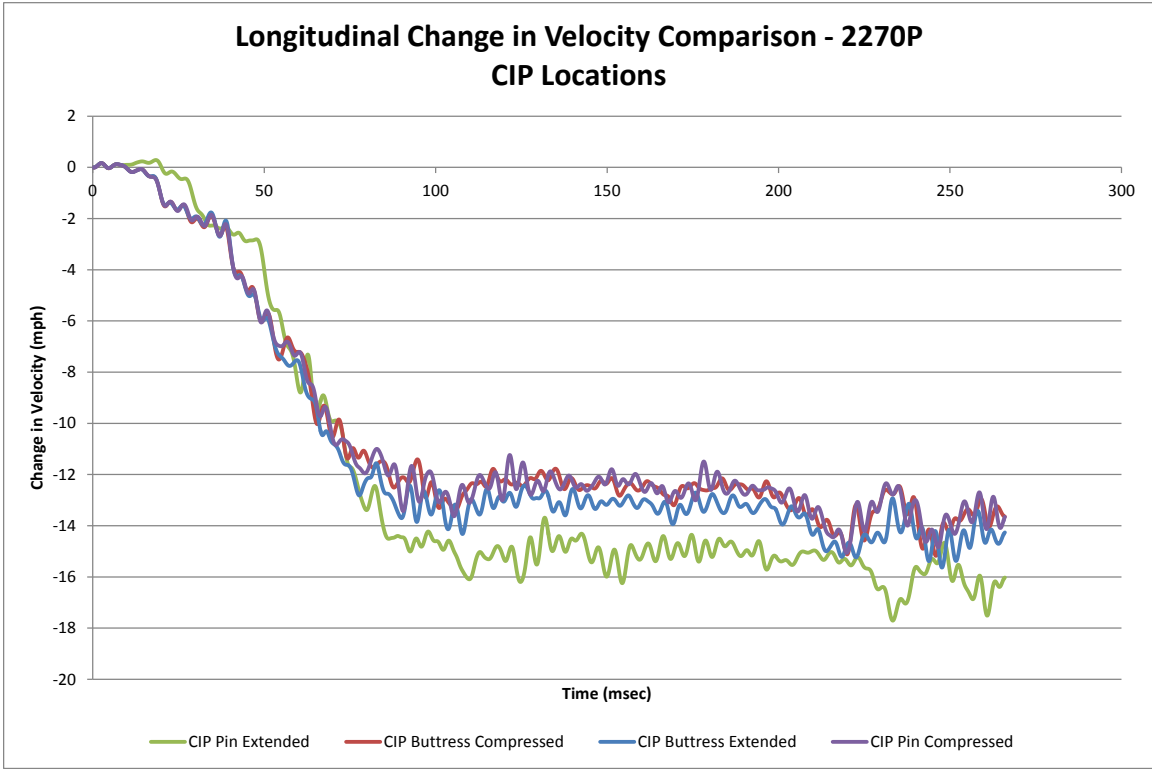


Figure 206. Longitudinal Change in Velocity, CIP Locations, 2270P Chevrolet Silverado

The lateral impact forces were calculated using the CFC60 filtered 50-msec global Y-accelerations multiplied by the vehicle mass. Each of the location simulations exhibited a similar force trend through the duration of the impact event, as shown in Figure 207. However, the simulations with impact location relative to the buttress with the expanded joint and relative to the pin with the compressed joint had peak lateral impact forces approximately 4 kips (18 kN) higher than observed for the other impact location simulations at 50 msec.

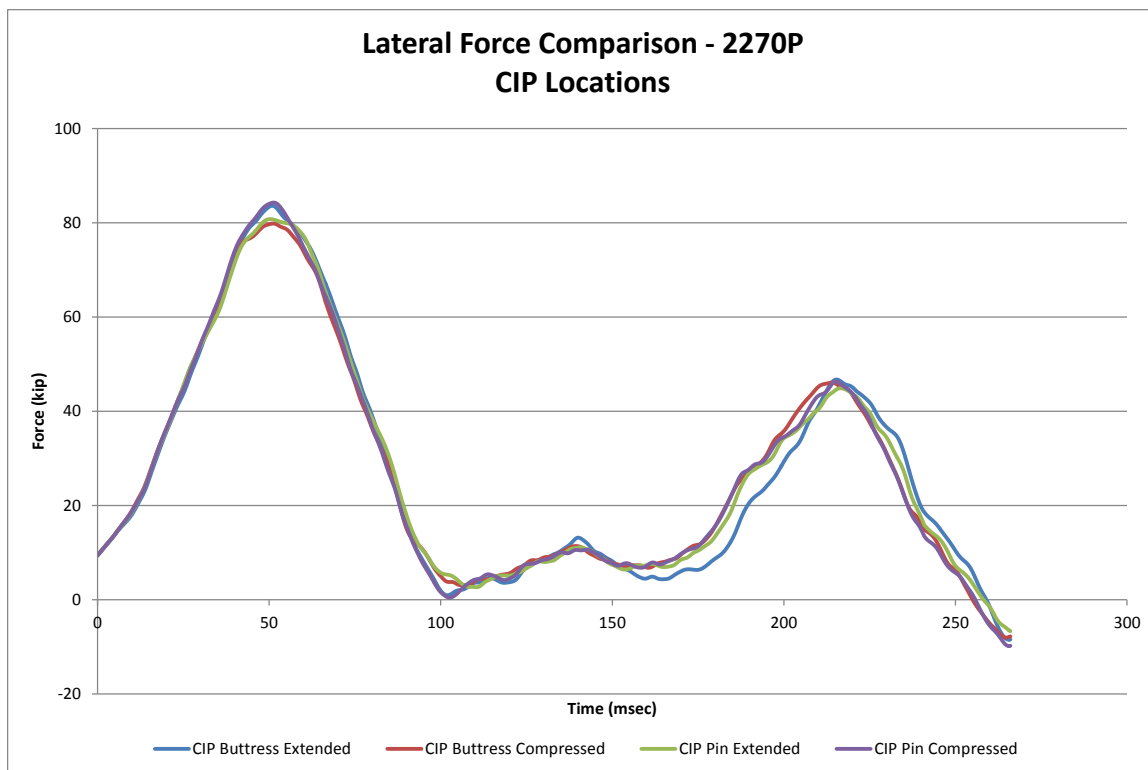


Figure 207. Lateral Force Comparison, CIP Locations, 2270P Chevrolet Silverado

The simulations which impacted the system upstream from the pin with the extended joint had a delayed roll and a maximum roll angle 16 percent greater than observed for the other impact location simulations, as shown in Figure 208. The roll angles for the other three impact location simulations were similar. However, the roll angles were still increasing at the end of the simulation, even after the desired information was obtained. Thus, it would be suggested that the simulations be re-run to determine the end results of the roll angles at these impact locations.

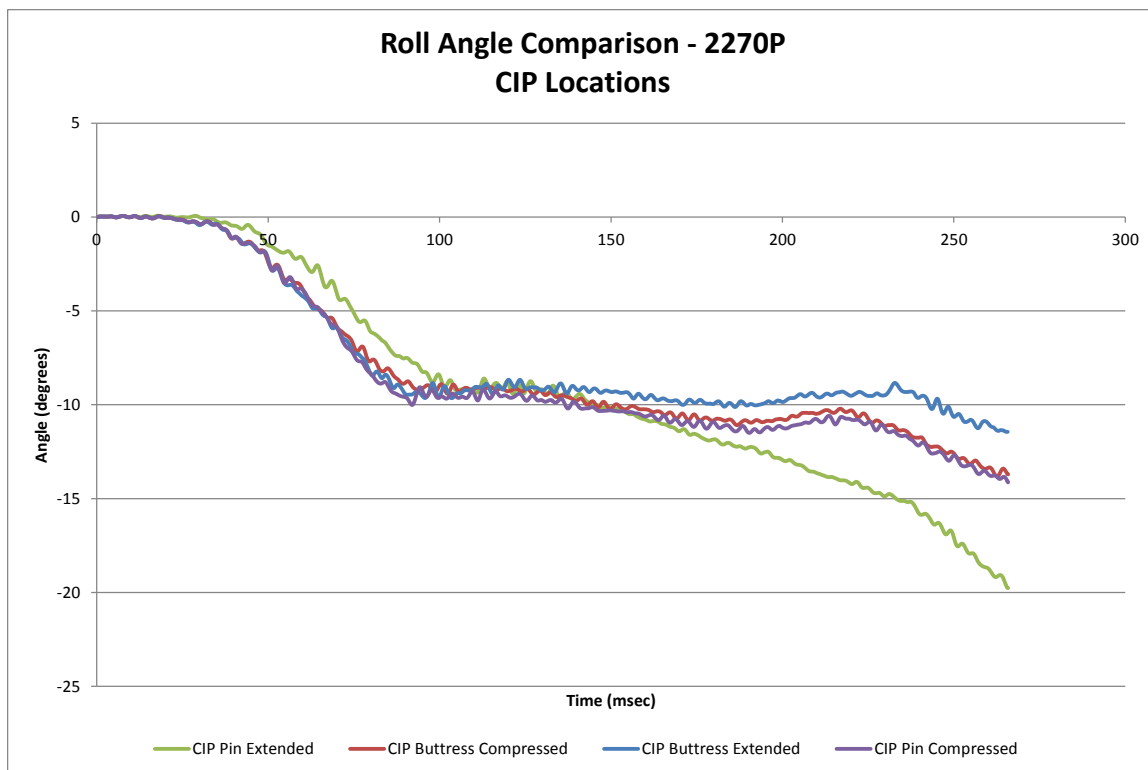


Figure 208. Roll Angle Comparison, CIP Locations, 2270P Chevrolet Silverado

Similarly, the simulation with respect to the pin with the extended joint had a delayed pitch of approximately 5 msec, and it did not follow a similar trend as the other simulations, as shown in Figure 209. The pitch angles for each impact location simulation were small, with a variance within 6 degrees. The yaw angles were similar to each other in each simulation, as shown in Figure 210. The simulation with respect to the pin and the extended joint had a peak yaw angle 12 percent larger than observed for the other three simulations.

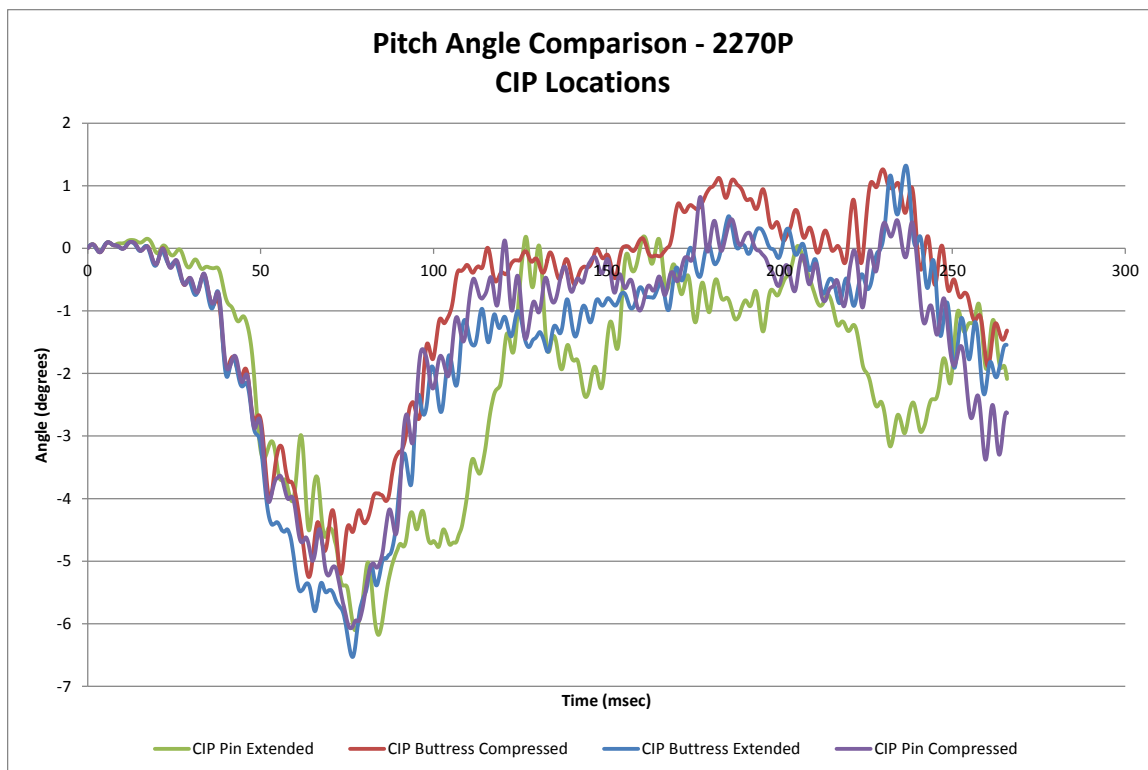


Figure 209. Pitch Angle Comparison, CIP Locations, 2270P Chevrolet Silverado

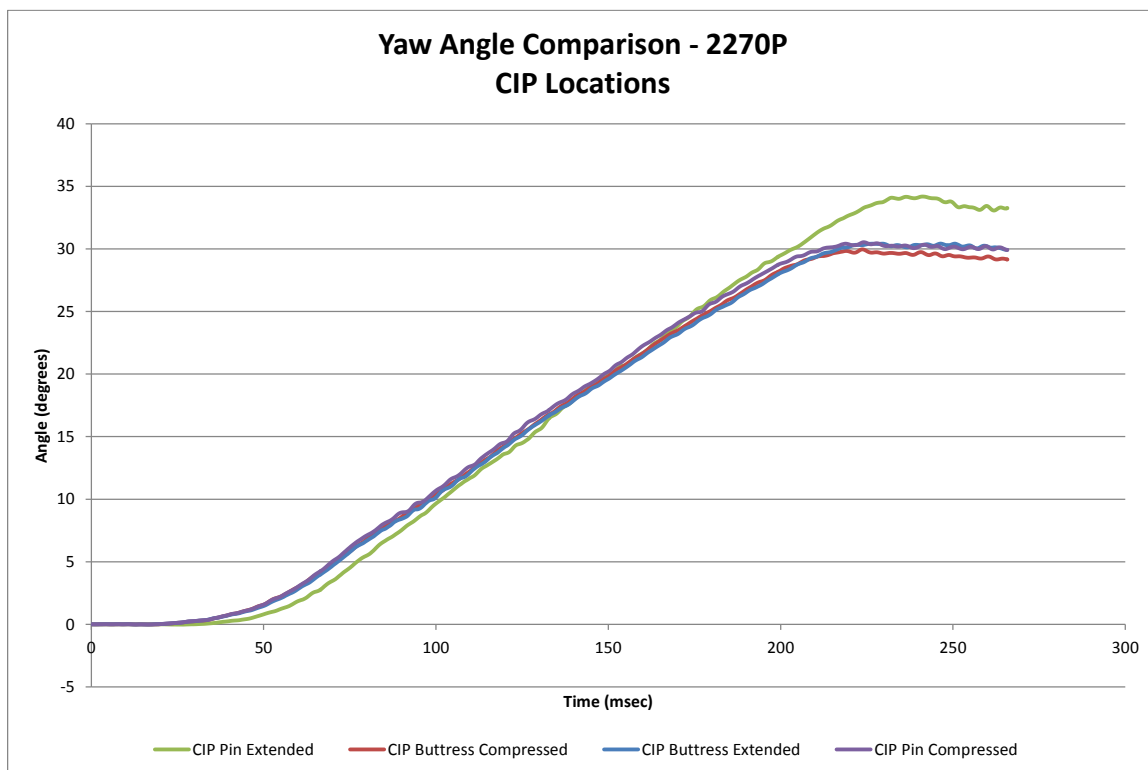


Figure 210. Yaw Angle Comparison, CIP Locations, 2270P Chevrolet Silverado

The von Mises and Tresca yield conditions were considered to evaluate the stresses within the joint parts. A description of each part in relation to each yield condition and the results are shown in Table 46. For some of the parts, the von Mises and Tresca yield conditions did not correspond to each other. The maximum stress of the vertical drop-down pin exceeded the Tresca yield condition in all the simulations at the suggest CIP locations in MASH, whereas the stresses did not exceed the von Mises yield condition. During the simulations with the Silverado model, the cover plate bolts experienced stresses that exceeded both the Tresca and von Mises yield conditions, thus causing permanent deformations. The simulations with respect to the buttress are being re-submitted due to an issue in properly determining the stresses within the cover plate bolts. Therefore, the results will be updated when the simulations are finished.

The horizontal gusset plates exceeded the yield conditions for all of the simulations. However, the peak stresses in the gusset plates occurred at the edges of the pin hole where the pin was bearing on the gusset plates, similar to what was shown previously in Figure 148. Due to the localization of the stresses, the gusset plate holes may have ovalized or torn out due to high bearing stresses, but they would not likely have ruptured, and could potentially be reloaded during subsequent impact events.

Table 46. RESTORE Barrier Component Stress Comparison, 2270P Silverado, CIP Locations

Simulation Parameters			Impact Location and Trial No.			
			31	35	41	71
			CIP Buttress Extended	CIP Buttress Compressed	CIP Pin Extended	CIP Pin Compressed
Vertical Pin	Max.Tresca Stress	Stress, ksi (MPa)	31.9 (220)	34.4 (237)	33.2 (229)	35.6 (246)
		$\tau \geq 0.5\sigma_y$?	Yes	Yes	Yes	Yes
	Max.von Mises Stress	Stress, ksi (MPa)	59.4 (410)	60.3 (416)	61.0 (421)	62.2 (429)
		$\sigma_{vm} \geq \sigma_y$?	No	No	No	No
Horizontal Gusset Plates	Max.Tresca Stress	Stress, ksi (MPa)	41.4 (286)	45.1 (311)	37.4 (258)	45.7 (315)
		$\tau \geq 0.5\sigma_y$?	Yes	Yes	Yes	Yes
	Max.von Mises Stress	Stress, ksi (MPa)	71.8 (495)	78.9 (544)	65.8 (454)	80.1 (552)
		$\sigma_{vm} \geq \sigma_y$?	Yes	Yes	Yes	Yes
Cover Plate Bolts	Max.Tresca Stress	Stress, ksi (MPa)	61.2 (422)	59.0 (407)	59.4 (410)	61.7 (425)
		$\tau \geq 0.5\sigma_y$?	Yes	Yes	Yes	Yes
	Max.von Mises Stress	Stress, ksi (MPa)	109.2 (753)	105.1 (724)	105.8 (729)	108.4 (748)
		$\sigma_{vm} \geq \sigma_y$?	Yes	Yes	Yes	Yes
Cover Plate Gussets	Max.Tresca Stress	Stress, ksi (MPa)	33.3 (229)	30.2 (208)	33.2 (229)	29.9 (206)
		$\tau \geq 0.5\sigma_y$?	Yes	No	Yes	No
	Max.von Mises Stress	Stress, ksi (MPa)	59.1 (408)	57.7 (398)	61.2 (422)	62.8 (433)
		$\sigma_{vm} \geq \sigma_y$?	No	No	No	Yes
Top Tube, Splice, and Termination	Max.Tresca Stress	Stress, ksi (MPa)	33.6 (231)	34.9 (241)	35.7 (246)	32.5 (224)
		$\tau \geq 0.5\sigma_y$?	Yes	Yes	Yes	Yes
	Max.von Mises Stress	Stress, ksi (MPa)	59.8 (412)	61.3 (423)	62.1 (428)	61.7 (426)
		$\sigma_{vm} \geq \sigma_y$?	No	No	No	No
Cover Plate	Max.Tresca Stress	Stress, ksi (MPa)	37.7 (260)	39.1 (269)	34.8 (240)	43.6 (300)
		$\tau \geq 0.5\sigma_y$?	Yes	Yes	Yes	Yes
	Max.von Mises Stress	Stress, ksi (MPa)	68.3 (471)	68.8 (474)	62.1 (428)	76.8 (530)
		$\sigma_{vm} \geq \sigma_y$?	Yes	Yes	No	Yes

The cover plate gussets had maximum stresses greater than the Tresca yield condition during simulations with the extended joint, whereas the simulations with the compressed joint did not have maximum stresses exceed the Tresca yield condition. The simulation upstream of the pin with the compressed joint had maximum stresses that exceeded the von Mises yield condition; however, did not exceed to Tresca yield condition. All of the stresses in the cover plate gussets that exceeded the yield conditions were within 6 percent of the yield strength.

The cover plate stresses during all of the impacts at the MASH suggested CIP locations exceeded the von Mises yield condition, except in the simulation relative to the pin with the extended joint. The majority of the stresses on the cover plate were

concentrated on the curved sides due to contact between the cover plate and the horizontal gusset plates.

The top tube, tube splices, and tube termination had peak stresses that exceeded the yield conditions in the simulations at each impact location based on the Tresca yield conditions. However, none of the simulations showed that the tube parts would exceed the von Mises yield condition.

12.3 Upstream Location Simulation Results

Impact points upstream from the pin and gusset plate assemblies were simulated at intervals of 10 ft (3.0 m). The impact point occurred 4 ft – 3 in. (1.3 m) upstream from locations of 10, 20, 30, and 40 ft (3.0, 6.1, 9.1, 12.2 m) away from the downstream end of the last concrete RESTORE barrier in order to determine the maximum load imparted to the ACJ hardware and investigate the potential for vehicle snag on posts when traveling toward a stiffened barrier.

The comparison of results for the Silverado vehicle model between the simulations at upstream impact locations is shown in Table 47. The simulations at each impact point successfully contained and redirected the Silverado model, as shown in Figures 211 through 214. The simulation end times were different, but all of the desired information was obtained through each simulation. However, shortly after becoming parallel to the system, the Chevrolet Silverado model in the simulation with the impact location 20 ft (6.1 m) upstream from the pin-and-gusset plate configuration when the joint was compressed experienced negative volumes within the ACJ bolts. The elements on the top, impact side, downstream RESTORE barrier bolt produced negative volumes,

and the model became unstable. Due to the model instability, the vehicle did not exit the system, and several results in Table 47 could not be obtained.

During the simulations with the impact location 20 and 40 ft (6.1 and 12.2 m) upstream from the pin, the exit velocity was slightly greater than the parallel velocity. Generally speaking, one may expect the parallel velocity to be greater than the exit velocity following additional energy losses.

Significant differences in damage of the Silverado model were not evident between the upstream impact location simulations and the interior impact simulation. The Silverado model was crushed on the left-front corner and engine hood in the upstream impact location simulations.

Table 47. Comparison Matrix of Upstream Impact Locations, 2270P Chevrolet Silverado

Simulation Parameters		Impact Location and Trial No.				
		45 10 ft Upstream Extended	46 20 ft Upstream Extended	67 20 ft Upstream Compressed	47 30 ft Upstream Extended	48 40 ft Upstream Extended
End Time, ms		316	416	216	516	566
Parallel Conditions	Time, ms	212	232	137	237	236
	Velocity, mph (km/h)	50.0 (80.5)	49.4 (79.5)	51.8 (83.4)	52.0 (86.6)	49.7 (80.0)
Exit Conditions	Velocity, mph (km/h)	49.8 (80.1)	49.9 (80.3)	NA	51.5 (82.9)	50.9 (82.0)
	Angle, deg.	4.8	5.8	NA	1.4	3.8
	Time, ms	276	306	NA	296	306
Length of Contact		8 ft - 10 in. (2.7 m)	11 ft - 2 in. (3.4 m)	NA	9 ft - 6 in. (2.9 m)	9 ft - 2 in. (2.8 m)
t*, ms		91.1	98.8	99.0	94.6	97.0
ORA, g's	Longitudinal	-9.18	8.4	-6.68	-7.59	-11.42
	Lateral	16.79	14.4	7.37	16.67	17.4
OIV, ft/s (m/s)	Longitudinal	-15.58 (-4.75)	-13.83 (-4.22)	-14.37 (-4.38)	-13.25 (-4.04)	-13.83 (-4.22)
	Lateral	23.14 (7.05)	18.34 (5.59)	18.78 (5.73)	19.06 (5.81)	19.89 (6.06)
Test Article Deflections, in. (mm)	Dynamic of Concrete	6.8 (173)	11.0 (279)	10.6 (269)	8.7 (221)	9.8 (249)
	Dynamic of Steel Rail	7.0 (178)	11.2 (284)	10.9 (277)	9.1 (231)	10.4 (264)
	Working Width	29.1 (739)	33.3 (846)	32.9 (836)	31.0 (787)	32.1 (815)
Location of Max. Deflection Upstream from Pin		20 ft (6.1 m)	20 ft (6.1 m)	20 ft (6.1 m)	20 ft (6.1 m)	40 ft (12.2 m)
Vehicle Stability	Max. Roll, deg.	-25	-32.9	-18.2	-28	-27.6
	Max. Pitch, deg.	-5.7	-20.5	-3.6	-18	-12.3
	Max. Yaw, deg.	30.3	31.9	28.3	27.1	29.3
Posts Hit by Leading Tire (wheel snag)		0	1	1	0	0
Max. Lateral Impact Force, kips (kN)		72.6 (322.9)	61.74 (274.6)	59.4 (264.1)	67.4 (299.8)	63.9 (284.2)

¹ Calculated using global Y-acceleration multiplied by mass.

² Impacted 4 ft – 3 in. (1.3 m) upstream from noted location.

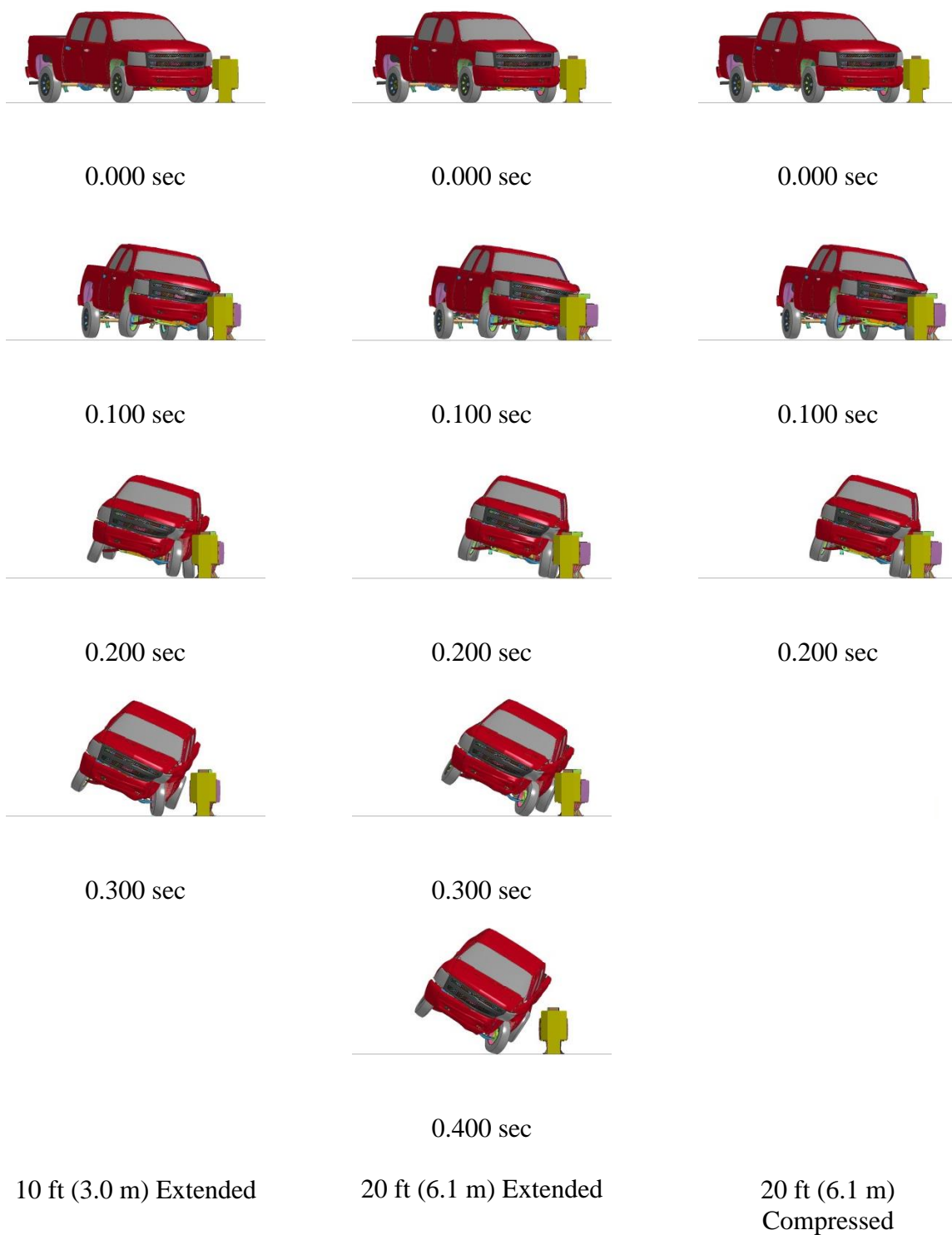


Figure 211. RESTORE Barrier Transition, 2270P Silverado Simulation Comparison, Upstream Impact Locations, Downstream View



Figure 212. RESTORE Barrier Transition, 2270P Silverado Simulation Comparison, Upstream Impact Locations, Downstream View

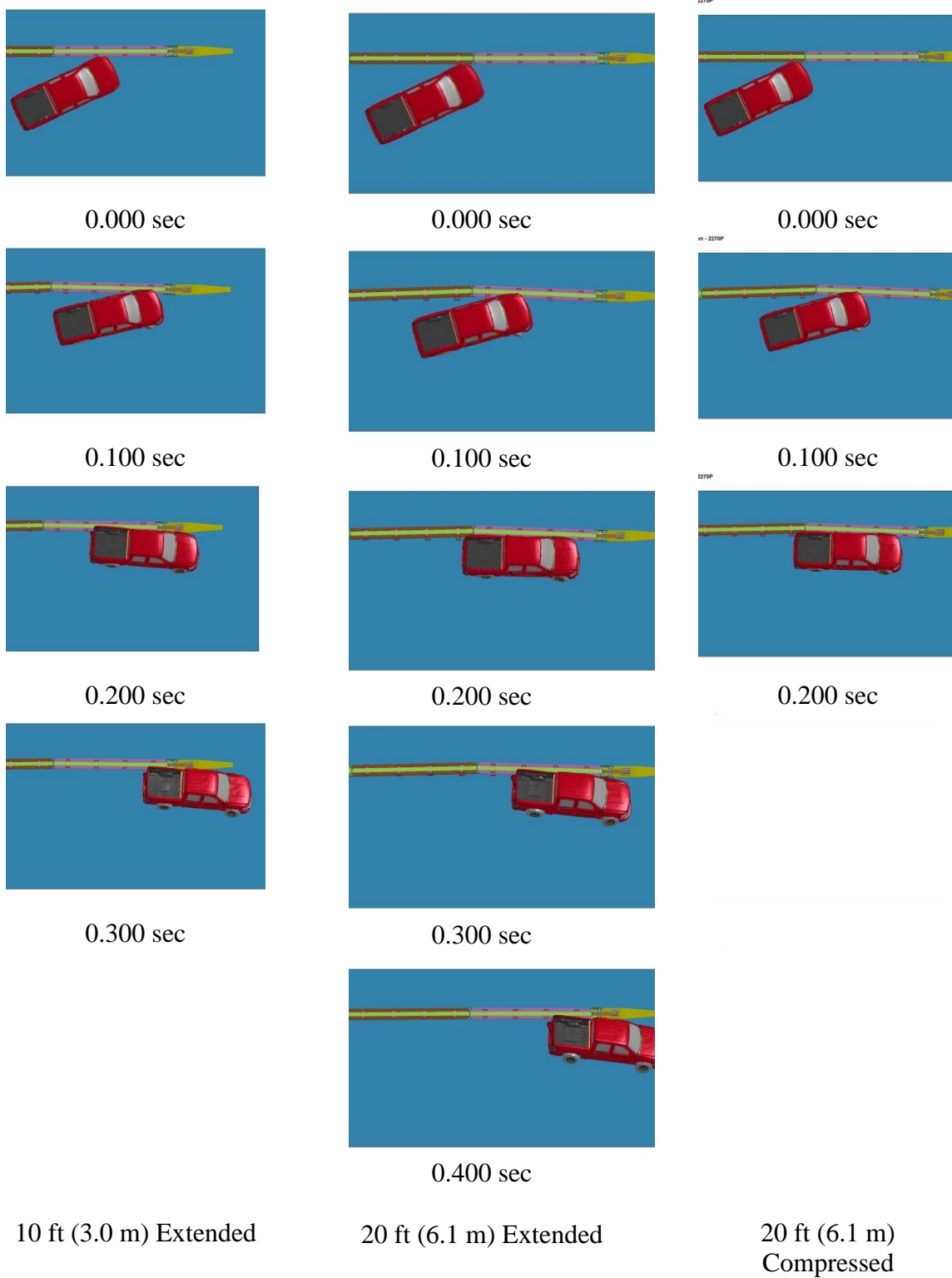


Figure 213. RESTORE Barrier Transition, 2270P Silverado Simulation Comparison, Upstream Impact Locations, Overhead View

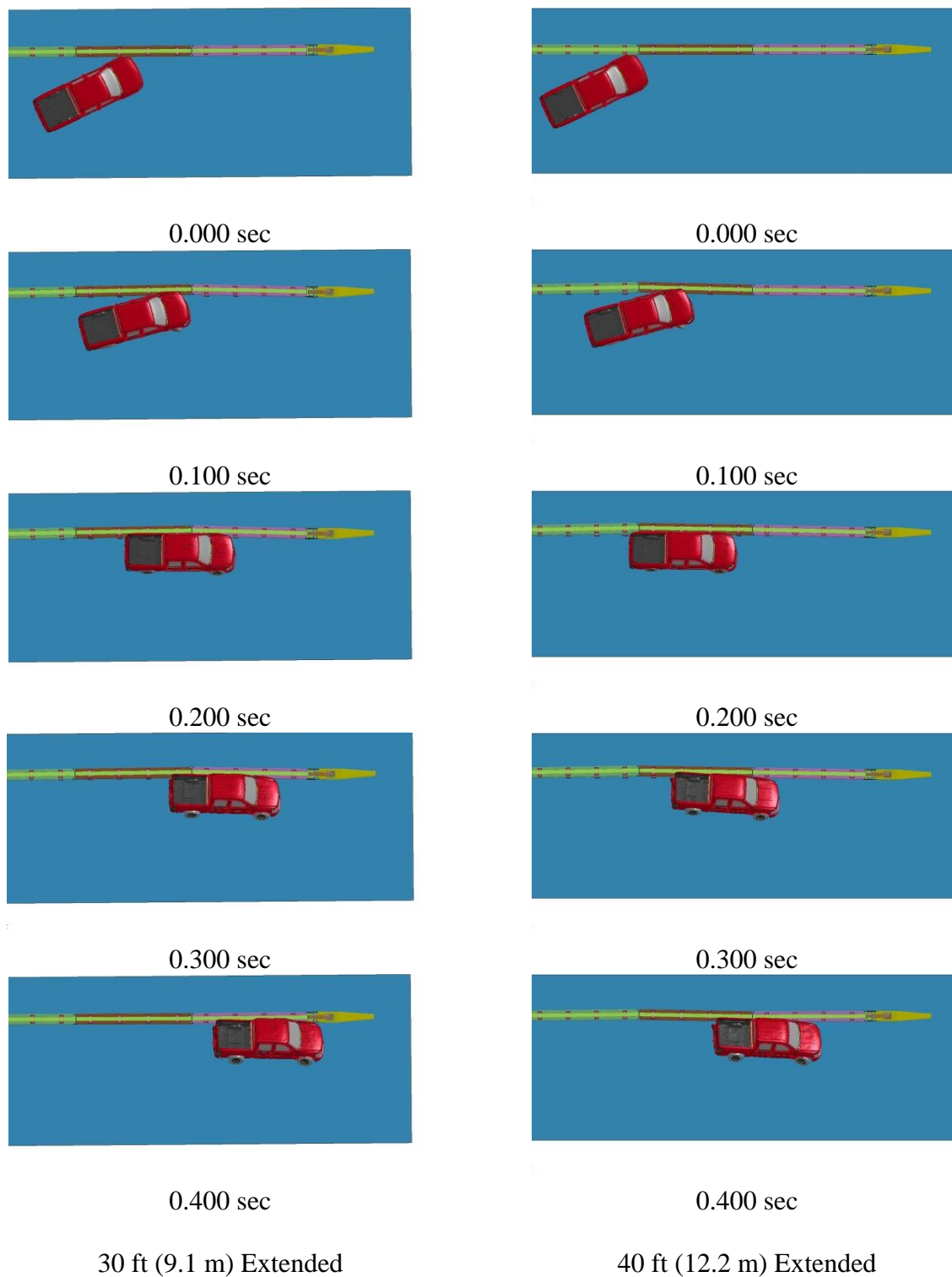


Figure 214. RESTORE Barrier Transition, 2270P Silverado Comparison, Upstream Impact Locations, Overhead View

The simulated dynamic barrier deflection of the RESTORE barrier at each impact location showed a trend where the deflections increased as the impact occurred farther upstream from the pin. However, the maximum dynamic deflection of 11.0 in. (279 mm) was found at the 20-ft (6.1-m) impact location simulation when considering impact locations of 10, 20, 30, and 40 ft (3.0, 6.1, 9.1, and 12.2 m). The simulation at the 20-ft (6.1-m) impact location with extended joint showed a 10 percent larger dynamic deflection than observed in the simulation at the interior location. The larger deflections were likely caused by the presence of a nearby hinge or pin, ACJ widening at 20 ft (6.1 m), and preventing the distribution of load across multiple barrier segments, thus changing the constraints of the system and increasing the dynamic barrier deflections.

The Silverado model at the 20-ft (6.1-m) location with the compressed and extended joint showed $2\frac{3}{4}$ in. (70 mm) of post contact across the upstream face of the second post downstream from impact by the left-front tire. The other simulations did not show any post contact.

The lateral change in velocity between of the impact location simulations were similar through approximately 50 msec, as shown in Figure 215. However, the lateral change in velocity for the simulation 10 ft (3.0 m) upstream from the pin was approximately 17 percent greater at 75 msec than observed at the other simulations. The longitudinal velocity for the simulations were nearly identical through approximately 50 msec, as shown in Figure 216. The simulation at the impact location 30 ft (9.1 m) upstream from the pin had the least longitudinal change in velocity through 500 msec. The longitudinal OIV were similar between each of the simulations. The lateral OIV for

the simulation 10 ft (3.0 m) upstream from the pin was the greater than the other simulations by approximately 15 percent. The other simulations had similar OIVs.

The ORA values were different for all of the simulations. The simulation 20 ft (6.1 m) upstream from the pin with the extended joint had a positive longitudinal ORA. The ORA values were expected to be negative due to the vehicle orientation. The simulation 20 ft (6.1 m) upstream from the pin with the compressed joint had the lowest lateral ORA value. However, the simulation terminated shortly after the Silverado model became parallel to the system. Thus, the ORA values for the simulation 20 ft (6.1 m) upstream of the drop-down pin with the compressed joint may not be accurate.

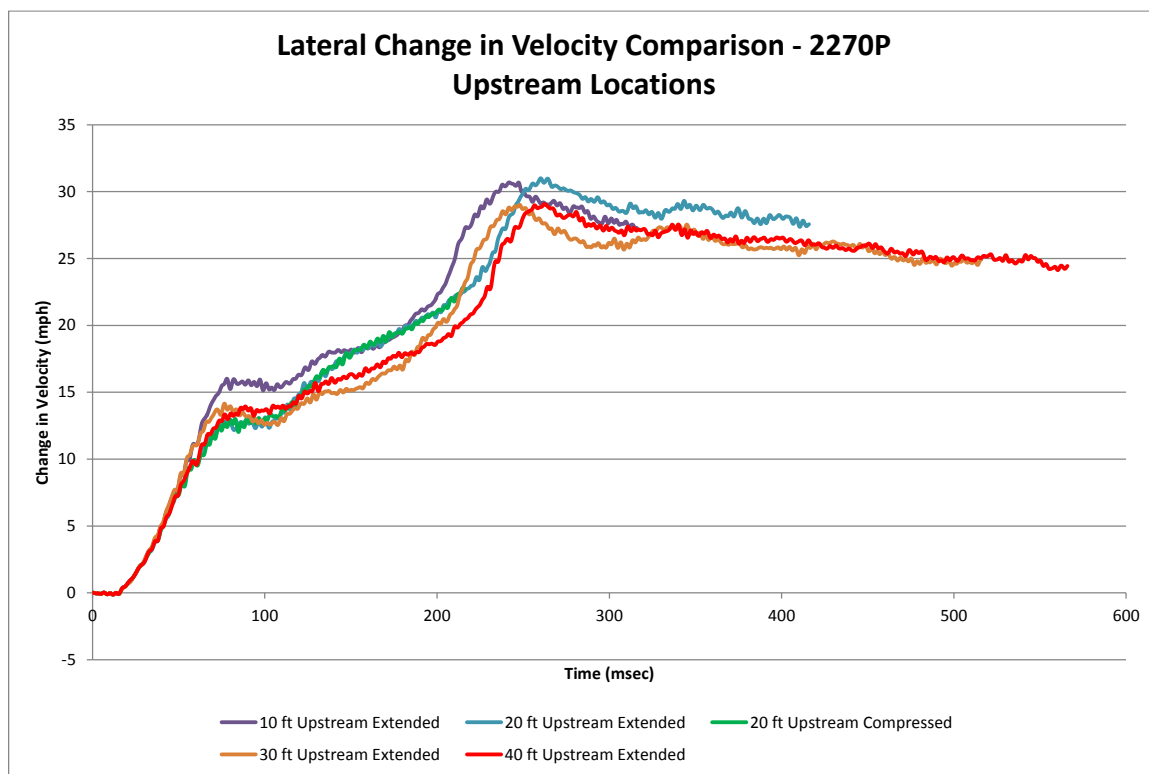


Figure 215. Lateral Change in Velocity, Upstream Impact Locations, 2270P Silverado

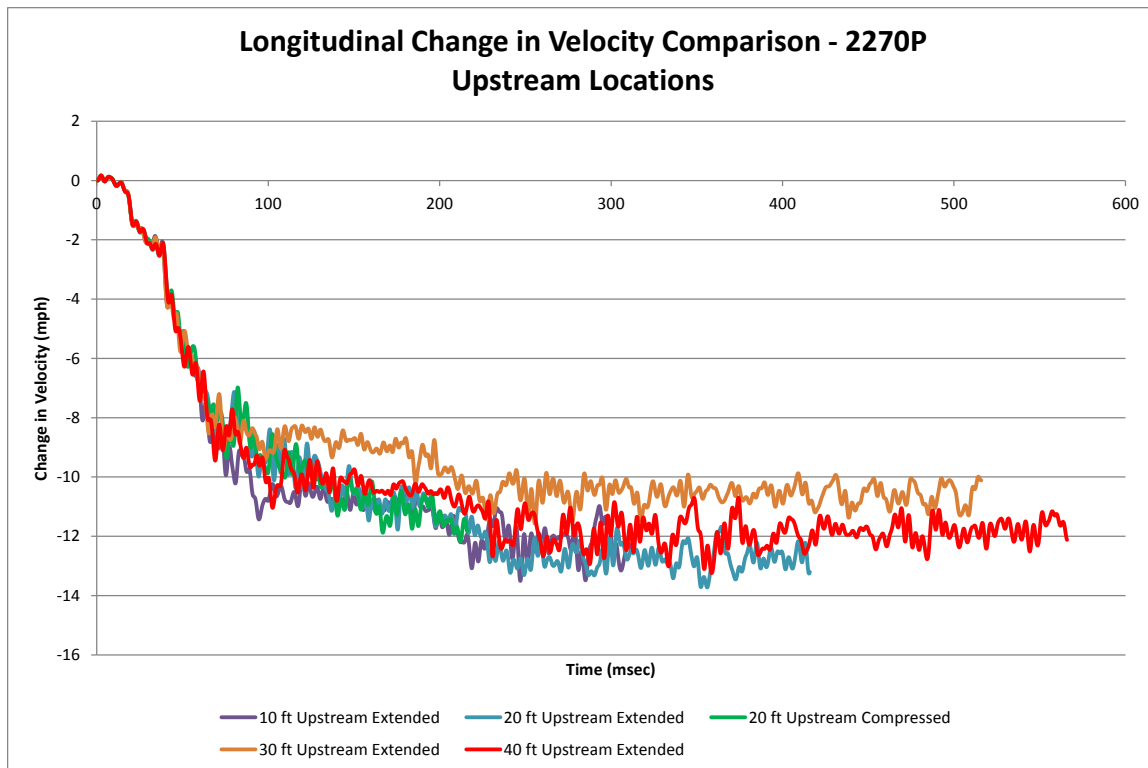


Figure 216. Longitudinal Change in Velocity, Upstream Impact Locations, 2270P Silverado

The lateral impact forces were calculated using the CFC60 filtered 50-msec global Y-accelerations multiplied by the mass. The simulation at 10 ft (3.0 m) upstream from the pin showed a higher peak lateral force as compared to the simulations at 20, 30, and 40 ft (6.1, 9.0, and 12.2 m) upstream from the pin, as shown in Figure 217. It was expected that there would be an increase in the lateral barrier force closer to the pin due to the constraint in the lateral y-direction, thus decreasing dynamic barrier deflections. The 10-ft (3.0-m) impact location simulation had approximately a 7 percent larger force than observed in the 30-ft (9.1-m) impact location simulation and approximately a 14 percent greater impact force than observed in the 20- and 40-ft (6.1- and 12.2-m) impact location simulations.

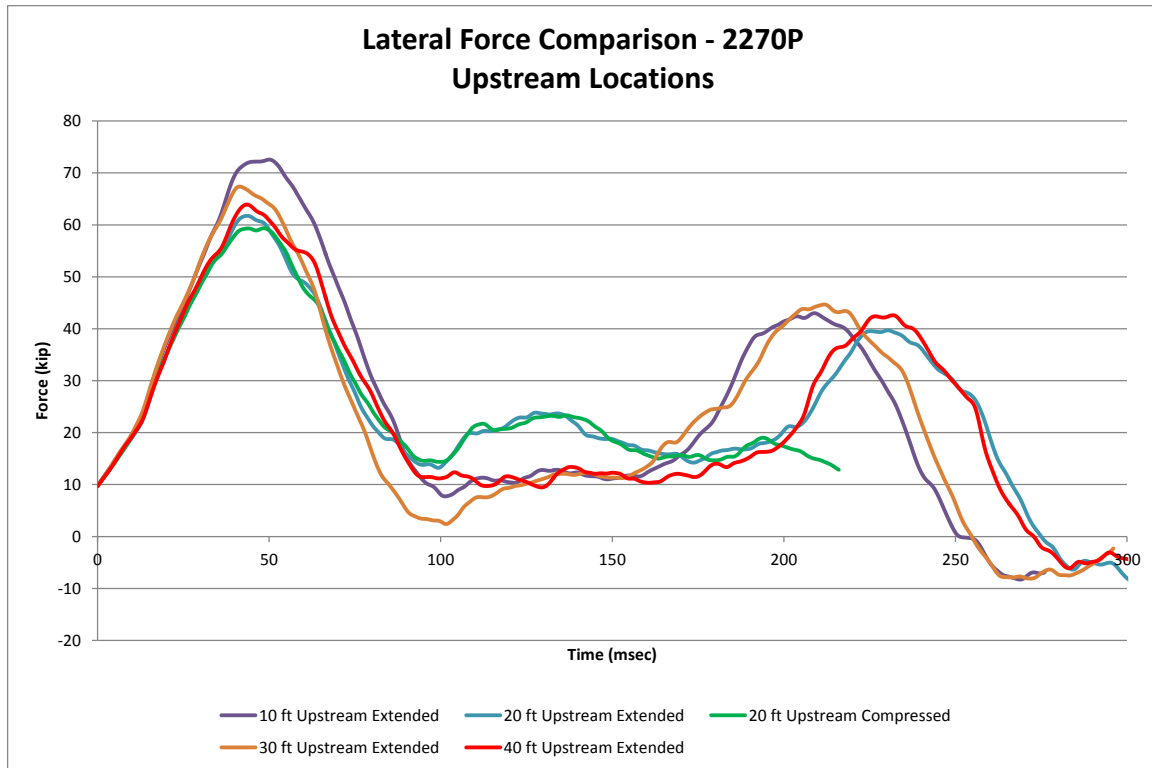


Figure 217. Lateral Force Comparison, Upstream Impact Locations, 2270P Silverado

The roll of the Silverado model at each impact location showed similar angles through approximately 100 msec, as shown in Figure 218. Slight divergence occurred between the different simulated roll angles between 100 and 200 msec. After 200 msec, the Silverado model experienced the greatest roll angle of -32.9 degrees at 400 msec at the 20-ft (6.1-m) impact location simulation with the extended joint, and it was still increasing at the end of the simulation. These peak roll angles were approximately 15 and 8 percent greater than observed for the 30- and 40-ft (9.0- and 12.2-m) impact location simulations, respectively.

The pitch of the Silverado model at each impact location showed similar angles through approximately 200 msec, as shown in Figure 219. Next, the pitch angles for each impact location varied up to 4 degrees from one another through the end of the simulated

impact events. Note that the pitch angles were still increasing by the time the simulation had ended.

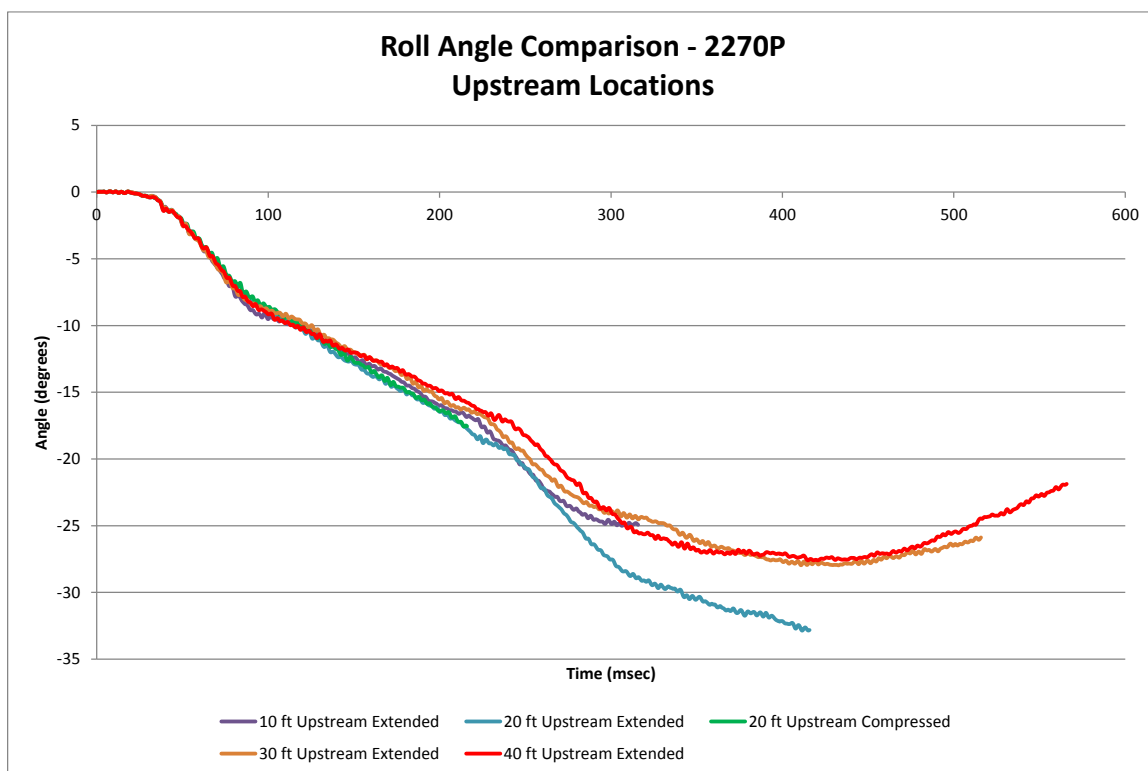


Figure 218. Vehicle Roll Comparison, Upstream Impact Locations, 2270P Silverado

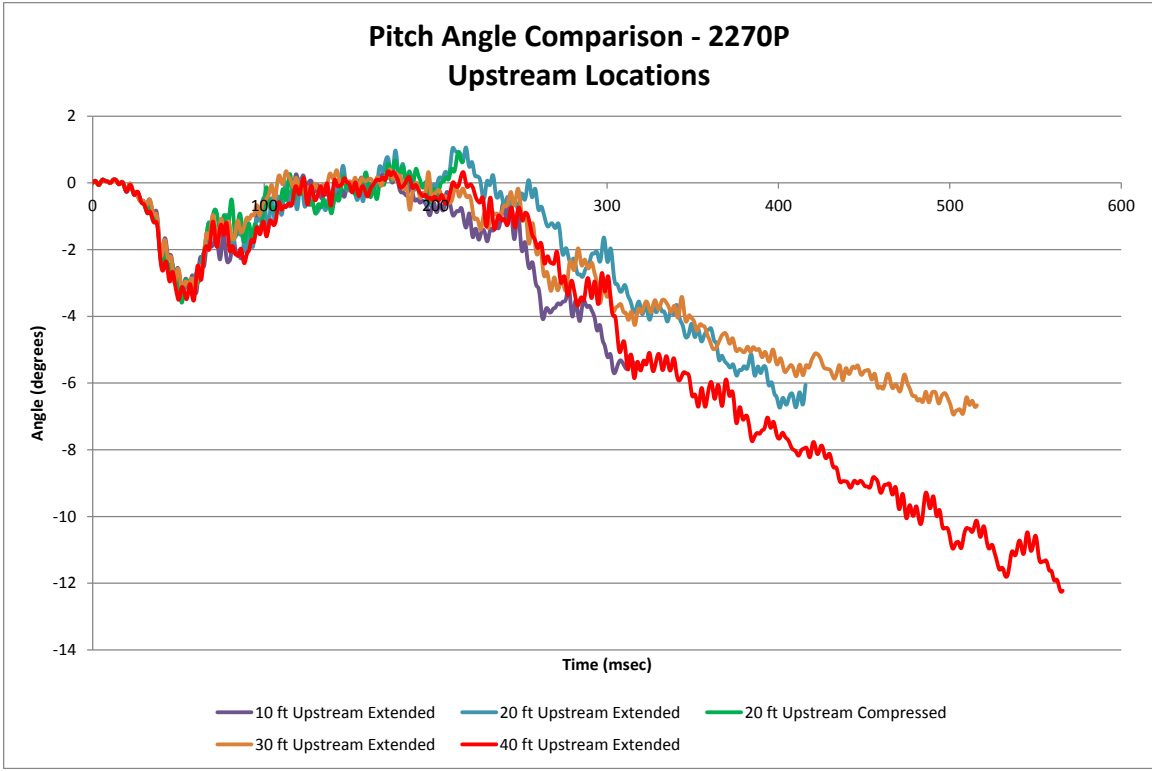


Figure 219. Vehicle Pitch Comparison, Upstream Impact Locations, 2270P Silverado

The simulation at 10-ft (3.0-m) upstream from the pin showed a faster change in yaw angle as compared to the simulations at 20-, 30- and 40-ft (6.1-, 9.0-, and 12.2-m), as shown in Figure 220. The yaw angle for the simulation at 10-ft (3.0-m) upstream from the pin was approximately 10 percent higher than observed for the simulations at 20-, 30- and 40-ft (6.1-, 9.0-, and 12.2-m) upstream from the pin at 200 msec. However, the maximum yaw angles for all of the impact location simulations were within 5 degrees.

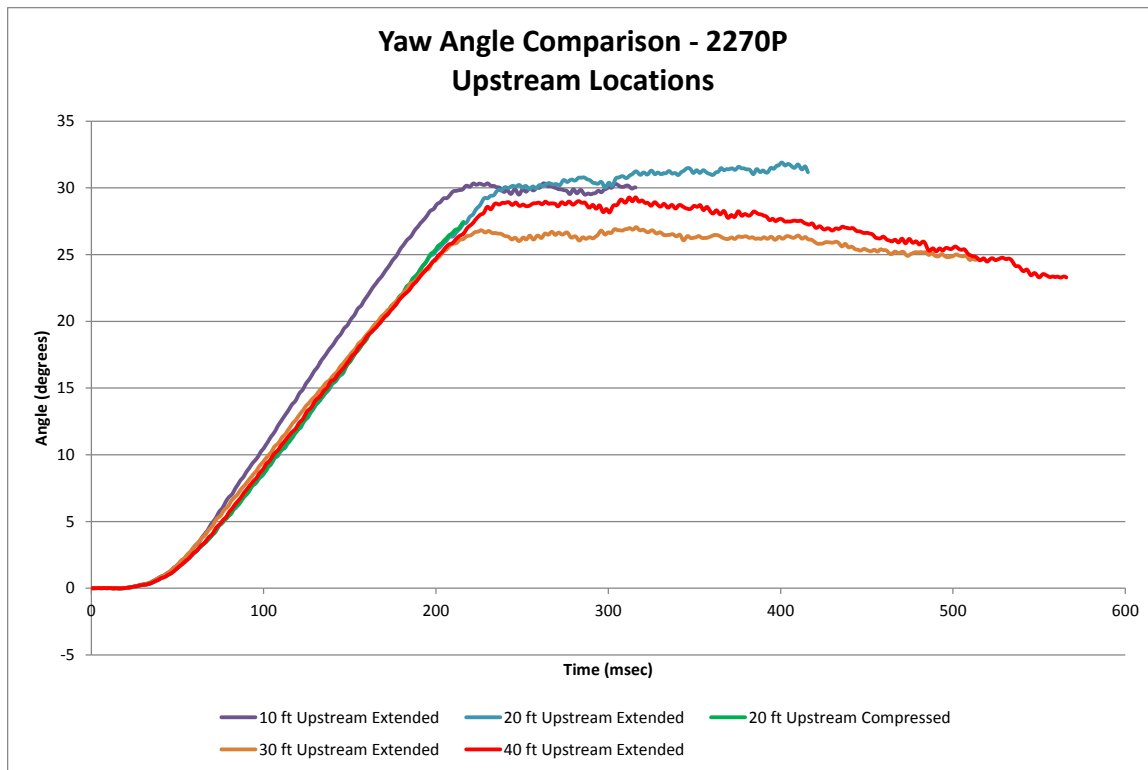


Figure 220. Vehicle Yaw Comparison, Upstream Impact Locations, 2270P Silverado

The von Mises and Tresca yield conditions were considered to evaluate the stresses within the parts of the pin and gusset plate assemblies. Each simulation with impact locations upstream from the transition hardware were compared to the interior Silverado simulation, as noted in Chapter 5 and shown in Table 48. The ACJ bolts had no visible permanent damage during test no. SFH-1. However, the top tube was deformed less than 1 in. (25 mm) above the ACJ just downstream from impact. The interior simulation was considered the baseline condition, as the full-scale test at the barrier components had minimal permanent deformations. The Silverado simulation at the interior location showed that the ACJ bolts had peak stresses that exceeded the Tresca and von Mises yield conditions. The impact location simulations upstream from the transition hardware showed Tresca stresses that were up to 35.2 percent greater than

observed for the interior location simulation. Similarly, the von Mises stresses for the upstream impact location simulations were up to 26.3 percent greater than the interior simulation. The simulations at 20-ft (6.1-m) upstream of the drop-down pin showed the largest difference as compared to the simulation at the interior location. Whereas the simulation at 40-ft (12.2-m) upstream of the pin had stresses relatively similar to the interior RESTORE barrier simulation. However, the ACJ bolts connected two adjacent rigid barriers, not allowing the concrete to fracture, which may have increased the stresses within the bolts.

The top tube and tube connections had maximum stresses that exceeded both the Tresca and von Mises yield conditions during the interior simulation impact event. Note the stresses presented were the maximum stresses for the top tube and tube splice connection. The maximum von Mises stress was 62.4 ksi (430 MPa) during the interior simulation, which satisfied the yield condition. With the exception of the simulation at 20 ft (6.1 m) upstream of the drop-down pin, the simulations at the upstream impact locations had lower maximum stresses than observed in the simulation at the interior location. The simulation of the 20-ft (6.1-m) impact location upstream from the pin with the compressed joint had the largest maximum stress difference of 8.8 percent.

Table 48. RESTORE Barrier Component Stress Comparison, 2270P Silverado, Upstream Locations

Simulation Parameters			Impact Location and Trial No.					
			NA	45	46	67	47	48
			Interior Model	10 ft Upstream Extended	20 ft Upstream Extended	20 ft Upstream Compressed	30 ft Upstream Extended	40 ft Upstream Extended
ACJ Bolts	Max. Tresca Stress	Stress, ksi (MPa)	57.5 (397)	66.0 (455)	76.2 (525)	77.8 (536)	65.6 (453)	60.1 (415)
		$\tau \geq 0.5\sigma_y$?	Yes	Yes	Yes	Yes	Yes	Yes
		% Different Than Interior	NA	14.7	32.5	35.2	14.1	4.5
	Max. von Mises Stress	Stress, ksi (MPa)	107.3 (740)	121.7 (839)	135.5 (934)	136.3 (940)	121.1 (835)	104.8 (723)
		$\sigma_{vm} \geq \sigma_y$?	Yes	Yes	Yes	Yes	Yes	No
		% Different Than Interior	NA	13.4	26.3	27	12.9	-2.3
Top Tube and Tube Splice	Max. Tresca Stress	Stress, ksi (MPa)	35.8 (247)	35.3 (244)	38.3 (264)	38.4 (265)	35.6 (246)	35.3 (244)
		$\tau \geq 0.5\sigma_y$?	Yes	Yes	Yes	Yes	Yes	Yes
		% Different Than Interior	NA	-1.4	7.0	7.1	-0.5	-1.4
	Max. von Mises Stress	Stress, ksi (MPa)	62.4 (430)	61.3 (423)	67.9 (468)	67.8 (467)	62.2 (429)	62.2 (429)
		$\sigma_{vm} \geq \sigma_y$?	Yes	No	Yes	Yes	No	No
		% Different Than Interior	NA	-1.8	8.8	8.6	-0.4	-0.3

12.4 Reverse-Direction Impact Location Simulation Results

Simulations of impact points in the reverse direction were performed at the slope-break point of the rigid concrete buttress, while traveling toward the RESTORE barrier as well as 4 ft – 3 in. (1.3 m) upstream from the upstream corner of the cover plate. These locations were evaluated with the joint extended to investigate vehicle snag and excessive OIVs and ORAs. Prior MASH testing on a concrete barrier with a horizontal flare rate of 6:1 over the full height has never been conducted. Therefore, a simulation effort was conducted to evaluate an impact at the horizontal slope-break point.

The comparison of results of the Silverado model in simulations under reverse-direction locations is shown in Table 49. The simulations at each impact point successfully contained and redirected the Silverado model, as shown in Figures 221 and 222. The simulation end times varied. However, all desired information was obtained through each impact event. The stresses in the transition hardware were acceptable, and they were not reported herein.

More extensive Silverado model damage occurred in the simulation in the reverse direction than observed in the simulations at the interior and upstream locations. The left-

front corner of the Silverado model was crushed inward farther, and the hood of the vehicle had more crush on the left side. Further, the top of the left-front and left-rear doors were separated from the vehicle during the simulation at the slope-break location. The door separation did not occur during the impact simulations at the interior or upstream locations. Overall, both simulated impacts in the reverse direction showed more vehicle model damage as compared to the upstream impact location simulations and the interior impact simulation. The increased damage to the Silverado model was expected as the buttress was stiffer than the RESTORE barrier and transition region.

Table 49. Comparison Matrix of Reverse-Direction Locations, 2270P Silverado

Simulation Parameters		Impact Location and Trial No.	
		39	63
		Reverse-Direction Slope-Break Point	Reverse-Direction CIP ³
End Time, ms		455	366
Parallel Conditions	Time, ms	209	230
	Velocity, mph (km/h)	46.6 (75.1)	49.7 (80.0)
Exit Conditions	Velocity, mph (km/h)	45.8 (73.8)	48.3 (77.8)
	Angle, deg.	7.4	3.2
	Time, ms	252	256
Length of Contact		4 ft - 11 in. (1.5 m)	7 ft - 3 in. (2.2 m)
t*, ms		83.4	89.4
ORA, g's	Longitudinal	11.36	10.80
	Lateral	17.28	18.21
OIV, ft/s (m/s)	Longitudinal	-21.42 (-6.53)	-17.62 (-5.37)
	Lateral	28.33 (8.64)	23.57 (7.19)
Test Article Deflections, in. (mm)	Dynamic of Concrete	0	0.6 (15)
	Dynamic of Steel Rail	0	0.4 (10)
	Working Width	22.3 (566)	22.9 (582)
Location of Max. Deflection Upstream from Pin		0 ft (0 m)	0 ft (0 m)
Vehicle Stability	Max. Roll, deg.	-29.3	-28.6
	Max. Pitch, deg.	-21.4	-14.5
	Max. Yaw, deg.	35.9	29.2
Posts Hit by Leading Tire (wheel snag)		0	0
Max. Lateral Impact Force, kips (kN) ¹		92.4 (411.0)	80.6 (358.7)
Max. Longitudinal Impact Force, kips (kN) ²		24.6 (109.4)	19.1 (85.0)

¹ Calculated using global Y-acceleration multiplied by mass.

² Calculated using local X- and Y- accelerations coupled with yaw, multiplied by mass.

³ Impacted 4 ft – 3 in. (1.3 m) upstream from cover plate edge.



Figure 221. RESTORE Barrier Transition, 2270P Silverado Simulation Comparison, Reverse-Direction Locations, Downstream View

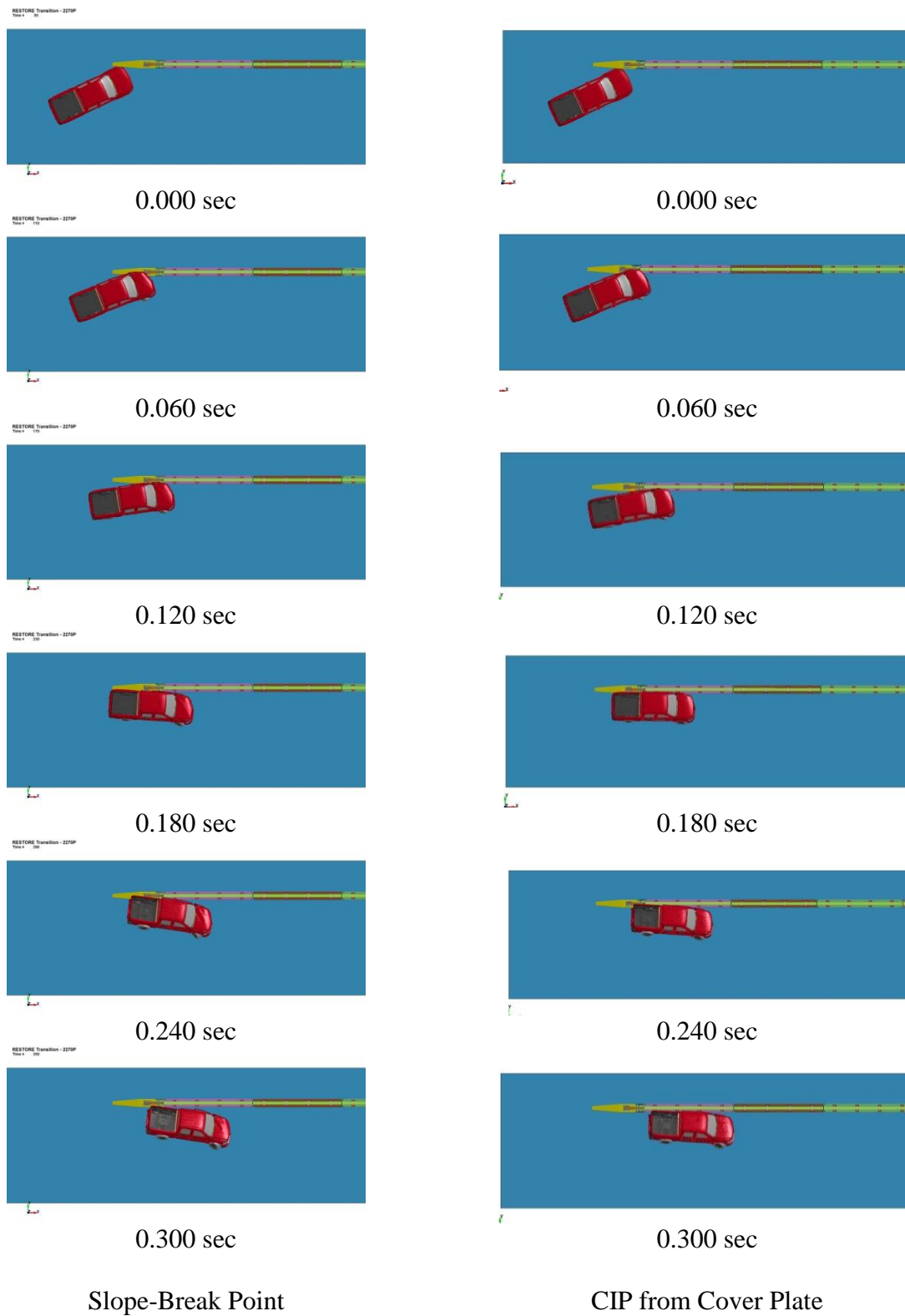


Figure 222. RESTORE Barrier Transition, 2270P Silverado Simulation Comparison, Reverse-Direction Locations, Overhead View

Since all degrees of freedom in the rigid concrete buttress were constrained, the buttress did not have any damage nor deflections. However, the upstream end of the RESTORE barrier dynamically deflected 0.6 in. (15 mm) during the simulation at the CIP location upstream from the cover plate corner. The Silverado model did not impact the RESTORE barrier in the simulation at the slope-break point, thus not causing any dynamic deflections.

The simulation where the Silverado model impacted the slope-break point had a 12 percent greater lateral change in velocity at 250 msec as compared to the CIP impact location, as shown in Figure 223. The longitudinal change in velocity was similar for both impact location simulations through 60 msec, as shown in Figure 224. However, as the Silverado model started to get further into the flared region of the buttress, the slope-break impact location simulation had greater changes in longitudinal velocity. By the end of the simulation, the slope-break point simulation had a 15 percent higher change in the longitudinal velocity at 350 msec.

The lateral and longitudinal ORA values were similar between the two simulations. The simulation at the slope-break point had higher lateral and longitudinal OIV values as compared to the CIP impact location simulation. Higher OIV and ORA values were expected due to impacting a rigid barrier. However they were within the limits presented in MASH.

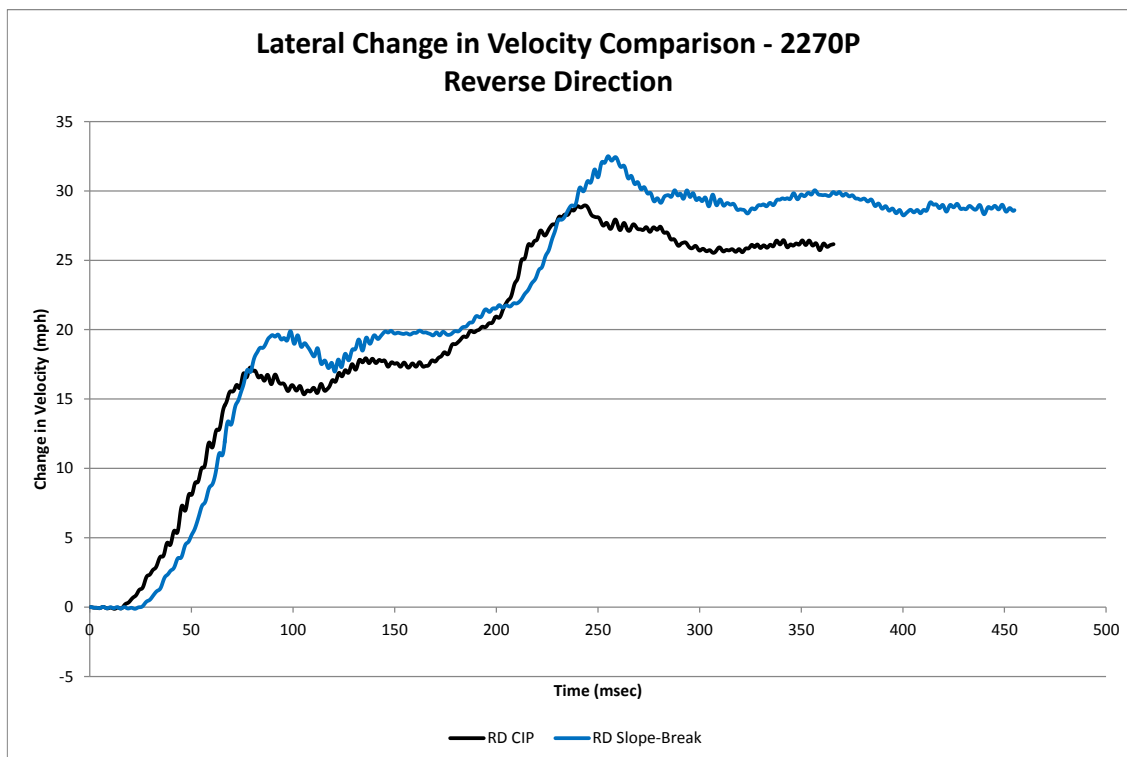


Figure 223. Lateral Change in Velocity, Reverse-Direction Locations, 2270P Silverado

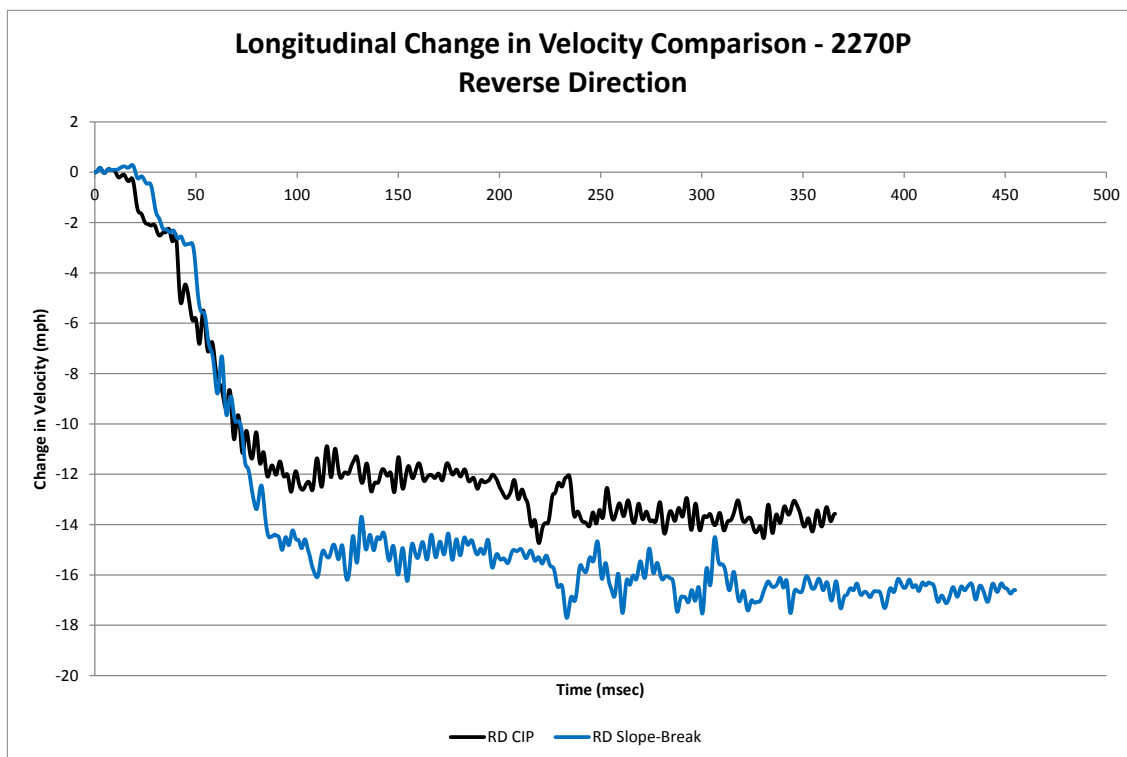


Figure 224. Longitudinal Change in Velocity, Reverse-Direction Locations, 2270P Silverado

The lateral impact forces were calculated using the CFC60 filtered 50-msec global Y-accelerations multiplied by the mass. The slope-break point location simulation experienced a 13 percent higher maximum lateral impact force than the simulation at the CIP location, as shown in Figure 225. After the peak force was reached, the two impact location simulations exhibited similar forces through the remainder of the impact event with the exception of a 5-kip (22-kN) difference in the tail slap. The longitudinal force was calculated using the local X- and Y- accelerations coupled with the yaw angle and multiplied by the mass of the vehicle model. The simulation at the slope-break point location experienced a 25 percent higher maximum longitudinal impact force as compared to the CIP location, as shown in Figure 226.

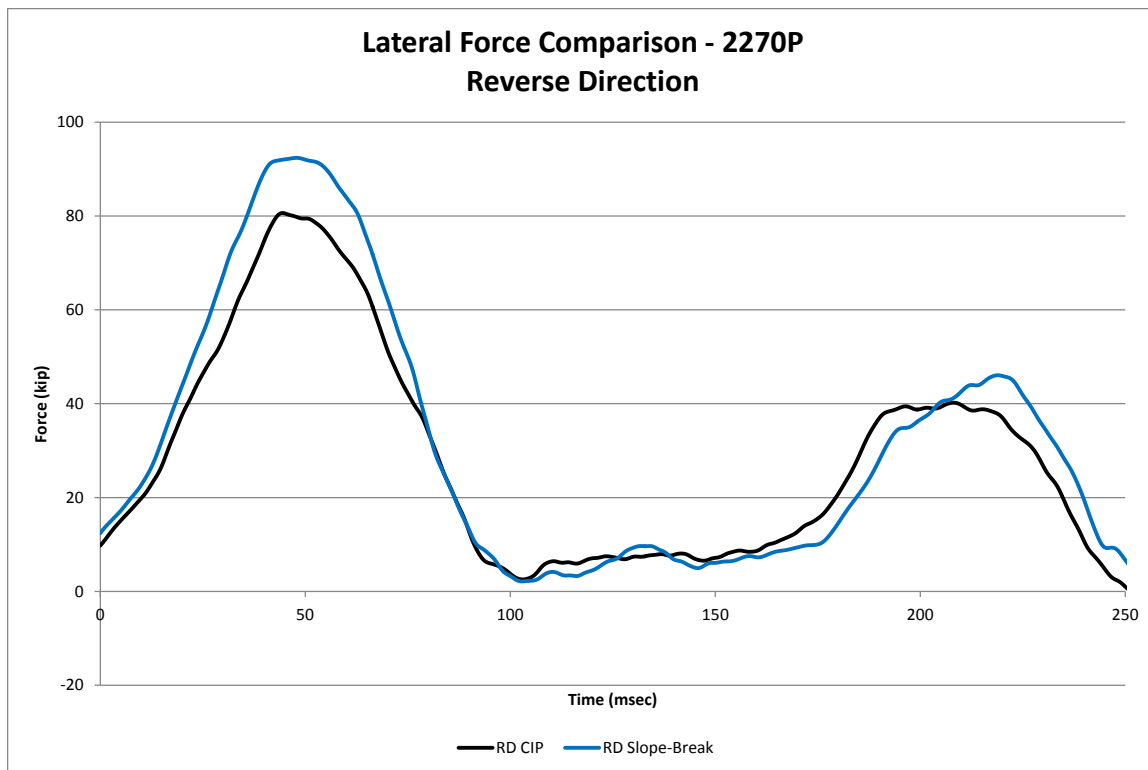


Figure 225. Lateral Force Comparison, Reverse-Direction Locations, 2270P Silverado

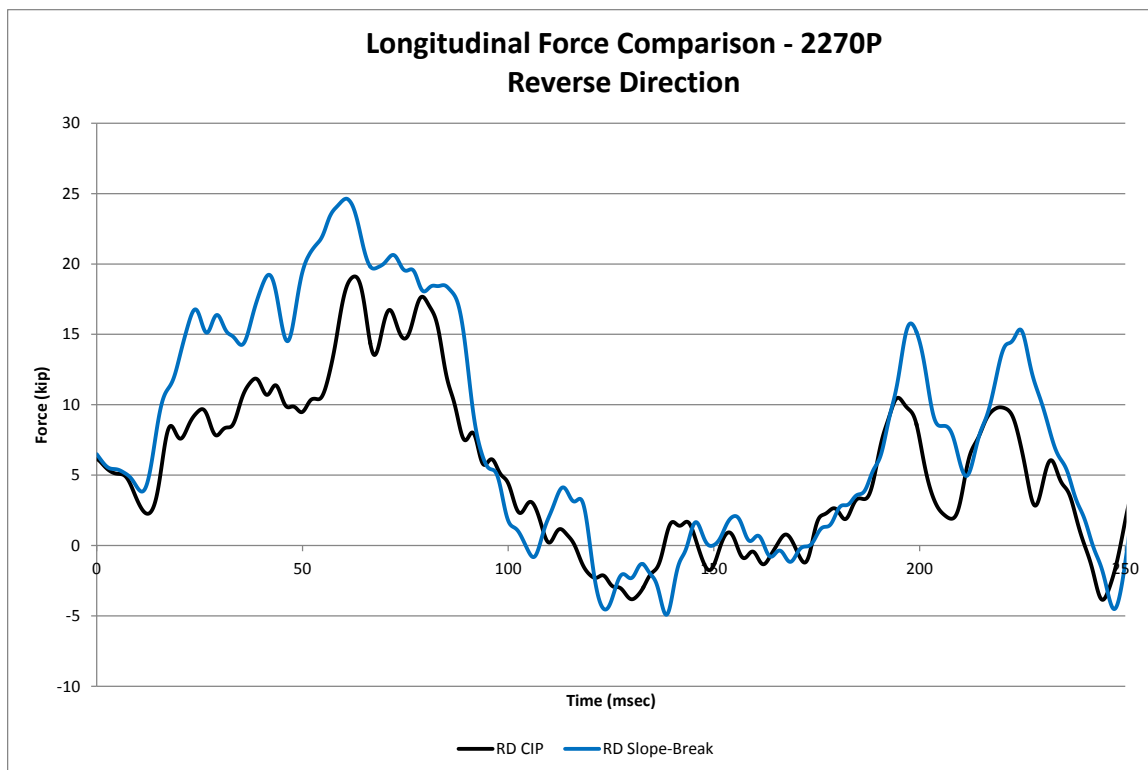


Figure 226. Longitudinal Force Comparison, Reverse-Direction Locations, 2270P Silverado

The roll angles for the Silverado model were similar through the course of the impact event, as shown in Figure 227. The vehicle model roll angles were still increasing at the time the simulations terminated. However, the pitch angles for the simulations at the slope-break point and the CIP location were different, as shown in Figure 228. The slope-break location simulation had a 33 percent larger initial peak and resulted in a 29 percent larger peak pitch angle at 375 msec as compared to the CIP location simulation. Note that the pitch angles were still increasing as the simulations ended.

The yaw angle for the simulation at the slope-break point location increased more quickly than the CIP location, as shown in Figure 229. The slope-break point simulation location had a maximum yaw angle 19 percent greater than observed at the CIP location.

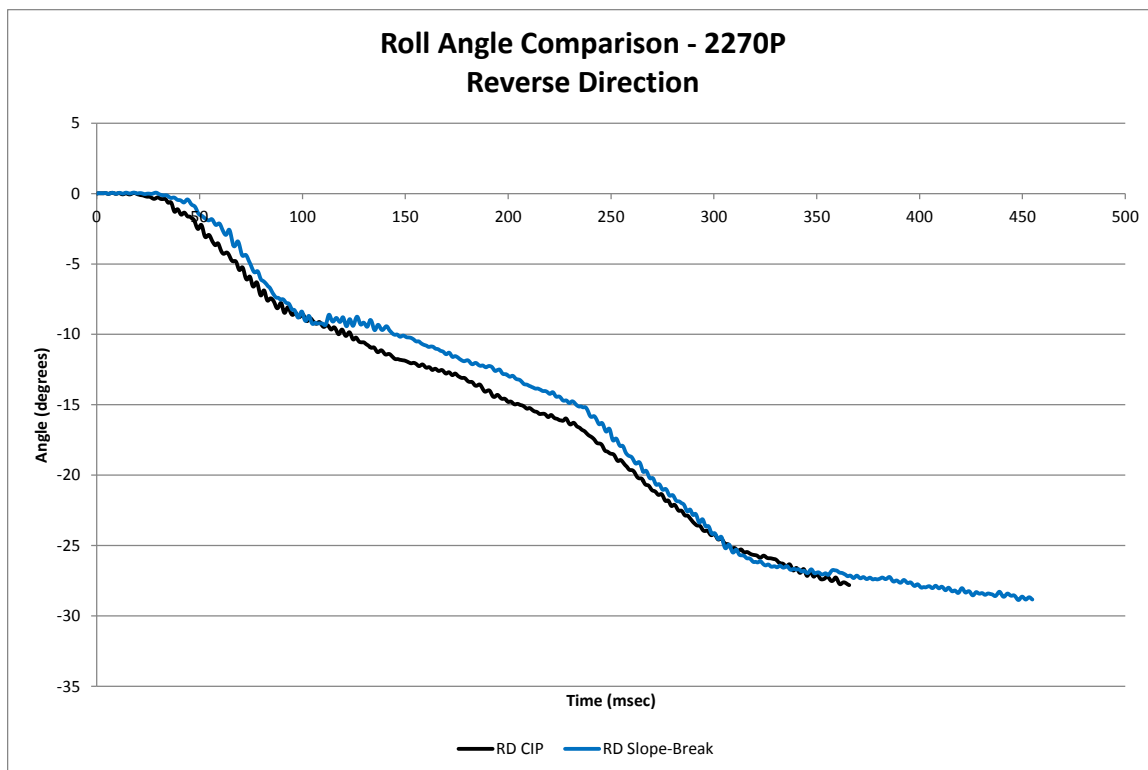


Figure 227. Roll Angle Comparison, Reverse-Direction Locations, 2270P Silverado

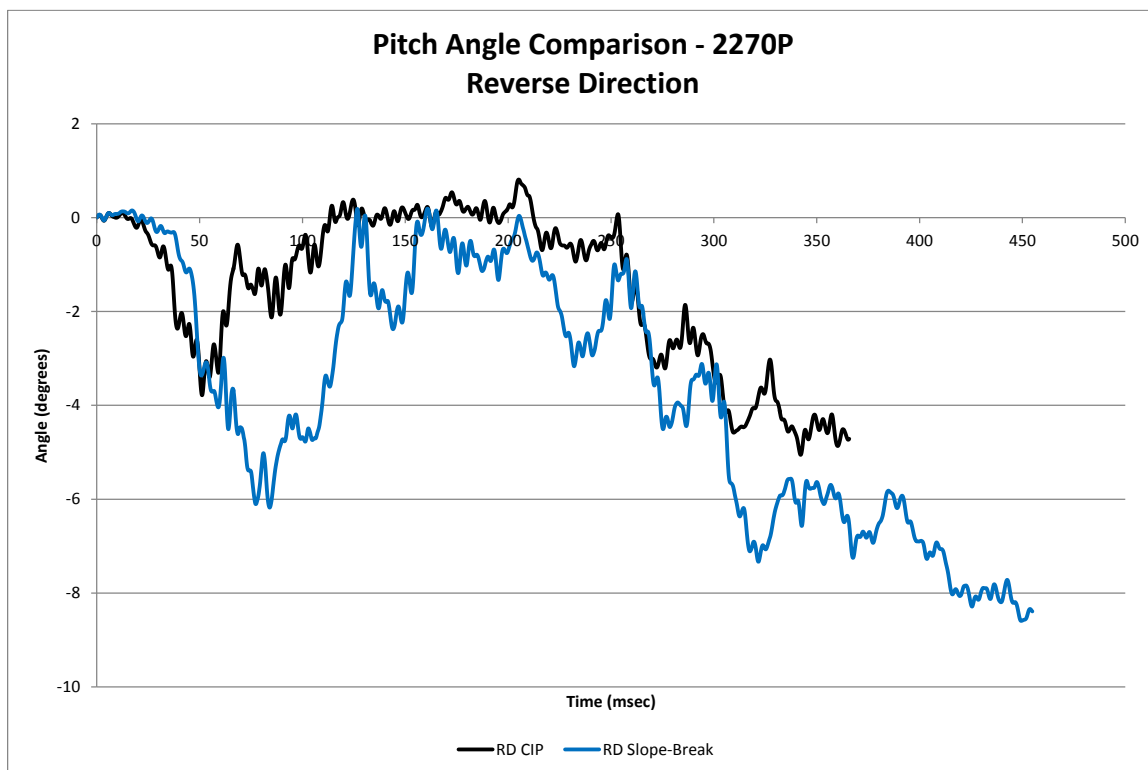


Figure 228. Pitch Angle Comparison, Reverse-Direction Locations, 2270P Silverado

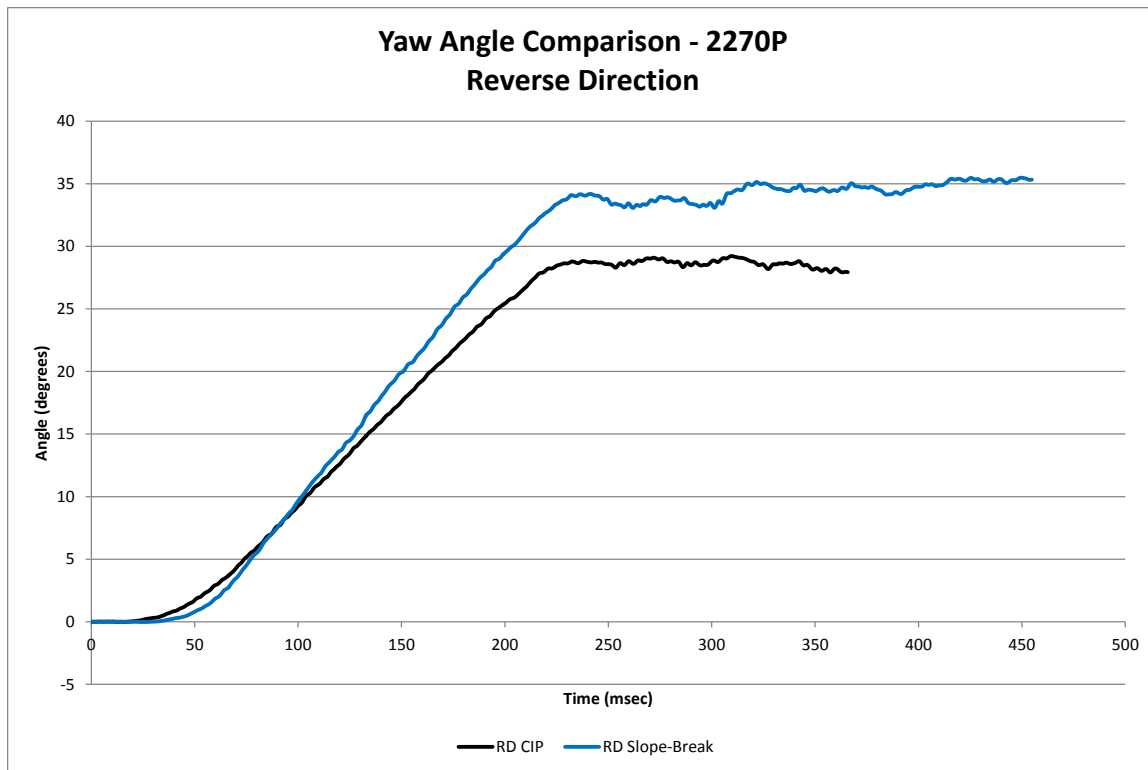


Figure 229. Yaw Angle Comparison, Reverse-Direction Locations, 2270P Silverado

12.5 2270P Simulation Summary

Various impact locations were simulated to evaluate the RESTORE barrier transition to a rigid concrete buttress according to MASH test designation no. 4-21 impact conditions. Impact locations at the suggested CIP location of 4 ft – 3 in. (1.3 m) in MASH were simulated with respect to the upstream buttress face and the drop-down pin locations. Impact locations were also simulated in 10 ft (3.0 m) increments upstream from the pin-and-gusset plate assemblies to find the worst-case critical impact points, as denoted in MASH. Further, two simulations in the reverse direction were used to determine if the transition can be used in median applications. The 2270P vehicle model, the Chevrolet Silverado, indicated that the pin and gusset plate assemblies with the rounded cover plates have the potential for being successfully used in a MASH TL-4

barrier transition that accommodates the degrees of freedom of the RESTORE barrier. Comparison plots between all of the impact locations with the pickup truck vehicle model are shown in Appendix M.

The simulations at the suggested CIP locations in MASH relative to the buttress face or pin did not cause major concerns for occupant safety. However, many of the stresses within the parts located within the pin and gusset plate assemblies exceeded both the Tresca and von Mises yield conditions. In order for the transition to be maintenance free, the vertical drop-down cover plate bolts were recommended to be re-designed, so that they do not exhibit excessive permanent deformations, which occurred in simulations at the suggested CIP locations in MASH during the Silverado model impacts. The original design intended for the vertical bolts to secure the cover plates and not experience much loading. The horizontal gusset plates exceeded the yield conditions. However, the localization of the stresses were at the edges of the pin holes and slots, which may have caused the holes to ovalize but not for the plates to rupture. The cover plate exceeded the yield conditions with the maximum stresses located on the rounded edges of the cover plate due to the cover plate contacting the horizontal gussets. The cover plate should maintain its structural capacity and could be impacted again if the permanent deformations did not cause the rounded edges to extend past the RESTORE or buttress face, which did not occur in the simulations. The cover plate gussets experienced stresses that exceeded the yield conditions in two of the simulations. However, the maximum stress was within 8 percent of yield, thus, the plate would likely have maintained structural capacity to be impacted again. The top tube, tube splice, and tube termination had stresses that exceeded the Tresca yield conditions; however, did not

exceed the von Mises yield condition. If the cover plate edges extended past the RESTORE or buttress face, the cover plates would need to be replaced due to an increased potential for snag behind the cover plate.

Through the simulations upstream from the transition hardware, the 20-ft (6.1-m) impact location upstream from the pin-and-gusset plate assemblies was observed to provide the worst-case impact location. At the 20-ft (6.1-m) impact location with the joint both extended and compressed, the system experienced dynamic deflections and ACJ bolt stresses greater than observed at other simulated impact locations. The RESTORE barrier was designed to distribute the impact force across multiple barrier segments. With the downstream end of the barrier segment pinned, the system did not distribute the impact force to as many RESTORE barrier segments, which likely increased deflections. The stresses in the ACJ bolts were up to 35 percent higher than observed in the interior location simulation. However, the loads and stresses in the ACJ bolts were likely higher than what would be expected due to the concrete RESTORE barrier segments being modeled with a rigid material model that was unable to fracture and spall, as was observed with the concrete beams in test no. SFH-1. Thus, the bolts were loaded more as the concrete segments were rigid and did not have any stress. Therefore, the system should be further evaluated, using larger bolts and full-scale crash tested using the most appropriate bolt size.

Lastly, the reverse-direction simulations found that the barrier successfully contained and redirected the pickup truck model. The lateral and longitudinal OIV values in the simulation at the slope-break point were up to 35 and 38 percent greater than observed in the simulations upstream from the drop-down pin. Similarly, the lateral and

longitudinal OIV values in the simulation at the reverse-direction CIP were up to 22 and 25 percent greater than observed in the simulations upstream from the drop-down pin. The OIV values were expected to be higher in reverse-direction impacts than observed for the impacts upstream from the drop-down pin due to primary contact with a rigid barrier. The simulation at the slope-break point resulted in up to 33 percent higher lateral impact forces and up to 32 percent longitudinal impact forces on the barrier as compared to the impact at the CIP location with respect to the cover plate. The increased forces as well as ORA and OIV values were believed to be acceptable as they did not negatively affect vehicle behavior and were below MASH limits. However, it may be advisable to consider flatter horizontal flare rates over the full barrier height in order to largely eliminate concerns for increased forces, ORAs, and OIVs.

In the simulations near the transition hardware, the vehicle model damage increased as compared to the interior location simulation. The greatest vehicle damage occurred during the slope-break point impact event. The top of the left-front and left-rear doors separated from the vehicle farther than observed in the interior location simulation. The impact locations upstream from the joint did not show significant changes in the vehicle model damage as compared to the interior location simulation.

It is recommended that the RESTORE barrier transition be full-scale crash tested at multiple impact points. MASH suggests that rigid transitions should be evaluated at the location 4 ft – 3 in. (1.3 m) upstream from the pin with the pickup truck to produce the largest load, risk for vehicle snag or pocketing, or risk for system failure. Through the simulation analysis, it was determined the compressed-joint impact location showed the highest lateral barrier force. However, the extended joint increased vehicle instability and

occupant risk values. The simulation with respect to the pin and the extended joint had a lateral ORA up to 14 percent greater than observed for the other impact locations.

Further, a lateral and longitudinal OIV was 16 and 12 percent greater, respectively, than observed for the other simulations occurred. The simulation with respect to the pin and extended joint had a peak roll angle up to 5 degrees greater than observed for the other impact locations. Therefore, the impact location 4 ft – 3 in. (1.3 m) upstream of the pin with the extended joint was recommended to be evaluated through full-scale crash testing.

The second impact location is 4 ft – 3 in. (1.3 m) upstream from the 20-ft (6.1-m) location with the extended joint. The simulation at 20 ft (6.1 m) with the compressed joint experienced negative volumes shortly after the vehicle became parallel to the system, so all of the desired results were not obtained. The simulated dynamic deflection, as well as roll, pitch, and yaw angles, were greatest at the 20-ft (6.1-m) impact location with the extended joint. Thus, the impact location has the greatest likelihood of vehicle snag and stability issues.

The third impact location may be the slope-break point of the horizontal flare rate of 6:1 on a concrete buttress. This slope-break point has never been full-scale crash tested according to MASH on full barrier heights and would need to be evaluated before considered for use on the roadway. Based on the simulation, the Silverado model did not exhibit poor vehicle behavior, so it may not have to be full-scale crash tested if further evaluation is completed. A 10:1 horizontal flare rate is suggested to be a starting point for the further evaluation.

13 CIP DETERMINATION – MODELING TEST DESIGNATION NO. 4-22

13.1 Purpose

In lieu of full-scale vehicle crash testing, further computer simulation was utilized to evaluate the transition design according to the MASH safety performance criteria for test designation no. 4-22. The F800 single-unit truck model impacted the barrier at a speed of 56.0 mph (90.1 km/h) and an angle of 15 degrees, as recommended by MASH. Several impact points were evaluated to determine vehicle and barrier performance. Multiple impact points were considered upstream from the buttress as well as in the reverse direction on the back side, as previously shown in in Figure 135. Two barrier configurations were considered due to the +/- 1½ in. (38 mm) construction tolerance: the joint fully extended and the joint fully compressed.

MASH states that computer simulation with LS-DYNA should be performed to evaluate the CIPs when practical and accessible. However, if computer simulation is unavailable, the CIP for a stiffness transition should be either 4 ft – 11 in. (1.5 m) upstream from the location with the greatest potential for wheel snag (i.e., upstream end of buttress) or 4 ft – 11 in. (1.5 m) upstream from the location with the potential for the largest load (i.e., drop-down pin) or deflection (i.e., upstream locations) for test designation no. 4-22. The largest load is expected to occur at an impact point near the pin and gusset plate assemblies due to the constraint in the lateral y-direction. However, impact locations farther upstream would need to be evaluated to determine the location of the maximum barrier deflection and/or flare rate. Higher flare rates upstream of the hinge location could potentially lead to vehicle instabilities and/or override. However, vehicle rollover on the traffic-side face is acceptable for SUT vehicles. Computer simulation was

used to investigate several CIP locations noted in MASH as well as other upstream impact locations to determine the worse-case vehicle and/or barrier performance. Each suggested CIP impact location in MASH was simulated with the Ford F800 vehicle model when the joint was fully extended and when the joint was fully compressed, as shown previously in Figure 136.

Impact locations farther upstream from the pin were simulated at intervals of 10 ft (3.0 m) and up to 40 ft (12.2 m) away from the pin. Each impact location was simulated at 4 ft – 11 in. (1.5 m) upstream from the four locations positioned at 10 ft (3.0 m) intervals, as shown previously in Figure 135 and with the joint fully extended. A location 20 ft (6.1 m) upstream from the pin, the compressed joint was also investigated to determine if restricted joint movement affected the results.

Lastly, the reverse-direction simulations evaluated performance at impact locations directly at the slope-break point of the rigid concrete buttress on the downstream end with a horizontal flare rate of 6:1. A horizontal flare rate of 6:1 over the full barrier height has not been previously crash tested under the MASH safety performance criteria. Also, the impact location 4 ft – 11 in. (1.5 m) upstream from the edge of the cover plate was simulated to evaluate vehicle snag behind the cover plate when the joint was fully extended.

13.2 CIP Location Simulation Results

Two reference locations were considered during simulations at the suggested MASH CIP locations. The first suggested CIP location was 4 ft – 11 in. (1.5 m) upstream from the location with the greatest potential for wheel snag (i.e., upstream end of buttress), while the second CIP location was 4 ft – 11 in. (1.5 m) upstream from the

location with the potential for largest load or deflection (i.e., drop-down pin). Based on the previous simulations with the single-unit truck model, the peak force is expected to occur during the secondary impact event which involves the rear axle. During the rounded cover plate implementation, the initial design had interference between the cover plate and the washers for the ACJ bolts when fully compressed. Therefore, the joint was ½ in. (13 mm) extended from the fully compressed configuration during the CIP simulations. However, the details are correct in the drawing set in Appendix K.

The comparison of results for the F800 model between the simulations at the suggested MASH CIP locations is shown in Table 50. The simulations at each impact point successfully contained and redirected the F800 model, as shown in Figures 230 through 233. The simulation end times were different for the simulations. However, the vehicles had redirected and were downstream from the buttress by the end of the simulations.

The simulated damage to the F800 vehicle models after the impact event for the suggested MASH CIP locations was similar to that observed for the interior location simulation. The left-front fender and left-side gas tank were crushed inward. However, slightly more denting occurred on the bottom left side of the box as compared to the interior location simulation.

Table 50. Comparison Matrix of CIP Locations, 10000S F800 Simulation

Simulation Parameters		Impact Location and Trial No.			
		32	36	42	72
		CIP Buttress Extended ²	CIP Buttress Compressed ²	CIP Pin Extended ²	CIP Pin Compressed ²
End Time, ms		550	505	450	620
Parallel Conditions	Time, ms	NA	NA	NA	NA
	Velocity, mph (km/h)	NA	NA	NA	NA
Exit Conditions	Velocity, mph (km/h)	48.8 (78.6)	49.3 (79.3)	48.9 (78.6)	48.7 (78.4)
	Angle, deg.	-4.9	-7.1	-5.0	-5.9
	Time, ms	410	400	389.5	389.5
Length of Contact		13 ft - 2 in. (4.0 m)	13 ft - 2 in. (4.0 m)	12 ft - 2 in. (3.7 m)	14 ft - 1 in. (4.3 m)
t*, ms		250.5	259.7	255.8	247.6
ORA, g's	Longitudinal	4.05	-5.63	-4.36	-5.03
	Lateral	8.21	9.7	12.98	8.62
OIV, ft/s (m/s)	Longitudinal	-6.86 (-2.09)	-7.32 (-2.23)	-7.86 (-2.40)	-7.12 (-2.17)
	Lateral	10.11 (3.08)	10.33 (3.15)	10.10 (3.08)	10.27 (3.13)
Test Article Deflections, in. (mm)	Dynamic of Concrete	0.8 (20)	0.7 (18)	0.9 (23)	0.7 (18)
	Dynamic of Steel Rail	0.6 (15)	0.6 (15)	0.6 (15)	0.5 (13)
	Working Width	83.0 (2,108)	79.0 (2,007)	68.0 (1,727)	84.0 (2,134)
Location of Max. Deflection Upstream of Pin		0 ft (0 m)	0 ft (0 m)	0 ft (0 m)	0 ft (0 m)
Vehicle Stability	Max Roll, deg.	-29.8	-25.8	-23.5	-24.1
	Max Pitch, deg.	-10.9	-7.6	-8.2	-9.1
	Max Yaw, deg.	10.5	10.3	10.6	9.8
Posts Hit by Leading Tire (wheel snag)		0	0	0	0
Max. Lateral Impact Force, kips (kN) ¹		81.2 (361.2)	91.4 (406.6)	98.7 (439.0)	82.4 (366.5)

¹ Calculated using global Y-acceleration multiplied by mass.

² Impacted 4 ft – 11 in. (1.5 m) upstream from noted location.

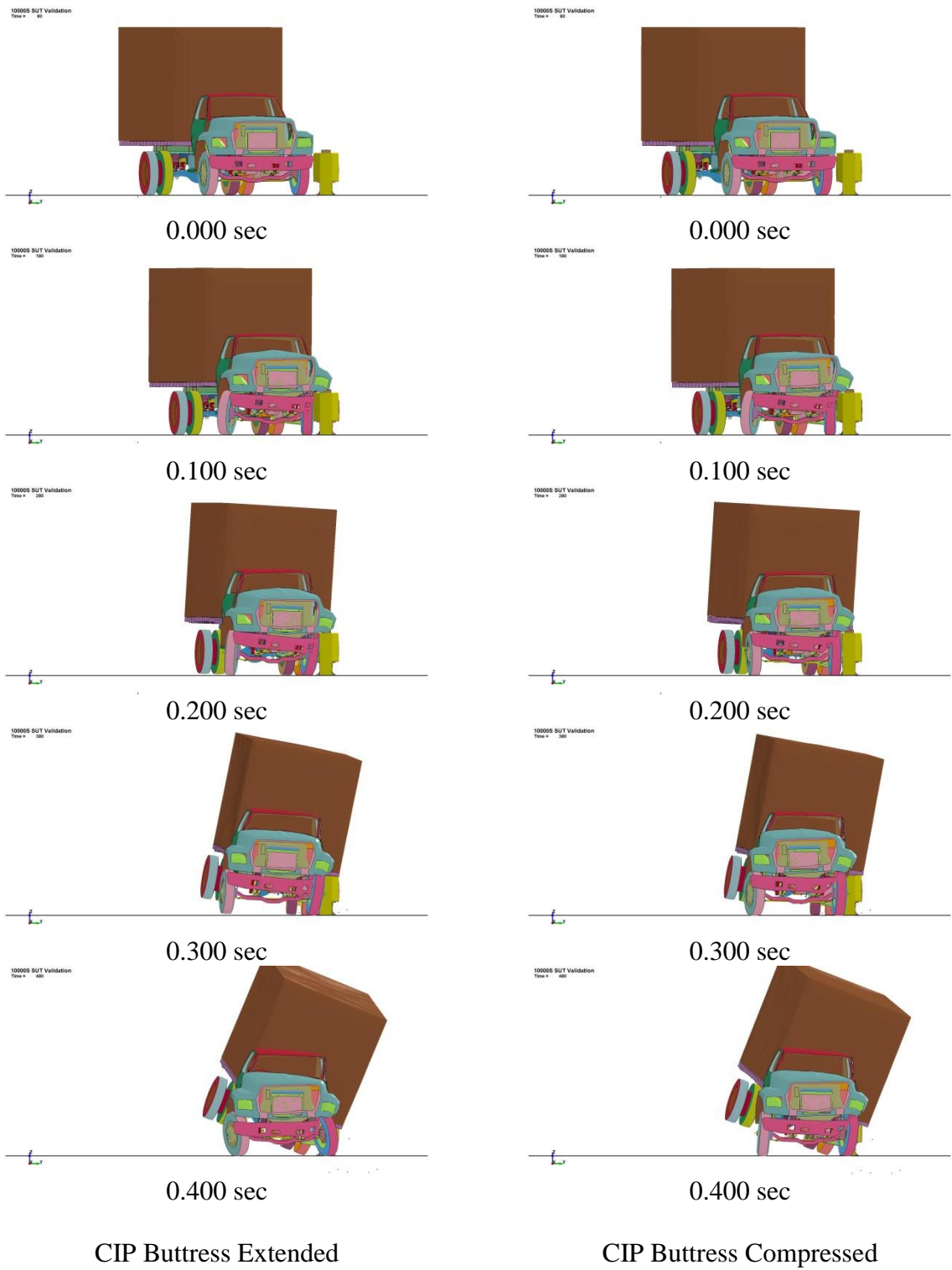


Figure 230. RESTORE Barrier Transition, 10000S F800 Simulation Comparison, CIP Locations, Downstream View

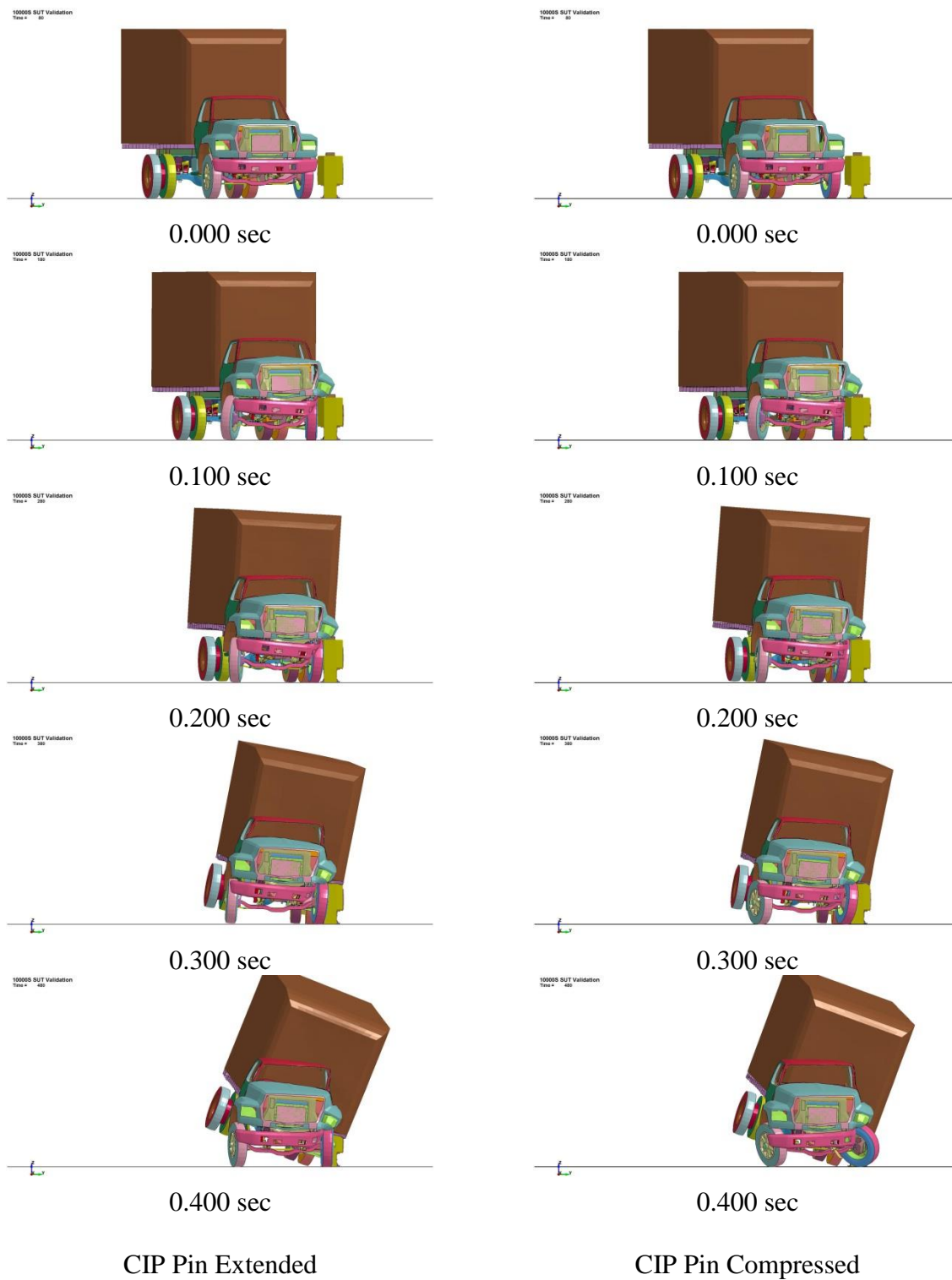


Figure 231. RESTORE Barrier Transition, 10000S F800 Simulation Comparison, CIP Locations, Downstream View

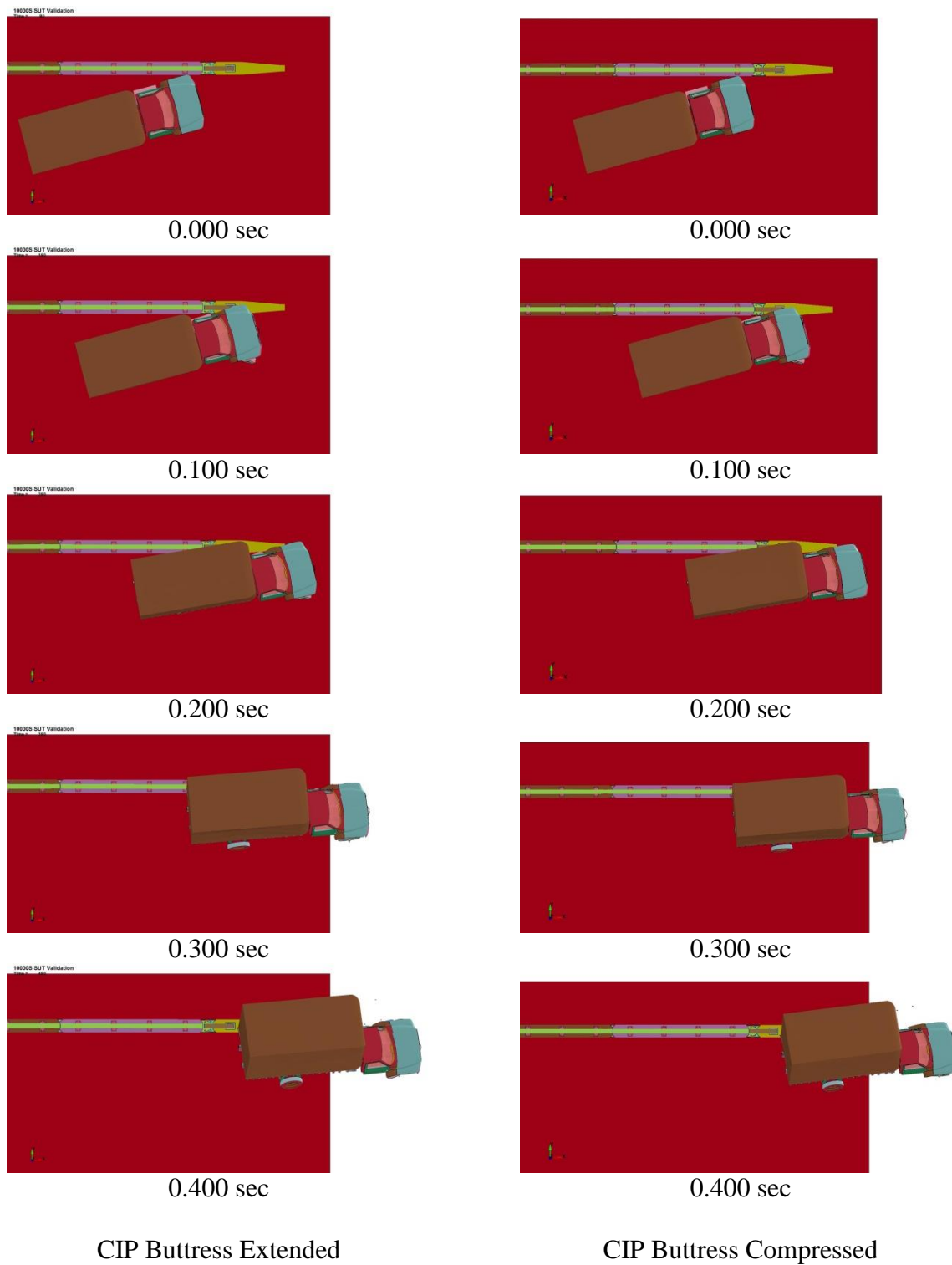


Figure 232. RESTORE Barrier Transition, 10000S F800 Simulation Comparison, CIP Locations, Overhead View

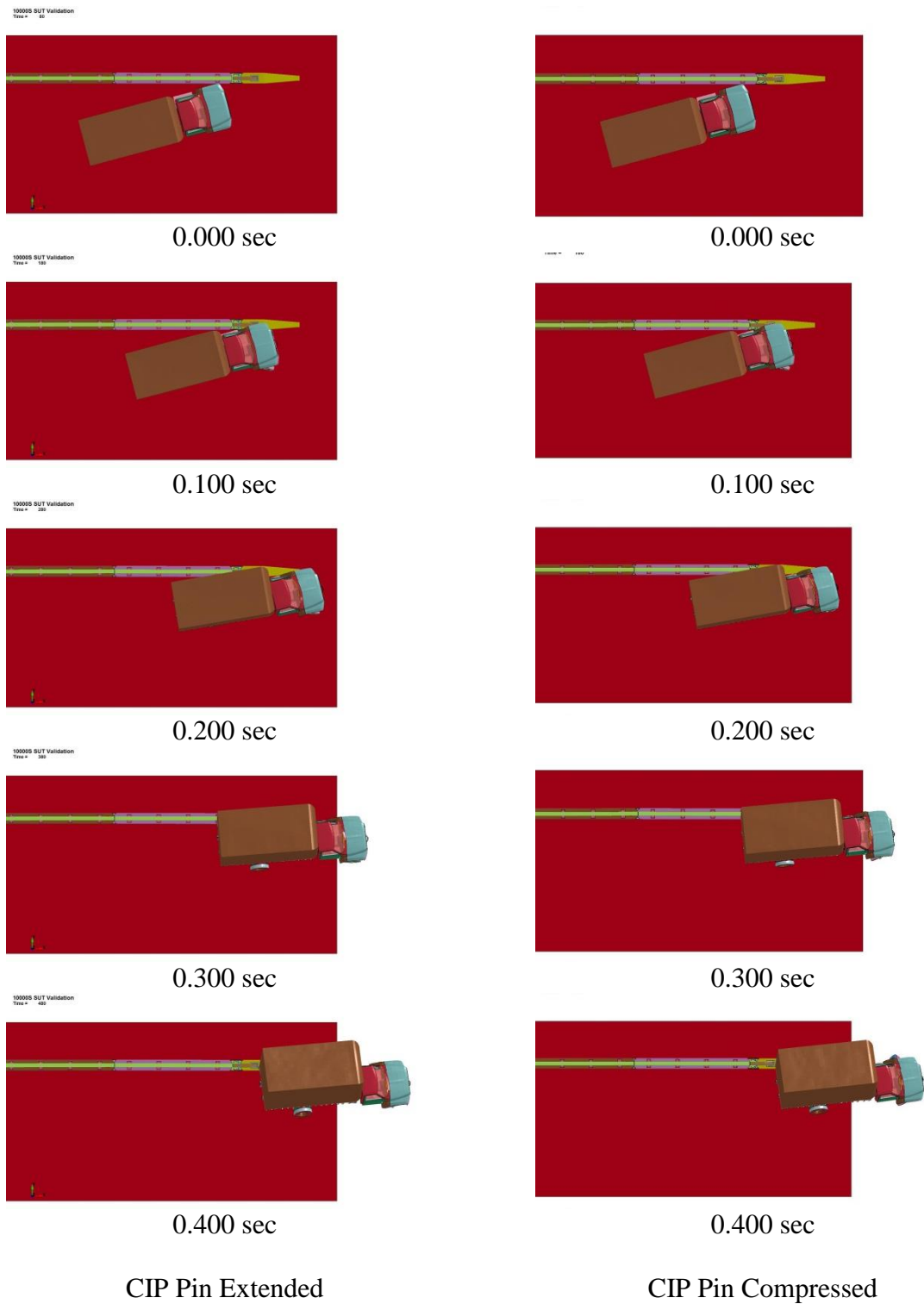


Figure 233. RESTORE Barrier Transition, 10000S F800 Simulation Comparison, CIP Locations, Overhead View

Since all degrees of freedom in the rigid concrete buttress were constrained, the buttress did not have any damage nor deflections. The simulations with the extended and the compressed joints showed similar dynamic deflections, with the maximum deflection located at the downstream end of the last RESTORE barrier segment (i.e., RESTORE barrier end nearest to the pin). The last RESTORE barrier segment experienced up to 2 degrees of rotation about the longitudinal x-axis during the simulations at the preferred MASH CIP locations. The vertical pin also rotated about the longitudinal x-axis to the extent allowed by the hole and slot tolerances within the gusset plates.

Occupant risk values are not a required evaluation criteria for test designation no. 4-22. However, the calculated OIV and ORA values in the lateral and longitudinal directions were obtained for comparison purposes. The lateral and longitudinal change in velocity for each simulation were similar, as shown in Figures 234 and 235. Between 250 and 300 msec, the lateral change in velocity decreased 2 mph (3.2 km/h) for the simulations with respect to the drop-down pin, so the lateral velocity of the vehicle was increasing during this time. In addition, the longitudinal change in velocity decreased more rapidly as well. The simulated lateral and longitudinal OIVs for the differed CIP locations and configurations corresponded well, with the exception of the simulation at the buttress with the compressed joint. The lateral OIV for that simulation was greater than observed for the other simulations, and the longitudinal OIV was less than observed for the other simulations. The longitudinal ORAs were similar as well. However the lateral ORA values ranged from 7.33 to 12.98 g's. The simulation at the buttress with compressed joint had the lowest ORA, and the simulation at the pin with extended joint had the highest ORA.

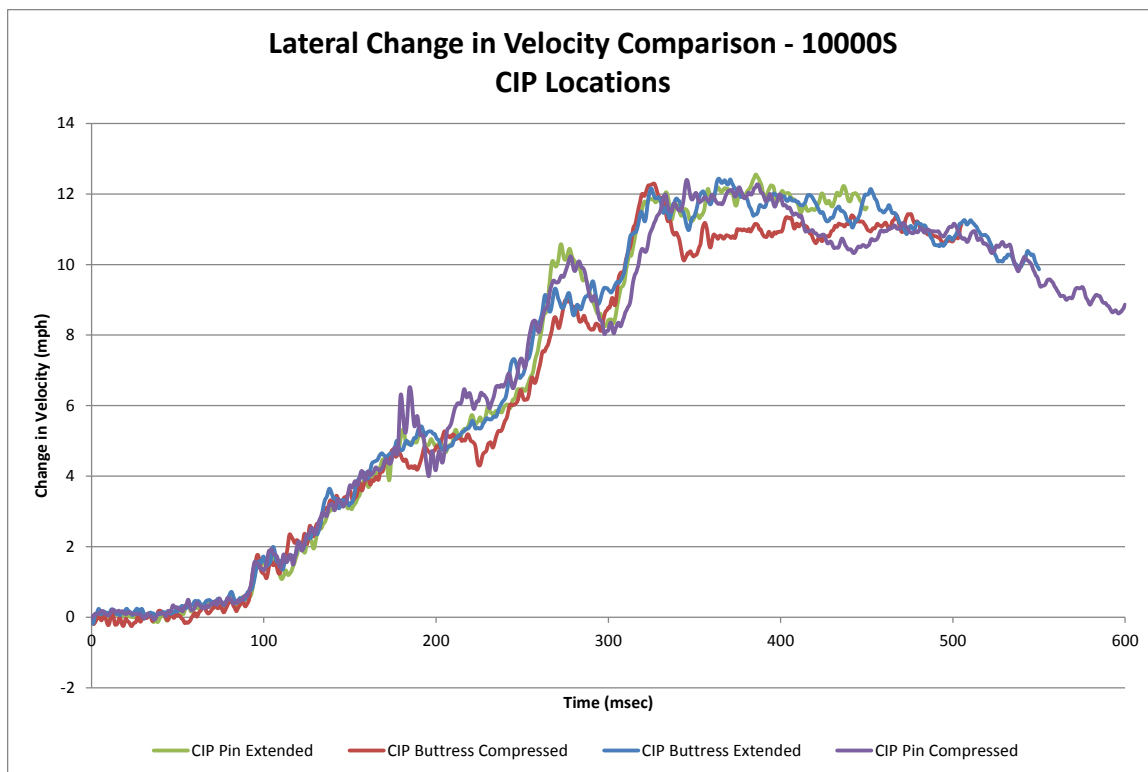


Figure 234. Lateral Change in Velocity, CIP Locations, 10000S F800 Simulation

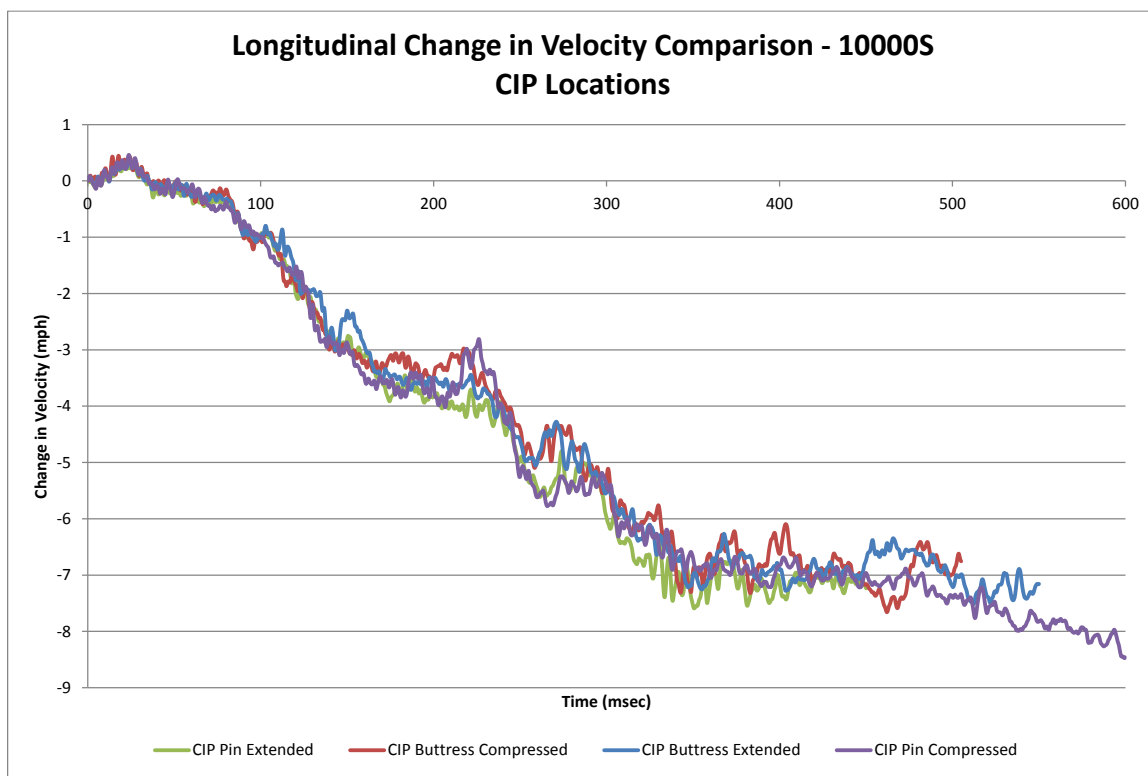


Figure 235. Longitudinal Change in Velocity, CIP Locations, 10000S F800 Simulation

The lateral impact forces were calculated using the CFC60 filtered 50-msec global Y-accelerations multiplied by the vehicle mass. Each of the location simulations exhibited a similar force trend through the duration of the impact event, as shown in Figure 236. Note that all of the simulations experienced its peak force during the secondary impact with the rear axle. As described in Chapter 6, the simulation in the interior region did not accurately predict the peak lateral barrier force, which occurred early in the impact event in full-scale crash test no. SFH-3. Thus, the lateral impact force in simulation may be underpredicted if the maximum force actually occurred early in the impact event. However, the lateral impact force due to tail-slap in the simulation corresponded well with that observed in the full-scale crash test. The peak lateral force shown during the simulation in relation to the pin with the extended joint was within 2 percent of the design load of 100 kips (445 kN).

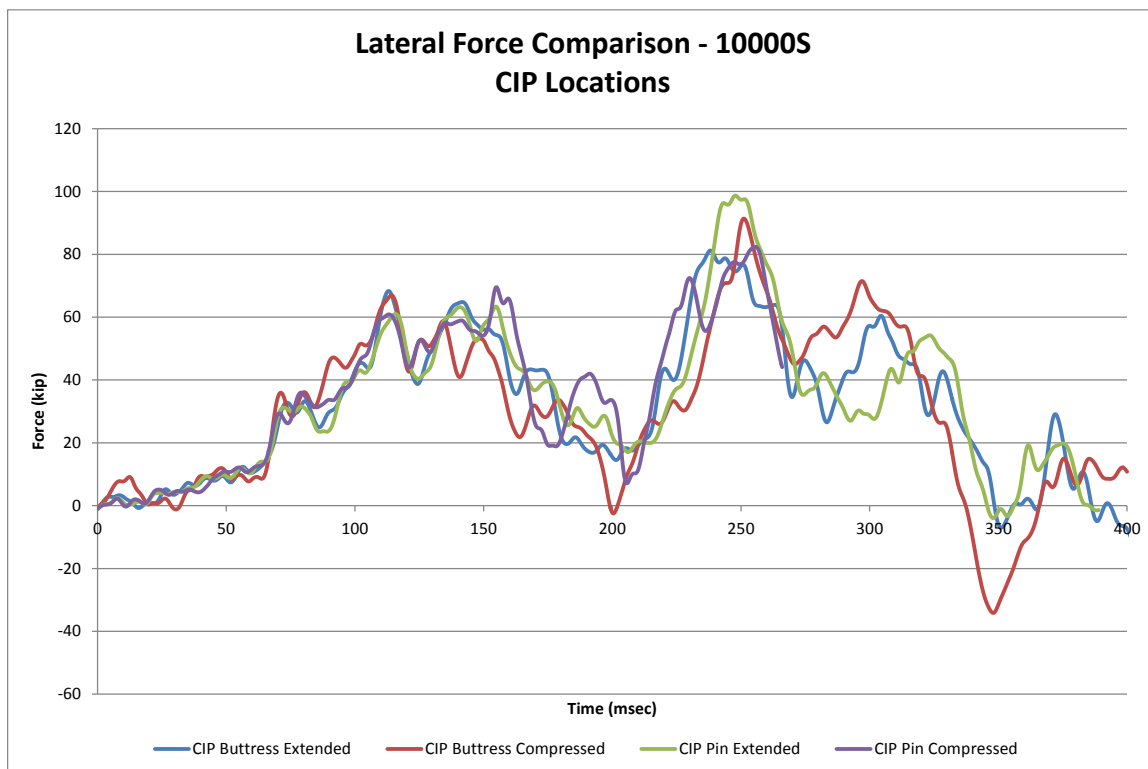


Figure 236. Lateral Force Comparison, CIP Locations, 10000S F800 Simulation

The simulated roll, pitch, and yaw angles were similar, as shown in Figures 237 through 239, respectively. The simulation with respect to the pin with the extended joint showed a faster change in roll angles between 300 and 450 msec as compared to that observed in the other simulations. The roll angles were still increasing as the simulation ended. The F800 model in each simulation started to pitch positively for the first 100 msec, where there was a decrease in pitch angles of approximately 2 degrees and plateaued for 50 msec. After the vehicle model's pitch angle plateaued, the pitch angle continued to decrease through the end of the simulation. There was slight deviation in pitch angle between 200 and 300 msec. Further, the yaw angle in the simulation relative to the pin with compressed joint varied slightly at 175 msec. The peak yaw angles were within 8.0 percent.

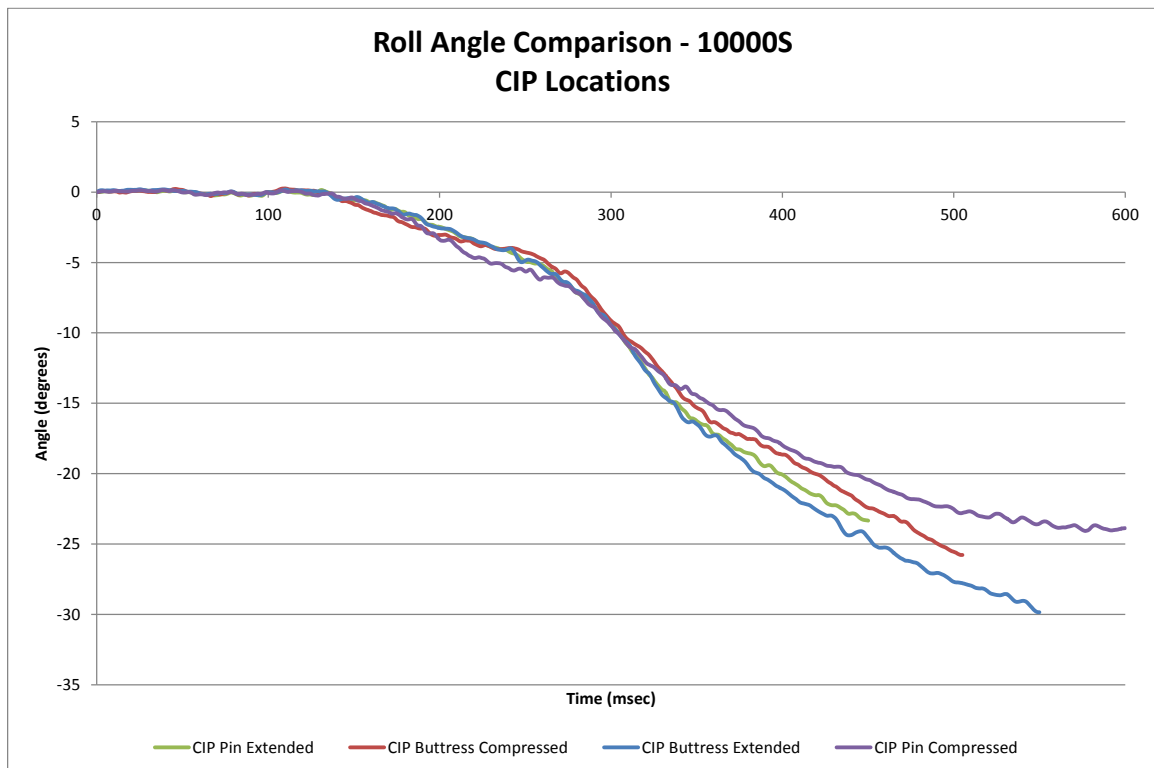


Figure 237. Roll Angle Comparison, CIP Locations, 10000S F800 Simulation

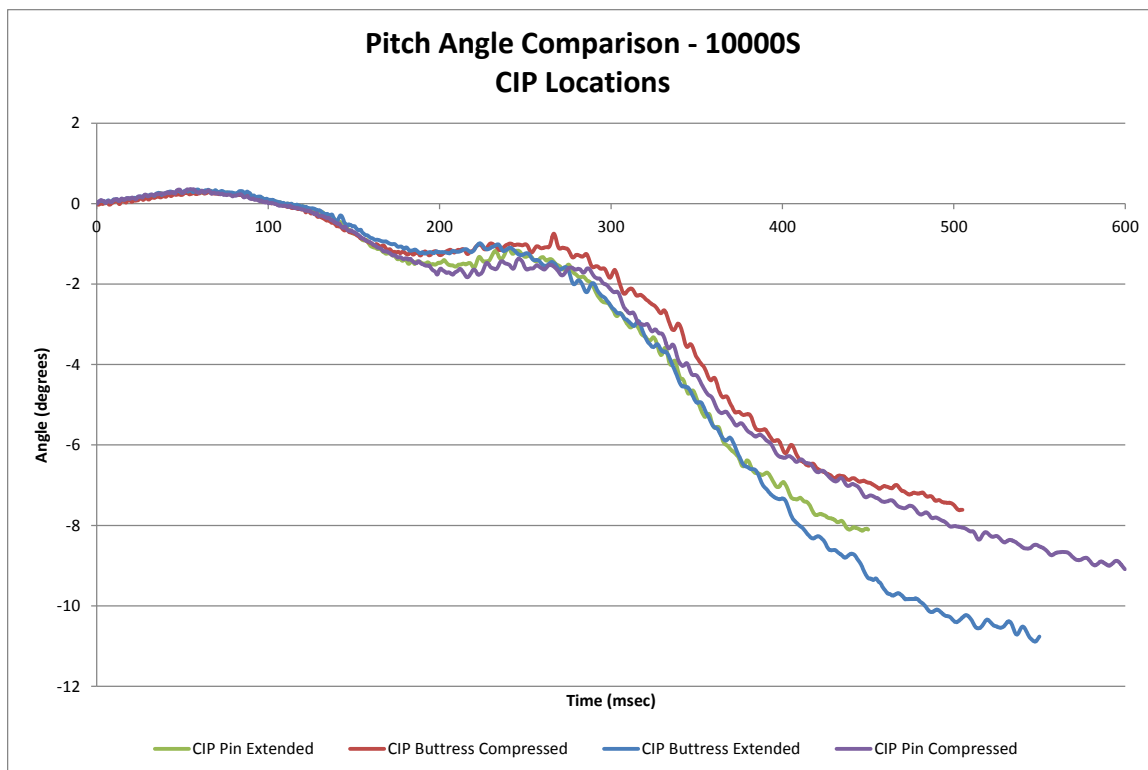


Figure 238. Pitch Angle Comparison, CIP Locations, 10000S F800 Simulation

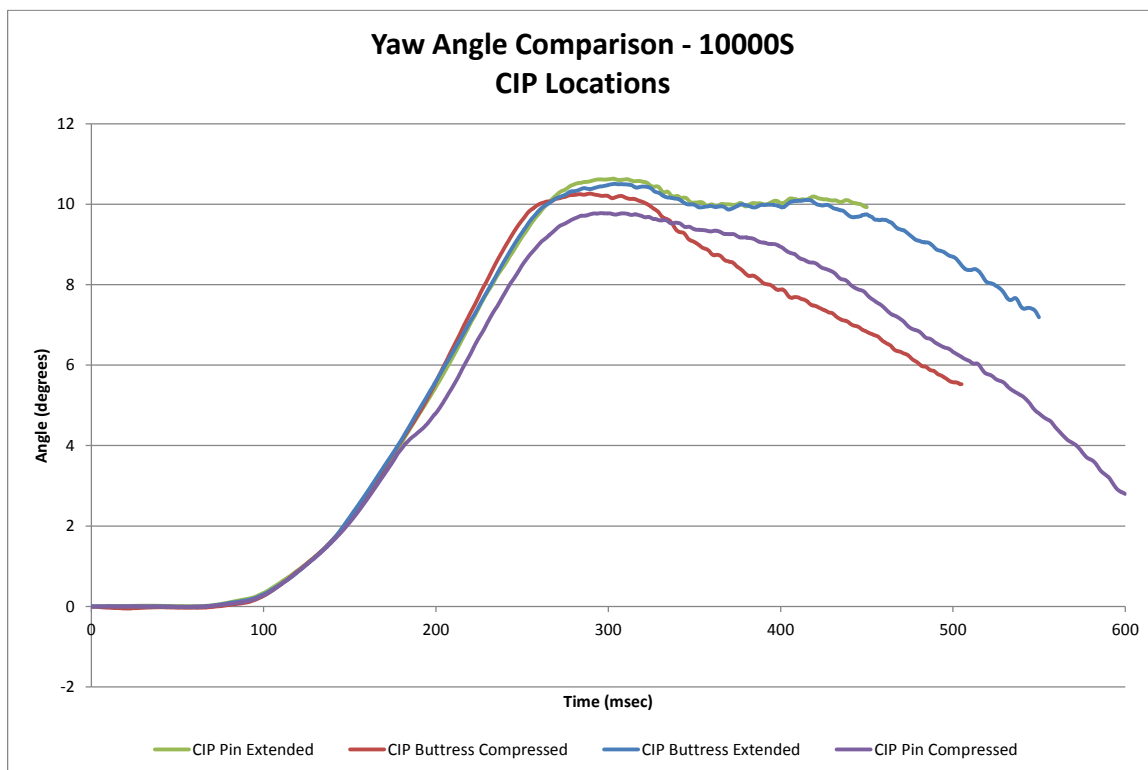


Figure 239. Yaw Angle Comparison, CIP Locations, 10000S F800 Simulation

The von Mises and Tresca yield conditions were considered to evaluate the stresses within the parts of the pin and gusset plate assemblies. A description of each part in relation to each yield condition, and the simulation results are shown in Table 51. For some of the parts, the von Mises and Tresca yield conditions did not correspond to each other. During the simulations, the maximum shear stress of the vertical pin exceeded the Tresca yield condition whereas the maximum von Mises stresses did not exceed the von Mises yield condition. Therefore, the vertical drop-down pin was likely to not yield during the impact events.

Table 51. RESTORE Barrier Component Stress Comparison, 10000S F800 Simulation, CIP Locations

Simulation Parameters			Impact Location and Trial No.			
			32 CIP Buttress Extended	36 CIP Buttress Compressed	42 CIP Pin Extended	72 CIP Pin Compressed
Vertical Pin	Max.Tresca Stress	Stress, ksi (MPa)	33.5 (231)	32.1 (221)	31.1 (215)	33.3 (230)
		$\tau \geq 0.5\sigma_y$?	Yes	Yes	No	Yes
	Max.von Mises Stress	Stress, ksi (MPa)	58.8 (401)	59.1 (408)	58.4 (403)	60.3 (416)
		$\sigma_{vm} \geq \sigma_y$?	No	No	No	No
Horizontal Gusset Plates	Max.Tresca Stress	Stress, ksi (MPa)	41.2 (284)	43.1 (297)	44.0 (303)	43.7 (301)
		$\tau \geq 0.5\sigma_y$?	Yes	Yes	Yes	Yes
	Max.von Mises Stress	Stress, ksi (MPa)	77.1 (532)	76.8 (529)	78.9 (544)	77.0 (531)
		$\sigma_{vm} \geq \sigma_y$?	Yes	Yes	Yes	Yes
Cover Plate Bolts	Max.Tresca Stress	Stress, ksi (MPa)	84.7 (584)	73.3 (505)	49.3 (340)	61.4 (423)
		$\tau \geq 0.5\sigma_y$?	Yes	Yes	No	Yes
	Max.von Mises Stress	Stress, ksi (MPa)	59.2 (408) ¹	138.4 (954)	97.5 (672)	107.7 (743)
		$\sigma_{vm} \geq \sigma_y$?	No	Yes	No	Yes
Cover Plate Gussets	Max.Tresca Stress	Stress, ksi (MPa)	29.2 (202)	46.0 (317)	32.2 (222)	33.2 (229)
		$\tau \geq 0.5\sigma_y$?	No	Yes	Yes	Yes
	Max.von Mises Stress	Stress, ksi (MPa)	54.1 (373)	82.0 (566)	58.1 (401)	60.2 (415)
		$\sigma_{vm} \geq \sigma_y$?	No	Yes	No	No
Top Tube, Splice, and Termination	Max.Tresca Stress	Stress, ksi (MPa)	42.0 (290)	48.1 (331)	68.6 (473)	56.9 (392)
		$\tau \geq 0.5\sigma_y$?	Yes	Yes	Yes	Yes
	Max.von Mises Stress	Stress, ksi (MPa)	72.8 (502)	83.3 (575)	119.7 (825)	98.8 (682)
		$\sigma_{vm} \geq \sigma_y$?	Yes	Yes	Yes	Yes
Cover Plate	Max.Tresca Stress	Stress, ksi (MPa)	48.9 (337)	73.0 (503)	49.7 (343)	67.9 (468)
		$\tau \geq 0.5\sigma_y$?	Yes	Yes	Yes	Yes
	Max.von Mises Stress	Stress, ksi (MPa)	88.0 (607)	131.4 (906)	86.7 (598)	120.1 (828)
		$\sigma_{vm} \geq \sigma_y$?	Yes	Yes	Yes	Yes

¹ Stress occurred at 100 msec when the SUT model was in contact with the system. However, the maximum stress occurred when the vehicle was downstream due to anomalies in the model, as shown in Figure 241.

The stresses in the cover plate bolts exceeded the Tresca and von Mises yield criteria for both simulations with the compressed joint (i.e., pin and buttress). The permanent deformations occurred due to excessive longitudinal loading from the upstream cover plate end being translated longitudinally, as shown in Figure 240. Failure was not enabled in the cover plate bolts as the plastic strain at failure was unknown. However, the bolts would have likely fractured due to the observed high stresses and excessive deformations. The cover plate bolts in the simulation relative to the buttress end with the extended joint had a maximum von Mises stress of 59.2 ksi (408 MPa) through the impact event. However, the stresses started to increase as the SUT model moved farther downstream from the joint due to unknown reasons and reached a maximum stress of 159.0 ksi (1,096 MPa), as shown in Figure 241. The simulation upstream of the buttress with compressed joint had von Mises stresses in the cover plate bolts up to 24 percent larger than the yield strength of the material due to a large longitudinal load applied to the cover plate configuration. The simulations at the pin also experienced higher von Mises stresses in the cover plate bolts. Therefore, it was recommended that either the cover plate bolts be redesigned with a larger diameter and evaluated for failure or the joint be redesigned so that cover plate bolts are not loaded significantly like the original design intent. Further, the cover plate bolt stresses in the extended joint simulations should be further evaluated to determine the cause for the excessive stresses when the SUT model was downstream of the pin and gusset plate assemblies.

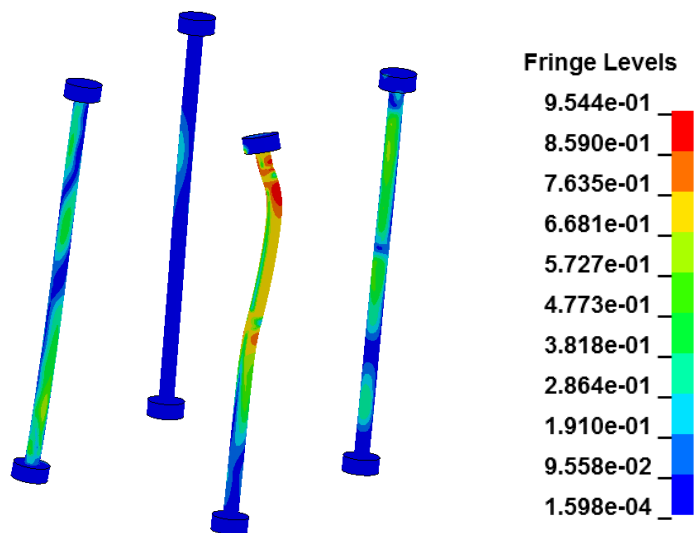


Figure 240. Von Mises Stress (GPa) of Cover Plate Bolts, Trial No. 36 at 100 msec, 10000S F800 Model

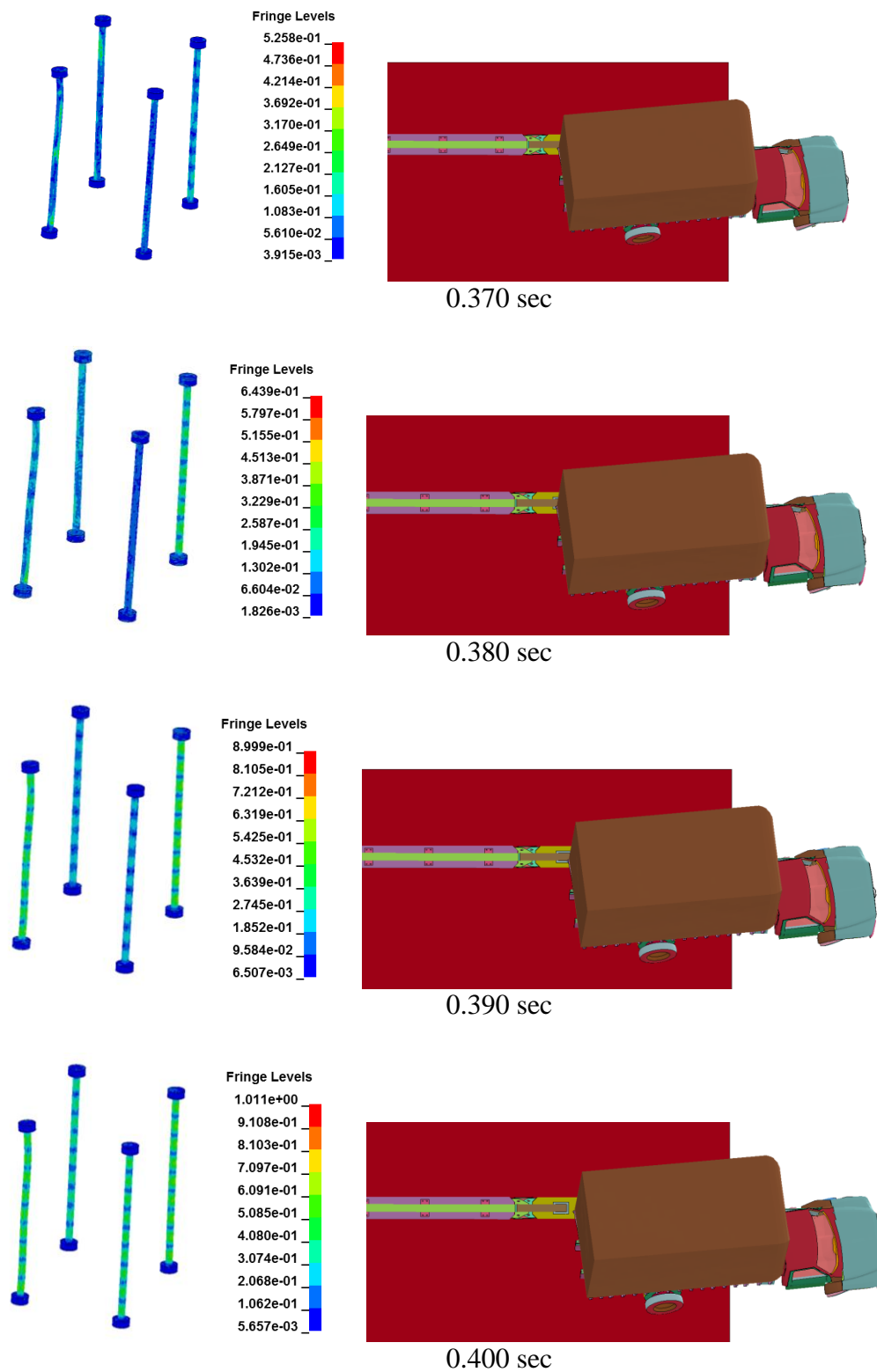


Figure 241. Cover Plate Bolt Von Mises Stress Anomalies (GPa), Trial 32

The stresses in the horizontal gusset plates exceeded the Tresca and von Mises yield conditions. However, the peak stresses in the gusset plates occurred at the plate edges where the cover plate strips were bearing due to vehicle impact on the cover plate, as shown in Figure 242. Bearing stress also occurred on the edges of the pin holes, similar to what was shown in previous simulations. Due to the localization of the stresses, the gusset plate corners may have bent, but they may likely have been able to withstand further impact events.

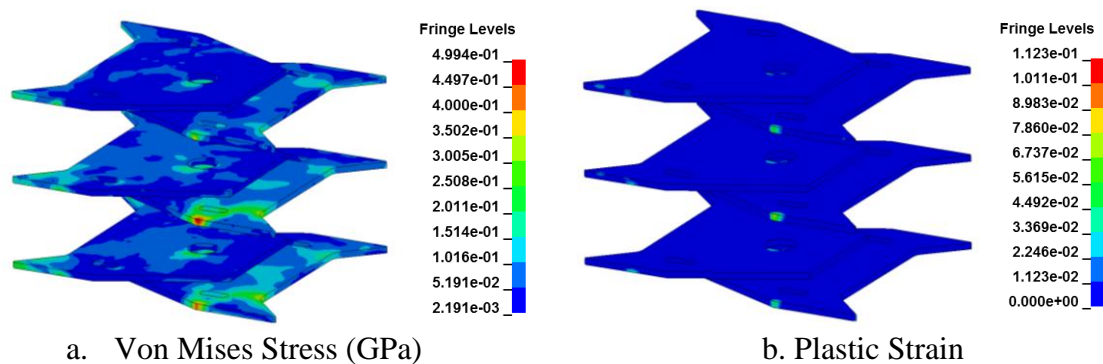


Figure 242. Von Mises Stress and Plastic Strain Comparison on Horizontal Gussets, Trial No. 32 at 240 msec, 10000S F800 Model

The cover plate gussets had slight deformations at the corner that connected the cover plate to the cover plate gussets. During the simulated impact event, the cover plate bolts restricted the lateral movement. However, the bolts did not restrict the longitudinal movement of the cover plate gussets, thus causing a localized force on the edges of the cover plate bolt holes. The cover plate stresses were concentrated on the edges of the plate. The maximum stresses were located at the top of the cover plate due to contact with the high bumper height of the SUT model, as shown in Figure 244. Therefore, the top of the cover plate would have likely bent, but it would have most likely maintained its function of preventing penetration between the horizontal gusset plates.

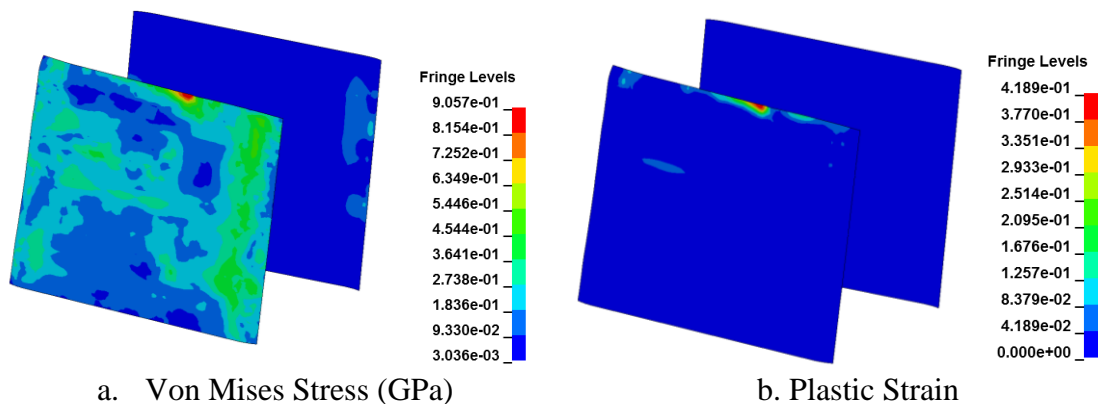


Figure 243. Von Mises Stress and Plastic Strain Comparison on Cover Plate, Trial No. 36 at 100 msec, 10000S F800 Model

The top tube, tube splices, and tube termination had peak stresses that exceeded Tresca and von Mises yield conditions in the simulations at each impact location. The von Mises stresses were up to 48 percent larger than the yield stress during the simulation upstream of the pin with extended joint. The top tube in full-scale vehicle crash test no. SFH-3 experienced permanent deformation. Thus, it was expected that the top tube would exceed the yield conditions. However, it is recommended that failure be further evaluated through simulation to determine if the top tube, tube splice, and tube termination would be able to effectively redirect the single-unit truck during a full-scale vehicle crash test. Further, modeling the top tube splice with the designed $\frac{1}{2}$ in. (13 mm) thickness would be recommended.

13.3 Upstream Location Simulation Results

Impact points upstream from the pin and gusset plate assemblies were simulated at intervals of 10 ft (3.0 m). The impact point occurred 4 ft – 11 in. (1.5 m) upstream from locations of 10, 20, 30, and 40 ft (3.0, 6.1, 9.1, 12.2 m) away from the downstream end of the last concrete RESTORE barrier in order to determine the maximum load

imparted to the ACJ hardware and investigate the potential for vehicle snag on posts when traveling toward a stiffened barrier.

The comparison of results for the F800 vehicle model between the simulations at upstream impact locations is shown in Table 52. Sequential photographs of the simulations at each impact point are shown in Figures 244 through 247. The simulations at 10 and 20 ft (3.0 and 6.1 m) upstream from the joint with the extended joint had model instabilities. When the large mesh size of the left-front fender impacted the smaller mesh size of the top tube rail, contact was not detected right away between the surfaces. When contact was detected, the model terminated. Thus, several results in Table 52 could not be obtained for those impact location simulations.

The vehicle damage observed during impacts upstream from the pin had more damage than observed for the suggested MASH CIP location simulations and the interior location simulation. The left side of the box had dents extending along its length on the lower quarter height of the box. The I-beams that supported the box had more deformations than what was observed in previous simulations. However, the crush on the left-front corner of the vehicle was approximately the same as observed in the interior location simulation.

Table 52. Comparison Matrix of Upstream Impact Locations, 10000S F800 Simulation

Simulation Parameters		Impact Location and Trial No.				
		57	58	68	59	60
		10 ft Upstream Extended ²	20 ft Upstream Extended ²	20 ft Upstream Compressed ²	30 ft Upstream Extended ²	40 ft Upstream Extended ²
End Time, ms		60	90	613	590	700
Parallel Conditions	Time, ms	NA	NA	301.9	331.9	330.4
	Velocity, mph (km/h)	NA	NA	49.9 (80.3)	49.4 (80.3)	49.1 (79.0)
Exit Conditions	Velocity, mph (km/h)	NA	NA	45.8 (73.8)	46.4 (74.7)	46.5 (74.8)
	Angle, deg.	NA	NA	3.3	4.4	4.8
	Time, ms	NA	NA	479.5	590	699.5
Length of Contact t*, ms		NA	NA	28 ft - 7 in. (8.7 m)	35 ft - 9 in. (10.9 m)	43 ft - 8 in. (13.3 m)
ORA, g's	Longitudinal	0	0	-9.28	-7.91	-6.64
	Lateral	0	0	8.05	9.39	7.61
OIV, ft/s (m/s)	Longitudinal	0	0	-6.59 (-2.01)	-5.81 (-1.77)	-6.03 (-1.84)
	Lateral	0	0	11.19 (3.41)	9.42 (2.87)	9.52 (2.90)
Test Article Deflections, in. (mm)	Dynamic of Concrete	1.1 (28)*	3.5 (89)*	12.5 (318)	12.0 (305)	13.0 (330)
	Dynamic of Steel Rail	1.2 (30)*	3.6 (91)*	12.6 (320)	12.5 (318)	13.6 (345)
	Working Width	23.4 (594)*	25.8 (655)*	67.0 (1,702)	69.0 (1,753)	74.0 (1,880)
Location of Max. Deflection Upstream of Pin		20 ft (6.1 m)	20 ft (6.1 m)	20 ft (6.1 m)	20 ft (6.1 m)	40 ft (12.2 m)
Vehicle Stability	Max Roll, deg.	-0.3*	-0.5*	-35.9	-30.1	-31.9
	Max Pitch, deg.	0.3*	0.4*	-10.7	-8.2	-10.7
	Max Yaw, deg.	-0.01*	0.2*	18.6	19.5	19.9
Posts Hit by Leading Tire (wheel snag)		0	0	0	0	0
Max. Lateral Impact Force, kips (kN) ¹		6.5 (28.9)*	14.7 (65.3)*	77.3 (343.8)	83.4 (370.8)	73.0 (324.5)

* Values calculated through simulation end time.

¹ Calculated using global Y-acceleration multiplied by mass.

² Impacted 4 ft – 11 in. (1.5 m) upstream from noted location.

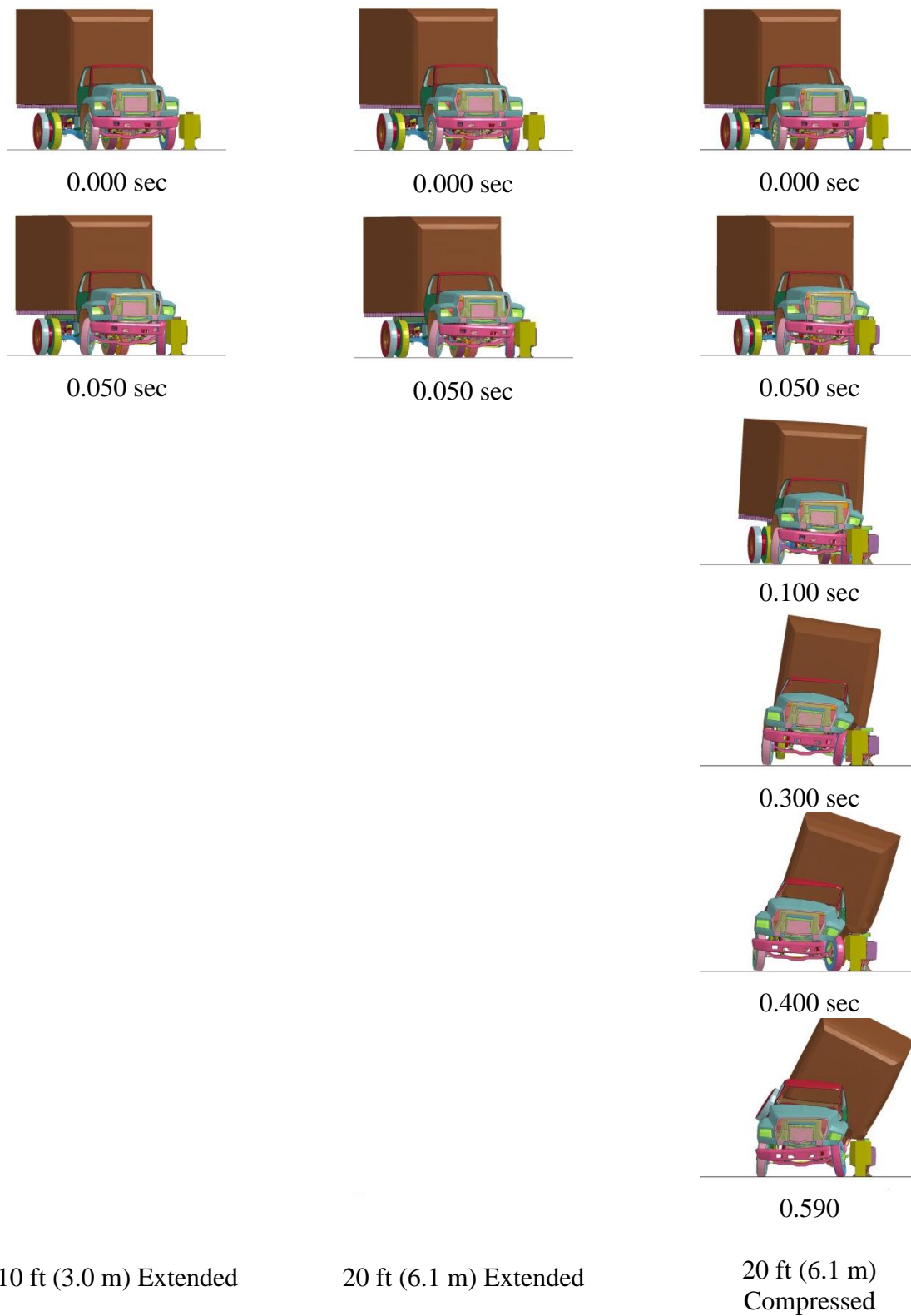


Figure 244. RESTORE Barrier Transition, 10000S F800 Simulation Comparison, Upstream Impact Locations, Downstream View

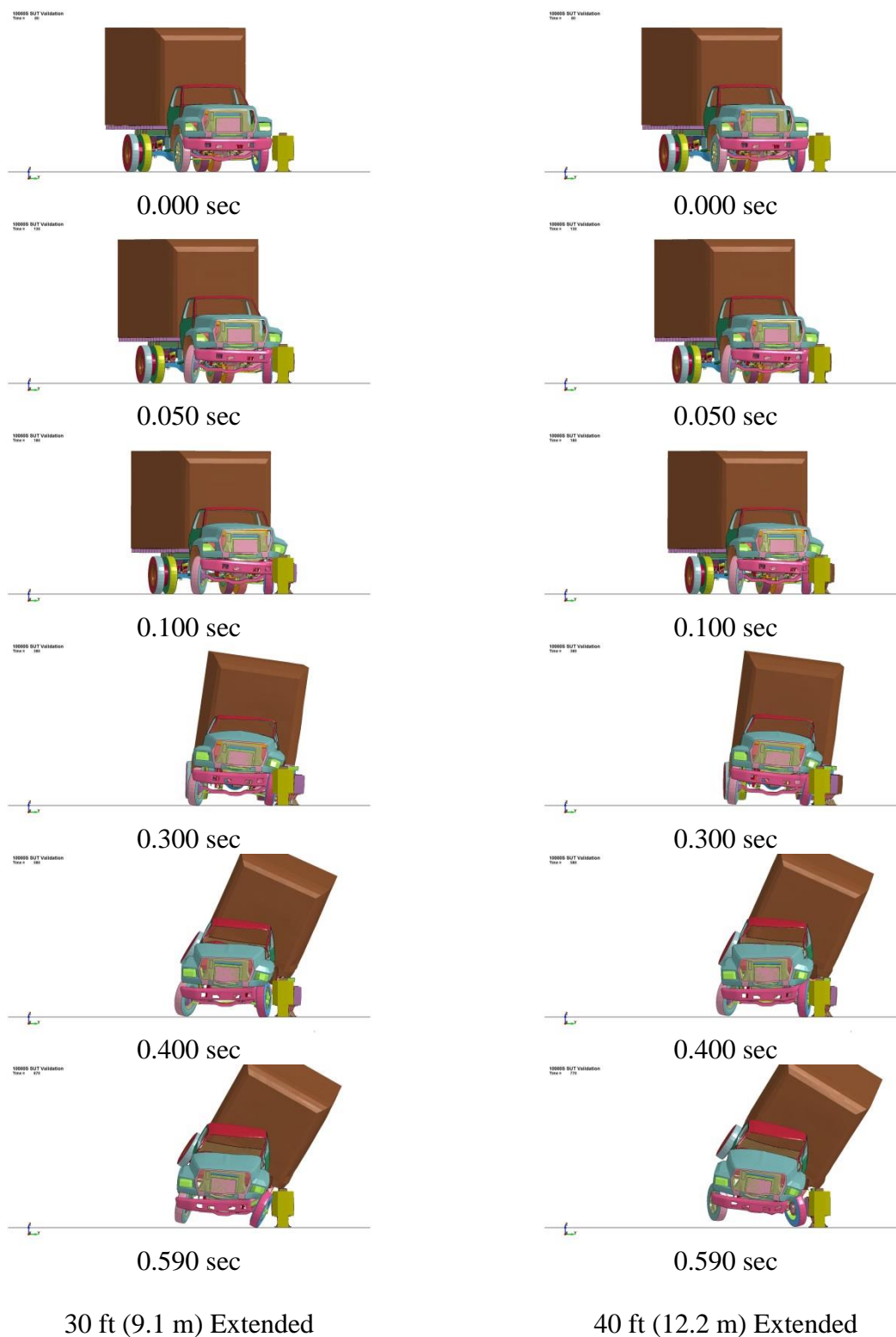


Figure 245. RESTORE Barrier Transition, 10000S F800 Simulation Comparison, Upstream Impact Locations, Downstream View

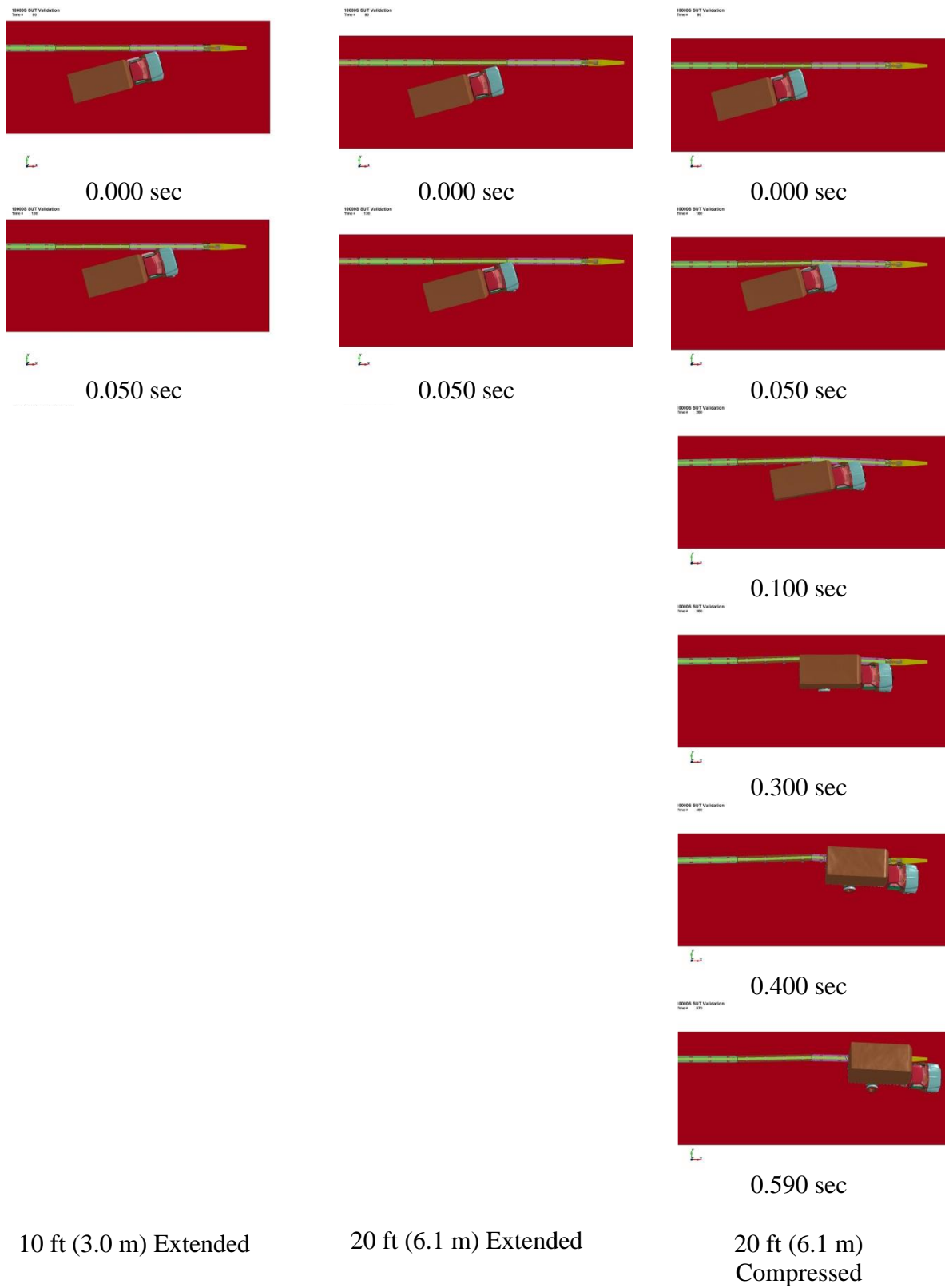


Figure 246. RESTORE Barrier Transition, 10000S F800 Simulation Comparison, Upstream Impact Locations, Overhead View

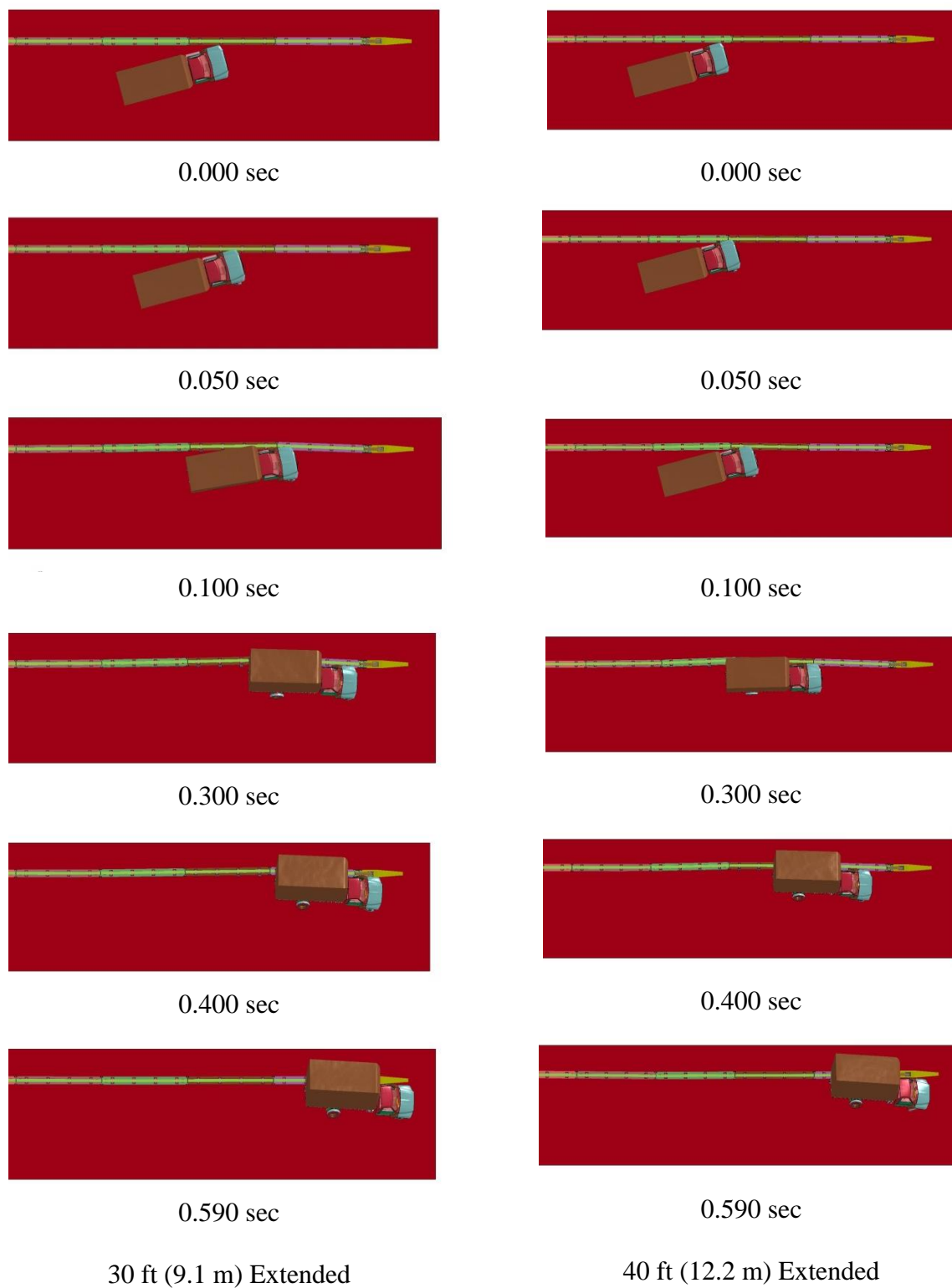


Figure 247. RESTORE Barrier Transition, 10000S F800 Simulation Comparison, Upstream Impact Locations, Overhead View

The maximum dynamic deflection was greatest in the 40-ft (12.2-m) impact location simulation. The deflections at the 40-ft (12.2-m) impact location simulation upstream from the pin exhibited 4.6 percent greater dynamic barrier deflections as compared to the interior location simulation, as described in Chapter 6. Further, the simulation at 40 ft (12.2 m) upstream from the joint had dynamic barrier deflections 3.8 percent larger than observed in the 20-ft (6.1-m) impact location and the 7.7 percent larger than the 30-ft (9.1-m) impact location. The simulated deflection at the 20-ft (6.1-m) impact location with the compressed joint was within 1 percent of the dynamic barrier deflection in the interior location simulation.

The lateral change in velocity between the simulations were similar through 600 msec, as shown in Figure 248. The peak lateral change in velocity between the simulations was within 2 mph (3.2 km/h). Similarly, the longitudinal change in velocity was similar between the simulations through 300 msec, as shown in Figure 249. The maximum change in longitudinal velocity during the simulation at 20 ft (6.1 m) upstream from the pin with compressed joint was 23 percent greater than observed in the other impact location simulations at approximately 400 msec.

Occupant risk values are not a required evaluation criteria for test designation no. 4-22. However, the calculated OIV and ORA values in the lateral and longitudinal directions were obtained for comparison purposes. The lateral and longitudinal OIV and ORA values could not be obtained for the simulations at 10 and 20 ft (3.0 and 6.1 m) upstream from the pin, because the simulations terminated before t^* could be obtained. The longitudinal OIV correlated well between each of the other simulations. The lateral OIV correlated well between the simulations at 30 and 40 ft (9.1 and 12.2 m) upstream

from the pin. The lateral OIV for the simulation at 20 ft (6.1 m) upstream from the pin with the compressed joint was approximately 16 percent larger than the other upstream location simulatinos. The lateral ORA values were within 28 percent of each other, and the longitudinal ORA values were within 19 percent of each other.

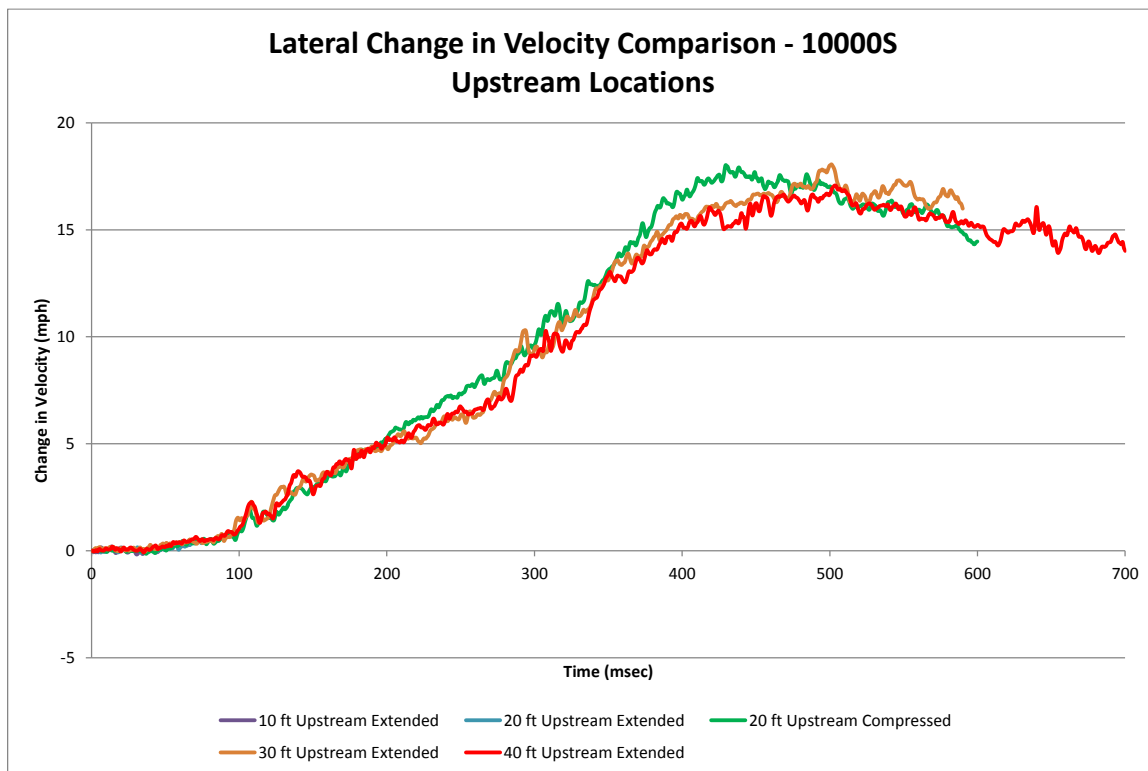


Figure 248. Lateral Change in Velocity, Upstream Impact Locations, 10000S F800 Simulation

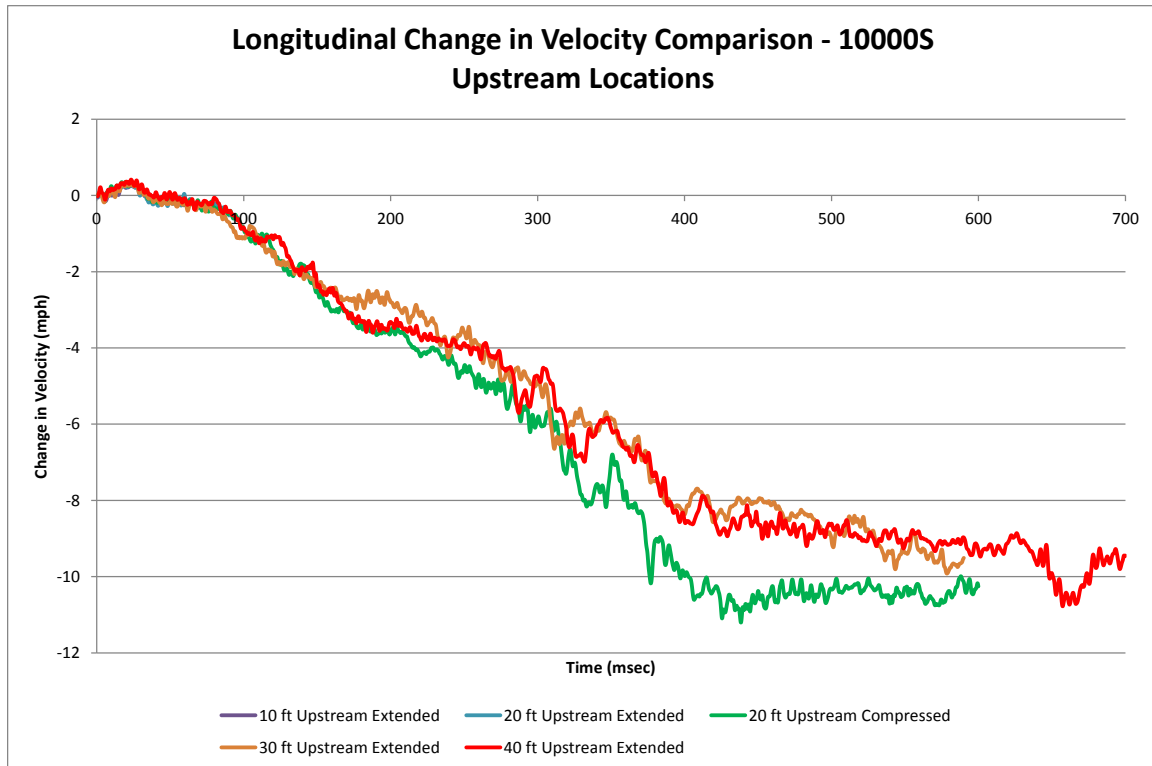


Figure 249. Longitudinal Change in Velocity, Upstream Impact Locations, 10000S F800 Simulation

The lateral impact forces were calculated using the CFC60 filtered 50-msec global Y-accelerations multiplied by the mass. The simulation at 30-ft (9.1-m) upstream from the pin showed the highest peak lateral force of 83.4 kips (371 kN) at approximately 320 msec, as shown in Figure 250. However, all simulations did not finish, thus higher impact loads may potentially have been experienced. The peak force for the simulation at 20 ft (6.1 m) upstream from the pin with the compressed joint was 7.9 percent lower than the 30 ft (9.0 m) location simulation and the peak force for the simulation at 40 ft (12.2 m) upstream from the pin was 14.2 percent lower than the 30 ft (9.1 m) location simulation. All of the simulations experienced its peak force during the secondary impact with the rear axle. As described earlier in Chapter 6, the simulation in the interior region did not accurately predict the peak lateral barrier force, which occurred early in the

impact event in full-scale vehicle crash test no. SFH-3. Thus, the simulated lateral impact force may be underpredicted if the maximum force actually occurred early in the impact event. However, the lateral impact force due to tail-slap in the simulation correlated well with that observed in the full-scale crash test.

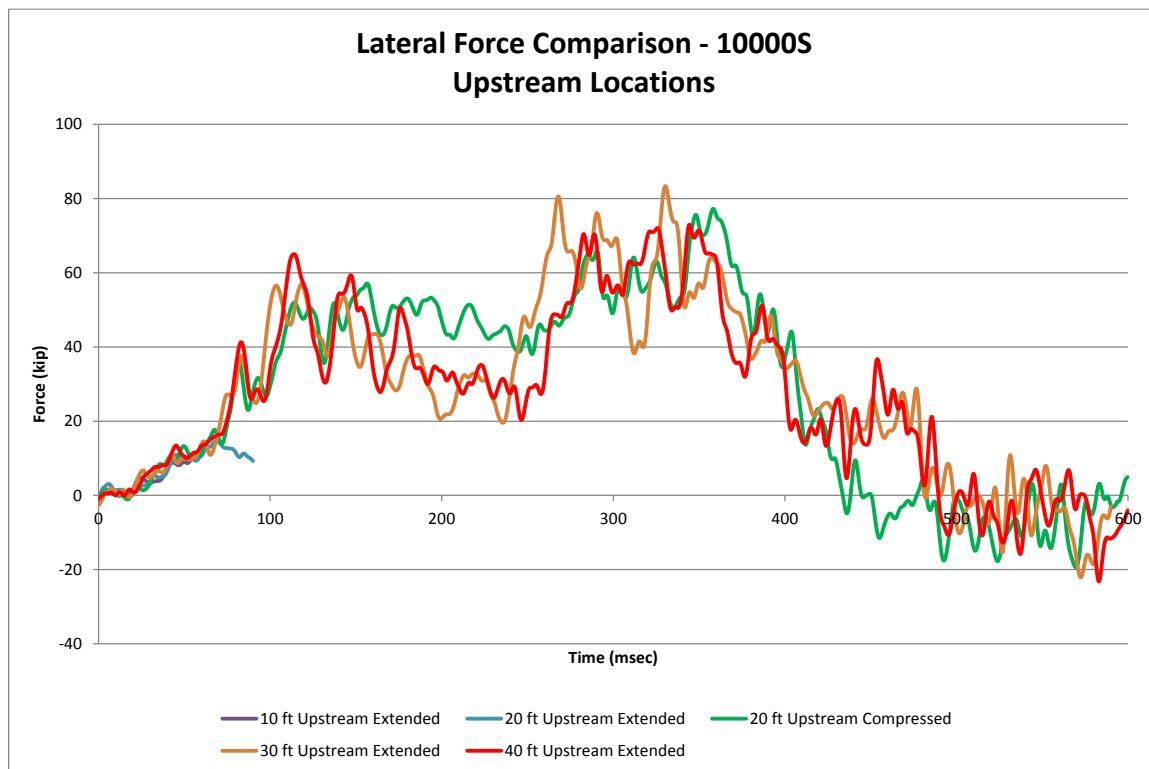


Figure 250. Lateral Force Comparison, Upstream Impact Locations, 10000S F800 Simulation

The roll angle of the F800 model at each impact location showed similar results through approximately 600 msec, as shown in Figure 251. However, the simulation at 20 ft (6.1 m) upstream from the pin with the compressed joint deviated slightly between 200 and 600 msec. The roll angles were still increasing when the simulations ended.

The pitch angles of the F800 model were nearly identical through 300 msec, as shown in Figure 252. The simulation at 20 ft (6.1 m) upstream from the pin with the compressed joint pitched more than observed in the other simulations and resulted in a 5

degree greater pitch angle at 600 msec. Note that the pitch angles in all the simulations were still increasing when the simulations ended.

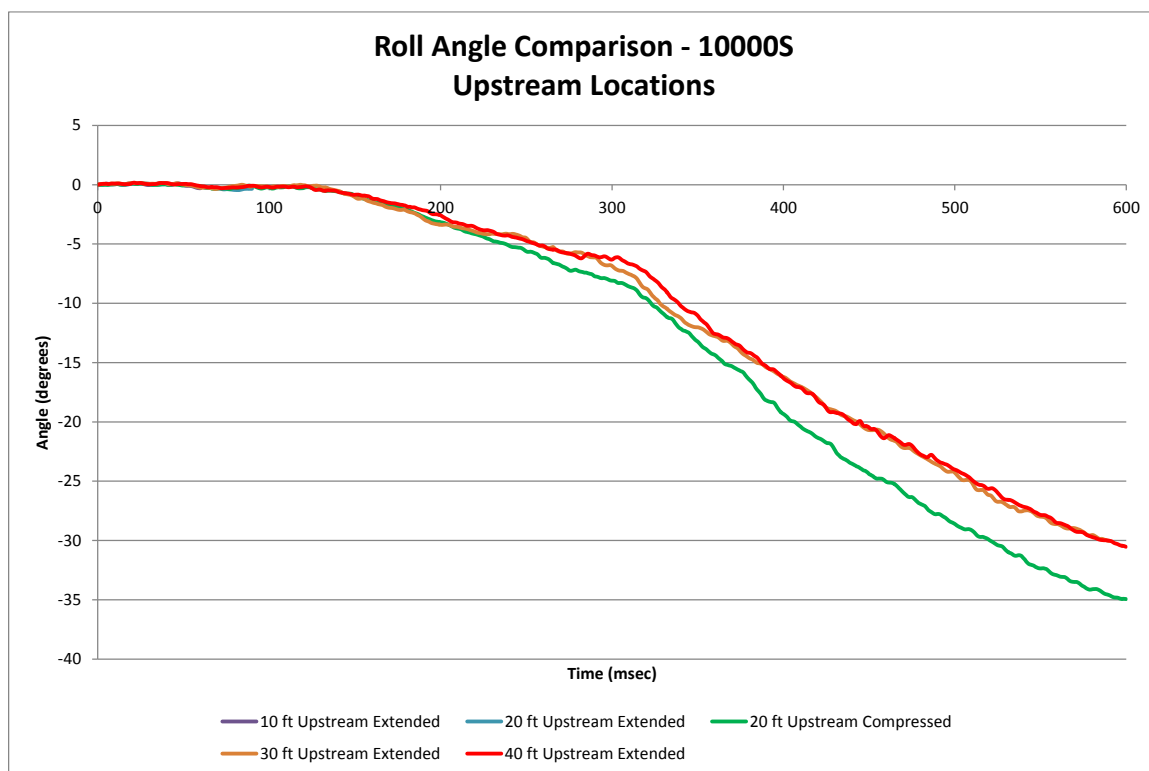


Figure 251. Vehicle Roll Comparison, Upstream Impact Locations, 10000S F800 Simulation

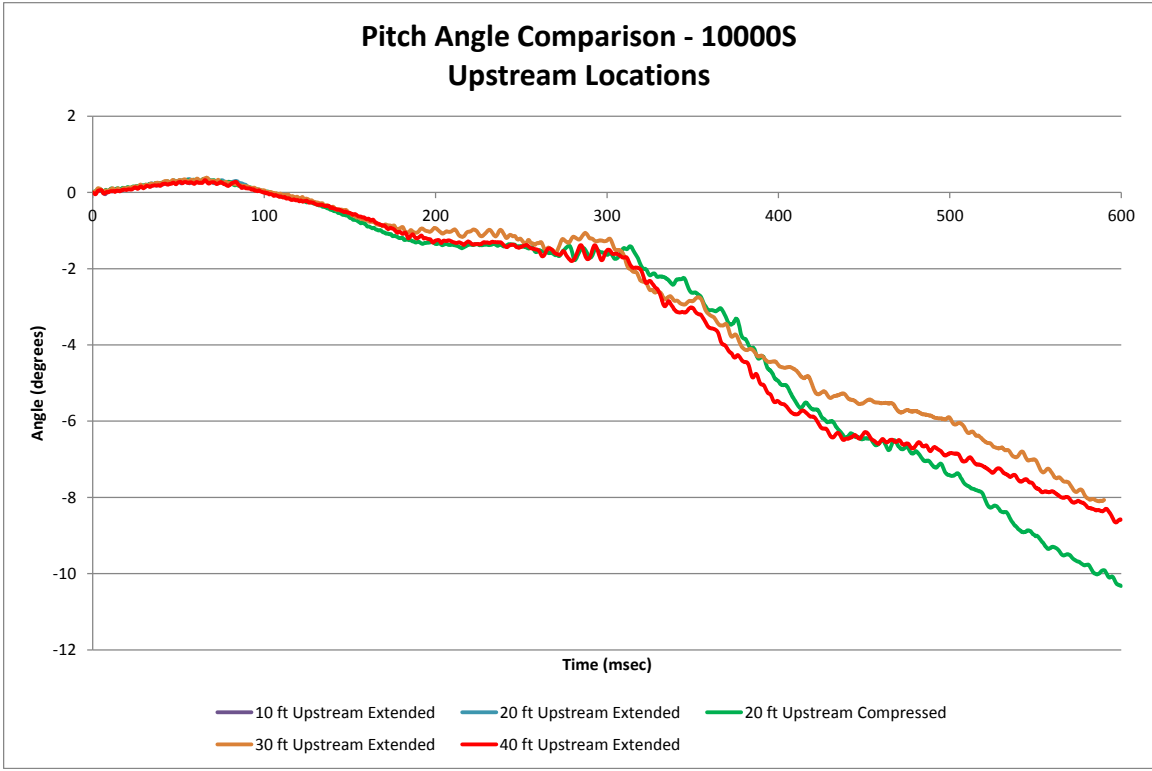


Figure 252. Vehicle Pitch Comparison, Upstream Impact Locations, 10000S F800 Simulation

The simulated yaw angles were similar through 150 msec, where they deviated slightly for the remainder of the impact event, as shown in Figure 253. The simulation with the impact location that was 20 ft (6.1 m) upstream from the pin with the compressed joint had a faster change in yaw angle between 250 msec and 400 msec than observed in the other simulations. However, the peak yaw angle for each simulation was within 6 percent of each other.

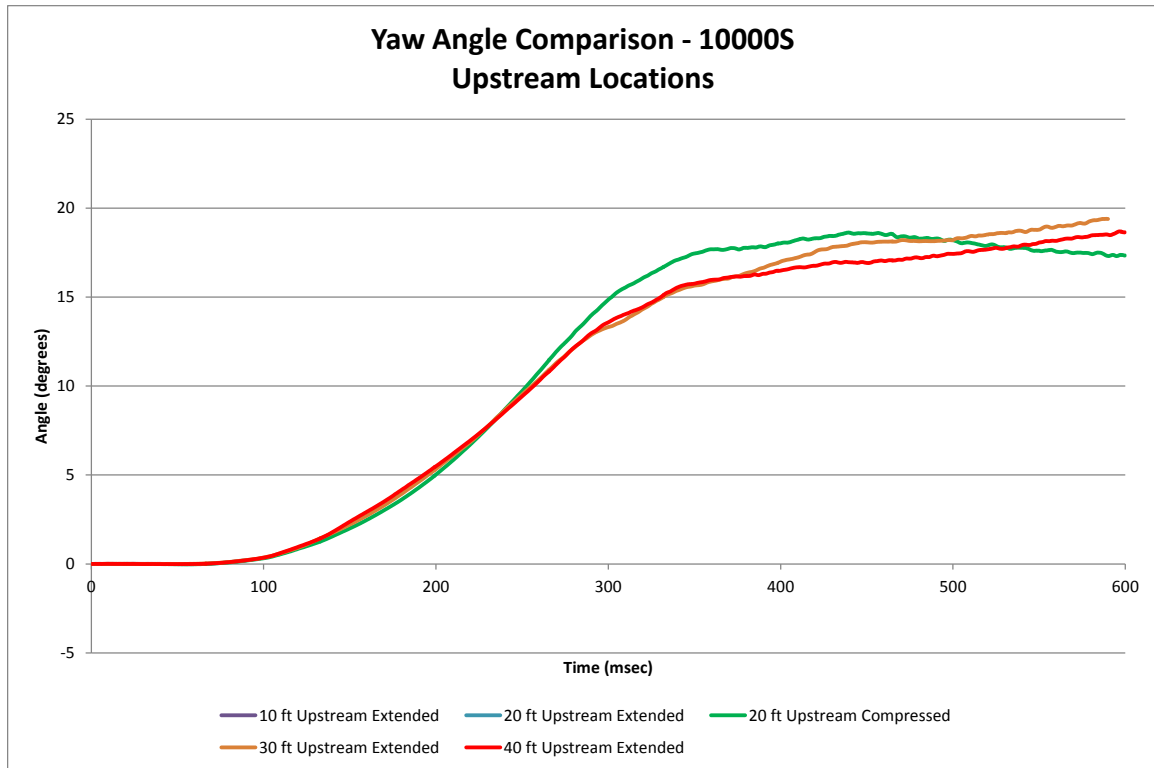


Figure 253. Vehicle Yaw Comparison, Upstream Impact Locations, 10000S F800 Simulation

The von Mises and Tresca yield conditions were used to evaluate the stresses within the parts of the pin and gusset plate assemblies. Each simulation with impact locations upstream from the transition hardware were compared to the interior simulation with F800 model, as noted in Chapter 6 and shown in Table 53. The interior location simulation was considered the baseline condition, as the ACJ bolts did not permanently deform. However, the top tube permanently deformed during test no. SFH-3. Similarly, the simulation at the interior impact location with the F800 vehicle model showed that the top tube would yield based on the Tresca and von Mises yield conditions. Note that failure was not enabled in the top tube material during the simulations. Therefore, further evaluation would need to be completed to determine if the top tube would be expected to fail during a full-scale vehicle crash test.

Table 53. RESTORE Barrier Component Stress Comparison, 10000S F800 Simulation, Upstream Locations

Simulation Parameters			Impact Location and Trial No.					
			NA	57	58	68	59	60
			Interior Model	10 ft Upstream Extended	20 ft Upstream Extended	20 ft Upstream Compressed	30 ft Upstream Extended	40 ft Upstream Extended
ACJ Bolts	Max. Tresca Stress	Stress, ksi (MPa)	69.2 (477)	60.0 (413)	52.4 (361)	76.0 (524)	68.0 (469)	70.0 (483)
		$\tau \geq 0.5\sigma_y$?	Yes	Yes	No	Yes	Yes	Yes
		% Different Than Interior	NA	-13.1	-24.2	10.0	-1.7	1.2
	Max. von Mises Stress	Stress, ksi (MPa)	120.0 (827)	104.4 (720)	101.2 (698)	133.3 (919)	119.3 (823)	123.4 (851)
		$\sigma_{vm} \geq \sigma_y$?	Yes	No	No	Yes	Yes	Yes
		% Different Than Interior	NA	-13.0	-15.6	11.1	-0.5	2.9
Top Tube and Tube Splice	Max. Tresca Stress	Stress, ksi (MPa)	64.8 (447)	64.1 (442)	63.2 (436)	71.5 (493)	70.5 (486)	53.0 (365)
		$\tau \geq 0.5\sigma_y$?	Yes	Yes	Yes	Yes	Yes	Yes
		% Different Than Interior	NA	-1.1	-2.4	10.3	8.8	-18.3
	Max. von Mises Stress	Stress, ksi (MPa)	115.3 (795)	119.4 (823)	111.0 (765)	124.0 (855)	123.8 (853)	93.8 (647)
		$\sigma_{vm} \geq \sigma_y$?	Yes	Yes	Yes	Yes	Yes	Yes
		% Different Than Interior	NA	3.6	-3.7	7.5	7.4	-18.6

¹ Through 60 msec, stresses may be inaccurate due to element penetration.

² Through 90 msec, stresses may be inaccurate due to element penetration.

Similar to top tube in the interior model, the Tresca and von Mises stresses exceeded the yield conditions for all of the simulations. Note that during the simulations at 10 and 20 ft (3.0 and 6.1 m) upstream from the pin with the extended joint, the large mesh size of the left-front fender of the F800 vehicle model penetrated the small mesh size of the top tube, which violated the contact definition and created higher localized stresses in the tube. However, the simulations at 20 ft (6.1 m) upstream from the pin with a compressed joint and 30 ft (9.1 m) upstream from the pin had observed stresses in the tube and tube splice which exceeded the ultimate strength of the material. Therefore, further evaluation with the designed tube splice thickness of ½ in. (13 mm) would be recommended.

Although the ACJ bolt stresses exceeded the Tresca and von Mises yield conditions in the simulations with the F800 vehicle model, they did not vary significantly from the ACJ bolt stresses in the interior location simulation. The 20-ft (6.1-m) impact location simulation with the compressed joint had the maximum ACJ bolt stresses, which were 11 percent greater than observed in the interior location simulation. Thus, larger

bolts may be needed within the transition region. However, the ACJ bolts connected two adjacent rigid barriers, not allowing the concrete to fracture, which may have increased the stresses within the bolts. Thus, concrete fracture may also be recommended to provide a more accurate result.

13.4 Reverse-Direction Impact Location Simulation Results

Simulations of impact points in the reverse direction were performed at the slope-break point of the rigid concrete buttress while traveling toward the RESTORE barrier as well as at 4 ft – 11 in. (1.5 m) upstream from the upstream corner of the cover plate. These locations were evaluated with the joint extended to investigate vehicle snag and vehicle stability. Prior MASH testing on a concrete barrier with a horizontal flare rate of 6:1 over the full height has never been conducted. Therefore, a simulation effort was conducted to evaluate an impact at the horizontal slope-break point.

The limited results for the F800 model in simulations under reverse-direction impact locations are shown in Table 54. The sequential photographs for each simulation through their respective end time are shown in Figures 254 and 255. Each simulation had model instabilities, which caused it to terminate early. The F800 model had a negative volume in the box frame at the rear of the vehicle during the slope-break impact, and the F800 model had a negative volume in the engine compartment during the CIP impact. Thus, parallel and exit conditions could not be obtained. The stresses in the transition hardware were minimal, thus they were not reported herein. The simulations did not run long enough to evaluate vehicle model damage or maximum impact loading.

Table 54. Comparison Matrix of Reverse-Direction Locations, 10000S F800 Model

Simulation Parameters		Impact Location and Trial No.	
		40	64
		Reverse-Direction Slope-Break Point	Reverse-Direction CIP ³
End Time, ms		170	185
Parallel Conditions	Time, ms	NA	NA
	Velocity, mph (km/h)	NA	NA
Exit Conditions	Velocity, mph (km/h)	NA	NA
	Angle, deg.	NA	NA
	Time, ms	NA	NA
Length of Contact		NA	NA
t*, ms		NA	NA
ORA, g's	Longitudinal	0	0
	Lateral	0	0
OIV, ft/s (m/s)	Longitudinal	0	0
	Lateral	0	0
Test Article Deflections, in. (mm)	Dynamic of Concrete	0.2 (5)*	0.5 (13)*
	Dynamic of Steel Rail	0.3 (8)*	0.5 (13)*
	Working Width	22.5 (572)*	22.8 (579)*
Location of Max. Deflection Upstream of Pin		0 ft (0 m)*	20 ft (6.1 m)*
Vehicle Stability	Max Roll, deg.	-1.7*	-3.1*
	Max Pitch, deg.	-1.8*	-1.7*
	Max Yaw, deg.	4.1*	5.1*
Posts Hit by Leading Tire (wheel snag)		0*	0*
Max. Lateral Impact Force, kips (kN) ¹		83.5 (371.5)*	76.2 (339.0)*
Max. Longitudinal Impact Force, kips (kN) ²		35.7 (158.8)*	30.4 (135.2)*

* Values calculated through simulation end time and may not provide maximum value.

¹ Calculated using global Y-acceleration multiplied by mass.

² Calculated using local X- and Y- accelerations coupled with yaw, multiplied by mass.

³ Impacted 4 ft – 11 in. (1.5 m) upstream from cover plate edge.



Figure 254. RESTORE Barrier Transition, 10000S F800 Simulation Comparison, Reverse-Direction Locations, Downstream View

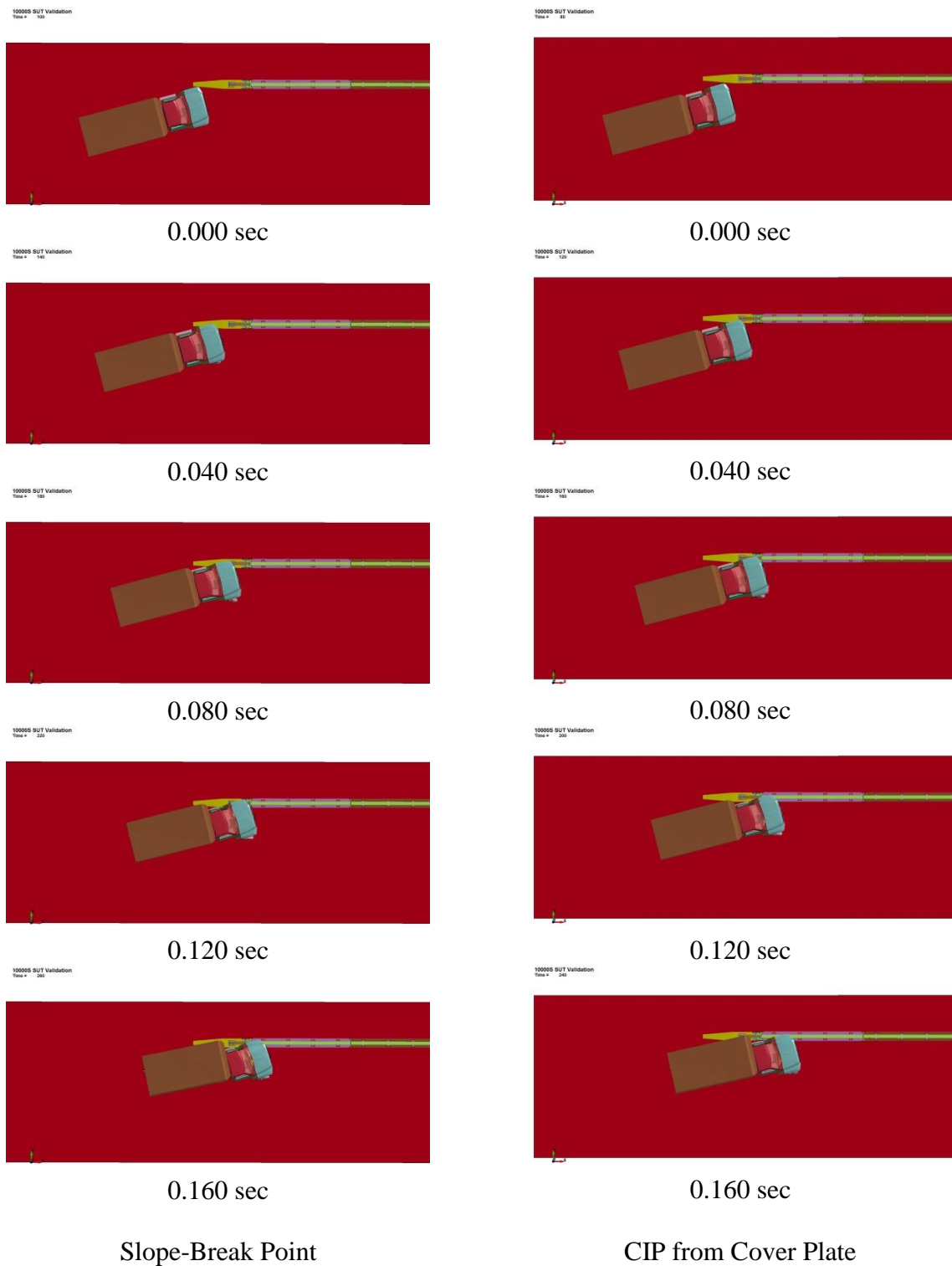


Figure 255. RESTORE Barrier Transition, 10000S F800 Simulation Comparison, Reverse-Direction Locations, Overhead View

Since all degrees of freedom in the rigid concrete buttress were constrained, the buttress did not have any damage nor deflections. However, the downstream end of the RESTORE barrier dynamically deflected 0.5 in. (13 mm) during the simulation at the CIP location upstream from the cover plate corner. For the simulation where the F800 vehicle model impacted the slope-break point, the RESTORE barrier deflected 0.2 in. (5 mm). The deflections of the RESTORE barrier located near the joint were due to the tolerances that were built into the pin holes and slots in the gusset plates.

The lateral change in velocity for each simulation was similar through approximately 100 msec, as shown in Figure 256. From 110 msec and 160 msec, the lateral change in velocity increased at a faster rate during the simulated impact at the slope-break point as compared to the CIP impact location simulation. The longitudinal change in velocity during the simulated impact at the CIP location had a positive change through 30 msec, as shown in Figure 257, which indicated the vehicle increased initially after impact. In the slope-break point simulation, a negative change in longitudinal velocity occurred throughout the impact. The peak longitudinal change in velocity was similar between the simulations at the time each simulation terminated. The lateral and longitudinal OIV and ORA values were not obtained, because the simulations did not run long enough to obtain a t^* time.

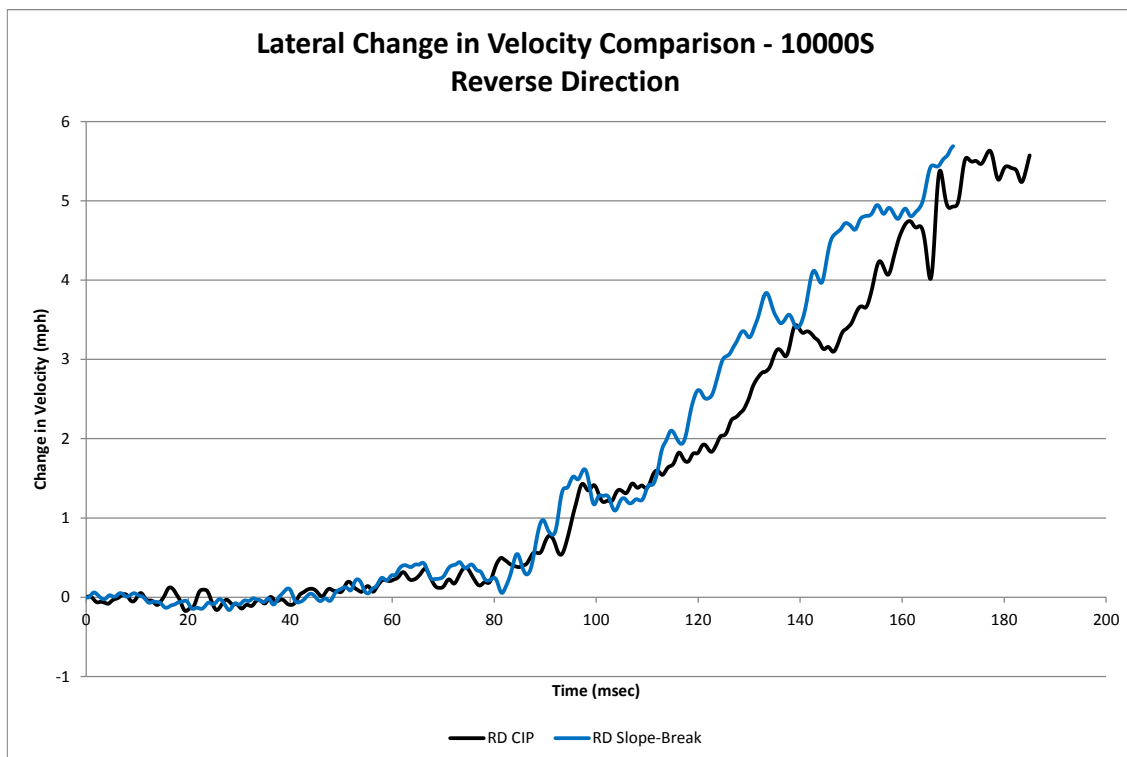


Figure 256. Lateral Change in Velocity, Reverse-Direction Locations, 10000S F800 Model

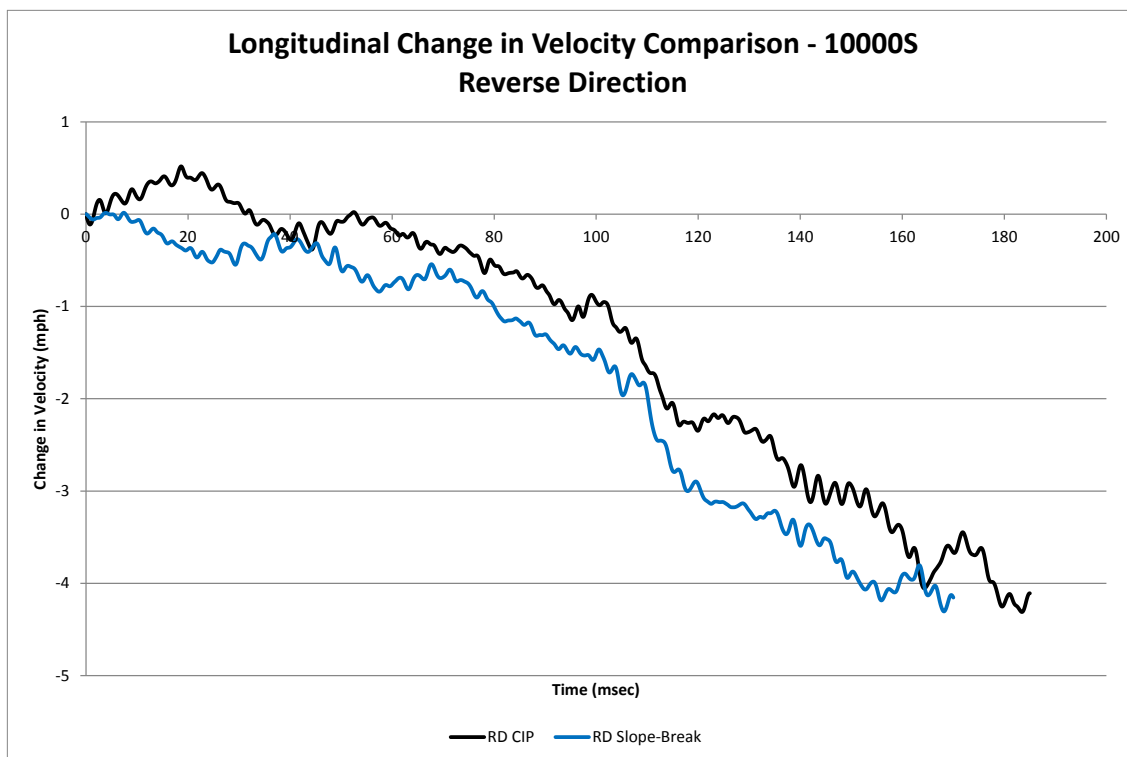


Figure 257. Longitudinal Change in Velocity, Reverse-Direction Locations, 10000S F800 Model

The lateral impact forces were calculated using the CFC60 filtered 50-msec global Y-accelerations multiplied by the mass. Each impact locations was on the rigid concrete buttress. The slope-break point location simulation had a peak lateral impact force of 83.5 kips (372 kN), which was 8.7 percent greater than observed in the CIP simulation, as shown in Figure 258. However, all simulations did not finish, thus higher impact loads potentially may have been experienced. The longitudinal barrier force was calculated using the local X- and Y- accelerations coupled with the yaw angle and multiplied by the mass of the vehicle model. The simulation at the slope-break point location had a peak longitudinal barrier force of 35.7 kips (159 kN), which was 14.8 percent greater than observed in the CIP simulation, as shown in Figure 259.

Due to model instabilities, tail slap did not occur in either simulation. The tail slap event typically produces the highest simulated lateral force during a reverse-direction impact event and thus could not be determined.

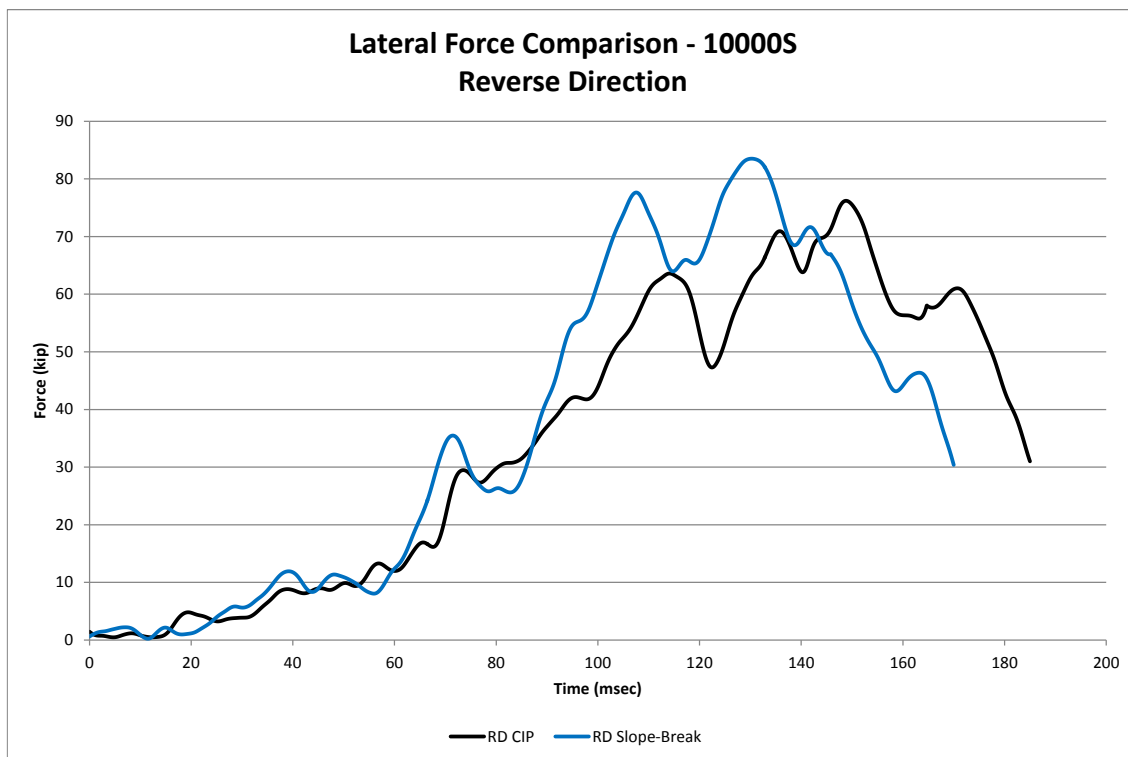


Figure 258. Lateral Force Comparison, Reverse-Direction Locations, 1000S F800 Model

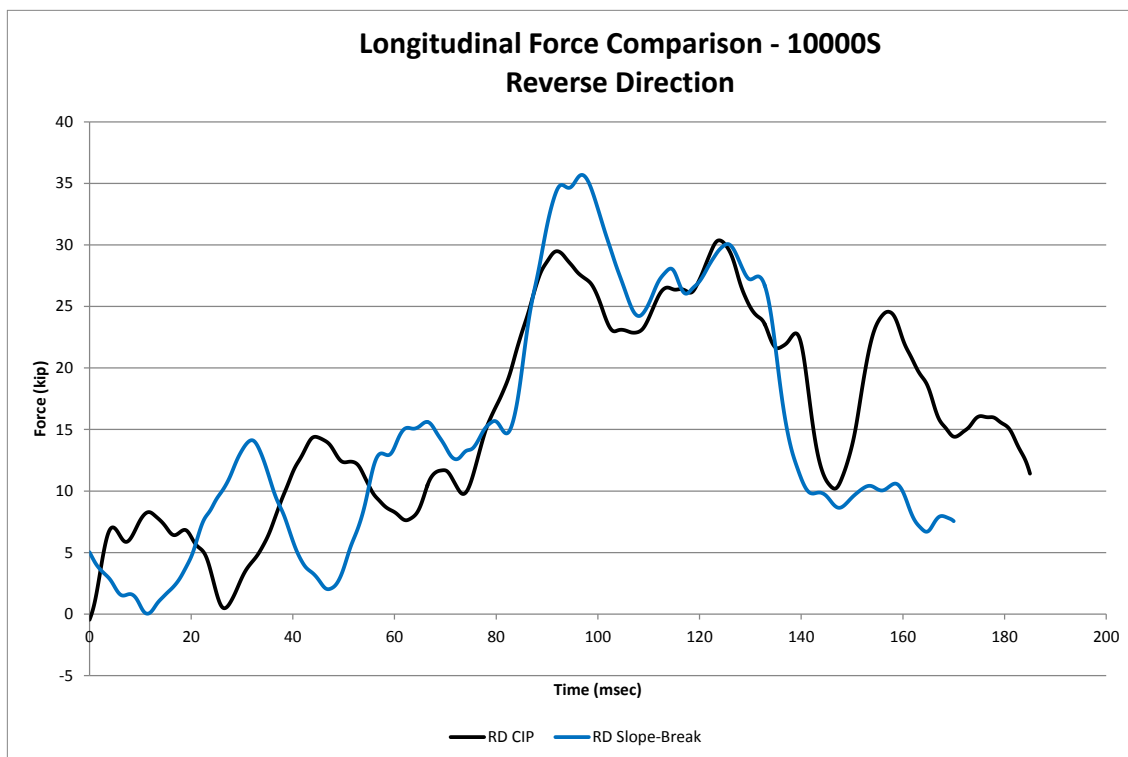


Figure 259. Longitudinal Force Comparison, Reverse-Direction Locations, 1000S F800 Model

In both of the reverse-direction simulations, the SUT model did not roll through approximately 90 msec, as shown in Figure 260. After 100 msec, the F800 vehicle models had a minimal positive roll angle before a minimal negative roll angle. The pitch angles for the simulations at the slope-break point and the CIP location were similar, as shown in Figure 261. The SUT models in both simulations had a minimal positive pitch angle through approximately 90 msec, when they proceeded to minimally pitch negatively. The yaw angle in the simulation at the slope-break point location increased more quickly than observed in the CIP location simulation, as shown in Figure 262. However, complete results were not obtained due to model instabilities.

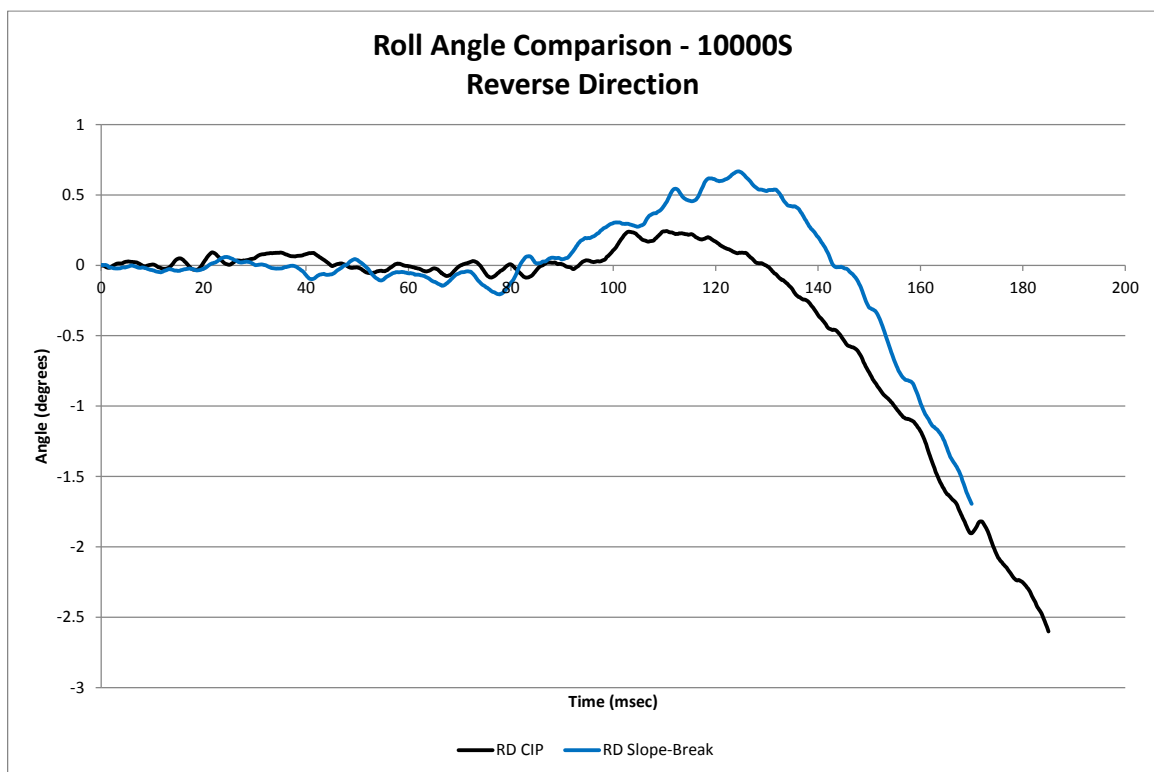


Figure 260. Roll Angle Comparison, Reverse-Direction Locations, 10000S F800 Model

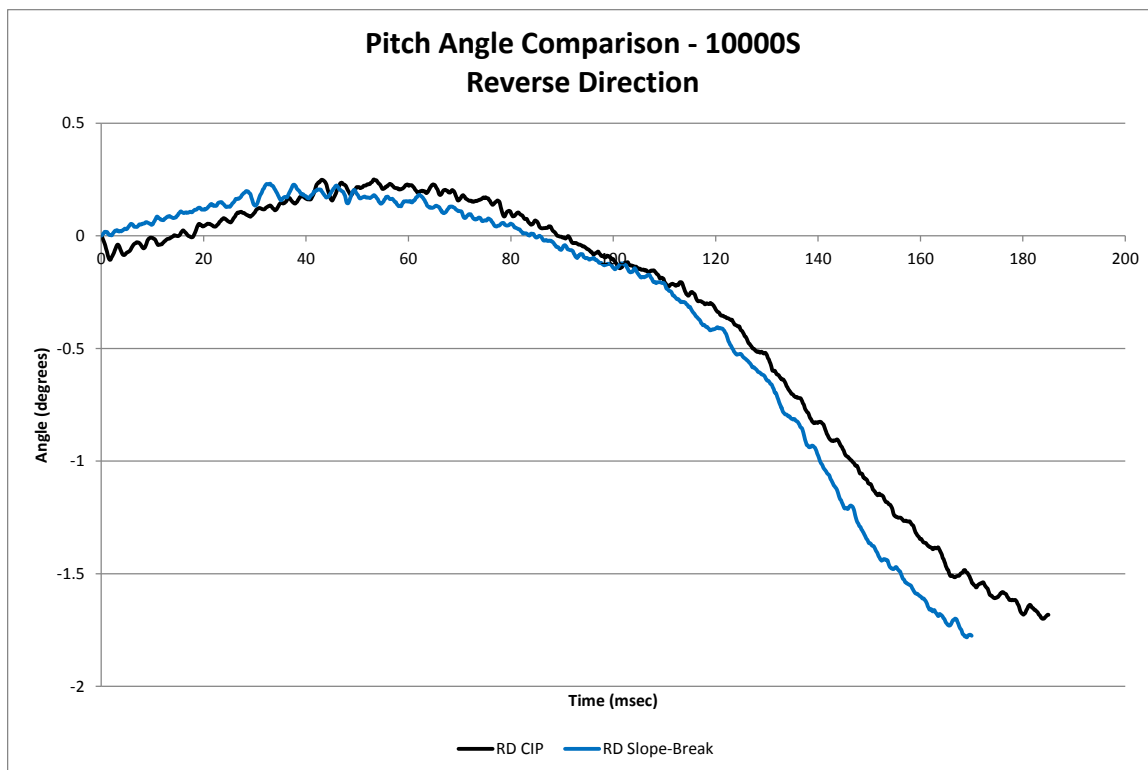


Figure 261. Pitch Angle Comparison, Reverse-Direction Locations, 10000S F800 Model

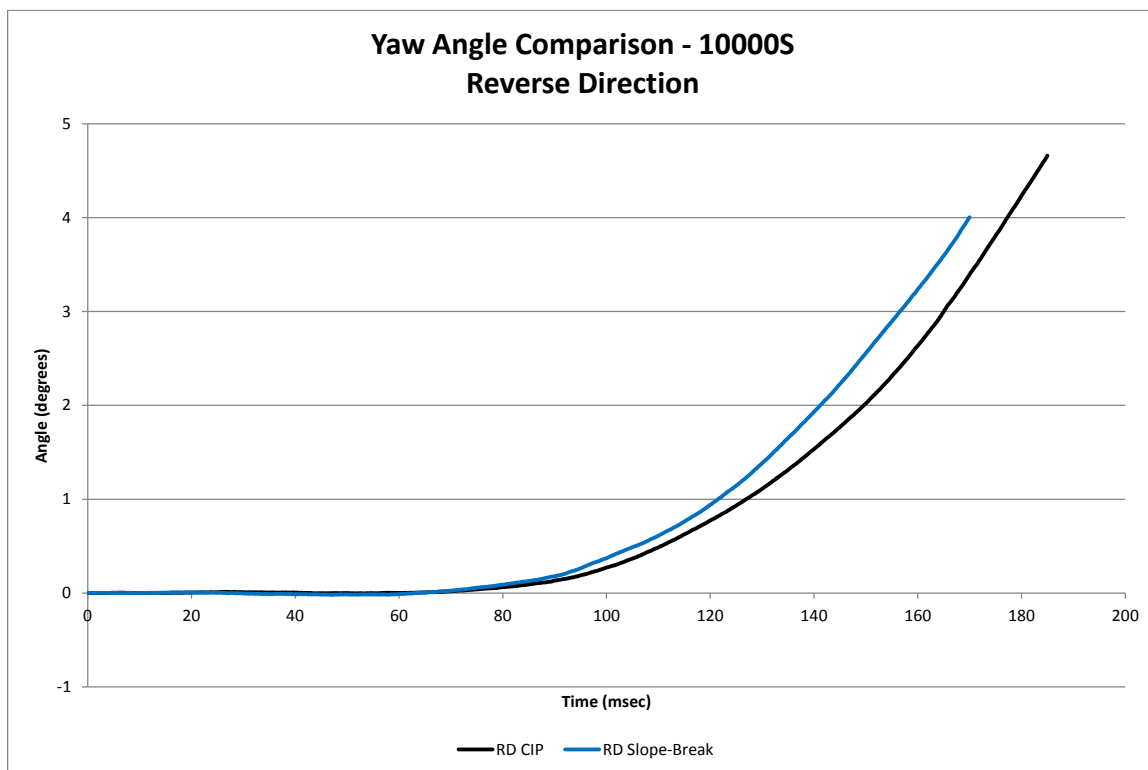


Figure 262. Yaw Angle Comparison, Reverse-Direction Locations, 10000S F800 Model

13.5 10000S Simulation Summary

Various impact locations were simulated to evaluate the RESTORE barrier transition to a rigid concrete buttress according to MASH test designation no. 4-22 impact conditions. Impact locations at the suggested CIP location of 4 ft – 11 in. (1.5 m) in MASH were simulated with respect to the upstream buttress face and the drop-down pin. Simulation impact distances in 10 ft (3.0 m) increments upstream from the pin-and-gusset plate assemblies were considered to find the worst-case critical impact points, as denoted in MASH. Further, two simulations in the reverse direction were used to determine if the transition can be used in median applications. The 10000S vehicle model, the Ford F800, indicated that the pin-and-gusset plate assemblies with the rounded cover plates have the potential to be successfully used as a MASH TL-4 barrier transition that accommodates the degrees of freedom from the RESTORE barrier. However, further evaluation is warranted. Comparison plots between all of the impact locations with the pickup truck vehicle model are shown in Appendix N.

In the simulations at the suggested CIP locations in MASH around the transition hardware, the peak lateral barrier force occurred when the rear axle contacted the barrier. The maximum lateral barrier force was 98.7 kips (439 kN) in the simulation upstream from the pin with the extended joint, which was up to 18 percent greater than observed in the interior simulation. This force was within 1 percent of the 100-kip (448-kN) lateral design load, as discussed previously in Chapter 2. However, the simulation in the interior region did not accurately predict the peak lateral barrier force, which occurred early in the impact event in the full-scale vehicle crash test. Thus, the simulation lateral impact force may underpredict the maximum force early in the impact event. The overall vehicle

performance was satisfactory. However, the roll and pitch angles of the SUT were still increasing at the end of the simulations and should be investigated further. The interior simulation showed that the SUT model roll angles did not correlate well after approximately 700 msec.

Through the stress analysis, the maximum von Mises stresses did not exceed the yield condition for the vertical drop-down pin. The cover plate bolts had maximum stresses that exceeded the yield conditions as well as experienced large longitudinal deformations. The large stresses and deformations were a cause for concern and would most likely result in fracture. Thus, it is recommended to redesign the joint to either lessen the forces imparted through the cover plate to the vertical bolts by having a part accommodate the longitudinal bearing or increase the structural capacity of the cover plate bolts by increasing the diameter of the bolts. Note that changes to the cover plate and bolt configuration may also change stresses imparted to other parts, thus requiring re-evaluation of the transition joint hardware. The horizontal gusset plates had maximum Tresca and von Mises stresses that exceeded the yield conditions at the edges of the plate where the cover plate strips were bearing due to the vehicle impact on the cover plate. Lastly, the cover plate experienced stresses that exceeded the Tresca and von Mises yield conditions. The stress locations were at the rounded edges and the top of the cover plates. If the cover plate edges extend past the RESTORE or buttress face, they may need to be replaced due to concerns for snag behind the cover plate. The stresses at the top of the cover plate would cause the plate to bend until it contacted the horizontal gusset plates, but it would not negatively affect the prevention of penetration behind the cover plate.

During simulations at the upstream impact locations, impacts at 10 and 20 ft (3.0 and 6.1 m) upstream from the pin with the extended joint terminated early due to model instabilities, and most results were not obtained. The model instabilities occurred when the F800 vehicle model's left-front fender contacted the upper tube. The vehicle model's fender mesh size was approximately 88 percent greater than that used for the upper tube mesh, and contact was not detected until after the fender mesh had penetrated into the upper tube. It is recommended that the fender mesh be refined, or an alternate contact is utilized to mitigate this problem. Thus, the simulations at the 10- and 20-ft (3.0- and 6.1-m) impact locations upstream from the pin with the extended joint should be re-evaluated to provide more complete results. However, the simulation at the 20-ft (6.1-m) impact location with the compressed joint completed successfully and was compared against the simulation results obtained at 30 and 40 ft (9.1 and 12.2 m) upstream from the pin with the extended joint.

The maximum simulated dynamic deflection was 13.0 in. (330 mm) for the 40-ft (12.2-m) impact location, which was greater than observed for the other impact locations. The F800 vehicle model's roll, pitch, and yaw behavior did not appear to be a problem in the simulations at each of the different upstream impact locations. However, they were still increasing when the simulations ended. The box roll angle was not very predictive during the interior location simulation, possibly due to the box attachment system having fewer and different constraints (i.e., shear plates and actual U-bolt diameter) than observed in full-scale vehicle crash test. Thus, it is recommended that the vehicle stability and contact problems at the upstream locations be further evaluated with a suspension that more closely resembles the full-scale crash test vehicle to determine if the stiffness

transition is capable of containing and safely redirecting a single-unit truck. The ACJ bolt as well as top tube and top tube splice stresses for the simulations at the upstream impact locations had maximum stresses that exceeded the Tresca and von Mises yield conditions. ACJ bolts were used to connect two adjacent rigid concrete barriers, where concrete fracture was not allowed to occur and may increase stresses in the bolts. However, an ACJ bolt with an increased diameter of 1¼ in. (32 mm) may reduce the stresses in the ACJ bolts within the transition region. Failure was not enabled in the model. However, the top tube and tube connection experienced stresses that well exceeded the yield conditions. Further work should be completed with an increased tube thickness of ½ in. (13 mm) which was what minimum thickness that exceeded the yield moment capacity of the outer tube. The increased tube thickness should minimize the stresses in the splice tube. Note that the top tube rail in test no. SFH-3 experienced plastic deformation above the ACJ just downstream from the impact point.

The simulations in the reverse direction experienced unresolvable errors that did not allow for the F800 vehicle model to exit the system. From the limited data, the simulated lateral barrier force due to the initial impact event was 8.7 percent greater at the slope-break point than observed in the suggested CIP location in MASH. The lateral barrier force due to the initial impact in the reverse direction was up to 14 percent greater than observed in the impacts at the suggested CIP locations in MASH and up to 25 percent greater than observed in the impacts upstream from the pin. Note that the tail-slap impact event will likely produce an even greater lateral barrier force in simulation. Further, the longitudinal barrier force due to the initial impact was 14.8 percent greater in the simulation at the slope-break point than observed in the suggested CIP location in

MASH. The vehicle roll, pitch, and yaw behaviors were only accurate through 170 msec for the simulation at the slope-break point and through 185 msec for the simulation at the CIP location, and all values were minimal. Thus, overall vehicle performance was unable to be evaluated in the reverse direction. However, based on the limited results, the lateral and longitudinal change in velocity did not appear to be different than the upstream impact locations and the barrier height in the direction of the SUT vehicle increases in height from 36 in. (914 mm) to 38 $\frac{1}{8}$ in. (968 mm). Therefore, the reverse direction impact locations do not appear to cause concern.

Based on the single-unit truck model simulations, it is recommended that the RESTORE barrier transition be subjected to full-scale crash testing at multiple impact points. MASH suggests that an impact be evaluated at the location 4 ft – 11 in. (1.5 m) upstream from the pin to produce the largest load or to produce the maximum vehicle snag. Through the simulation effort, the maximum lateral barrier load was experienced during the simulation with respect to the pin when the joint was full extended. The maximum lateral load was within 1 percent of the design load of 100 kips (445 kN). Further, the vehicle had the largest peak roll angle of 30 degrees at 500 msec, and the roll angles were still increasing as the simulation ended. Thus, has the greatest potential for vehicle rollover. However, the maximum roll angle occurred after the vehicle was no longer in contact with the system and was positioned downstream of the downstream end of the buttress.

The impacts upstream from the pin should may provide further insight if evaluated further before full-scale testing is recommended. The simulations at 10 and 20 ft (3.0 and 6.1 m) upstream from the pin with the extended joint had contact issues

between the left-front fender and the top tube. Thus, it is suggested to remesh the fender in the F800 model to improve contact between the two parts and re-simulate impacts between the suggested CIP location and the 20-ft (6.1-m) location. However, if further simulation is not desired, a full-scale crash test at the 20-ft (6.1-m) location showed the greatest potential for system failure with large lateral deflections, and excessive stresses within the ACJ bolts. If the ACJ bolt diameter were increased, tube splice thickness was increased, and additional elastomer posts were implemented, the 20 ft (6.1 m) impact location may be neglected due to improving the lateral barrier deflections and stresses within the bolts and tube assembly.

Similarly, the F800 model instabilities in the reverse direction should may be further investigated. The simulations in the reverse direction experienced negative volumes in the F800 model. Thus, complete results in the reverse-direction simulations were not obtained, and further evaluation may be recommended. However, the lateral and longitudinal changes in velocity were not significantly different than the upstream impact locations through 180 msec. Similarly, the simulated roll, pitch, and yaw angles did not cause concern in the reverse direction impacts. Thus, the full-scale crash tests in the reverse direction are most likely not needed for the SUT.

14 SUMMARY, CONCLUSIONS, AND RECOMMENDATIONS

14.1 Summary and Conclusions

The objective of this study was to develop a stiffness transition between the RESTORE barrier and a rigid concrete buttress. The MASH TL-4 RESTORE barrier experienced a maximum dynamic deflection of 13.9 in. (353 mm) and 15.1 in. (384 mm) at the top of the concrete barrier and the top of the steel tube, respectively, and rotated backward during the impact event with the 10000S single-unit truck. However, the RESTORE barrier was not crash tested and evaluated with any special termination system. In order to terminate the RESTORE barrier and protect the ends, a transition from the RESTORE barrier to a rigid concrete barrier was desired. LS-DYNA computer simulation was used to evaluate a prototype stiffness transition, identify potential design modifications, and investigate critical impact points for future use in a full-scale crash testing program according to the MASH TL-4 safety performance criteria.

A literature search was performed to review existing connections between portable concrete barriers, stiffness transition techniques, barrier transitioning requirements, and design impact loads, which can be found in Chapter 2. In Chapter 3, the previous work research and development program associated with the RESTORE barrier, including computer simulation, component testing, and full-scale crash tests was summarized. Results from the prior full-scale vehicle crash tests and baseline simulation models at the interior impact location were summarized.

In Chapter 4, MASH test designation no. 4-10 simulated two 1100C small car vehicle models, the Dodge Neon and Toyota Yaris, impacting the RESTORE barrier model, with results compared to full-scale crash test no. SFH-2. Each vehicle was

targeted to impact 3 ft – 7 in. (1.1 m) upstream from the upstream face of the first post downstream from the impact location. Multiple methods were explored to determine the most accurate simulated barrier force for comparison to results from the full-scale crash test, including: (1) 50-msec average, CFC60 filtered, local lateral and longitudinal accelerations extracted at the vehicle model's c.g. coupled with the calculated Euler yaw angle multiplied by vehicle mass; (2) 50-msec average, CFC60 filtered, global lateral accelerations extracted at the vehicle model's c.g. multiplied by the vehicle mass; (3) contact forces between the vehicle and the barrier components with a CFC 60 filter applied; and (4) contact forces between the vehicle and the barrier components with a CFC 60 filter and a 50-msec moving average applied. The local x- and y-accelerations extracted at the vehicle model c.g., coupled with yaw and multiplied by the vehicle mass, was the same procedure that was utilized to calculate the lateral barrier force in the actual full-scale crash tests into the RESTORE barrier. The global y-accelerations multiplied by the vehicle mass produced the best estimate/prediction for peak lateral barrier force, as compared to test no. SFH-2, which was within 3.9 percent for the Yaris model and 13.1 percent for the Neon model. The global y-acceleration multiplied by the vehicle mass was selected for calculating lateral barrier forces with the small car vehicle.

The small car in test no. SFH-2 had impacted the first two posts downstream from the impact location. The Yaris model impacted the first two posts downstream from the impact location, whereas the Neon model did not impact any posts. The roll and yaw angles were similar for both simulations and the full-scale crash test. The Neon model's simulated pitch angle of -2.6 degrees was within 2 degrees of the maximum pitch angle observed in test no. SFH-2. However, the Yaris model's simulated pitch angle was over

15 degrees and still increasing at the end of the simulation, which was unrepresentative of the pitch angle observed in the full-scale crash test. Based on the comparison between the simulations and the full-scale crash test, the Dodge Neon model more closely resembled the actual roll, pitch, and yaw behaviors, as well as the ORA and OIV values. The Toyota Yaris more closely predicted the vehicle snag on the posts, system deflections, and lateral barrier forces.

In Chapter 5, MASH test designation no. 4-11 simulated the Chevrolet Silverado vehicle model impacting the RESTORE barrier model, with results compared to full-scale crash test no. SFH-1. Each vehicle was targeted to impact 4 ft – 3 in. (1.3 m) upstream from the ACJ between two adjacent barriers. Based on the comparison between the simulation and the full-scale crash test results, the Chevrolet Silverado had simulated roll and pitch angles that compared well with the full-scale crash test results. The simulated Silverado yaw angles compared well through 200 msec, which was shortly after the vehicle became parallel to the barrier system. The lateral and longitudinal occupant impact velocities were within 13 percent of each other in the simulation and full-scale crash test. However, the longitudinal ORA was 57 percent greater and lateral ORA was 33 percent greater in the simulation than observed in the full-scale crash test. However, the Silverado model's rear axle is likely stronger than observed for the full-scale vehicle, which usually overestimates the secondary impact forces and vehicle accelerations. Multiple methods were explored to determine the most accurate simulated barrier force, which were explained previously. The global y-accelerations multiplied by the vehicle mass provided the best estimate/prediction for peak lateral barrier force, which was within 3.3 percent for the Silverado model when compared to test no. SFH-1.

The global y-acceleration multiplied by the vehicle mass was selected for calculating lateral barrier forces with the pickup truck vehicle. The left-front tire in test no. SFH-1 impacted the first two posts downstream from the impact location. However, the Silverado model in the simulation only impacted the second post downstream from the impact location.

In Chapter 6, MASH test designation no. 4-12 simulated the Ford F800 vehicle model impacting the RESTORE barrier model, with results compared to full-scale crash test no. SFH-3. The simulation vehicle model and the full-scale crash test vehicle had notable differences. The connection of the box to the frame in the F800 simulation model did not include any shear plates and used ½-in. (13-mm) diameter U-bolts as opposed to the ⅜-in. (10-mm) thick shear plates and the ⅝-in. (16-mm) diameter U-bolts, used in test no. SFH-3. The suspension for the F800 vehicle model did not have failure enabled, which did not allow the front axle to disengage as it did in test no. SFH-3. Each vehicle was targeted to impact 4 ft – 11 in. (1.5 m) upstream from the ACJ between two adjacent barriers. Based on the comparison between the simulation and the full-scale crash test, the simulated impact with the F800 model had relatively similar roll, pitch, and yaw angles, as compared to the full-scale crash test. However, the roll angles found in simulation started to deviate from those observed in the full-scale crash test after 700 msec. The dynamic barrier deflections between the simulation and the full-scale crash test were within 10 percent, and the working width was within 14 percent of one another. Multiple methods were explored to determine the best estimate/prediction for simulated barrier force, as described earlier. During test no. SFH-3, a peak lateral barrier force of 105.0 kips (467 kN) occurred during the initial impact. However, all of the simulated

maximum barrier forces resulted from a tail slap event. When comparing forces at the tail slap event, the global y-acceleration extracted from the vehicle model's c.g., multiplied by the vehicle mass, resulted in a maximum lateral force approximately 8 percent less than observed in test no. SFH-3. Thus, the global y-acceleration multiplied by the vehicle mass was selected for calculating lateral barrier forces due to the similarity between simulated and measured tail slap forces. During test no. SFH-3, the vehicle's left-front tire contacted the first post downstream from impact. In the simulation with the F800 model, the left-front tire did not contact any of the posts.

In Chapter 7, different transition design considerations were discussed in regards to design impact force, degrees of freedom, tolerances, geometry (height, width, and shape), stiffness, and roadway geometry. The initial transition design was configured to mitigate vehicle snag, reduce the risk for rollover, have limited maintenance for passenger car vehicles, and provide structural continuity. The desired transition concept would maintain the current 20-ft (6.1-m) long RESTORE barrier segments. Further, the transition was to be designed for use in a median application, where traffic could travel in either direction and on either side at some point. Based on the literature review and the results from test no. SFH-3, a lateral design impact load of 100 kips (445 kN) was selected for configuring and designing the transition joint hardware. A coefficient of friction of 0.45 was calculated for vehicle-to-barrier contact during the full-scale crash test with the SUT vehicle (test no. SFH-3), which was also used to determine a longitudinal design load of 45 kips (200 kN) for use within the transition region.

The RESTORE barrier displaced in the y-direction and rotated about the z-axis. Displacements in the x- and z-directions and rotations about the x- and y-axes were

minimal. Since the concrete buttress was configured to be rigid, the transition system and joint hardware was designed to have minimal displacements and rotations. The interior joint hardware, denoted as the ACJ, could accommodate $\pm 1/4$ in (6 mm) of construction tolerances. Since the barrier system could have extended installation lengths, an increased construction tolerance of $\pm 1/2$ in. (38 mm) was desired for the transition system. The concrete buttress was desired to have a nearly identical geometry to the $30\frac{1}{8}$ -in. (765-mm) tall RESTORE barrier segment and transition to a 36-in. (914-mm) tall vertical concrete barrier. The stiffness and capacity of the RESTORE barrier near the transition joint was to be evaluated through simulation. Analytical calculations would be used to suggest changes in the number and/or size of the elastomer posts or metal skids, if needed.

Through static testing, an 8 percent superelevation was considered acceptable for the current RESTORE barrier configuration, which would be further explored after the barrier design was finalized. The available tolerances in the RESTORE barrier allowed it to be installed on the minimal horizontal curve radius of 1,300 ft (396.2 m) and vertical grade of up to 9 percent. Lastly, slight modifications to the RESTORE barrier were desired, which included moving the splice of the top tube assembly to a location above the ACJ for ease of construction.

The design considerations were considered during a concept development and design effort provided in Chapter 8. Through three phases of concept development, three general groups were created, including: a drop-down RESTORE barrier or bollard concept; a pin and loop or female-female concept; or an adjustable-length end fitting. However, the adjustable-length concept was not pursued due to the desire to maintain the

current 20-ft (6.1-m) long RESTORE barrier segments. The drop-down RESTORE barrier or bollard concept included a bollard that was embedded into the ground and extended upward through the pentagon hole in the RESTORE barrier to act as a pivot for the downstream end. The bollard was assumed to act as a cantilever beam, and a section with the required structural capacity would not fit into the existing openings of the RESTORE barrier. Thus, this concept was not pursued, as the RESTORE barrier segments would need to be modified.

A pin and loop concept with eight loops was already incorporated within the RESTORE barrier model, as created by Schmidt [19] and shown in Chapter 9. Five loops were removed to only incorporate three loops, similar to the desired connection. The pin in the model had a 1 $\frac{3}{4}$ -in. (44-mm) diameter section, and it was modeled as rigid and constrained in all directions to simulate a rigid barrier connection. The initial simulations had failure enabled in the $\frac{3}{4}$ -in. (19-mm) diameter rebar loops, and the loops fractured. Failure was removed within the loops and excessive deformations occurred, which did not resemble the rigid connection that was desired. After increasing the diameter of the loops to 1 $\frac{1}{4}$ in. (32 mm) and re-enabling failure, the loops did not fracture nor deform. A force investigation with the Dodge Neon, Toyota Yaris, and Chevrolet Silverado vehicle model impacts determined that the largest peak lateral force occurred at locations closer to the vertical pin. Simulations with impacts at 5 ft (3.0 m) upstream from the pin had peak forces up to 8, 10, and 13 percent greater than simulations with impacts at 20 and 40 ft (6.1 and 12.2 m) upstream from the pin with the Dodge Neon, Toyota Yaris, and Chevrolet Silverado vehicle models, respectively. The simulations showed small roll, pitch, and yaw angles. Thus, vehicle stability was not a concern, and the pin and loop

concept was feasible for the transition system. However, rebar loops were not desired for the female-female connection due to the need to embed the loops into the RESTORE barrier, which would modify the barrier segment and require a special concrete beam. Thus, horizontal gusset plates were desired for attachment to the end of the RESTORE concrete beams.

The pin and loop concept utilized horizontal gusset plates for the female-female connection, as shown in Chapter 8. Throughout the design process, multiple analysis techniques were used to determine the analytical representation of the distributed forces on each part within the transition configuration. Two cases were used to distribute the 100-kip (445-kN) lateral impact point load, located $30\frac{1}{8}$ in. (765 mm) above ground and at the top of the RESTORE concrete beam, to the RESTORE gusset plates. The RESTORE gusset plates transfer the impact force to the buttress gusset plates through shear and bending on the vertical drop-down pin.

The maximum resultant shear force on the pin was 98.8 kips (439 kN), which required the drop-down pin diameter of 2 in. (51 mm) using ASTM A572 Grade 50 steel. The diameter of the pin to resist bending was calculated to be approximately $2\frac{1}{4}$ in. (57 mm) for ASTM A572 Grade 50 steel. However, the 2-in. (51-mm) pin diameter was selected for initial evaluation through computer simulation and stress analysis. The maximum lateral and longitudinal shear forces of 97.7 and 15 kips (435 and 67 kN), respectively, were used to configure the gusset plates to be 8 in. (203 mm) wide and $\frac{1}{2}$ in. (13 mm) thick using ASTM A572 Grade 50 steel. A 3-dimensional vector analysis with the 100-kip (445-kN) lateral load and the 45-kip (200-kN) longitudinal load was used to determine the required capacity for the back plate, gusset to back plate welds, and size of

connection bolts. All of the horizontal gusset plates and black plate were ½-in. (13-mm) thick, ASTM A572 Grade 50 steel. The RESTORE barrier gusset plates utilized a standard hole for the drop-down pin, whereas the buttress gusset plates utilized a slot to accommodate the +/- 1½ in. (38 mm) construction tolerances. The nominal vertical gap between horizontal gusset plates was 5 ¹¹/₁₆ in. (144 mm). The bolts that connected the back plate to the barriers were calculated to be 1¼ in. (32 mm) diameter, ASTM A325 steel. However, a 1-in. (25-mm) diameter bolt would be evaluated through simulation, which is the current bolt specification in the RESTORE barrier and ACJ connection. Lastly, a top tube splice with dimensions of 7¼ in. x 3¼ in. x ½ in. (184 mm x 83 mm x 13 mm) was required to provide an elastic moment capacity greater than provided for the outer tube. However, a top tube splice with dimensions of 7¼ in. x 3¼ in. x ⁵/₁₆ in. (184 mm x 83 mm x 8 mm) was required to provide a plastic moment capacity greater than provided for the outer tube. The inner tube splice would need to be 29 in. (737 mm) long with two ½-in. (13-mm) diameter connection bolts to secure it within the outer tube. However, a more aggressive approach was considered, and ¼-in. (6-mm) thick steel splice rail was simulated.

In Chapter 10, a model of the preferred transition concept was configured with the pin and gusset plate assemblies, rigid concrete buttress, and ten RESTORE barrier segments. One end of the RESTORE barrier was connected to the rigid concrete buttress with the pin and gusset plate assembly, and the other end of the system was not constrained. To simulate the extents of the +/- 1½-in. (38-mm) construction tolerances within the joint, simulations were run with either the joint fully extended or fully compressed, where the pin would be in contact with each side of the slots based on the

configuration being simulated. The initial simulations looked at the gusset plate configuration with wide gusset plates so that they were nearly flush with the front faces of the RESTORE barrier and buttress. The Yaris model penetrated the vertical gaps between the horizontal gusset plates and snagged on the upstream buttress face, and negative volumes occurred within the Silverado model's engine compartment due to contact with the upstream buttress face. Thus, a cover plate was desired to mitigate concerns for vehicle snag within the joint. A trial cover plate was added that incorporated a rigid plate with nodes merged to the edges of the horizontal gusset plates. The cover plate reduced vehicle snag in the initial simulations.

A straight cover plate was designed to shield the vertical spaces between the horizontal gusset plates. The cover plate accommodated the +/- 1½-in. (38-mm) construction tolerances and incorporated three ½-in. (13-mm) thick gusset plates that were placed within the horizontal gusset plates. The cover plate gussets were secured with two ⅝-in. (16-mm) diameter bolts that extended vertically through all of the plates. The cover plate was designed to be 20 in. x 18½ in. x ⅝ in. (508 mm x 470 mm x 16 mm). However, a more aggressive thickness of ½ in. (13 mm) was considered for evaluation through simulation. The Yaris and Silverado vehicle models extended behind and snagged on the upstream edge of the straight cover plate when the joint was fully extended, which caused vehicle instability. Therefore, a modified cover plate design was considered that used rounded edges on the upstream and downstream sides. The initial intention for the cover plate bolts was to secure the cover plate but transfer minimal load through them. Thus, three 17-in. x 1½-in. x ⅝₁₆-in. (432-mm x 38-mm x 8-mm) steel strips were attached to the back side of the cover plate, so that the metal strips started to

bear on the horizontal gusset plates before the bolts were loaded simulated impact events. Therefore, the cover plate with the rounded edges was recommended for further evaluation using computer simulation.

Through a more intensive simulation effort, as noted in Chapters 11 through 13, several different impact points were evaluated to investigate and evaluate vehicle and barrier performance. MASH states that computer simulation with LS-DYNA should be performed to investigate CIPs when practical and accessible. If the computer simulation is unavailable, the CIP for a longitudinal stiffness transition could be selected based on the suggested CIP distances noted in MASH for impacts upstream from: (1) the location with the greatest potential for wheel snag (i.e., upstream end of buttress) or (2) the location with the potential for the largest load (i.e., drop-down pin or joint) or deflection (i.e., upstream locations). The suggested CIP distances in MASH for each vehicle were simulated upstream from both the pin and the buttress face in extended and compressed joint configurations. These locations were used to determine the maximum lateral loading imparted to the pin and gusset plate hardware as well as the propensity for vehicle snag and instability. Impact locations farther upstream were also simulated at intervals of 10 ft (3.0 m), up to 40 ft (12.2 m) upstream, from the drop-down pin to determine the maximum barrier deflection as well as potential for vehicle instability. Each impact location was simulated at the CIP distance upstream from the 10 ft (3.0 m) interval. Lastly, impact locations in the reverse direction were simulated at the slope-break point of the horizontal flare and the CIP distance upstream of the edge from the cover plate with the joint fully extended.

The maximum Tresca and von Mises stresses were determined in the pin and gusset hardware and the original ACJ hardware for each simulation. Material failure was not enabled throughout the barrier model. Thus, the maximum stresses were then compared to the Tresca and von Mises yield conditions.

In Chapter 11, different impact locations were simulated with the Dodge Neon and Toyota Yaris vehicle models at the suggested CIP location in MASH of 3 ft – 7 in. (1.1 m). Each simulation had an impact velocity of 62.1 mph (100 km/h) and an angle of 25 degrees. For simulations at the suggested CIP locations in MASH into the transition hardware, the vehicle was contained and redirected, and occupant risk values did not cause major concerns. However, many stresses within the parts located in the pin and gusset plate assemblies exceeded the Tresca and von Mises yield conditions. The cover plate bolts were intended to maintain the cover plate in the joint and not transfer the impact load to the horizontal gusset plates. However, the cover plate bolt stresses exceeded the yield conditions and permanently deformed. The horizontal gussets and the cover plate gussets also exceeded the yield conditions. The maximum stresses on the gussets were localized, and the parts would likely maintain their structural capacity during repeated impacts. Stresses in the cover plate exceeded the yield conditions and permanently deformed. The maximum stresses of the cover plate were located on the rounded edges due to contact with the horizontal gusset plates, but they would maintain adequate structural capacity for preventing vehicle penetration between the horizontal gusset plates. The ACJ bolts had maximum stresses that exceeded the yield conditions in all of the upstream impact location simulations. Since the RESTORE barrier segments were modeled with a rigid material, the concrete segments could not have stress and did

not fracture or spall as observed in the full-scale crash testing program. Thus, the ACJ bolts experienced higher loads which resulted in higher stresses than what was expected. The stresses in the bolts were 26 larger than those observed in the interior location simulation and would like need to be redesigned with a larger diameter to lower the stresses. The maximum shear stress in the top tube and inner tube splice exceeded the Tresca yield conditions in all of the upstream and suggested MASH CIP impact location simulations. However, the maximum von Mises stresses did not exceed the yield condition in the simulations at the buttress at 10 and 40 ft (3.0 and 12.2 m) upstream from the drop-down pin.

The simulated roll and yaw angles for the small car models were within the suggested limits noted in MASH and did not cause concern. The simulated pitch angles for the Neon model were minimal. However, the simulated pitch angles for the Yaris model were similar to the simulation at the interior location with angles over 15 degrees and still increasing. The Neon vehicle model simulation had model instabilities when the left-front tire impacted an elastomer post downstream from impact during the simulation at 20 ft (6.1 m) upstream from the pin with the compressed joint. The Neon model did not impact any posts during the interior location simulation, which may be an indication that post snag is more evident at that impact location. The Yaris model impacted two posts during the impacts at 20 and 40 ft (6.1 and 12.2 m) upstream from the drop-down pin, similar to that observed in the simulation at the interior location. Extensive vehicle damage was found in the Neon model during the simulation at the slope-break point in the reverse direction. Occupant compartment deformations in the left-front toe pan exceeded 11 in. (279 mm), which is over the MASH limit of 9 in. (229 mm). All of the

OIV and ORA values through the simulations in the transition region were within the MASH limits.

In Chapter 12, different impact locations were simulated with the Chevrolet Silverado vehicle model at the suggested CIP location in MASH of 4 ft – 3 in. (1.3 m). Each simulation had an impact velocity of 62.1 mph (100 km/h) and an angle of 25 degrees. In the simulations at the suggested CIP locations in MASH into the transition hardware, the vehicle was contained and redirected, and occupant risk values did not cause major concerns. A stress analysis was completed on each of the parts within the pin and gusset plate assemblies similar to that performed in Chapter 11. The vertical drop-down pin had stresses that exceeded the Tresca yield condition but did not exceed the von Mises yield condition. The cover plate bolts and horizontal gusset plates had stresses that exceeded both yield conditions. The cover plate bolts also had excessive permanent deformations. The horizontal gusset plate stresses were localized at the edges of the pin holes and slots, which may have caused the holes to ovalize, but not for the plates to rupture. The cover plate stresses exceeded the yield conditions with concentrated maximum stresses on the curved edges. The cover plate should maintain its structural capacity and could be impacted again if the permanent deformations do not create a snag point by protruding past the face of the RESTORE barrier or buttress. The top tube and inner tube splice experienced maximum shear stresses that exceeded the Tresca yield condition at each impact location, whereas none of the simulations at the suggested CIP locations in MASH experienced von Mises stresses in the top tube that exceeded the yield condition. Similarly, all of the upstream impact location simulations, except at 20 ft (6.1 m), had stresses in the top tube and inner tube splices that did not exceed the von Mises

yield condition. During the simulation at 20 ft (6.1 m) upstream from the pin with the compressed joint, negative volumes occurred in the ACJ bolts shortly after the vehicle model became parallel to the barrier. The damage to the Silverado vehicle model was greatest at the slope-break impact location. The top of the left-front and left-rear doors separated away from the vehicle farther than what was seen in the interior location simulation. The simulated roll angles for impacts upstream from the pin with extended joint, 20 ft (6.1 m) upstream of the pin with extended joint, and both reverse-direction locations were still increasing when the simulations ended. Similarly, the simulated pitch angles were still increasing when the simulations ended for all upstream impact locations and reverse-direction locations. The ORA and OIV values were within the limits of MASH and were not a concern.

In Chapter 13, different impact locations were simulated with the Ford F800 vehicle model at the suggested CIP location in MASH of 4 ft – 11 in. (1.5 m). Each simulation had an impact velocity of 56.0 mph (90.1 km/h) and an angle of 15 degrees. Large stresses occurred in the cover plate bolts and cover plate gussets in the simulation at the suggested CIP location in MASH upstream from the buttress with the compressed joint. The cover plate bolts had stresses 24 percent larger than the yield strength with large deformations in the longitudinal direction, which occurred as the cover plate translated downstream. As a result of the longitudinal translation of the cover plate, the cover plate gussets had maximum stresses 24 percent larger than the material yield strength. The vertical drop-down pin did not exceed the von Mises yield conditions during any simulated impact event. The horizontal gusset plates had maximum stresses localized around the cover plate bolts that exceeded the yield conditions and would

ovalize, thus potentially causing material rupture. The top tube and inner tube splice experienced maximum shear and von Mises stresses that exceeded the yield conditions and were large enough to potentially fail. A maximum lateral barrier force of 98.7 kips (439 kN) occurred in the simulations at the suggested CIP location in MASH, thus correlating with the selected design load of 100 kips (445 kN). However, the peak lateral load was not imparted to the joint hardware, because the vehicle had already traveled downstream while in contact with the concrete buttress. For simulations at impact locations upstream from the pin, the 10- and 20-ft (3.0- and 6.1-m) locations with the extended joint had contact issues between the large mesh size of the left-front bumper and the small mesh size of the top tube rail, which caused the simulations to become unstable and terminate shortly after vehicle impact. Thus, the maximum load imparted to the pin and gusset plate assemblies was not likely observed and further simulations may be necessary to investigate the maximum loading on the pin and gusset plate assembly. Neither of the simulations in the reverse direction completed as they both terminated due to negative volumes within the F800 vehicle model shortly after impact. Further evaluation is recommended in the reverse direction.

14.2 Recommendations

Further simulation is recommended with the splice tube thickness of $\frac{1}{2}$ in. (13 mm) as opposed to the $\frac{1}{4}$ in. (6 mm) used throughout this research effort. The $\frac{1}{2}$ -in. (13-mm) thickness was the required thickness that was necessary to provide greater or equivalent elastic moment capacity to that provided by the outer tube. Further, the increased thickness would minimize splice tube stresses that had exceeded the yield conditions for simulations with all vehicle models. Excessive cover plate bolt

deformations and stresses above yield had occurred. Multiple options could be implemented. A redesign of the configuration could be performed to increase the number of horizontal gusset plates within the assembly. However, any redesigned transition hardware would require an evaluation with all of the upstream impact location simulations. Thus, this solution was not desired. A second option could be to redesign the cover plate assembly to restrict the longitudinal plate movement and loading, which caused the excessive deformations. However, a logical method to accommodate this modification was unavailable. Lastly, the diameter of the vertical cover plate bolts could be increased to withstand additional longitudinal loading and reduce the plastic deformations. By increasing the diameter of the bolts, higher stresses may occur in other parts. However, it is believed to be the most logical option to reduce the potential for failure and yield within the vertical bolts.

High stresses above the yield conditions within the ACJ bolts should potentially be mitigated. First, the RESTORE barrier concrete beams could be modeled with a material formulation that allows for fracture, thus providing a more accurate representation of the stresses in the bolts. Unfortunately, a reliable concrete material model with fracture may not exist and/or is not well known. Thus, evaluation was unable to determine if the RESTORE barrier concrete beams were needed to be redesigned. Due to the increased forces, and the constraint in the y-direction, it is recommended that the RESTORE barrier should be evaluated further to determine if the concrete beams need to be redesigned within the transition region. Second, the bolt diameter could be increased from 1 in. (25 mm) to 1¼ in. (32 mm), which was the diameter identified in the 3-dimensional analysis noted in Chapter 8. The ACJ bolt diameter increase is

recommended to be changed at least through 40 ft (12.2 m) upstream of the pin and gusset plate assemblies. The stresses within the ACJ bolts at 40 ft (12.2 m) did not appear to cause failure within the bolts, as compared to the stresses in the ACJ bolts after the interior simulation.

A gradual stiffness transition is recommended in order to decrease the lateral barrier deflections found at the 20- and 40-ft (6.1- and 12.2-m) impact locations upstream from the pin and gusset plate assembly. Several methods may be used to increase the transition stiffness near the pin, including: adding elastomer posts; using a stiffer joint between barriers; and incorporating larger ACJ bolts.

The buttress horizontal flare rate of 6:1 caused concern for reverse-direction impacts at the slope-break point, especially with the excessive occupant compartment deformation that occurred to the Dodge Neon. It is recommended that a flatter flare rate of 10:1 or flatter may be implemented to reduce safety concerns. However, further design variations should be evaluated through simulation or full-scale vehicle crash testing.

It is recommended that the single-unit truck model be modified in order to evaluate the RESTORE barrier transition model over a longer duration. A refined fender mesh size or an improved contact definition may mitigate model instability between the fender and upper tube rail. Further simulations should then be conducted at impact locations between the suggested CIP locations in MASH from the pin to 20 ft (6.1 m) upstream from the pin to investigate the maximum load imparted to the pin and gusset plate assemblies. Further, simulation models and definitions should be improved for used in reverse-direction impacts.

Further calculations are warranted to finalize the internal steel reinforcement for the preferred concrete buttress as only a preliminary design was completed, and a flatter flare rate has been recommended. Further, the bolt and epoxy anchorage system for the tube termination and back plate were not designed. Therefore, these anchor systems must be designed.

In general, full-scale vehicle crash testing is recommended for evaluating the safety performance of the prototype pin and gusset plate transition system according to the AASHTO MASH TL-4 impact safety standards. Unfortunately the SUT simulations did not run completely or revealed excessive permanent deformations and high stresses for many impact locations. Thus, full-scale vehicle crash testing is not recommended without further redesign, modification and/or simulation. However, if full-scale crash testing was desired, the recommendations to change the transition parts would need to be completed prior to testing. Thus, the smallest testing program would be as follows:

- 3 ft – 7 in. (1.1 m) upstream from buttress face with extended joint and 1100C vehicle;
- 4 ft – 3 in. (1.3 m) upstream from pin with extended joint and 2270P vehicle;
and
- 4 ft – 11 in. (1.5 m) upstream from pin with extended joint and 10000S vehicle.

The CIP location for the small car is 3 ft – 7 in. (1.1 m) upstream from the buttress face with extended joint. This impact location was selected due to the higher potential for vehicle snag behind the cover plate and snag on the upstream buttress face. The CIP location for the pickup truck is 4 ft – 3 in. (1.3 m) upstream from the pin with

extended joint. This simulation showed the largest dynamic barrier deflection, as well as largest roll, pitch, and yaw angles, as compared to other impact locations at the suggested CIP locations in MASH. The CIP location for the single-unit truck is 4 ft – 11 in. (1.5 m) upstream from the pin with the extended joint. This location was selected due to the highest lateral load applied to the transition system hardware. Note that the simulation did not have a long run time, so there remains a potential for greater roll angles and further instabilities.

Further full-scale crash testing that could be done would include a second CIP location for the small car at 3 ft – 7 in. (1.1 m) upstream from the 20-ft (6.1-m) impact location with the extended joint. The extended joint provided the largest lateral barrier force, greater lateral barrier deflections, and post contact with both vehicle models, as compared to the other upstream impact location simulations. A second CIP location for the pickup truck at 4 ft – 3 in. (1.3 m) upstream of the 20-ft (6.1-m) impact location with extended joint could also be full-scale crash tested. This impact location had the greatest dynamic barrier deflection, and largest roll, pitch, and yaw angles, as compared to other upstream impact location simulations. Lastly, a second impact location at 4 ft – 11 in. (1.5 m) upstream from the 20-ft (6.1-m) location with compressed joint would be recommended for the single-unit truck. This location was selected due to the larger vehicle roll angles while still increasing at the end of the simulation and lateral barrier deflections similar to the interior location simulation, which causes a greater concern for snag at the ACJ just downstream from impact. However, with the increased ACJ bolt diameter, the large deflections would likely be reduced, which would mitigate the potential for post contact and the need for these full-scale crash tests.

15 REFERENCES

1. Infrastructure Quarterly, Volume 3, Issue 1, Garver, 2011.
2. Lundstrom, L.C., Skeels, P.C., Englund, B.R., and Rogers, R.A., *A Bridge Pararpet Designed For Safety*, General Motors Proving Ground, presented at 44th Annual Highway Research Board Meeting, January 1965.
3. Hellriegel, E.J., *Development of the Narrow Median Concrete Barrier in New Jersey*, Presented at the 38th Annual Meeting of Institute of Traffic Engineers, August, 1968.
4. Nordlin, E.F., Field, R.N., Stoker, J.R., Pelkey, R.A., and Halterman, J.A., *Dynamic Tests of Concrete Median Barrier Series XVI*, State of California Transportation Agency, Division of Highways, August 1967.
5. Bronstad, M.E., Calcote L.R., and Kimbar, Jr, C.E., *Concrete Median Barrier Research*, Final Report to Federal Highway Administration, Southwest Research Institute, June 1976.
6. McDevitt, C.F. "Basics of Concrete Barriers", *Public Roads*, Federal Highway Administration, Washington D.C, March 2000.
7. Albuquerque, F.D.B., Evaluation of the In-Service Safety Performance of Safety-Shape and Vertical Concrete Barriers, Dissertation, University of Nebraska – Lincoln, July, 2011.
8. Albuquerque, F.D.B. and Sicking, D.L., *Evaluation of the In-Service Safety Performance of Safety-Shape and Vertical Concrete Barriers*, Final Report to the Midwest States Pooled Fund Program, Research Report No. TRP-03-259-11, Midwest Roadside Safety Facility, University of Nebraska-Lincoln, December 16, 2011.
9. Rosenbaugh, S.K., Development of a TL-5 Vertical Faced Concrete Median Barrier Incorporating Head Ejection Criteria, Thesis, University of Nebraska - Lincoln, September 2007.
10. Rosenbaugh, S.K. Sicking, D.L., and Faller, R.K., *Development of a TL-5 Vertical Faced Concrete Median Barrier Incorporating Head Ejection Criteria*, Final Report to the Midwest States Pooled Fund Program, Research Report No. TRP-03-194-07, Midwest Roadside Safety Facility, University of Nebraska-Lincoln, December 10, 2007.
11. Rosenbaugh, S.K., Faller, R.K., and Sicking, D.L., *Head Ejection During Barrier Impacts*, Journal of Transportation Engineering, American Society of Civil Engineers (ASCE), Vol. 138, Number 1, January 2012, pages 1-11.
12. Jewell, J.R., Rowhani, P., Stoughton, R., and Crozier, W., *Vehicular Crash Tests of a Slip-Formed, Single Slope, Concrete Median Barrier*, Final Report to the California

Dept. of Transportation, CALTRANS, Division of New Technology, Materials and Research, December 1997.

13. Beason, W.L., Ross, H.E., Perera, H.S., and Marek, M., *Single-Slope Concrete Median Barrier*, Transportation Research Record No. 1302, Transportation Research Board, National Research Council, Washington, D.C., 1991.
14. Beason, W.L., Ross, H.E., Perera, H.S., Campise, W.L., and Bullard, D.L., *Development of a Single-Slope Concrete Median Barrier*, Final Report to the Texas State Department of Highways and Public Transportation, Research Report No. 9429CDK-1, Texas Transportation Institute, Texas A&M University, June 1989.
15. *Manual for Assessing Safety Hardware (MASH)*, American Association of State Highway and Transportation Officials (AASHTO), Washington, D.C., 2009.
16. Schmidt, J.D., Development of a New Energy-Absorbing Roadside/Median Barrier System with Restorable Elastomer Cartridges, Dissertation, University of Nebraska – Lincoln, November 2012.
17. Schmidt, J.D., Faller, R.K., Sicking, D.L., Reid, J.D., Lechtenberg, K.A., Bielenberg, R.W., Rosenbaugh, S.K., and Holloway, J.C., *Development of a New Energy-Absorbing Roadside/Median Barrier System with Restorable Elastomer Cartridges*, Final Report to the Federal Highway Administration and Nebraska Department of Roads, Research Report No. TRP-03-281-13, Midwest Roadside Safety Facility, University of Nebraska-Lincoln, July 16, 2013.
18. Schmidt, J.D., Schmidt, T.L., Faller, R.K., Sicking, D.L., Reid, J.D., Lechtenberg, K.A., Bielenberg, R.W., Rosenbaugh, S.K., and Holloway, J.C., *Evaluation of Energy Absorbers for use in a Roadside/Median Barrier*, Final Report to the Federal Highway Administration and Nebraska Department of Roads, Research Report No. TRP-03-280-14, Midwest Roadside Safety Facility, University of Nebraska-Lincoln, February 6, 2014.
19. Schmidt, J.D., Rosenbaugh, S.K., Faller, R.K., Bielenberg, R.W., Reid, J.D., Holloway, J.C., Lechtenberg, K.A., and Kohtz, J.E., *Design and Evaluation of an Energy Absorbing, Reusable Roadside/Median Barrier, Phase 3*, Final Report to the Federal Highway Administration and Nebraska Department of Roads, Research Report No. TRP-03-317-15, Midwest Roadside Safety Facility, University of Nebraska-Lincoln, July 29, 2015.
20. Schmidt, J.D., Schmidt, T.L., Rosenbaugh, S.K., Faller, R.K., Bielenberg, R.W., Reid, J.D., Holloway, J.C., and Lechtenberg, K.A., *MASH TL-4 Crash Testing, Evaluation of the RESTORE Barrier*, Final Report to the Federal Highway Administration and Nebraska Department of Roads, Research Report No. TRP-03-318-15, Midwest Roadside Safety Facility, University of Nebraska-Lincoln, November 3, 2015.

21. Schmidt, J.D., Rosenbaugh, S.K., Bielenberg, R.W., Faller, R.K., Reid, J.D., and Schmidt, T.L., *MASH TL-4 Design and Evaluation of a Restorable, Energy-Absorbing Concrete Barrier*, Paper No. 16-0650, Accepted for Presentation and Publication, Journal of the Transportation Research Board, Transportation Research Record No. 2588, Transportation Research Board, Washington D.C., Submitted March 9, 2016.
22. Sheikh, N.M., Bligh, R.P., and Menges, W.L., *Determination of Minimum Height and Lateral Design Load for MASH TL-4 Bridge Rails*, Final report to the Texas Department of Transportation, Research Report no. 9-1002-5, Texas Transportation Institute, Texas A&M University, December, 2011.
23. Sheikh, N.M., Bligh, R.P., and Holt, J.M., Minimum Rail Height and Design Impact Load for Longitudinal Barriers That Meet Test Level 4 of Manual for Assessing Safety Hardware, Transportation Research Record No. 2309, Transportation Research Board, Washington, D.C., July 2012.
24. Hallquist, J.O. *LS-DYNA Keyword User's Manual*. Livermore, CA: Livermore Software Technology Corporation, May 26, 2014, Revision 5471.
25. Polivka, K.A., Eller, C.M., Faller, R.K., Sicking, D.S., Rohde, J.R., Reid, J.D., Bielenberg, B.W., Allison, E.M., *Development of the Midwest Guardrail System (MGS) W-Beam to Thrie Beam Transition Element*, Final Report to the Midwest States Regional Pooled Fund Program, Transportation Research Report No. TRP-03-167-07, Project No. SPR-3(017)-Year 16, Midwest Roadside Safety Facility, University of Nebraska-Lincoln, Lincoln, NE, November 26, 2007.
26. Rosenbaugh, S.K., Lechtenberg, K.A., Faller, R.K., Sicking, D.L., Bielenberg, R.W., and Reid, J.D., *Development of the MGS Approach Guardrail Transition Using Standardized Steel Posts*, Final Report to the Midwest States' Regional Pooled Fund Program, Research Report No. TRP-03-210-10, Midwest Roadside Safety Facility, University of Nebraska-Lincoln, December 21, 2010.
27. Ross, H.E., Sicking, D.L., Zimmer, R.A., and Michie, J.D., *Recommended Procedures for the Safety Performance Evaluation of Highway Features*, National Cooperative Highway Research Program (NCHRP) Report 350, Transportation Research Board, Washington, D.C., 1993.
28. Graham, J.L., Loumiet, J.R., and Migletz, J., *Portable Concrete Barrier Connectors*, Final Report to the Federal Highway Administration, Research Report No. FHWA-TS-88-006, Graham – Migletz Enterprises, Inc., November 1987.
29. Federal Highway Administration, *Portable Concrete Barrier Connection Systems*, U.S. Department of Transportation, Washington, D.C., November 1985.
30. Ivey, D.L., Walker, K.C., Ross, Jr., H.E., Beason, W.L., and Koppa, R.J., *Barriers in Construction Zones Volume 3: Appendices B, C, D, and E*, Final Report to the Federal

- Highway Administration, Research Report No. RF3825, Texas Transportation Institute, Texas A&M University, April 1985.
31. Rosenbaugh, S.K., Bielenberg, R.W., Faller, R.K., Reid, J.D., Rohde, J.R., Sicking, D.L., Lechtenberg, K.A., and Holloway, J.C., *Termination and Anchorage of Temporary Concrete Barriers*, Final Report to the Midwest States' Regional Pooled Fund Program, Research Report No. TRP-03-209-09, Midwest Roadside Safety Facility, University of Nebraska-Lincoln, October 29, 2009.
 32. Bielenberg, R.W., Rosenbaugh, S.K., Faller, R.K., Reid, J.D., and Lechtenberg, K.A., *Transition of Temporary Concrete Barrier*, Journal of Transportation Safety & Security, Taylor & Francis, Volume 4, Number 2, Available online November 16, 2011, May 2012, pages 137-159.
 33. Bligh, R.P., and Menges, W.L., *Median Barrier Gate*, Technical Memorandum, Task Report No. 0-5210-9, Texas Transportation Institute, June 15, 2010.
 34. Bligh, R.P., Arrington, D.R., Sheikh, N.M., Silvestri, C., and Menges, W.L., *Development of a MASH TL-3 Median Barrier Gate*, Final Report to the Texas Department of Transportation, Research Report No. FHWA/TX-11/9-1002-2, Texas Transportation Institute, Texas A&M University, June 2011.
 35. Bligh, R.P., Arrington, D.R., Sheikh, N.M., Meza, R., and Silvestri, C., *Low-Cost Median Barrier Gate*, Transportation Research Record No. 2309, Transportation Research Board, Washington, D.C., July 2012.
 36. Gutierrez, D.A., Development of a MASH TL-3 Transition Between Guardrail and Portable Concrete Barriers, Thesis, University of Nebraska - Lincoln, May, 2014.
 37. Gutierrez, D.A., Bielenberg, R.W., Faller, R.K., Reid, J.D., and Lechtenberg, K.A., *Development of a MASH TL-3 Transition Between Guardrail and Portable Concrete Barriers*, Final Report to the Nebraska Department of Roads and Smart Work-Zone Deployment Initiative, Research Report No. TRP-03-300-14, Midwest Roadside Safety Facility, University of Nebraska-Lincoln, June 26, 2014.
 38. Lingenfelter, J.L., Bielenberg, R.W., Faller, R.K., Reid, J.D., and Lechtenberg, K.A., *Evaluation of a MASH TL-3 Transition Between Guardrail and Portable Concrete Barriers*, Draft Report in Progress to the Nebraska Department of Roads and Smart Work-Zone Deployment Initiative, Midwest Roadside Safety Facility, University of Nebraska-Lincoln, 2016.
 39. Bielenberg, R.W., Faller, R.K., Sicking, D.L., Reid, J.D., and Lechtenberg, K.A., *Design and Evaluation of the SAFER Barrier Installed on Portable Concrete Barrier*, Final Report to Rogers and Hemmer, Research Report No. TRP-03-257-11, Midwest Roadside Safety Facility, University of Nebraska-Lincoln, July 28, 2011.

40. Reid, J.D., Bielenberg, R.W., Faller, R.K., Lechtenberg, K.A., and Sicking, D.L., *Racetrack SAFER Barrier on Temporary Concrete Barriers*, International Journal of Crashworthiness, Taylor & Francis, Volume 18, No. 4, May 2013, pages 343-355.
41. Bielenberg, R.W., Faller, R.K., Rohde, J.R., Reid, J.D., Sicking, D.L., and Holloway, J.C., *Development of Tie-Down and Transition Systems for Temporary Concrete Barrier on Asphalt Road Surfaces*, Final Report to the Midwest States' Regional Pooled Fund Program, Research Report No. TRP-03-180-06, Midwest Roadside Safety Facility, University of Nebraska-Lincoln, February 23, 2007.
42. Bielenberg, R.W., Faller, R.K., Sicking, D.L., Rohde, J.R., and Reid, J.D., *Tie-Downs and Transitions for Temporary Concrete Barriers*, Paper No. 06-1276, Transportation Research Record No. 1984, Journal of the Transportation Research Board, TRB AFB20 Committee on Roadside Safety Design, Transportation Research Board, Washington D.C., January 2006.
43. Soyland, K., Faller, R.K., Sicking, D.L., and Holloway, J.C., *Development and Testing of an Approach Guardrail Transition to a Single Slope Concrete Median Barrier*, Final Report to the Missouri Highway and Transportation Department, Research Report No. TRP-03-47-95, Midwest Roadside Safety Facility, University of Nebraska-Lincoln, November 1995.
44. Faller, R.K., Soyland, K., and Sicking, D.L., *Approach Guardrail Transition for Single Slope Concrete Barriers*, Transportation Research Record No. 1528, Transportation Research Board, Washington, D.C., September 1996.
45. Wiebelhaus, M.J., Terpsma, R.J., Lechtenberg, K.A., Reid, J.D., Faller, R.K., Bielenberg, R.W., Rohde, J.R., and Sicking, D.L., *Development of a Temporary Concrete Barrier to Permanent Concrete Median Barrier Approach Transition*, Final Report to the Midwest States' Regional Pooled Fund Program, Research Report No. TRP-03-208-10, Midwest Roadside Safety Facility, University of Nebraska-Lincoln, July 15, 2010.
46. Sheikh, N.M., and Menges, W.L., *Transition Design for Pinned-Down Anchored Temporary Barrier to Rigid Concrete Barrier*, Final Report to the Roadside Safety Research Program Pooled Fund, Research Report No. 405160-34-1, Texas Transportation Institute, Texas A&M University, November 2012.
47. Polivka, K.A., Faller, R.K., Ritter, M.A., and Rosson, B.T., *Development of the TBC-8000 Bridge Railing*, Draft Report to the U.S. Department of Agriculture, Forest Service, Forest Products Laboratory, Report No. TRP-03-30-93, Midwest Roadside Safety Facility, Civil Engineering Department, University of Nebraska-Lincoln, September 5, 2000.
48. Faller, R.K., Rosson, B.T., Ritter, M.A., and Duwadi, S.R., *Railing Systems for Use on Timber Deck Bridges*, Transportation Research Record No. 1656, Journal of the Transportation Research Board, Transportation Research Board, Washington, D.C., July 1999, 110-119.

49. Rosson, B.T., Faller, R.K., and Ritter, M.A., *Performance Level 2 and Test Level 4 Bridge Railings for Timber Decks*, Transportation Research Record No. 1500, Transportation Research Board, Washington, D.C., July 1995.
50. *Guide Specifications for Bridge Railings*, American Association of State Highway and Transportation Officials, Washington, D.C., 1989.
51. Faller, R.K., Ritter, M.A., Rosson, B.T., Fowler, M.D., and Duwadi, S.R., *Two Test Level 4 Bridge Railing and Transition Systems for Transverse Timber Deck Bridges*, Paper No. 5B0110, Transportation Research Record No. 1996, Volume 1, Fifth International Bridge Engineering Conference, Tampa, Florida, April 3-5, 2000, Transportation Research Board, Washington, D.C., 334-351.
52. Polivka, K.A., Faller, R.K., Rosson, B.T., Fowler, M.D., Keller, E.A., *Two Test Level 4 Bridge Railing and Transition Systems for Transverse Glue-Laminated Timber Decks*, Final Report Submitted to the United States Department of Agriculture-Forest Service-Forest Products Laboratory, Transportation Report No. TRP-03-71-01, Performed by the Midwest Roadside Safety Facility, University of Nebraska-Lincoln, January 30, 2002.
53. Faller, R.K., Reid, J.D., Rohde, J.R., Sicking, D.L., and Keller, E.A., *Two Approach Guardrail Transitions for Concrete Safety Shape Barriers*, Final Report to the Iowa Department of Transportation, Research Report No. TRP-03-69-98, Midwest Roadside Safety Facility, University of Nebraska-Lincoln, May 15, 1998.
54. Faller, R.K., Reid, J.D., and Rohde, J.R., *Approach Guardrail Transition for Concrete Safety Shape Barriers*, Transportation Research Record No. 1647, Transportation Research Board, Washington, D.C., November 1998.
55. *AASHTO Guide Specifications for Bridge Railings*, American Association of State Highway and Transportation Officials (AASHTO), Washington, D.C., 1989.
56. *AASHTO LRFD Bridge Design Specifications, Customary U.S. Units, 7th Edition*, American Association of State Highway and Transportation Officials (AASHTO), Washington, D.C., 2014.
57. Eller, C.M. and Reid, J.D., *Determination of Impact Forces From Vehicle-to-Barrier Crashes*, Final Report to the University of Nebraska Honors Program, Midwest Roadside Safety Facility, University of Nebraska-Lincoln, April 2007.
58. Rosenbaugh, S.K., Faller, R.K., Bielenberg, R.W., Sicking, D.L., Reid, J.D., and Tadros, M.K., *Phase I Development of an Aesthetic Precast Concrete Bridge Rail, Final Report to the Nebraska Department of Roads*, Final Report to the Nebraska Department of Roads, Research Report No. TRP-03-239-12, Midwest Roadside Safety Facility and University of Nebraska-Omaha, University of Nebraska-Lincoln, February 13, 2012.

59. Polivka, K.A., Hascall, J.A., Faller, R.K., Rohde, J.R., Holloway, J.C., Sicking, D.L., and Kurz, K., *Design and Evaluation of CYRO's Paraglas Soundstop TL-4 Noise Barrier System*, Final Report to CYRO Industries, Inc., Research Report No. TRP-03-160-05, Midwest Roadside Safety Facility, University of Nebraska-Lincoln, April 22, 2005.
60. Faller, R.K., Kurz, K., Polivka, K.A., Sicking, D.L., Humphries, E., and Hascall, J., *A Test Level 4 Noise Wall for Attachment to Concrete Traffic Barriers*, Paper No. 06-1784, Transportation Research Record No. 1984, Journal of the Transportation Research Board, TRB AFB20 Committee on Roadside Safety Design, Transportation Research Board, Washington D.C., January 2006.
61. Wiebelhaus, M.J., Polivka, K.A., Faller, R.K., Rohde, J.R., Sicking, D.L., Holloway, J.C., Reid, J.D., and Bielenberg, R.W., *Evaluation of Rigid Hazards Placed in the Zone of Intrusion*, Final Report to the Midwest States' Regional Pooled Fund Program, Research Report No. TRP-03-151-08, Midwest Roadside Safety Facility, University of Nebraska-Lincoln, January 3, 2008.
62. *Tentative Service Requirements For Bridge Rail Systems*, National Cooperative Highway Research Report Program (NCHRP) Report No. 86, Washington, D.C., 1970.
63. Bligh, R.P., Briaud, J.L., Kim, K.M., and Abu-Odeh, A., *Design of Roadside Barrier Systems Placed on MSE Retaining Walls*, Final Report to the National Cooperative Highway Research Program, Research Report No. 663, Texas Transportation Institute, Texas A&M University, 2010.
64. Bligh, R.P., Briaud, J.L., Abu-Odeh, A., Kim, K., and Saez, S., *Design Guidelines for TL-3 through TL-5 Roadside Barrier Systems Placed on Mechanically Stabilized Earth (MSE) Retaining Walls*, Interim Report, Research Report No. NCHRP 22-20(2), Texas Transportation Institute, Texas A&M University.
65. Unreferenced Facts Noted in Reference [64], pg. 7.
66. Abu-Odeh, A.Y., Kim, K.M., Williams, W.F., Buth, C.E., and Patton, C., *Crash Wall Design for Mechanically Stabilized Earth (MSE) Retaining Wall Phase I: Engineering Analysis and Simulation*, Final Report to the Washington State Department of Transportation, Research Report No. 405160-15, Texas Transportation Institute, Texas A&M University, March 2011.
67. Abu-Odeh, A. and Kim, K.M., *Evaluation of the Performance of a Crash Wall Design for Protection of Mechanically Stabilized Earth Retaining Walls*, Paper No. 11-2977, Journal of the Transportation Research Board, Transportation Research Board, Washington D.C., 2010.
68. Bullard, D.L., Bligh, R.P., and Menges, W.L., *Appendix B: MASH TL-4 Testing and Evaluation of the New Jersey Safety Shape Bridge Rail*, Final Report to the National

Cooperative Highway Research Program, Project No. 22-14, Texas Transportation Institute, Texas A&M University, March 2010.

69. Cota, K.A., McDonnell, J., Hardy, K., and Bush, P., Webinar to update AASHTO/FHWA Joint Implementation Plan Regarding *AASHTO Manual for Assessing Safety Hardware* [PowerPoint slides], August 17, 2015.
70. Hirsch, T.J., *Analytical Evaluation of Texas Bridge Rails to Contain Buses and Trucks*, Report No. FHWA TX 78-230-2, Final Report to the Texas State Department of Highways and Public Transportation, Texas Transportation Institute, Texas A&M University, August 1978.
71. Rosenbaugh, S.K., Faller, R.K., Hascall, J.A., Allison, E.M., Bielenberg, R.W., Rohde, J.R., Polivka, K.A., Sicking, D.L., and Reid, J.D., *Development of a Stand-Alone Concrete Bridge Pier Protection System*, Final Report to the Midwest States' Regional Pooled Fund Program, Research Report No. TRP-03-190-08, Midwest Roadside Safety Facility, University of Nebraska-Lincoln, April 18, 2008.
72. *Building Code Requirements for Structural Concrete (ACI 318-14) and Commentary (ACI 318R-14): An ACI Standard*, Reported by ACI Committee 318, American Concrete Institute, Farmington Hills, MI, August 2014.
73. Bligh, R.P. Sheikh, N.M., Menges, W.L., and Heck, R.R., *Development of Low-Deflection Precast Concrete Barrier*, Final Report to the Texas Department of Transportation, Report FHWA/TX-05/0-4162-3, Texas A&M Transportation Institute, Texas A&M University, College Station, Texas, January 2005.
74. FHWA/NHTSA National Crash Analysis Center, Finite Element Model of Dodge Neon, Model Year 1996, Version 7, Posted July 3, 2006.
75. FHWA/NHTSA National Crash Analysis Center, Finite Element Model of Chevy Silverado, Model Year 2007, Version 2, Posted February 27, 2009.
76. Mohan, P., Marzougui, D., Arispe, E., and Story, C., Component and Full-Scale Tests of the 2007 Chevrolet Silverado Suspension System, National Crash Analysis Center, Contract No. DTFH61-02-X-00076, July 2009.
77. *Vehicle Damage Scale for Traffic Investigators*, Second Edition, Technical Bulletin No. 1, Traffic Accident Data (TAD) Project, National Safety Council, Chicago, Illinois, 1971.
78. *Collision Deformation Classification – Recommended Practice J224 March 1980*, Handbook Volume 4, Society of Automotive Engineers (SAE), Warrendale, Pennsylvania, 1985.
79. Ray, M.H., Plaxico, C.A., and Anghileri, M., *Procedures for Verification and Validation of Computer Simulations Used for Roadside Safety Applications*, Final

- Report to NCHRP Project 22-24, National Cooperative Highway Research Program, Transportation Research Board, March 2010.
80. FHWA/NHTSA National Crash Analysis Center, Finite Element Model of Toyota Yaris, Model Year 2010, Posted December 21, 2011.
 81. *A Policy on Geometric Design of Highways and Streets*, 6th Edition, American Association of State Highway and Transportation Officials (AASHTO), Washington, D.C., 2011, pp 3-32 and 3-161.
 82. Bateman, R.J., Design of Cable-to-Post Attachments for Use in a Non-Proprietary, High-Tension, Cable Median Barrier, Thesis, University of Nebraska - Lincoln, May, 2013.
 83. Bateman, R.J., Faller, R.K., Bielenberg, R.W., Sicking, D.L., Reid, J.D., Stolle, C.S., Lechtenberg, K.A., and Rosenbaugh, S.K., *Design of Cable-to-Post Attachments for Use in a Non-Proprietary, High-Tension, Cable Median Barrier*, Final Report to the Midwest States' Regional Pooled Fund Program, Research Report No. TRP-03-285-13, Midwest Roadside Safety Facility, University of Nebraska-Lincoln, August 29, 2013.
 84. Bates, B.R., RISA-2D Educational Version 1.0, RISA Technologies, 2002.
 85. American Institute of Steel Construction (AISC), Steel Construction Manual, Fourteenth Edition, Second Printing, February 2012.
 86. Salmon, C.G., and Johnson, J.E., *Steel Structures Design and Behavior – Emphasizing Load and Resistance Factor Design*, Third Edition, Harper & Row, Publishers, Inc., 1990.
 87. Beer, F.P., Johnston, E.R.Jr., DeWolf, J.T., *Mechanics of Materials*, Fourth Edition, Published by McGraw-Hill, Inc., 2006.
 88. Young, W.C., *Roark's Formulas for Stress & Strain*, Sixth Edition, Published by McGraw-Hill, Inc., 1989.
 89. Dowling, N. E., *Mechanical Behavior of Materials: Engineering Methods for Deformations, Fracture, and Fatigue*, Boston: Pearson, 2013.

16 APPENDICES

Appendix A. MASH TL-4 Safety Criteria

Three full-scale vehicle crash tests are recommended for evaluating longitudinal barriers according to the MASH TL-4 safety performance criteria [15]. According to TL-4 of MASH, longitudinal barrier systems must be subjected to three full-scale vehicle crash tests. The three full-scale crash tests are as follows:

1. Test Designation No. 4-10 consists of a 2,425-lb (1,100-kg) passenger car impacting the system at a nominal speed and angle of 62 mph (100 km/h) and 25 degrees, respectively.
- c. Test Designation No. 4-11 consists of a 5,000-lb (2,268-kg) pickup truck impacting the system at a nominal speed and angle of 62 mph (100 km/h) and 25 degrees, respectively.
- d. Test Designation No. 4-12 consists of a 22,046-lb (10,000-kg) single-unit truck impacting the system at a nominal speed and angle of 56 mph (90 km/h) and 15 degrees, respectively.

The test conditions of TL-4 longitudinal barriers are summarized in Table 55.

Table 55. MASH TL-4 Crash Test Conditions [15]

Test Article	Test Designation No.	Test Vehicle	Impact Conditions			Evaluation Criteria ¹
			Speed		Angle (deg)	
			mph	km/h		
Longitudinal Barrier	4-10	1100C	62	100	25	A,D,F,H,I
	4-11	2270P	62	100	25	A,D,F,H,I
	4-12	10000S	56	90	15	A,D,G

¹ Evaluation criteria explained in Table 56

Evaluation criteria for full-scale vehicle crash testing are based on three appraisal areas: (1) structural adequacy; (2) occupant risk; and (3) vehicle trajectory after collision. Criteria for structural adequacy are intended to evaluate the ability of the median barrier to contain and redirect impacting vehicles. Occupant risk evaluates the degree of hazard to occupants in the impacting vehicle. Vehicle trajectory after collision is a measure of

the potential for the post-impact trajectory of the vehicle to result in secondary collisions with other vehicles or fixed objects, thereby increasing the risk of injury to the occupant of the impacting vehicle and to other vehicles. These evaluation criteria are summarized in Table 56 and defined in greater detail in MASH. Therefore, these test conditions and evaluation criteria were used to establish guidelines for designing the new barriers.

Table 56. MASH Evaluation Criteria for Longitudinal Barriers [15]

Structural Adequacy	A. Test article should contain and redirect the vehicle or bring the vehicle to a controlled stop; the vehicle should not penetrate, underride, or override the installation although controlled lateral deflection of the test article is acceptable.		
Occupant Risk	D. Detached elements, fragments or other debris from the test article should not penetrate or show potential for penetrating the occupant compartment, or present an undue hazard to other traffic, pedestrians, or personnel in a work zone. Deformations of, or intrusions into, the occupant compartment should not exceed limits set forth in Section 5.3 and Appendix E of MASH.		
	F. The vehicle should remain upright during and after collision. The maximum roll and pitch angles are not to exceed 75 degrees.		
	G. It is preferable, although not essential, that the vehicle remain upright during and after collision.		
	H. Occupant Impact Velocities (OIV) (see Appendix A, Section A5.3 of MASH for calculation procedure) should satisfy the following limits:		
	Occupant Impact Velocity Limits		
	Component	Preferred	Maximum
Longitudinal and Lateral	30 ft/s (9.1 m/s)	40 ft/s (12.2 m/s)	
I. The Occupant Ridedown Acceleration (ORA) (see Appendix A, Section A5.3 of MASH for calculation procedure) should satisfy the following limits:	Occupant Ridedown Acceleration Limits		
Component	Preferred	Maximum	
Longitudinal and Lateral	15.0 g's	20.49 g's	

Appendix B. RESTORE Barrier Drawing Set

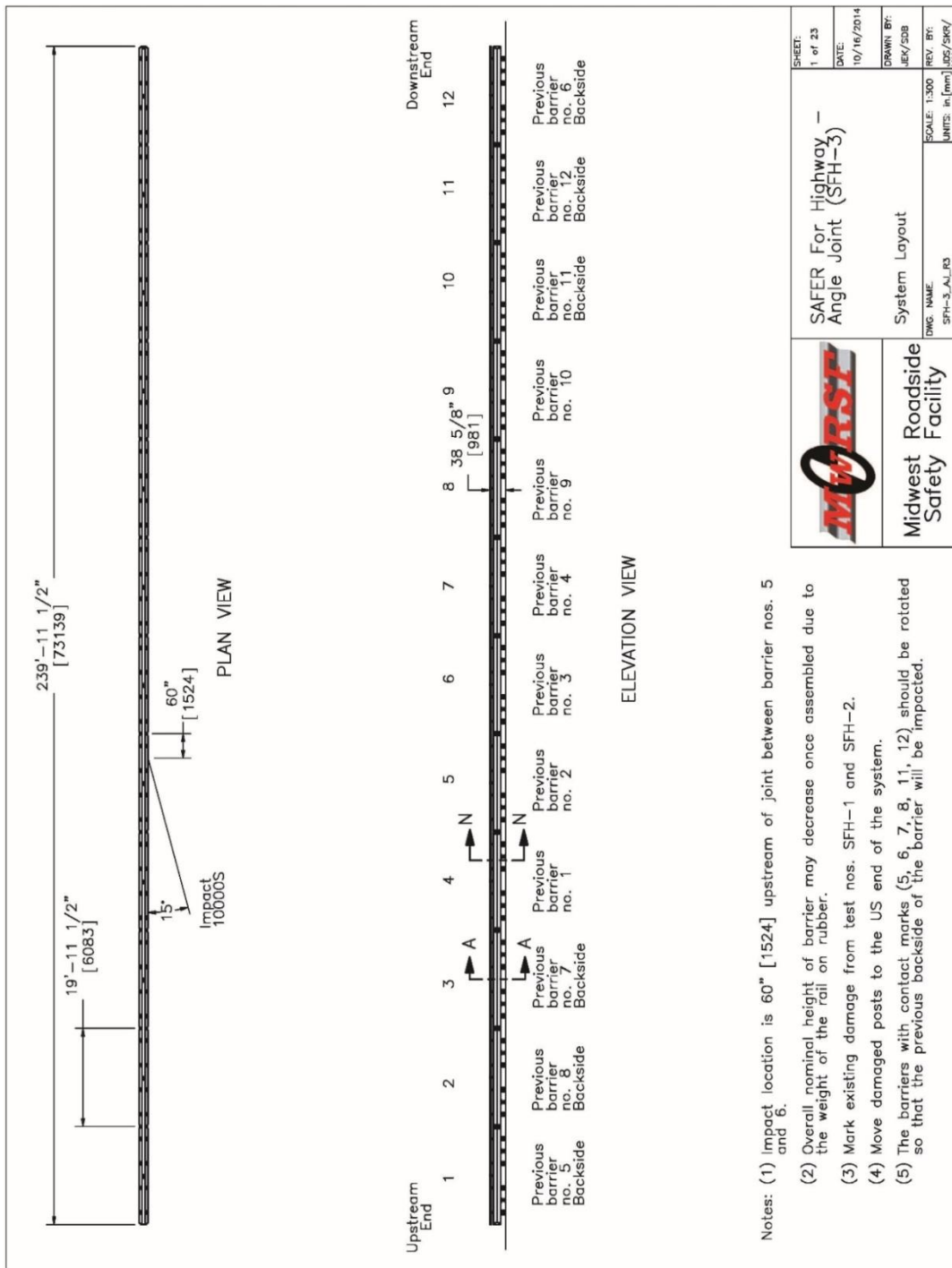


Figure B-1. System Layout, RESTORE Barrier [20]

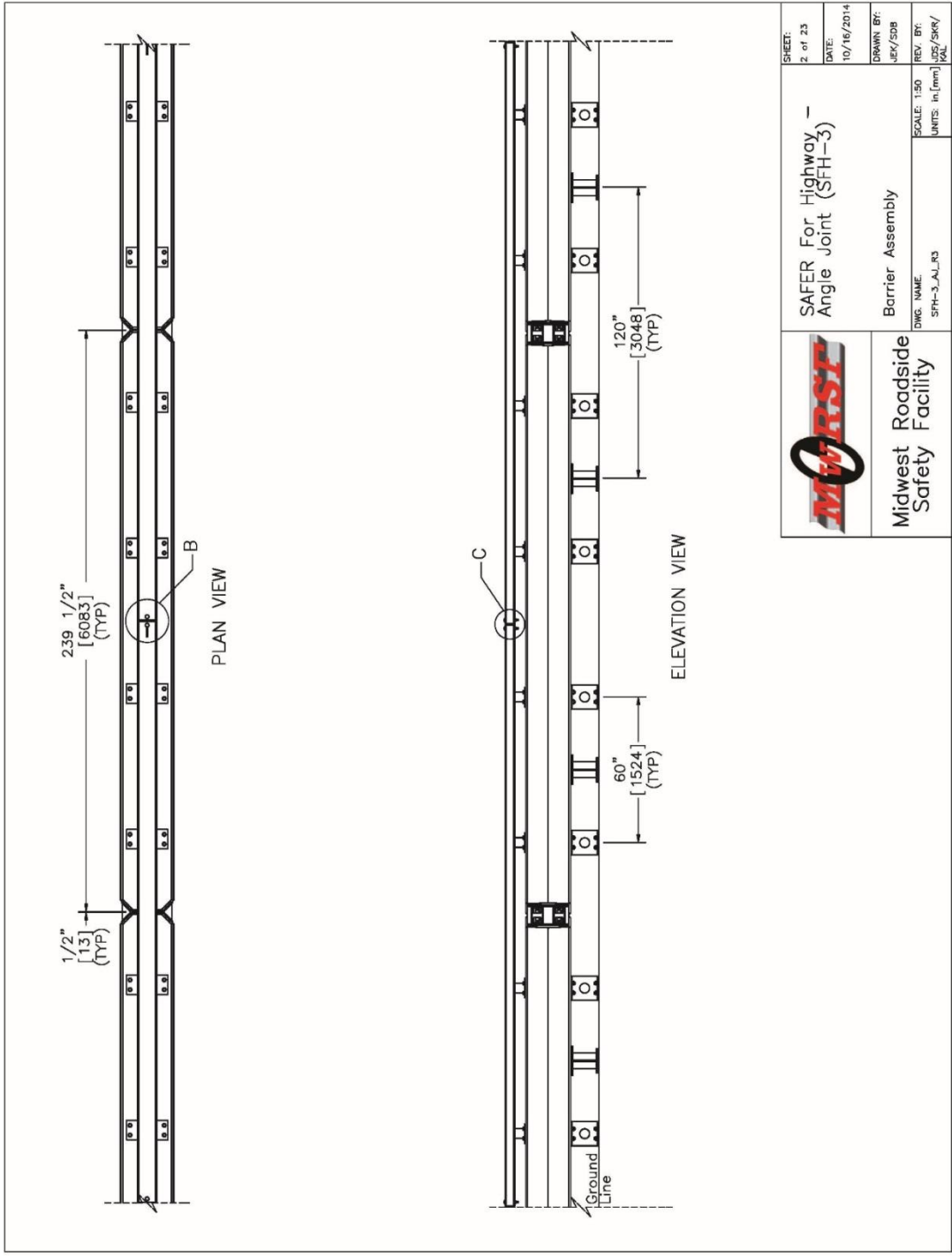


Figure B-2. Barrier Assembly, RESTORE Barrier [20]

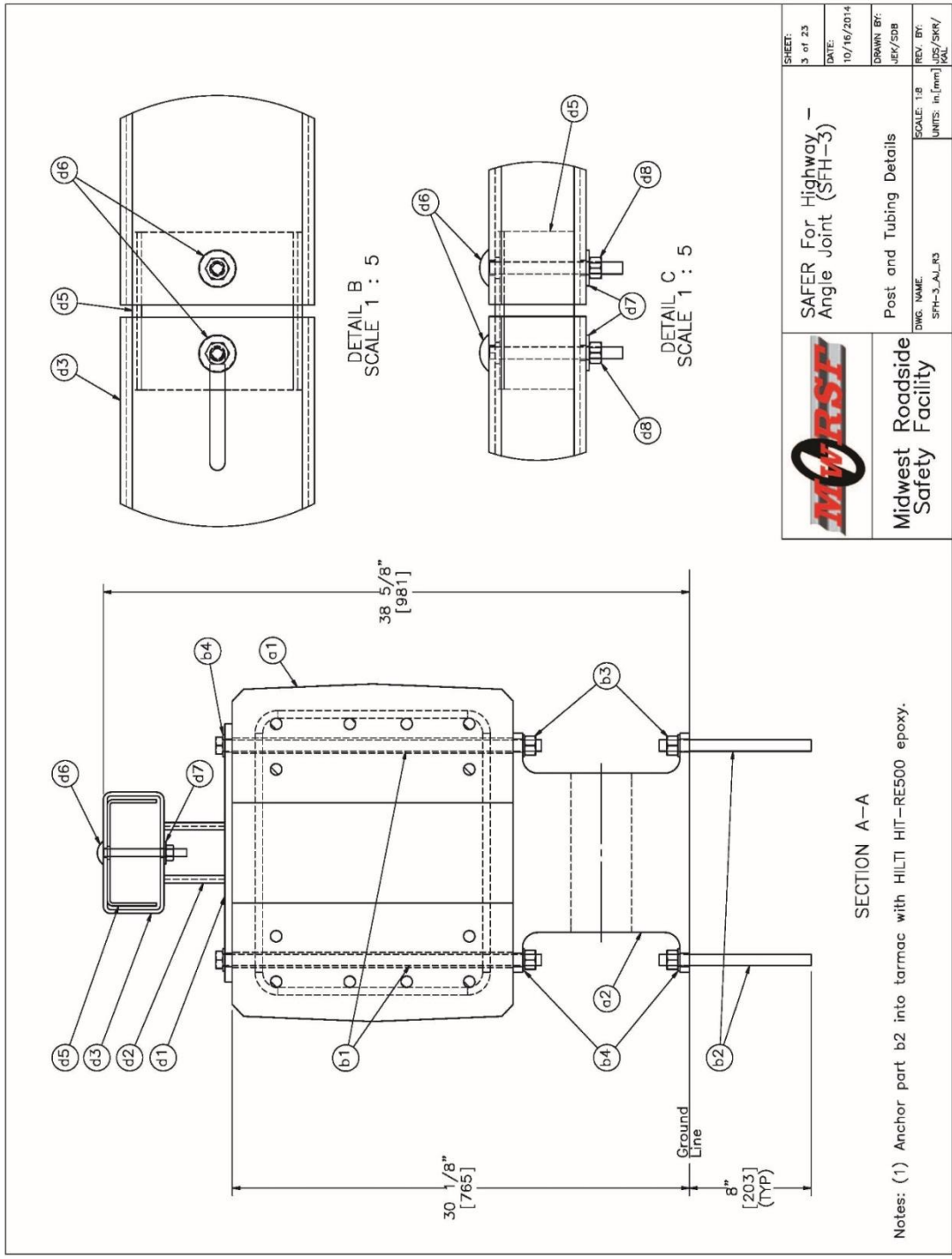


Figure B-3. Post and Tubing Details, RESTORE Barrier [20]

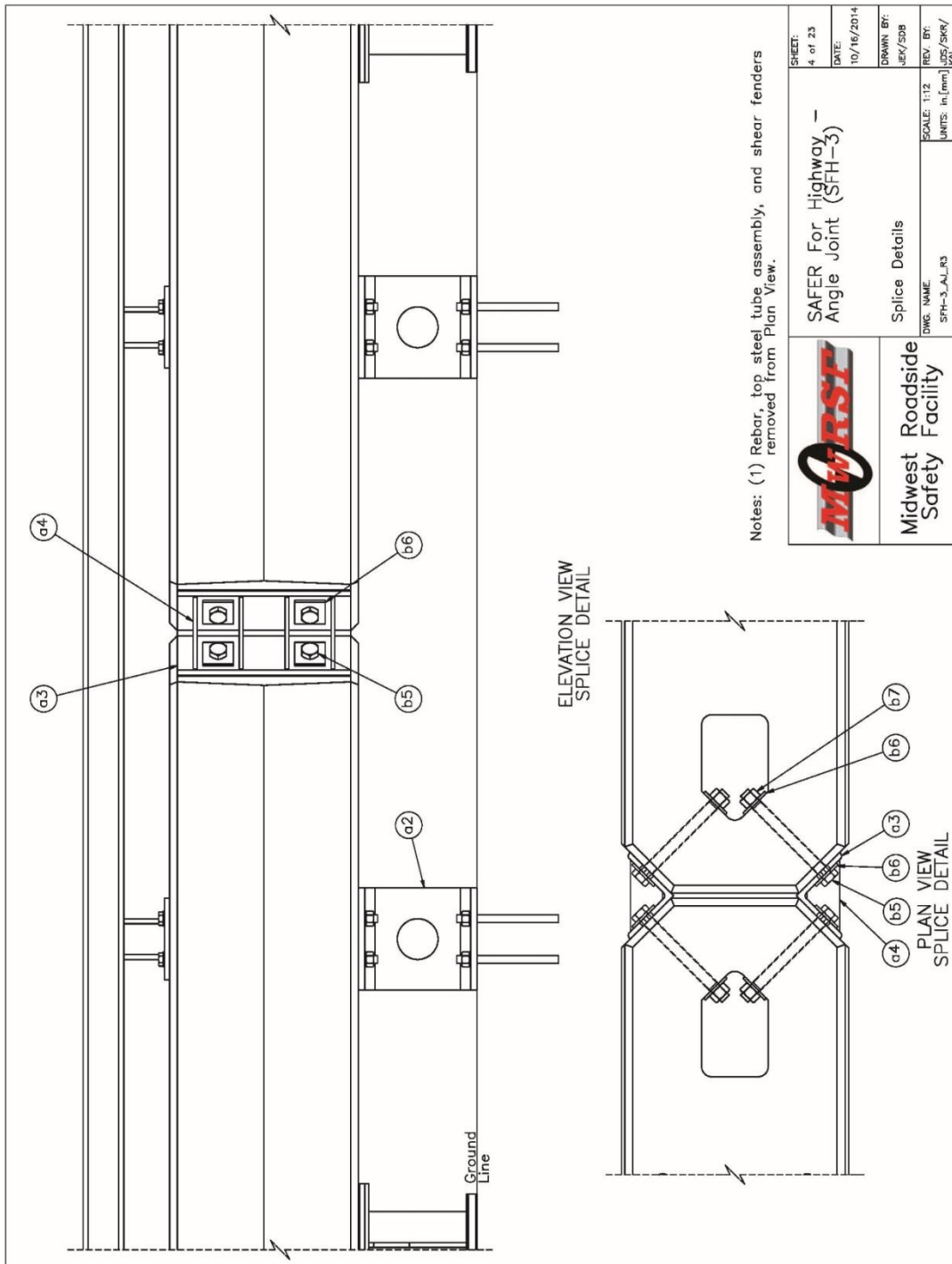


Figure B-4. Splice Details, RESTORE Barrier [20]

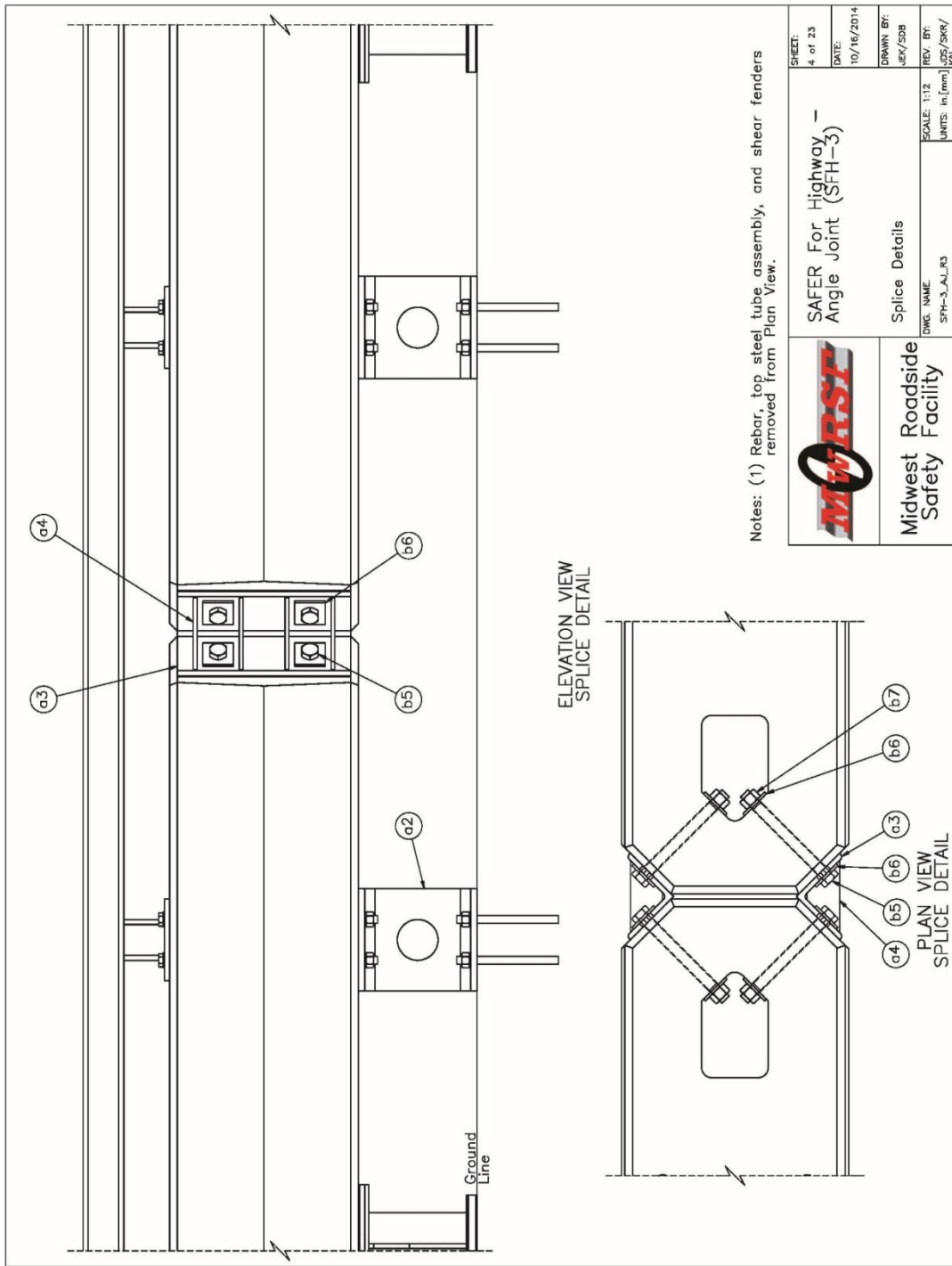


Figure B-5. Splice Details, RESTORE Barrier [20]

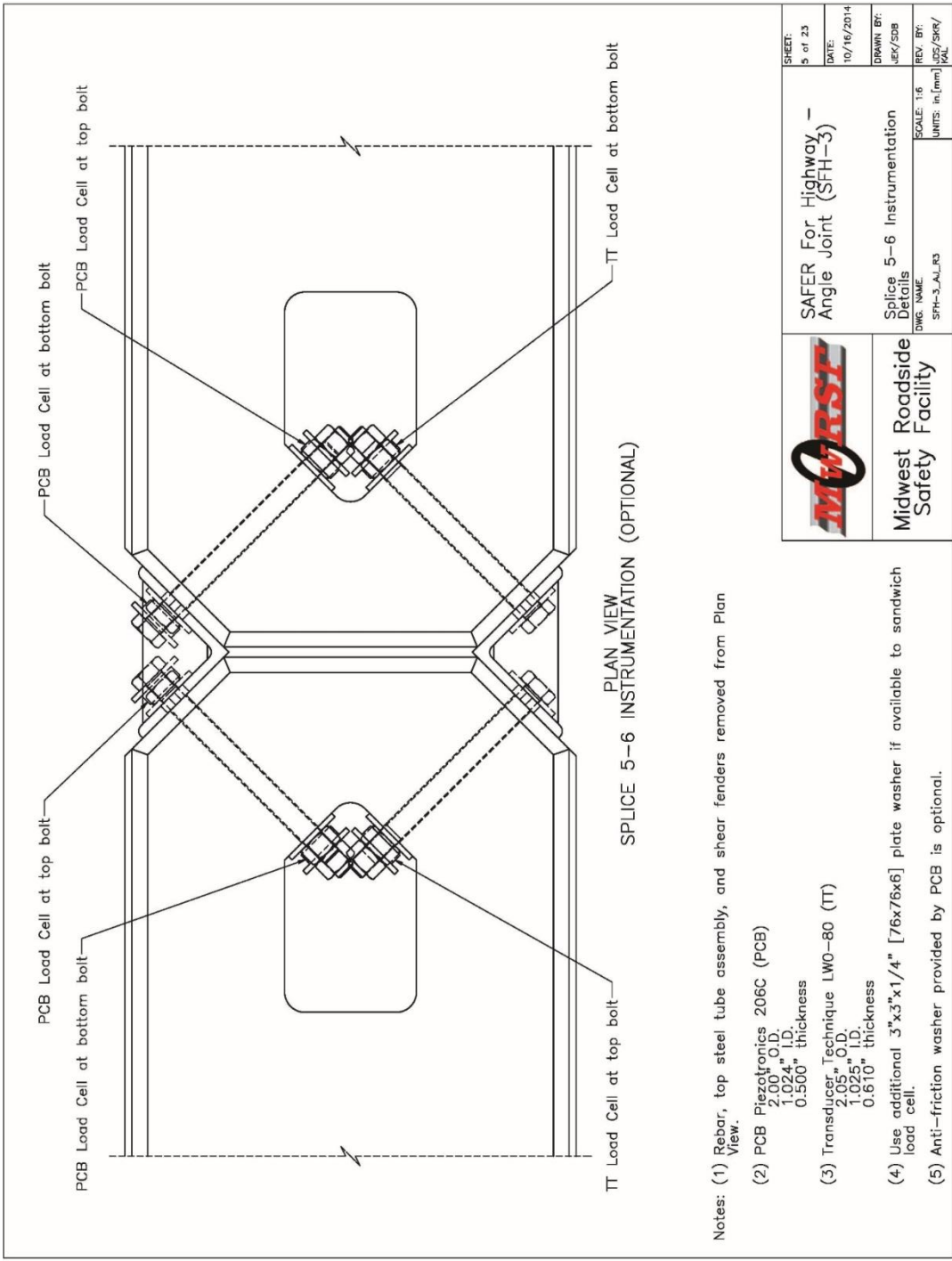


Figure B-6. Splice 5-6 Instrumentation Details, RESTORE Barrier [20]

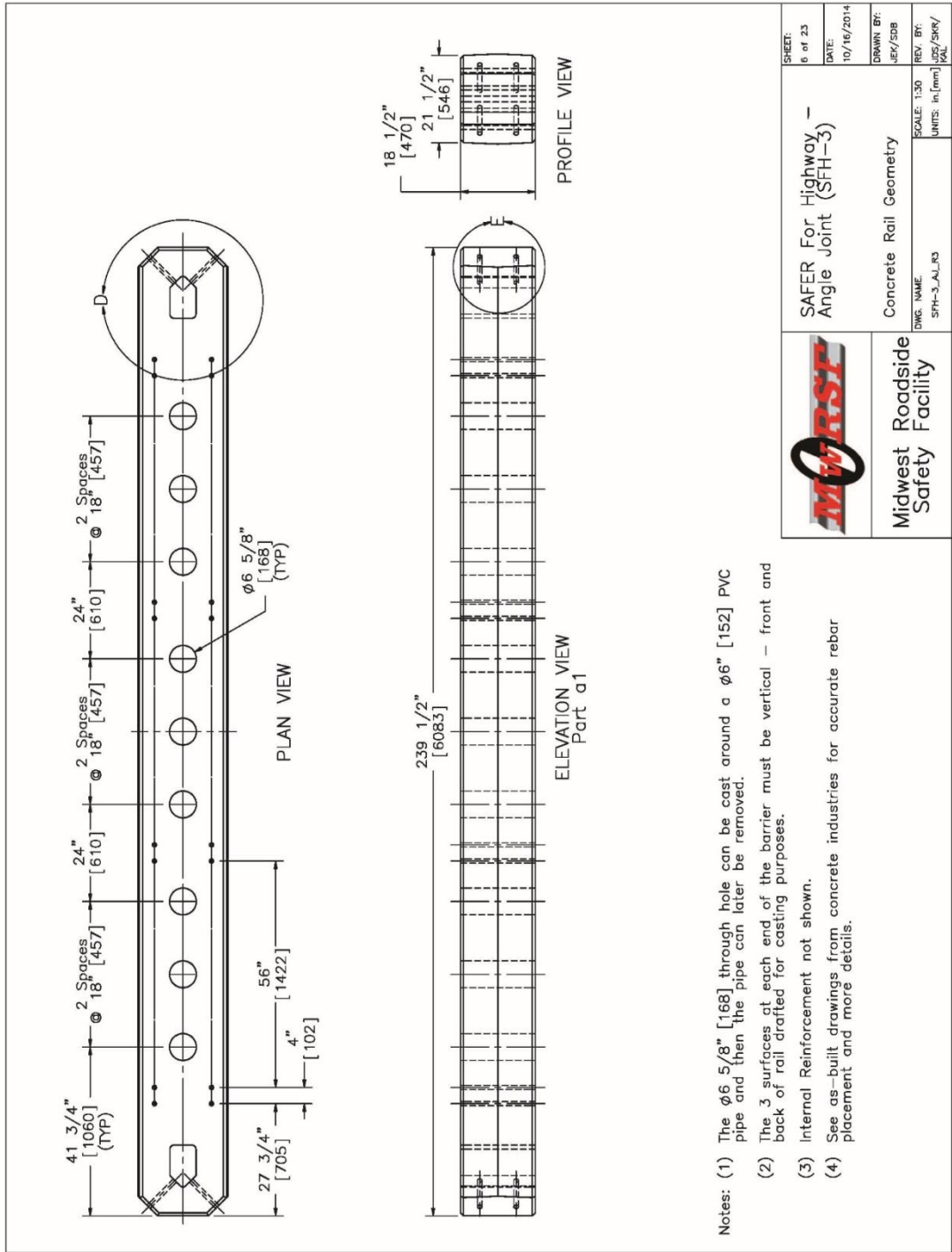
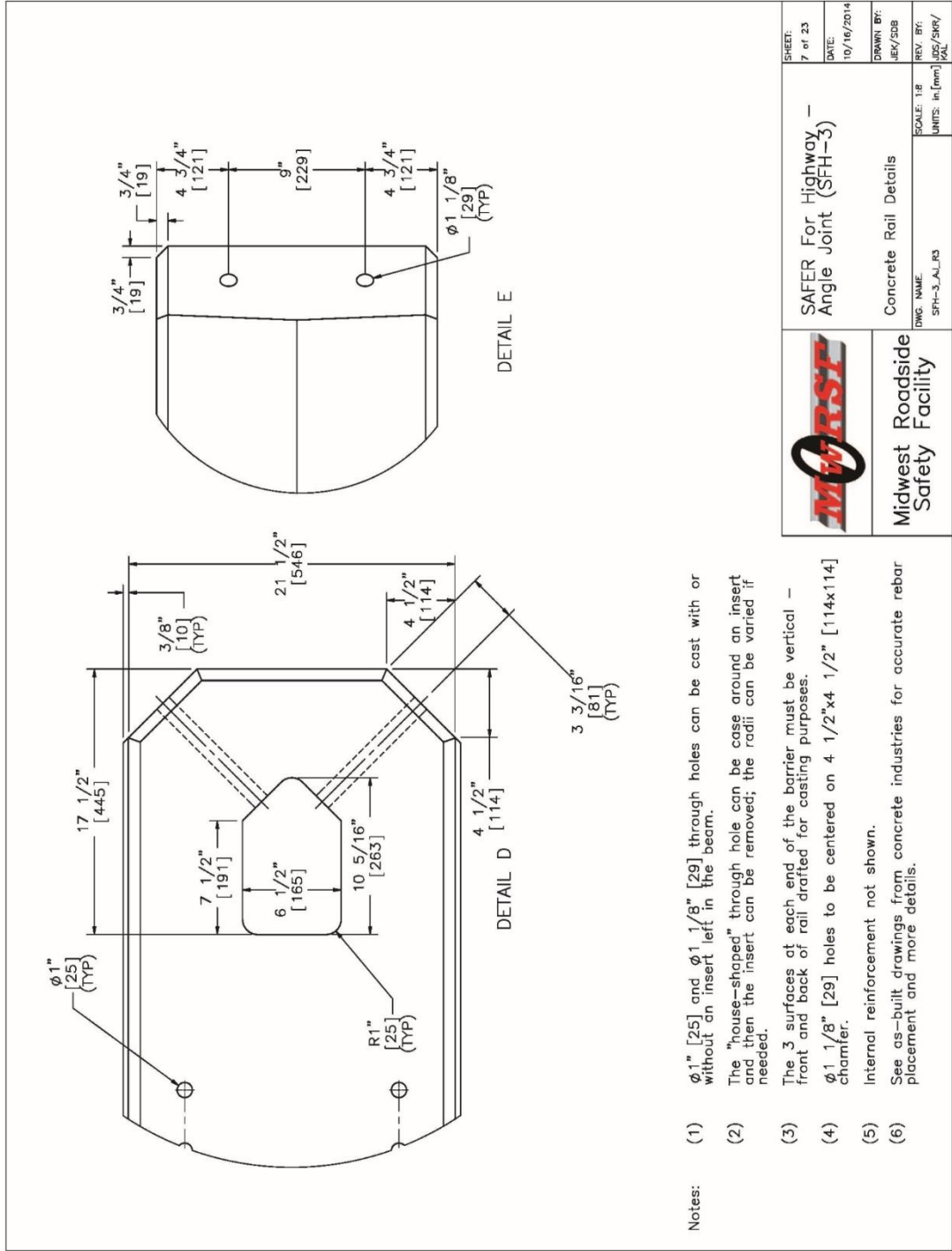


Figure B-7. Concrete Beam Geometry, RESTORE Barrier [20]




	SAFER For Highway - Angle Joint (SFH-3)	SHEET: 7 of 23 DATE: 10/16/2014
	Concrete Rail Details DWG. NAME: SFH-3_A_L1.R3	SCALE: 1:8 UNITS: in./mm REV. BY: JEC/SK/KAL DATE:

Figure B-8. Concrete Beam Details, RESTORE Barrier [20]

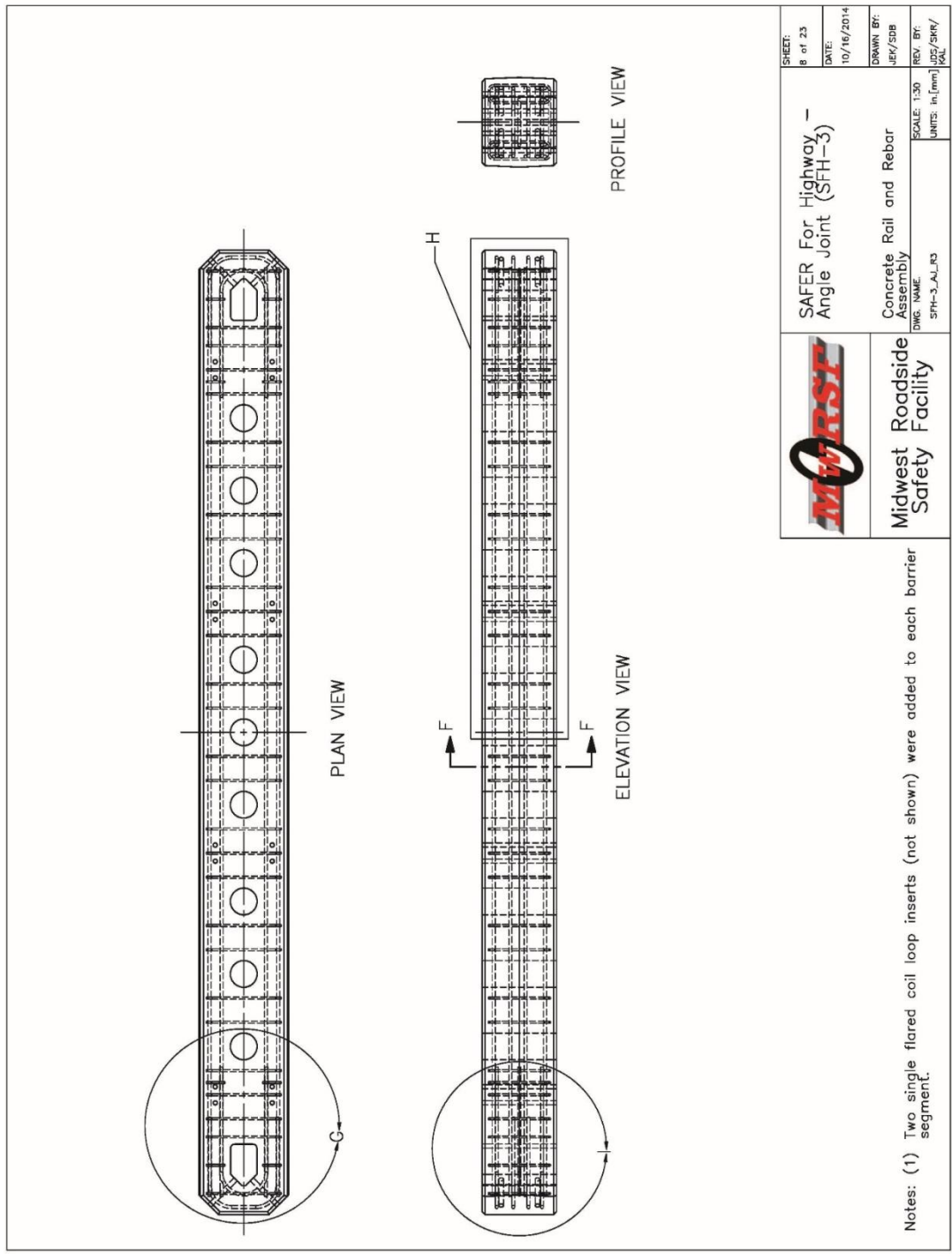
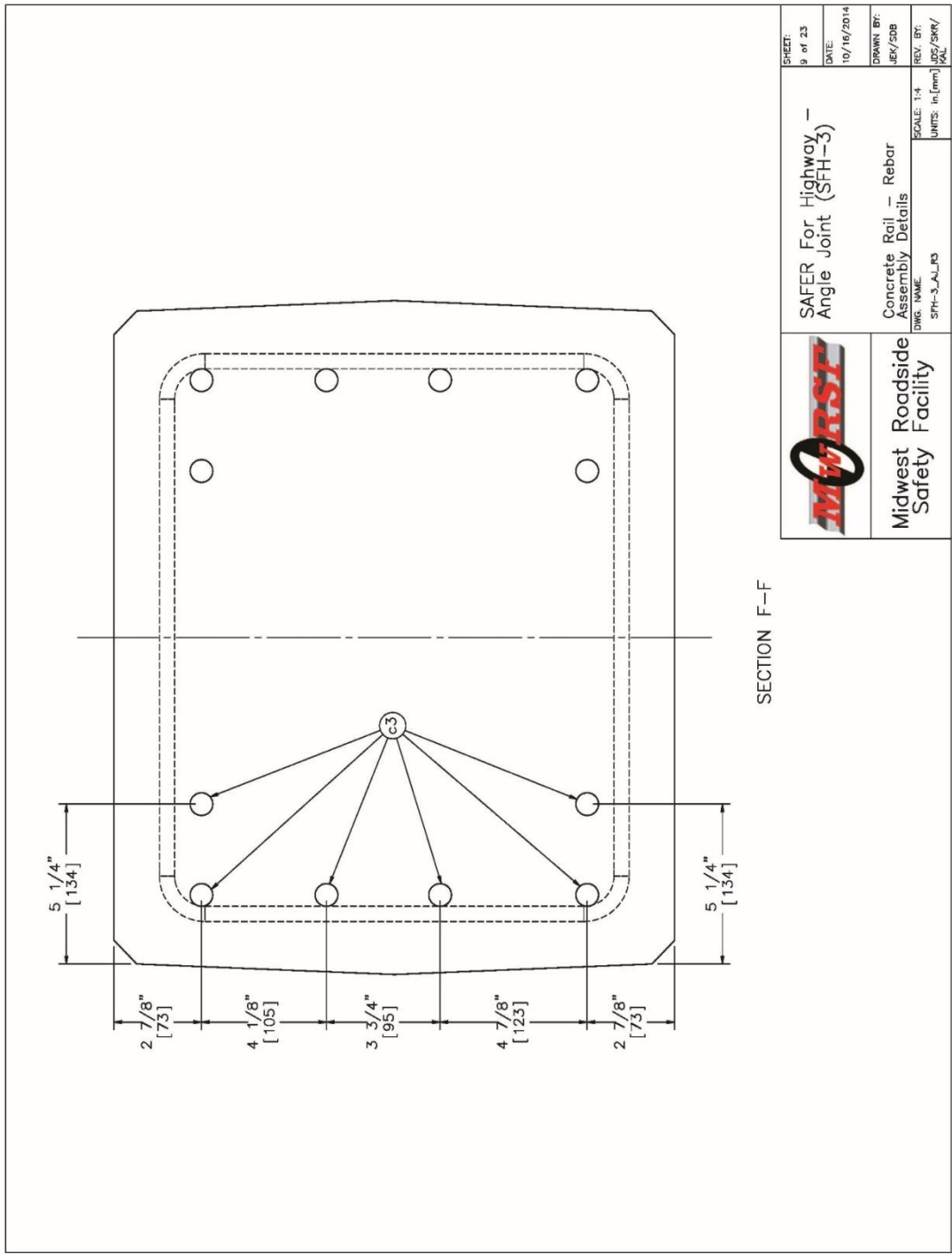
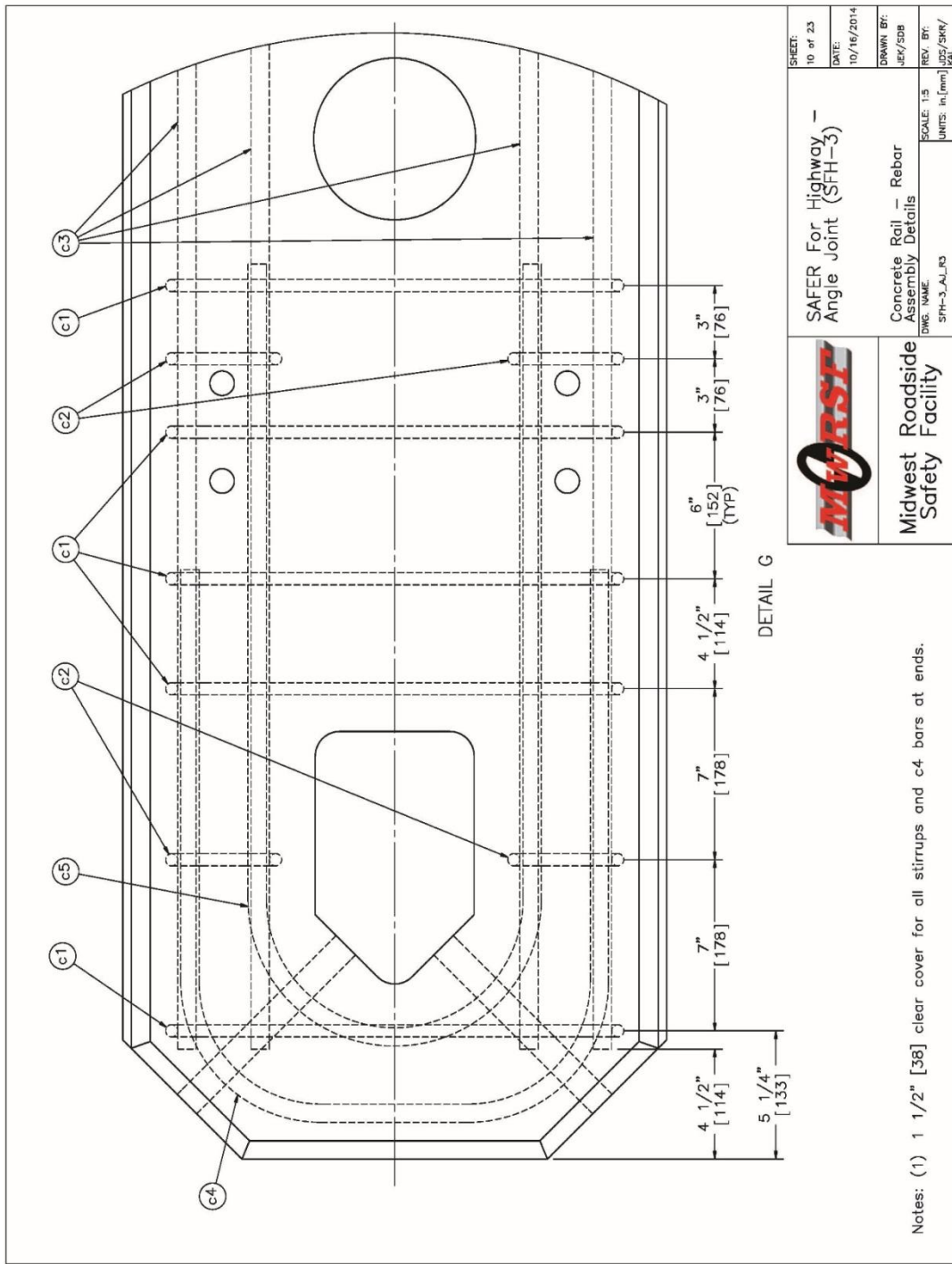


Figure B-9. Concrete Beam and Rebar Assembly, RESTORE Barrier [20]



SECTION F-F

Figure B-10. Concrete Beam, Rebar Assembly Details, RESTORE Barrier [20]



	SAFER For Highway - Angle Joint (SFH-3)	SHEET: 10 of 23 DATE: 10/16/2014
	Concrete Rail - Rebar Assembly Details DWG. NAME: SFH-3_AJ_R3	DRAWN BY: JEM/SDB REV. BY: JDS/SBK/JCL SCALE: 1:5 UNITS: in./mm

Figure B-11. Concrete Beam, Rebar Assembly Details, RESTORE Barrier [20]

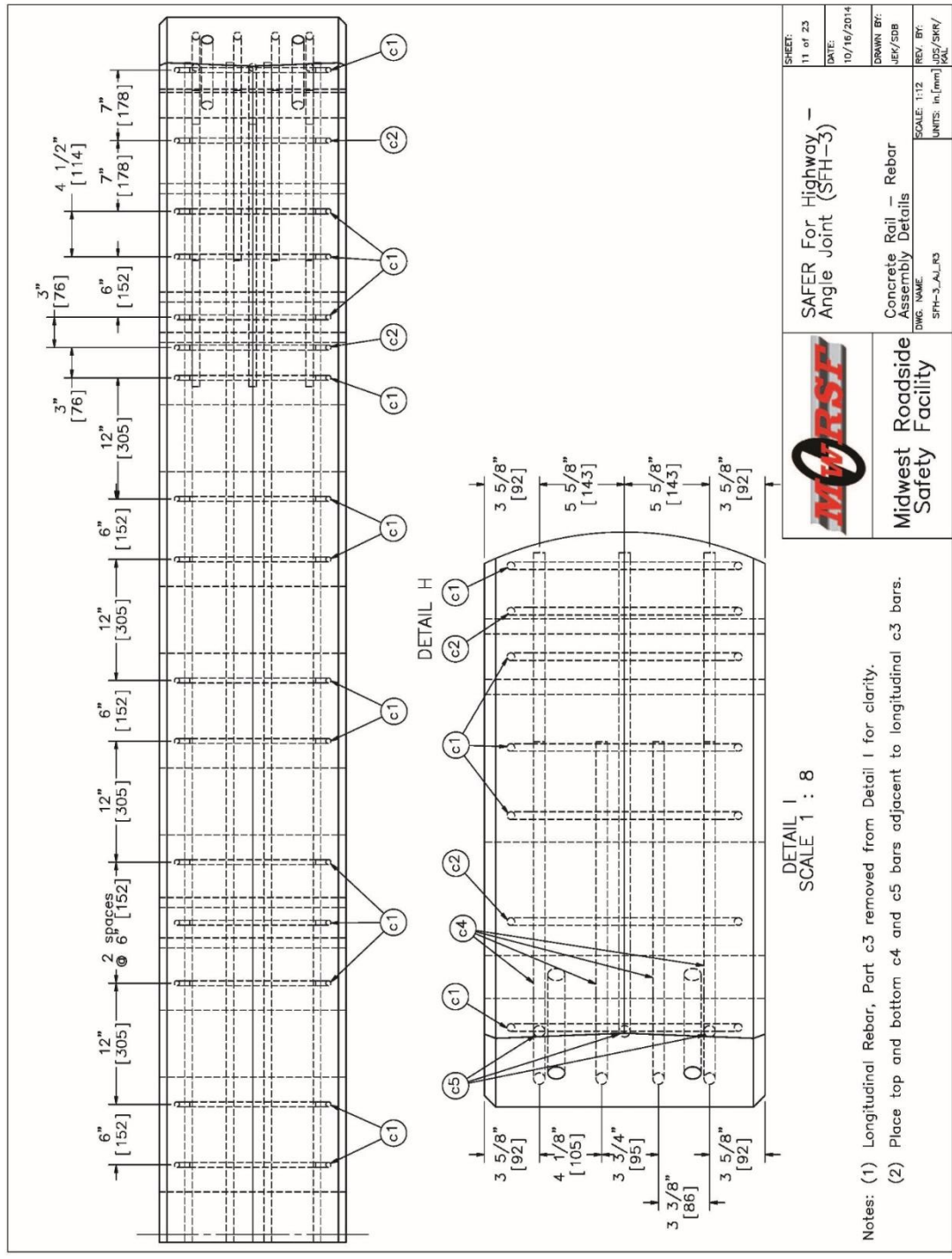


Figure B-12. Concrete Beam, Rebar Assembly Details, RESTORE Barrier [20]

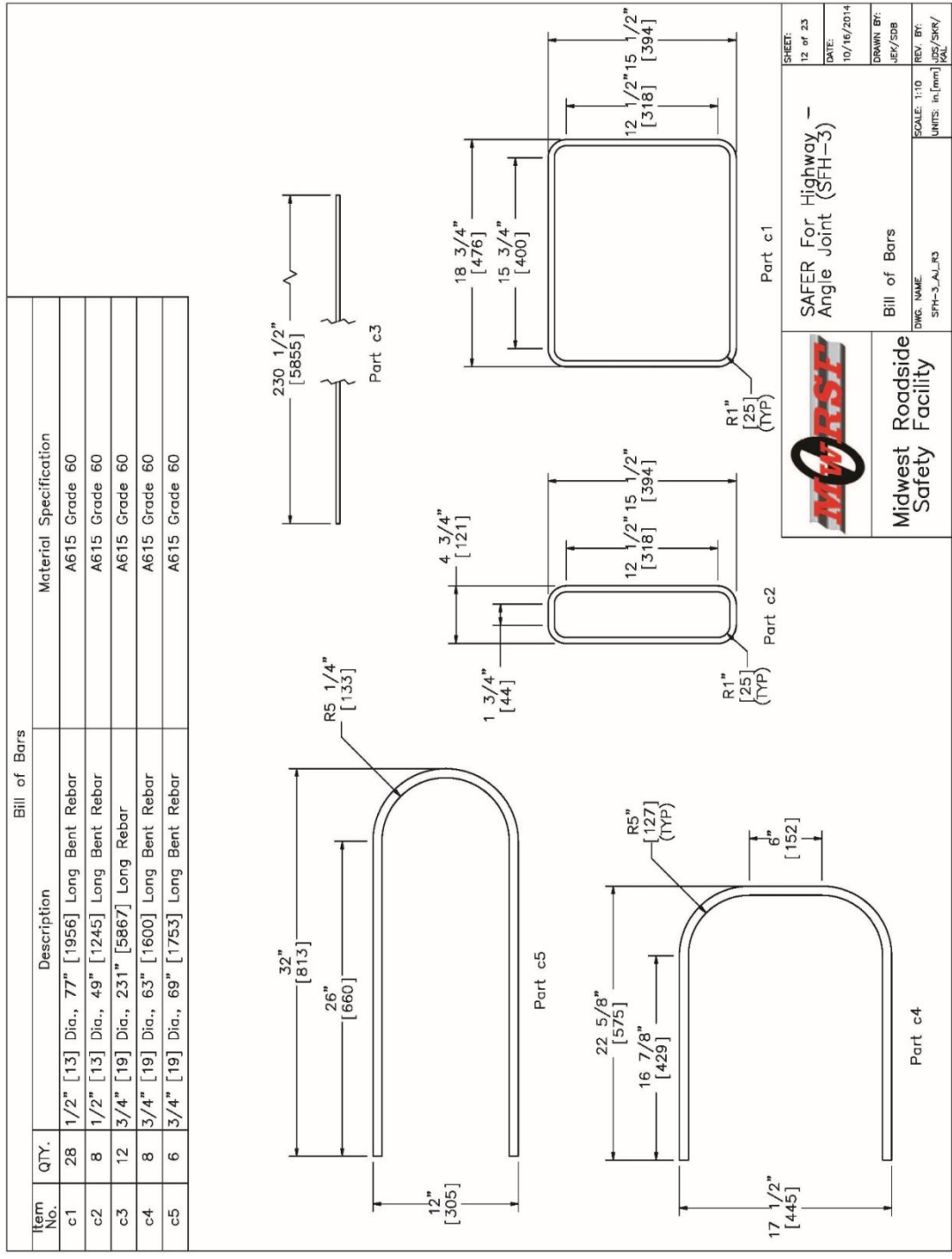


Figure B-13. Bill of Bars, RESTORE Barrier [20]

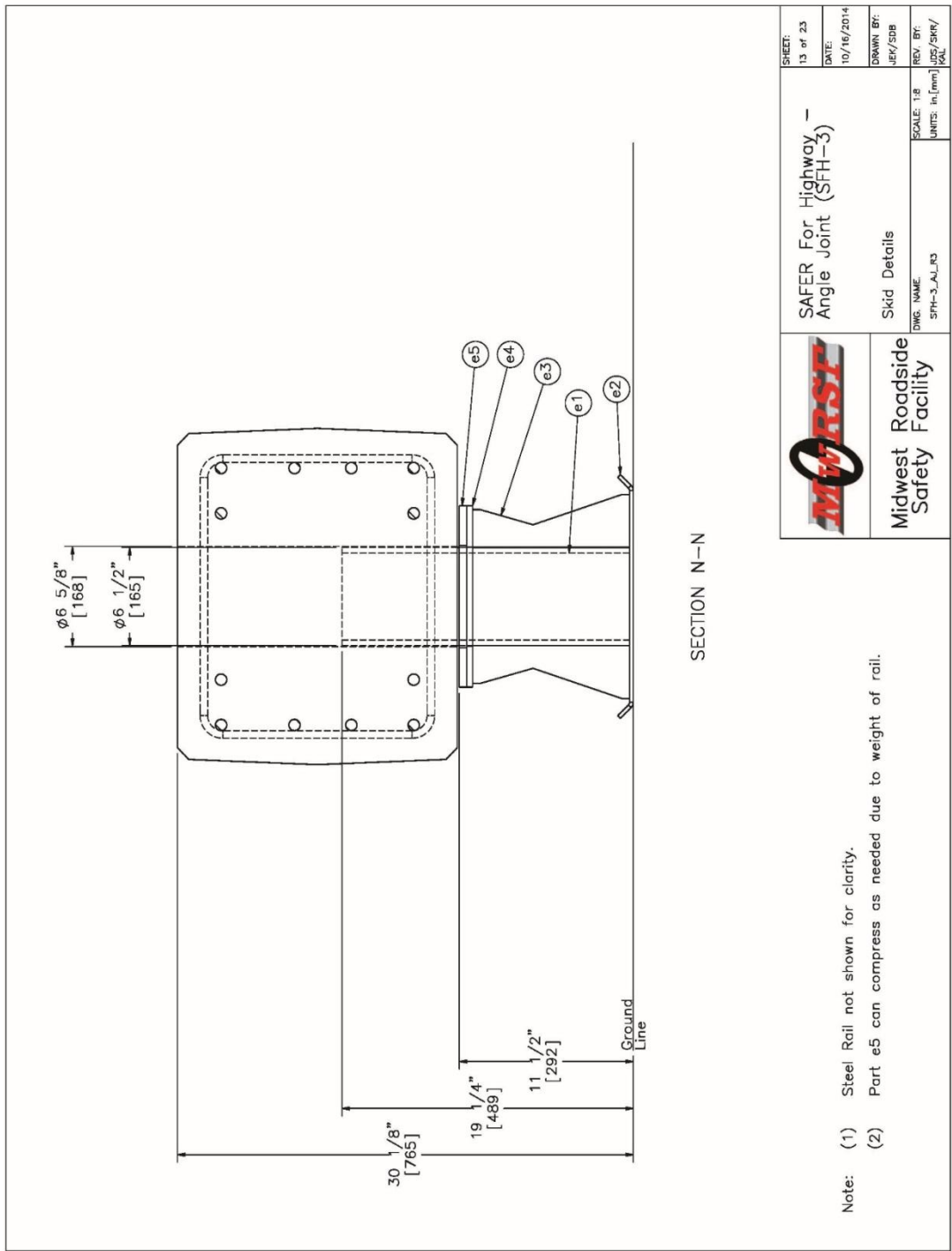


Figure B-14. Skid Details, RESTORE Barrier [20]

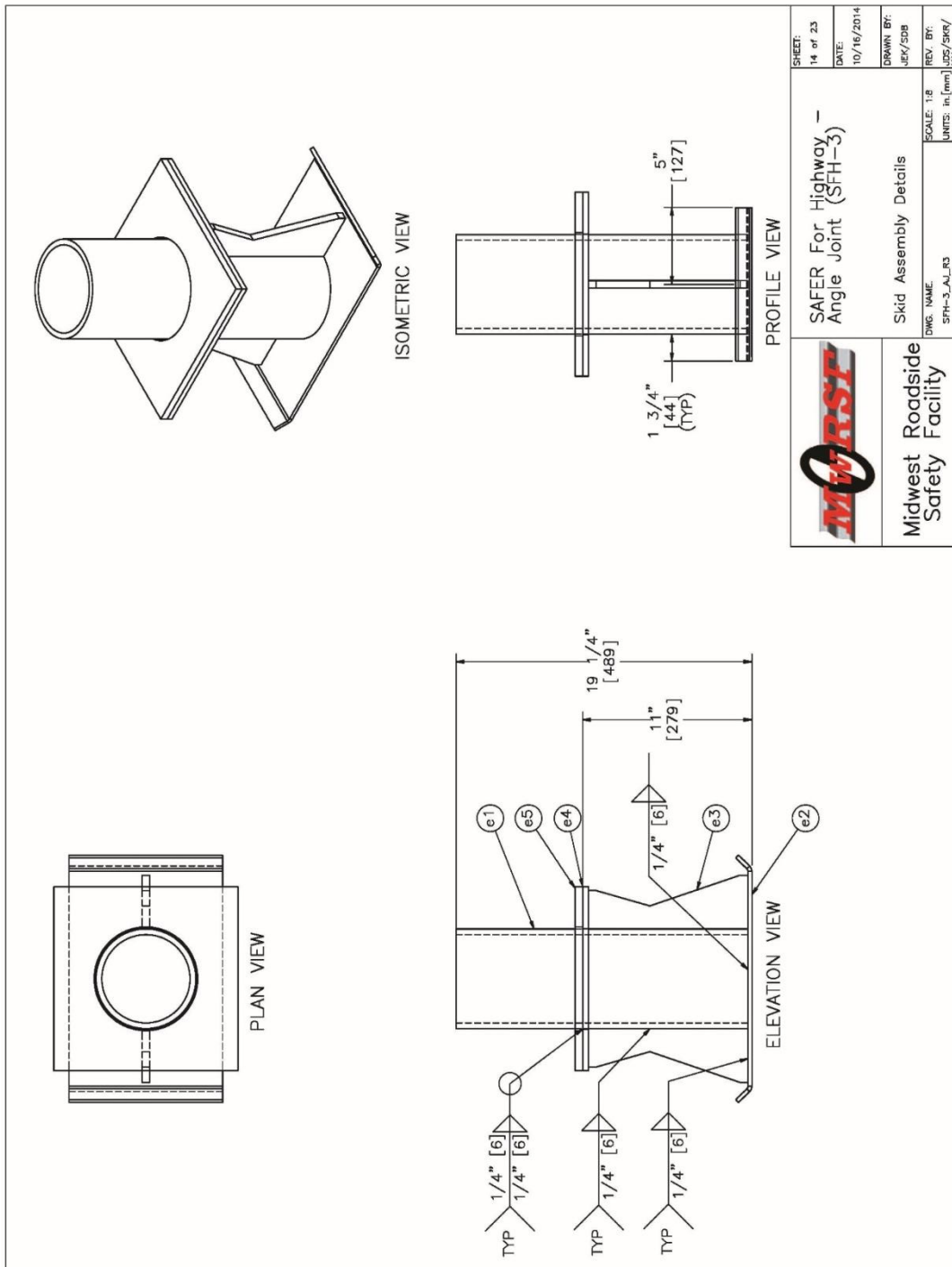


Figure B-15. Skid Assembly Details, RESTORE Barrier [20]

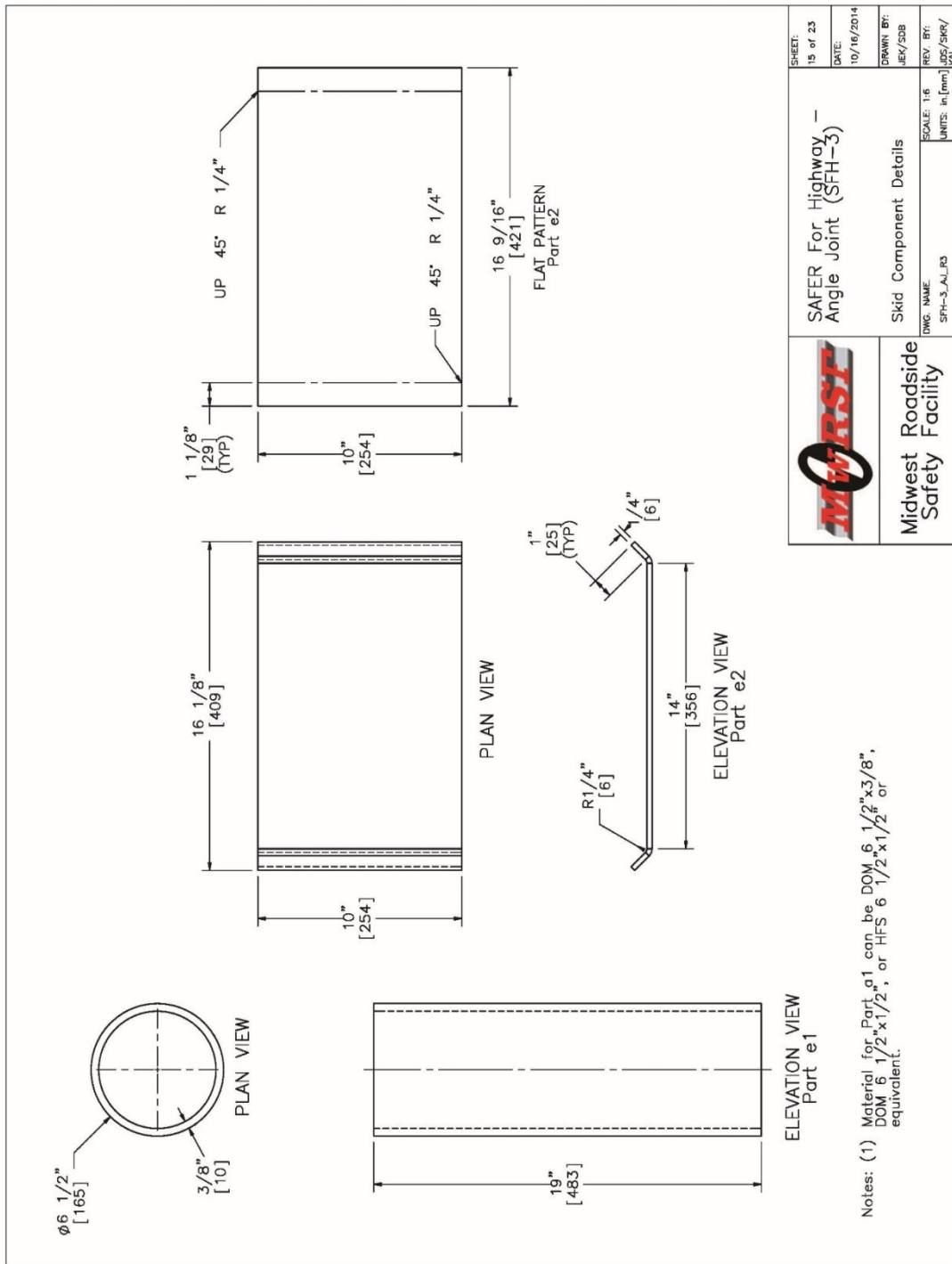


Figure B-16. Skid Component Details, RESTORE Barrier [20]

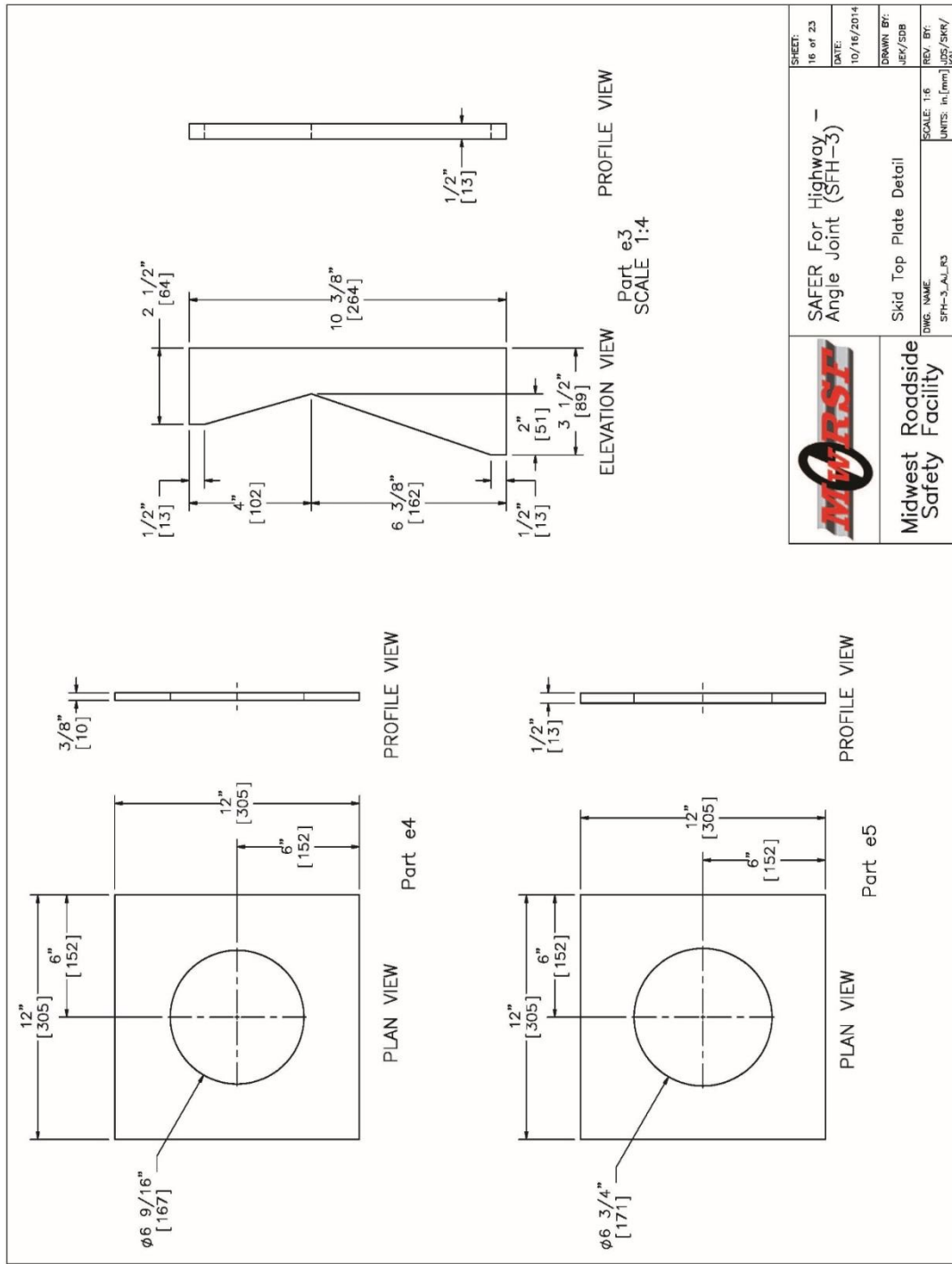


Figure B-17. Skid Top Plate Detail, RESTORE Barrier [20]

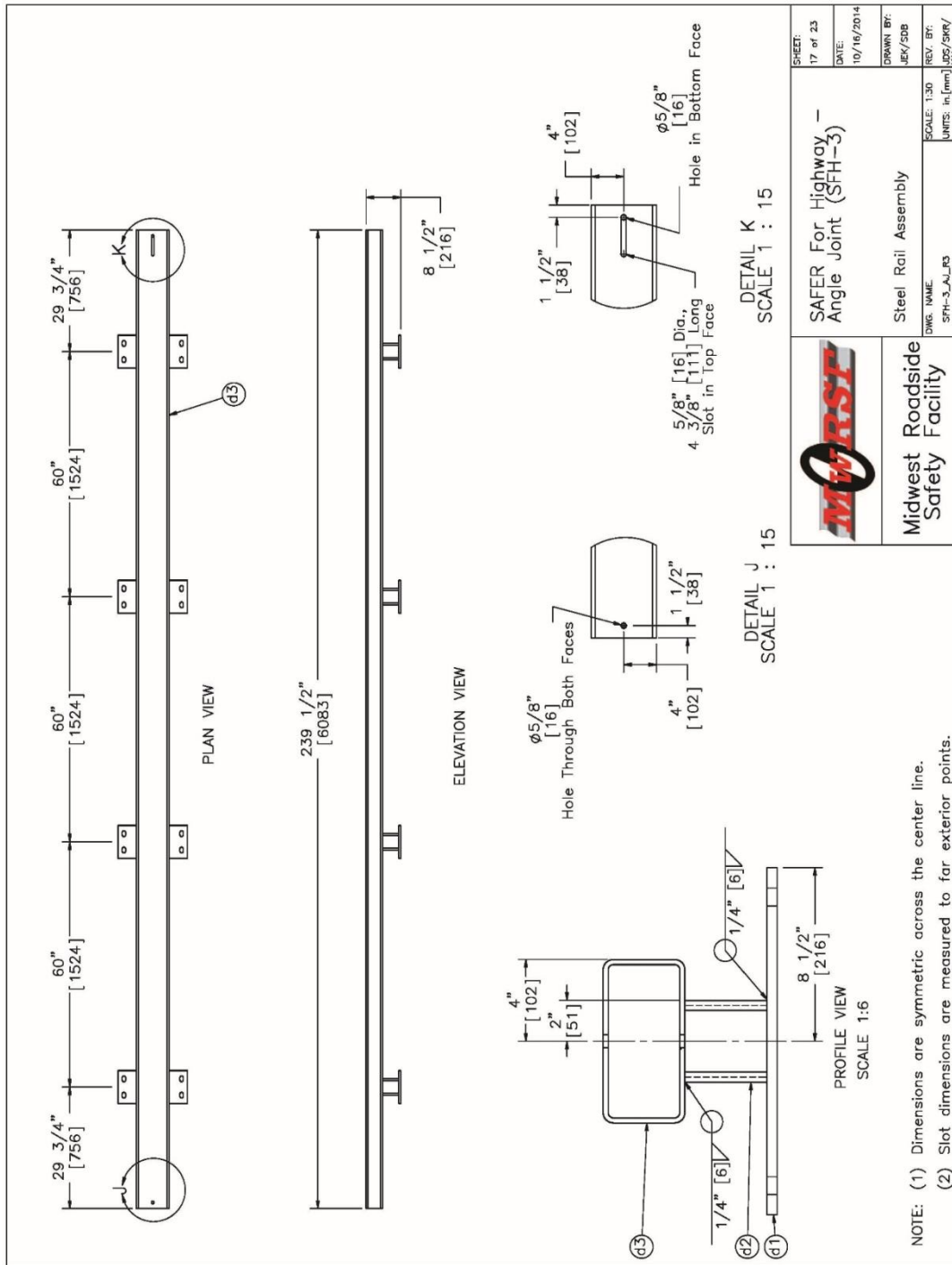


Figure B-18. Upper Tube Assembly, RESTORE Barrier [20]

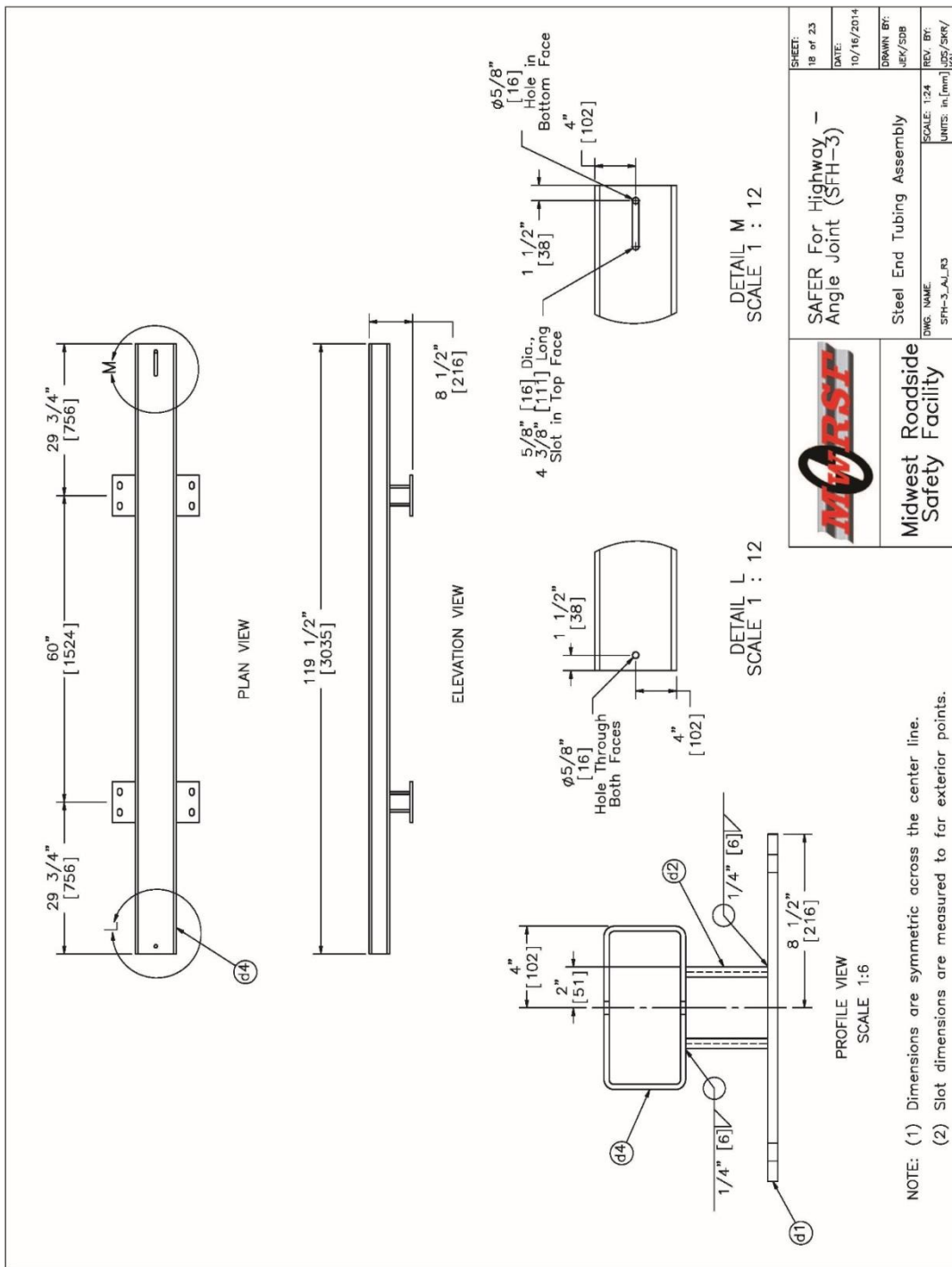


Figure B-19. Steel End Tubing Assembly, RESTORE Barrier [20]

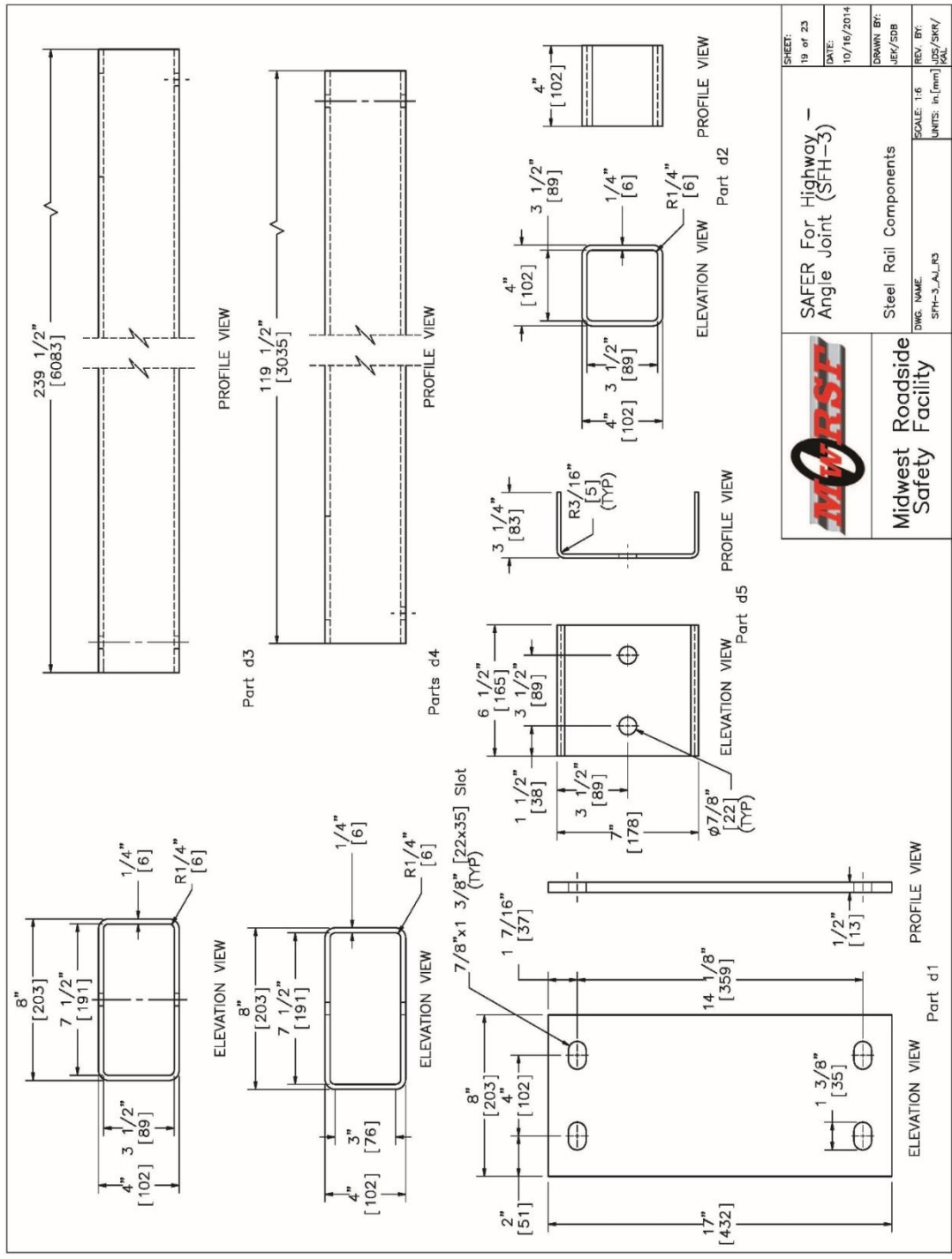


Figure B-20. Steel Tubing Components, RESTORE Barrier [20]

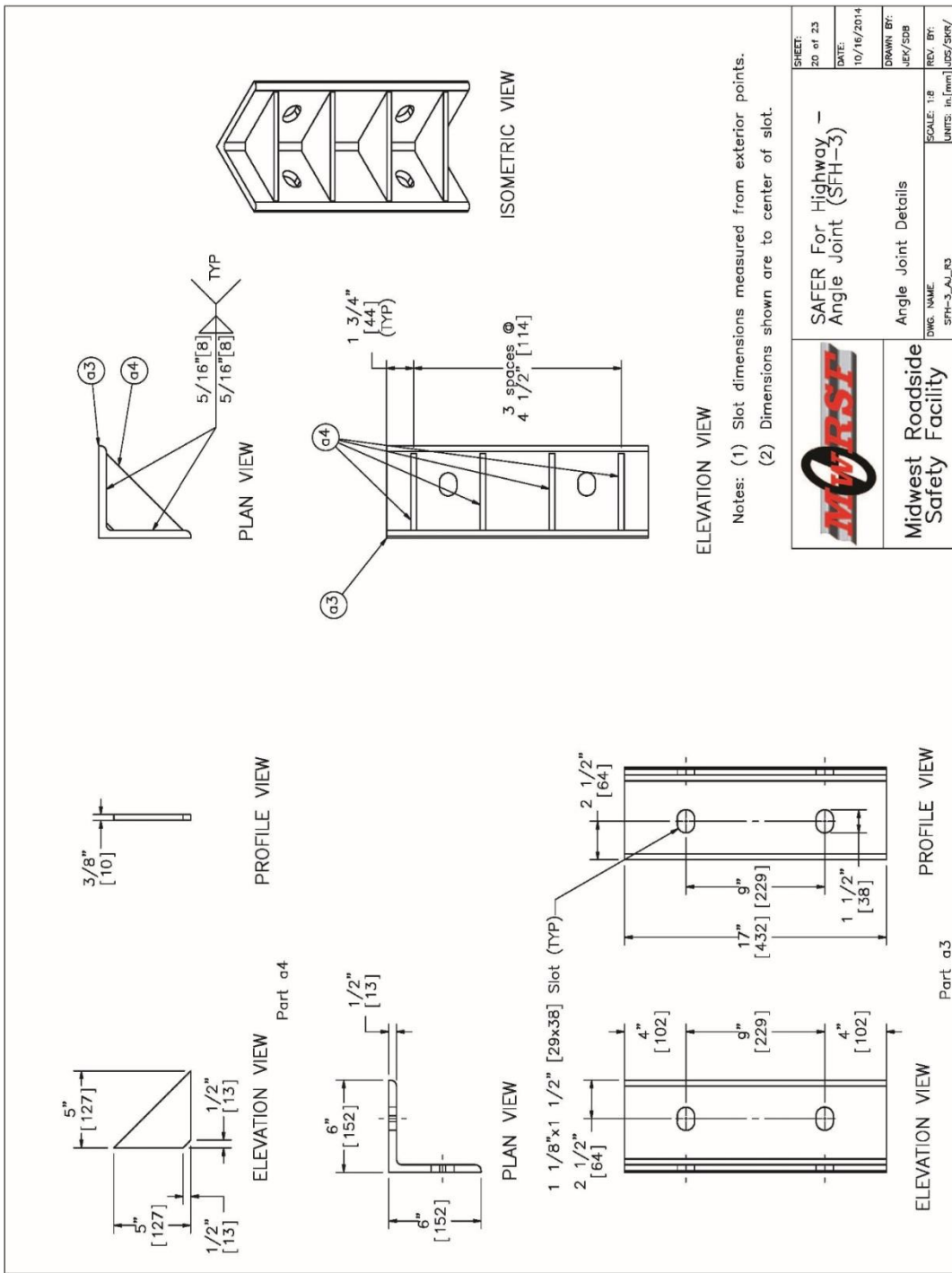


Figure B-21. Angle Joint Details, RESTORE Barrier [20]

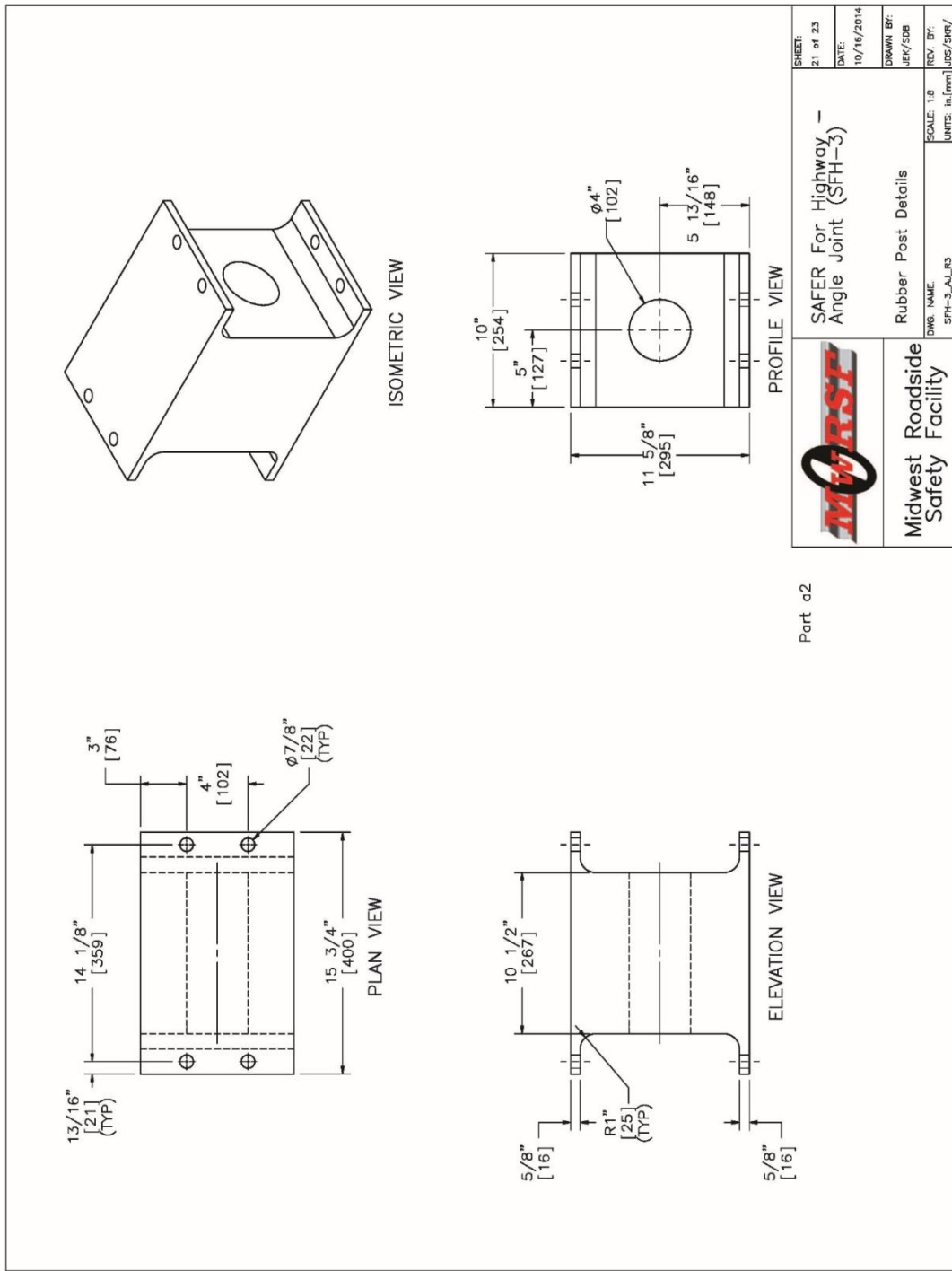


Figure B-22. Rubber Post Details, RESTORE Barrier [20]

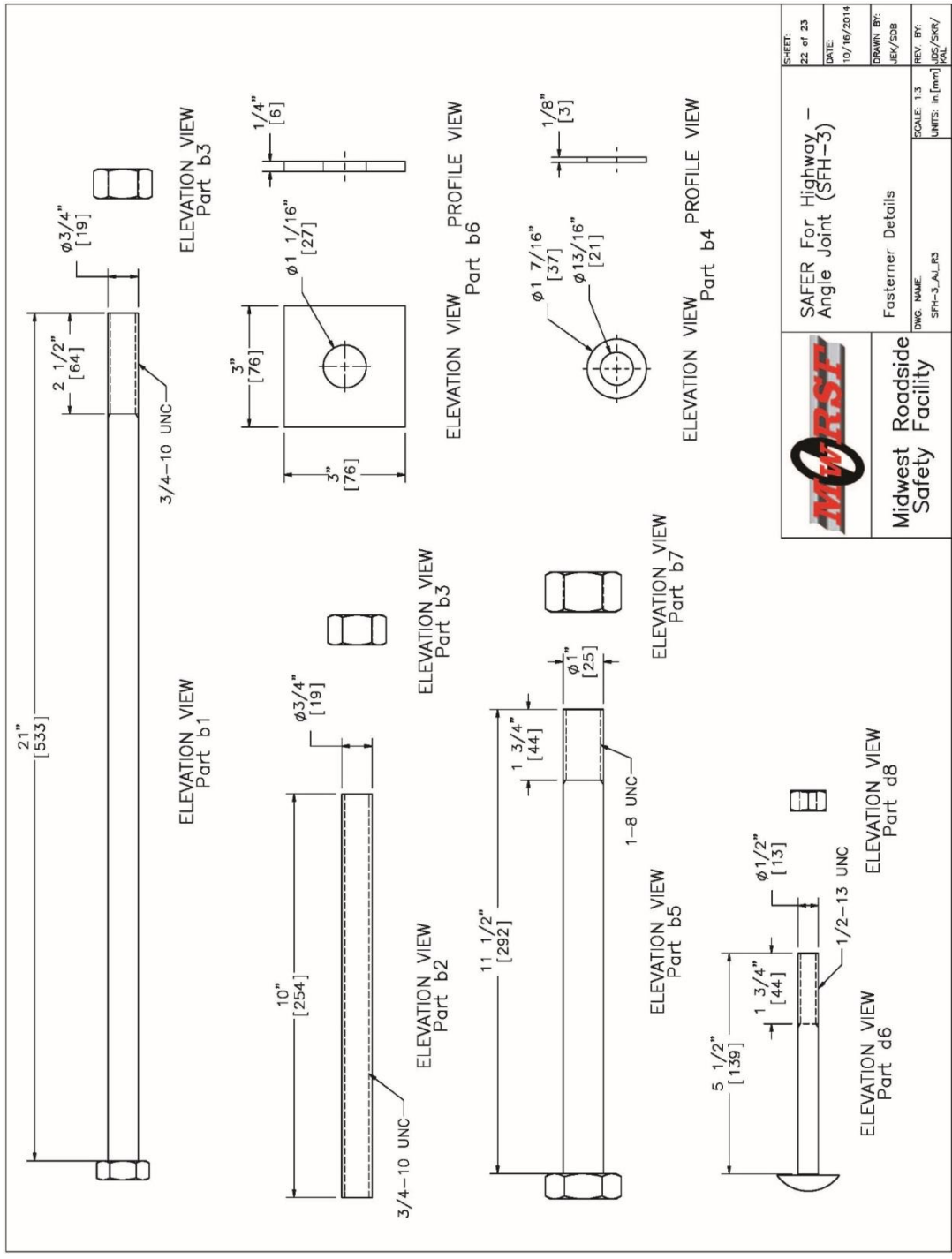



Figure B-23. Fastener Details, RESTORE Barrier [20]

Item No.	QTY.	Description	Material Specification	Hardware Guide
a1	12	Lightweight Concrete Rail	min f'c=5 ksi [34.5 MPa], density=110 pcf	-
a2	48	Morse E46496 Shear Fender	ASTM D2000	-
a3	22	6"x6"x1/2" [152x152x13], 17" [432] Long L-Bracket	A992 Galvanized	-
a4	88	5"x5"x3/8" [127x127x10] Gusset Plate	A572 Grade 50 Galvanized	-
b1	192	3/4" [19] Dia. UNC, 21" [533] Long Hex Bolt	Grade 5 Galvanized	FBX20a
b2	192	3/4" [19] Dia. UNC, 10" [254] Long Threaded Rod	ASTM A193 Grade B7 Galvanized	-
b3	384	3/4" [19] Dia. UNC Heavy Hex Nut	ASTM A194 Grade 2H Galv.	-
b4	576	3/4" [19] Dia. Flat Washer	ASTM F436 Galv.	-
b5	88	1" [25] Dia. UNC, 11 1/2" [292] Long Hex Head Bolt	ASTM A325 Galv.	FBX24b
b6	176	3"x3"x1/4" [76x76x6] Square Washer	A572 Grade 50 Galvanized	-
b7	88	1" [25] Dia. UNC Heavy Hex Nut	ASTM A563 DH Galv.	FNX24b
c1	336	1/2" [13] Dia., 77" [1956] Long Bent Rebar	A615 Grade 60	-
c2	96	1/2" [13] Dia., 49" [1245] Long Bent Rebar	A615 Grade 60	-
c3	144	3/4" [19] Dia., 231" [5867] Long Rebar	A615 Grade 60	-
c4	96	3/4" [19] Dia., 63" [1600] Long Bent Rebar	A615 Grade 60	-
c5	72	3/4" [19] Dia., 69" [1753] Long Bent Rebar	A615 Grade 60	-
d1	48	17"x8"x1/2" [431x203x13] Anchor Plate	ASTM A572 Grade 50 Galvanized	-
d2	48	4"x4"x1/4" [102x102x6], 4" [102] Long Tube	A500 Grade B Galvanized	-
d3	11	8"x4"x1/4" [203x102x6], 239 1/2" [6083] Long Tube	A500 Grade B Galvanized	-
d4	2	8"x4"x1/4" [203x102x6], 119 1/2" [3035] Long End Tube	A500 Grade B Galvanized	-
d5	12	12 3/4"x6 1/2"x3/16" [324x165x5] Bent Plate	ASTM A572 Grade 50 Galvanized	-
d6	24	1/2" [13] Dia. UNC, 5 1/2" [140] Long Dome (Round) Head Bolt	ASTM A307 Grade A Galvanized	-
d7	24	1/2" [13] Dia. Flat Washer	ASTM F844 Galvanized	FWC12a
d8	24	1/2" [13] Dia. UNC Heavy Hex Nut	A563A Galvanized	FNX12b
d9	-	Epoxy	HILTI HIT-RE500	-
e1	24	6 1/2" [165] Dia., 3/8" [10] Thick, 19" [483] Long Steel Pipe	AISI 1026	-
e2	24	16 9/16"x10"x1/4" [421x254x6] Base Plate	ASTM A572 Grade 50 Steel	-
e3	48	3 1/2"x10 3/8"x1/2" [89x264x13] Plate Gusset	ASTM A572 Grade 50 Steel	-
e4	24	12"x12"x3/8" [305x305x10] Top Plate	ASTM A572 Grade 50 Steel	-
e5	24	12"x12"x1/2" [305x305x13] EPDM Rubber Sheet	Minimum 50 durometer	-



Midwest Roadside Safety Facility

Bill of Materials

DWG. NAME: SFH-3_A1_B3
SCALE: 1:8
UNITS: in./mm

SAFER For Highway - Angle Joint (SFH-3)

SHEET: 23 of 23
DATE: 10/16/2014
DRAWN BY: JEK/SDB
REV. BY: JDE/SBK/
VAL

Figure B-24. Bill of Materials, RESTORE Barrier [20]

**Appendix C. Accelerometer and Rate Transducer Data Plots, 1100C Interior
Simulation**

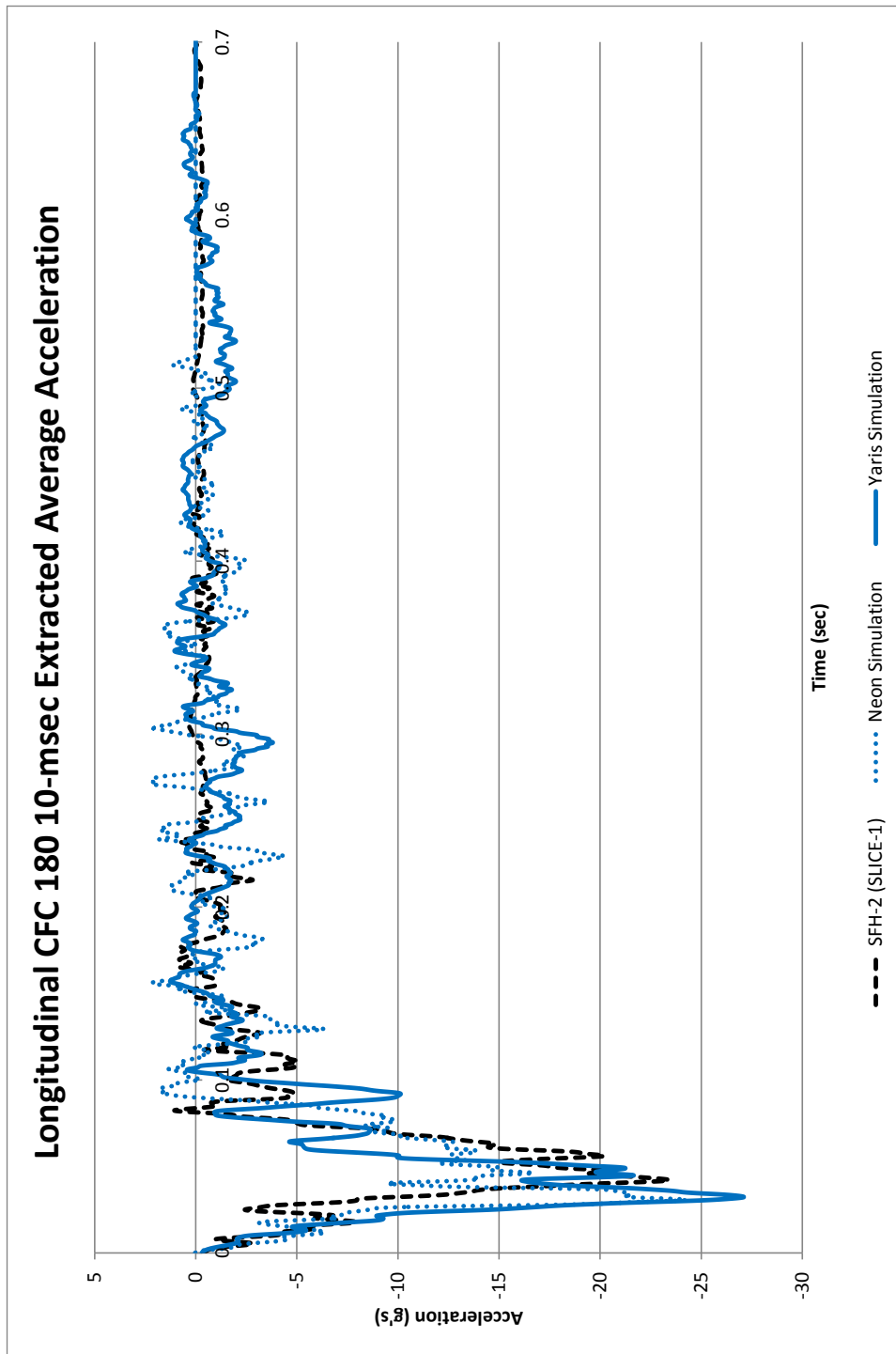


Figure C-1. 10-ms Average Longitudinal Deceleration Comparison, 1100C Vehicles

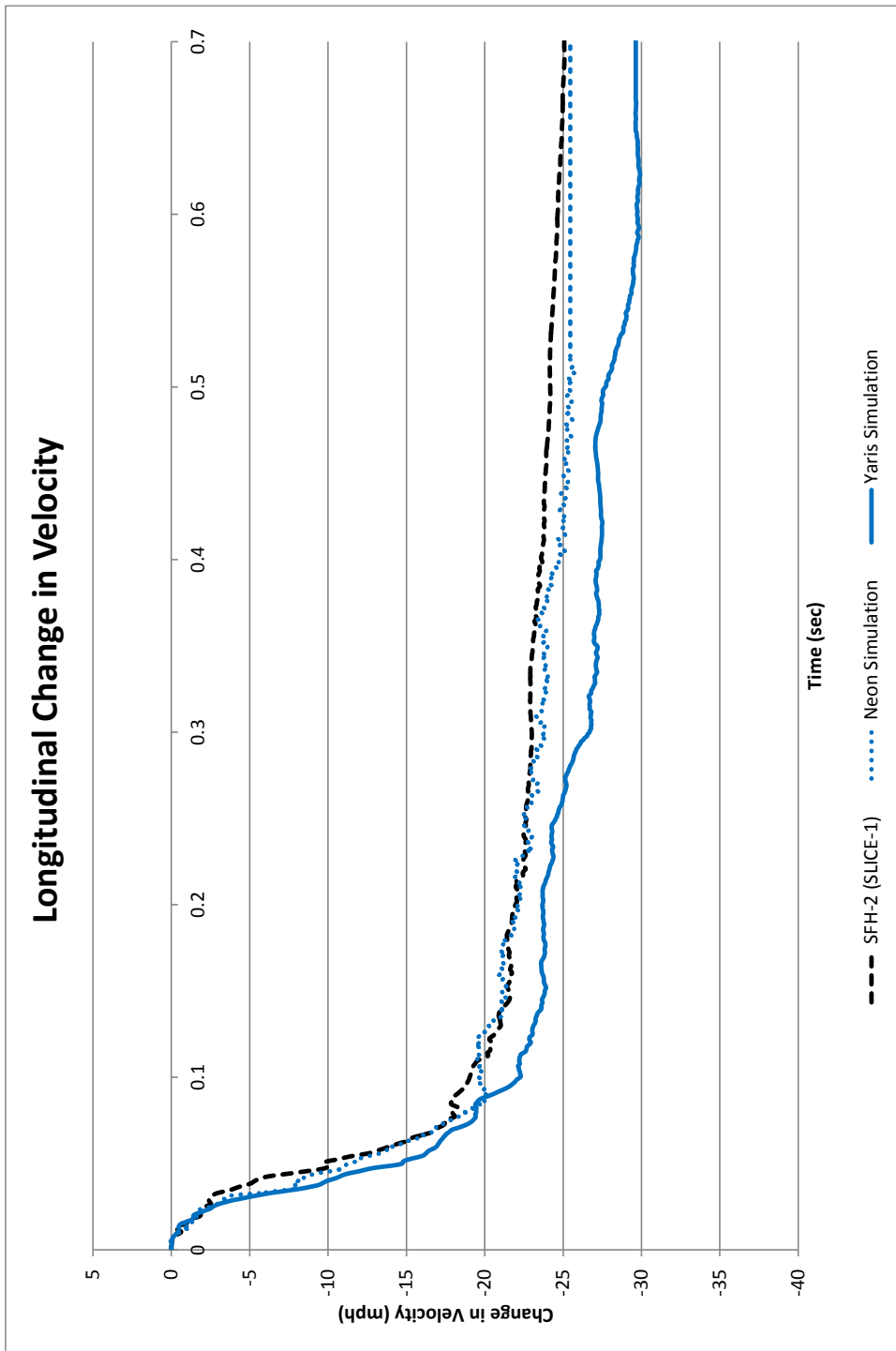


Figure C-2. Longitudinal Occupant Impact Velocity Comparison, 1100C Vehicles

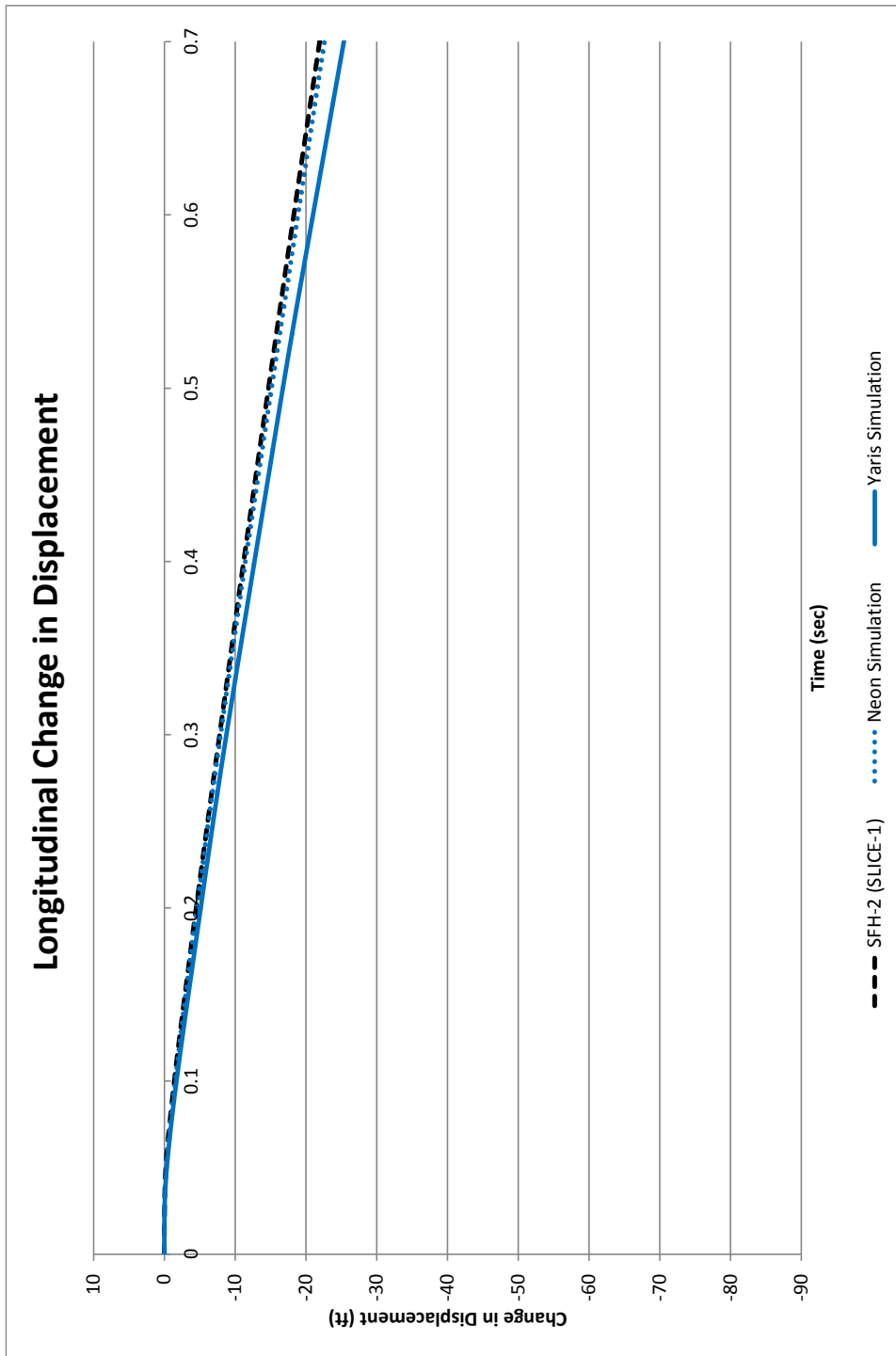


Figure C-3. Longitudinal Occupant Displacement Comparison, 1100C Vehicles

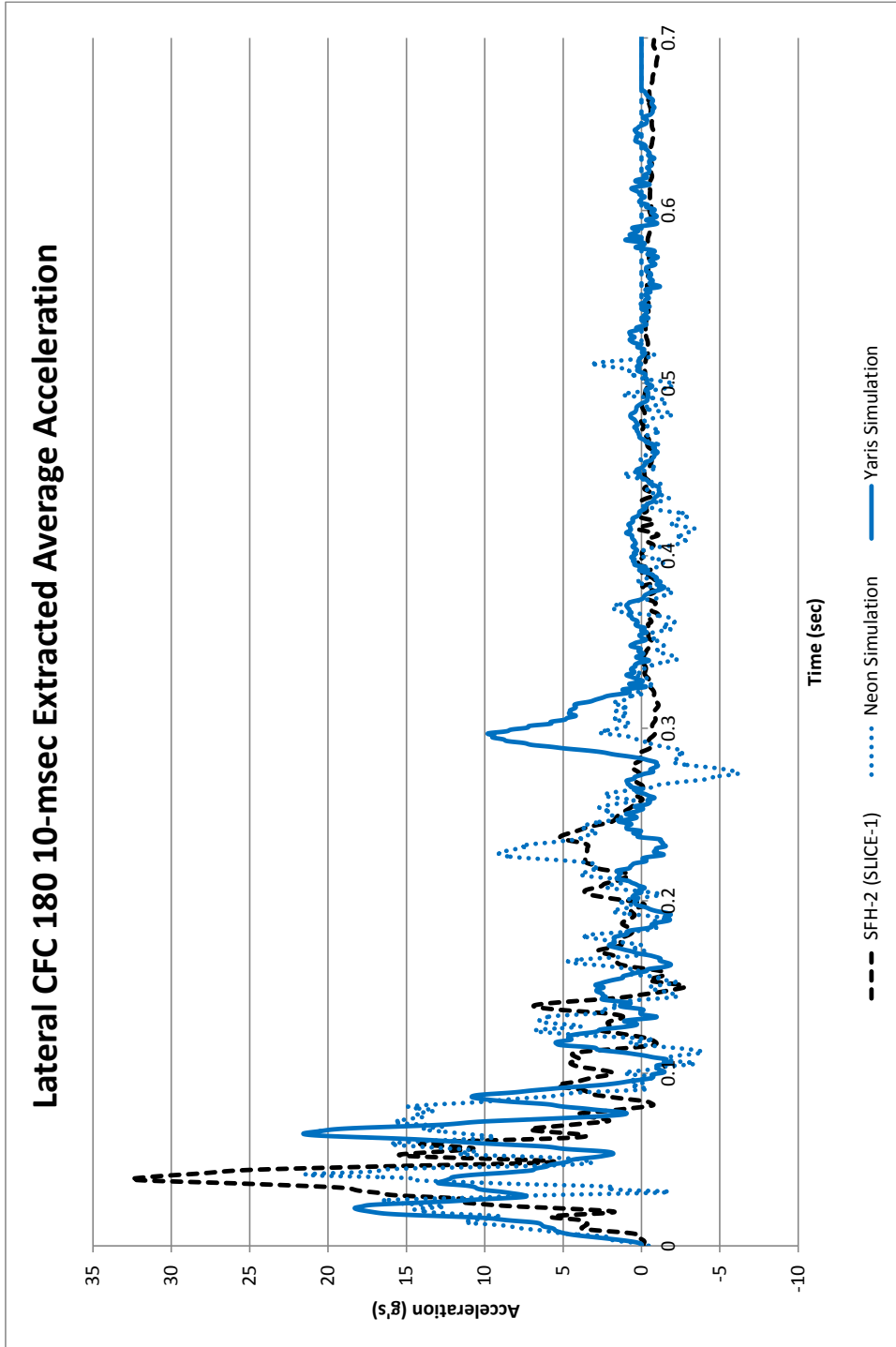


Figure C-4. 10-ms Average Lateral Deceleration Comparison, 1100C Vehicles

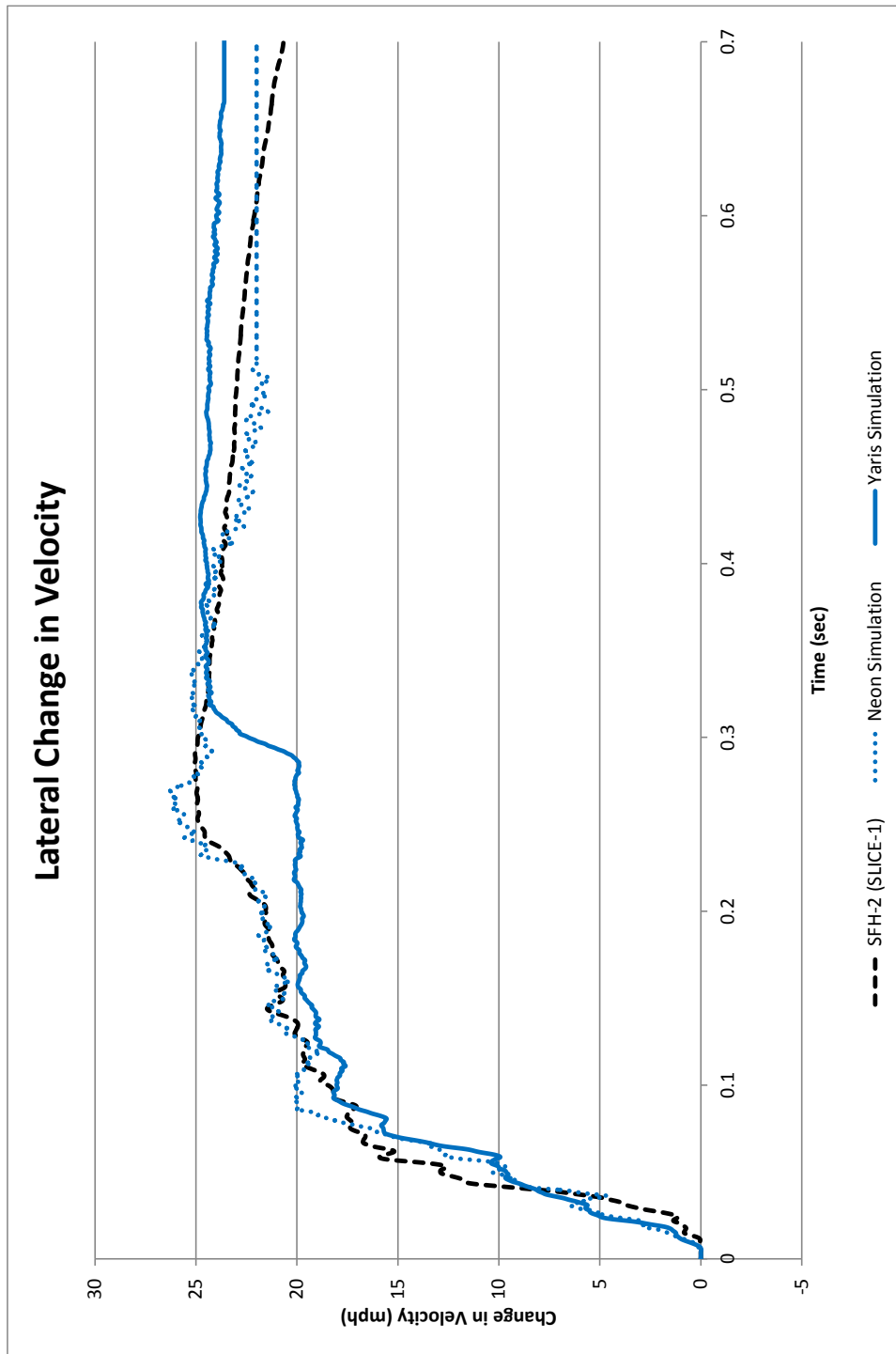


Figure C-5. Lateral Occupant Impact Velocity Comparison, 1100C Vehicles

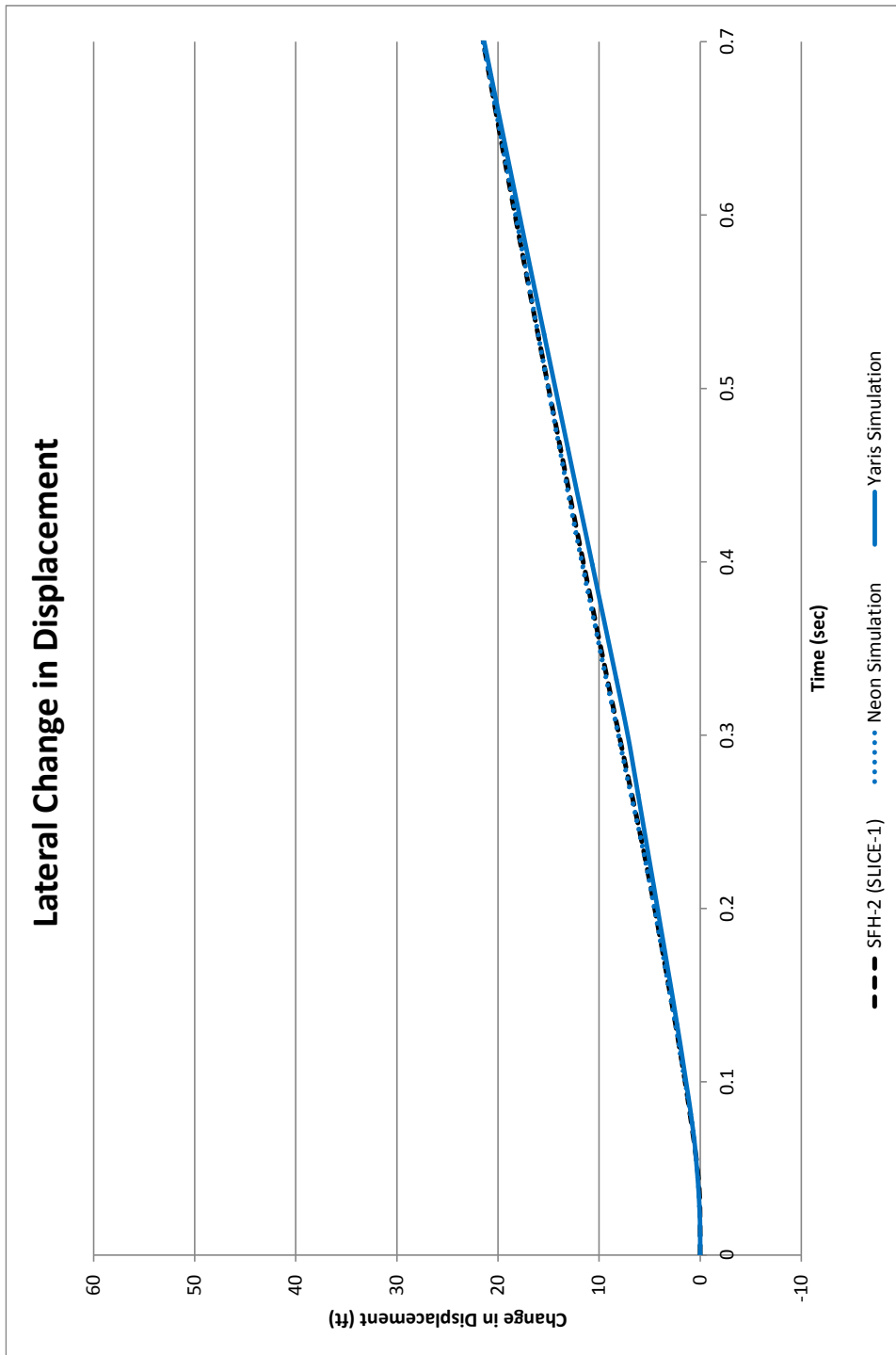


Figure C-6. Lateral Occupant Displacement Comparison, 1100C Vehicles

Appendix D. Accelerometer and Rate Transducer Data Plots, 2270P Interior Simulation

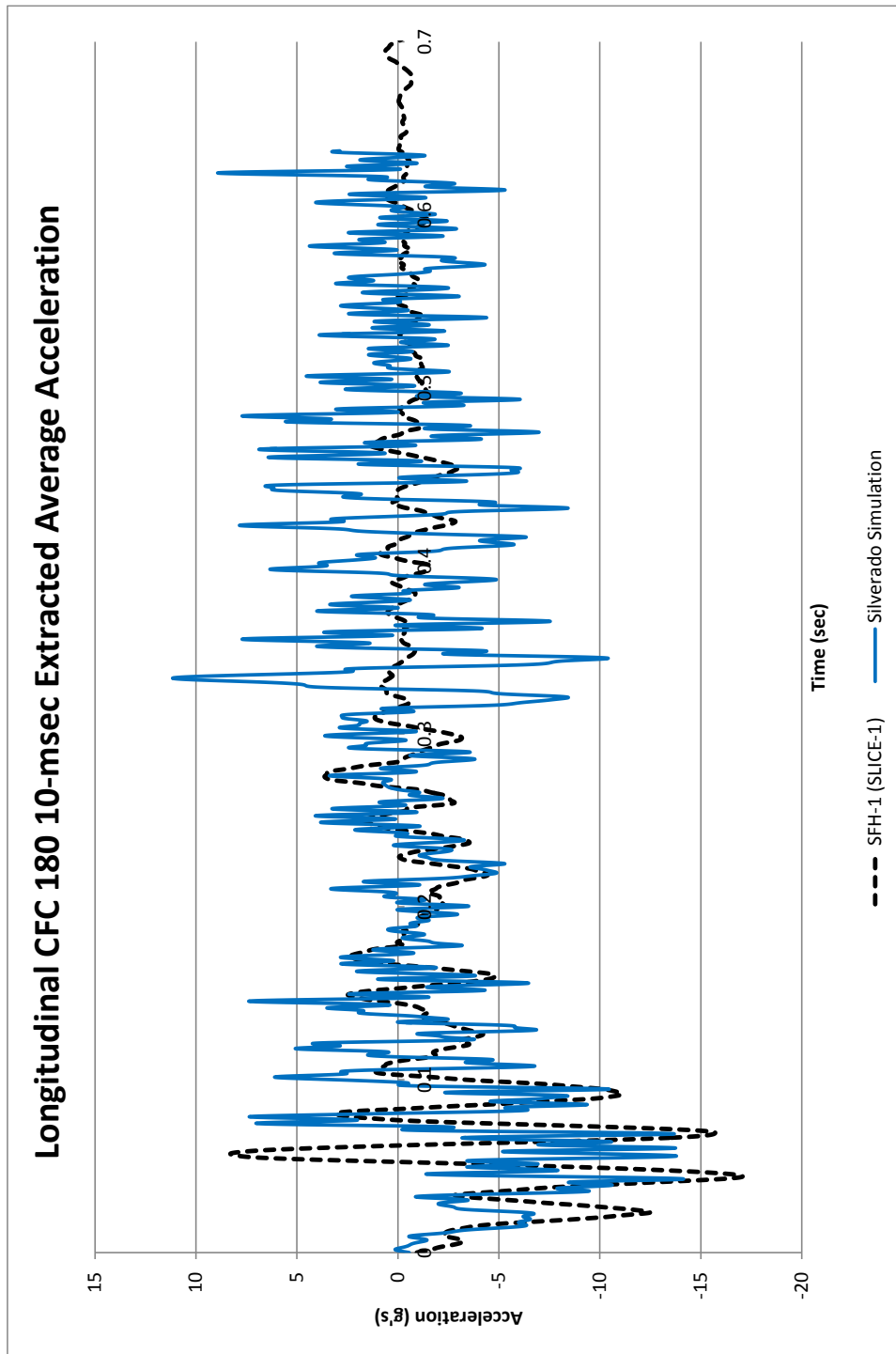


Figure D-1. 10-ms Average Longitudinal Deceleration Comparison, 2270P Vehicles

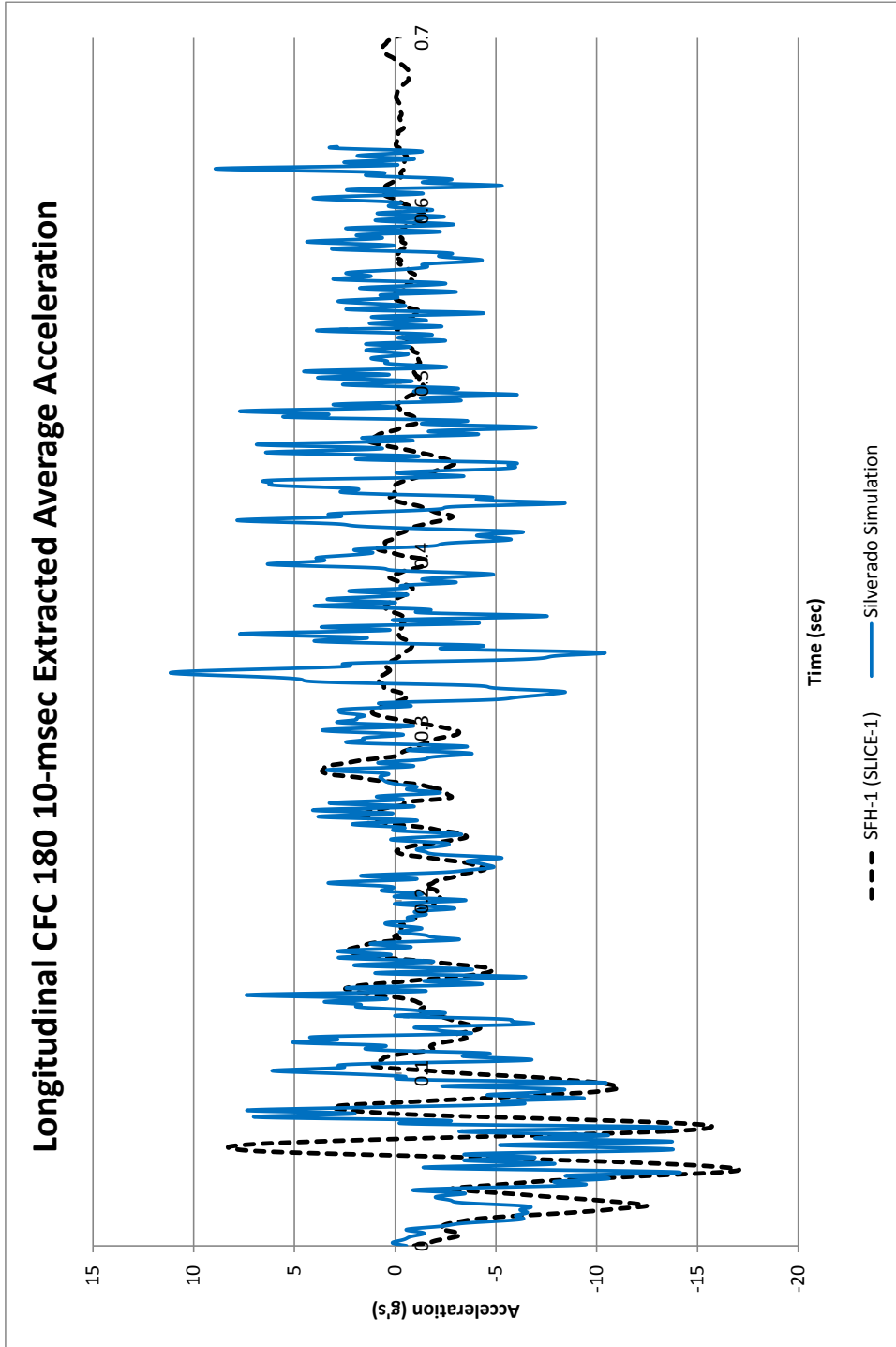


Figure D-2. 10-ms Average Longitudinal Deceleration Comparison, 2270P Vehicles

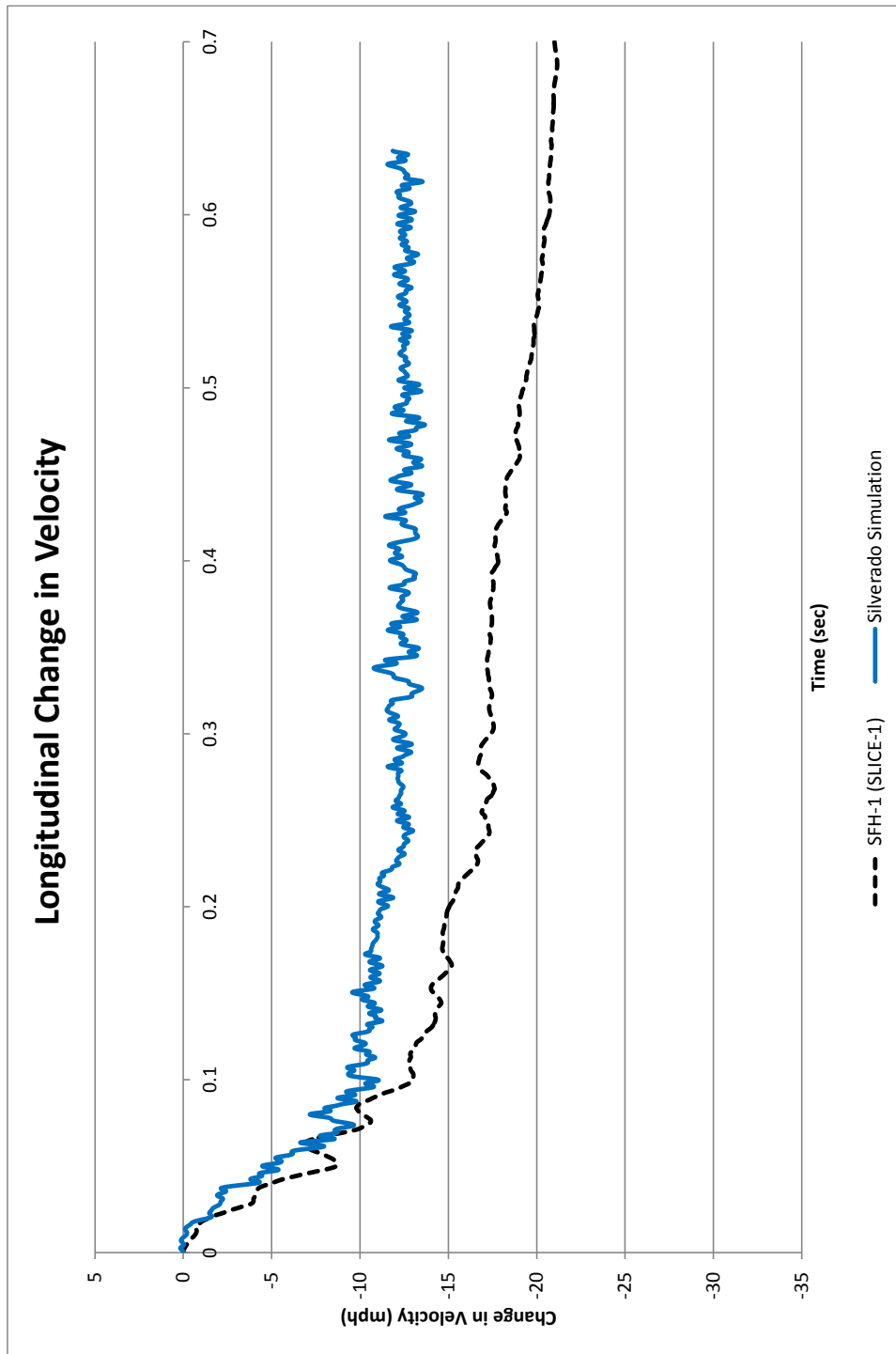


Figure D-3. Longitudinal Occupant Impact Velocity Comparison, 2270P Vehicles

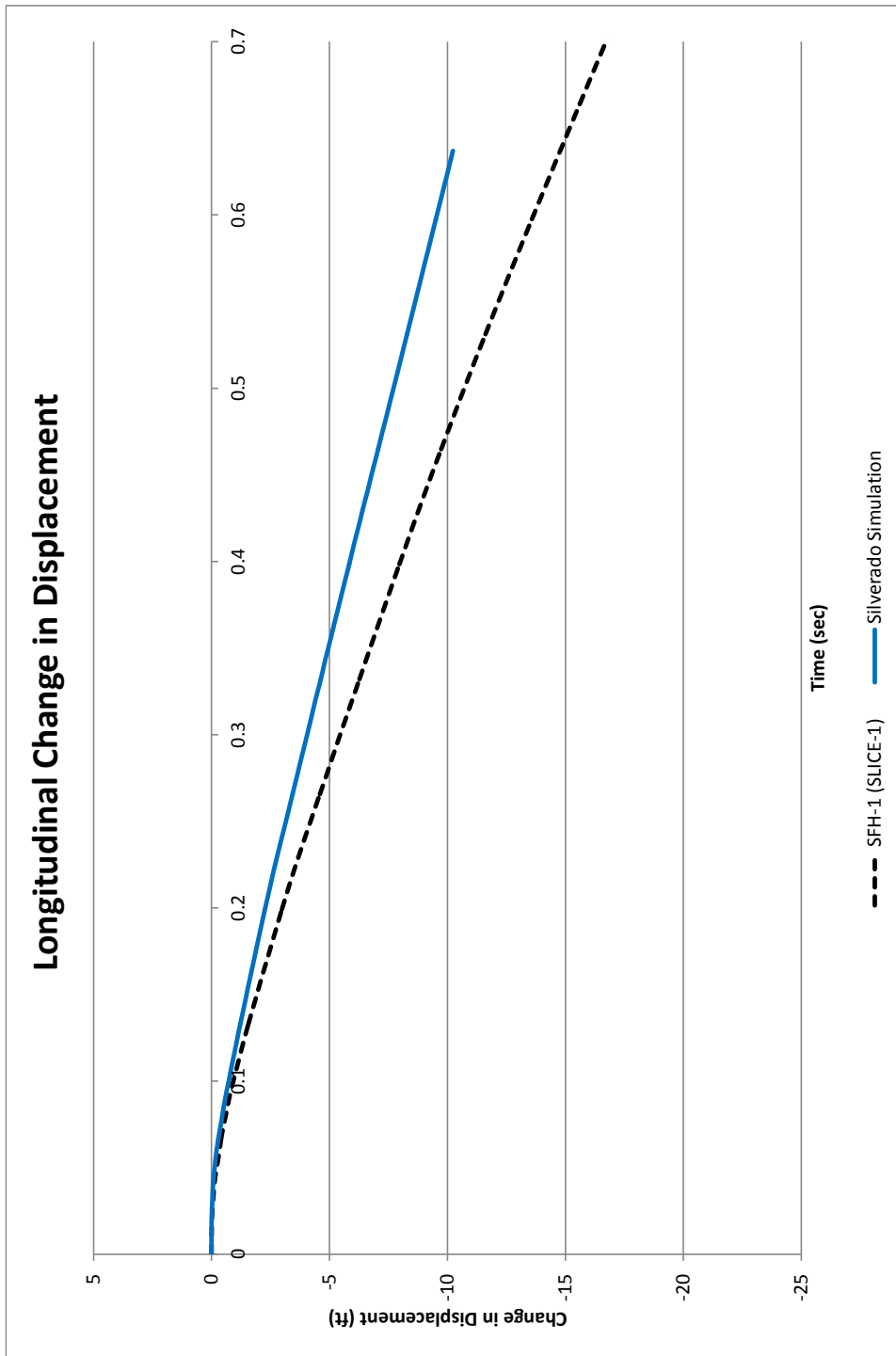


Figure D-4. Longitudinal Occupant Displacement Comparison, 2270P Vehicles

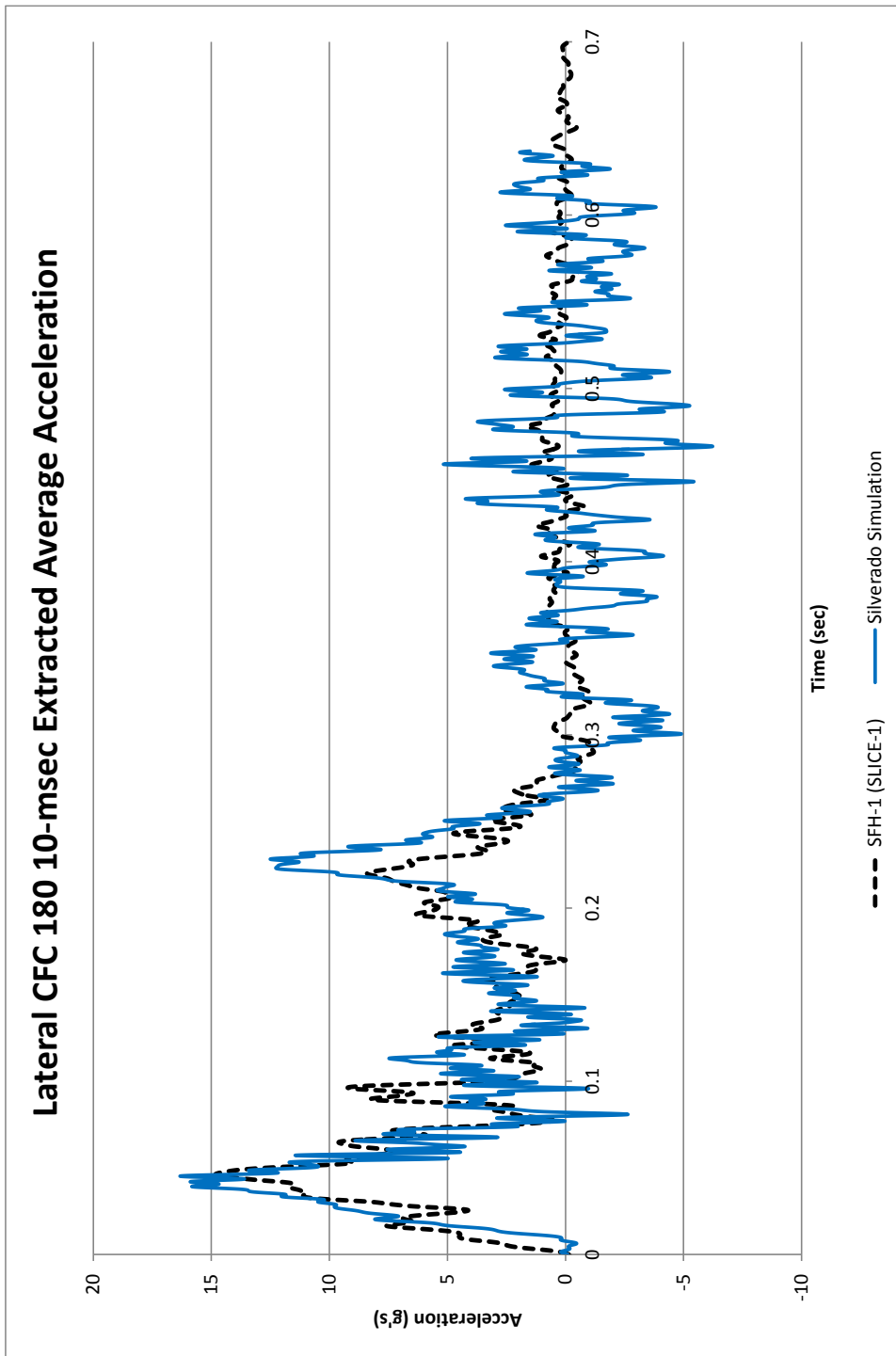


Figure D-5. 10-ms Average Lateral Deceleration Comparison, 2270P Vehicles

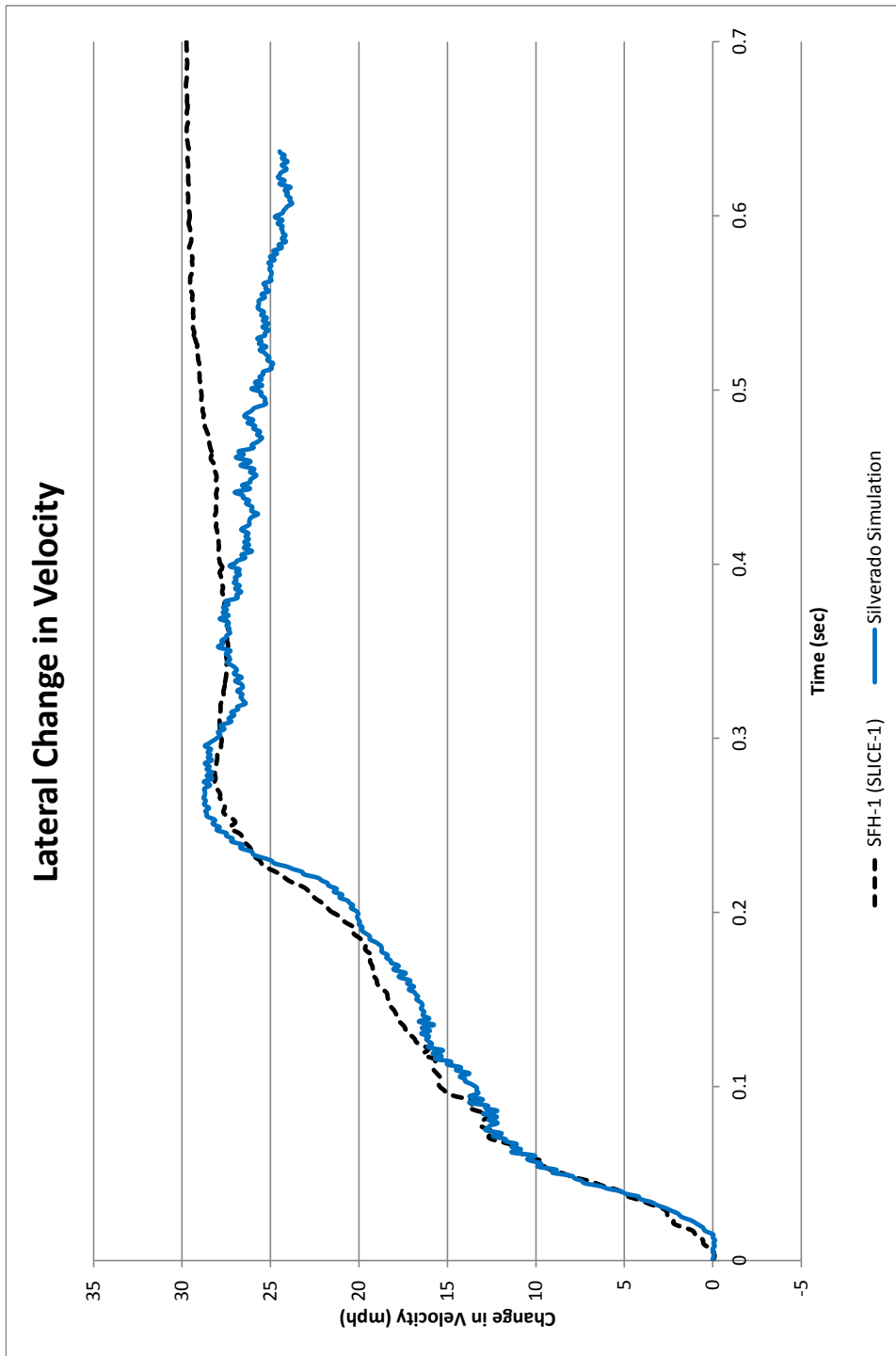


Figure D-6. Lateral Occupant Impact Velocity Comparison, 2270P Vehicles

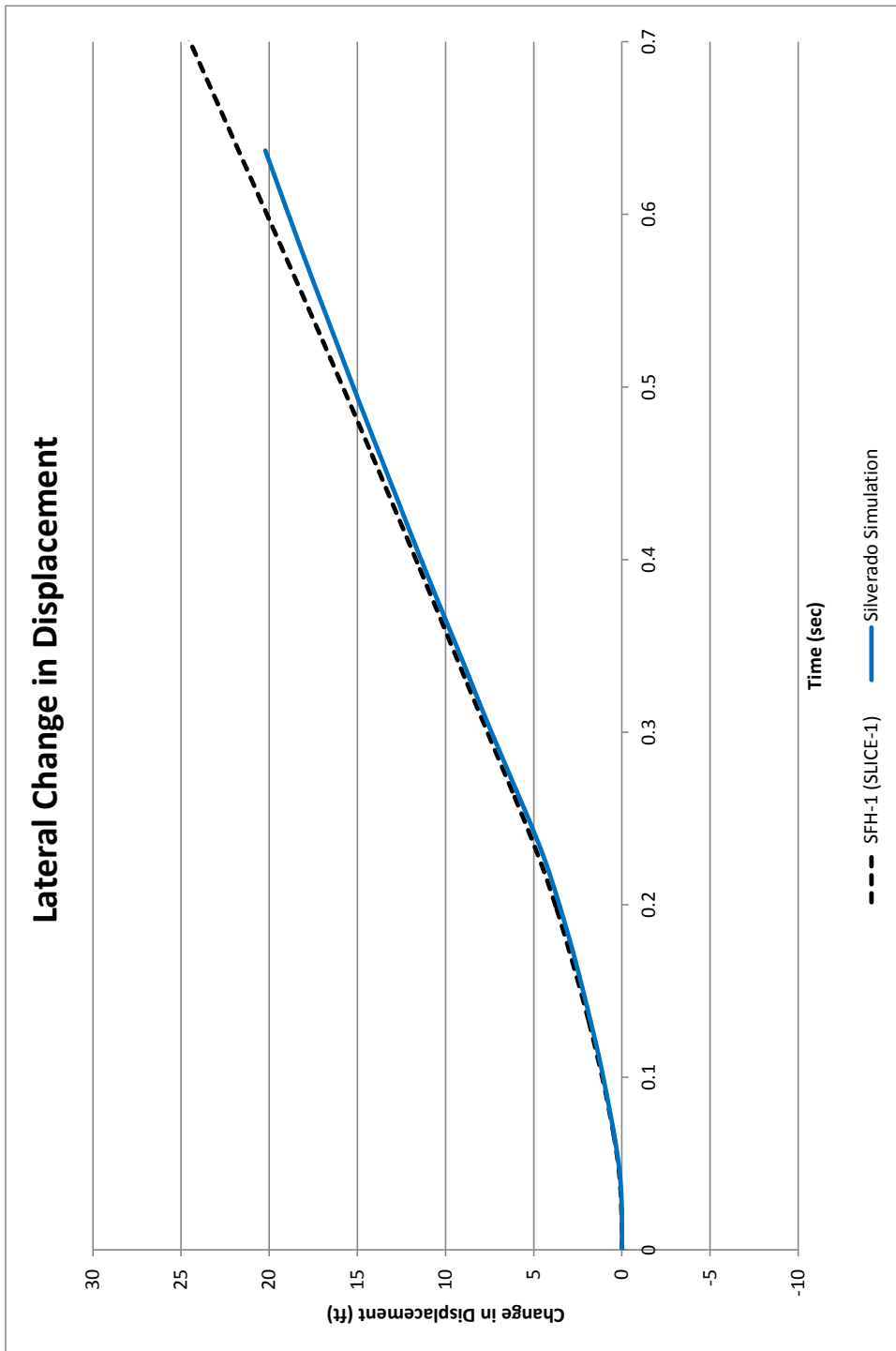


Figure D-7. Lateral Occupant Displacement Comparison, 2270P Vehicles

Appendix E. Accelerometer and Rate Transducer Data Plots, 1000S Interior Simulation

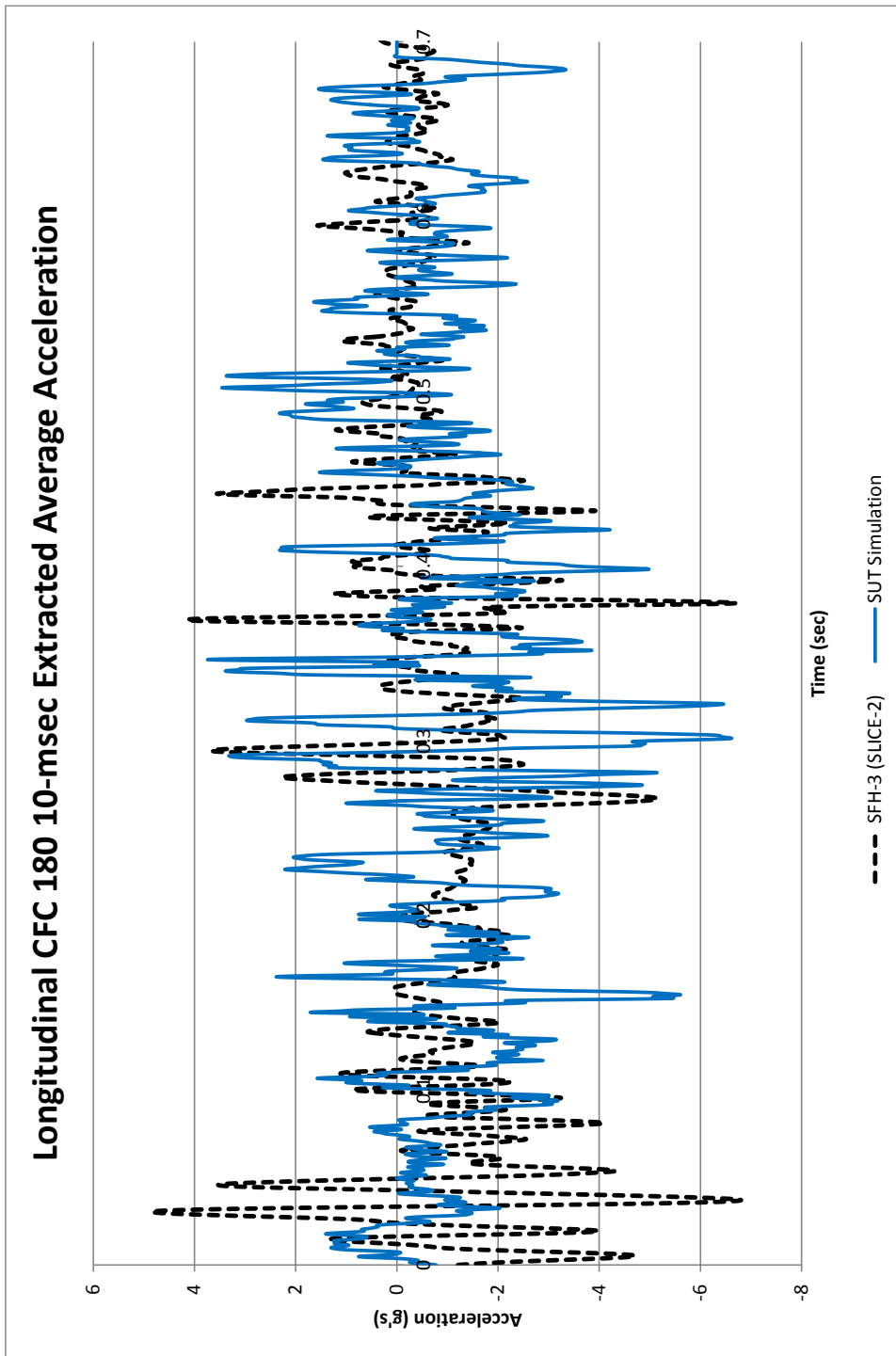


Figure E-1. 10-ms Average Longitudinal Deceleration Comparison, 10000S Vehicles

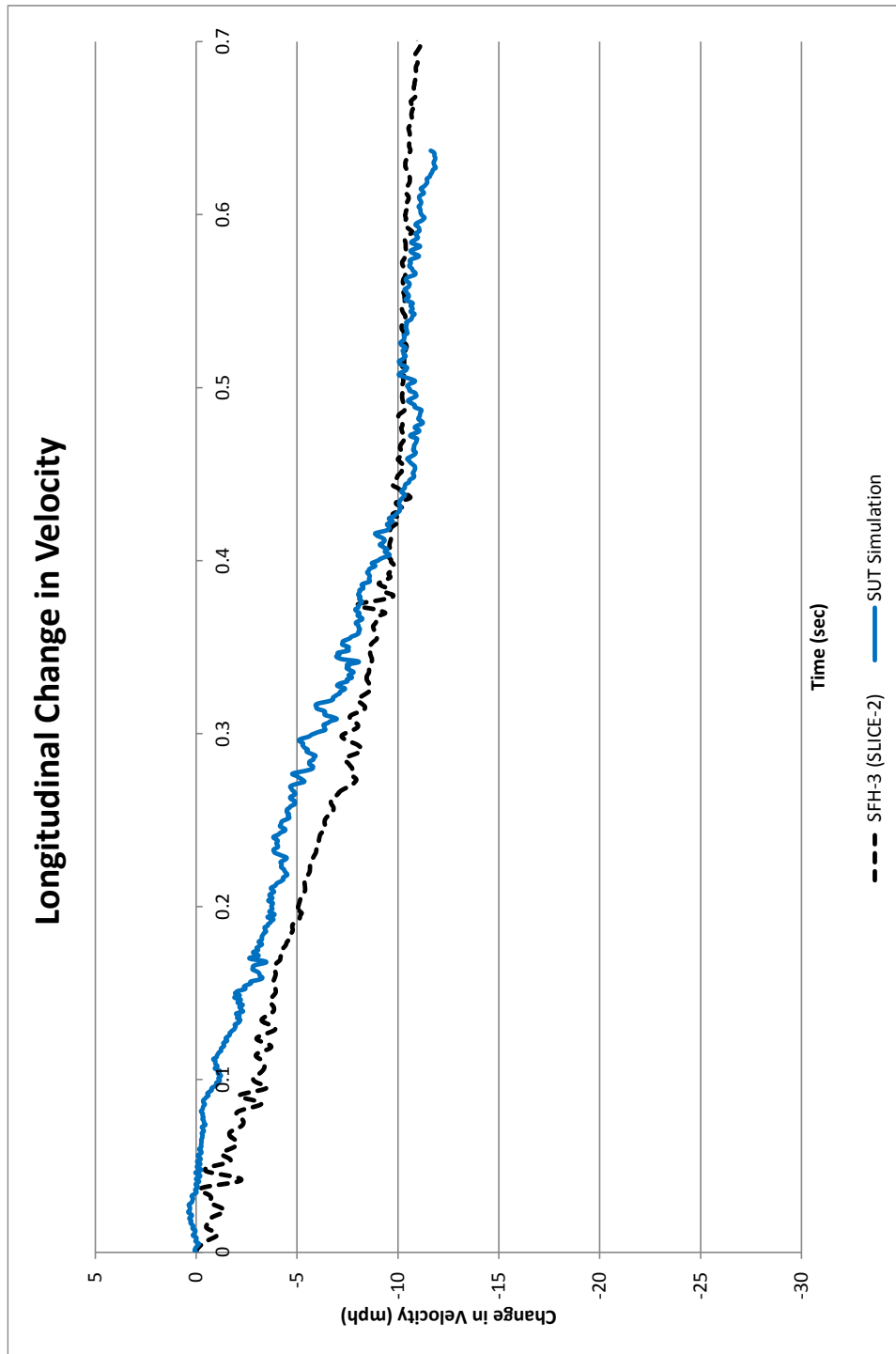


Figure E-2. Longitudinal Occupant Impact Velocity Comparison, 1000S Vehicles

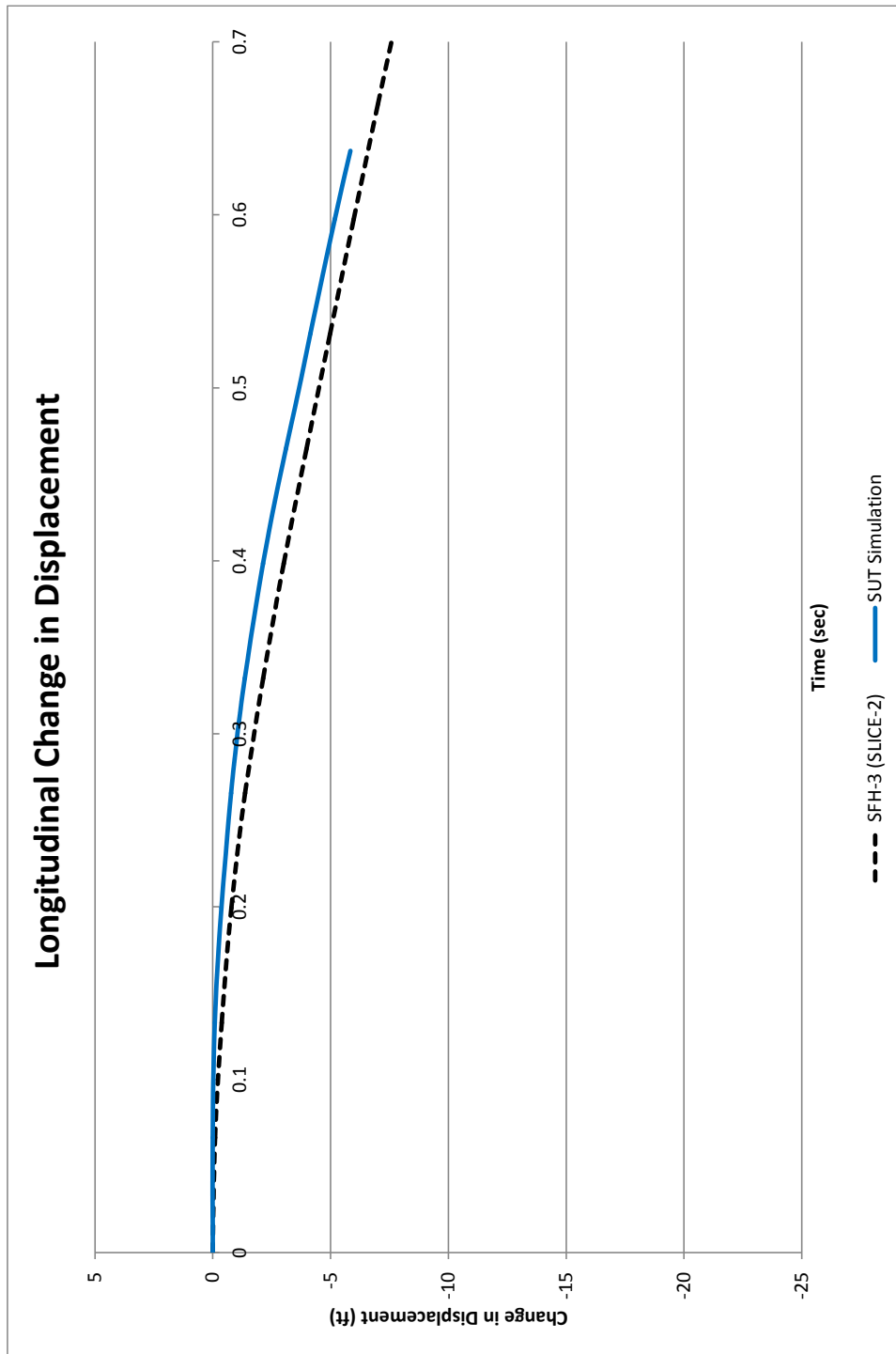


Figure E-3. Longitudinal Occupant Displacement Comparison, 10000S Vehicles

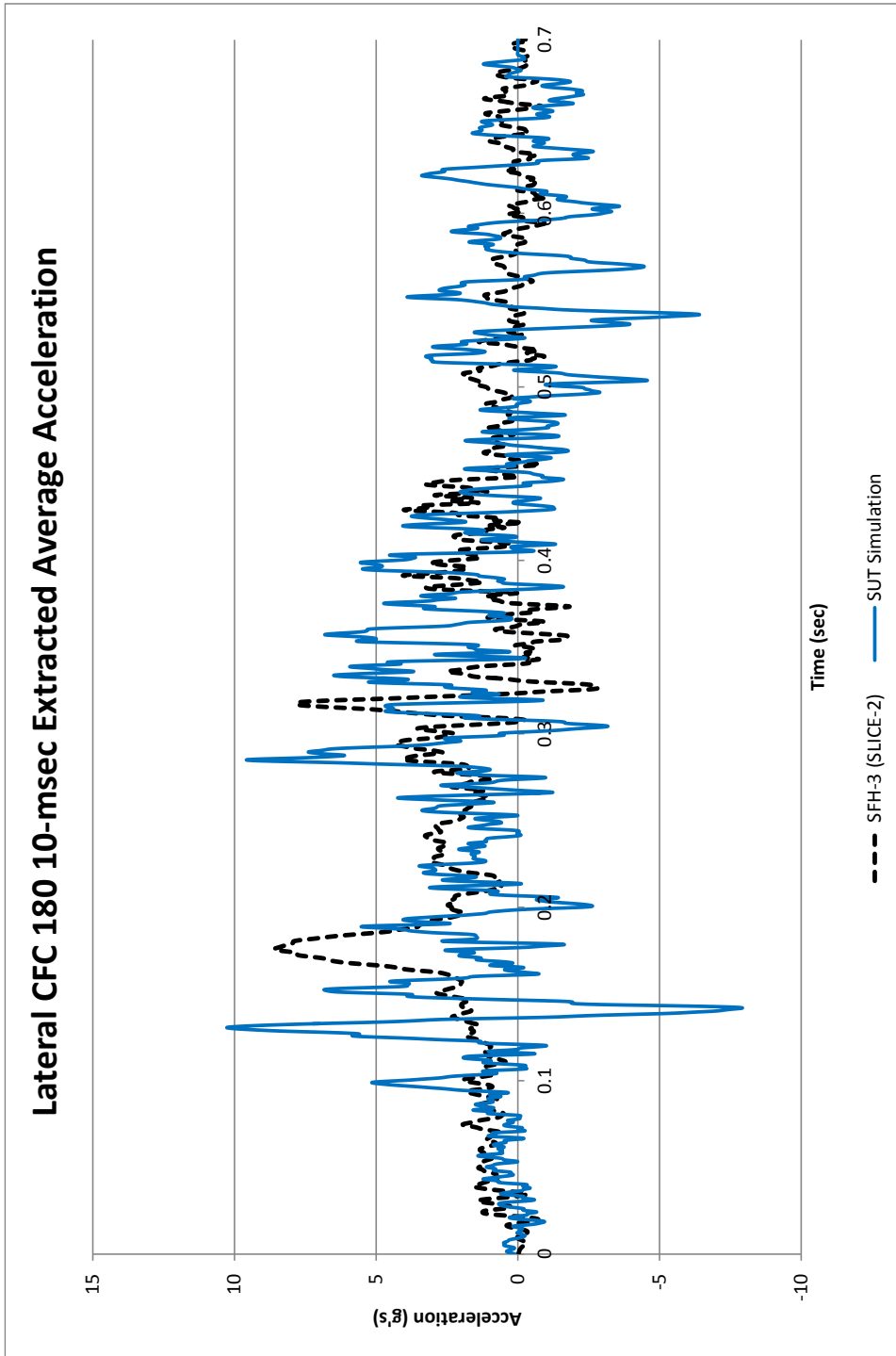


Figure E-4. 10-ms Average Lateral Deceleration Comparison, 10000S Vehicles

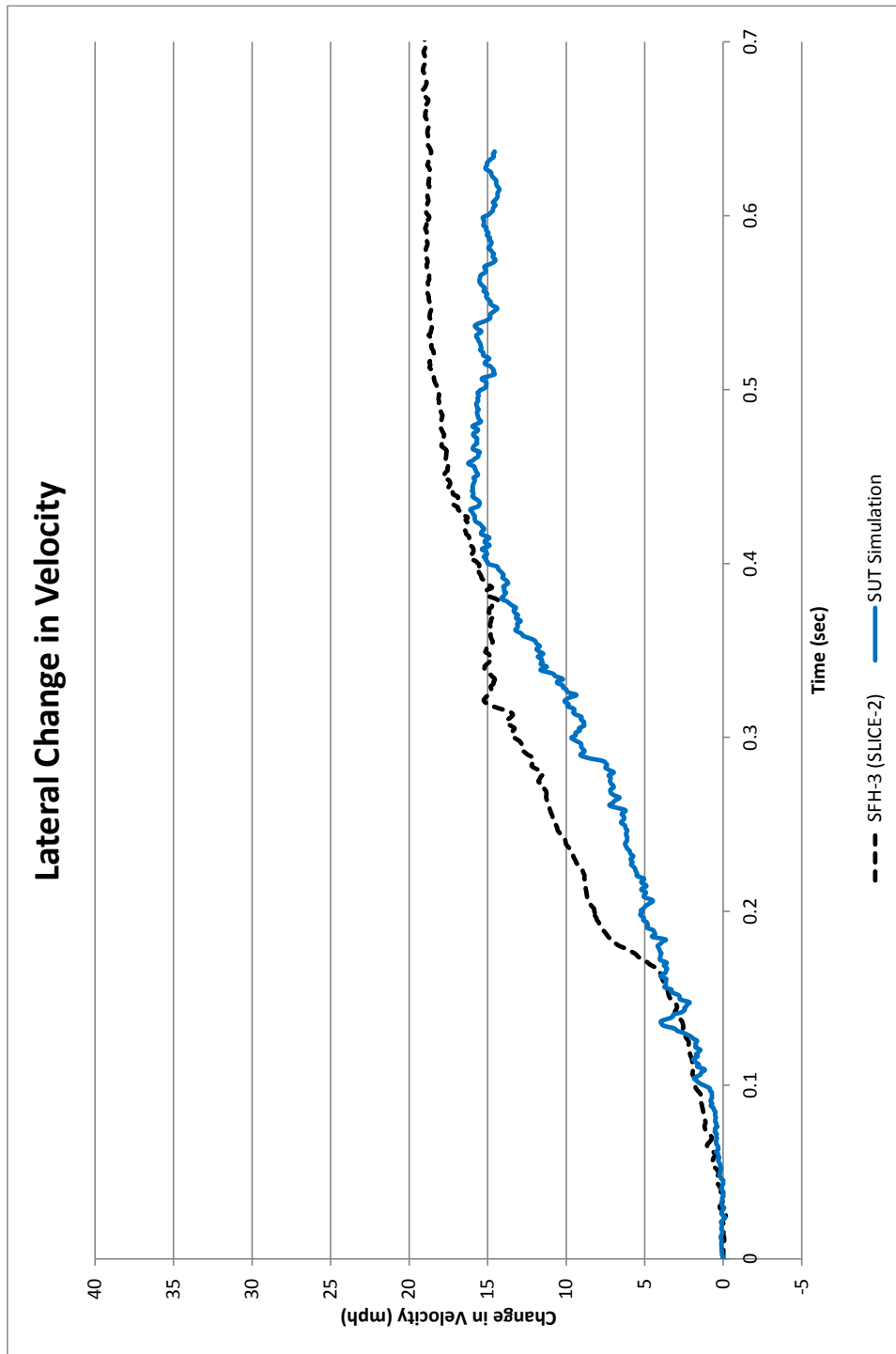


Figure E-5. Lateral Occupant Impact Velocity Comparison, 10000S Vehicles

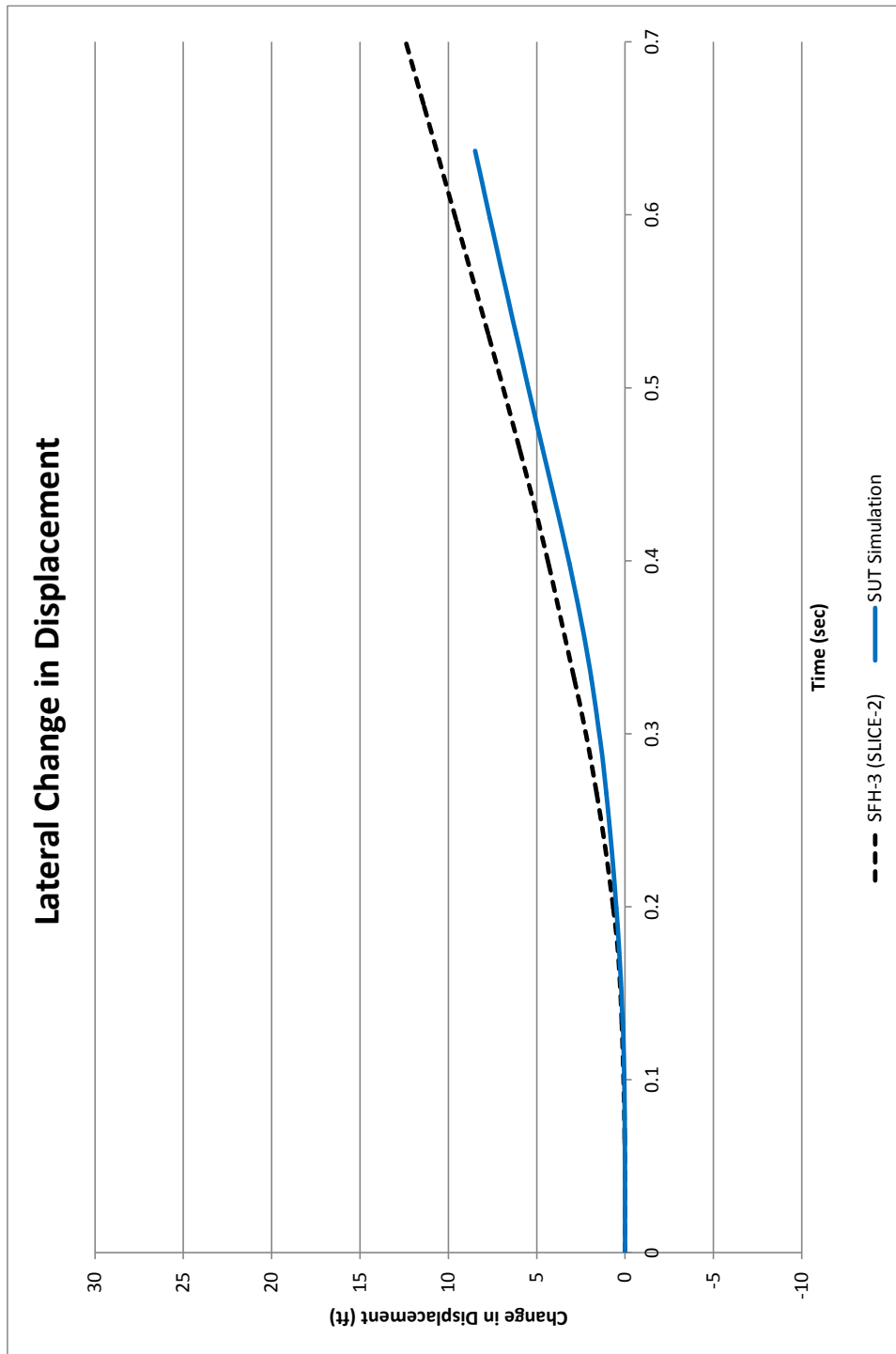


Figure E-6. Lateral Occupant Displacement Comparison, 10000S Vehicles

Appendix F. Design Concepts

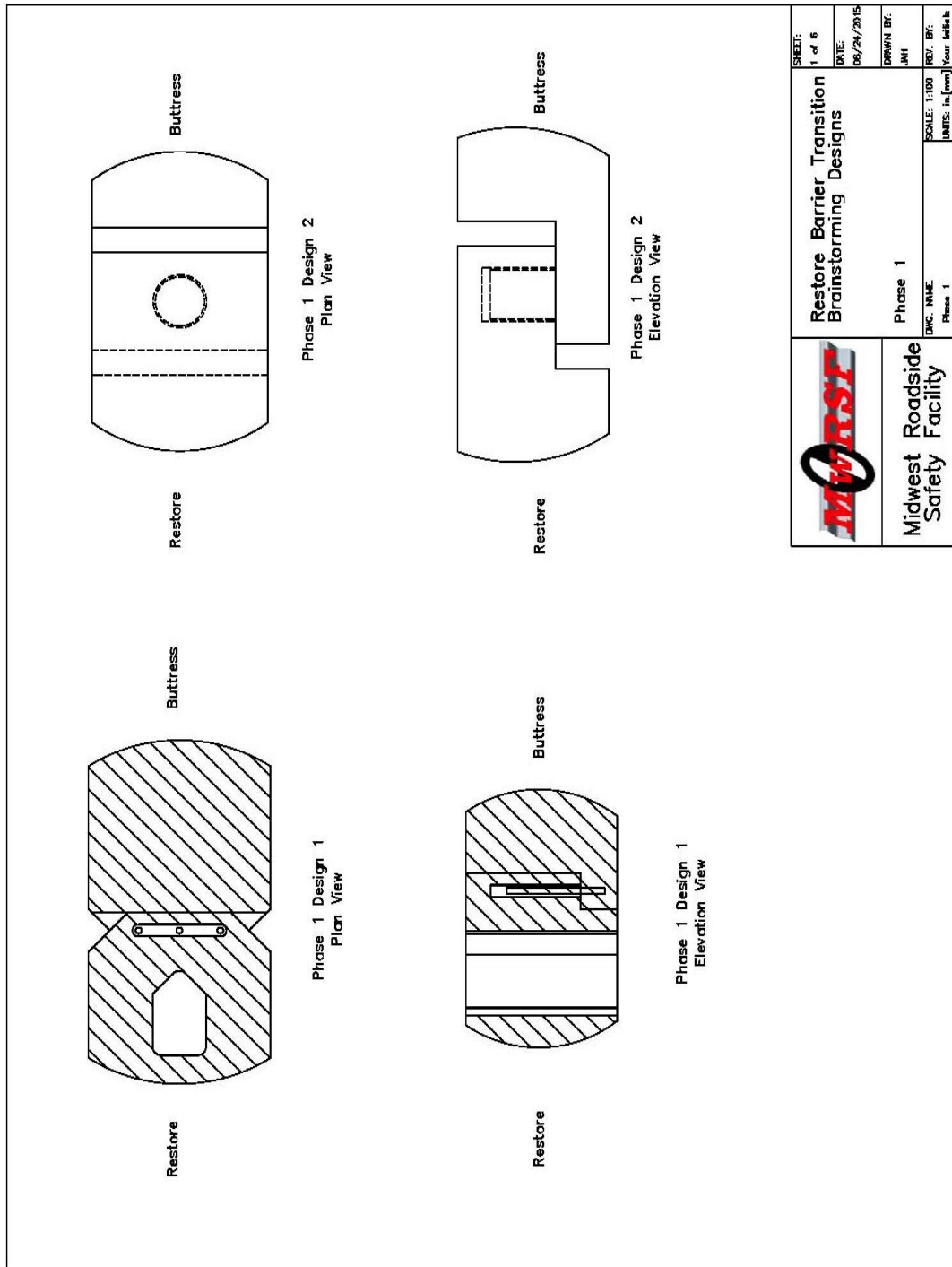
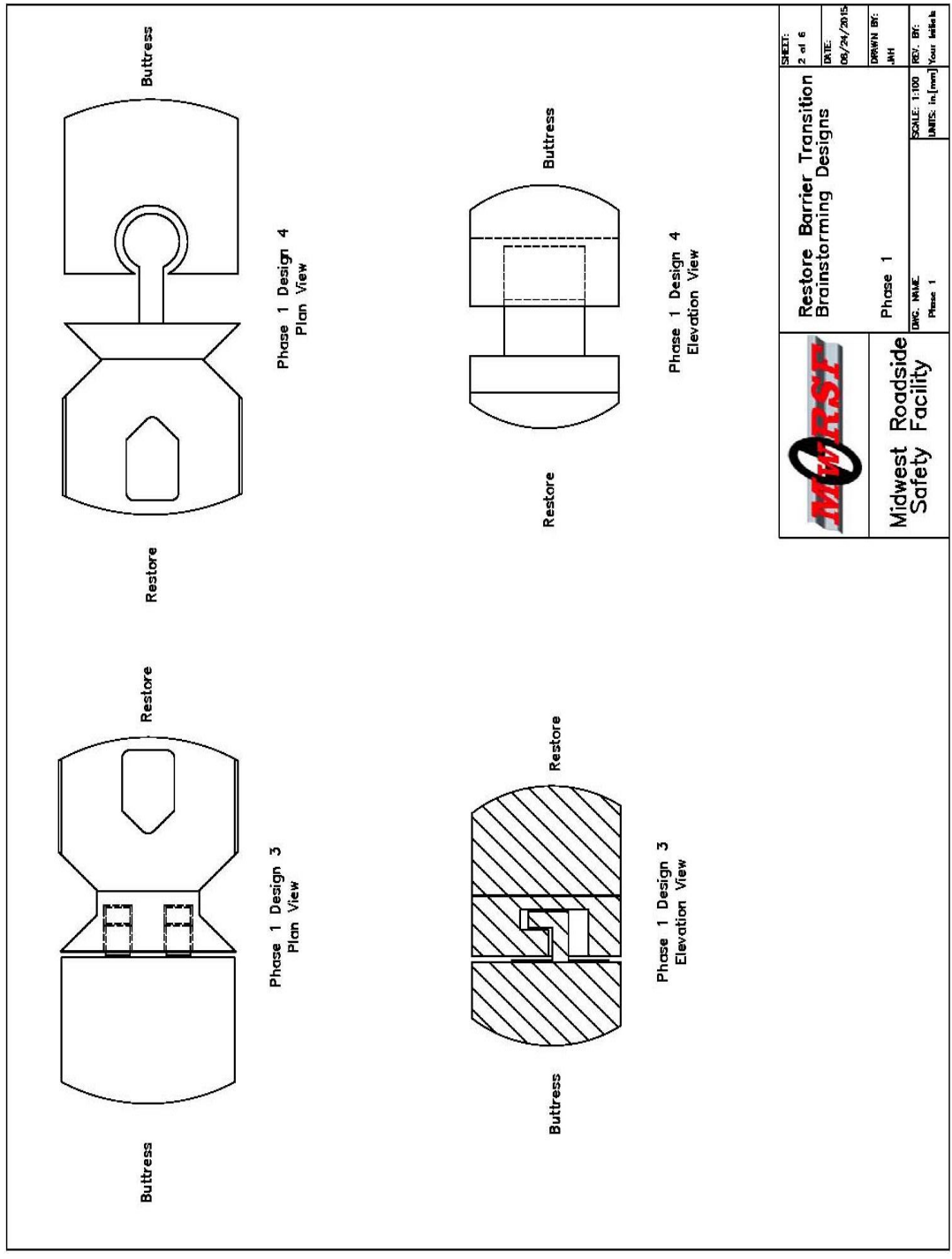


Figure F-1. RESTORE Barrier Transition Brainstorming Designs – Phase 1




	Restore Barrier Transition Brainstorming Designs	
	Phase 1 Dwg. Name: Phase 1	SCALE: 1/100 UNITS: in (mm) Your table
SHEET: 2 of 6		DATE: 08/24/2015
DRAWN BY: JMH		REV. BY: Your table

Figure F-2. RESTORE Barrier Transition Brainstorming Designs – Phase 1

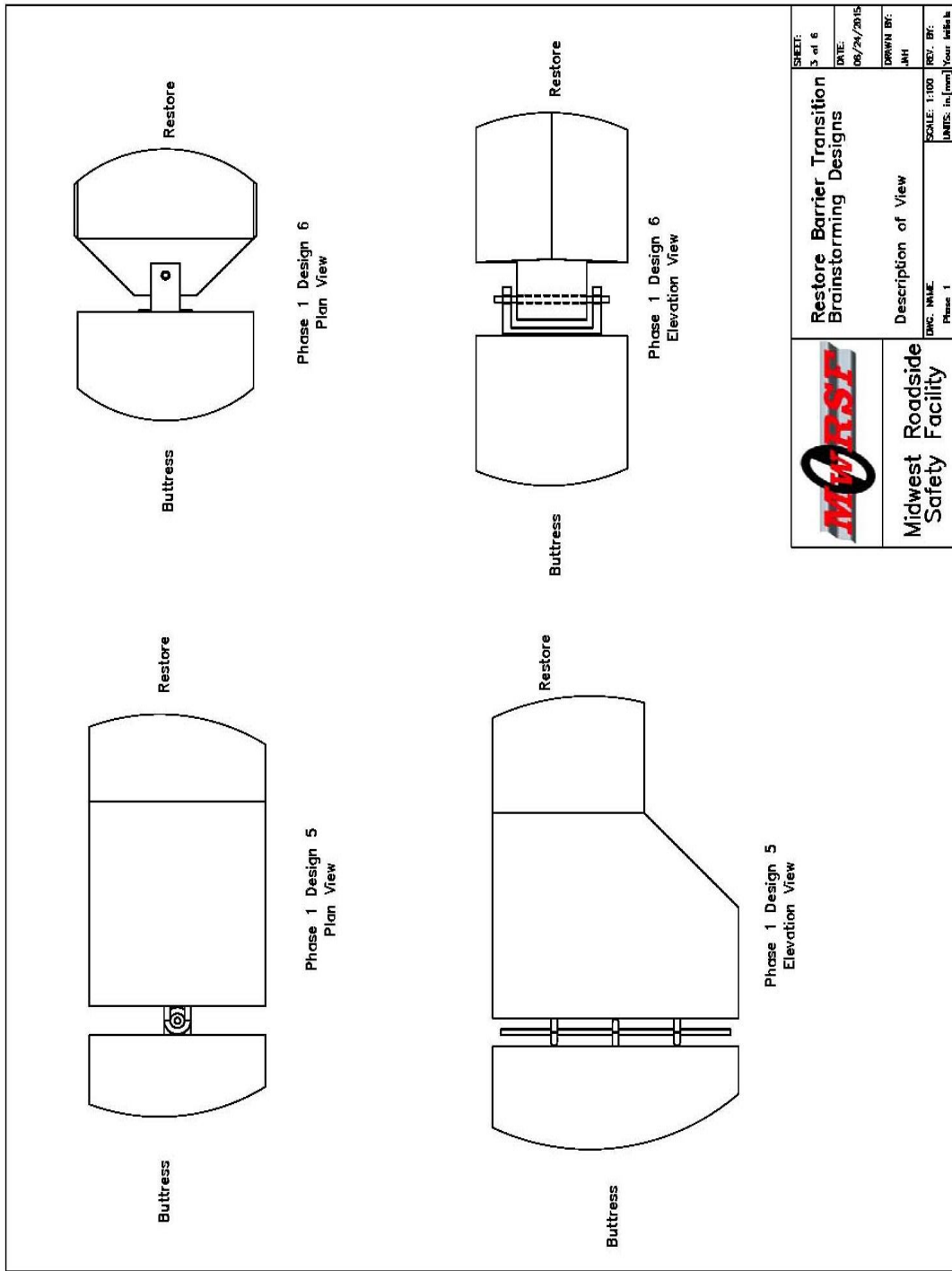


Figure F-3. RESTORE Barrier Transition Brainstorming Designs – Phase 1

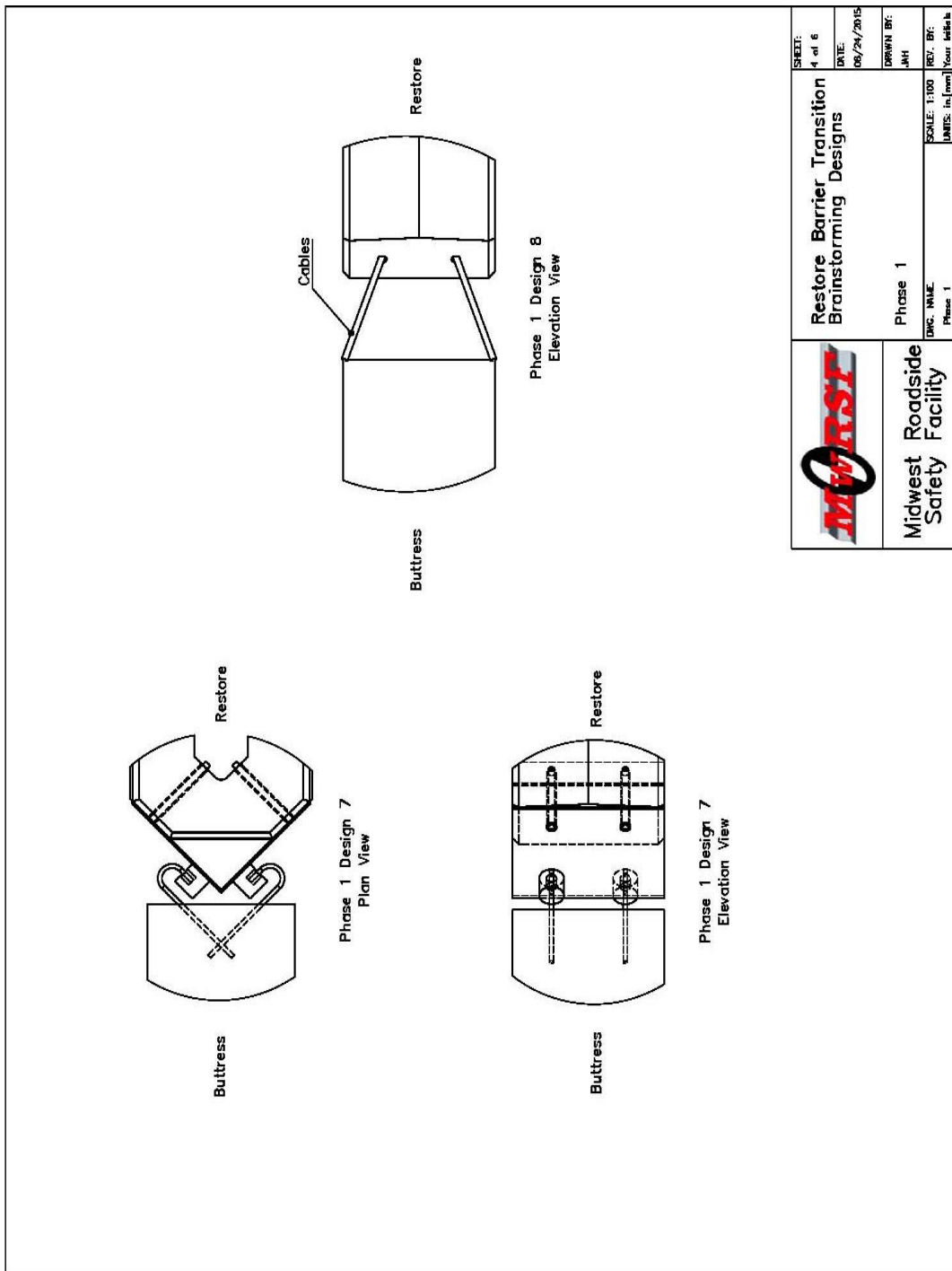
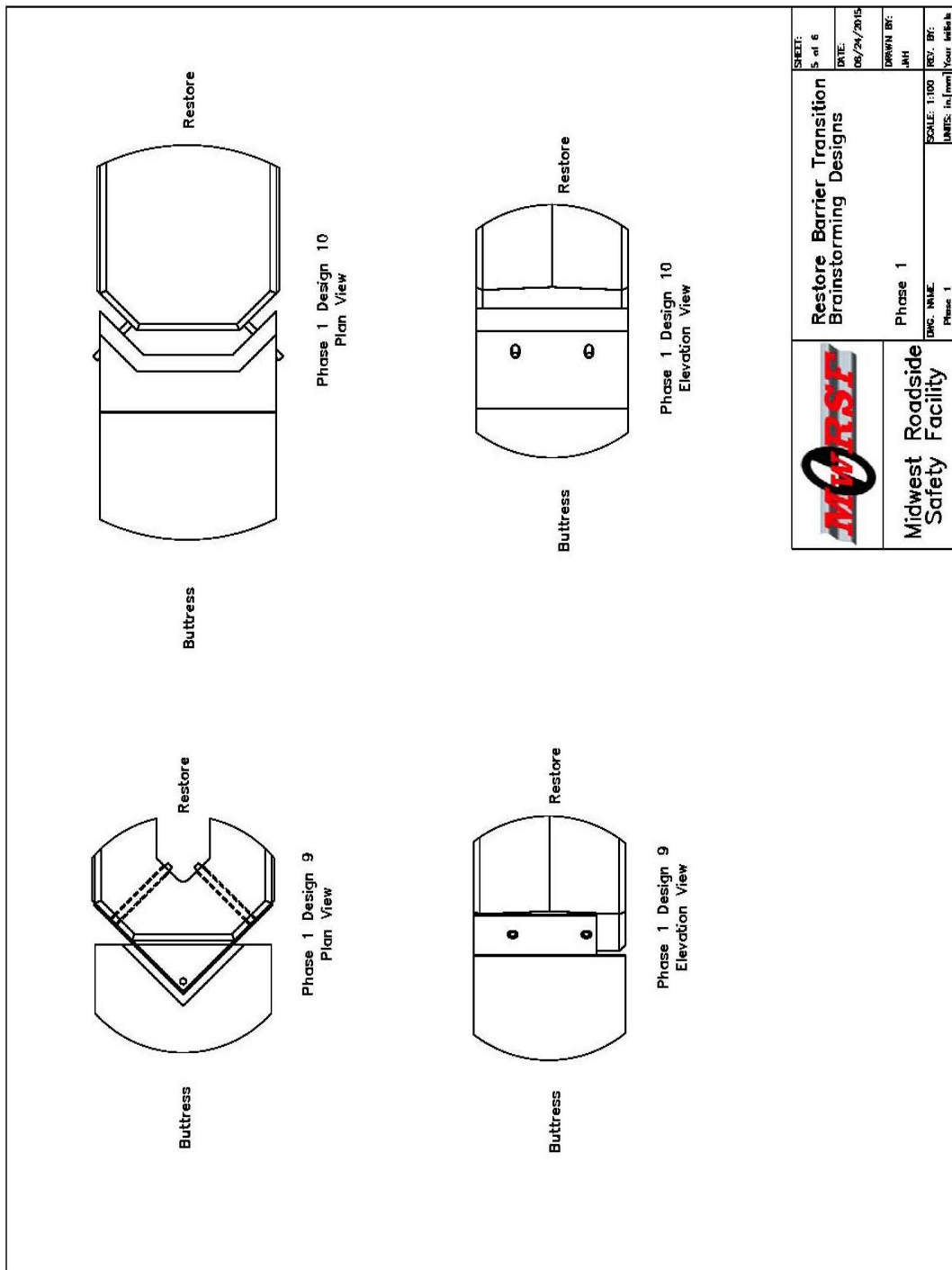


Figure F-4. RESTORE Barrier Transition Brainstorming Designs – Phase 1




 Midwest Roadside Safety Facility	Restore Barrier Transition Brainstorming Designs	SHEET: 5 of 6
	Phase 1 Dwg. Name: Phase 1	DATE: 06/24/2015
SCALE: 1/100 UNITS: in. (mm)		DRAWN BY: JWH
REV. BY: Your initials		REV. BY: Your initials

Figure F-5. RESTORE Barrier Transition Brainstorming Designs – Phase 1

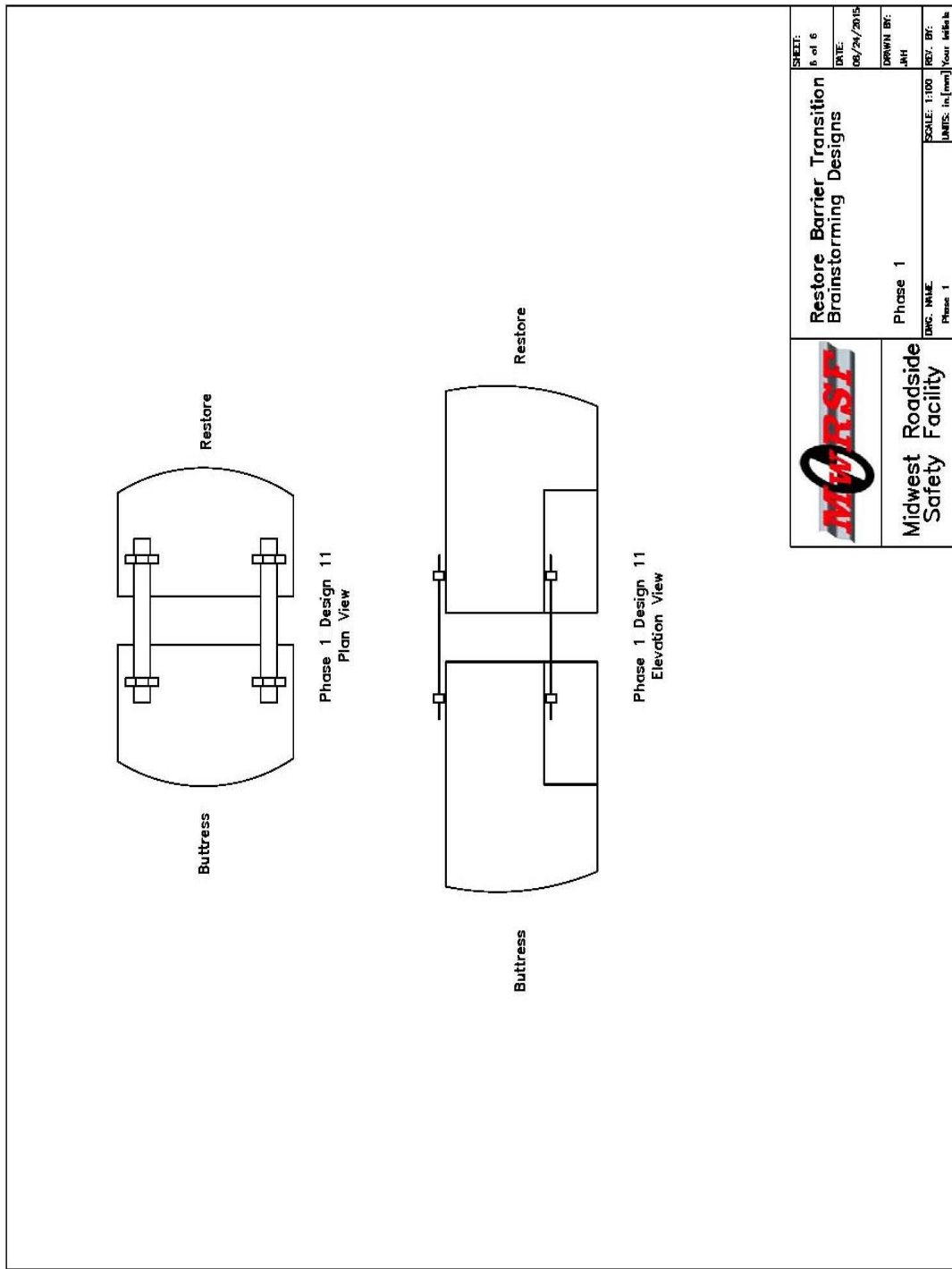
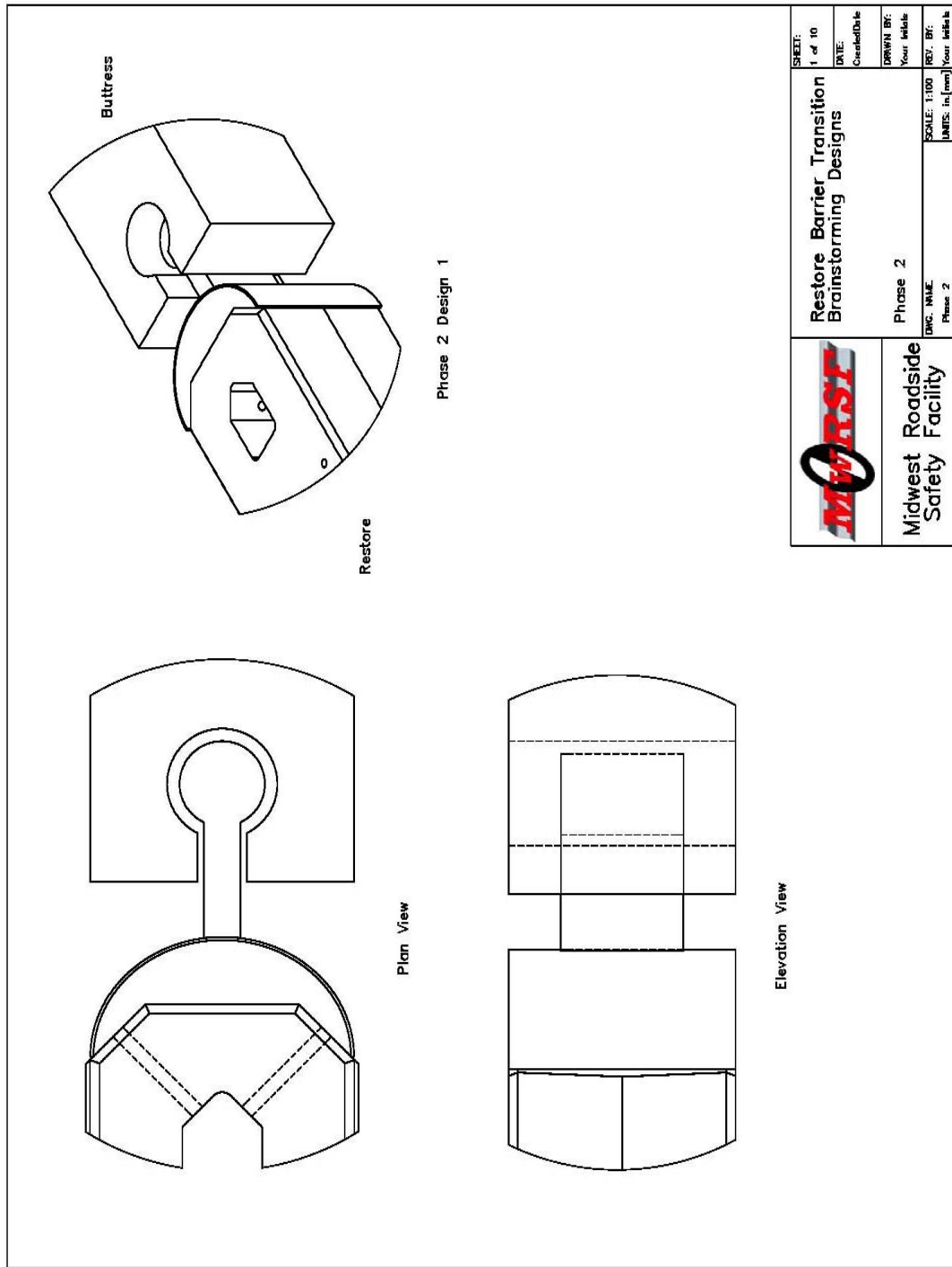


Figure F-6. RESTORE Barrier Transition Brainstorming Designs – Phase 1




 Midwest Roadside Safety Facility	Restore Barrier Transition Brainstorming Designs	SHEET: 1 of 10
	Phase 2 DWG. NAME: Phase 2	DATE: Create/Date
	Phase 2 DWG. NAME: Phase 2	DRAWN BY: Your Initials
	Phase 2 DWG. NAME: Phase 2	SCALE: 1/100 UNITS: in (mm)
		REV. BY: Your Initials

Figure F-7. RESTORE Barrier Transition Brainstorming Designs – Phase 2

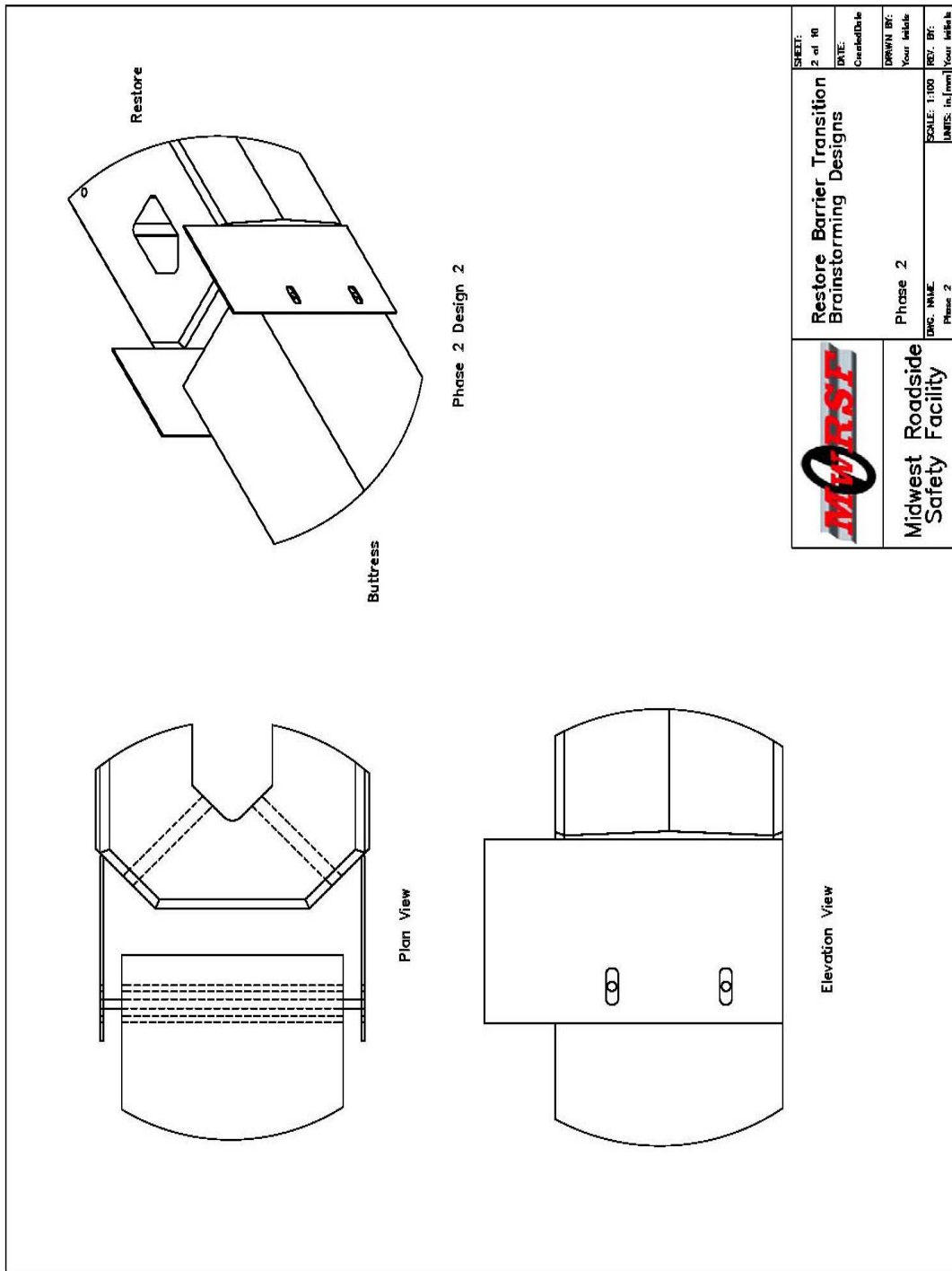


Figure F-8. RESTORE Barrier Transition Brainstorming Designs – Phase 2

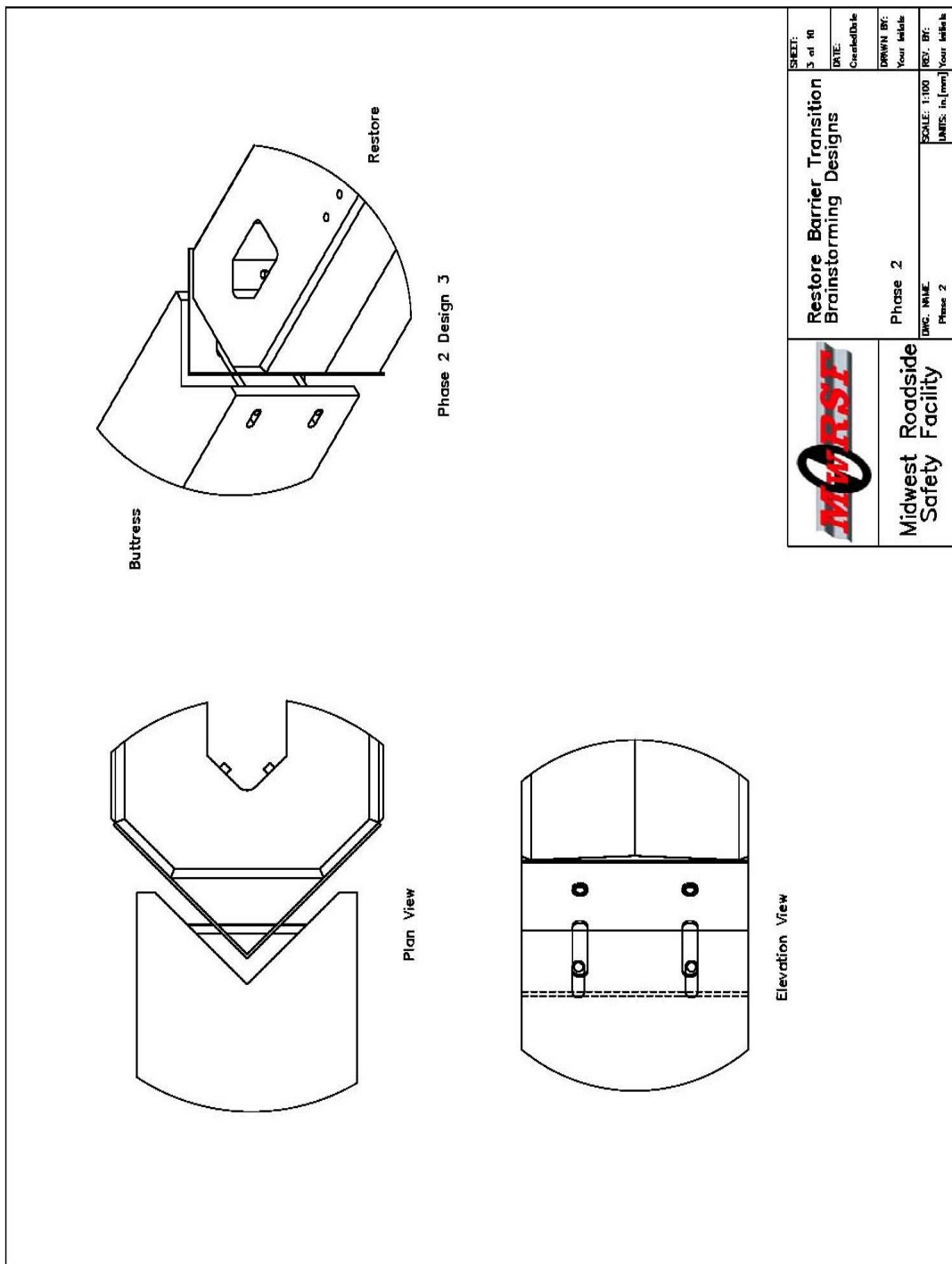
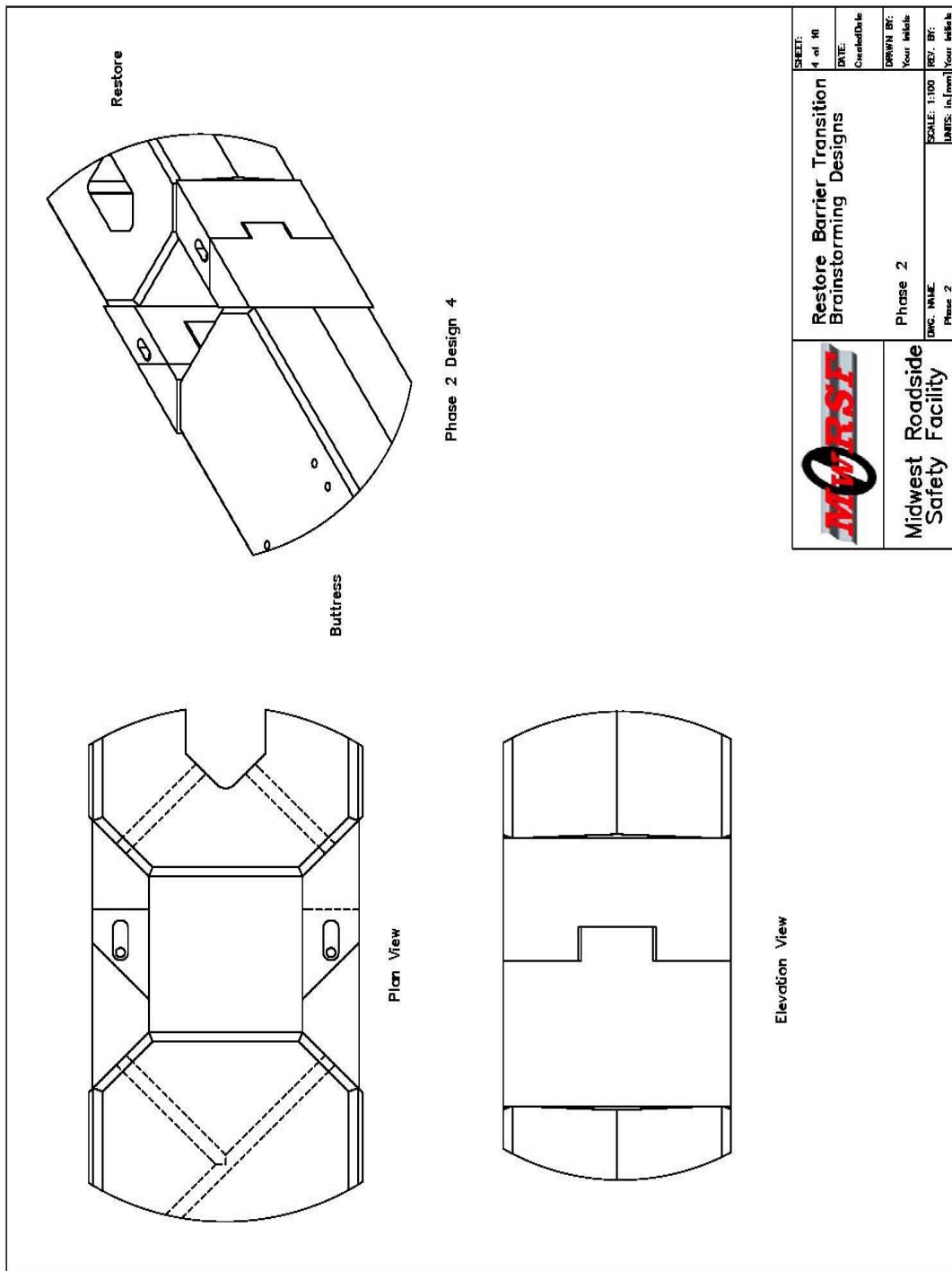


Figure F-9. RESTORE Barrier Transition Brainstorming Designs – Phase 2




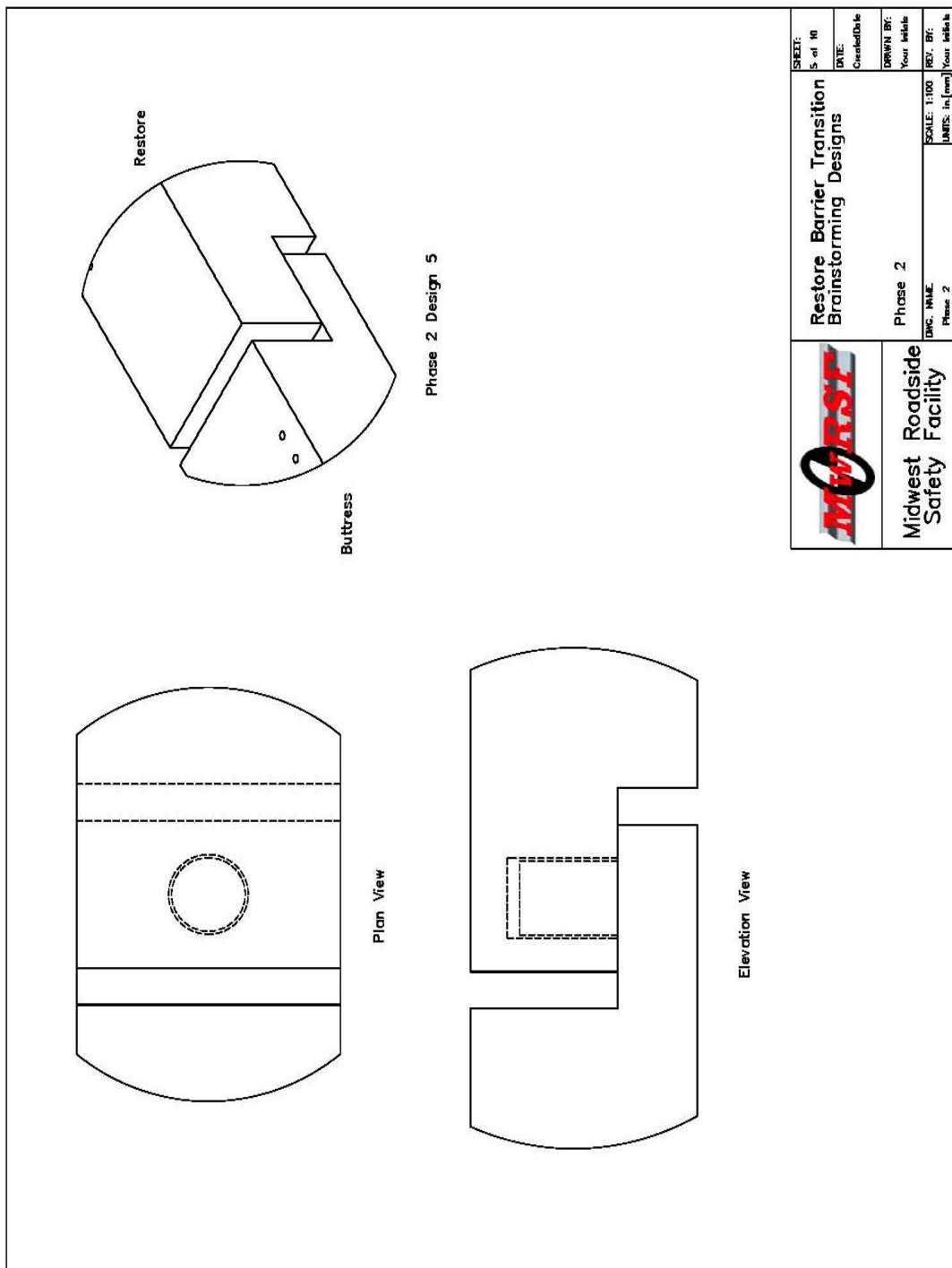
	Restore Barrier Transition Brainstorming Designs	SHEET: 4 of 10
	Phase 2 <small>DWG. NAME</small>	DATE: Created/Date
Midwest Roadside Safety Facility	Phase 2 <small>DWG. NAME</small>	DRAWN BY: Your Initials
	Phase 2 <small>DWG. NAME</small>	SCALE: 1/100 UNITS: in. (mm)
		REV. BY: Your Initials
		REV. BY: Your Initials

Figure F-10. RESTORE Barrier Transition Brainstorming Designs – Phase 2




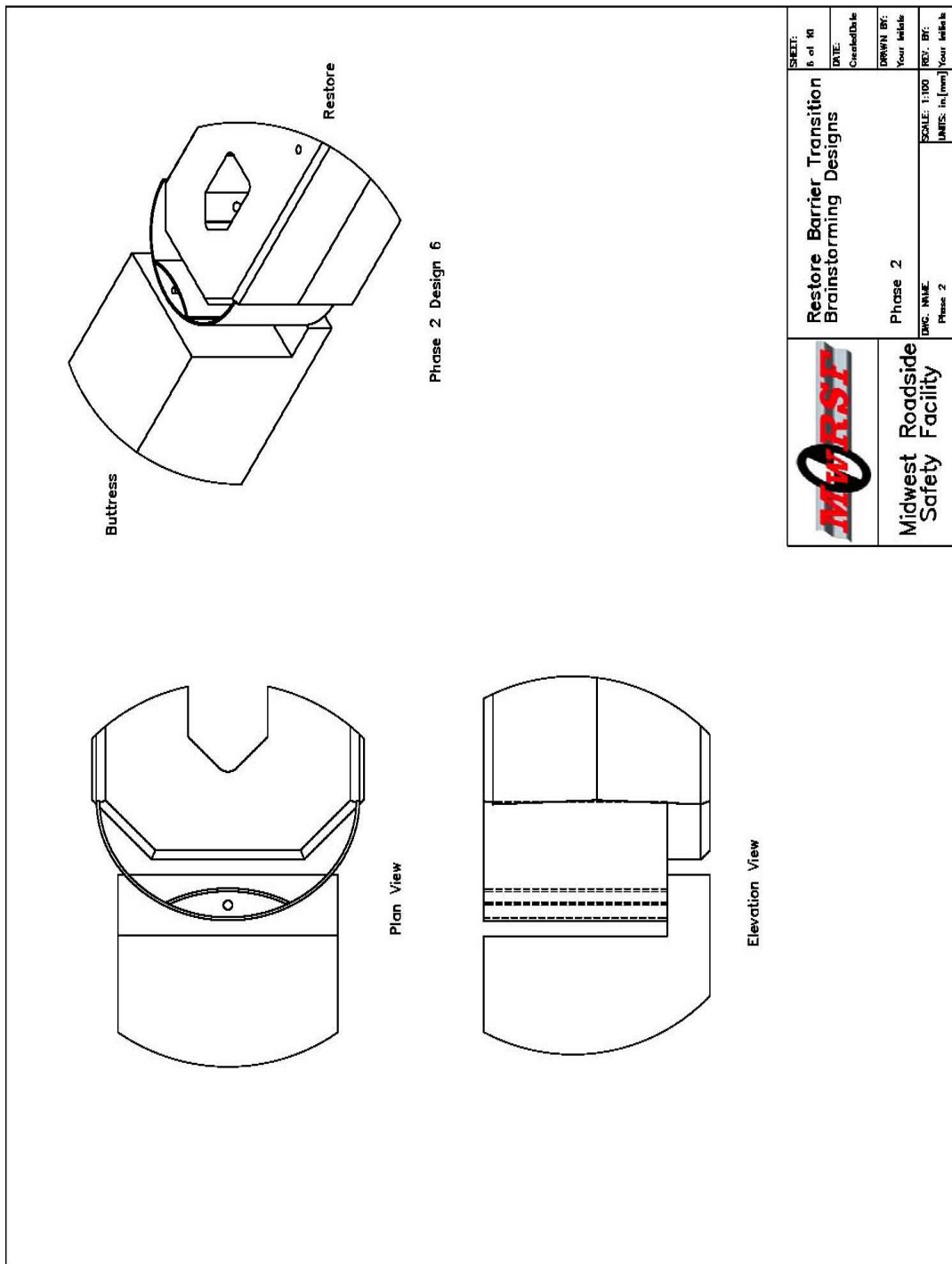
	Restore Barrier Transition Brainstorming Designs	SHEET: 5 of 10
	Phase 2	DATE: Created/Date
Phase 2	DRAWN BY: Your Initials	SCALE: 1:100
Phase 2	REV. BY: Your Initials	UNITS: in [mm]

Figure F-11. RESTORE Barrier Transition Brainstorming Designs – Phase 2




 Midwest Roadside Safety Facility	Restore Barrier Transition Brainstorming Designs Phase 2	SHEET: 6 of 10
	DATE: Complete	DRAWN BY: Your details
SCALE: 1:100 UNITS: in./mm		REV. BY: Your details

Figure F-12. RESTORE Barrier Transition Brainstorming Designs – Phase 2

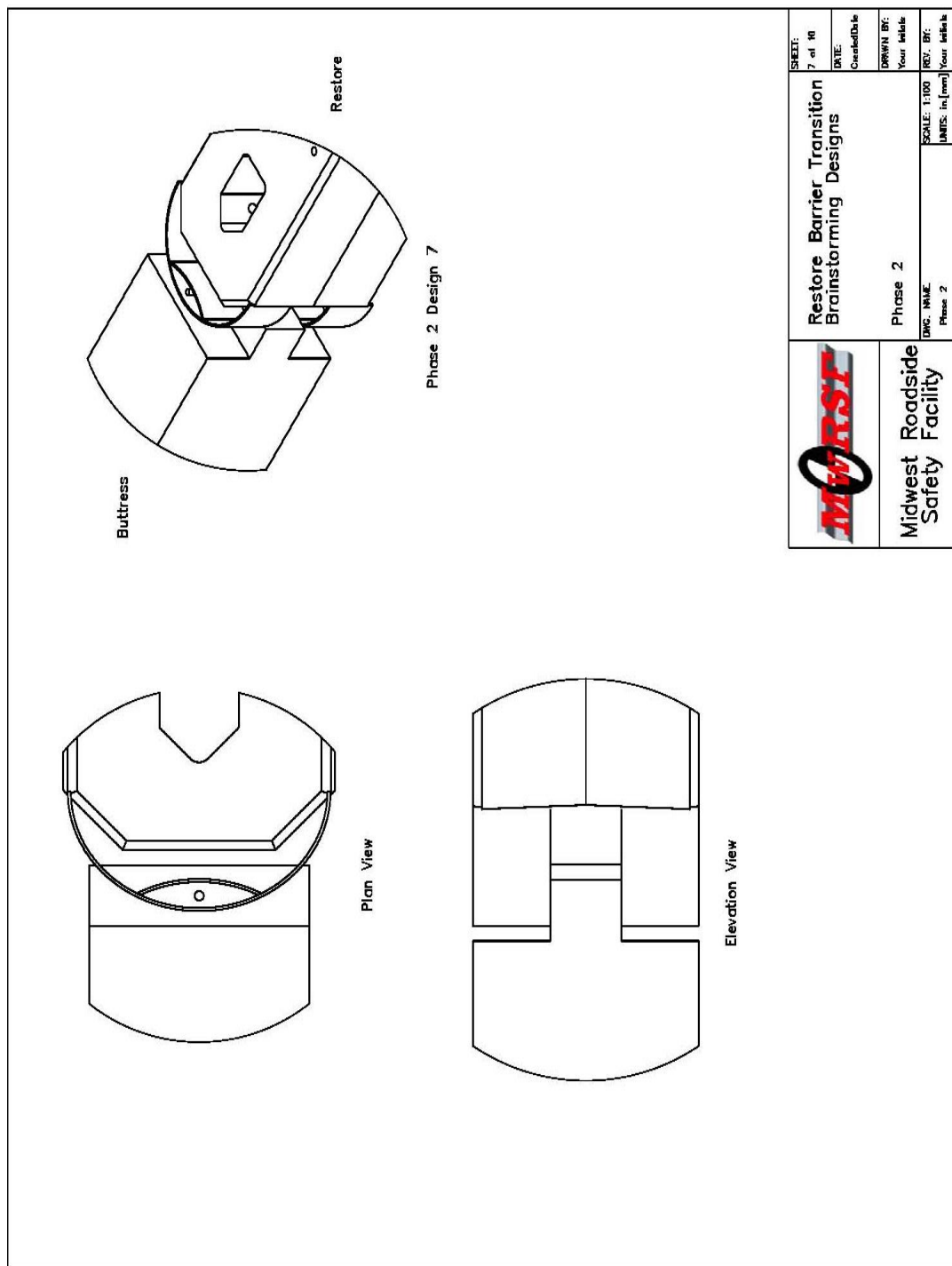


Figure F-13. RESTORE Barrier Transition Brainstorming Designs – Phase 2

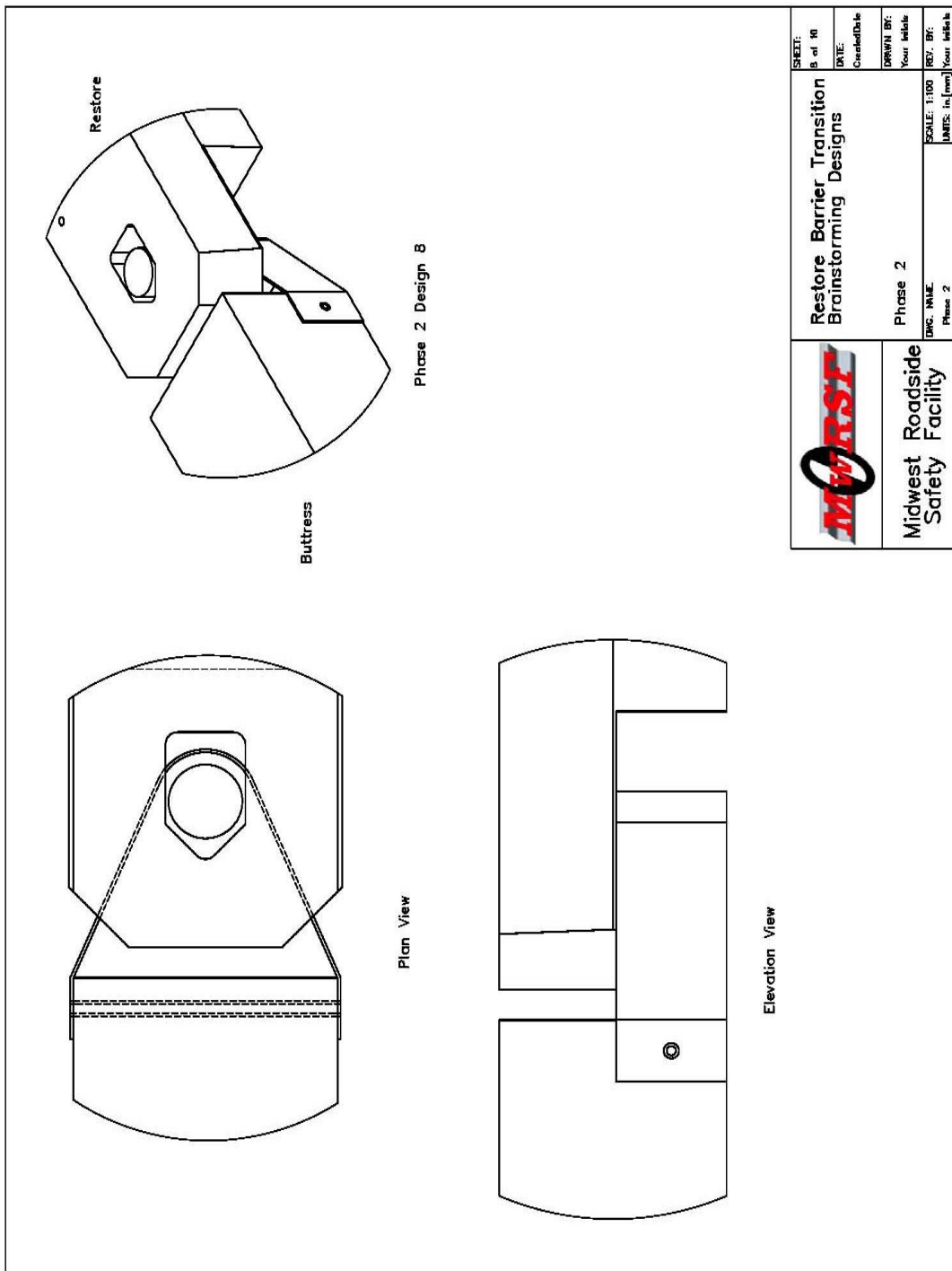


Figure F-14. RESTORE Barrier Transition Brainstorming Designs – Phase 2

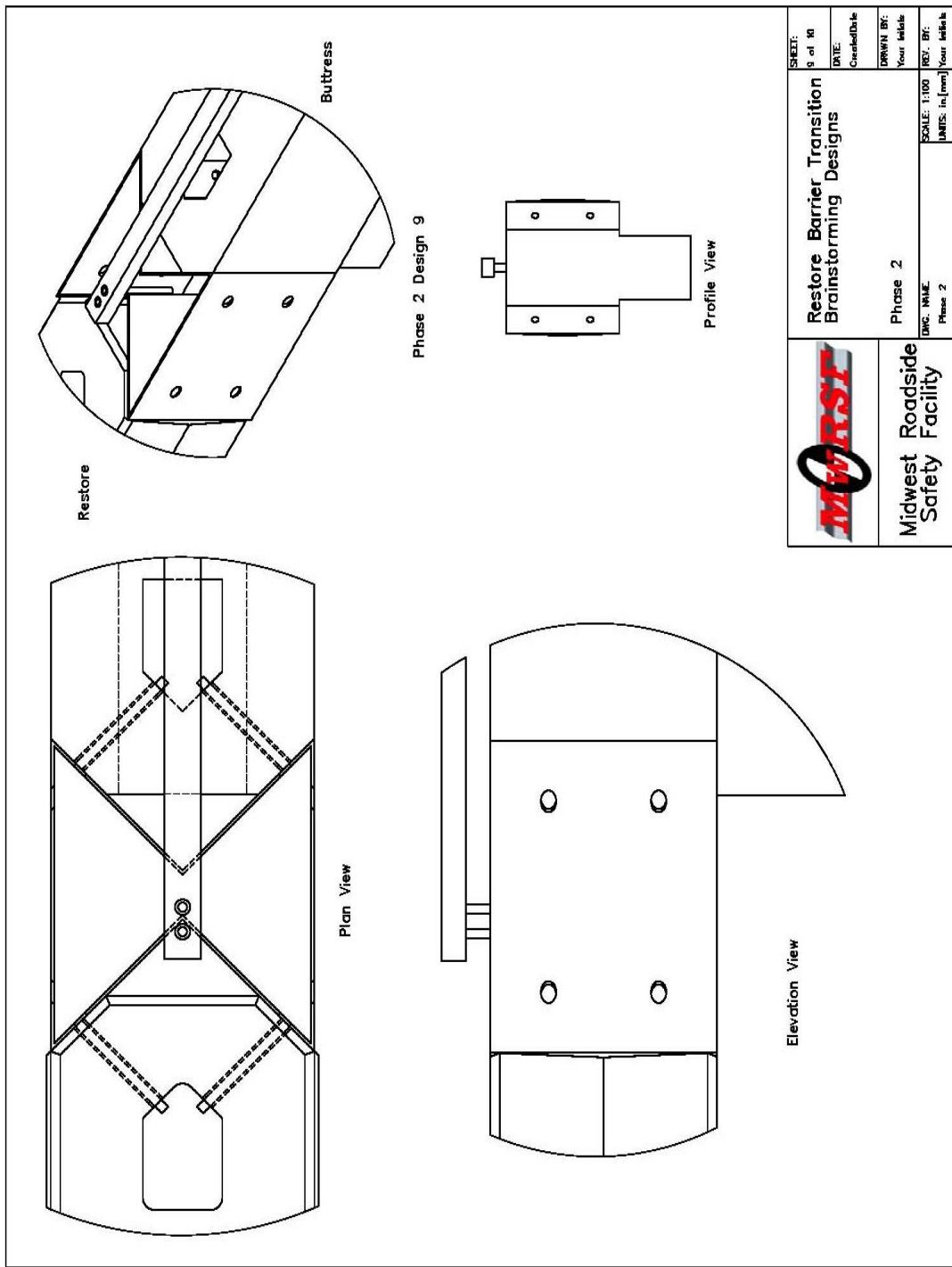
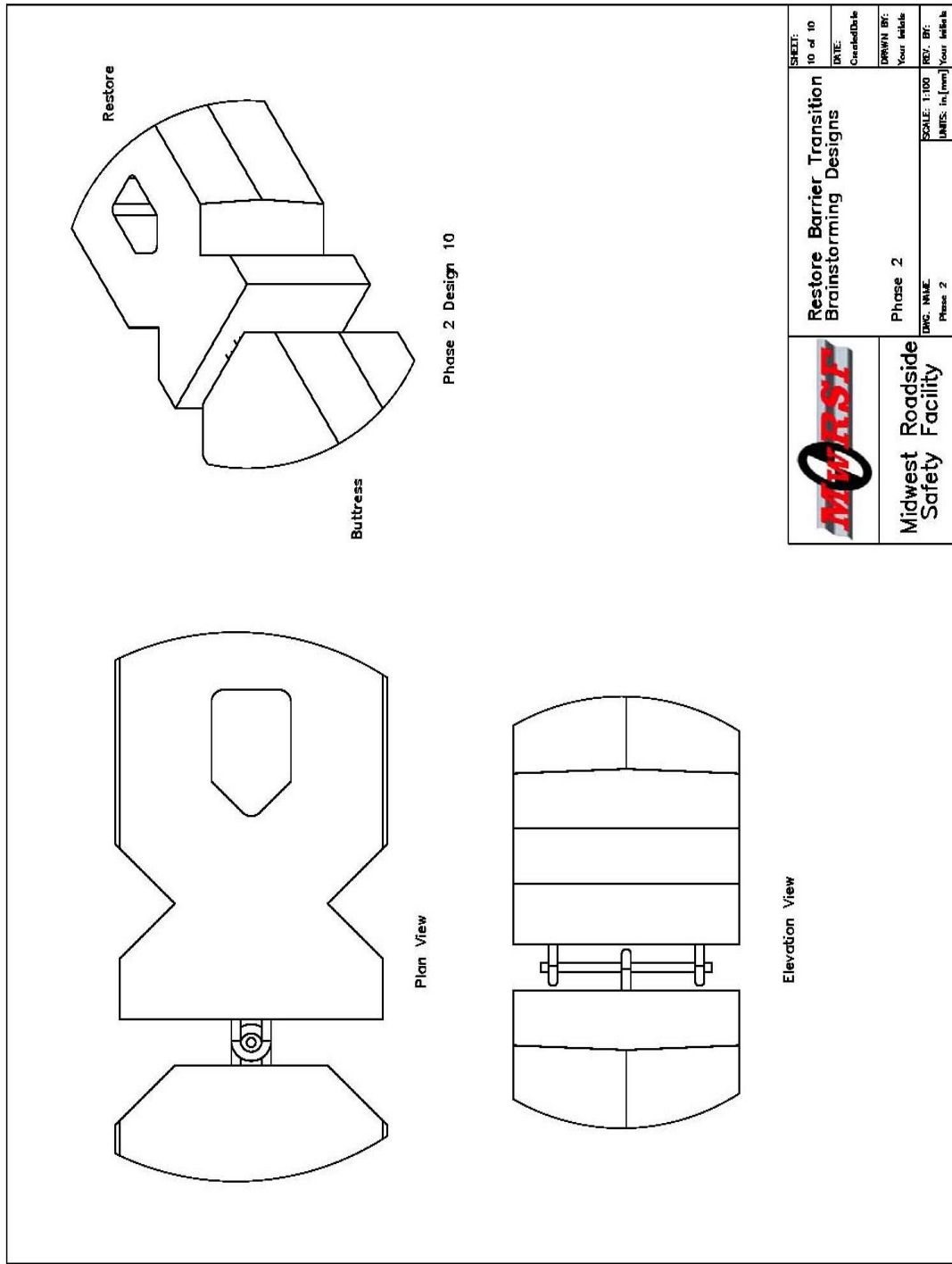


Figure F-15. RESTORE Barrier Transition Brainstorming Designs – Phase 2




 Midwest Roadside Safety Facility	Restore Barrier Transition Brainstorming Designs	SHEET: 10 of 10
	Phase 2 DWG. NAME: Phase 2	DATE: Create/Date
	SCALE: 1/100 UNITS: in./mm	DATE: Your date
		REV. BY: Your initials

Figure F-16. RESTORE Barrier Transition Brainstorming Designs – Phase 2

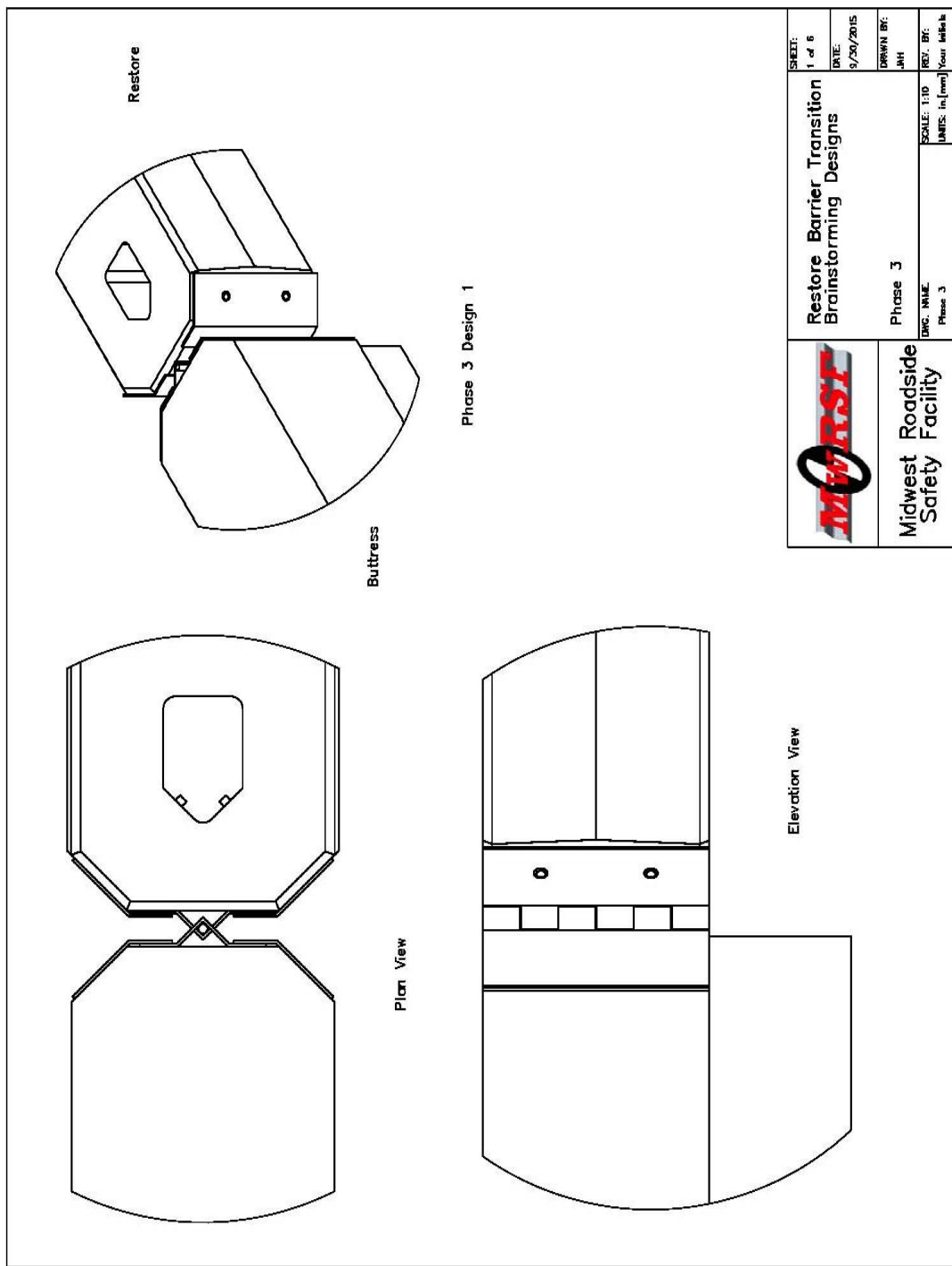


Figure F-17. RESTORE Barrier Transition Brainstorming Designs – Phase 3

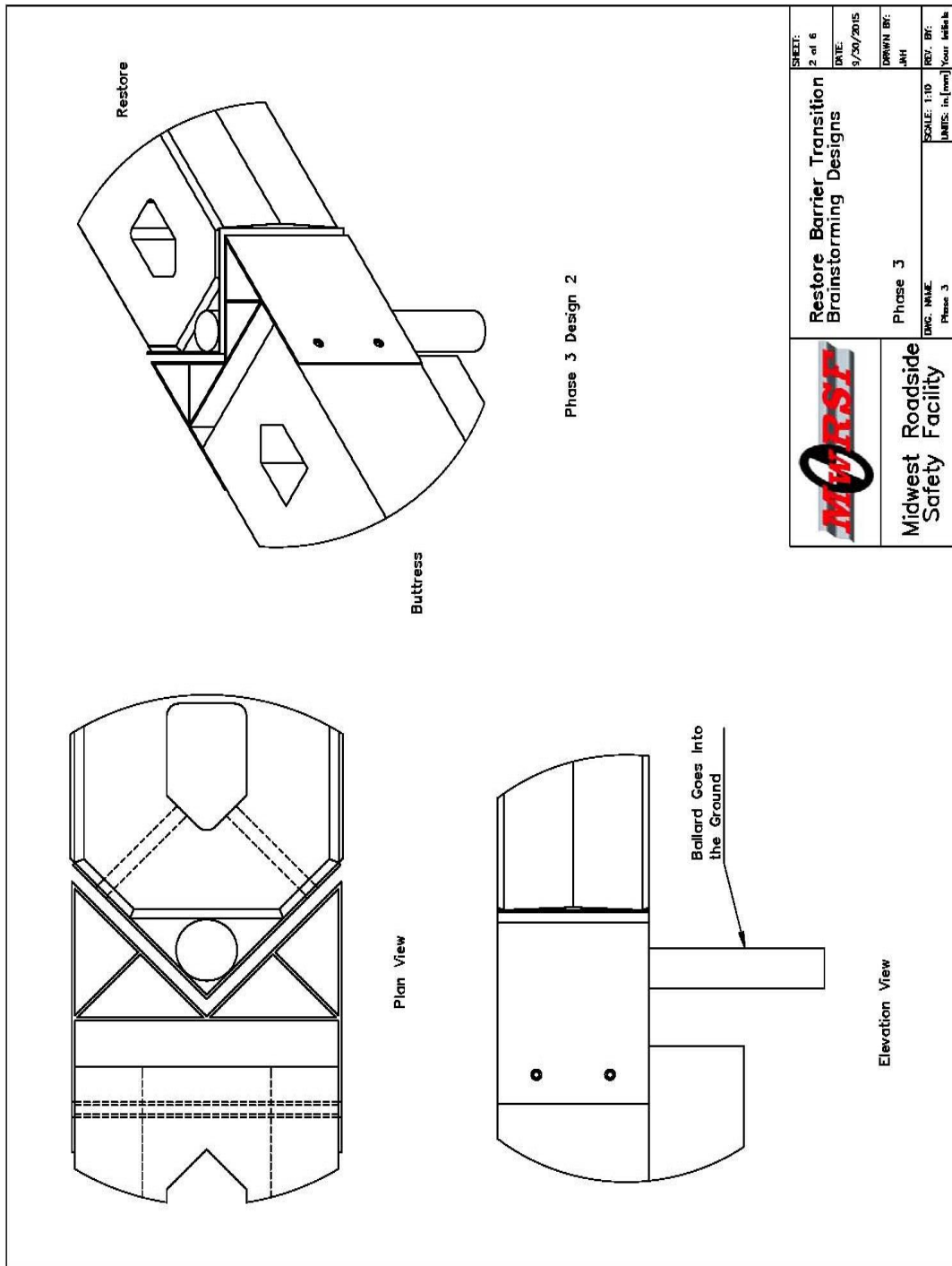
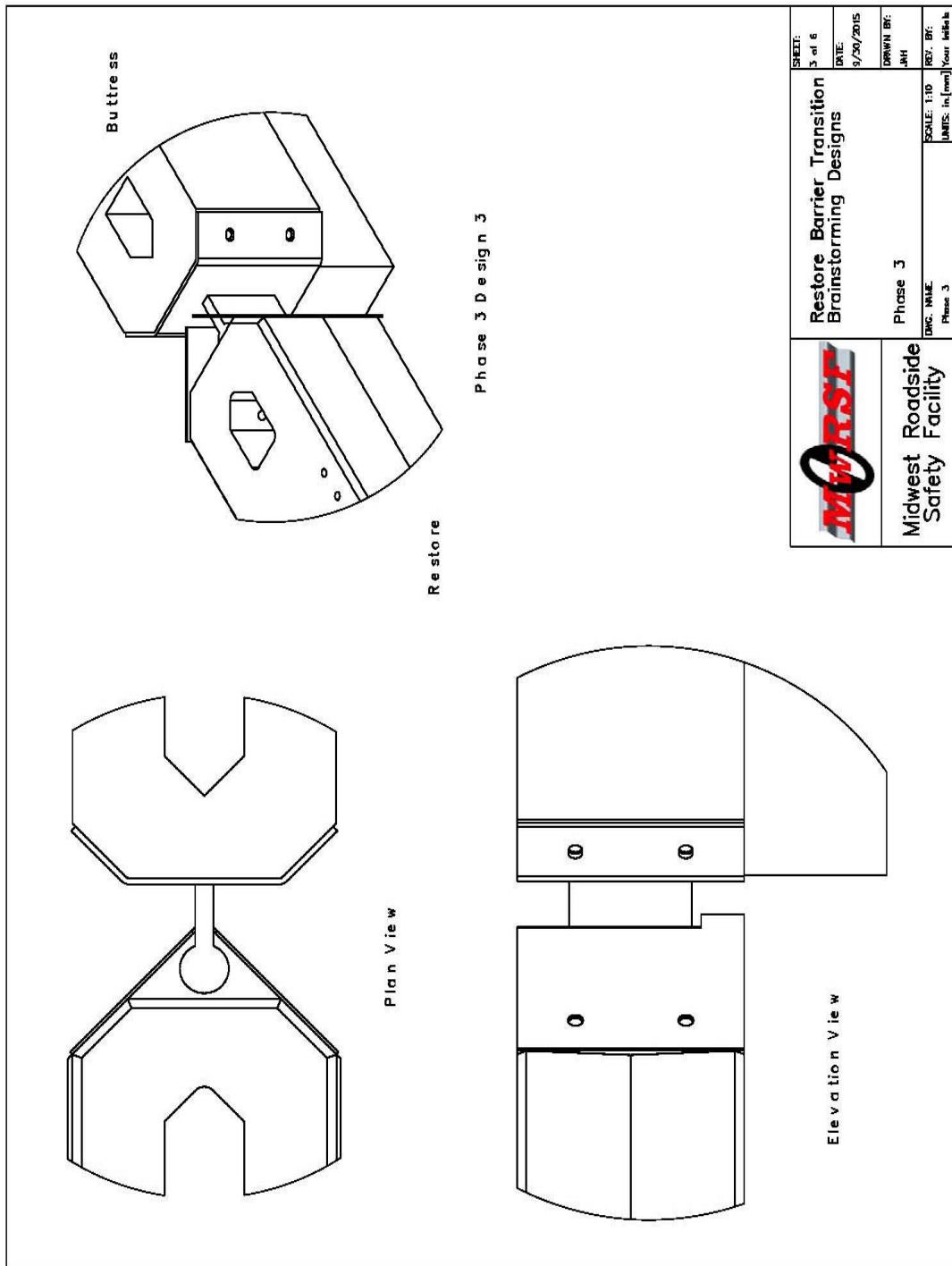


Figure F-18. RESTORE Barrier Transition Brainstorming Designs – Phase 3




	Restore Barrier Transition Brainstorming Designs	SHEET: 3 of 6
	Phase 3 Dwg. Name: Phase 3	DATE: 9/20/2015
Midwest Roadside Safety Facility	SCALE: 1/10 UNITS: in. (mm)	DRAWN BY: JWH
		REV. BY: Your initials

Figure F-19. RESTORE Barrier Transition Brainstorming Designs – Phase 3

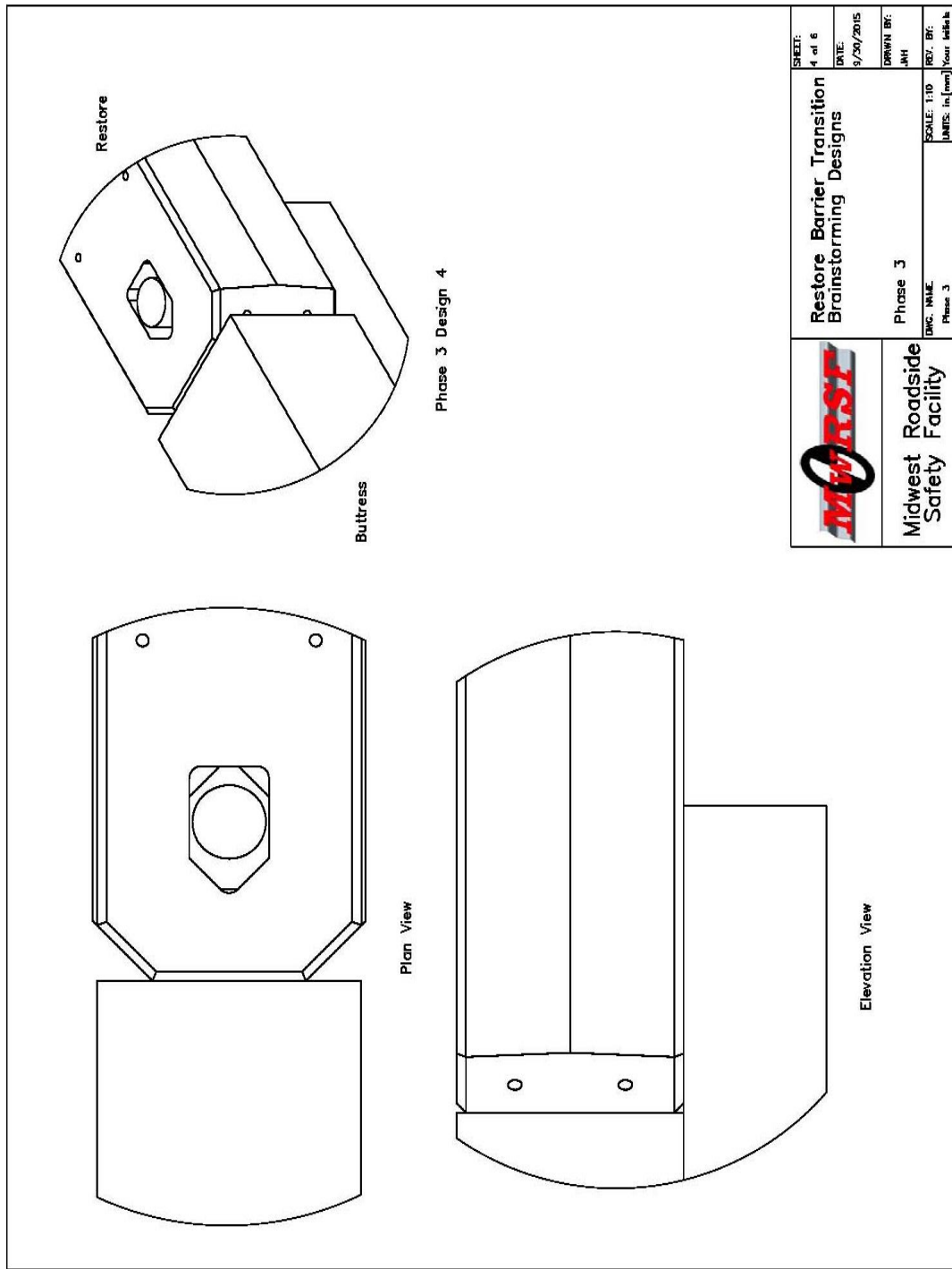
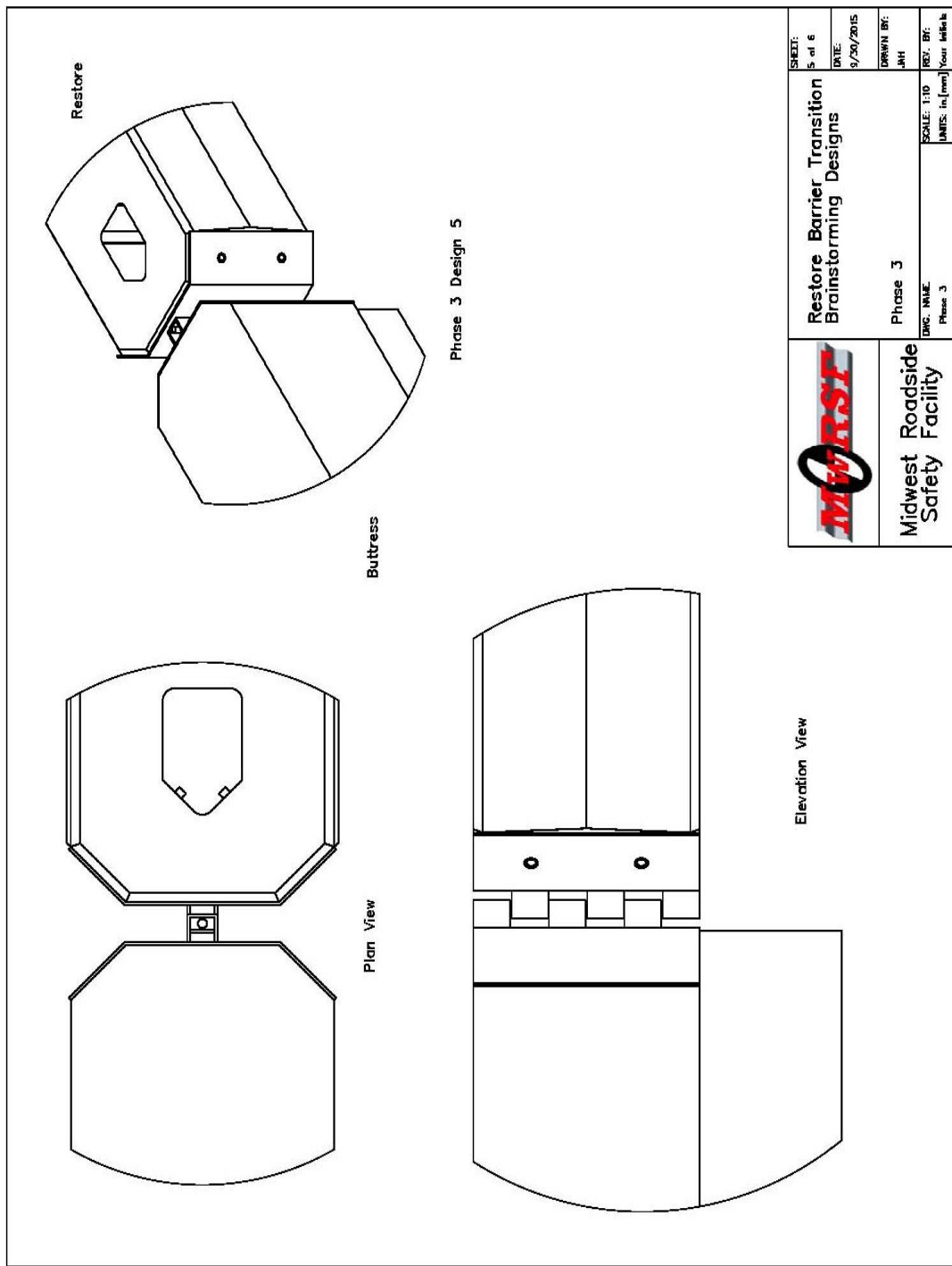


Figure F-20. RESTORE Barrier Transition Brainstorming Designs – Phase 3




 Midwest Roadside Safety Facility	Restore Barrier Transition Brainstorming Designs	SHEET: 5 of 6
	Phase 3 ENG. NAME: Phase 3	DATE: 9/20/2015
SCALE: 1:10 UNITS: in./mm	DRAWN BY: JMH	REV. BY: Your initials

Figure F-21. RESTORE Barrier Transition Brainstorming Designs – Phase 3

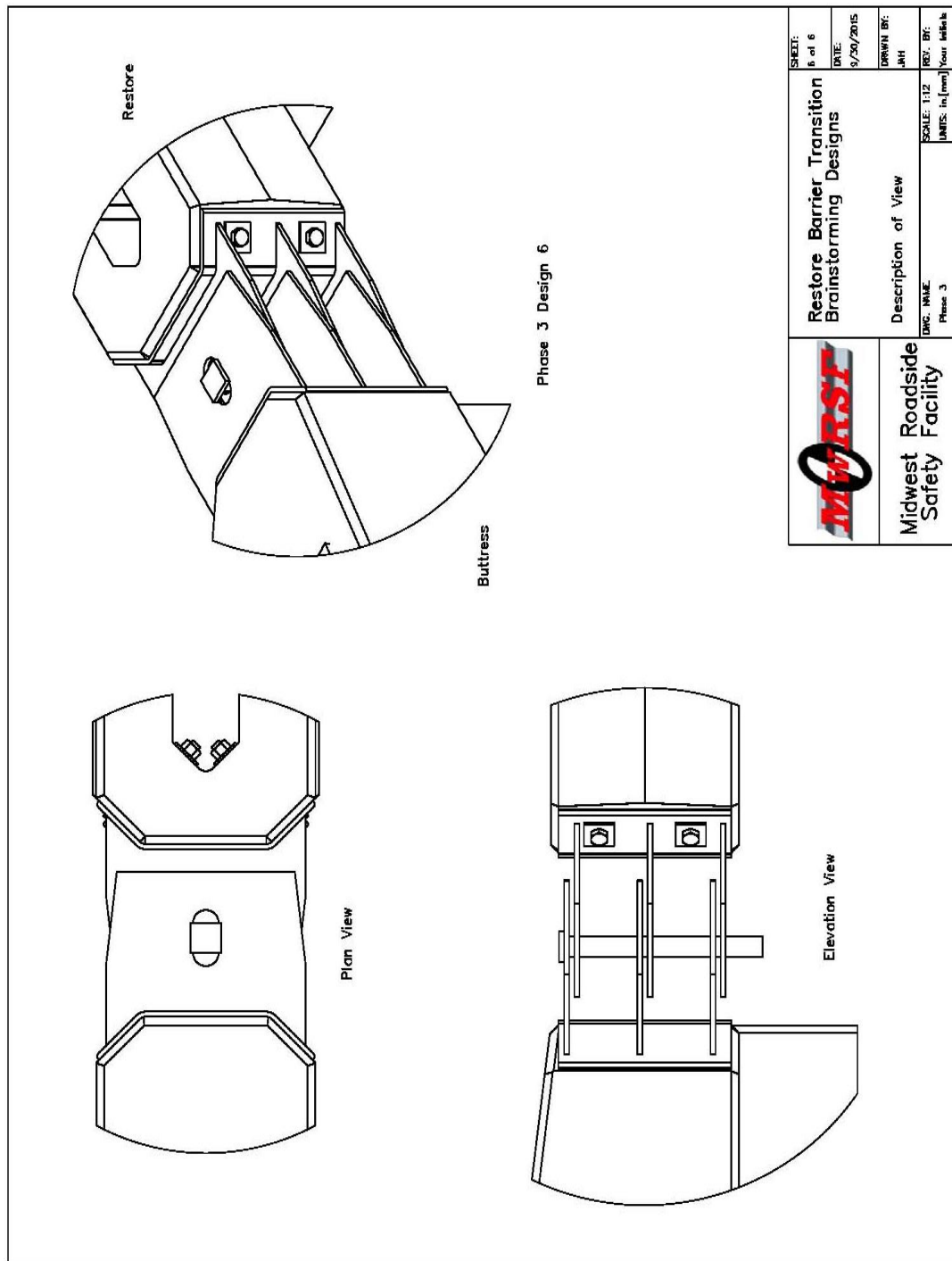


Figure F-22. RESTORE Barrier Transition Brainstorming Designs – Phase 3

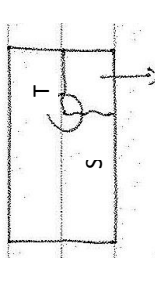
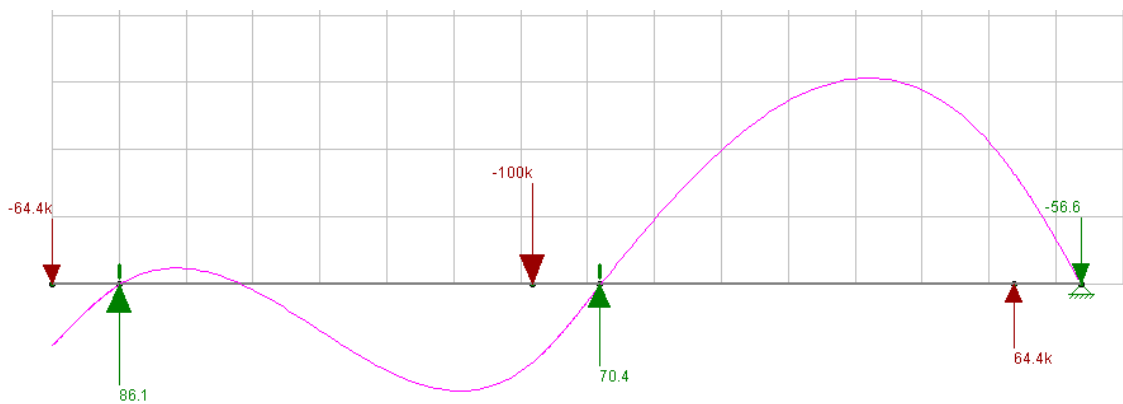
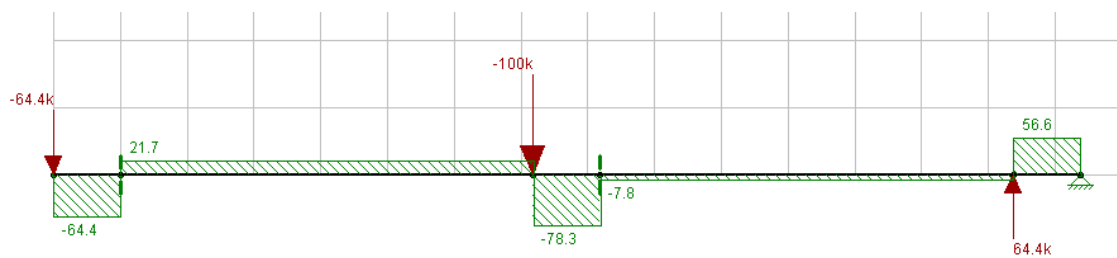
			
Shear Dist	4.75 in	Shear Dist	4 in
Tens Dist	5.25 in	Tens Dist	4.375 in
Thickness	0.5 in	Thickness	0.5 in
Hole Dia	2.5 in	Hole Dia	2.5 in
Fu	58 ksi	Fu	65 ksi
Fy	36 ksi	Fy	50 ksi
Agv	2.375 in ²	Agv	2.1875 in ²
Anv	1.75 in ²	Anv	1.5625 in ²
Agt	2.625 in ²	Agt	2 in ²
Ant	2 in ²	Ant	1.375 in ²
Rupture	132.9 k	Rupture	131.75 k
Yield	167.3 k	Yield	161.5625 k
φ	0.75	φ	0.75
φLeft	99.68 k	φLeft	98.81 k
φRight	125.48 k	φRight	121.17 k
A36			
			
Shear Dist	4.75 in	Shear Dist	4 in
Tens Dist	4 in	Tens Dist	4.375 in
Thickness	0.5 in	Thickness	0.5 in
Hole Dia	2.5 in	Hole Dia	2.5 in
Fu	65 ksi	Fu	65 ksi
Fy	50 ksi	Fy	50 ksi
Agv	2.1875 in ²	Agv	2 in ²
Anv	1.5625 in ²	Anv	1.375 in ²
Agt	2 in ²	Agt	2.1875 in ²
Ant	1.375 in ²	Ant	1.5625 in ²
Rupture	129.6875 k	Rupture	131.75 k
Yield	155 k	Yield	161.5625 k
φ	0.75	φ	0.75
φLeft	97.27 k	φLeft	98.81 k
φRight	116.25 k	φRight	121.17 k
A572			

Figure F-23. Block Shear Calculations and Surfaces of Horizontal Gusset Plates

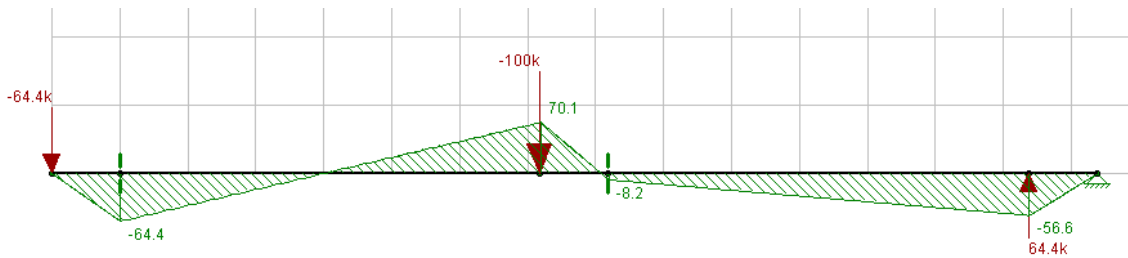
Appendix G. RISA Indeterminate Beam Analysis



a. Reactions and Deflected Shape

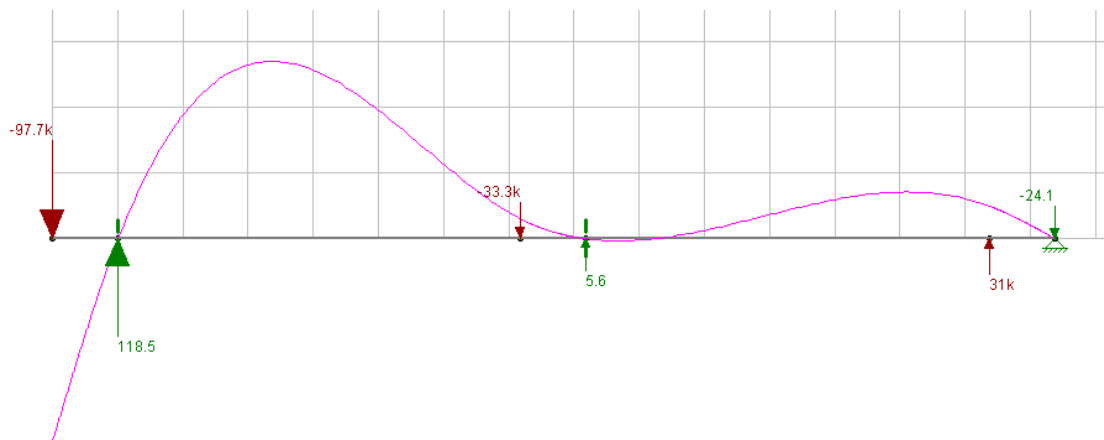


b. Shear Diagram

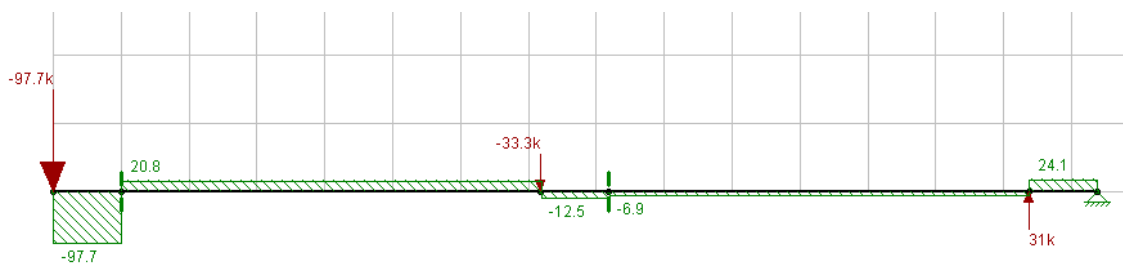


c. Moment Diagram

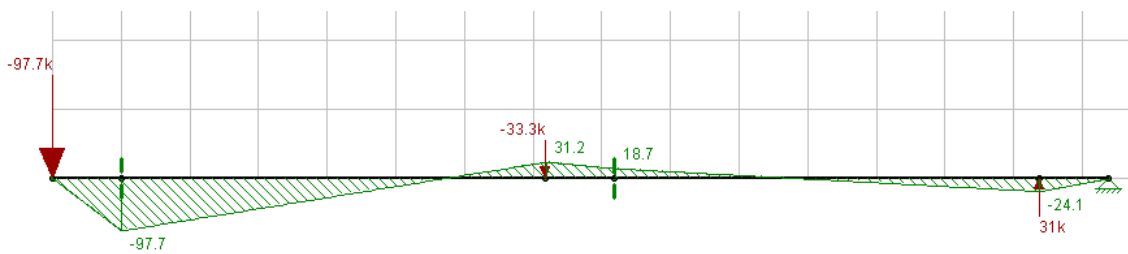
Figure G-1. Case 1 RISA Analysis



a. Reactions and Deflected Shape



b. Shear Diagram



c. Moment Diagram

Figure G-2. Case 2 RISA Analysis

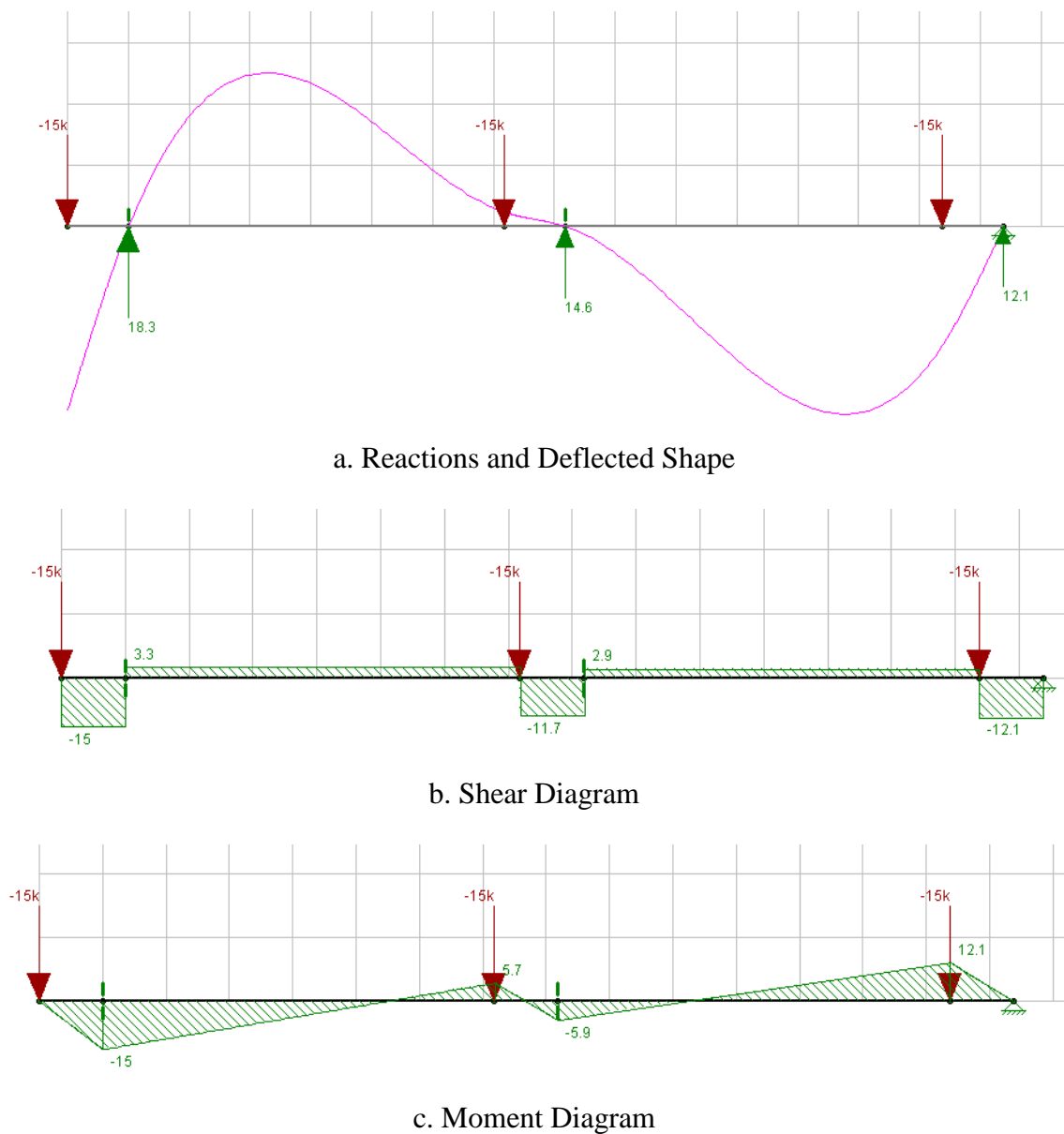


Figure G-3. Longitudinal Loading RISA Analysis

Appendix H. Concrete Buttress – Preliminary Design Only – Internal Reinforcement and Footer

A preliminary design was configured for the internal reinforcement for a rigid concrete buttress and foundation system, as described in Chapter 7. However, the design was never finalized as the scope of the project was focused on the design of a transition concept involving pin-and-gusset hardware. The reinforcement was designed utilizing yield-line theory [70], as noted previously in Section 2.8. Three different segments were considered for the concrete buttress, as the shape transitions between a modified “T” shape to a vertical shape. To assist in the design, spreadsheets were created to determine the required steel in the three different buttress segments. The three segments included a modified “T” shape with a 30 in. (762 mm) height, a modified “T” shape a the 36 in. (914 mm) height, and a 36-in. (914-mm) tall vertical barrier, as shown in Figure H-2. The buttress was 10 ft (3.0 m) long. As noted in Chapter 7, the design lateral impact load was 100 kips (445 kN).

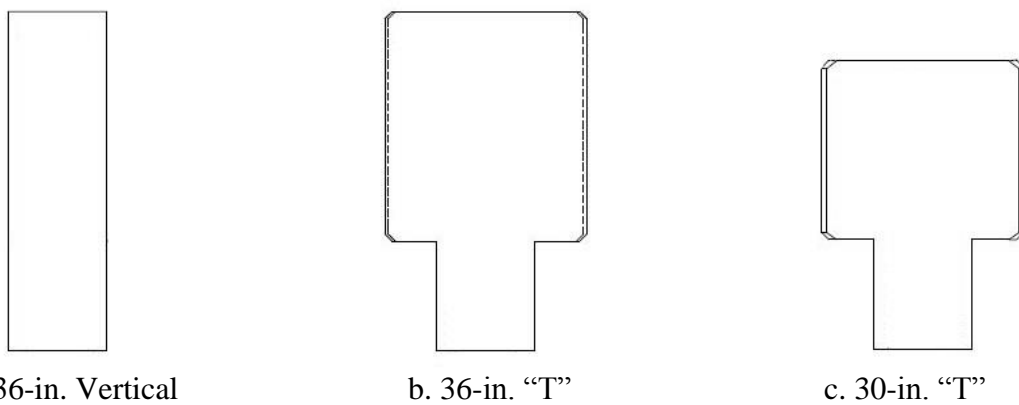


Figure H-2. Profile Barrier Segments for Simplification of Reinforcement Design

The yield-line equations for the end sections are provided in Equations 50 and 51. The ultimate flexural resistance of the wall and beam and the ultimate moment capacity of the beam were calculated using the Whitney stress block procedure for doubly-

reinforced concrete design, which uses a rectangular compressive stress distribution to replace the parabolic stress distribution in reinforced concrete. In order to calculate the length of the stress block, a parabolic assumption was made, as shown in Equation 52. The concrete buttress was designed to have a 28-day compressive strength of 5,000 psi (34.5 MPa). The distribution length for the lateral impact force with the yield-line analysis involving a single-unit truck is 3.5 ft (1.1 m). The steel reinforcement had a yield strength of 60 ksi (413.7 GPa) and a modulus of elasticity of 29,000 ksi (199,948 GPa). The analysis showed that the critical length for the yield lines to develop were greater than half of the length of the buttress. Thus, there was no interior section to the buttress. Further, a reduction factor equal to $\phi=0.9$ and a β_1 factor equal to 0.80 were used within the calculation of the flexural resistance values or the moment capacity.

$$L_c = \frac{L_t}{2} + \sqrt{\left(\frac{L_t}{2}\right)^2 + H \frac{(M_b + M_w H)}{M_c}} \quad (50)$$

$$R_w = \frac{M_b}{L_c - \frac{L_t}{2}} + \frac{M_w H}{L_c - \frac{L_t}{2}} + \frac{M_c L_c^2}{H \left(L_c - \frac{L_t}{2}\right)} \quad (51)$$

$$(0.85f'_c b)a^2 + (0.003E_s A'_s - A_s f_y)a - (0.003E_s A'_s \beta_1 d') = 0 \quad (52)$$

Where: L_c = Critical wall length over which the yield line mechanism occurs

L_t = Longitudinal length of distribution of impact force, ft (m)

M_c = Ultimate flexural resistance of wall about horizontal axis, kip-ft/ft (kN-m/m)

M_b = Ultimate moment capacity of beam at top of wall, kip-ft (kN-m)

M_w = Ultimate flexural resistance of wall about vertical axis, kip-ft/ft (kN-m/m)

H = Height of wall, ft (m)

R_w = Nominal railing redirecive capacity to transverse loads, kips (kN)

A_s = Area of reinforcing steel on tension face, in.² (mm²)

A'_s = Area of reinforcing steel on compression face, in.² (mm²)

f_y = Yield stress of reinforcing steel, ksi (MPa)

f_c' = Compressive strength of concrete, psi (MPa)
 b = Width of beam considered, in. (mm)
 a = Length of Whitney stress block, in. (mm)
 E_s = Modulus of elasticity of reinforcement, psi (Pa)
 β_1 = Ratio of depth of rectangular stress block to depth of neutral axis
 d' = Distance between compression end to centroid of compression reinforcement, in. (mm)

Lastly, a shear check was performed to determine if the stirrups had adequate capacity to exceed the shear force. The buttress was assumed as a simple-simple support where the 100-kip (445-kN) lateral design load, distributed over the 3.5 ft (1.1 m) length, would be evenly distributed to the two supports to obtain the design shear force (V_u). The shear capacity of the rail, shear strength of the shear reinforcement, and the nominal shear strength were determined using Equations 53 through 55. A strength reduction factor of $\phi=0.75$ was used. The shear reinforcement was considered adequate if the shear force determined from the lateral design load (V_u) was less than or equal to the nominal shear strength (ϕV_n).

$$V_c = 2\sqrt{f_c'bd} \quad (53)$$

$$V_s = \frac{A_v f_y d}{s} \quad (54)$$

$$\phi V_n = \phi(V_c + V_s) \quad (55)$$

Where: V_c = Nominal shear force of the concrete, kip (kN)
 V_s = Nominal shear strength from shear reinforcement, kip (kN)
 ϕV_n = Nominal shear strength, kip (kN)
 s = Spacing of shear reinforcement, in. (mm)
 d = Distance between compression face and centroid of tension reinforcement, in. (mm)
 ϕ = Strength reduction factor

The calculations are provided in Figure H-3 through Figure H-5. A clear cover of 1½ in. (38 mm) was used throughout the design. A total of four longitudinal no. 7 bars equally spaced in the interior 10½ in. (267 mm) wide section were required through the

sections that were changing shape within the buttress. The beam required eight longitudinal no. 7 bars throughout the profile changes. At the end with the vertical wall, the buttress required ten longitudinal no. 7 bars spaced equally through the height of the barrier. The upstream and downstream ends of the buttress required no. 5 stirrups to accommodate the shear load in the buttress.

30 in. (762 mm) Modified "T"										
Mc stirrups			Mb beam			Mw wall			Shear Check	
As/bar	in. ²	0.31	As/bar	in. ²	0.6	As/bar	in. ²	0.6	φVn	36.33
# of rebar		1	# of rebar		4	# of rebar		2	Vc	kip 33.68
d_bar	in.	0.625	d_bar	in.	0.875	d_bar	in.	0.875	Vs	kip 14.76
As=As'	in. ²	0.31	As=As'	in. ²	2.4	As=As'	in. ²	1.2		
Clear Cover	in.	1.5	Clear Cover	in.	1.5	Clear Cover	in.	1.5	w	k/ft 28.57
Length (b)	in.	10	Length (b)	in.	18.5	Length (b)	in.	30	Ra	50
Width	in.	10.5	Width	in.	21.5	Width	in.	10.5	Rb	50
d	in.	8.69	d	in.	18.94	d	in.	7.94		
d'	in.	1.81	d'	in.	2.56	d'	in.	2.56	Vu>φVn?	
variable a		42.5	variable a		78.625	variable a		127.5	increase reinforce	
variable b		8.37	variable b		64.8	variable b		32.4		
variable c		-39.11	variable c		-428.04	variable c		-214.02		
a_pos	in.	0.87	a_pos	in.	1.96	a_pos	in.	1.17		
a_neg	in.	4.65	a_neg	in.	6.60	a_neg	in.	6.60		
a	in.	0.87	a	in.	1.96	a	in.	1.17		
T	kip	18.6	T	kip	144	T	kip	72		
Cc	kip	36.80	Cc	kip	153.89	Cc	kip	149.78		
Cs	kip	-18.20	Cs	kip	-9.89	Cs	kip	-77.78		
Cc+Cs	kip	18.60	Cc+Cs	kip	144.00	Cc+Cs	kip	72.00		
CHECK		good	CHECK		good	CHECK		good		
Mult	k-in	178.6	Mult	k-in	2601.7	Mult	k-in	682.8		
φMult	k-ft/ft	16.1	φMult	k-ft	195.1	φMult	k-ft/ft	20.5		
Mc	k-ft/ft	16.1	Mb	k-ft	195.13	Mw	k-ft/ft	20.49		
END SECTION										
Lc	ft	8.181785								
φRw	kip	105.2348								

Figure H-3. RESTORE Barrier Transition Buttress Internal Reinforcement Calculations

36 in. (914 mm) Modified "T"								
Mc stirrups			Mb beam			Mw wall		
As/bar	in. ²	0.2	As/bar	in. ²	0.6	As/bar	in. ²	0.6
# of rebar		2	# of rebar		4	# of rebar		2
d_bar	in.	0.625	d_bar	in.	0.875	d_bar	in.	0.875
As=As'	in. ²	0.4	As=As'	in. ²	2.4	As=As'	in. ²	1.2
Clear Cover	in.	1.5	Clear Cover	in.	1.5	Clear Cover	in.	1.5
Length (b)	in.	12	Length (b)	in.	24.5	Length (b)	in.	36
Width	in.	10.5	Width	in.	21.5	Width	in.	10.5
d	in.	8.69	d	in.	18.94	d	in.	7.94
d'	in.	1.81	d'	in.	2.56	d'	in.	2.56
variable a		51	variable a		104.125	variable a		153
variable b		10.8	variable b		64.8	variable b		32.4
variable c		-50.46	variable c		-428.04	variable c		-214.02
a_pos	in.	0.89	a_pos	in.	1.74	a_pos	in.	1.08
a_neg	in.	4.65	a_neg	in.	6.60	a_neg	in.	6.60
a	in.	0.89	a	in.	1.74	a	in.	1.08
T	kip	24	T	kip	144	T	kip	72
Cc	kip	45.62	Cc	kip	181.19	Cc	kip	165.48
Cs	kip	-21.62	Cs	kip	-37.19	Cs	kip	-93.48
Cc+Cs	kip	24.00	Cc+Cs	kip	144.00	Cc+Cs	kip	72.00
CHECK		good	CHECK		good	CHECK		good
Mult	k-in	227.3	Mult	k-in	2664.7	Mult	k-in	721.6
φMult	k-ft/ft	17.0	φMult	k-ft	199.8	φMult	k-ft/ft	18.0
Mc	k-ft/ft	17.0	Mb	k-ft	199.85	Mw	k-ft/ft	18.04
END SECTION								
Lc	ft	8.660804						
φRw	kip	98.42082						

Figure H-4. RESTORE Barrier Transition Buttress Internal Reinforcement Calculations

36 in. (914 mm) Vertical Barrier								
Mc stirrups			Mw wall			Shear Check		
As/bar	in. ²	0.31	As/bar	in. ²	0.6	ϕV_n		52.45
# of rebar		2	# of rebar		5	Vc	kip	40.41
d_bar	in.	0.625	d_bar	in.	0.875	Vs	kip	29.53
As=As'	in. ²	0.62	As=As'	in. ²	3			
Clear Cover	in.	1.5	Clear Cover	in.	1.5	w	k/ft	28.57
Length (b)	in.	10	Length (b)	in.	36	Ra		50
Width	in.	10.5	Width	in.	10.5	Rb		50
d	in.	8.69	d	in.	7.94			
d'	in.	1.81	d'	in.	2.56			
variable a		42.5	variable a		153	Vu> ϕV_n ? section good		
variable b		16.74	variable b		81			
variable c		-78.21	variable c		-535.05			
a_pos	in.	1.17	a_pos	in.	1.62			
a_neg	in.	4.66	a_neg	in.	6.60			
a	in.	1.17	a	in.	1.62			
T	kip	37.2	T	kip	180			
Cc	kip	49.89	Cc	kip	248.47			
Cs	kip	-12.69	Cs	kip	-68.47			
Cc+Cs	kip	37.20	Cc+Cs	kip	180.00			
CHECK		good	CHECK		good			
Mult	k-in	316.9	Mult	k-in	1402.4			
ϕ Mult	k-ft/ft	28.5	ϕ Mult	k-ft/ft	35.1			
Mc	k-ft/ft	28.5	Mw	k-ft/ft	35.06			
END SECTION								
Lc	ft	5.508532						
ϕR_w	kip	104.7367						

Figure H-5. RESTORE Barrier Transition Buttress Internal Reinforcement Calculations

A torsional beam or footer was designed to transfer the load from the barrier into the footing by lateral shear and moment about the longitudinal axis. The footer design process was described earlier in Section 2.8, and the calculation spreadsheet can be found in Figure H-6. A safety factor of $\phi=0.75$ was used during the design. The initial footer was designed to be 30 in. wide by 30 in. deep (762 mm by 762 mm) and extended under

the length of the buttress and throughout the RESTORE barrier, if a footing was not already present. The steel reinforcement consisted of no. 4 stirrups spaced at 12 in. (305 mm) and four no. 6 longitudinal bars evenly spaced. An initial drawing of the reinforcement within the buttress and the footer is shown in Figures H-7 through H-10.

$$T_c = kx^2yv_{tc} \quad (56)$$

Where: T_c = Torsion capacity of the concrete, k-in (kN-m)

k = Coefficient for concrete capacity

x = Depth of the footer, in. (mm)

y = Width of the footer, in. (mm)

v_{tc} = Limiting pure torsion shear stress of concrete, ksi (MPa)

END SECTION (A-A)		END SECTION (B-B)		END SECTION (C-C)	
Torsion Moment	$T=Mc*Lcr$	Torsion Moment	$T=Mc*Lcr$	Torsion Moment	$T=Mc*Lcr$
Mc	16.1 k-ft/ft	Mc	17 k-ft/ft	Mc	28.5 k-ft/ft
Lcr	6.32 ft	Lcr	8.669 ft	Lcr	5.508 ft
ϕ Torsion	0.75	ϕ Torsion	0.75	ϕ Torsion	0.75
T	1221.024 k-in	T	1768.476 k-in	T	1883.736 k-in
Tn	1628.032 k-in	Tn	2357.968 k-in	Tn	2511.648 k-in
Torsion Cap. Concrete	$Tc=kx^2yv_{tc}$	Torsion Cap. Concrete	$Tc=kx^2yv_{tc}$	Torsion Cap. Concrete	$Tc=kx^2yv_{tc}$
fc'	5 ksi	fc'	5 ksi	fc'	5 ksi
$v_{tc}=6\text{sqrt}(fc')$	0.424264 ksi	$v_{tc}=6\text{sqrt}(fc')$	0.424264 ksi	$v_{tc}=6\text{sqrt}(fc')$	0.424264 ksi
k	0.133	k	0.133	k	0.133
x (depth)	30 in	x (depth)	30 in	x	30 in
y (width)	30 in	y (width)	30 in	y	30 in
Tc	1523.532 k-in	Tc	1523.532 k-in	Tc	1523.532 k-in
Torsion Cap from Stirrups	$Ts=Tn-Tc$	Torsion Cap from Stirrups	$Ts=Tn-Tc$	Torsion Cap from Stirrups	$Ts=Tn-Tc$
Ts	104.4997 k-in	Ts	834.4357 k-in	Ts	988.1157 k-in
Stirrup Design		Stirrup Design		Stirrup Design	
clear cover dist	2 in	clear cover dist	2 in	clear cover dist	2 in
Select. Bar number	4	Select. Bar number	4	Select. Bar number	4
Select. Bar area	0.2 in ²	Select. Bar area	0.2 in ²	Select. Bar area	0.2 in ²
stirrup diameter	0.5 in	stirrup diameter	0.5 in	stirrup diameter	0.5 in
x _o	25.5 in	x _o	25.5 in	x _o	25.5 in
y _o	25.5 in	y _o	25.5 in	y _o	25.5 in
A _o =0.85x _o y _o	552.7125 in ²	A _o =0.85x _o y _o	552.7125 in ²	A _o =0.85x _o y _o	552.7125 in ²
f _y	60 ksi	f _y	60 ksi	f _y	60 ksi
At/S=Ts/(2Aof _y)	0.001576 in ² /in	At/S=Ts/(2Aof _y)	0.012581 in ² /in	At/S=Ts/(2Aof _y)	0.014898 in ² /in
Spacing Needed	126.9391 in.	Spacing Needed	15.89709 in.	Spacing Needed	13.42464 in.
Spacing Chosen < Needed	12 in.	Spacing Chosen < Needed	12 in.	Spacing Chosen < Needed	12 in.
At	0.018907 in ²	At	0.150971 in ²	At	0.178776 in ²
Long Reinforcement		Long Reinforcement		Long Reinforcement	
f _{yt}	60 ksi	f _{yt}	60 ksi	f _{yt}	60 ksi
Ph=2(y _o +x _o)	102 in	Ph=2(y _o +x _o)	102 in	Ph=2(y _o +x _o)	102 in
Al=(At/S)Ph(f _{yt} /f _y)	0.160707 in ²	Al=(At/S)Ph(f _{yt} /f _y)	1.283254 in ²	Al=(At/S)Ph(f _{yt} /f _y)	1.519594 in ²
Bar Selected	6	Bar Selected	6	Bar Selected	6
Bar Area	0.44 in ²	Bar Area	0.44 in ²	Bar Area	0.44 in ²
Number of Bars	4	Number of Bars	4	Number of Bars	4
Bar select Area > Al	1.76 in ²	Bar select Area > Al	1.76 in ²	Bar select Area > Al	1.76 in ²

Figure H-6. Torsional Footer Design Spreadsheet, RESTORE Barrier Transition Buttress

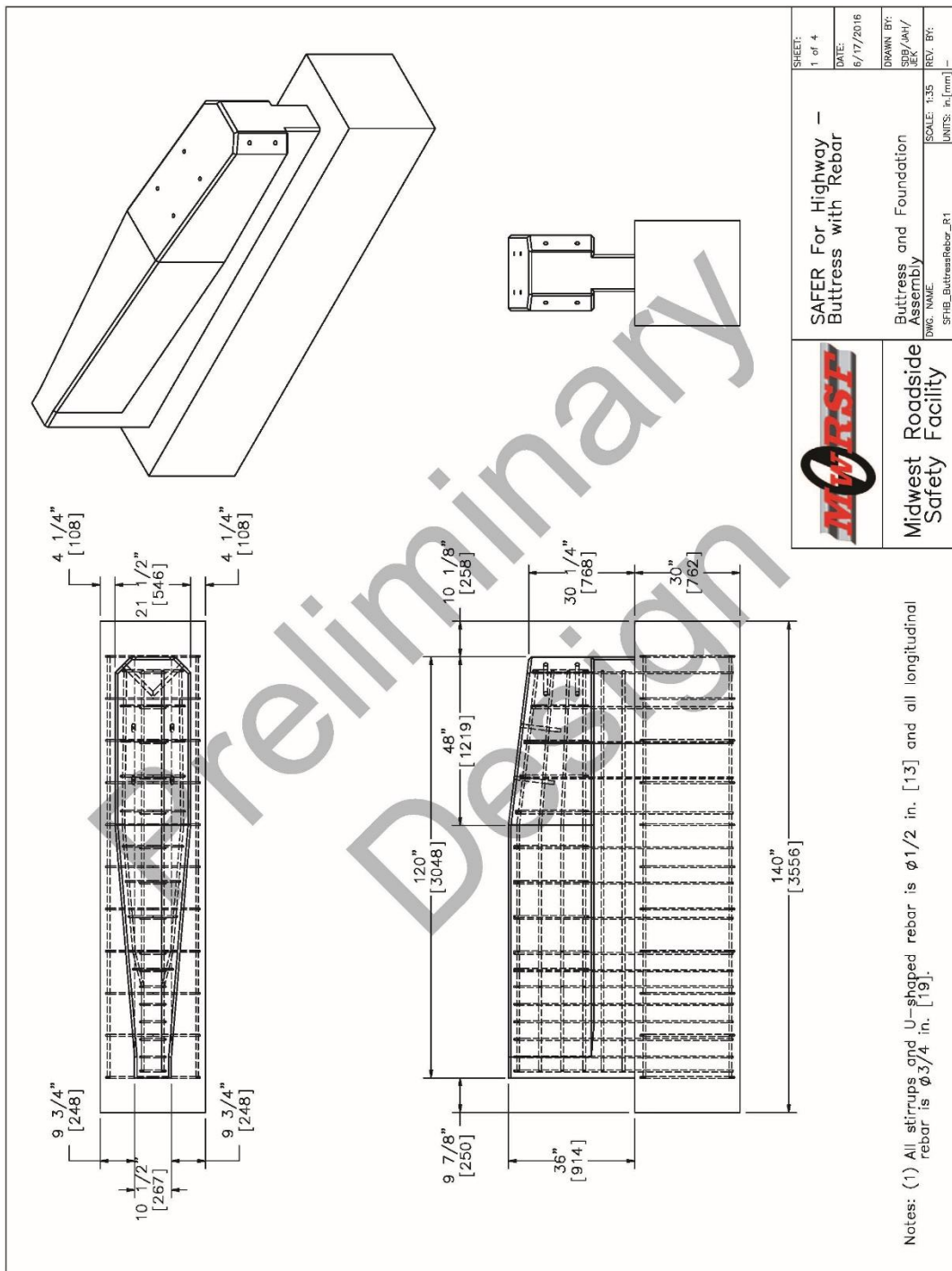
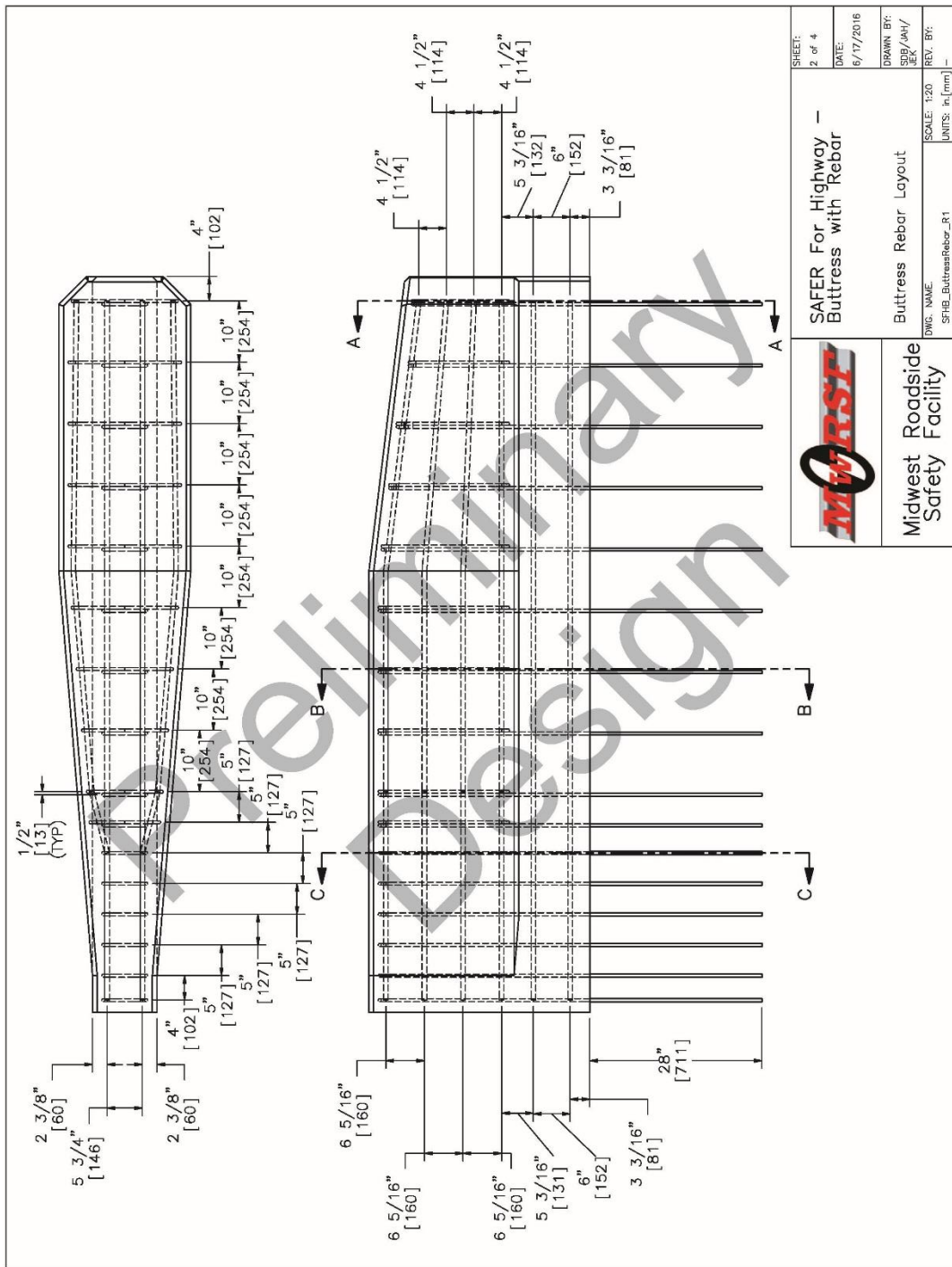


Figure H-7. Buttress and Foundation Assembly




 Midwest Safety Facility	SAFER For Highway -- Buttress with Rebar	SHEET: 2 of 4
	Buttress Rebar Layout	DATE: 6/17/2016
DWG. NAME: SFHB_ButtressRebar_R1	SCALE: 1:20 UNITS: in, (mm)	DRAWN BY: SDB/AH/ J.E.K.
		REV. BY: -

Figure H-8. Buttress Rebar Layout

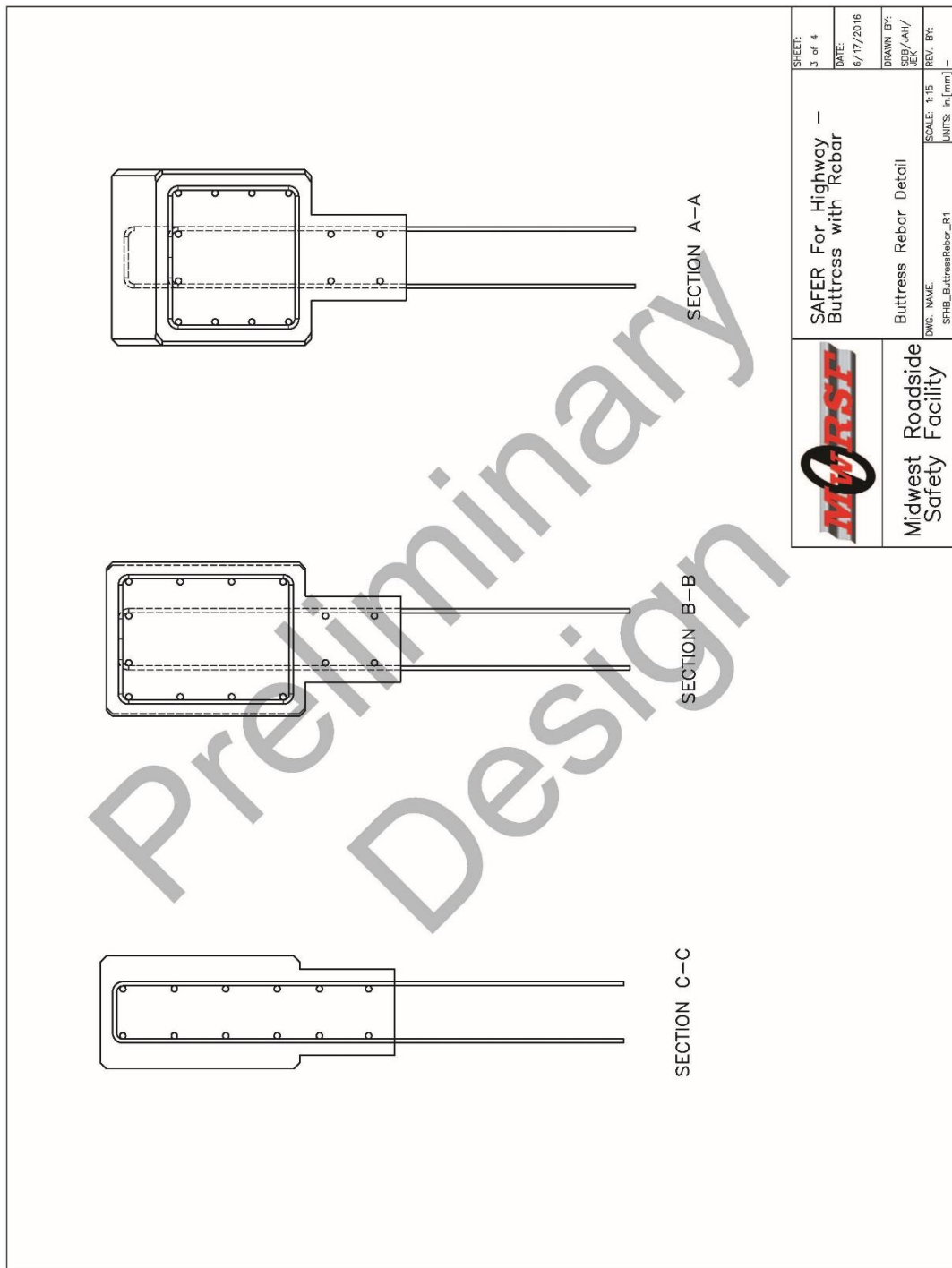


Figure H-9. Buttress Rebar Detail

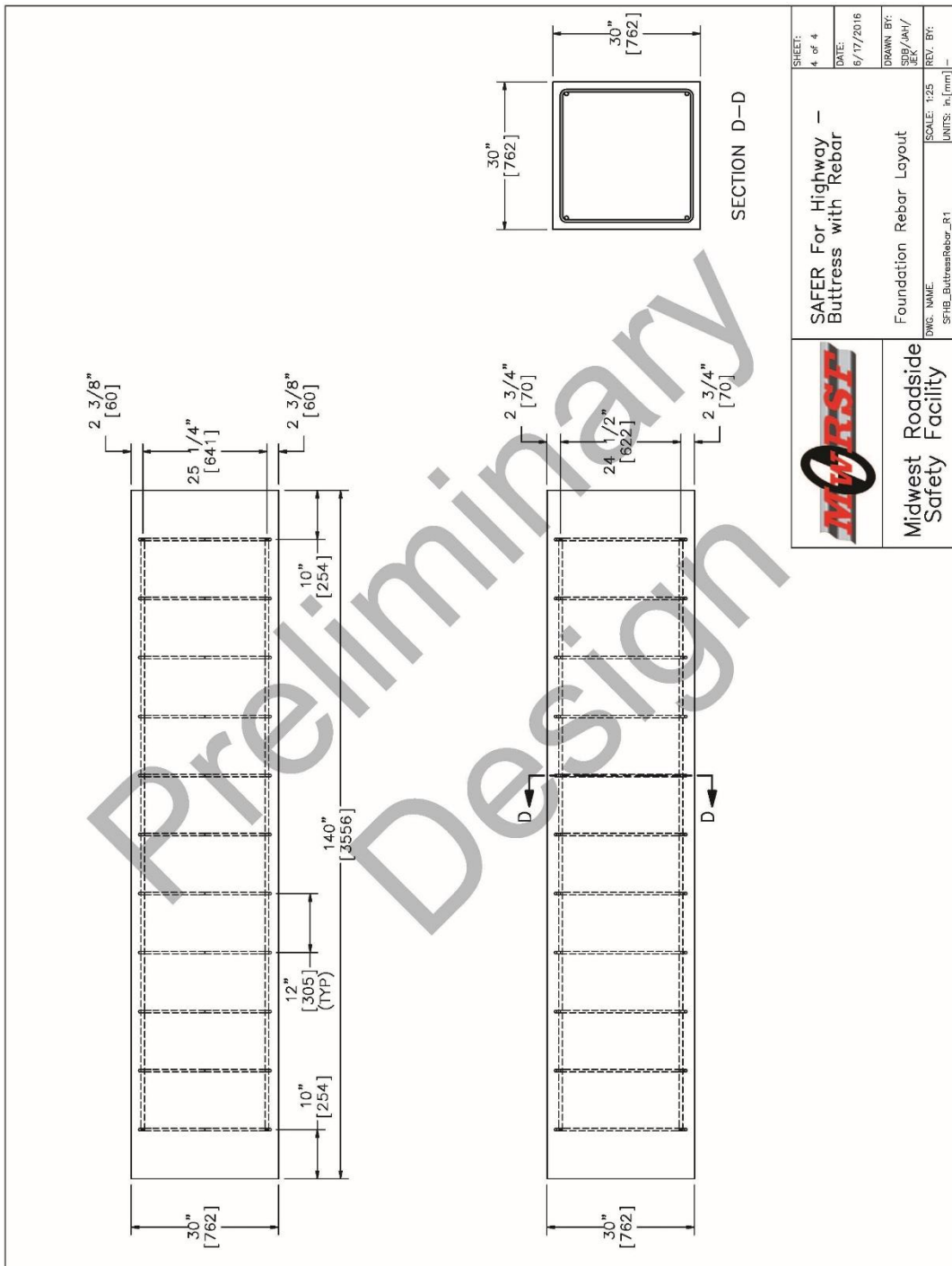


Figure H-10. Foundation Rebar Layout

Appendix I. RESTORE Barrier Transition with No Cover Plate

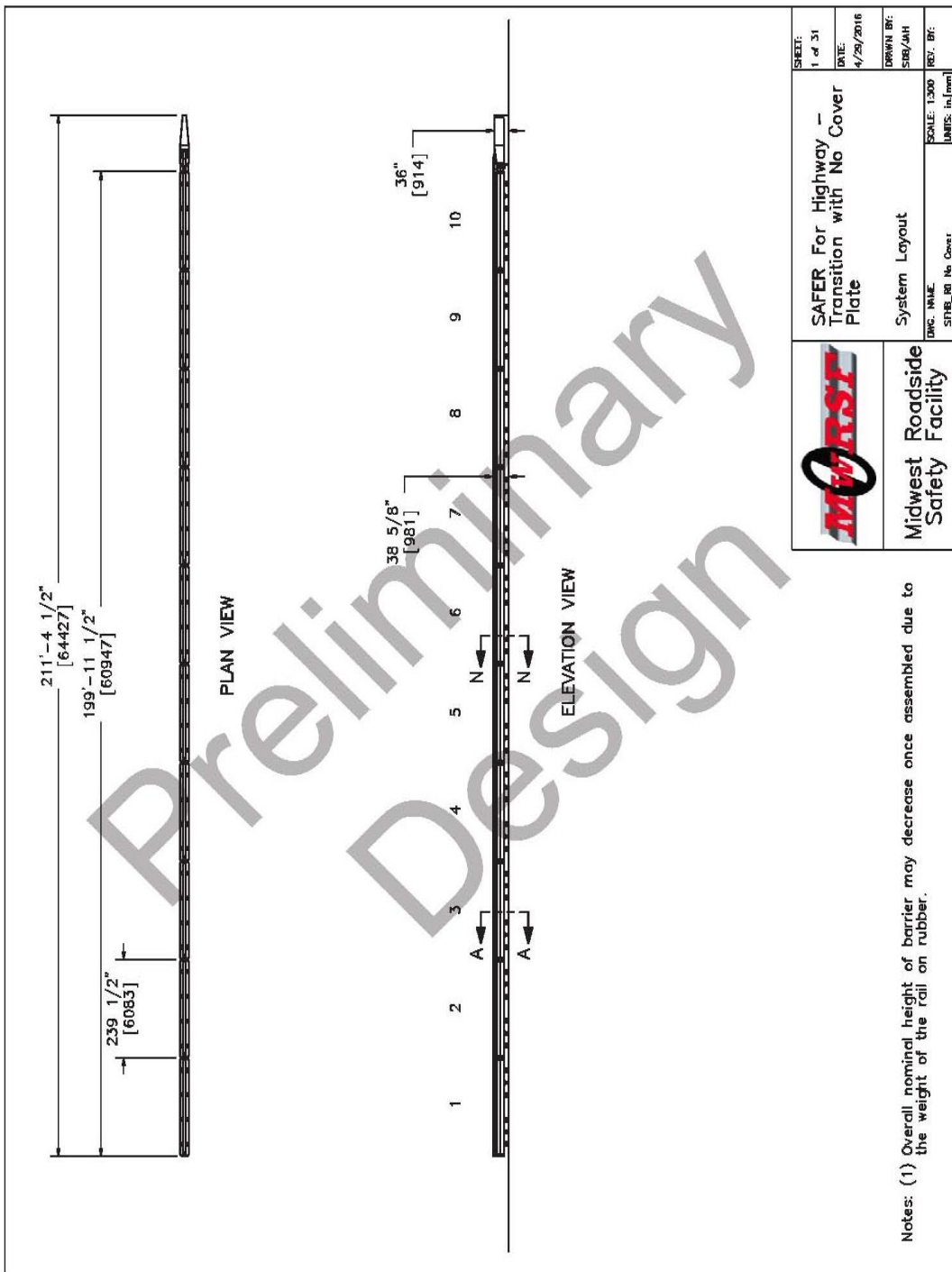


Figure I-1. System Layout, No Cover Plate, RESTORE Barrier Transition

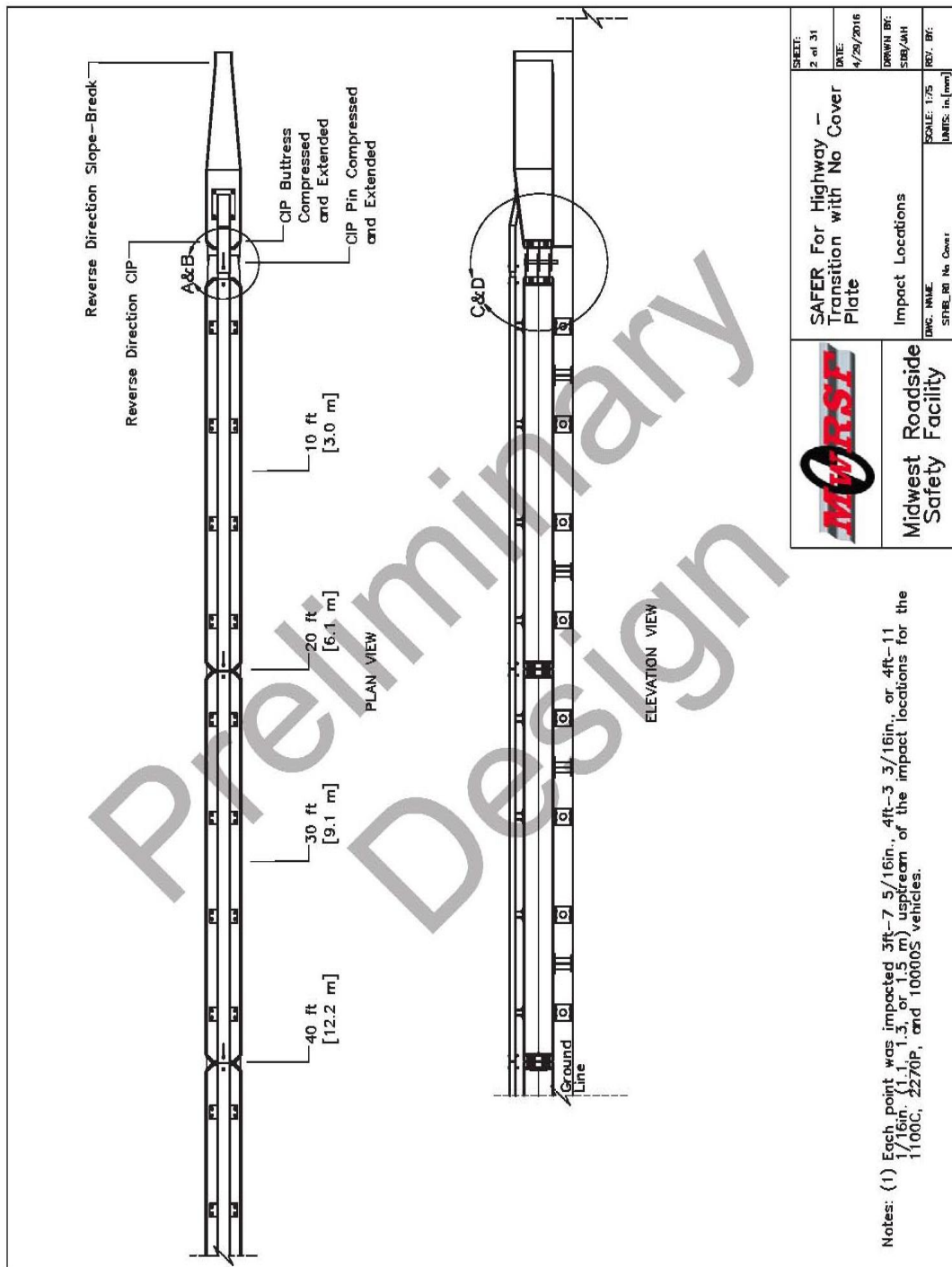
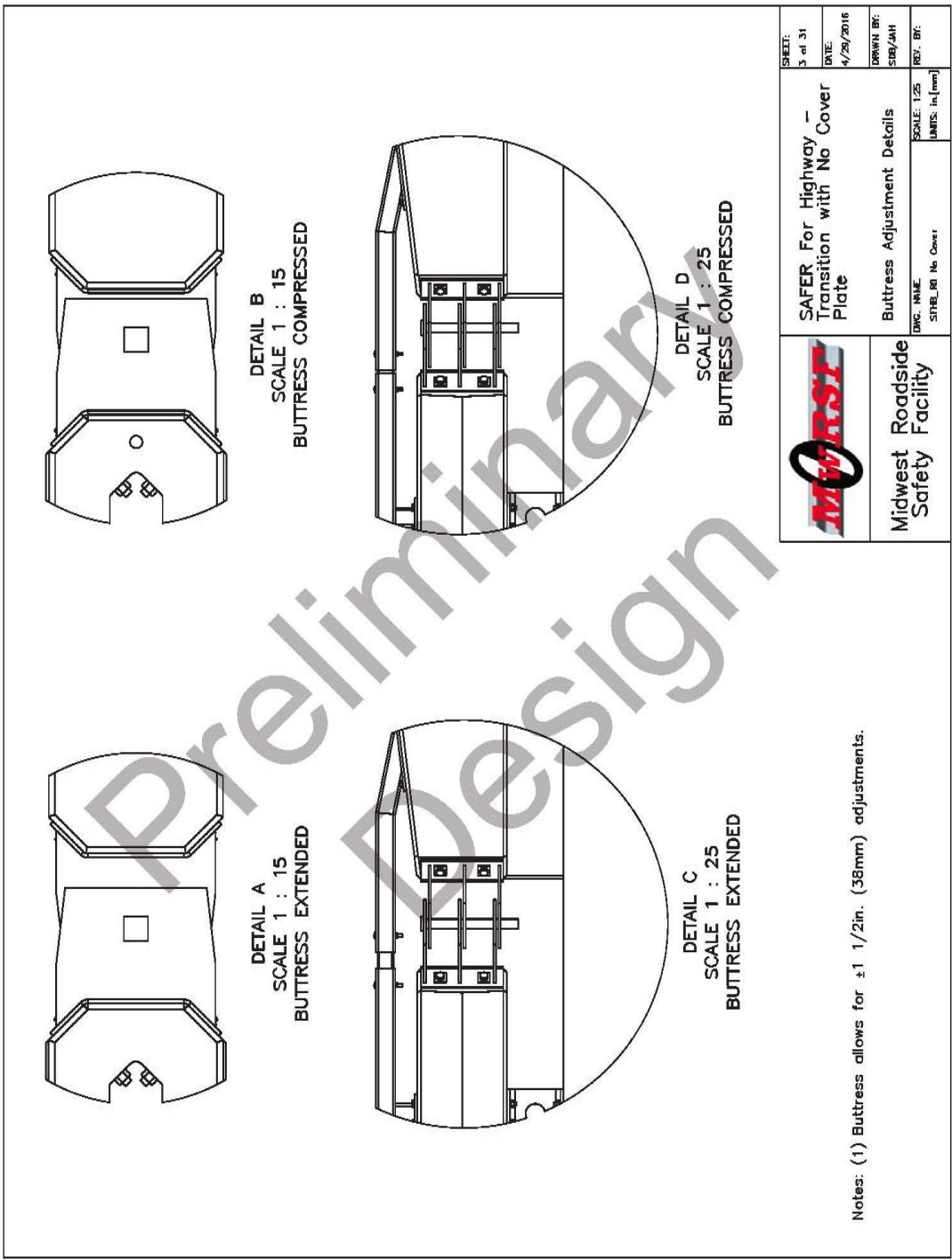


Figure I-2. System Layout, No Cover Plate, RESTORE Barrier Transition




 Midwest Roadside Safety Facility	SAFER For Highway – Transition with No Cover Plate	SHEET: 3 of 31 DATE: 4/29/2016
	Buttress Adjustment Details	DRAWN BY: SSB/JAH REV. BY: REV. BY:
DWG. NAME: STRS_BI No Cover	SCALE: 1:25 UNITS: in./mm	

Figure I-3. Barrier Adjustment Details, No Cover Plate, RESTORE Barrier Transition

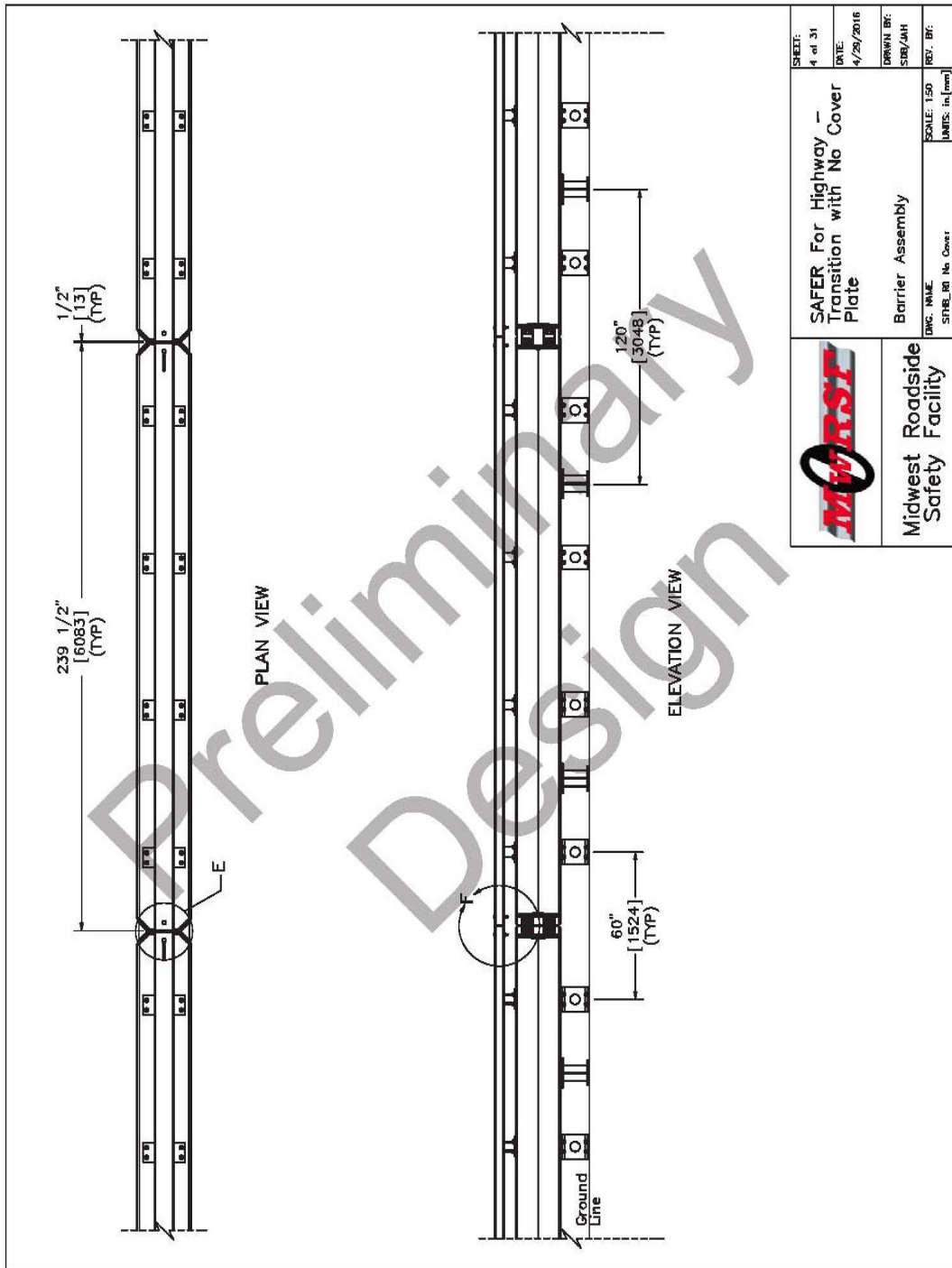


Figure I-4. Barrier Assembly, No Cover Plate, RESTORE Barrier Transition

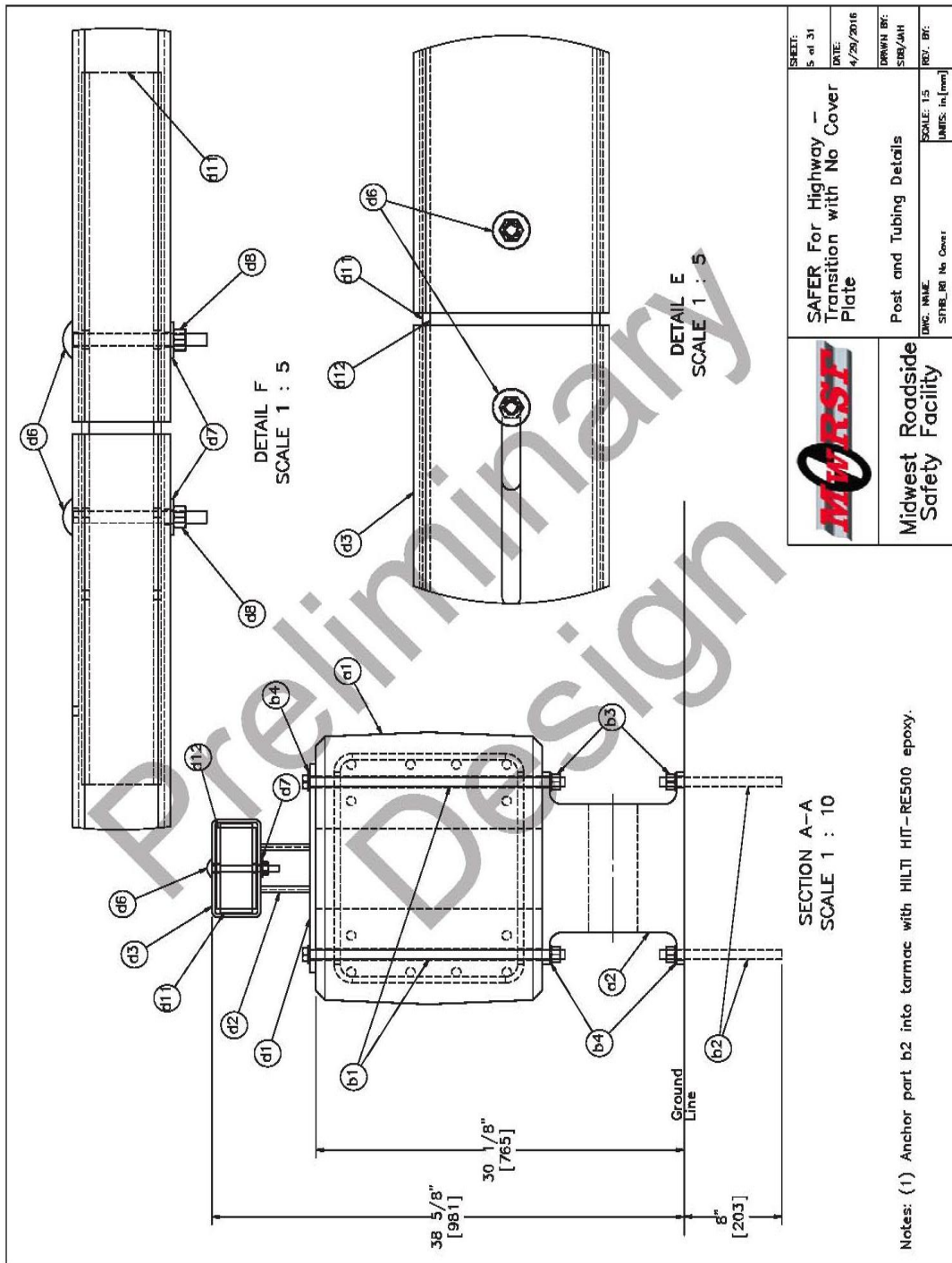


Figure I-5. Post and Tubing Details, No Cover Plate, RESTORE Barrier Transition

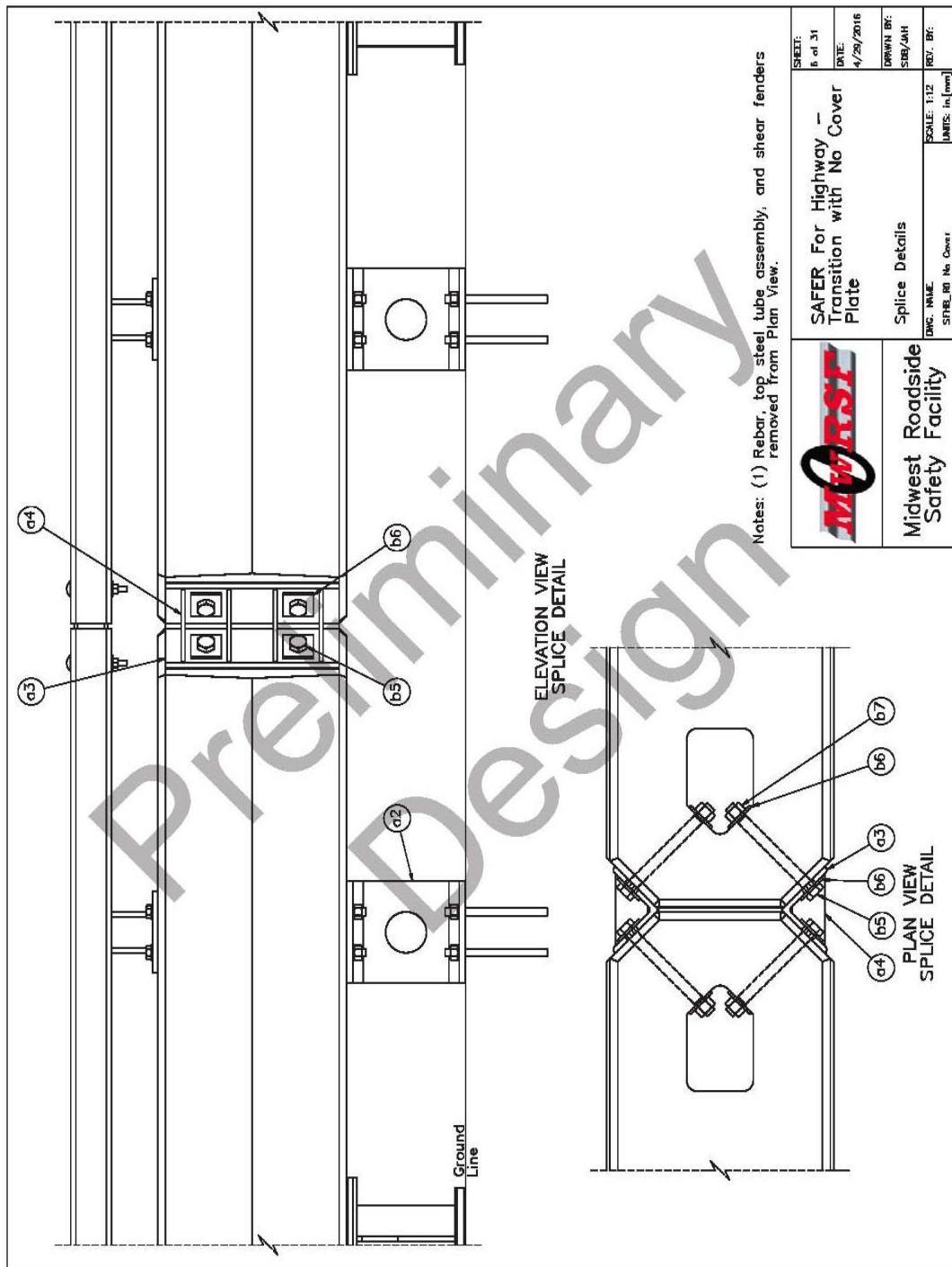


Figure I-6. Splice Details, No Cover Plate, RESTORE Barrier Transition

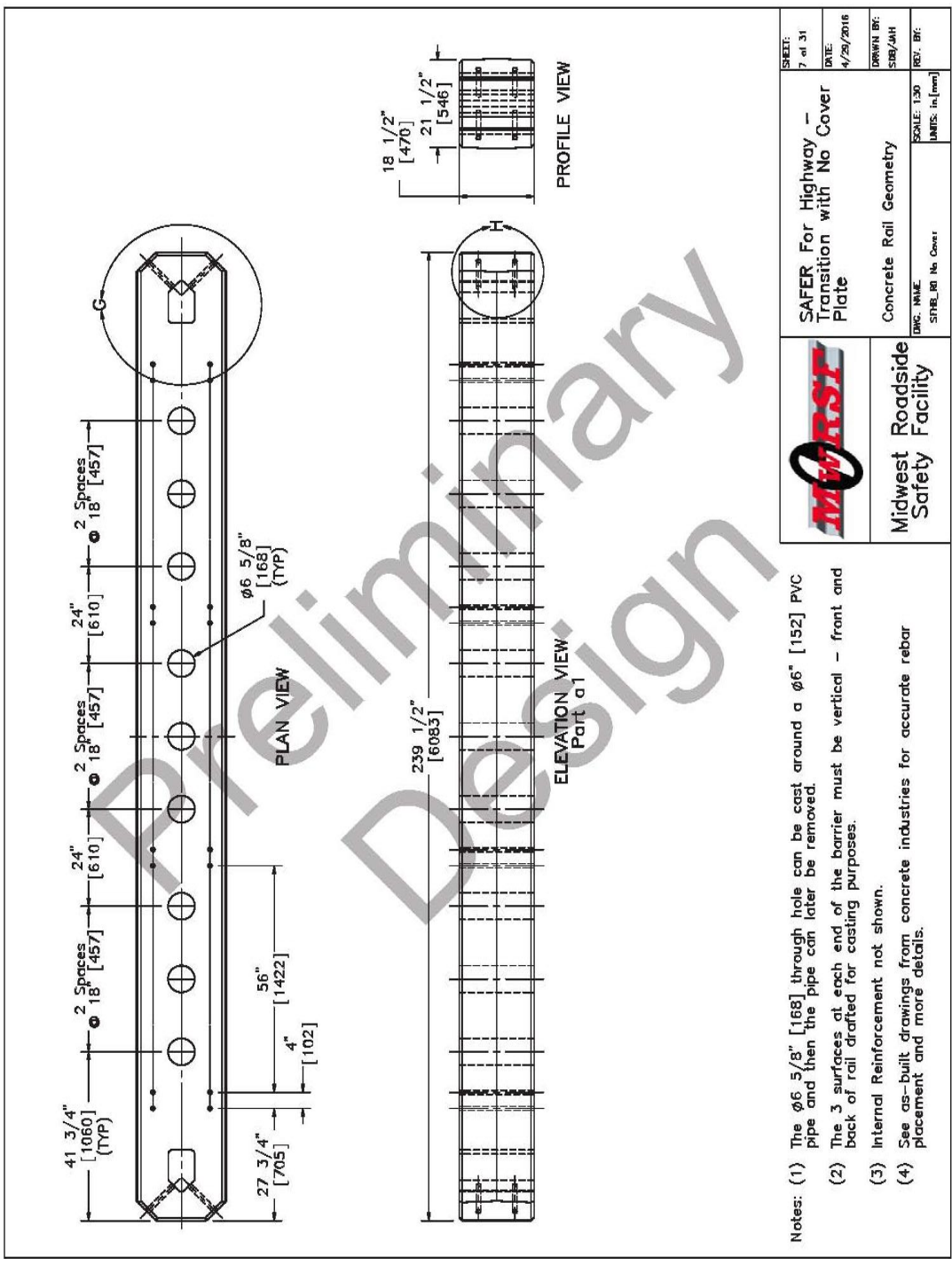


Figure I-7. Concrete Rail Geometry, No Cover Plate, RESTORE Barrier Transition

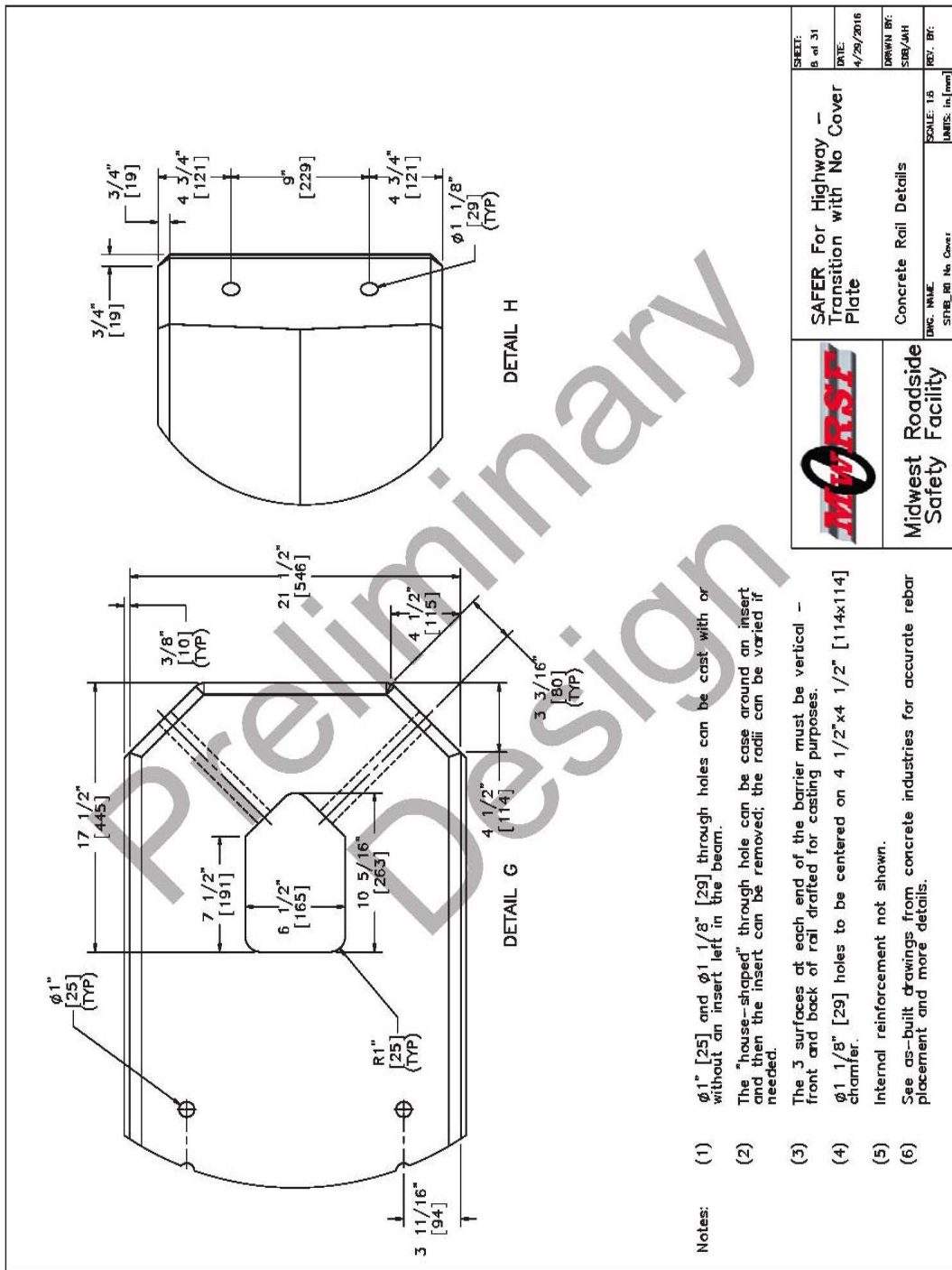


Figure I-8. Concrete Rail Details, No Cover Plate, RESTORE Barrier Transition

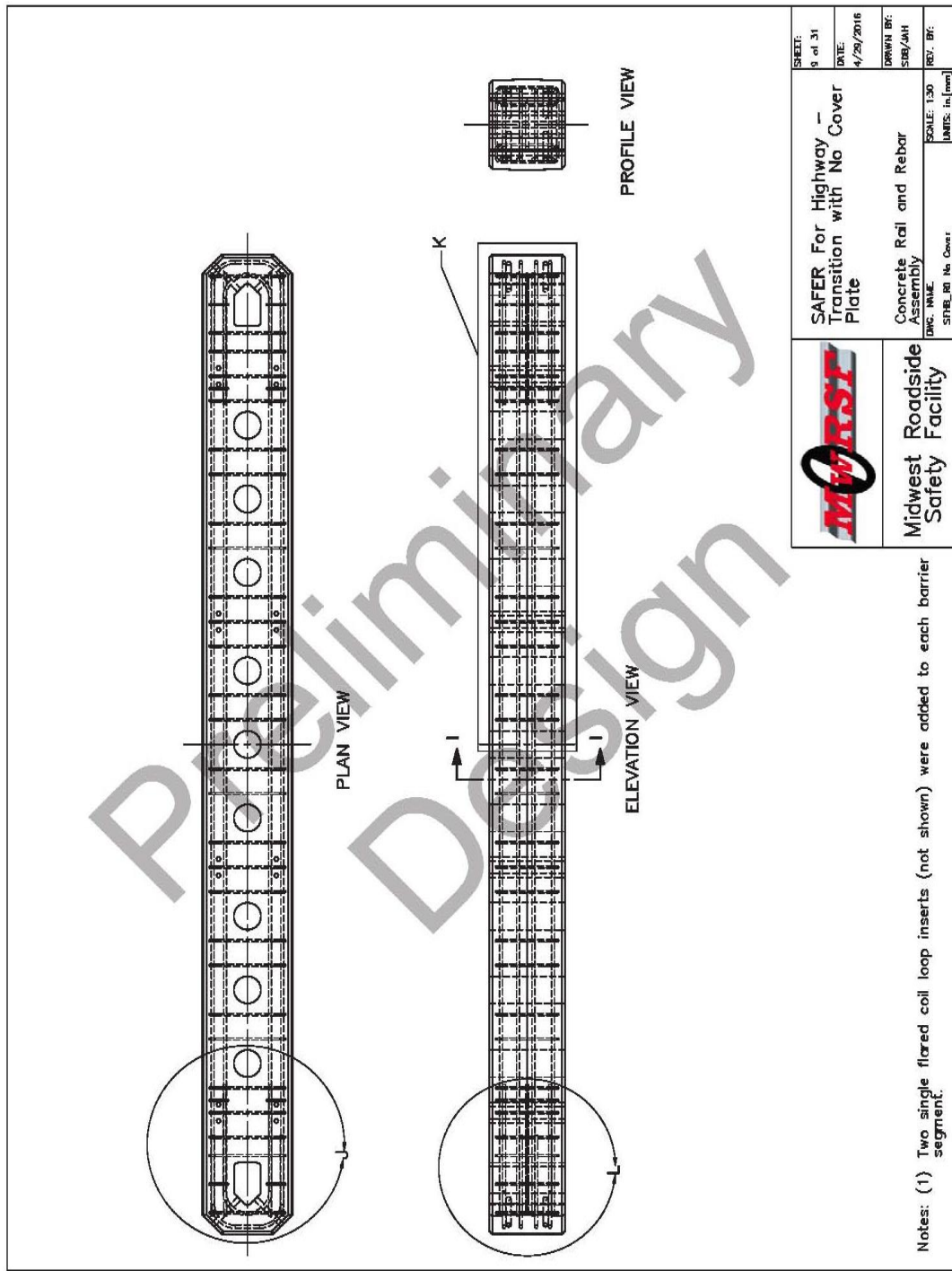


Figure I-9. Concrete Rail and Rebar Assembly, No Cover Plate, RESTORE Barrier Transition

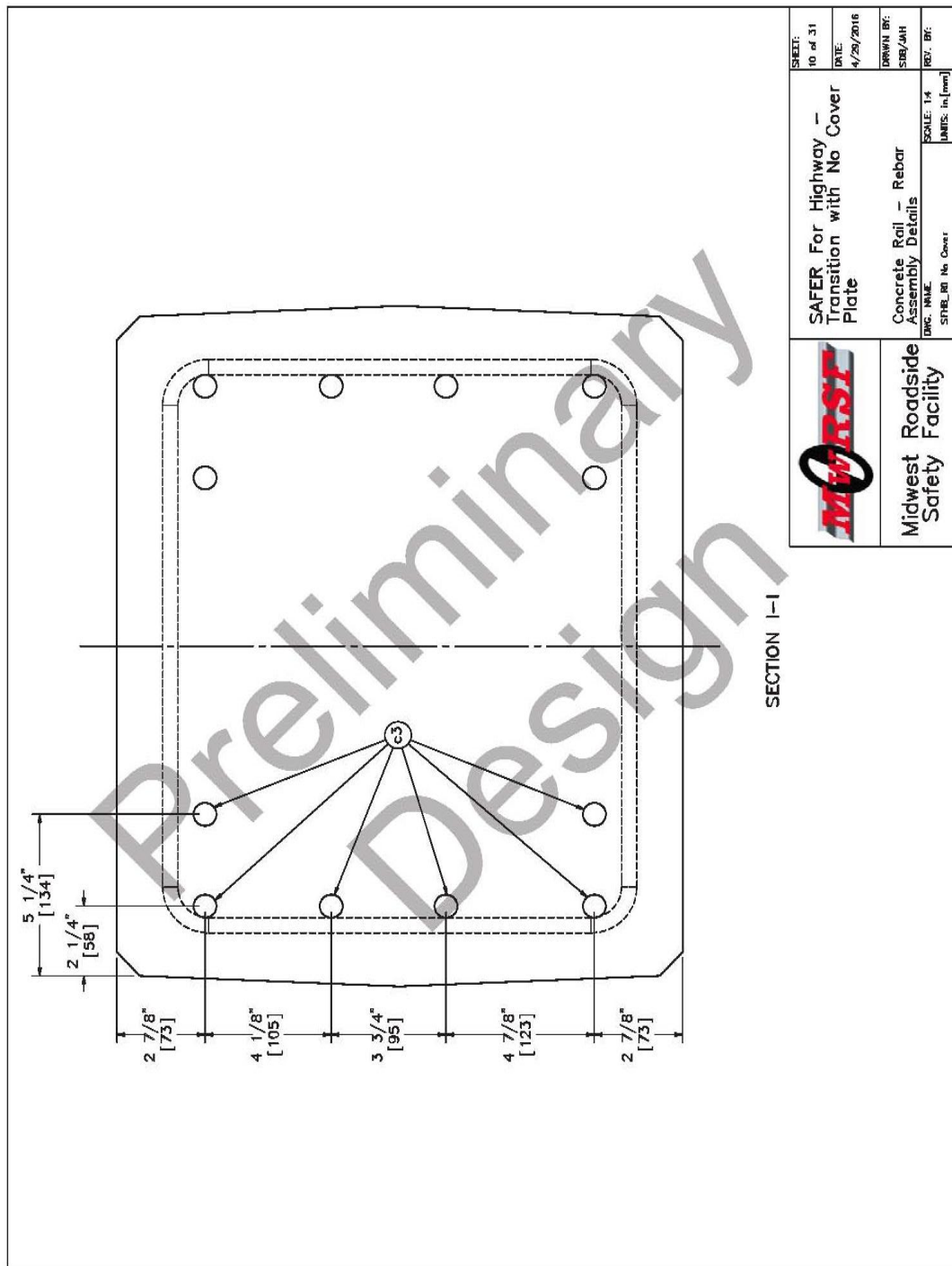


Figure I-10. Concrete Rail Rebar Assembly Details, No Cover Plate, RESTORE Barrier Transition

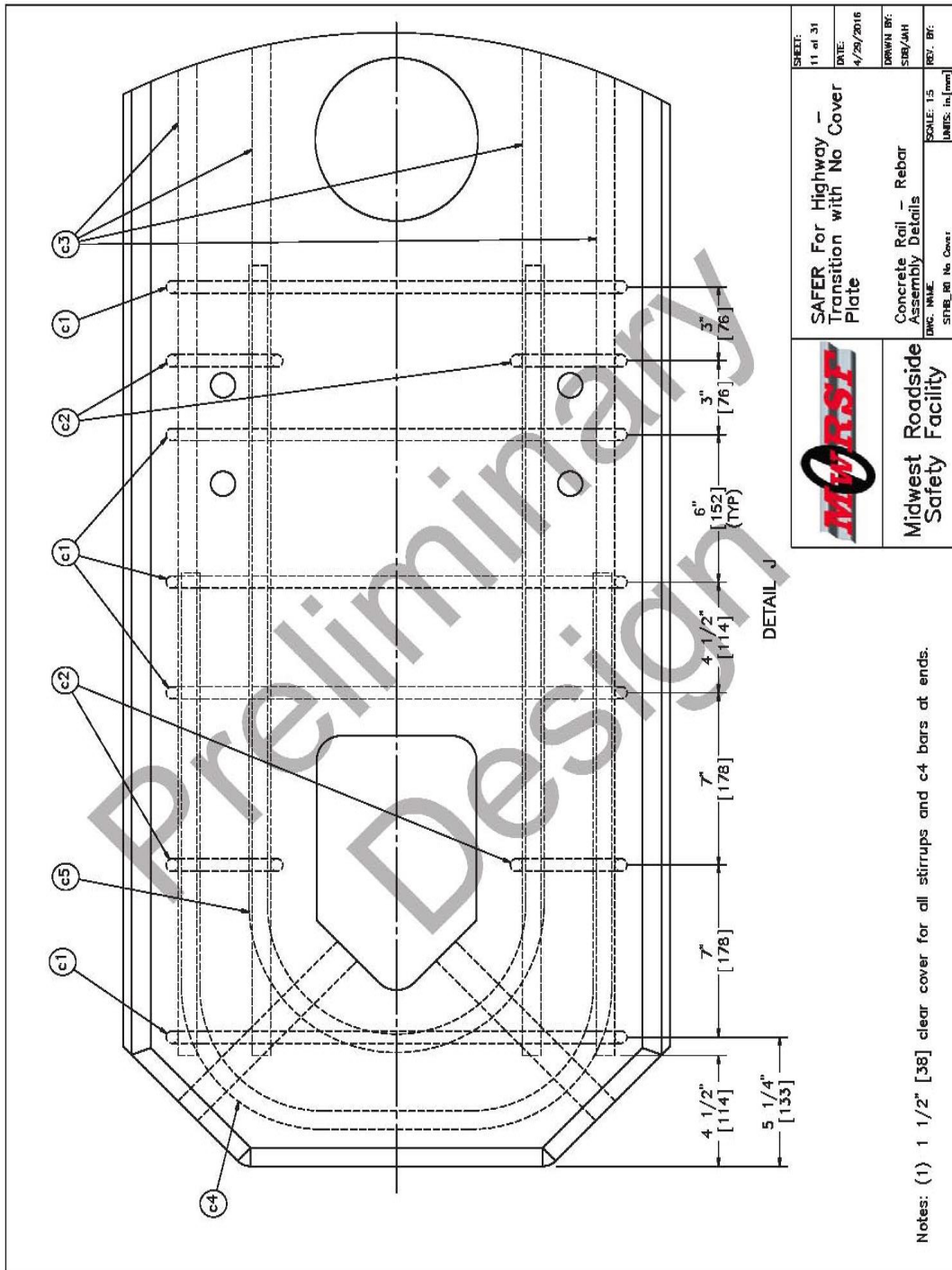


Figure I-11. Concrete Rail Rebar Assembly Details, No Cover Plate, RESTORE Barrier Transition

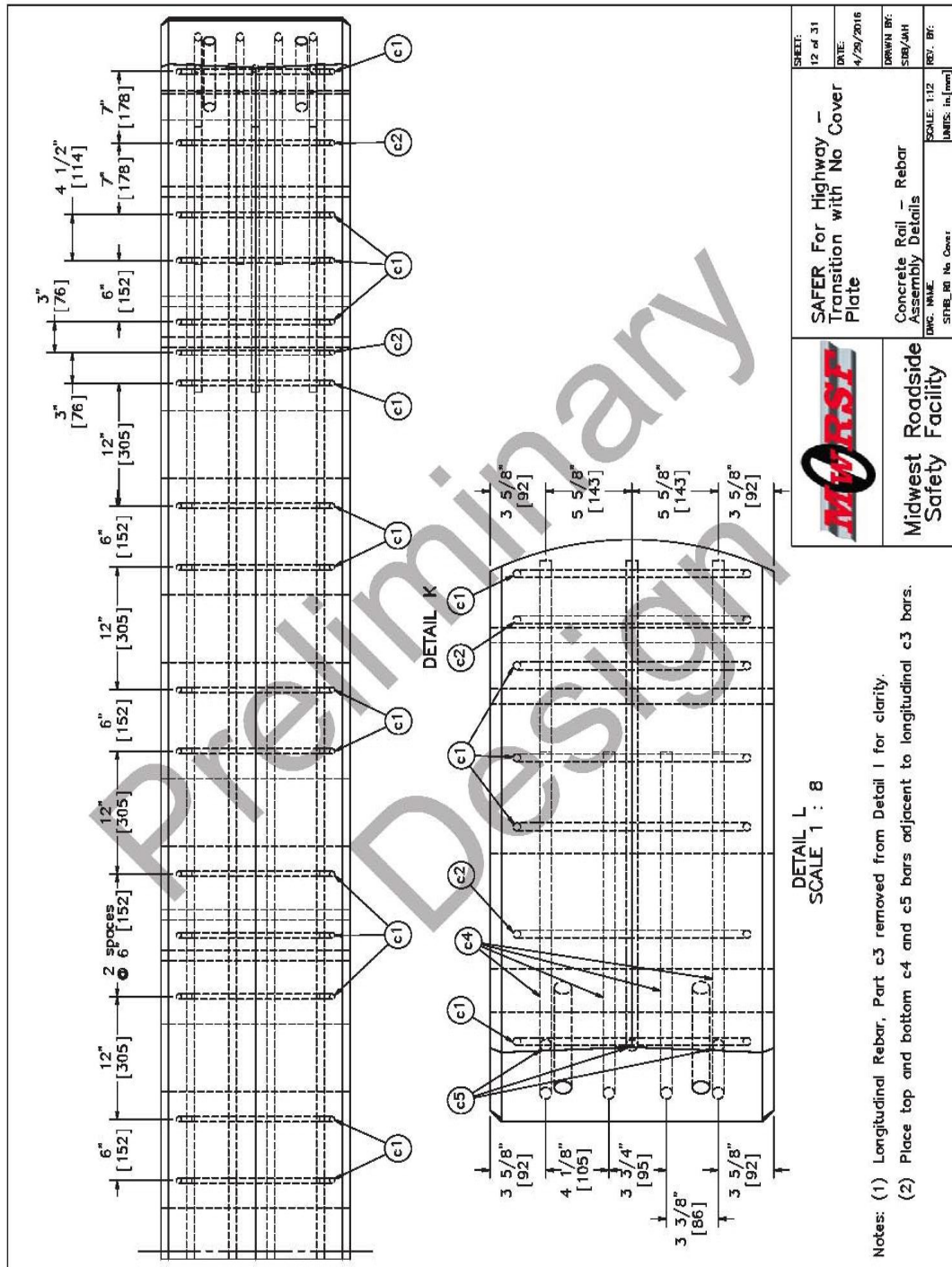


Figure I-12. Concrete Rail Rebar Assembly Details, No Cover Plate, RESTORE Barrier Transition

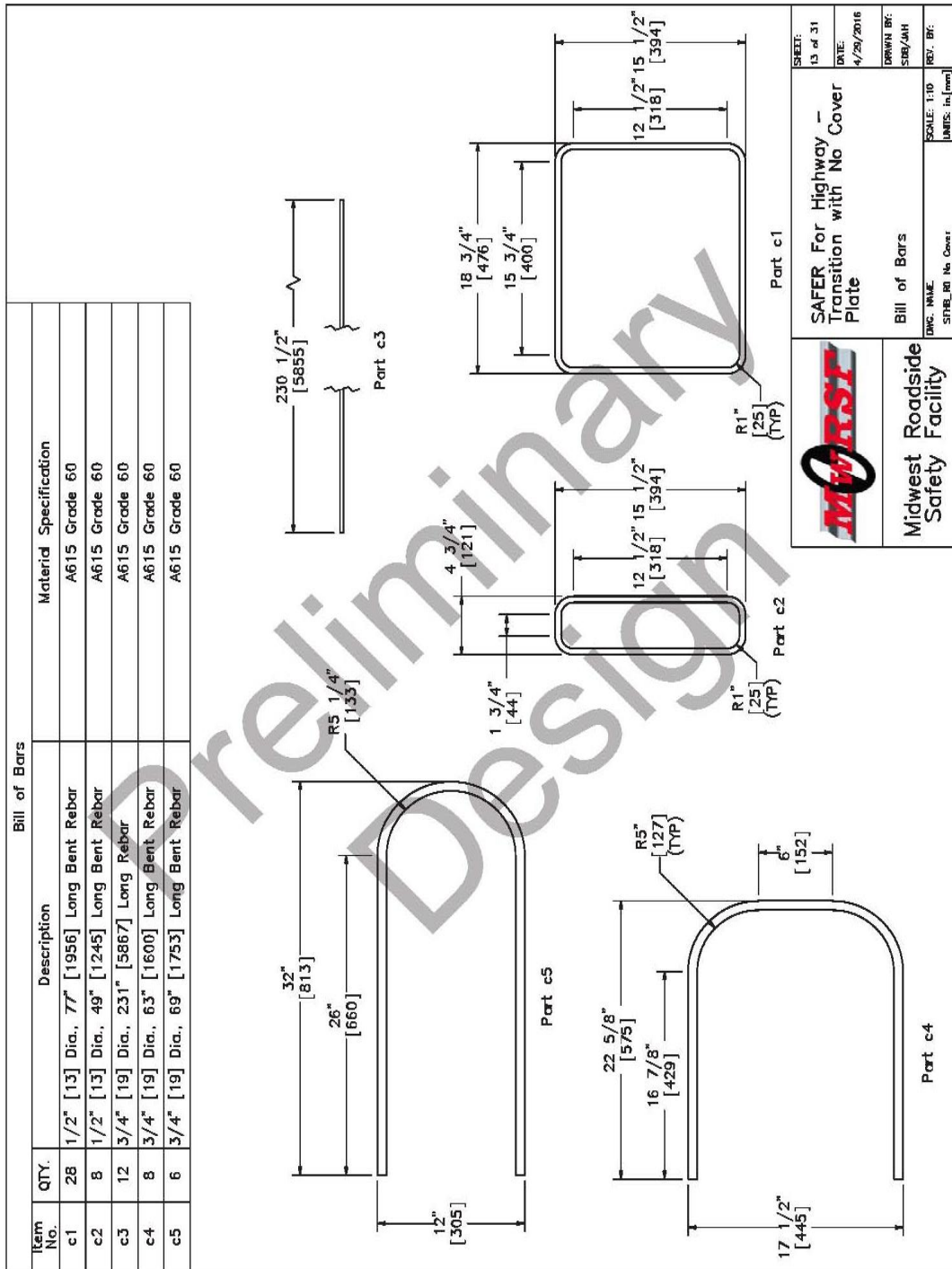


Figure I-13. Bill of Bars, No Cover Plate, RESTORE Barrier Transition

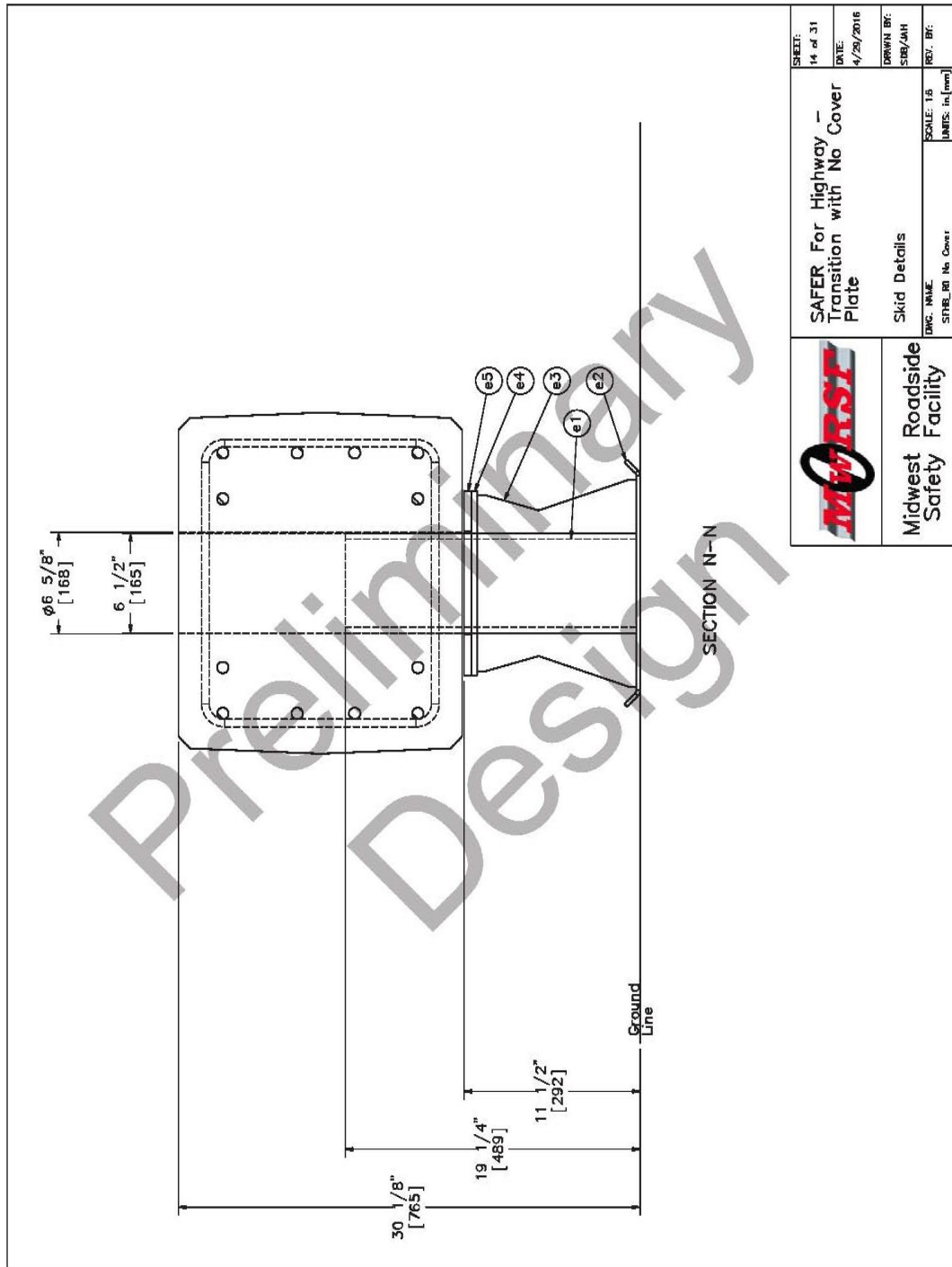


Figure I-14. Skid Details, No Cover Plate, RESTORE Barrier Transition

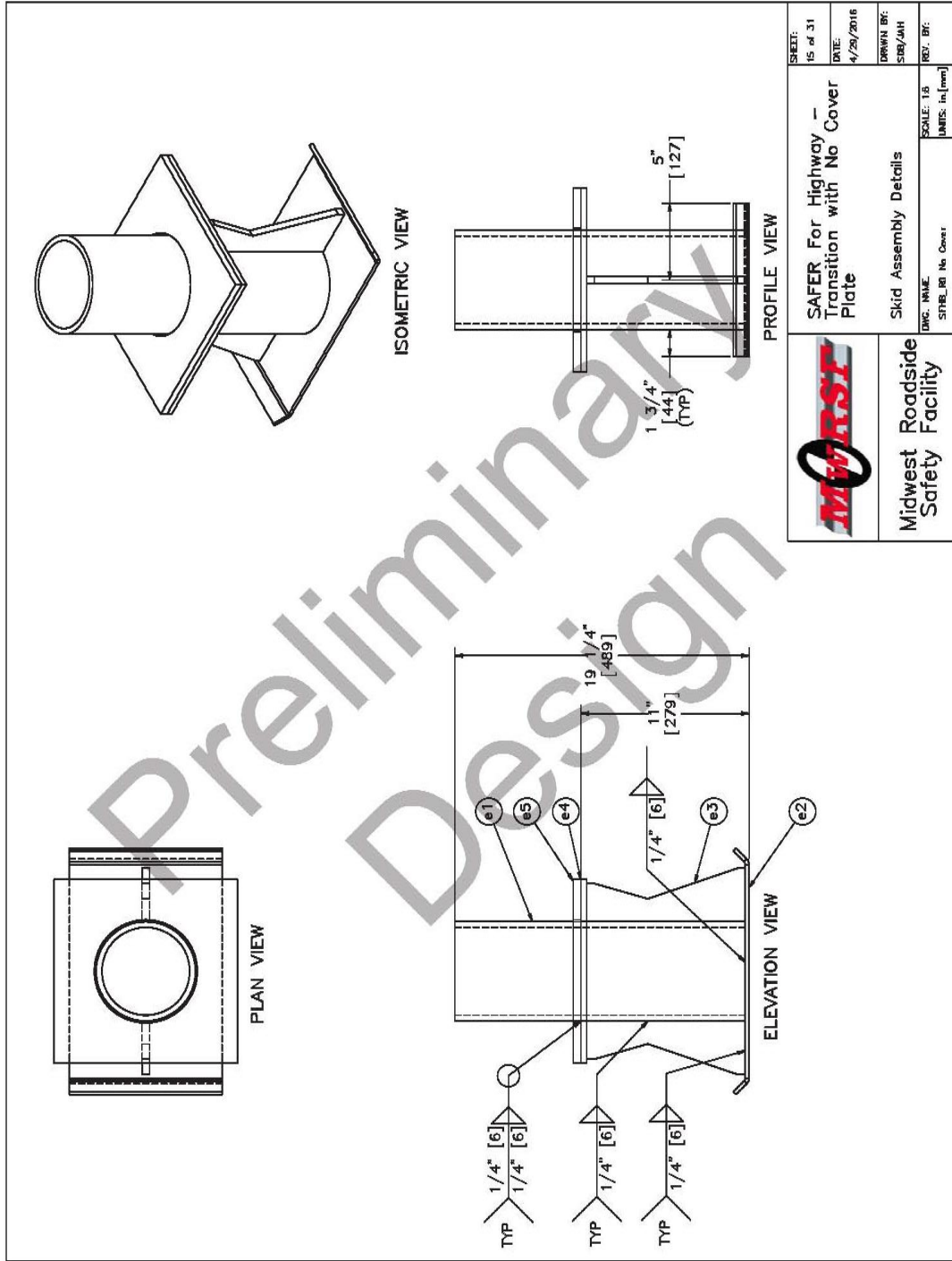


Figure I-15. Skid Assembly Details, No Cover Plate, RESTORE Barrier Transition

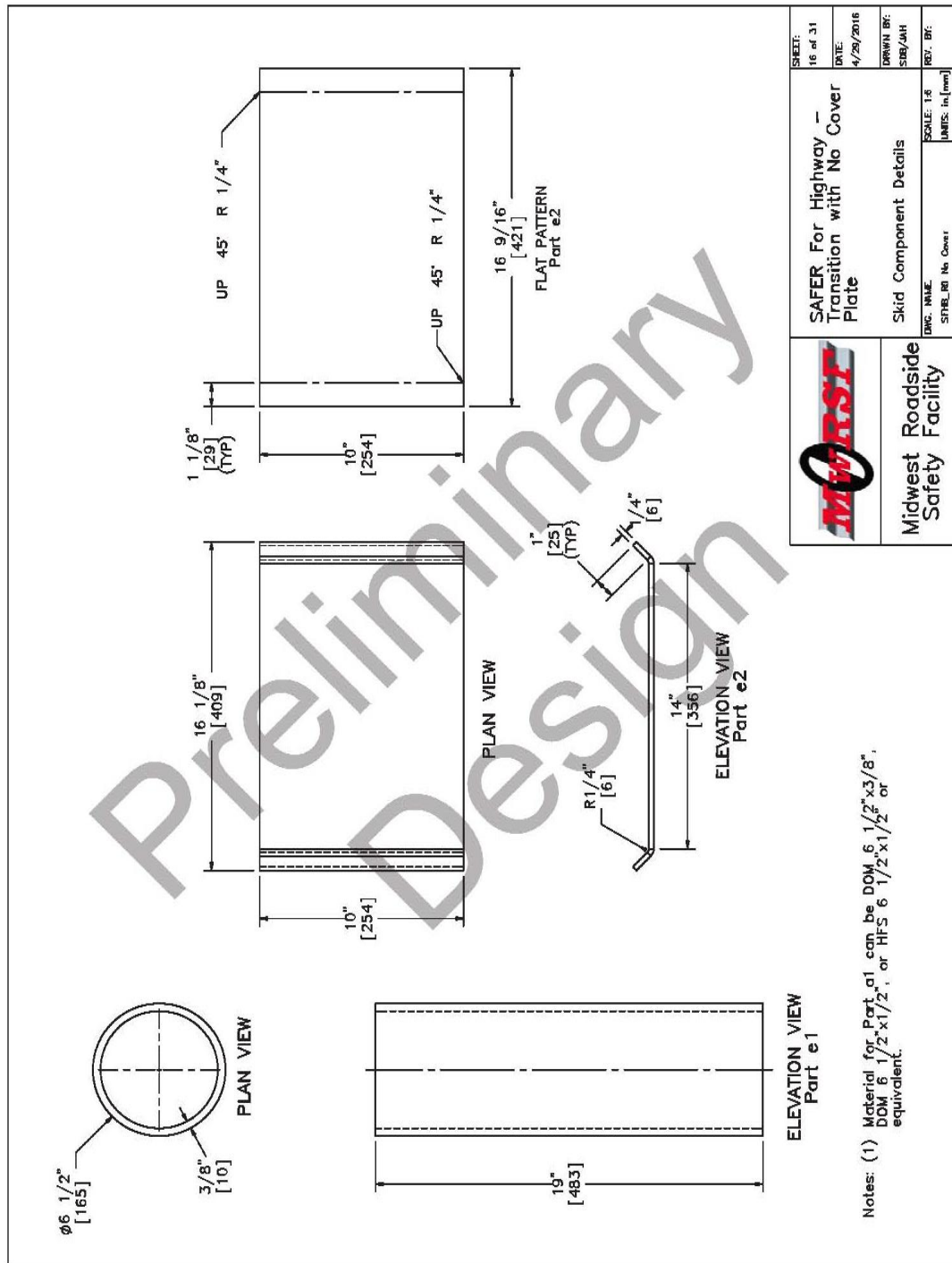


Figure I-16. Skid Component Details, No Cover Plate, RESTORE Barrier Transition

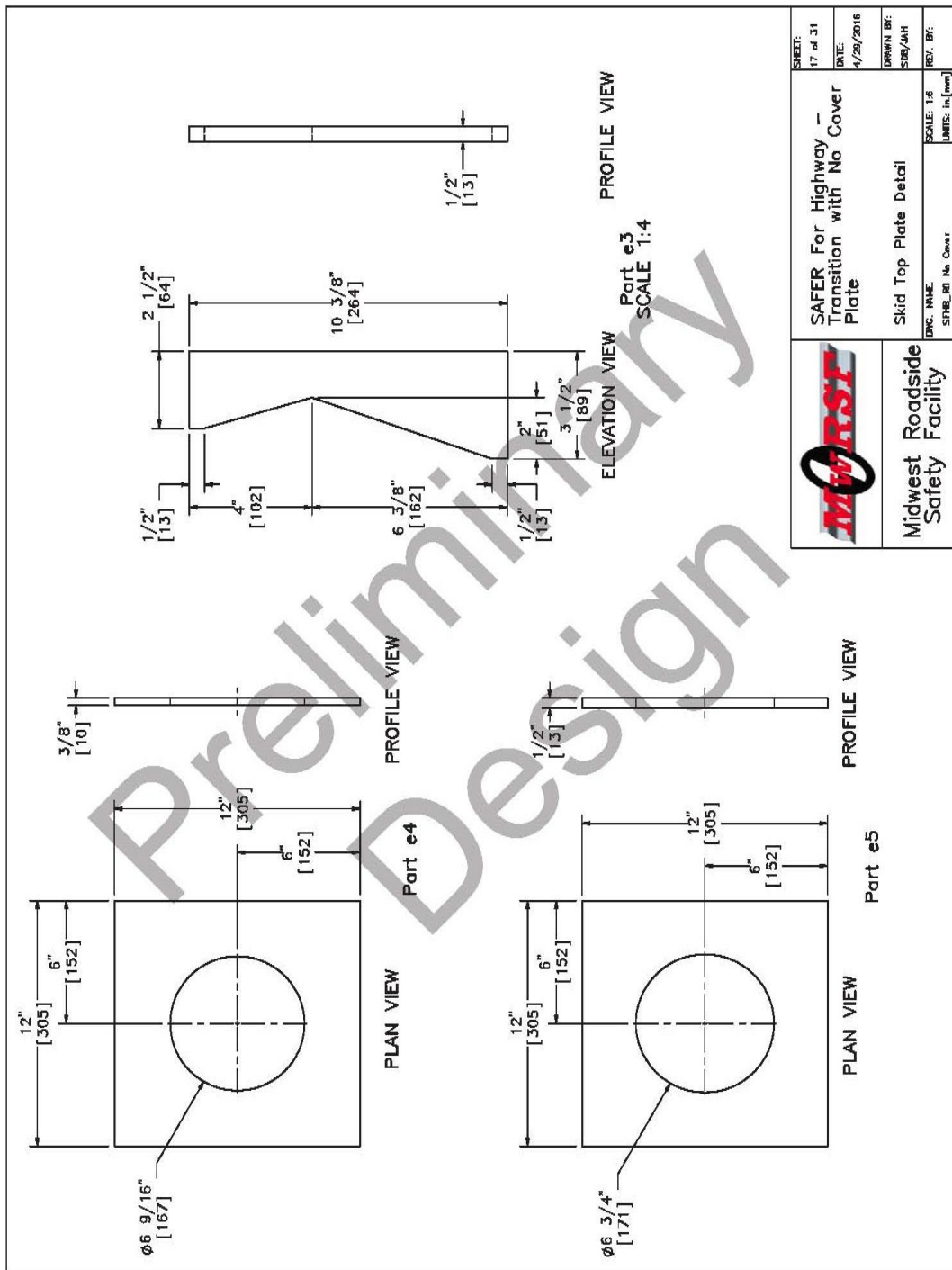


Figure I-17. Skid Top Plate Detail, No Cover Plate, RESTORE Barrier Transition

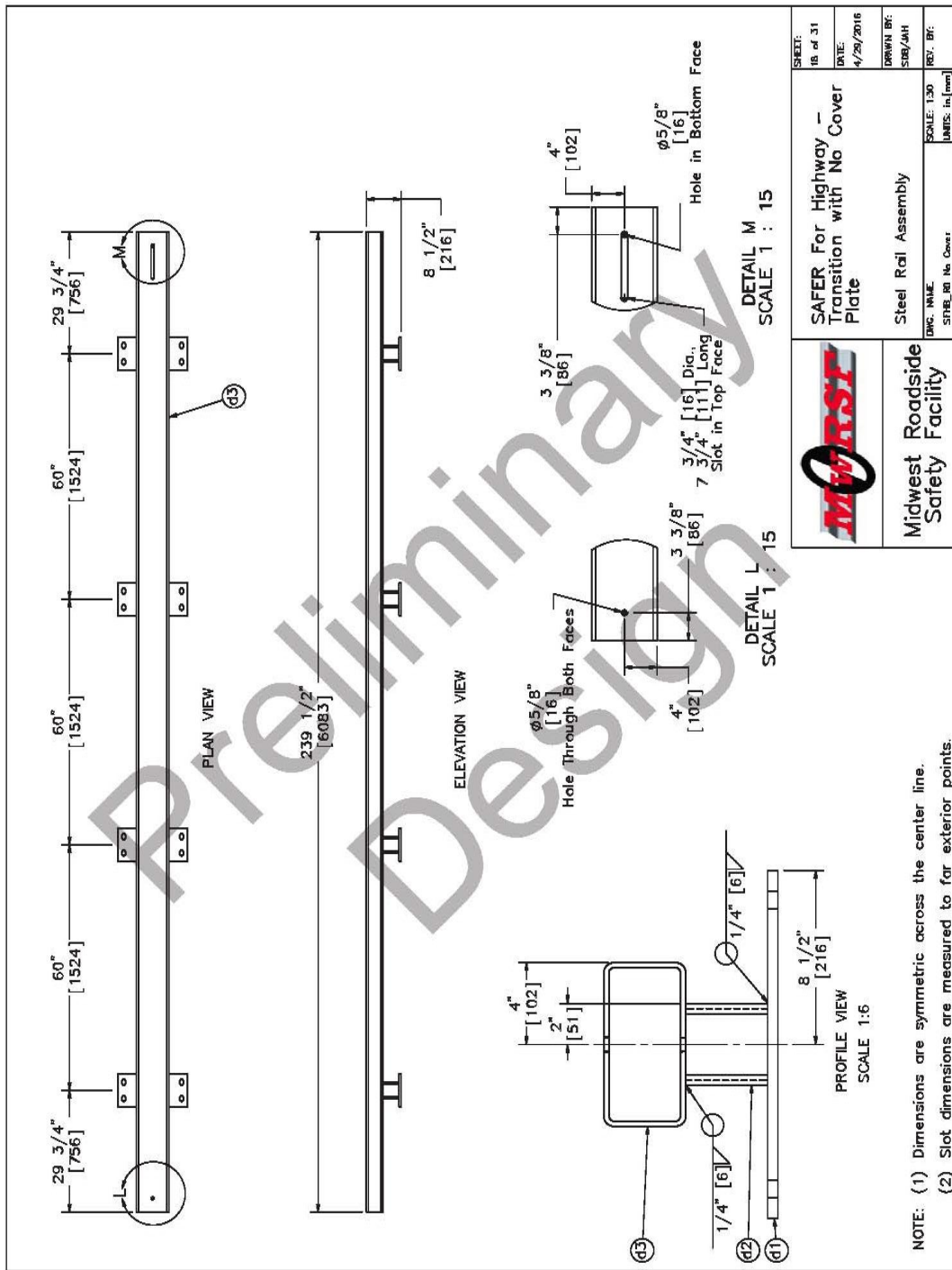


Figure I-18. Steel Rail Assembly, No Cover Plate, RESTORE Barrier Transition

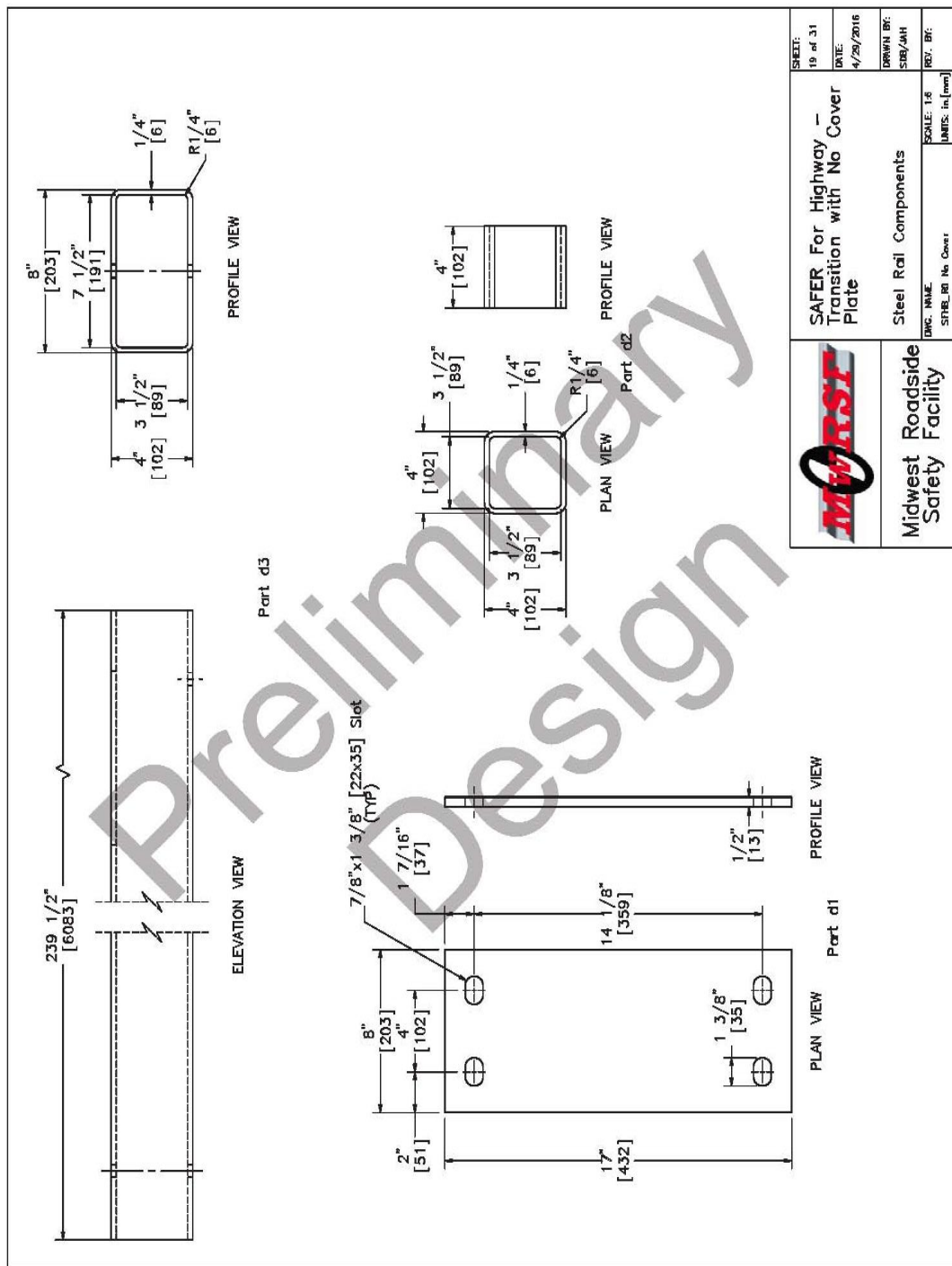


Figure I-19. Steel Rail Components, No Cover Plate, RESTORE Barrier Transition

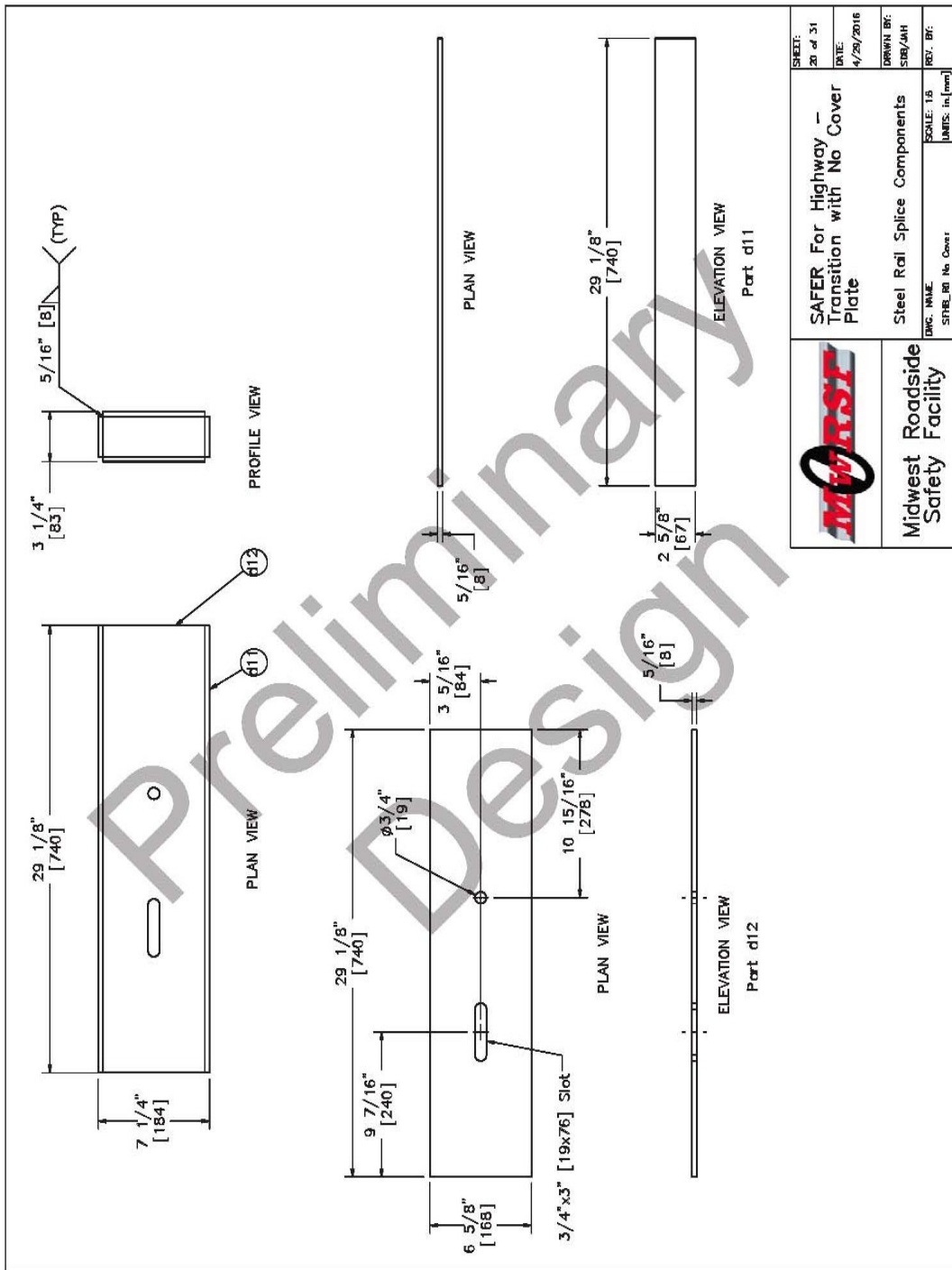


Figure I-20. Steel Rail Splice Components, No Cover Plate, RESTORE Barrier Transition

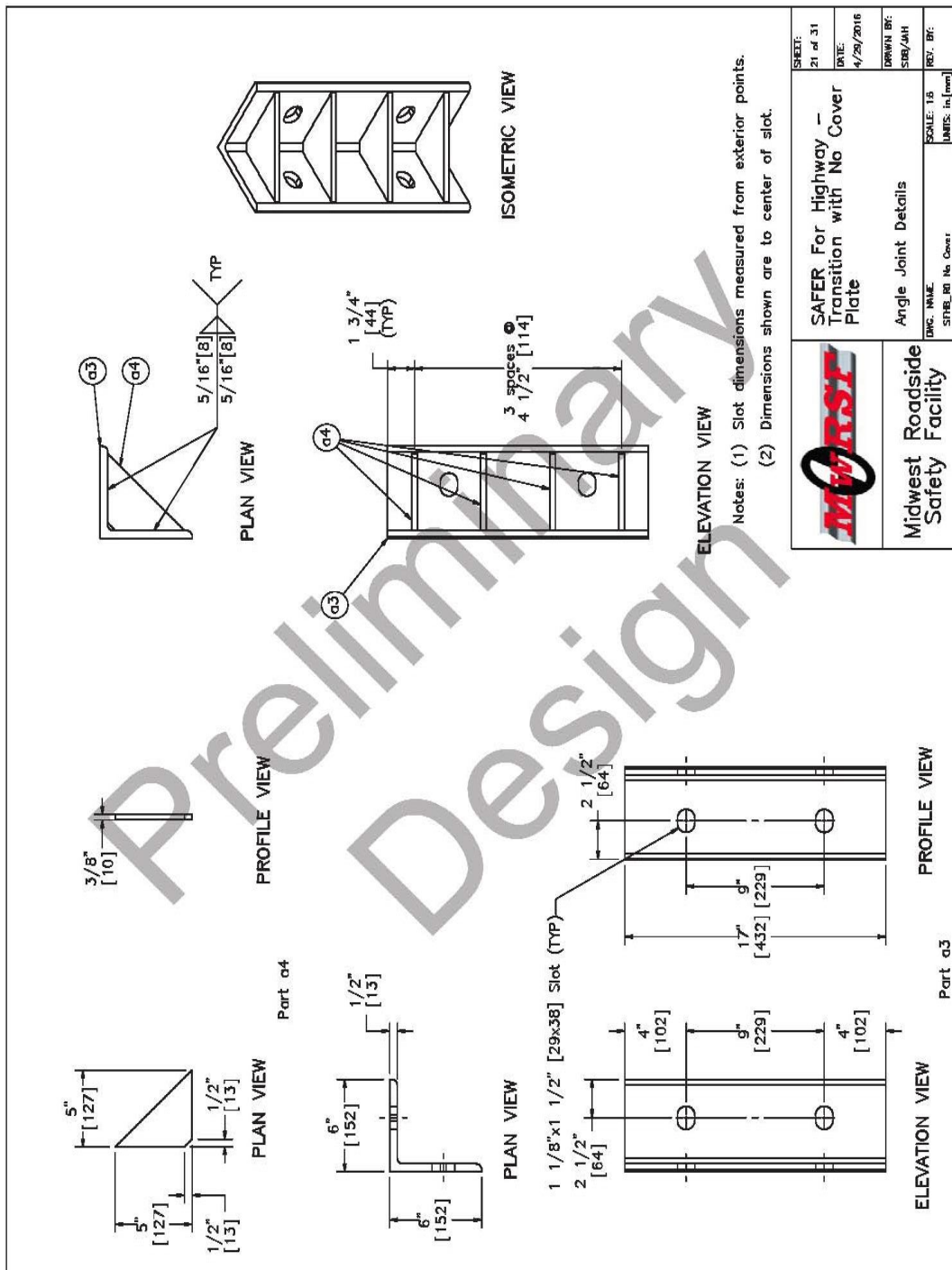


Figure I-21. Angle Joint Details, No Cover Plate, RESTORE Barrier Transition

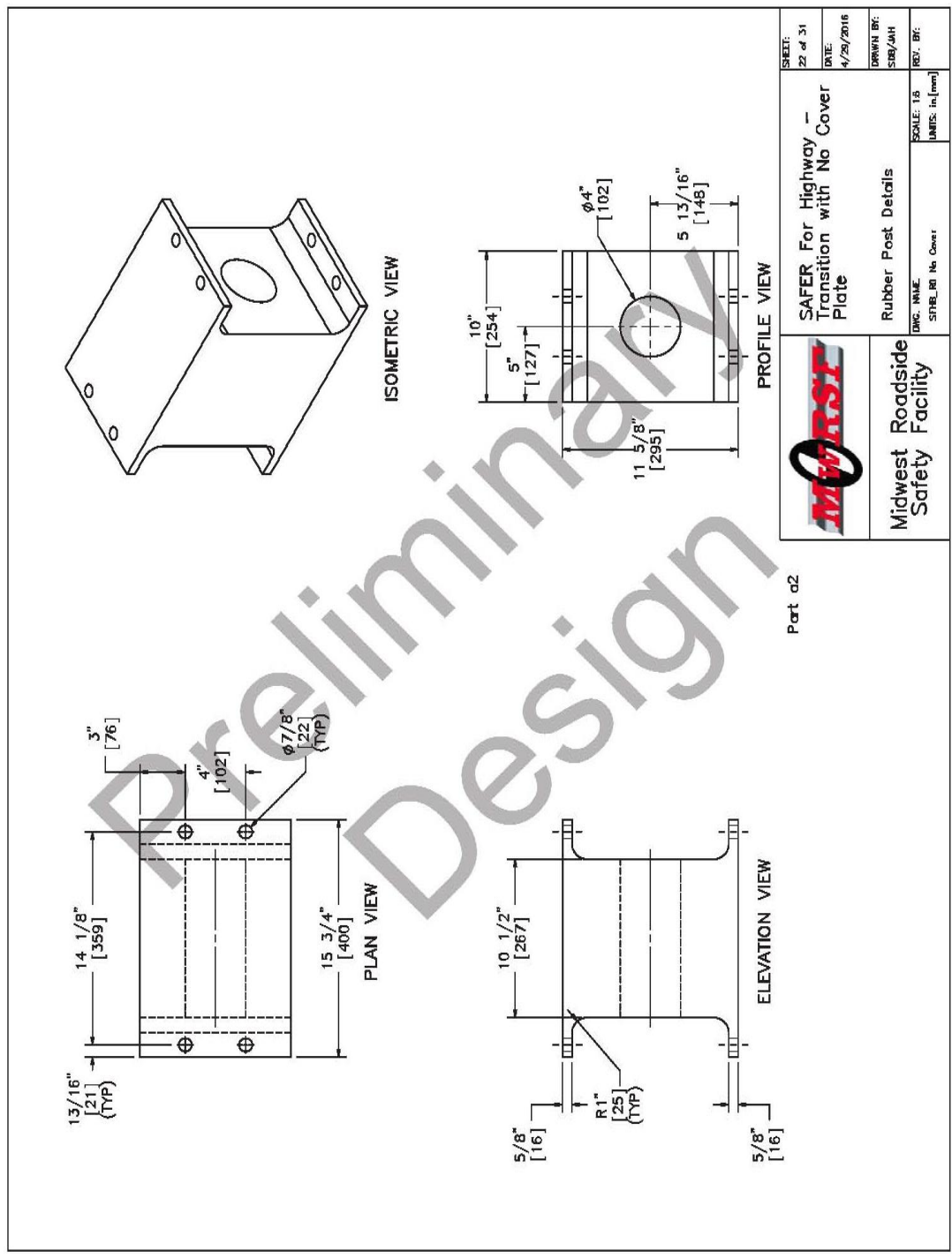


Figure I-22. Rubber Post Details, No Cover Plate, RESTORE Barrier Transition

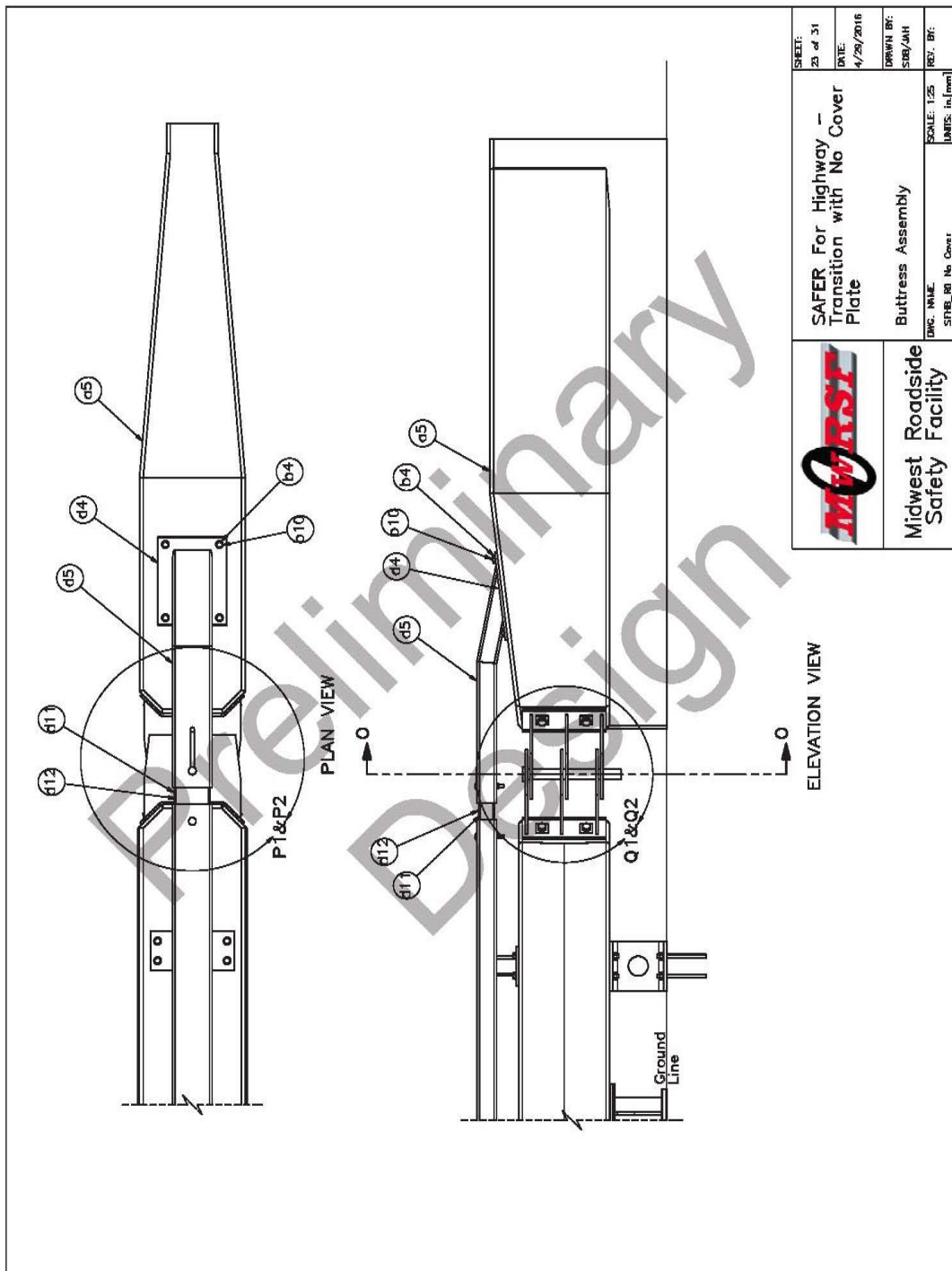


Figure I-23. Buttress Assembly, No Cover Plate, RESTORE Barrier Transition

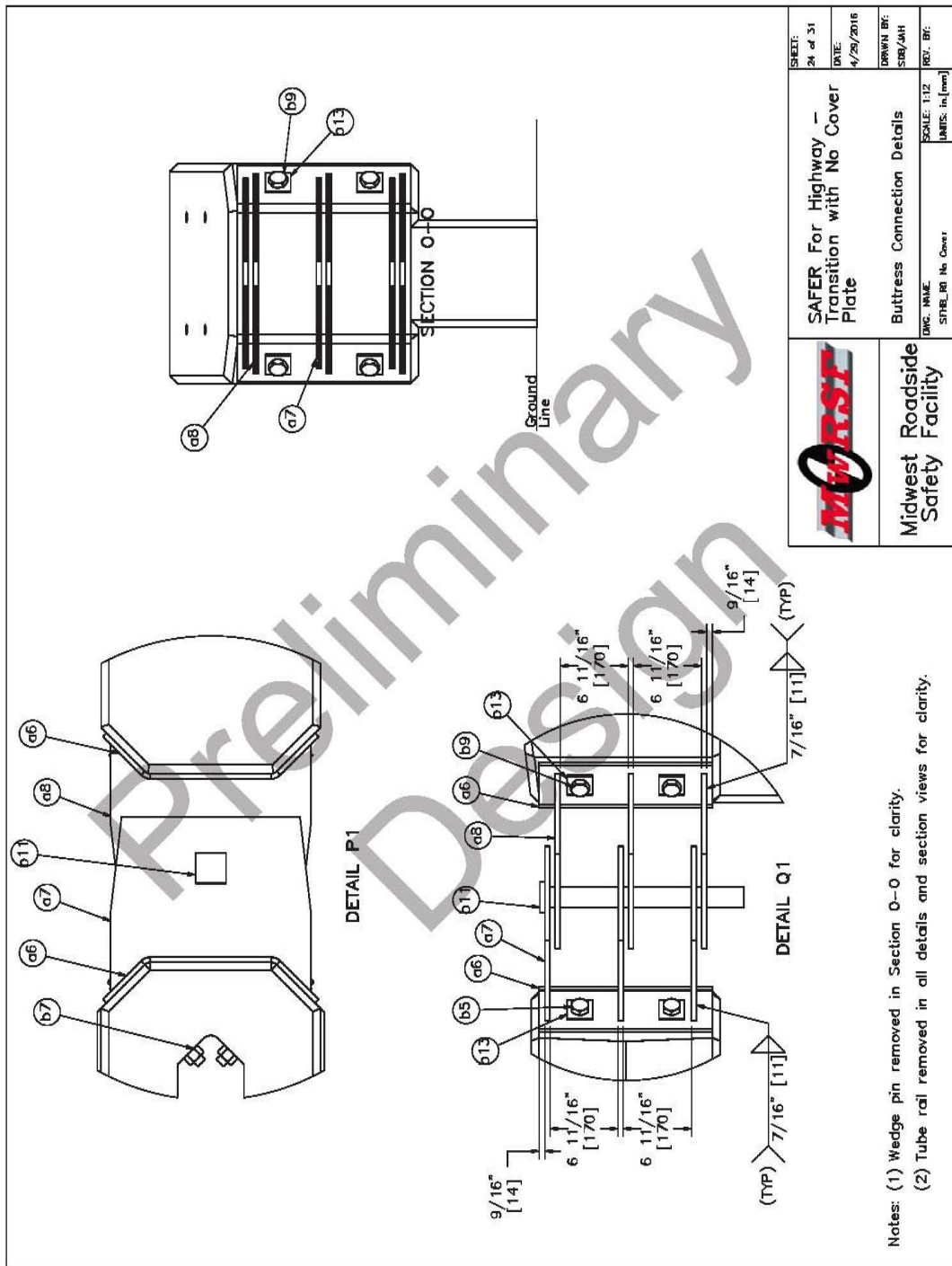


Figure I-24. Buttress Connection Details, No Cover Plate, RESTORE Barrier Transition

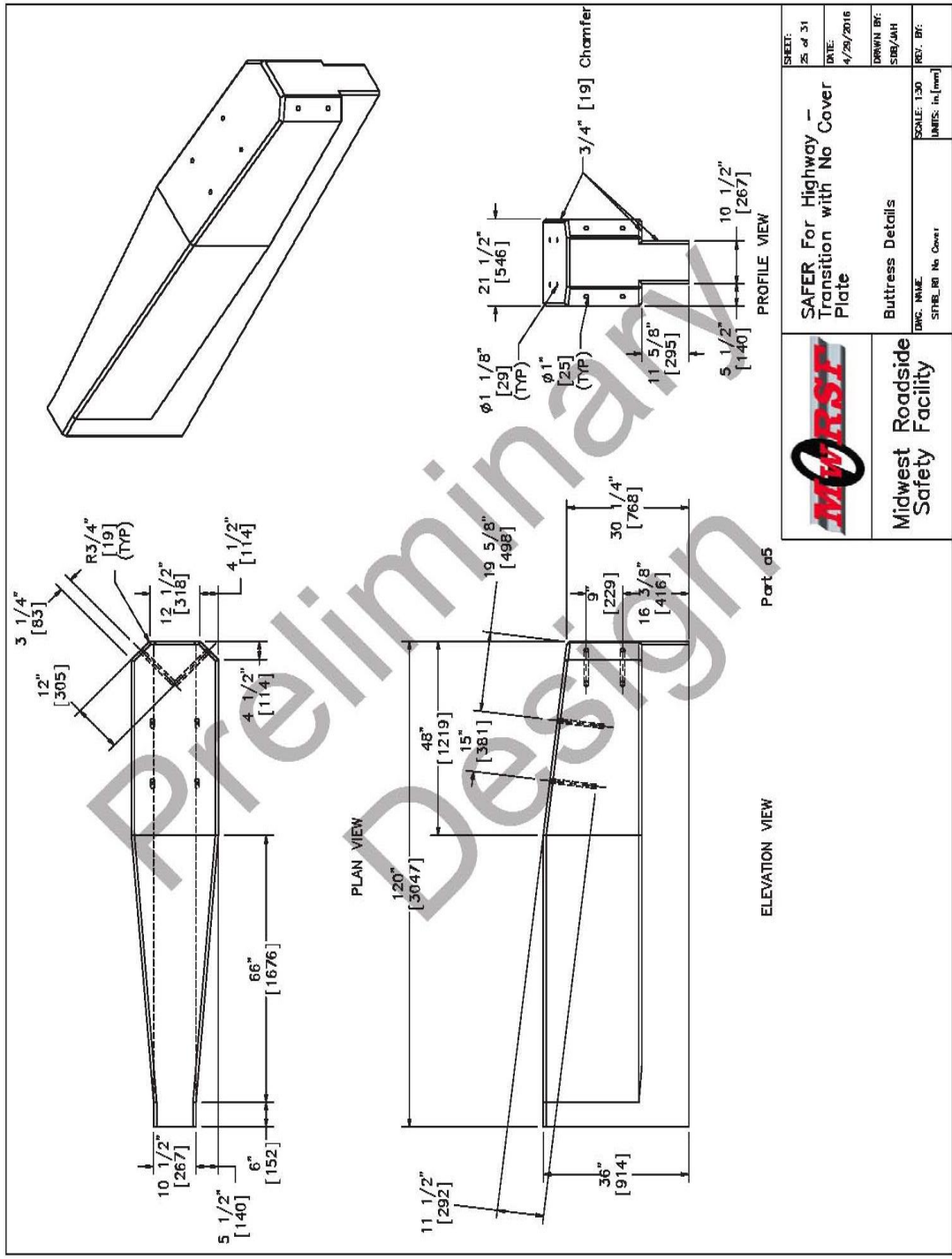



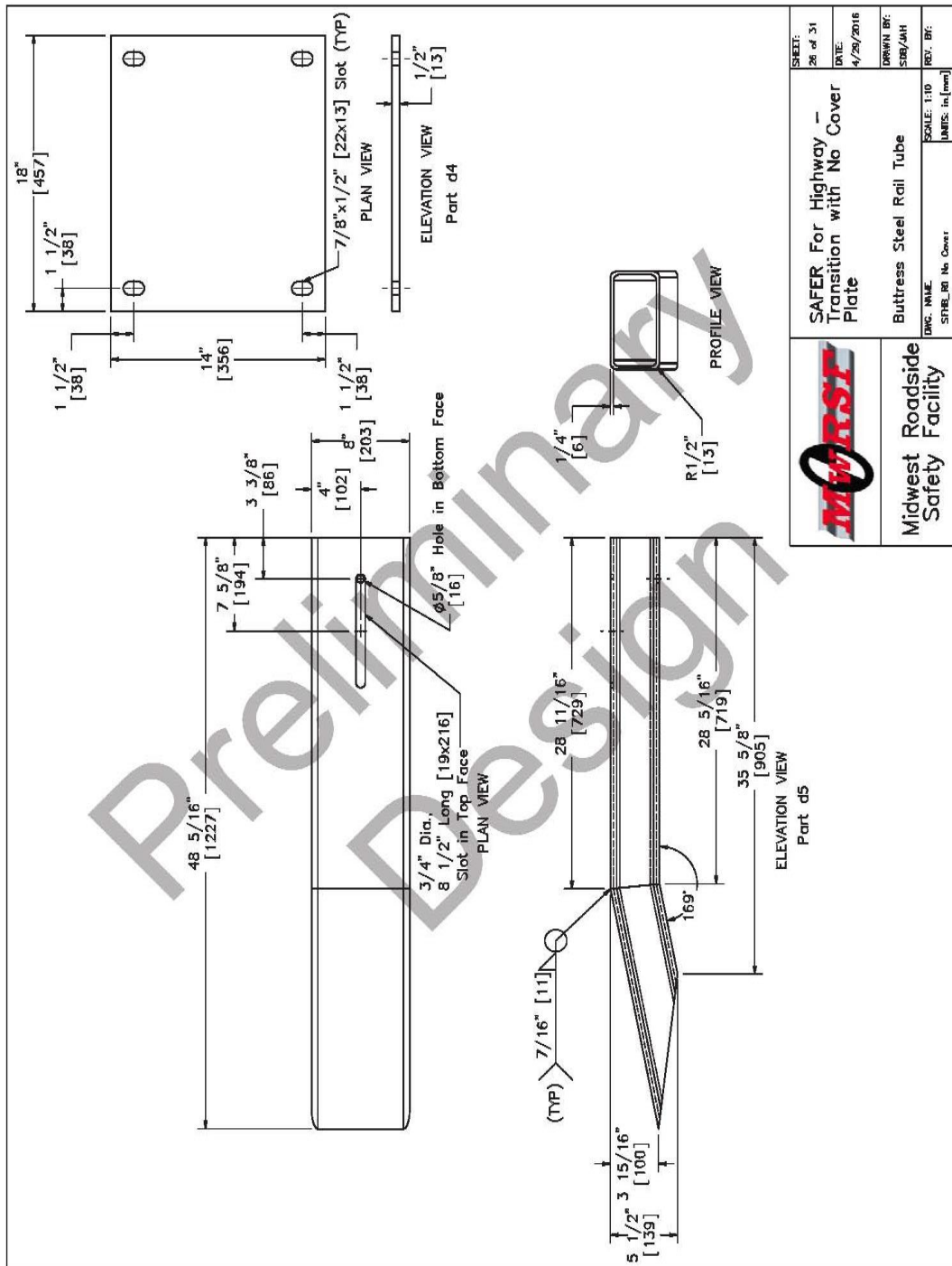
Figure I-25. Buttress Details, No Cover Plate, RESTORE Barrier Transition

		Midwest Roadside Safety Facility	
SAFER For Highway Transition with No Cover Plate		Buttress Details	
SHEET: 25 of 31	DATE: 4/29/2016	DRAWN BY: SIB/JAH	SCALE: 1:30
REV. BY:	SPEC. BY: No Cover	UNIT: In. [mm]	DATE:

Part 05

ELEVATION VIEW

PROFILE VIEW



	SAFER For Highway - Transition with No Cover Plate	SHEET: 26 of 31 DATE: 4/29/2016 DRAWN BY: SIB/DAH SCALE: 1:10 UNITS: in, (mm)
	Midwest Roadside Safety Facility	Butress Steel Rail Tube Dwg. Name: STBLR1 No Cover

Figure I-26. Butress Steel Rail Tube, No Cover Plate, RESTORE Barrier Transition

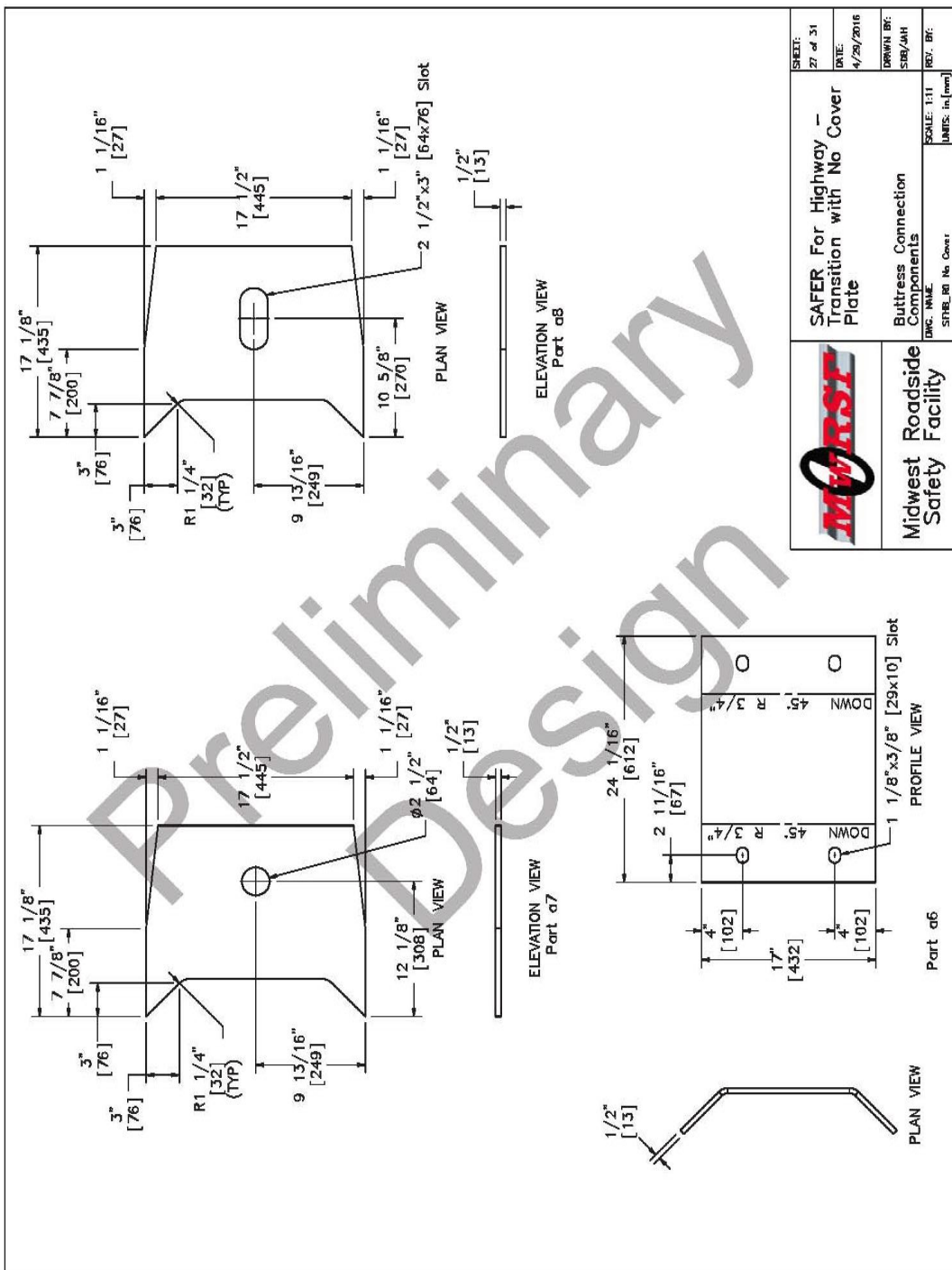
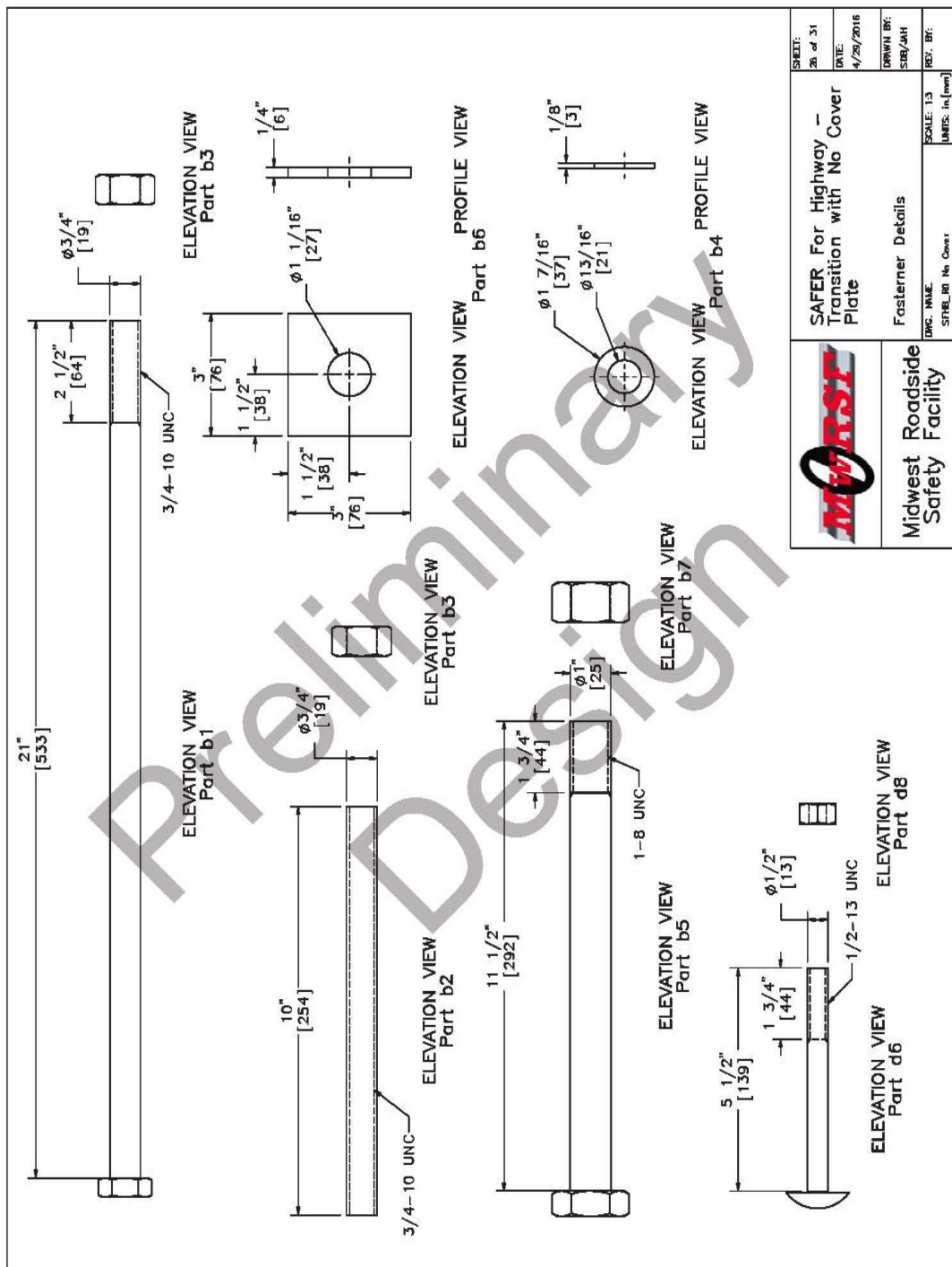
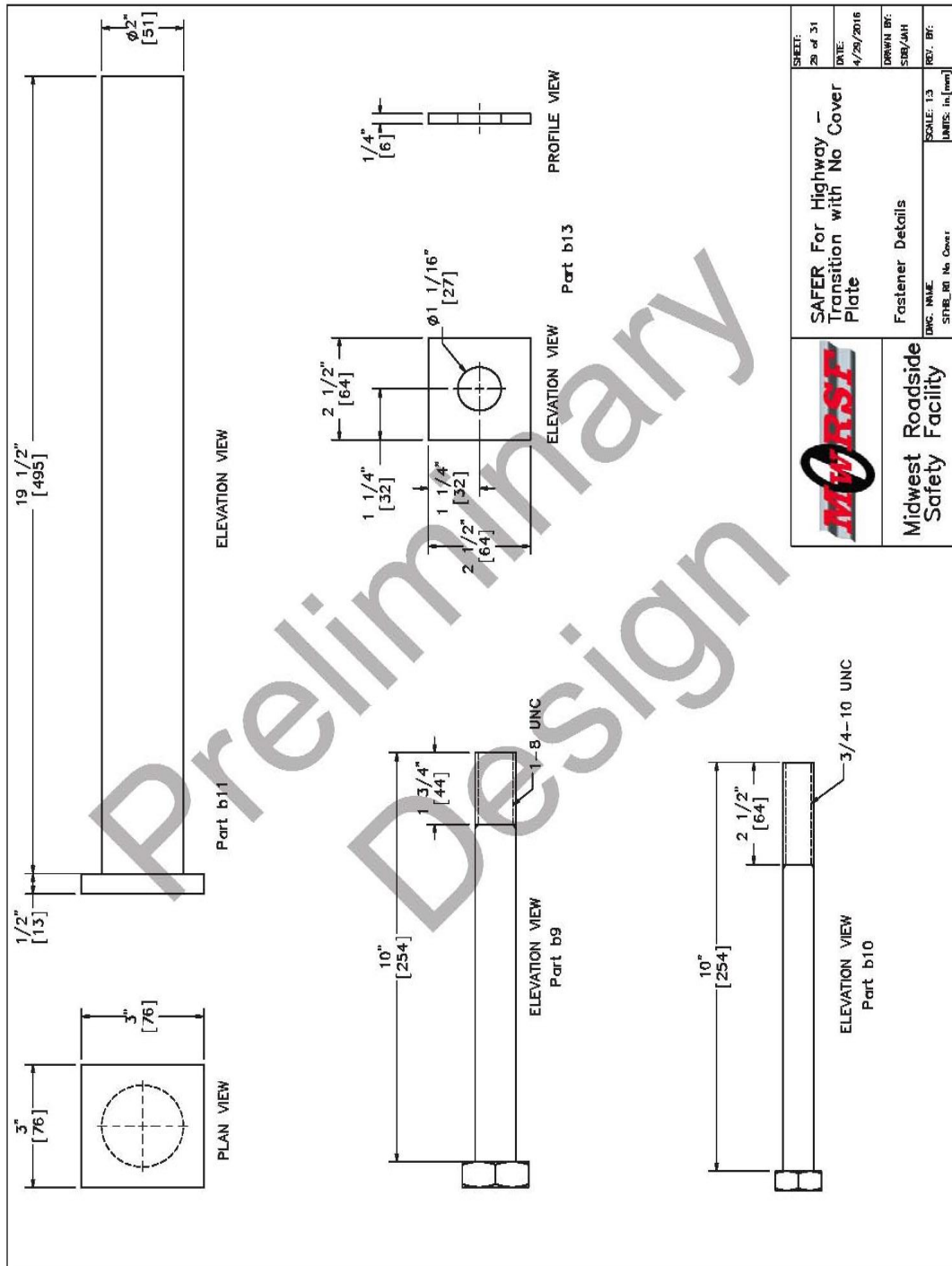


Figure I-27. Buttruss Connection Components, No Cover Plate, RESTORE Barrier Transition



	SAFER For Highway - Transition with No Cover Plate	SHEET: 28 of 31 DATE: 4/29/2016 DRAWN BY: SDB/AH REV. BY:
	Midwest Roadside Safety Facility	FASTENER No. Cover: SCALE: 1:3 UNITS: in (mm)

Figure I-28. Fastener Details, No Cover Plate, RESTORE Barrier Transition




	SAFER For Highway - Transition with No Cover Plate	SHEET: 29 of 31 DATE: 4/29/2016 DRAWN BY: SDB/AH REV. BY:
	Midwest Roadside Safety Facility	FASTENER NAME: FASTENER No. Cover: SCALE: 1:3 UNITS: in (mm)

Figure I-29. Fastener Details, No Cover Plate, RESTORE Barrier Transition

Item No.	QTY.	Description	Material Specification	Hardware Guide
a1	10	Lightweight Concrete Rail	min f'c=5 ksi [34.5 MPa], density=110 pcf	-
a2	40	Morse E46496 Shear Fender	ASTM D2000	-
a3	18	6"x6"x1/2" [152x152x13], 17" [432] Long L-Bracket	A992 Galvanized	-
a4	72	5"x5"x3/8" [127x127x10] Gusset Plate	A572 Grade 50 Galvanized	-
a5	1	Concrete Buttress	min f'c=5 ksi [34.5 MPa], density=110 pcf	-
a6	2	24 1/16"x1/2"x17" [611x13x432] Barrier Bracket	A992 Galvanized	-
a7	3	19 5/8"x17 1/8"x1/2" [498x435x13] Restore Gusset	A572 Grade 50 Galvanized	-
a8	3	19 5/8"x17 1/8"x1/2" [498x435x13] Buttress Gusset	A572 Grade 50 Galvanized	-
b1	160	3/4" [19] Dia. UNC, 21" [533] Long Hex Bolt	Grade 5 Galvanized	FBX20a
b2	160	3/4" [19] Dia. UNC, 10" [254] Long Threaded Rod	ASTM A193 Grade B7 Galvanized	-
b3	320	3/4" [19] Dia. UNC Heavy Hex Nut	ASTM A194 Grade 2H Galv.	-
b4	484	3/4" [19] Dia. Flat Washer	ASTM F436 Galv.	-
b5	76	1" [25] Dia. UNC, 11 1/2" [292] Long Hex Head Bolt	ASTM A325 Galv.	FBX24b
b6	144	3"x3"x1/4" [76x76x6] Square Washer	A572 Grade 50 Galvanized	-
b7	76	1" [25] Dia. UNC Heavy Hex Nut	ASTM A563 DH Galv.	FNX24b
b9	4	1" [25] Dia. UNC, 10" [254] Long Hex Head Bolt	ASTM A325 Galv.	FBX24b
b10	4	3/4" [19] Dia. UNC, 10" [254] Long Hex Bolt	Grade 5 Galvanized	FBX20a
b11	1	2" Dia. x 19 1/2" Long [51x495] Gusset Pin	A572 Grade 50 Galvanized	-
b13	8	2 1/2"x2 1/2"x1/4" [64x64x6] Square Washer	A572 Grade 50 Galvanized	-



Midwest Roadside Safety Facility

SAFER For Highway Transition with No Cover Plate

Bill of Materials

SYMB: 00 No Cover

SCALE: 1:8

UNITS: In (mm)

SHEET: 30 of 31

DATE: 4/29/2016

DRAWN BY: [Blank]

SRB/AH

REV. BY: [Blank]

Figure I-30. Bill of Materials, No Cover Plate, RESTORE Barrier Transition

Item No.	QTY.	Description	Material Specification	Hardware Guide
c1	280	1/2" [13] Dia., 77" [1956] Long Bent Rebar	A615 Grade 60	-
c2	80	1/2" [13] Dia., 49" [1245] Long Bent Rebar	A615 Grade 60	-
c3	120	3/4" [19] Dia., 231" [5867] Long Rebar	A615 Grade 60	-
c4	80	3/4" [19] Dia., 63" [1600] Long Bent Rebar	A615 Grade 60	-
c5	60	3/4" [19] Dia., 69" [1753] Long Bent Rebar	A615 Grade 60	-
d1	40	17"x8"x1/2" [431x203x13] Anchor Plate	ASTM A572 Grade 50 Galvanized	-
d2	40	4"x4"x1/4" [102x102x6], 4" [102] Long Tube	A500 Grade B Galvanized	-
d3	10	8"x4"x1/4" [203x102x6], 239 1/2" [6083] Long Tube	A500 Grade B Galvanized	-
d4	1	18"x14"x1/2" [457x356x13] Anchor Plate	ASTM A572 Grade 50 Galvanized	-
d5	1	8"x4"x1/4" [203x102x6], 42 1/4" [1073] Bent Tube	A500 Grade B Galvanized	-
d6	20	1/2" [13] Dia. UNC, 5 1/2" [140] Long Dome (Round) Head Bolt	ASTM A307 Grade A Galvanized	-
d7	18	1/2" [13] Dia. Flat Washer	ASTM F844 Galvanized	-
d8	20	1/2" [13] Dia. UNC Heavy Hex Nut	A563A Galvanized	FNX12b
d9	-	Epoxy		
d11	20	29 1/8"x2 5/8"x5/16" [740x67x8] Splice Side Plate	ASTM A572 Grade 50 Galvanized	-
d12	20	29 1/8"x6 5/8"x5/16" [740x168x8] Splice Top Plate with Slot	ASTM A572 Grade 50 Galvanized	-
e1	20	6 1/2" [165] Dia., 3/8" [10] Thick, 19" [483] Long Steel Pipe	AISI 1026	-
e2	20	16 9/16"x10"x1/4" [421x254x6] Base Plate	ASTM A572 Grade 50 Steel	-
e3	40	3 1/2"x10 3/8"x1/2" [89x264x13] Plate Gusset	ASTM A572 Grade 50 Steel	-
e4	20	12"x12"x3/8" [305x305x10] Top Plate	ASTM A572 Grade 50 Steel	-
e5	20	12"x12"x1/2" [305x305x13] EPDM Rubber Sheet	Minimum 50 durometer	-



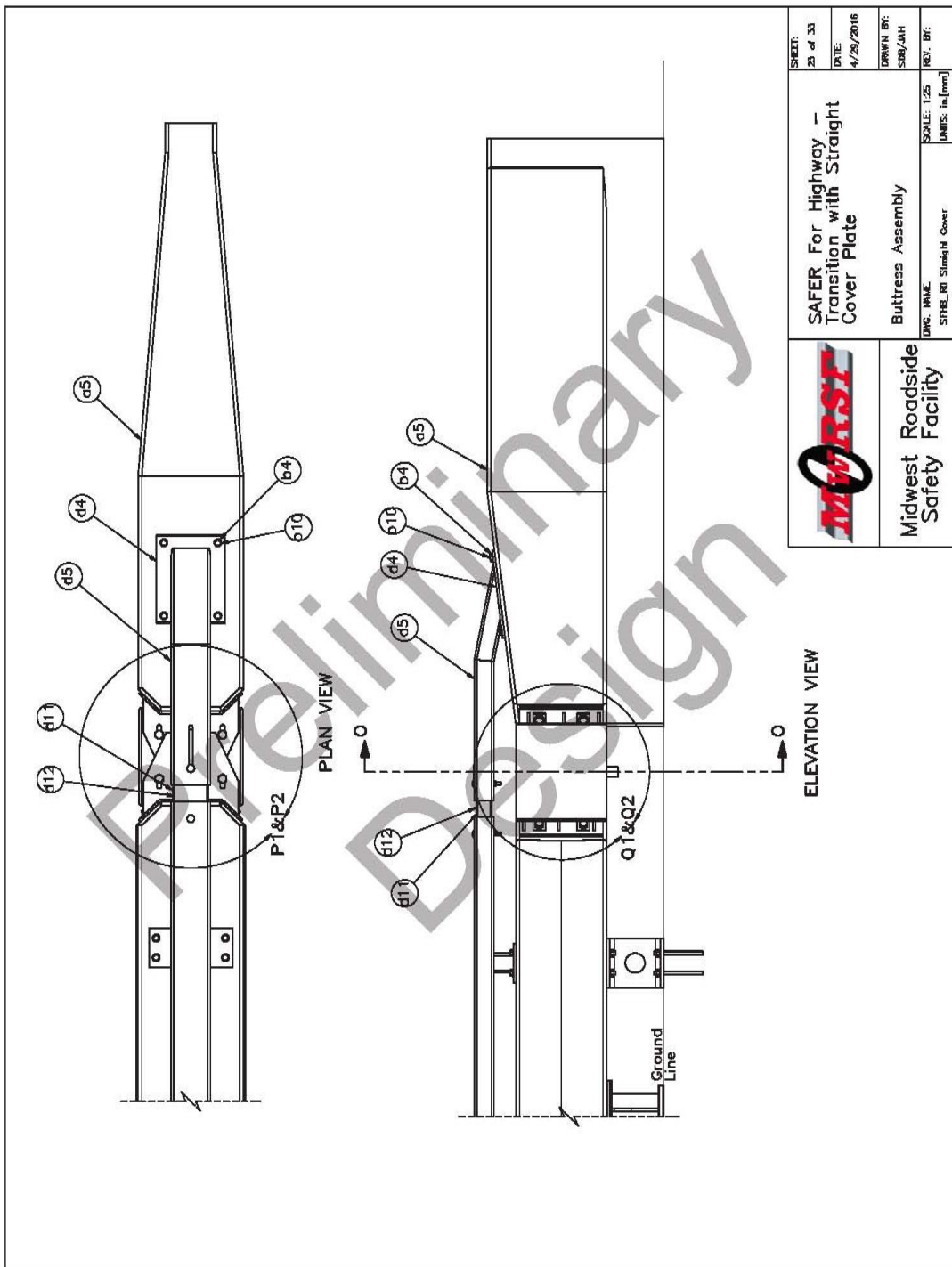
Midwest Roadside Safety Facility

SAFER For Highway Transition with No Cover Plate		SHEET: 31 of 31
Bill of Materials		DATE: 4/29/2016
SCALE: 1:6		DRAWN BY: SDB/AH
UNCS: In. (mm)		REV. BY:

Figure I-31. Bill of Materials, No Cover Plate, RESTORE Barrier Transition

Appendix J. RESTORE Barrier Transition with Straight Cover Plate Drawing Modifications

Note the drawing set is not a complete drawing set. Only page nos. 23 through 33 are included herein due to the other pages being similar to the drawing sets located in either Appendix G or Appendix K. If the full drawing set is needed, please feel free to contact MwRSF.




	SAFER For Highway - Transition with Straight Cover Plate	
	BUTTRESS ASSEMBLY BUTTRESS ASSEMBLY SHEET NO Straight Cover	SCALE: 1/25 DIMS: in./mm
SHEET: 23 of 33	DATE: 4/28/2016	DRAWN BY: SBB/JAH
		REV. BY: JAMES

Figure J-1. Buttress Assembly, Straight Cover Plate, RESTORE Barrier Transition

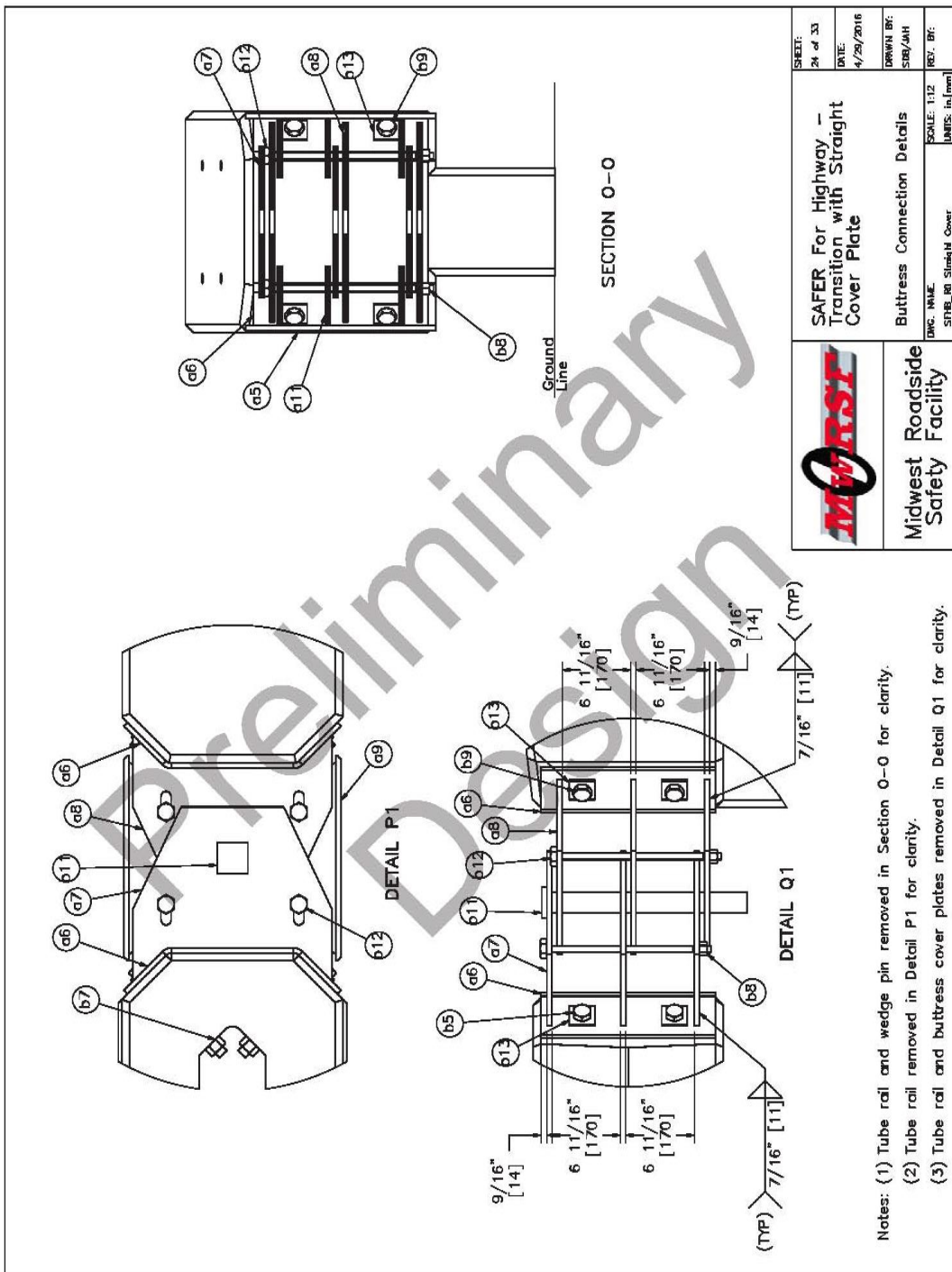
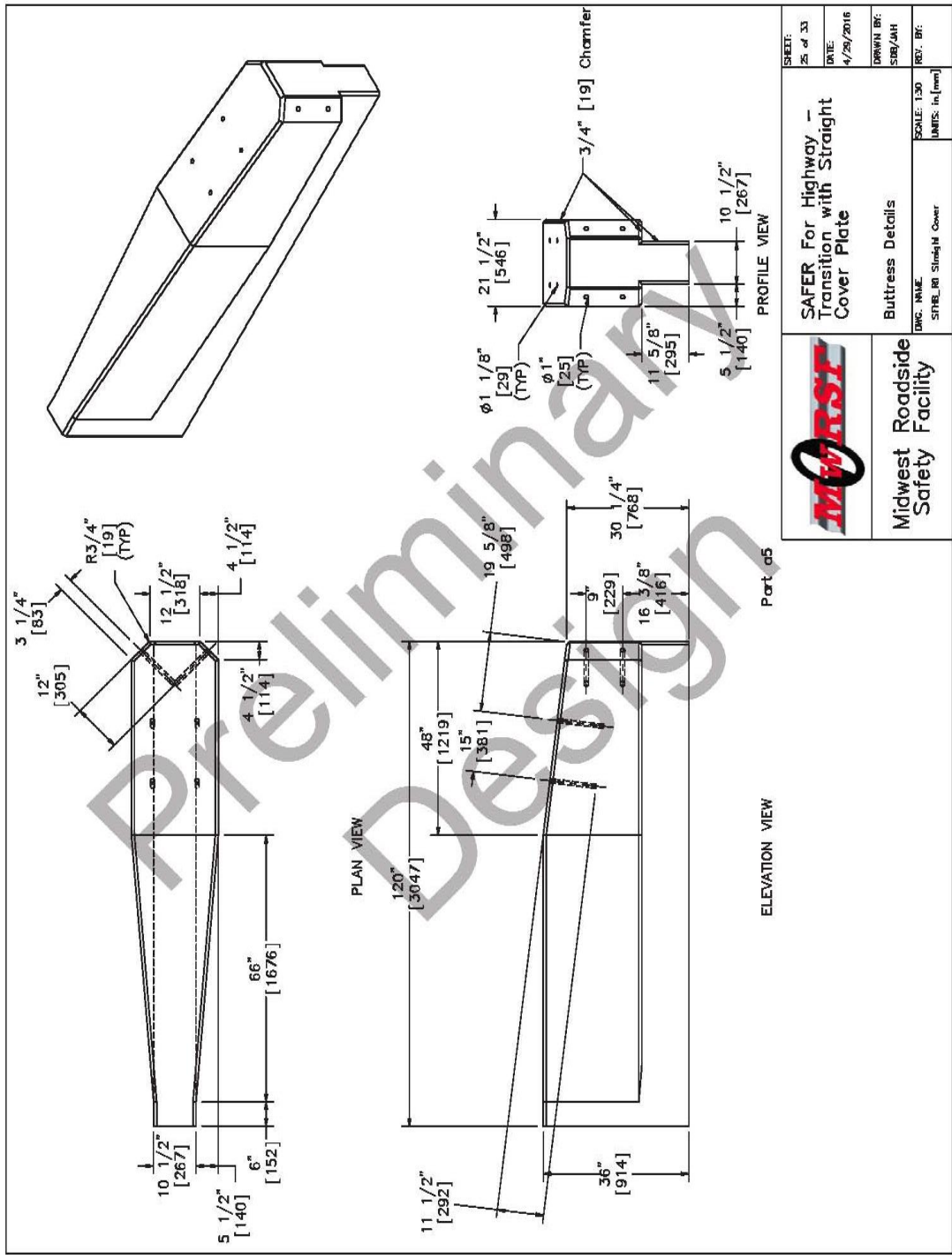


Figure J-2. Buttress Connection Details, Straight Cover Plate, RESTORE Barrier Transition




		SAFER For Highway - Transition with Straight Cover Plate	
Midwest Roadside Safety Facility		Buttress Details	
DWG. NAME STRUT_RI Straight Cover	SCALE: 1:30 UNITS: in./mm	DRAWN BY: SMB/JAH	DATE: 4/29/2016
		REV. BY:	SHEET: 25 of 33

Figure J-3. Buttress Details, Straight Cover Plate, RESTORE Barrier Transition

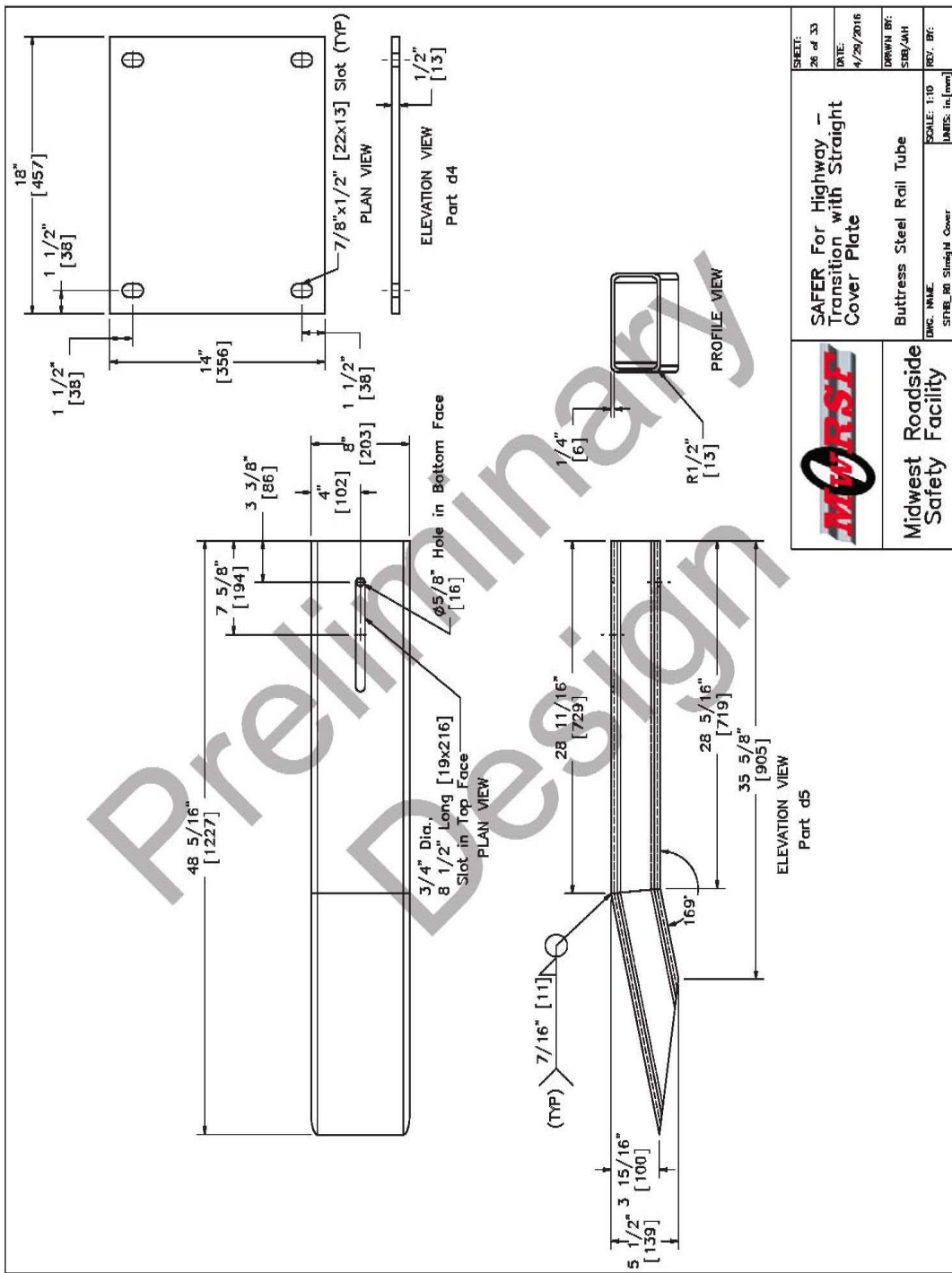
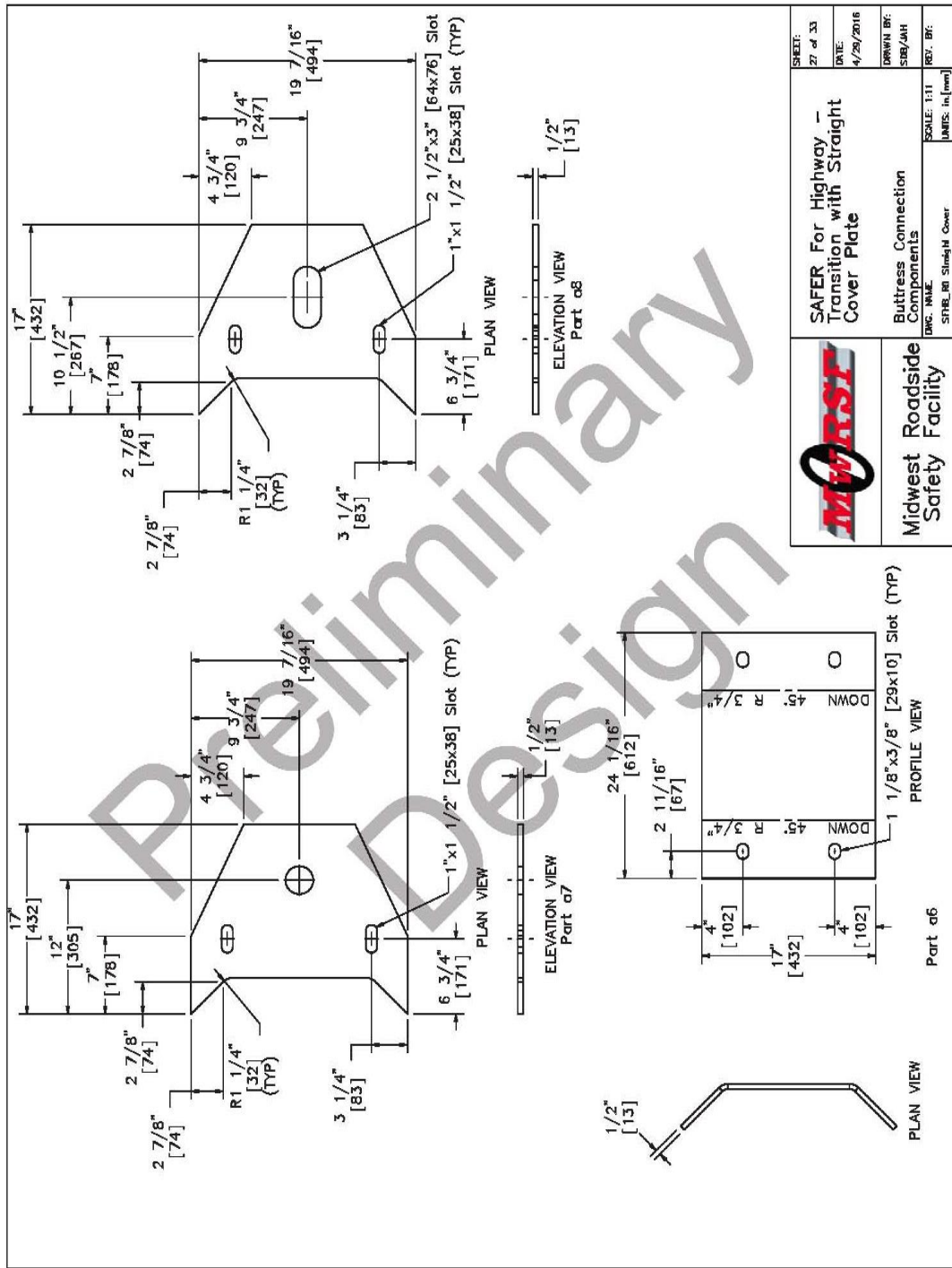


Figure J-4. Buttruss Steel Rail Tube, Straight Cover Plate, RESTORE Barrier Transition



	SAFER For Highway - Transition with Straight Cover Plate	SHEET: 27 of 33
	Buttruss Connection Components	DATE: 4/29/2016
Midwest Roadside Safety Facility	SCALE: 1:1 UNITS: in (mm)	DRAWN BY: SBG/AH
Dwg. Name: STRBTR Straight Cover		REV. BY:

Figure J-5. Buttruss Connection Components, Straight Cover Plate, RESTORE Barrier Transition

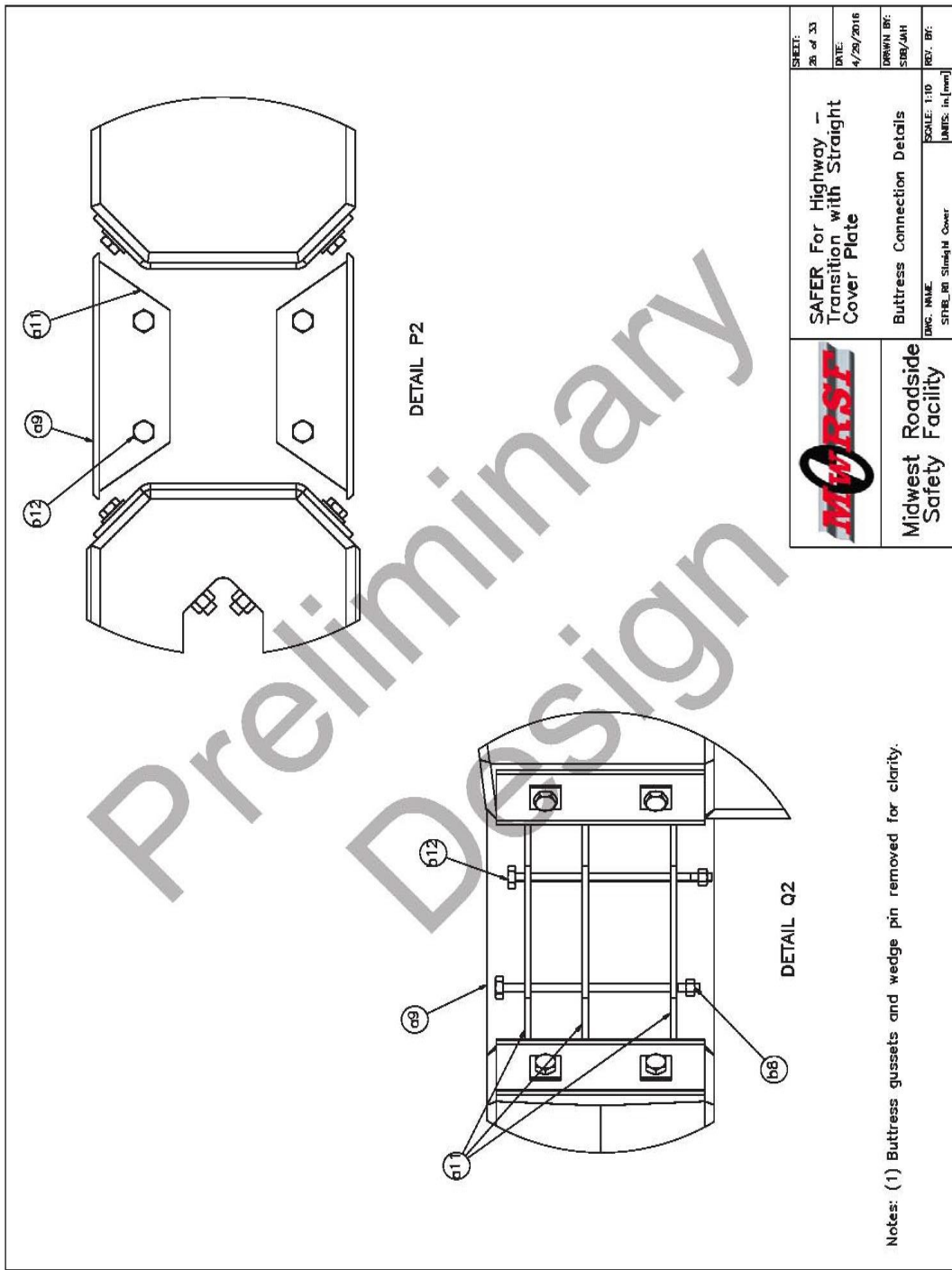


Figure J-6. Buttress Connection Details, Straight Cover Plate, RESTORE Barrier Transition

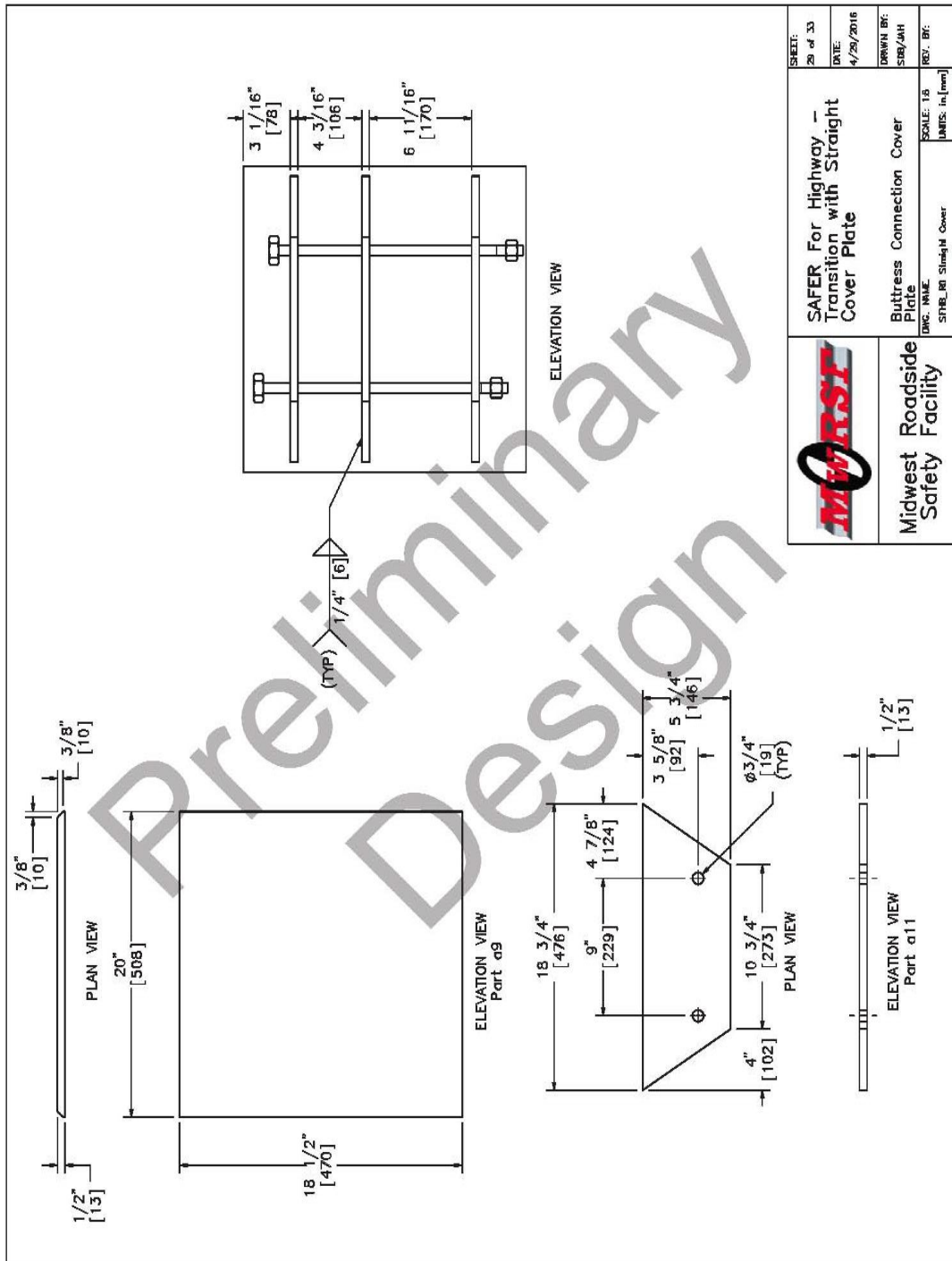


Figure J-7. Buttruss Connection Cover Plate, Straight Cover Plate, RESTORE Barrier Transition

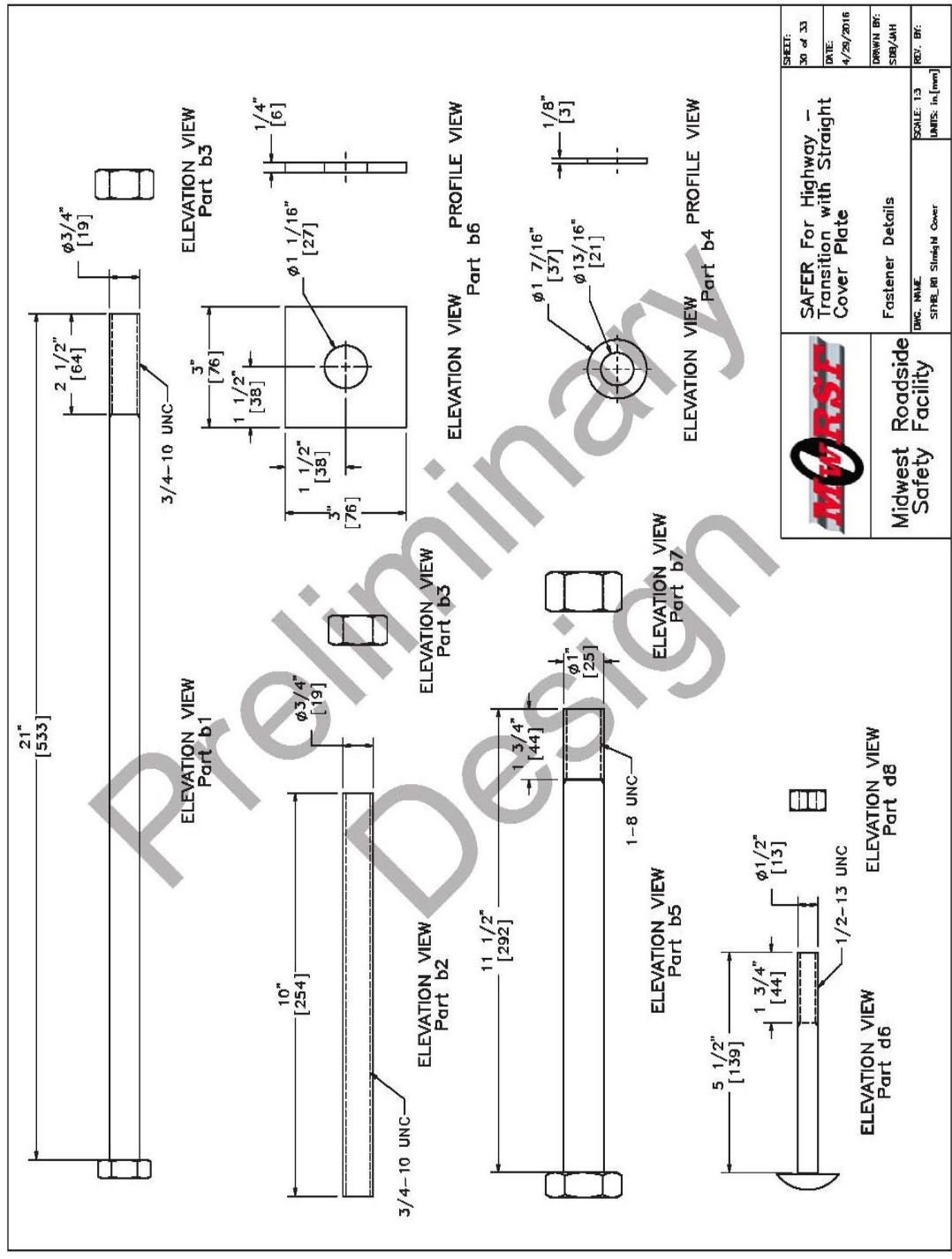
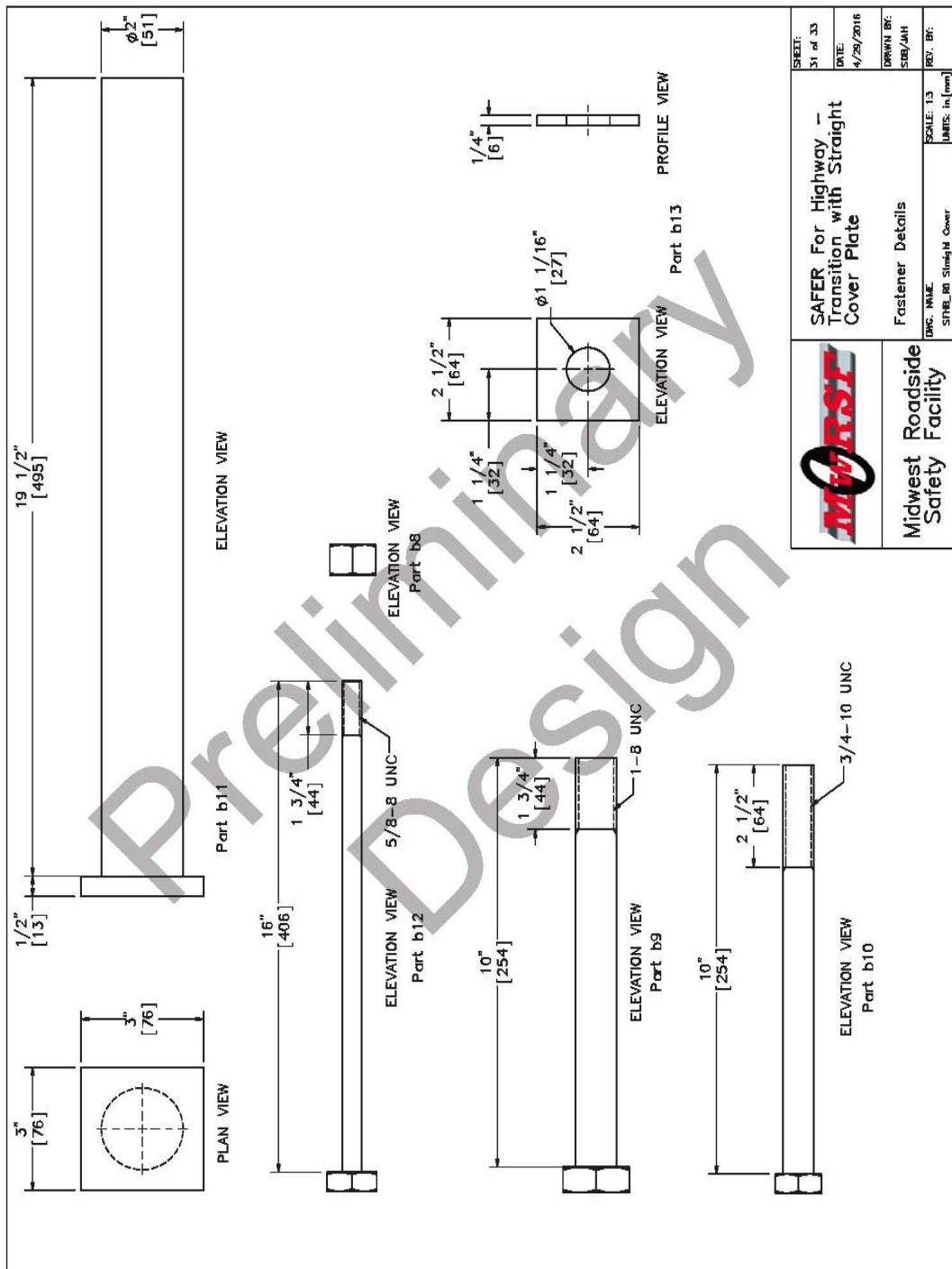


Figure J-8. Fastener Details, Straight Cover Plate, RESTORE Barrier Transition




	SAFER For Highway - Transition with Straight Cover Plate
	Fastener Details
Dwg. Name: STRB_RR Straight Cover	Scale: 1:3 Units: in. (mm)
SHEET: 31 of 33 DATE: 4/29/2016 DRAWN BY: SSB/SHH REV. BY:	Midwest Roadside Safety Facility

Figure J-9. Fastener Details, Straight Cover Plate, RESTORE Barrier Transition

Item No.	QTY.	Description	Material Specification	Hardware Guide
a1	10	Lightweight Concrete Rail	min f'c=5 ksi [34.5 MPa], density=110 pcf	-
a2	40	Morse E46496 Shear Fender	ASTM D2000	-
a3	18	6"x6"x1/2" [152x152x13], 17" [432] Long L-Bracket	A992 Galvanized	-
a4	72	5"x5"x3/8" [127x127x10] Gusset Plate	A572 Grade 50 Galvanized	-
a5	1	Concrete Buttruss	min f'c=5 ksi [34.5 MPa], density=110 pcf	-
a6	2	24 1/16"x1/2"x17" [611x13x432] Barrier Bracket	A992 Galvanized	-
a7	3	19 7/16"x17"x1/2" [494x432x13] Restore Gusset	A572 Grade 50 Galvanized	-
a8	3	19 7/16"x17"x1/2" [494x432x13] Buttruss Gusset	A572 Grade 50 Galvanized	-
a9	2	20"x18 1/2"x5/8" [508x470x16] Straight Cover Plate	A992 Galvanized	-
a11	6	18 3/4"x5 1/2"x1/2" [476x140x13] Straight Cover Plate Gusset	A572 Grade 50 Galvanized	-
b1	160	3/4" [19] Dia. UNC, 21" [533] Long Hex Bolt	Grade 5 Galvanized	FBX20a
b2	160	3/4" [19] Dia. UNC, 10" [254] Long Threaded Rod	ASTM A193 Grade B7 Galvanized	-
b3	320	3/4" [19] Dia. UNC Heavy Hex Nut	ASTM A194 Grade 2H Galv.	-
b4	484	3/4" [19] Dia. Flat Washer	ASTM F436 Galv.	-
b5	76	1" [25] Dia. UNC, 11 1/2" [292] Long Hex Head Bolt	ASTM A325 Galv.	FBX24b
b6	144	3"x3"x1/4" [76x76x6] Square Washer	A572 Grade 50 Galvanized	-
b7	76	1" [25] Dia. UNC Heavy Hex Nut	ASTM A563 DH Galv.	FNX24b
b8	4	5/8" [16] Dia. UNC Heavy Hex Nut	ASTM A194 Grade 2H Galv.	FNX16b
b9	4	1" [25] Dia. UNC, 10" [254] Long Hex Head Bolt	ASTM A325 Galv.	FBX24b
b10	4	3/4" [19] Dia. UNC, 10" [254] Long Hex Bolt	Grade 5 Galvanized	FBX20a
b11	1	2" Dia. x 19 1/2" Long [51x495] Gusset Pin	A572 Grade 50 Galvanized	-
b12	4	5/8" [25] Dia. UNC, 16" [406] Long Hex Head Bolt	ASTM A325 Galv.	FBX16b
b13	8	2 1/2"x2 1/2"x1/4" [64x64x6] Square Washer	A572 Grade 50 Galvanized	-



Midwest Roadside Safety Facility

SAFER For Highway - Transition with Straight Cover Plate

Bill of Materials

SCALE: 1/8"
UNITS: in (mm)

Midwest Roadside Safety Facility

SAFER For Highway - Transition with Straight Cover Plate


DATE: 4/29/2016

DRAWN BY: SFB/JAH

REV. BY:

Figure J-10. Bill of Materials, Straight Cover Plate, RESTORE Barrier Transition

Item No.	QTY.	Description	Material Specification	Hardware Guide
c1	280	1/2" [13] Dia., 77" [1956] Long Bent Rebar	A615 Grade 60	-
c2	80	1/2" [13] Dia., 49" [1245] Long Bent Rebar	A615 Grade 60	-
c3	120	3/4" [19] Dia., 231" [5867] Long Rebar	A615 Grade 60	-
c4	80	3/4" [19] Dia., 63" [1600] Long Bent Rebar	A615 Grade 60	-
c5	60	3/4" [19] Dia., 69" [1753] Long Bent Rebar	A615 Grade 60	-
d1	40	17"x8"x1/2" [431x203x13] Anchor Plate	ASTM A572 Grade 50 Galvanized	-
d2	40	4"x4"x1/4" [102x102x6], 4" [102] Long Tube	A500 Grade B Galvanized	-
d3	10	8"x4"x1/4" [203x102x6], 239 1/2" [6083] Long Tube	A500 Grade B Galvanized	-
d4	1	18"x14"x1/2" [457x356x13] Anchor Plate	ASTM A572 Grade 50 Galvanized	-
d5	1	8"x4"x1/4" [203x102x6], 42 1/4" [1073] Bent Tube	A500 Grade B Galvanized	-
d6	20	1/2" [13] Dia. UNC, 5 1/2" [140] Long Dome (Round) Head Bolt	ASTM A307 Grade A Galvanized	-
d7	18	1/2" [13] Dia. Flat Washer	ASTM F844 Galvanized	-
d8	20	1/2" [13] Dia. UNC Heavy Hex Nut	A563A Galvanized	FNX12b
d9	-	Epoxy		
d11	20	29 1/8"x2 5/8"x5/16" [740x67x8] Splice Side Plate	ASTM A572 Grade 50 Galvanized	-
d12	20	29 1/8"x6 5/8"x5/16" [740x168x8] Splice Top Plate with Slot	ASTM A572 Grade 50 Galvanized	-
e1	20	6 1/2" [165] Dia., 3/8" [10] Thick, 19" [483] Long Steel Pipe	AISI 1026	-
e2	20	16 9/16"x10"x1/4" [421x254x6] Base Plate	ASTM A572 Grade 50 Steel	-
e3	40	3 1/2"x10 3/8"x1/2" [89x264x13] Plate Gusset	ASTM A572 Grade 50 Steel	-
e4	20	12"x12"x3/8" [305x305x10] Top Plate	ASTM A572 Grade 50 Steel	-
e5	20	12"x12"x1/2" [305x305x13] EPDM Rubber Sheet	Minimum 50 durometer	-



Midwest Roadside Safety Facility

Bill of Materials

STYBLBI Straight Cover

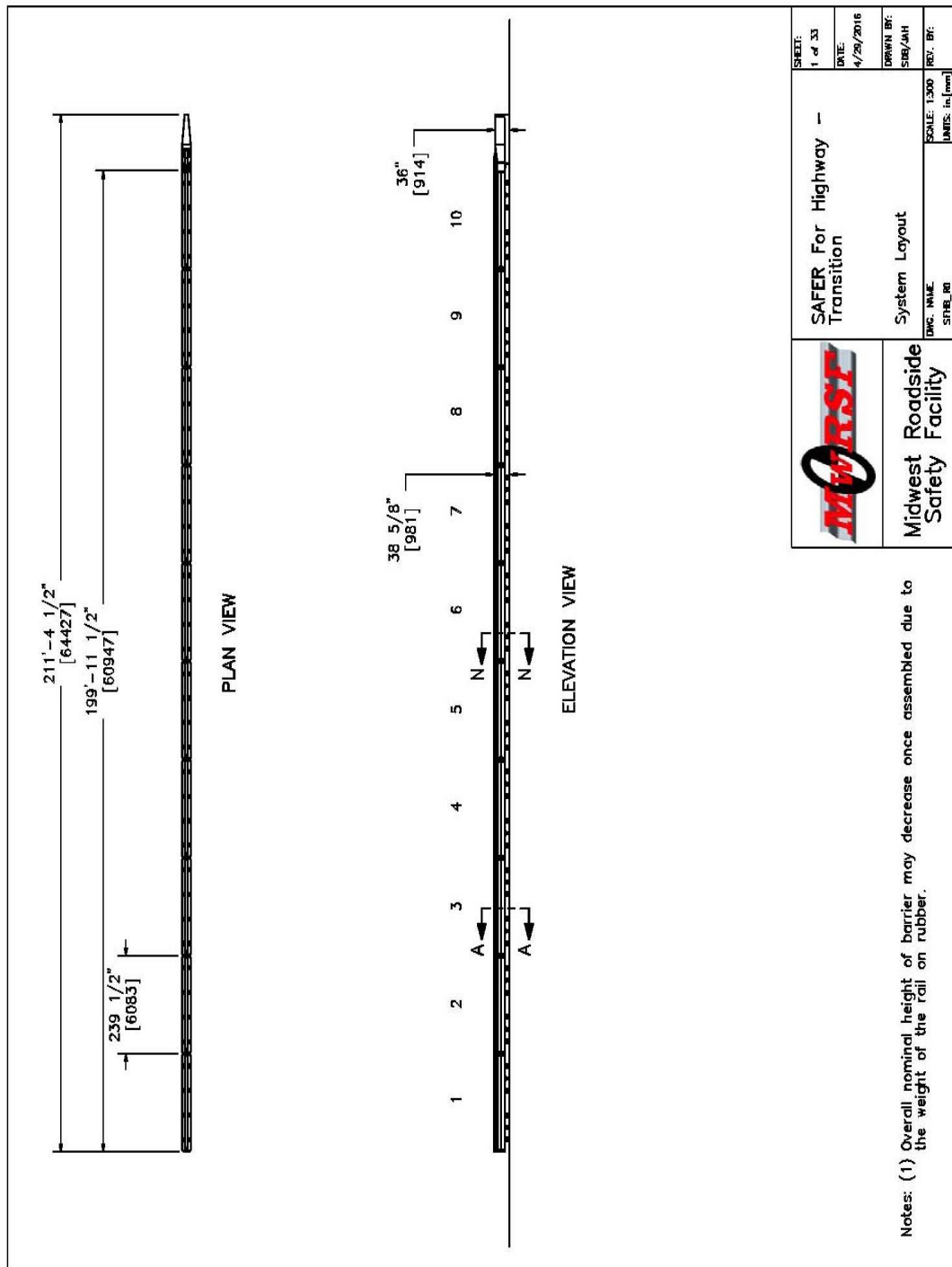
SAFER For Highway Transition with Straight Cover Plate

SCALE: 1:5
UNITS: in. (mm)

SHEET: 33 of 33
DATE: 4/29/2016
DRAWN BY: SDB/AH
REV. BY:

Figure J-11. Bill of Materials, Straight Cover Plate, RESTORE Barrier Transition

Appendix K. RESTORE Barrier Transition with Rounded Cover Plate Drawing Set



	SAFER For Highway - Transition	SHEET: 1 of 33
	System Layout	DATE: 4/29/2016
Midwest Roadside Safety Facility	Dwg. Name: STPB_00	DRAWN BY: SMB/SAH
	SCALE: 1:200 DIMES. in. (mm)	REV. BY:

Notes: (1) Overall nominal height of barrier may decrease once assembled due to the weight of the roll on rubber.

Figure K-1. System Layout, RESTORE Barrier Transition

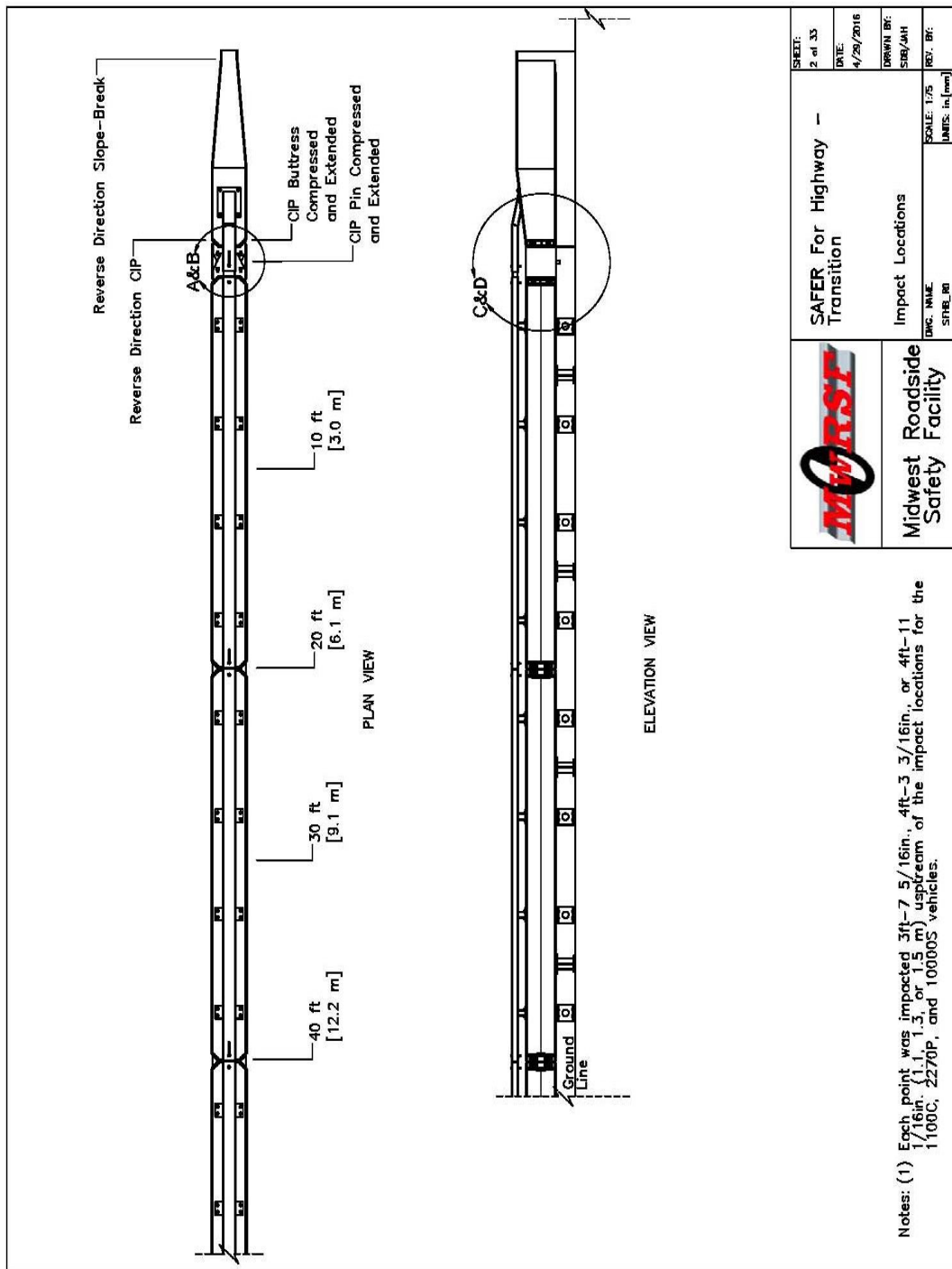


Figure K-2. System Layout, RESTORE Barrier Transition

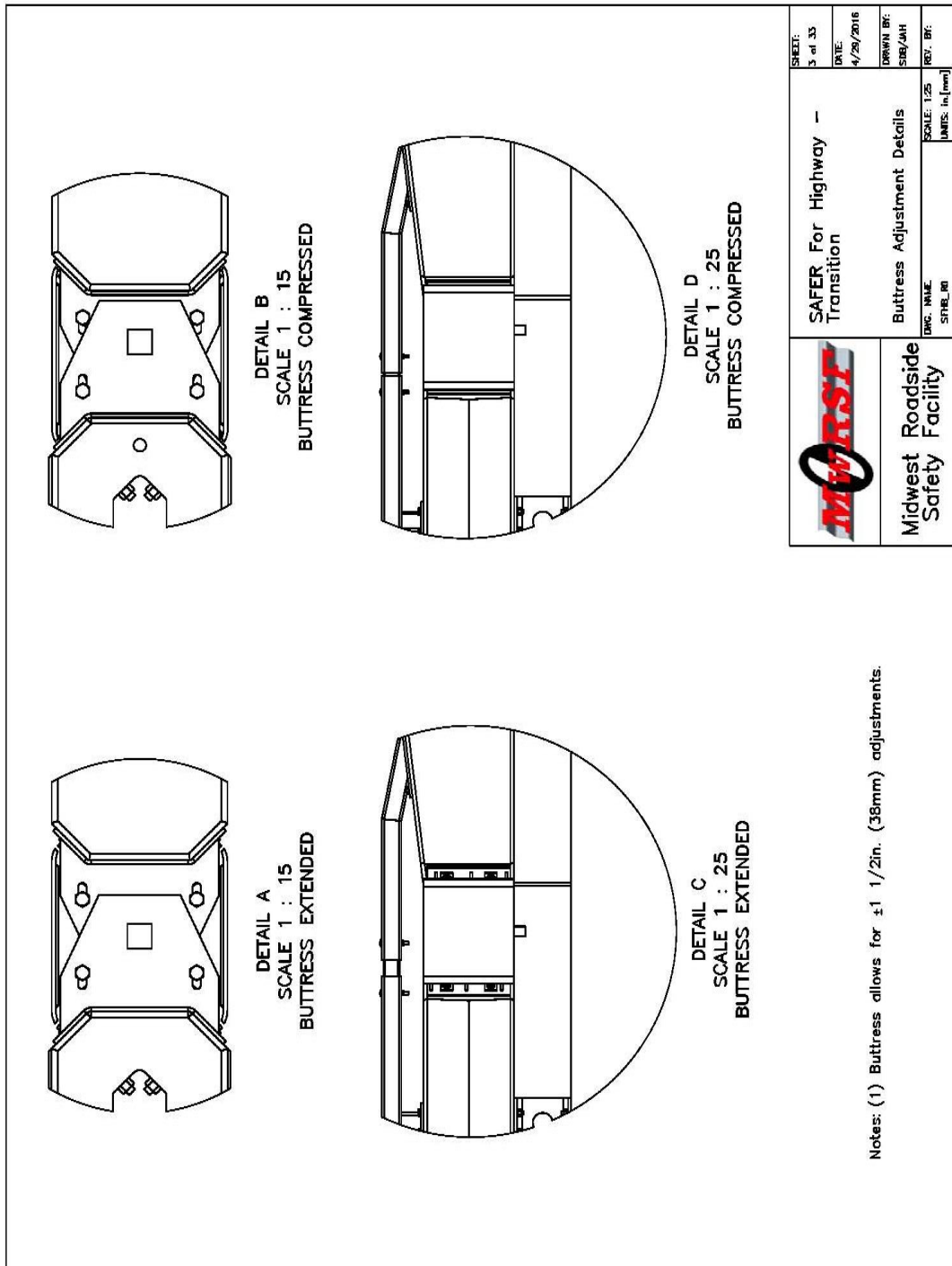
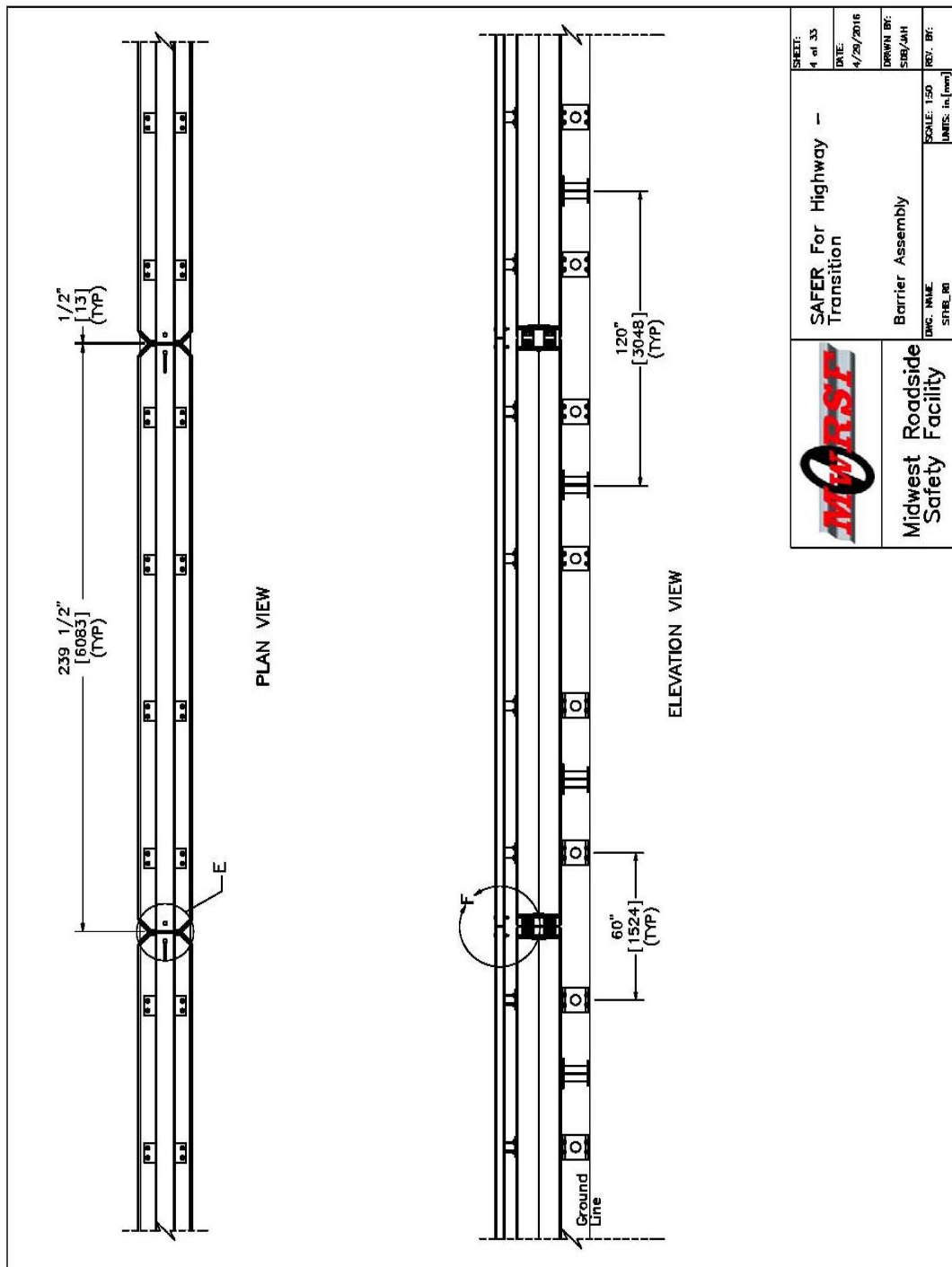


Figure K-3. Barrier Adjustment Details, RESTORE Barrier Transition




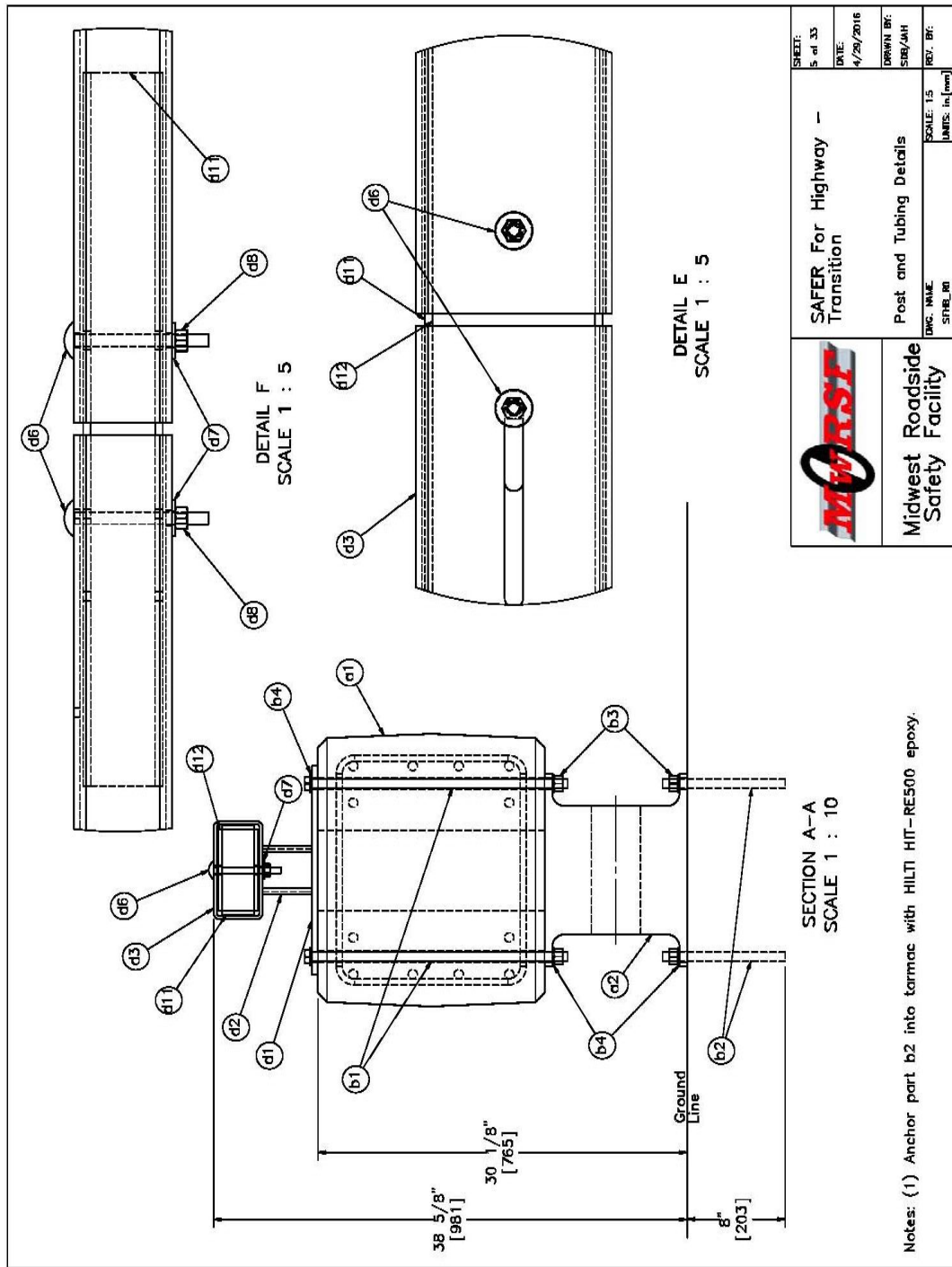
 Midwest Roadside Safety Facility	SAFER For Highway - Transition Barrier Assembly	SHEET: 4 of 33
	DMC: NAME STABLE_ID	DATE: 4/29/2016
SCALE: 1:50 UNITS: in. (mm)	DRAWN BY: SDB/AH	REV. BY:

Figure K-4. Barrier Assembly, RESTORE Barrier Transition



Notes: (1) Anchor part b2 into tarmac with HILTI HIT-RE500 epoxy.

	SAFER For Highway - Transition	SHEET: 5 of 33 DATE: 4/29/2016
	Post and Tubing Details	DRAWN BY: SBB/AH DWC: NAME SFB: RI
Midwest Roadside Safety Facility	SCALE: 1:5 UNITS: in (mm)	REV: BF

Figure K-5. Post and Tubing Details, RESTORE Barrier Transition

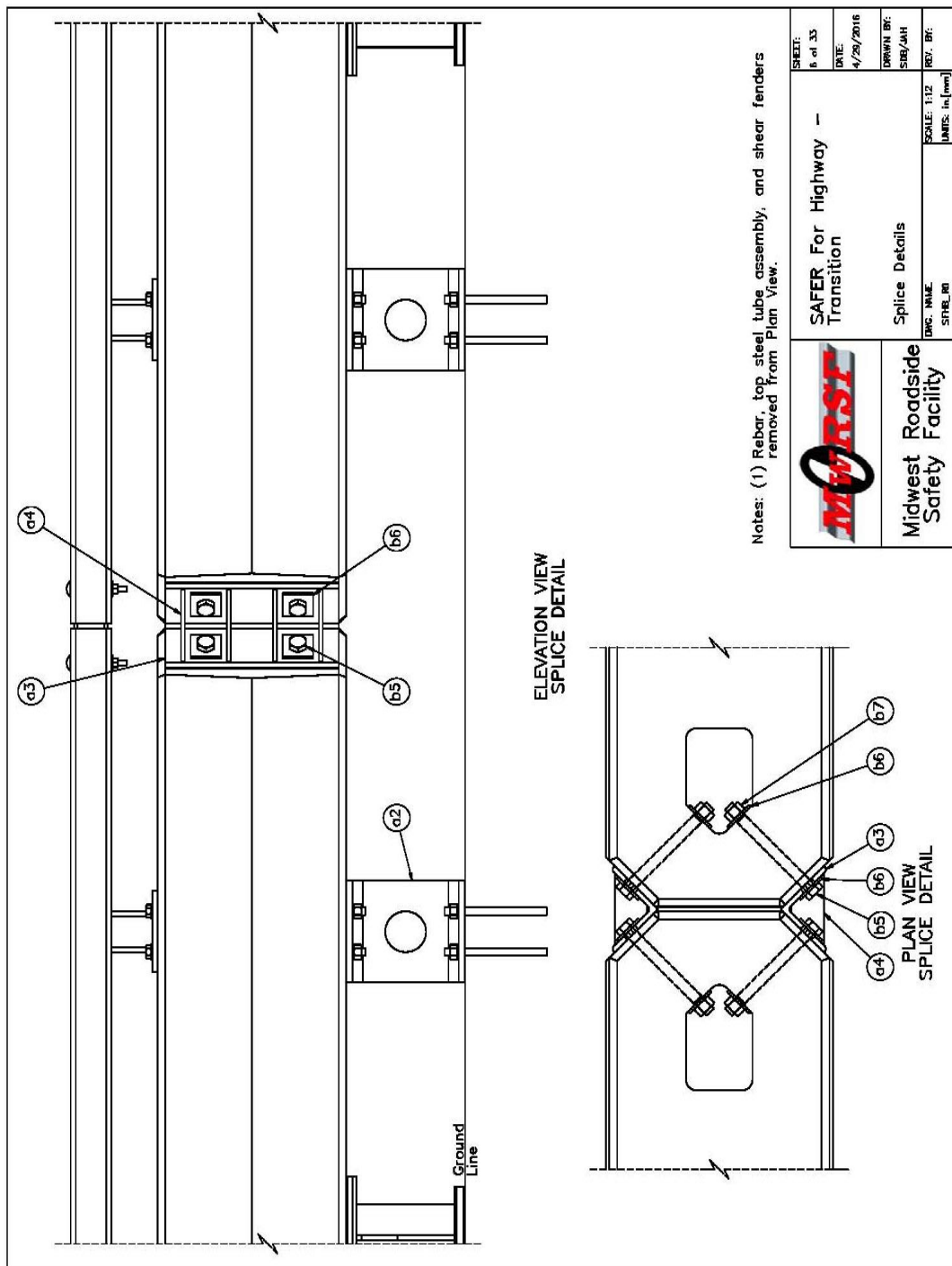


Figure K-6. Splice Details, RESTORE Barrier Transition

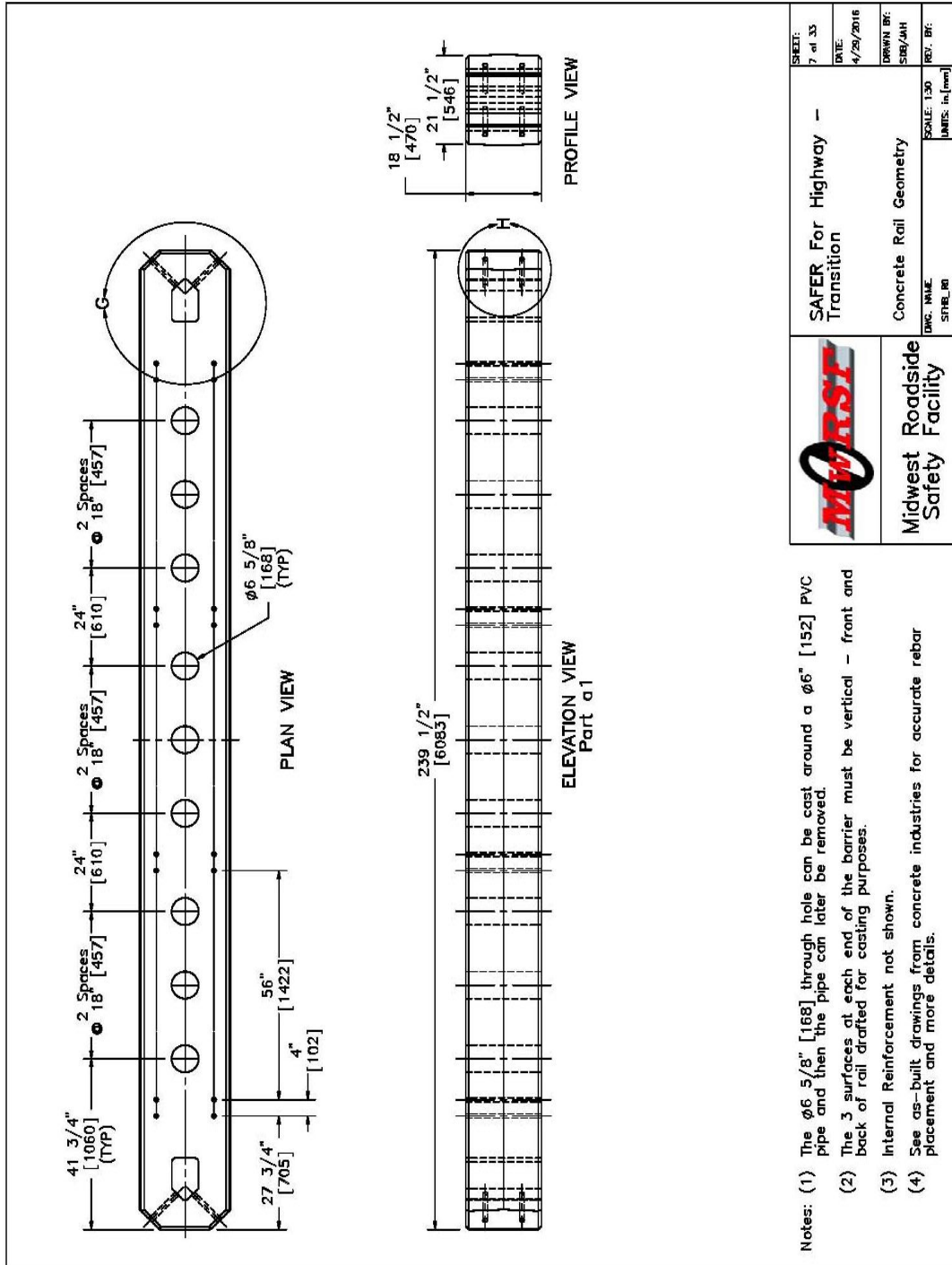
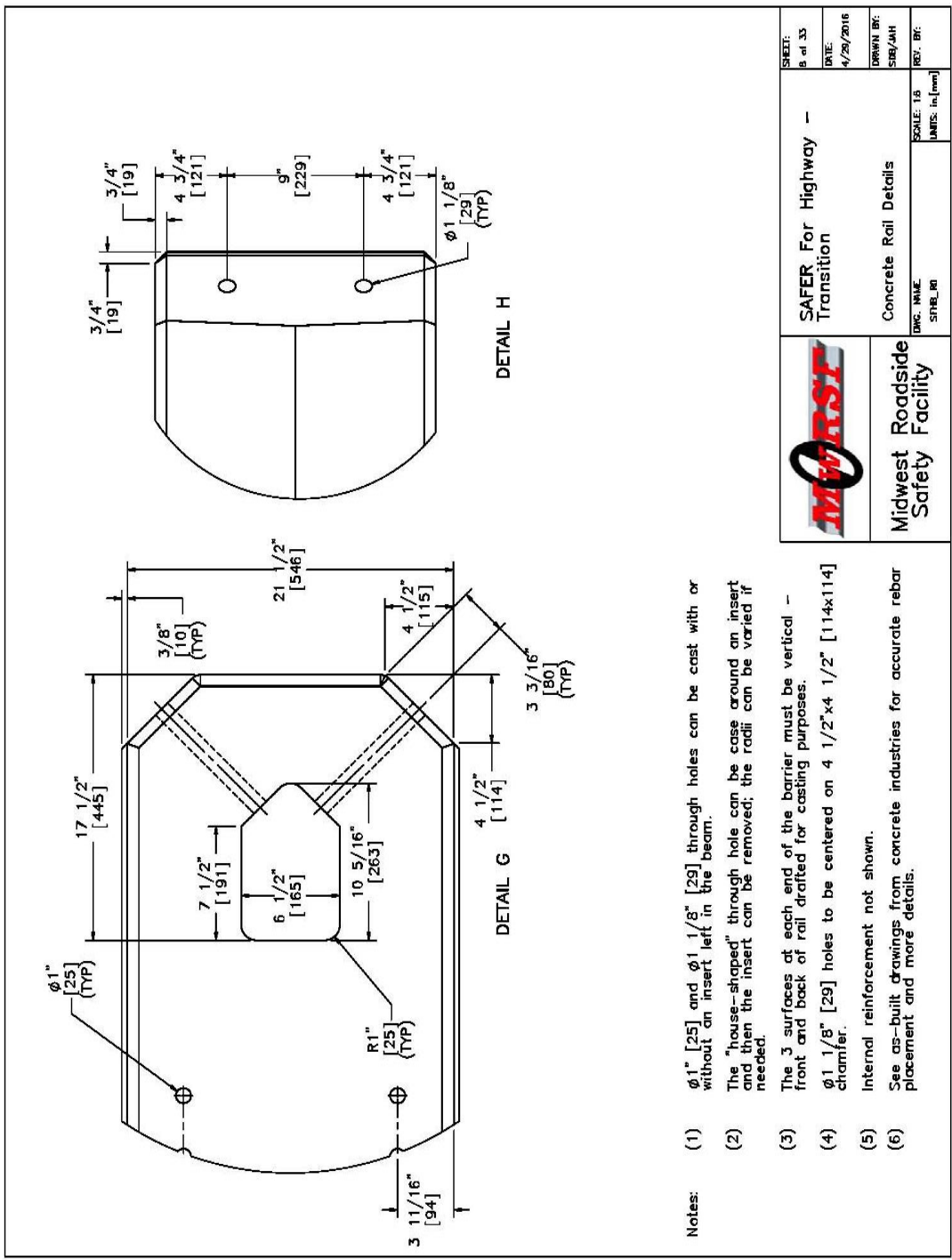
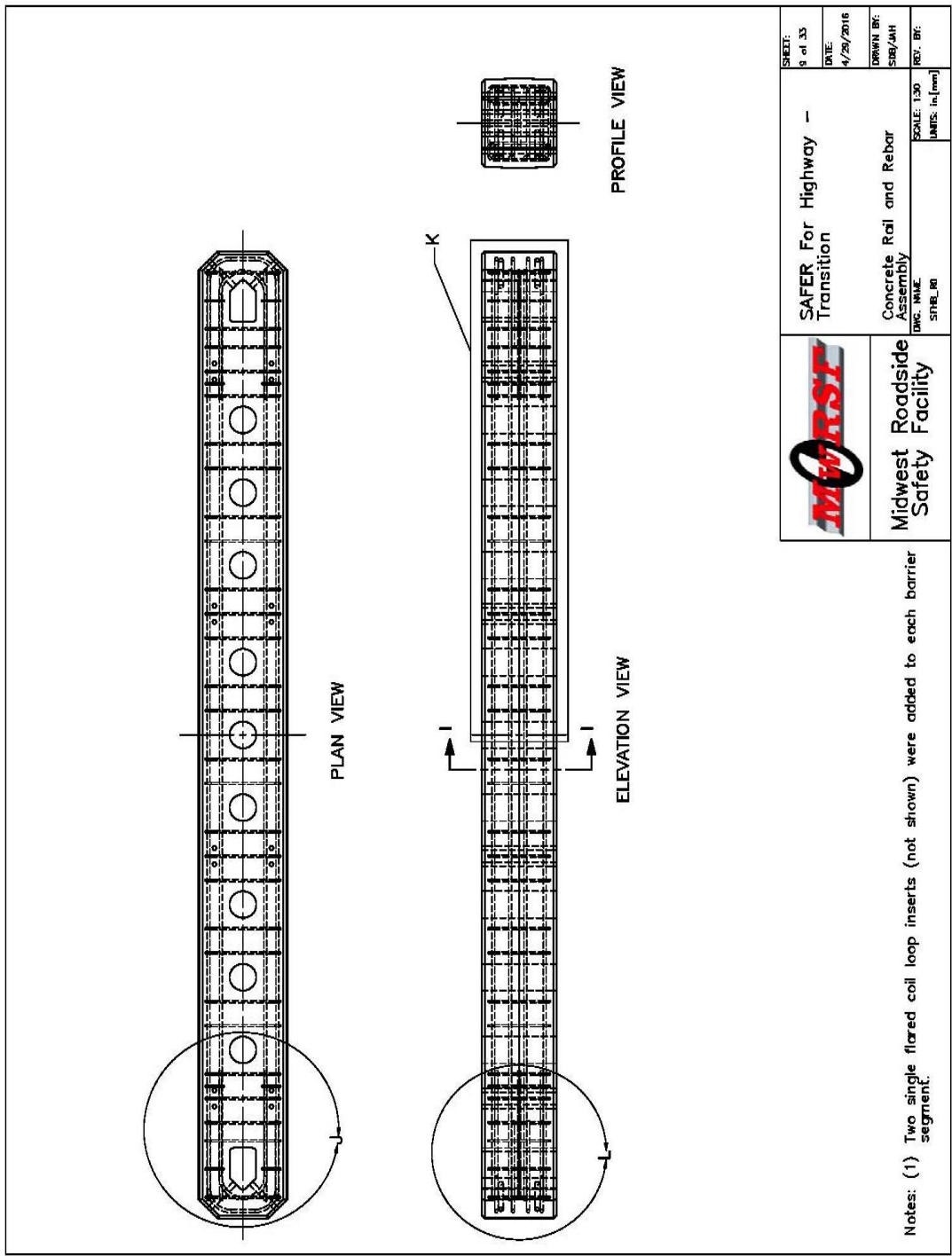


Figure K-7. Concrete Rail Geometry, RESTORE Barrier Transition



- Notes:
- (1) $\phi 1"$ [25] and $\phi 1 1/8"$ [29] through holes can be cast with or without an insert left in the beam.
 - (2) The "house-shaped" through hole can be case around an insert and then the insert can be removed; the radii can be varied if needed.
 - (3) The 3 surfaces at each end of the barrier must be vertical - front and back of rail drafted for casting purposes.
 - (4) $\phi 1 1/8"$ [29] holes to be centered on $4 1/2" \times 4 1/2"$ [114x114] chamfer.
 - (5) Internal reinforcement not shown.
 - (6) See as-built drawings from concrete industries for accurate rebar placement and more details.

Figure K-8. Concrete Rail Details, RESTORE Barrier Transition




 Midwest Roadside Safety Facility	SAFER For Highway Transition	SHEET: 9 of 33 DATE: 4/29/2016
	Concrete Rail and Rebar Assembly Dwg. Name: SPSL_R0	SCALE: 1:30 UNITS: in. [mm]

Figure K-9. Concrete Rail and Rebar Assembly, RESTORE Barrier Transition

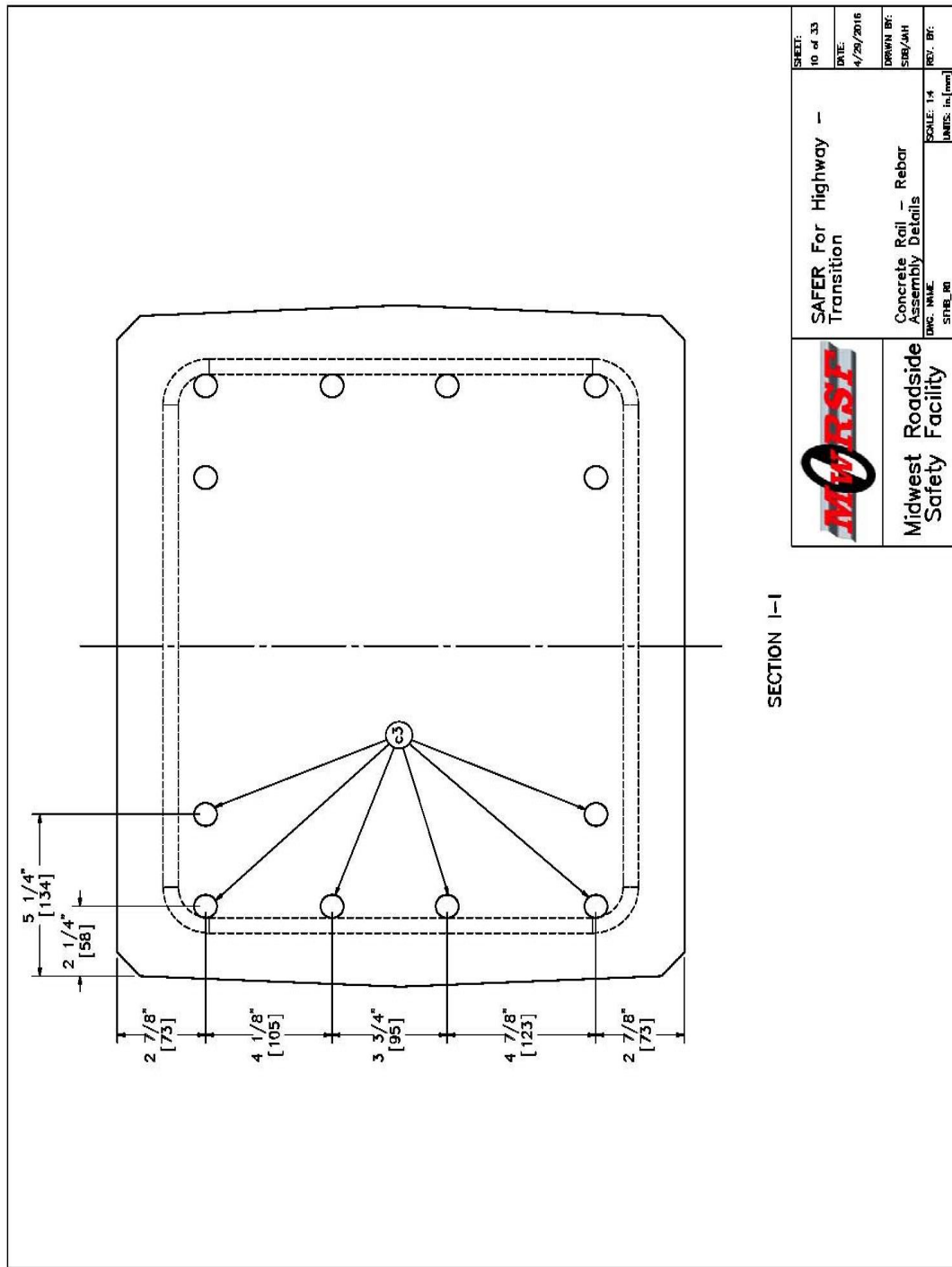


Figure K-10. Concrete Rail Rebar Assembly Details, RESTORE Barrier Transition

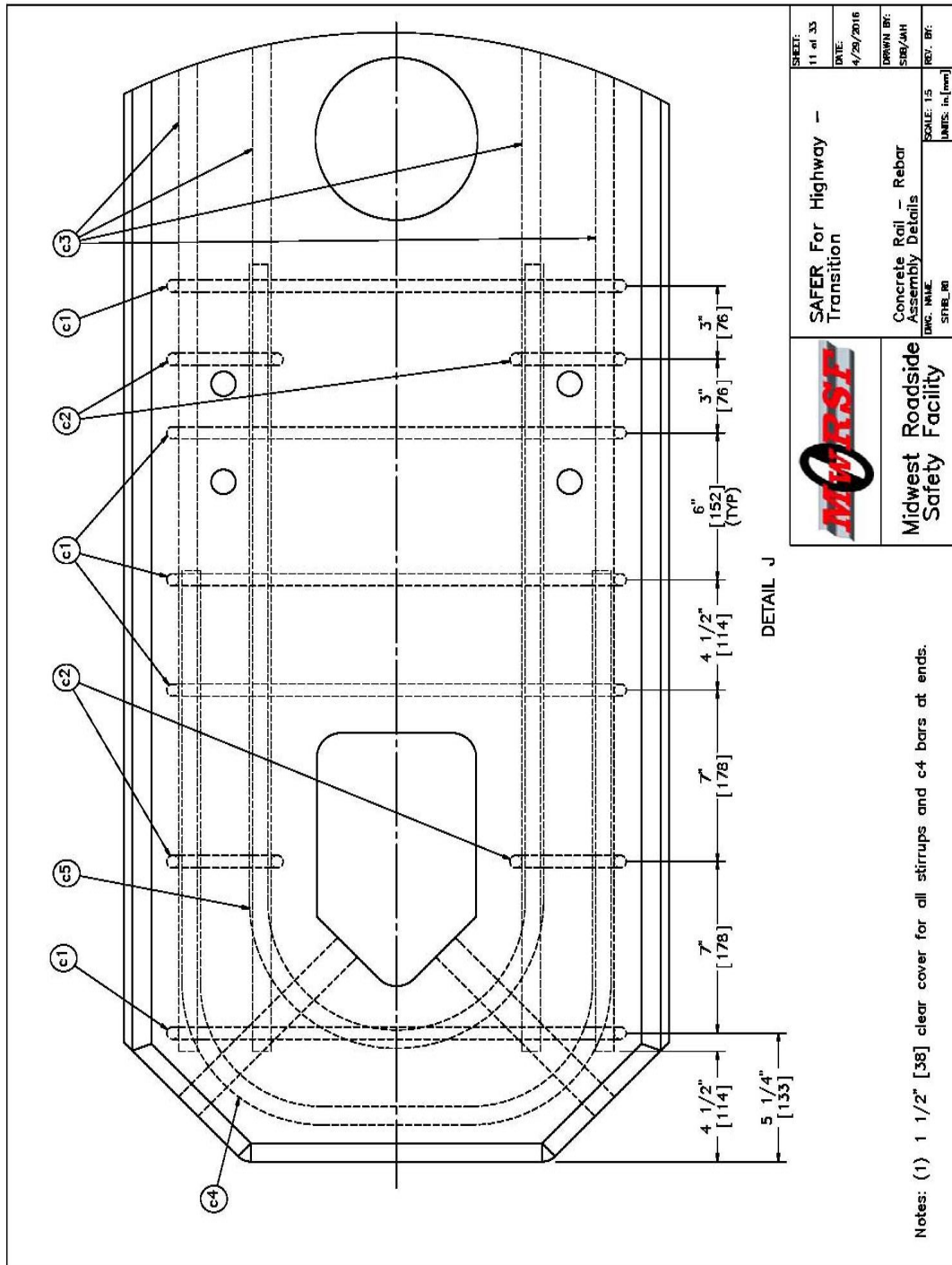
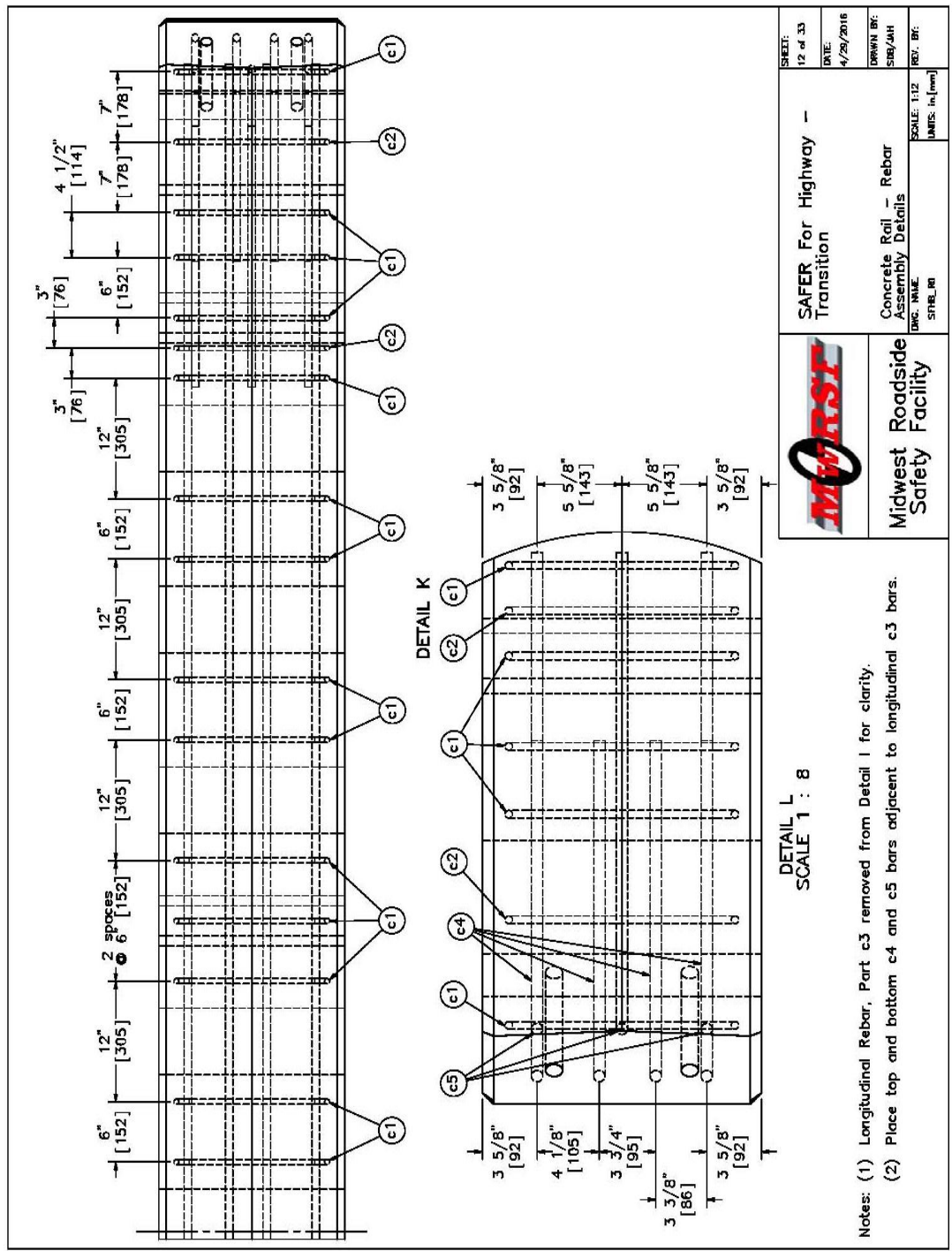


Figure K-11. Concrete Rail Rebar Assembly Details, RESTORE Barrier Transition



Notes: (1) Longitudinal Rebar, Part c3 removed from Detail I for clarity.
 (2) Place top and bottom c4 and c5 bars adjacent to longitudinal c3 bars.

	SAFER For Highway - Transition	SHEET: 12 of 33 DATE: 4/29/2016 DRAWN BY: SSB/AH DWG. NAME: Concrete Rail - Rebar Assembly Details SCALE: 1:12 UNITS: in. (mm) SFB:RI
	Midwest Roadside Safety Facility	

DETAIL L
 SCALE 1 : 8

Figure K-12. Concrete Rail Rebar Assembly Details, RESTORE Barrier Transition

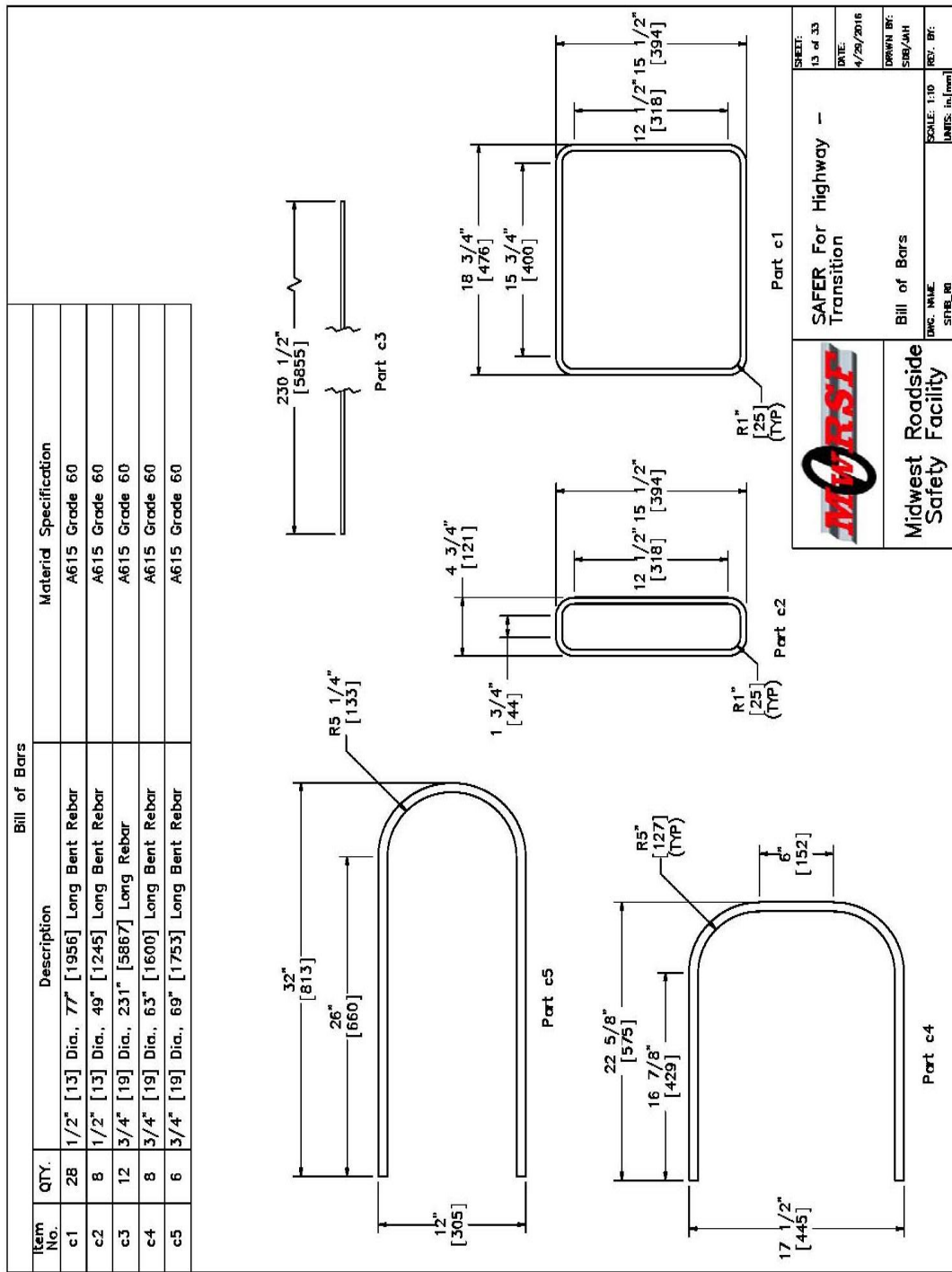


Figure K-13. Bill of Bars, RESTORE Barrier Transition

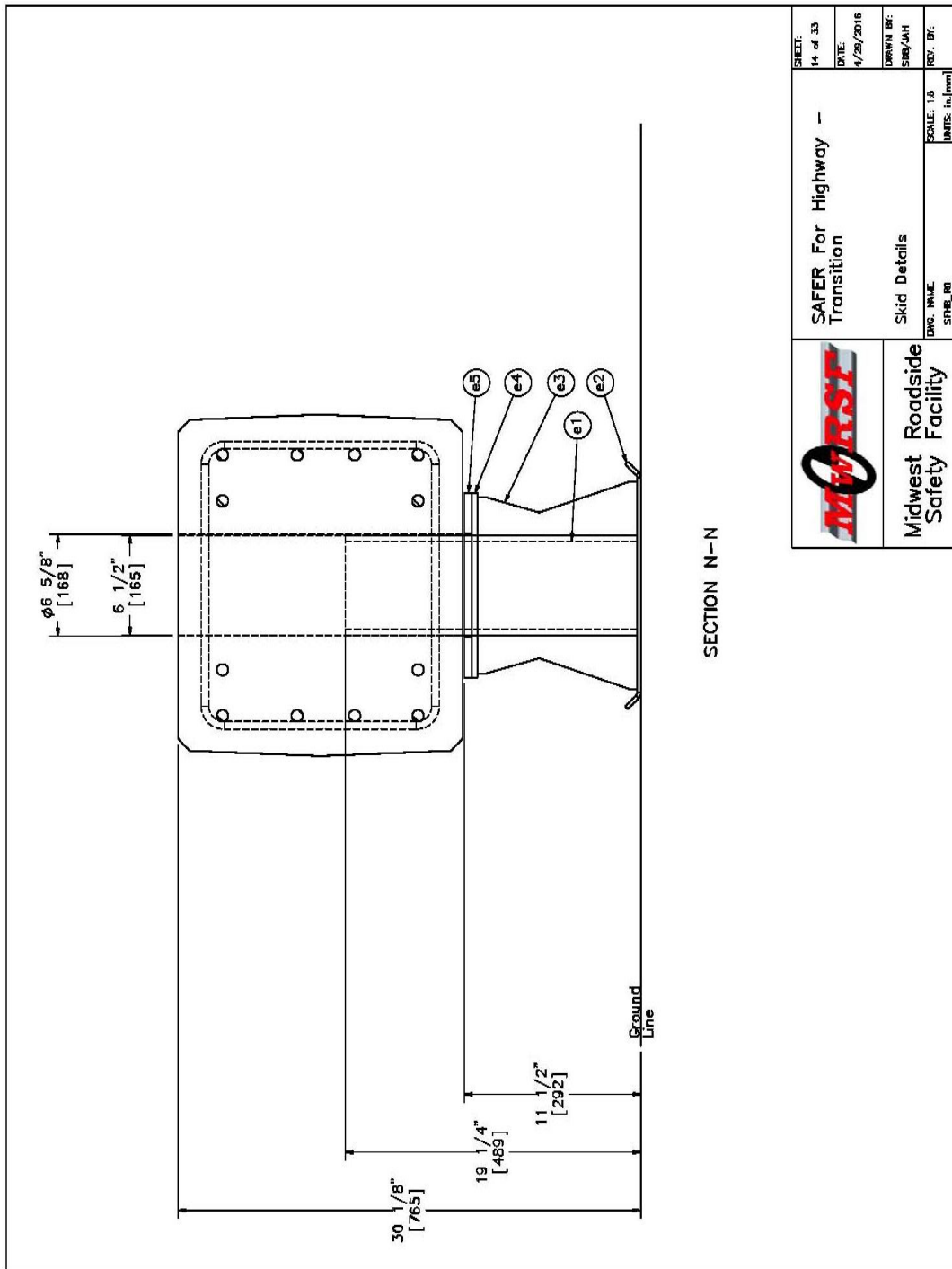


Figure K-14. Skid Details, RESTORE Barrier Transition

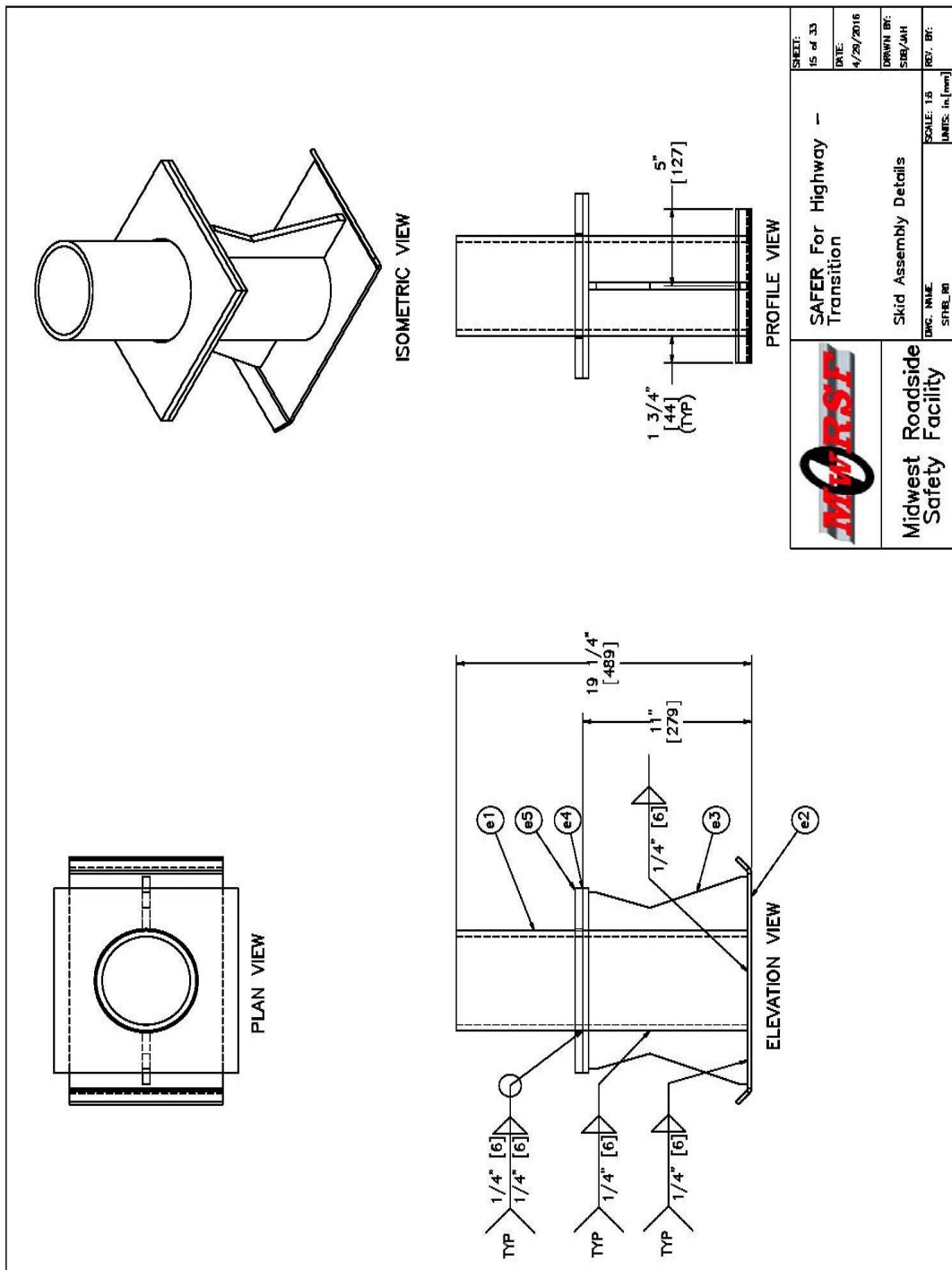
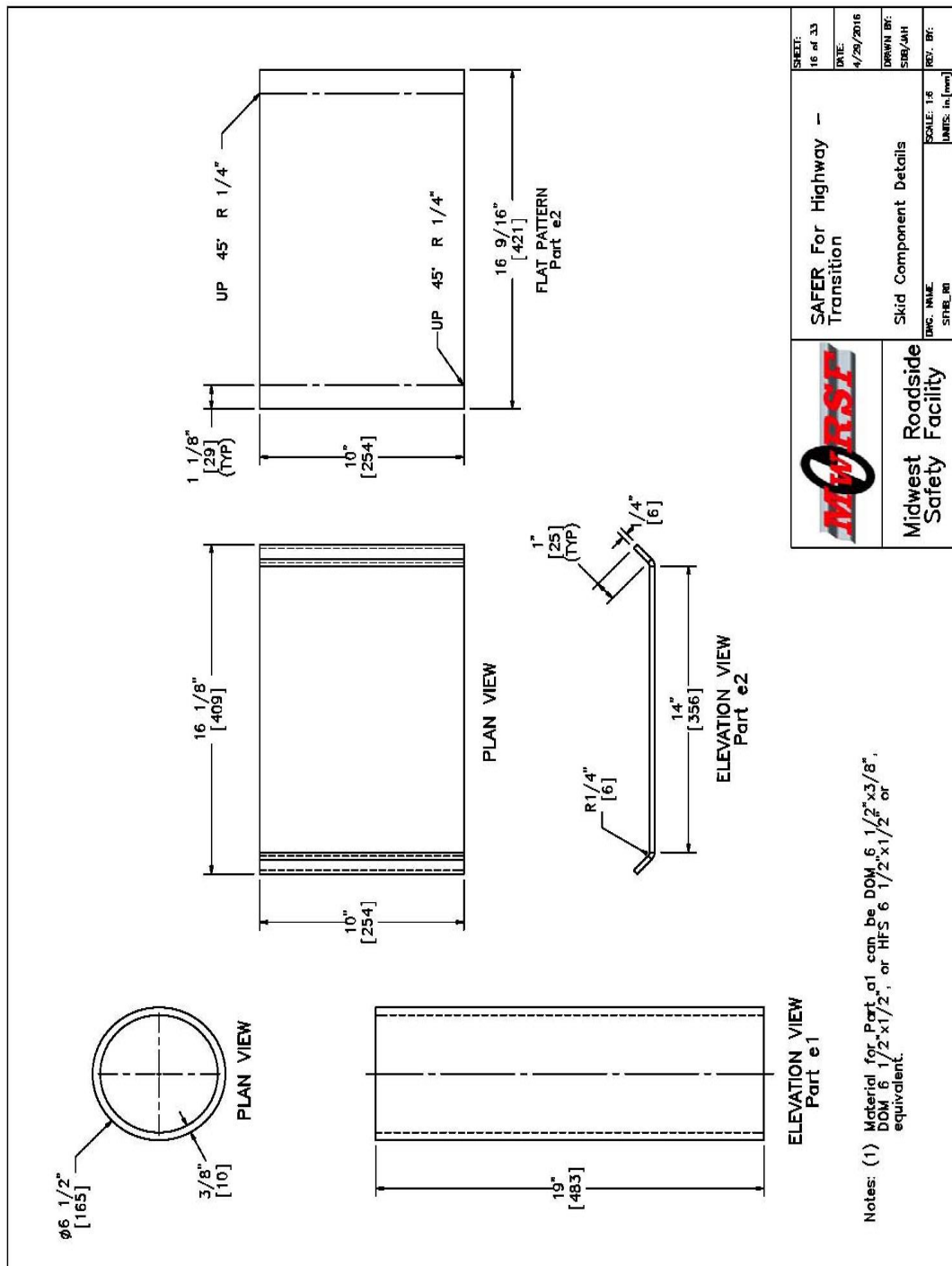
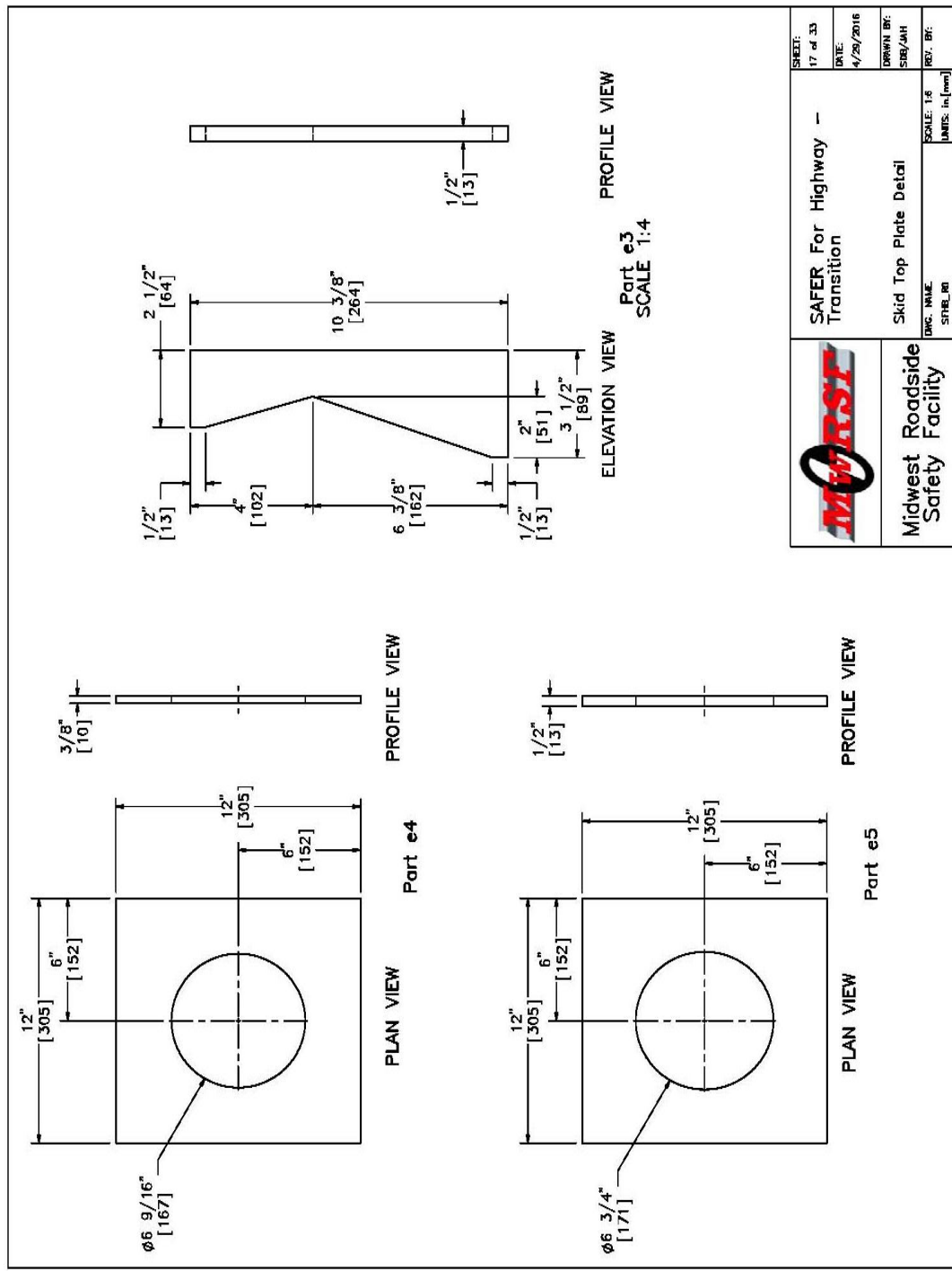


Figure K-15. Skid Assembly Details, RESTORE Barrier Transition



	SAFER For Highway - Transition	SHEET: 16 of 33
	Skid Component Details	DATE: 4/29/2016
Midwest Roadside Safety Facility	Dwg. Name: SFHB_00	DRAWN BY: SMB/AH
	SCALE: 1:6 UNITS: in. (mm)	REV. BY:

Figure K-16. Skid Component Details, RESTORE Barrier Transition




 Midwest Roadside Safety Facility	SAFER For Highway Transition	SHEET: 17 of 33
	Skid Top Plate Detail	DATE: 4/29/2016
DWG. NAME: SKID_PLATE	SCALE: 1:8	DRAWN BY: SBB/AH
SPFBLR0	UNITS: in, (mm)	REV. BY:

Figure K-17. Skid Top Plate Detail, RESTORE Barrier Transition

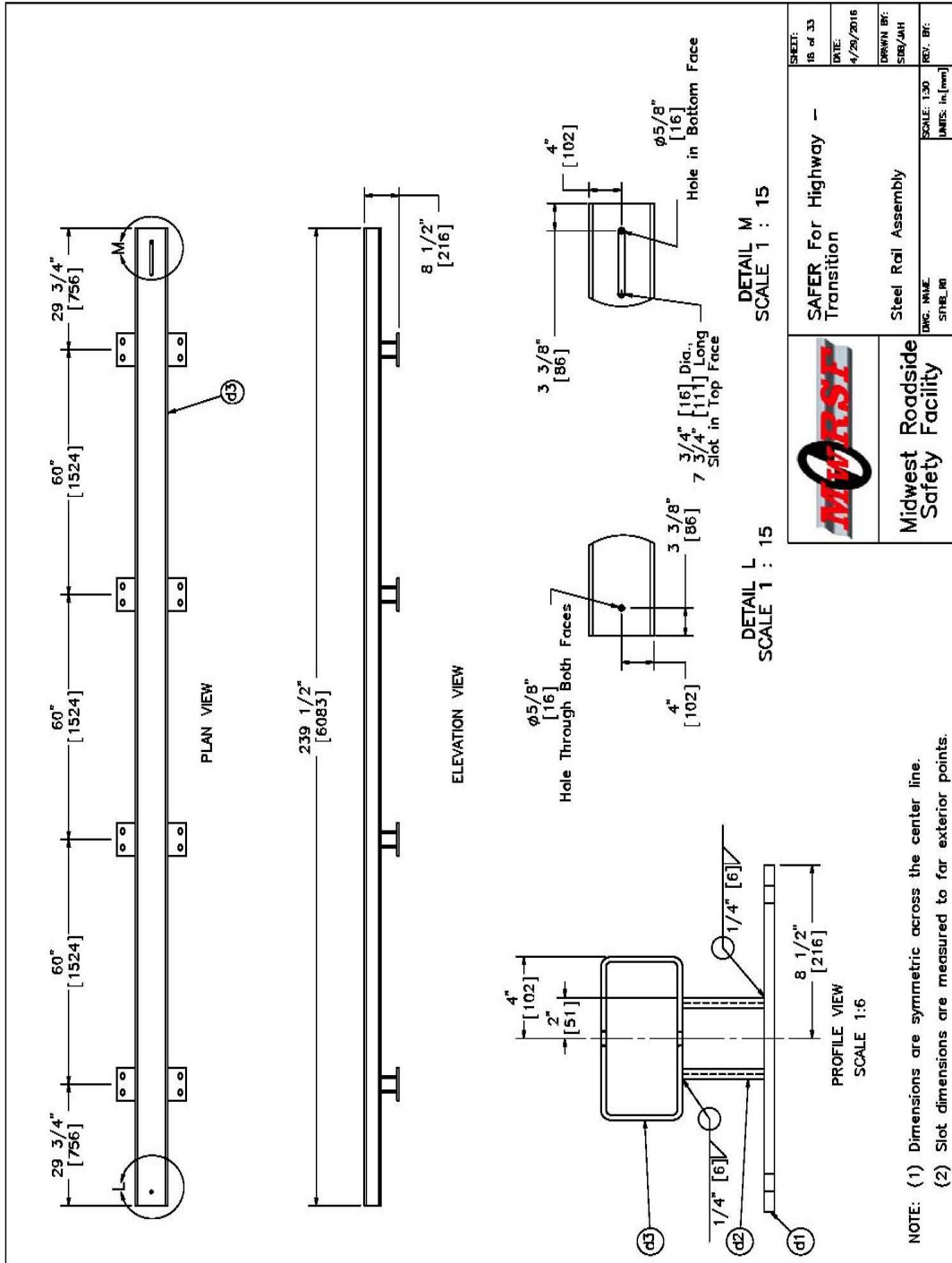


Figure K-18. Steel Rail Assembly, RESTORE Barrier Transition

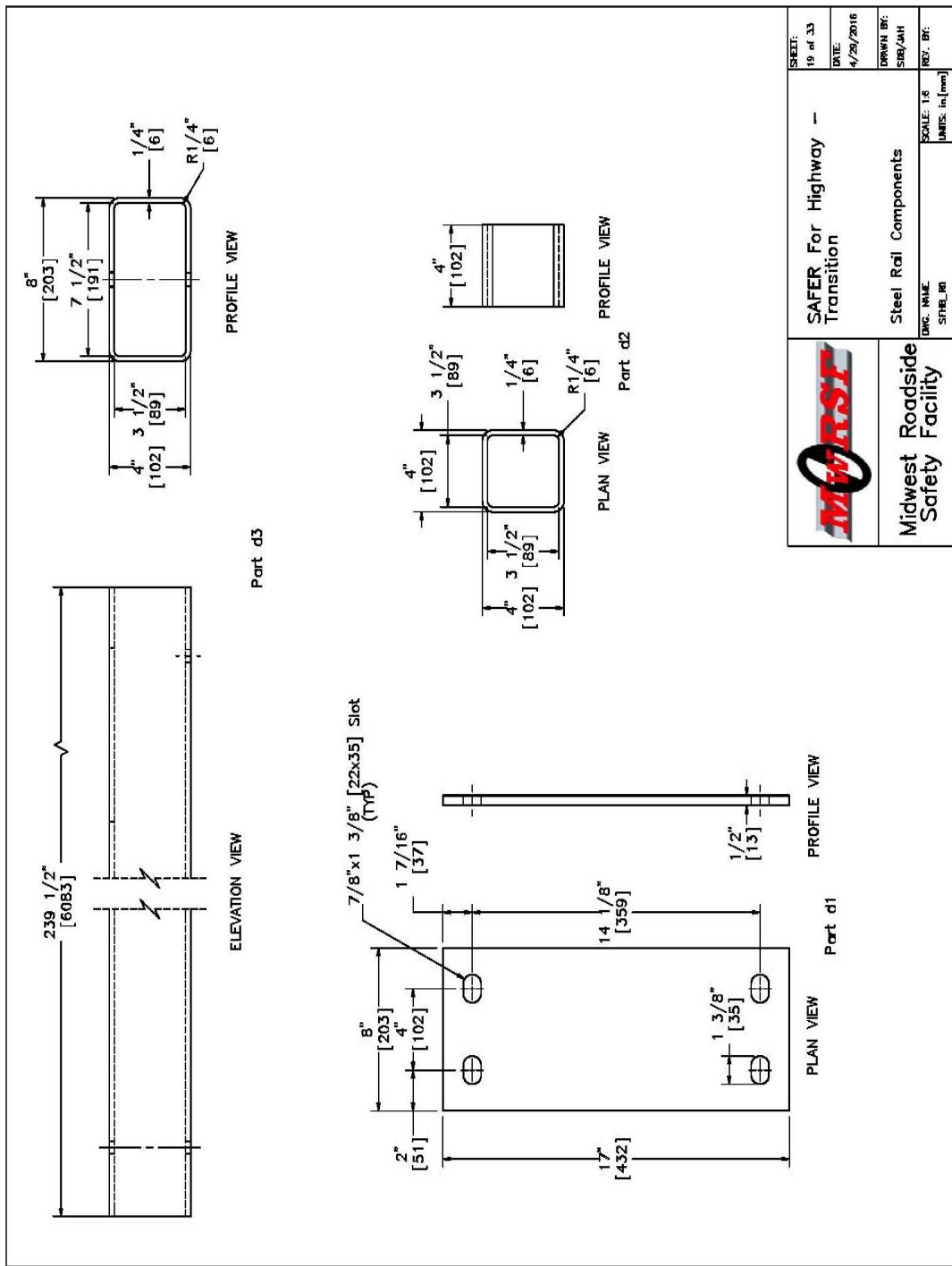
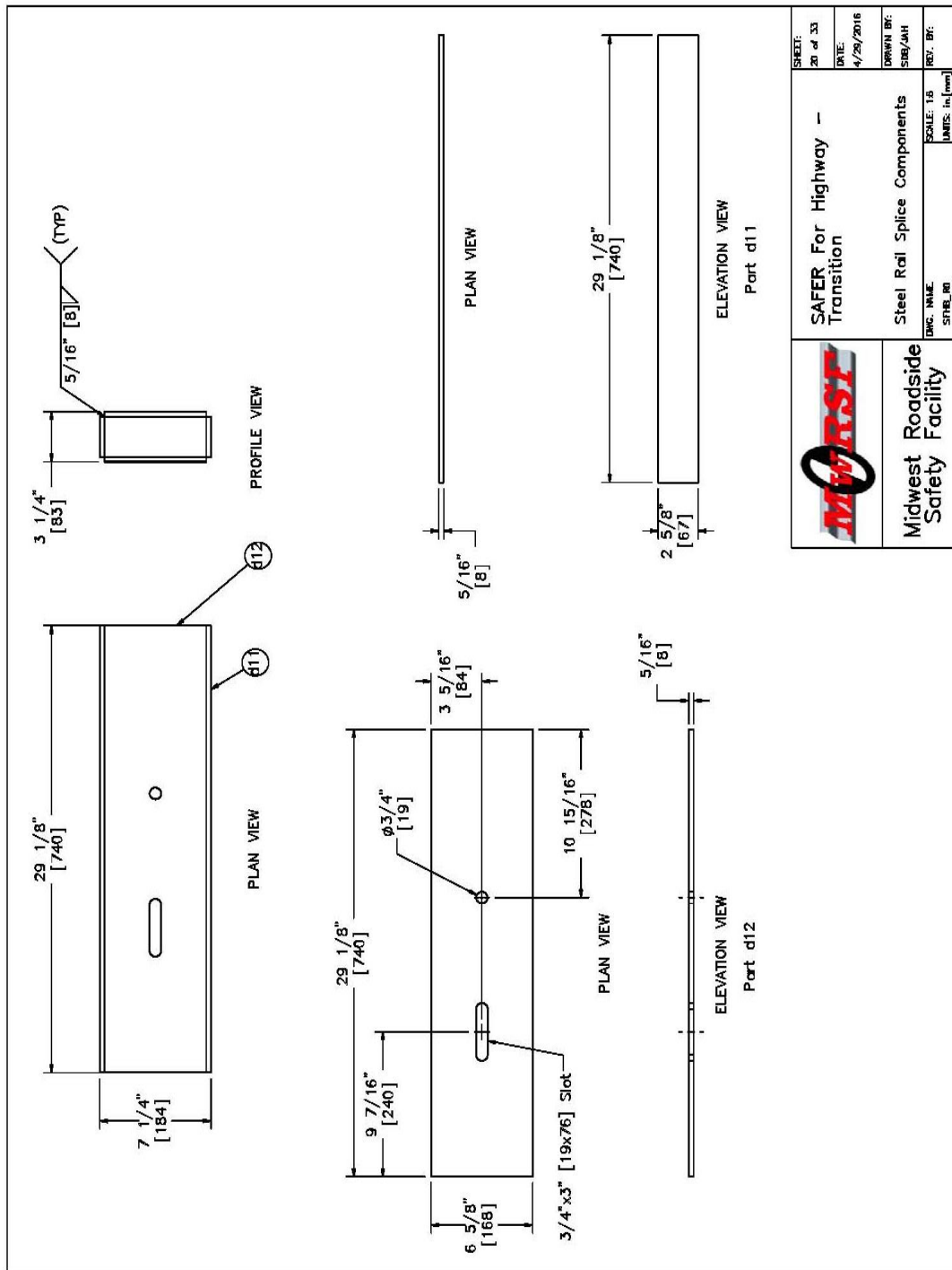


Figure K-19. Steel Rail Components, RESTORE Barrier Transition




 Midwest Roadside Safety Facility	SAFER For Highway Transition	SHEET: 20 of 33 DATE: 4/29/2016
	Steel Rail Splice Components <small>DWG. NAME: STSPL_R1</small>	DRAWN BY: SBB/ahh SCALE: 1:5 <small>DIMS: in, [mm]</small>

Figure K-20. Steel Rail Splice Components, RESTORE Barrier Transition

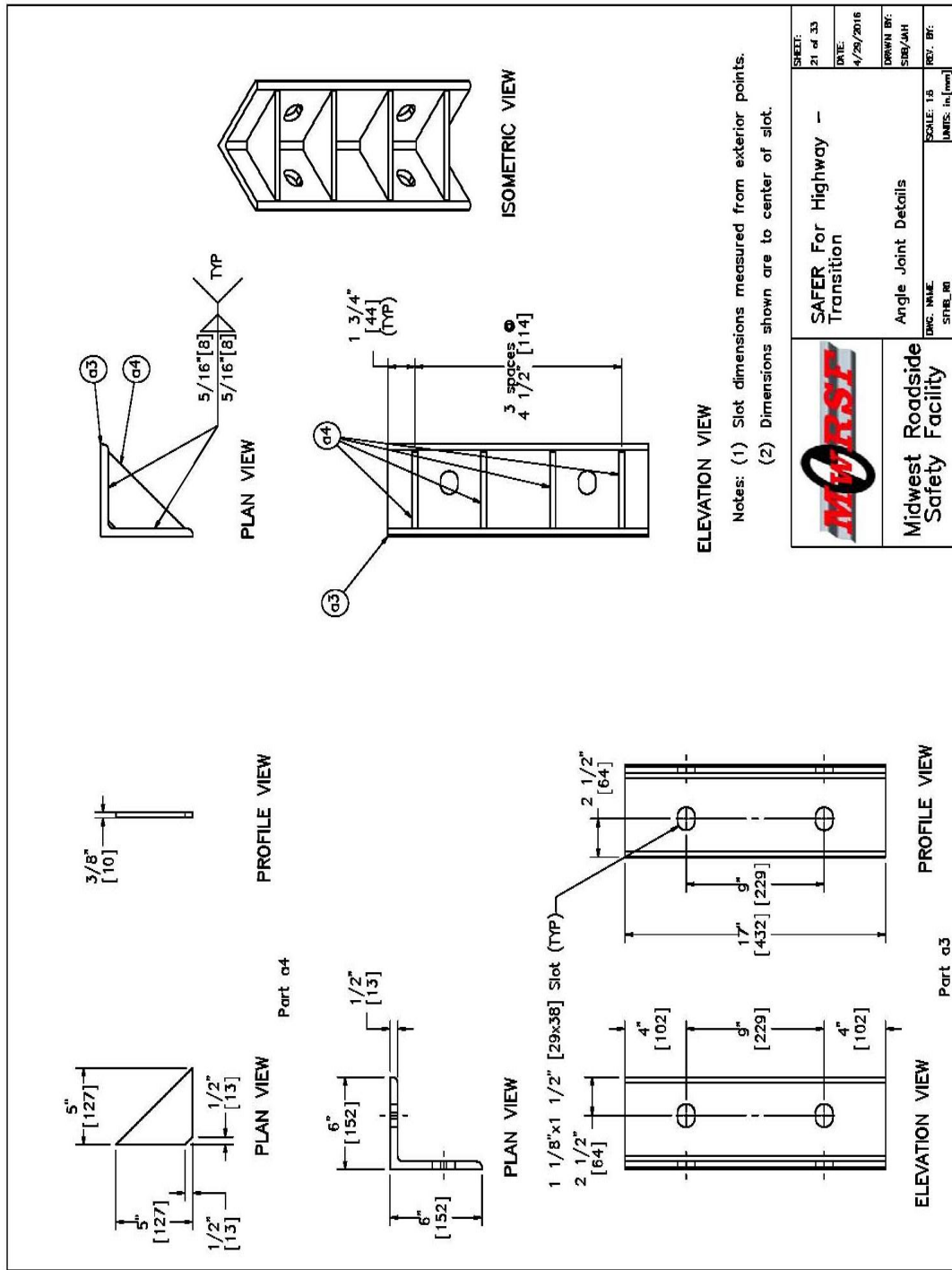


Figure K-21. Angle Joint Details, RESTORE Barrier Transition

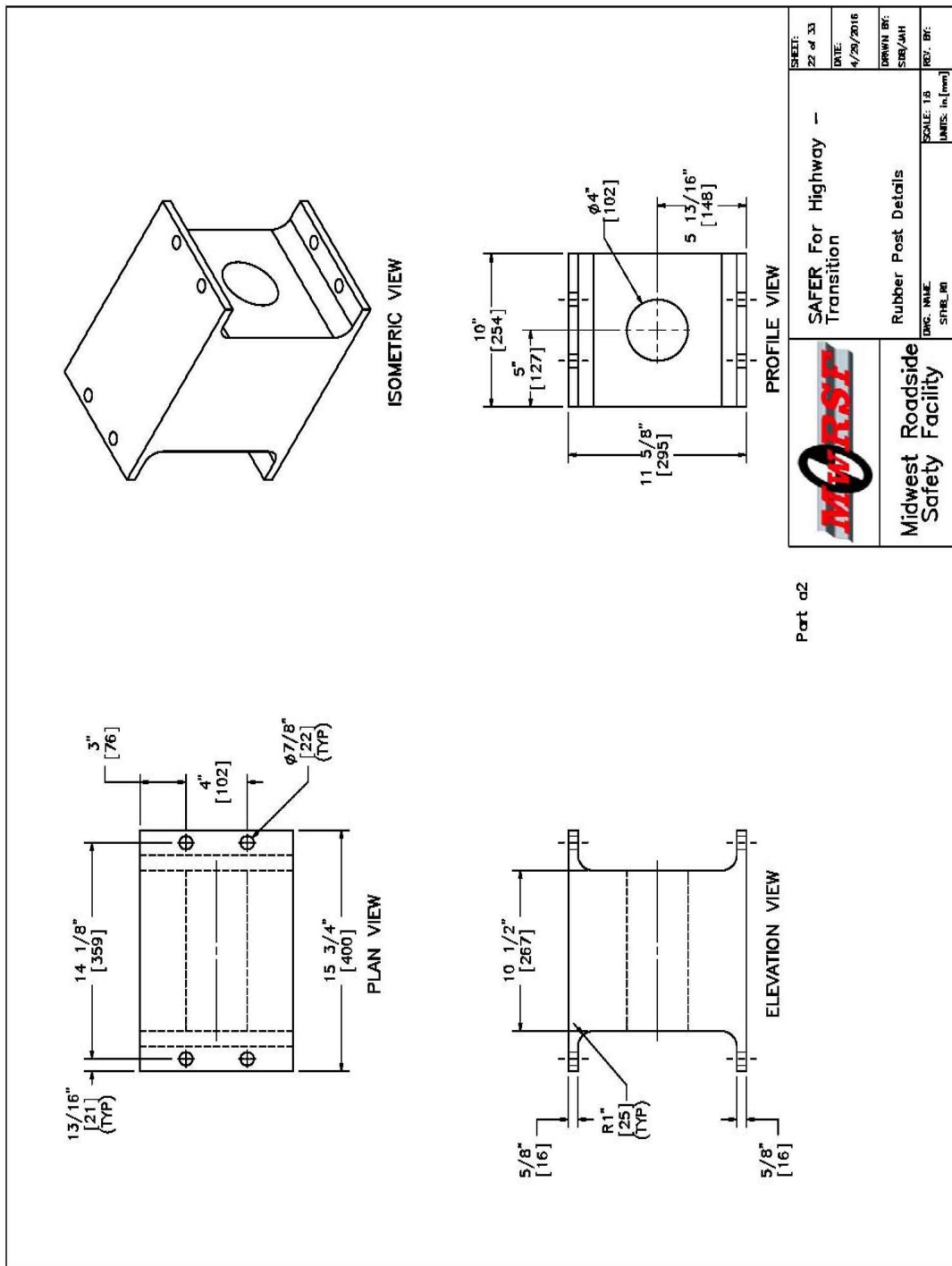


Figure K-22. Rubber Post Details, RESTORE Barrier Transition

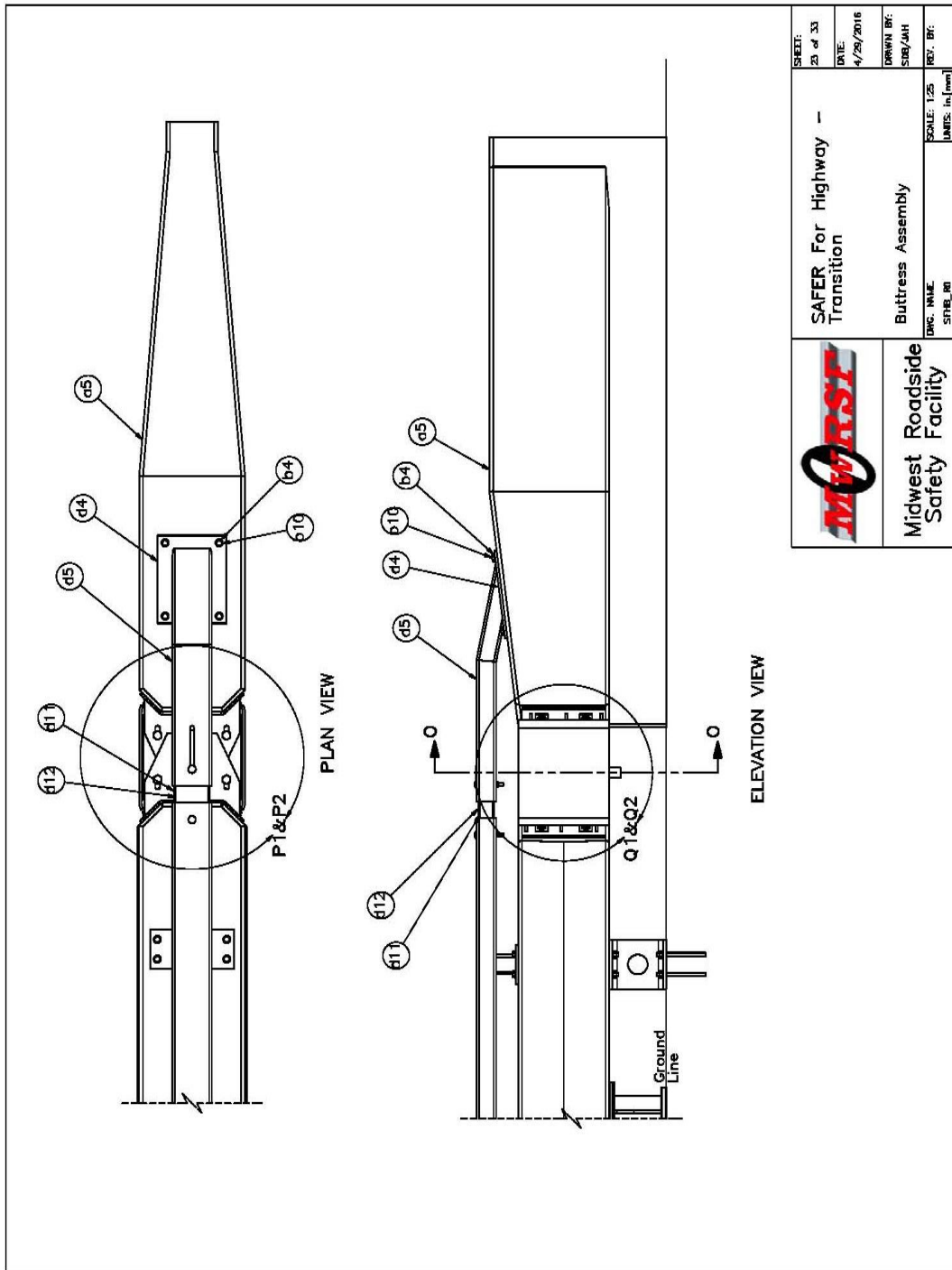


Figure K-23. Buttruss Assembly, RESTORE Barrier Transition

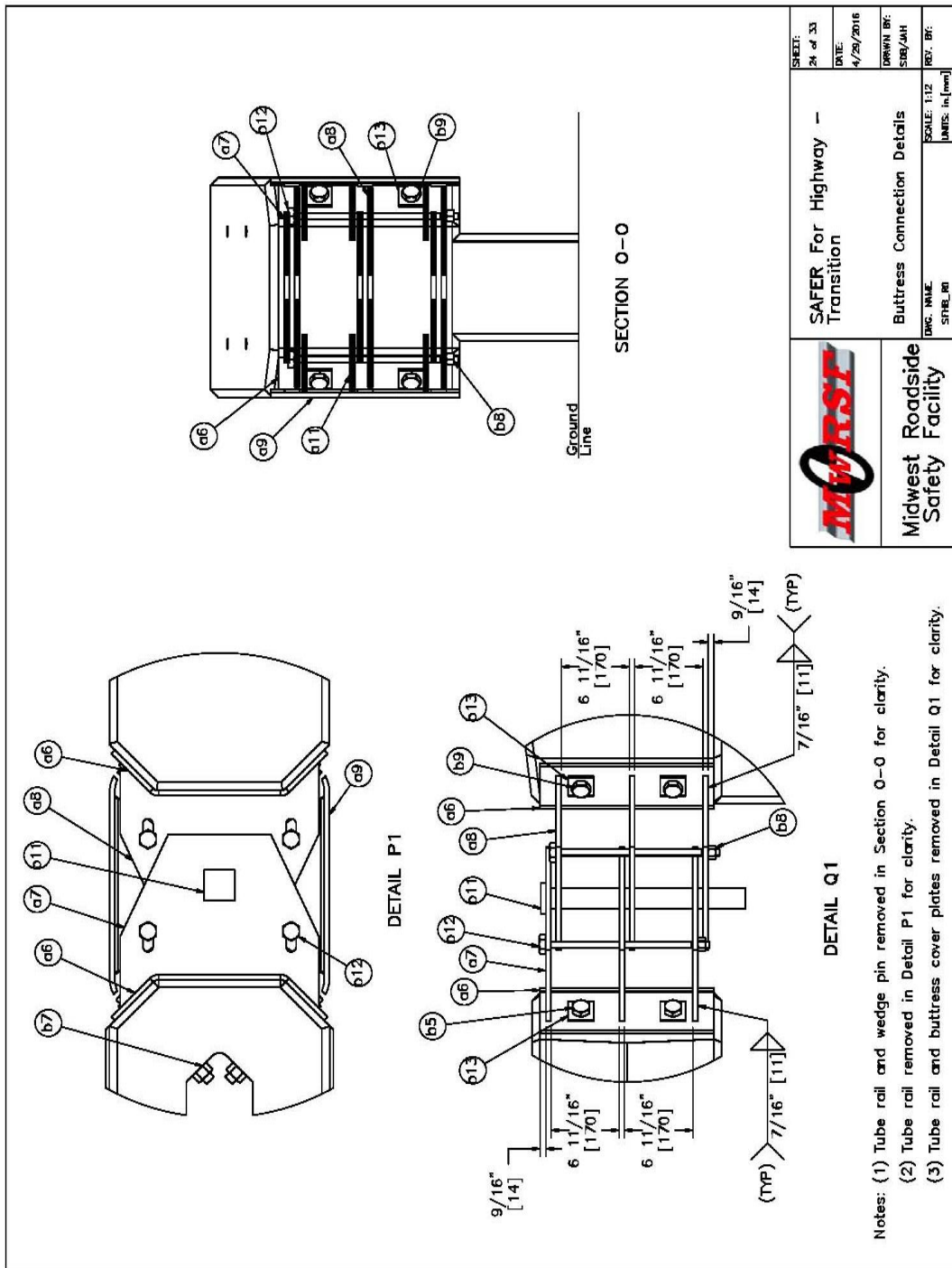
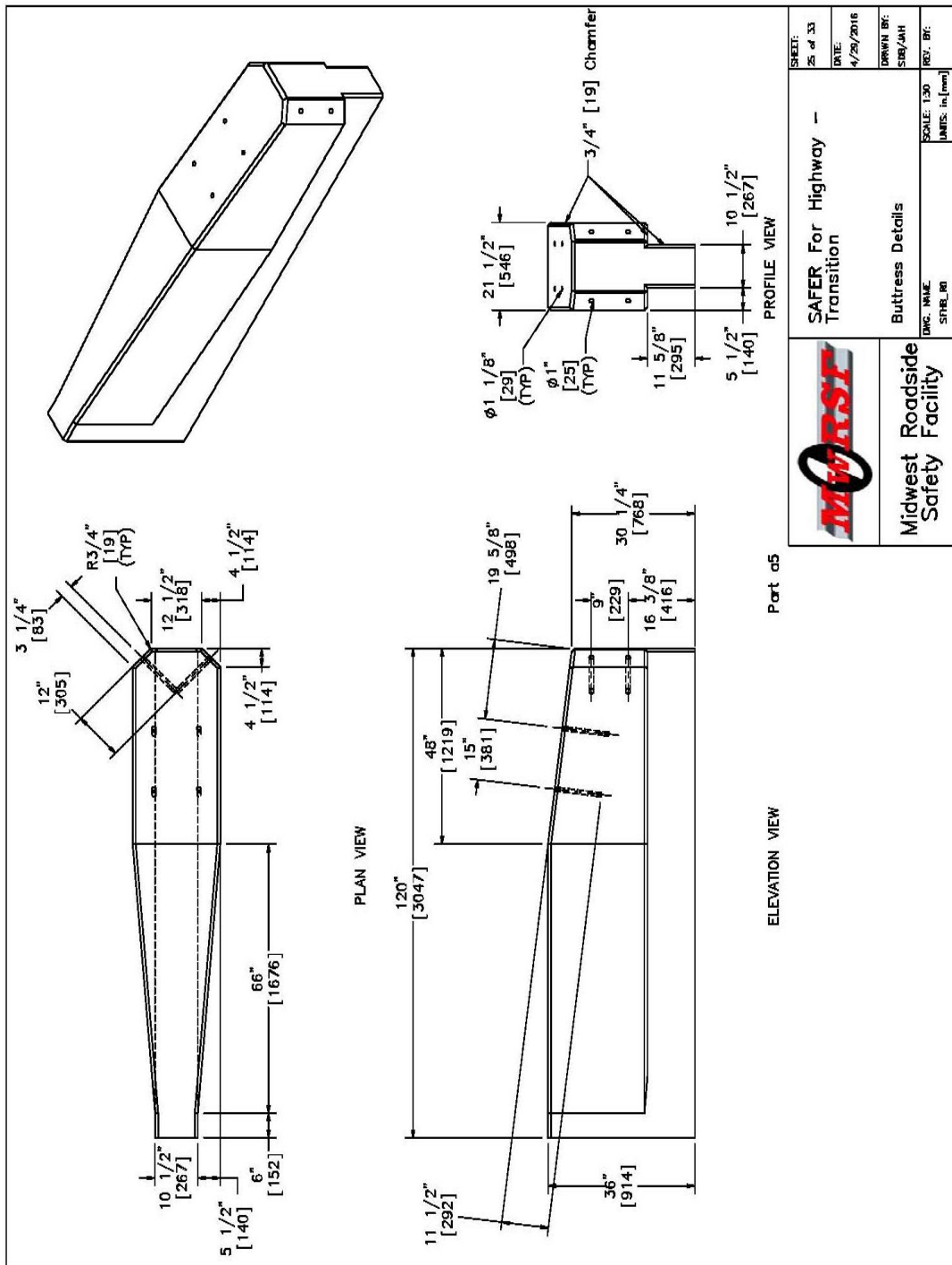


Figure K-24. Butress Connection Details, RESTORE Barrier Transition




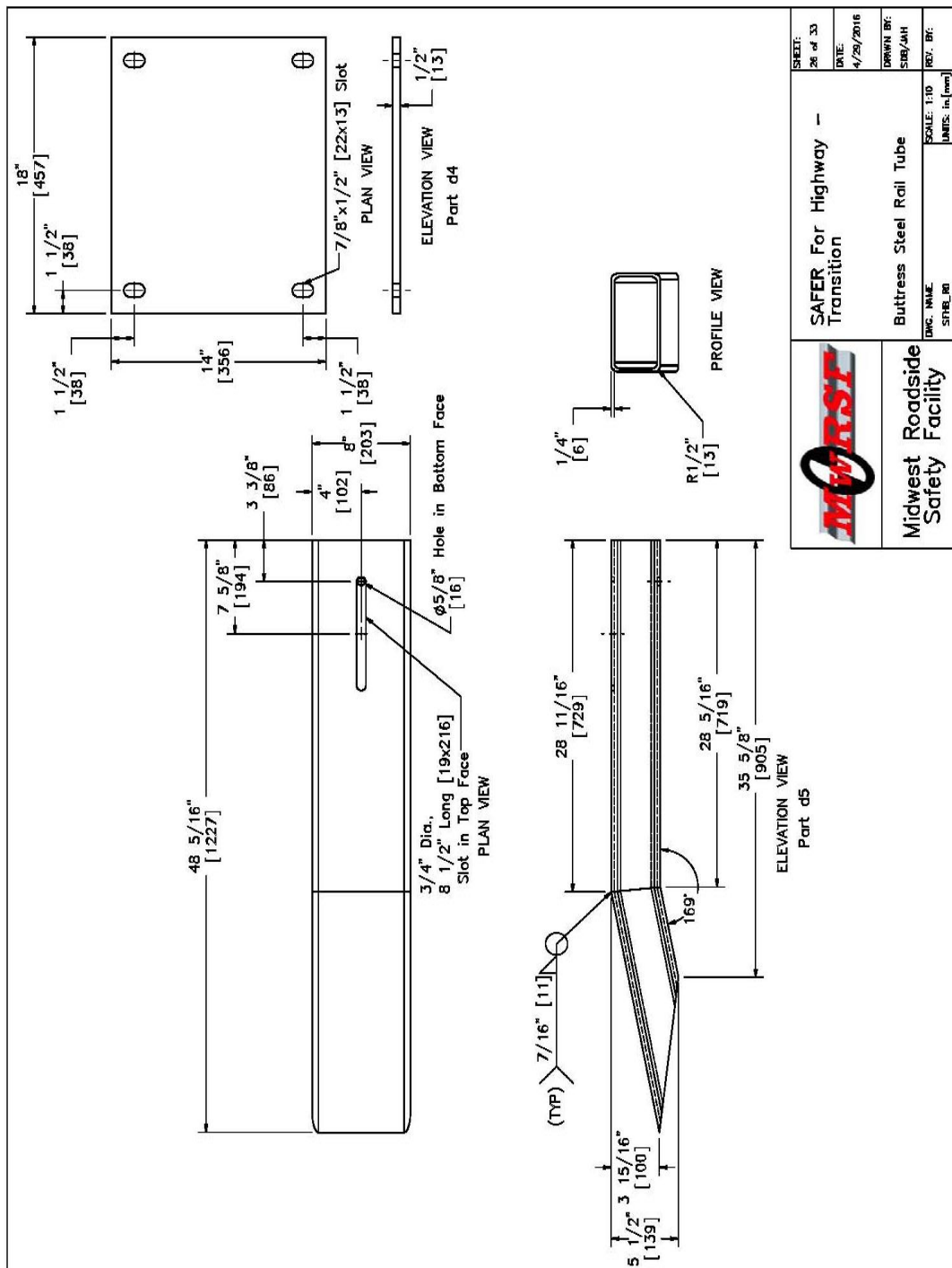
 Midwest Roadside Safety Facility	SAFER For Highway - Transition	SHEET: 25 of 33 DATE: 4/29/2016 DRAWN BY: SDB/JAH REV. BY:
	Buttriss Details	SCALE: 1:30 DIMS: in [mm]

Figure K-25. Buttriss Details, RESTORE Barrier Transition




	SAFER For Highway Transition	SHEET: 26 of 33 DATE: 4/29/2016 DRAWN BY: SBB/JAH REV. BY:
	Buttruss Steel Rail Tube	DWG. NAME: SRRB_R0 SCALE: 1:10 UNITS: in (mm)
Midwest Roadside Safety Facility		

Figure K-26. Buttruss Steel Rail Tube, RESTORE Barrier Transition

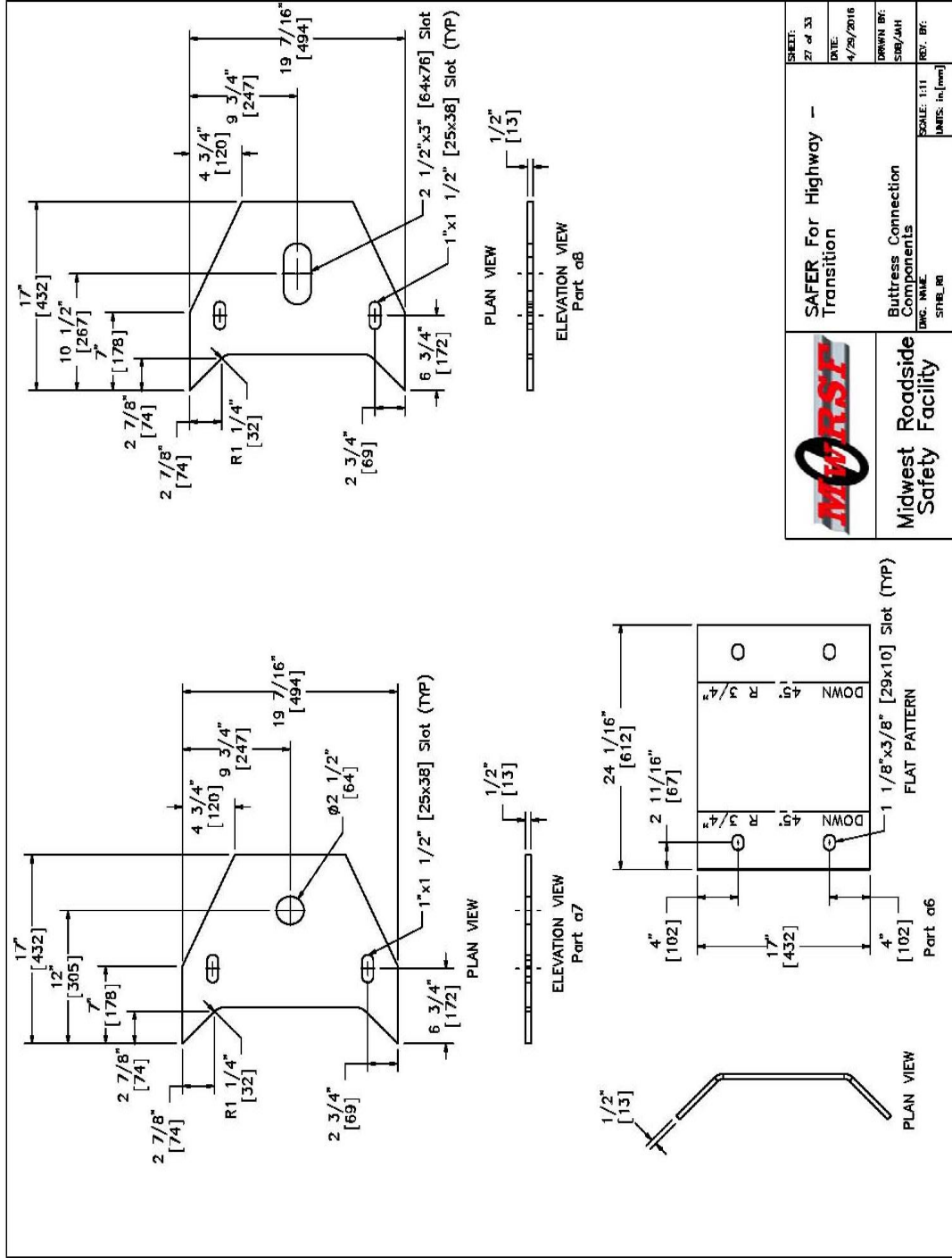


Figure K-27. Buttress Connection Components, RESTORE Barrier Transition

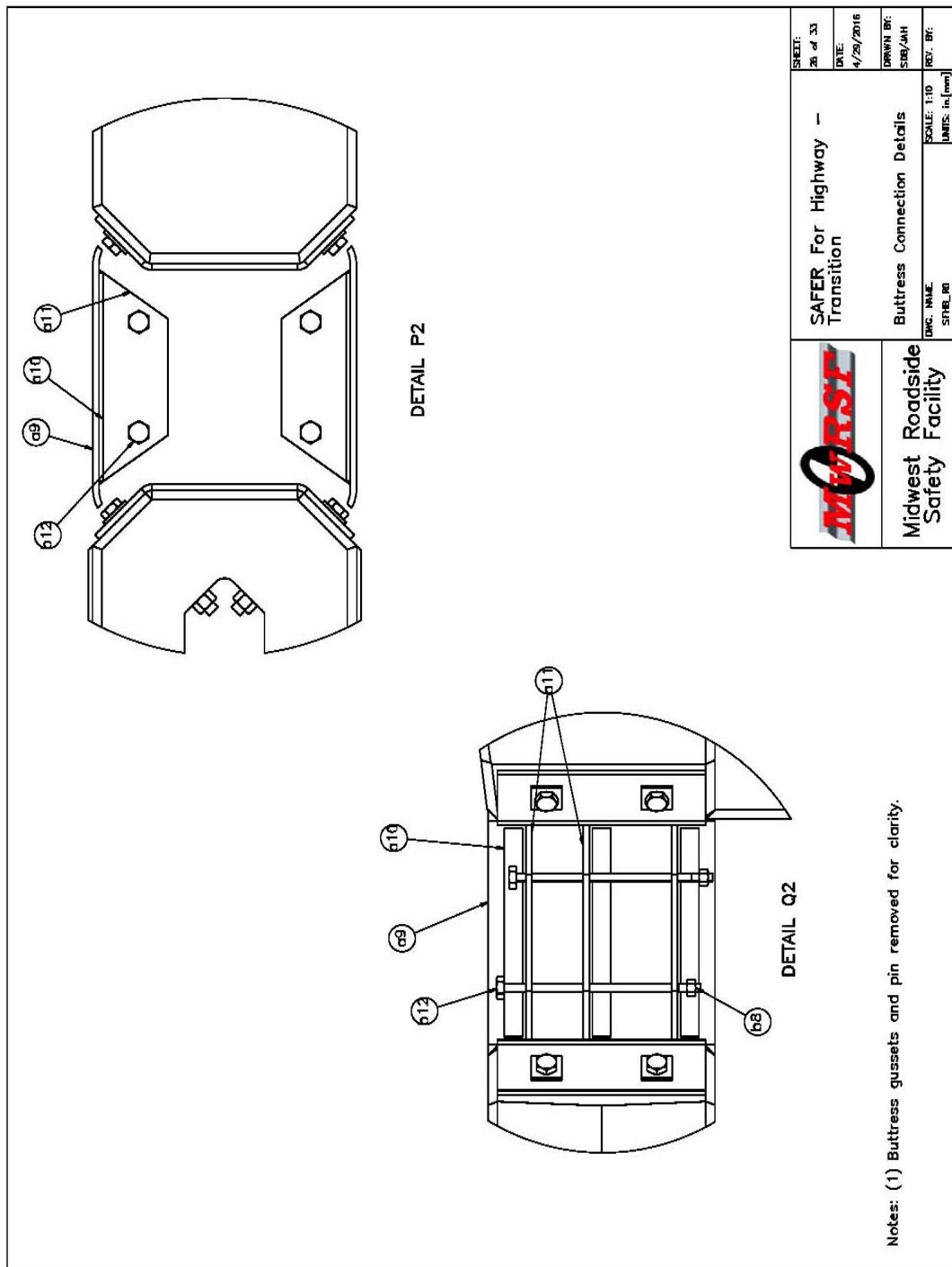


Figure K-28. Buttress Connection Details, RESTORE Barrier Transition

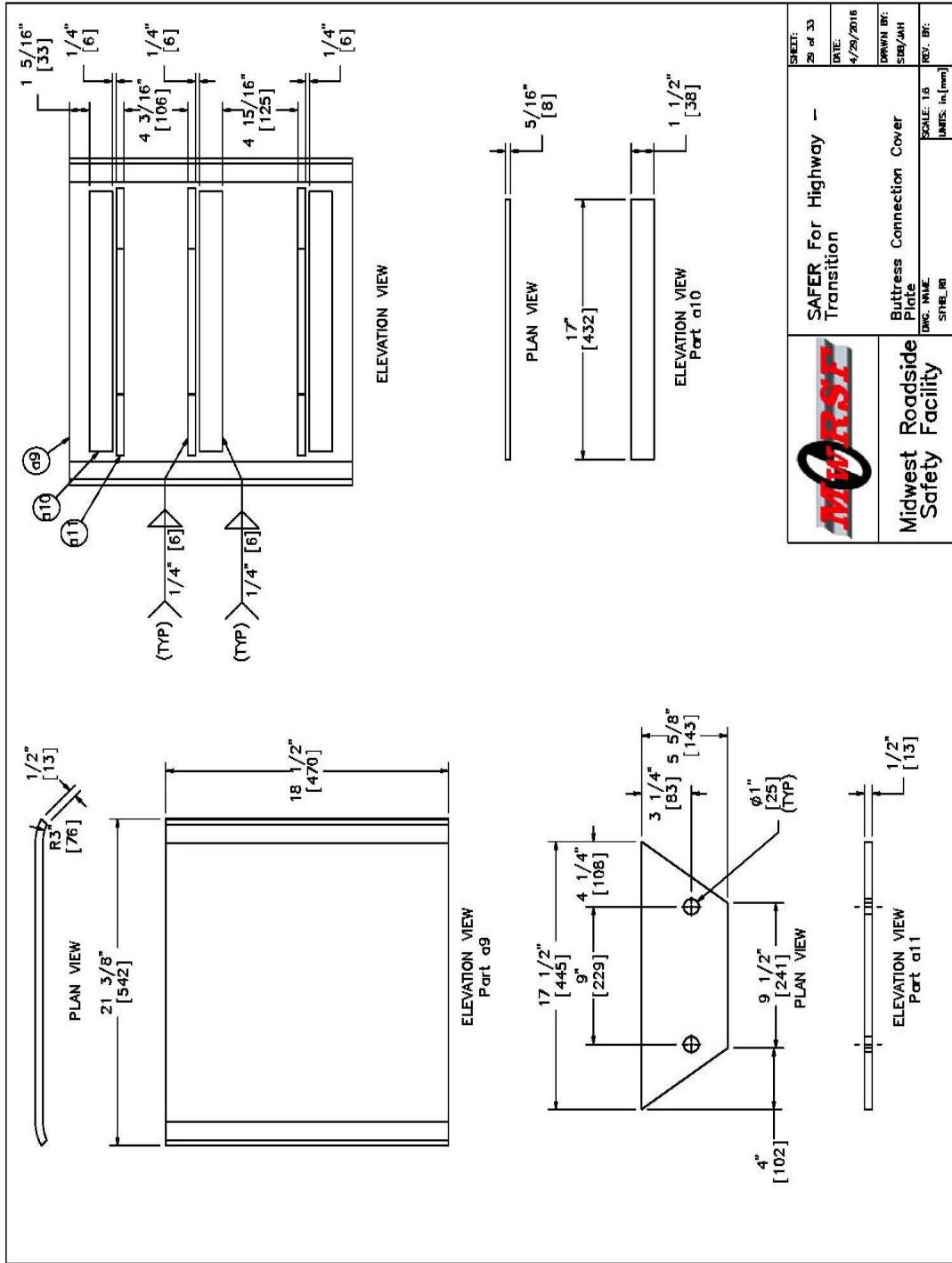


Figure K-29. Buttress Connection Cover Plate, RESTORE Barrier Transition

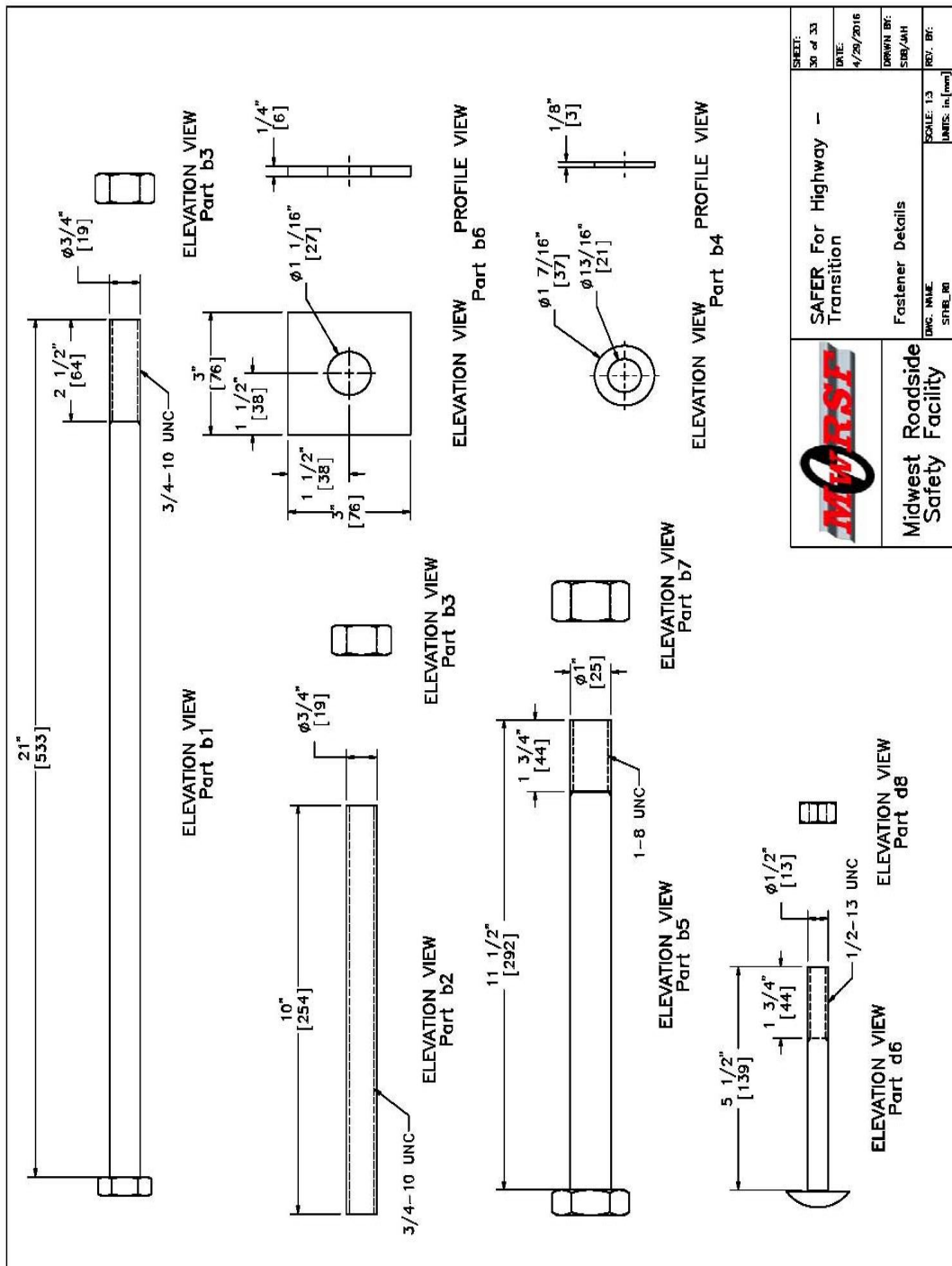


Figure K-30. Fastener Details, RESTORE Barrier Transition

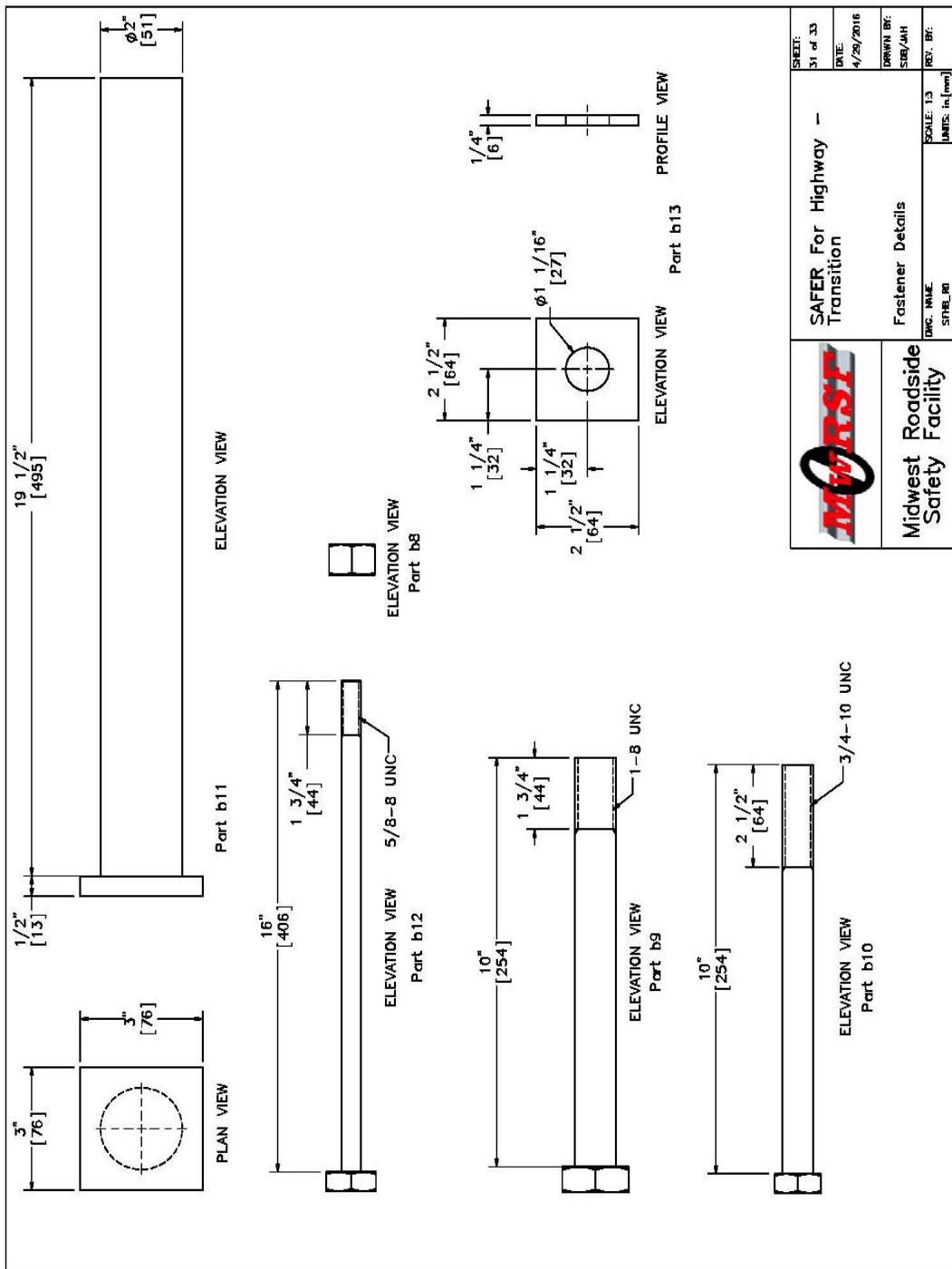



Figure K-31. Fastener Details, RESTORE Barrier Transition

Item No.	QTY.	Description	Material Specification	Hardware Guide
a1	10	Lightweight Concrete Rail	min f'c=5 ksi [34.5 MPa], density=110 pcf	-
a2	40	Morse E46496 Shear Fender	ASTM D2000	-
a3	18	6"x6"x1/2" [152x152x13], 17" [432] Long L-Bracket	A992 Galvanized	-
a4	72	5"x5"x3/8" [127x127x10] Gusset Plate	A572 Grade 50 Galvanized	-
a5	1	Concrete Buttress	min f'c=5 ksi [34.5 MPa], density=110 pcf	-
a6	2	24 1/16"x1/2"x17" [611x13x432] Barrier Bracket	A992 Galvanized	-
a7	3	19 7/16"x17"x1/2" [494x432x13] Restore Gusset	A572 Grade 50 Galvanized	-
a8	3	19 7/16"x17"x1/2" [494x432x13] Buttress Gusset	A572 Grade 50 Galvanized	-
a9	2	21 5/16"x18 1/2"x5/8" [541x470x16] Cover Plate	A992 Galvanized	-
a10	6	17"x1 1/2"x11/32" [432x38x9] Cover Plate Support	A992 Galvanized	-
a11	6	17 1/2"x5 1/2"x1/2" [445x140x13] Cover Plate Gusset	A572 Grade 50 Galvanized	-
b1	160	3/4" [19] Dia. UNC, 21" [533] Long Hex Bolt	Grade 5 Galvanized	FBX20a
b2	160	3/4" [19] Dia. UNC, 10" [254] Long Threaded Rod	ASTM A193 Grade B7 Galvanized	-
b3	320	3/4" [19] Dia. UNC Heavy Hex Nut	ASTM A194 Grade 2H Galv.	-
b4	484	3/4" [19] Dia. Flat Washer	ASTM F436 Galv.	-
b5	76	1" [25] Dia. UNC, 11 1/2" [292] Long Hex Head Bolt	ASTM A325 Galv.	FBX24b
b6	144	3"x3"x1/4" [76x76x6] Square Washer	A572 Grade 50 Galvanized	-
b7	76	1" [25] Dia. UNC Heavy Hex Nut	ASTM A563 DH Galv.	FNX24b
b8	4	5/8" [16] Dia. UNC Heavy Hex Nut	ASTM A194 Grade 2H Galv.	FNX16b
b9	4	1" [25] Dia. UNC, 10" [254] Long Hex Head Bolt	ASTM A325 Galv.	FBX24b
b10	4	3/4" [19] Dia. UNC, 10" [254] Long Hex Bolt	Grade 5 Galvanized	FBX20a
b11	1	2" Dia. x 19 1/2" Long [51x495] Gusset Pin	A572 Grade 50 Galvanized	-
b12	4	5/8" [25] Dia. UNC, 16" [406] Long Hex Head Bolt	ASTM A325 Galv.	FBX16b
b13	8	2 1/2"x2 1/2"x1/4" [64x64x6] Square Washer	A572 Grade 50 Galvanized	-



Midwest Roadside Safety Facility

SAFER For Highway Transition


Bill of Materials

ENC. NAME: SP18B_01

SHEET: 32 of 33
 DATE: 4/29/2016
 DRAWN BY: SDB/DAH
 SCALE: 1:5
 UNITS: in. (mm)

Figure K-32. Bill of Materials, RESTORE Barrier Transition

Item No.	QTY.	Description	Material Specification	Hardware Guide
c1	280	1/2" [13] Dia., 77" [1956] Long Bent Rebar	A615 Grade 60	-
c2	80	1/2" [13] Dia., 49" [1245] Long Bent Rebar	A615 Grade 60	-
c3	120	3/4" [19] Dia., 231" [5867] Long Rebar	A615 Grade 60	-
c4	80	3/4" [19] Dia., 63" [1600] Long Bent Rebar	A615 Grade 60	-
c5	60	3/4" [19] Dia., 69" [1753] Long Bent Rebar	A615 Grade 60	-
d1	40	17"x8"x1/2" [431x203x13] Anchor Plate	ASTM A572 Grade 50 Galvanized	-
d2	40	4"x4"x1/4" [102x102x6]. 4" [102] Long Tube	A500 Grade B Galvanized	-
d3	10	8"x4"x1/4" [203x102x6]. 239 1/2" [6083] Long Tube	A500 Grade B Galvanized	-
d4	1	18"x14"x1/2" [457x356x13] Anchor Plate	ASTM A572 Grade 50 Galvanized	-
d5	1	8"x4"x1/4" [203x102x6]. 42 1/4" [1073] Bent Tube	A500 Grade B Galvanized	-
d6	20	1/2" [13] Dia. UNC, 5 1/2" [140] Long Dome (Round) Head Bolt	ASTM A307 Grade A Galvanized	-
d7	18	1/2" [13] Dia. Flat Washer	ASTM F844 Galvanized	-
d8	20	1/2" [13] Dia. UNC Heavy Hex Nut	A563A Galvanized	FNX12b
d9	-	Epoxy		
d11	20	29 1/8"x2 5/8"x5/16" [740x67x8] Splice Side Plate	ASTM A572 Grade 50 Galvanized	-
d12	20	29 1/8"x6 5/8"x5/16" [740x168x8] Splice Top Plate with Slot	ASTM A572 Grade 50 Galvanized	-
e1	20	6 1/2" [165] Dia., 3/8" [10] Thick, 19" [483] Long Steel Pipe	AISI 1026	-
e2	20	16 9/16"x10"x1/4" [421x254x6] Base Plate	ASTM A572 Grade 50 Steel	-
e3	40	3 1/2"x10 3/8"x1/2" [89x264x13] Plate Gusset	ASTM A572 Grade 50 Steel	-
e4	20	12"x12"x3/8" [305x305x10] Top Plate	ASTM A572 Grade 50 Steel	-
e5	20	12"x12"x1/2" [305x305x13] EPDM Rubber Sheet	Minimum 50 durometer	-



Midwest Roadside Safety Facility

Bill of Materials

SCALE: 1:8
UNITS: in. (mm)

SAFER For Highway Transition

SHEET: 33 of 33	DATE: 4/29/2016
DRAWN BY: SIM/JAH	REV. BY:

Figure K-33. Bill of Materials, RESTORE Barrier Transition

Appendix L. Comparison Bar Graphs for 1100C Vehicles

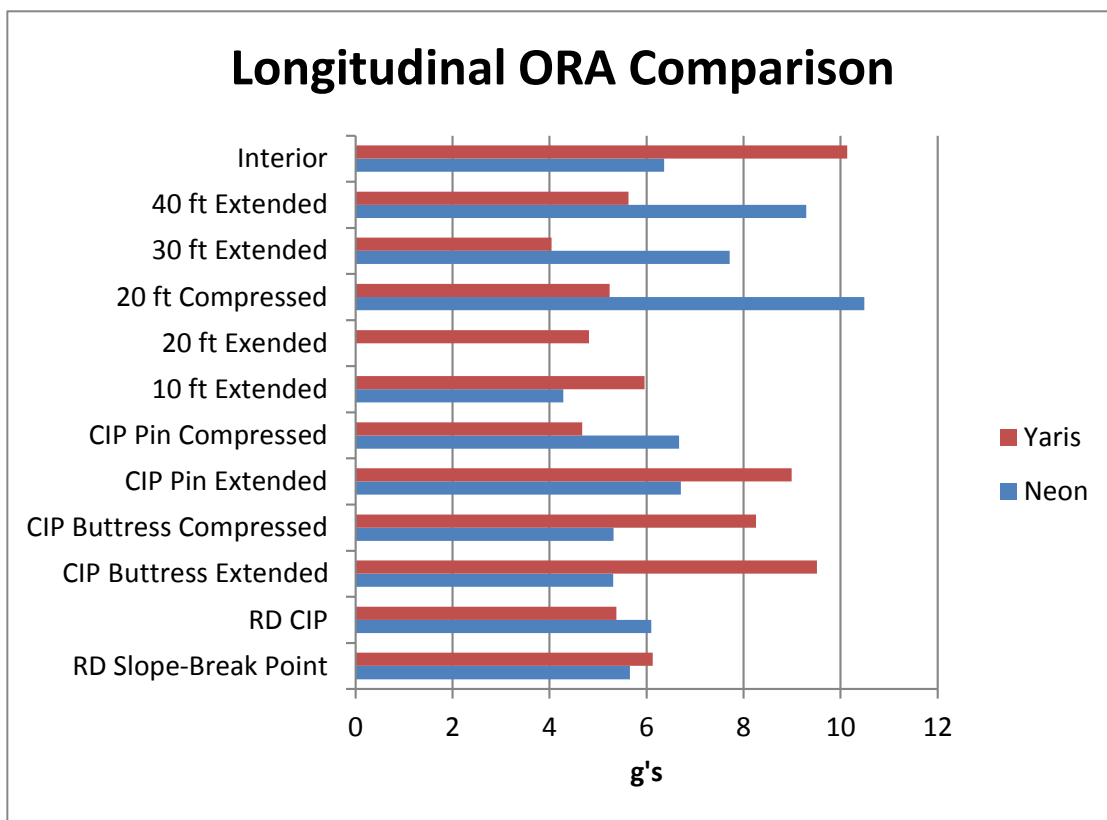
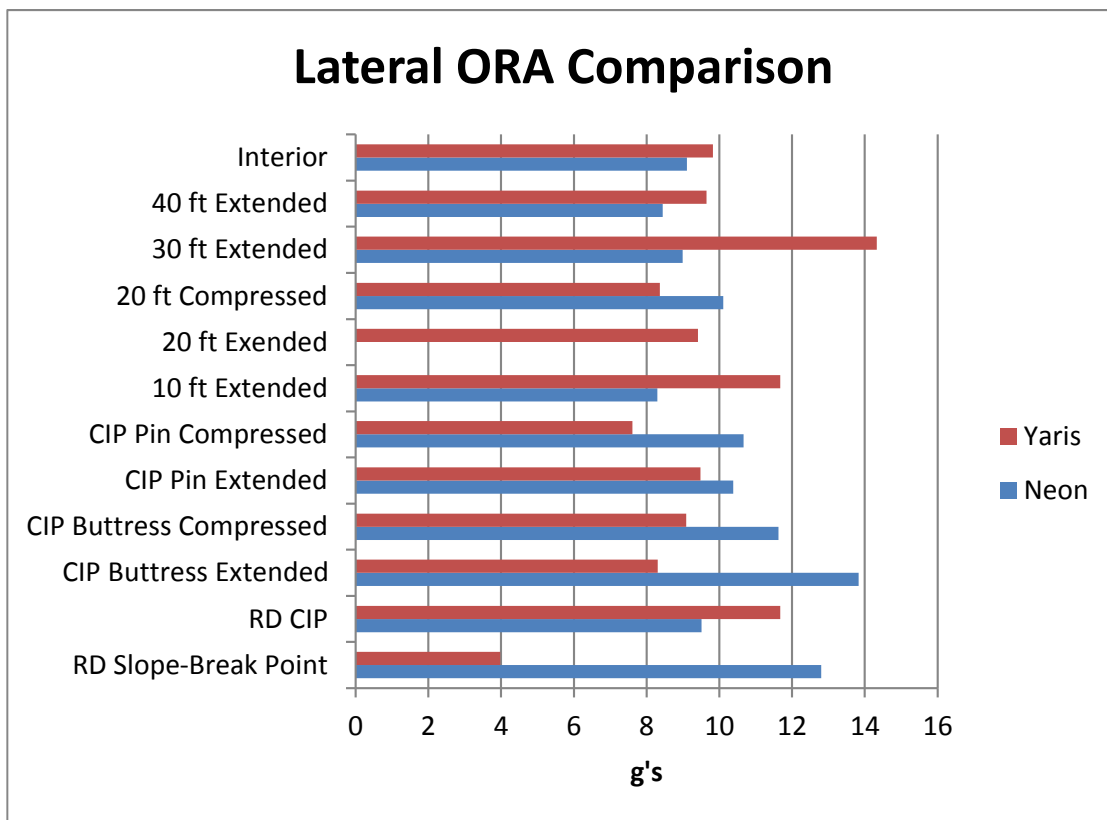


Figure L-1. Lateral and Longitudinal ORA Comparison, 1100C Simulations

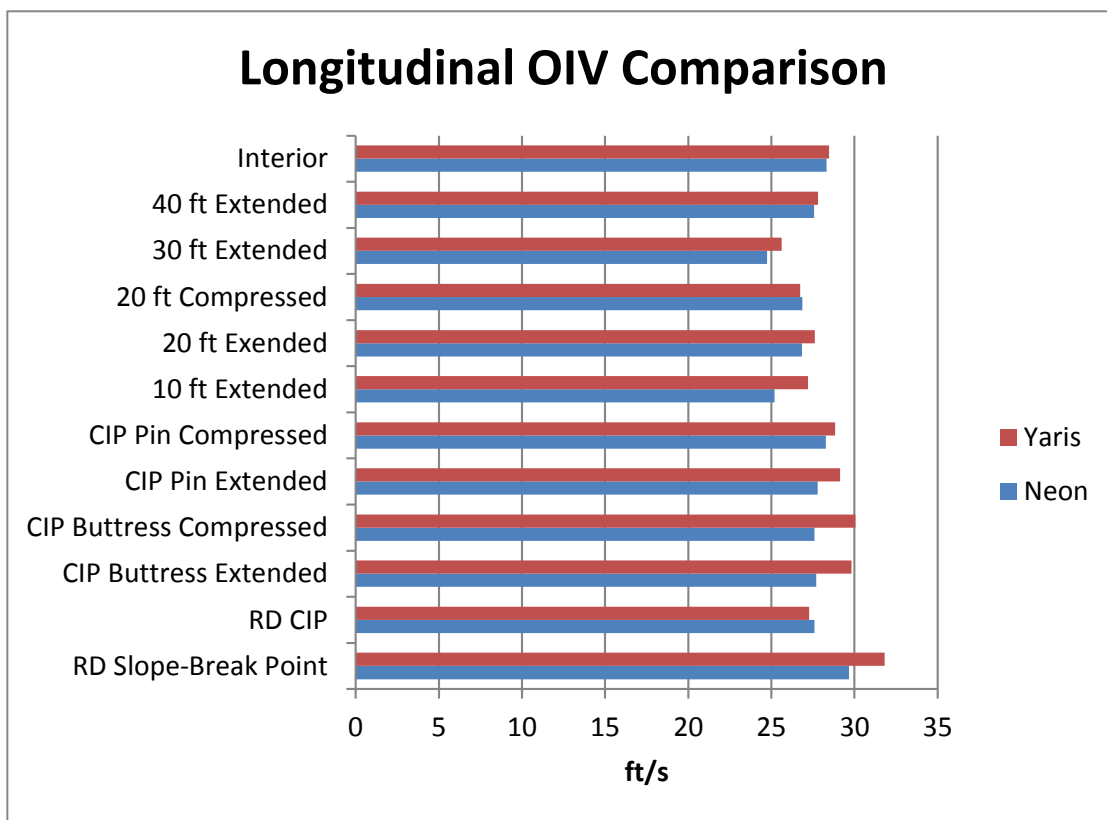
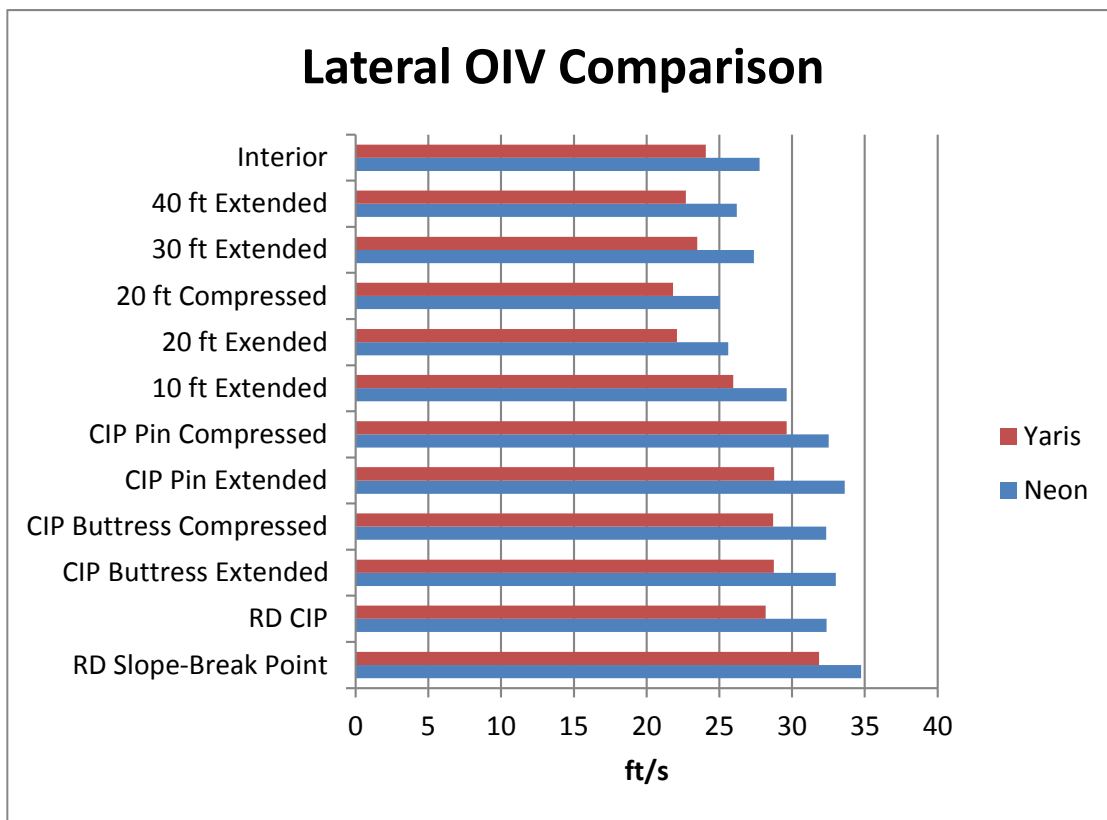


Figure L-2. Lateral and Longitudinal OIV Comparison, 1100C Simulations

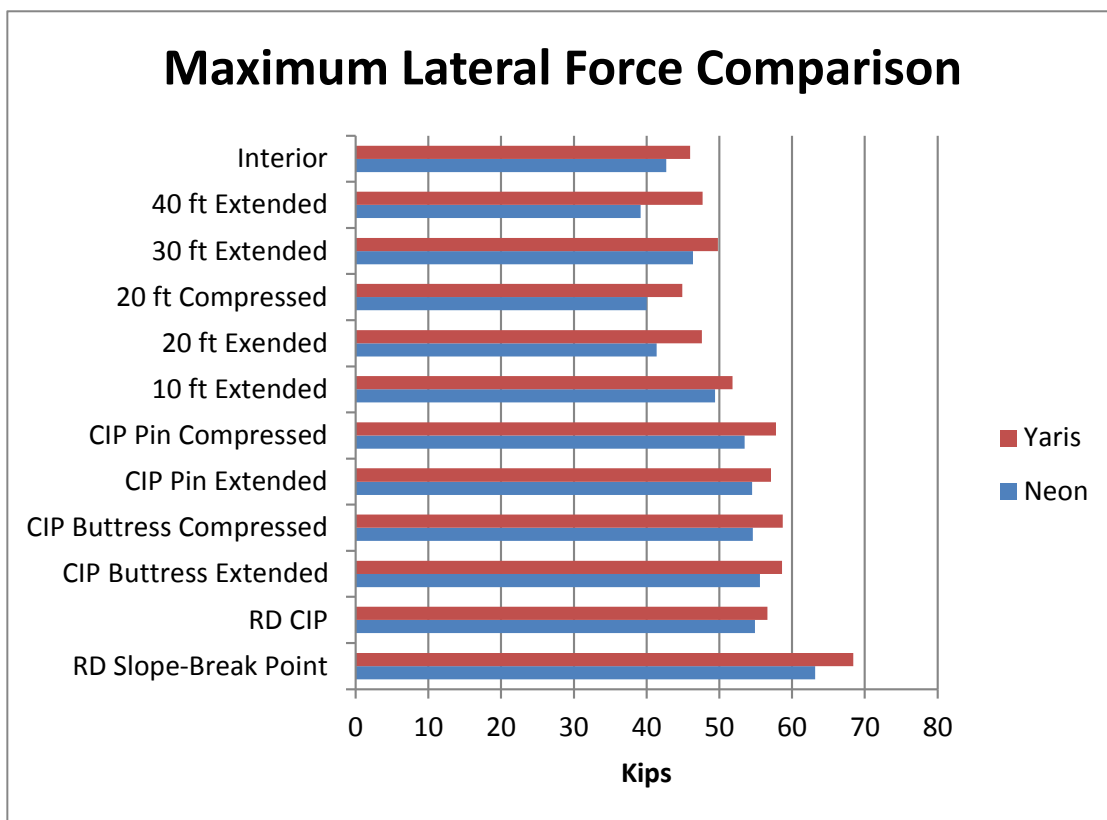
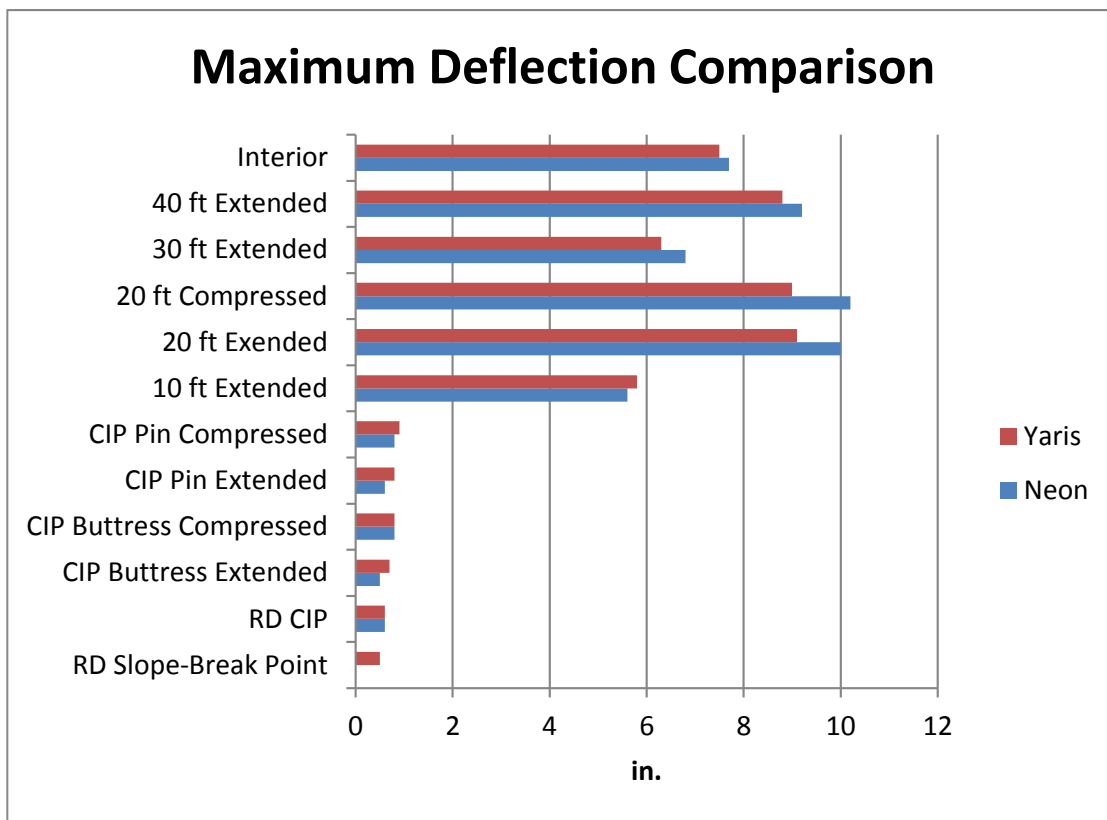


Figure L-3. Maximum Deflection and Lateral Force Comparisons, 1100C Simulations

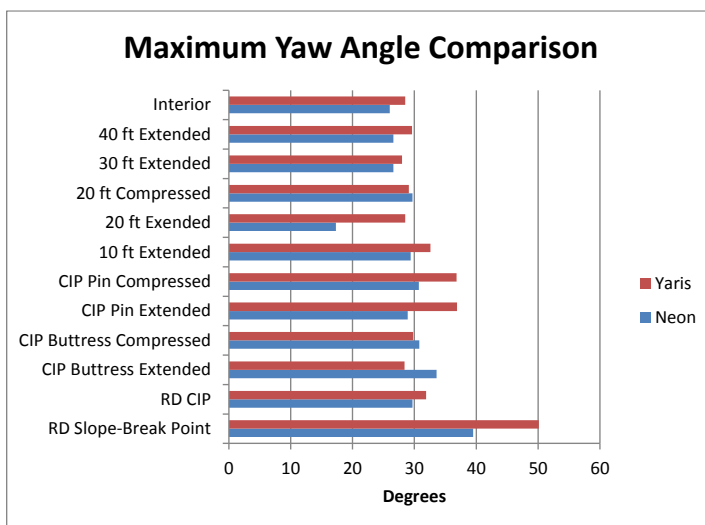
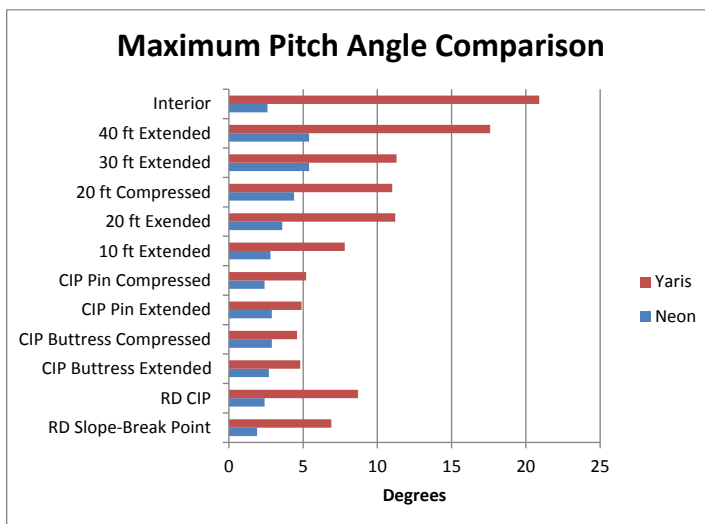
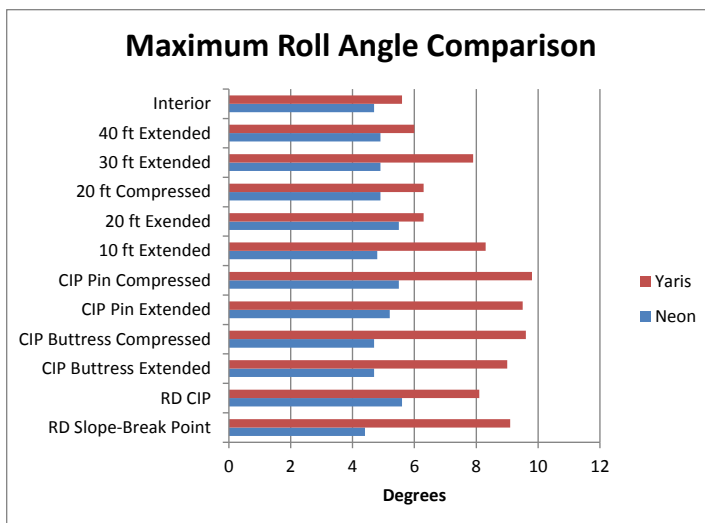


Figure L-4. Maximum Roll, Pitch, and Yaw Angle Comparisons, 1100C Simulations

Appendix M. Comparison Bar Graphs for 2270P Vehicle

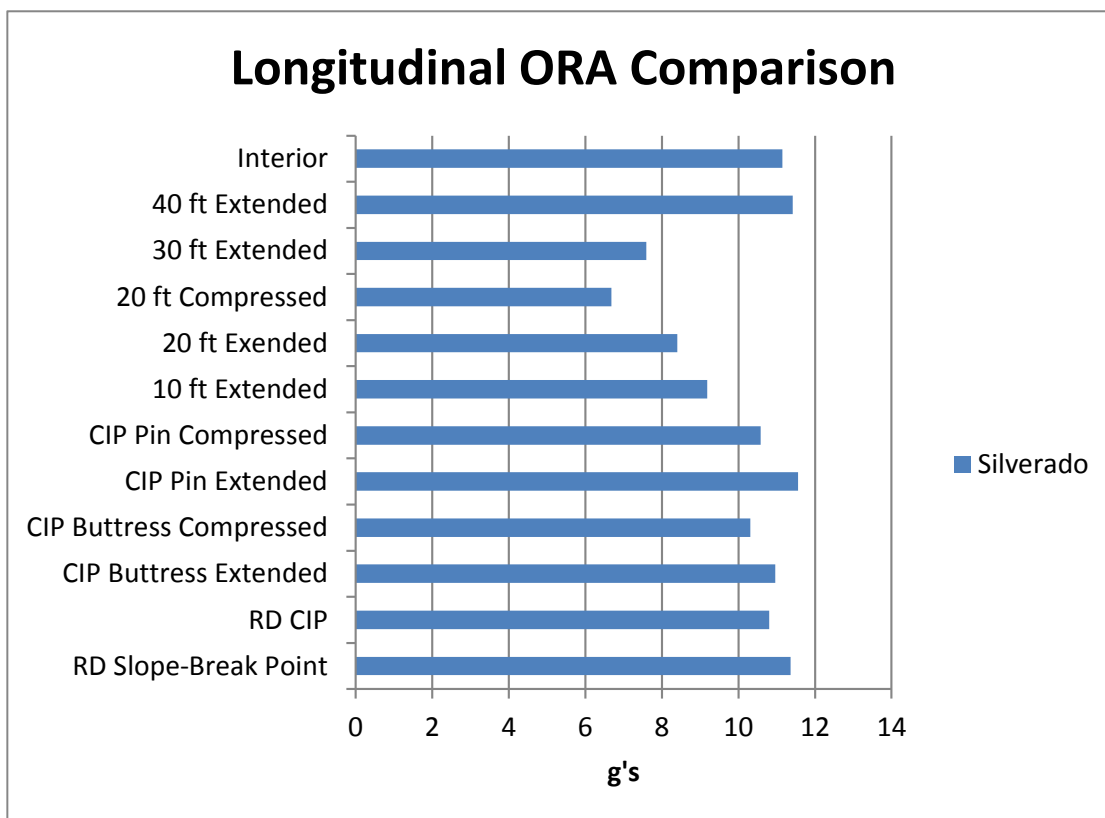
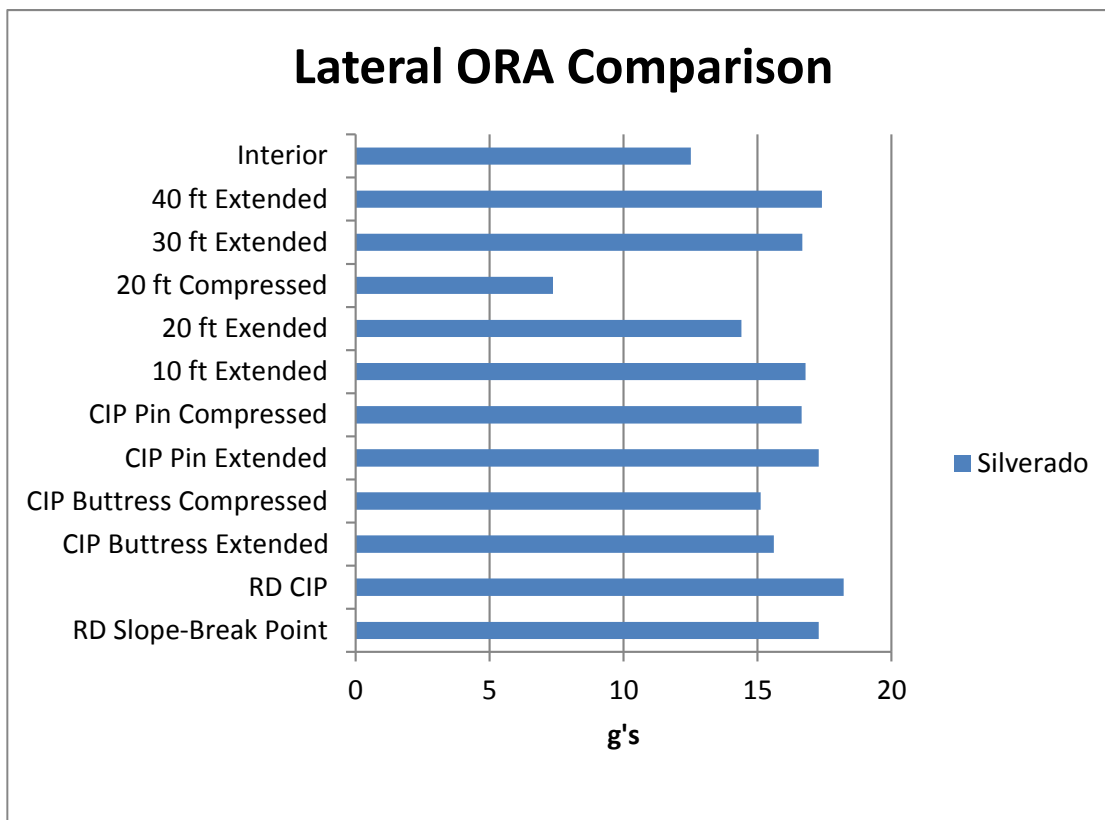


Figure M-1. Lateral and Longitudinal ORA Comparison, 2270P Simulations

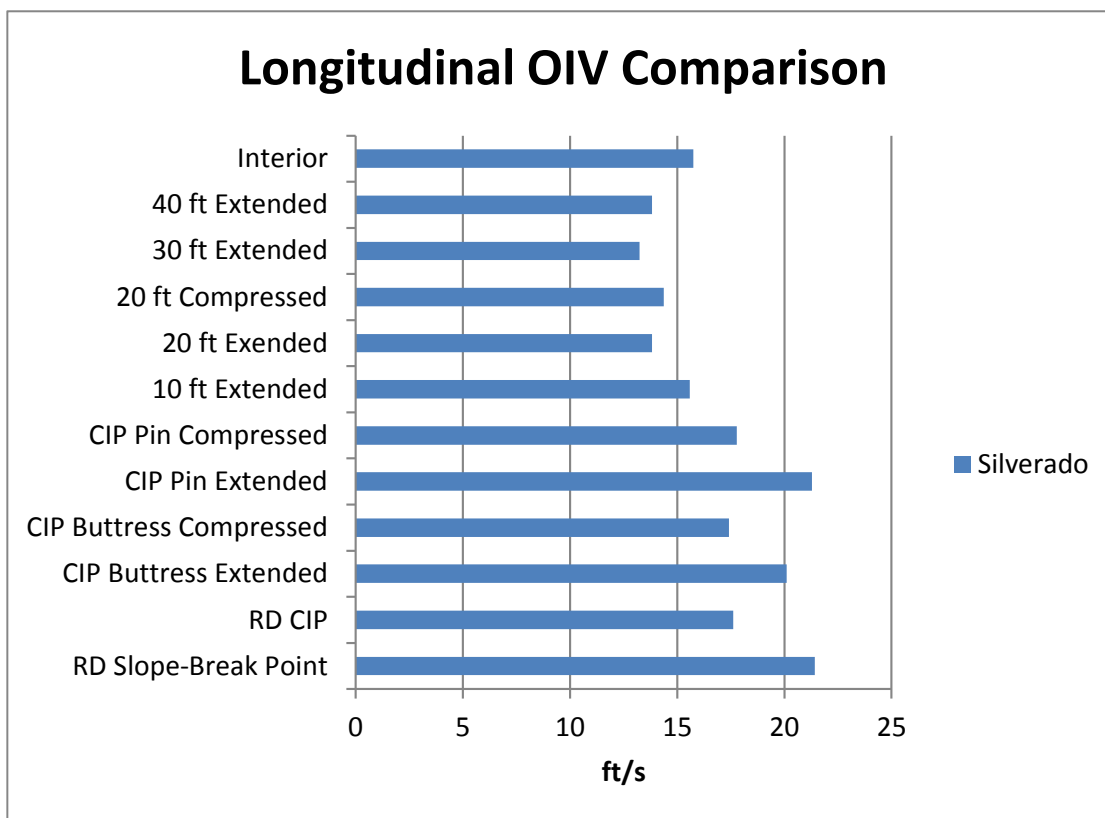
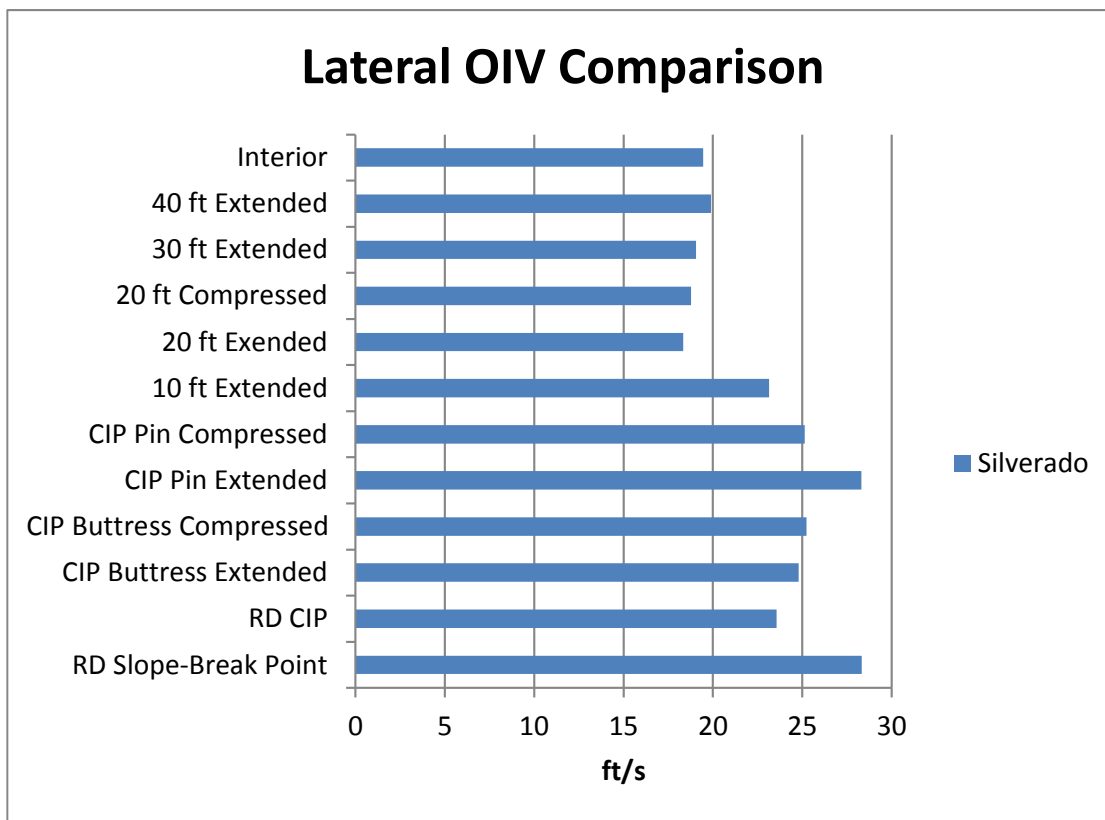


Figure M-2. Lateral and Longitudinal OIV Comparison, 2270P Simulations

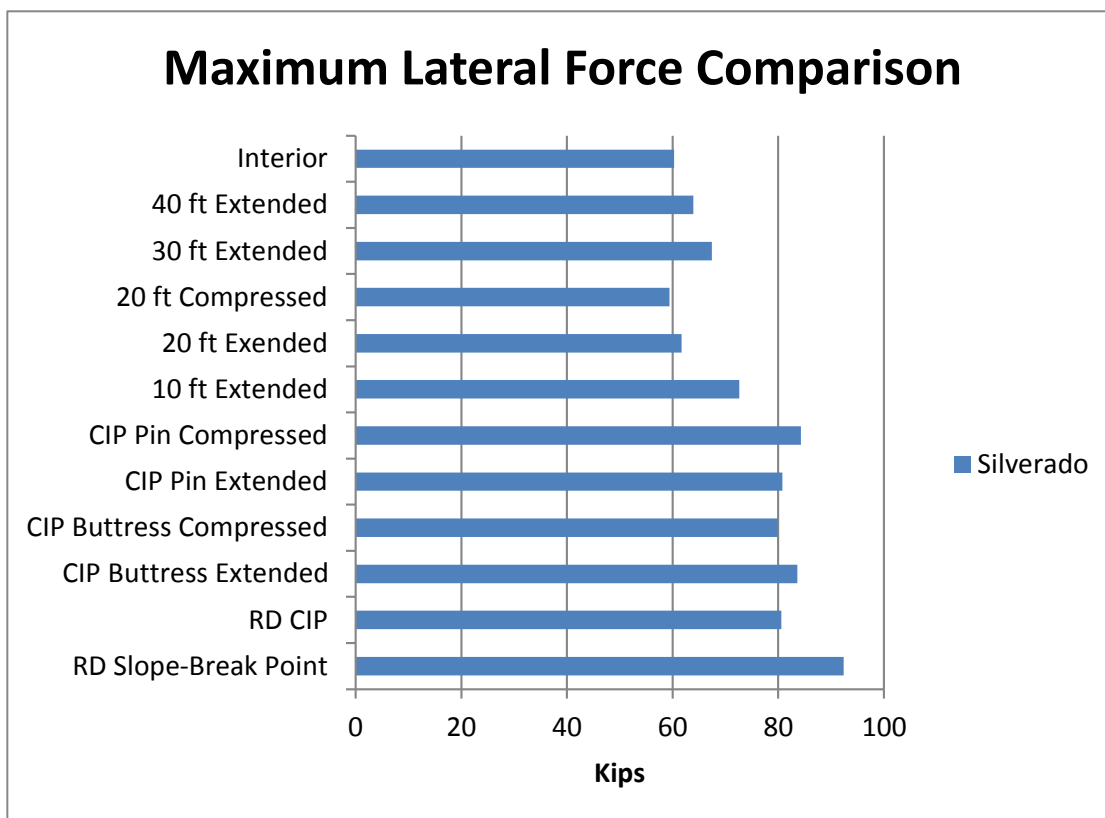
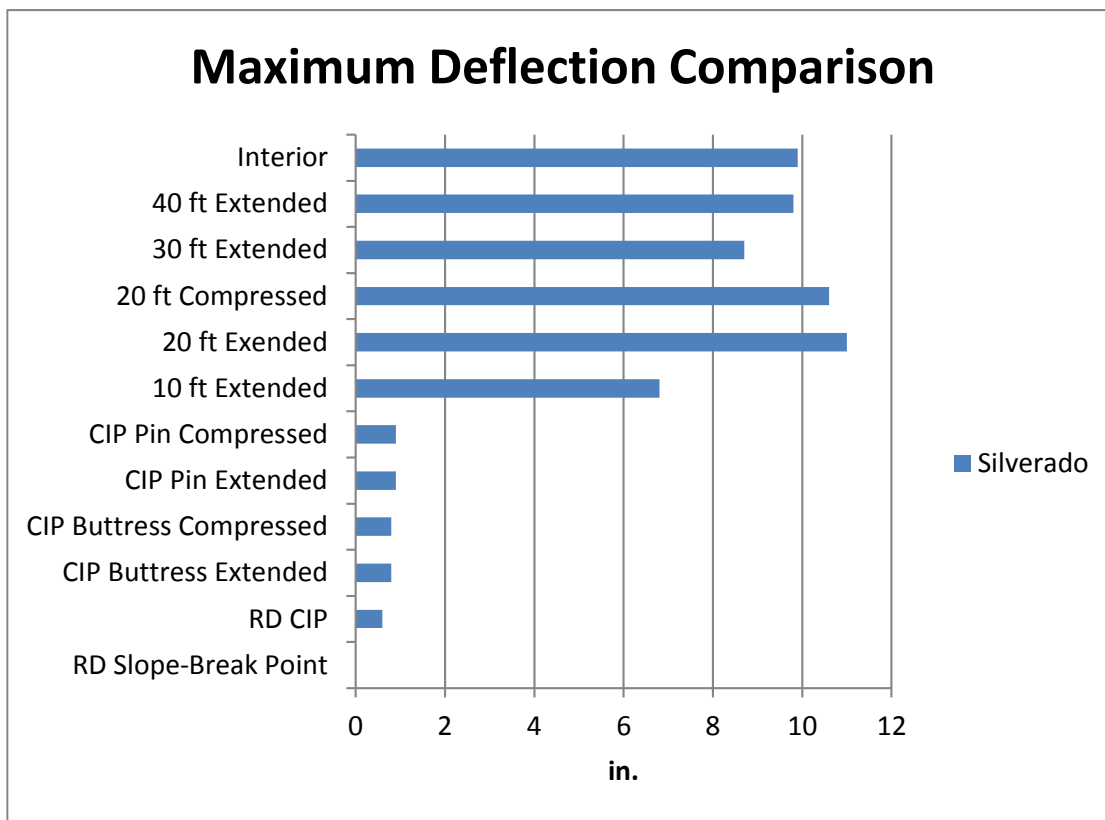


Figure M-3. Maximum Deflection and Lateral Force Comparisons, 2270P Simulations

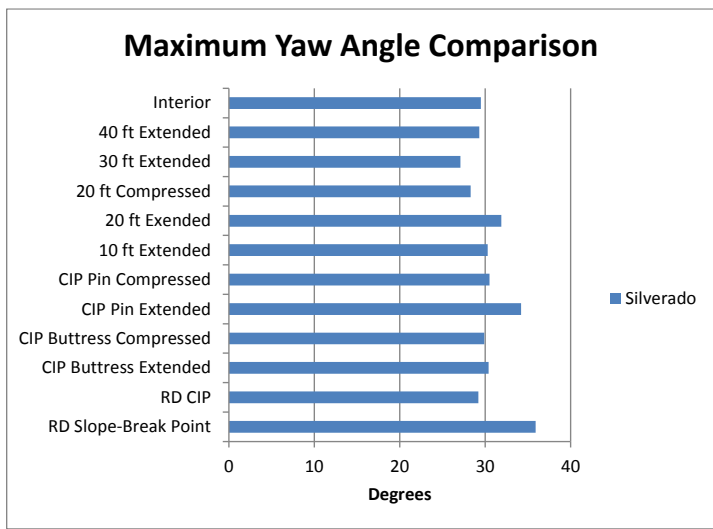
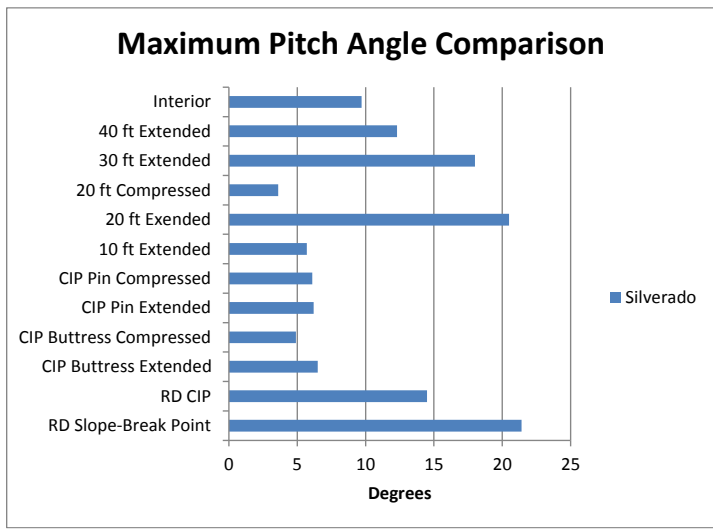
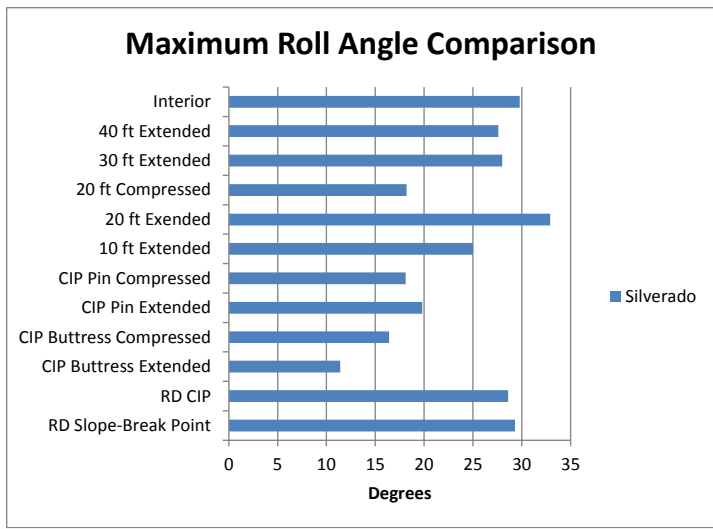


Figure M-4. Maximum Roll, Pitch, and Yaw Angle Comparisons, 2270P Simulations

Appendix N. Comparison Bar Graphs for 1000S Vehicle

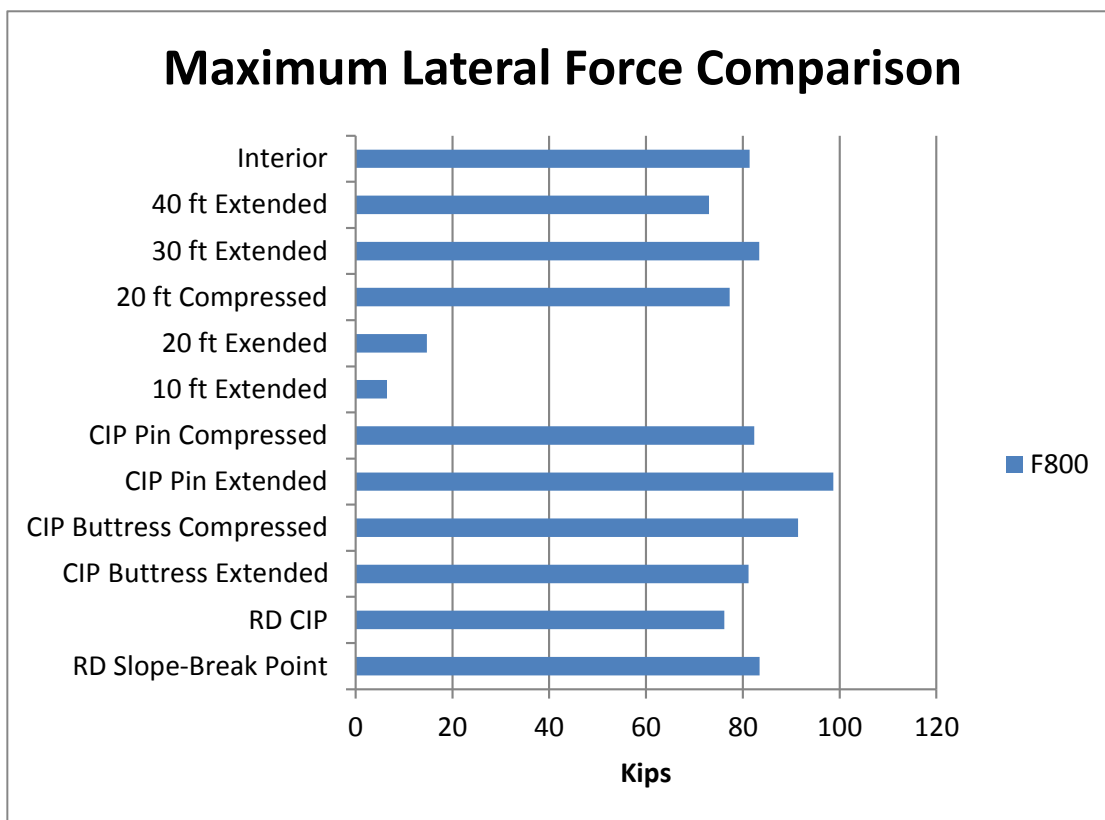
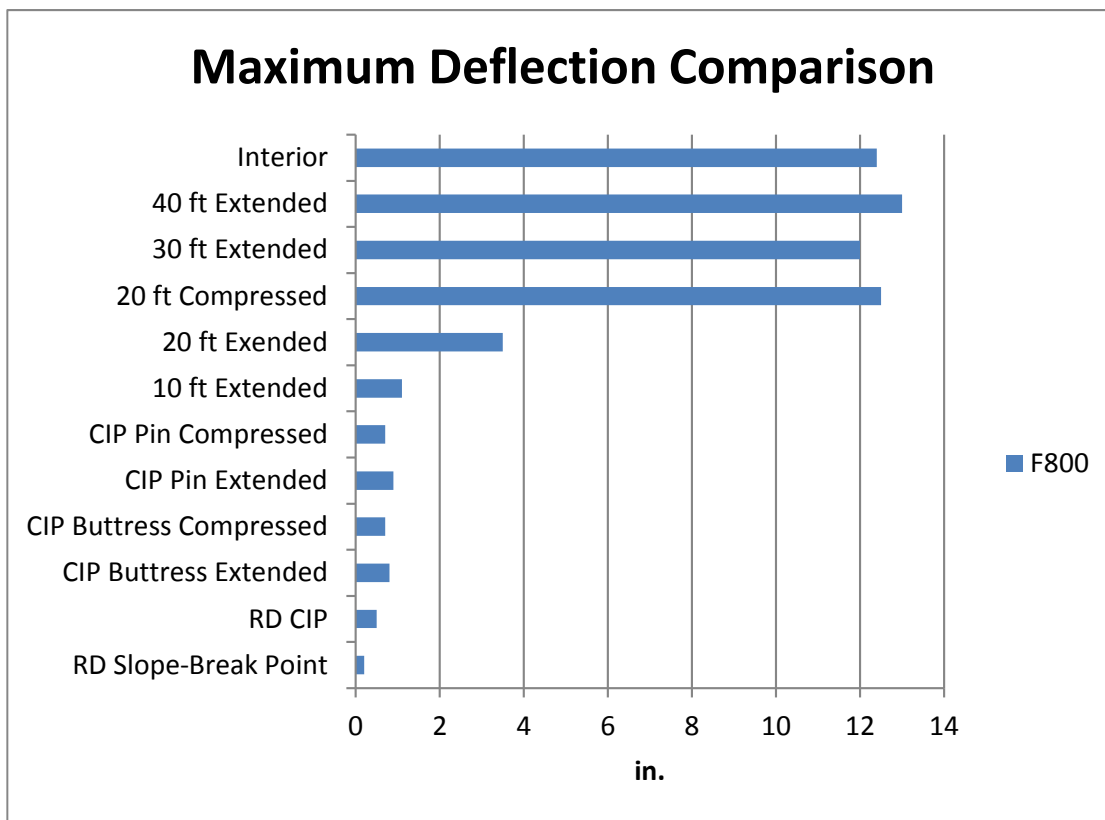


Figure N-1. Maximum Deflection and Lateral Force Comparisons, 10000S Simulations

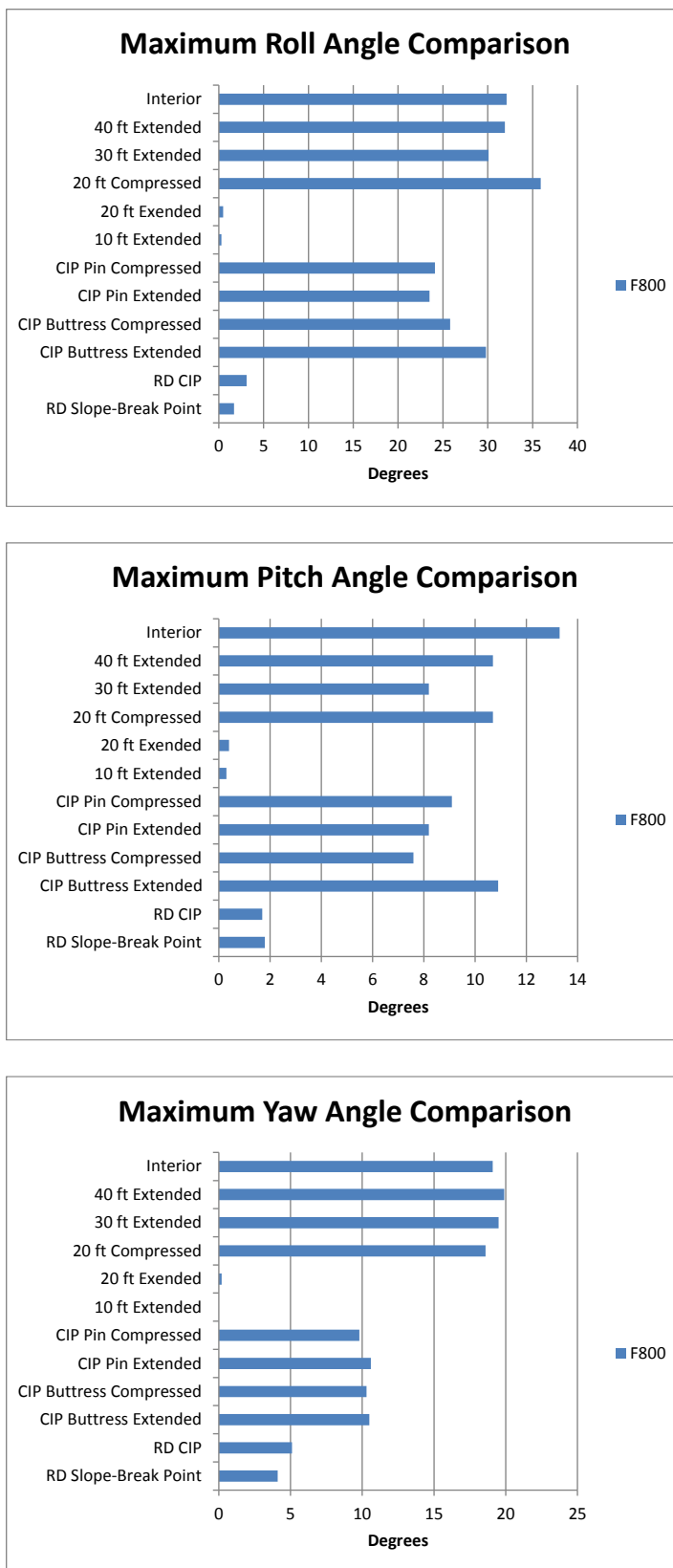


Figure N-2. Maximum Roll, Pitch, and Yaw Angle Comparisons, 10000S Simulations

END OF DOCUMENT